FRACTURE BEHAVIOR CHARACTERIZATION OF CONVENTIONAL AND HIGH PERFORMANCE STEEL FOR BRIDGE APPLICATIONS

William Norfleet Collins

Dissertation submitted to the Faculty of the
Virginia Polytechnic Institute and State University
in partial fulfillment of the requirements for the degree of

Doctor of Philosophy
In
Civil Engineering

Roberto T. Leon, Chair

William J. Wright, Co-Chair

Thomas E. Cousins

Norman E. Dowling

Richard E. Weyers

August 26, 2014

Blacksburg, Virginia

Keywords: Brittle failures; Material failures; Cracking; Toughness; Steel; Bridges; Fracture

FRACTURE BEHAVIOR CHARACTERIZATION OF CONVENTIONAL AND HIGH PERFORMANCE STEEL FOR BRIDGE APPLICATIONS

William Norfleet Collins

(ABSTRACT)

The work described herein examines the fracture behavior of steels used in bridge applications. As part of Transportation Pooled Fund (TPF) Project 5-238, Design and Fabrication Standards to Eliminate Fracture Critical Concerns in Steel Members Traditionally Classified as Fracture Critical, researchers aim to take advantage of advances made in both steel production technology and in the field of fracture mechanics.

Testing and analysis of both conventional and High Performance Steel (HPS) grades of bridge steel was conducted as part of this study. This includes both Charpy V-Notch testing, as well as more rigorous elastic-plastic fracture toughness testing. Analysis includes the application of the master curve methodology to statistically characterize fracture behavior in the ductile to brittle transition region. In addition, a database of historic bridge fracture toughness data was compiled and re-analyzed using plasticity corrections to estimate elastic-plastic fracture toughness. Correlations between Charpy V-Notch impact energy and fracture toughness, which forms the basis for the current material specification, were also examined. Application of fracture toughness characterization of both new and historic data results in updated methodologies for addressing fracture in bridge design.

Acknowledgements

I cannot adequately express the gratitude that I have for everyone who has supported me over the past few years. My committee members, Dr. Bill Wright, Dr. Roberto Leon, Dr. Tommy Cousins, Dr. Norman Dowling, and Dr. Richard Weyers, have provided much insight, guidance, and wisdom throughout this process, and for this I am extremely grateful. My family and I are extremely thankful for the funding provided by the Via Fellowship and Transportation Pooled Fund programs. I offer thanks to Brett Farmer, Dennis Huffman, Dr. Dave Mokarem, and Terry Phillips for their help in many facets of this research. I am grateful for the help and support of Dr. Robert Connor and Ryan Sherman at Purdue University, Dr. Rick Link and colleagues at the United States Naval Academy, and Dr. Kim Wallin at VTT in Finland. There are times when I would have been lost if not for the technical guidance of these men. Numerous graduate students have provided friendship and assistance throughout this process, including Marc Maguire, Kacie D'Alessandro, Amey Bapat, and Kedar Halbe, as well as countless others.

The strength of any organization lies with its people, and the Charles E. Via, Jr. Department of Civil and Environmental Engineering is a wonderful example of this. Support and encouragement from all of the faculty and staff has been amazing, and I am exceedingly grateful for the relationships that I have formed, both professional and personal. Whether working at the lab or on campus, or on fishing, hunting, or camping trips, the impact of the time we have spent together and the conversations we have had cannot be overstated.

Words cannot convey the gratitude I have for my parents, sister, and extended family. The love, guidance, and support they have provided for my entire life has made me who I am, and for this I am forever grateful. Lastly, I would like to thank my boys, Liam and Levi, and my wife, Kate Collins, for their love, support, and patience throughout this process. When we embarked on this this two year adventure six years ago, we had no idea what was in store for our lives. I wouldn't trade this time for anything.

TABLE OF CONTENTS

TABLE OF FIGURES

TABLE OF TABLES

Chapter 1: Introduction

Two and three girder steel bridge systems categorized as Fracture Critical (FC), along with other bridges containing designated Fracture Critical Members (FCMs), have been avoided by design engineers and transportation officials in the United States since the late 1960's. Although these systems can be very efficient and economical for use in medium and long span bridges, the performance history of older bridges and the extensive inspection program required has resulted in the limited implementation of these designs.

Prior to the mid-twentieth century, fracture of steel bridges was not a recognized problem for design engineers. Although brittle fractures and failures were acknowledged as early as the late 1800's in standpipes and tanks (Shank 1953), the mechanics of fracture had not been fully investigated and were not very well understood. With the emergence of welded connections taking prevalence over rivets, fracture was elevated to the forefront of design during World War II as multiple American and British-built ships experienced catastrophic brittle fractures (Biggs 1958). It was not until 1967 however, when the fracture and collapse of the U.S. 35 Highway Bridge (Silver Bridge) resulted in the loss of 46 lives, that bridge officials recognized the importance of fracture critical members (NTSB 1970). As a result of this catastrophe, the Federal Highway Administration (FHWA) called for the development and implementation of a new fracture control plan (FCP) for steel bridges (Frank and Galambos 1972).

Based on the behavior of structural steel economically available at the time, the FCP relied heavily on design and construction details, as well as inspection requirements, to ensure the safety of steel bridges. The requirements for bridges deemed to be Fracture Critical, or those

containing FCMs, were such that building and maintaining this type of bridge system became economically unfeasible. The practice of general avoidance of FC bridges remains in place today, both with designers and bridge officials.

Recent advances in the production of structural steel have resulted in new High Performance Steel (HPS) that have improved performance properties in comparison to both conventional and previously available high strength steels (Wright 1997). Performance benefits of the new HPS included an optimization of strength, ductility, resistance to corrosion, weldability, and most notably, fracture toughness. In addition, technological innovations in steel production have made HPS more economical than it has been in the past. HPS structural members meeting the improved performance properties can be regularly produced today. To take full advantage of these performance benefits in bridge design, an understanding of HPS fracture behavior is needed.

1.1 Transportation Pooled Fund Project

FHWA Transportation Pooled Fund (TPF) Project 5-238, Design and Fabrication Standards to Eliminate Fracture Critical Concerns in Steel Members Traditionally Classified as Fracture Critical, was initiated with the objective of taking advantage of the inherent fracture performance benefits of HPS. The project includes the examination of material characteristics, fatigue, fracture design and detailing specifications, fabrication methodology, and shop and field inspections to be used for bridges designed and built with HPS.

The experimental program of this TPF includes the behavior characterization of multiple grades of HPS, as well as fracture testing of full scale girders. Researchers at Purdue University

and Virginia Tech are collaborating in these efforts. The end goal of this research is to create specifications for a new class of Fracture Critical bridges which will take advantage of the improved performance of HPS. This will eliminate or greatly reduce the extensive inspection requirements, thus making two and three girder steel bridge systems more competitive in the marketplace.

1.2 Scope and Objectives of This Study

TPF 5-238 will use results from material characterization tests and full scale fracture tests to set specifications for a new category of fracture critical bridges using HPS steel. The main objectives of this study are to fully characterize the fracture behavior of multiple heats, plates, and grades of HPS. Specifically, HPS material testing includes:

- Yield and Tensile Strength
- Charpy V-Notch Impact Toughness
- Fracture Toughness at Static and Dynamic Rates
- Crack Arrest Toughness

Analysis of this data may result in the development of correlations between Charpy V-Notch (CVN) tests and quantifiable fracture and performance parameters. Development of appropriate specifications and material requirements would be based on these correlations, enabling producers and designers to easily verify the fracture characteristics of plate steel being produced for bridge applications.

In addition to the work being done on HPS, five plates of conventional bridge steel removed from in-service structures will be examined to determine fracture toughness. This data,

combined with existing bridge fracture datasets, will be examined in terms of modern analysis techniques to be compared with the performance of the HPS grades of steel

1.3 Original Contribution

This study provides an original contribution to the field of civil engineering through the development of fracture toughness datasets of HPS grade bridge steels. Many behavior characteristics of HPS have been examined and documented in the past. Lacking in this data is the complete characterization of HPS fracture toughness, even though increased toughness is marketed as a performance benefit. In addition, the application of the master curve methodology for bridge fracture data is another important original contribution of this work. This has the potential to greatly influence the design and material toughness specifications of steel bridges, as it allows statistical fracture toughness characterization in the ductile to brittle transition region.

1.4 Dissertation Organization

This dissertation is organized into nine chapters and follows the manuscript format. A literature review of current fracture control methodology, experimental programs, HPS development, and material testing is presented in Chapter 2. Chapter 3 introduces the experimental procedures being used in this study, including steel specimen layout. Manuscripts of papers ready to be submitted to technical journals make up Chapters 4 through 6. Chapters 4 and 5 present historical bridge fracture data within the context of this study, and examine the relationship between Charpy V-Notch impact tests and the master curve reference temperature. The third manuscript, found in Chapter 6, presents the static fracture toughness testing and characterization of HPS steel. Chapter 7 contains results of HPS dynamic initiation and crack

arrest toughness testing, and Chapter 8 presents results of fracture initiation testing of conventional bridge steels. Lastly, Chapter 9 provides a summary of the work presented in the previous chapters and presents conclusions and recommendations for future work based upon the results of all testing and analysis.

Chapter 2: Literature Review

2.1 Introduction to Fracture Mechanics

Most evaluation and design processes are based on a comparison between some characteristic material capacity property (typically yield or tensile strength) and demand (typically an applied stress field). The use of fracture mechanics in engineering methodologies introduces a new variable into these evaluations and design processes. Fracture mechanics compares not only the applied stress and a material property (fracture toughness), but also includes the size of an assumed or known flaw present in the material. Thus, fracture mechanics is the study of a material's behavior under a given stress state in the presence of a flaw. The ability of a material to resist fracture in the presence of that flaw is said to be its fracture toughness.

At the atomic level, a material will fracture only if a degree of stress exists that is sufficient to break the atomic bonds. However, experimental studies have revealed that fracture resistance is typically three to four times smaller than the theoretical cohesive strength of a brittle material (Anderson 1995). This is due to the increase in stress at internal flaws.

Typically the stress raiser effect of internal flaws is illustrated through the use of an elliptically shaped through-hole in a material, as shown in Figure 2-1. The length of the flaw is defined by 2a, and the width by 2b, while the radius of curvature is defined by ρ. A gross cross-sectional stress, S, is applied perpendicular to the major axis of the elliptical flaw.

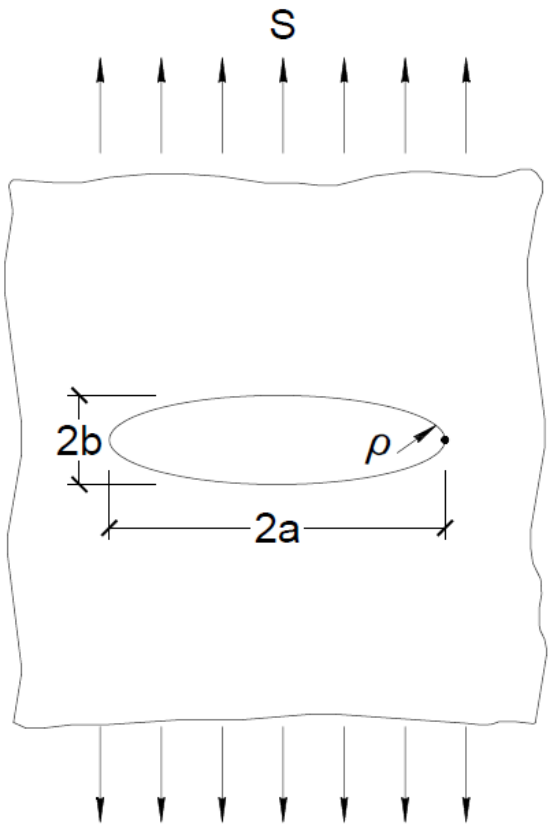

Figure 2-1. Elliptical Hole in a Flat Plate

As the aspect ratio of the flaw is increased (i.e., *a*>>*b*), the ellipse begins to resemble a sharp crack. Examining the stress at the tip of the crack (σ), indicated by a dot in the figure, it can be shown that the local stress is inversely proportional to the radius of curvature (Anderson 1995). This stress is represented in Equation 2.1.

$$\sigma = S\left(2\sqrt{\frac{a}{\rho}} + 1\right) \qquad \text{Eq. 2.1}$$

where σ is the stress at the tip of the ellipse, S is the applied stress, a is half of the flaw length, and ρ is the radius of curvature of the ellipse. It can be seen from Eq. 2-1 that as the radius of

curvature gets smaller, the stress increases. Thus, for an infinitely sharp crack, the stress at the crack tip approaches infinity. Clearly it is impossible for infinite stresses to exist in real materials. However, it can be seen that flaws have the ability to cause large increases in stress that can lead to failure well before the material's yield strength is reached.

2.1.1 Fracture Modes

When discussing fracture, it is important to note the direction of the applied stress field in relation to the crack orientation. There are three modes of fracture that can be examined independently or combined to form mixed-modes. The three fracture modes are presented visually in Figure 2-2 . Mode I exists where loading is applied normal to the crack plane, causing an opening of the crack. Modes II and III refer to shear loading, either in plane or out of plane. When fracture toughness values are presented, fracture modes I, II, and III are represented by subscripts. Typical engineering problems including a crack involve tensile stresses, and Mode I fracture is of primary interest. All discussions of fracture in this study are Mode I unless explicitly noted otherwise.

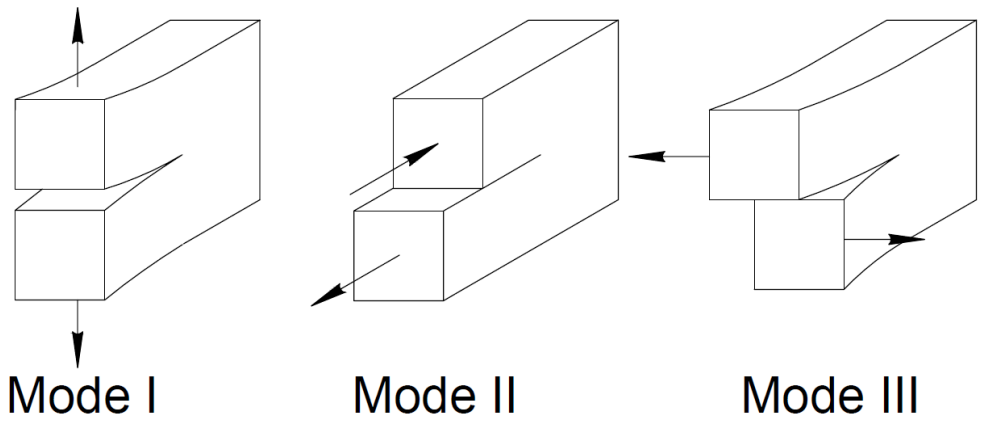

Figure 2-2. Three Modes of Fracture Loading

2.1.2 Linear Elastic Fracture Mechanics

Early fracture research by Griffith employed an energy approach to describe behavior at a crack or flaw (Griffith 1920). Griffith postulated that a crack in a material can only grow if the propagation causes either a reduction or no change in the potential energy state. Working from this, Griffith was able to develop an expression for the stress level that would cause fracture initiation, σ_f. This expression included the modulus of elasticity of the material, details concerning flaw size and geometry, and the surface energy of the material. Although this approach works well for ideally brittle materials such as glass, it greatly underestimates the toughness of materials capable of plastic deformation such as steel. Accounting only for the energy released by broken atomic bonds, this neglected the energy dissipation occurring near the crack tip due to dislocations. For this reason, modifications to Griffith's approach were made by both Irwin and Orowan to allow for small amounts of plasticity at the crack tip relative to specimen geometry (Irwin 1948, Orowan 1948).

This approach was then expanded upon by Irwin (Anderson 1995), who defined an energy release rate, *G*. This represents the amount of energy (*U*) per unit crack area (*A*) that is required to extend the crack, as shown in Equation 2.2.

$$G = -\frac{dU}{dA} \qquad \text{Eq. 2.2}$$

Here *dU* is the change in potential energy and *dA* is the change in crack surface area. This was initially very useful in describing the necessary crack driving force in the presence of a flaw, as it was possible to examine changes in resistance as the crack propagated. However,

application of the energy release rate in both testing and design was difficult, and new approaches were developed.

It has already been shown that a sharp crack in a material causes a dramatic increase in the stress at the crack tip. Stress fields in front of the crack tip can be expressed in terms of series functions. These functions include one singular and multiple non-singular terms. When examining the stress field very close to the crack tip, these non-singular terms disappear, and we are left with a single term that can describe the stresses in the vicinity of the crack tip. This term, the stress intensity factor, is represented by *K*, and defines the amplitude of the stresses near an ideally infinite sharp crack tip in ideally linear-elastic and isotropic materials.

Mathematically speaking, *K* is the limit of the stress field as you approach the crack tip because no stress can be defined at the crack tip. It is more convenient, however, to express K in a more general form, shown in Equation 2.3.

$$K = F\,S\sqrt{\pi a} \qquad \text{Eq. 2.3}$$

In this equation, *F* is a function defining loading and geometry, *S* is the applied gross nominal stress, and *a* is a variable representing crack length. Closed form solutions for a multitude of crack geometries have been developed and can be found in most fracture mechanics texts.

For ideally linear-elastic materials the relationship between the energy release rate, *G*, and the stress intensity factor, *K*, is given by Equation 2.4.

$$G = \frac{K^2}{E'} \qquad \text{Eq. 2.4}$$

G and *K* are as previously defined, and *E'* an effective modulus related to the elastic modulus of the material. For plane stress conditions *E'* is just the elastic modulus, while for plane strain the modulus is modified by Poisson's ratio.

As mentioned previously, these formulations assume ideally linear-elastic behavior, and can only account for limited amounts of plasticity at the crack tip. Because of this and the use of the theory of linear elasticity in the derivation of the presented equations, this approach to fracture mechanics is known as Linear Elastic Fracture Mechanics (LEFM).

In ductile materials such as structural steel, yielding can occur in the vicinity of the crack tip causing blunting. Blunting is the process by which crack tip sharpness is decreased due to plastic deformation. This increases the radius of the crack tip, relaxing the actual stresses at this location. When excessive yielding occurs in the region preceding the crack tip, violating limits on plastic zone size, the LEFM approach no longer represents the true state of stress at the flaw. Because of this, a new approach is necessary to characterize behavior of materials that exhibit excessive non-linear deformation.

2.1.3 Elastic Plastic Fracture Mechanics

Researchers found that LEFM was inadequate in characterizing most structural steels due to high ductility and toughness. During testing, excessive crack tip blunting invalidated the LEFM approach, leaving an important class of materials with no comprehensive approach to fracture characterization (Anderson 1995). This void led to research into what would become Elastic Plastic Fracture Mechanics (EPFM).

Plastic zone corrections, beyond that originally introduced by Irwin, can account for limited amounts of plasticity at the crack tip (Dowling 1999). Application of this approach is

done by increasing the crack size in Equation 2.3. The crack size, *a*, is replaced by an effective crack size, a_e, which is increased by the length of the plastic zone. Because the calculation of plastic zone length is dependent on stress intensity, applying this plastic zone correction is an iterative process. In addition to the difficulties of applying this correction, permissible yielding is still limited, and large amounts of plasticity at the crack tip cannot be analyzed.

Two EPFM approaches attempt to account for large amounts of plasticity. These are the crack-tip opening displacement (CTOD) and the J-Integral. CTOD was initially developed as a test method for examining the fracture toughness of structural steels when LEFM approaches failed. The J-Integral concept was initially developed mathematically, and test methods were later developed to physically verify the approach.

In the early 1960's it was proposed that fracture behavior of a material could be characterized by the opening of crack faces at the original crack length (Wells 1961). CTOD, represented by δ, is the opening between the initially sharp crack, and the crack that has been blunted due to plastic deformation. The degree of blunting increases in proportion to the fracture toughness of the material being tested, and CTOD can be used to characterize fracture toughness. For limited amounts of plasticity, CTOD can be directly related to LEFM parameters, as seen in Equation 2.5.

$$\delta = \frac{4}{\pi}\frac{G}{\sigma_{ys}} \qquad \text{Eq. 2.5}$$

In this equation δ is CTOD, σ_{ys} is yield stress, and *G* is as previously defined. Application of CTOD to engineering structures requires empirical driving force estimates and design reference curves, making it much more difficult to apply than LEFM parameters.

The J-integral concept, developed independently by both Rice and Cherepanov (Rice 1968 and Cherepanov 1967), is equal to the work performed per unit area of fracture surface on a nonlinear elastic body containing a crack (Zhu and Joyce 2012). The J-Integral relates to the difference in absorbed energy under loading for incremental changes in crack size. Thus, it can be thought of as elastic-plastically analogous to the linear elastic energy release rate, *G*. For the unique case of a linear elastic material, the J-Integral is equal to the energy release rate.

Mathematically, the J-Integral was originally defined as a path-independent line integral enclosing the crack tip. This integral evaluates the strain energy around the crack tip, as shown in Equation 2.6.

$$J = \int_{0}^{\Gamma} \left(w dy - T_i \frac{\partial u_i}{\partial x} ds \right) \qquad \text{Eq. 2.6}$$

In this equation Γ defines the path around the crack tip, w is the strain energy density, T_i are the components of an applied traction, u_i are components of the displacement vector, and *ds* is the incremental length around the contour Γ. This is presented schematically in Figure 2-3.

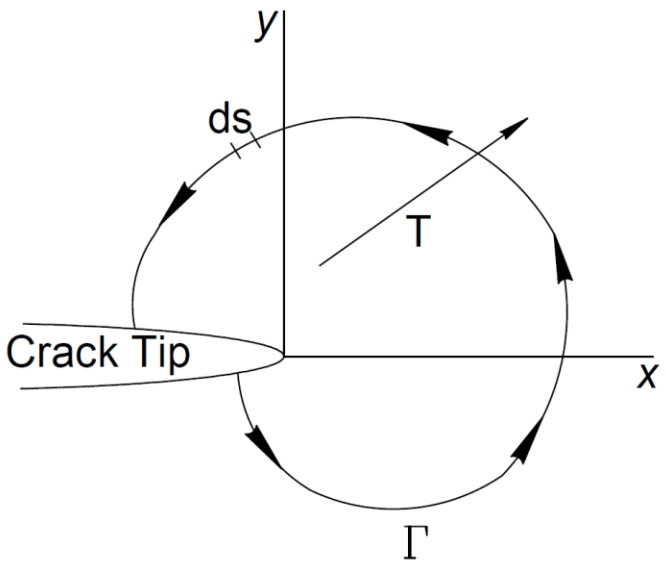

Figure 2-3. J-Integral Contour Schematic

Although initially presented in this manner, the J-Integral concept did not gain traction with researchers until experimental test methods were developed for its evaluation. Multiple researchers were able to prove that the J-Integral uniquely defines stress and strain at the crack tip in nonlinear materials. This makes the J-Integral a parameter of both energy and stress intensity (Anderson 1995).

Application of the J-Integral to engineering problems is much easier than that of CTOD, due to the fact that it does characterize the stress intensity at a flaw. Critical J-Integral values, *J*, can be converted to elastic plastic fracture toughness values, K_J, using the material's elastic modulus and Poisson's ratio, *v*, as shown in Equation 2.7. With this relationship, elastic plastic fracture evaluation can be performed in the same manner as linear elastic fracture evaluation.

$$K_J = \sqrt{J \frac{E}{1 - v^2}} \qquad \text{Eq. 2.7}$$

2.2 Introduction to Measures of Fracture Toughness

Quantifiable measures of fracture toughness have evolved as understanding of fracture mechanics and fracture testing methods have been developed. Current fracture testing specifications and their associated measures of toughness have recently been consolidated into a single document, ASTM E 1820-08 Standard Test Methods for Fracture Toughness (ASTM 2008) Understanding past testing methods and techniques is imperative in contextualizing results of historical data sets, i.e. it is imperative to understand the state of testing when the research was conducted. Current and past fracture toughness testing techniques are presented herein in a succinct manner. It is beyond the scope of the present study to present the entire chronicle of fracture mechanics, or the record of fracture testing methods. Others have presented the development of fracture mechanics and testing, including Anderson (1995), Cotterell (2002), and Zhu and Joyce (2012). It is also beyond the scope of this study to introduce all former and current fracture toughness test methods. Although more fracture toughness tests exist and are in use, this review presents only the methods that are the most common in bridge steel research and have relevance to the current study.

2.2.1 Charpy V-Notch Impact Fracture Toughness

For over 100 years, the Charpy V-Notch Impact test has been the benchmark of fracture toughness testing for material qualification in the structural steel industry. Noted for its time and economic efficiency, as well as ease of specimen fabrication and test procedure, the CVN Impact

test is standardized in ASTM E 23-07, along with other notched bar impact tests (ASTM 2007). The CVN specimen is a small, rectangular bar with a radiused "V notch" centered on the length. Placed on an anvil, the specimen is contacted with a swinging drop hammer, and the amount of energy absorbed by the material as fracture occurs is measured. The absorbed energy is the CVN toughness of the material, and is extremely dependent on test temperature. Typical behavior exhibited by steel specimens includes brittle, cleavage fracture at low temperatures, termed lower shelf behavior. As test temperature is increased, the toughness also increases in what is known as the brittle to ductile transition region. Finally, at high temperatures, steels exhibit ductile behavior and high CVN toughness values, and their behavior is said to be on the upper shelf. A typical CVN curve of HPS 70W steel is presented in Figure 2-4 displaying lower shelf, transition, and upper shelf behavior.

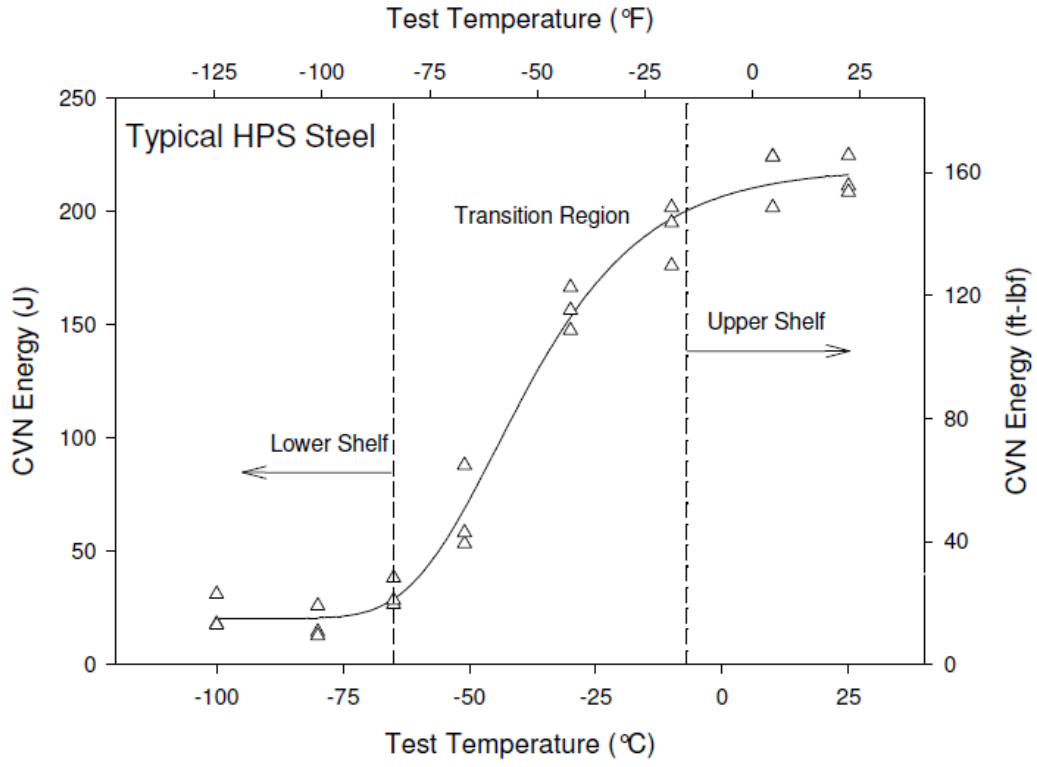

Figure 2-4. Typical CVN Behavior for HPS Steel

Other parameters that can be recorded from CVN testing are lateral expansion of the broken specimen and percentage of the shear fracture on the failure surface, both of which typically show the same temperature dependence as the absorbed energy. However, CVN fracture toughness is not directly applicable to fracture mechanics parameters or design calculations (Dowling 1999).

2.2.2 Fracture Mechanics-Based Fracture Toughness

In the late 1960's and early 1970's, the beginning of earnest examination of fracture in bridges, LEFM was still the prevailing method of fracture analysis. Elastic plastic fracture mechanics test methods were being investigated. Reliable test methods were yet to be developed, and research was still being performed with the use of LEFM. Fracture toughness, the ability of a material to resist fracture initiation in the presence of a sharp crack, was defined in terms of K.

The use of LEFM in testing was very useful for material evaluation as it yielded a single value, representing the toughness at initiation of brittle fracture. As long as the critical toughness of a material, K_c, is greater than the applied stress intensity, K, the material is able to resist fracture initiation. Because of limitations on plastic zone size in the validity of LEFM parameters, materials exhibiting slow stable crack growth prior to fracture are difficult to characterize. Valid K_c testing for Mode I fracture values (K_{Ic}) require plane strain fracture behavior, which is dependent on specimen size. Rolled steel plate thickness is often too thin to obtain valid plane strain results at reasonable test temperatures. Nonetheless, test data obtained from tests beyond validity limits has often been presented in the literature, and has been used in the characterization of structural steels (Barsom et al. 1972, Roberts et al. 1977).

K-based fracture toughness, like CVN toughness, is a temperature dependent property. Fracture behavior, when examined with respect to changing temperature, follows a pattern similar to CVN energy, shown in Figure 2-4 above, with a well-defined lower shelf and a brittle to ductile transition region. Upper shelf values of fracture initiation toughness are difficult to characterize, due to the absence of a single value of toughness in the presence of large amounts of stable tearing. More information on temperature dependence and the brittle to ductile transition region can be found in the discussion on the Master Curve, Section 2.3.1.

Advances in testing methodologies were needed to account for tests where large amounts of plasticity were present, as previously discussed. Structural steels are too tough to be characterized with LEFM, requiring the development of test methods using EPFM. The two most common EPFM parameters used by researchers of structural steel are CTOD, and the J-integral. Both of these parameters provide measures of fracture toughness in the presence of plastic deformation, and have much less stringent validity requirements than linear elastic K-based approaches (Anderson 1995).

Thickness dependent validation requirements of LEFM are not as stringent when applying EPFM. However, it is extremely important to control the amount of constraint experienced at the crack front. Concerns about constraint can be eliminated by properly following specimen geometry guidelines presented in ASTM E 1820-08 and ASTM E 1921-08 (ASTM 2008). Typical specimens used in all fracture mechanics testing consist of variations of two main specimen types: the compact tension (C(T)) specimen, and the single edge bend (SE(B)) specimen, as shown in Figure 2-5. Fracture toughness specimens are typically defined

by dimension W, a, and B, representing width, crack length, and thickness, respectively. Width, W, and crack length, a, are represented schematically in Figure 2-5.

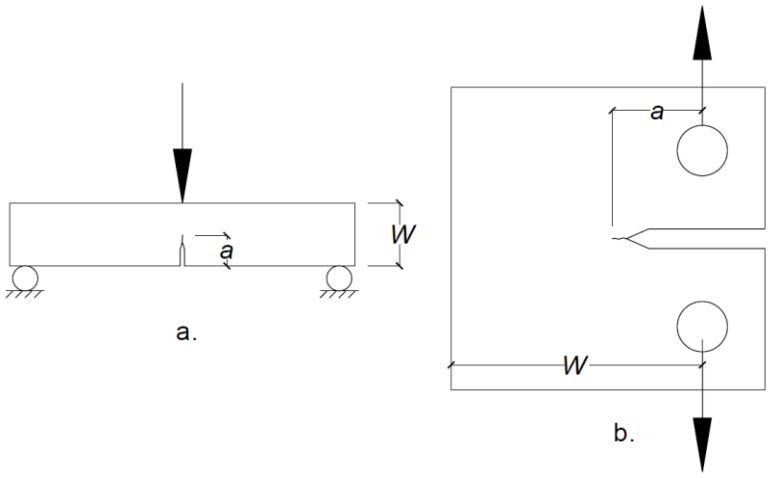

Figure 2-5. Typical Fracture Mechanics Specimens: a. SE(B) and b. C(T)

C(T) specimens are loaded in tension through the use of clevis grips and pins, while SE(B) specimens are loaded in a three-point bend setup. Both can be used to perform static, intermediate, and dynamic load rate tests, although the SE(B) does offer advantages as its smaller size allows experiments to reach high strain rates without the use of large drop tower test equipment. In all test geometries the specimen thickness is denoted in terms of xT, where x is specimen thickness in inches. Thus one and two inch thick specimens are said to be 1T and 2T, respectively. All specimen thicknesses follow this same nomenclature.

Differences between LEFM and EPFM fracture toughness testing have yielded an array of parameters that can be used in the evaluation of engineering structures. Single value parameters of interest to this study are briefly defined here. For EPFM parameters, only J-Integral values are discussed, although for each J-based toughness parameter there is a corresponding CTOD-based parameter.

Plane-strain fracture toughness, K_{Ic}, is a LEFM parameter representing a lower bound fracture toughness corresponding to a plane-strain stress state. Historically, this is the most commonly used fracture toughness parameter. Validity of K_{Ic} testing can be difficult, especially with high toughness materials that experience substantial plasticity and stable tearing.

Two EPFM parameters describe brittle cleavage fracture initiation. In terms of the J-Integral, these are J_c and J_u. J_c is a well-defined parameter that corresponds to a cleavage fracture prior to any ductile tearing. The parameter J_u relates to fracture after an undefined amount of ductile tearing occurs. If J_c is obtained from test record, it is typically considered to be the critical toughness value. J_u on the other hand, is typically not used. As ductile tearing progresses, test specimens can experience loss of crack-tip constraint, which can lead to unconservative toughness values if J_u is considered to be the critical value of fracture toughness. For this reason, a parameter was defined that represented the onset of ductile tearing (Wallin 2011). J_{Ic} represents the toughness at the initiation of ductile crack growth. This is defined in ASTM E1820-08 as the *J* value corresponding to 0.2 mm. (0.008 in.) of crack extension (ASTM 2008). As previously discussed, critical J-Integral values can be converted into a corresponding K_J fracture toughness, and evaluated against calculated stress intensity values.

2.2.3 Crack Arrest Toughness

While fracture toughness parameters *K*, *J*, and CTOD represent the ability of a material to resist fracture initiation in the presence of a crack, crack arrest toughness of a material, represented by K_a, is the ability of a material to stop a brittle fracture that has already initiated. Standardized in ASTM E 1221-12 (ASTM 2012), crack arrest toughness is not a commonly used

parameter, although it has been used to characterize steels for naval and nuclear applications (Joyce, et al. 2010).

In order to obtain crack arrest values, it is necessary to initiate a brittle crack by loading a specimen that contains fracture susceptible details, such as fatigue pre-cracking or a brittle weld deposit. Once fracture is initiated it is necessary to remove the driving force in order to capture the arrest ability of the material. Crack arrest toughness has been shown to follow a similar temperature dependence of that seen in fracture toughness measures. However, because of the necessary test parameters of initiating fracture and immediately removing the driving force, researchers have had difficulty in characterizing crack arrest toughness in the upper transition region (Link, et al. 2009). Crack arrest toughness testing has not previously been used to characterize bridge steels, but the ability to describe the capacity of a material to arrest dynamic fracture events is very promising.

2.3 Material Fracture Characterization

Knowing that fracture toughness is dependent on temperature and strain rate, it is important to be able to characterize a material in terms of one or both of these variables. In other industries, fracture behavior is characterized by what is known as the Master Curve, a statistically based function that describes the toughness of steels in the brittle to ductile transition region based on elastic plastic fracture toughness test data. Characterization of material toughness in the US bridge industry has typically been performed by applying correlations that relate CVN impact data to static, intermediate, and dynamic load rate fracture toughness, K, over a full range of temperatures.

2.3.1 Master Curve and Reference Temperature, T_o

The Master Curve approach is a method that characterizes fracture toughness of a material in the brittle to ductile transition region based on elastic plastic toughness, K_J. An exponential curve anchored to a reference temperature, T_o, has been shown to be applicable to ferritic steels. The process for determining this curve, along with its tolerance bounds, is presented in ASTM E 1921-08 (ASTM 2008).

Based on a weakest link flaw distribution model, the Master Curve uses a three parameter Weibull distribution to define the probability of failure due to cleavage fracture in a theoretically homogenous material. The reference temperature, T_o, is the temperature at which the median cleavage initiation toughness is equal to 100 MPa√m (91 ksi√in). Data from varying specimen sizes are size corrected to 1T thickness. This size correction is performed to take into account the distribution of flaws in a material. A thick specimen will inherently have more flaws than a thin specimen, and thus will have a higher incidence of fracture. Reference temperature, T_o can reliably be calculated with as few as six specimens tested at a single temperature. The reference temperature may also be determined from test data at multiple test temperatures, providing researchers with two testing options for reference temperature determination: single- and multi-temperature testing. The shape of the median fracture toughness is then given by

$$K_{Jc(med)} = 30 + 70e^{(0.019(T-T_o))} \qquad \text{Eq. 2.8}$$

where K_{Jc} is in MPa√m, and T and T_o, test temperature and reference temperature, respectively, are given in degrees Celsius.

Both upper and lower bound limits of the Master Curve are calculated using

$$K_{Jc(0.xx)} = 20 + \left[ln\left(\frac{1}{1-0.xx}\right)\right]^{1/4}\{11 + 77e^{(0.019(T-T_o))}\} \qquad \text{Eq. 2.9}$$

where K_{Jc}, T, and T_o are as previously defined, and xx represents the selected cumulative probability of failure. For example, for 5 and 95 per cent boundary limits, 0.xx would be equal to 0.05 and 0.95, respectively. A typical Master Curve with T_o equal to -75 C (-103 °F), along with upper and lower bound limits was determined using the above equations. As can be seen in Figure 2-6, the tolerance bounds used on this example are 5 and 95 per cent. The data for this figure was provided as an example in ASTM E 1921-08, and was obtained from a plate of A533B steel.

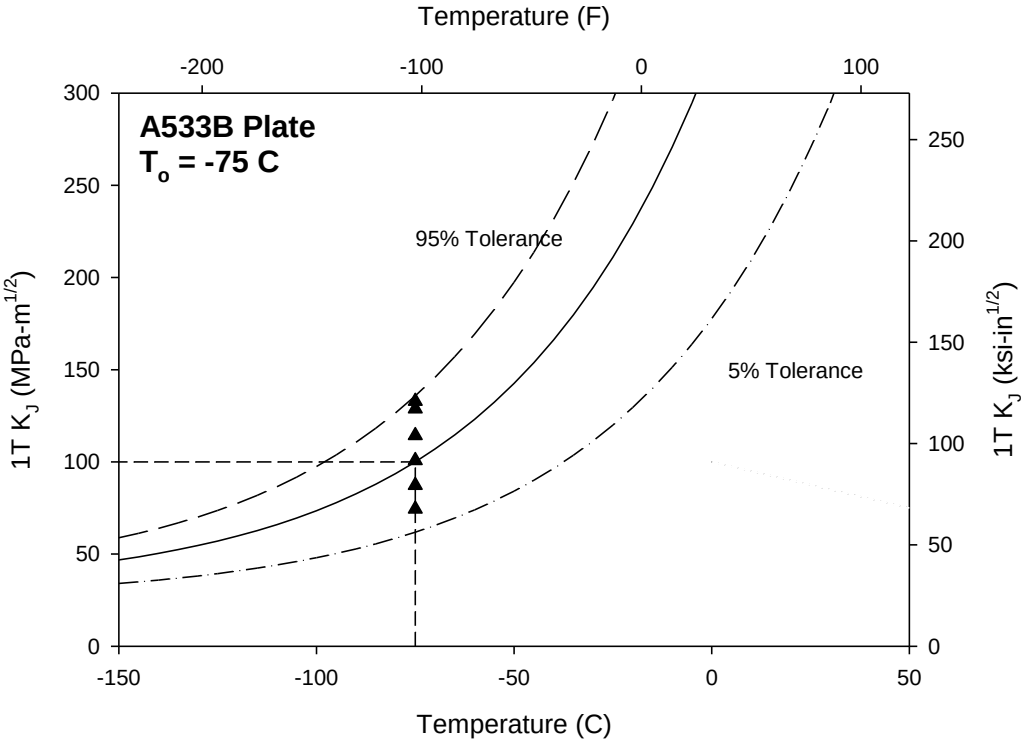

Figure 2-6. Typical Master Curve A533B Steel, Adapted from ASTM E 1921

Provisions for the application of the master curve methodology to crack arrest toughness are presented in the crack arrest specification. With respect to temperature, crack arrest toughness behavior follows the same exponential master curve as fracture initiation toughness. Two main aspects differentiate between initiation and arrest master curves. The first is that arrest data is not size adjusted. While cleavage fracture toughness is dependent on the distribution of discrete initiation sites throughout the material matrix, arrest is more of a global mechanism. Because of this there are no statistical size corrections for crack arrest data. The second main difference is found in the determination of tolerance bounds. Tolerance bounds for fracture initiation are based on statistical flaw distribution and can be determined based solely on the median toughness reference temperature. Tolerance bounds for arrest data are developed upon the variance of actual test data with respect to the master curve. Thus, arrest data with very little scatter produces tight tolerance bounds and vice versa, while the bounds for initiation curves are independent of data variation.

The Master Curve provides a statistically verified characterization of fracture toughness in the brittle to ductile transition region. This allows for the defining of behavior at highway bridge service temperatures. The literature provides further background for the Master Curve, including the effects of strain rate, constraint conditions, and material inhomogeneity (McCabe, et al. 2007, Wallin 1997, Wallin 2001, and Wallin, et al. 2004). A thorough introduction to the application of the master curve methodology, as well as an example data set, is presented in Chapter 4.

2.3.2 CVN Correlations

As previously stated, CVN toughness values are not directly applicable to fracture mechanics problems. Relationships have been proposed to correlate CVN toughness to fracture mechanics based toughness values. The correlation used in setting the AASHTO material toughness specifications is the Barsom and Rolfe Two Stage correlation (Barsom 1974). The correlation is based on both loading rate and temperature to account for the difference between an impact load rate and the in-service load rate for highway bridges.

2.3.2.1 Barsom and Rolfe Two Stage Correlation, 1974

The premise of this correlation is that CVN toughness values can be converted to K-based fracture parameters depending on the rate of loading (Barsom 1974). Toughness of standard CVN test values are empirically correlated to K through the use of

$$\frac{K^2}{E} = 5\ (CVN) \qquad \text{Eq. 2.10}$$

where K is fracture toughness in psi$\sqrt{\text{in}}$, E is the material's modulus of elasticity in psi, and CVN is the absorbed CVN energy in ft-lbf. If the CVN specimen is tested with an impact hammer, K corresponds to K_{Id}, the dynamic fracture toughness of the material. When CVN is tested statically, K corresponds to K_{Ic}. Because CVN impact values are typically used to qualify structural steels, the correlation equation provides a link to dynamic fracture toughness. Barsom and Rolfe found that effects of strain rate could be taken into account by shifting, with respect to temperature, the resulting fracture toughness values. The temperature shift is related to the yield stress of the material by

$$T_{shift} = 215 - 1.5\sigma_{ys} \quad \text{Eq. 2.11}$$

where the temperature shift is given in degrees Fahrenheit, and yield stress is in ksi. The equation is only applicable for yield strength ranges between 26 and 140 ksi (180 and 965 MPa). For highway bridge applications, it was proposed that loading rates are neither static nor dynamic, but somewhere in between. For this reason, the temperature shift used in setting AASHTO material toughness standards is only 75% of the shift presented in Equation 2.11. It is important to note that this correlation is only applicable to CVN data located in the lower shelf and lower half of the transition toughness range.

2.3.2.2 Barsom and Rolfe Single Stage Correlation, 1970

An earlier version of the Barsom and Rolfe CVN-K correlation did not take into account loading rate, and used a direct correlation between CVN impact and static K_{Ic} values (Barsom and Rolfe 1970). This relationship is represented by

$$\frac{{K_{Ic}}^2}{E} = 2\,(CVN)^{3/2} \quad \text{Eq. 2.12}$$

where all variables are as previously defined.

2.3.2.3 Corten and Sailors Correlation, 1971

Corten and Sailors also presented a correlation between CVN impact and fracture toughness which does not consider the rate of loading, Equation 2.13 (Corten and Sailors 1971, Sailors and Corten 1972).

$$K_{Ic} = 15.5\ (CVN)^{1/2} \qquad \text{Eq. 2.13}$$

where K_{Ic} is given in ksi√in and *CVN* is given in ft-lbf.

2.3.2.4 Marandet and Sanz Correlation, 1977

Marandet and Sanz (1977) developed a CVN-K correlation from low carbon steels with 142 yield strengths ranging from 215 to 1100 MPa (31 to 160 ksi). This correlation does not include rate effects, and relates CVN impact toughness to static fracture toughness through Equation 2.14.

$$K_{Ic} = 19\sqrt{CVN} \qquad \text{Eq. 2.14}$$

2.3.2.5 Roberts and Newton Lower Bound Correlation, 1984

Roberts and Newton presented a loading rate independent correlation, intended to represent a lower bound of fracture toughness (Roberts and Newton 1984). The relationship between impact CVN and *K* is very similar to that of Corten and Sailors, and is presented as Equation 2.15.

$$K_{Ic} = 9.35\ (CVN)^{0.63} \qquad \text{Eq. 2.15}$$

where K_{Ic} is given in ksi√in and *CVN* is given in ft-lbf.

2.3.2.6 British Standard 7910 CVN-T_o Relationship

A relationship directly connecting CVN toughness to the Master Curve Reference Temperature, T_o, is presented in British Standard 7910 (BS 7910) (British Standards Institute 2005). The relationship is based on knowing the CVN test temperature at a specific energy value of 27 or 40 J (20 or 29 ft-lbf). This temperature is then converted into a reference temperature by subtracting18 or 24 C for the 27 or 40 J temperatures, respectively. This temperature adjustment can be seen in Equations 2.16 and 2.17.

$$T_o = T_{27} - 18C \qquad \text{Eq. 2.16}$$

$$T_o = T_{40} - 24C \qquad \text{Eq. 2.17}$$

The more conservative of these two values is then used in Equation 2.18, which is equivalent to the Master Curve equation presented in ASTM E 1921-08. In the BS 7910 equation the size correction and probability of failure are built into the equation, as seen with the variables B and P_f for thickness and failure probability, respectively.

$$K_{mat} = 20 + \left[11 + 77e^{\{0.019(T-T_o-T_K)\}}\right]\left(\frac{25}{B}\right)^{1/4}\left\{ln\left(\frac{1}{1-P_f}\right)\right\}^{1/4} \qquad \text{Eq. 2.18}$$

In this equation temperatures are in Celsius, fracture toughness is in MPa√m, and thickness is in millimeters. An additional factor is added to the equation to account for the scatter in CVN impact test data. This is the variable T_K, which is recommended to be 25 °C, unless CVN test data shows that another value should be used. Applying this temperature adjustment

factor to the original equations provides a direct correlation between CVN and T_o. Equations 2.19 and 2.20 represent this modification to the previously presented equations.

$$T_o = T_{27} - 18C + 25C \quad \text{Eq. 2.19}$$

$$T_o = T_{40} - 24C + 25C \quad \text{Eq. 2.20}$$

2.3.2.7 CVN-Master Curve Relationship

Based on a slightly modified BS7910 approach, ASTM E 1921-08 presents a relationship that is intended to be a guide for determining a starting test temperature for determining T_o (ASTM 2008). Some researchers, however, have used it as a correlation for comparison purposes (Alstadt 2008). The relationship is based on knowing the CVN test temperature at a specific energy value of 28 or 41 J (21 or 30 ft-lbf), and is dependent on specimen size. A constant value, *C*, is used to adjust the CVN test temperature, yielding a reference temperature, T_o. Constant values for C can be found in Table 2-1 (ASTM 2008).

Table 2-1. Constants for Test Temperature Selection Based on CVN

Specimen Size	Constant C (°C)	
(nT)	28 J	41 J
0.4	-32	-38
0.5	-28	-34
1	-18	-24
2	-8	-14
3	-1	-7
4	2	-4

Reference temperature, T_o, is then determined from Equation 2.21.

$$T_o = T_{CVN} + C \qquad \text{Eq. 2.21}$$

In this equation T_o is the reference temperature used in the Master Curve, T_{CVN} is the CVN test temperature, and C is a value taken from Table 2-1.

2.4 Fracture in Bridge Steels

Of the nearly 200,000 steel bridges in service in the United States, since the 1950's there have only been two failures resulting in catastrophic loss of life (Albrecht and Wright 2000). Of these two failures, the Point Pleasant Bridge and the I-35W bridge in Minneapolis, only the Point Pleasant Bridge collapsed due to fracture. In fact, other bridges have experienced fractures, sometimes of multiple girders, without structural failure. Even two girder bridges designated as fracture critical have been able to remain in service after being subjected to full depth girder fractures including (a) the US 52 Bridge in Savannah, Illinois in 1976, (b) the Interstate 79 over Neville Island bridge, Glenfield, Pennsylvania in 1977, and (c) the US 422 Bridge in Pottstown, Pennsylvania in 2003 (Fisher, et al. 1977, Schwendeman and Hedgren 1978). Milwaukee's three girder Hoan Bridge experienced full depth fracture in two girders, with partial depth fracture in the third, without full collapse (Connor, et al. 2007). Fisher presents a comprehensive list of highway bridges that have fractured (Fisher 1984).

Historically, the understanding was that brittle fractures occurred in bridges due to the growth of fatigue cracks that reach critical size. Brittle fracture has been documented for numerous cases, and was the focus for much of the early fracture research on structural steels. Weld defects have also resulted in the fracture of highway bridge girders. These fractures

resulted in AASHTO banning electro-slag welding in 1977. However, this directive was rescinded in 2000 (FHWA 2000).

Recently researchers have observed that fractures do occur in bridge girders without a preceding fatigue crack or identifiable weld defects. These fractures initiate from locations in bridges experiencing tri-axial constraint, usually due to the detailing of welded connections (Mahmoud, et al. 2005). Constraint-induced fracture (CIF) is an extremely dynamic event, and was found to be the cause of fractures in both the US 422 and Hoan bridges (Connor, et al. 2007). In the 1970's some researchers were concerned with so-called pop-in cracking, where fractures initiate in a weld or heat-affected zone despite the absence of prior fatigue cracking (Hartbower 1979). In spite of this, emphasis was placed on the control of fatigue crack growth to prevent brittle fracture, and little attention was given to issues concerning any other cause of fracture.

2.5 Fracture Control Plan and Specifications

2.5.1 History of Fracture Control Plan

Material toughness requirements for bridge steels, specified in terms of CVN, were first introduced in 1968 (Wright 2002). The requirements were based on the experience of the ship building industry, where it was known that a minimum CVN value of 20 J (15 ft-lb) typically prevented brittle fracture. This value was chosen because it was known that fractures in ships were rare when steel met or exceeded this toughness level. Following the FHWA's call for an updated fracture control plan, The American Iron and Steel Institute (AISI) initiated Project 168 at U.S. Steel Research (Barsom 1974). The objective of the research was to investigate the

fracture toughness of structural steels for bridge applications. Analysis of results served in the formation of ASTM material toughness requirements and the American Association of State and Highway Transportation Officials (AASHTO) fracture control plan (AASHTO 1978).

Initially the CVN toughness requirements were the same for all steel bridges, regardless of layout or geometry. Eventually higher material toughness requirements were put in place for bridges with member's whose fracture would result in failure of the entire structure. The delineation between redundant and non-redundant structural design became the distinction between non-fracture critical and FC bridges and members.

The current FCP consists of three interrelated factors which are used to prevent fractures from occurring in steel bridges: material toughness requirements, control of weld flaws through welding inspection and fabrication guidelines, and in-service inspection criteria. The original 1978 AASHTO Guide Specifications for Fracture Critical Non-Redundant Steel Bridge Members contained design and review responsibilities, qualification and certification of welders and inspectors, material toughness requirements, and fabrication requirements and procedures. The 1978 Guide Specifications have been updated multiple times, and the majority of the fracture control plan can now be found in Section 12 of the AASHTO/AWS D1.5M/D1.5 Bridge Welding Code (AASHTO/AWS 2010).

Current material toughness requirements for all steels used in bridge applications can be found in both the AASHTO LRFD Bridge Design Specifications (AASHTO 2008) and ASTM A 709-13 (ASTM 2013). The AASHTO Manual for Bridge Evaluation contains the in-service inspection requirements and criteria for all types of highway bridges (AASHTO 2011). Because the focus of this research lies with fracture behavior and material toughness of HPS steels, the

literature review will concentrate on this aspect of the FCP. Details of the FCP pertaining to fabrication and inspection are only briefly addressed.

2.5.2 Fracture Critical Definitions and Designations

Definitions of FC are found in the FCP and are as follows (AASHTO/AWS 2010):

> *2.1 Fracture critical members or member components (FCMs) are tension members or tension components of members whose failure would be expected to result in collapse of the bridge.*
>
> *2.2 Tension components of a bridge member consist of components of tension members and those portions of a flexural member that are subject to tension stress. Any attachment having a length in the direction of the tension stress greater than 4 inches (101.6 mm.) that is welded to a tension component of a "fracture critical" member shall be considered part of the tension component and, therefore, shall be considered "fracture critical."*

Design and review responsibilities are also found in the FCP, where the engineer is fully responsible for the design of the bridge, including the selection of materials, structural details, and welding requirements. The determination of what is categorized as fracture critical members and member components is also the responsibility of the engineer.

2.5.3 Material Toughness Requirements

CVN impact toughness values have historically been used as quality control and assurance measures in the steel industry. All material toughness values found in the FCP are in

terms of CVN impact toughness. Although not a direct test of fracture toughness, CVN values have been correlated to data from more rigorous and informative fracture tests. The correlations between CVN impact toughness and static critical plane-strain fracture toughness values, K_{Ic}, were empirically determined from data developed through the use of LEFM technology (Barsom 1974). Although the field of fracture mechanics has advanced beyond LEFM, correlations from the 1970's are still used to determine and set material specifications for today's bridge steels. A detailed discussion of CVN-K correlations is presented in Section 2.4.

Because the fracture toughness of ferritic steels is known to vary dramatically with changes in temperature, higher toughness requirements are needed for steels in bridges located in colder climates (Anderson 1995). For this reason, AASHTO divided the United States into three service temperature regions based on the lowest anticipated service temperature (LAST), with CVN test temperatures adjusted accordingly. States are given the authority to determine their LAST based on historically recorded temperatures. A contour map showing an approximation of the three design zones is presented in Figure 2-7. This figure was adapted from AASHTO's temperature contour map developed for bearing design (AASHTO 2008). Table 2-2 presents the temperature limits of the three zones (AASHTO 2008). Qualifying impact tests are not performed at the LAST, however, due to a temperature shift employed in the CVN-K_{Ic} correlation procedure.

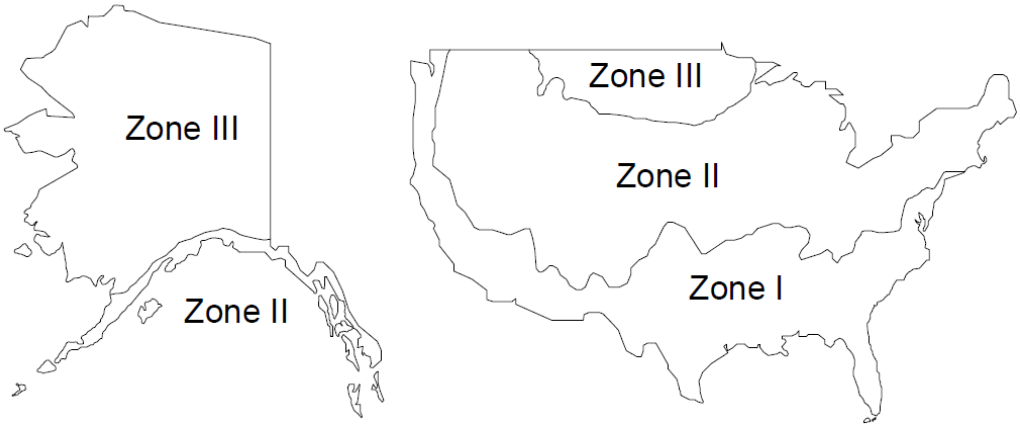

Figure 2-7. Approximate LAST Zones

Table 2-2. Temperature Zone Designations

Temperature Zone	Minimum Service Temperature
I	-18°C (0°F) and above
II	-19°C (-1°F) to -34°C (-30°F)
III	-35°C (-31°F) to -51°C (-60°F)

Alternative FCPs based on different material toughness requirements were proposed, but due to the available technology in the steel making industry, these alternatives were determined to be too costly, and aspects of the FCP other than material toughness were relied upon to prevent fractures in steel bridges. Some of the alternatives advocated CVN testing at bridge service temperatures (Hartbower 1979) and including a required level of dynamic toughness sufficient to arrest cracks occurring suddenly in local brittle zones (Dexter, et al. 2004). At the time it was thought that bridge fractures typically occurred at fatigue cracks, and dynamic pop-in type cracks were not considered. If a material could prevent fracture from crack growth up to the end of fatigue life this was considered sufficient. It was reasoned that setting toughness

requirements any higher would not extend service life (Barsom 1973). Also, significantly higher steel toughness was not economically feasible at the time.

Presented in Table 2-3 are the current AASHTO material toughness requirements for FC tension members, as specified in ASTM A 709-13 (ASTM 2013). Each energy value is taken as the average of three samples tested at the specified temperature. It can be seen that the steels primarily being examined in this research, HPS 70 and HPS 100, have requirements of 48 J (35 ft-lbf) at -23°C (-10°F) and -34°C (-30°F), respectively. Toughness requirements for HPS 485W (70W) and HPS 690W (100W) do not change based on temperature zones.

Table 2-3. Fracture Critical Tension Component Impact Test Requirements

Grade	Thickness, mm. (in.)	Minimum Average Energy, J (ft-lbf)		
		Zone I	Zone II	Zone III
250F (36F)	to 100 (4) incl.	34 (25) at 21°C (70°F)	34 (25) at 4°C (40°F)	34 (25) at -12°C (10°F)
345F (50F), 345SF (50SF), 345WF (50WF)	to 50 (2) incl.	34 (25) at 21°C (70°F)	34 (25) at 4°C (40°F)	34 (25) at -12°C (10°F)
	over 50 to 100 (2 to 4) incl.	41 (30) at 21°C (70°F)	41 (30) at 4°C (40°F)	41 (30) at -12°C (10°F)
HPS 345WF (HPS 50WF)	to 100 (4) incl.	41 (30) at -12°C (10°F)	41 (30) at -12°C (10°F)	41 (30) at -12°C (10°F)
HPS 485WF (HPS 70WF)	to 100 (4) incl.	48 (35) at -23°C (-10°F)	48 (35) at -23°C (-10°F)	48 (35) at -23°C (-10°F)
HPS 690 WF (HPS 100WF)	to 65 (2.5) incl.	48 (35) at -34°C (-30°F)	48 (35) at -34°C (-30°F)	48 (35) at -34°C (-30°F)
	over 65 to 100 (2.5 to 4) incl.	not permitted	not permitted	not permitted

It is known that lateral constraint within a plate increases with thickness, creating a state of triaxial tensile stress ahead of a crack tip, reducing fracture toughness (Barsom and Rolfe 1987). Thus the CVN requirements are based on the thickness of the plate being used in the bridge. Earlier versions of this table specified different toughness values for structural members depending on whether they were mechanically fastened or welded, but the requirement has been removed to simplify the specification. All applications are now held to the same standard. Details of the required number of CVN specimens, as well as their location and orientation can be found within ASTM A 709-13.

2.5.4 Welding and Fabrication Requirements

All information in the FCP related to welding and fabrication is currently found in Section 12 of the AASHTO/AWS Bridge Welding Code (AASHTO/AWS 2010). Related to changing technology in the welding industry, updates of all welding information are found in the

AASHTO Guide Specifications, as well as details concerning welder and inspector certification and qualification. Also included in are requirements for thermal cutting, repair of welds and base metal, straightening, curving, and cambering, and preheat and interpass temperature control.

2.5.5 In-Service Inspection Guidelines

As stated above, in-service inspection guidelines and specifications are presented in the AASHTO Manual for Bridge Evaluation (AASHTO 2011). AASHTO requires that bridges with FCMs have a very close, visual "hands-on" inspection, which often necessitates intensive cleaning of the structure and the use of expensive access equipment. It is recommended that all bridges be inspected at a minimum frequency of 24 months. Although owners can petition for less frequent inspections, this is not allowed for bridges deemed to have fracture critical members. In addition, many older FC bridges may require the use of advanced inspection techniques to monitor fatigue crack growth, which can be time consuming and costly. These arduous requirements for in-service inspection create a large cost for bridge owners, and are a major reason for the limited use of bridges with FCMs.

For additional details on the inspection of FC bridges, AASHTO makes reference to the Inspection of Fracture Critical Bridge Members, FHWA Report IP-86-26 (FHWA 1986) and the Bridge Inspector's Reference Manual (BIRM) (Ryan, et al. 2012). Additional guidelines for the in-service inspection of bridges with FCMs can be found in the Recording and Coding Guide for Structure Inventory and Appraisal of the Nation's Bridges, FHWA Report PD-96-001 (FHWA 1996).

2.6 Fracture Toughness Programs Examining Conventional Bridge Steels

Several independent studies have investigated the fracture toughness of conventional steels used in bridge application, some for the development of the FCP material toughness requirements and others for the evaluation of them. The studies include CVN impact tests, as well as more informative fracture mechanics tests. Some of the experimental programs also include fracture tests of full scale bridge girders although the focus of this review is on the results of small scale fracture tests. Applicable data from these studies will be presented in Chapters 4 and 5, including analysis within the context of the current study.

2.6.1 Barsom, Sovak, and Novak 1972

The experimental program was instituted following the fracture and collapse of the Point Pleasant Bridge, and formed the basis for the original material toughness requirements of the AASHTO FCP. The study was divided into a material characterization program and a full scale girder fracture program. Taken together, the results investigate the fracture behavior of A572 bridge steels.

Fracture toughness of A572 Steels, the initial part of the program, examined and characterized the fracture behavior of the steel through the use of small scale fracture mechanics tests (Barsom, et al. 1972). Test specimens fabricated from 1.5 in. (38 mm) thick plates of grades 50 and 62 ksi (345 and 428 MPA) A572 steel. CVN specimens were tested at impact, intermediate, and slow loading rates, characterizing the material over the full temperature transition. All CVN specimens were sampled from plates centered at the third point of plate thickness.

Fatigue pre-cracked SE(B) and C(T) specimens were tested using the latest LEFM technology available, yielding plane-strain fracture toughness values, K_c. Experiments were again performed at slow, intermediate, and dynamic loading rates, corresponding to crack tip strain rates of 10^{-5}, 10^{-3}, and 10 sec^{-1}, respectively. The state of fracture testing at the time necessitated the use of large specimens to achieve valid test results. Although compact tension specimens were fabricated at 2T, 4T, and 7T sizes, specimen thickness was limited by the as-rolled thicknesses of the plates. Researchers had difficulty in obtaining valid plane-strain behavior at temperatures above -140° F (-96 C) due to the validity requirements relating specimen thickness and test temperature. Even without valid data within a reasonable temperature range, relationships between CVN and K_c were presented. Dynamic tear and Nil-Ductility tests were also performed on the steel, the results of which agreed with all other test results.

The effect of strain rate was observed in the K_c data as the transition region experienced a temperature shift, decreasing in temperature as the strain rate was increased. Effects of temperature and plate thickness were also noted.

The second phase of the project, Low-Temperature Tests of Simulated Bridge Members, tested six full scale bridge girders fabricated from A36 and A572 grade 50 steels (Schilling, et al. 1972). Girders were purposefully designed with poor fatigue details, including cover end plates and transverse stiffeners. Loaded cyclically to create fatigue cracking, the girders were then loaded at low temperatures with impulse loads applied at a 1 second rate to approximate traffic loading until fracture occurred. It was shown that all girders exhibited sufficient toughness to resist fracture at -30 °F (-35 °C).

Comparisons with small specimen data for the A36 steel showed that the calculated stress intensity of the girders at fracture was consistently about 30 per cent lower than expected. Results of the A572 steel were not as consistent, with some girders achieving lower stress intensities than the small specimen tests, while others exhibited higher toughness. It was postulated that higher material toughness would not increase the service life of these bridge girders since the critical fatigue crack size was already approaching the fatigue life of the member.

2.6.2 Irwin and Roberts 1972

The initial phase of an FHWA investigation into the fracture behavior of bridge steels, this study examines the methods used to determine fracture toughness (Irwin and Roberts 1972). Three different bridge materials were used as part of this study: A36, A441, and A514 steel. Each type of material was examined through numerous test methods including CVN impact, static and dynamic fracture toughness, and R-curve characterization. Although presented in this report, the results of these material tests are included in a more comprehensive manner with the additional data collected with phase two of this project (Roberts, et al. 1974).

Introduced in this report is the “leak-before-burst” fracture criterion, adopted from the pressure vessel industry. Employing this criterion assumes that the length of a surface crack will be approximately twice the plate thickness as it grows into a through crack. If toughness were guaranteed that could prevent fracture initiation from a defect of this length, a pressure vessel would leak prior to catastrophic failure, and thus the flaw would be detected. Irwin and Roberts recommend using this approach in setting toughness standards for bridges. In the calculation of required stress intensity, it is recommended that an anticipated nominal service stress should be

used. Multiple CVN-K_c correlations are examined, but the authors state that more data is needed to make any conclusive recommendations.

As the primary goal of this study was to validate test methods for evaluating fracture toughness of bridge steels, recommendations are made to this end. The authors feel that the combination of CVN, K_c, and R-curve testing provides sufficient information for researchers examining the fracture resistance of bridge steels.

2.6.3 Wolff and Martin 1973

Steel components from four different in-service bridges were sampled in order to characterize their physical, chemical, and metallurgical properties, and to quantify levels and causes of deterioration (Wolff and Martin 1973). The bridge components were removed from structures in Maine, West Virginia, Vermont, and New York, constructed in 1904, 1906, 1935, and 1915, respectively. Testing included multiple visual inspections and non-destructive tests, chemical composition analyses, and destructive testing such as tensile, CVN, hardness, fatigue crack growth, and fracture toughness testing.

Three CVN impact specimens were tested from each bridge component at 20, 0, and -30 °F (-6, -18, and -34 °C), as well as room temperature (ranging from 70 to78 °F), for a total of 12 specimens tested per component. Tests of both the Maine and West Virginia steels proved the materials to be of poor quality. CVN energy values for the Maine steel was never able to leave the lower shelf region, while the West Virginia steel did reach lower transition at 78°F (26 °C), although only one specimen exceeded 10 ft-lbf (14 J). Steel from the New York bridge was able to enter the transition region at 75 °F (24 °C), with an average value of 31 ft-lbf (42 J) at this temperature. The steel sampled from the Vermont bridge exhibited the best impact properties,

reaching upper shelf behavior at room temperature, and mid-transition at 0 and 20°F (-18 and -7 °C). It should be noted that for this steel upper shelf behavior averaged 51 ft-lbf (69 J), while mid-transition ranged from 14 to 26 ft-lbf (19 to 35 J). The authors of the study attributed the poor impact performance to elevated phosphorus levels in the steels.

For each steel sample, six C(T) specimens were fabricated and tested in accordance with ASTM E 399-72. All specimens were fabricated with a depth to thickness ratio of 4:1, and initial crack size to depth ratios ranged from 0.51 to 0.63. Three specimens of each plate were tested at 75°F (24 °C), while the other three were tested at -30°F (-34 °C). No tests from any of the four sources met the validity requirements to produce a value of K_{Ic}. Conditional stress intensity values, K_Q, were reported however. Failures of all specimens at the lower test temperature were described as brittle and unstable, and values ranged from 31 to 45 ksi√in (34 to 49 MPa√m). At the warmer test temperature, results were lower than expected for structural steels, with values ranging from 28 to 42 ksi√in (31 to 46 MPa√m). In general, the fracture tests followed the same pattern as the impact tests, with the Vermont steel performing the best and the Maine and West Virginia samples performing poorly.

Based on the results of these fracture toughness tests, the researchers calculated critical flaw sizes for a shallow and deep surface cracks. Using stress levels of 50, 75, and 100 per cent of yield, the authors concluded that it was unlikely for a critical defect to develop unnoticed in any of these bridges under normal service conditions.

2.6.4 Roberts, Irwin, Krishna, and Yen 1974

As the second part of the FHWA's investigation into the fracture toughness of bridge steels, this study examined eight different steels commonly used in the bridge industry (Roberts,

et al. 1974). The eight steels examined in this study are A7, A36, A242, A440, A441, A588, A514, and A517. This report included the steels tested as part of phase one of the study. Specimens were machined from 22 plates of 0.5, 1, and 2 in. (12.7, 25.4, and 50.8 mm.) thickness. Data for both static and dynamic fracture toughness, as well as dynamic tear and Charpy impact data were obtained over a broad range of temperatures, fully characterizing the temperature dependence of the materials. The findings of the experimental program were then compared to the AASHTO material toughness requirements current at that time.

For each type of steel full temperature transition curves were developed using Charpy specimens, both standard notched and fatigue precracked specimens. These tests were performed at three different loading rates, designated impact, intermediate, and slow bend. Typical results at low temperatures indicated a convergence of fracture energy on the lower shelf for both specimen types and all testing speeds. Above this bottom shelf convergence, a temperature shift was observed as loading rates were increased. Higher rate tests displayed lower toughness when compared with slower rate tests at the same temperature. A similar shift was observed in the relationship between notched and precracked specimens, with precracked specimens displaying lower toughness.

Static and dynamic toughness tests were performed on three point bend specimens of varying thicknesses. Rate dependence was also observed in these tests, with dynamic toughness, K_{Id}, data displaying a reduction in toughness compared with static fracture toughness, K_c, tested at the same temperature. Values from R-curve tests were used to extend the static K_c results to higher temperature ranges. Fracture toughness data was compared with predicted toughness

values obtained using the Barsom temperature shift *CVN*-K_c correlation. In general this correlation proved to be a reasonable estimate of K_c.

In addition to small scale test specimens, four full scale beams were constructed and tested at a temperature of -50 °F (-45 °C). All four W14x30 beams were made of A36 steel, and each had a precracked coverplate detail in order to facilitate fracture. Two of the beams failed in catastrophic fashion due to rapid crack propagation, while the other two failed due to web buckling and plastic hinge formation, respectively. Using fracture mechanics and small specimen test data, failure loads were estimated with reasonable results. However, the authors of the report cautioned that more full scale testing was needed to validate the prediction methods used.

Results of the study were examined in light of the AASHTO material toughness standards at that time. The majority of the steels met the CVN requirements in at least one of the three temperature zones, with 11 of the 22 plates meeting requirement for the lowest temperature zone. Only the A7 steel was unable to meet the material toughness requirements for any of the temperature zones. Comparing CVN requirements with fracture toughness data, the authors indicated that the requirements current at that time were adequate for normal redundant bridge design. Concern over dynamic fracture led the authors to caution that requirements were not adequate for non-redundant structures. This was due to the fact that CVN requirements were based on correlations with static K_c values.

2.6.5 Hartbower and Sunbury 1975

This study examines the fracture toughness of steels from two California bridges that were simultaneously being constructed in 1970 (Hartbower and Sunbury 1975). While the concrete deck was being placed, one of the three tension flanges of the Bryte Bend bridge

experienced a brittle fracture. The Tuolumne River bridge, simultaneously under construction, was employing the same types of steel, ASTM A517 Grades F and H. At the time of design and material purchase, fracture toughness of A517 steel was assumed to be adequate for bridges and no toughness requirements existed, although material toughness specifications were implemented prior to this study. Following the fracture of the Bryte Bend flange, a review of both bridges was ordered. This report examined the variability in fracture toughness of the A517 steels, as well as the A514/517 steels used in the retrofits of each bridge.

Tension, CVN impact, drop weight tear, C(T) fracture toughness, and fatigue crack growth tests were employed to assess the variability found across multiple variables. Variability was evaluated among different heats, grades (H and F), ignots, and types of steel (A514 and A517). Variability with respect to plate thickness and rolling direction was also examined. Seventy six plates of steel were examined across thirty heats.

Initial CVN impact testing was performed in triplicate at the LAST for each bridge. This corresponded to 0 °F (-18 °C) for the Tuolumne bridge and 20 °F (-7 °C) for the Bryte Bend bridge. In addition to this, single specimens were also tested at -40, 0, room temperature, and 120 °F (-40, -18, room temperature, and 49 °C). Other test temperatures were then chosen based on the results of these tests in order to characterize the material over the full temperature transition range. Steels sampled from the two bridges exhibited very low toughness, with no tests meeting the AASHTO CVN requirements existing at the time of testing. CVN tests of steel provided for repair of both bridges by and large were shown to meet or exceed these requirements.

Fracture toughness testing was performed in accordance with ASTM E 399-70. Due to the expense and difficulty of fracture toughness testing, only selected plates and heats were

tested. Sixty seven fatigue pre-cracked C(T) specimens were tested over a temperature range from -320 to 200 °F (-196 to 93 °C). Forty two of these specimens had a thickness of one inch, while the other twenty five were two inches thick. Only twenty specimens total (ten of each thickness) met all validity criteria for K_{Ic} testing.

Results of the study led to recommendations for a design review of the two bridges, including extensive evaluation of susceptibility to fatigue crack growth. In addition, the authors recommended that due to toughness variability between heats and plates of A514/517 steels that rigorous test requirements be put into place prior to use in bridge construction. The final recommendation made in this study is an increase in the CVN requirements for future bridges fabricated from A514/517 steel from 25 to 30 ft-lbf (34 to 41 J).

2.6.6 Roberts and Krishna 1977

The fracture behavior of three different heats of A36 bridge steels were examined through both CVN impact tests and intermediate rate fracture toughness tests (Roberts and Krishna 1977). Data was obtained from two 1.5 in. (38.1 mm.) thick plates and one 2 in. (50.8 mm.) thick plate. The data obtained was used to test the validity of the AASHTO CVN requirements and the specified sampling procedures.

Specimens were machined from three locations in each of the three plates for a total of nine test locations. This was done to examine the difference between Heat (H) and Plate (P) sampling frequencies. These two sampling frequencies differ in that one impact test, defined as a group of three CVN specimens, must be made for each heat in H frequency, while one test is required for each plate produced in P frequency. It was shown that H frequency is not adequate for steel to be used in fracture critical details. Going beyond P frequency sampling, the authors

recommended that each piece of steel being used in a fracture critical application be tested. This recommendation means that if multiple pieces are cut from the same plate, each individual piece needs to be tested.

This test program also examined the Barsom *CVN*-K_c temperature shift correlation. K_c values were obtained through the use of three point bend specimens loaded at an intermediate rate, which produced failure in approximately one second. It was shown that this correlation produced conservative results for the collected data.

2.6.7 Roberts, et al. 1977

The primary goal of the FHWA project was to examine the effects of flaw size on the fracture performance of bridge girders (Roberts, et al. 1977). Testing was performed on 24 full size bridge girders fabricated from A36, A588, and A514 steels. Fatigue prone details such as transverse stiffeners, cover plates, flange transitions, and lateral attachments were included to introduce fatigue cracks within approximately 2 million cycles of loading. Similar to other full scale tests, impulse loads were then applied at low temperatures to initiate fracture.

In addition to the large scale tests, complimentary small scale fracture mechanics tests were performed for each plate thickness. Standard CVN impact tests were performed, along with Nil-Ductility and pre-cracked CVN tests, the latter of which was performed to examine the effects of notch acuity on correlations between CVN and plane-strain fracture toughness values. Data from standard CVN testing was used, along with the Barsom and Rolfe temperature shift, to determine the approximate test temperatures for three point bend fracture toughness tests. The results were compared with both the large scale test results and the CVN data.

Results showed that the slow bend K_{Ic} tests best approximated the stress intensity values in large scale testing, confirming that this 1 second loading rate approximates full scale conditions. Examination of both CVN and *K* results revealed that the empirical Barsom and Rolfe correlation process was conservative for the majority of steels tested. The only exception to this was the A36 rolled flange plate, for which the correlation yielded unconservative results. Temperature shifts related to load rate were also confirmed, as the observed shift was always greater than or equal to that predicted by Barsom's empirical approximation.

2.6.8 Kendrick, Smith, and Crozier 1980

This project examined the fracture behavior of typical structural steels used in bridge construction (Kendrick, et al. 1980). Two plates each of A36 and A441 steel were tested, investigating their fracture resistance at various loading rates. The resulting data was used to evaluate existing CVN-K_c correlations and to develop a new method of predicting fracture behavior of structural steels.

For each of the four plates of steel a battery of tests were performed. Tensile tests were conducted at 32 and 70 °F (0 and 21 °C) and a CVN temperature transition curve was developed. Pre-cracked Charpy specimens were also tested over various temperature ranges at both static and impact loading rates. Four compact tension specimens were tested at 32 °F (0 °C) for each plate, two at static load rates and two at intermediate bridge load rates.

Evaluation of *CVN-K* correlations were made with multiple correlation procedures. The Barsom and Rolfe Two Stage Correlation, codified in material toughness specifications for bridges, was shown to be unconservative due to the temperature shift employed. The report recommended that toughness specifications need to be based on CVN impact tests conducted at

the anticipated service temperature. CVN limits based on material yield stress and component size were also recommended. Meeting these limits eliminates brittle fracture by ensuring that a structure experiences yielding prior to fracture initiation.

2.6.9 Crosley 1984

Following reported cracks in the support columns of the Fort Duquesne bridge, the Pennsylvania Department of Transportation initiated an investigation into the bridge's potential for fracture (Crosley 1984). This investigation included the testing of tensile, CVN, and fracture toughness specimens taken from core samples of the flange, which was composed of 2.5 in. (63.5 mm.) A517 steel plate. Existing cracks and welded repairs were also studied as part of this analysis.

Twenty four CVN impact tests were performed over a range of temperatures, and two disk shaped compact tension specimens were tested at an intermediate load rate at a temperature of -30 °F (-34 °C). Because specimens were machined from cores of the flange steel, their orientation with respect to plate rolling direction is unknown. However, the same orientation was used for both types of specimens.

Neither of the two fracture toughness specimens were able to produce purely valid K_{Ic} values, although the results can still be used to analyze the fracture performance of the material. Using the Barsom temperature shift *CVN*-K_c correlation, the author of the study compared the CVN results to the invalid fracture toughness data. This correlation proved to be an accurate prediction of fracture toughness for the two tests performed.

2.6.10 Ripling, Crosley, and Armstrong 1990

The two phase program examined the transition behavior of bridge steels and weldments. Part one involved the examination of the micro-mechanics of fracture (Ripling, et al 1991). Laboratory testing showed that yield strength and fracture of low carbon steel could be greatly influenced by two metallurgical variables and three external service variables. The variables are the individual ferrite grain strength and diameter, and the temperature, strain rate, and residual strain at testing, respectively. Physical microstructure evidence showed that commonly used loading rate and temperature dependence of stress and fracture are to be expected.

The second and larger part of the study examined the fracture behavior of one and two inch (25 and 50 mm) thick A572, A852, and A514 plates, as well as different weldments (Ripling, et al. 1990). At the time of this study, elastic-plastic fracture techniques had been established. Thus, testing was performed with CTOD specimens, as well as standard K_c and CVN test methods. CTOD tests were chosen because of their applicability to specimens of various thicknesses. This allowed researchers to effectively study the impact of thickness, something that was not possible with the validity requirements of K-based testing. In the report, Ripling is critical of the use of K_c in setting fracture toughness standards for bridges, due to its invalidity beyond plane-strain behavior. CVN limits are set to avoid plane-strain fracture, and the argument is made that these limits are based on tests that are either invalid, or not measured in a usable temperature range.

Examining the Barsom and Rolfe correlation, the study showed that it worked well for most cases, providing conservative estimates of fracture toughness. However, the two-stage correlation including temperature shift yielded unconservative results for the two inch [50 mm]

thick A852 and A514 heat treated plates. Although further research into the reasons for this are necessary, it was hypothesized that this unconservativism is due to the sampling location of CVN specimens. Although CVN specimens are sampled from quarter thickness points, cracks initiate at the plate midplane, where constraint is highest. Sampling of CVN specimens from the midline of plates is recommended if this behavior is observed in other test programs.

2.7 Development of HPS Grade Bridge Steels

The history of structural steels includes many steel grades that can be considered high strength and high performance, although a distinction should be made between the two. Traditional high strength steels, commonly used in bridges in the 1960's and 1970's, have earned a poor reputation for performance in areas other than strength. Difficulty in welding these steels created defects that could cause fractures just after fabrication, even prior to erection (Dexter, et al. 1994). Advances in steel production technology have allowed bridge engineers to follow the lead of other industries in using high performance steels. HPS steels can not only exhibit higher strength than conventional steels, but can also show better weldability, fracture toughness, durability, and ductility.

2.7.1 History of HPS Bridge Steels

A cooperative research program was implemented in 1994 to develop high performance steels for bridge applications. Gaining from the experience of the ship building industry in producing steels of extremely high strength and toughness, FHWA worked with the US Navy and AISI in this endeavor (Hamby, et al. 2002). Initial goals of the program were to develop HPS 70W and HPS 100W weathering steels with improved weldability and adequate AASHTO Zone

III toughness. However, with the immediate success of HPS 70W, bridge engineers requested an HPS version of grade 50 weathering steel, which became a part of the development program.

Three years after the start of this cooperative research effort, the first HPS 70W highway bridge was put into service in 1997. Since that time, bridge girders have been fabricated both exclusively with HPS 70W, and with HPS 70W and conventional steel to create an optimized, hybrid system. There are currently more than 140 bridges in the United States fabricated with HPS grade steel (Steel Market Development Institute 2011).

2.7.2 Present Day HPS Grade Bridge Steels

As with the development of any new material, changes in the composition of HPS have occurred over time as production methods and techniques have been refined. Refinements in steel chemistry were made to ensure consistently reproducible strength, toughness, weldability, and weathering capabilities. The current required chemical composition of HPS 50W, 70W, and 100W are presented in Table 2-4 (ASTM 2013).

Table 2-4. Heat Analysis Chemical Requirements

Element	Composition, %	
	HPS 345W (HPS 50W) HPS 485W (HPS 70W)	HPS 690W (100W)
Carbon	0.11 max	0.08 max
Manganese 2.5 in. [65 mm] and under	1.10-1.35	0.95-1.50
Manganese over 2.5 in. [65 mm]	1.10-1.50	N/A
Phosphorus	0.020 max	0.015 max
Sulfur	0.006 max	0.006 max
Silicon	0.30-0.50	0.15-0.35
Copper	0.25-0.40	0.90-1.20
Nickel	0.25-0.40	0.65-0.90
Chromium	0.45-0.70	0.40-0.65
Molybdenum	0.02-0.08	0.40-0.65
Vanadium	0.04-0.08	0.04-0.08
Columbium	No Requirement	0.01-0.03
Aluminum	0.010-0.040	0.020-0.050
Nitrogen	0.015 max	0.015 max

Because the total allowed alloy percentage is less than 8 per cent and the carbon content is capped at well under 0.2 per cent, HPS grades are considered low-carbon, low-alloy steels. This limit on carbon allows HPS to retain ductility and toughness, as well as improving weldability. This low level of carbon allows for welding with little or no preheating (Wilson, et al. 1988). However, higher carbon content is usually associated with higher strength. For this reason, other alloys are introduced into the melt to increase strength. Some of these elements included for strength increase purposes are manganese, silicon, copper, nickel, chromium, vanadium, and molybdenum (Degarmo 2003). Limits have also been set on phosphorus, sulfur, and nitrogen, as these elements can have detrimental effects on the performance of a heat.

Many of these alloying elements provide multiple benefits to HPS. Inclusion of copper and nickel in HPS, called the Cu-Ni system, has been optimized to produce desired toughness

and strength, as well as corrosion resistance important in weathering steels. Copper also improves the hardenability of the steel. Inclusion of molybdenum also helps reduce embrittlement and, along with chromium, retards tempering during post-roll processing.

For the interested reader, details on the development of the chemical composition of HPS is presented in the literature (Gross and Stout 1995, Gross and Stout 2001, Gross, et al. 1998, Wilson 2002). Grades 345 (50) and 485 (70) steels are available as-rolled, control-rolled, thermo-mechanical control processed (TMCP), or quenched and tempered (Q&T) (ASTM 2013). Questions have arisen over the consistency of the TMCP process with thick plates. Thus, more research is needed to determine the effect of TMCP on material behavior.

2.8 Fracture Toughness Programs Examining HPS Bridge Steel

Although there was much research involved in the development of HPS for bridge applications, little has been done in terms of characterizing the material's fracture behavior. Only one previous program has been implemented to study this behavior. A brief overview of this study is provided here.

2.8.1 Fracture Initiation Resistance of I-Girders Fabricated from HPS, 2003

This research was designed to evaluate the ability of bridge girders fabricated from HPS 485W (70W) and HPS 690W (100W) to resist initiation of brittle fracture (Wright 2003). The focus of this research was on the testing of six full scale bridge girders. Prior to full scale girder tests, both materials were characterized through CVN impact testing and fracture mechanics testing. A total of seventy two C(T) specimens were tested over a range of temperatures at both static and dynamic loading rates. Of these seventy two specimens, only three yielded valid K_c

tests results, while the others required elastic-plastic analysis to characterize the fracture behavior. Because of this, all data is presented in terms of J.

Similar to previous full scale girder fracture investigations, each specimen was cyclically loaded at room temperature to create fatigue cracks. Girders were then cooled and subjected to an over load in attempts to produce fracture. If fracture did not occur, fatigue cracks were grown to larger sizes and overloads were again applied. Results indicated that girders fabricated from HPS 70W were able to reach their elastic limit load prior to fracture failure. However, the higher strength HPS 100W was unable to reach yield on the net section prior to fracture. Recommendations included setting CVN material toughness criteria to ensure yielding of the net section for both grades of HPS.

2.9 Literature Review Summary

The main purpose of this literature review was to assess the current state of practice for material toughness specification in fracture critical steel bridge applications. This included a brief introduction into fracture mechanics and testing methodology for fracture toughness, as well as a history of bridge fractures. A review of the fracture control plan was presented, including its development and current requirements for flaw control through weld and fabrication detailing, in-service inspection criteria, and material toughness specifications. A discussion of previous experimental programs focusing on the fracture of conventional bridge steels was provided. These programs provided the basis and validation of the current fracture control plan. The development of high performance steels for bridge applications was also summarized, including the history of its development and implementation, and the current state of HPS in the

bridge industry. Finally, the study examining the fracture behavior of modern HPS was presented in this literature review.

Chapter 3: Experimental Procedure

This section presents details of the specific plates of steel tested as part of this research program. Within each plate, the locations and orientations of all specimens are presented. Experimental testing procedures, including tensile, CVN, static and dynamic fracture toughness, and crack arrest testing methods, are also presented in this section.

In total, 636 fracture specimens are fabricated and tested as part of this study. This includes 246 CVN impact, 209 static fracture toughness, 126 dynamic fracture toughness, and 55 crack arrests specimens.

3.1 Plate Designations and Sampling Procedure

3.1.1 Plate Designations

Test specimens were fabricated from eight different HPS plates of varying grade and thickness. Each plate was designated a letter for specimen and testing numbering purposes. Details of each tested HPS plate, including letter designation, grade, thickness, and heat number can be found in Table 3-1.

Table 3-1. Designations and Details of HPS Plates

Letter Designation	Grade, MPa (ksi)	Thickness, mm. (in.)	Heat/ID Number
A	485 (70)	25.4 (1.0)	801W10170
C	690 (100)	19 (0.75)	W24549 55 W4
D	485 (70)	63.5 (2.5)	U5191-6A
E	690 (100)	38.1 (1.5)	P60017 W24549
F	690 (100)	50.8 (2.0)	T1W24594
H	485 (70)	31.8 (1.25)	HT813C7220
I	485 (70)	31.8 (1.25)	HT822H34790
J	485 (70)	38.1 (1.5)	821T06770

In addition to these HPS plates, fracture toughness specimens were fabricated from five different conventional steels sampled from in-service bridges. Each of these plates was also given a letter or number designation, and the details of these five plates can be found in Table 3-2. Because these plates were taken from in-service bridge members, the plate heat numbers are unknown. For this reason, grades presented in Table 3-2 are average yield strength values taken from tensile tests.

Table 3-2. Designations and Details of Conventional Plates

Letter Designation	Grade, MPa (ksi)	Thickness, mm. (in.)
R	330 (48)	25.4 (1.0)
B	282 (41)	38.1 (1.5)
4	243 (35)	31.8 (1.25)
P	190 (28)	63.5 (2.5)
M	241 (35)	12.7 (0.5)

3.1.2 Sampling Procedure and Specimen Layout

Specimens were fabricated from the plates at specific locations and in specific orientations. All tension specimens were sampled at mid-thickness and oriented with the

longitudinal axis in the direction of rolling. As specified in ASTM A 673-07, CVN specimens are to be centered at one-quarter plate thickness (ASTM 2007). All CVN and SE(B) specimens tested as part of this study were located at this depth. The only exceptions to this are in plates C and M, where plate thickness prohibited this practice. For plate C specimens were centered at one-third plate thickness, while plate M specimens were centered at mid-thickness. In addition, a limited number of CVN tests were performed for each HPS plate sampled at mid-thickness. A limited number of SE(B) specimens were also sampled from the conventional steel plates at mid-thickness.

The majority of CVN specimens and all of the SE(B) and crack arrest specimens were oriented such that the crack propagates perpendicular to the rolling direction of the plate. This is referred to as L-T orientation, as seen in Figure 3-1. For comparison purposes a limited number of CVN tests were performed on specimens from the T-L orientation. Crack arrest specimens were fabricated at plate thickness unless the plate was greater than 50.8 mm. (2 in.), in which case the specimens were centered at mid-thickness and cut down to 50.8 mm. (2 in.). Like CVN and SE(B) specimens, crack arrest specimens were machined in the L-T orientation.

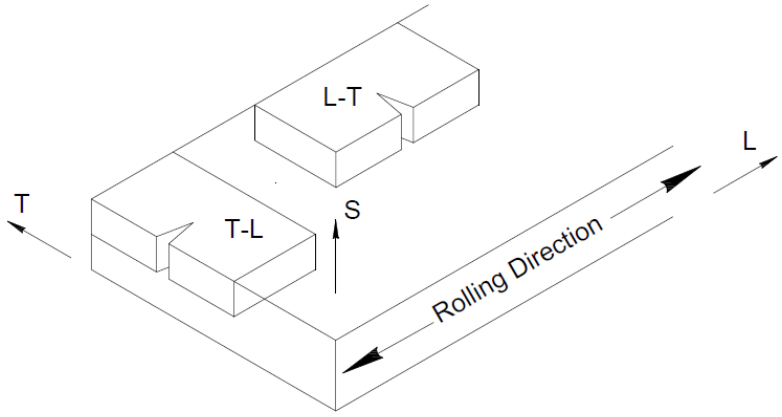

Figure 3-1. Specimen Orientation Designations

Specimen identification marking included the plate letter as well as a unique identifying number. CVN specimens were designated with only these two markings. SE(B) specimens were identified with a prime following the letter and number designation, while arrest and tension specimens were labeled with an a and t following the number designations, respectively. Following this pattern, specimen labels A1, A1', A1a, and A1t would indicate the first CVN, SE(B), arrest, and tension specimens removed from plate A.

Large plate sizes make saw-cutting specimens difficult, so smaller sections are typically cut out to provide a manageable section of plate. Specimens are then removed from these smaller sections. If the smaller sections are removed from the original plate with the use of a cutting torch, care is taken to avoid the heat affected zone when sampling specimens.

3.1.2.1 Plate A Specimen Layout

Plate A is a Grade HPS 485 W (70W) 25.4 mm. (1 in.) thick plate with dimensions of 2440 mm. and 1520 mm. (86 in. and 60 in.) in the longitudinal and transverse directions, respectively. A rectangular section measuring 250 by 430 mm. (10 by 17 in.) was removed from the corner of the full plate and specimens were located within this section as shown in Figure 3-2, Figure 3-3, and Figure 3-4. CVN and SE(B) specimens are centered at the quarter thickness point of the plate, except for CVN specimens A25, A26, and A27, which are centered at plate mid-thickness. Tension specimens A1t and A2t are centered at plate mid-thickness.

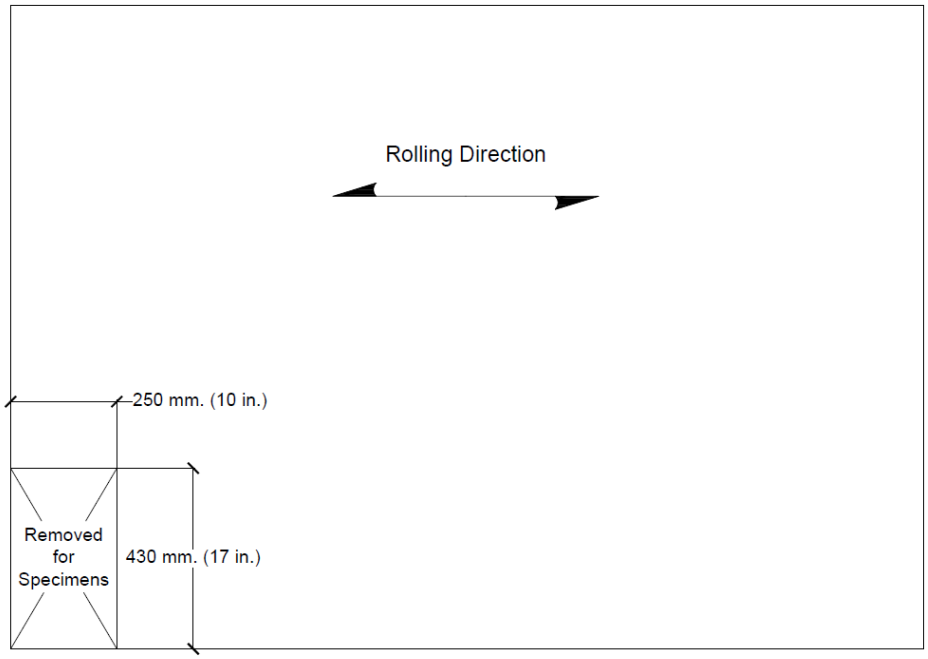

Figure 3-2. Plate A

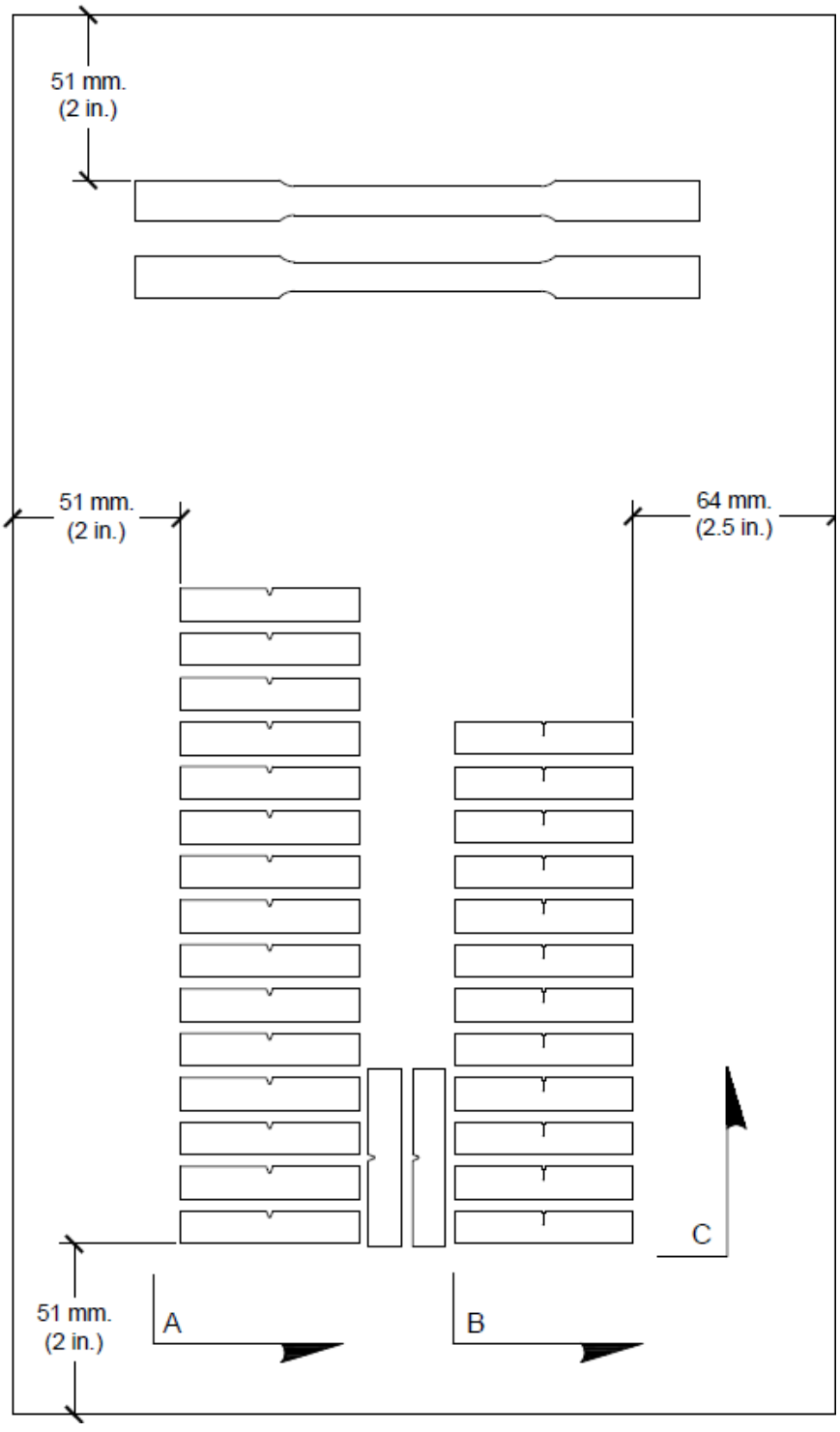

Figure 3-3. Plate A Specimen Cutout

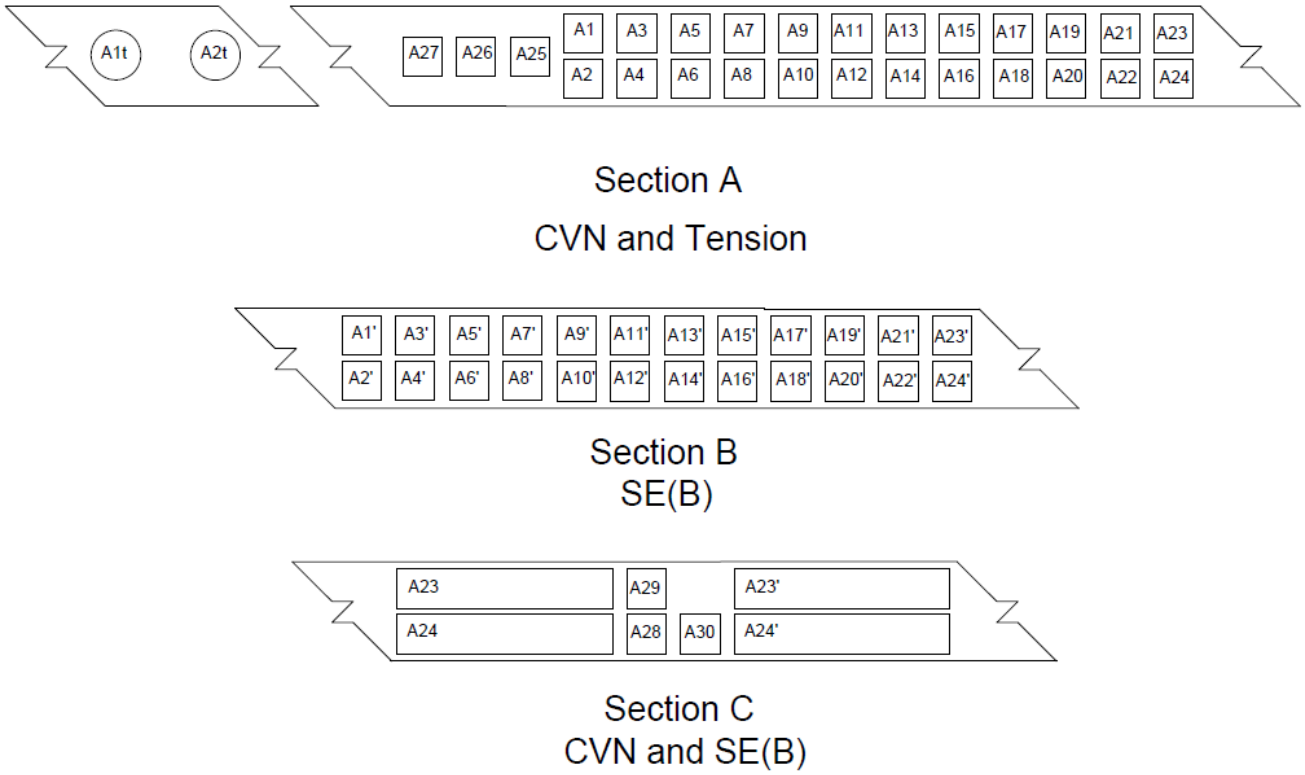

Figure 3-4. Plate A Specimen Section Views

3.1.2.2 Plate C Specimen Layout

Plate C is a Grade HPS 690 W (100W) 19 mm. (0.75 in.) thick plate with dimensions of 1580 mm. and 1170mm. (62 in. and 46 in.) in the longitudinal and transverse directions, respectively. A rectangular section measuring 305 by 430 mm. (12 by 17 in.) was removed from the corner of the full plate and specimens were located within this section as shown in Figure 3-5, Figure 3-6, and Figure 3-7. All CVN and SE(B) specimens are centered at the third point thickness of the plate, except for CVN specimens C25, C26, and C27, which are centered at plate mid-thickness. Tension specimens are also centered at mid-thickness.

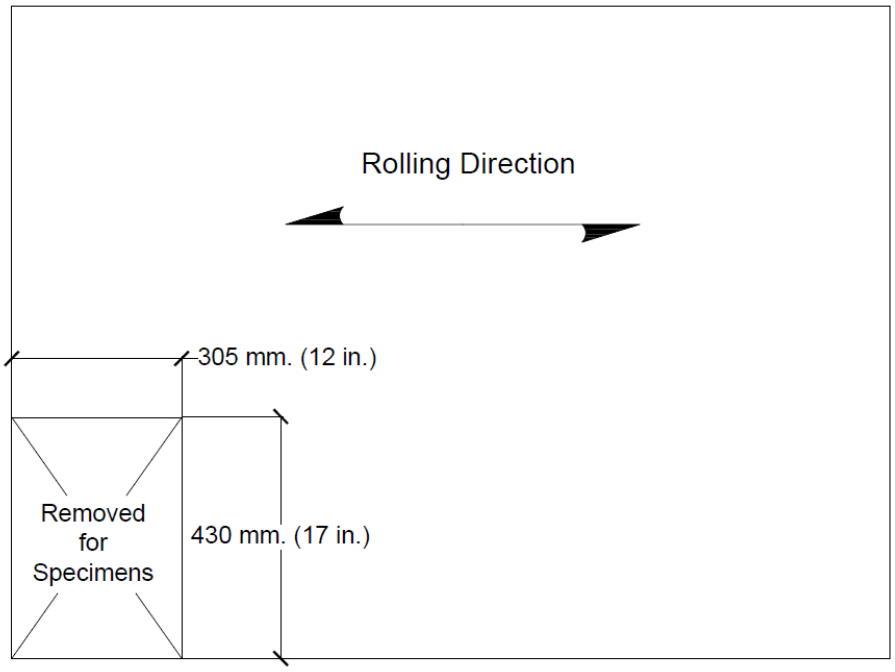

Figure 3-5. Plate C

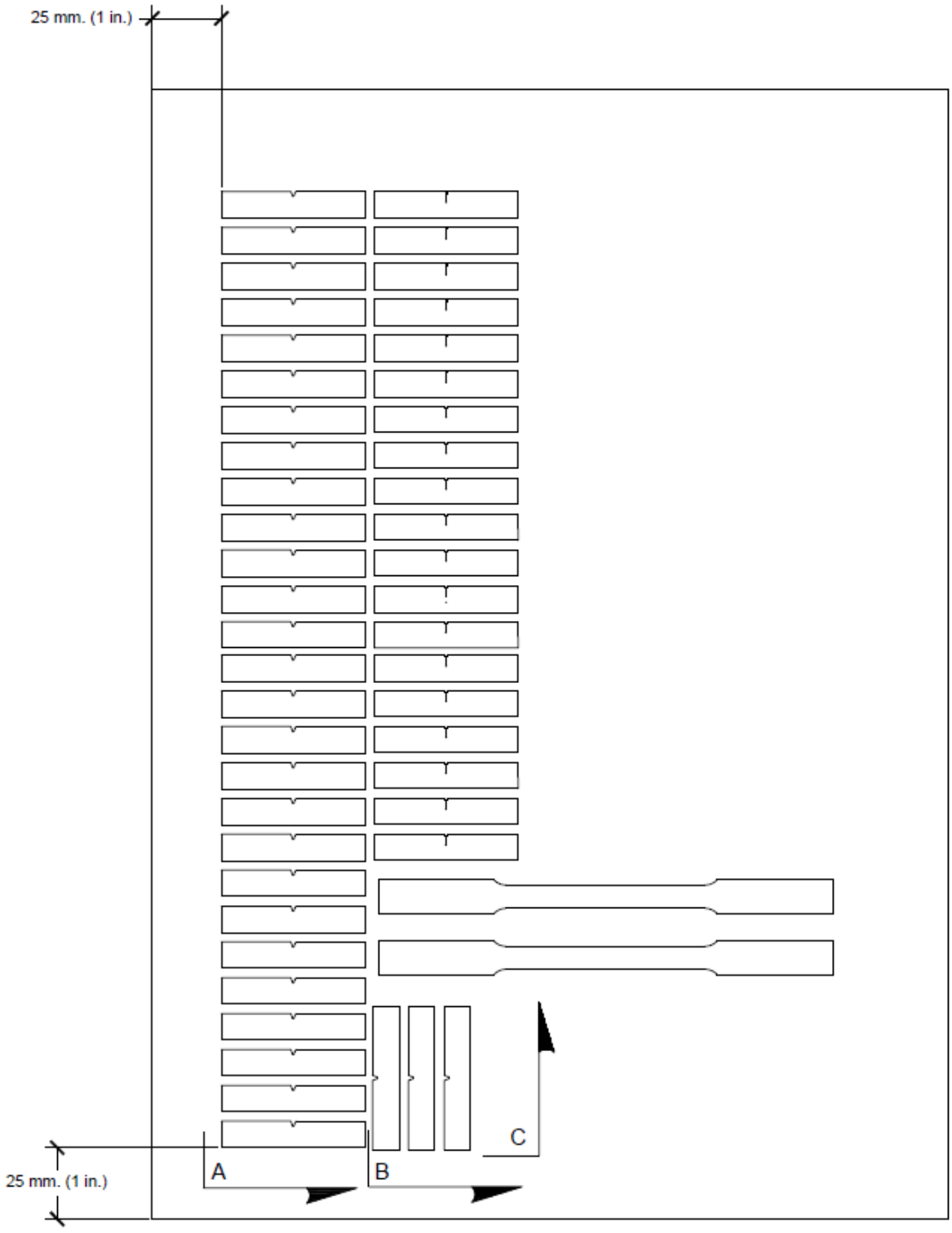

Figure 3-6. Plate C Specimen Cutout

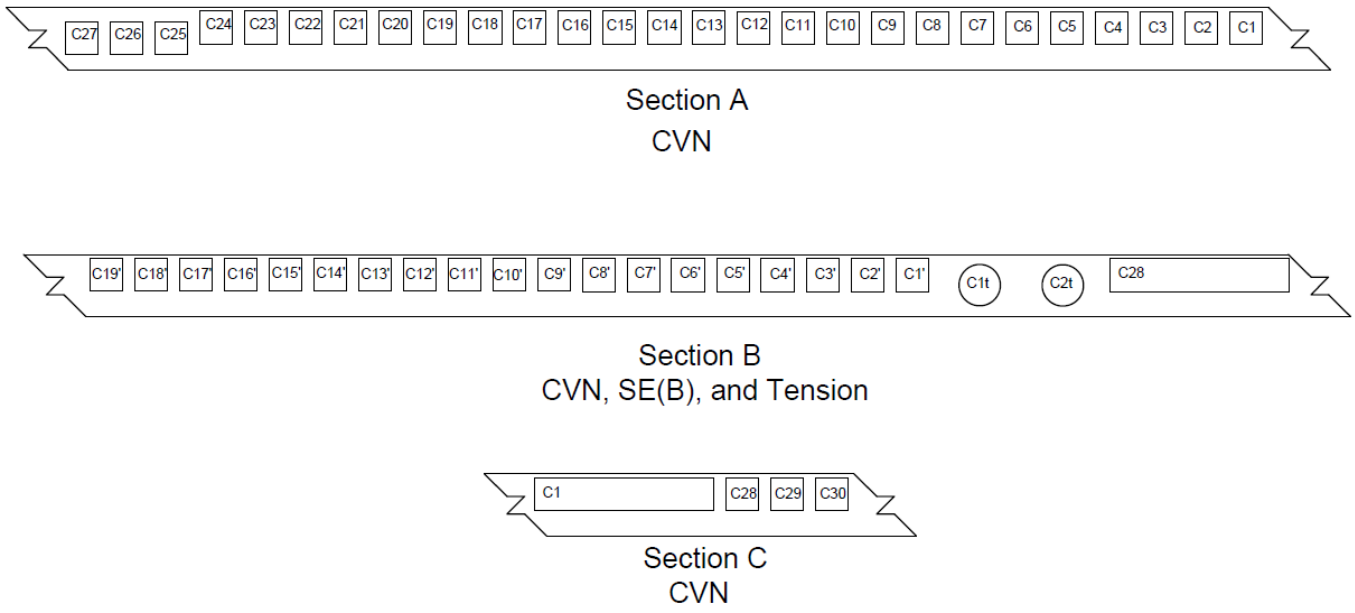

Figure 3-7. Plate C Specimen Section Views

3.1.2.3 Plate D Specimen Layout

Plate D is a Grade HPS 485 W (70W) 64 mm. (2.5 in.) thick plate with irregular dimensions. Semi-rectangular sections measuring roughly 270 by 480 mm. (10.5 by 19 in.) and 890 by 460 mm. (35 by 18 in.) were removed for CVN and SE(B) specimens, and crack arrest specimens, respectively, as can be seen in Figure 3-8.

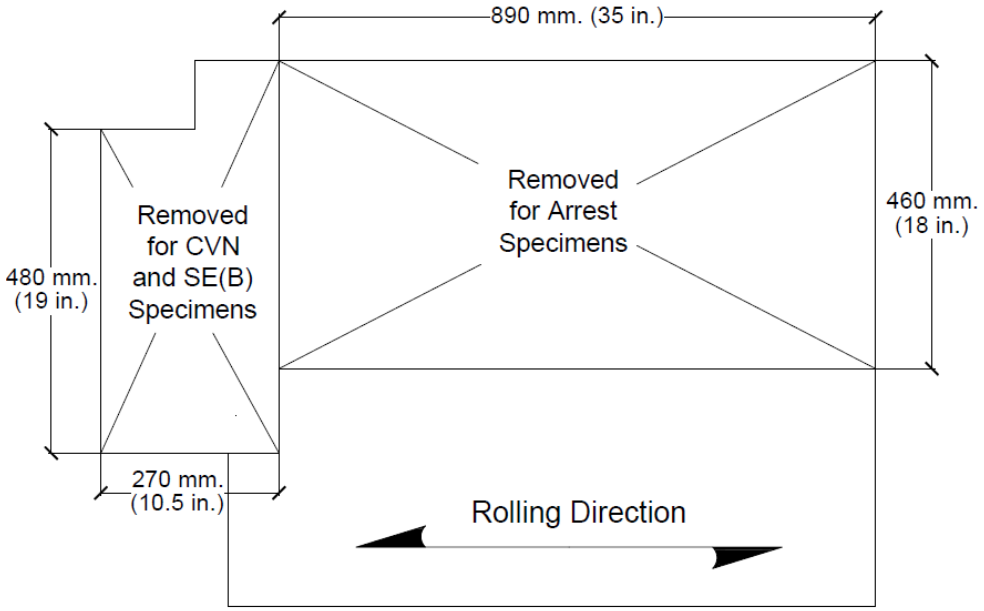

Figure 3-8. Plate D

CVN and SE(B) specimens are centered at the quarter thickness point of the plate, except for CVN specimens D25, D31, and D36, which are centered at plate mid-thickness. Mid-thickness specimens are located in between the layers of quarter-thickness specimens. To keep saw-cutting organized, blanks were numbered as cutting progressed, but not all were used for specimens. For this reason, there are no specimens corresponding to D26-D30, or D32-35. Layout details for all CVN and SE(B) specimens can be seen in Figure 3-9 and Figure 3-10. Crack arrest specimens, also oriented in the L-T direction, were centered at plate mid-thickness. Layout of crack arrest specimens can be seen in Figure 3-11.

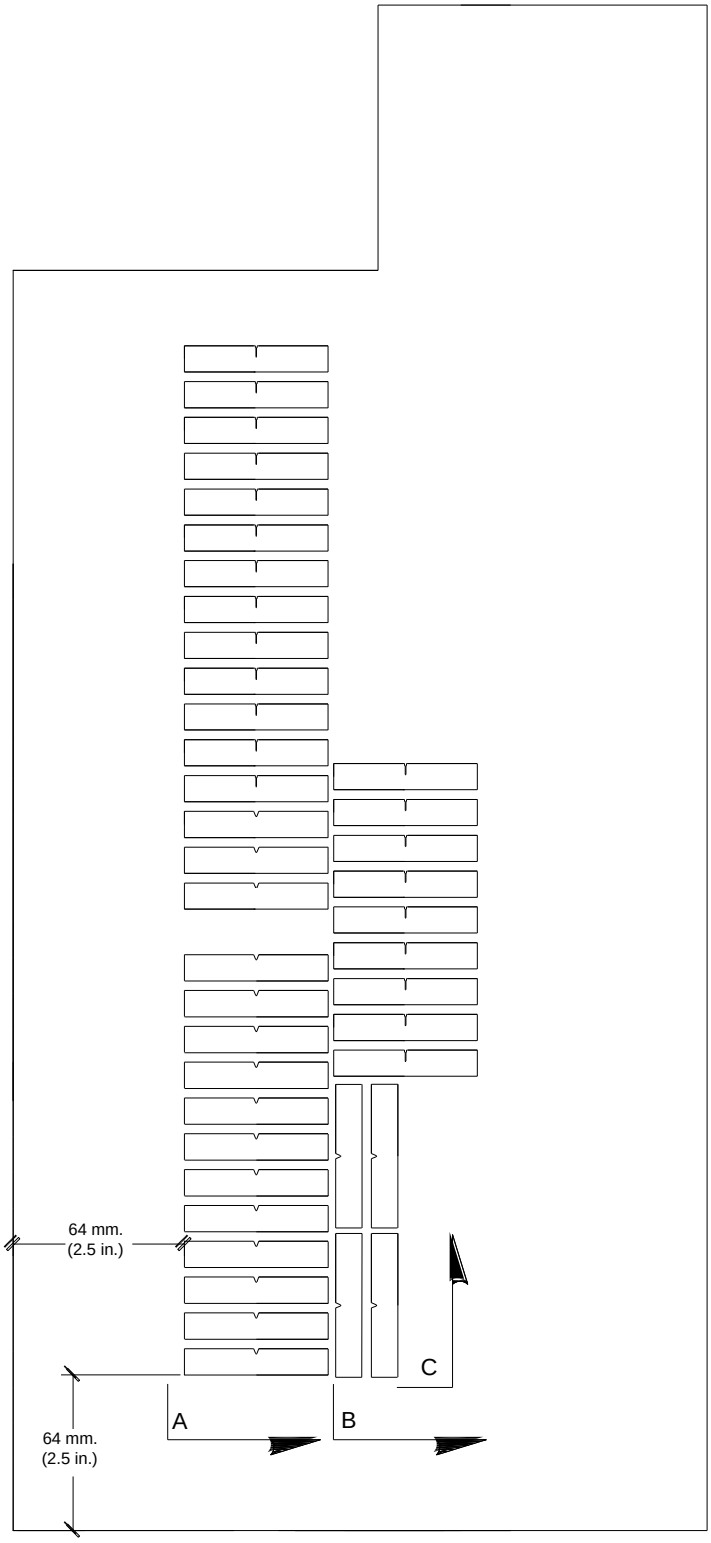

Figure 3-9. Plate D Specimen Cutout

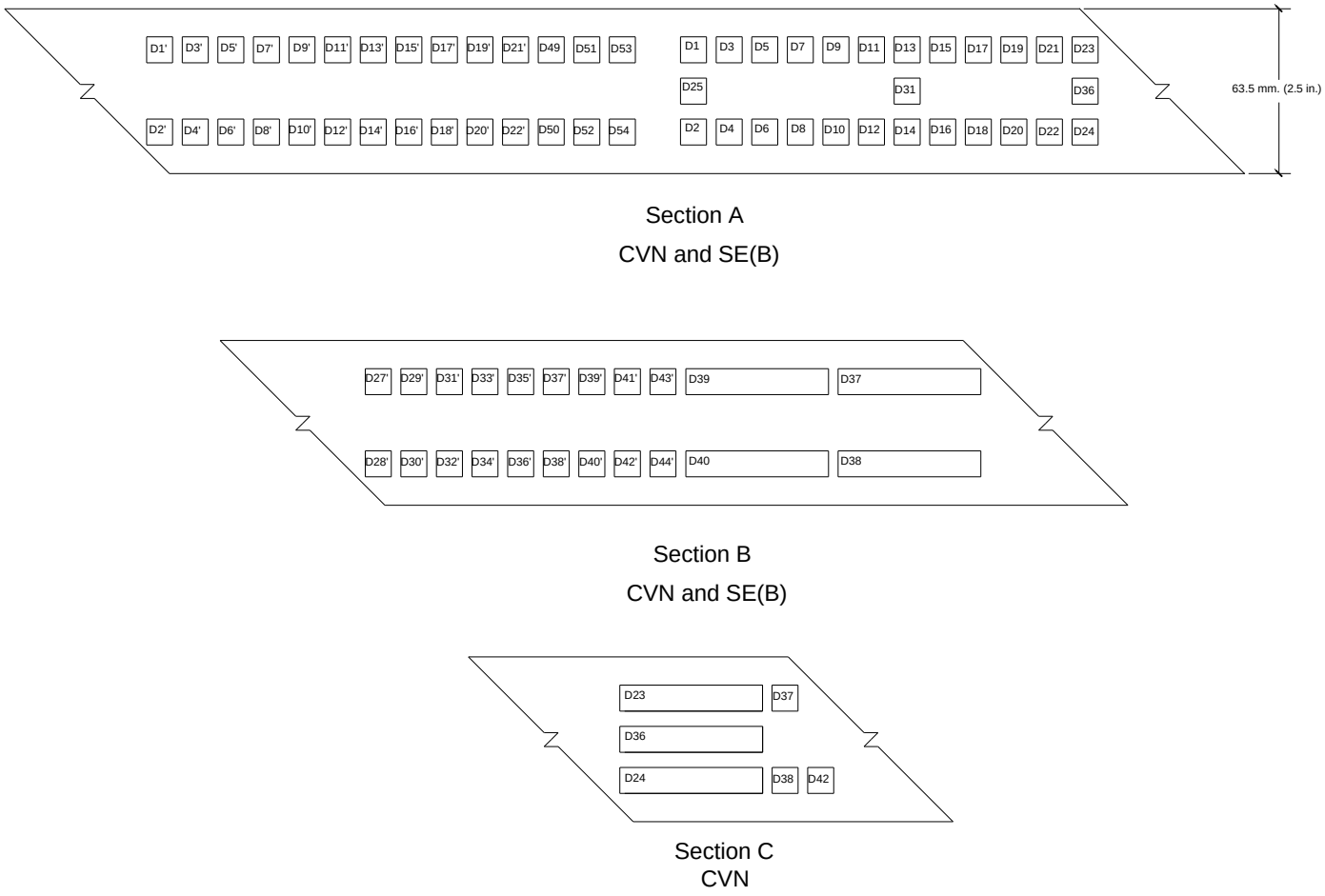

Figure 3-10. Plate D Specimen Layout

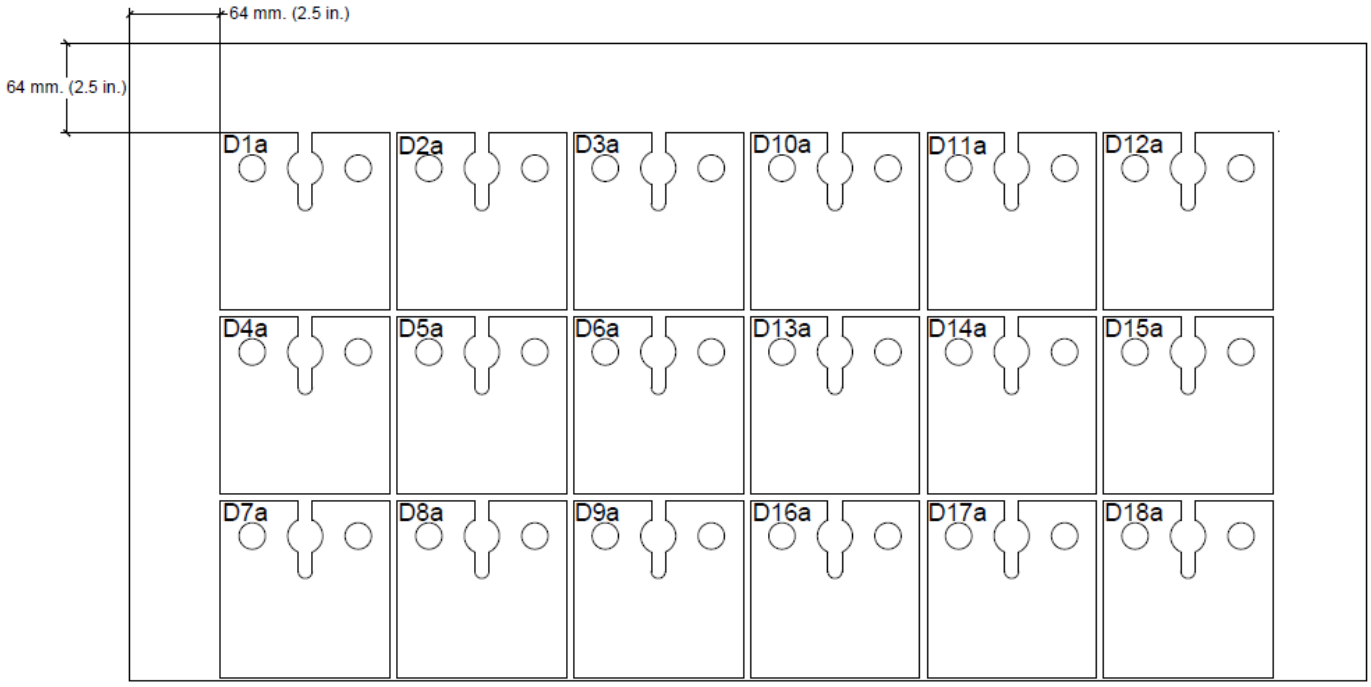

Figure 3-11. Plate D Arrest Specimen Layout

3.1.2.4 Plate E Specimen Layout

Plate E is a Grade HPS 690 W (100W) 38.1 mm. (1.5 in.) thick plate with irregular dimensions. Rectangular sections measuring roughly 203 by 432 mm. (8 by 17 in.) and 965 by 470 mm. (38 by 18.5 in.) were removed for CVN and SE(B) specimens, and crack arrest specimens, respectively, as can be seen in Figure 3-12. In between these two sections, a piece of steel was removed to be used in the fabrication of the crack arrest test setup. Because the original plate was over 5.5 m (18 ft.) long, only the end of the plate containing the test specimens is shown.

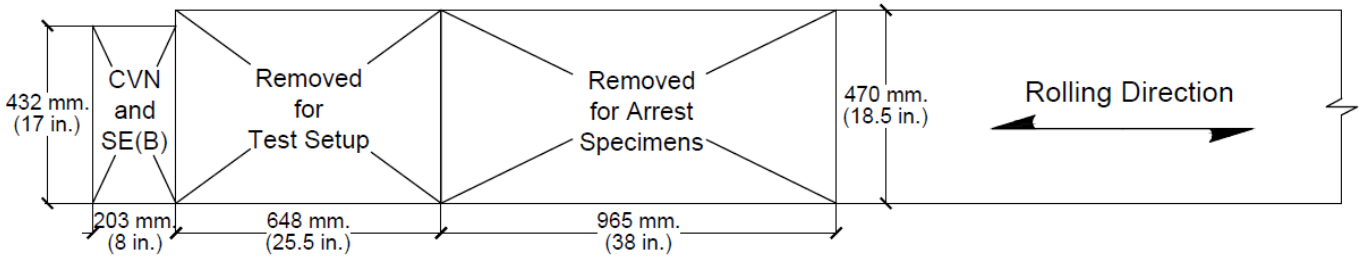

Figure 3-12. Plate E

CVN and SE(B) specimens are centered at the quarter thickness point of the plate, except for CVN specimens E25, E26, and E27, which are centered at plate mid-thickness. Layout details for all CVN and SE(B) specimens can be seen in Figure 3-13 and Figure 3-14. Crack arrest specimens were taken at full plate thickness, and the layout can be seen in Figure 3-15.

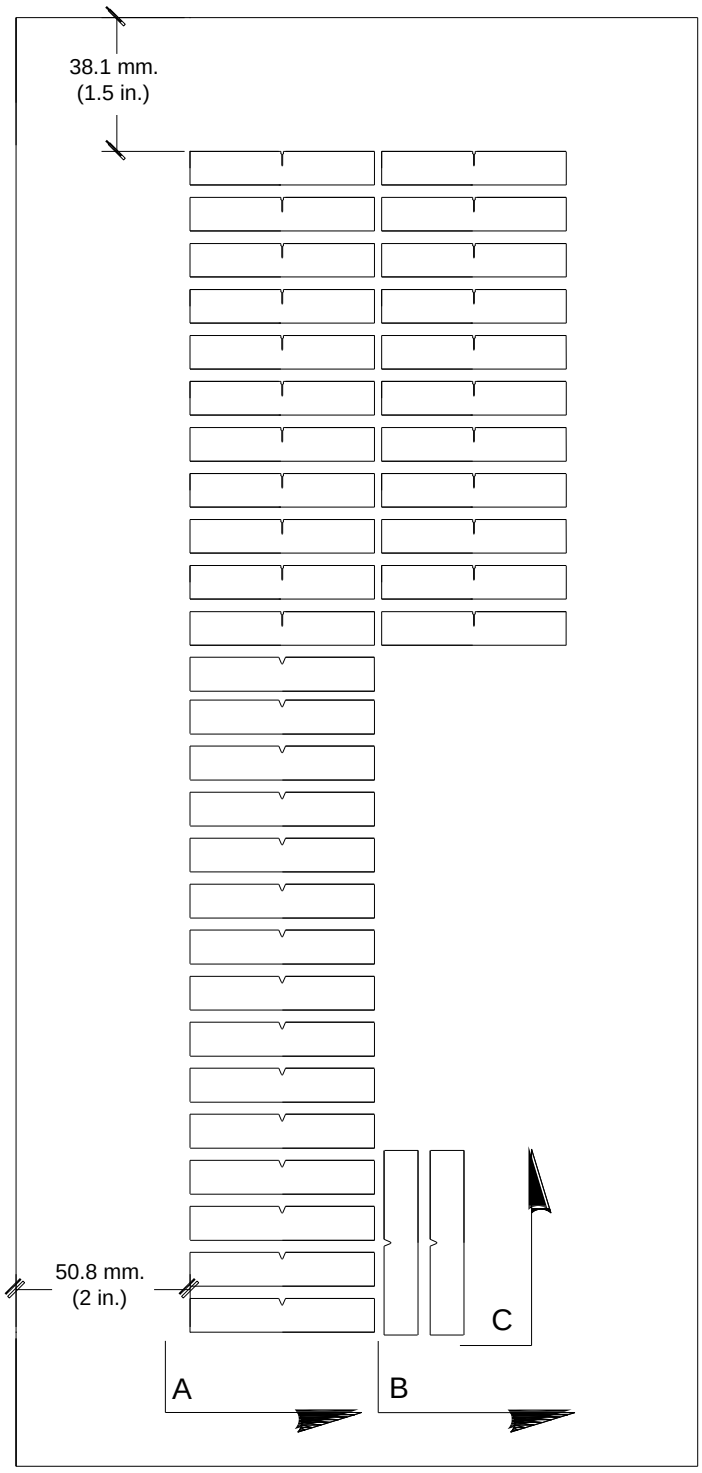

Figure 3-13. Plate E Specimen Cutout

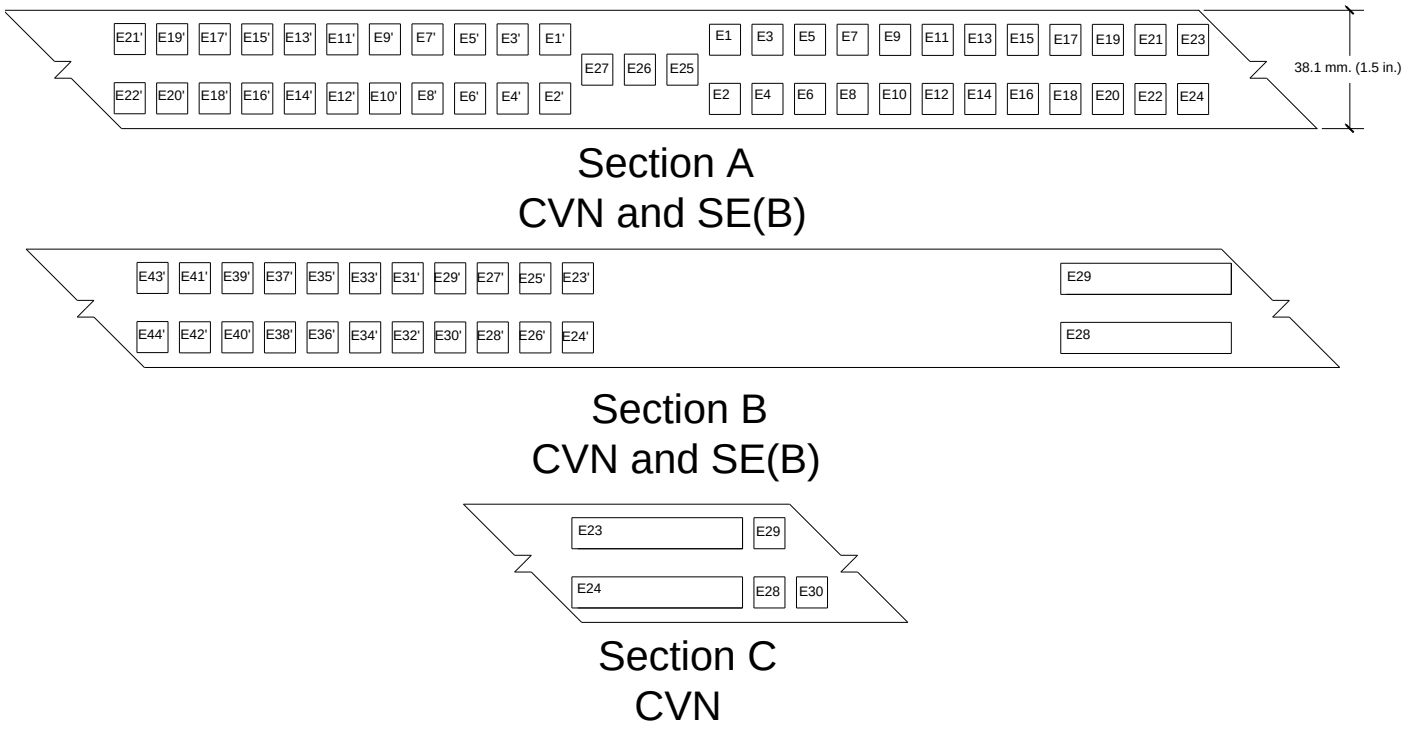

Figure 3-14. Plate E Specimen Layout

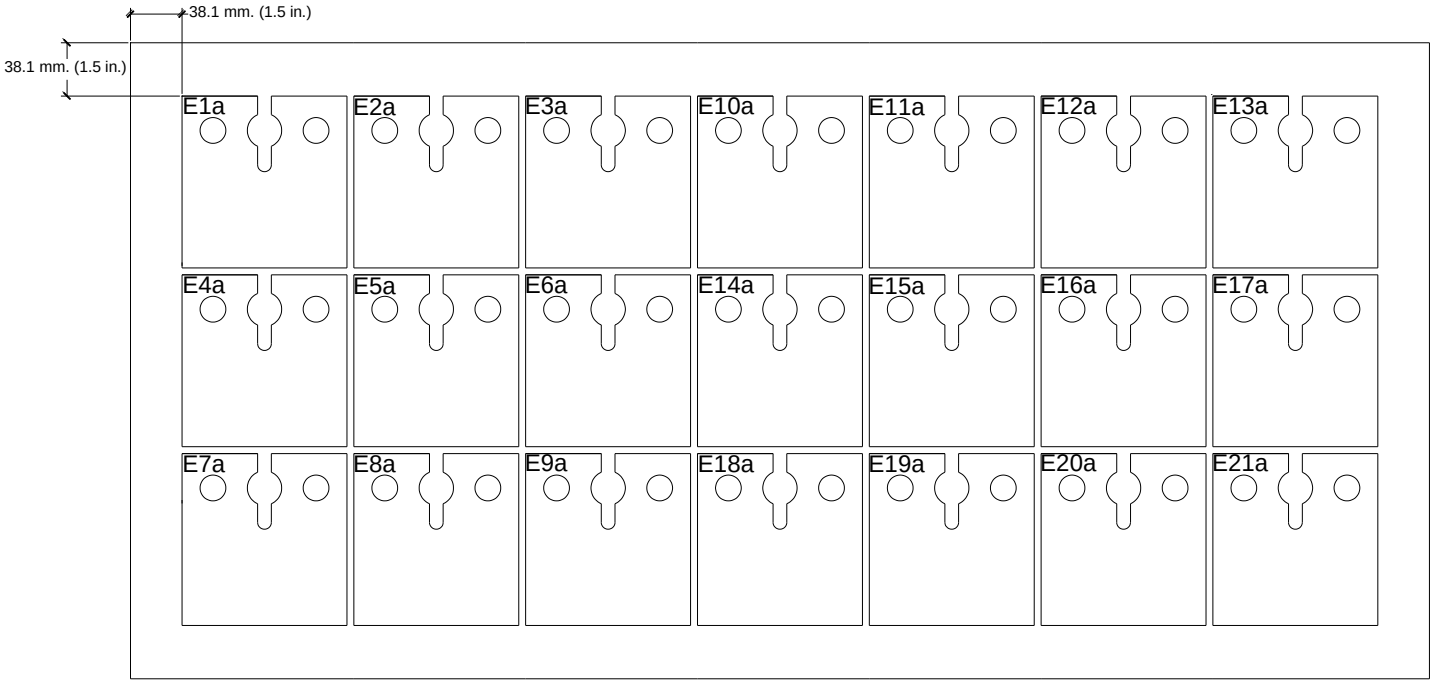

Figure 3-15. Plate E Arrest Specimen Layout

3.1.2.5 Plate F Specimen Layout

Plate F is a Grade HPS 690 W (100W) 50.8 mm. (2 in.), approximately 914 mm. (36 in.) square. Rectangular sections measuring roughly 254 by 457 mm. (10 by 18 in.) and 394 by 914 mm. (15.5 by 36 in.) were removed for CVN and SE(B) specimens, and crack arrest specimens, respectively, as can be seen in Figure 3-16. Like Plate E, a piece of Plate F was removed for test setup fabrication.

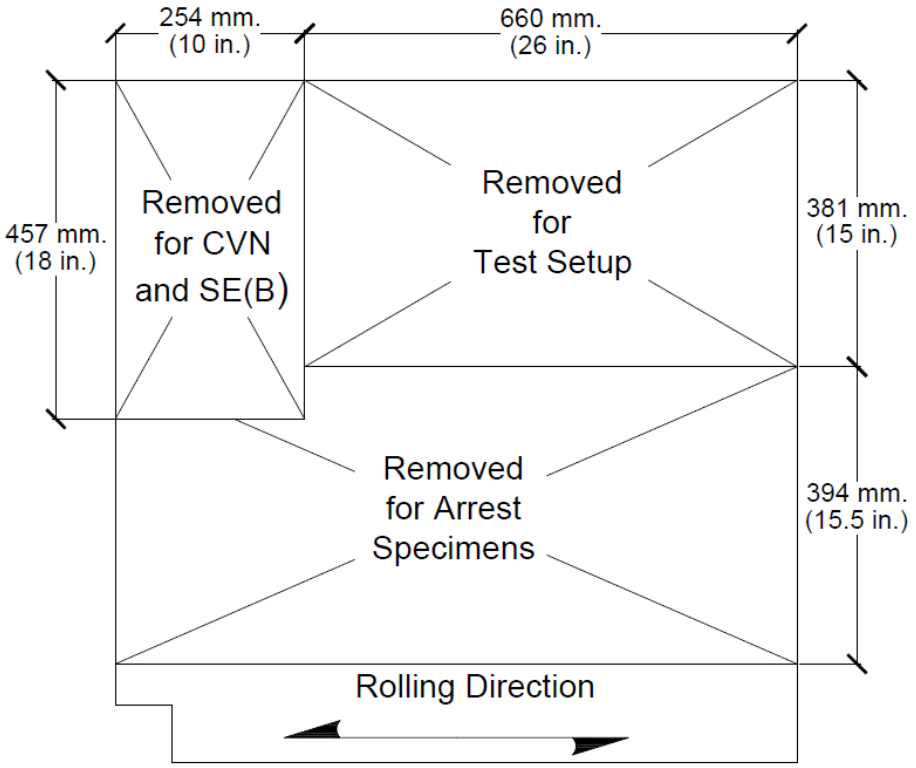

Figure 3-16. Plate F

CVN and SE(B) specimens are centered at the quarter thickness point of the plate, except for CVN specimens F25, F26, and F27, which are centered at plate mid-thickness. Layout details for all CVN and SE(B) specimens can be seen in Figure 3-17 and Figure 3-18. SE(B) specimen F21' was damaged in machining, so a second F21' was machined from an extra blank. The

original location of F21’ is denoted with a star (F21’*) while the actual F21’ is shown with normal identification. Full plate thickness crack arrest specimens were fabricated, sampled from Plate F as shown in Figure 3-19.

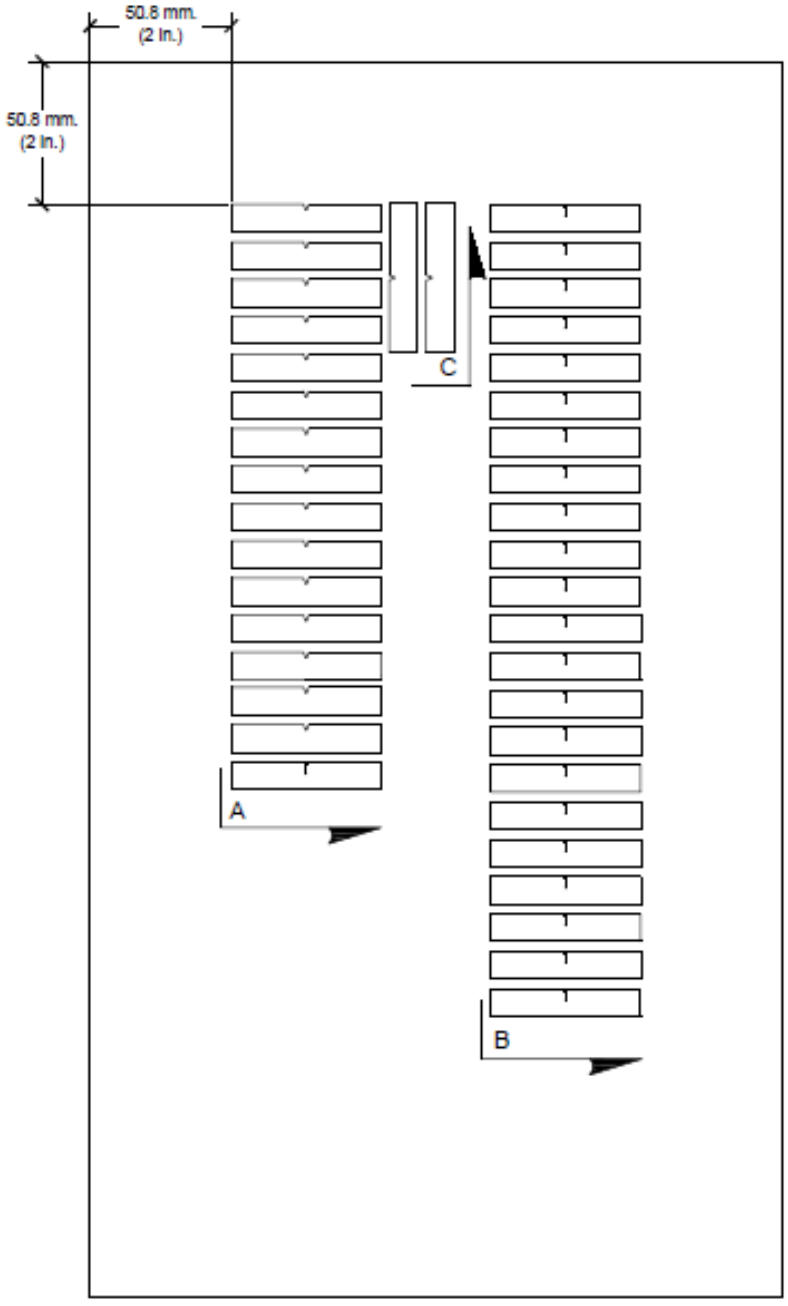

Figure 3-17. Plate F Specimen Cutout

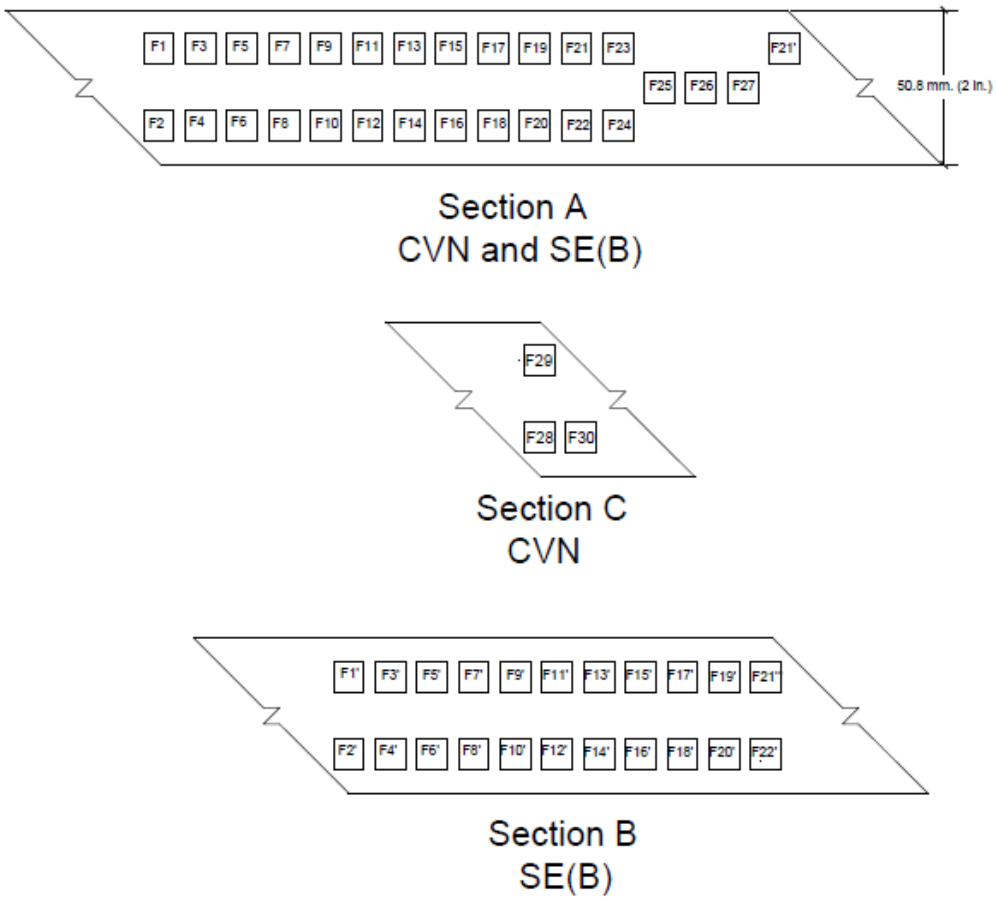

Figure 3-18. Plate F Specimen Layout

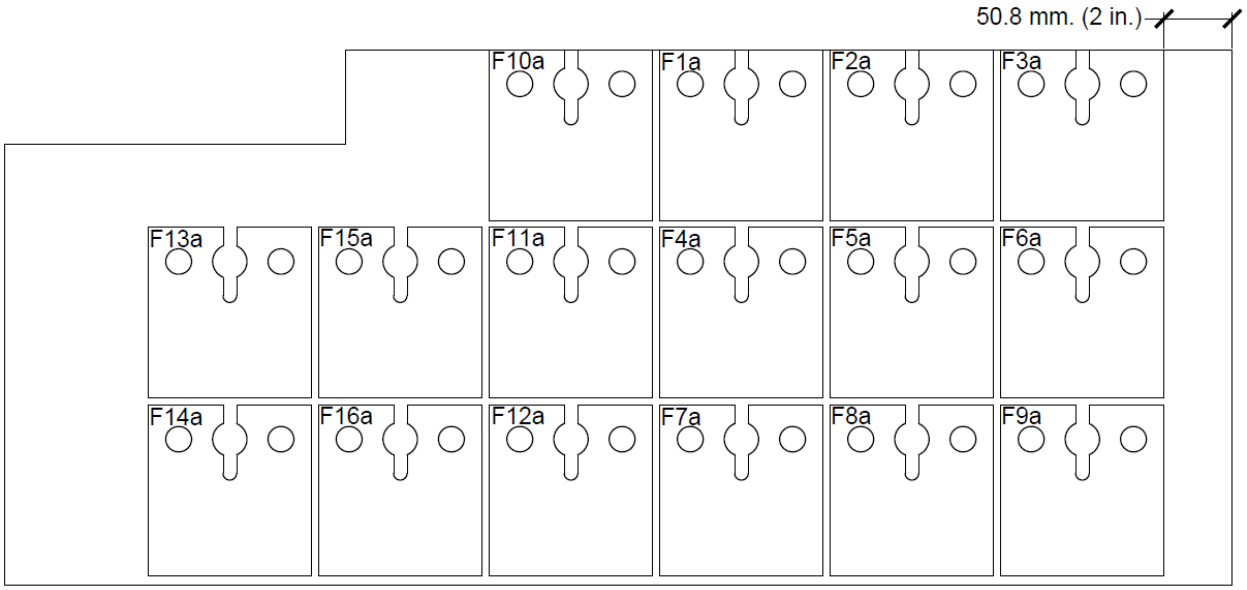

Figure 3-19. Plate F Arrest Specimen Layout

3.1.2.6 Plate H Specimen Layout

Plate H is a Grade HPS 485 W (70W) 31.8 mm. (1.25 in.) thick plate with dimensions of 914 mm. and 508 mm. (36 in. and 20 in.) in the longitudinal and transverse directions, respectively. Rectangular sections measuring 254 by 152 mm. (10 by 6 in.) and 178 by 89 mm. (7 by 3.5 in.) were removed from the full plate, and specimens were located within these sections as shown in Figure 3-20, Figure 3-21, and Figure 3-22. CVN and SE(B) specimens are centered at the quarter thickness point of the plate, except for CVN specimens H25, H26, and H27, which are centered at plate mid-thickness. CVN specimen H6 was damaged in the machining process, and was replaced with specimen H32. The location of the damaged specimen is identified with the label H6*. Tension specimens H1t and H2t are centered at plate mid-thickness.

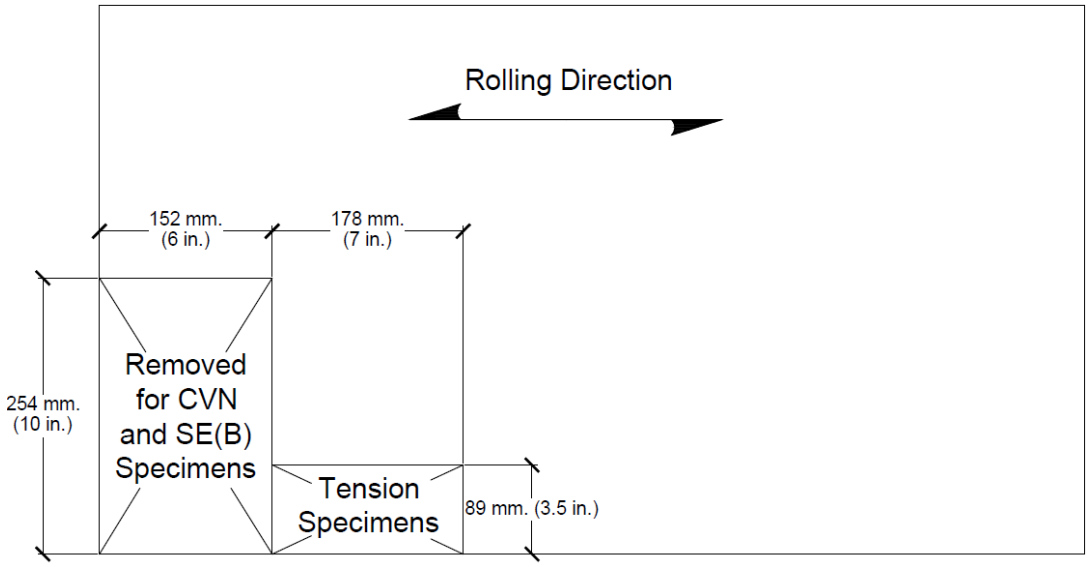

Figure 3-20. Plate H

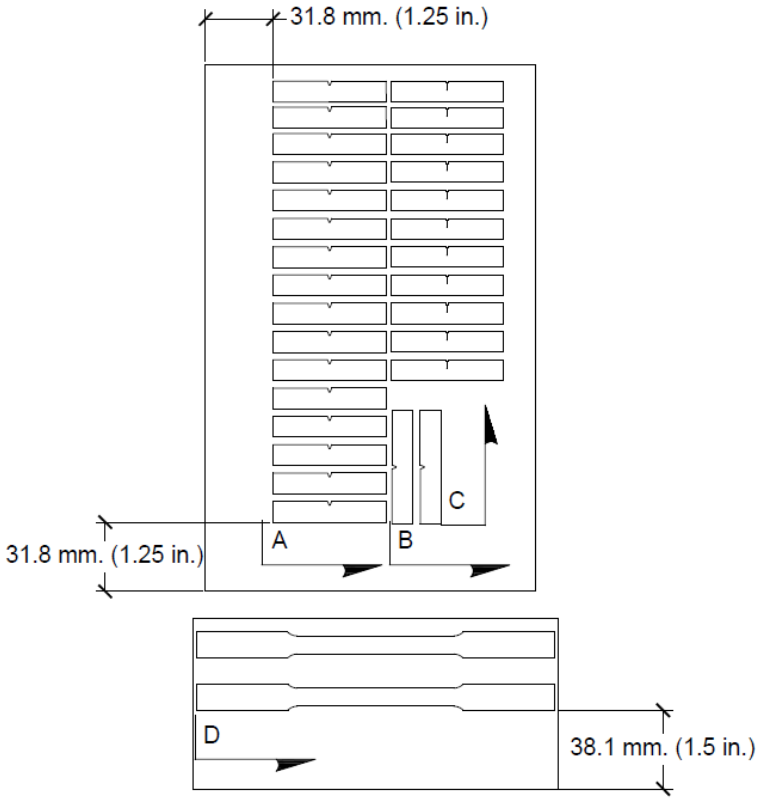

Figure 3-21. Plate H Specimen Cutouts

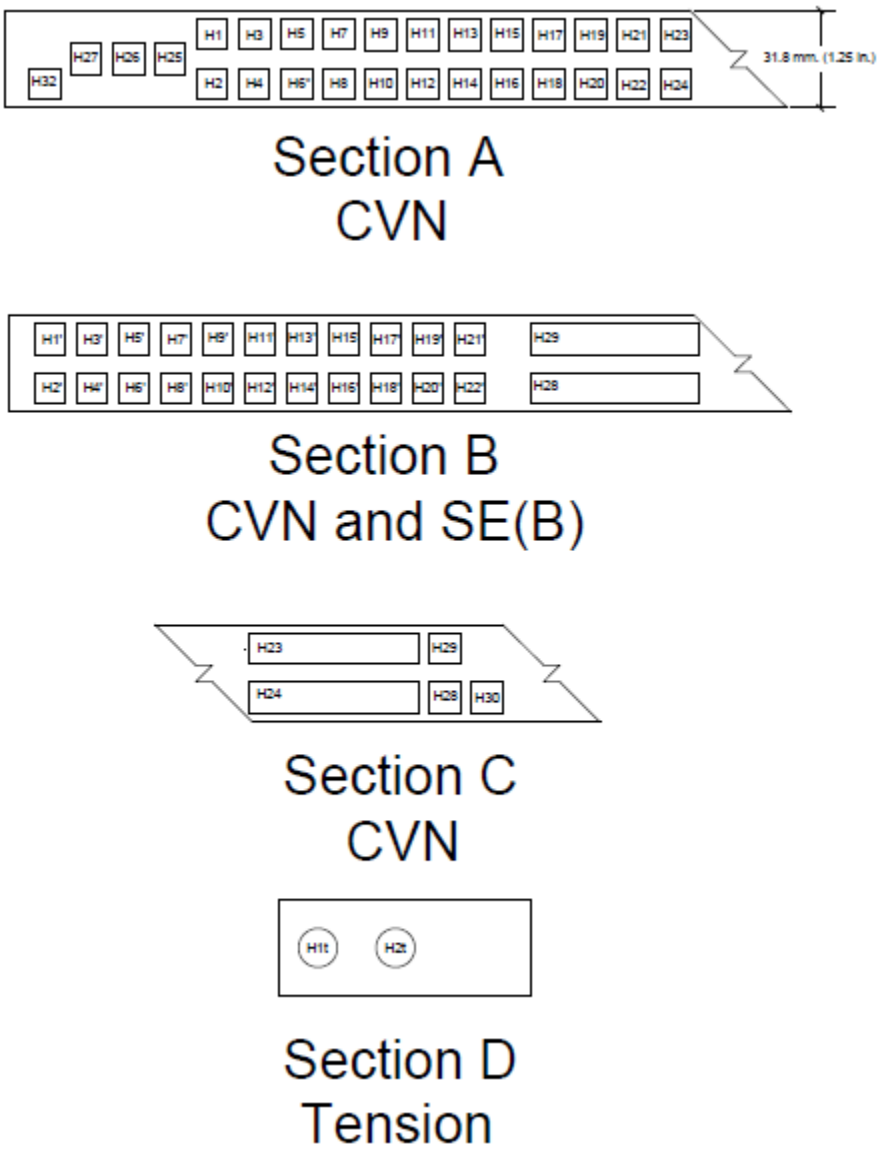

Figure 3-22. Plate H Specimen Layout

3.1.2.7 Plate I Specimen Layout

Plate I is a Grade HPS 485 W (70W) 31.8 mm. (1.25 in.) thick plate with dimensions of 914 mm. and 660 mm. (36 in. and 26 in.) in the longitudinal and transverse directions, respectively. Rectangular sections measuring 305 by 152 mm. (12 by 6 in.) and 178 by 89 mm. (7 by 3.5 in.) were removed from the full plate, and specimens were located within these sections

as shown in Figure 3-23, Figure 3-24, and Figure 3-25. CVN and SE(B) specimens are centered at the quarter thickness point of the plate, except for CVN specimens I25, I26, and I27, which are centered at plate mid-thickness. Tension specimens I1t and I2t are centered at plate mid-thickness.

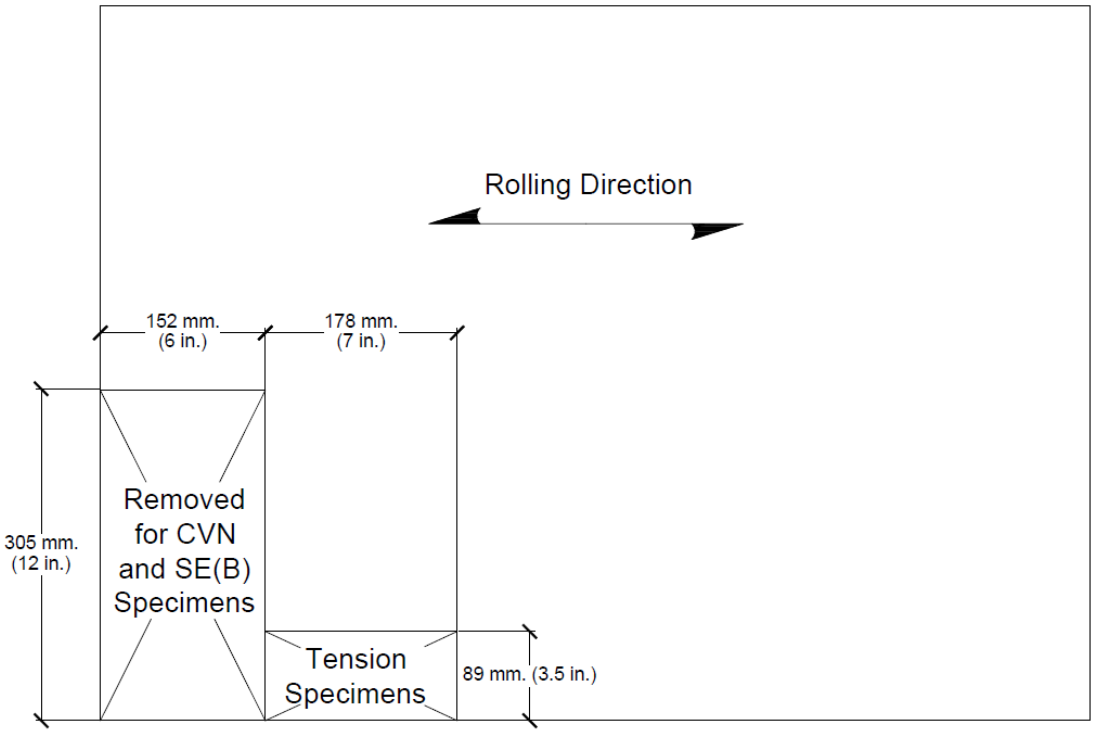

Figure 3-23. Plate I

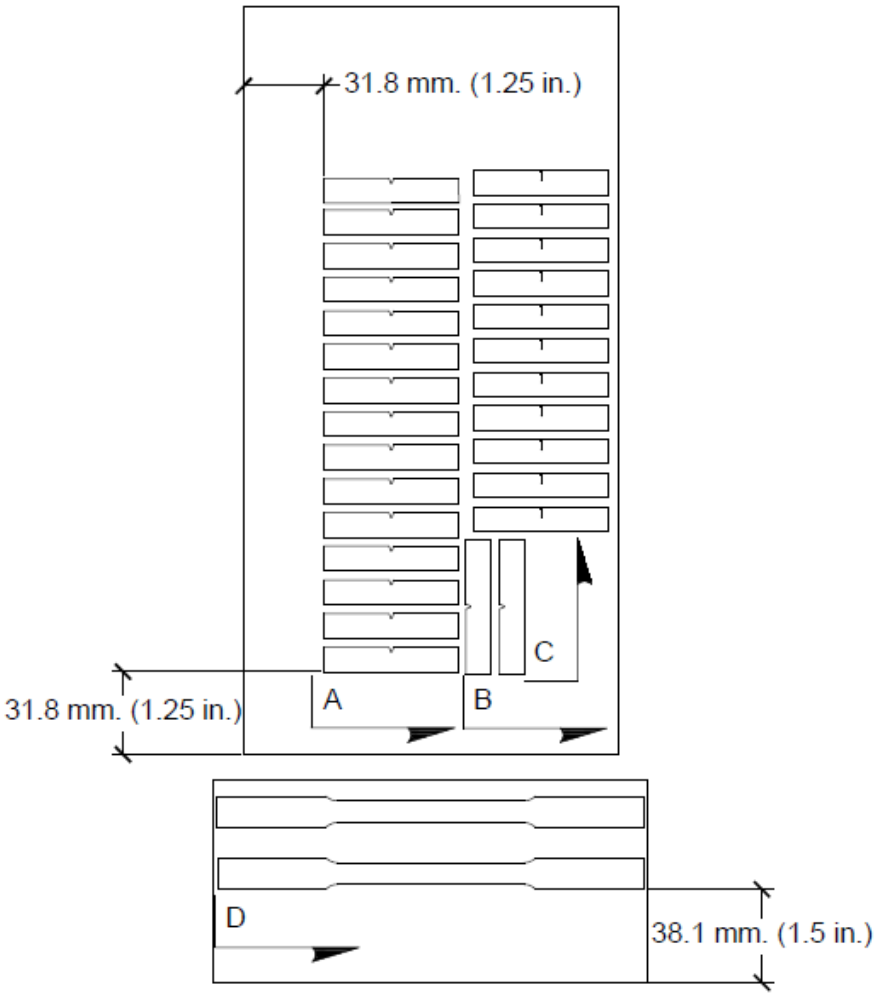

Figure 3-24. Plate I Specimen Cutouts

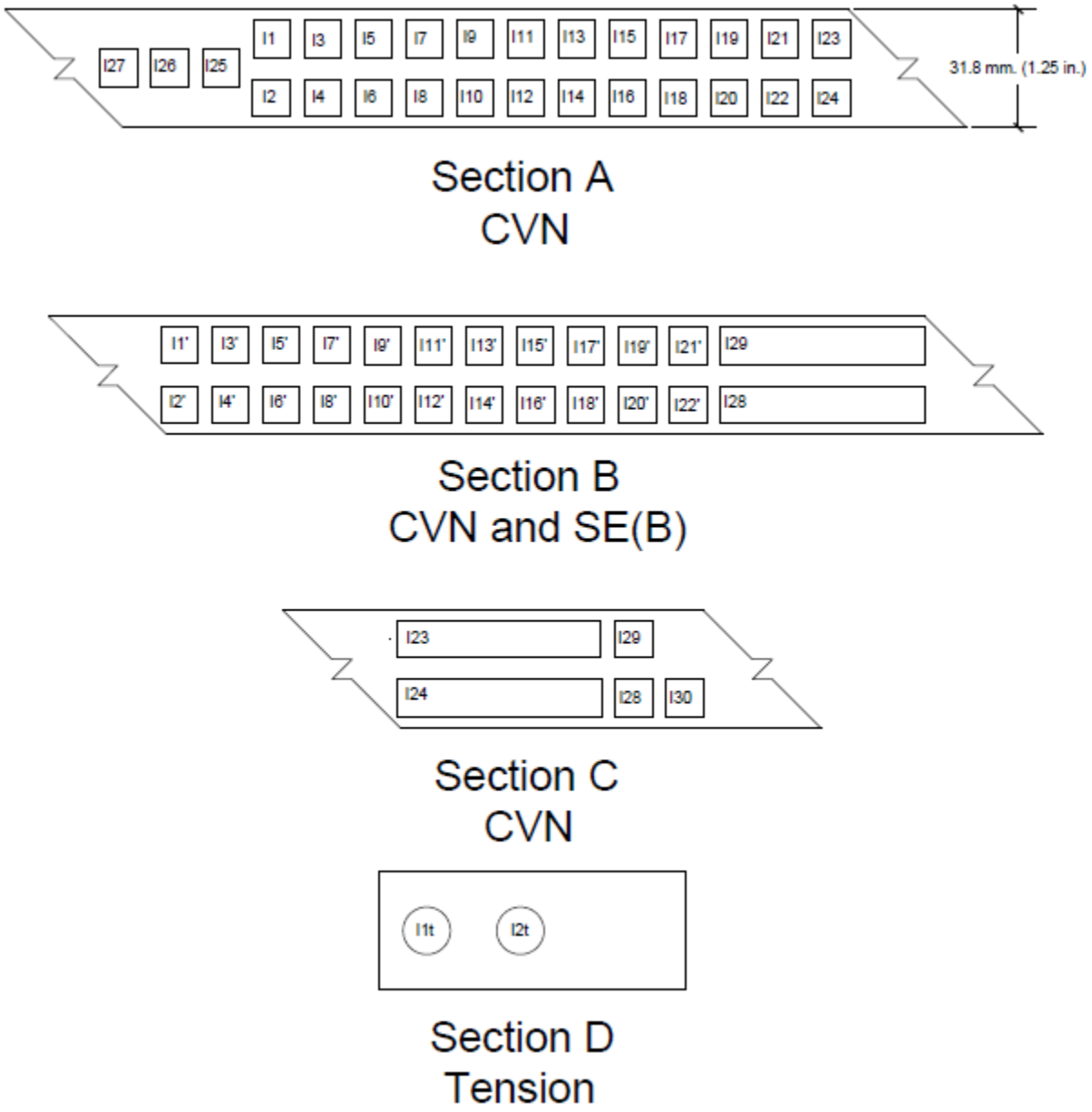

Figure 3-25. Plate I Specimen Layout

3.1.2.8 Plate J Specimen Layout

Plate J is a Grade HPS 485 W (70W) 38.1 mm. (1.5 in.) thick plate with dimensions of 457 mm. and 864 mm. (18 in. and 34 in.) in the longitudinal and transverse directions, respectively. A rectangular section measuring 381 by 216 mm. (15 by 8.5 in.) was removed from

the full plate and specimens were located within this section as shown in Figure 3-26, Figure 3-27, and Figure 3-28. CVN and SE(B) specimens are centered at the quarter thickness point of the plate, except for CVN specimens J25, J26, and J27, which are centered at plate mid-thickness. Tension specimens J1t and J2t are centered at plate mid-thickness.

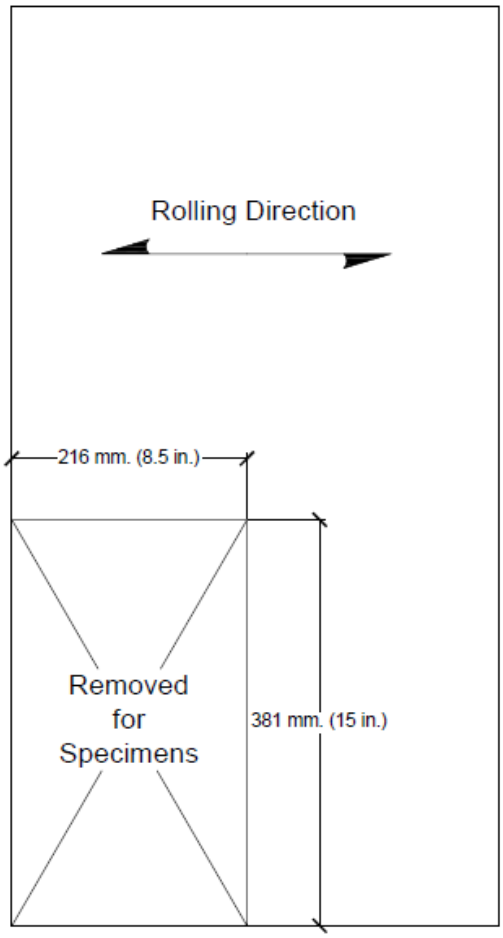

Figure 3-26. Plate J

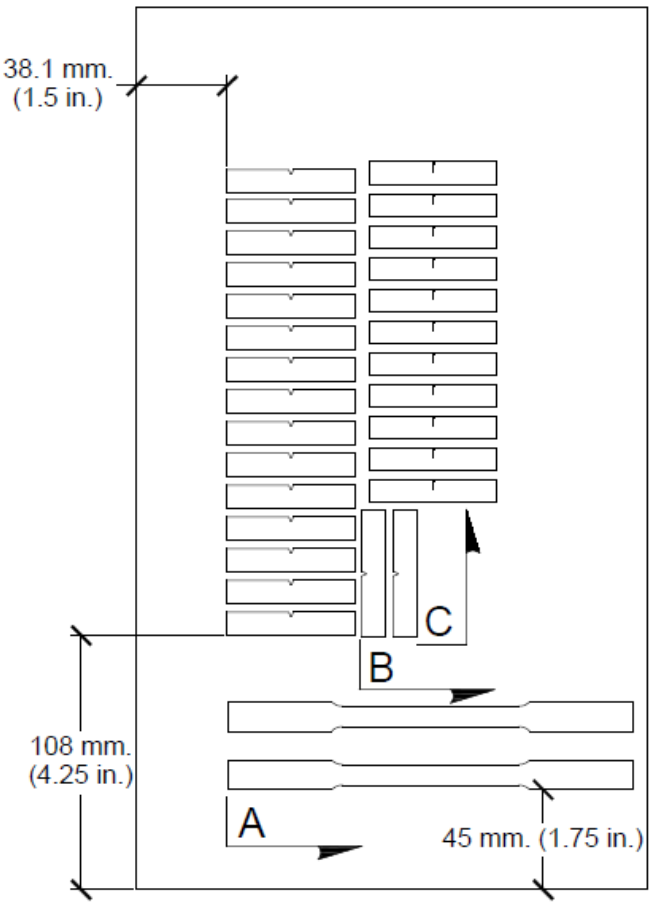

Figure 3-27. Plate J Specimen Cutout

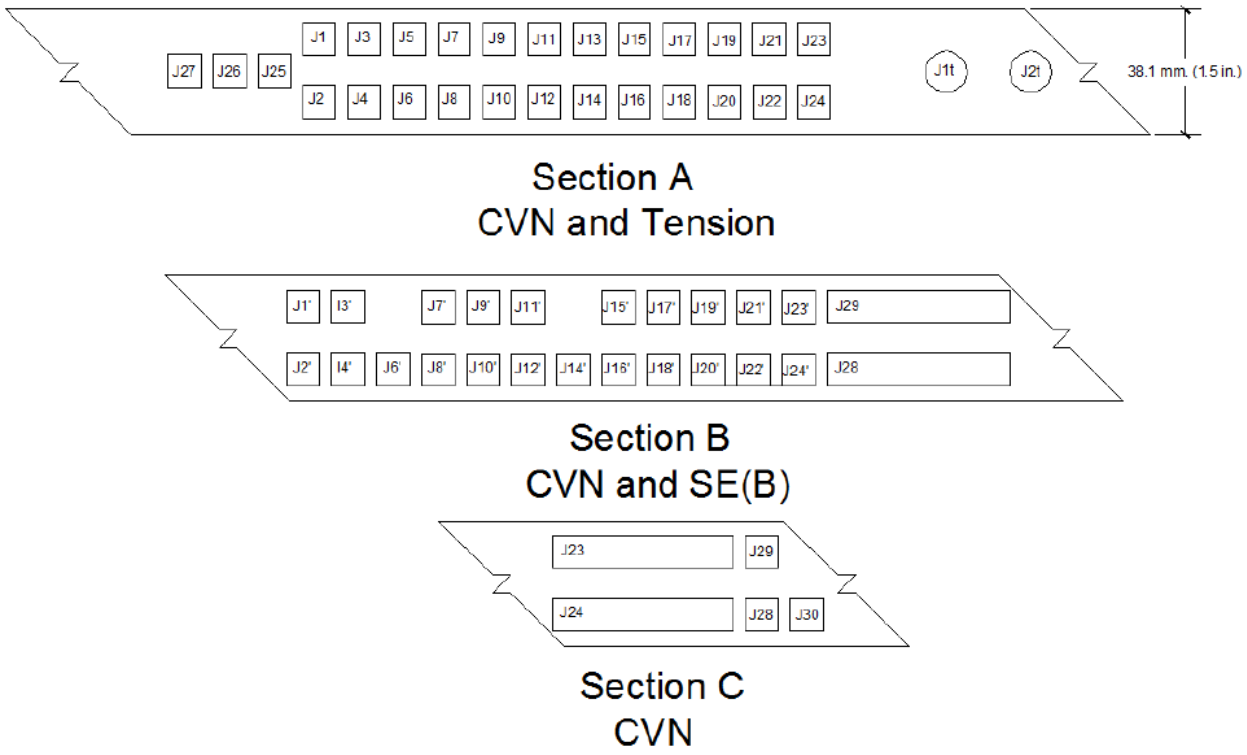

Figure 3-28. Plate J Specimen Layout

3.1.2.9 Plate R Specimen Layout

Plate R is a section of a main girder tension flange from the Railroad Flat Car (RRFC) research project at Purdue University. The plate is 25.4 mm. (1 in.) thick, and approximately 152 and 165 mm. (6 and 6.5 in.) in the transverse and longitudinal directions, respectively. Tension and CVN specimens were sampled from a different location within the plate and tested by researchers at Purdue. Seventeen SE(B) specimens were fabricated from the provided plate, twelve centered at quarter-thickness and five from mid-thickness. All specimens were sampled in the L-T orientation, as shown in Figure 3-29.

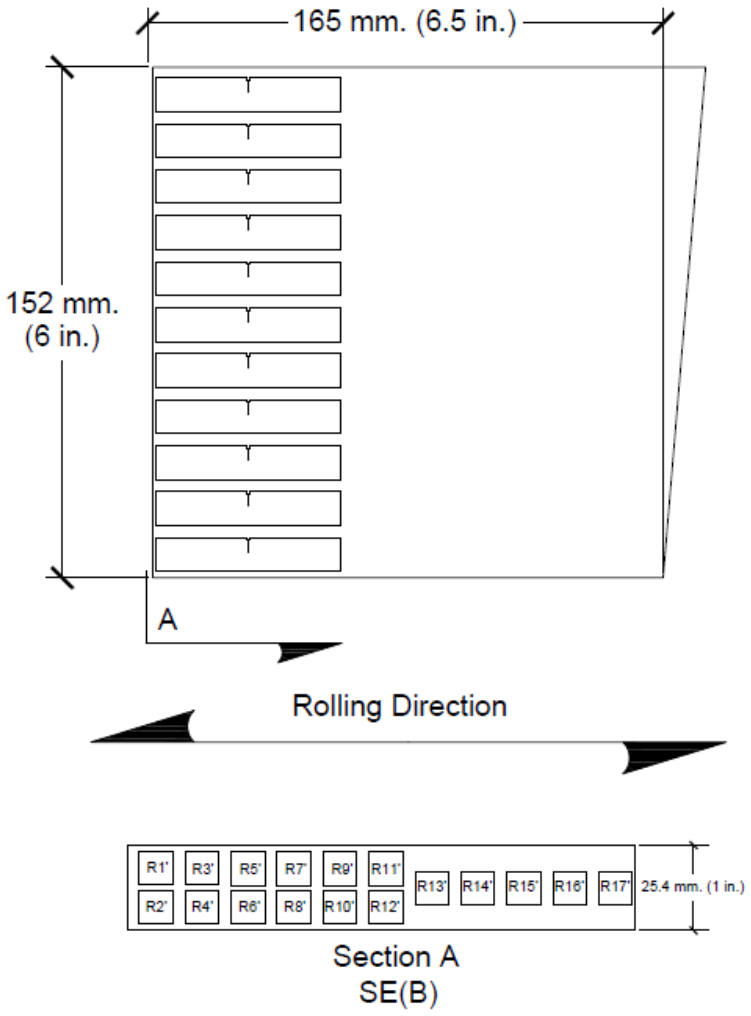

Figure 3-29. Plate R Specimen Layout

3.1.2.10 Plate B Specimen Layout

Plate B is a section of a tension flange from the Diefenbaker bridge in Canada. This was a fracture critical bridge that experienced a fracture due to a highly constrained detail. The square plate is 25.4 mm. (1 in.) thick, with dimensions of 152 and 152 mm. (6 and 6 in.) in the transverse and longitudinal directions, respectively. Tension and CVN specimens were sampled from the plate and tested by researchers at Purdue. Eighteen SE(B) specimens were fabricated

from the provided plate, twelve centered at quarter-thickness and six from mid-thickness. All specimens were sampled in the L-T orientation, as shown in Figure 3-30.

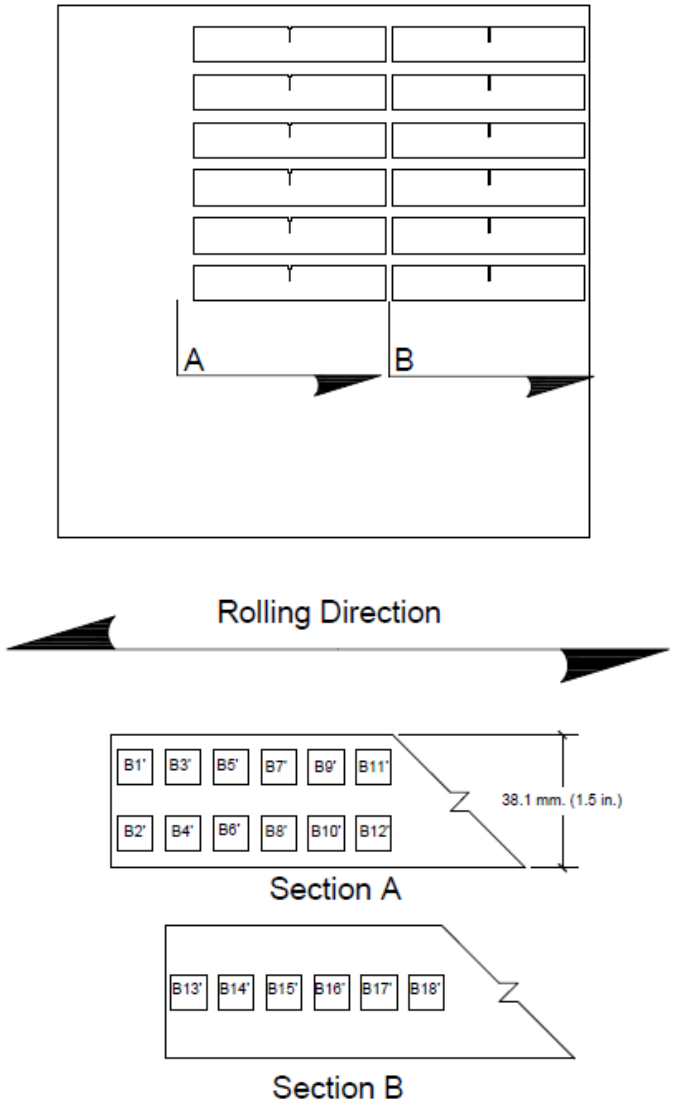

Figure 3-30. Plate B Specimen Layout

3.1.2.11 Plate 4 Specimen Layout

Plate 4 is a section of a tension flange from the US 422 bridge over the Schuylkill River in Pottstown, PA. This bridge also experienced a fracture due to a highly constrained detail. The

plate is 31.8 mm. (1.25 in.) thick, with original dimensions of 159 and 146 mm. (6.25 and 5.75 in.) in the transverse and longitudinal directions, respectively. Tension and CVN specimens were removed from the plate and tested by researchers at Purdue University. Eighteen SE(B) specimens were fabricated from the provided plate, twelve centered at quarter-thickness and six from mid-thickness. All specimens were sampled in the L-T orientation, as shown in Figure 3-31.

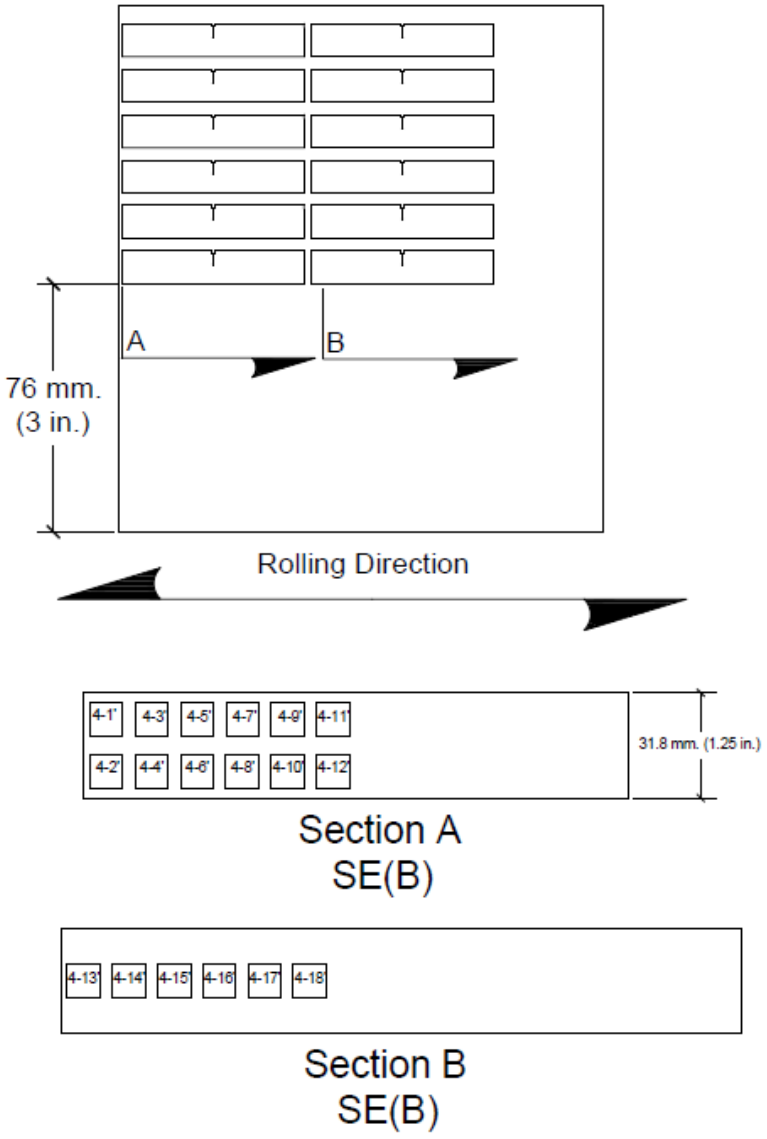

Figure 3-31. Plate 4 Specimen Layout

3.1.2.12 Plate P Specimen Layout

Plate P is from a tension flange on a plate girder bridge located at the Transportation Technology Center, Inc.'s railroad testing facility. This bridge had remained in service at the test center for several years after experiencing a fracture that was able to arrest. The plate is 63.5 mm. (2.5 in.) thick, with dimensions of 152 and 152 mm. (6 and 6 in.) in the transverse and longitudinal directions, respectively. Tension and CVN specimens removed from the plate were tested by researchers at Purdue. Eighteen SE(B) specimens were fabricated from the plate, twelve centered at quarter-thickness and six from mid-thickness. All specimens were sampled in the L-T orientation, as shown in Figure 3-32.

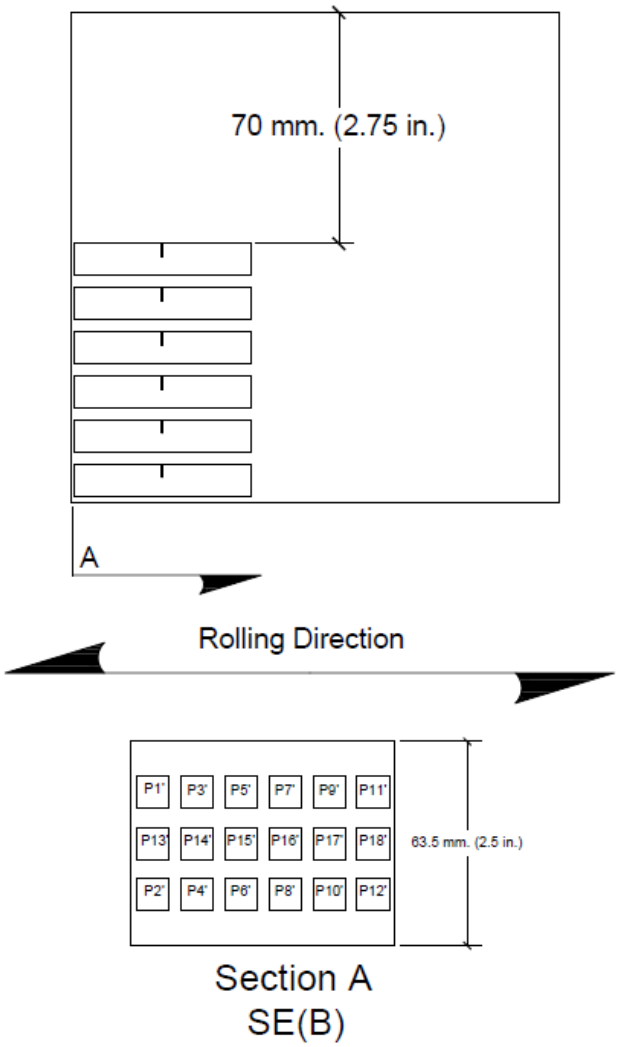

Figure 3-32. Plate P Specimen Layout

3.1.2.13 Plate M Specimen Layout

Plate M was removed from the cover plate on a tension chord of the old Milton Madison bridge. This fracture critical deck truss was tested to failure by researchers at Purdue University, who also sampled and tested CVN and tension specimens from the same plate. The provided section included two plates connected with four rivets. The two plates were 9.5 mm. (0.375 in.) and 12.7 mm. (0.5 in.) with approximate original dimensions of 171 and 305 mm. (6.75 and 12 in.) in the transverse and longitudinal directions, respectively. Twelve SE(B) specimens were

fabricated from the 12.7 mm. (0.5 in.) plate, all centered at plate mid-thickness. The rivets were spaced at 140 mm. (5.5 in.) center-to-center in the longitudinal direction, and SE(B) specimens were centered between the rivets. All specimens were sampled in the L-T orientation, as shown in Figure 3-33.

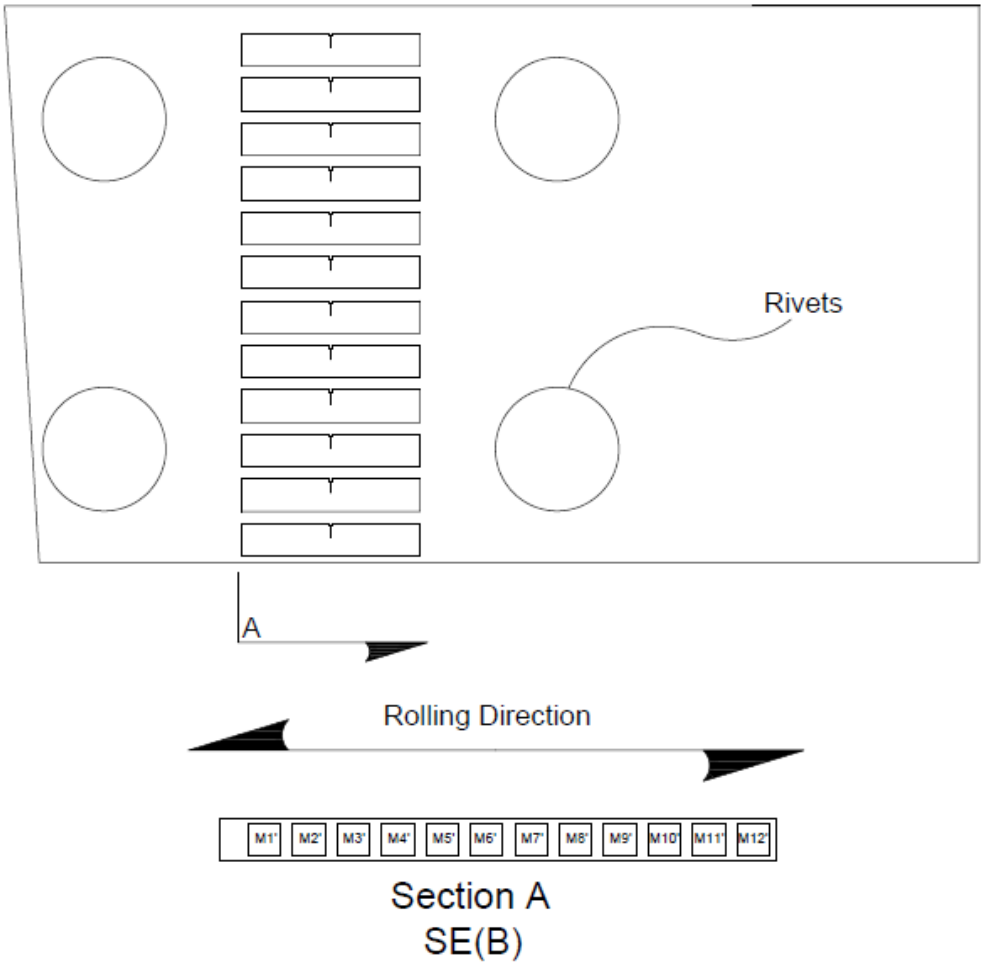

Figure 3-33. Plate M Specimen Layout

3.1.3 Test Specimen Geometry

Various test specimens were used in an array of test methods. Presented herein are the different specimens used in this study.

3.1.3.1 Tension Test Specimens

Round tensile specimens in accordance with ASTM E8-08 were fabricated with a diameter of 9 mm. (0.35 in.) and a total reduced section length of 75 mm. (3 in.), as seen in Figure 3-34 (ASTM 2008).

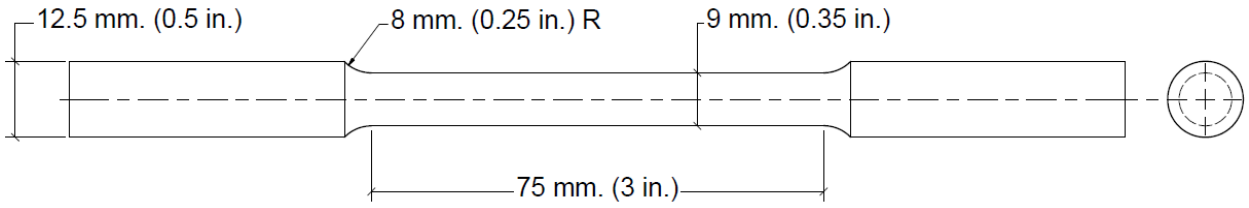

Figure 3-34. Tension Specimen Geometry

3.1.3.2 Charpy V-Notch Specimens

Typical CVN specimens used in impact testing are described in ASTM E 23-07 (ASTM 2007). Specimens are 10 mm. (0.394 in.) square by 55 mm. (2.165 in.) in length. A 2 mm. (0.079 in.) deep notch with a 0.25 mm. (0.01 in.) radius is broached into the center of the specimen, as seen in Figure 3-35.

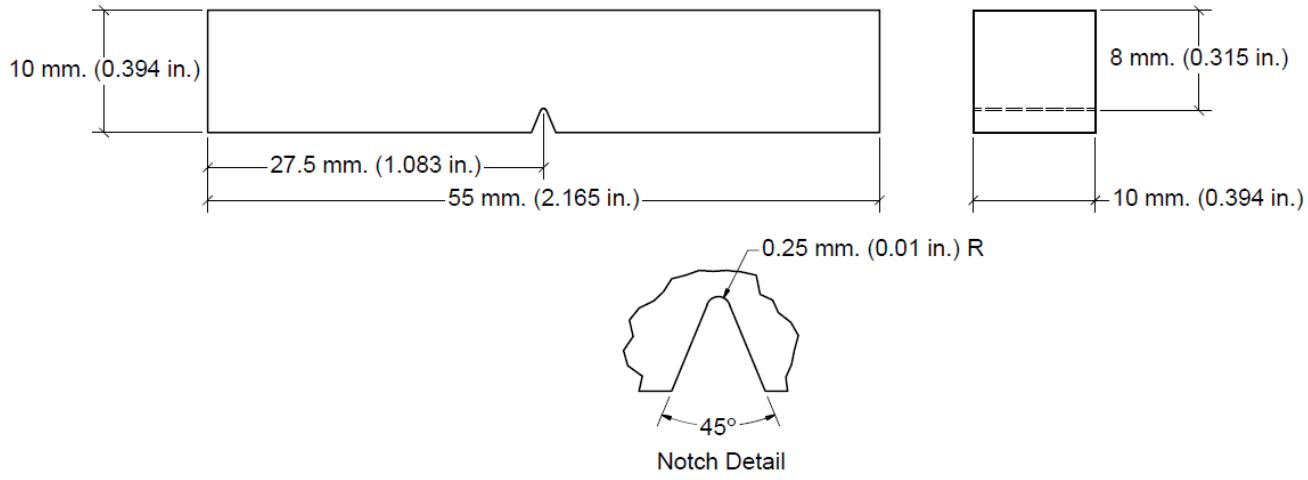

Figure 3-35. CVN Specimen Geometry

3.1.3.3 SE(B) Specimens

Geometry requirements for SE(B) fracture toughness specimens can be found in ASTM E1921-08 and E1820-08 (ASTM 2008). The chosen specimen for use in this study is commonly referred to as a pre-cracked Charpy SE(B). The specimen blank geometry is the same as described above for the CVN specimen. The specimen is different at the notch however, as fracture toughness testing requires a sharp crack front. To ease fatigue pre-cracking, an EDM notch is cut into the center of the SE(B) blank, as seen in Figure 3-36. The notch width and end radius corresponds with the diameter and radius of EDM wire, while the shoulders cut into the face of the specimen facilitate the use of a clip gage during testing.

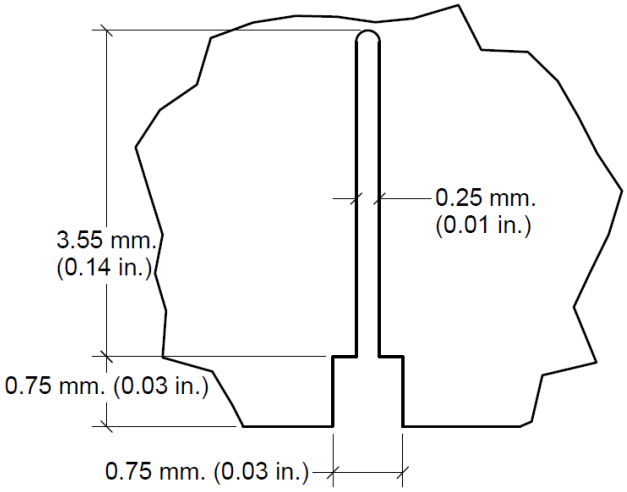

Figure 3-36. SE(B) Specimen Notch Details

Typically fracture toughness specimens are defined by dimensions B and W, which represent the thickness and height of the specimen, respectively. Also used to define specimen geometry is dimension a, which is the length of the crack. These dimensions can be seen on an SE(B) specimen in Figure 3-37. As mentioned above, all SE(B) specimens used in this study use CVN specimen geometry with dimensions B and W both equal to 10 mm. (0.394 in.).

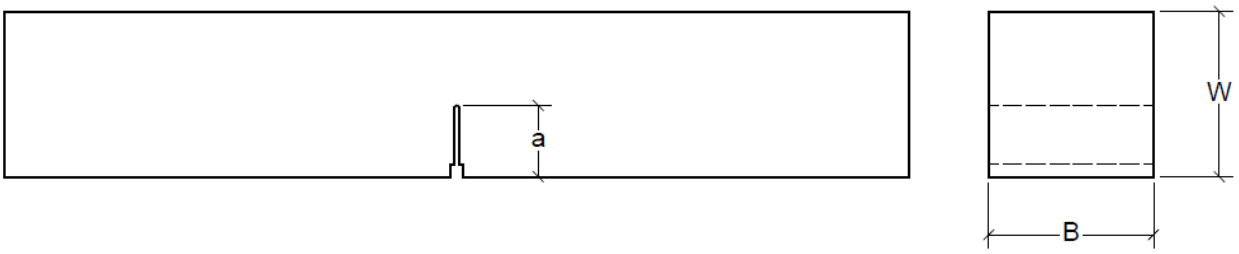

Figure 3-37. SE(B) Specimen Dimensions

To ensure a straight crack front during testing, side grooves are machined on the specimen sides after the completion of fatigue pre-cracking. Side grooves used in this study have a depth of 1 mm. (0.0394 in.) and an included angle of 45 degrees, and are centered on the specimen in line with the fatigue crack. Side grooves are located on two opposite sides of the specimen, perpendicular to the notched face, as can be seen in Figure 3-38. In this figure, the previously discussed notch has been machined into the bottom of the specimen.

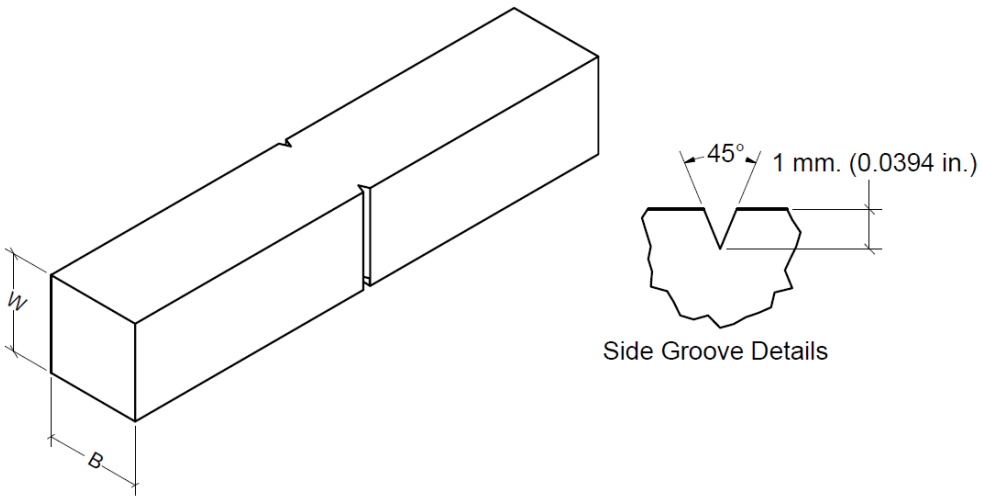

Figure 3-38. SE(B) Side Groove Location and Dimensions

3.1.3.4 Crack Arrest Specimens

Specimens used for crack arrest testing are modified C(T) specimens with geometry requirements described in ASTM E1221-12 (ASTM 2012). C(T) specimen geometry is defined in a similar manner to SE(B) specimens, with dimensions *B* and *W* defining thickness and width, respectively. Crack arrest testing is typically performed at plate thickness, so in this study *B* varied from plate to plate. Specimen width *W*, however, measured from the load line to the end of the specimen, was held constant at 102 mm. (4 in.) for all specimens. Wedge loading is applied through a 25.4 mm. (1.0 in.) diameter hole, centered on a 10.2 mm. (0.4 in.) slot that is machined to extend from the load line 30 mm. (1.2 in.) into the specimen. Initial machining geometry as described above can be seen in Figure 3-39. Additionally, 19 mm. (0.75 in.) diameter holes are also included in fabrication to accommodate clevis grips.

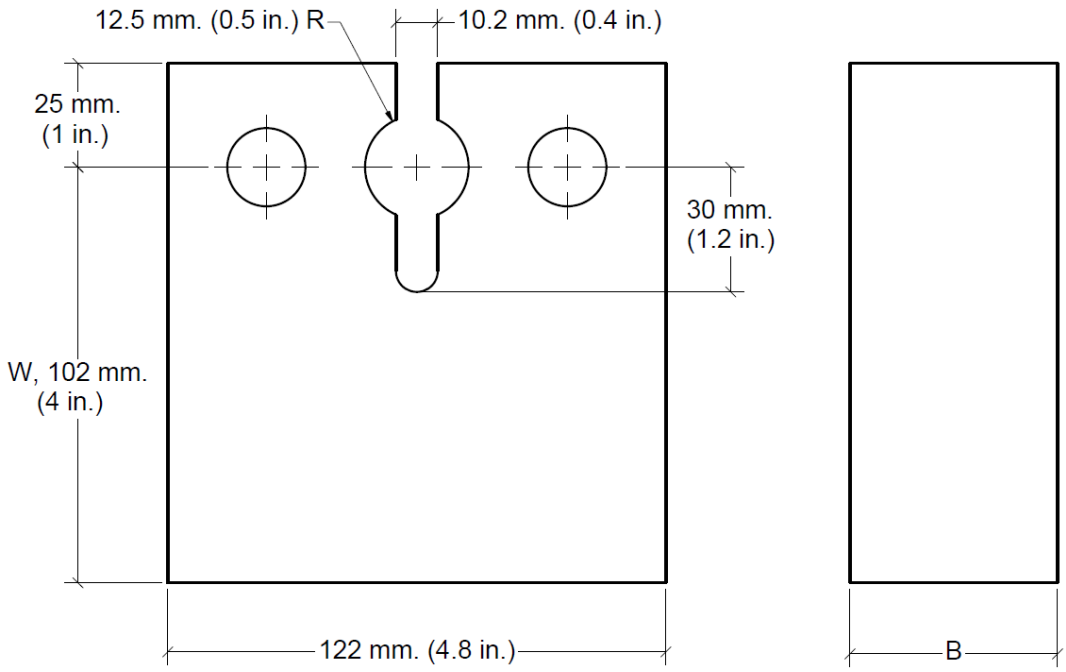

Figure 3-39. Crack Arrest Specimen Geometry

Using a buildup rod, a brittle weld is deposited at the bottom of the slot, and then an EDM cut notch is machined into this deposit. The distance from the load line to the end of the notch, the initial crack length, a_o, is 28 mm. (1.1 in.). This places the end of the initial crack within the weld deposit, approximately 2.5 mm. (0.1 in.) from the base metal. Similar to the SE(B) specimens, side grooves are also employed on crack arrest specimens. The two side grooves on crack arrest specimens are machined to a total depth of 25% specimen thickness with an included angle of 45 degrees. Details of the weld deposit, notch, and side grooves can be seen in Figure 3-40.

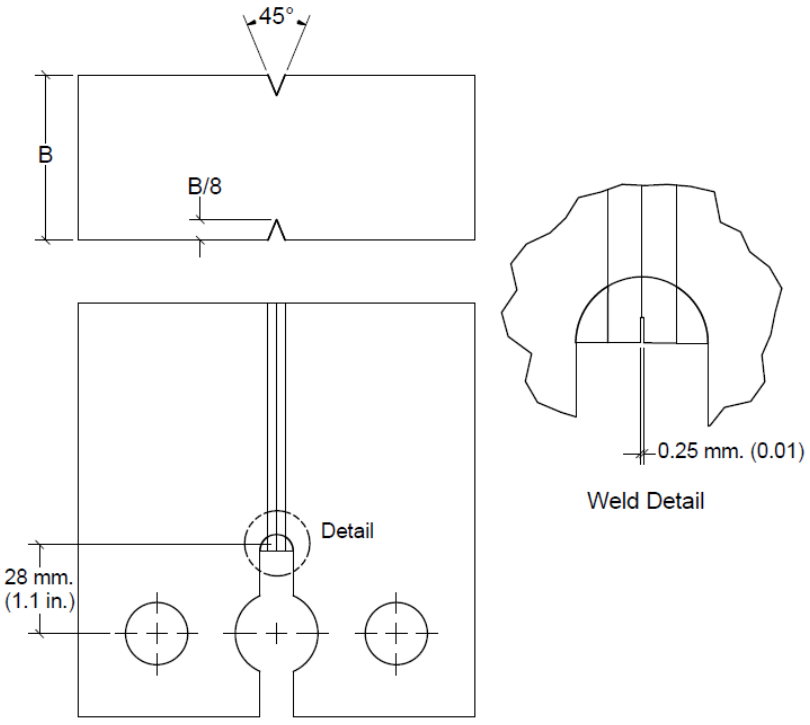

Figure 3-40. Crack Arrest Specimen Details

3.2 Material Characterization Testing Procedures

3.2.1 Tensile Testing

Tensile testing was performed on a 100 kN (22 kip) Instron electro-mechanical test machine. Tests were performed in accordance with ASTM E8-08 (ASTM 2008). An Instron 5982 Type 1 extensometer was attached to each specimen prior to testing in order to measure elongation, as seen in Figure 3-41. Measurements were made until specimens reached 5 per cent elongation, at which point the gages were removed. After extensometer removal, elongation was measured by the movement of the load frame crosshead.

Figure 3-41. Tensile Test Specimen with Extensometer

Upon completion of the test, the records of both the extensometer and the crosshead were combined to form the final stress-stain curve of the specimen. Yield strength of each specimen was evaluated using the 0.2 per cent offset method. Tensile strength evaluation was made by dividing the maximum attained load by the original cross-sectional area of the specimen. All tensile testing was performed at room temperature, and records of each test temperature were maintained.

3.2.2 Charpy V-Notch Impact Testing

CVN tests of HPS were performed on a friction compensated Tinius Olsen impact test machine with a maximum capacity of 400 J (300 ft-lb), seen in Figure 3-42. Prior to the beginning of testing this impact test machine was verified using NIST low and high energy specimens and was found to be in calibration.

Figure 3-42. Impact Test Machine

This impact machine uses an analog scale to indicate absorbed energy at fracture. Prior to testing the pendulum arm is raised and locked into place with a safety latch. Once the dial indicator is turned to full scale reading, a test specimen is placed on the anvil with the notch centered, oriented vertically, and facing away from the striking surface of the impact hammer. The safety latch is then removed and the hammer is released, allowing the arm to swing and causing the hammer to strike the back face of the specimen. The height of the swinging pendulum after fracture is then related to energy absorption, and is indicated on the dial. Energy values below 80 per cent of machine capacity are considered valid. Indicated values above this limit are considered invalid due to pendulum speed validity requirements.

Because full temperature transition curves were desired, CVN specimens were cooled using a methanol cooling bath capable of temperatures as low as -80 °C (-112 °F). Specimens were deposited in the bath once the desired temperature was obtained, and left to cool prior to testing. Temperatures were monitored using a sample CVN specimen with an embedded thermo-couple. Specimens were removed from the cooling bath and placed on the anvils with the use of Charpy centering tongs, which had also been placed in the cooling bath. Measures were taken to ensure that the time between removal from temperature bath and impact was less than five seconds. If an error occurred and specimens were removed from the cooling bath for longer than five seconds prior to testing, they were again placed in the methanol bath for re-cooling.

When lower-shelf behavior could not be obtained at -80 °C (-112 °F), liquid nitrogen was used to cool specimens to lower test temperatures. Specimens were placed in an insulated container with the thermo-couple embedded specimen, and liquid nitrogen was introduced. Temperatures were allowed to drop below the desired test temperature, and then specimens were removed from the container and placed on a metal plate along with the thermo-couple embedded specimen, as seen in Figure 3-43. The temperature of the embedded CVN was monitored as the specimens gradually warmed up, and tests were completed as the desired temperature was reached.

Figure 3-43. CVN Specimen Reaching Desired Test Temperature

Charpy V-Notch impact testing of the conventional bridge steels taken from in-service structures was conducted by researchers at Purdue University. Testing protocols for these tests were similar to those described above.

3.2.3 Fracture Toughness Testing

Fracture toughness tests were performed on specimens from both HPS and conventional bridge steel plates. Specimens were prepared with specialized machining as described above, as well as fatigue pre-cracking, prior to testing. All pre-cracking and testing of fracture toughness specimens is performed on an MTS Landmark servo-hydraulic test machine. Software used for pre-cracking and testing was developed by researchers at the Naval Academy (Joyce and Link 2012).

3.2.3.1 Fatigue Pre-Cracking Procedure

Fatigue pre-cracking is performed on the same three point bend test apparatus that is used for fracture toughness testing, as seen in Figure 3-44. For both pre-cracking and testing, CMOD is measured using the Tension Measurement SFDG-08 clip gage, also shown in Figure 3-44. The span of the test setup is equal to four times the specimen width, or 40 mm. (1.575 in.) as required in ASTM E1820-08 (ASTM 2008).

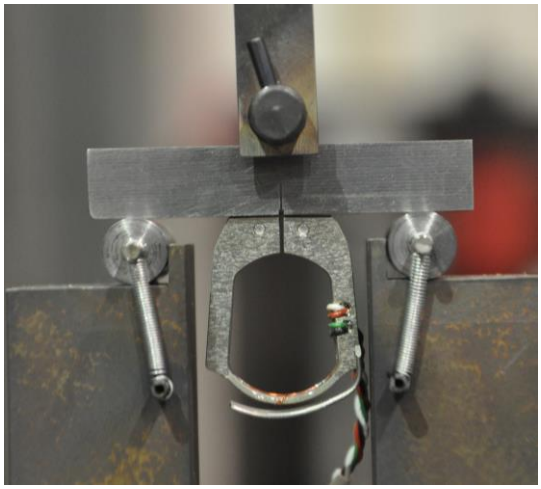

Figure 3-44. SE(B) Cracking and Testing Apparatus

Original EDM specimen notches are machined to a depth of 4.3 mm. (0.17 in.). This depth was chosen to minimize fatigue pre-cracking time. An initial crack length, a_o, of W/2 is desirable for reference temperature testing. Because ASTM E 1921-08 requires a minimum of 0.6 mm. (0.024 in.) of crack extension beyond the machined notch, an initial notch depth of 4.3 mm. (0.17 in.) produces an acceptable fatigue pre-crack at an a_o/W ratio equal to 0.5.

Pre-cracking is performed at room temperature, which is recorded as part of the test record. Because test temperatures are much colder than pre-cracking temperatures, there are

stringent rules in place to avoid warm prestressing during the pre-crack process. Limits on stress intensity values during the last segment of pre-cracking are prescribed in ASTM E1921-08. The first half of the pre-crack is run in a load shedding approach, as described in ASTM E647-13 (ASTM 2013). In this process, the stress intensity is stepped down from a start of 17.5 MPa√m (16 ksi√in) to 14.3 MPa√m (13 ksi√in) during the first half of crack growth. Once the crack has reach 0.3 mm. (0.012 in.) beyond the initial notch, the specimen is turned around to complete pre-cracking at a constant stress intensity of 14.3 MPa√m (13 ksi√in). Turning the specimen helps to ensure a straight crack front by eliminating small errors that may occur due to mis-alignment.

Once the fatigue pre-crack has reached the desired length, each specimen is re-machined with side grooves, as previously described. Side grooves eliminate any crack curvature that often occurs at the ends of specimen. Eliminating this tunneling effect provides a straight fatigue crack front for fracture toughness testing.

3.2.3.2 Fracture Toughness Testing Procedure

Fracture toughness testing of SE(B) specimens is performed on the same testing apparatus shown in Figure 3-44. Reference temperature determination is the desired outcome of the testing, thus ASTM E 1921-08 and E 1820-08 methods were followed (ASTM 2008). Test specimens are centered on the apparatus using a jig that enables proper alignment. A clip gage connected to the front face of the specimen measures crack mouth opening displacement (CMOD).

A small amount of pre-load is applied to the specimen to hold the specimen in place on the fixture while the environmental chamber is reaching the desired test temperature. More

information on the environmental cooling chamber can be found in Section 3.3.5. Once the desired test temperature has stabilized, testing can begin. Three to five elastic loading-unloading cycles are performed to check specimen alignment. Once proper alignment is verified, testing begins.

Load is applied to the specimen in displacement control mode. Static tests are performed at a rate that is equivalent to approximately 0.1 MPa√m/sec (0.091 ksi√in) in the elastic regime of the test. Dynamic tests are performed at the highest rate attainable by the servo-hydraulic test machine. Depending on toughness, this resulted in dynamic test rates ranging from 1000 to 5000 MPa√m/sec (910 to 4550 ksi√in/sec).

For reference temperature determination no elastic compliance unloadings are necessary, as the master curve method does not correct for slow stable crack growth. If testing at temperatures well above T_o, beyond temperature ranges where cleavage fracture is expected to occur, it is necessary to perform unloadings in order to generate a resistance curve. However, the majority of testing is focused on evaluating cleavage fracture initiation toughness, so unloadings are typically not used. Graphical examples of typical test records both with and without unloadings are presented in Figure 3-45 and Figure 3-46. Both of these figures display plots of load versus CMOD.

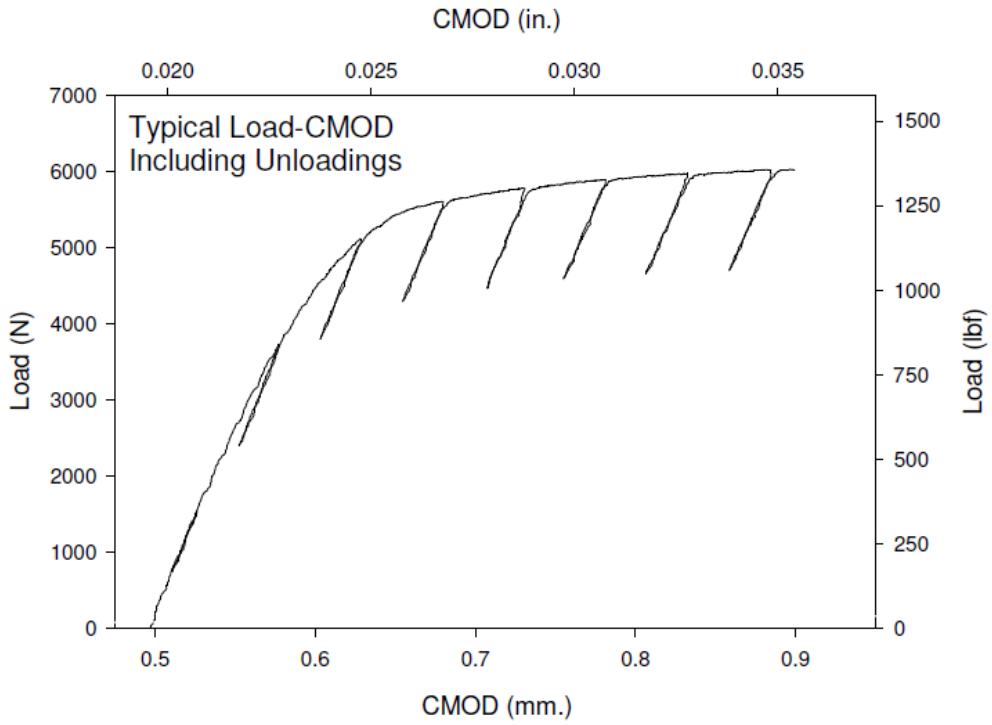

Figure 3-45. Typical Load-CMOD Plot with Elastic Compliance Unloadings

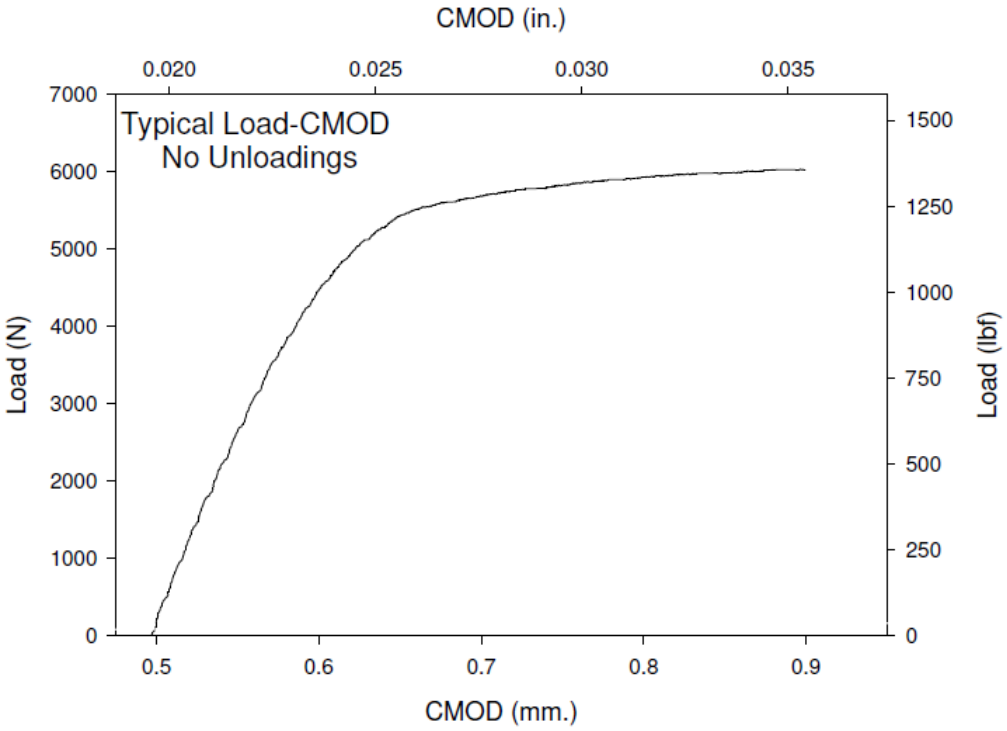

Figure 3-46. Typical Load-CMOD Plot without Elastic Compliance Unloadings

3.2.3.3 Fracture Toughness Data Analysis

Once fracture has occurred, specimens are removed from the cooling chamber and are placed on a hot plate for heat tinting. This changes the color of the fatigue crack and fracture surfaces, allowing for accurate measurement of initial crack size. Digital photographs of crack surfaces are scaled in AutoCAD, and nine-point measurements of initial crack size are made in accordance with ASTM E1820-08. An example of a measured crack is shown in Figure 3-47. The light blue section of this specimen is the fatigue crack, while the golden is the fractured surface. The silver surface is the remaining ligament of the specimen that was broken after heat tinting.

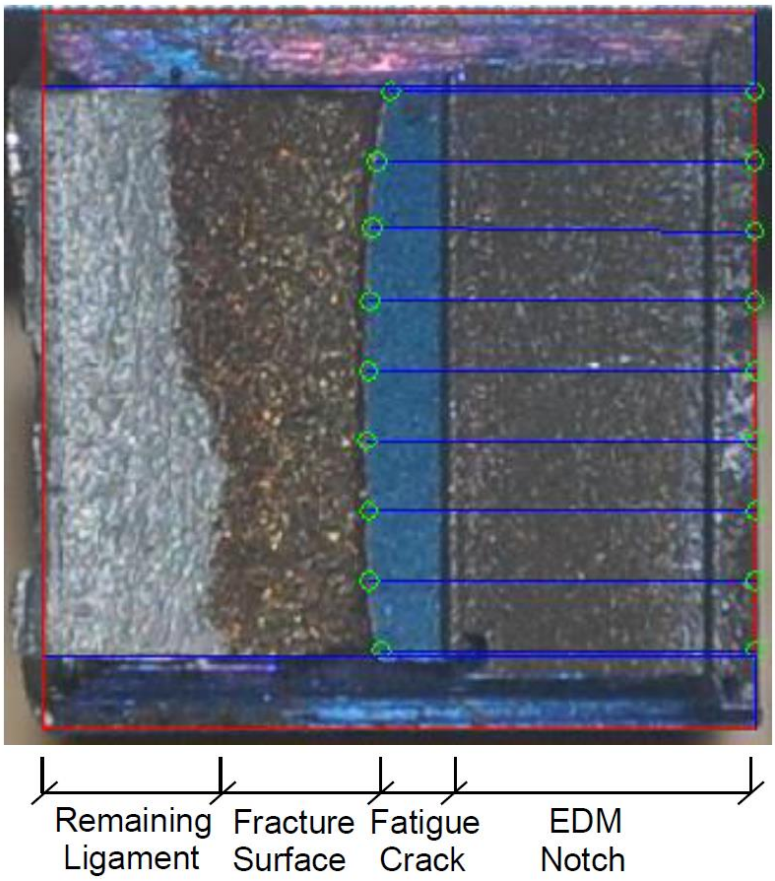

Figure 3-47. Measured Fracture Surface of Typical SE(B) Specimen

Calculation of the J-Integral is then made using the measured initial crack size, specimen geometry, and load-CMOD test record. It is also possible to use the load line displacement (LLD) rather than CMOD. However, for this study CMOD measurements are used because the clip gage resolution and stability are better than that of the load line displacement test record.

Adjustments to the modulus of elasticity are made until the elastic compliance method predicts an initial crack size corresponding to the optically measured fatigue crack. Testing specifications allow for up to 10 per cent deviation from expected elastic modulus in this calculation. Any test record requiring more than a 10 per cent adjustment is considered to be invalid due to specimen misalignment.

The J-Integral at the onset of cleavage fracture, J_c, is the parameter used for reference temperature determination. This is experimentally calculated by separating the elastic and plastic components of the J-Integral, signified by J_e and J_p. These two values are given in Equations 3.1 and 3.2.

$$J_e = \frac{(1 - v^2){K_e}^2}{E} \qquad \text{Eq. 3.1}$$

$$J_p = \frac{\eta A_p}{B_N b_o} \qquad \text{Eq. 3.2}$$

In Equation 3.1, J_e is the elastic component of the J-Integral, v is Poisson's ratio, E is the material modulus of elasticity, and K_e is an elastic fracture toughness value, calculated as shown in Equation 3.3.

$$K_e = \frac{\mathrm{PS}}{(BB_N)^{1/2}W^{3/2}} f\left({}^{a_o}/_{W}\right) \qquad \text{Eq. 3.3}$$

For calculating the elastic fracture toughness, P is the load at fracture, S is the span length of the test apparatus, B is the gross specimen thickness, B_N is the nominal specimen thickness, W is specimen width, and $f(a_o/W)$ is a function related to initial crack size, a_o, and specimen width, W. This function is presented in Equation 3.4.

$$f\left({}^{a_o}/_{W}\right) = \frac{3\left({}^{a_o}/_{W}\right)^{1/2}}{2\left[1+2\left({}^{a_o}/_{W}\right)\right]} \frac{1.99 - \left({}^{a_o}/_{W}\right)\left(1-{}^{a_o}/_{W}\right)\left[2.15 - 3.93\left({}^{a_o}/_{W}\right) + 2.7\left({}^{a_o}/_{W}\right)^2\right]}{\left(1-{}^{a_o}/_{W}\right)^{3/2}} \qquad \text{Eq. 3.4}$$

In Equation 3.2, J_p is the plastic component of the J-Integral, η is a dimensionless parameter relating plastic work to crack growth resistance, A_p is the plastic area under the Load-CMOD or Load-LLD curve, B_N is the nominal specimen thickness, and b_o is the initial remaining ligament. The plastic eta factor, η, varies upon the type of test record being examined. For LLD, η is taken to be 1.9. When CMOD is used, η varies as a function of specimen geometry, as shown in Equation 3.5.

$$\eta = 3.784 - 3.101\left({}^{a_o}/_{W}\right) + 2.018\left({}^{a_o}/_{W}\right)^2 \qquad \text{Eq. 3.5}$$

The plastic area under the Load-CMOD or Load-LLD curve, A_p, is graphically shown in Figure 3-48. This area is calculated using an unloading line from the point of fracture. This unloading line is parallel to the initial elastic slope, $1/C_o$.

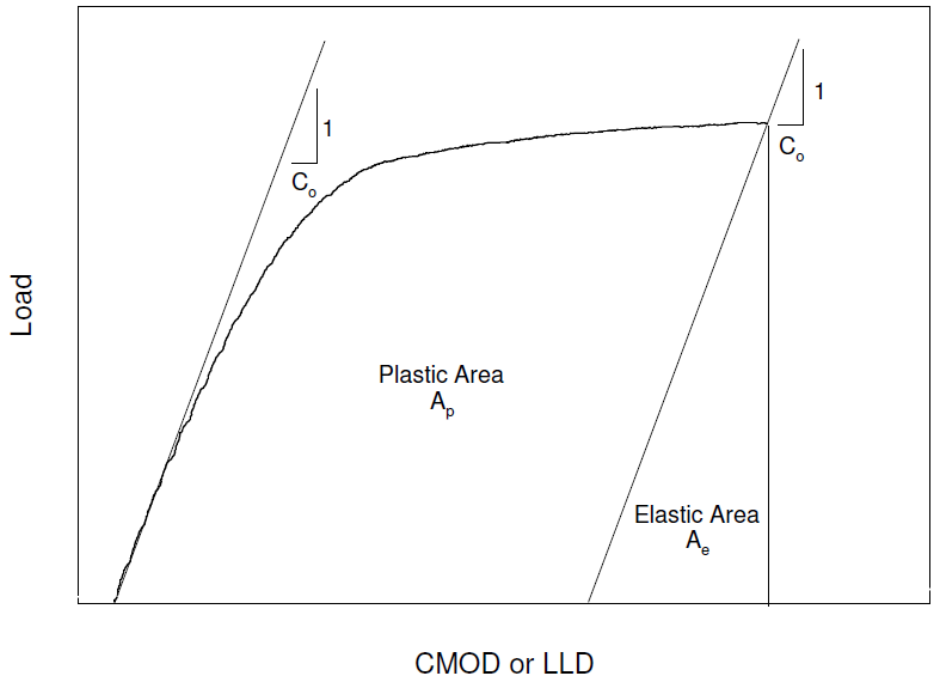

Figure 3-48. Plastic and Elastic Portions of Test Record

These two components, J_e and J_p, are combined to arrive at the critical J-Integral value at the onset of cleavage fracture, J_c. This critical J-Integral value is then converted into an equivalent elastic plastic stress intensity value, K_J, as presented in Chapter 2. Elastic plastic stress intensity values are then used in the determination of the reference temperature, T_o for individual plates or heats of steel. It should be noted that J_c values are only considered to be conditional until a multitude of validity requirements are met.

3.2.4 Crack Arrest Testing

3.2.4.1 Crack Arrest Testing Procedure

Crack arrest testing was performed on an MTS Insight 150 kN (33 kip) electro-mechanical machine, in accordance with ASTM E1221-12 (ASTM 2012). Load is applied

cyclically to the specimen through a wedge and split pin apparatus, as shown in Figure 3-49. Various configurations are allowed for crack arrest testing. For this study the specimens rest on the shoulders of the split pin and are not in contact with the base plate.

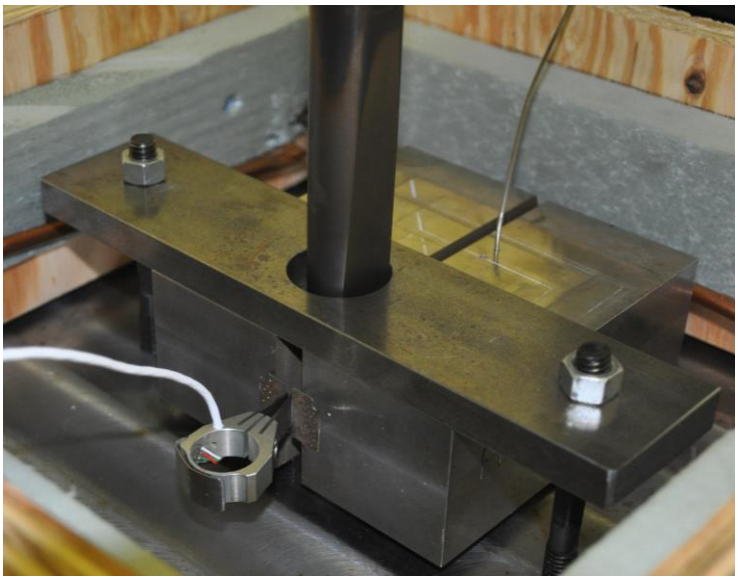

Figure 3-49. Crack Arrest Specimen Prior to Testing

A Tension Measurement DG-25 clip gage is used to record CMOD as the test is performed. Common nomenclature for crack arrest testing uses δ to represent CMOD. Load is applied in displacement control at a rate of approximately 8 mm/min (0.3 in/min) until δ reaches a maximum value calculated by Equation 3.6. If fracture occurs prior to any unloading cycles, this limit should be reduced when testing subsequent specimens.

$$\delta_{1_{max}} = \frac{0.69\sigma_{ys}W\sqrt{B_N/B}}{Ef(a_o/W)} \qquad \text{Eq. 3.6}$$

For Equation 3.6, one signifies the first loading cycle, $f(a_o/W)$ is a specimen geometry related function as defined in Equation 3.7, and all other variables are as previously defined.

$$f(a_o/W) = (1 - a_o/W)^{0.5}\left(0.748 - 2.176(a_o/W) + 3.56(a_o/W)^2 - 2.55(a_o/W)^3 + 0.62(a_o/W)^4\right) \quad \text{Eq. 3.8}$$

When this limit is reached, the wedge is extracted from the specimen. This wedge extraction is the reason for the hold-down plate seen in Figure 3-49. The wedge is extracted completely from the specimen with the clip gage constantly recording CMOD. This allows for a record of displacement offset that occurs at zero force. It is common for load readings to reverse into tension during wedge extraction. To counter this, thread tape is applied to the wedge to reduce friction with split pins, although this does not eliminate the load reversal. This is not thought to influence test results.

Once wedge extraction is complete, the next cycle of loading begins. The wedge is again introduced into the specimen, applying load to the specimen until a fracture event occurs, or the next CMOD limit is reached. CMOD loading limits for all cycles following the first are given by Equation 3.8.

$$\delta_{n_{max}} = [1 + 0.25(n-1)]\left[\frac{0.69\sigma_{ys}W\sqrt{B_N/B}}{Ef(a_o/W)}\right] \quad \text{Eq. 3.8}$$

The variable n signifies the cycle number in this equation, and all other variables are as previously defined. This process continues until fracture occurs, or the maximum CMOD limit is reached. This displacement limit, beyond which point the specimen is not likely to yield a successful result, is presented in Equation 3.9.

$$\delta_{o\,limit} = \frac{1.5\sigma_{ys}W\sqrt{B_N/B}}{Ef(a_o/W)} \quad \text{Eq. 3.9}$$

If this limit is reached without fracture initiation, the test is stopped and the specimen re-machined to remove the material in the area of the plastic zone around the started notch. Specimens are then tested again at a lower temperature, where fracture initiation may occur.

Similar to SE(B) fracture toughness specimens, crack arrest specimens are heat tinted and photographed to allow for accurate measurements of the fracture surface. The nine point measurement process used for fracture toughness testing is not used on crack arrest specimens. Crack arrest point measurements are made with a visual average along three lines of measurement, as seen in Figure 3-50. This allows more room for judgment, as arrested cracks rarely form perfectly straight or flat. Limits on crack straightness are greatly relaxed in comparison to those in place for fracture toughness testing. The photograph presented as Figure 3-50 shows the arrested crack surface measured from the end of the started notch. Additional measurements are also taken from the starter notch to the load line. The distance from the load line to the arrested surface represents the starter notch is the initial crack length, a_o. The final arrested crack length, a_a, is measured from the load line to the visual average discussed above.

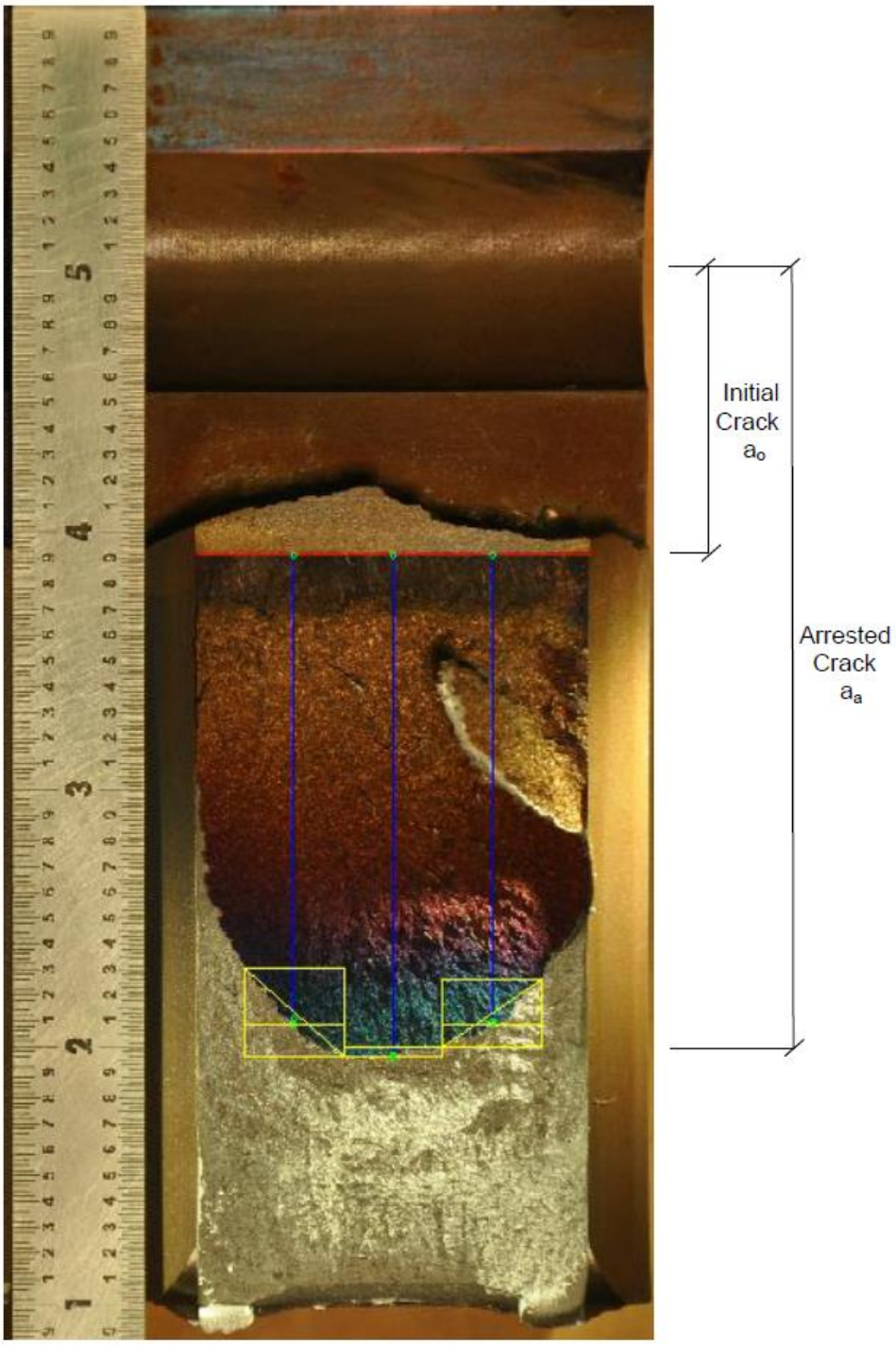

Figure 3-50. Measured Fracture Surface of Typical Crack Arrest Specimen

3.2.4.2 Crack Arrest Data Analysis

Crack arrest toughness values for each specimen are determined from the final arrested crack length and data taken from the Load-CMOD test record. The calculation of crack arrest toughness is done with the use of Equation 3.10.

$$\mathrm{K}_{Qa} = Edf(a/W)\frac{\sqrt{B_N/B}}{\sqrt{W}} \qquad \text{Eq. 3.10}$$

In this equation for a conditional value of crack arrest toughness, *d* is a function related to multiple CMOD values as defined by Equation 3.11. All other variables are as previously defined with a_a used in place of a_o in the geometry function defined by Equation 3.8.

$$d = 0.5\left[\delta_o + \delta_a - \left(\delta_p\right)_1 - \left(\delta_p\right)_{n-1}\right] \qquad \text{Eq. 3.11}$$

In this equation, δ_o represents the CMOD at the onset of unstable crack growth, δ_a represents the displacement just after crack arrest, $(\delta_p)_1$ represents the displacement offset at the end of the first loading cycle, and $(\delta_p)_{n-1}$ represents the CMOD offset at the start of the last loading cycle. These points are all indicated graphically on the typical test record plot shown in Figure 3-51.

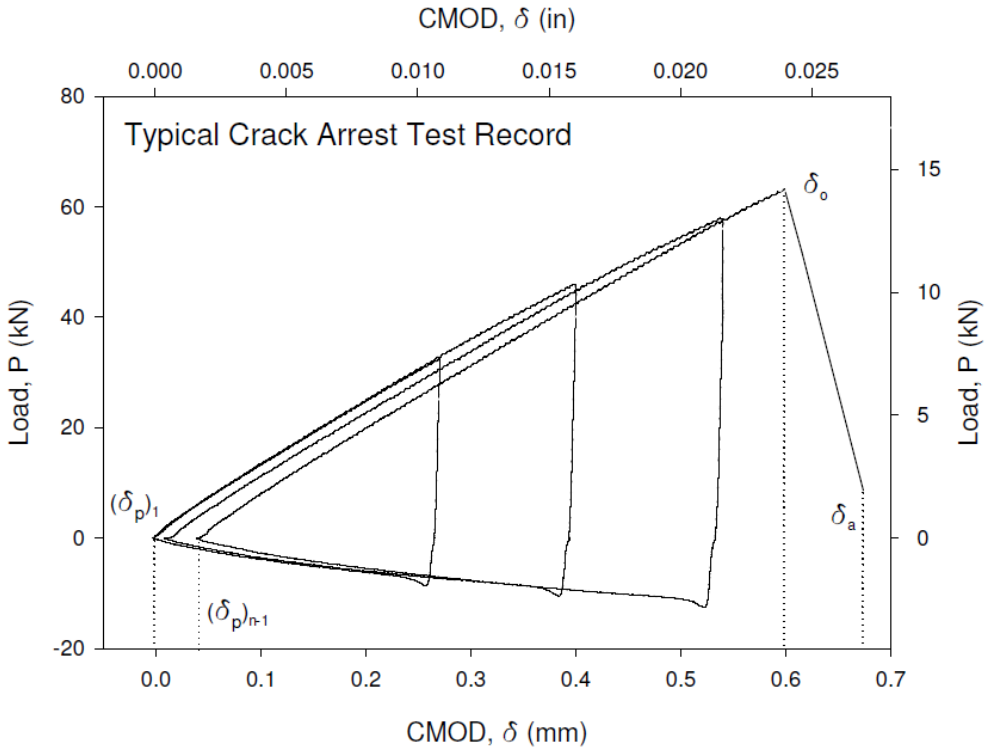

Figure 3-51. Typical Crack Arrest Test Record

As with fracture toughness testing, crack arrest toughness values are considered to be conditional until it can be shown that all validity requirements have been met.

3.2.5 Specimen Cooling Chamber

For both fracture toughness and crack arrest testing, extremely low test temperature are required. These temperatures are obtained and consistently maintained through the use of a liquid nitrogen delivery system. An adjustable environmental chamber was fabricated out of foam and plywood. The chamber was designed to be easily adaptable to either of the two test setups it was needed for, as shown on the crack arrest apparatus in Figure 3-52.

Figure 3-52. Environmental Chamber on Crack Arrest Apparatus

A cryogenic hose connects a tank of liquid nitrogen to an electronically controlled solenoid valve, which in turn leads to a copper pipe with multiple perforations inside of the cooling chamber. The operation of the normally-closed valve is performed by a programmable digital controller connected to a thermocouple inside the chamber. For fracture toughness testing, the thermocouple is embedded in a dummy SE(B) specimen that is placed near the actual test specimen during testing. As previously stated, during crack arrest testing the thermocouple wire is embedded in the crack arrest specimen.

Once a set point temperature is entered, the controller signals for the valve to open if the thermocouple reading was greater than the set point. The controller then measures the rate of change of the temperature, closing and opening the valve as necessary to regulate the temperature. The ability of the controller to regulate valve opening, combined with the insulation provided by the chamber, allow for extremely stable test temperatures. Once set point temperatures are given time to stabilize, test temperatures do not fluctuate by more than $\pm$1 °C.

Chapter 4: "State-of-the-Art Fracture Characterization Part I: Master Curve Analysis of Legacy Bridge Fracture Data"

William Collins, William Wright, Robert Connor, Roberto Leon, and Ryan Sherman

Abstract

Advances in the field of fracture mechanics over the past four decades have allowed for a greater understanding of brittle fracture. Inclusive are how to account for plasticity occurring in fracture specimens and how to statistically define data scatter in the ductile-brittle transition region. This is particularly important for structural steels, which typically possess high ductility and toughness. The material toughness aspect of the fracture control plan for bridges in the United States was developed from a database of linear-elastic tests, many of which were invalid due to specimen plasticity. The first of two papers presents a re-analysis of legacy bridge fracture data, applying plasticity corrections and characterizing behavior using the master curve methodology. Results of the study indicate that the methodology can be used to accurately describe the temperature dependence and associated scatter of fracture behavior in the ductile-brittle transition region. This can be used to define cleavage fracture tolerance bounds for a given data set, which is a necessary step towards the development of a performance based fracture design specification.

4.1 Introduction

Following the 1967 collapse of the Silver Bridge in Point Pleasant, West Virginia, research was directed towards the prevention of structural failure due to brittle fracture in highway bridges (NTSB 1970; Frank and Galambos 1972). The efforts led to the development and

implementation of a fracture control plan (FCP), consisting of three aspects: material toughness specifications, in-service inspection requirements, and fabrication guidelines (AASHTO 1978). Material toughness specifications were mandated in terms of minimum Charpy V-Notch (CVN) impact requirements, an indirect and imperfect measure of fracture toughness (ASTM 2007; ASTM 2013). Using the most modern and appropriate test methods available at the time, many research programs investigated the correlation between CVN impact energy values and linear-elastic fracture toughness (Barsom, et al. 1972; Hartbower and Sunbury 1975; Roberts, et al. 1974). The correlation techniques and the material specifications of the FCP, coupled with the AASHTO fatigue design provisions and shop inspection requirements appear to be effective, as no bridges constructed after the implementation of the FCP have failed due to fracture. However, advances in design codes and in the field of fracture mechanics demonstrate that it is appropriate to revisit how the bridge industry addresses the prevention of brittle fracture, specifically as it relates to the class of structural members referred to as fracture critical members (FCMs).

Modern fracture toughness testing of structural steels involves an elastic-plastic analysis, as a purely linear-elastic analysis is inadequate in defining behavior of ductile, high toughness materials, such as structural steel. Elastic-plastic methods were not well understood at the time that the majority of fracture research on bridge steels was conducted nearly 40 years ago. For this reason, the majority of bridge fracture data has been generated in terms of K_{Ic}, a parameter known as plane-strain critical fracture toughness. Meeting the numerous validity requirements for K_{Ic} testing proved difficult for researchers examining structural steels, and many tests were deemed to be invalid. Material toughness specifications were originally set to correspond with the K_{Ic} limits of validity, thus attempting to avoid a plane strain fracture failure (Alstadt, et al. 2014). These toughness specifications have been modified over time to reach their present state,

but the basic premise and correlation between K_{Ic} and CVN remains the same. The history of the development and evolution of the toughness specifications has been presented in detail elsewhere (Barsom 1974; Alstadt, et al. 2014). The approach is at odds with current performance- and reliability-based design codes (AASHTO 2010).

Rapid, brittle fracture occurring across grain boundaries, known as cleavage fracture, has been studied extensively in the past four decades, and the understanding of this behavior has advanced greatly during this time. Elastic-plastic fracture analysis of test results can now account for plasticity occurring prior to failure that would have previously produced invalid test results (ASTM 2008). In addition to this, a method that statistically accounts for scatter in fracture data has been developed, providing quantifiable confidence in behavior previously thought to be too variable to characterize. The analysis technique has been standardized in ASTM E 1921 and is known as the master curve method (ASTM 2013). Through the research conducted by the authors, it has been shown that the master curve methodology provides statistical bounds that represent fracture behavior of structural steels used in the bridge industry. Presented herein is a re-evaluation of historic bridge fracture data in terms of elastic-plastic fracture mechanics and the master curve methodology.

4.2 Cleavage Fracture and the Master Curve

Cleavage Fracture Initiation

Fracture toughness of a given grade of steel is highly dependent on temperature. At low temperatures, a steel typically behaves in a brittle manner exhibiting low levels of fracture toughness, known as lower shelf behavior. High temperatures typically result in ductility and

plasticity, with no cleavage failure occurring. The plateau reached where ductile tearing instability and plastic collapse control is typically referred to as upper shelf behavior. The zone between the upper and lower shelf, where small changes in temperature can result in large changes in toughness, is known as the transition region. These behavior regions are represented schematically in Figure 4-1. The images in each region represent specimen fracture surfaces and their typical fracture behavior. On the lower shelf cleavage fracture occurs globally along the entire face of a fatigue crack. In the transition region ductile tearing occurs outward from a fatigue crack until an initiation site is reached, triggering cleavage fracture. The fracture surface on the upper shelf exhibits ductile tearing from a fatigue crack, with no occurrence of cleavage fracture.

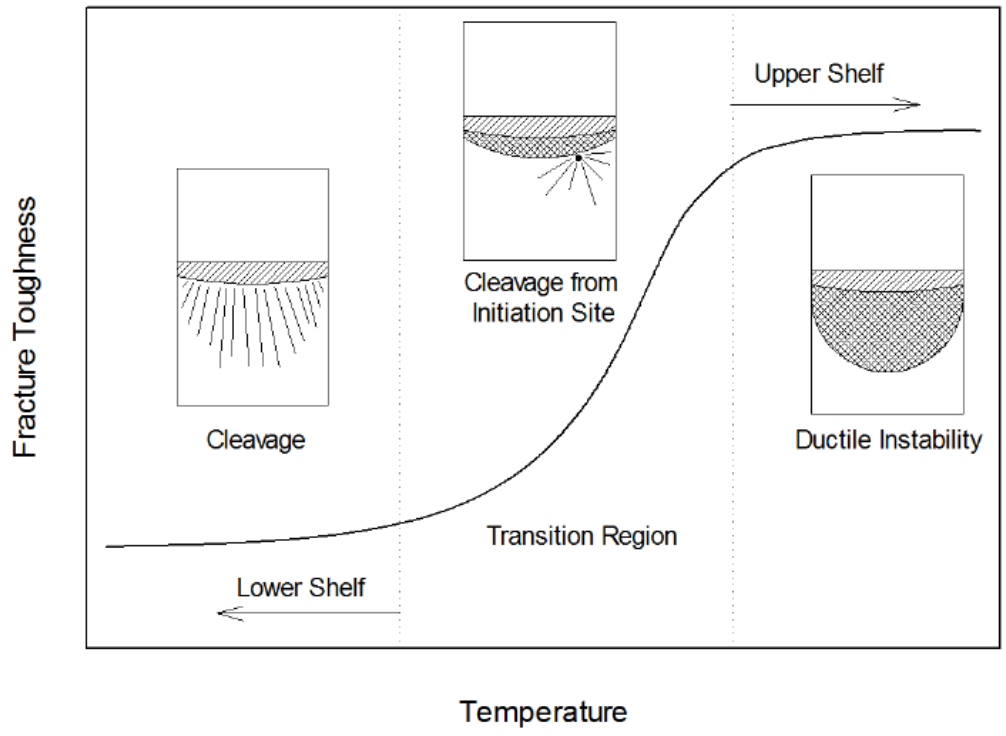

Figure 4-1. Representations of Fracture Mechanism and Temperature Dependence

Cleavage fracture occurs both on the lower shelf and within the transition region. Although structural steel is considered to be a homogenous material for the purposes of general analyses, this assumption is only valid on a global scale, as locally there exist numerous points of discontinuity in the microstructure. These discontinuities, often inclusions, precipitates, or grain boundaries, act as initiation points for fracture. Fracture behavior on the lower shelf, where toughness is reduced, is characterized by initiation from multiple points throughout the material. As temperature and toughness increase, moving fracture behavior into the transition region, plasticity begins to greatly affect the toughness of the material. Yielding and ductile tearing may occur in advance of a crack tip until a sufficiently large initiation site is sampled and cleavage initiation occurs. Due to this variability in behavior and the fact that flaw distribution plays a key role in fracture initiation, cleavage in the transition region is considered to be a stochastic event. As such, behavior in this region can be characterized using statistical modeling methods. These different fracture mechanisms can be seen represented on specimen fracture surfaces in Figure 4-1.

Master Curve Introduction

Traditionally, fracture data in the transition region has been characterized as being highly scattered. Early in the development of fracture mechanics, the scatter was attributed to discrepancies arising from evolving test methods (McCabe, et al. 2007). As advances were made in test methodologies, it became apparent that data scatter was caused by material microstructure. Landes and Shaffer (1980) first described this scatter in terms of the critical J-Integral, J_c, an elastic-plastic parameter representing the rate of energy release as a crack surface is formed during a fracture event. A two-parameter Weibull model was initially employed to represent the probability of failure at a given level of J-integral. Observing noticeable trigger

point sites on specimen fracture surfaces, Landes and Shaffer were able to determine that scatter in cleavage initiation data could be represented by taking into account the distribution of these points throughout the material matrix. When compared to thin specimens, thicker specimens inherently will exhibit lower fracture toughness due to a larger number of flaws and inclusions (i.e., weakest link analogy). Applying this knowledge, Landes and Shaffer were able to develop a size correction capable of adjusting J-integral values for specimens of differing thicknesses.

Wallin (1984) then applied these principles to fracture toughness expressed in terms of an equivalent critical stress intensity factor, K_c, a parameter more applicable to engineering problems than the J-integral. Critical J-integral, J_c, values can be converted to elastic-plastic equivalent critical fracture toughness values, K_{Jc}, by using the material modulus of elasticity, E, and Poisson's ratio, ν, by:

$$K_{Jc} = \sqrt{J_c \frac{E}{1 - \upsilon^2}} \qquad \text{Eq. 4.1}$$

Extensive work was done in examining the scatter found in structural steel fracture data, and a three-parameter Weibull distribution model was adopted to account for the observed phenomenon of an absolute minimum toughness value, K_{min} = 20 MPa√m (18 ksi√in). Specimen size correction and statistical scatter models were applied to an empirical fit describing the relationship between temperature and fracture toughness, and standardized as the master curve concept in ASTM E 1921-97, "Determination of Reference Temperature, T_o, for Ferritic Steels in the Transition Range."

The master curve refers to the exponential function, empirically derived from fracture data of ferritic steels and weld metals, relating toughness and temperature. Typically the master

curve is used to represent median fracture toughness, which is the toughness value at a given temperature for which a specimen has a 50 per cent probability of failure. As the exponential shape applies to all ferritic steels, the curve can be defined by a single temperature which corresponds to a specific toughness value. This temperature is known as the reference temperature, T_o, and is rooted to the median toughness curve at a value of 100 MPa√m (91 ksi√in). The median toughness with respect to temperature is given as:

$$K_{Jc(med)} = 30 + 70e^{[0.019(T-T_o)]} \qquad \text{Eq. 4.2}$$

In this equation, $K_{Jc(med)}$ is the median elastic-plastic critical fracture toughness in MPa√m, T is test temperature in degrees Celsius, and T_o is the reference temperature in degrees Celsius.

Specimen size is normalized prior to application of the master curve methodology to account for distribution of initiation sites throughout the material matrix. Thickness is designated using xT nomenclature, where 'x' is the specimen thickness in inches. Thus, a 25.4 mm (1 in) thick specimen is said to be of thickness 1T. Master curve data is typically normalized to a 1T specimen thickness, although any thickness may be chosen. Thickness normalization is performed through:

$$K_{Jc(x)} = K_{min} + \left[K_{Jc(o)} - K_{min}\right]\left(\frac{B_o}{B_x}\right)^{1/4} \qquad \text{Eq. 4.3}$$

where $K_{Jc(x)}$ is the elastic-plastic critical fracture toughness adjusted to a desired thickness, B_x, absolute minimum toughness, K_{min} = 20 MPa√m (18 ksi√in), $K_{Jc(o)}$ is the fracture toughness at a known thickness, B_o.

Scatter in test data is accounted for using a three-parameter Weibull distribution, for which two of the parameters have been empirically determined. The three parameters used are absolute minimum toughness, Weibull slope, b = 4, and a scale parameter. The scale parameter is determined based upon the number of valid data in a sample, and is built in to the master curve methodology. Applying the probability of failure from the Weibull distribution, tolerance bounds can be determined in units of MPa√m with Eq. 4.4, where 0.xx represents the desired probability of failure, and temperature values are given in degrees Celsius.

$$K_{Jc(0.xx)} = 20 + \left[ln\left(\frac{1}{1-0.xx}\right)\right]^{1/4}\{11 + 77e^{[0.019(T-T_o)]}\} \qquad \text{Eq. 4.4}$$

A typical master curve with a reference temperature of -30 °C (-22 °F) and tolerance bounds of 5 and 95 per cent is shown in Figure 4-2.

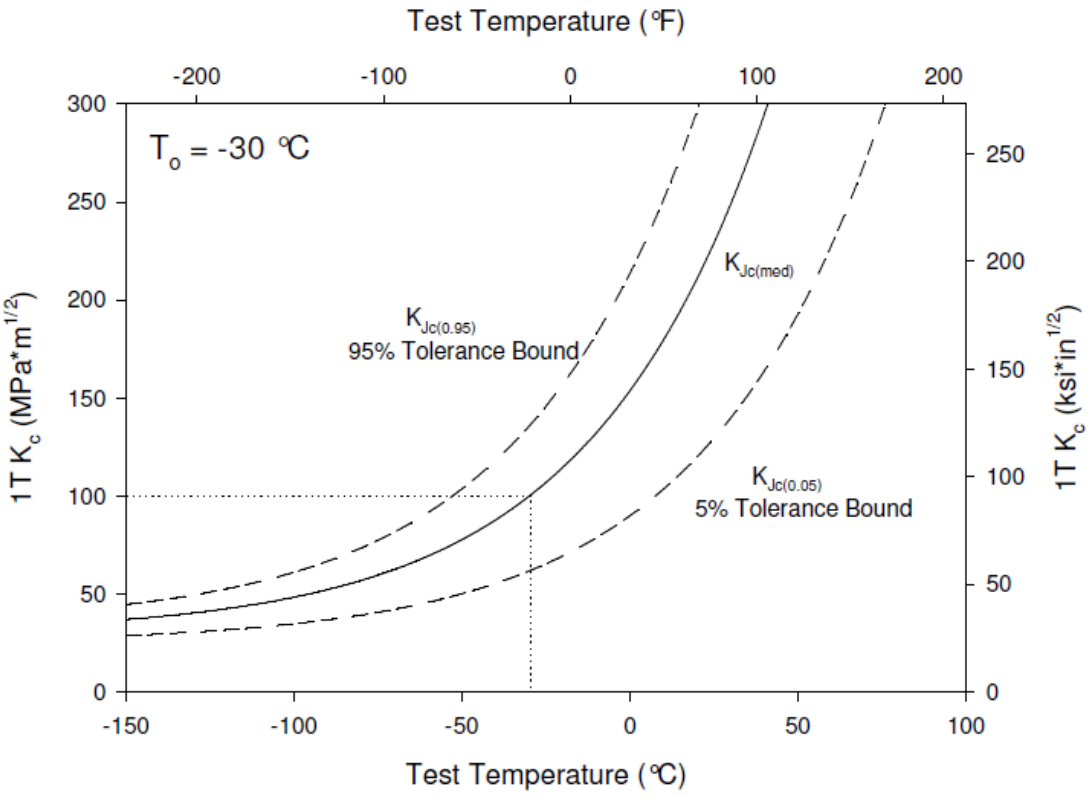

Figure 4-2. Typical Master Curve with Tolerance Bounds

Application of Master Curve Methodology

ASTM E1921 (2013) places two validity limits on K_{Jc} data for use with the master curve methodology. The first is an actual toughness limit, $K_{Jc(limit)}$, that is defined by Eq. (5). The limit equation is defined using the specimen's initial remaining ligament, b_o in millimeters, which is the difference between the specimen width, W, and the initial crack, a_o. Also included in this equation is the material 0.2 per cent offset yield stress, σ_{ys}, in MPa, and modulus of elasticity in GPa. The purpose of the limit is to ensure adequate crack tip constraint in the specimen.

$$K_{Jc(limit)} = \sqrt{\frac{E b_o \sigma_{ys}}{30(1-\upsilon^2)}} \qquad \text{Eq. 4.5}$$

Any toughness value that exceeds this limit is censored in the ASTM E1921 master curve analysis. The second limit is placed on slow stable crack growth preceding cleavage fracture. Any data obtained from a specimen with crack growth beyond the initial fatigue crack exceeding the smaller of 1 mm. (0.04 in.) or 5 per cent of the original ligament length, b_o, is also censored. In both cases, censored values may be used in place of the original datum for master curve analysis. If the limit is violated, $K_{Jc(limit)}$ is the censored value for master curve purposes. When the crack growth limit is violated, the corresponding toughness at that amount of crack growth is used. In the case of both limits being exceeded, the smaller of the two is used as the censoring value.

To obtain the reference temperature for a dataset of size N, fracture toughness and test temperature data are entered into Eq. 4.6. Accounting for censored data values, δ_i is equal to one if the "ith" datum is valid, and zero if it is censored. Using this equation, a provisional value of the reference temperature, T_{oQ}, is determined through iteration. This calculation is limited to data experimentally obtained at temperatures within a range of $\pm$50°C from the provisional reference temperature.

$$\sum_{i=1}^{N} \delta_i \frac{e^{[0.019(T_i - T_{oQ})]}}{11 + 76.7e^{[0.019(T_i - T_{oQ})]}} - \sum_{i=1}^{N} \frac{\left(K_{Jc(i)} - 20\right)^4 e^{[0.019(T_i - T_{oQ})]}}{\left\{11 + 76.7e^{[0.019(T_i - T_{oQ})]}\right\}^5} = 0 \qquad \text{Eq. 4.6}$$

The provisional value of the reference temperature is considered to be the true reference temperature, T_o, only if the size of the data set meets validity requirements. Data collected at temperatures well below the reference temperature are considered to make reduced accuracy contributions towards T_o determination. For this reason, each valid datum is assigned a weighting factor, n_i, determined by the test temperature. These weighting factors are given in

Table 4-1. Summing all weighting factors must result in a value greater than one for the provisional value of the reference temperature, T_{oQ}, to be considered a valid reference temperature, T_o.

Table 4-1. ASTM E1921 Weighting Factors for Multi-Temperature Analysis

$(T-T_o)$ Range, °C	1T $K_{Jc(med)}$ Range, MPa√m	Weighting Factor, n_i
50 to -14	212 to 84	1/6
-15 to -35	83 to 66	1/7
-36 to -50	65 to 58	1/8

4.3 Historical Bridge Fracture Database

Data from nine fracture studies was compiled to form a large database of more than 800 individual fracture toughness values of US bridge steels. All available studies found in the literature that included both CVN impact energy values and fracture mechanics based fracture toughness values were included. The experimental programs re-analyzed in this study are presented in Table 4-2, arranged in order of publication date. As discussed above, fracture toughness test methods have evolved over time, and this is evident when examining the compiled database. The majority of the test programs employed some form of ASTM E 399, the Standard Test Method for Linear-Elastic Plane-Strain Fracture Toughness K_{Ic} of Metallic Materials (ASTM 2006). In addition to different test methods and specimen types, various types and grades of steel were studied. It is important to note that not all of fracture toughness and CVN impact data were presented numerically. Many of the studies used only graphical representations of the data, resulting in the introduction of a small amount of digitizing error into the re-analysis. Each study examined is presented below, with a brief discussion of key testing details and, in some instances, assumptions made for re-analysis.

Table 4-2. Historical Bridge Fracture Database

Database Source	Reference
Toughness Criteria for Structural Steels- Fracture Toughness of A572 Steels	Barsom, et al. 1972
The Determination of the Physical, Chemical, and Metallurgical Characteristics of Steels Furnished from Typical Highway Bridges	Wolff and Martin 1973
Fracture Toughness of Bridge Steels- Phase II	Roberts, et al. 1974
Variability of Fracture Toughness in A514/517 Plate	Hartbower and Sunbury 1975
Determination of Tolerable Flaw Sizes in Full Size Welded Bridge Details	Roberts, et al. 1977
Fracture Behavior of A36 Bridge Steels	Roberts and Krishna 1977
Fracture Toughness of Structural Grade Bridge Steels Part II	Kendrick, et al. 1980
Fort Duquesne Bridge: Fracture Analysis of Flange Cores	Crosley 1984
Brittle-Ductile Transition of Bridge Steels	Ripling, et al. 1990

Barsom, et al. 1972

The experimental program was instituted following the fracture and collapse of the Point Pleasant Bridge, and formed the basis for the original material toughness requirements of the AASHTO fracture control plan. Testing was performed prior to the standardization of fracture testing methods, and conformed to a tentative ASTM method for determining plane-strain fracture toughness. Toughness testing was performed on single edge bend (SE(B)) specimens loaded in three-point bending. Fatigue pre-cracking to a nominal depth of $a_o/W=0.5$ was performed prior to testing. Fracture initiation was examined at three different strain rates: slow, intermediate, and dynamic. Slow rates conformed to fracture toughness testing protocol, while intermediate rate tests represented a one second highway bridge loading rate (Madison 1969). Dynamic rates were conducted as fast as physically possible using a drop-weight machine, and strain rates in the range of 5 to 10 micro strain per second were typical. All plates had a thickness

of 38.1 mm. (1.5 in.), and fracture specimens were tested at full thickness. For each fracture toughness specimen, geometric and test record data were tabulated. Numerical values of CVN impact data were not provided, and information was only presented in a graphical format.

Wolff and Martin 1973

Steel was sampled from bridges constructed in the states of Maine, West Virginia, Vermont, and New York in 1904, 1906, 1935, and 1915, respectively. Six compact tension (C(T)) specimens were tested from each bridge, three each at 24 and -34 °C (75 and -30 °F). Testing conformed with ASTM E 399-72, although the majority of the tests did not meet the validity requirements of the standard. Fatigue pre-cracking of each specimen was conducted prior to fracture testing, with a_o/W ratios ranging from 0.51 to 0.63. All fracture toughness and CVN data were presented in tabulated fashion, including test record data.

Roberts, et al. 1974

Examined as part of this study were eight different types of bridge steel: A7, A36, A242, A440, A441, A588, A514, and A517. All fracture toughness tests were performed on SE(B) specimens with nominal fatigue cracks of 25.4 mm. (1.0 in.). The majority of tests were conducted at dynamic rates, with a relatively small number of tests conducted at intermediate bridge loading rates. In addition to the fracture toughness testing, resistance curve testing was attempted using large C(T) specimens. However, stable crack growth was not achieved and static rate critical fracture toughness values were calculated from the data obtained during these tests. For an unknown reason, initial fatigue crack lengths were not reported for any specimen fabricated from A441 steel. To re-analyze this data, the average a_o/W ratio for all other tests in

this study was used to calculate initial crack lengths for all A441 specimens. All fracture toughness and CVN data was tabulated in this report.

Harbower and Sunbury 1975

Following the discovery of cracks in two bridges under construction in California, this project examined the toughness of the steels used in both their construction and repair. Seven heats of A514/517 grades F and H were examined from two different producers. All plates used in the study had a thickness of 57 mm. (2.25 in.), and C(T) specimens of thickness 1T and 2T were fabricated. Testing was performed at static rates in accordance with ASTM E 399-72, with fatigue pre-cracking to a nominal a_o/W ratio of 0.5. Although fracture toughness data was tabulated in this report, CVN impact data presentation was limited to a graphical format.

Roberts, et al. 1977

The primary purpose of this test program was to examine tolerable flaw sizes in full scale bridge girders. As part of the study, fracture toughness testing was performed on three types of steel: A36, A588, and A514. Specimens of SE(B) geometry and various thicknesses were tested at intermediate and dynamic rates. Fatigue pre-cracks oriented perpendicular to the direction of plate rolling were induced in the specimens prior to testing. Although testing conformed to ASTM E 399-72, efforts were made to account for excessive plasticity occurring in specimens. Plastic zone size corrections were made to calculated linear-elastic fracture toughness values. This effort enabled the researchers to reasonably quantify toughness beyond the validity limits of the linear-elastic test methods. All data in this report, including test record information, fracture toughness, and CVN impact values, were presented in tabular format.

Roberts and Krishna 1977

This study examined the fracture toughness of three heats of A36 steel at an intermediate bridge loading rate. Data was obtained from two 38.1 mm. (1.5 in.) thick plates and one 50.8 mm. (2.0 in.) thick plate. All testing was performed on SE(B) specimens of full plate thickness with nominal fatigue cracks of 25.4 mm. (1.0 in.). Tested in accordance with ASTM E 399-72, all fracture toughness data, as well as CVN impact data, are presented numerically.

Kendrick, et al. 1980

The project examined the fracture behavior of typical structural steels used in bridge construction. Two plates each of A36 and A441 steel were tested, investigating their fracture resistance at various loading rates. Compact tension specimens of thickness 2T were tested at both intermediate and static load rates. Testing was not performed in accordance with standardized test methods, as small cyclic loads were superimposed on the standard loading. It was reported that these cyclic loads did not significantly change the fracture behavior of the material. Fracture toughness and CVN impact data were tabulated in this report.

Crosley 1984

Following reported cracks in the support columns of the Fort Duquesne bridge, the Pennsylvania Department of Transportation initiated an investigation examining the fracture potential of the bridge. Fracture toughness specimens were taken from core samples of the bridge flange, which was composed of a 63.5 mm. (2.5 in.) thick A517 steel plate. Two disk shaped compact tension (DC(T)) specimens were fabricated from the cores, and fatigue crack and fracture orientation was unknown. Both fracture toughness tests were performed at -34 °C (-30 °F). Neither of the two specimens were able to produce purely valid K_{Ic} values, although the

results were still used to analyze the fracture performance of the material. All fracture data obtained in this report was presented numerically.

Ripling, et al.1990

The only study in this database to employ elastic-plastic fracture toughness test methods, the report examined the toughness of four different bridge steels. Plates of 25.4 and 50.8 mm. (1.0 and 2.0 in.) thicknesses were used to fabricate SE(B) specimens of A572, A588, A514, and A852 steel. In addition, 76.2 mm. (3.0 in.) thick C(T) specimens were made from the A852 steel. Crack tip opening displacement (CTOD) tests were performed in accordance with the BS5762-79 test method for all SE(B) specimens. The A852 C(T) specimens were tested following a tentative ASTM method for CTOD determination. CTOD and the J-integral are uniquely related, making it possible to calculate an elastic-plastic equivalent critical fracture toughness value, K_J. In order to use this conversion, certain details pertaining to specimen geometry must be known. Unfortunately, initial fatigue crack size for each specimen was not included in this report. For this reason it was assumed that the ratio of a_o/W was equal to 0.5 for each specimen, and initial crack size was determined from this relationship. In addition to this assumption, all CTOD and CVN data was presented graphically with no tabulated values.

4.4 Data Analysis Procedures

As previously mentioned, the majority of the data being examined as part of this study were developed using linear-elastic fracture mechanics (LEFM) test methods. Due to the high toughness and ductility of structural steel, many tests resulted in invalid K_{Ic} data per the E 399 ASTM specification. Although load-displacement test records for these tests are unavailable, it is possible to approximate the amount of plasticity occurring at the crack tip of a specimen. With

this information, an estimate of cleavage fracture toughness can be made using the method described below. Although not a true measure of elastic-plastic fracture toughness, applying this plasticity correction provides a more meaningful measure of toughness that can then be characterized with the master curve methodology.

In addition to plasticity corrections and assumptions made about individual data sets, there are other aspects of the database that must be accounted for when applying the master curve methodology. Clearly the values compiled herein were not obtained with the intention of establishing the reference temperature of the material. Issues relating to specimen geometry, test rate, and quantity of data were encountered in the re-analysis. How these details were handled is important in the evaluation of the dataset and are therefore, explained below.

Fracture Toughness Plasticity Corrections

Elastic-plastic fracture mechanics (EPFM) test methods for evaluation of the J-integral include the evaluation of the area under the load-displacement curve at the time of fracture initiation. The test record is divided into elastic and plastic components, and these components of J_c are analyzed independently. The elastic portion of the critical J-integral value, J_e, is calculated from a linear-elastic value of fracture toughness, K_e, reversing Eq. (1). The value of K_e is simply the LEFM evaluation of toughness at the point of cleavage failure, represented for bend specimens by:

$$K_e = \frac{PS}{\sqrt{BB_N}W^{3/2}} f\left(a_o/W\right) \qquad \text{Eq. 4.7}$$

where P is the load at fracture, S is the span, B is gross specimen thickness, B_N is net specimen thickness, and $f(a_o/W)$ is a geometric function including initial crack size and specimen width

(ASTM 2013). The formulation of this equation is geometry dependent, and takes a slightly different form for various other specimen geometries. Specimen geometry also influences the form of the function evaluating a_o/W ratio. Changes to these functions due to specimen geometry have been widely published (ASTM 2006).

As the J-integral represents the release rate of energy per area of fracture surface formed, the plastic component, J_p, is a function of plastic energy divided by specimen thickness and remaining ligament size. Both components of the J-integral are then combined to form the elastic-plastic J_c. Because experimental reports do not typically contain load-displacement records, it is not possible to evaluate J_p directly. Based on available data, only an elastic evaluation of fracture toughness is possible.

To evaluate each fracture toughness specimen, the load at failure, P_{max}, was used to calculate fracture toughness, K_{max}, using Eq. 4.7 with appropriate modifications made for specimen geometry. An estimate of plastic zone size, r_p, preceding a crack was developed by Irwin (1960), who showed that it could be used to estimate an effective crack size, a_{eff}, slightly larger than the true crack. As shown in Figure 4-3, half of the assumed plastic zone length in front of the advancing crack, r_y, is used increase the specimen crack size.

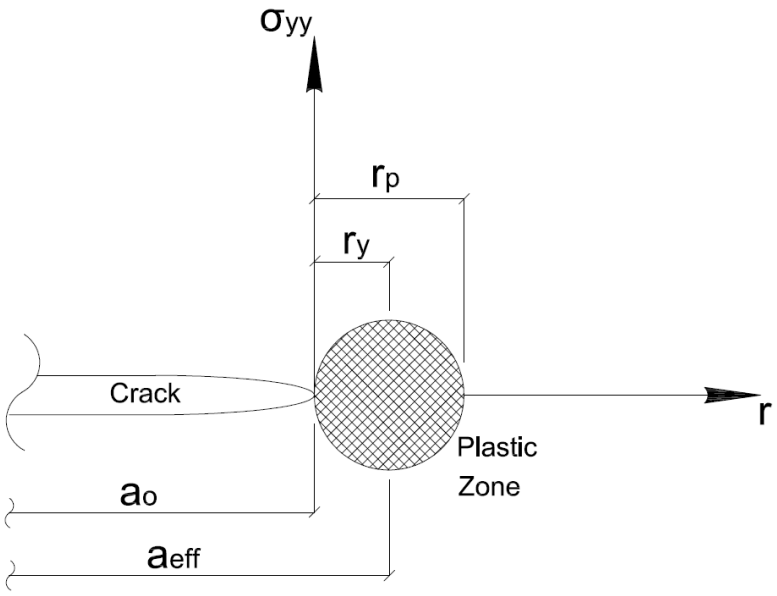

Figure 4-3. Plastic Zone Size Crack Length Correction

Assuming a state approaching plane-strain, this length is given by (Anderson 1995):

$$r_y = \frac{1}{6\pi}\left(\frac{K_{max}}{\sigma_{ys}}\right)^2 \qquad \text{Eq. 4.8}$$

Using this estimate of plastic zone size, a plasticity corrected effective fracture toughness, K_{eff}, can be calculated iteratively by:

$$K_{eff} = \frac{K_{max}\sqrt{a_{eff}}\, f\left({}^{a_{eff}}/_{W}\right)}{\sqrt{a_o}\, f\left({}^{a_o}/_{W}\right)} \qquad \text{Eq. 4.9}$$

Test specimens experiencing large amounts of yielding have extremely large plastic zones in front of the advancing crack. When this occurs the iterative process described above does not converge on a solution of fracture toughness. For this reason it is necessary to quantify

the amount of specimen plasticity at the point where convergence does not occur. This can be done by defining the parameter α, as shown in Eq. 4.10, as an estimate of plasticity (Wallin 2011).

$$\alpha = \frac{b_o}{\left(K/\sigma_{ys}\right)^2} \qquad \text{Eq. 4.10}$$

When α equals 2.5, the parameter serves as the specimen size validity limit for linear-elastic plane-strain fracture toughness, K_{Ic} (ASTM 2006). Using K_{max} as the value of fracture toughness in Eq. 4.10, this parameter was compared against the convergence success of the plasticity correction iteration scheme. Specimen geometry clearly influenced the outcome of the procedure, as it was seen that convergence did not occur for SE(B) specimens when α reached values lower than 0.8, while for C(T) specimens the convergence threshold was approximately 0.7.

Extension of plasticity correction beyond the convergence of the iterative procedure was possible by examining the relationship between α and the normalized increase in fracture toughness due to plasticity correction, K_{eff}/K_{max}. This can be seen for both SE(B) and C(T) specimens in Figure 4. All data for which the iteration scheme converged were included in the fit. Values of α greater than 10, although included in the data fit, have been truncated from the plots for clarity. The fit lines for both specimen types indicate that convergence failed at approximately K_{eff}/K_{max} equal to 1.35. For this reason, the extension of plasticity correction beyond the iterative procedure was capped at a 35 per cent increase in fracture toughness. The upper limit is shown for both SE(B) and C(T) specimens in Figure 4-4.

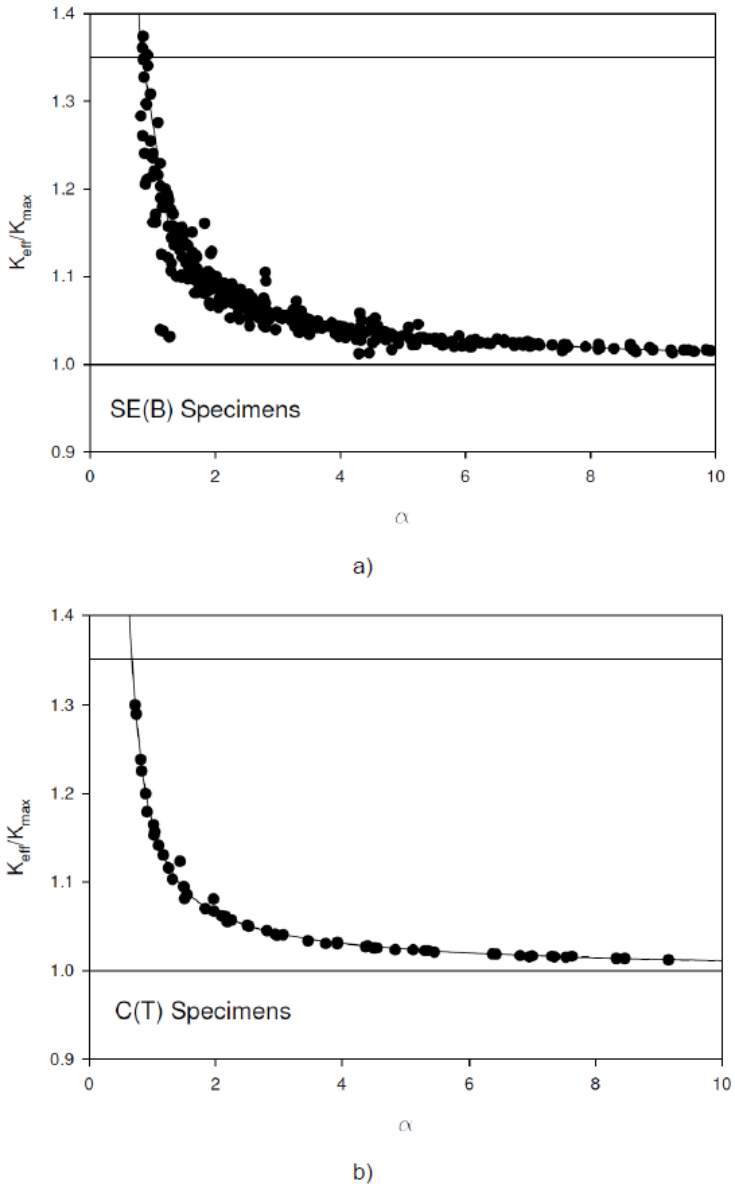

Figure 4-4. Plasticity Correction in a) SE(B) and b) C(T) Specimens

Clearly there exists a point where K_{max}, due to an extreme amount of yielding, no longer corresponds with cleavage fracture initiation. Examinations of limit load solutions for typical specimen and crack size geometries reveal that α in the range of 0.3 to 0.5 corresponds with limit load failure. Because of this, α equal to 0.5 was chosen as the cutoff for plasticity corrections. Any specimen for which K_{max} produced α less than or equal to this limit was censored from the

master curve analysis of that data series. In the case of the Wolff and Martin study, this eliminated the entire data series from re-analysis, as every specimen produced values of α well below 0.5. Data falling below this limit, although not used in the determination of reference temperature, are still included in their respective data sets as ductile failures.

Master Curve Analysis Procedure

Because they were not tested with the intention of determining a reference temperature, many of the specimens in the compiled database fail to meet the requirements set forth in the master curve standard. In many instances it is difficult to quantify the effects of these requirements on the individual data sets, while in others it is impossible to even check the requirements due to a lack of information. Understanding that this may introduce error into the master curve analysis, it is important to identify these aspects of the database.

Fatigue pre-cracking to an a_o/W ratio between 0.45 and 0.55 is required in fracture toughness specimens being used to determine reference temperature. Requirements on crack front straightness and fatigue stress intensity limits also exist in the master curve standard. Although more than a third of the test specimens in the database fall within the specified crack length ratio, many specimens do not meet this requirement. Some of the studies do not report detailed information regarding fatigue pre-cracking procedures. The ones that do provide this information indicate that fatigue cracking was performed at stress intensity values higher than what is currently allowed for reference temperature determination. In addition, very little information is provided about pre-crack geometry. Examination of the database revealed it was not possible to identify specimens that did not meet crack front straightness criteria. To discard all specimens not meeting pre-crack requirements, or specimens for which not enough information is provided to make an evaluation of these requirements, would essentially eliminate

the entire database. For this reason, all specimens were evaluated as if meeting the pre-crack provisions of the master curve methodology, knowing that this may introduce a degree of error into the evaluation.

Although the master curve methodology was developed for quasi-static fracture initiation, the shape of the curve and the statistical limits apply to dynamic fracture initiation as well, and provision for elevated loading rates is now included in ASTM E1921-13 (ASTM 2013). Test rates for fracture specimens are typically presented in terms of stress intensity rate, with the prescribed rate for reference temperature determination falling in the range of 0.1 to 2 MPa√m/sec (0.09 to 1.8 ksi√in/sec), which is considered to be a quasi-static rate. Most studies in the compiled database present test rates in terms of crack tip strain rate or time to maximum load. These values can be roughly converted into stress intensity rates, providing more meaningful measures of fracture toughness test rates. (Details of these rate estimations and their application can be found in the companion paper for this study.) However, because loading rates of fracture toughness tests have been directly tied to bridge loading rates, this convention will be followed in the master curve examination of the database discussed and compiled herein. Data will be presented in terms of three distinct loading rates: static, intermediate, and dynamic. Examination of the estimated stress intensity rates of the database shows a clear delineation in rates for the three categories. Static tests are those that conform to the quasi-static loading rate range of 0.1 to 2 MPa√m/sec (0.09 to 1.8 ksi√in/sec). Dynamic rates have been classified as those that exceed 10,000 MPa√m/sec (9100 ksi√in/sec). Intermediate rates, corresponding to an approximate time to maximum load of 1 second, are those rates in between, the majority of which fall between 20 and 100 MPa√m/sec (18 and 91 ksi√in/sec).

As discussed above, reference temperature validity is dependent on data set size and individual test temperature. Many of the data sets contained in the database contain too few tests, tests outside of the reference temperature $\pm$50°C range, or a combination of both. When a data set did not reach the weighted validity limit of $\Sigma n_i = 1.0$, the temperature bounds for master curve analysis were removed, allowing for all specimens to be included in the reference temperature evaluation regardless of test temperature. Sparse data sets not containing enough points to reach a weighting factor of 1.0 regardless of test temperature were evaluated with the understanding that these led to reduced accuracy determinations of the reference temperature. Any reference temperature determined from a sparse data set, or from an analysis with temperature bounds removed, is designated as a conditional reference temperature, T_{oQ}. Application of the plasticity correction and the master curve methodology can be found for an example data set in 4.7.

4.5 Evaluation of Master Curve Approach

The entire database examined contains 801 fracture toughness tests in 94 data sets. However, upon the examination of the degree of plasticity in each specimen, it was determined that only 681 of the tests correspond to cleavage fracture. Designated as ductile failures, the 120 specimens for which α was less than 0.5 were censored from the master curve analysis of their respective data sets. They are presented in Figure 4-5 as the solid symbols, while the open symbols correspond to cleavage fracture. Values plotted here correspond to the 'original' fracture data, after the plasticity correction procedure has been applied. From Figure 4-5, it is clear that the data appear to be extremely scattered, with no apparent trend. Examining the data of structural bridge steels, it is easily understood why fracture toughness in the transition region

has been considered too variable to accurately characterize. Beyond an absolute minimum fracture toughness appearing to exist around 25 MPa√m (23 ksi√in), there is no discernable pattern to the data scatter.

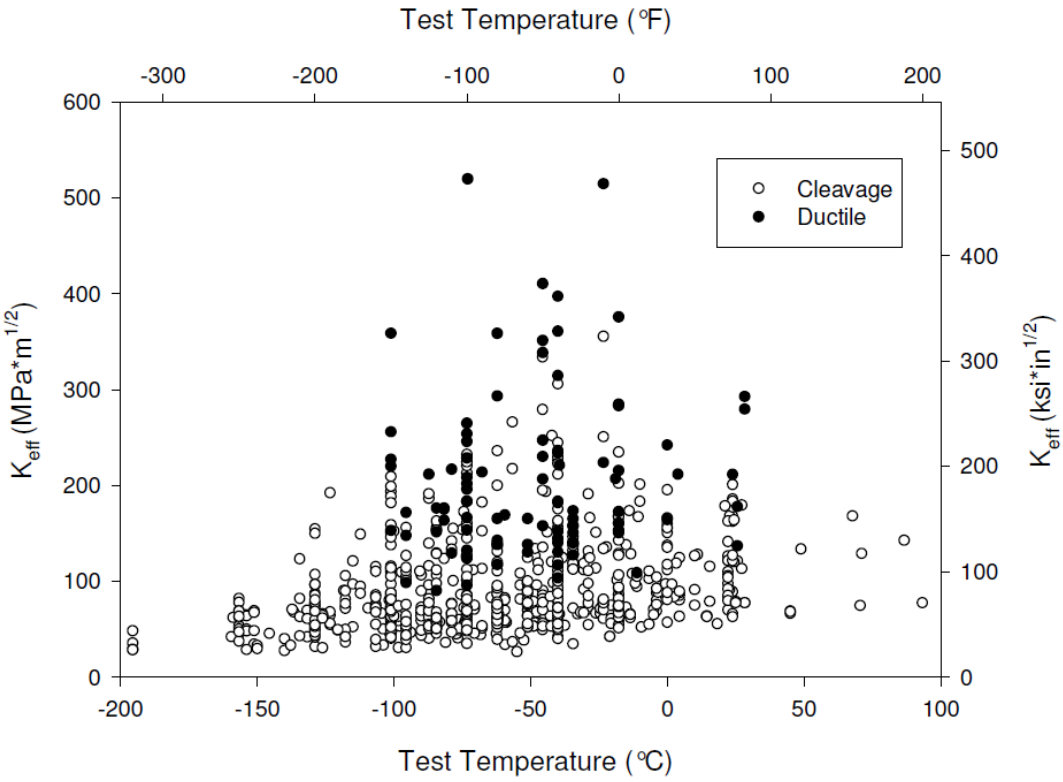

Figure 4-5. Raw Fracture Toughness of Entire Database

Once data have been size corrected and a reference temperature determination has been made for each data set according to ASTM E1921 with the adjustments previously discussed, the entire database can be presented on a single graph by plotting fracture toughness in terms of test temperature minus reference temperature, $T-T_o$. The normalization, seen in Figure 4-6, adjusts all of the toughness data along the temperature axis, presenting the data as if the master curve were anchored at a reference temperature equal to 0 °C. Vertical lines indicate the $\pm$50 °C temperature range within which data are used in reference temperature determination. Statistical tolerance

bounds of 1 and 99 per cent and 5 and 95 per cent are also shown, providing the bounds for the data scatter. No secondary temperature axis is provided on these plots because $T-T_o$ does not actually correspond to a true temperature.

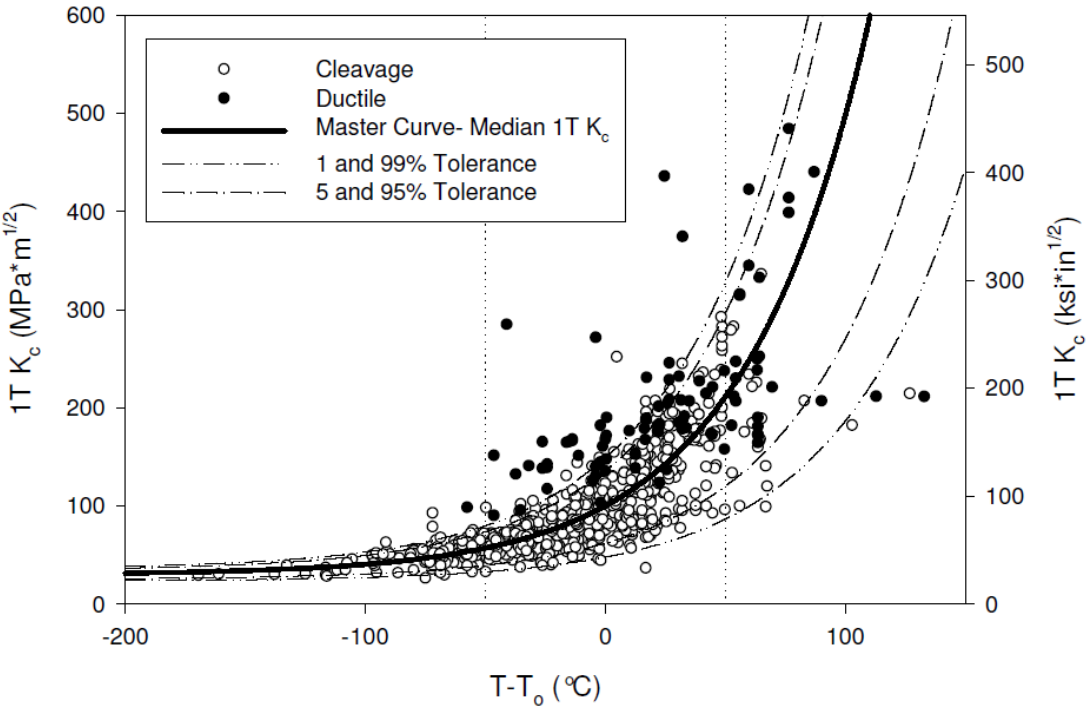

Figure 4-6. $T-T_o$ Normalized Fracture Toughness of Entire Database

Evaluating the number of data falling below a given tolerance bound provides an indication of the effectiveness of the Weibull distribution to describe the data scatter. Examining the entire database it was found that 1.2 and 6.0 per cent of the data fell below the 1 and 5 per cent tolerance bounds, respectively. Removing the fracture specimens not corresponding to cleavage fracture, as seen in Figure 4-7, reduces the total number of data, causing an increase in the percentage of points falling below the tolerance bounds. Visually it can be seen that the removal of ductile failure specimens from the database improves the scatter bounding of upper tolerance limits. For cleavage fracture data alone, 1.2 and 6.6 per cent of the data fell below the 1

and 5 per cent tolerance bounds, respectively. The counts and percentages for data falling below various tolerance bounds is presented in Table 4-3. Reference temperatures for each data set are tabulated in 4.8.

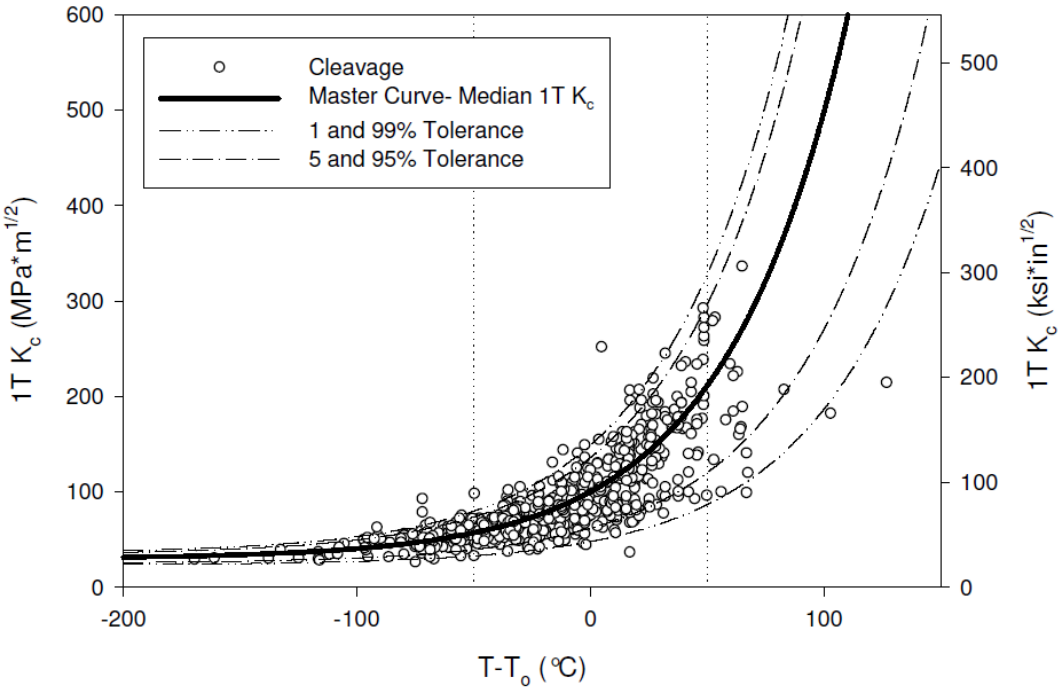

Figure 4-7. T-T_o Normalized Fracture Toughness of Cleavage Fracture Data

Table 4-3. Count and Percentages of Data Falling Below Tolerance Bounds

Tolerance Bound	Total Fracture Database (801)		Ductile Failure Excluded (681)	
	# of Data Below Tolerance Bound	Percentage Below	# of Data Below Tolerance Bound	Percentage Below
10%	100	12.5	94	13.8
5%	48	6.0	45	6.6
2%	21	2.6	19	2.8
1%	10	1.2	8	1.2

4.6 Conclusions

A database of legacy US bridge steel fracture toughness was compiled, re-analyzed, and characterized using state-of-the-art methods to represent the fracture behavior and data scatter in the lower shelf and transition regions using the master curve methodology. Extension of fracture toughness measures beyond LEFM were applied to the database through plasticity corrections. The corrections allow for the estimation of the material's true elastic-plastic fracture toughness. This is extremely beneficial as the majority of US bridge fracture data was obtained prior to the development and refinement of elastic-plastic fracture test methods. The results confirm that cleavage fracture in the transition region is a statistically based event that can be modeled using known probabilistic methods. Although the tolerance bounds predicted from the Weibull distribution of the master curve methodology did not perfectly bound the fracture behavior of the database, the results are within reason.

Application of the master curve methodology allows for the statistical characterization of cleavage fracture behavior, making it possible to move towards performance based fracture design. Current AASHTO material specifications are out of step with the rest of the reliability based design code. The master curve methodology provides a necessary tool in the reliability assessment of bridge fracture data.

4.7 Example of Master Curve Application to a Data Set

An example of plasticity correction and master curve application to a data set is provided herein. Chosen for this example is a data set from Roberts, et al. (1977). The selected data set is composed of intermediate rate fracture toughness test data for an A36 steel beam flange. This

was chosen as an example because it displays many of the application features and assumptions previously discussed including plasticity correction, censored ductile failure, and relaxed temperature limits. Eleven specimens comprise the data set, sampled from a 36.5 mm. (1.44 in.) thick flange of a rolled W36x260. All specimens were SE(B) geometry, with a width of 76.2 mm. (3.0 in.), machined to a thickness of 35.5 mm. (1.40 in.). Original test data is provided in Table 4-4.

Table 4-4. A36 Flange, Intermediate Data: Roberts, et al. 1977

Specimen ID	Test Temperature, °C (°F)	a_o, mm. (in.)	P_{max}, kN (kip)
13.316	-159 (-255)	25.4 (1.000)	61.4 (13.8)
13.313	-157 (-250)	25.4 (1.000)	54.7 (12.3)
13.320	-129 (-200)	26.2 (1.030)	68.9 (15.5)
13.307	-129 (-200)	25.9 (1.020)	77.8 (17.5)
13.312	-123 (-190)	26.2 (1.030)	91.6 (20.6)
13.314	-101 (-150)	27.9 (1.100)	105.9 (23.8)
13.309	-101 (-150)	24.5 (0.965)	110.3 (24.8)
13.304	-101 (-150)	39.1 (1.540)	100.1 (22.5)
13.310	-84 (-120)	25.6 (1.010)	191.7 (43.1)
13.302	-73 (-100)	26.2 (1.030)	154.8 (34.8)
13.315	-68 (-90)	27.8 (1.095)	215.7 (48.5)

Using the provided maximum load at fracture and specimen geometry, K_{max} was determined using Eq. 4.7. Because no specimen side grooves were used in this data set, nominal and gross thicknesses are equal. Using Eq. 4.10, a quantitative measure of plasticity in each specimen was determined, and plastic zone size was estimated using Eq. 4.8. Yield strength of each specimen was adjusted for test temperature and loading rate using the correction developed my Madison and Irwin (Madison and Irwin 1974). Plasticity adjusted crack sizes were used in an iterative manner with Eq. 4.9 to determine effective fracture toughness. Each of these values can

be seen in Table 4-5. Stress intensity values that did not converge on a value using the iterative procedure were capped at a 35 per cent increase above K_{max}, as previously discussed. These values are indicated by an asterisk in the table.

Table 4-5. A36 Flange, Intermediate Plasticity Corrected Data

Specimen ID	K_{max}, MPa√m (ksi√in)	α	K_{eff}, MPa√m (ksi√in)
13.316	41.5 (37.7)	11.5	42.0 (38.2)
13.313	37.0 (33.6)	9.9	37.5 (34.1)
13.320	47.8 (43.5)	5.8	49.1 (44.6)
13.307	53.5 (48.7)	4.1	55.5 (50.5)
13.312	63.5 (57.8)	2.4	68.1 (61.9)
13.314	78.1 (71.1)	1.5	87.6 (79.7)
13.309	72.3 (65.8)	1.9	79.6 (72.4)
13.304	113.3 (103.1)	0.5	153.0 (139.2)*
13.310	130.6 (118.9)	0.4	176.4 (160.5)*
13.302	107.3 (97.7)	0.6	144.9 (131.9)*
13.315	158.4 (144.2)	0.3	213.9 (194.6)*

Effective stress intensity values were compared with the limit of Eq. 4.5 prior to the application of the master curve methodology. All data were found to be below the prescribed limit, and each toughness value was normalized to a 1T equivalent toughness using Eq. 4.3. Discarding any datum with α less than 0.5, Eq. 4.6 was solved iteratively. A provisional reference temperature value was determined at -88 °C (-126 °F). Specimens 13.316 and 13.313 fell outside of the $\pm$50 °C temperature range and were not included in the iterative solution for T_{oQ}. However, the sum of the weighting factors for each specimen, as shown in Table 4-6, did not reach the validity limit of 1.0. For this reason the temperature bounds were relaxed, and 13.316 and 13.313 were used in the determination of a new provisional reference temperature, which was found to be -85 °C (-121 °F). Figure 4-8 displays the 1T plasticity corrected effective

fracture toughness data, as well as the master curve for the data set with 5 and 95 per cent tolerance bounds. Vertical lines indicate the $\pm$50 °C temperature range that was not applied for the analysis of this data set. Other than the specimens exhibiting ductile failure, all data fall within the specified tolerance bounds.

Table 4-6. A36 Flange, Int. Specimen Weighting Factors for Master Curve Validity

Specimen ID	Weighting Factors, n_i
13.316	0
13.313	0
13.320	1/8
13.307	1/8
13.312	1/7
13.314	1/6
13.309	1/6
13.304	-
13.310	-
13.302	1/6
13.315	-
	$\Sigma = 0.893$

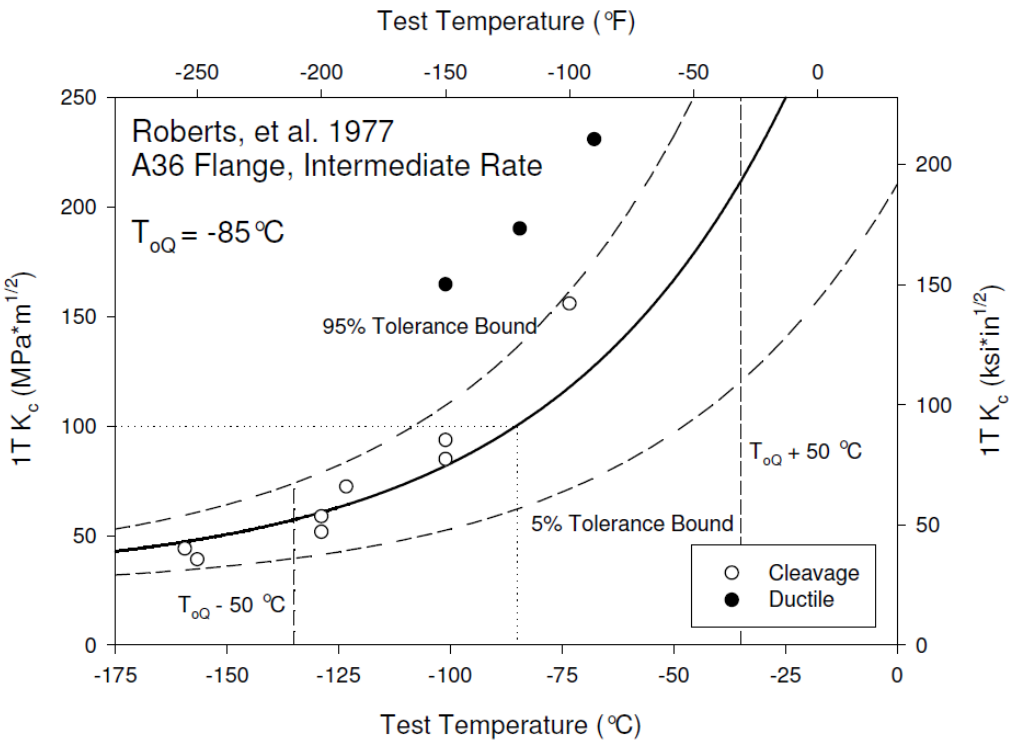

Figure 4-8. Master Curve for A36 Flange, Intermediate Data Set

4.8 Supplemental Data: Reference Temperatures for Each Data Set

Reference temperatures for each individual data set examined as part of this study are presented in Table 4-7. Data sets are identified by the type of steel and designation provided by the authors of the respective studies. All reference temperatures are presented normalized to 1T thickness, and are associated with the median toughness curve. Data sets meeting test number requirements are designated as T_o. Sparse data sets and data sets analyzed with relaxed temperature bounds are presented as provisional reference temperatures, T_{oQ}.

Table 4-7. Reference Temperatures for all Data Sets in Database

Source	Data Set	Rate	1T T_o, °C (°F)	1T T_{oQ}, °C (°F)
Barsom, et al. 1972	A572- 50	Static	-79 (-110)	
		Intermediate		-24 (-11)
		Dynamic		-3 (27)
	A572- 62	Static	-26 (-15)	
Roberts, et al. 1974	A7	Static		27 (81)
		Dynamic		24 (75)
	A36 0.5"	Static		-47 (-53)
		Dynamic	-7 (19)	
	A36 1"	Static		-97 (-143)
		Dynamic		0 (32)
	A36 2"	Dynamic		-6 (21)
	A242, 0.5"	Static		-99 (-146)
		Intermediate		-83 (-117)
		Dynamic	-18 (0)	
	A242, 1"	Static		20 (68)
		Intermediate		35 (95)
		Dynamic	13 (55)	
	A242 2"	Intermediate		15 (59)
		Dynamic		13 (55)
	A440 0.5"	Static		-160 (-256)
		Intermediate		-77 (-107)
		Dynamic	-42 (-44)	
	A440 1"	Static		-74 (-101)
		Intermediate		-34 (-29)
		Dynamic	-10 (14)	
	A440 2"	Intermediate		-63 (-81)
		Dynamic		13 (55)
	A441 0.5"	Static		-67 (-89)
		Dynamic		-35 (-31)
	A441 1"	Dynamic	15 (59)	
	A441 2"	Dynamic		47 (117)
	A588 0.5"	Static		-48 (-54)
		Intermediate		-25 (-13)
		Dynamic	-27 (-17)	
	A588 1"	Static		-98 (-144)
		Intermediate		-83 (-117)

		Dynamic	-29 (-20)	
	A588 2"	Intermediate		-16 (3)
		Dynamic		1 (34)
	A514 1"	Dynamic		-45 (-49)
	A514 2"	Dynamic		-55 (-67)
Hartbower and Sunbury 1975	A514 F, L	Static	-59 (-74)	
	A514 F, M	Static		-103 (-153)
	A517 F, A	Static		-109 (-164)
	A514 H, R	Static		-43 (-45)
	A517 H, Z	Static		-24 (-11)
	A517 H, AL	Static		-4 (25)
	A517 H, CK-1	Static	62 (144)	
Roberts, et al. 1977	A36 0.375"	Intermediate		-123 (-189)
		Dynamic		-57 (-71)
	A36 2"	Intermediate	-90 (-130)	
		Dynamic	-7 (19)	
	A36 3"	Intermediate	-126 (-195)	
		Dynamic		-7 (19)
	A36 Web	Intermediate		-68 (-90)
		Dynamic		-20 (-4)
	A36 Flange	Intermediate		-85 (-121)
		Dynamic		-6 (21)
	A588 0.375"	Intermediate	-127 (-197)	
		Dynamic		-39 (-38)
	A588 2"	Intermediate	-71 (-96)	
		Dynamic		-5 (23)
	A588 3"	Intermediate	-118 (-180)	
		Dynamic		-25 (-13)
	A588 Web	Intermediate	-123 (-189)	
		Dynamic		-49 (-56)
	A588 Flange	Intermediate	-122 (-188)	
		Dynamic		-28 (-18)
	A514 0.375"	Intermediate		-60 (-76)
		Dynamic	-72 (-98)	
	A514 1.5"	Intermediate	-105 (-157)	
		Dynamic		-79 (-110)
	A514 2"	Intermediate	-119 (-182)	
		Dynamic		-95 (-139)
Roberts and Krishna	A36 496T0881	Intermediate	-51 (-60)	

1977	A36 491T1031	Intermediate	-47 (-53)	
	A36 402P7031	Intermediate	-98 (-144)	
Kendrick, et al. 1980	A36 A	Intermediate		-26 (-15)
	A36 B	Static		8 (46)
		Intermediate		-3 (27)
	A441 C	Static		-36 (-33)
		Intermediate		-39 (-38)
	A441 D	Static		-33 (-27)
		Intermediate		-28 (-18)
Crosley 1984	A517	Intermediate		-49 (-56)
Ripling, et al. 1990	A514 Grade B, A	Static	-100 (-148)	
	A514-85A, B	Static	-122 (-188)	
	A572-82, C	Static		-36 (-33)
	A572-82, D	Static	-40 (-40)	
	A588-82 Grade B, E	Static		-38 (-36)
	A588-82 Grade B, F	Static	-50 (-58)	
	A852-85, H	Static		-96 (-141)
	A852-85, L	Static	-82 (-116)	
	A852-85, M	Static	-61 (-78)	

4.9 Acknowledgements

The authors would like to thank Kim Wallin from VTT Technical Research Centre of Finland for his guidance and feedback during this study. They would also like to thank Richard Link of the US Naval Academy for his advice and assistance. Funding for this study was provided by the FHWA. The opinions expressed in this paper are those of the authors, and do not reflect the position of the FHWA.

Notation

The following symbols are used in this paper:

a_{eff} = Effective crack size following plasticity correction

a_o = Initial crack size

b_o = Initial remaining ligament size

B = Specimen thickness

B_N = Net specimen thickness

B_o = Initial specimen thickness used in thickness adjustment

B_x = Desired specimen thickness for thickness adjustment

C(T) = Compact tension specimen geometry

CVN = Charpy V-notch impact test

E = Modulus of Elasticity

J_c = Critical value of J-integral at failure

J_e = Elastic component of J-integral calculation

J_p = Plastic component of J-integral calculation

K = Fracture toughness and stress intensity

K_c = Critical fracture toughness

K_e = Elastic fracture toughness

K_{eff} = Effective fracture toughness following plasticity correction

K_{Ic} = Mode I critical plane-strain fracture toughness

K_{Jc} = Elastic-plastic equivalent fracture toughness converted from J-integral

$K_{Jc(0.xx)}$ = Elastic-plastic fracture toughness tolerance limit of xx per cen

$K_{Jc(i)}$ = Elastic-plastic fracture toughness of ith specimen

$K_{Jc(limit)}$ = Elastic-plastic fracture toughness limit in master curve analysis

$K_{Jc(med)}$ = Median elastic-plastic fracture toughness

$K_{Jc(o)}$ = Initial elastic-plastic fracture toughness used in thickness adjustment

$K_{Jc(x)}$ = Size adjusted fracture toughness for specimen of thickness B_N

K_{max} = Linear-elastic fracture toughness calculated at maximum load

K_{min} = Absolute minimum fracture toughness equal to 20 MPa√m (18 ksi√in)

n_i = Weighting factor assigned to ith specimen

P_{max} = Maximum load, typically occurring at failure

r_p = Estimated plastic zone size

r_y = Effective crack length increase due to estimated plastic zone size

S = Span length in bend bar testing

SE(B) = Single edge bend specimen geometry

T_i = Test temperature of ith specimen

T_o = Reference temperature, rooted at median toughness equal to 100 MPa√m (91 ksi√in)

T_{oQ} = Provisional reference temperature prior to validation

W = Width of specimen

α = Quantitative estimate of specimen plasticity

δ_i = Validity of ith specimen in master curve analysis, valid = 1, invalid = 0

v = Poisson's ratio

σ_{ys} = 0.2% offset yield strength

Chapter 5: "State-of-the-Art Fracture Characterization Part II: Examination of Correlations between Charpy V-Notch and the Master Curve Reference Temperature, T_o"

William Collins, William Wright, Robert Connor, Roberto Leon, and Ryan Sherman

Abstract

Many material toughness specifications, including the AASHTO fracture control plan for highway bridges promulgated in 1978, rely on Charpy V-Notch (CVN) requirements to prevent brittle fracture. It has long been recognized that this is at best an indirect approach to the problem and significant advances in the understanding of fracture behavior have taken place in the four decades since this approach was put in place. These advances include (1) the ability to characterize the scatter of fracture data in the ductile to brittle transition region through a method known as the master curve methodology and (2) numerous proposals for better correlation procedures to relate CVN values to more rigorous fracture mechanics parameters. This paper, the second of two companion papers, presents an analysis of 29 permutations of methods for correlating CVN to reference temperature, T_o. Results indicate that although no method acts as a true predictor for reference temperature, the dispersion of the estimated values is quantifiable, allowing for fracture to be treated like other design limit states. Additionally, the current basis of the material toughness was examined, revealing that the accepted temperature shift can predict unconservative fracture toughness values.

5.1 Introduction

In order to prevent brittle fracture in highway bridges, AASHTO (1978) developed and implemented a fracture control plan (FCP) consisting of a combination of material toughness specifications, fabrication guidelines, and in-service inspection requirements. Although it has long been recognized that Charpy V-Notch (CVN) values are not the best predictors of brittle fracture behavior, material toughness specifications are mandated in terms of CVN impact test energy values. Required CVN values for different applications and service conditions are mandated in ASTM A709 (2013) and the AASHTO LRFD Bridge Design Specifications (2010). Impact test specifications for fracture critical tension components are presented in Table 5-1.

Table 5-1. ASTM A709-13 Fracture Critical Tension Component CVN Requirements

Grade	Thickness, mm. (in.)	Minimum Average Energy, J (ft-lbf)		
		Zone I	Zone II	Zone III
250F (36F)	to 100 (4) incl.	34 (25) at 21°C (70°F)	34 (25) at 4°C (40°F)	34 (25) at -12°C (10°F)
345F (50F), 345SF (50SF), 345WF (50WF)	to 50 (2) incl.	34 (25) at 21°C (70°F)	34 (25) at 4°C (40°F)	34 (25) at -12°C (10°F)
	over 50 to 100 (2 to 4) incl.	41 (30) at 21°C (70°F)	41 (30) at 4°C (40°F)	41 (30) at -12°C (10°F)
HPS 345WF (HPS 50WF)	to 100 (4) incl.	41 (30) at -12°C (10°F)	41 (30) at -12°C (10°F)	41 (30) at -12°C (10°F)
HPS 485WF (HPS 70WF)	to 100 (4) incl.	48 (35) at -23°C (-10°F)	48 (35) at -23°C (-10°F)	48 (35) at -23°C (-10°F)
HPS 690 WF (HPS 100WF)	to 65 (2.5) incl.	48 (35) at -34°C (-30°F)	48 (35) at -34°C (-30°F)	48 (35) at -34°C (-30°F)
	over 65 to 100 (2.5 to 4) incl.	not permitted	not permitted	not permitted

The CVN values have been related to true fracture mechanics toughness parameters, such as fracture toughness, K, through correlation procedures. The majority of the correlations were

developed as single point CVN-K relationships. Validity limits on fracture toughness testing at the time of the correlation development limited the relationships to behavior on the lower shelf of CVN temperature transition curves.

Over the last four decades, advances in the understanding of fracture mechanics and ductile-brittle transition region behavior have made it possible to better characterize the fracture behavior of bridge steels (ASTM 2013). Application of the master curve methodology to legacy bridge steel fracture data sets has shown that data scatter in the transition region can be statistically characterized (Collins, et al. submitted). This paper examines proposed relationships between CVN impact tests and the master curve reference temperature, T_o, for the database presented in the first part of this companion papers (Collins, et al. submitted). Establishment of a CVN correlation with the master curve will allow for the development of performance- and reliability-based material toughness specifications.

5.2 Charpy V-Notch Testing

Charpy V-Notch testing, as described in ASTM E23 (2007), measures the absorbed energy at fracture of a notched bar specimen subjected to dynamic loading from an impact hammer. Although traditionally used as a measure of fracture toughness in material qualification tests, there are numerous differences between CVN testing and true fracture mechanics tests. Providing only a qualitative measure of material toughness, CVN test values cannot be used directly in fracture mechanics analyses, and thus are not usable in structural integrity assessment (Anderson 1995). CVN test values over a range of temperatures exhibit three typical fracture behavior regimes: lower shelf, transition region, and upper shelf. The three different behavior regimes are displayed schematically in Figure 5-1. The CVN temperature transition curve is

shifted and distorted when compared with curves developed from fracture mechanics test data. Differences in notch acuity cause the curve to shift horizontally along the temperature axis. Sharp notches, like fatigue cracks, cause lower toughness at a given temperature when compared with blunter notches, like those on CVN specimens. A sharp crack will also cause a decrease in upper shelf toughness when compared with a blunt notch. Rate effects also cause a shift of the transition curve along the temperature axis. Dynamic tests display lower toughness at a given temperature than static tests. However, due to an increase in yield strength at higher test rates, materials typically exhibit higher upper shelf toughness when tested at dynamic rates. Rate and notch acuity effects on fracture toughness are presented schematically in Figure 5-1.

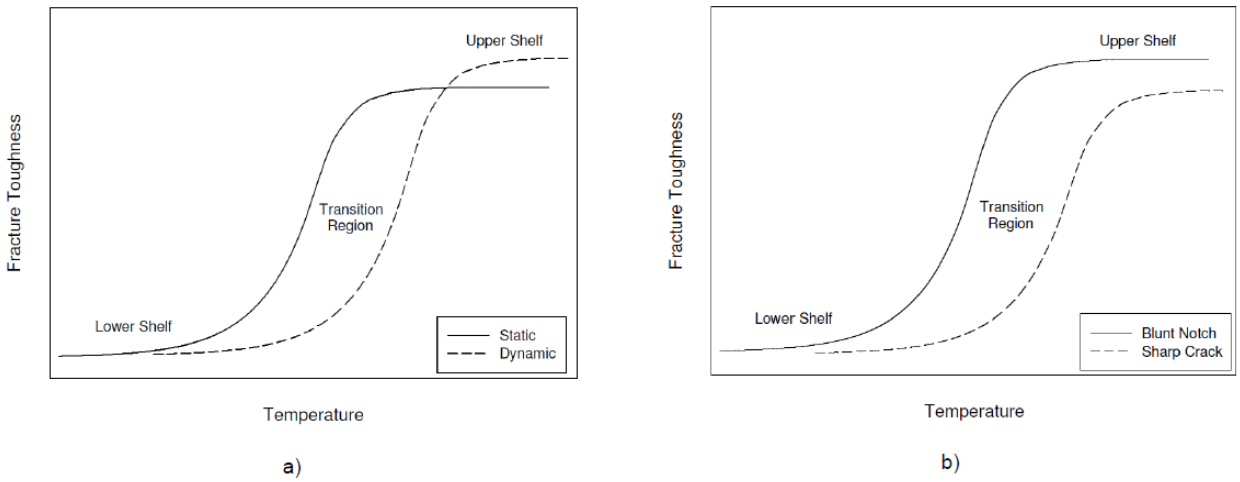

Figure 5-1. Schematic Representation of a) Rate and b) Notch Acuity Effects

Although these differences exist between CVN and fracture mechanics tests, it is thought that the two can be associated through a careful correlation methodology (Wallin 2011). This belief is justified by the fact that both CVN and the more rigorous fracture toughness J-integral tests relate to energy dissipation during a fracture event. J-integral testing examines the energy released during an elastic-plastic fracture event. Results of J-integral testing can be used to

determine an elastic-plastic fracture toughness parameter, which can directly be applied to fracture mechanics problems. Because of the commonality between the two types of tests, it is typical to use CVN tests in place of more expensive, time consuming, and rigorous fracture mechanics tests. In addition to bridge design specifications, numerous industries specify material toughness requirements in terms of mandatory CVN values. The bases of these specifications typically are developed from more rigorous fracture toughness testing, and the empirically derived relationships between these values and CVN tests (Barsom 1975, BSI 2005).

5.3 Existing Correlation Methods

Numerous empirically derived correlation methods have been proposed to relate CVN energy values to true fracture mechanics parameters, either fracture toughness, K, or master curve reference temperature, T_o. The reference temperature represents the temperature at which the median toughness value of the exponential master curve is equal to 100 MPa√m (91 ksi√in). A detailed description of the reference temperature and the master curve methodology can be found in the first part of this paper (Collins, et al. submitted). Twelve different correlation methods were examined as part of this study. The majority of these methods were developed as direct one-to-one correlation procedures relating a single CVN data point to a single fracture toughness value. Only the Wallin (2011) method and the British Standard (2005) methods relate CVN values to reference temperatures instead of single point toughness values. Additionally, most correlation methods do not consider changes in test rate, predicting either static or dynamic fracture toughness. Rate considerations, if not implicitly included in the correlation method, are discussed later in this paper. Presented below are the correlation methods examined as part of this study. Although predominantly published in imperial units, all correlation methods have

been converted and are presented here in SI units. The exception to this is when temperature shifts are involved, as these conversions are not convertible between different temperature scales. Readers should remember that most of these correlations were developed in order to provide a conservative approach for design and were not intended originally to predict the actual fracture toughness of any particular test specimen.

Barsom and Rolfe Original Correlation

An early correlation proposed by Barsom and Rolfe (1970) was developed to relate CVN energy directly to linear elastic plane strain fracture toughness, K_{Ic}. The correlation equation does not consider the effects of rate, predicting only static fracture toughness as:

$$K_{Ic} = 0.471\sqrt{E \times CVN^{3/2}} \qquad \text{Eq. 5.1}$$

where K_{Ic} is plain strain linear elastic static fracture toughness in MPa√m, E is modulus of elasticity in GPa, and CVN in the Charpy V-Notch impact toughness in J. The correlation equation, as well as others proposed by Barsom and other researchers, was developed from a database composed of nine steels having yield stresses in the range of 250 to 1700 MPa (36 to 246 ksi).

Barsom and Rolfe Two Stage Correlation

The Barsom and Rolfe Two Stage correlation method is so named because it requires a toughness correlation and then a rate-induced temperature shift. This correlation forms the basis for the current AASHTO material toughness specifications (Barsom 1975). Charpy V-Notch energy values are related to dynamic fracture toughness by:

$$K_{ID} = 0.804\sqrt{E \times CVN} \quad \text{Eq. 5.2}$$

where K_{ID} is dynamic fracture toughness, and all other variables are as previously defined. As rate changes do not influence the shape of a toughness temperature transition curve, but move it along the horizontal temperature axis, a temperature shift is needed to predict toughness at non-dynamic loading rates. Transitioning from dynamic fracture toughness to an intermediate or static value requires a shift to lower temperatures, provided by:

$$T_{shift} = 215 - 1.5\sigma_{ys} \quad \text{Eq. 5.3}$$

where T_{shift} is the temperature shift applied to the dynamic toughness test temperature in Fahrenheit, and σ_{ys} is yield stress in ksi. Application of this shift produces the temperature for a static fracture toughness test corresponding to the calculated toughness value. To obtain an intermediate rate fracture toughness temperature, 75 per cent of this shift is applied. The procedure was intended for fracture toughness values exhibiting lower shelf and lower transition behavior.

British Standard 7910 Correlation Methods

Presented in Annex J of the British Standards Institution's BS 7910 (2005) are multiple correlation methods for predicting static fracture toughness of ferritic steels. Methods J.2.1 and J.2.4 predict lower bound fracture toughness, K, at service temperature, while method J.2.2 provides an estimate of the master curve reference temperature, T_o. The correlation method presented in J.2.1 includes an adjustment for the thickness of the structural component being analyzed given by:

$$K = \left[\left(12\sqrt{CVN} - 20\right)\left({}^{25}/_{B}\right)^{0.25}\right] + 20 \qquad \text{Eq. 5.4}$$

where K is the material toughness in MPa√m, B is component thickness in mm, and CVN is as previously defined. The procedure is intended for use when CVN energy values are known at service temperatures.

Method J.2.2 predicts the reference temperature when data for a full Charpy V-Notch temperature transition curve is available. The equations are based on correlations originally proposed by Wallin (1989). Test temperatures corresponding to CVN impact test values of 27 and 40 J (20 and 30 ft-lbf) are adjusted as shown by Eq. (5) and Eq. (6) to provide an estimated reference temperature:

$$T_o = T_{27J} - 18°C + T_k \qquad \text{Eq. 5.5}$$

$$T_o = T_{40J} - 24°C + T_k \qquad \text{Eq. 5.6}$$

where T_o is reference temperature, T_{27J} and T_{40J} correspond to test temperatures at CVN energy levels of 27 and 40 J, respectively, and T_k is a temperature term used to account for scatter in CVN data. All temperatures are in degrees Celsius. BS 7910 recommends that T_k =25 °C unless experimental data supports the use of a lower value.

The correlation presented in J.2.4 provides a lower bound service temperature toughness value. The resulting value is intended to act as a cap on the previous British Standard equations in the case of a material exhibiting low upper shelf toughness, where the CVN impact values are simply related to fracture toughness by:

$$K = (0.54 \times \text{CVN}) + 55 \qquad \text{Eq. 5.7}$$

where all variables are as defined previously. Although intended to be used together in estimating a conservative material toughness value, each of the BS 7910 methods has been analyzed independently in this study.

Corten and Sailors Correlation Methods

Employing the fracture toughness database used in the development of the two Barsom and Rolfe correlation methods, Corten and Sailors (1971) attempted to identify and eliminate causes of scatter in the data. This included the removal of both the extremely low and extremely high CVN energy values, leaving only values in the range of 7 to 68 J (5 to 50 ft-lb). Also removed from the database were any tests for which the steel was thought to have had an inhomogenous structure, including steel exhibiting extreme through thickness microstructure gradients and weld metals. The refinement in the database and the addition of a few other data points resulted in a "second generation" correlation method given by:

$$K_{Ic} = 14.6 \times \text{CVN}^{1/2} \qquad \text{Eq. 5.8}$$

where the two variables are as previously defined. The equation does not consider rate effects, and is only used to predict static fracture toughness values. Dynamic toughness estimates are made using the empirically derived relationship:

$$K_{ID} = 15.6 \times \text{CVN}^{0.375} \qquad \text{Eq. 5.9}$$

Marandet and Sanz Correlation

Marandet and Sanz (1977) developed a CVN-K correlation from low carbon steels with yield strengths ranging from 215 to 1100 MPa (31 to 160 ksi). The equation does not include rate effects, and relates CVN impact toughness to static fracture toughness through:

$$K_{Ic} = 19\sqrt{CVN} \qquad \text{Eq. 5.10}$$

Roberts and Newton Lower Bound Correlation

Noting that various existing correlation methods were conservative at different stages of fracture behavior, Roberts and Newton (1984) proposed a new CVN-K correlation. The so called lower bound method was developed to provide a conservative estimate of fracture toughness at both lower shelf and transition region behavior. The lower bound correlation method is provided by:

$$K_{Ic} = 8.47 \times \mathrm{CVN}^{0.63} \qquad \text{Eq. 5.11}$$

where all variables are as previously defined.

Rolfe-Novak-Barsom Upper Shelf Correlation

The correlation is unique as it is the only method examined not intended for toughness at or below the transition region of fracture behavior. The Rolfe-Novak-Barsom correlation relates upper shelf CVN energy to static fracture toughness values (Rolfe and Novak 1970, Barsom and Rolfe, 1970). The inclusion of material yield stress directly in the correlation equation is also unique as only one other method considers the influence of material yield stress. Although the intention of this study is to examine correlations to cleavage fracture, this procedure was included because for most grades of steel a fracture toughness of 100 MPa√m (median master curve fracture toughness at the reference temperature) corresponds to CVN values not typically

associated with upper shelf behavior for structural steels. Fracture toughness is estimated through:

$$K_{Ic} = 0.159\sigma_{ys}\sqrt{\frac{25.43 \times CVN}{\sigma_{ys}} - 0.25} \quad \text{Eq. 5.12}$$

where all variables are as previously defined and yield stress, σ_{ys}, is in MPa. The correlation was developed from a database including eleven steels of various grades (Barsom and Rolfe 1987)

Wallin Correlation

Similar to the British Standard methods in that it relates CVN toughness with the master curve reference temperature, T_o, the Wallin (2011) method attempts a more theoretical approach to the correlation development. Starting with an equation similar to BS7910 J2.2, the correlation includes the effects of material yield stress and upper shelf toughness as:

$$T_o = T_{28J} - C + \frac{\sigma_{ys}}{12} + \frac{1000}{CVN_{US}} \quad \text{Eq. 5.13}$$

Where T_{28J} is the test temperature corresponding to a CVN value of 28 J (21 ft-lbf) in degrees Celsius, C is a constant depending on fracture specimen type, σ_{ys} is material yield stress in MPa, and CVN_{US} is the Charpy V-Notch impact energy value in J corresponding to upper shelf behavior. The upper shelf energy values is included in the correlation in order to account for low upper shelf toughness materials, where 28 J (21 ft-lbf) does not correspond with cleavage fracture behavior. Constant C is 77 °C and 87 °C for C(T) and SE(B) specimens, respectively.

5.4 Data Analysis Procedures

Each CVN data set was characterized with a five parameter exponential sigmoid function of the form:

$$CVN(T) = \mathrm{a} + \frac{b}{\left[1 + e^{-(T-c)/d}\right]^f} \qquad \text{Eq. 5.14}$$

where *CVN* and *T* are CVN energy and temperature, respectively, and *a*, *b*, *c*, *d*, and *f* are five fitted parameters.

The function is capable of describing the "S" shaped fracture behavior along the temperature transition curve, defining lower shelf, transition, and upper shelf behavior. Two typical examples of sigmoid functions fit to CVN data sets demonstrate the amount of associated scatter, seen in Figure 5-2 and Figure 5-3. Data in Figure 5-2 is from Roberts, et al. (1977) and consists of a small number of few data points, most likely the reason for the lack of scatter. In Figure 5-3, CVN data from Roberts and Krishna (1977) displays significantly more scatter. Vertical lines in each figure represents the three AASHTO lowest anticipated service temperature (LAST) zones of -18, -34, and -51 °C (0, -30, and -60 °F) and the three current fracture critical CVN test temperatures of 21, 4, and -12 °C (70, 40, and 10 °F) (AASHTO 2010, ASTM 2013).

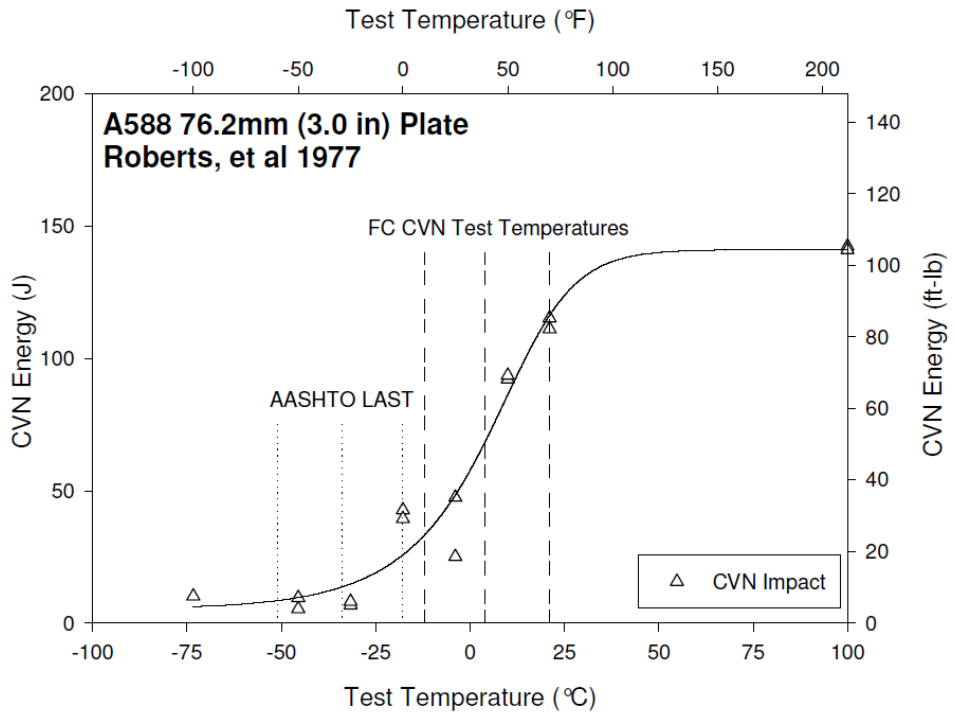

Figure 5-2. Sigmoid Fit to CVN Data from A588, Roberts, et al. 1977

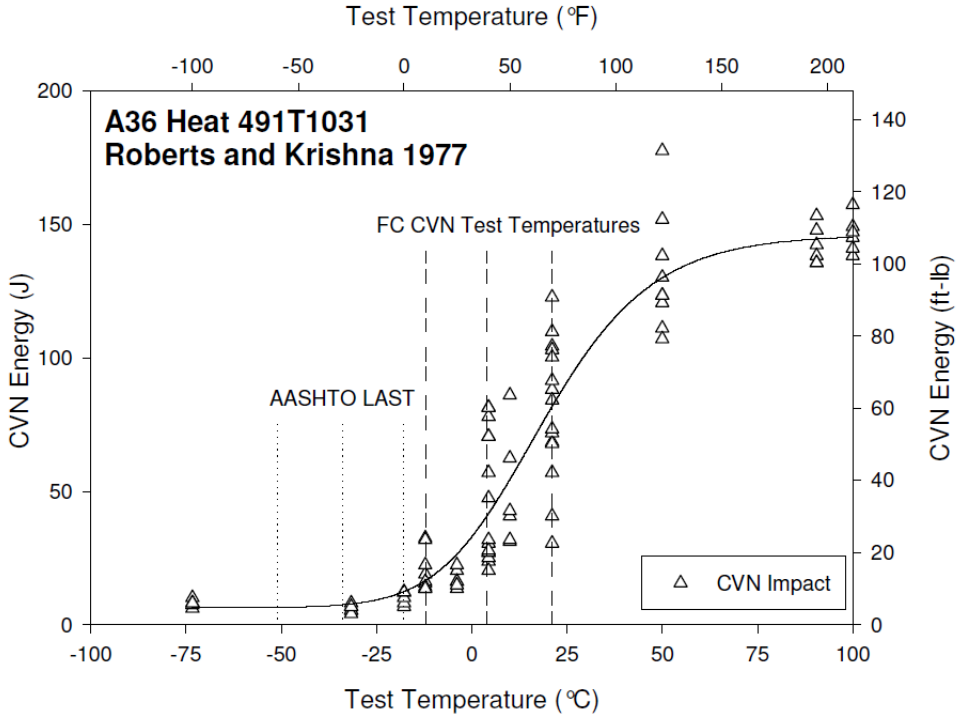

Figure 5-3. Sigmoid Fit to CVN Data from A36, Roberts and Krishna 1977

To utilize the benefits of the master curve methodology presented in Part I, all correlation methods have been used to predict a material reference temperature. The method used was to select the temperature corresponding to the CVN value for which each correlation predicted a fracture toughness value of 100 MPa√m (91 ksi√in). Temperature values for given CVN toughness energies were taken from the sigmoid fit, eliminating ambiguity in the selection of values in the presence of data scatter. Additionally, it was determined that using values from a best-fit line was more appropriate for correlations to the reference temperature, which describes the location of the median toughness transition curve.

In many cases, the required CVN energy values corresponding to 100 MPa√m (91 ksi√in) are higher than those typically attributed to cleavage failure. For this reason, most methods were also evaluated at a CVN value of 27 J (20 ft-lb). Resulting fracture toughness and temperature values were used to determine the reference temperature occurring on the same median toughness master curve. This process is described below in more detail for a specific data set.

Certain CVN test values, both high and low, are not present in all data sets. For conservatism, the lowest test temperature was selected if the minimum recorded CVN values were above the desired energy level. Data sets not attaining desired CVN values at upper shelf were not included in the evaluation of that particular correlation method. Thus, not all correlation methods were evaluated with all 94 available data sets.

Only one of the correlation methods, the Barsom and Rolfe Two-Stage method, includes a temperature shift correction for fracture toughness testing rates. All other methods predict single rate fracture toughness. Because the compiled bridge fracture database consists of fracture toughness tests and corresponding reference temperatures at multiple rates, a rate correction

procedure was needed. A reference temperature adjustment for different stress intensity rates has been proposed by Wallin (1997), verified by other researchers (Gao and Dodds 2005, Gao, et al. 2008), and recommended for use in ASTM E 1921 (2013). The reference temperature adjustment is given by:

$$T_{o,est} = \frac{(T_o + 273.15)\Gamma}{\Gamma - \ln \dot{K}} - 273.15 \qquad \text{Eq. 5.15}$$

where $T_{o,est}$ is the master curve reference temperature for the desired rate in degrees Celsius, T_o is the known static reference temperature in degrees Celsius, $\dot{K}$ is stress intensity rate in MPa√m/sec, and Γ is defined by:

$$\Gamma = 9.9e^{\left[\left(\frac{T_o+273.15}{190}\right)^{1.66}+\left(\frac{\sigma_{ys}}{722}\right)^{1.09}\right]} \qquad \text{Eq. 5.16}$$

where σ_{ys} is the 0.2 per cent offset static yield stress and T_o is as previously defined. The temperature adjustment was used for all methods not implicitly containing a rate adjustment. For this calculation the stress intensity rate of each master curve was estimated as the average of the stress intensity rates for each test comprising the data set. In addition to this rate adjustment, each method correlating CVN energies directly to fracture toughness values was evaluated using the Barsom and Rolfe temperature shift presented above. This was done to examine the Barsom and Rolfe temperature shift independent of the correlation method being used.

5.5 Evaluation of Correlation Methods

Evaluation Procedure

As previously discussed, twelve correlation methods were examined in this study. The diversity of variables in the application of these methods however, led to 29 permutations of the CVN-T_o correlation methods. This includes the selection of temperature for different CVN values, and the two different rate adjustments. Each of these permutations was applied to each of the 94 data sets as applicable, and the resulting estimate of reference temperature was compared with the calculated actual or provisional reference temperature presented in Part I of this study.

In order to identify the correlation approach that best approximates reference temperature, a quantitative measure is required. Due to the fact that many of the correlation methods were developed in order to provide a conservative estimate of toughness instead of a true prediction, it is difficult to evaluate the performance of each method with standard statistical approaches. Examining the results of the analyses, all of the methods display a conservative temperature shift when evaluated against a line with a slope of one, indicating ideal correlation, shown in Figure 5-4. For this reason, the fit of each method was examined against a vertically shifted line with a slope of one. The shift implemented, T_{adj}, was adjusted so as to minimize the dispersion. Dispersion about the fitted line was evaluated using the standard deviation calculated using the shifted line as the expected value instead of the mean. Thus, although not a true standard deviation by definition, it can be used as a standard deviation about the adjusted correlation line. All rates were included in this evaluation, as well as both valid and provisional reference temperature values. A graphical representation of this approach is shown in Figure 2 for a generic data set. Any data point falling below the 45 degree correlation line represents an unconservative prediction.

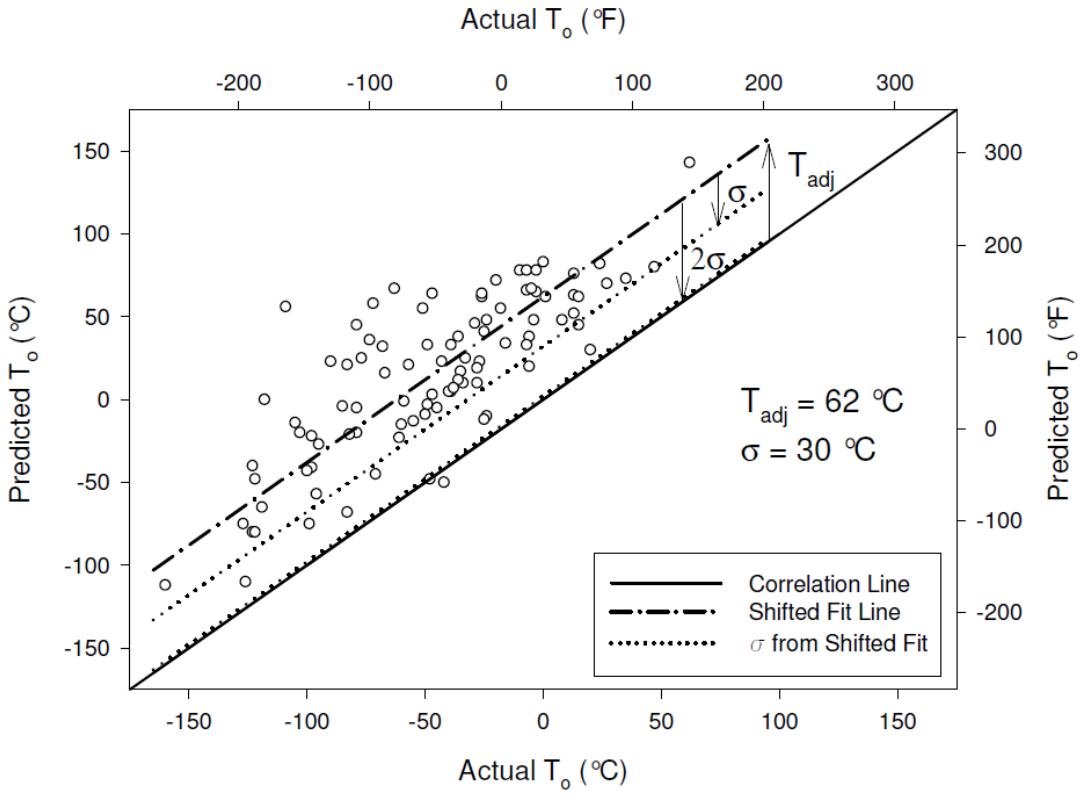

Figure 5-4. Correlation Fit Quantification Approach

In this example the adjusted correlation line has been shifted from the 45 degree correlation line by 62 °C. The standard deviation of the correlation data is 30 °C. It should be noted that the dispersion about the adjusted correlation line for each method was evaluated, comparing predicted error to the inverse of the standard normal cumulative distribution. This resulted in a straight line plot for each correlation method, meaning that the distribution of values for each method can be considered standard normal.

Correlation Method Evaluation

The results from each correlation method are summarized in Table 5-2. The multiple permutations of each method are identified by the CVN value corresponding with the selected temperature, any temperature addition needed to obtain reference temperature, and the rate

adjustment applied to the correlation. Each method has listed the shift applied to the correlation line, T_{adj}, as well as the measure of dispersion, σ, calculated from this line. For example, the Corten and Sailors correlation predicts that a CVN value of 27 J (20 ft-lbf) corresponds to a fracture toughness value of 75.9 MPa√m (69.0 ksi√in). On the exponential master curve, this toughness values is 33 °C below the reference temperature. A temperature addition of 33 °C is made to each test temperature corresponding to a CVN of 27 J (20 ft-lbf) to predict reference temperature. Rate adjustments are made to each datum as appropriate using the K-Rate adjustment method, and dispersion of the entire database is minimized about a 45 degree line shifted from the correlation line by T_{adj} = 62.0 °C, resulting in a standard deviation of 32.9 °C.

Table 5-2. Evaluation of CVN-T_o Correlation Methods

Correlation Method	CVN Value	Temperature Addition	Rate Adjustment	T_{adj}	σ
	J (ft-lbf)	°C		°C	°C
Barsom and Rolfe Original	37 (27)	N/A	B&R	66.4	38.1
			K-Rate	51.6	33.8
	27 (20)	19	B&R	74.9	37.3
			K-Rate	59.4	32.9
Barsom and Rolfe Two-Stage	77 (57)	N/A	B&R	16.4	35.9
	27 (20)	46	B&R	29.6	35.1
BS 7910 J.1	69 (51)	N/A	K-Rate	68.7	31.0
BS 7910 J.2	27 (20)	N/A	K-Rate	27.9	33.0
		T_k	K-Rate	49.1	32.8
BS 7910 J.3	40 (30)	N/A	K-Rate	33.2	33.9
		T_k	K-Rate	54.5	33.8
BS 7910 J.5	83 (61)	N/A	K-Rate	75.6	32.7
Corten and Sailors	47 (35)	N/A	B&R	75.2	37.8
			K-Rate	59.4	34.1
	27 (20)	33	B&R	77.9	37.3
			K-Rate	62.0	32.9
Corten and Sailors Dynamic	27 (20)	57	B&R	40.6	35.1
			K-Rate	60.9	34.7
Marandet and Sanz	28 (21)	N/A	B&R	57.2	37.3
			K-Rate	44.2	32.9
Roberts and Newton	50 (37)	N/A	B&R	77.1	38.3
			K-Rate	60.8	34.7
	27 (20)	33	B&R	88.9	37.3
			K-Rate	71.6	33.0
Rolfe-Novak-Barsom Upper Shelf	Varies	N/A	B&R	72.7	41.5
			K-Rate	57.0	35.5
	27 (20)	varies	B&R	81.1	44.0
			K-Rate	64.4	37.3
Wallin	28 (21)	N/A	K-Rate	11.2	34.2

The Barsom and Rolfe Two Stage correlation method predicts dynamic fracture toughness of 100 MPa√m (91 ksi√in) at a temperature corresponding to a CVN value of 77 J (57 ft-lbf). Adjusting these CVN temperature values with the Barsom and Rolfe rate correction of Eq. (3), the predicted reference temperature values are compared with the actual valid and provisional reference temperatures in Figure 5-5. Many of the steels included in the database did not reach CVN values of 77 J (57 ft-lbf), so the evaluation of this method only contains 81 data sets. Dispersion of the data as calculated using the previously described standard deviation method is not presented in the figure, as only the correlation line and the shifted fit line are shown.

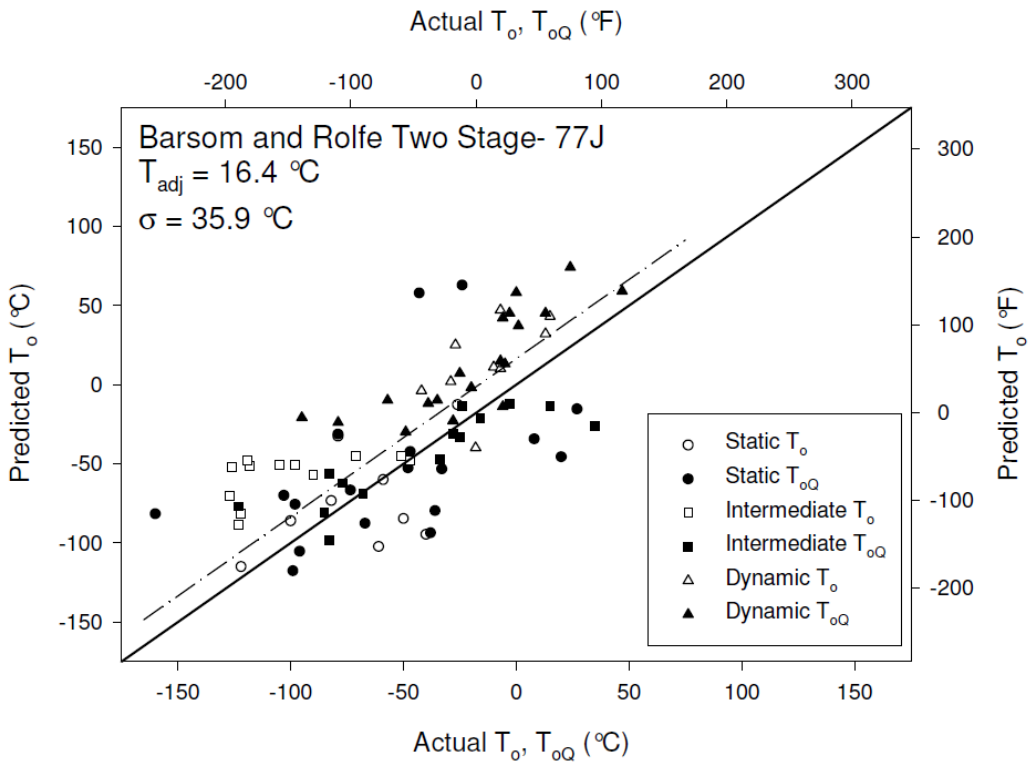

Figure 5-5. Barsom and Rolfe Two Stage Evaluated at 77 J

Following the evaluation procedure described above resulted in an adjusted fit line shifted by 16.4 °C with a standard deviation of 35.9 °C. Thus, unconservative predictions occur at 0.46 standard deviations from the expected correlation line. The interpretation is that 32 per cent of the predictions should be unconservative. However, as CVN values of 77 J (57 ft-lbf) are not typically associated with cleavage fracture and this correlation was only developed to be applicable in the lower transition region, it is necessary to apply this method at a lower CVN value. Temperatures corresponding to a CVN value of 27 J (20 ft-lbf) correspond to a dynamic fracture toughness value of 59 MPa√m (54 ksi√in). On the median toughness master curve, 59 MPa√m (54 ksi√in) occurs 46 °C below the reference temperature. To estimate the reference temperature 46 °C was added to the selected temperature prior to the application of the Barsom and Rolfe temperature shift. Although selecting temperatures at this CVN level improved the performance of this method, numerous unconservative values were still predicted, as shown in Figure 5-6.

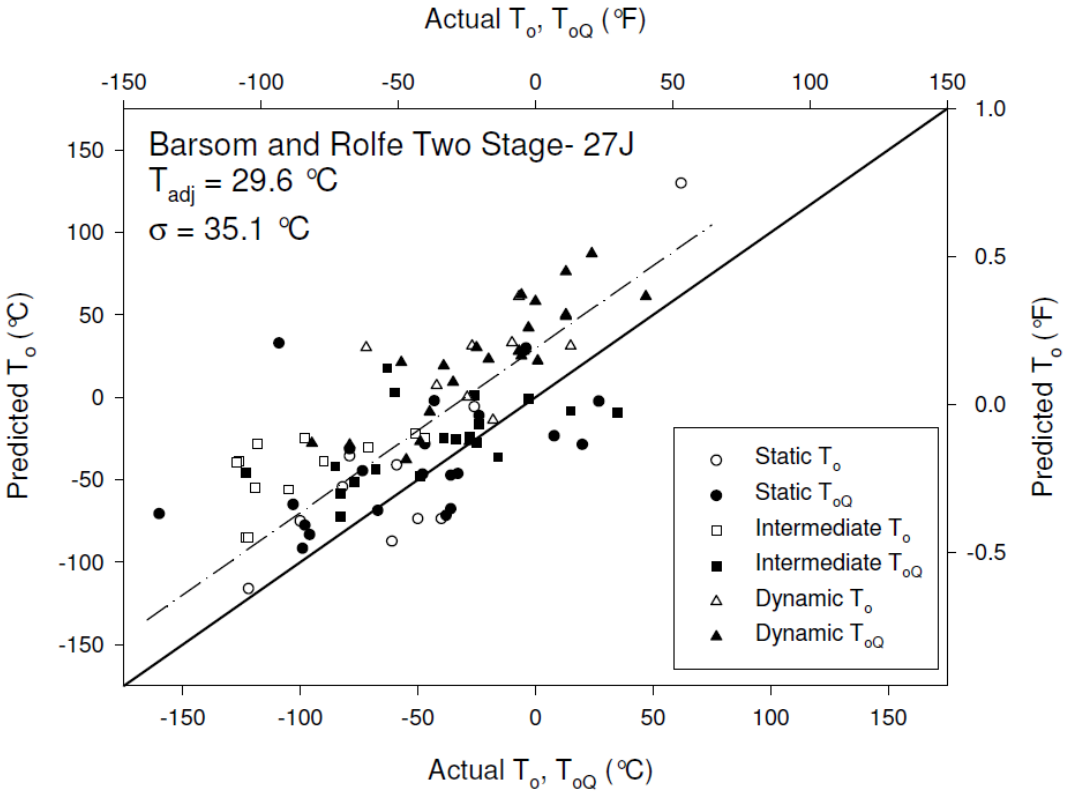

Figure 5-6. Barsom and Rolfe Two Stage Evaluated at 27 J

However, if the predictions are examined at different rates separately, as shown in Figure 5-7 and Figure 5-8, it can be seen that the Barsom and Rolfe Two Stage method conservatively predicts dynamic reference temperature values. Static values are not predicted as well, indicating that it is not the correlation itself but the applied temperature shift that is the cause of the unconservatism. As the temperature shift forms the basis for the selection of CVN test temperatures in the current material toughness specification, this is concerning.

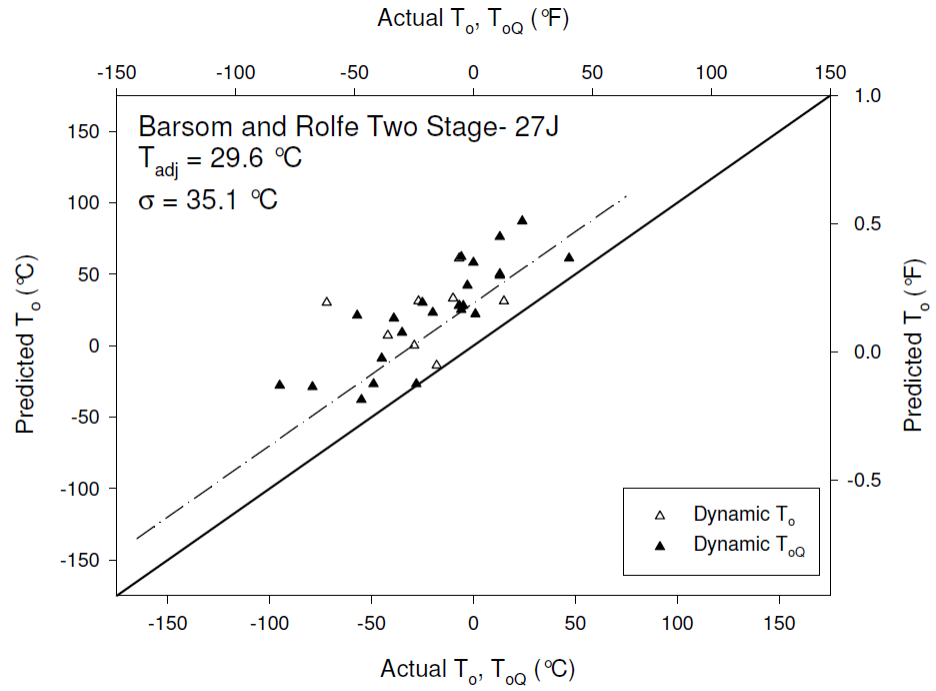

Figure 5-7. Dynamic Barsom and Rolfe Two Stage at 27 J

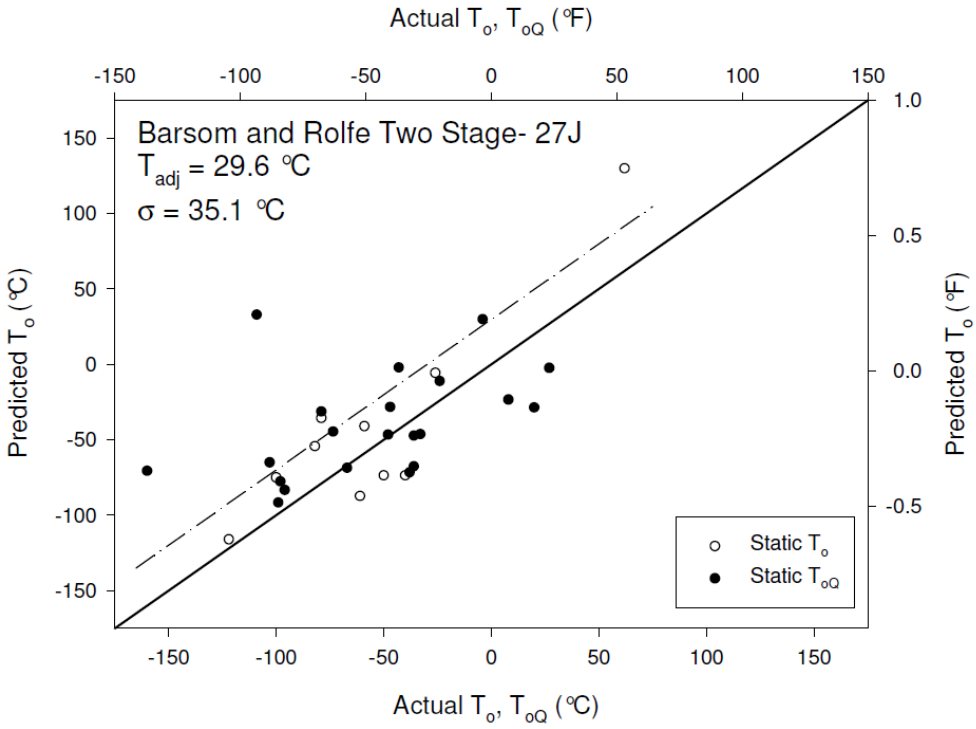

Figure 5-8. Static Barsom and Rolfe Two Stage at 27 J

The most conservative correlation is the Roberts and Newton Lower Bound evaluated at 27 J (20 ft-lbf) and using the Barsom and Rolfe temperature shift to account for rate differences. The correlation, presented in Eq. 5.11, predicts a fracture toughness of 79 MPa√m (72 ksi√in) at the temperature corresponding to this CVN level, which is 22 °C below the reference temperature on the exponential master curve. For this reason, 22 °C was added to the selected CVN temperature prior to the application of the rate adjustment in order to predict reference temperature. The comparison of estimated values with actual reference temperatures is seen in Figure 5-9. An adjusted correlation line with a temperature shift of 88.9 °C and a standard deviation of 37.3 °C indicate that the procedure will statistically predict unconservative values in less than one per cent of all analyzed cases. However, when examined closer it is clear that the dynamic reference temperature values are much more conservative than the intermediate and static rate values. This is due to the fact that the Barsom and Rolfe shift is applied in reverse, moving from a static to a dynamic prediction. This is not the application procedure intended in the development of this temperature shift. These extremely conservative dynamic values cause this method to appear more conservative than it truly is.

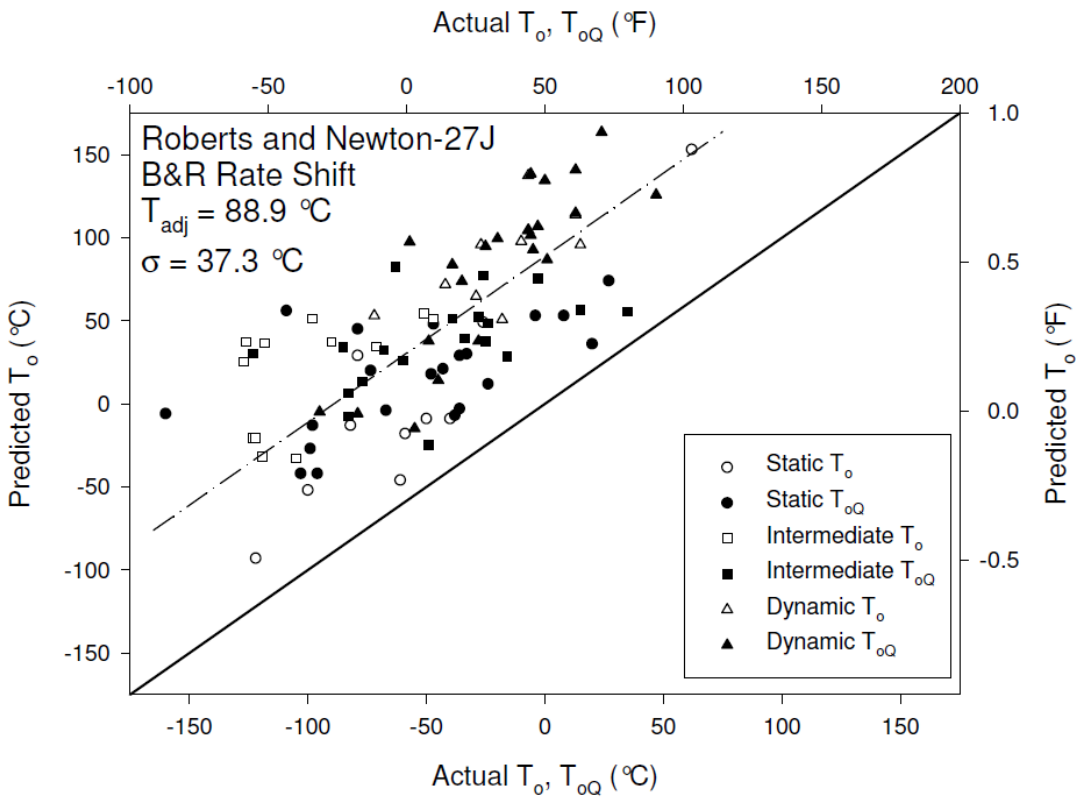

Figure 5-9. Roberts and Newton Lower Bound Evaluated at 27 J with B&R Shift

Excessive amounts of data scatter, indicated by the large standard deviations shown in Table 5-2, suggest that none the correlation methods examined proved to be adequate predictors of reference temperature for this bridge fracture database. Selection of a correlation method must then be based on other considerations. Ease of application, verification for larger data sets of other steels, and desired amounts of conservatism should all be considered in choosing a CVN-T_o correlation method. The estimation method presented in BS 7910 J.2, the evaluation of which is seen in Figure 5-10, is quite simple in application.

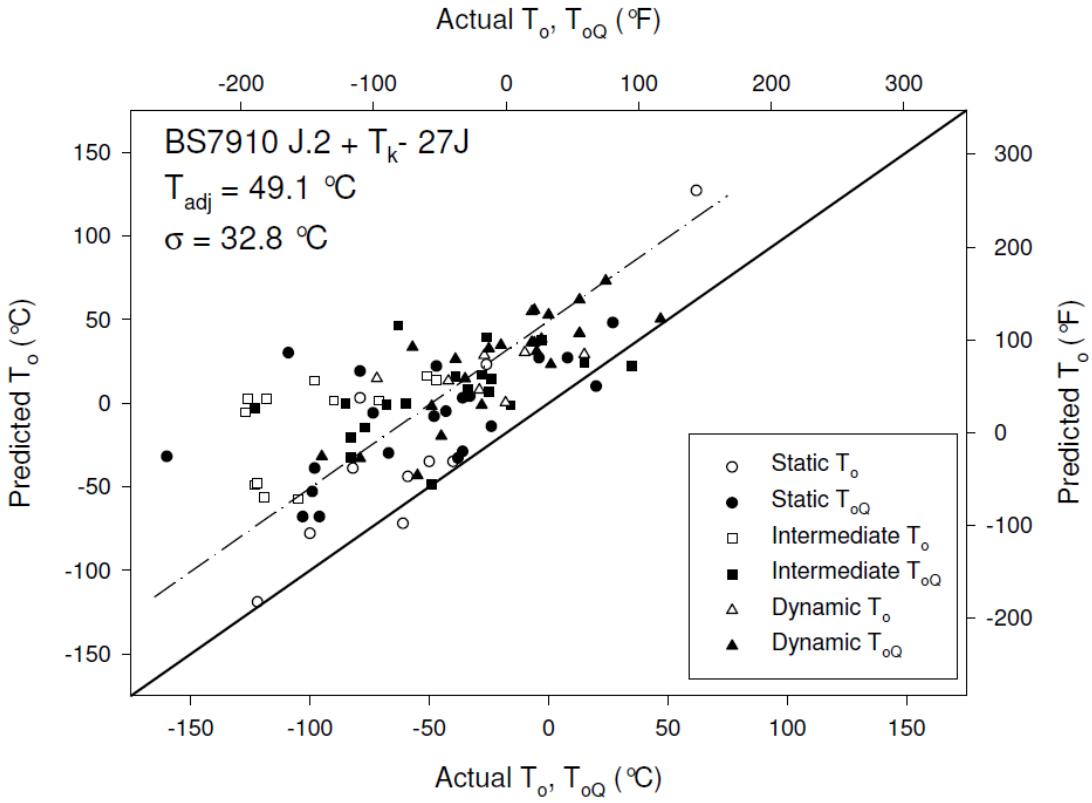

Figure 5-10. BS 7910 J.2 + T_k

Including the variable T_k = 25 °C, static reference temperature is estimated as the test temperature corresponding to a CVN value of 27 J (20 ft-lbf), plus 7 °C. For the bridge database compiled in this study the method resulted in the lowest standard deviation for correlations with CVN values at a level associated with cleavage fracture. In addition, the correlation showed a relatively high level of conservatism with the shifted correlation line 1.5 standard deviations above the actual reference temperature. This statistically corresponds to a conservative prediction for more than 93 per cent of estimates. Perhaps most importantly, the method has been empirically verified for a large database of structural steels, and because of this has been accepted in other industries.

5.6 Flaw Tolerance Application Example

Using CNV-T_o correlations and the master curve tolerance bounds, material toughness specifications now have the ability to be statistically based on tolerable flaw geometry from a real structure. Considering a plate girder bridge located in AASHTO's Zone II fabricated from A709 grade 345 steel, the example will present the approach to setting a performance based material toughness specification. Although some research has been done to quantify the ability of inspectors to locate cracks on bridges, there still exists a large amount of variability concerning the defining of a detectable crack size (Moore, et al. 2001). Because of this variability, the example will utilize an approach that has been proposed in other industries to set tolerable flaw sizes. The leak-before-burst approach has been used with steel pressure vessels, and has in the past been proposed for use in bridge applications (Dowling 1999, Irwin and Roberts 1972). The approach is based on the analysis of a fatigue crack grown from the surface of a structural component until it has reached through the material's full thickness. Because of the elliptical shape of a growing crack, the total crack length on the original surface will be twice the material thickness when the crack reaches the opposite surface. In a bridge application this is an extremely conservative scenario, as a through thickness crack would be readily apparent to an inspector due to rust bleed. In all likelihood the crack would have been discovered in a routine inspection well prior to this amount of growth.

To satisfy this approach, a fatigue crack growing in a 76 mm. (3.0 in.) thick flange of a plate girder would need toughness adequate to tolerate a crack of 152 mm. (6.0 in.). A simplified approximation of this geometry can be used with known fracture mechanics solutions to determine the necessary material toughness. The flange can be modeled as a flat plate in pure tension with an applied tensile stress $0.55F_y$, which represents the AASHTO design stress level.

Defining the length of the crack on the original surface as 2a, the necessary toughness is calculated by:

$$K = 0.55F_y\sqrt{\pi a} \qquad \text{Eq. 5.17}$$

Applying this solution, the toughness needed to resist fracture initiation under this condition is 92.7 MPa√m (84.4 ksi√in). Adjusting this toughness value for plate thickness using the size master curve size adjustments presented in the first part of this companion paper results in a 1T required toughness of 116 MPa√m (106 ksi√in). Application of master curve's one per cent tolerance bound results in a static reference temperature of -104 °C (-155 °F) in order to achieve the desired toughness at service temperature. For this desired reference temperature, a test temperature and CVN can be selected for material toughness specifications using the BS 7910 J.2 correlation procedure shown in Eq. (5), with T_k = 25 °C. The application of this correlation indicates that to achieve the desired reference temperature, CVN impact values must be equal to 27 J (20 ft-lbf) at -104 °C (-155 °F).

As previously discussed, this correlation method contains a conservative temperature shift of 49.1 °C, with a standard deviation of 32.8 °C. Thus, the selected correlation method estimates reference temperature with a conservative value to 1.5 standard deviations, which corresponds to a probability of failure of 6.7 per cent. The failure probabilities of the master curve and the CVN-T_o correlations can be combined assuming that they are independent. This assumption is reasonable due to the fact that the dispersion in the master curve methodology is due to flaw distribution in the material, while the uncertainty in the correlation comes from the analysis method itself.

Applying the BS 7910 J.2 correlation with the master curve methodology, requiring CVN values of 27 J (20 ft-lbf) at -104 °C (-155 °F) will provide adequate toughness to prevent static fracture initiation of a through thickness fatigue crack of 152 mm. (3.0 in.) in Zone II, with a 7.6 per cent probability of failure. If CVN specifications mandate that all tests be greater than 27 J (20 ft-lbf) at this temperature, this failure probability can be considered to be conservative. This is due to the fact that all CVN values were selected for analysis from the sigmoid fit. Requiring all CVN tests to be above the specified value essentially uses a lower bound for the correlation. The added conservatism to the correlation process is not accounted for in the calculated probability of failure.

5.7 Conclusions and Recommendations

Twenty nine permutations of correlation methods used to predict master curve reference temperature from Charpy V-Notch tests were evaluated using the legacy bridge fracture database presented in Part I of this study (Collins, et al. submitted). A quantitative measure of fit was developed in an attempt to determine the best correlation procedure. The analysis led to ability proposed design procedure to statistically predict flaw tolerance in a bridge structure by setting CVN material toughness requirements.

The current basis for the AASHTO material toughness specifications was examined using this methodology. The results revealed that although the Barsom and Rolfe Two Stage process can conservatively predict dynamic fracture toughness values, the temperature shift employed can lead to unconservative estimates of intermediate and static rate toughness. Fortunately, unaccounted for conservatism is present in this analysis, as CVN values were selected from fit

lines. However, this unquantified conservatism should not be relied upon when alternative methods are available.

It is clear from the analyses of the multiple correlation procedures that none of the CVN-T_o methods is an acceptable predictor of reference temperature. Selection of a correlation method can be made based on desired conservatism in the fracture mechanics analysis. Although more work is necessary in quantifying tolerable flaw sizes, loading rates, and acceptable tolerance levels, this procedure represents a large step forward for the management of fracture in highway bridges. The tools now exist to treat fracture in a manner that is consistent with other design limit states.

5.8 Acknowledgements

The authors would like to thank both Kamal Rojiani of Virginia Tech and Marc Maguire of Utah State University for their guidance and feedback concerning the statistical analysis used in this study. Funding for this study was provided by the FHWA. The opinions expressed in this paper are those of the authors, and do not reflect the position of the FHWA.

Notation

The following symbols are used in this paper:

B = Specimen thickness

CVN = Charpy V-notch impact test

CVN_{us} = Charpy V-notch impact test at upper shelf behavior

E = Modulus of Elasticity

F_y = Material yield strength used in design

K = Fracture toughness and stress intensity

$\dot{K}$ = Stress intensity rate

K_{Ic} = Mode I critical plane-strain fracture toughness

K_{ID} = Mode I dynamic fracture toughness

T_{27J} = Test temperature corresponding to CVN of 27J

T_{28J} = Test temperature corresponding to CVN of 28J

T_{40J} = Test temperature corresponding to CVN of 40J

T_{adj} = Temperature shift from line of perfect correlation

T_k = Temperature adjustment based on CVN scatter in BS 7910

T_o = Reference temperature corresponding to median fracture toughness of 100 MPa$\sqrt{m}$

$T_{o,est}$ = Reference temperature adjusted for rate using K-Rate adjustment

T_{shift} = Temperature shift rate adjustment in Barsom and Rolfe Two Stage correlation

Γ = Material fitting coefficient used in K-Rate adjustment

σ = Measure of dispersion calculated as standard deviation from shifted correlation line

σ_{ys} = 0.2% offset yield strength

Chapter 6: "Fracture Toughness Characterization of HPS-485W (70W) and 690W (100W) for Bridge Girder Applications"

William Collins, William Wright, Robert Connor, Roberto Leon, and Ryan Sherman

Abstract

The use of high performance steel (HPS) in new bridge construction continues to increase as engineers and owners recognize the potential for cost savings and performance benefits. One advantage of HPS is the increase in fracture toughness when compared with conventional bridge steel. However, little work has been done to characterize HPS fracture toughness, and current material specifications do not take advantage of this improvement in performance. This paper presents the fracture toughness testing and analysis of eight A709 HPS 690W (100W) and 485W (70W) steel plates. Fracture toughness values are used to determine tolerable flaw sizes for varying flange geometries. Comparison is made with tolerable flaw sizes based on toughness estimations of current fracture critical material toughness specifications. Results indicate that current production of HPS is producing toughness far in excess of that mandated in the specification.

6.1 Introduction

The history of structural steel includes many steel grades that can be considered high strength and high performance, although a distinction should be made between the two. Traditional high strength steels, commonly used in bridges in the 1960's and 1970's, have earned a poor reputation for performance in areas other than strength. Difficulty in welding these steels

can create defects that may cause fractures just after fabrication, even prior to erection (Dexter, et al. 1994). Advances in steel production technology have allowed bridge engineers to follow the lead of other industries in using high performance steels. Current A709 HPS grade steels can not only exhibit higher strength than conventional steels, but can also show better weldability, fracture toughness, durability, and ductility (Wright 1997).

However, although these performance benefits are widely known and accepted, very little research has been performed to document the HPS fracture toughness. Only a few previous studies have examined the fracture behavior of A709 HPS grade steels (Wright 2003). Results of these studies indicate that HPS grade steels have exceptionally high fracture toughness when compared with traditional bridge steels. In order for bridge engineers to take advantage of the increased toughness that HPS offers, this performance benefit must be carefully quantified and documented. This paper addresses this need by carrying out a large experimental and accompanying analytical work on the fracture behavior of HPS 485W (70W) and HPS 690W (100W) steel grades. The paper also describes how this new data can be applied to the design of steel bridge girders.

6.2 Background

A cooperative research program was implemented in 1994 to develop high performance steels for bridge applications (Wright 2003). Building upon the experience of the ship building industry in producing steels of extremely high strength and toughness, the Federal Highway Administration (FHWA) worked with the United States Navy (USN) and the American Iron and Steel Institute (AISI) to develop HPS weathering steels with improved weldability and adequate American Association of State Highway and Transportation Officials (AASHTO) Zone III

toughness (Hamby, et al, 2002). Two decades after the initial cooperative research and development program began, almost 150 bridges in the United States have been fabricated with HPS grade steel (Steel Market Development Institute 2011), including the replacement Tappan Zee bridge currently under construction in New York.

As with the development of any new material, changes in the chemical composition of HPS have occurred over time as production methods and techniques have been refined. Improvements in steel chemistry have resulted in consistently reproducible superior strength, toughness, weldability, and weathering properties for HPS steels. Because the total allowed alloy percentage is less than 8 per cent and the carbon content is capped at well under 0.2 per cent, HPS grades are considered low-carbon, low-alloy steels. The limit on carbon allows HPS to retain ductility and toughness, as well as to provide improved weldability. For example, these HPS steels can be welded with little or no preheating (Wilson, et al. 1988). Further details on the chemical composition of HPS and its development are presented in the literature (Gross and Stout 1995, Gross and Stout 2001, Gross, et al. 1998, Wilson 2002).

Numerous research programs have examined various aspects of the mechanical behavior of HPS; a good summary can be found in Kayser, et al. (2006). Comparatively speaking, scant work has been done to understand the fracture behavior of HPS, however, and current bridge code CVN requirements for HPS have no quantitative basis (Altstadt, et al. 2014). Current AASHTO fracture critical tension component Charpy V-Notch (CVN) impact test requirements, including HPS grades 485W (70W) and 690W (100W) examined as part of this study, are provided in Table 6-1. The impact test requirements are presented in both ASTM A709-13 and AASHTO LRFD Bridge Design Specifications (2008).

Table 6-1. ASTM A709-13 Fracture Critical Tension Component CVN Requirements

Grade	Thickness, mm. (in.)	Minimum Average Energy, J (ft-lbf)		
		Zone I	Zone II	Zone III
250F (36F)	to 100 (4) incl.	34 (25) at 21°C (70°F)	34 (25) at 4°C (40°F)	34 (25) at -12°C (10°F)
345F (50F), 345SF (50SF), 345WF (50WF)	to 50 (2) incl.	34 (25) at 21°C (70°F)	34 (25) at 4°C (40°F)	34 (25) at -12°C (10°F)
	over 50 to 100 (2 to 4) incl.	41 (30) at 21°C (70°F)	41 (30) at 4°C (40°F)	41 (30) at -12°C (10°F)
HPS 345WF (HPS 50WF)	to 100 (4) incl.	41 (30) at -12°C (10°F)	41 (30) at -12°C (10°F)	41 (30) at -12°C (10°F)
HPS 485WF (HPS 70WF)	to 100 (4) incl.	48 (35) at -23°C (-10°F)	48 (35) at -23°C (-10°F)	48 (35) at -23°C (-10°F)
HPS 690 WF (HPS 100WF)	to 65 (2.5) incl.	48 (35) at -34°C (-30°F)	48 (35) at -34°C (-30°F)	48 (35) at -34°C (-30°F)
	over 65 to 100 (2.5 to 4) incl.	not permitted	not permitted	not permitted

The material toughness specifications, along with inspection and fabrication guidelines to control weld flaws and in-service inspection criteria, form the basis for AASHTO's fracture control plan (FCP). Originally introduced in 1978 as the AASHTO Guide Specifications for Fracture Critical Non-Redundant Steel Bridge Members (AASHTO 1978), the FCP has been updated multiple times, with the majority of the FCP now found in Section 12 of the AASHTO/AWS D1.5M/D1.5 Bridge Welding Code (AASHTO/AWS 2010). In spite of the advances in steel production and the increased understanding of fracture mechanics over this time period, the material toughness values presented in Table 6-1 have undergone no significant changes, with only small increases in toughness and seemingly arbitrary adjustments to testing temperatures.

6.3 Objectives

The objective of this study is to characterize the fracture behavior of HPS-485 (70 W) and HPS-690 (100 W) according to the most modern fracture approaches and to correlate this data to the traditional CVN approach. Therefore, the experimental work carried out as part of this work includes both standard Charpy V-Notch (CVN) impact testing and elastic-plastic fracture mechanics tests. Elastic-plastic fracture toughness tests were performed using Charpy-sized single edge bend (SE(B)) specimens (Figure 6-3), and the results were characterized with the application of the master curve methodology. In addition, correlations between CVN and fracture toughness values were used to compare experimental material behavior with existing material toughness specifications.

6.4 Experimental Setup

Eight HPS plates from different heats, provided by both steel mills and fabricators, were examined as part of this study. Each plate was designated a letter for specimen and testing number purposes. Plates A, D, H, I, and J were grade HPS 485W (70W), while C, E, and F were grade HPS 690W (100W). Plate thickness varied from 25.4 mm. (1.0 in.) to 63.5 mm. (2.5 in.) and 19 mm. (0.75 in.) to 50.8 mm. (2.0 in.) for grades 485 and 690, respectively. Table 6-2 provides a summary of each plate examined, including grade, thickness, and heat number.

Table 6-2. HPS Plate Details

Letter Designation	Grade, ksi (Mpa)	Thickness, in. (mm)	Heat Number
A	70 (485)	1.0 (25.4)	801W10170
C	100 (690)	0.75 (19)	W24549 55 W4
D	70 (485)	2.5 (63.5)	U5191-6A
E	100 (690)	1.5 (38.1)	P60017 W24549
F	100 (690)	2.0 (50.8)	T1W24594
H	70 (485)	1.25 (31.8)	HT813C7220
I	70 (485)	1.25 (31.8)	HT822H34790
J	70 (485)	1.5 (38.1)	821T06770

Test specimens were fabricated from the plates at specific locations and in specific orientations. As specified in ASTM A673-07, CVN specimens are to be centered at one-quarter plate thickness. The majority of CVN and SE(B) specimens tested in this study were located at one-quarter depth except for plate C, where plate thickness prohibited this practice. Specimens from plate C were centered at one-third plate thickness. Also, three CVN specimens were sampled and tested from mid-thickness of each plate for comparison purposes. Specimen locations with respect to plate through thickness are designated 1/2T, 1/3T, and 1/4T for mid-thickness, one-third thickness, and one-quarter thickness, respectively.

The CVN and SE(B) specimens were oriented so that fracture would propagate perpendicular to the rolling direction of the plate, referred to as L-T orientation, as shown in Figure 6-1. For comparison purposes a number of CVN tests were conducted on specimens from the T-L orientation.

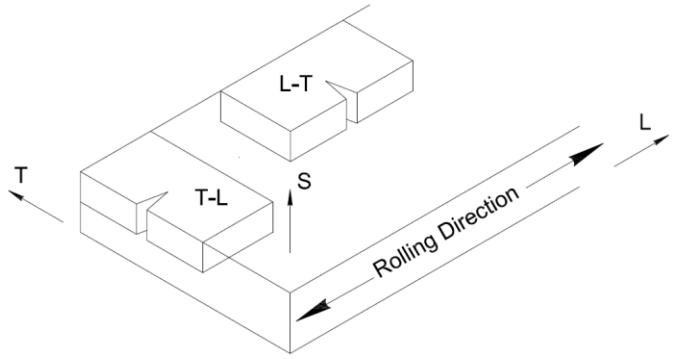

Figure 6-1. Fracture Specimen Orientation Designations

6.5 Fracture Toughness Testing and Analysis Procedures

Charpy V-Notch Impact Testing

CVN impact energy values were obtained on a friction compensated Tinius Olsen impact test machine with a maximum capacity of 400 J (300 ft-lb). Prior to the beginning of testing the impact test machine was verified using NIST low and high energy specimens and was found to be in calibration. Absorbed energy values above 80 per cent of machine capacity are considered invalid due to pendulum speed requirements. Dimensions of a standard CVN specimen are shown in Figure 6-2. Additional details including permissible geometry variation and surface finish requirements can be found in ASTM E23-07 (ASTM 2007).

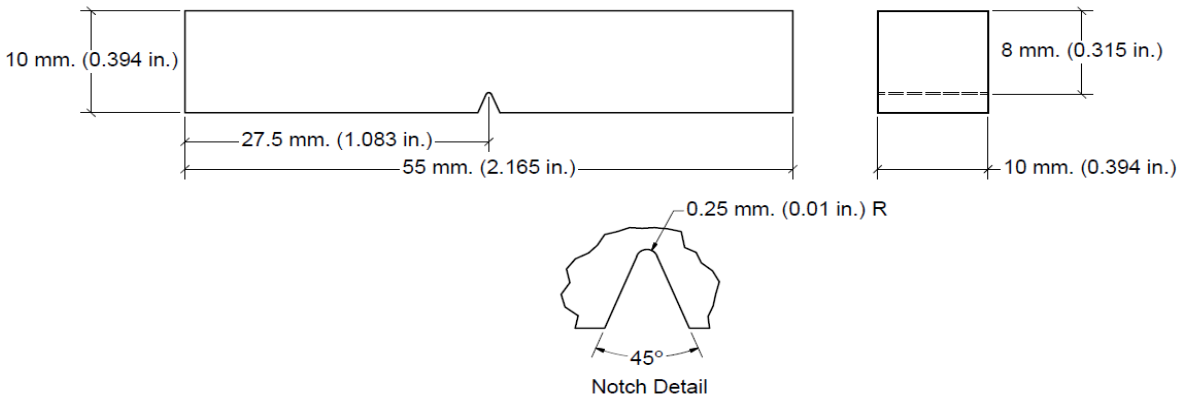

Figure 6-2. Typical Geometry of Charpy V-Notch Specimen

For each plate being examined, CVN specimens were tested in accordance with ASTM E23-07 over a range of temperatures in order to develop a full temperature transition curve. Specimens were cooled to sub-ambient temperatures using a methanol cooling bath capable of reaching -80 °C (-112 °F). When lower-shelf behavior could not be obtained at -80 C (-112°F), liquid nitrogen was used to cool specimens to lower test temperatures. Specimens were placed in an insulated container with a companion thermo-couple embedded specimen, and liquid nitrogen was introduced. Temperatures were allowed to decrease to below the desired test temperature, and then specimens were removed from the container and placed on a metal plate along with the thermo-couple embedded specimen. The temperature of the embedded CVN was monitored as the specimen temperature increased, and testing was performed at the desired temperature. CVN specimens located at mid-thickness, as well as those oriented in the T-L direction, were all tested at -51 °C (-60 °F), corresponding to an AASHTO Zone III temperature.

Fracture Toughness Testing

Fracture toughness testing was performed in accordance with ASTM E1921-13 using Charpy-sized SE(B) specimen geometry on an MTS Landmark servo-hydraulic test machine.

Although the specimen blank geometry matches that of the CVN, the notch detail is different, as fracture toughness testing requires a sharp crack front. Figure 6-3 shows the blank specimen prior to fatigue pre-cracking, as well as after the cutting of side grooves. Prior to testing each specimen is cyclically loaded in order to initiate a fatigue crack. This process is performed in accordance with ASTM E647-13, using a stress intensity of 17.5 MPa√m (16 ksi√in) for the first half of crack growth. The specimen is then rotated and pre-cracking is completed at a constant stress intensity of 14.3 MPa√m (13 ksi√in). Specimens were fatigue loaded until the initial crack length, a_o, reached a nominal length of W/2, or 5 mm. (0.197 in.).

To ease fatigue pre-cracking, an electrical discharge machine (EDM) notch is cut into the center of the SE(B) blank. The size of the notch itself corresponds with the 0.25 mm. (0.01 in.) diameter of EDM wire, while shoulders are cut into the face of the specimen to facilitate the use of a clip gage during testing. Fracture toughness specimens are typically defined by dimensions B and W, which represent the thickness and height of the specimen, respectively. Also used to define specimen geometry is dimension a, which is the length of the crack. To provide a straight crack front during testing, side grooves are machined on the specimen sides after the completion of fatigue pre-cracking. Side grooves used in this study have a depth of 1 mm. (0.0394 in.) and an included angle of 45 degrees, and are centered on the specimen in line with the fatigue crack. Side grooves are located on two opposite sides of the specimen, perpendicular to the notched face.

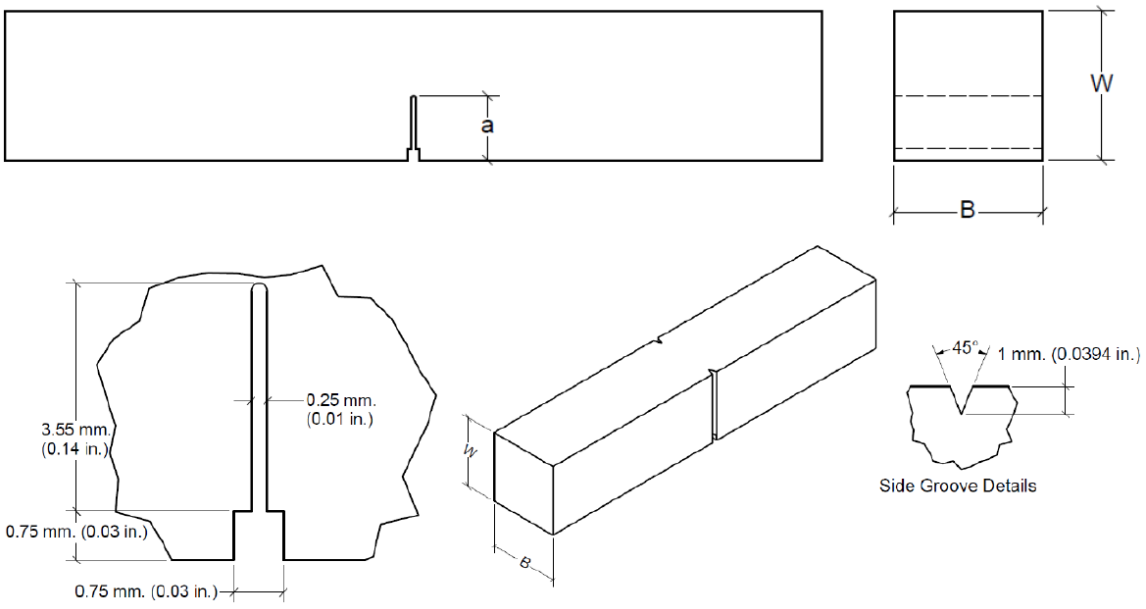

Figure 6-3. SE(B) Specimen Details

Both fatigue pre-cracking and fracture toughness testing were performed on the same three point bend test apparatus, shown in Figure 6-4. The span of the test setup is equal to four times the specimen width, or 40 mm. (1.575 in.) as required in ASTM E1820-08. The clip gage shown in the figure is used to measure crack mouth opening displacement (CMOD) during pre-cracking and testing. Prior to testing, multiple elastic unloadings are performed in order to calculate the crack length based on compliance equations, verifying proper specimen alignment within the test fixture. Exact fatigue crack lengths are unknown until optical measurements are made after fracture toughness testing is completed. During post-test evaluation, material elastic modulus adjustments of up to ten per cent are permitted to align compliance calculated crack lengths with the optically measured initial crack size. If an adjustment of more than ten per cent is required to match compliance and measured crack size, the test is considered to be invalid.

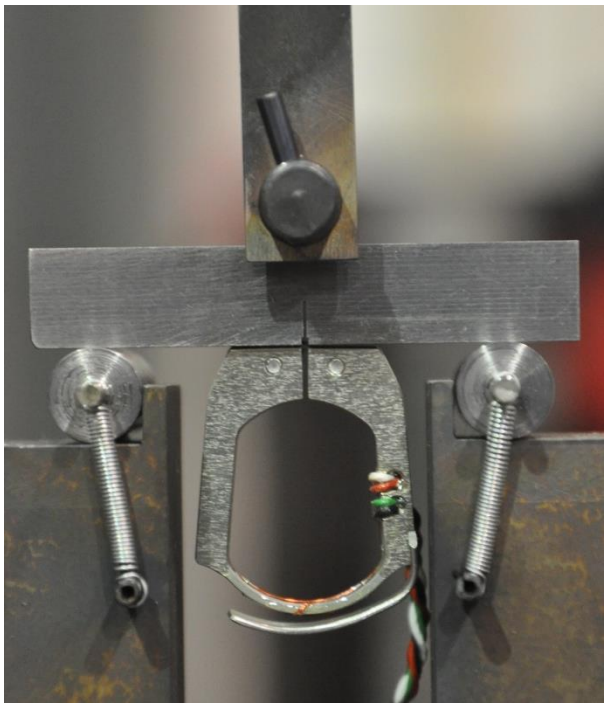

Figure 6-4. SE(B) Specimen with Clip Gage in Test Fixture

Similar to CVN testing, fracture toughness tests were performed at sub-ambient temperatures. Liquid nitrogen was used to cool specimens inside an environmental chamber, using a thermocouple, process controller, and cryogenic servo-valve to regulate temperature within + 1 °C of the desired test temperature. Nominal stress intensity rates of 0.1 MPa√m/sec (0.091 ksi√in) were used for all tests. Upon completion of testing, specimens were heat tinted in order to clearly differentiate between the fatigue crack and the fracture surface. Load and CMOD test records were used with specimen geometry and optically measured fatigue crack size to calculate the J integral at the point of failure, J_c, a measure of the elastic-plastic energy release rate as the fracture event occurs, which can be converted into an elastic-plastic equivalent critical fracture toughness, K_J. Fracture toughness data were then used with their respective test temperatures to characterize fracture behavior through the application of the master curve methodology.

Application of Master Curve Methodology

Presented herein is a brief introduction to the master curve methodology and its application to fracture toughness data sets. Interested readers can find a more thorough overview, including information on the background and development of the method, in McCabe, et al. (2007). More details concerning the application of the master curve methodology to bridge fracture data sets, including specific examples, can be found in companion papers by Collins, et al. (submitted 2014a, b).

Fracture behavior in the ductile to brittle transition region is described by an exponential function relating fracture toughness and temperature, commonly referred to as the master curve. Specifically, the master curve describes the median toughness of a material, which is the toughness value at a given temperature for which a specimen has a 50 per cent probability of failure. The exponential master curve only pertains to behavior in the ductile-brittle transition regime, and does not describe upper shelf behavior. The exponential form representing median toughness is given by:

$$K_{Jc(med)} = 30 + 70e^{[0.019(T-T_o)]} \qquad \text{Eq. 6.1}$$

where $K_{Jc(med)}$ is the median elastic-plastic critical fracture toughness in MPa√m, T is test temperature in degrees Celsius, and T_o is the reference temperature in degrees Celsius. As the general shape of the exponential curve applies to all ferritic steels, this behavior can be defined by a single temperature value. The single temperature, known as the reference temperature, T_o, is anchored to the median toughness curve at a value of 100 MPa√m (91 ksi√in). Scatter of data about this median toughness curve can be statistically accounted for with tolerance bounds that consider the distribution of cleavage fracture initiation sites throughout material thickness. The

statistical fracture toughness tolerance bounds, where 0.xx represents the desired probability of failure, are given by:

$$K_{Jc(0.xx)} = 20 + \left[ln\left(\frac{1}{1-0.xx}\right)\right]^{1/4}\{11 + 77e^{[0.019(T-T_o)]}\} \quad \text{Eq. 6.2}$$

Thus, all fracture toughness data must be size-corrected to account for specimen size prior to reference temperature determination. Specimen thickness is designated using xT nomenclature, where x is the specimen thickness in inches. Thus, a 25.4 mm. (1 in.) thick specimen is said to be of thickness 1T. Master curve data is typically normalized to a 1T specimen thickness, although any thickness may be chosen. Thickness adjustment is performed by:

$$\mathrm{K}_{Jc(x)} = K_{min} + \left[K_{Jc(o)} - K_{min}\right]\left(\frac{B_o}{B_x}\right)^{1/4} \quad \text{Eq. 6.3}$$

where $K_{Jc(x)}$ is the elastic-plastic critical fracture toughness adjusted to a desired thickness, B_x, absolute minimum toughness, K_{min} = 20 MPa√m (18 ksi√in), $K_{Jc(o)}$ is the fracture toughness at a known thickness, B_o. A typical 1T master curve characterized by a reference temperature equal to -30 °C (-34 °F), is presented in Figure 6-5, along with 5 and 95 per cent tolerance bounds. Dotted lines represent the anchoring of the median toughness curve to 100 MPa√m (91 ksi√in).

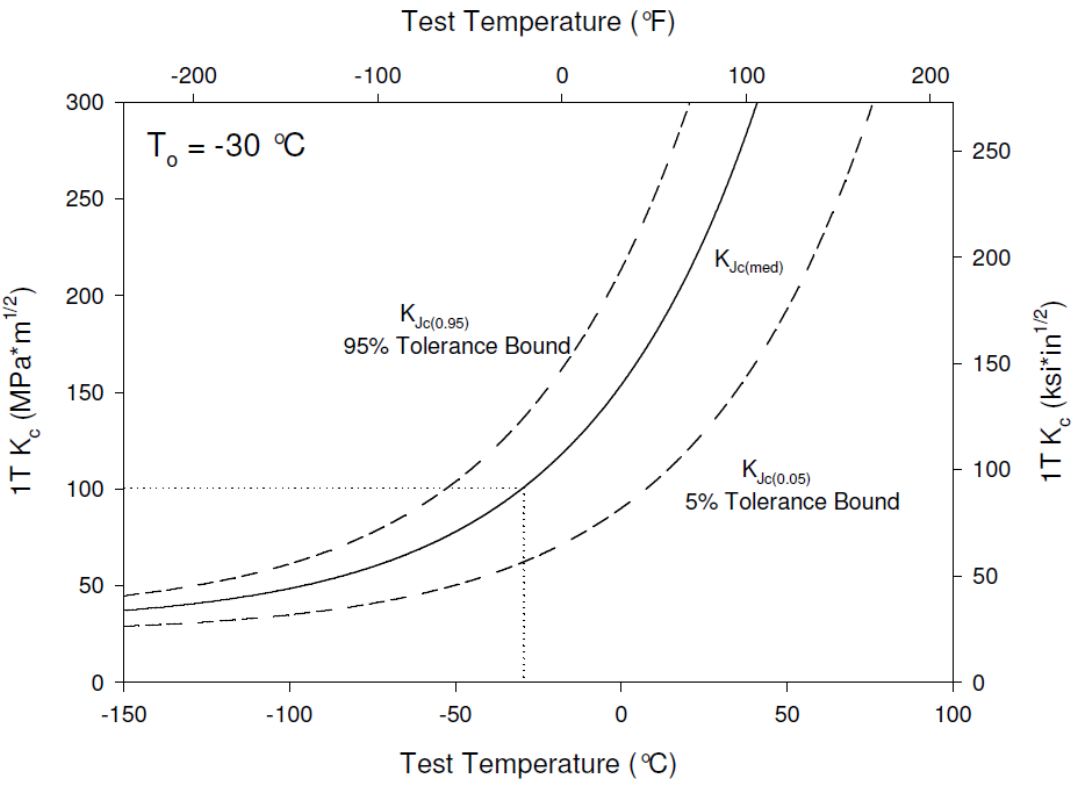

Figure 6-5. Typical Master Curve with Tolerance Bounds

Determination of reference temperature is conducted in accordance with ASTM E1921-13. Valid master curve evaluation can be performed with as few as six fracture toughness tests (ASTM 2013). Each valid datum is assigned a weighting factor depending on the difference between test temperature and calculated reference temperature. In order for the reference temperature to be considered valid, the weighting factors must sum to a total equal to or greater than one. Any reference temperature determined from a data set with a weighting factor sum less than one must be considered provisional, represented by T_{oQ}.

Adequate levels of constraint are guaranteed through a specimen size related fracture toughness limit, $K_{Jc(limit)}$, calculated by:

$$K_{Jc(limit)} = \sqrt{\frac{E b_o \sigma_{ys}}{30(1-\upsilon^2)}} \qquad \text{Eq. 6.5}$$

where the specimen's initial remaining ligament, b_o is in millimeters, which is the difference between the specimen width, W, and the initial crack, a_o. Also included in this equation is the material 0.2 per cent offset yield stress, σ_{ys}, in MPa, and modulus of elasticity in GPa. Any test values that exceed the limit are censored, and the limit value itself is substituted into the data set for reference temperature determination. Censored values, although used in the evaluation of the master curve, are not assigned validity weighting factors.

6.6 Test Results

Charpy V-Notch Impact Test Results

A total of 246 CVN impact tests were performed for the eight different plates of HPS. Impact energy values of 1/4T L-T CVN specimens from each plate were plotted with respect to test temperature in order to develop a transition curve. The general form of the five parameter sigmoid function is provided by:

$$CVN(T) = \mathrm{a} + \frac{b}{\left[1 + e^{-(T-c)/d}\right]^f} \qquad \text{Eq. 6.6}$$

where *CVN* and *T* are CVN energy and temperature, respectively, and *a*, *b*, *c*, *d*, and *f* are five fitted parameters.

As previously mentioned, the exception to this is plate C, which had specimens sampled at 1/3T due to thickness limitations. A five parameter sigmoidal fit was applied to each data set

to capture the lower shelf, transition, and upper shelf behavior, as shown in Figure 6-6 through Figure 6-8 for the three 690W (100W) plates. AASHTO temperature zones of -18, -34, and -51 °C (0, -30, and -60 °F) are represented by vertical dotted lines in each of these plots. The mandated fracture critical CVN test temperature is shown with a vertical dashed line, and the specified minimum average energy value of 48 J (35 ft-lbf) is designated with an X. This requirement is easily achieved by all steels, with sigmoid fit values of 139, 147, and 144 J (102, 108, and 106 ft-lbf) for plates C, E, and F, respectively. The examined plates even displayed behavior well above the toughness requirements at the AASHTO Zone III temperature of -51 °C (-60 °F), with average test values of 66.5, 89.5, and 98 J (49, 66, and 72 ft-lbf). It should also be noted that for these three plates of HPS 690W (70W), there was little difference in toughness due to changes in specimen orientation or through thickness sampling location.

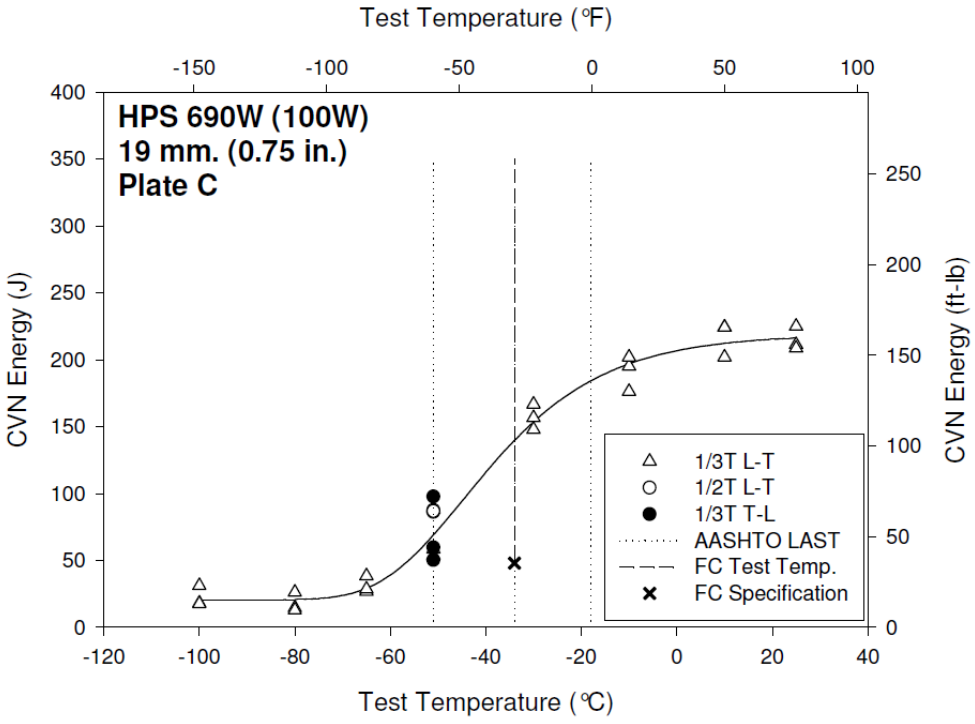

Figure 6-6. CVN Data for Plate C, HPS 690W, 19 mm.

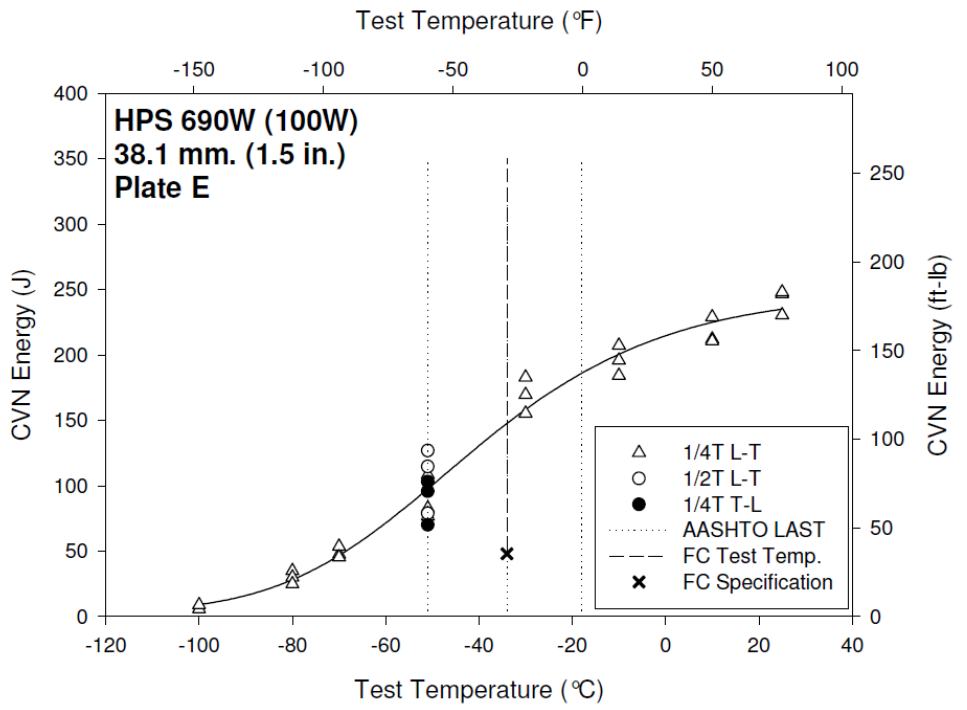

Figure 6-7. CVN Data for Plate E, HPS 690W, 38.1 mm.

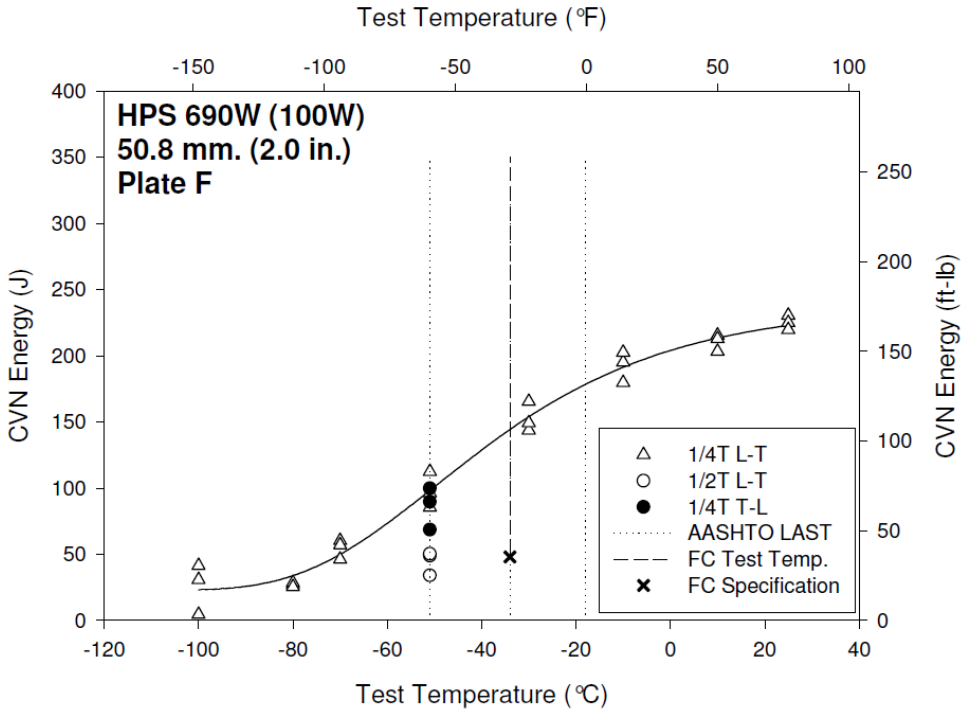

Figure 6-8. CVN Data for Plate F, HPS 690W, 50.8 mm.

The CVN test results of HPS 485W (70W) are presented in Figure 6-9 through Figure 6-13. Specimens machined from 485W (70W) also exhibited toughness much greater than that required in the current fracture critical specification. However, plates A and J did not display typical temperature transition behavior, with no well-defined upper or lower toughness shelves. The lack of clearly defined upper and lower shelf behavior may be due to the fact that specimens were not tested at more extreme temperatures. More testing at both colder and warmer temperatures may have produced data that would allow for the sigmoid fit to exhibit more typical behavior. As the behavior of the steel within service temperature ranges was desired, it was determined that further testing at extreme temperatures was not necessary.

Different from that of HPS 690W (100W), the fracture critical toughness test temperature of HPS 485W (70W) is -23 °C (-10 °F), shown as a vertical dashed line. The required minimum average energy remains at a value of 48 J (35 ft-lbf), represented again by an X. Although more scatter exists in the 485W (70W) data than in the 690W (100W) data, it is clear that the toughness of the steel at -23 °C (-10 °F) greatly exceeds that required in the specification. Sigmoidal fit values at the test specification temperature range from 213.5 J (157.5 ft-lbf) for plate A, to 342 J (252 ft-lbf) for plate I, with an average of 278.5 J (205 ft-lbf) for all five plates. Zone III CVN toughness values also greatly exceed the required minimum energy, with average values ranging from 161.5 J (119 ft-lbf) for plate A to 288.5 J (213 ft-lbf) for plate H, and an average of 209 J (154 ft-lbf) across the five plates.

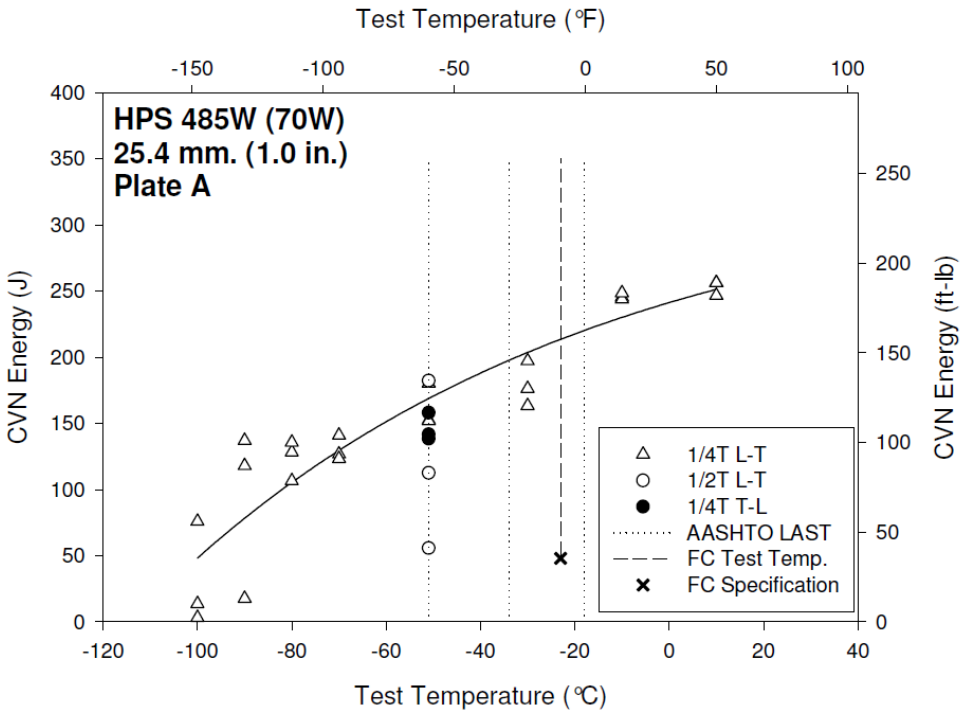

Figure 6-9. CVN Data for Plate A, HPS 485W, 25.4 mm.

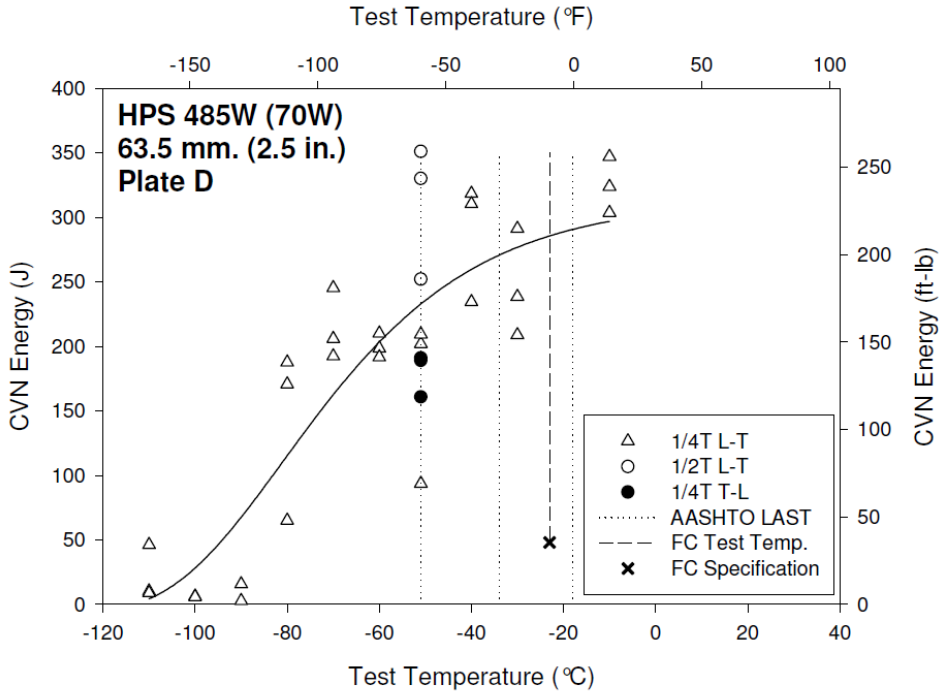

Figure 6-10. CVN Data for Plate D, HPS 485W, 63.5 mm.

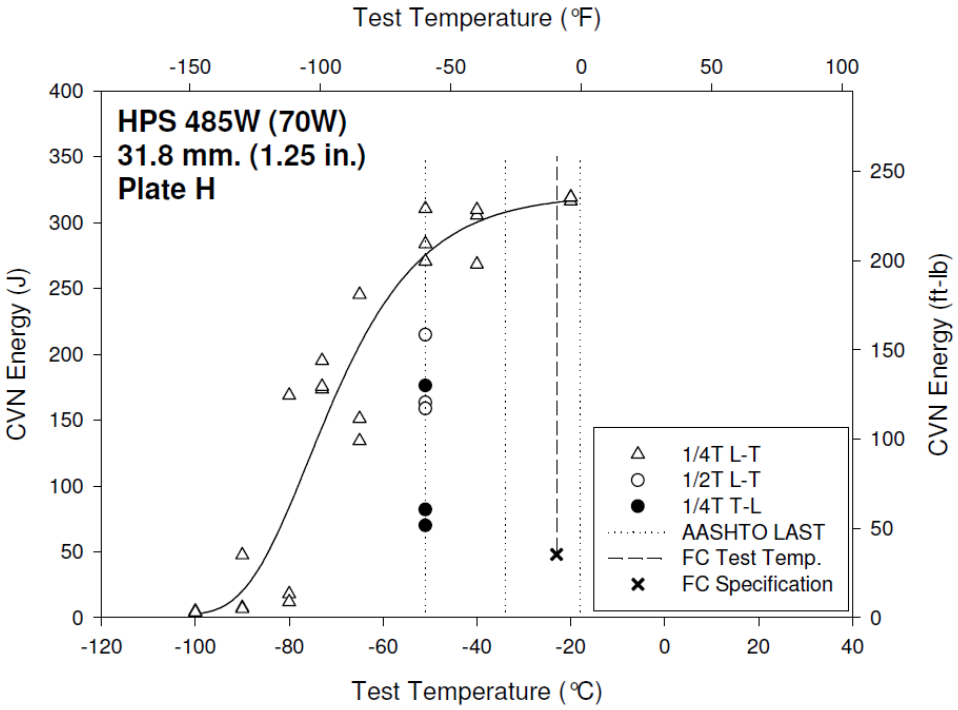

Figure 6-11. CVN Data for Plate H, HPS 485W, 31.8 mm.

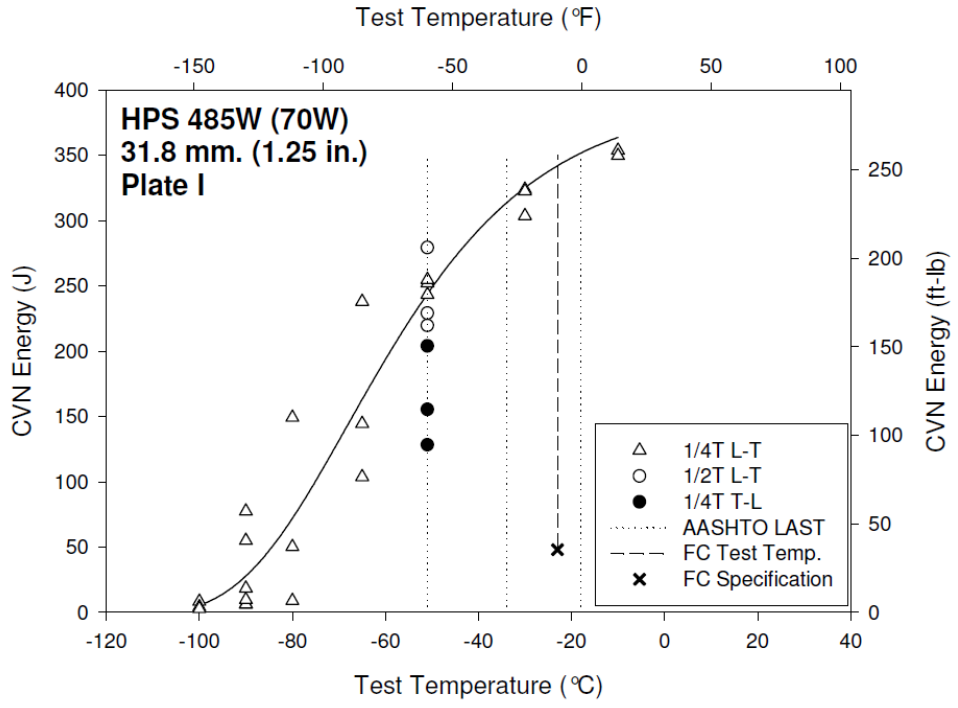

Figure 6-12. CVN Data for Plate I, HPS 485W, 31.8 mm.

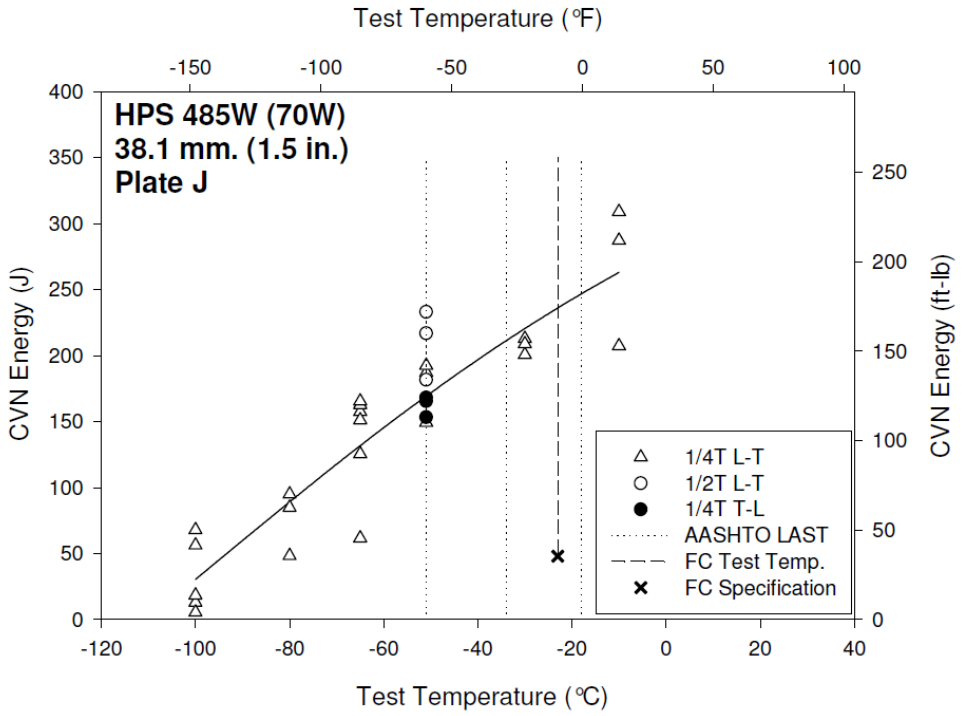

Figure 6-13. CVN Data for Plate J, HPS 485W, 38.1 mm.

Examination of HPS 485W (70W) CVN data reveals that differences in specimen orientation and through thickness sampling do have an effect on impact energy values when compared with 1/4T L-T specimens. The effect is not consistent between plates, however. No reason for this apparent difference in behavior could be ascertained, other than the fact that it may be attributed to general impact toughness variability.

Fracture Toughness Test Results

A total of 114 pre-cracked Charpy-sized SE(B) specimens were prepared from the eight different plates of HPS for static fracture toughness testing. The master curve methodology was applied to each data set in order to determine the 1T reference temperature, T_o, of each plate of HPS. Data indicates that the three plates of HPS 690W (100W) have reference temperatures of -80, -102, and -95 °C, for plates C, E, and F, respectively. Following the exponential master curve

allows for evaluation of fracture toughness at bridge service temperatures. At the AASHTO Zone III temperature of -51 °C (-60 °F), the presented reference temperatures correspond to median 1T fracture toughness values of 150, 213, and 191 MPa√m (137, 194, and 174 ksi√in) for plates C, E, and F, respectively. The average reference temperature is -92 °C (-134 °F), which corresponds to a median 1T fracture toughness of 183 MPa√m (166 ksi√in) at -51 °C (-60 °F). Examination of the master curve tolerance bounds at service temperatures presents expected toughness values with a provided amount of statistical confidence. Material exhibiting a T_o of -92 °C (-134 °F) has 1T toughness values of 105 and 77 MPa√m (96 and 70 ksi√in) at the five and one per cent tolerance bounds, respectively.

Analysis of all three HPS 690W (100W) data sets resulted in valid reference temperatures with weighting factors greater than 1.0. Size corrected 1T fracture toughness data for HPS 690W (100W) plates C, E, and F are presented in Figure 6-14 through Figure 6-16, along with their median toughness master curve and associated 5 and 95 per cent tolerance bounds. Although presented in these plots, neither uncensored data exceeding the specimen constraint limit or invalid data were used in the calculation of the reference temperature.

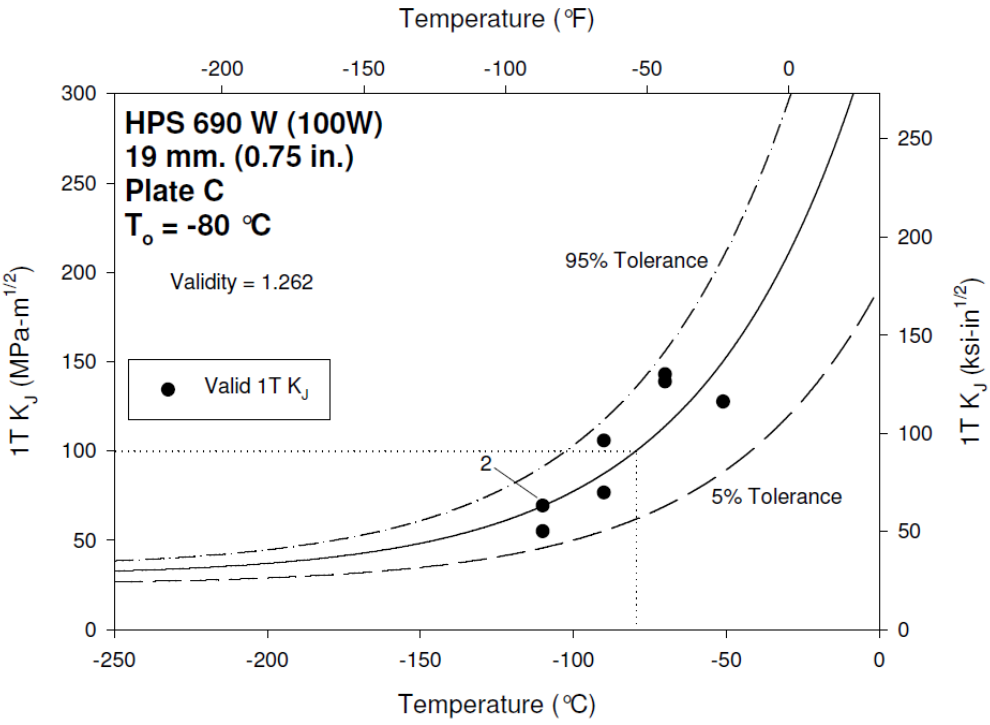

Figure 6-14. Fracture Toughness Data and Master Curve for Plate C, HPS 690W, 19 mm.

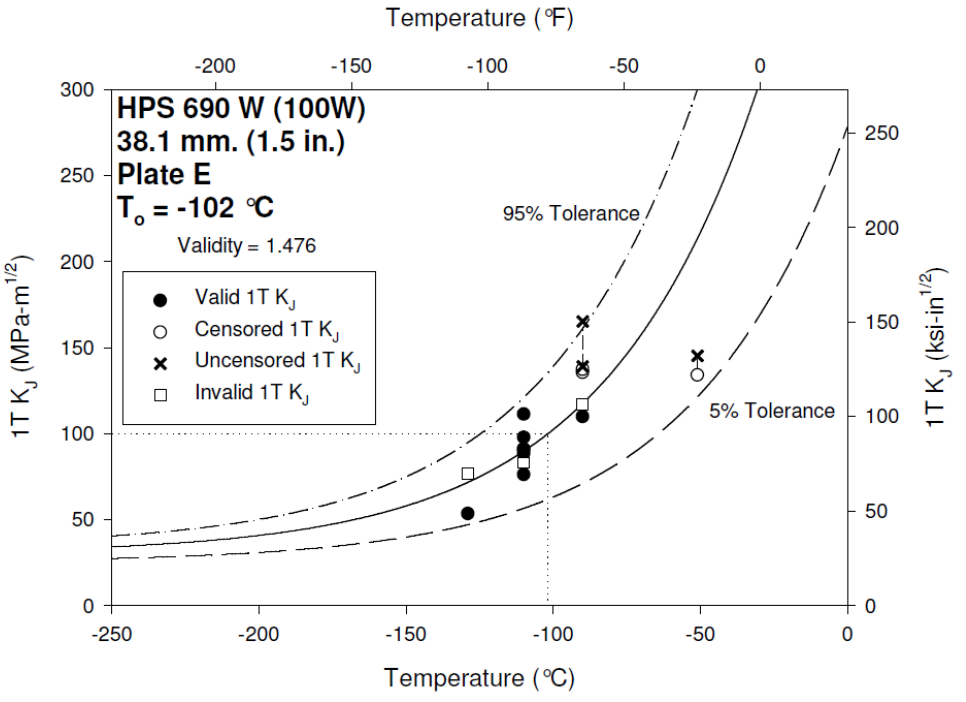

Figure 6-15. Fracture Toughness Data and Master Curve for Plate E, HPS 690W, 38.1 mm.

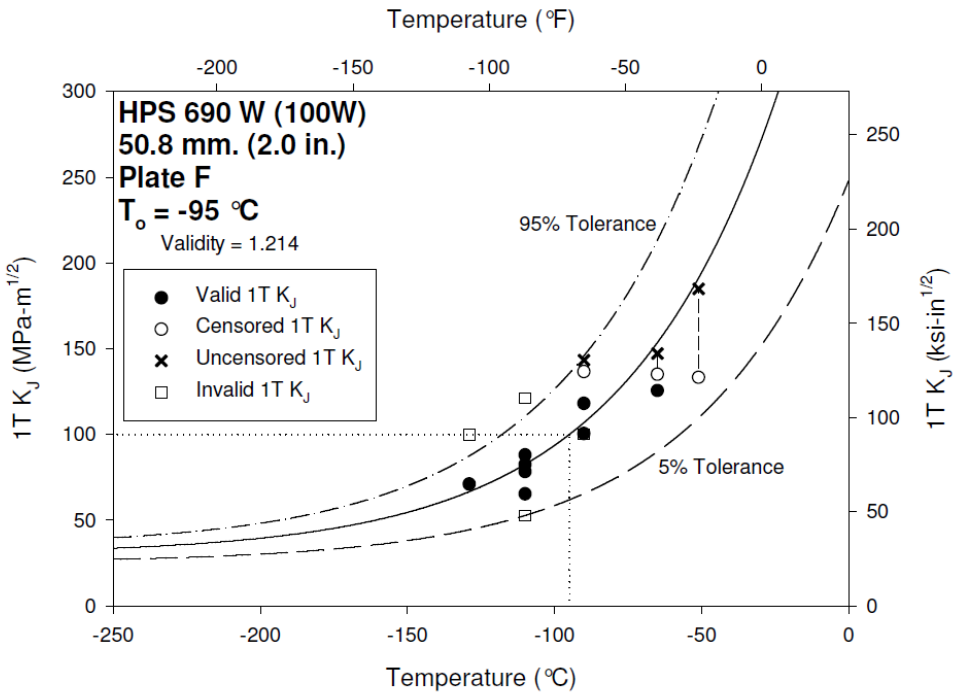

Figure 6-16. Fracture Toughness Data and Master Curve for Plate F, HPS 690W, 50.8 mm.

Master curve evaluation of static fracture toughness data for HPS 485W (70W) yielded extremely low reference temperatures, indicating high toughness at bridge service temperatures. The five plates of HPS 485W (70W) examined yielded 1T reference temperatures ranging from -134 °C (-209 °F) for plate J to -181 °C (-294 °F) for plate D, with an average value of -164 °C (-263 °F). Median fracture toughness values at -51 °C (-60 °F) for these reference temperatures range from 369 to 862 MPa√m (336 to 785 ksi√in). Although ASTM E1921-13 presents no upper bound in the master curve standard, the exponential function is only intended to be representative of fracture behavior on the lower shelf and in the transition region. Because of this, it should be noted that materials with extremely low reference temperatures may experience ductile tearing prior to reaching these extremely high median toughness values predicted at much warmer service temperatures. Lower fracture toughness values from tolerance bounds, however,

are attainable and can be applied to fracture mechanics problems in design and analysis. The average 1T reference temperature of -164 °C (-263 °F) produces five and one percent fracture toughness values of 339 and 232 MPa√m (308 and 211 ksi√in), respectively, at -51 °C (-60 °F).

Due to excessive numbers of specimens fracturing above the master curve censoring limit as well as some invalid tests, plates A and I did not achieve a weighting factor of 1.0. For this reason the reference temperatures of these two plates must be considered conditional, T_{oQ}, and are presented as such. Fracture toughness data of the five HPS 485W (70W) plates, size corrected to 1T, is seen in Figure 6-17 through Figure 6-21, along with the 5 and 95 per cent tolerance bounds. Again, neither invalid data points nor uncensored data that violated the size dependent constraint limit were included in the reference temperature calculation.

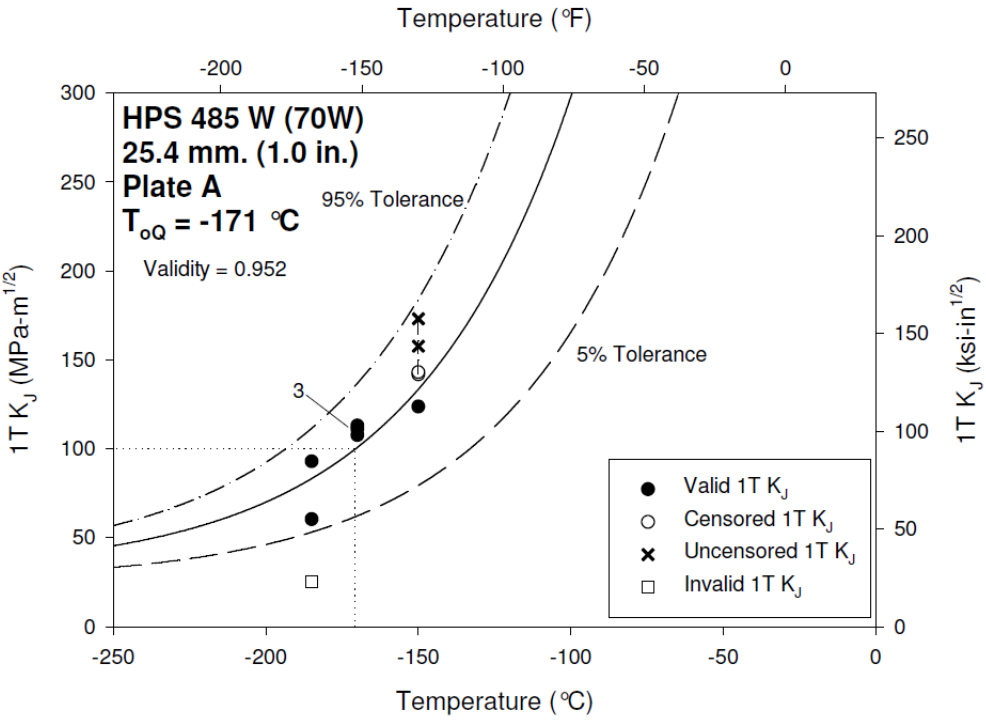

Figure 6-17. Fracture Toughness Data and Master Curve for Plate A, HPS 485W, 25.4 mm.

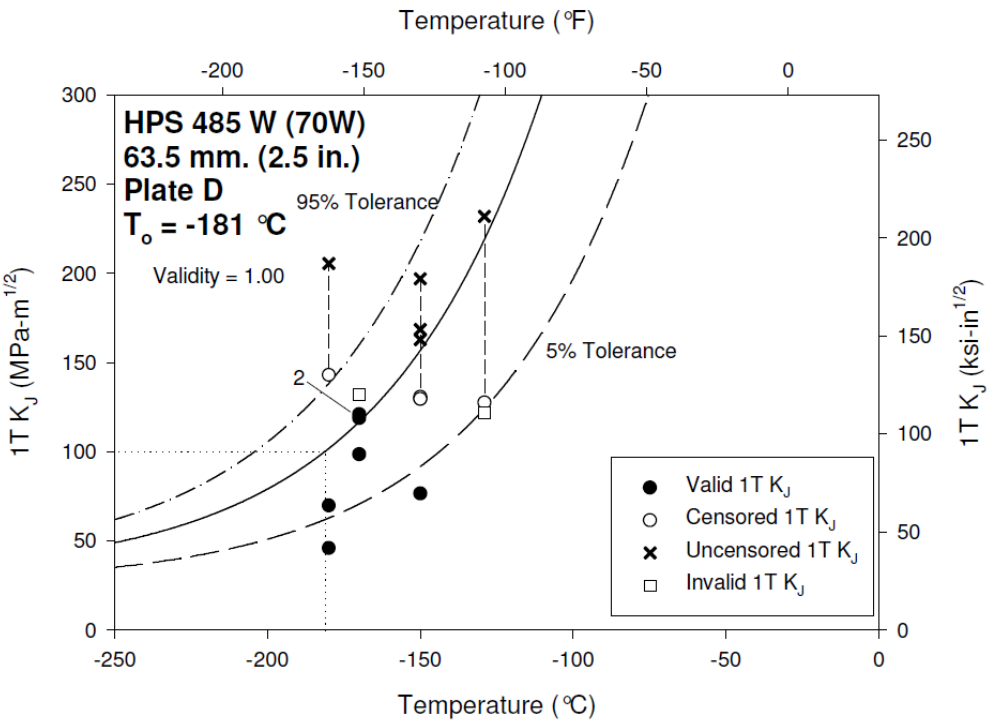

Figure 6-18. Fracture Toughness Data and Master Curve for Plate D, HPS 485W, 63.5 mm.

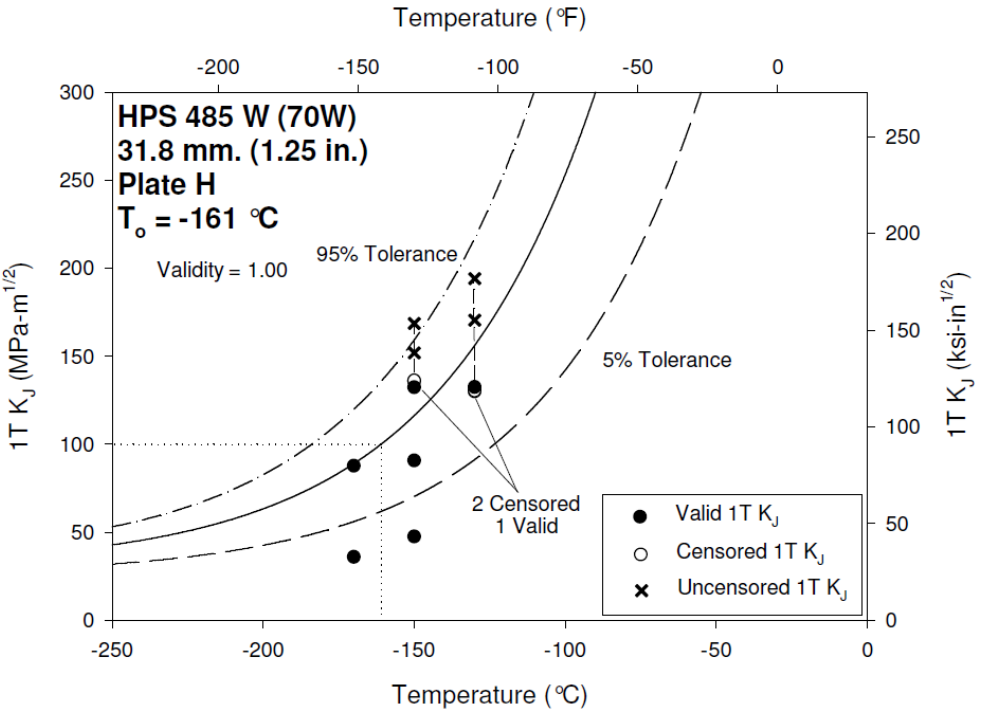

Figure 6-19. Fracture Toughness Data and Master Curve for Plate H, HPS 485W, 31.8 mm.

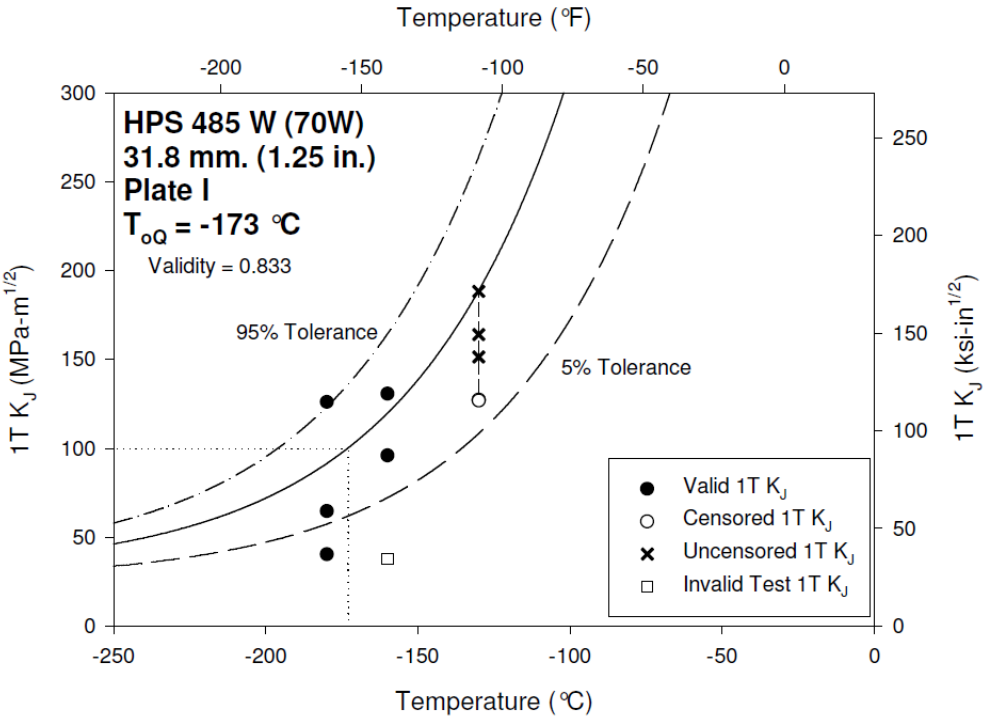

Figure 6-20. Fracture Toughness Data and Master Curve for Plate I, HPS 485W, 31.8 mm.

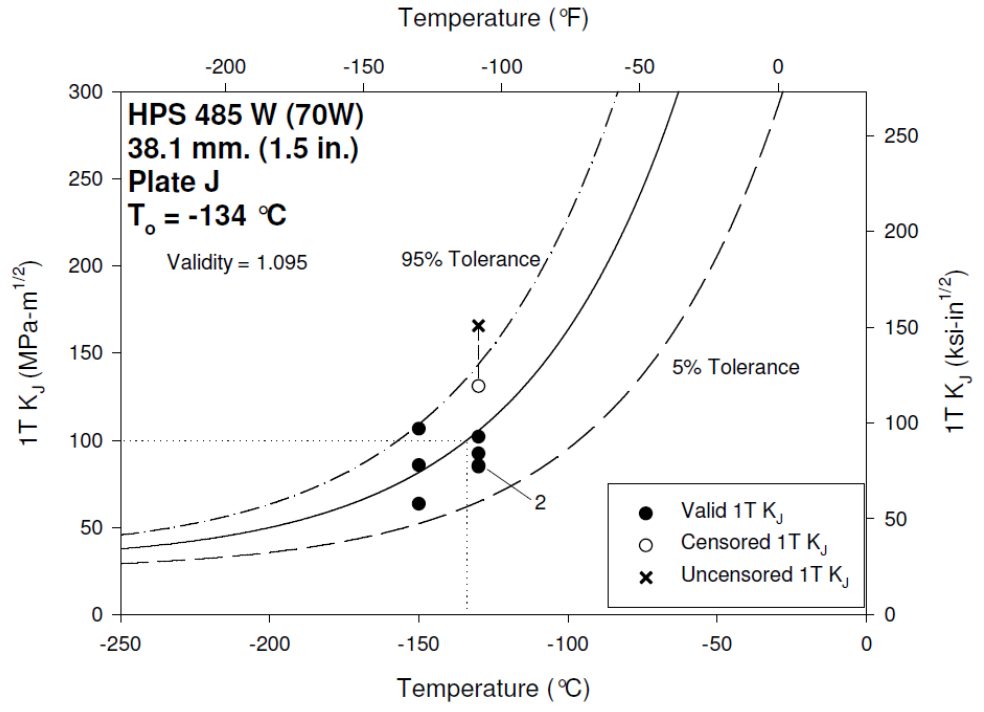

Figure 6-21. Fracture Toughness Data and Master Curve for Plate J, HPS 485W, 38.1 mm.

6.7 Flaw Tolerance Capability

The benefit of using true fracture mechanics parameters to characterize material toughness is that, in contrast with CVN impact energy values, they are directly applicable to engineering problems. Fracture toughness values can be used with known solutions for various structural geometries and load combinations to calculate tolerable flaw sizes. With this knowledge, it is possible to examine real structures and determine acceptable damage, flaw, or fatigue crack size.

Considering an HPS 485W (70W) built-up bridge girder with a tension flange of thickness 76 mm. (3.0 in.) and width 610 mm. (24.0 in.), the size of a tolerable flaw can be determined for a provided level fracture toughness. The flange with a growing through-thickness fatigue crack (Figure 6-22b) can be modeled as a flat plate in tension with an applied tensile stress of $0.55F_y$, which represents the AASHTO design service stress. Defining the total length of the fatigue crack as 2a, the required fracture toughness is calculated using:

$$K = f(\alpha)0.55F_y\sqrt{\pi a} \qquad \text{Eq. 6.7}$$

where K is the provided fracture toughness and $f(\alpha)$ is a function based on the relationship between crack geometry and plate size (Dowling 1999). Using the average one per cent tolerance value of toughness for HPS 485W (70W) plate with reference temperature, T_o, equal to -164 °C (-263 °F) and adjusted for flange thickness using the master curve size correction in Eq. 6.3, the available fracture toughness of the flange is 181 MPa√m (165 ksi√in). This results is a total crack size of 2a equal to 277 mm. (10.9 in.), with only a one per cent probability of failure.

However, a through-thickness center crack of 277 mm. (10.9 in.) reduces the flange area by over 45 per cent. Under the applied service stress of $0.55F_y$ on the gross cross-section, this

reduction in area results in a fully yielded net cross-section. A fatigue crack of this size will result in net section failure due to rupture. Thus, the HPS 485W (70W) has adequate toughness to eliminate cleavage fracture, with less than a one per cent probability of failure. This same exercise can be performed for various other flaw and plate geometries, as well as for HPS 690W (100W), with the toughness values presented above.

6.8 Comparison with Current CVN Requirements

Fracture Toughness Estimate

As previously mentioned, no fracture mechanics analysis can be performed using CVN impact energy values. However, there exist empirical correlation relationships between CVN and fracture toughness, and between CVN and reference temperature. A widely accepted correlation between CVN values and reference temperature is presented in the British Standard Institution's BS 7910 (2005) which was shown by Collins, et al. to be applicable to bridge steels (submitted 2014a, b). Method J.2.2 predicts reference temperature based on a full Charpy V-Notch temperature transition curve. Test temperatures corresponding to CVN impact test values of 27 and 40 J (20 and 30 ft-lbf) are adjusted by Eq. 6.8 and Eq. 6.9 to provide an estimated reference temperature:

$$T_o = T_{27J} - 18°C + T_k \qquad \text{Eq. 6.8}$$

$$T_o = T_{40J} - 24°C + T_k \qquad \text{Eq. 6.9}$$

where To is reference temperature, T_{27J} and T_{40J} correspond to test temperatures at CVN energy levels of 27 and 40 J, respectively, and T_k is a temperature term used to consider scatter

in CVN data. All temperatures are in degrees Celsius. BS 7910 recommends that T_k =25 °C unless experimental data supports the use of a lower value. Unfortunately, current fracture critical CVN specifications require an average CVN energy of 48 J (35 ft-lbf) at -23 and -34 C (-10 and -30 F), for HPS 485W (70W) and HPS 690W (100W), respectively. Examining the CVN data presented above, the difference in temperature between 48 and 40 J (35 and 30 ft-lbf) is -4 °C for HPS 690W (100W) and -2 °C for 485W (70W). Using this temperature adjustment, along with Eq. 6.9, the estimated reference temperatures currently specified for fracture critical bridges are -37 and -24 °C (-35 and -11 °F) for HPS 690W (100W) and 485W (70W), respectively. These reference temperatures provide 1T, one percent tolerance, fracture toughness in Zone III of 42 MPa√m (38 ksi√in) for HPS 690W (100W) and 38 MPa√m (35 ksi√in) for HPS 485W (70W). The toughness values guaranteed by the AASHTO material toughness specifications are significantly lower than the toughness observed in the HPS examined in this study.

HPS Behavior Comparison with Current Specifications

Using the specification estimated reference temperatures and corresponding fracture toughness values, a similar exercise to that shown above can be performed to illustrate the flaw tolerance currently established through material toughness specifications. Two different flaw geometries are considered for the same 76 mm. (3.0 in.) thick by 610 mm. (24 in.) wide plate subject to a tensile stress of 0.55 F_y. Figure 6-22 presents the different geometries for a) an edge cracked plate and b) a through thickness center cracked plate. Performing the master curve size adjustment, the 1T, 1 per cent tolerance, fracture toughness values presented above at AASHTO Zone III become 37 MPa√m (34 ksi√in) for HPS 690W (100W) and 34 MPa√m (31 ksi√in) for HPS 485W (70W).

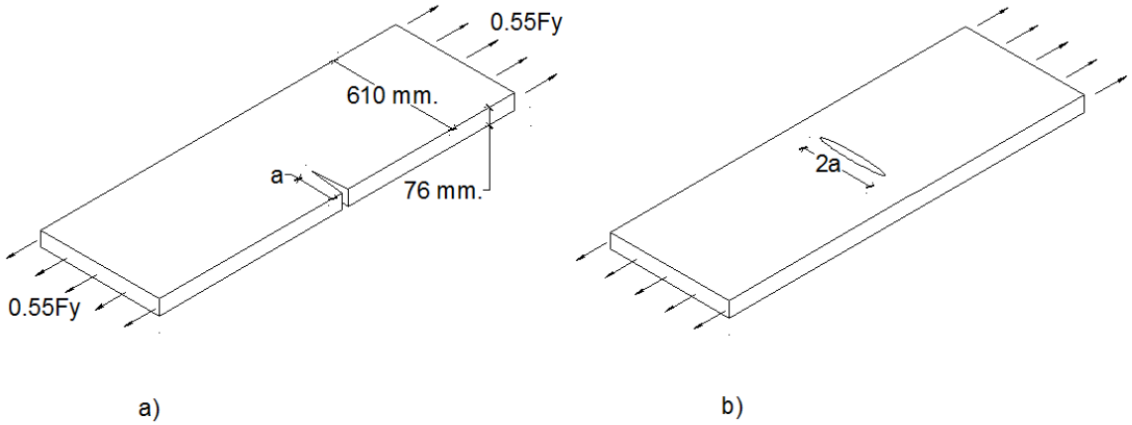

Figure 6-22. Geometry of Plate with a) Edge Crack, b) Through-Thickness Center Crack

Using the 3T specification estimated one per cent tolerance fracture toughness values, tolerable flaw sizes were calculated. The flaw sizes are presented in Table 3 for both geometries and grades of HPS. In addition to the specification determined tolerable flaw sizes, Table 6-3 also contains tolerable flaw sizes calculated based on toughness values from fracture toughness testing. It is clear that the tolerable flaw sizes based on the current specification are significantly smaller than those determined from the data. Material toughness specifications allow for HPS 485W (70W) edge crack size tolerance of 4.1 mm. (0.16 in.), compared with the 89.7 mm. (3.50 in.) crack size that the material is capable of allowing, more than a 20 times increase in flaw tolerance capacity. The difference between the specification determined tolerable flaw size and the data determined flaw size for the center cracked plate displays a similar disparity.

Table 6-3. Calculated Tolerable Flaw Size Comparison

Grade	Toughness Determination	Edge Crack, a	Center Crack, 2a
		mm. (in.)	mm. (in.)
HPS 485W (70W)	Specification	4.1 (0.16)	10.3 (0.41)
	Data	89.7 (3.50)	277 (10.90)
HPS 690W (100W)	Specification	2.4 (0.09)	6.0 (0.24)
	Data	7.0 (0.27)	17.7 (0.70)

Flaw sizes tolerable in HPS 690W (100W) are, in general, significantly smaller than those in 485W (70W). This is due to the fact that the applied stress is greater on the 690W (100W) material, resulting in a much larger stress intensity at the tip of the flaw. However, although the sizes of flaws are smaller for the HPS 690W (100W), the difference between the specification determined and data determined values are still great. Given the described geometry and loading, HPS 690W (100W) is capable of resisting fracture initiation in the presence of 7.0 mm. (0.27 in.) and 17.7 mm. (0.70 in.) flaws for the edge crack and center crack, respectively. In comparison, the material toughness specification provides toughness only capable of tolerating flaws of 2.4 mm. (0.09 in.) and 6.0 mm. (0.24 in.) for the same crack geometries. In addition, it should be noted that failure probabilities are not equal for this comparison. Flaws calculating from toughness data have a one per cent probability of failure due to cleavage fracture. Specification estimated flaw sizes, although using the one per cent tolerance bound from the master curve, in reality have a higher probability of failure. This is due to the scatter associated with the CVN-T_o correlation procedure, which was not considered as part of this analysis. Thus, the disparity between data determined and specification determined flaw sizes is actually greater than it appears.

6.9 Conclusions

Results of the CVN tests indicate that all plates greatly exceed the minimum required material toughness specifications prescribed in ASTM A709-13. CVN test results at the AASHTO Zone III temperature of -51 °C (-60 °F) also exceeded the minimum toughness requirements despite this being well below the fracture critical prescribed test temperatures of -

23 and 34 °C (-10 and -30 °F). Fracture toughness testing and analysis produced average master curve reference temperatures of -92 and -164 °C (-134 and -263°F) for HPS 690W (100W) and 485W (70W), respectively. In comparison, reference temperature estimates based on CVN toughness specifications produces values of -37 °C (-35 °F) for HPS 690W (100W) and -24 °C (-11 °F) for HPS 485W (70W).

Examination of tolerable flaw sizes based on these reference temperatures reveal that HPS steels are being produced that can tolerate much larger flaws than the minimum toughness requirements would indicate. The test data from this study shows that HPS 690W (100W) is capable of tolerating flaws nearly three times larger than the current specification mandates, while flaws in HPS 485W (70W) can be more than twenty times the size that the current specification dictates. In fact, under the conditions examined in this study, HPS 485W (70W) has the fracture toughness capacity to reach flaw sizes resulting in net section yielding with only a one per cent probability of cleavage fracture. Although not every combination of loading and flaw geometry is capable of producing this result, this level of toughness has the potential to change the way that fracture is considered with respect to steel bridge design. Based on the results of this study, the material toughness specifications should be changed in order to take advantage of the superior toughness exhibited by A709 HPS grade steels.

6.10 Acknowledgements

The authors would like to thank Richard Link, Jim Joyce, and Steve Graham of the United States Naval Academy for their advice and assistance. Funding for this study was provided by TPF- 5(238). The opinions expressed in this paper are those of the authors, and do not reflect the position of the FHWA.

Notation

The following symbols are used in this paper:

a = Flaw size in a member

a_o = Initial crack size in specimen

B = Specimen thickness

B_o = Initial specimen thickness used in thickness adjustment

B_x = Desired specimen thickness for thickness adjustment

CMOD = Crack mouth opening displacement measurement

CVN = Charpy V-notch impact test

$f(\alpha)$ = Function relating crack length to member size for a given geometry

F_y = Yield stress

J_c = Critical value of J-integral at failure

K = Fracture toughness and stress intensity

K_c = Critical fracture toughness

K_{Jc} = Elastic-plastic equivalent fracture toughness converted from J-integral

$K_{Jc(limit)}$ = Elastic-plastic fracture toughness limit in master curve analysis

$K_{Jc(med)}$ = Median elastic-plastic fracture toughness

$K_{Jc(o)}$ = Initial elastic-plastic fracture toughness used in thickness adjustment

$K_{Jc(x)}$ = Size adjusted fracture toughness for specimen of thickness B_N

K_{min} = Absolute minimum fracture toughness equal to 20 MPa√m (18 ksi√in)

SE(B) = Single edge bend specimen geometry

T_{27J} = Test temperature corresponding to CVN value of 27 J (20 ft-lbf)

T_{40J} = Test temperature corresponding to CVN value of 27 J (30 ft-lbf)

T_k = Temperature term related to CVN scatter, recommended to be 25 °C

T_o = Reference temperature, rooted at median toughness equal to 100 MPa√m (91 ksi√in)

T_{oQ} = Provisional reference temperature prior to validation

W = Width of specimen

Chapter 7: Additional HPS Fracture Data and Analysis

As presented in Chapter 6, the static fracture toughness of eight plates of HPS was examined, and the results were analyzed using the master curve methodology. Tension testing was also performed as part of the material characterization of the plates, the results of which can be found in Appendix A. Additionally, CVN data presented graphically in Chapter 6 can be found in tabulated format in Appendix B. Due to the limited format of journal manuscripts, not all details of individual fracture toughness tests were presented in the previous chapter. Load-displacement records and fracture surface images of each statically tested HPS specimen can be found in Appendix C. Tabulated details about each specimen are presented in Appendix D.

In addition to the static fracture toughness testing performed for reference temperature determination, attempts were made to develop resistance curves in order to characterize the ductile tearing resistance of HPS. Unfortunately the clip gage used to measure CMOD was limited to a maximum opening of 2.0 mm. (0.08 in.). For the majority of the plates examined, this limit was not enough displacement to record adequate amounts of crack growth. Thus, no meaningful analysis of resistance curves was possible. Appendix E presents the test records for each attempted resistance curve.

As discussed in Chapter 2, much debate has centered on the effect of elevated loading rates on bridge steel fracture toughness. Original toughness specifications were based on an intermediate loading rate approximating a time to maximum load of one second, although at the time some researchers argued for the use of dynamic loading rates (Hartbower 1979). The idea of the intermediate bridge loading rate still influences current material toughness specifications, dictating the temperature shift used to arrive at CVN test temperatures from lower service

temperatures. Although debate about the effects of bridge loading rates on fracture toughness persists, it is important to understand material behavior under differing loading rates. To this end, dynamic fracture initiation and crack arrest toughness testing was performed on the same HPS plates examined in Chapter 6. Presented in this chapter are the results and analyses of these tests.

7.1 HPS Dynamic Fracture Toughness Data and Analysis

Following the same procedures used for static fracture toughness testing, all eight plates of HPS 690W (100W) and HPS 485W (70W) were examined at dynamic test rates. Although all dynamic tests were performed at the fastest attainable rate of the servo-hydraulic test frame being used, final stress intensity rate is a function of critical fracture toughness value. In general, higher toughness specimens take longer to break than specimens exhibiting low toughness. Although final stress intensity rates ranged from 1000 to 5000 MPa√m/sec (910 to 4550 ksi√in/sec), all rates are simply designated as dynamic because they are of the same order of magnitude. This grouping of dynamic rates by order of magnitude is addressed in ASTM E1921-13. In this report dynamic reference temperatures are designated by $T_{o,Dyn}$. Details of dynamic toughness testing of HPS steel presented in this chapter, including individual test records and scaled images of fracture surfaces, are presented in Appendix F. Dynamic HPS fracture toughness data is tabulated in Appendix G.

7.1.1 Dynamic Fracture Toughness of HPS 690W (100W)

Charpy-sized SE(B) specimens machined from HPS 690W (100W) plate C were tested dynamically at temperatures of -51 and -34 °C (-60 and -30 °F), resulting in a 1T dynamic reference temperature of -51 °C (-60 °F). All tests conducted at this temperature resulted in valid

data, with only one limit censored test at -34 °C (-30 °F), providing a weighting validity factor of 1.167. The dynamic reference temperature represents a 29 °C shift in temperature between static and dynamic testing rates. Plate C dynamic fracture toughness data, along with the master curve and corresponding 5 and 95 per cent tolerance bounds are shown in Figure 7-1.

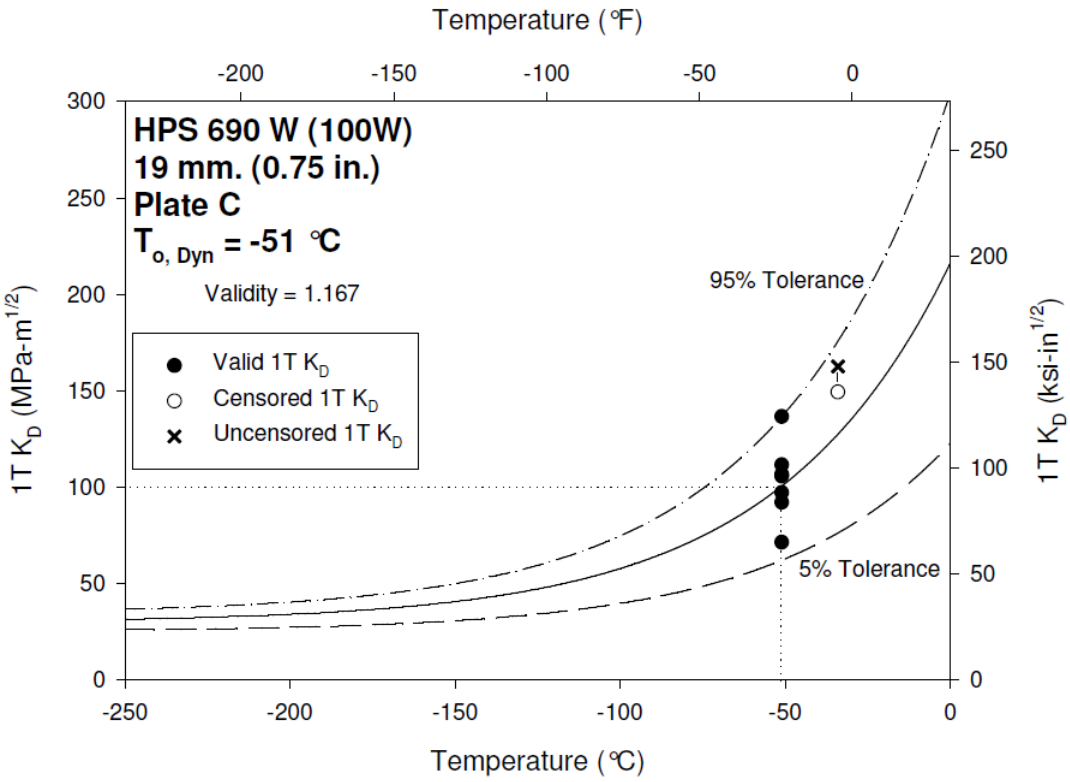

Figure 7-1. Dynamic Fracture Toughness Data and Master Curve for Plate A

Dynamic fracture toughness testing of plate E was performed at temperatures ranging from -51 to -100 °C (-60 to -148 °F). Analysis of the test data resulted in a 1T dynamic reference temperature of -54 °C (-65 °F), and a weighting factor of 1.690. Compared with the plate's static reference temperature of -102 °C (-152 °F), this represents a temperature shift of 48 °C. Figure 7-2 presents the dynamic fracture toughness data of plate E, along with the corresponding master curve.

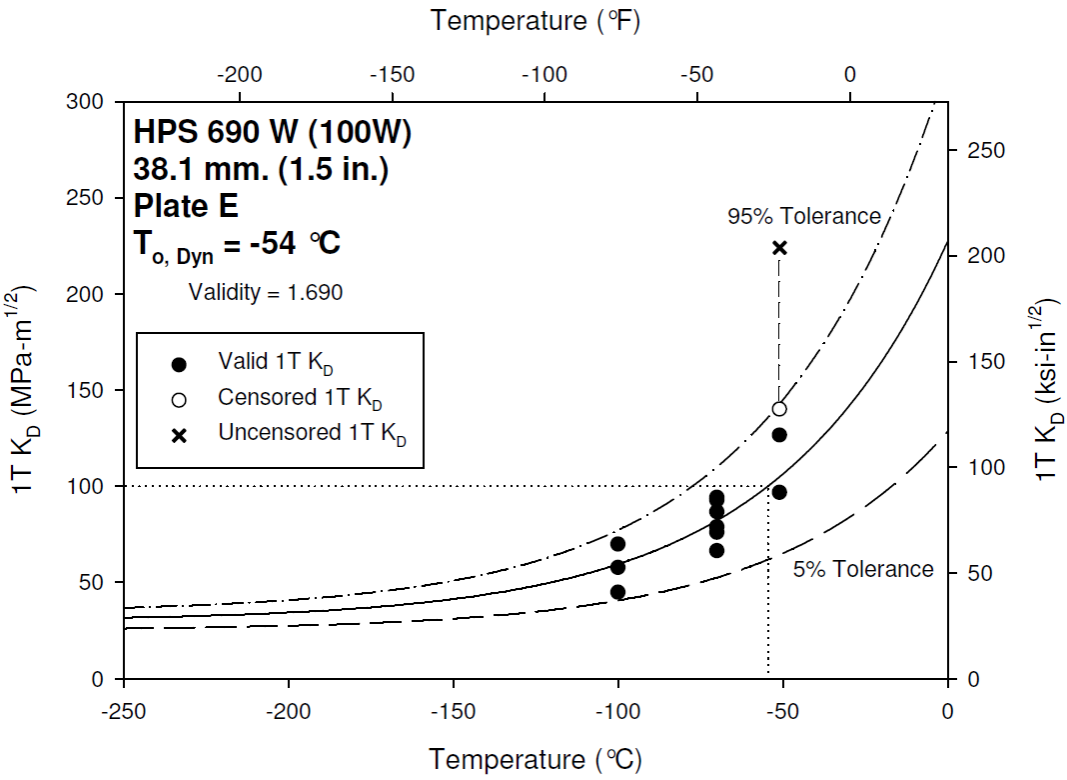

Figure 7-2. Dynamic Fracture Toughness Data and Master Curve for Plate E

HPS 690W (100W) plate F was tested dynamically at temperatures ranging from -51 to -90 °C (-60 to –130 °F). Dynamic fracture toughness data of plate F is very similar to that of plate E, with a 1T dynamic reference temperature of -57 °C (-71 °F) and a weighting factor of 1.762. The dynamic reference temperature represents a shift of 38 °C when compared with the plate's static reference temperature. The dynamic fracture toughness data of plate F, along with the calculated master curve and tolerance bounds is presented in Figure 7-3.

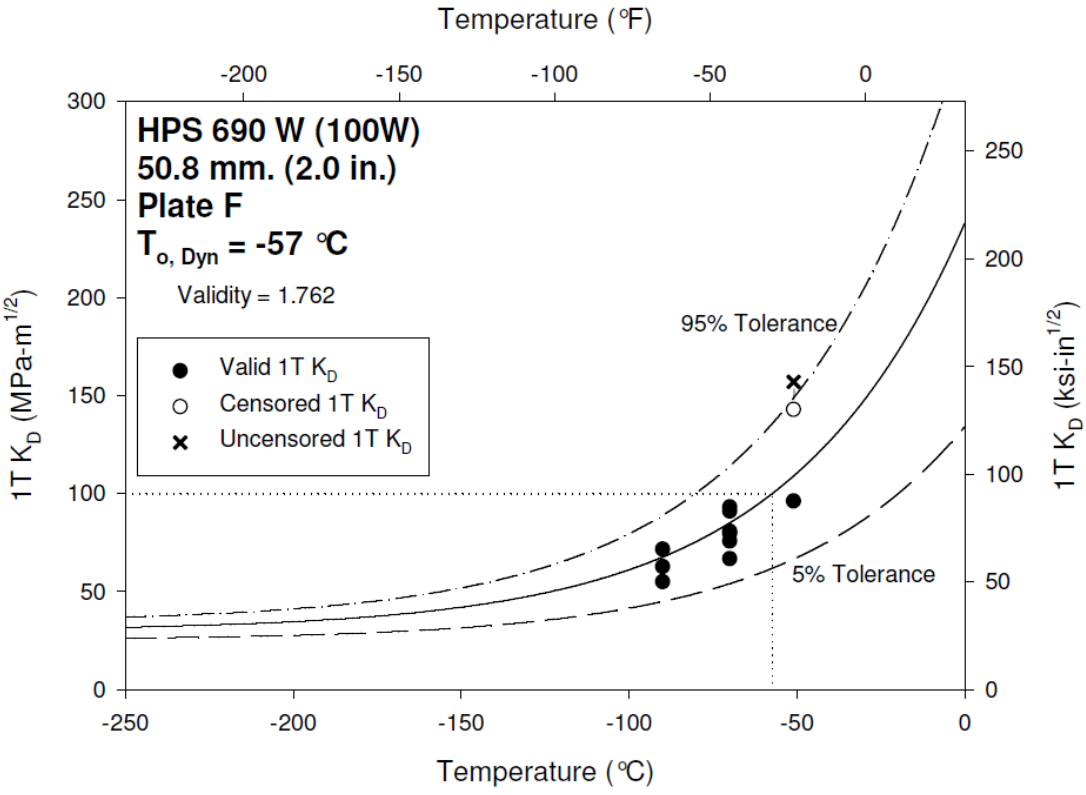

Figure 7-3. Dynamic Fracture Toughness Data and Master Curve for Plate F

The average dynamic reference temperature of the three HPS 690W (100W) plates examined is -54 °C (-65 °F), representing an average temperature shift of 38 °C when compared with static data. The shift is slightly more than that calculated using the stress intensity rate based temperature shift introduced in Chapter 5. Evaluation of Eq. 5.15 and Eq. 5.16 for the average static reference temperature of -92 °C (-134 °F) estimates a dynamic reference temperature of -69 °C (-92 °F) for a rate of 3000 MPa√m/sec (2730 ksi√in/sec), which corresponds to a shift of 23 °C.

7.1.2 Dynamic Fracture Toughness of HPS 485W (70W)

Test specimens machined from HPS 485W (70W) plate A were tested dynamically at temperatures of -100 and -120 °C (-148 and -184 °F). The resulting dynamic reference

temperature of the plate was determined to be -113 °C (-171 °F), with a weighting validity factor of 1.50. This reference temperature represents a shift of 58 °C when compared with the static reference temperature presented in Chapter 6. The prediction of dynamic reference temperature based on Eq. 5.15 and Eq. 5.16 is -132 °C (-206 °F). Figure 7-4 presents the dynamic fracture toughness of plate A, along with the corresponding master curve and 5 and 95 per cent tolerance bounds. Similar to the static analyses, invalid test data are plotted for reference only, and were not used in the calculation of the reference temperature.

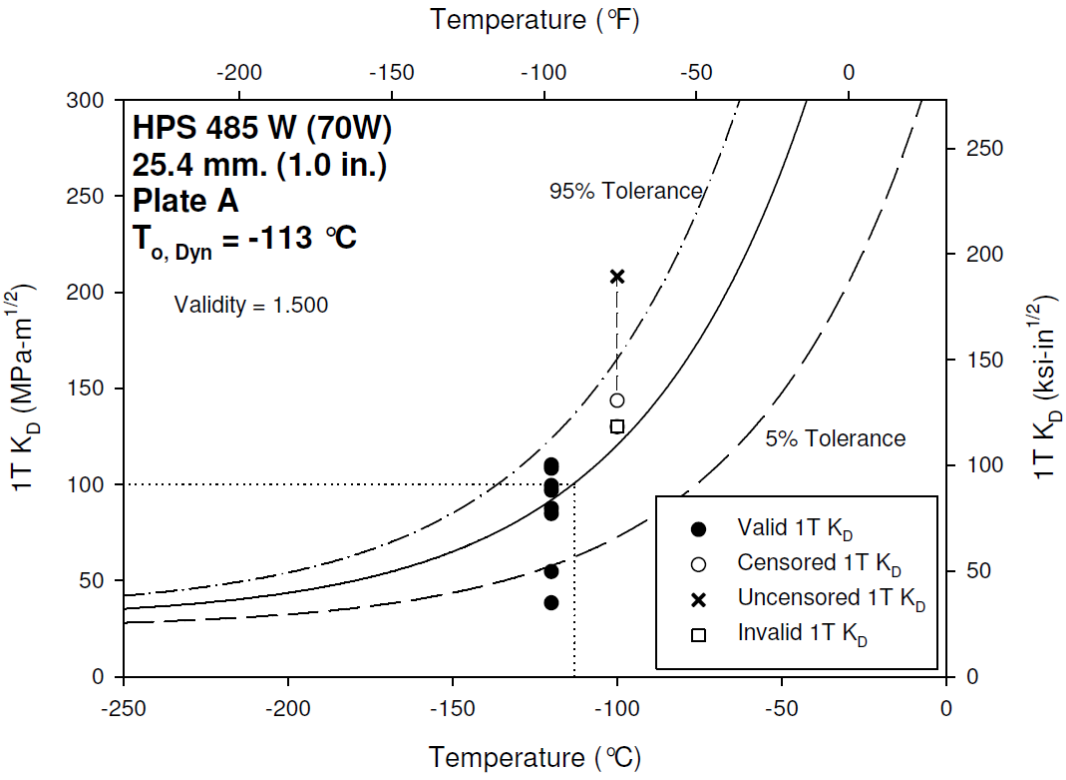

Figure 7-4. Dynamic Fracture Toughness Data and Master Curve for Plate A

Dynamic toughness testing of plate D produced interesting results. Multiple specimens violated the toughness limit resulting in the insertion of censored data. However, in spite of these specimens attaining high toughness values, other tests at the same temperatures resulted in much

lower values. Master curve analysis of this data set yielded a dynamic 1T reference temperature of -111 °C (-168 °F) with a weighting validity factor of 1.619. This would indicate a valid reference temperature. However, visual inspection of the data and master curve, as shown in Figure 7-5, indicates that censored values dominate the determination of $T_{o, Dyn}$, causing the master curve to unconservatively over predict dynamic fracture toughness values.

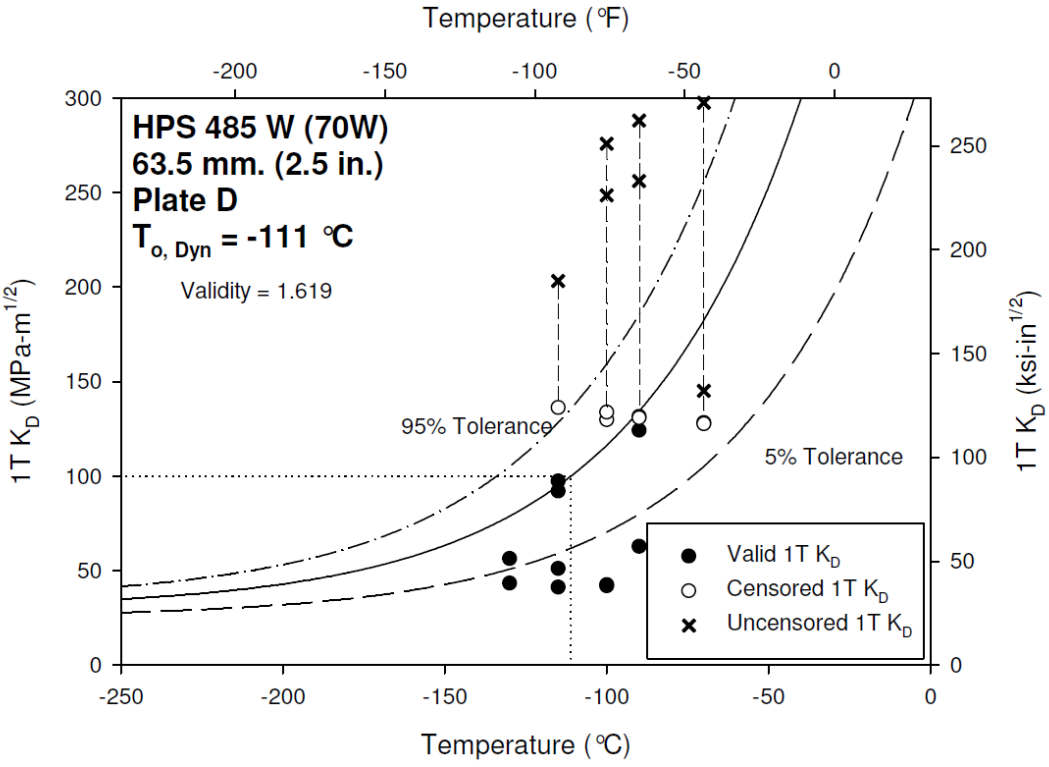

Figure 7-5. Dynamic Fracture Toughness Data and Master Curve for Plate D

If the data set is re-analyzed ignoring the censored values, a new 1T dynamic reference temperature is calculated, which seems to better capture the valid data. This analysis produces a dynamic reference temperature of -86 °C (-123 °F) and a validity weighting value of 1.440. This analysis, results of which are shown if Figure 7-6, is not in accordance with ASTM E1921-13, although it does seem to better represent fracture behavior than the previous analysis. Neither of

the approaches, however, provides a value that is close to the dynamic reference temperature predicted by Eq. 5.15 and Eq. 5.16. This approach estimates $T_{o, Dyn}$ equal to -144 °C (-227 °F), which seems to be very unconservative when compared with test data.

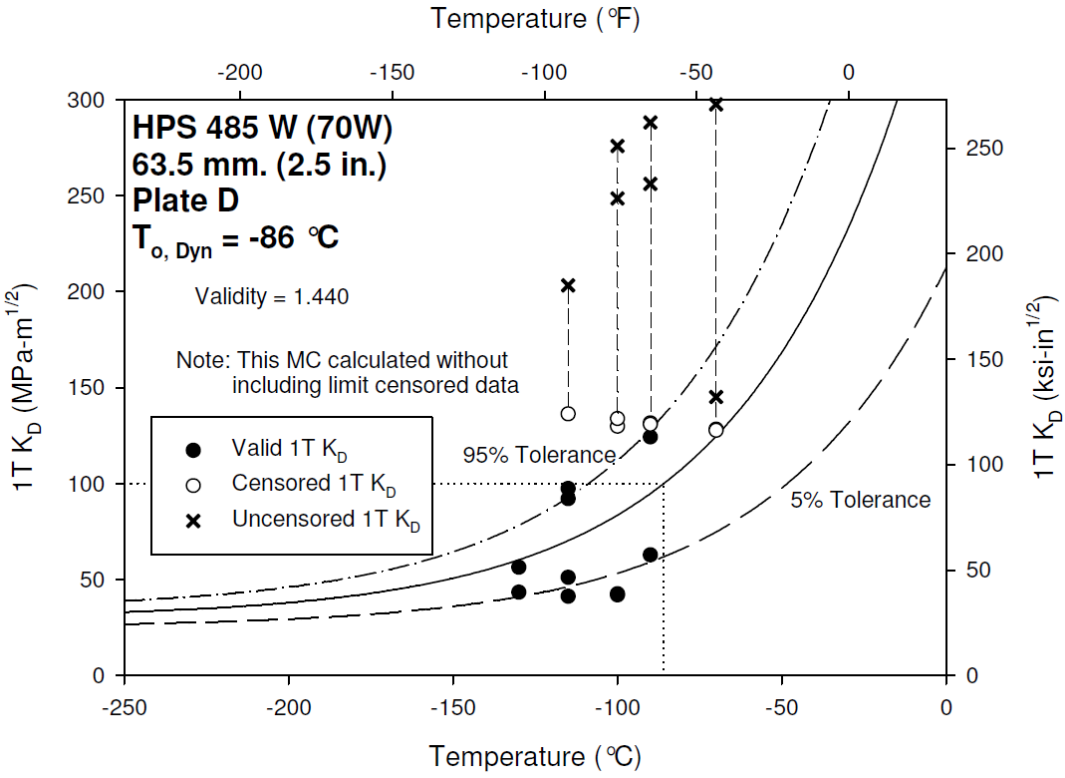

Figure 7-6. Dynamic Fracture Toughness Data and Alternate Master Curve for Plate D

Analysis of dynamic fracture toughness data for both plates H and I resulted in similar scenario to that of plate D. The original analysis of dynamic fracture toughness data for HPS 485W (70W) plate H resulted in a provisional 1T dynamic reference temperature of -105 °C (-157 °F), with a validity factor of 0.881. Ignoring censored values in an alternative master curve analysis results in a dynamic reference temperature of -84 °C (-119 °F) and a validity factor of 0.857. Again, neither of these dynamic reference temperature values aligns with the rate adjusted estimate based off of the static reference temperature. Using a rate of 3000 MPa√m/sec (2730

ksi√in/sec) and static T_o = -161 °C (-258 °F), Eq. 5.15 and Eq. 5.16 predict a dynamic reference temperature of -123 °C (-189 °F). Examining the data presented in Figure 7-7 and Figure 7-8, this is clearly an unconservative prediction of dynamic reference temperature.

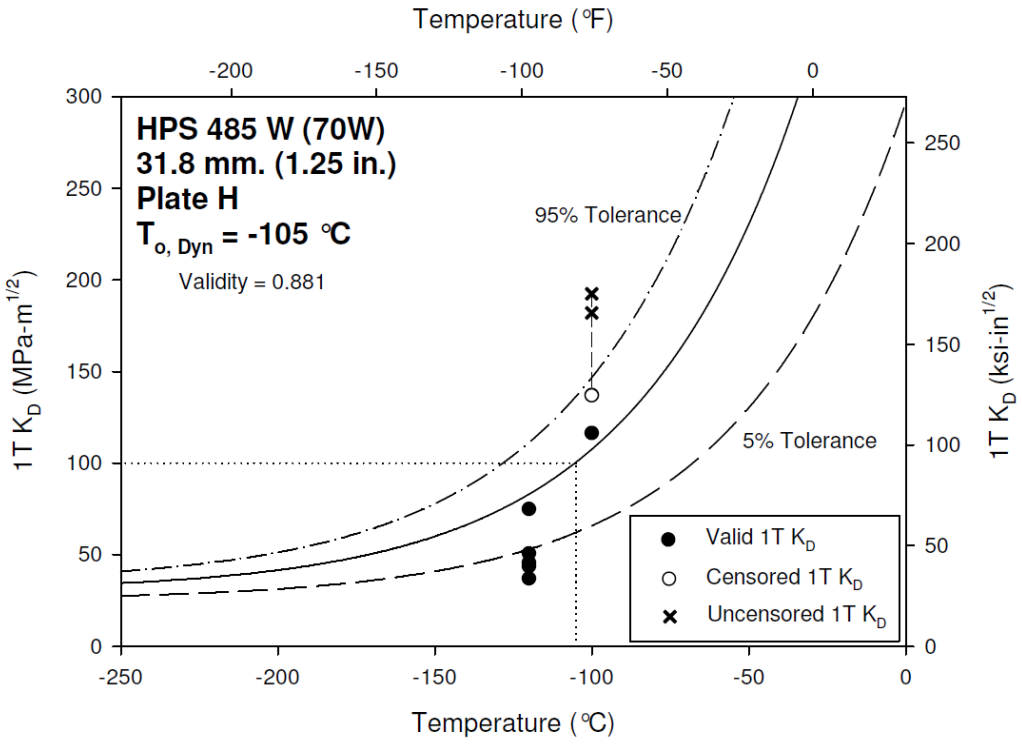

Figure 7-7. Dynamic Fracture Toughness Data and Master Curve for Plate H

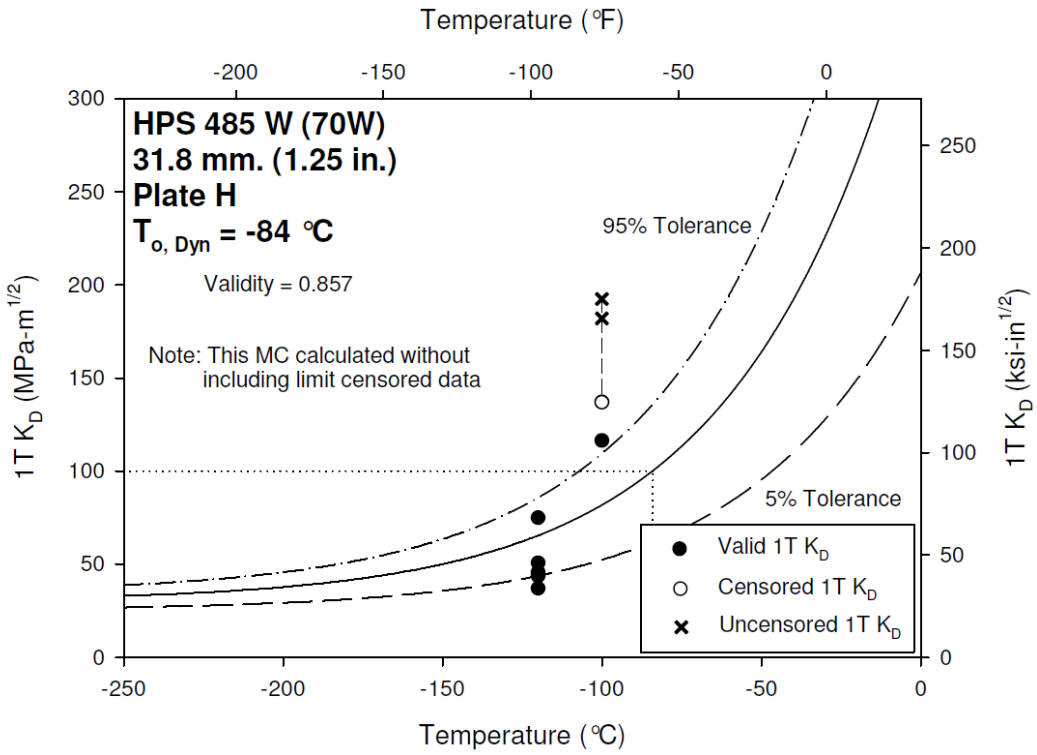

Figure 7-8. Dynamic Fracture Toughness Data and Alternate Master Curve for Plate H

The initial analysis of plate I dynamic fracture toughness data results in a provisional 1T dynamic reference temperature of -119 °C (-182 °F) with a weighted validity factor of 0.643. An alternate analysis of dynamic reference temperature without using limit censored data results in a $T_{o, Dyn}$ value of -69 °C (-92 °F), which visually appears to better represent the valid data than the previous analysis. In this alternate analysis, the weighted validity factor is only 0.286, however, due to the fact that two of the valid tests were performed at temperatures more than 50 °C from the calculated reference temperature. Once again, the dynamic reference temperature estimated from the static value appears to be unconservative, as it predicts a temperature of -135 °C (-211 °F). Plate I dynamic fracture toughness data and the two different master curve analyses are presented in Figure 7-9 and Figure 7-10.

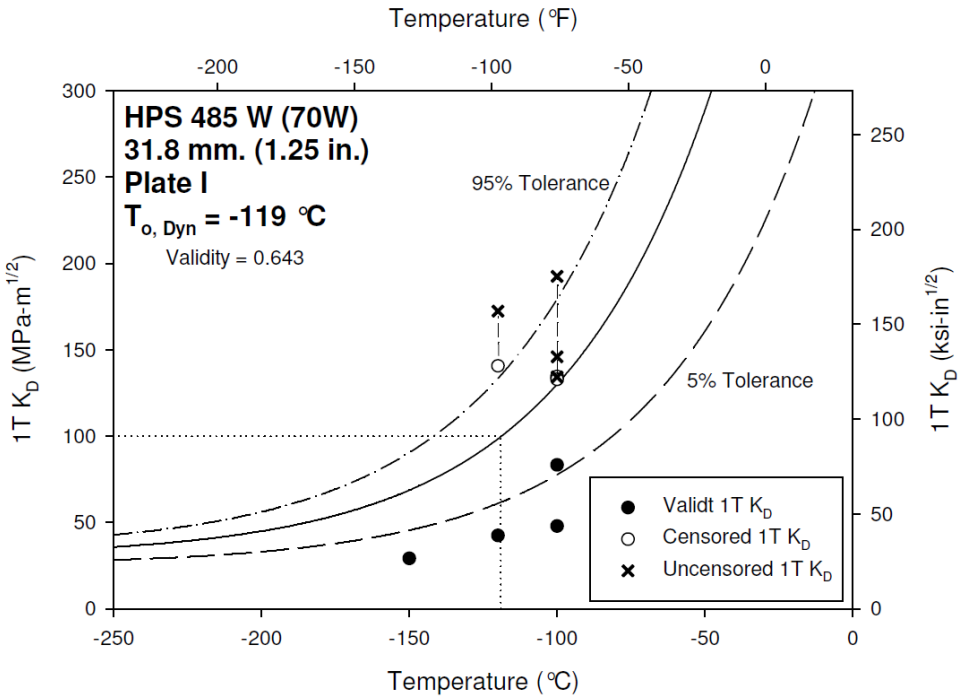

Figure 7-9. Dynamic Fracture Toughness Data and Master Curve for Plate I

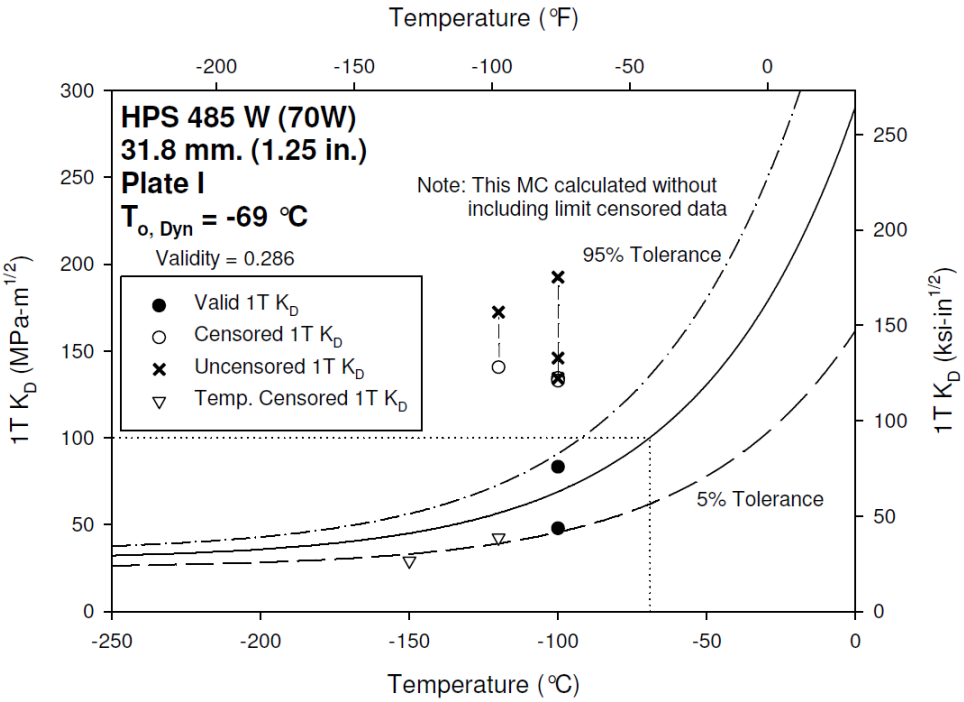

Figure 7-10. Dynamic Fracture Toughness Data and Alternate Master Curve for Plate I

Test specimens from HPS 485W (70W) plate J were tested dynamically over a range of temperatures between -70 and -100 °C (-94 and -148 °F). Fracture toughness values led to the determination of a 1T dynamic reference temperature equal to -61 °C (-78 °F) with a weighted validity value of 1.196. As seen in Figure 7-11, this analysis seems to properly characterize dynamic fracture behavior, with the 5 and 95 per cent tolerance thresholds bounding the data. However, the dynamic reference temperature predicted from the static value of -134 °C (-209 °F) is once again unconservative, as it estimates a value of -97 °C (-143 °F).

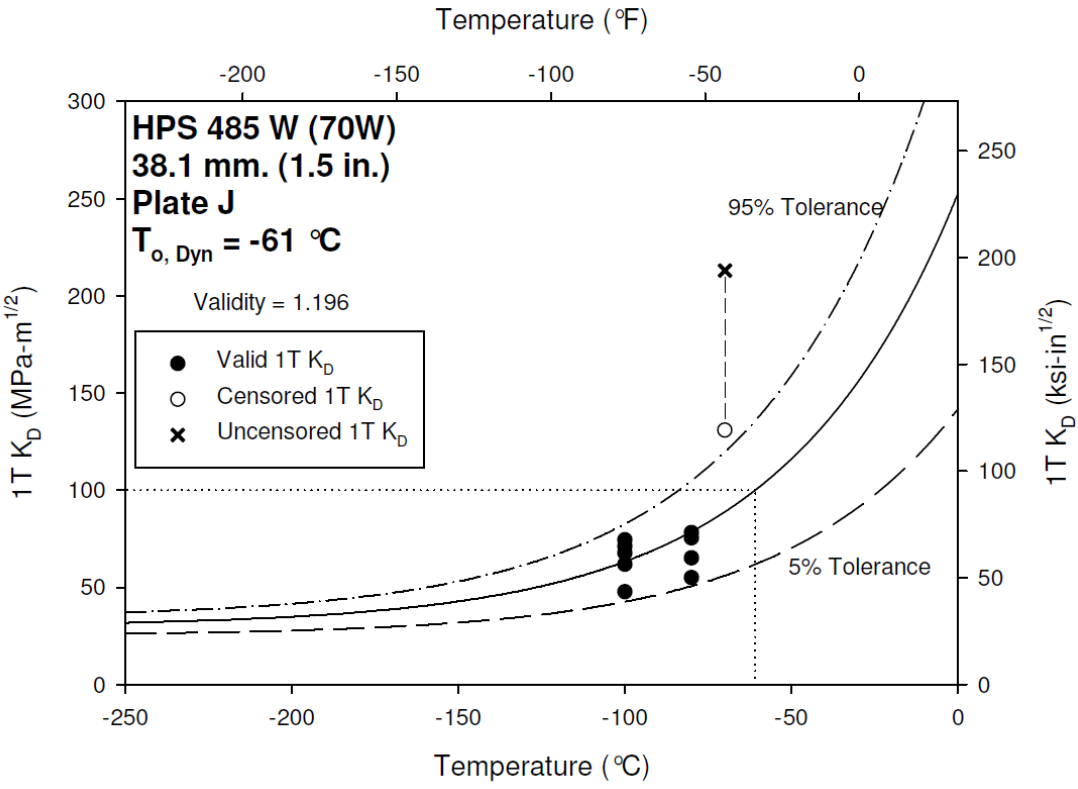

Figure 7-11. Dynamic Fracture Toughness Data and Master Curve for Plate J

7.1.3 Summary of HPS Dynamic Fracture Toughness

Determination of dynamic reference temperatures for HPS 485W (70W) proved to be difficult. Values of $T_{o, Dyn}$ were not nearly as consistent between plates of HPS 485W (70W) as was seen in the HPS 690W (100W) data. Dynamic 1T reference temperatures varied from -61 to -119 °C (-78 to -182 °F) for the five plates. Discrepancies even arose for data with valid reference temperature calculations, seemingly due to limit censored values. Additionally, the rate adjustment presented in Eq. 5.15 and Eq. 5.16 that seems to provide an adequate estimate for HPS 690W (100W) appears to predict unconservative dynamic reference temperatures for HPS 485W (70W). A summary of each static, dynamic, and predicted dynamic reference temperature is presented in Table 7-1. In this table, dynamic reference temperatures presented are those calculated excluding limit censored data, as discussed above. Also, no distinction is made between provisional and valid reference temperatures is made in Table 7-1.

Table 7-1. Summary of Calculated HPS Reference Temperatures

Letter Designation	Grade, ksi (Mpa)	T_o, °C (°F)	$T_{o, Dyn}$, °C (°F)	Predicted $T_{o, Dyn}$, °C (°F)
A	70 (485)	-171 (-276)	-113 (-171)	-132 (-206)
C	100 (690)	-80 (-112)	-51 (-60)	-58 (-72)
D	70 (485)	-181 (-294)	-81 (-114)	-144 (-227)
E	100 (690)	-102 (-152)	-54 (-65)	-78 (-108)
F	100 (690)	-95 (-139)	-57 (-71)	-72 (-97)
H	70 (485)	-161 (-258)	-84 (-119)	-123 (-189)
I	70 (485)	-173 (-279)	-69 (-92)	-135 (-211)
J	70 (485)	-134 (-209)	-61 (-78)	-97 (-143)

7.2 HPS Crack Arrest Toughness Data and Analysis

Crack arrest testing proved to be extremely difficult. A total of 55 crack arrest specimens were fabricated from plates D, E, and F. Of these, only 41 specimens fractured during testing, and only 10 of these produced valid crack arrest toughness, K_{Ia}, values. For the majority of specimens for which fracture initiation occurred, the specimen was unable to arrest the propagating crack, leaving only a small remaining ligament intact. Other specimens were able to stop crack propagation, but arrested crack lengths proved to be too long for validity purposes. Unlike invalid fracture initiation toughness, it is difficult to glean any information from invalid arrest tests. This is due to the large amounts of plasticity preceding the crack, reduced crack driving force, and reflective stress waves occurring in the fracturing specimen. The effects of these factors are not currently well understood. For this reason, only data meeting all ASTM E1221-12 validity criteria will be presented herein. All test records and fracture surface measurements have been recorded for specimens exhibiting crack arrest behavior, and are presented in Appendix H. Tabulated specimen information for valid tests can be found in Appendix I. Specimen information for invalid test specimens exhibiting some amount of arrest toughness can also be found in Appendix I.

For the two plates of HPS 690W (100W), only five crack arrest tests proved to be valid. Plate E produced valid tests at test temperatures of -35 and -50 °C (-31 and -58 °F), while plate F produced two valid tests at -35 °C (-31 °F) and one at -20 °C (-4 °F). Plates E and F produced provisional crack arrest reference temperatures, T_{KIaQ}, of -7 and -1 °C (19 and 30 °F), respectively. Clearly neither of these data sets produced a validity weighting factor greater than one. Crack arrest data, along with the provisional master curves, can be seen in Figure 7-12 and

Figure 7-13. Unlike tolerance bounds for initiation toughness, which are statistically based off of the master curve itself due to flaw distribution probability, crack arrest tolerance bounds are determined by the scatter of test data. For this reason, and the lack of valid tests, tolerance bounds are not provided for the crack arrest master curves.

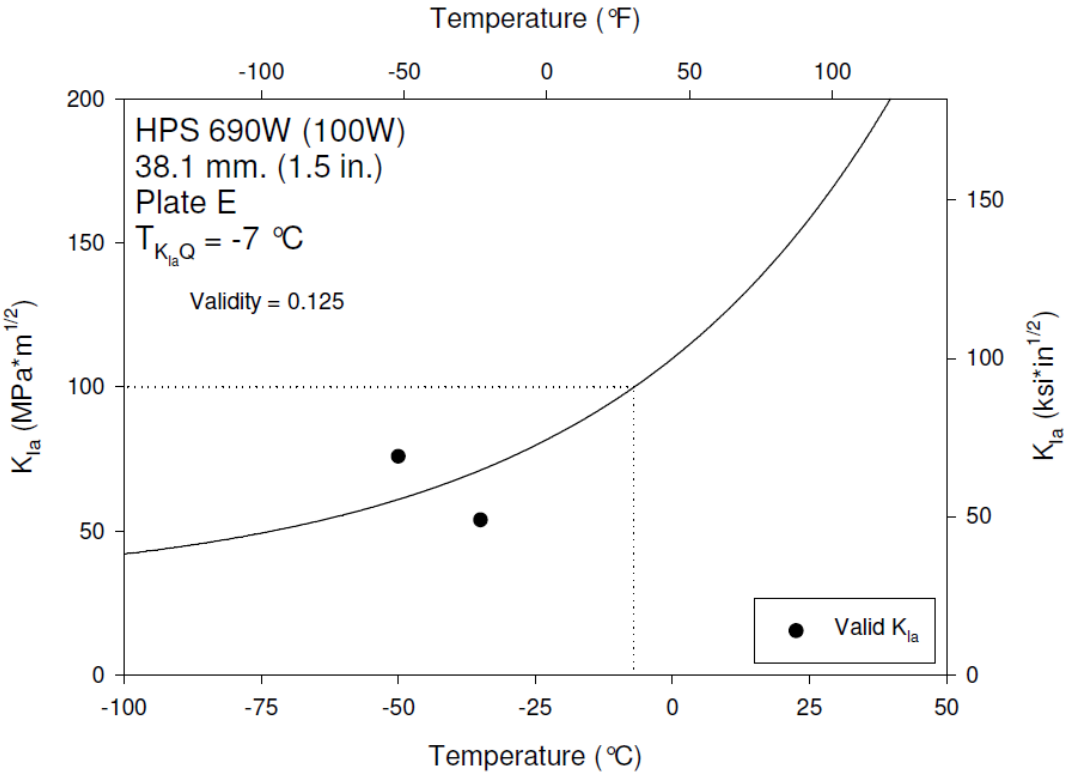

Figure 7-12. Crack Arrest Toughness Data and Master Curve for Plate E

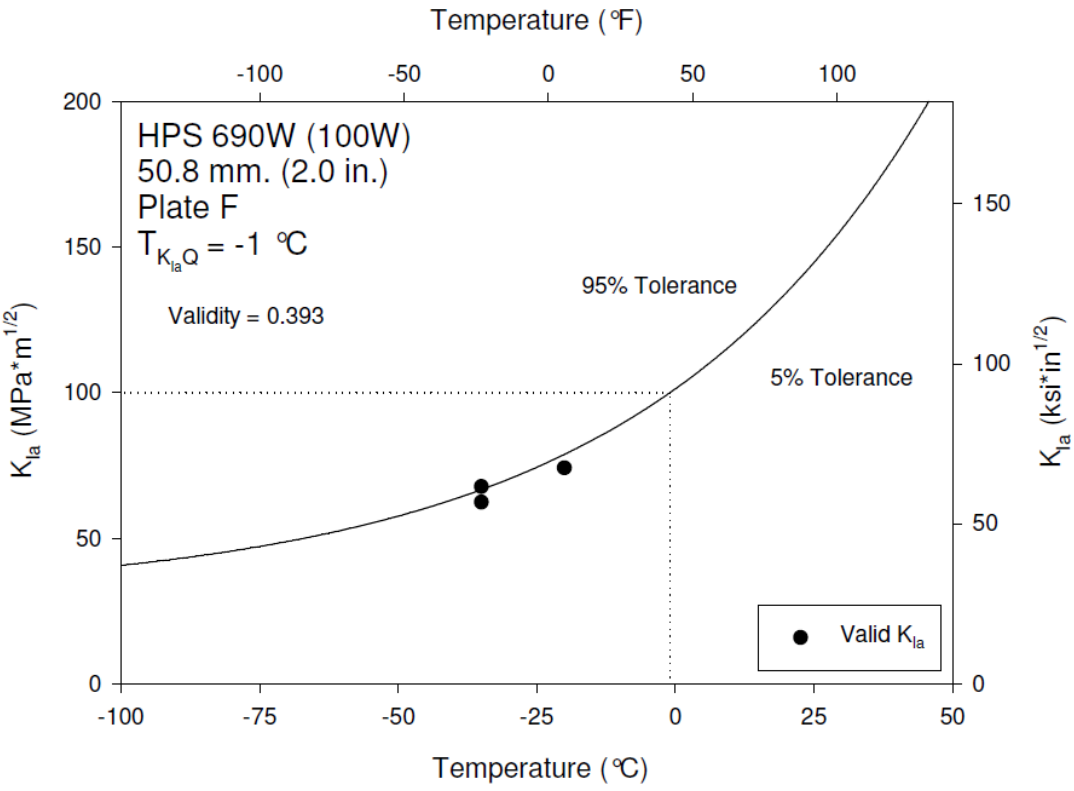

Figure 7-13. Crack Arrest Toughness Data and Master Curve for Plate F

HPS 485W (70W) plate D produced five valid crack arrest test values. Two valid tests were performed at a test temperature of -50 °C (-58 °F), while the other three valid tests were performed at -35 °C (-31 °F). These five valid crack arrest tests resulted in a provisional crack arrest reference temperature of -2 °C (28 °F), with a validity factor of 0.557. Plate D crack arrest toughness data and corresponding master curve are presented in Figure 7-14.

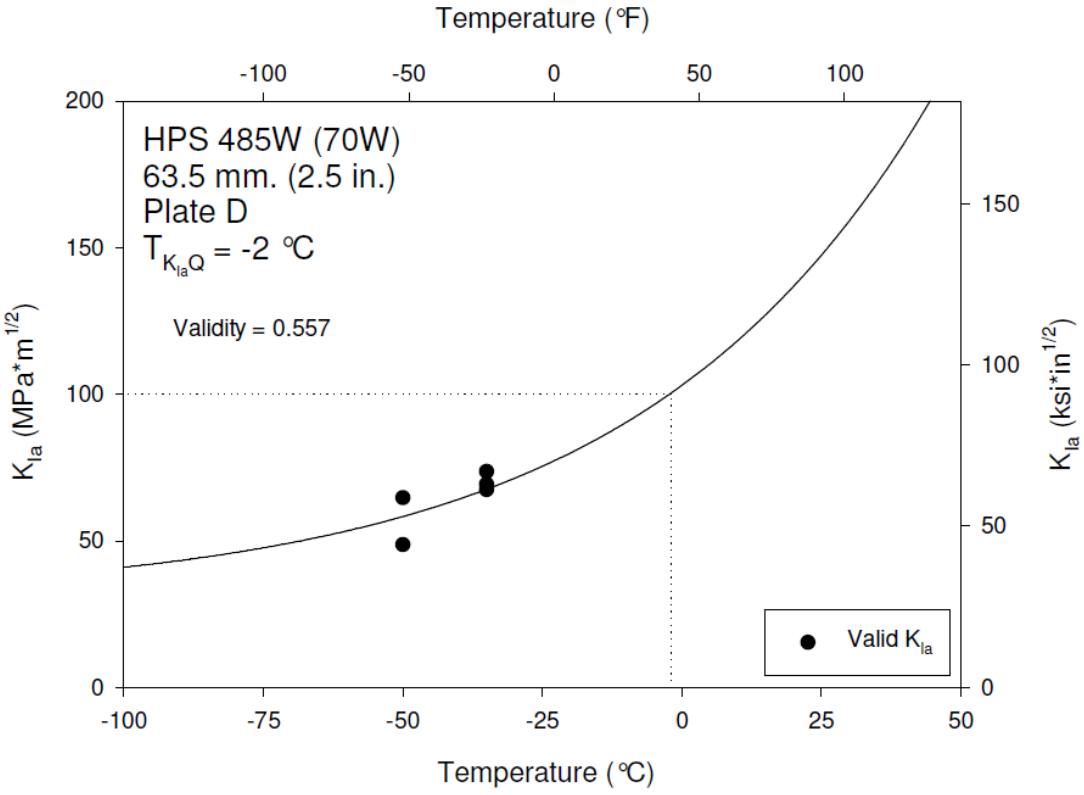

Figure 7-14. Crack Arrest Toughness Data and Master Curve for Plate D

7.2.1 Summary of HPS Crack Arrest Toughness

Crack arrest testing proved to be extremely difficult, and very few valid test results were obtained. Of 55 crack arrest specimens fabricated of the three heats of HPS, only 10 produced valid crack arrest toughness values. Because of this, it was not possible to calculate valid crack arrest reference temperatures. An estimate of crack arrest reference temperature was made for each of the three plates examined, and results are summarized in Table 7-2. For comparison, static and dynamic reference temperatures are also included. No distinction between valid and provisional reference temperatures is made in Table 7-2.

Table 7-2. Summary of HPS Crack Arrest Reference Temperatures

Letter Designation	Grade, ksi (Mpa)	T_o, °C (°F)	$T_{o, Dyn}$, °C (°F)	T_{KIa}, °C (°F)
D	70 (485)	-181 (-294)	-81 (-114)	-2 (28)
E	100 (690)	-102 (-152)	-54 (-65)	-7 (19)
F	100 (690)	-95 (-139)	-57 (-71)	-1 (30)

Chapter 8: Conventional Bridge Steel Data and Analysis

As presented in Chapters 4 and 5, a large database of historic bridge fracture data was compiled and analyzed in terms of modern elastic-plastic fracture mechanics. Each data set was evaluated using the master curve methodology, and either valid or provisional reference temperatures were determined for each. Due to limited space within the format of a journal manuscript, it was not possible to individually present all of the data examined. For this reason, data from the compiled database can be found in appendices. Appendix J contains plots of all legacy CVN data, while master curve plots of each data set can be found in Appendix K. Evaluation plots for each CVN-T_o correlation method are found in Appendix L.

In addition to the compilation of legacy data, fracture toughness testing was performed on five plates of conventional bridge steels from various sources. Most of these plates are at or below the minimum strength levels for which the master curve methodology is considered to be applicable. Details of the plates, as well as specimen layout and orientation, can be found in Chapter 3. Unfortunately, an error in an analysis spreadsheet miscalculated the master curve limit ensuring specimen constraint. Explained in Chapter 4, and presented in Eq. 4.5, the limit ensuring adequate constraint for each of the five conventional steel plates is significantly lower than the limit for HPS plates due to lower yield strengths. This error originally estimated the limit to be higher than it truly is for the conventional steels. Although the error was discovered during analysis, testing was complete at this point, and numerous specimens violated the limit. Censored values, although used in reference temperature determination, do not count towards the validity of the master curve. If the error had been discovered during testing, more tests would

have been performed at lower temperatures in an attempt to stay below the toughness limit, possibly producing more valid tests.

Presented herein is the fracture data and corresponding analysis of the five conventional bridge steel plates. Individual test records for each specimen, as well as images of scaled fractures surfaces, can be seen in Appendix M. Tabulated fracture toughness data for each specimen is found in Appendix N. Additionally, resistance curve plots were developed for a few plates of conventional steel. Similar to the resistance curves produced for HPS grades clip gage capacity limited the amount of crack growth measurable during testing. Plots of resistance curves for conventional steel can be found in Appendix O.

8.1 Fracture Toughness of Conventional Bridge Steel

Test specimens machined from Purdue University's Railroad Flat Car project, plate R, were tested over a temperature range from -150 to -195 °C (-238 to -319 °F). Using only test data from specimens sampled at one-quarter thickness in the L-T orientation, a 1T reference temperature of -192 °C (-314 °F) was determined. Due to multiple data points exceeding the provided limit, the weighting validity value for the analysis of this plate is only 0.5. Fracture toughness data for plate R along with the corresponding master curve and 5 and 95 per cent tolerance bounds is presented in Figure 8-1. Data from specimens sampled at mid-plate thickness which are designated as 1/2T, although presented in this plot, were not used in this master curve analysis.

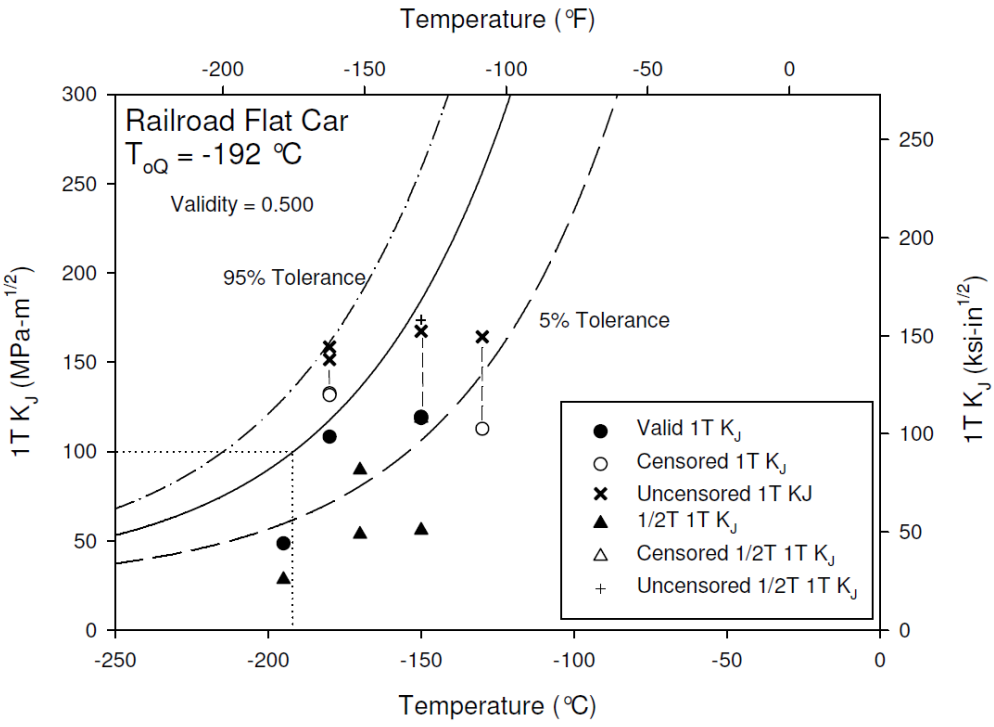

Figure 8-1. Fracture Toughness Data and Master Curve for Plate R

In an attempt to better characterize plate R with a non-provisional reference temperature, another master curve analysis was performed using all fracture toughness data. This analysis included the specimens sampled from one-quarter thickness as well as those from mid-thickness. Including mid-thickness specimens caused a positive shift in the reference temperature, and also added to the validity weighting value. The reference temperature for this alternate analysis of plate R is -180 °C (-292 °F), with a validity value of 1.119. The fracture toughness data of plate R is presented with the alternate master curve and tolerance bounds in Figure 8-2.

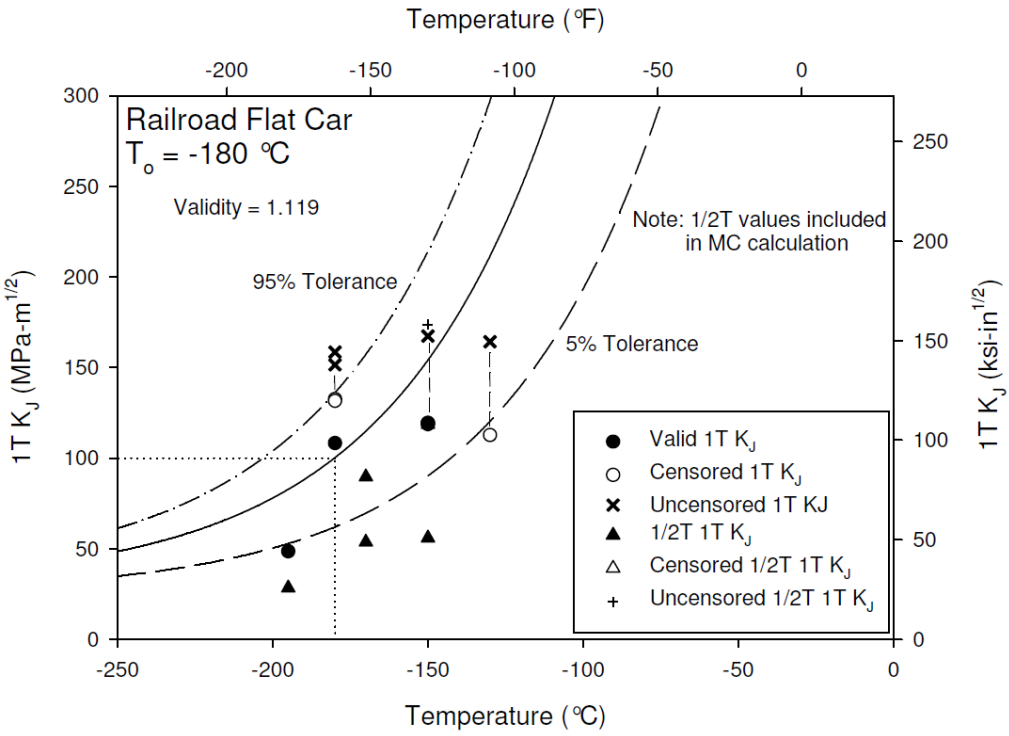

Figure 8-2. Fracture Toughness Data and Alternate Master Curve for Plate R

Fracture toughness of specimens machined from samples of the Diefenbaker bridge, plate B, were tested over a range of temperatures from -120 to -150 °C (-184 to -238 °F). Calculation of a reference temperature for this data set, including only data from specimens sampled at one-quarter plate thickness, produced a value of -150 °C (-238 °F) with a weighting factor of 0.83. This fracture toughness data with resulting master curve and tolerance bounds are presented in Figure 8-3. Present in this plot is invalid data. As described in Chapter 6, this is due to the failure of the compliance equation to properly calculate the true initial fatigue crack length as measured optically following specimen heat tinting. Invalid data was not included in reference temperature calculation, and is only included in data plots for comparison purposes.

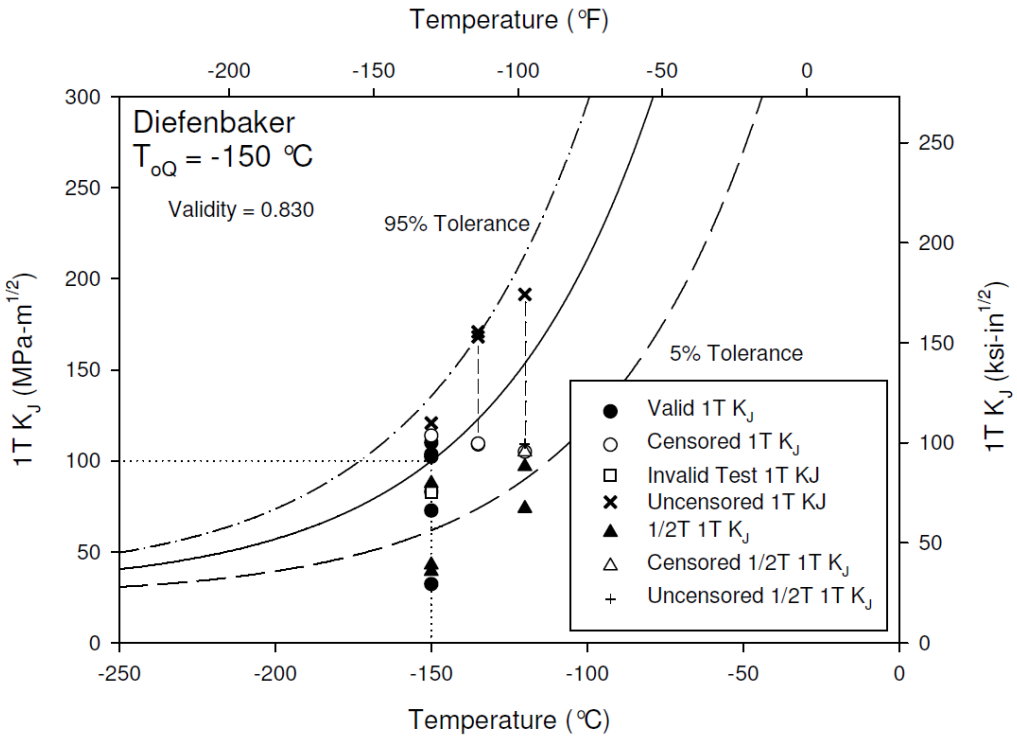

Figure 8-3. Fracture Toughness Data and Master Curve for Plate B

Similar to the analysis performed for plate R, an alternate calculation of reference temperature for plate B was performed including data sampled at plate mid-thickness. Again, this alternate analysis caused a positive shift in calculated reference temperature and an increase in the weighting validity value. The reference temperature determined in the master curve analysis of plate B is -141 °C (-222 °F), and the weighting factor is 1.667, indicating a valid master curve. Fracture toughness data for plate B along with the alternate master curve and corresponding 5 and 95 per cent tolerance bounds can be found in Figure 8-4.

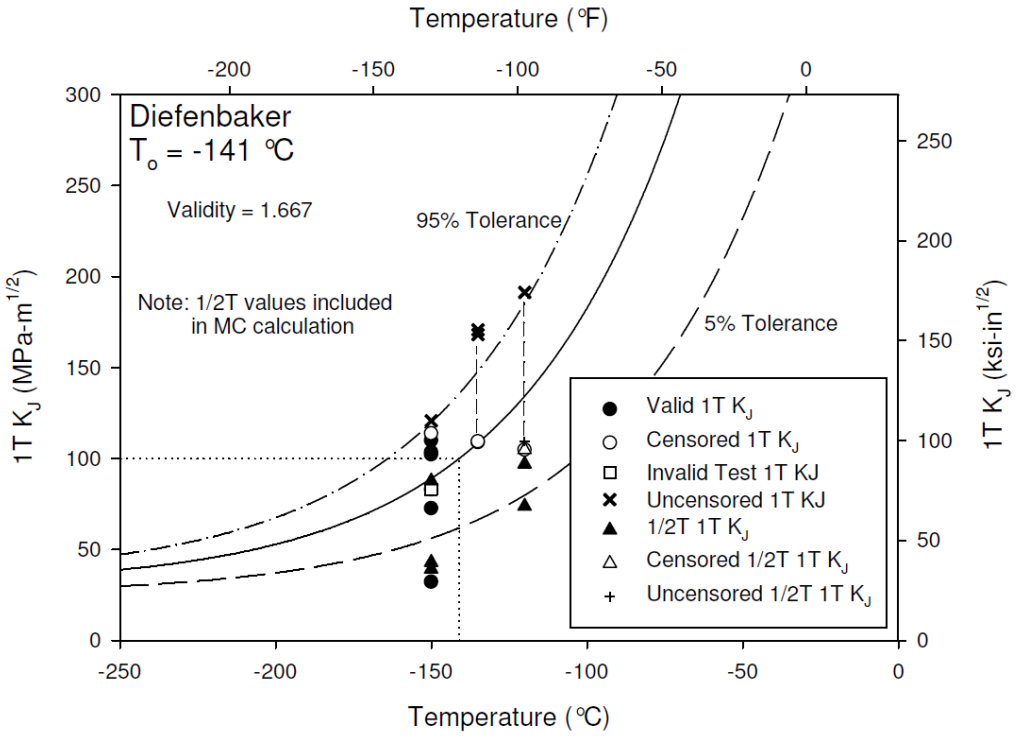

Figure 8-4. Fracture Toughness Data and Alternate Master Curve for Plate B

Fracture toughness testing of SE(B) specimens from the Route 422 bridge, designated as plate 4, resulted in only one toughness value below the master curve limit. All other values exceeded the limit and were censored for master curve calculations. Analysis of all specimens sampled at one-quarter plate thickness resulted in a provisional reference temperature of -87 °C (-125 °F) and a weighted validity factor of only 0.167. Unlike the previous two plates, specimens sampled from mid-thickness also produced fracture toughness values exceeding the low toughness limit. For this reason, these values were not used in an alternate reference temperature calculation as it would not have increased the validity of the analysis. Plate 4 fracture toughness data and corresponding provisional master curve can be seen in Figure 8-5.

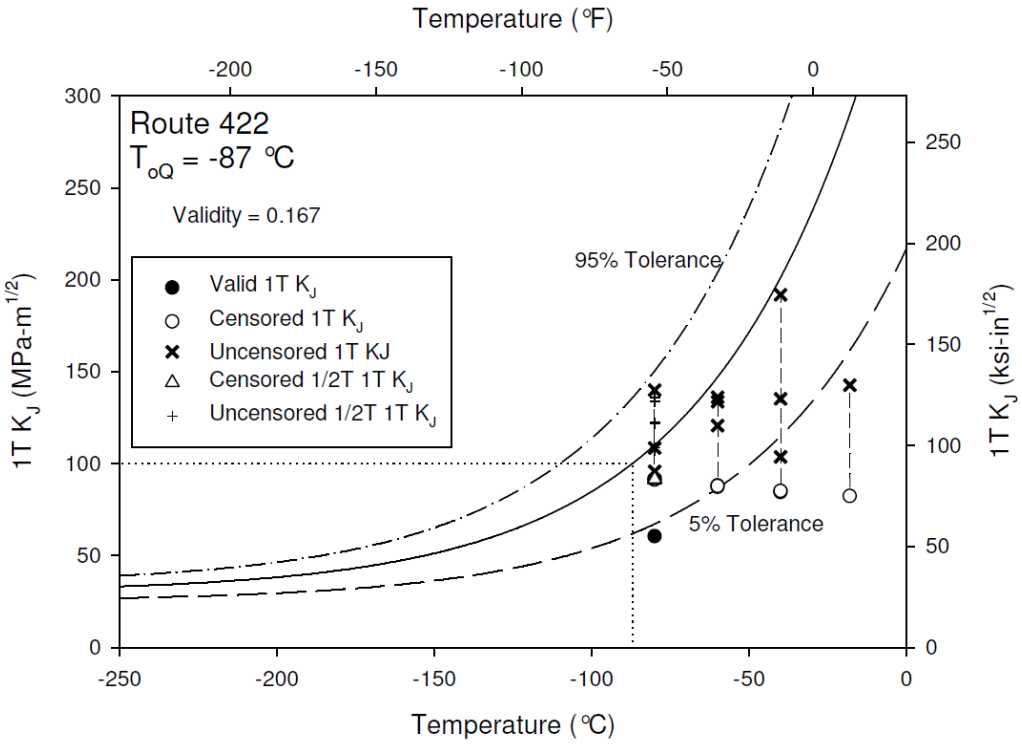

Figure 8-5. Fracture Toughness Data and Master Curve for Plate 4

Like tests performed on specimens from plate 4, fracture toughness testing of plate from the Pueblo bridge, designated as P, only yielded a single value not exceeding the master curve constraint limit. Analysis of fracture toughness data from plate P produced a provisional reference temperature of -96 °C (-141 °F) and a weighting factor of 0.167. Again, no specimens sampled from plate mid-thickness produced fracture toughness values less than the toughness limit, so no alternate analysis was performed with this data set. Plate P fracture toughness and associated master curve is presented in Figure 8-6.

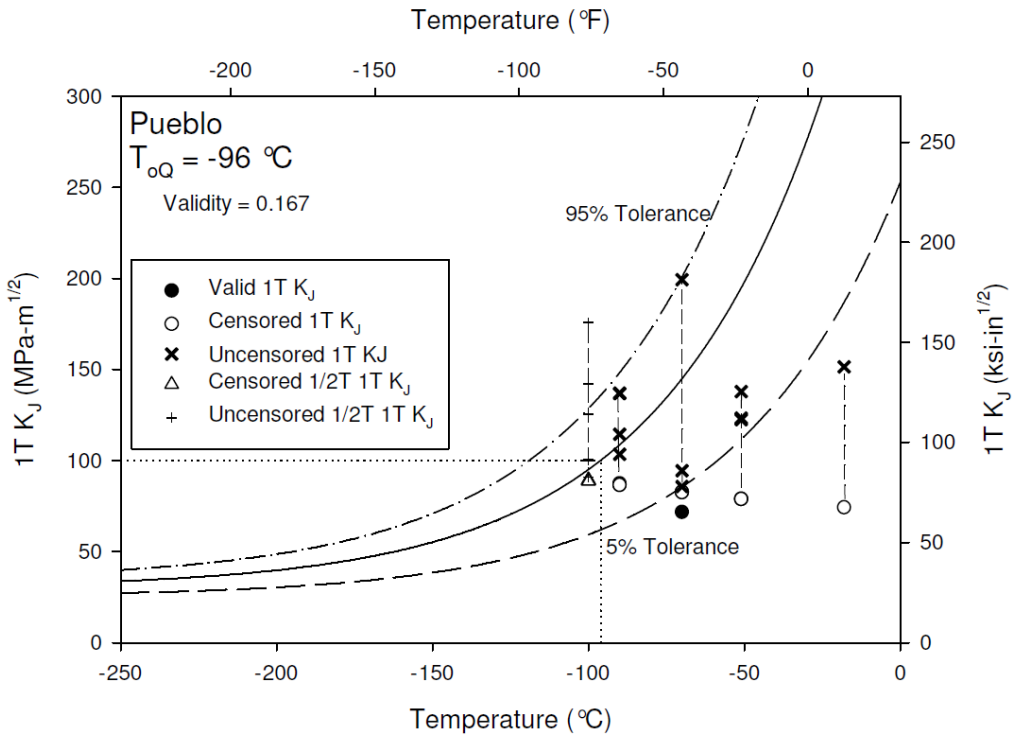

Figure 8-6. Fracture Toughness Data and Master Curve for Plate P

Fracture toughness tests were performed on specimens sampled from plate of the old Milton Madison bridge, designated plate M, at temperatures between -80 and -130 °C (-112 and 202 °F). Because the thickness of plate M was only 12.7 mm. (0.5 in.), all specimens were sampled from mid-thickness. Unfortunately only three valid tests fell below the toughness limit, producing a weighted validity factor of 0.429 and a provisional reference temperature of -100 °C (-148 °F). The plate M provisional master curve and corresponding tolerance bounds, along with fracture toughness test results, can be found in Figure 8-7

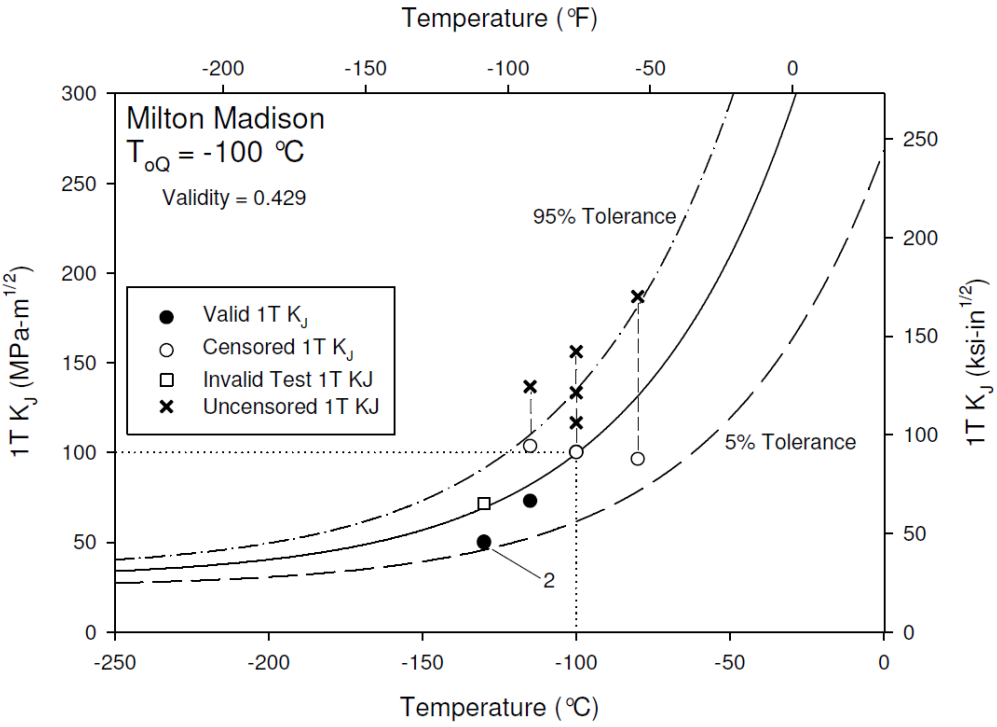

Figure 8-7. Fracture Toughness Data and Master Curve for Plate M

8.2 Summary of Conventional Bridge Steel Testing

Although mistakes were made in the testing of these plates, information can still be gleaned from the results. Having provisional and valid reference temperatures for these five plates of conventional bridge steel allows for more refined analysis of large scale tests performed on these materials. Estimations of tolerable flaw sizes, similar to those made in Chapter 6, can be made and compared with behavior observed in large scale laboratory and field testing.

Clearly low strength steels present challenges in terms of fracture toughness testing using Charpy-sized SE(B) specimens. Awareness of limits controlling constraint should improve validity of reference temperature determinations in the future. Although promising due to the limited amount of material needed to characterize a given plate, more work still needs to be done

to verify that SE(B) specimens of this size can be used for evaluation of in-service structures whose material may be of low strength.

Chapter 9: Conclusions and Recommendations

Many advances have taken place in the four decades since the inception of AASHTO's original fracture control plan. Specifically, steel production and fabrication have made high performance materials much more economically feasible for the bridge industry. Also, advances in the understanding of elastic-plastic fracture mechanics have made possible the characterization of materials with high toughness and ductility, including structural steel. Consequently, this research has focused on the fracture behavior characterization of modern HPS grade steels and on the re-analysis and characterization of historic US bridge fracture in terms of modern elastic-plastic fracture mechanics methods. Original contribution to the field of civil engineering is provided through the development of the HPS fracture toughness database. Additionally, application of the master curve methodology in the characterization of bridge fracture data, both new and historic, is another important original contribution of this work.

This chapter provides a summary of the work presented throughout this document. The first section of this chapter summarizes the testing and analysis performed in the previous chapters and provides an overview of the main conclusions. The second section of this chapter presents recommendations for future work.

9.1 Summary and Conclusions

Chapter 4 introduced a compiled database comprised of over 800 US bridge steel fracture toughness tests. Plasticity corrections were applied to each test, allowing for an estimation of each material's elastic-plastic fracture toughness. The re-analysis of this data is extremely important as the majority of the database was developed prior to the establishment and

refinement of elastic-plastic fracture test methods. Re-analyzed data sets were then evaluated using the master curve methodology, characterizing fracture behavior in the ductile to brittle transition region, including the statistical description of data scatter. Although the tolerance bounds do not exactly bound the fracture behavior of the database, results indicate that cleavage is a statistically based event that can be modeled using known probabilistic methods. This statistical characterization of fracture behavior allows for the possibility of performance based fracture design for highway bridges.

In Chapter 5, the legacy database compiled in Chapter 4 was used to evaluate twenty nine permutations of Charpy V-Notch to reference temperature correlation methods. This evaluation revealed that the Barsom and Rolfe Two Stage correlation method, currently employed in the AASHTO material toughness specification, can unconservatively predict intermediate and static rate toughness. Other correlation methods, although not acceptable as exact predictors of reference temperature, provide quantifiable levels of conservatism in the estimation of fracture toughness. It was shown that method J.2.2 of BS 7910 (Eq. 5.5) provides an adequate estimate of reference temperature, and thus fracture toughness. This method is recommended based on its use and performance in this study. Used in conjunction with the statistically based tolerance bounds of the master curve as presented in Chapter 4, this CVN-T_o correlation allows for the setting of CVN impact values that can be tied to fracture mechanics toughness parameters, and thus to statistically based prediction of fracture behavior. This represents the possibility for advancement in the management of fracture in highway bridges, allowing for the treatment of fracture in a manner consistent with other design limit states.

Chapter 6 presented static fracture toughness data for eight plates ofA709 HPS 690W (100W) and HPS 485W (70W), each characterized using the master curve methodology. Tolerance bounds of the master curve were used to predict acceptable flaw sizes for various geometry and loading configurations in a modeled bridge girder tension flange. In addition, correlation methods presented in Chapter 5 were used to estimate reference temperatures for the CVN values currently found in the material toughness specification. This allowed for a comparison between tolerable flaw sizes based on fracture toughness data and those based on correlations from the current minimum toughness standards.

Results of CVN testing indicate that HPS is currently being produced at toughness levels much greater than currently mandated. Flaw tolerance examination showed that HPS 690W (100W) can tolerate cracks three times larger than what is currently allowed based on material toughness specifications, while HPS 485W (70W) can tolerate cracks up to twenty times larger than what is currently acceptable as per material toughness specification. In certain flaw configurations, HPS 485W (70W) displayed adequate toughness to have only a one per cent probability of cleavage fracture prior to crack growth reaching the point of net section yielding. Based on the results of this study it is clear that material toughness specifications should be updated in order to take advantage of the superior toughness exhibited by A709 HPS grade steels.

Chapters 7 and 8 presented additional fracture toughness data obtained as part of this study. In Chapter 7, additional fracture toughness data obtained on eight plates of A709 HPS 690W (100W) and HPS 485W (70W) was presented. This included dynamic fracture testing and characterization on the same eight plates examined in Chapter 6, and crack arrest toughness

testing of three of the plates. Static fracture toughness data for five different conventional bridge steels was presented in Chapter 8. For each data set, the master curve methodology was applied to characterize material toughness with respect to temperature. Dynamic HPS toughness data was also analyzed with rate adjustment equations to compare with static data. It was shown that rate adjustment estimates work well for HPS 690W (100W), but for HPS 485W (70W) the rate adjustments can predict unconservative estimates of dynamic toughness. Obtaining valid crack arrest data proved to be very difficult. Out of 55 total specimens tested, only 10 resulted in valid data. This lack of valid test results makes drawing conclusions very problematic.

Data collected on the five different conventional bridge steels can be used in conjunction with the additional testing being performed at Purdue University. Difficulty was had in obtaining valid reference temperatures for these plates, in part due to the materials' low yield strengths. Use of Charpy-sized SE(B) specimens in evaluation of in-service structures is promising due to the small amount of material needed. However, more evaluation is needed to know whether or not this specimen size is capable of reliably characterizing fracture behavior of low strength steels.

9.2 Recommendations for Future Work

A large amount of testing and data analysis was performed as part of this study. However, no single study is capable of answering all questions related to a given topic, and typically solving one problem may lead to even more questions. For this reason, all studies have limitations and require further exploration, and this research is no different. The following are some identified limitations of this work, and recommendations for further study.

- Currently there is no quantifiable rationale for setting flaw tolerance sizes in steel bridge girders. Work is currently being performed at Purdue University to quantify bridge inspectors' abilities to identify flaws of various sizes and geometries. This information is needed before realistic flaw tolerance values can be selected for material toughness specifications.

- Although this work represents a large increase in the HPS fracture toughness database, it is still a relatively small study. Analysis of many more heats of HPS is needed for a statistically significant review of material toughness specifications to be made.

- This work only included the testing and evaluation of HPS 485W (70W) and HPS 690W (100W). The fracture toughness HPS 345W (50W) was not evaluated as part of this study. Because it is very commonly used in the bridge industry, fracture toughness evaluation of HPS 345W (50W) is needed.

- True stress intensity rates occurring in highway bridges are not currently known. Current specifications are based on an intermediate loading rate, but this evaluation is out of step with modern fracture mechanics knowledge. Before new fracture toughness specifications can be made it is necessary to know the true stress intensity rates that need to be accounted for. It is recommended that a parametric study be performed with varying bridge geometries, girder shapes, flaw sizes and locations, and loading rates.

- Crack arrest testing produced very few valid results, making crack arrest toughness evaluation difficult. Testing procedures and analysis for crack arrest testing need to be evaluated and refined before it can become a viable test for bridge steel fracture behavior.

If testing procedures improve, making evaluation of crack arrest toughness more viable, it will be necessary to fully characterize the arrest behavior of HPS for use in bridge applications.

- Clearly there are difficulties in the fracture toughness evaluation of low strength steels. More work is needed to determine whether use of Charpy-sized SE(B) specimens can be used to characterize bridge steels of low strength.

References

Albrecht, Pedro and Wright, William. (2000). "Fatigue and Fracture of Steel Bridges." *Fracture Mechanics: Applications and Challenges*, ESIS Publication 26, M. Fuentes and M. Elices Eds., Elsevier Publisher, 211-234.

Alstadt, Steven A. (2008). "A deterministic damage tolerant design procedure for fracture critical members in steel bridges." PhD Dissertation, Purdue University, West Lafayette, IN.

Alstadt, S., Wright, W., and Connor, R. (2014). "Proposed Revisions to the Current Charpy V-Notch Requirements for Structural Steel Used in U.S. Bridges." *J. Bridge Eng.*, 19(1), 131-140.

American Association of State Highway and Transportation Officials/American Welding Society. (2010). *Bridge Welding Code*. AASHTO, Washington, D.C.

American Association of State Highway and Transportation Officials (AASHTO). (1978). *Guide Specifications for Fracture Critical Non-Redundant Steel Bridge Members*. AASHTO, Washington, D.C.

American Association of State Highway and Transportation Officials (AASHTO) (2008). *LRFD Bridge Design Specifications:* Third Edition. AASHTO. Washington, D.C.

American Association of State Highway and Transportation Officials (AASHTO) (2010). *Manual for Bridge Evaluation*. AASHTO. Washington, D.C.

American Society for Testing and Materials (ASTM). (2007), "Standard Test Methods for Notched Bar Impact Testing of Metallic Materials." E 23-07, West Conshohocken, Pa.

American Society for Testing and Materials (ASTM). (2013), "Standard Test Method for Determination of Reference Temperature, T_o, for Ferritic Steels in the Transition Range" E 1921-13, West Conshohocken, Pa.

American Society for Testing and Materials (ASTM). (2008), "Standard Test Method for Fracture Toughness" E 1820-08, West Conshohocken, Pa.

American Society for Testing and Materials (ASTM). (2008), "Standard Test Methods for Tension Testing of Metallic Materials" E 8-08, West Conshohocken, Pa.

American Society for Testing and Materials (ASTM). (2012), "Standard Test Method for Determining Plane-Strain Crack-Arrest Fracture Toughness, K_{Ia}, of Ferritic Steels" E 1221-12, West Conshohocken, Pa.

American Society for Testing and Materials (ASTM). (2007), "Standard Specification for Sampling Procedure for Impact Testing of Structural Steel." A673-07, West Conshohocken, Pa.

American Society for Testing and Materials (ASTM). (2013), "Standard Specification for Structural Steel for Bridges" A 709-13, West Conshohocken, Pa.

American Society for Testing and Materials (ASTM). (2013), "Standard Test Method for Measurement of Fatigue Crack Growth Rates" E 647-13, West Conshohocken, Pa.

Anderson, T.L. (1995). *Fracture Mechanics- Fundamentals and Applications*, 2nd Edition. CRC Press LLC, 2000 Corporate Blvd., N.W., Boca Raton, Florida 33431.

Barsom, J. M. (1975). "Development of the AASHTO Fracture-Toughness Requirements for Bridge Steels." *Eng. Fracture Mech.*, 7(3), 605-618.

Barsom, John. M. (1973). *Toughness Criteria for Structural Steels- Investigation of Toughness Criteria for Bridge Steels- AISI Project 168*. U.S. Steel Research Laboratory Report No. 97.018-001(5), Monroeville, PA.

Barsom, John. M. (1974). "The Development of AASHTO Fracture-Toughness Requirements for Bridge Steels." *U.S.- Japan Cooperative Science Seminar, Tohoku University, Sendai, Japan.*

Barsom, J. M. and Rolfe, S. T. (1970). "Correlations Between K_{Ic} and Charpy V-Notch Test Results in the Transition Temperature Range." *Impact Testing of Metals, ASTM STP 466*, 281-302.

Barsom, J. M. and Rolfe, S. T. (1987). *Fracture and Fatigue Control in Structures- Applications of Fracture Mechanics*, 2nd Edition. Prentice-Hall, Inc. A Division of Simon and Schuster, Englewood Cliffs, NJ.

Barsom, J. M., Sovak, J. F., and Novak, S. R. (1972). *AISI Project 168- Toughness Criteria for Structural Steels: Fracture Toughness of A572 Steels*. U.S. Steel Research Laboratory Report 97.021-002 (2), Monroeville, PA.

Biggs, W. D. (1958). "The Problem of Brittle Fracture." Murex Welding Processes Limited, Waltham Cross, Hertfordshire, England.

British Standards Institute (BSI), (2005). BS 7910:2005. "Guide to methods for assessing the acceptability of flaws in metallic structures." British Standards Institute, London.

Cherepanov, G. P. (1967). "The propagation of cracks in a continuous medium." *Journal of Applied Mathematics and Mechanics*, 31(3), 503-512.

Collins, W., Wright, W., Connor, R., Leon, R., and Sherman, R. (2014). "State of the Art Fracture Characterization Part I: Master Curve Analysis of Legacy Bridge Fracture Data." *J. Bridge Eng.*, submitted.

Collins, W., Wright, W., Connor, R., Leon, R., and Sherman, R. (2014). "State of the Art Fracture Characterization Part II: Examination of Correlations between Charpy V-Notch and the Master Curve Reference Temperature, T_o." *J. Bridge Eng.*, submitted.

Connor, R. J., Kaufmann, E. J., Fisher, J. W., and Wright, W. J. (2007). "Prevention and Mitigation Strategies to Address Recent Brittle Fractures in Steel Bridges." *Journal of Bridge Engineering*, 12(2), 164-173.

Cotterell, B. (2002). "The Past, Present, and Future of Fracture Mechanics." *Engineering Fracture Mechanics*, 69, 533-553.

Corten, H. T. and Sailors, R. H. (1971). "Relationship between Material Fracture Toughness Using Fracture Mechanics and Transition Temperature Tests," *T. & A.M. Report No. 346*, Heavy Section Steel Technology Program, Technical Report No. 15, University of Illinois, Urbana, IL.

Crosley, P. B. (1984). *Fort Duquesne Bridge: Fracture Analysis of Flange Cores*. FHWA-TS-84-210. Washington, D.C.

Degarmo, P. E., Black, J. T., Kohser, R. A. (2003). *Materials and Processes in Manufacturing*, 9th ed., John Wiley & Sons, Inc., Hoboken, NJ.

Dexter, R. J., Lu, L., and Fisher, J. W. (2004). "Application of High Performance Steel in New and Retrofit Structures." *Proceedings of the third Materials Engineering Conference*, San Diego, California, November 13, 1994, 336-343.

Dexter, R. J., Wright, W. J., and Fisher, J. W. (2004). "Fatigue and Fracture of Steel Girders." *Journal of Bridge Engineering*, 9(3), 278-286.

Dowling, Norman E. (1999). *Mechanical Behavior of Materials, Engineering Methods for Deformation, Fracture, and Fatigue*, 2nd Ed. Prentice-Hall, Inc. Upper Saddle River, New Jersey 07458.

Federal Highway Administration (1986). *Inspection of Fracture Critical Bridge Members-Supplement to the Bridge Inspector's Training Manual*. FHWA Report No FHWA-IP-86-26, Washington, D.C.

Federal Highway Administration (1996). *Recording and Coding Guide for the Structure Inventory and Appraisal of the Nation's Bridges*. FHWA Report No FHWA-PD-96-001, Washington, D.C.

Federal Highway Administration (2000). *Narrow-Gap Electroslag Welding for Bridges*. U.S. Department of Transportation, Federal Highway Administration Memorandum, March 20, 2000, Washington, D.C.

Fisher, J. W., Roberts, R., and Pense, A. W. (1977). ''Evaluation of fracture of Lafayette Street bridge.'' *Journal of the Structural Division, ASCE.* 103(7), 1339–1357.

Fisher, J. W. (1984). *Fatigue and fracture in steel bridges*, Wiley, New York.

Frank, K. H., and Galambos, C. F. (1972). ''Application of fracture mechanics to analysis of bridge failure.'' *Proeeding., Specialty Conference on Safety and Reliability of Metal Structures*, ASCE, New York.

Gao, X. and Dodds, R. H. (2005). "Loading Rate Effects on Parameters of the Weibull Stress Model for Ferritic Steels." *Eng. Fracture Mech.*, 72, 2416-2425.

Gao, X., Joyce, J. A., and Roe, C. (2008). "An Investigation of the Loading Rate Dependence of the Weibull Stress Parameters." *Eng. Fracture Mech.*, 75, 1451-1467.

Griffith, A. A. (1920). "The Phenomena of Rupture and Flow in Solids." *Philosophical Transactions*, A(221), 163-198.

Gross, J. H. and Stout, R. D. (1995). "Evaluation of a Production Heat of an Improved Cu-Ni 70W/100W Steel." ATLSS Reports, paper 11, Bethlehem, PA.

Gross, J. H. and Stout, R. D. (2001). "ATLSS Studies on Chemical Composition and Processing of High Performance Steels." ATLSS Reports, paper 207, Bethlehem, PA.

Gross, J. H., Stout, R. D., and Dawson, H. M. (1998). "Copper-Nickel High-Performance 70W/100W Bridge Steels - Part II." ATLSS Reports, paper 228, Bethlehem, PA.

Hamby, G., Clinton, G., Nimis, R., and Lwin, M. (2002). *High Performance Steel Designers' Guide*, Second Edition, April 2002. U.S. Department of Transportation, Federal Highway Administration, Western Resource Center. Washington, D.C.

Hartbower, Carl E. (1979). "Reliability of the AASHTO Temperature Shift in Material Toughness Testing." Structural Engineering Series No. 7, August 1979.

Hartbower, C. E. and Sunbury, R. D. (1975). *Variability of Fracture toughness in A514/517 Plate*. FHWA RD-78-110. Washington, D.C.

Irwin, G. R. (1948). "Fracture Dynamics." *Fracture of Metals, American Society for Metals*, Cleveland, OH., 147-166.

Irwin, G. R. (1957). "Analysis of Stresses and Strains near the End of a Crack Traversing a Plate." *Journal of Applied Mechanics*, 24, 361-364.

Irwin, G. R. (1960). "Plastic zone near a crack and fracture toughness." *Seventh Sagamore Ordnance Materials Research Conference*, Raquette Lake, NY, 63-78.

Irwin, G. R., and Roberts, R. (1972). *Fracture Toughness of Bridge Steels- Phase I Report*, Lehigh University, Bethlehem, PA.

Joyce, J. A., and Link, R. E. (2012). *Automated Software for Unloading Compliance Testing*. U.S. Naval Academy. Annapolis, MD.

Joyce, J. A., Link, R. E., Roe, C., and Sobotka, J. C. (2010). "Dynamic and Static Characterization of Compact Crack Arrest Tests of Navy and Nuclear Steels." *Engineering Fracture Mechanics*, 77, 337-347.

Kayser, C., Swanson, J., and Linzell, D. (2006). "Characterization of Material Properties of HPS-485W (70 W) TMCP for Bridge Girder Applications." *J. Bridge Eng.*, 11(1), 99-108.

Kendrick, C. B., Smith, R. D., and Crozier, W. F. (1980). *Fracture Toughness of Structural Grade Bridge Steels Part II*. FHWA/CA/TL-80/11. Washington, D.C.

Landes, J. D. and Shaffer, D. H. (1980). "Statistical Characterization of Fracture in the Transition Region." *Fracture Mechanics: Twelfth Conference, ASTM, STP 700,* American Society for Testing and Materials, 368-382.

Link, R. E., Joyce, J. A., and Roe, C. (2009). "Crack Arrest Testing of High Strength Structural Steels for Naval Applications." *Engineering Fracture Mechanics*, 76, 402-418.

Madison, R. B. (1969). "Application of Fracture Mechanics to Bridges." *Lehigh University Institute of Research, Fritz Engineering Laboratory Report No. 335.2,* Bethlehem, PA.

Madison, R. B., and Irwin, G. R. (1974). "Dynamic K_c Testing of Structural Steel." *J. of the Structural Division*, 100(ST7), 1331-1349.

Mahmoud, H. N., Connor, R. J., and Fisher, J. W. (2005). "Finite Element Investigation of the Fracture Potential of Highly Constrained Details in Steel Plate Members." *Computer-Aided Civil and Infrastructure Engineering*, 20, 383-392.

Marandet, B. and Sanz, G. (1977). "Evaluation of the Toughness of Thick Medium Strength Steels by LEFM and Correlations between KIc and CVN." *ASTM STP 631*, ASTM, West Conshohocken, PA, 72-95.

McCabe, D. E., Merkle, J. G., and Wallin, K. (2007). *An Introduction to the Development and Use of the Master Curve Method*. ASTM Stock Number: MNL52 ASTM International 100 Barr Harbor Drive PO Box C700 West Conshohocken, PA.

National Transportation Safety Board (1970). *Highway Accident Report NTSB Number: HAR-71/0*. Washington, D.C.

Orowan, E. (1948). "Fracture and Strength of Solids." *Reports on Progress in Physics*, 12, 185-232.

Rice, J. R. (1968). "A Path Independent Integral and the Approximate Analysis of Strain Concentration by Notches and Cracks." *Journal of Applied Mechanics*, 35, 379-386.

Ripling, E. J., Crosley, P. B., and Armstrong, R. W. (1990). *Brittle-Ductile Transition of Bridge Steels Volume I: Final Report*. FHWA-RD-90-008. Washington, D.C.

Ripling, E. J., Crosley, P. B., and Armstrong, R. W. (1991). *Brittle-Ductile Transition of Bridge Steels Volume II: Microstructural Aspects of the Ductile-Brittle (D-B) Transition*. FHWA-RD-90-009. Washington, D.C.

Roberts, R., Fisher, J. W. Irwin, G. R., K. D. Boyer, Hausammann, H., Krishna, G. V., Morf, V., and Stockbower, R. E. (1977). *Determination of Tolerable Flaw Sizes in Full Size Welded Bridge Details*. FHWA-RD-77-170. Washington, D.C.

Roberts, R., Irwin, G. R., Krishna, G. V., and Yen, B. T. (1974). *Fracture Toughness of Bridge Steels- Phase II Report.* FHWA-RD-74-59. Washington, D.C.

Roberts, R. and Krishna, G. V. (1977). *Fracture Behavior of A36 Bridge Steels*. FHWA-RD-77-156. Washington, D.C.

Roberts, R. and Newton, C. (1984). "Report on Small-Scale Test Correlations with K_{Ic} Data." *WRC Bulletin*, 299.

Rolfe, S. T. and Novak, S. R. (1970). "Slow-Bend K_{Ic} Testing of Medium-Strength High-Toughness Steels," *Review of Developments in Plane Strain Fracture Toughness Testing, ASTM STP 463*, ASTM, West Conshohocken, PA, 124-159.

Ryan, T. W., Mann, J. E., Chill, Z. M., and Ott, B. T. (2012). *Bridge Inspector's Reference Manual (BIRM)*, FHWA Publication No. FHWA NHI 12-049, Arlington, VA.

Sailors, R. H., and Corten, H. T. (1972). "Relationship Between Material Fracture toughness using fracture mechanics and transition temperature tests." *ASTM Special Technical Publication 514.*

Schilling, C. G., Klippstein, K. H., Barsom, J. M., Novak, S. R., and Blake, G. T. (1972). *Toughness Criteria for Structural Steels- Low-Temperature Tests of Simulated Bridge Members-AISI Project 168 (3)* U.S. Steel Research Laboratory Report No. 97.021-001 (3), Monroeville, PA.

Schwendeman, L.P., and Hedgren, A.W. (1978). "Bolted repair of fractured I-79 girder." *Journal of the Structural Division, ASCE,* 104(2), 134-143.

Shank, M. E. (1953). *Brittle Failure in Carbon Plate Steel Structures other than Ships*. National Research Council's Committee on Ship Structural Design. National Academy of Sciences, Washington, D.C.

Steel Market Development Institute. (2011). *Guide Specifications for Highway Bridge Fabrication with High Performance Steel,* Third Edition, April 2011. Washington, D.C.

Wallin, K. (1989). "A Simple Theoretical Charpy-V-K_{Ic} Correlation for Irradiation Embrittlement." *Innovative Approaches to Irradiation Damage and Fracture Analysis*, Marriott, D. L., Mager, T. R., and Bamford, W. H., ed., PVP, Vol. 170, The American Society of Mechanical Engineers, New York, NY.

Wallin, Kim. (1997). "Effect of Strain Rate on the Fracture Toughness Reference Temperature To for Ferritic Steels." *Recent Advances in Fracture, Proceedings of a Symposium held at the Annual Meeting of The Minerals, Metals, and Materials Society*. Orlando, FL. 171-183.

Wallin, Kim. (2011). *Fracture Toughness of Engineering Materials, Estimation and Application*. EMAS Publishing- a FESI Subsidiary, Birchwood Park, Warrington, UK.

Wallin, K. (1984). "The scatter in K_{Ic} Results." *Eng. Fracture Mechanics,* 19(6), 1085-1093.

Wallin, K., Nevasmaa, P., Laukkanen, A., and Planman, T. (2004). "Master Curve Analysis of inhomogeneous Ferritic Steels." *Engineering Fracture Mechanics,* 71, 2329-2346.

Wallin, K., Planman, T., Valo, M., and Rintamaa, R. (2001). "Applicability of miniature size bend specimens to determine the master curve reference temperature T_o." *Engineering Fracture Mechanics,* 68. 1265-1296.

Wells, A. A. (1961). "Unstable Crack Propagation in Metals: Cleavage and Fast Fracture." *Proceedings of the Crack Propagation Symposium,* 1(84). Cranfield, UK.

Wilson, A. D. (2002). "Development of an improved HPS-100W Steel for bridge applications." *Proceedings from Material Solutions Conference 2002,* Columbus, OH.

Wilson, A. D., Hamburg, E. G., Colvin, D. J., Thompson, S. W., and Krauss, G. (1988). "Properties and microstructures of copper precipitation aged plate steels." *ASM International,*, 259-275.

Wolff, A. K. and Martin, A. D. (1973). *The Determination of the Physical, Chemical, and Metallurgical Charateristics of Steels Furnished from Typical Highway Bridges*. FHWA-RD-74-4. Washington, D.C.

Wright, William J. (1997). "High-Performance Steel: Research to Practice." *Public Roads Magazine,* 60(4).

Wright, William J. (2002). "Fracture Toughness Requirements for Highway Bridges: Past and Future Trends." *Progress in Structural Engineering and Materials*, 4(1), 96-104.

Wright, William J. (2003). "Fracture Initiation and Resistance of I-Girders Fabricated from High Performance Steels." PhD Dissertation, Lehigh University, Bethlehem, PA.

Zhu, X., and Joyce, J. (2012). "Review of Fracture Toughness (G, K, J, CTOD, CTOA) Testing and Standardization." *Engineering Fracture Mechanics,* 85, 1-46.

APPENDIX A: HPS Tensile Testing Plots

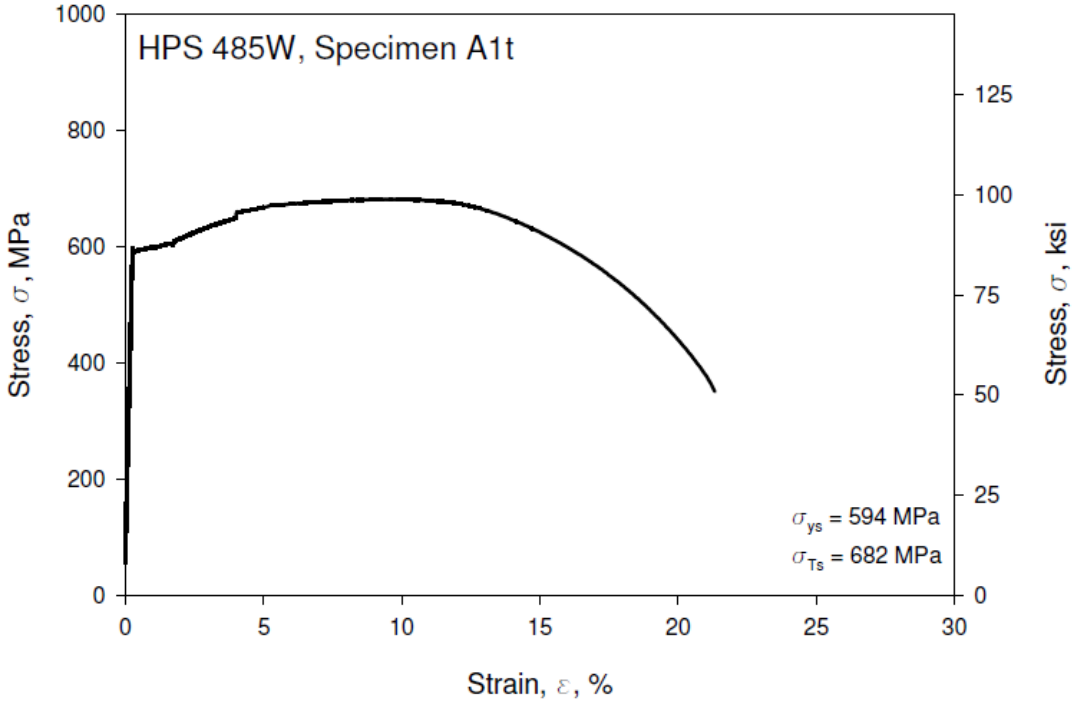

Figure A-1, Tension Test Data, Specimen A1t, HPS 485W, 25.4 mm.

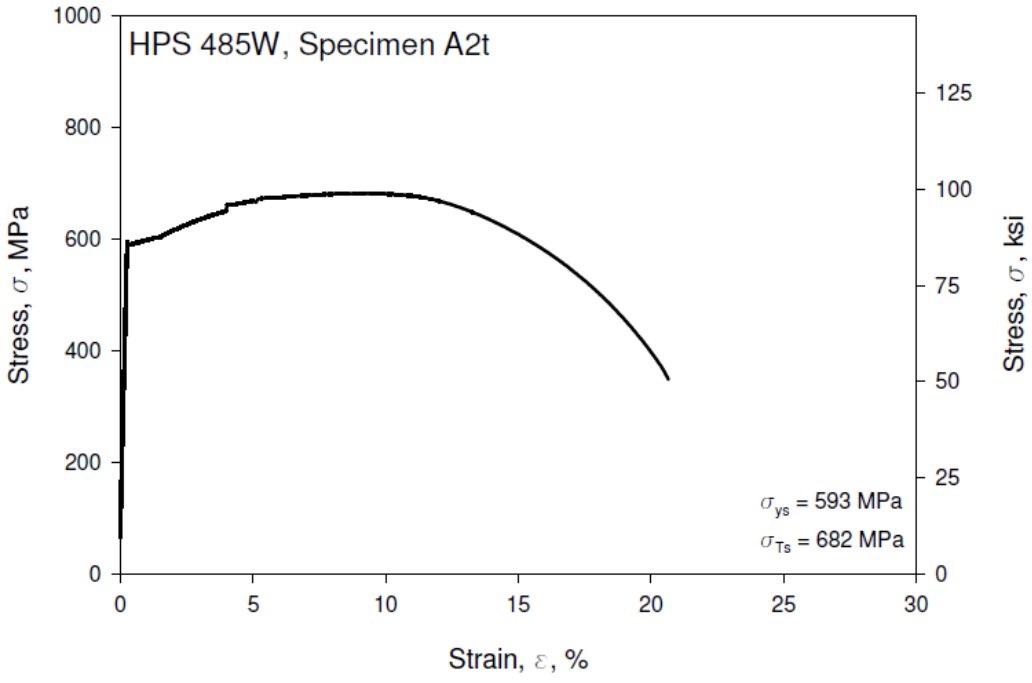

Figure A-2. Tension Test Data, Specimen A2t, HPS 485W, 25.4 mm.

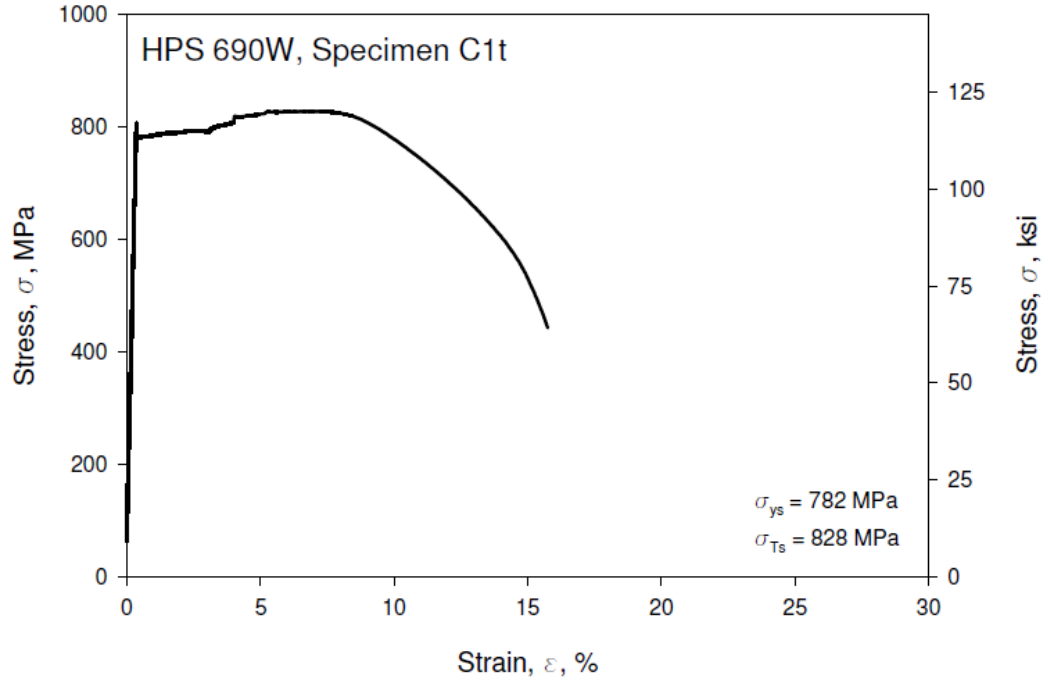

Figure A-3. Tension Test Data for Specimen C1t, HPS 690W, 19 mm.

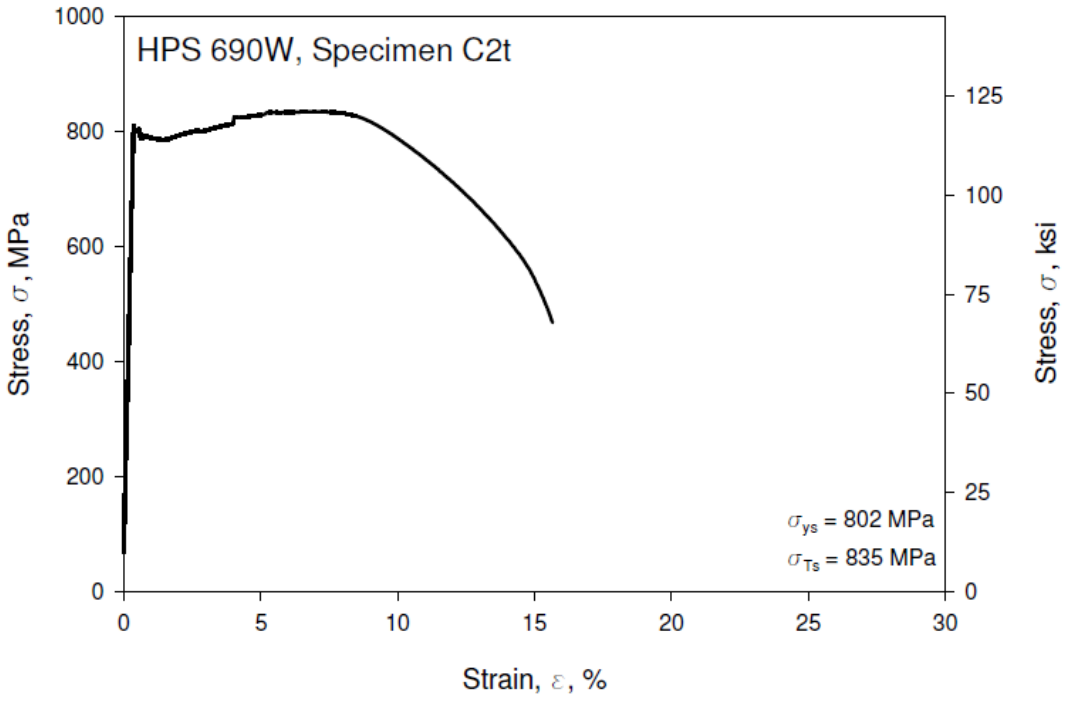

Figure A-4. Tension Test Data for Specimen C2t, HPS 690W, 19 mm.

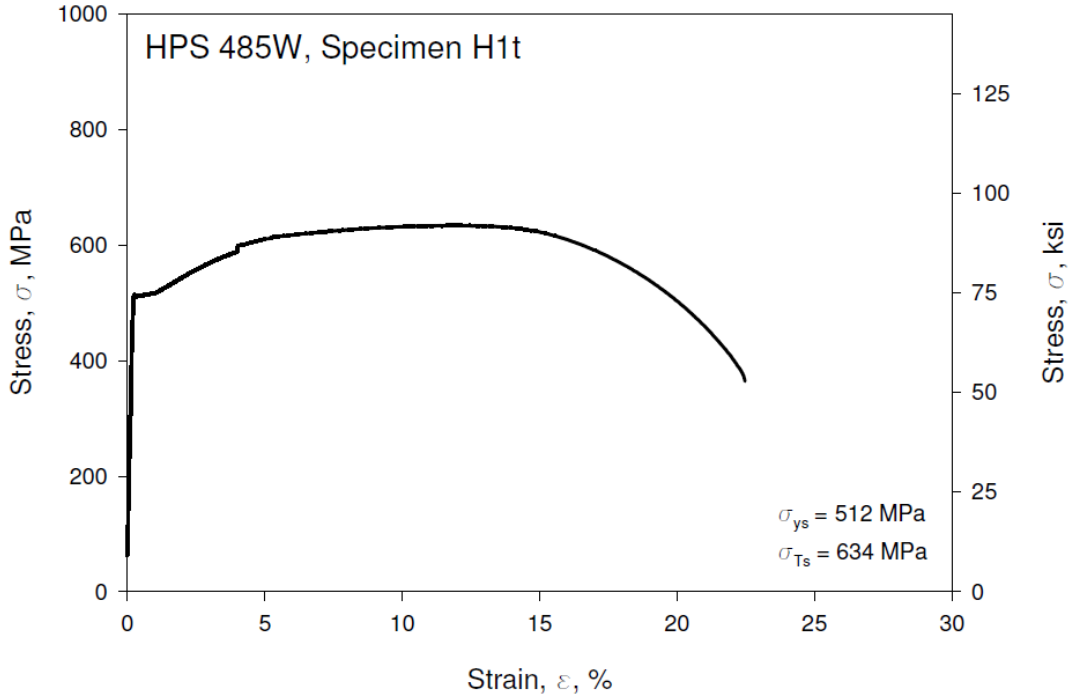

Figure A-5. Tension Test Data for Specimen H1t, HPS 485W, 31.8 mm.

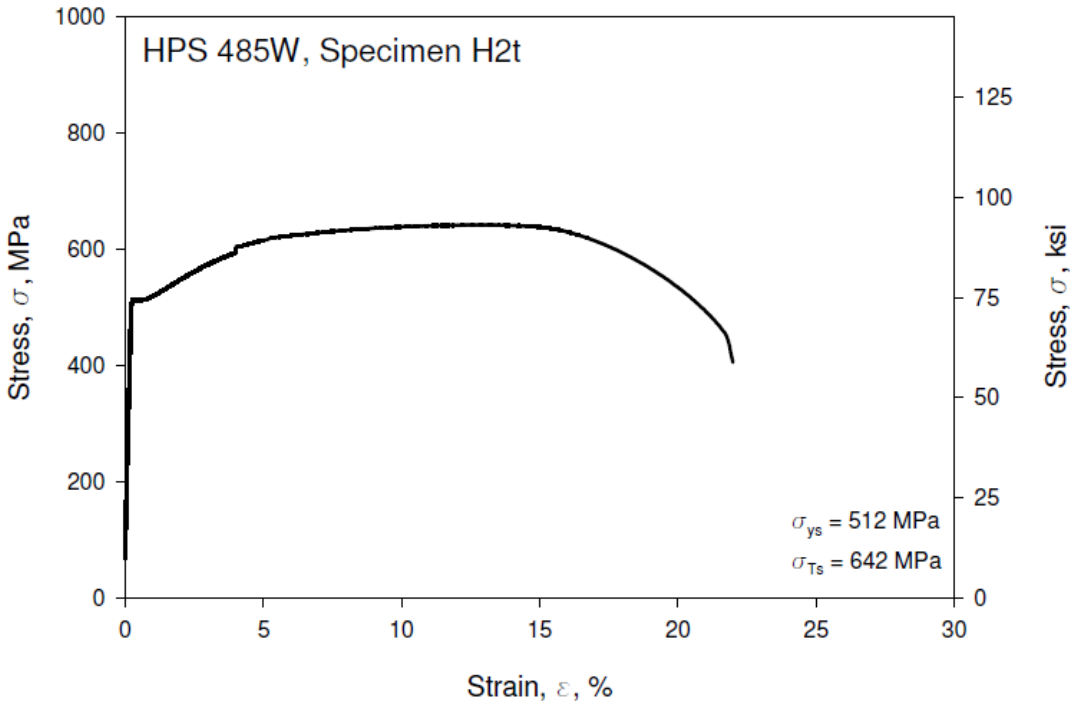

Figure A-6. Tension Test Data for Specimen H2t, HPS 485W, 31.8 mm.

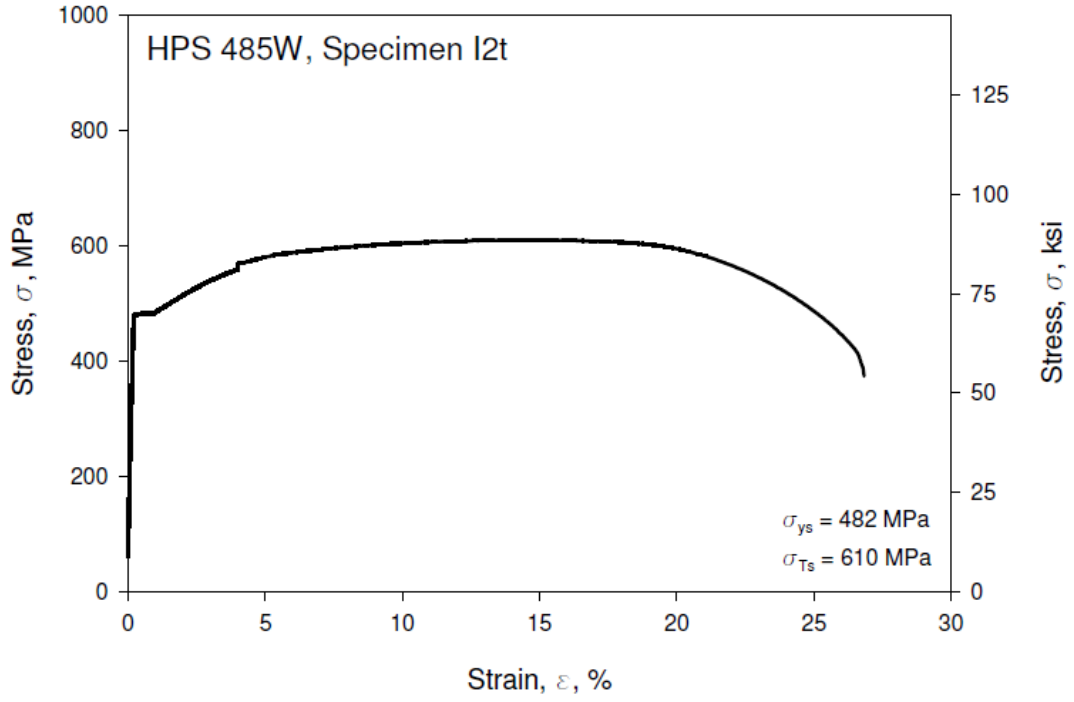

Figure A-7. Tension Test Data for Specimen I2t, HPS 485W, 31.8 mm.

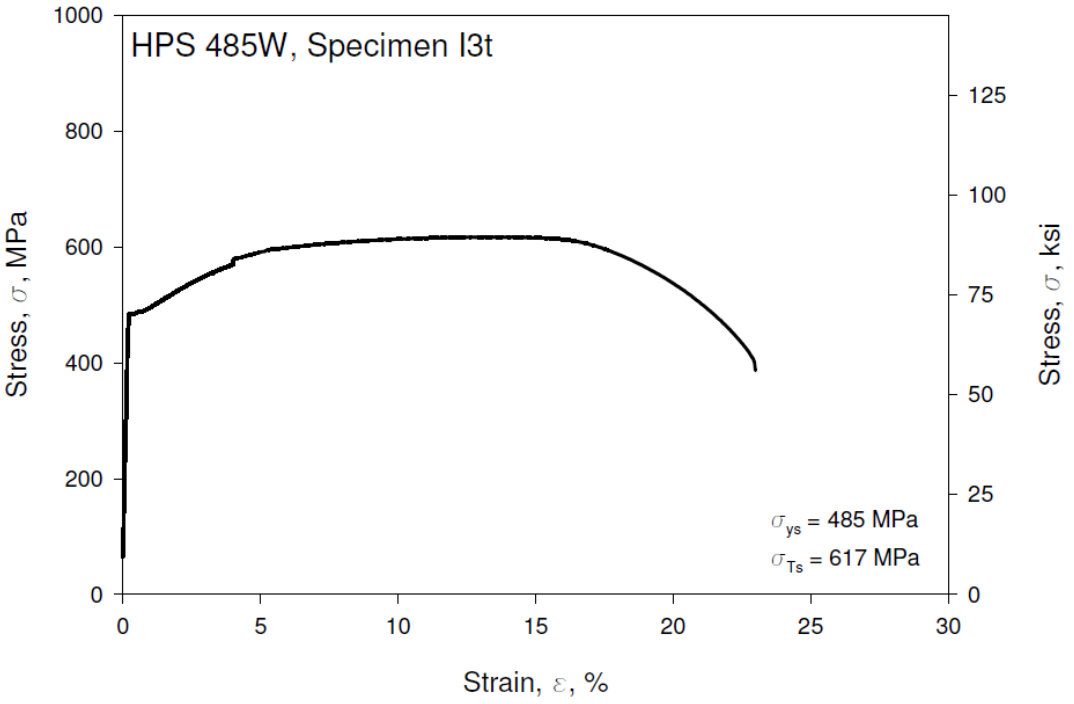

Figure A-8. Tension Test Data for Specimen I3t, HPS 485W, 31.8 mm.

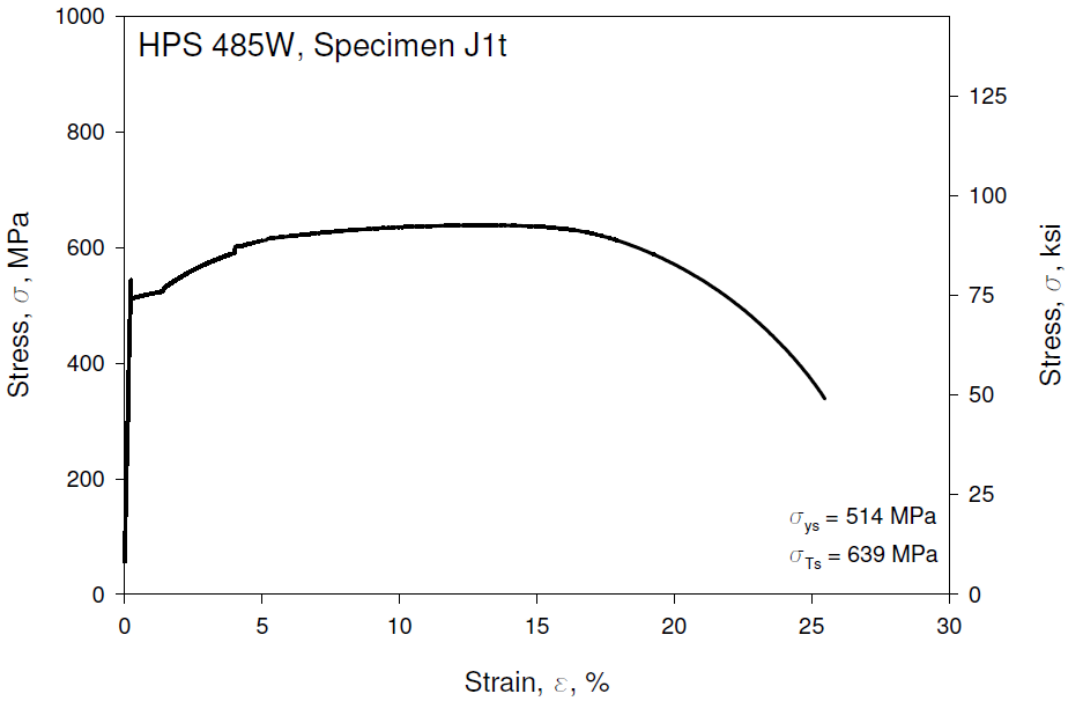

Figure A-9. Tension Test Data for Specimen J1t, HPS 485W, 38.1 mm.

APPENDIX B: Tabulated HPS CVN Data

Table B-1. CVN Data for Plate A, HPS 485W, 25.4 mm.

Specimen ID	Orientation	Through-Thickness Location	Test Temperature		CVN Impact Energy	
			°C	°F	J	ft-lbf
A1	L-T	1/4 T	-100	-148	3	2.25
A2	L-T	1/4 T	-100	-148	14	10
A3	L-T	1/4 T	-100	-148	76	56
A4	L-T	1/4 T	-70	-94	127	93.5
A5	L-T	1/4 T	-70	-94	123	91
A6	L-T	1/4 T	-70	-94	141	104
A7	L-T	1/4 T	-30	-22	176	130
A8	L-T	1/4 T	-30	-22	197	145.5
A9	L-T	1/4 T	-30	-22	163	120.5
A10	L-T	1/4 T	-10	14	246	181
A11	L-T	1/4 T	-10	14	244	180
A12	L-T	1/4 T	-10	14	249	183.5
A13	L-T	1/4 T	10	50	256	189
A14	L-T	1/4 T	10	50	247	182
A15	L-T	1/4 T	10	50	256	189
A16	L-T	1/4 T	-80	-112	128	94.5
A17	L-T	1/4 T	-80	-112	106	78.5
A18	L-T	1/4 T	-80	-112	136	100
A19	L-T	1/4 T	-90	-130	118	87
A20	L-T	1/4 T	-90	-130	137	101
A21	L-T	1/4 T	-90	-130	18	13
A22	L-T	1/4 T	-51	-60	153	112.5
A23	L-T	1/4 T	-51	-60	180	133
A24	L-T	1/4 T	-51	-60	152	112
A25	L-T	1/2 T	-51	-60	56	41
A26	L-T	1/2 T	-51	-60	182	134.5
A27	L-T	1/2 T	-51	-60	113	83
A28	T-L	1/4 T	-51	-60	158	116.5
A29	T-L	1/4 T	-51	-60	142	104.5
A30	T-L	1/4 T	-51	-60	138	102

Table B-2. CVN Data for Plate C, HPS 690W, 19 mm.

Specimen ID	Orientation	Through-Thickness Location	Test Temperature		CVN Impact Energy	
			°C	°F	J	ft-lbf
C1	L-T	1/3 T	-80	-112	26	19.25
C2	L-T	1/3 T	-80	-112	15	10.75
C3	L-T	1/3 T	-80	-112	13	9.5
C4	L-T	1/3 T	-65	-85	27	19.75
C5	L-T	1/3 T	-65	-85	28	21
C6	L-T	1/3 T	-65	-85	38	28.25
C7	L-T	1/3 T	-30	-22	148	109
C8	L-T	1/3 T	-30	-22	167	123
C9	L-T	1/3 T	-30	-22	157	115.5
C10	L-T	1/3 T	-10	14	176	130
C11	L-T	1/3 T	-10	14	195	144
C12	L-T	1/3 T	-10	14	202	149
C13	L-T	1/3 T	10	50	225	165.5
C14	L-T	1/3 T	10	50	202	149
C15	L-T	1/3 T	10	50	225	165.5
C16	L-T	1/3 T	25	77	212	156
C17	L-T	1/3 T	25	77	209	154
C18	L-T	1/3 T	25	77	225	166
C19	L-T	1/3 T	-100	-148	18	13.25
C20	L-T	1/3 T	-100	-148	31	23
C21	L-T	1/3 T	-100	-148	18	13
C22	L-T	1/3 T	-51	-60	88	65
C23	L-T	1/3 T	-51	-60	54	39.5
C24	L-T	1/3 T	-51	-60	58	43
C25	L-T	1/2 T	-51	-60	86	63.5
C26	L-T	1/2 T	-51	-60	88	64.5
C27	L-T	1/2 T	-51	-60	87	64
C28	T-L	1/3 T	-51	-60	60	44
C29	T-L	1/3 T	-51	-60	50	37
C30	T-L	1/3 T	-51	-60	98	72

Table B-3. CVN Data for Plate D, HPS 485W, 63.5 mm.

Specimen ID	Orientation	Through-Thickness Location	Test Temperature		CVN Impact Energy	
			°C	°F	J	ft-lbf
D1	L-T	1/4 T	-80	-112	188	138.5
D2	L-T	1/4 T	-80	-112	171	126
D3	L-T	1/4 T	-80	-112	65	48
D4	L-T	1/4 T	-60	-76	199	146.5
D5	L-T	1/4 T	-60	-76	210	155
D6	L-T	1/4 T	-60	-76	192	141.5
D7	L-T	1/4 T	-40	-40	319	235
D8	L-T	1/4 T	-40	-40	311	229
D9	L-T	1/4 T	-40	-40	235	173
D10	L-T	1/4 T	-51	-60	94	69
D11	L-T	1/4 T	-51	-60	202	149
D12	L-T	1/4 T	-51	-60	210	154.5
D14	L-T	1/4 T	-100	-148	6	4.5
D15	L-T	1/4 T	-100	-148	6	4.25
D16	L-T	1/4 T	-30	-22	239	176
D17	L-T	1/4 T	-30	-22	292	215
D18	L-T	1/4 T	-30	-22	209	154
D19	L-T	1/4 T	-10	14	347	256
D20	L-T	1/4 T	-10	14	304	224
D21	L-T	1/4 T	-10	14	324	239
D22	L-T	1/4 T	-70	-94	206	152
D23	L-T	1/4 T	-70	-94	246	181
D24	L-T	1/4 T	-70	-94	193	142
D25	L-T	1/2 T	-51	-60	351	259
D31	L-T	1/2 T	-51	-60	252	186
D36	L-T	1/2 T	-51	-60	330	243.5
D37	T-L	1/4 T	-51	-60	191	141
D38	T-L	1/4 T	-51	-60	161	118.5
D42	T-L	1/4 T	-51	-60	189	139.5
D49	L-T	1/4 T	-110	-166	10	7.5
D50	L-T	1/4 T	-110	-166	46	34
D51	L-T	1/4 T	-110	-166	9	6.5
D52	L-T	1/4 T	-90	-130	3	2
D53	L-T	1/4 T	-90	-130	16	11.5

Table B-4. CVN Data for Plate E, HPS 690W, 38.1 mm.

Specimen ID	Orientation	Through-Thickness Location	Test Temperature		CVN Impact Energy	
			°C	°F	J	ft-lbf
E1	L-T	1/4 T	-80	-112	35	25.75
E2	L-T	1/4 T	-80	-112	30	22
E3	L-T	1/4 T	-80	-112	25	18.25
E4	L-T	1/4 T	-70	-94	47	35
E5	L-T	1/4 T	-70	-94	54	39.5
E6	L-T	1/4 T	-70	-94	45	33.5
E7	L-T	1/4 T	-30	-22	170	125
E8	L-T	1/4 T	-30	-22	155	114.5
E9	L-T	1/4 T	-30	-22	183	135
E10	L-T	1/4 T	-10	14	185	136
E11	L-T	1/4 T	-10	14	196	144.5
E12	L-T	1/4 T	-10	14	208	153
E13	L-T	1/4 T	10	50	229	169
E14	L-T	1/4 T	10	50	212	156.5
E15	L-T	1/4 T	10	50	211	155.5
E16	L-T	1/4 T	-100	-148	6	4.25
E18	L-T	1/4 T	-100	-148	9	6.5
E19	L-T	1/4 T	25	77	247	182
E20	L-T	1/4 T	25	77	231	170
E21	L-T	1/4 T	25	77	248	183
E22	L-T	1/4 T	-51	-60	77	56.5
E23	L-T	1/4 T	-51	-60	109	80
E24	L-T	1/4 T	-51	-60	83	61
E25	L-T	1/2 T	-51	-60	115	84.5
E26	L-T	1/2 T	-51	-60	127	93.5
E27	L-T	1/2 T	-51	-60	79	58
E28	T-L	1/4 T	-51	-60	96	70.5
E29	T-L	1/4 T	-51	-60	103	76
E30	T-L	1/4 T	-51	-60	70	51.5

Table B-5. CVN Data for Plate F, HPS 690W, 50.8 mm.

Specimen ID	Orientation	Through-Thickness Location	Test Temperature		CVN Impact Energy	
			°C	°F	J	ft-lbf
F1	L-T	1/4 T	-80	-112	27	20
F2	L-T	1/4 T	-80	-112	28	21
F3	L-T	1/4 T	-80	-112	25	18.75
F4	L-T	1/4 T	-70	-94	60	44.5
F5	L-T	1/4 T	-70	-94	46	34
F6	L-T	1/4 T	-70	-94	57	42
F7	L-T	1/4 T	-30	-22	144	106
F8	L-T	1/4 T	-30	-22	166	122
F9	L-T	1/4 T	-30	-22	149	110
F10	L-T	1/4 T	-10	14	195	144
F11	L-T	1/4 T	-10	14	203	149.5
F12	L-T	1/4 T	-10	14	180	132.5
F13	L-T	1/4 T	10	50	204	150
F14	L-T	1/4 T	10	50	216	159
F15	L-T	1/4 T	10	50	213	157
F16	L-T	1/4 T	-100	-148	4	3.25
F17	L-T	1/4 T	-100	-148	31	22.75
F18	L-T	1/4 T	-100	-148	41	30.5
F19	L-T	1/4 T	25	77	231	170
F20	L-T	1/4 T	25	77	225	166
F21	L-T	1/4 T	25	77	220	162
F22	L-T	1/4 T	-51	-60	96	71
F23	L-T	1/4 T	-51	-60	85	63
F24	L-T	1/4 T	-51	-60	113	83
F25	L-T	1/2 T	-51	-60	49	36
F26	L-T	1/2 T	-51	-60	34	25
F27	L-T	1/2 T	-51	-60	50	37
F28	T-L	1/4 T	-51	-60	100	73.5
F29	T-L	1/4 T	-51	-60	90	66
F30	T-L	1/4 T	-51	-60	69	50.5

Table B-6. CVN Data for Plate H, HPS 485W, 31.8 mm.

Specimen ID	Orientation	Through-Thickness Location	Test Temperature		CVN Impact Energy	
			°C	°F	J	ft-lbf
H1	L-T	1/4 T	-80	-112	18	13.25
H2	L-T	1/4 T	-80	-112	12	8.75
H3	L-T	1/4 T	-80	-112	169	124.5
H4	L-T	1/4 T	-40	-40	306	225.5
H5	L-T	1/4 T	-40	-40	310	228.5
H32	L-T	1/4 T	-40	-40	269	198
H7	L-T	1/4 T	-100	-148	4	3
H8	L-T	1/4 T	-100	-148	5	3.5
H9	L-T	1/4 T	-100	-148	4	3
H10	L-T	1/4 T	-65	-85	246	181
H11	L-T	1/4 T	-65	-85	134	99
H12	L-T	1/4 T	-65	-85	151	111.5
H13	L-T	1/4 T	-20	-4	317	233.5
H14	L-T	1/4 T	-20	-4	319	235.5
H15	L-T	1/4 T	-20	-4	319	235.5
H16	L-T	1/4 T	-73	-99	174	128
H17	L-T	1/4 T	-73	-99	176	129.5
H18	L-T	1/4 T	-73	-99	195	144
H19	L-T	1/4 T	-90	-130	47	35
H20	L-T	1/4 T	-90	-130	7	5.5
H21	L-T	1/4 T	-90	-130	7	5
H22	L-T	1/4 T	-51	-60	311	229
H23	L-T	1/4 T	-51	-60	284	209.5
H24	L-T	1/4 T	-51	-60	271	199.5
H25	L-T	1/2 T	-51	-60	163	120.5
H26	L-T	1/2 T	-51	-60	215	158.5
H27	L-T	1/2 T	-51	-60	159	117
H28	T-L	1/4 T	-51	-60	70	51.5
H29	T-L	1/4 T	-51	-60	176	130
H30	T-L	1/4 T	-51	-60	82	60.5

Table B-7. CVN Data for Plate I, HPS 485W, 31.8 mm.

Specimen ID	Orientation	Through-Thickness Location	Test Temperature		CVN Impact Energy	
			°C	°F	J	ft-lbf
I1	L-T	1/4 T	-80	-112	9	6.5
I2	L-T	1/4 T	-80	-112	149	110
I3	L-T	1/4 T	-80	-112	50	37
I4	L-T	1/4 T	-65	-85	238	175.5
I5	L-T	1/4 T	-65	-85	144	106.5
I6	L-T	1/4 T	-65	-85	104	76.5
I7	L-T	1/4 T	-30	-22	324	239
I8	L-T	1/4 T	-30	-22	323	238
I9	L-T	1/4 T	-30	-22	304	224
I10	L-T	1/4 T	-10	14	354	261
I11	L-T	1/4 T	-10	14	400	295
I12	L-T	1/4 T	-10	14	350	258
I13	L-T	1/4 T	-100	-148	8	6
I14	L-T	1/4 T	-100	-148	4	3
I15	L-T	1/4 T	-100	-148	3	2
I16	L-T	1/4 T	-90	-130	55	40.5
I17	L-T	1/4 T	-90	-130	77	57
I18	L-T	1/4 T	-90	-130	6	4.5
I19	L-T	1/4 T	-90	-130	6	4.5
I20	L-T	1/4 T	-90	-130	18	13.5
I21	L-T	1/4 T	-90	-130	9	7
I22	L-T	1/4 T	-51	-60	252	186
I23	L-T	1/4 T	-51	-60	255	188
I24	L-T	1/4 T	-51	-60	244	179.5
I25	L-T	1/2 T	-51	-60	220	162
I26	L-T	1/2 T	-51	-60	279	206
I27	L-T	1/2 T	-51	-60	229	169
I28	T-L	1/4 T	-51	-60	155	114.5
I29	T-L	1/4 T	-51	-60	204	150.5
I30	T-L	1/4 T	-51	-60	128	94.5

Table B-8. CVN Data for Plate J, HPS 485W, 38.1 mm.

Specimen ID	Orientation	Through-Thickness Location	Test Temperature		CVN Impact Energy	
			°C	°F	J	ft-lbf
J1	L-T	1/4 T	-80	-112	95	70
J2	L-T	1/4 T	-80	-112	48	35.5
J3	L-T	1/4 T	-80	-112	85	62.5
J4	L-T	1/4 T	-65	-85	157	116
J5	L-T	1/4 T	-65	-85	62	45.5
J6	L-T	1/4 T	-65	-85	151	111.5
J7	L-T	1/4 T	-30	-22	201	148
J8	L-T	1/4 T	-30	-22	213	157
J9	L-T	1/4 T	-30	-22	209	154
J11	L-T	1/4 T	-100	-148	13	9.5
J12	L-T	1/4 T	-100	-148	56	41.5
J13	L-T	1/4 T	-100	-148	5	4
J14	L-T	1/4 T	-100	-148	18	13.5
J15	L-T	1/4 T	-100	-148	68	50
J16	L-T	1/4 T	-65	-85	163	120
J17	L-T	1/4 T	-65	-85	125	92.5
J18	L-T	1/4 T	-65	-85	166	122
J19	L-T	1/4 T	-10	14	309	228
J20	L-T	1/4 T	-10	14	208	153
J21	L-T	1/4 T	-10	14	288	212
J22	L-T	1/4 T	-51	-60	187	138
J23	L-T	1/4 T	-51	-60	193	142
J24	L-T	1/4 T	-51	-60	149	110
J25	L-T	1/2 T	-51	-60	217	160
J26	L-T	1/2 T	-51	-60	182	134
J27	L-T	1/2 T	-51	-60	233	172
J28	T-L	1/4 T	-51	-60	166	122
J29	T-L	1/4 T	-51	-60	153	113
J30	T-L	1/4 T	-51	-60	168	124

APPENDIX C: HPS Static Test Records and Fracture Surfaces

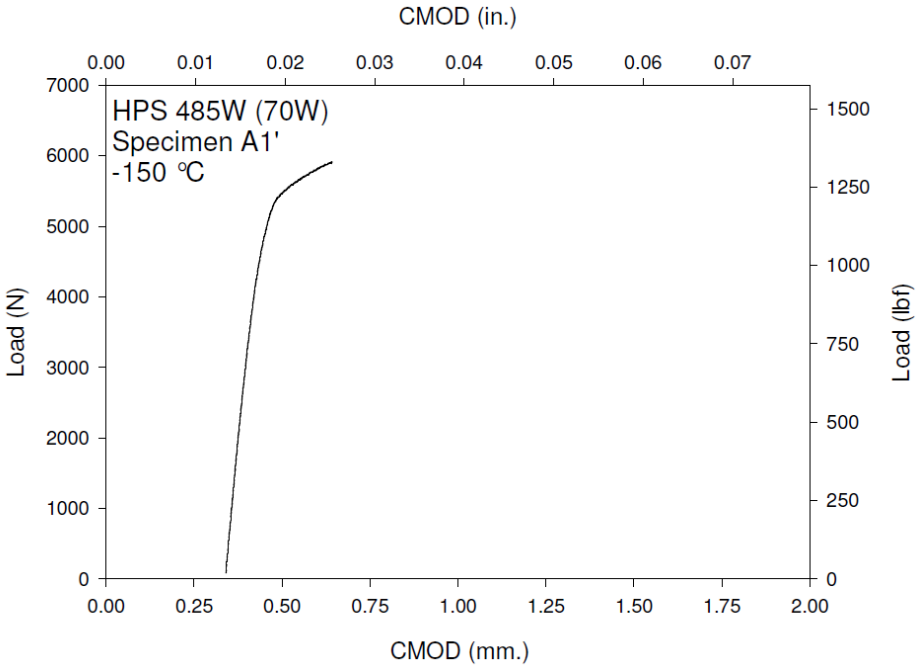

Figure C-1. Specimen A1' Test Record

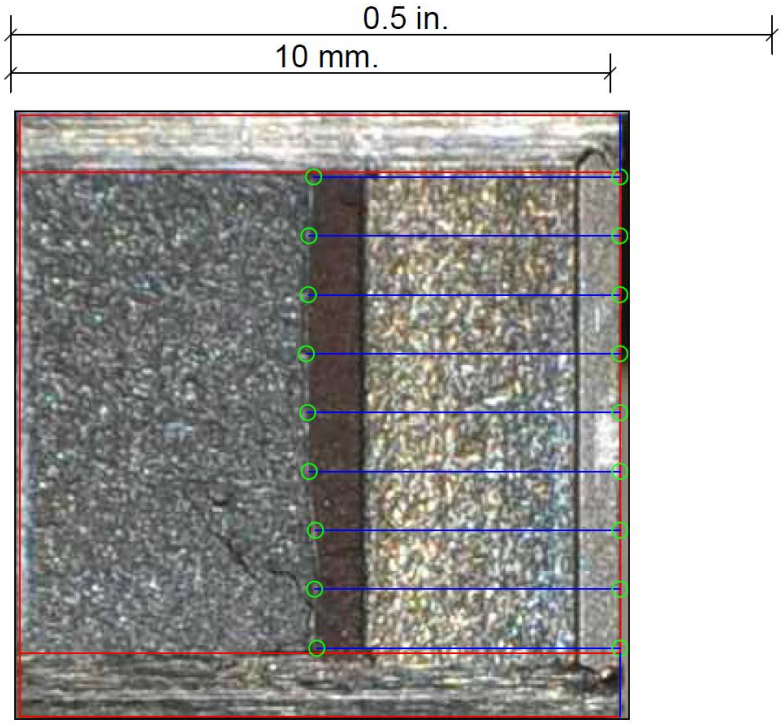

Figure C-2. Specimen A1' Fracture Surface

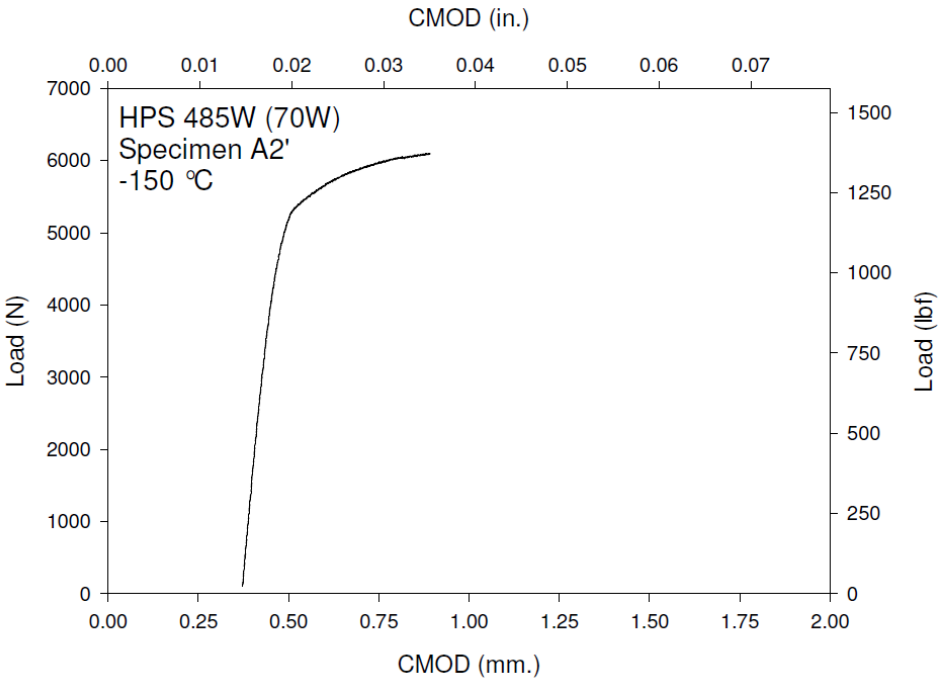

Figure C-3. Specimen A2' Test Record

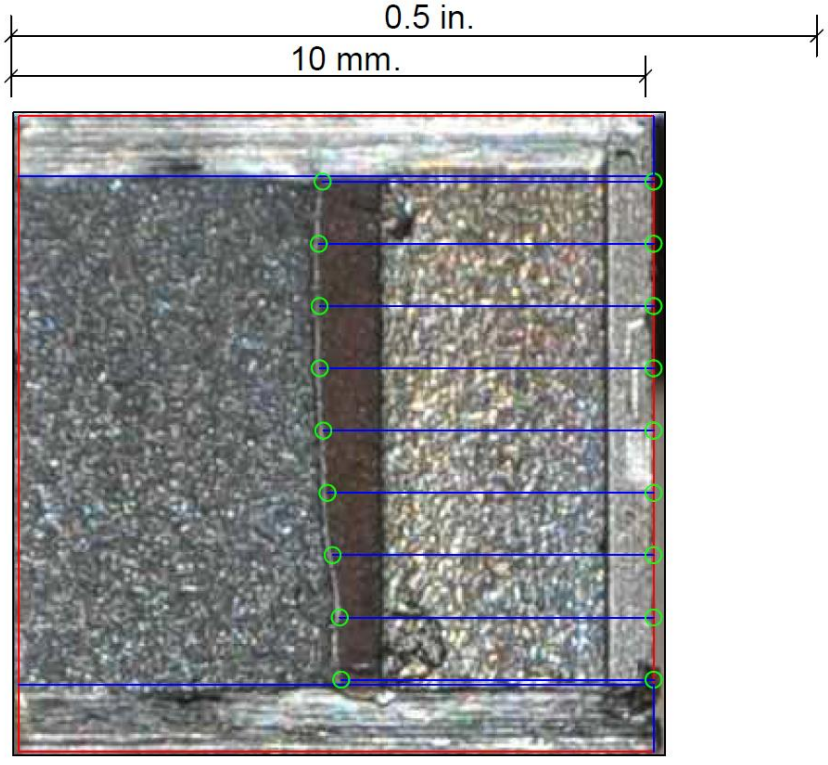

Figure C-4. Specimen A2' Fracture Surface

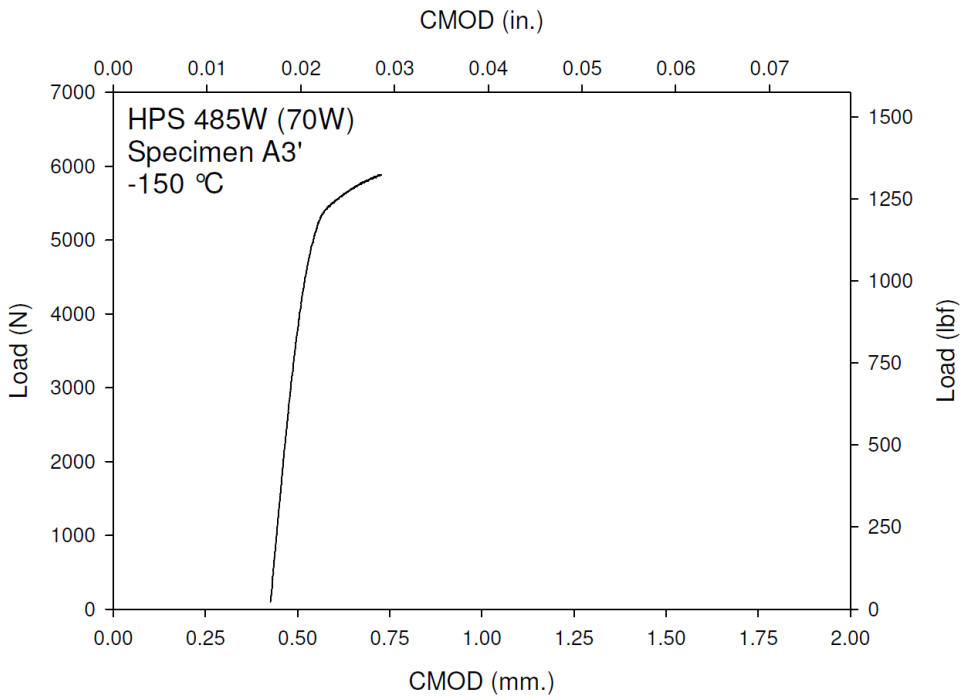

Figure C-5. Specimen A3' Test Record

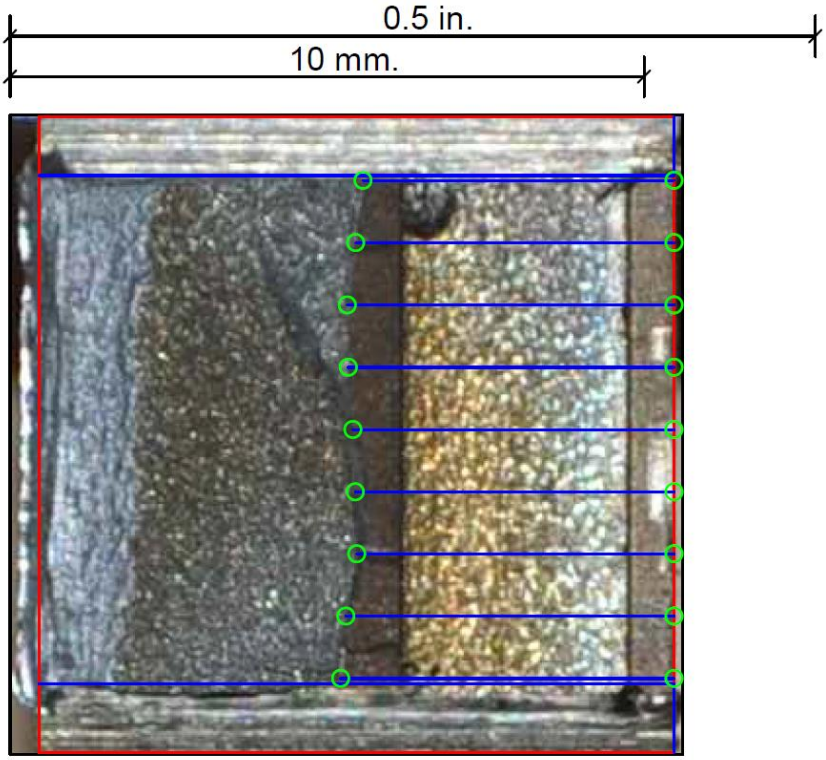

Figure C-6. Specimen A3' Fracture Surface

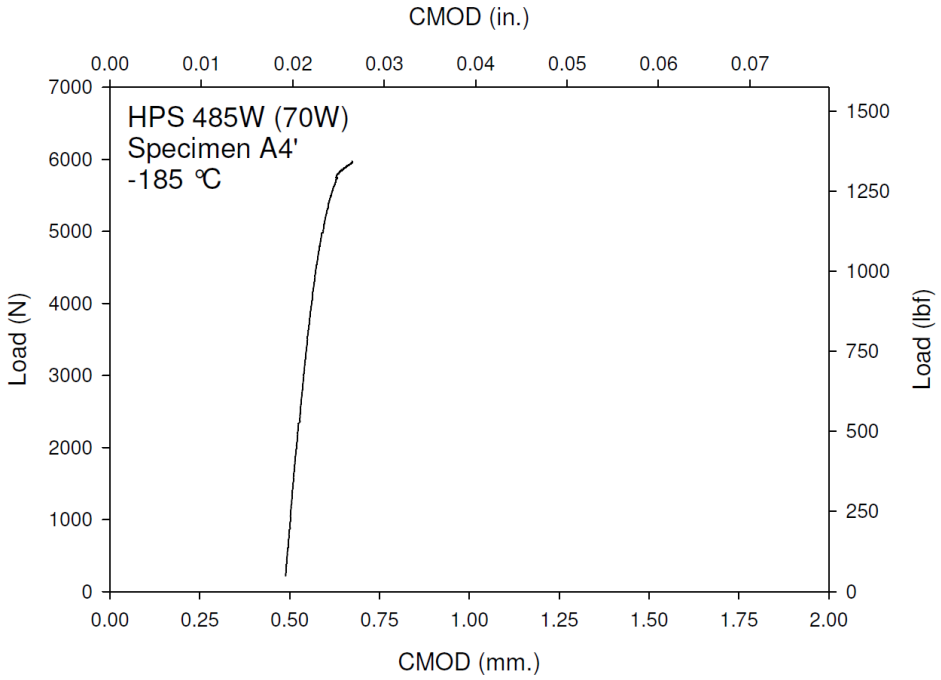

Figure C-7. Specimen A4' Test Record

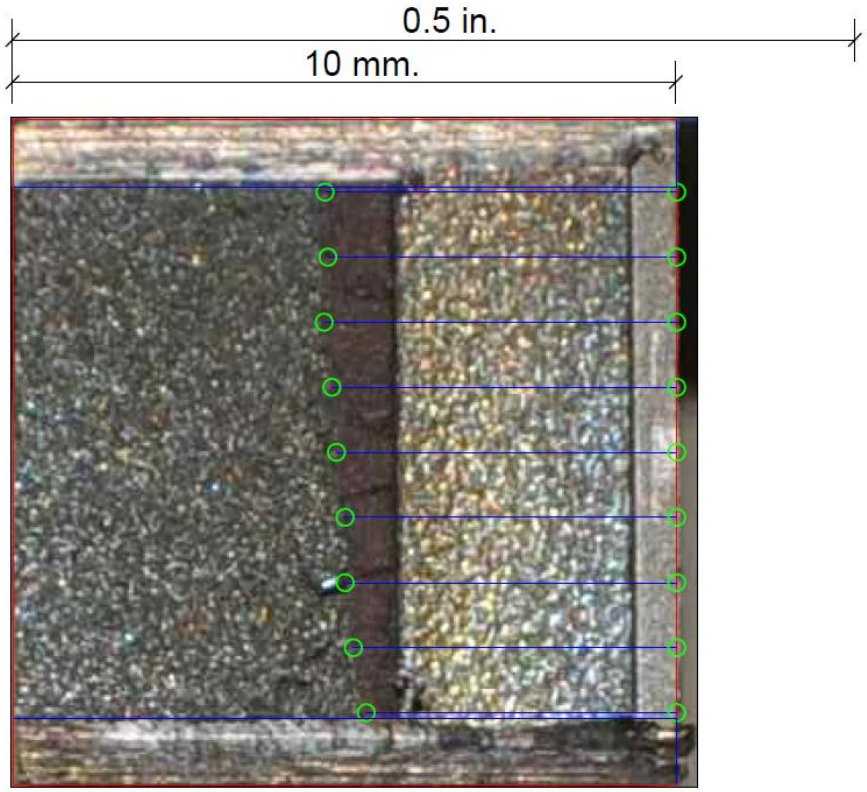

Figure C-8. Specimen A4' Fracture Surface

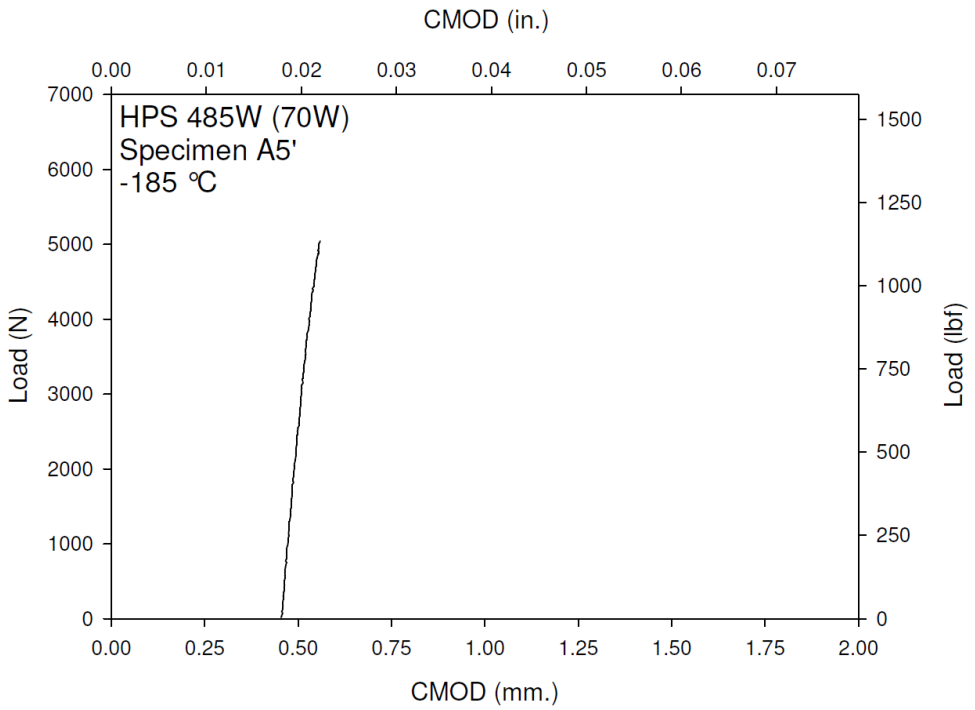

Figure C-9. Specimen A5' Test Record

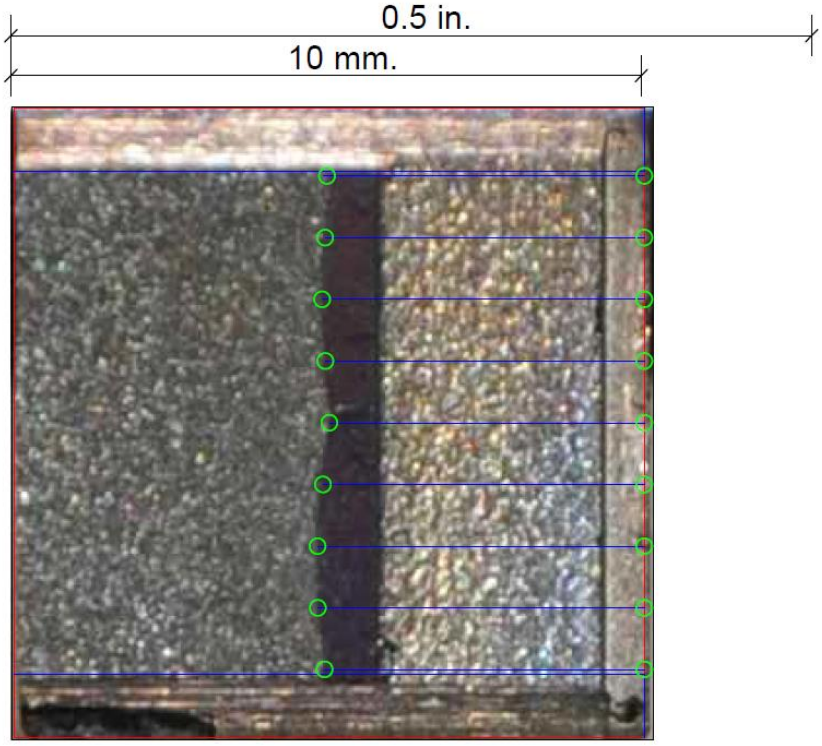

Figure C-10. Specimen A5' Fracture Surface

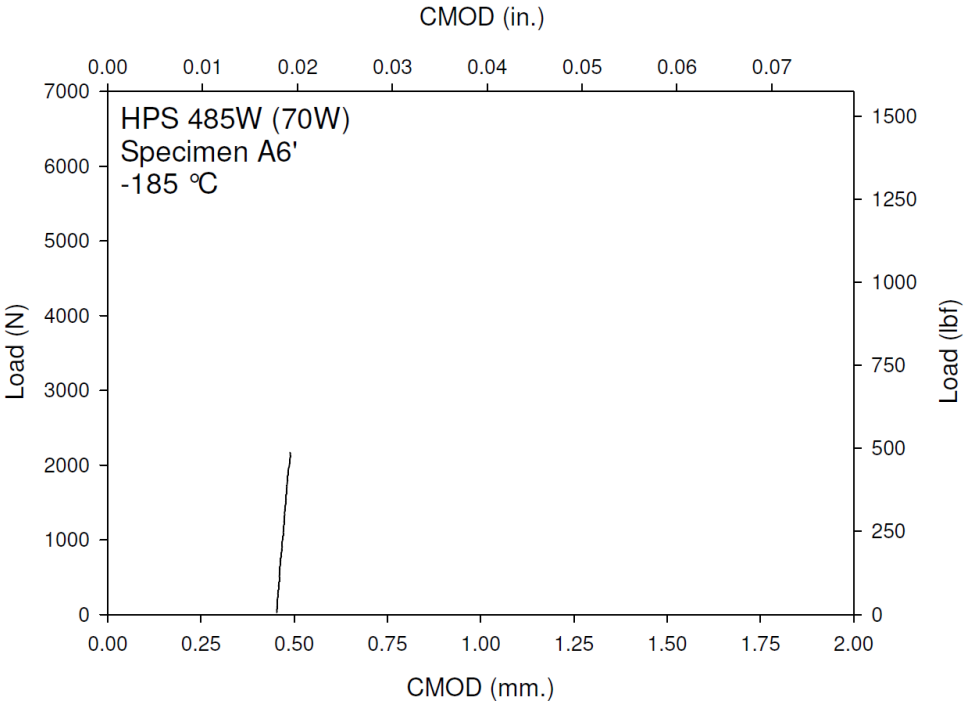

Figure C-11. Specimen A6' Test Record

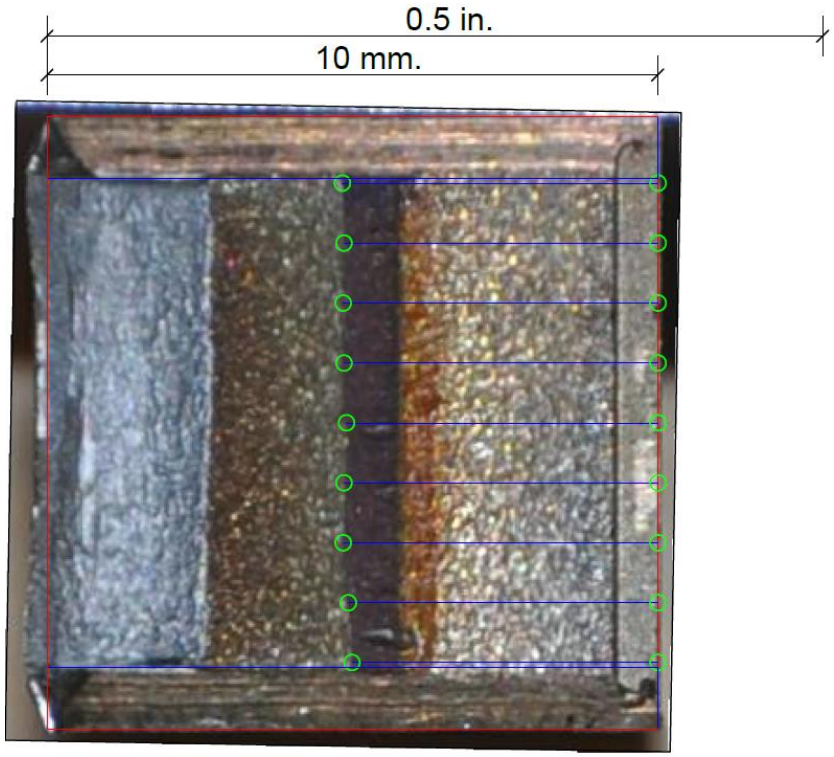

Figure C-12. Specimen A6' Fracture Surface

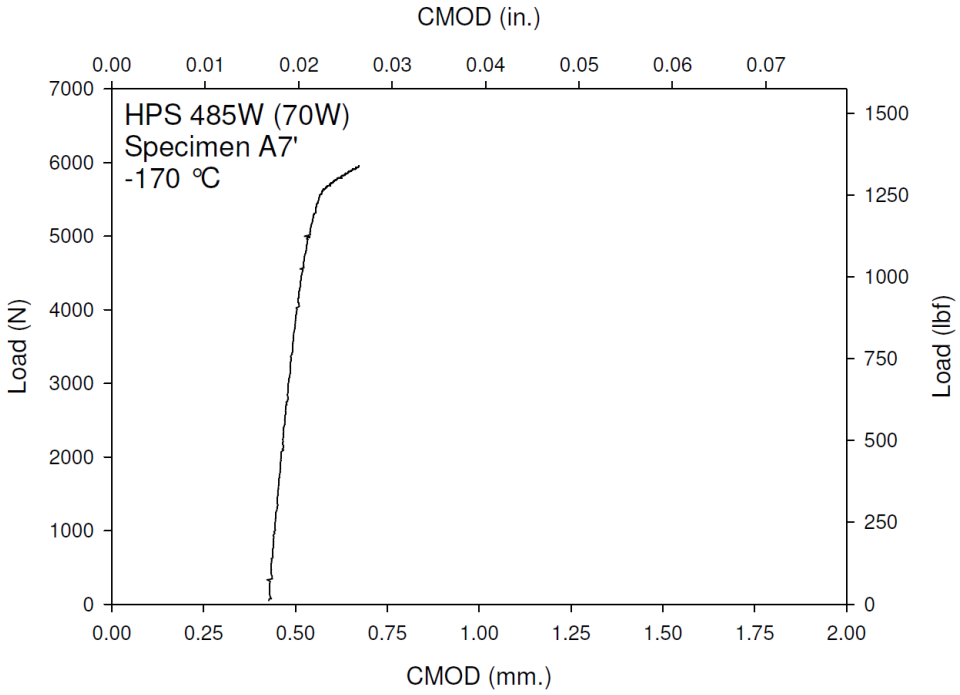

Figure C-13. Specimen A7' Test Record

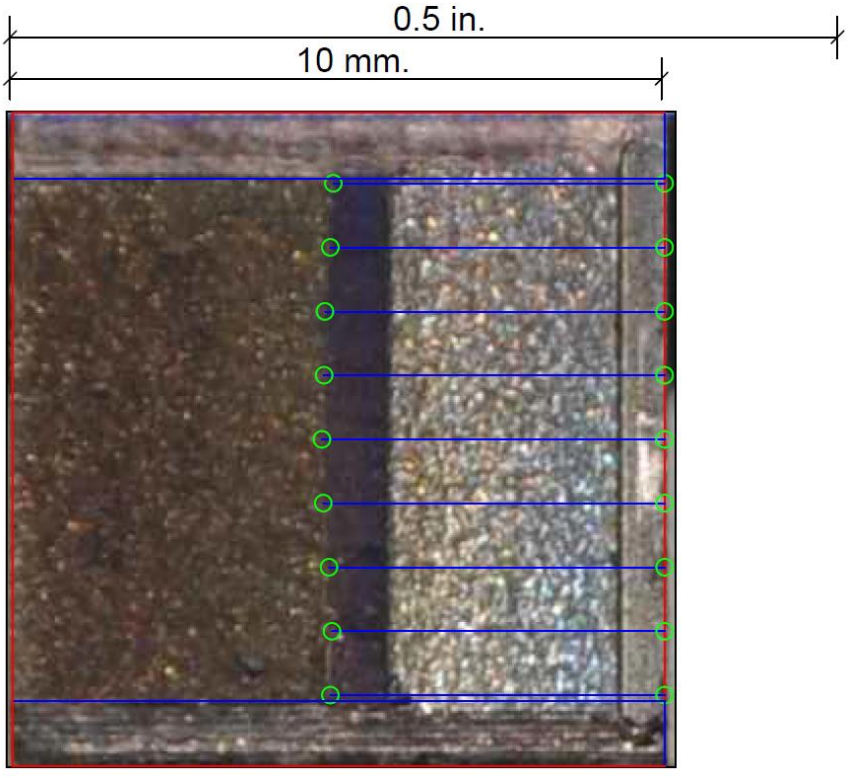

Figure C-14. Specimen A7' Fracture Surface

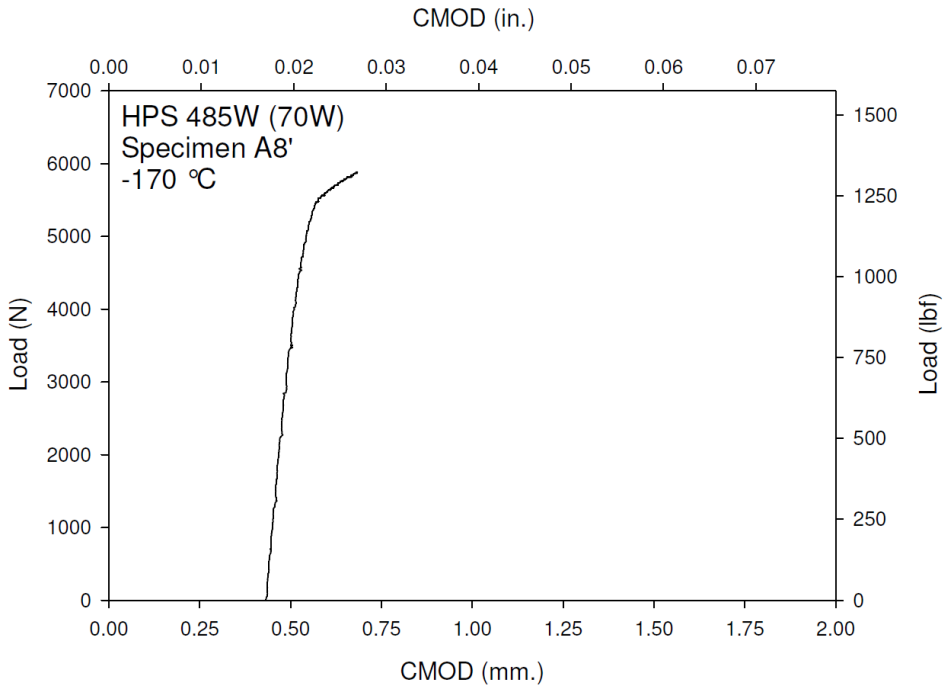

Figure C-15. Specimen A8' Test Record

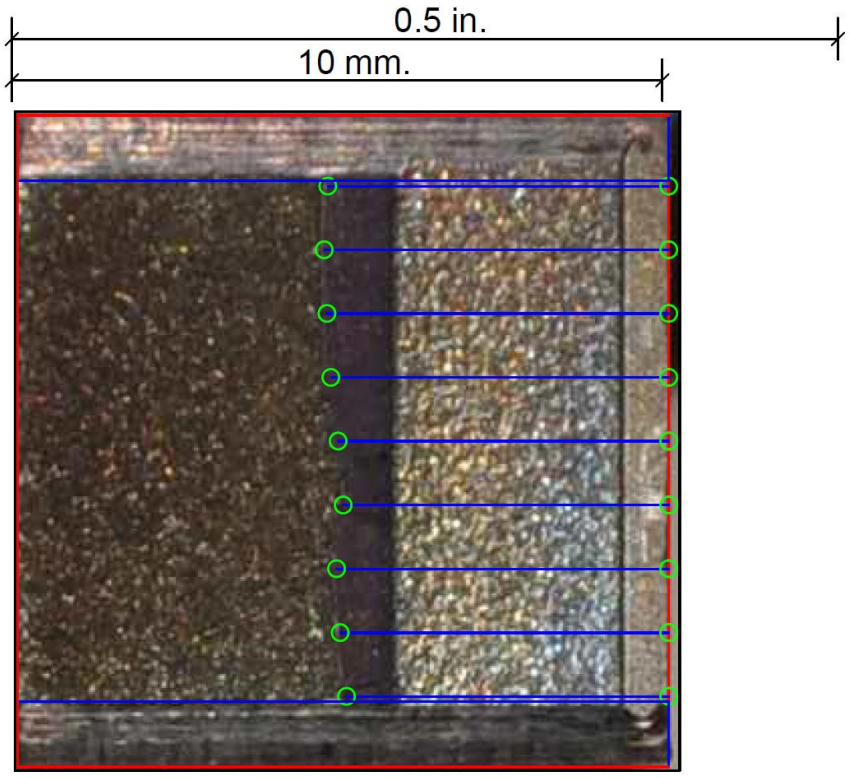

Figure C-16. Specimen A8' Fracture Surface

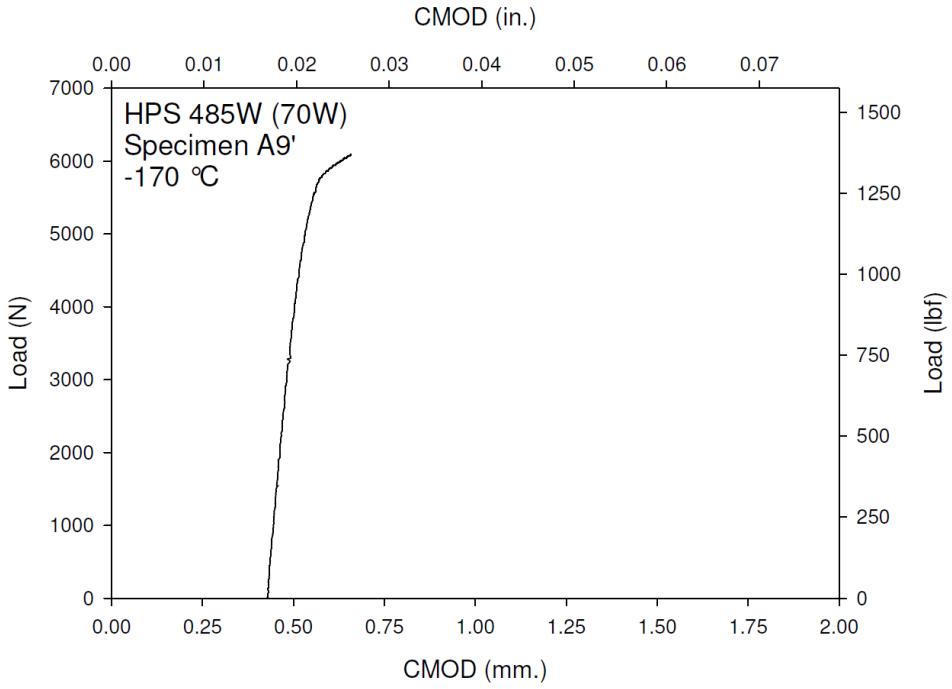

Figure C-17. Specimen A9' Test Record

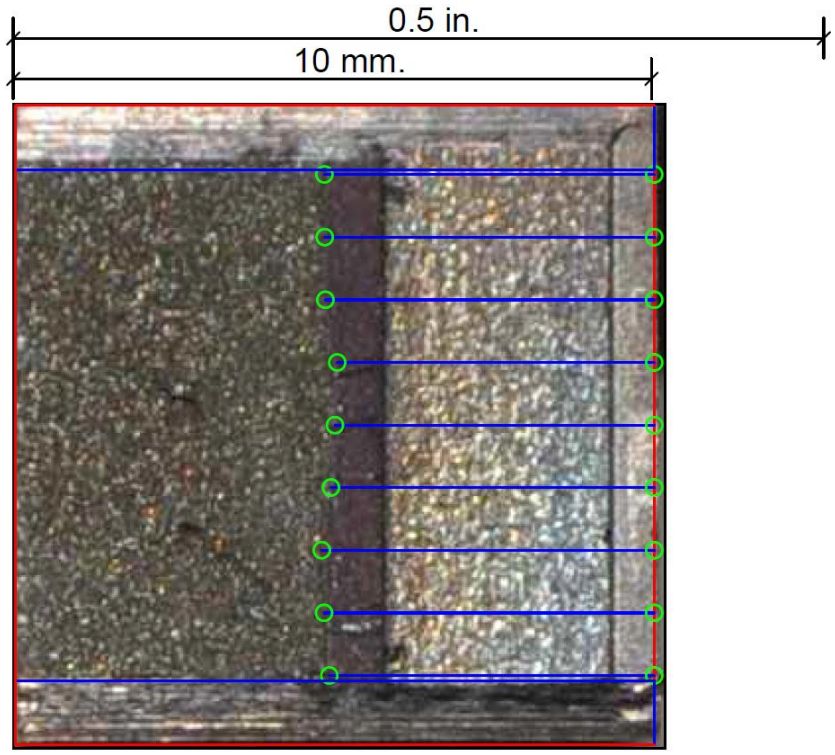

Figure C-18. Specimen A9' Fracture Surface

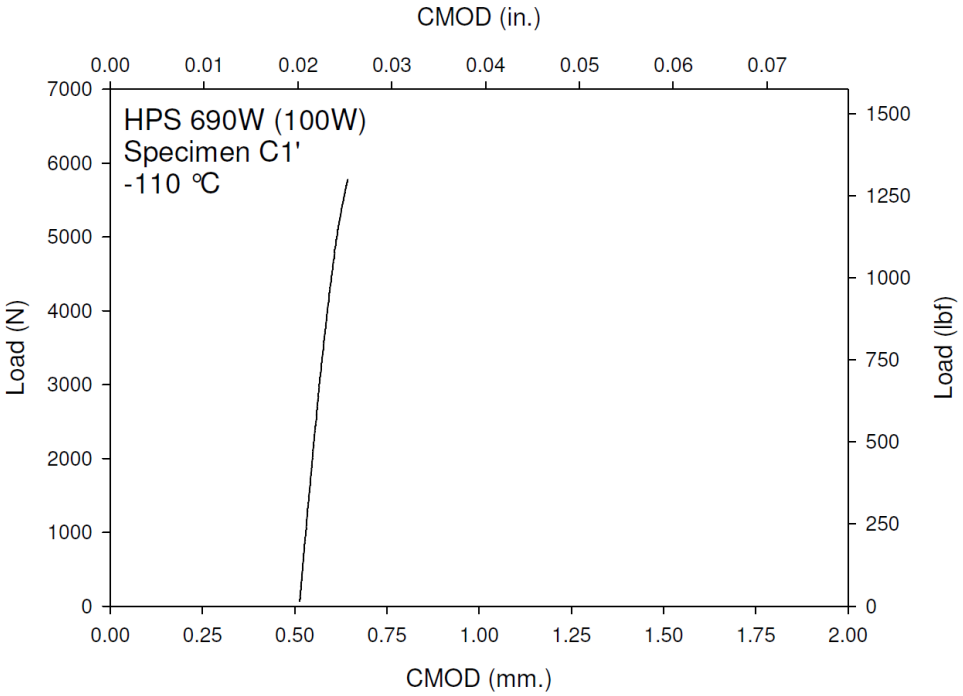

Figure C-19. Specimen C1' Test Record

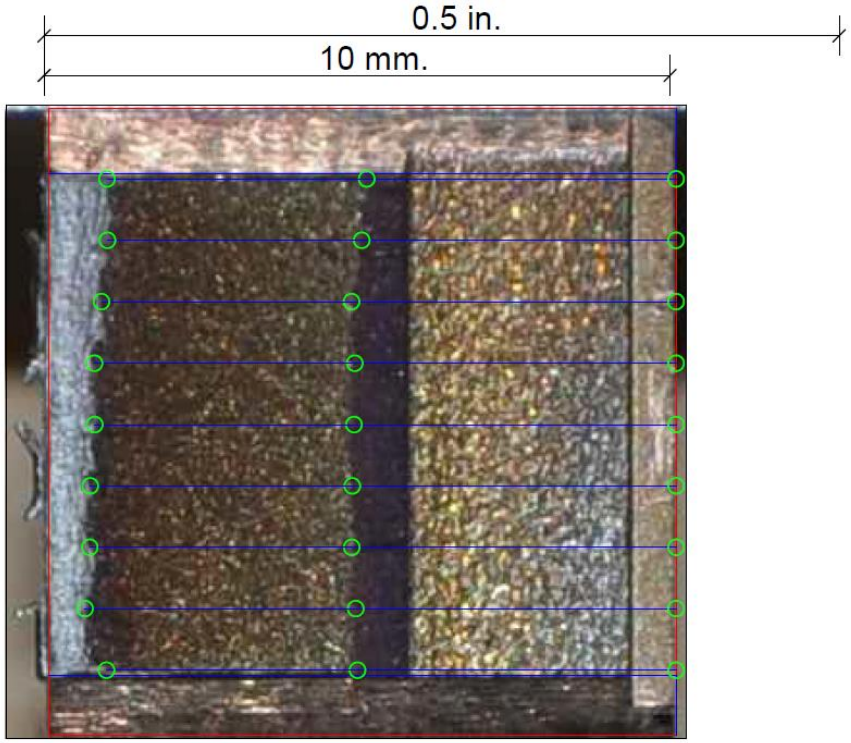

Figure C-20. Specimen C1' Fracture Surface

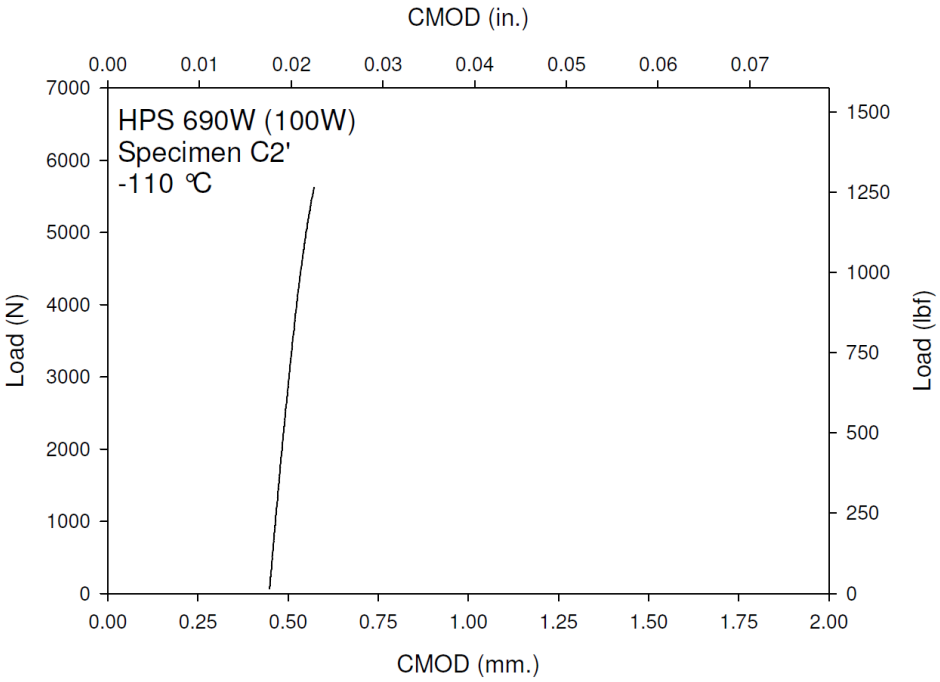

Figure C-21. Specimen C2' Test Record

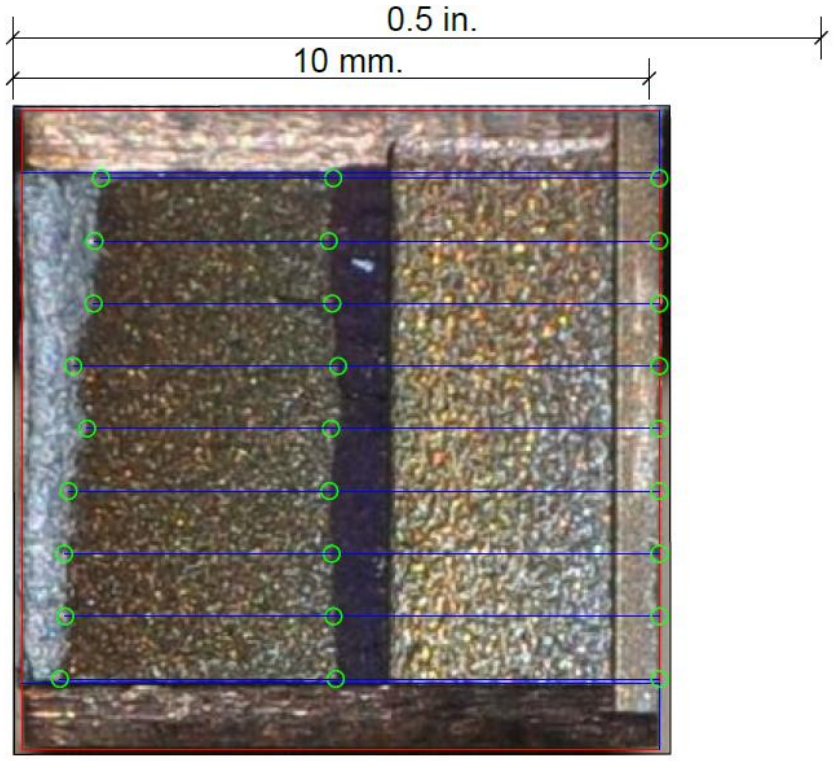

Figure C-22. Specimen C2' Fracture Surface

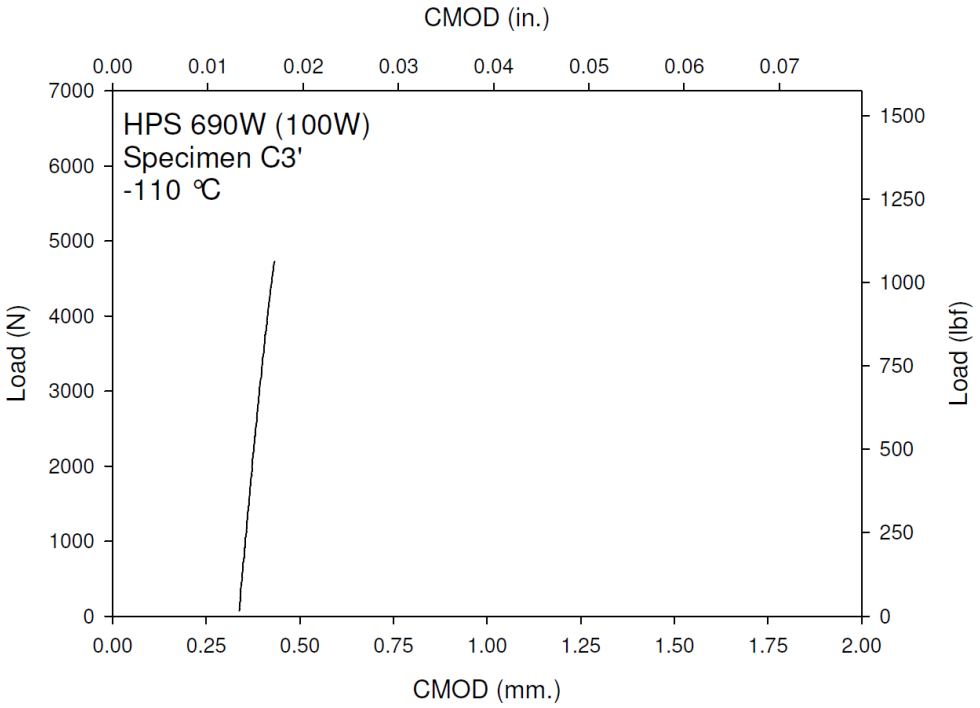

Figure C-23. Specimen C3' Test Record

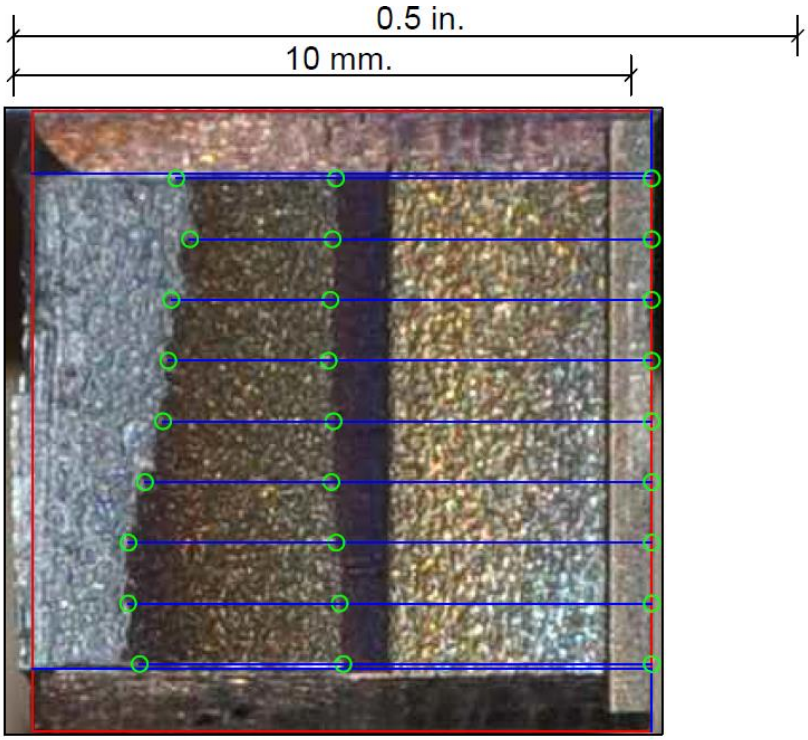

Figure C-24. Specimen C3' Fracture Surface

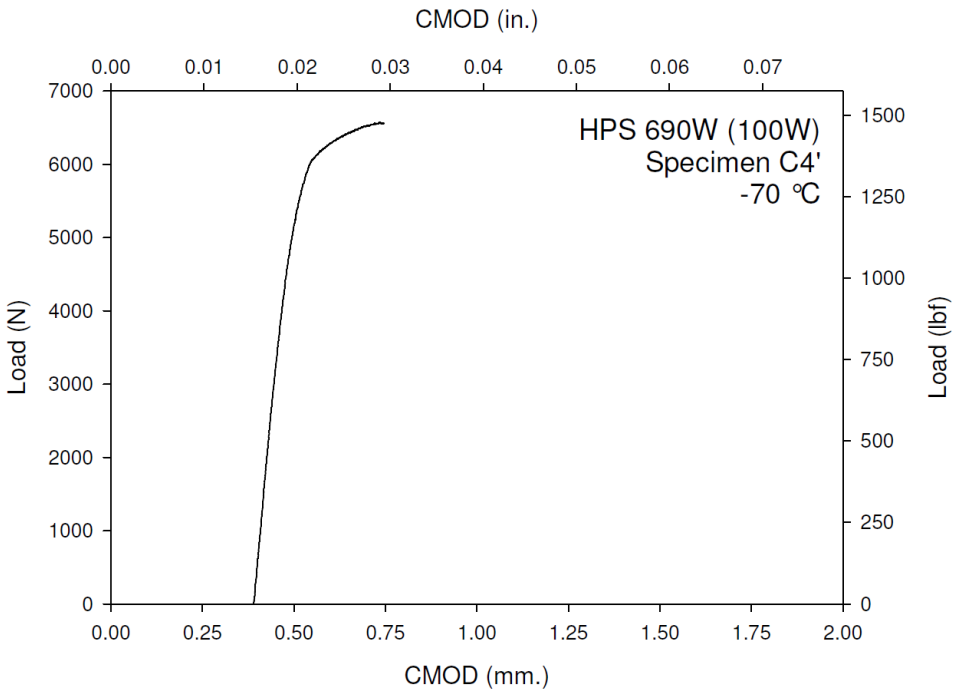

Figure C-25. Specimen C4' Test Record

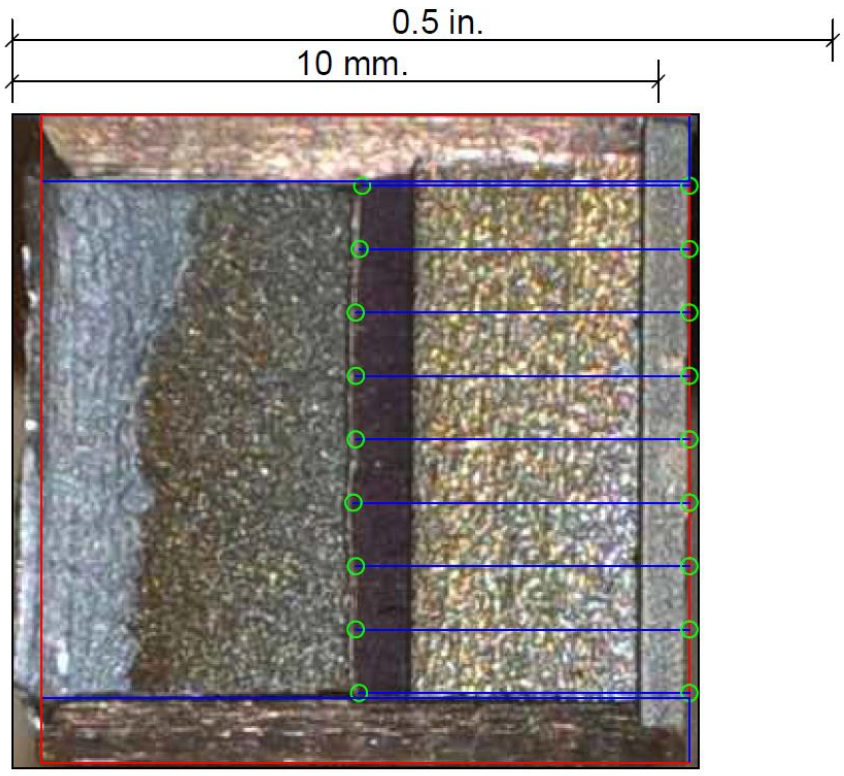

Figure C-26. Specimen C4' Fracture Surface

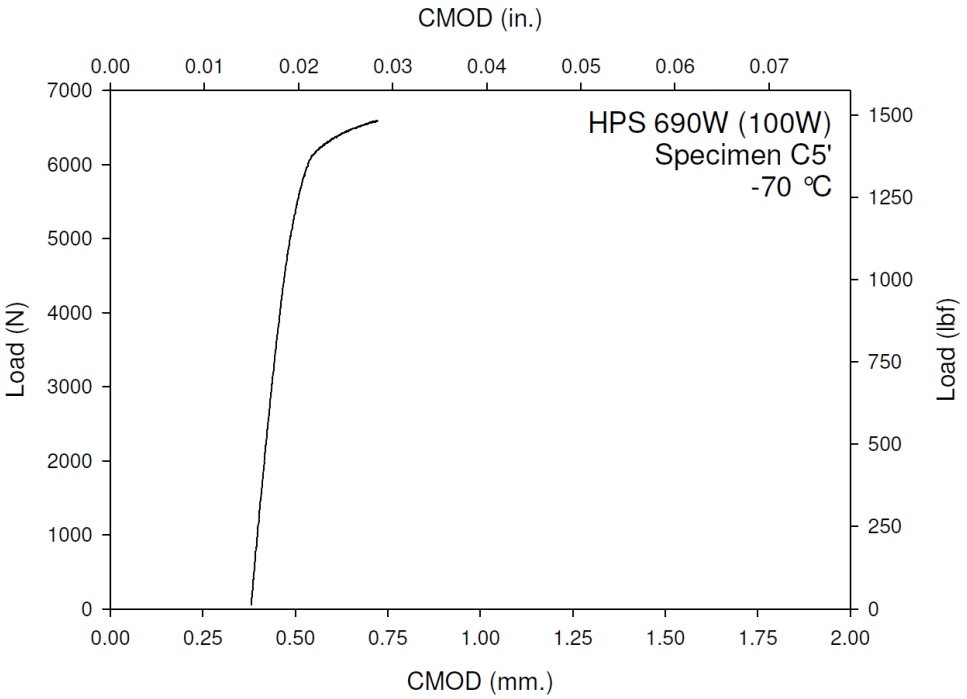

Figure C-27. Specimen C5' Test Record

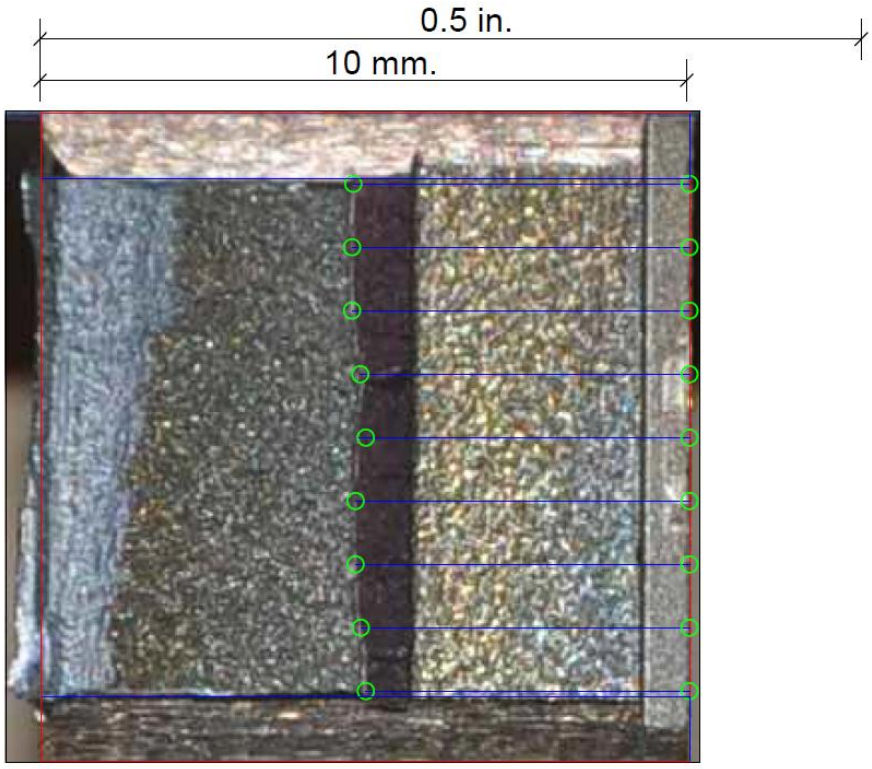

Figure C-28. Specimen C5' Fracture Surface

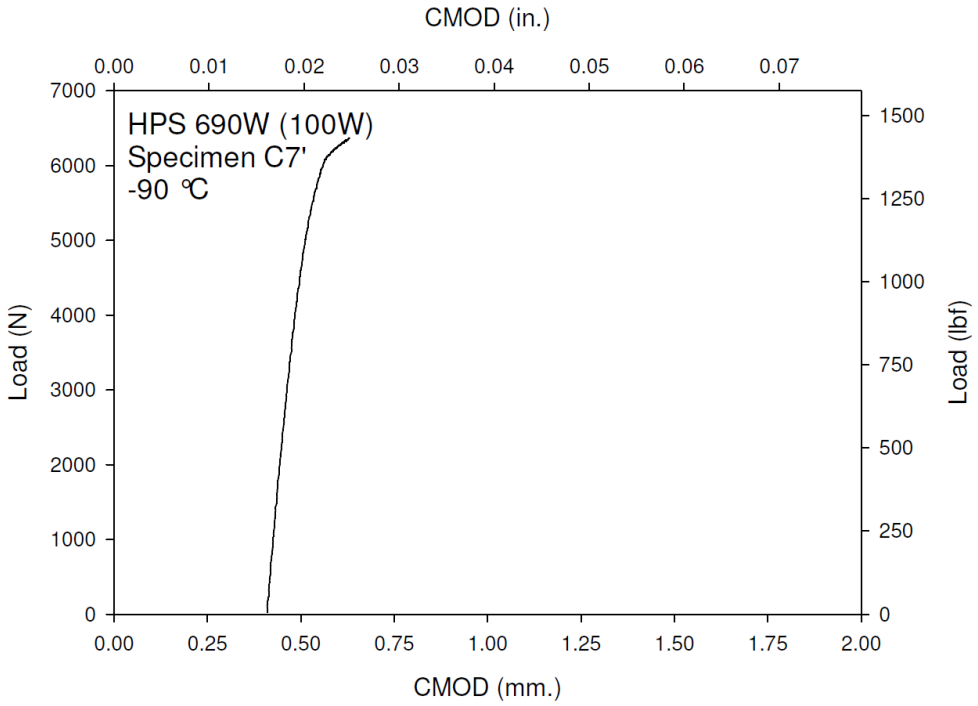

Figure C-29. Specimen C7' Test Record

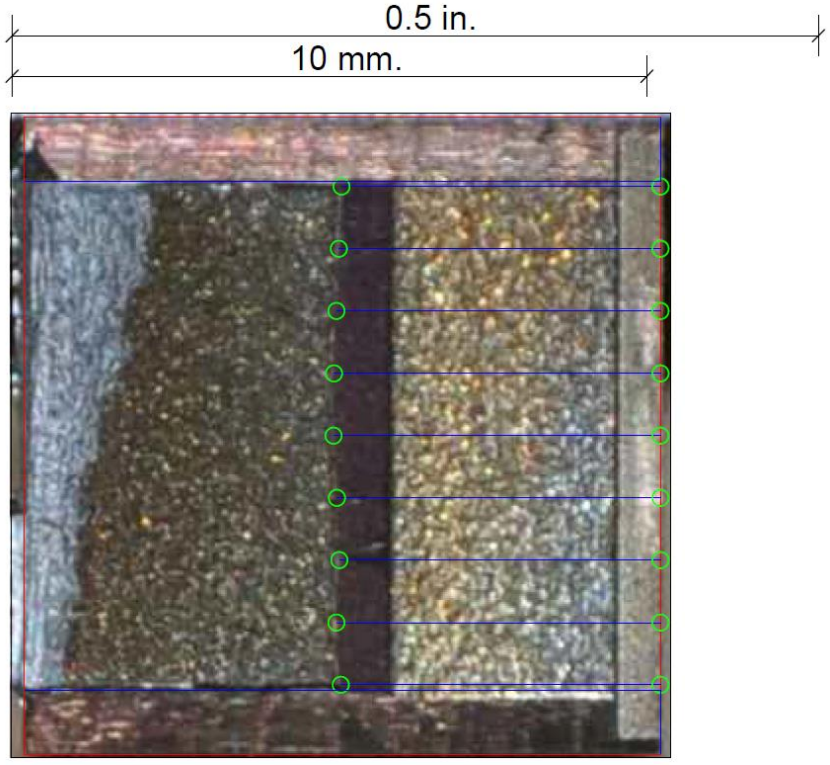

Figure C-30. Specimen C7' Fracture Surface

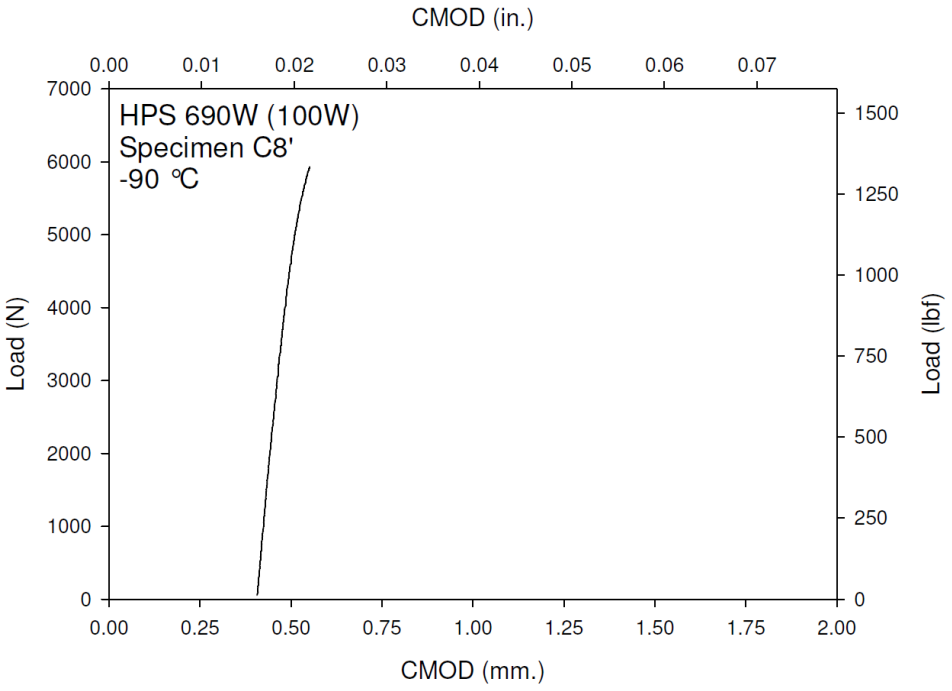

Figure C-31. Specimen C8' Test Record

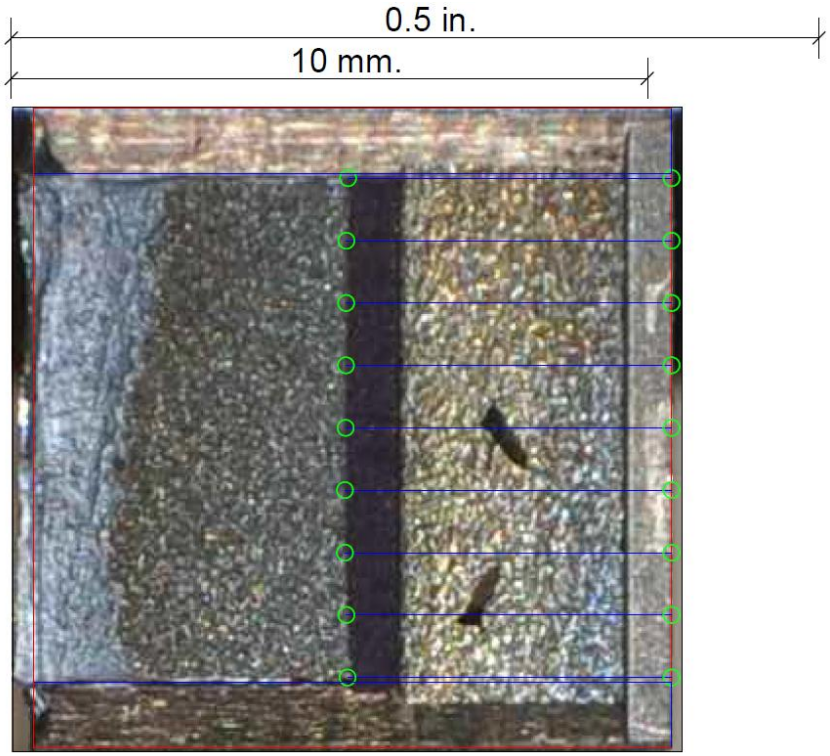

Figure C-32. Specimen C8' Fracture Surface

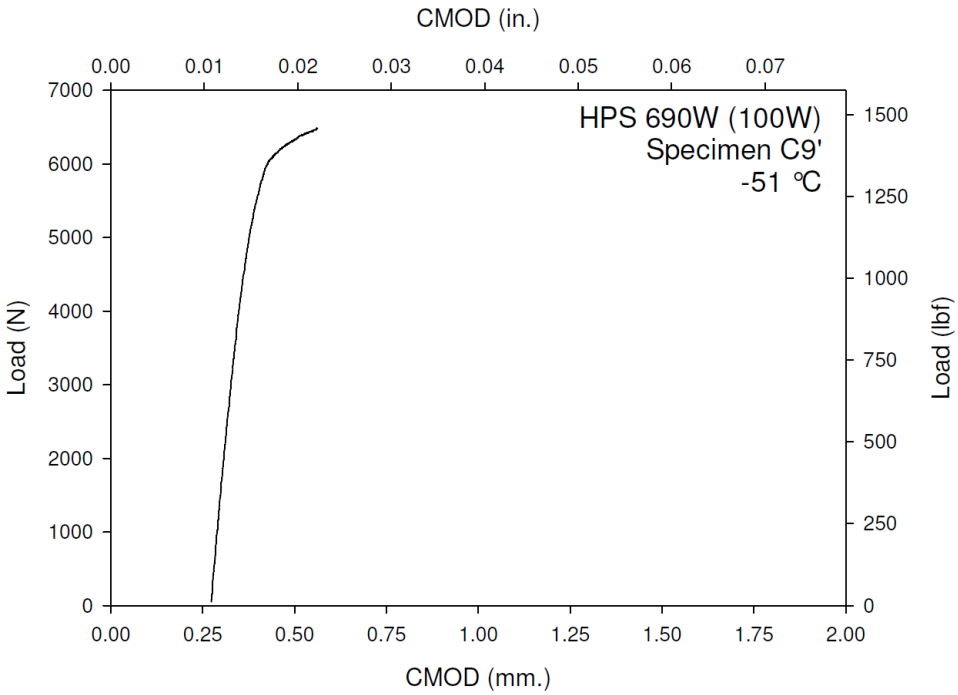

Figure C-33. Specimen C9' Test Record

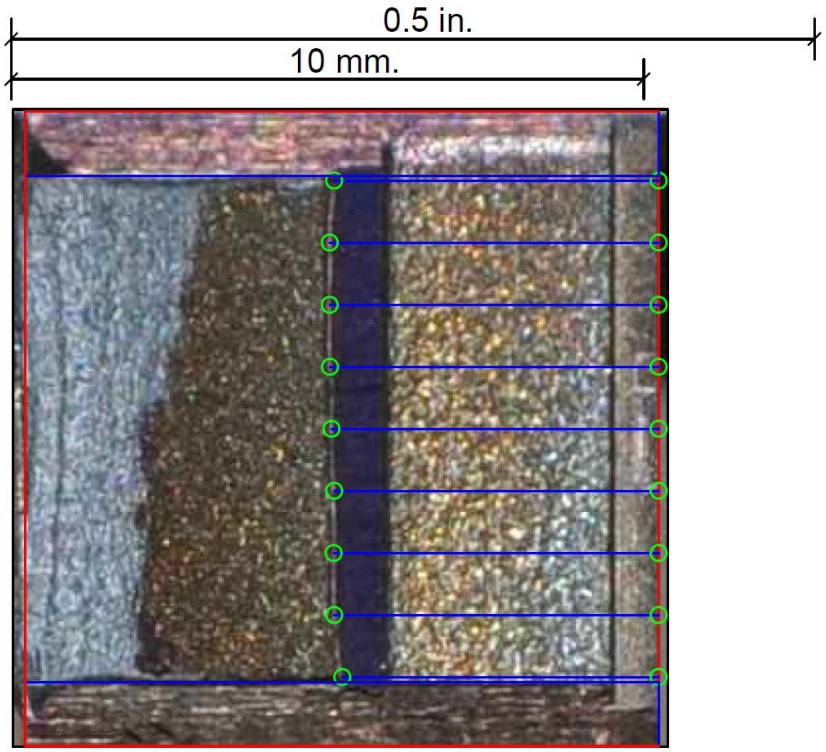

Figure C-34. Specimen C9' Fracture Surface

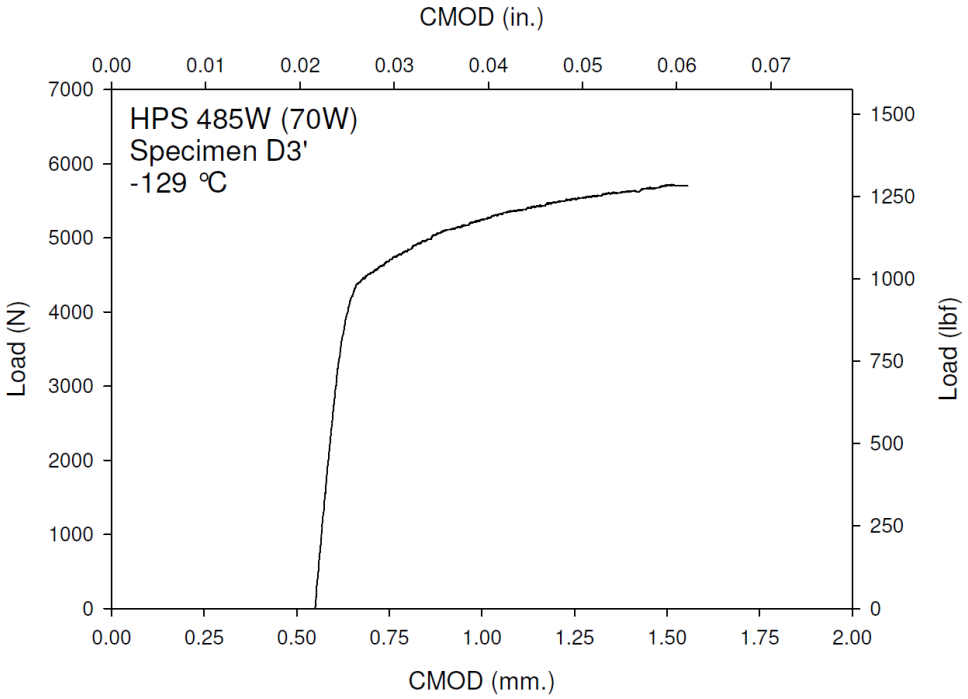

Figure C-35. Specimen D3' Test Record

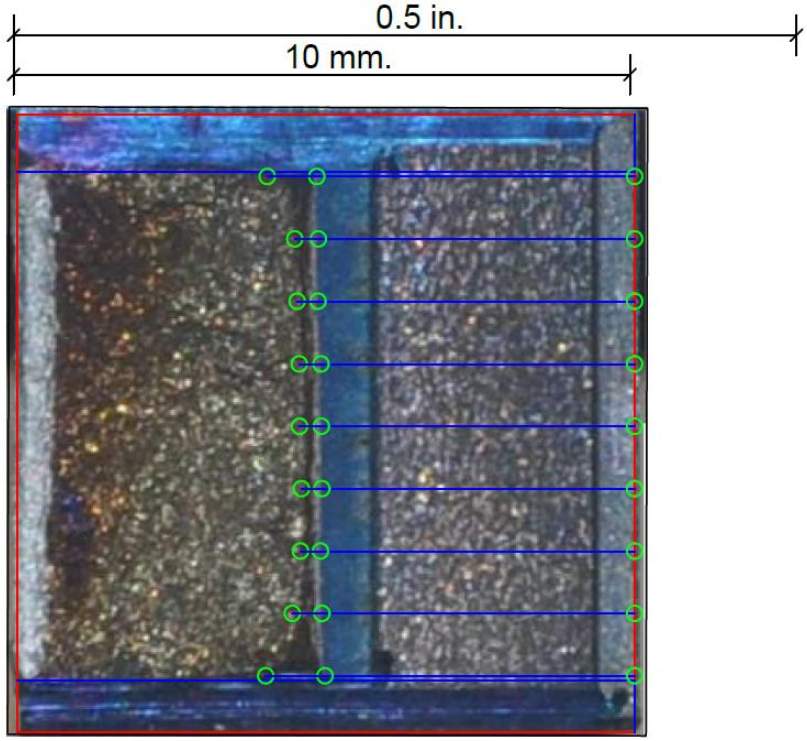

Figure C-36. Specimen D3' Fracture Surface

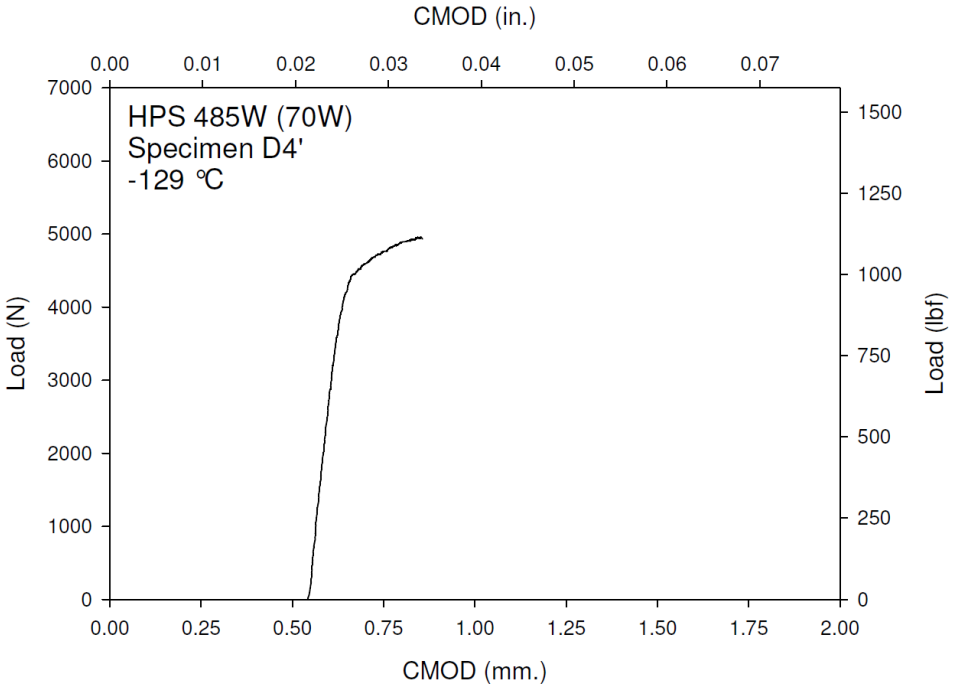

Figure C-37. Specimen D4' Test Record

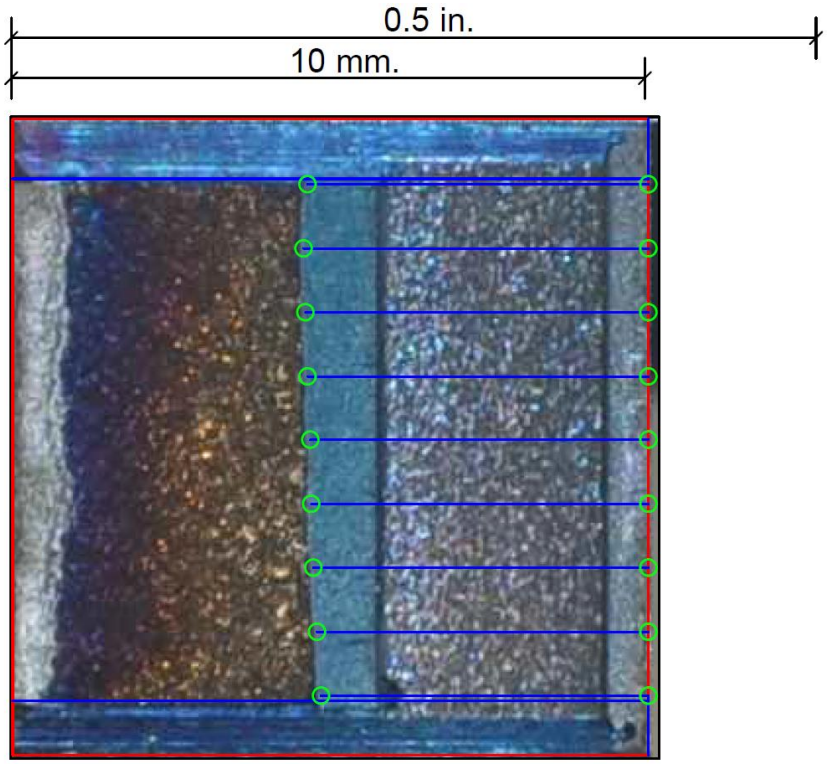

Figure C-38. Specimen D4' Fracture Surface

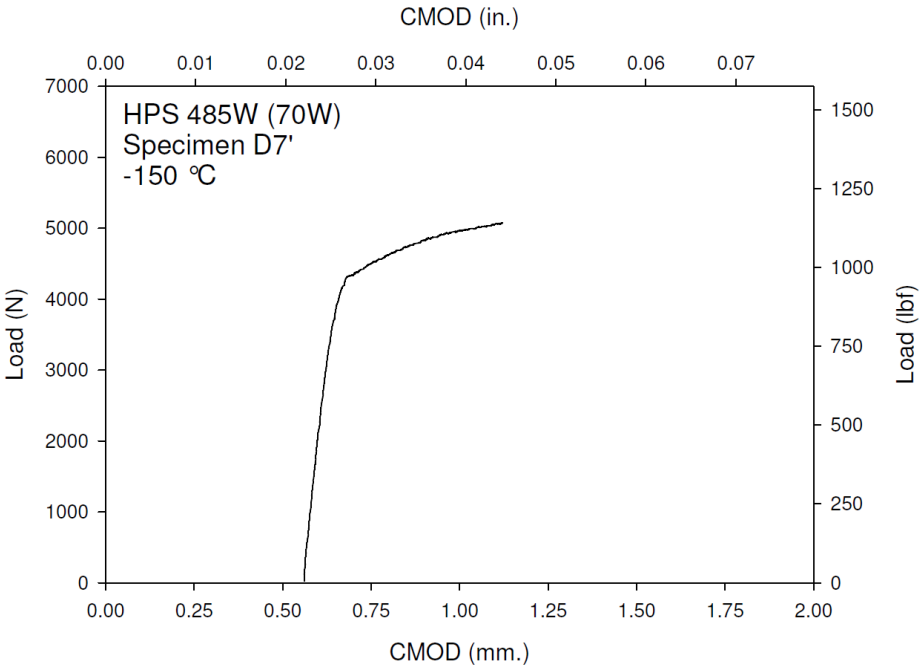

Figure C-39. Specimen D7' Test Record

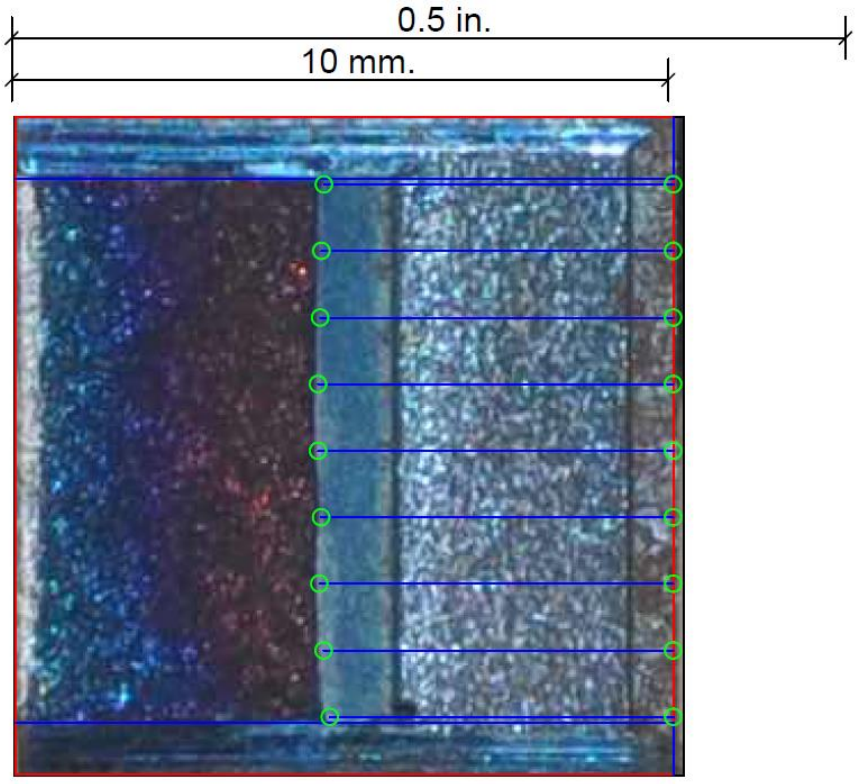

Figure C-40. Specimen D7' Fracture Surface

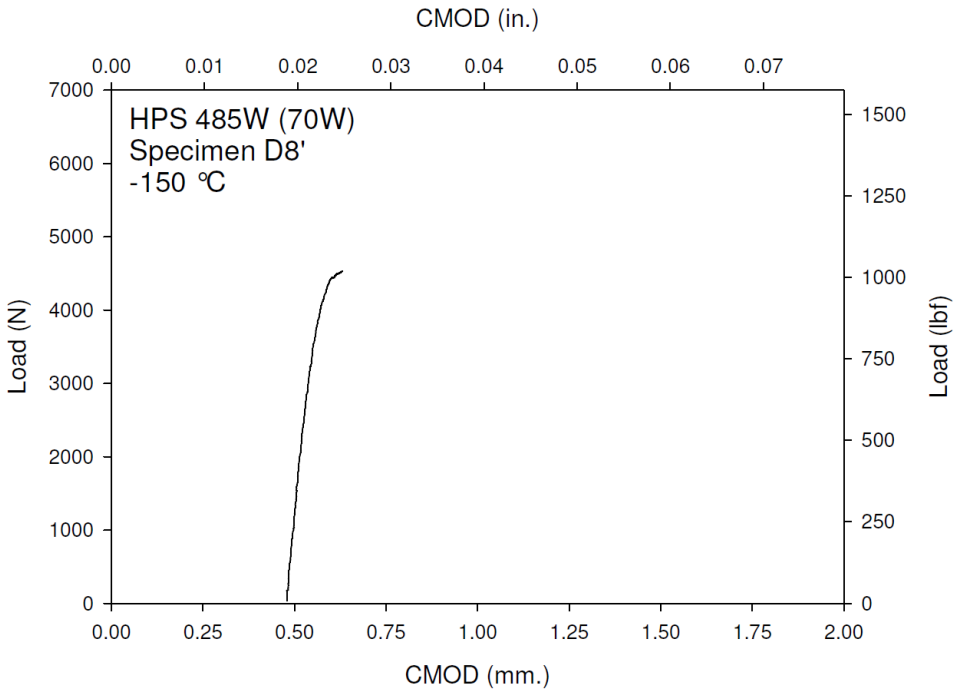

Figure C-41. Specimen D8' Test Record

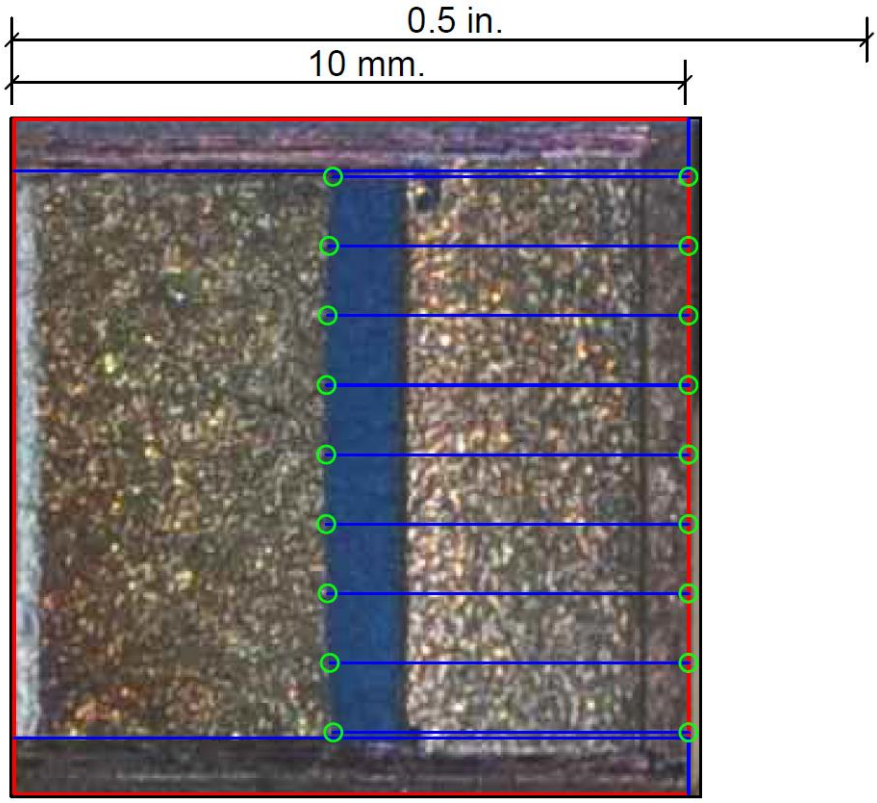

Figure C-42. Specimen D8' Fracture Surface

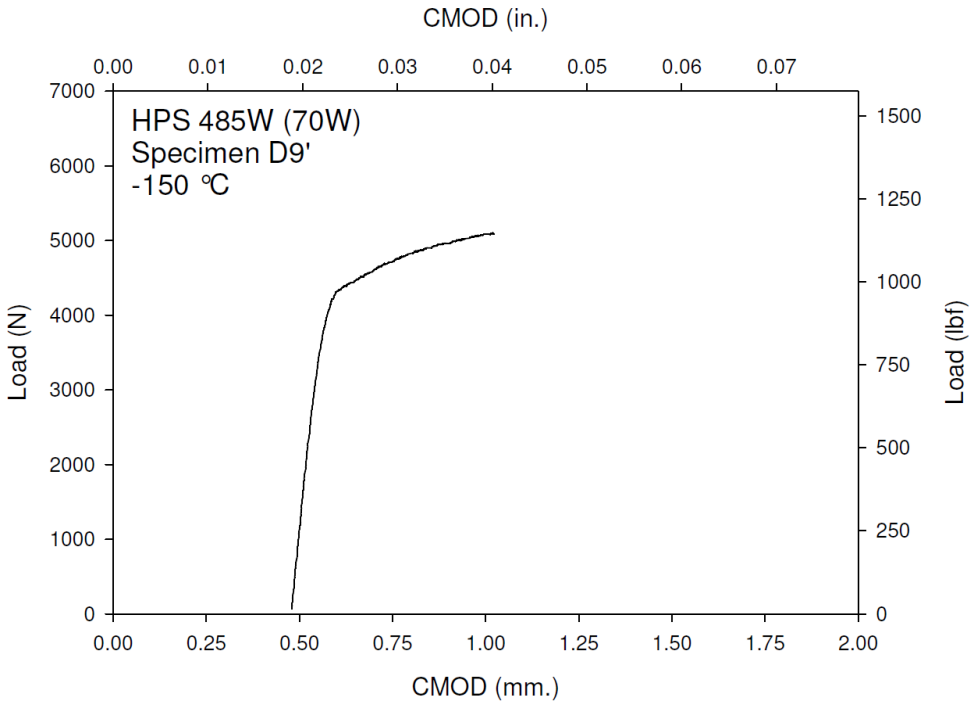

Figure C-43. Specimen D9' Test Record

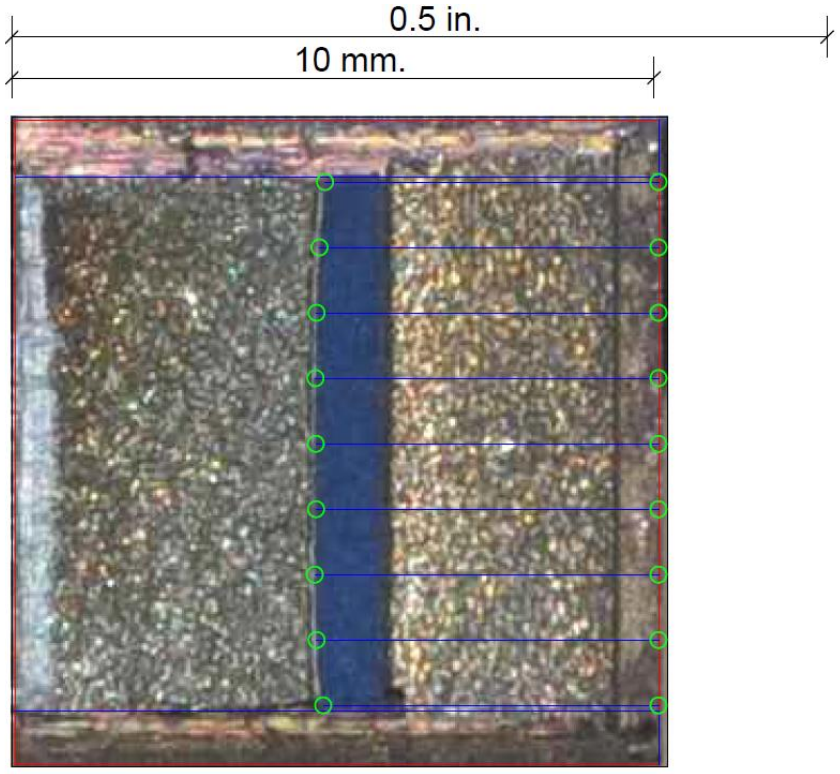

Figure C-44. Specimen D9' Fracture Surface

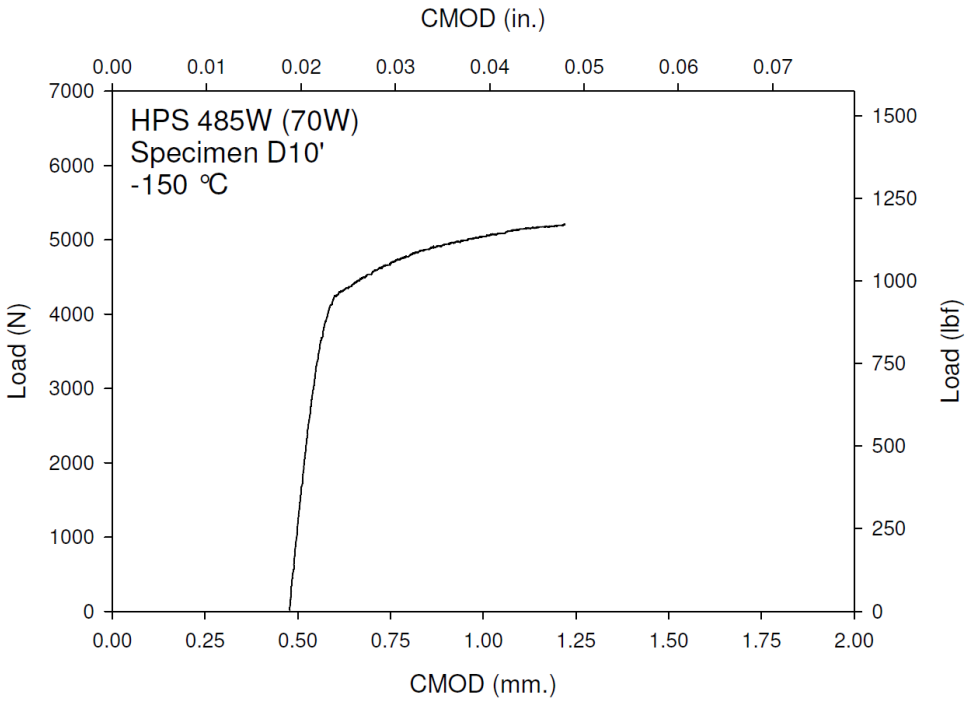

Figure C-45. Specimen D10' Test Record

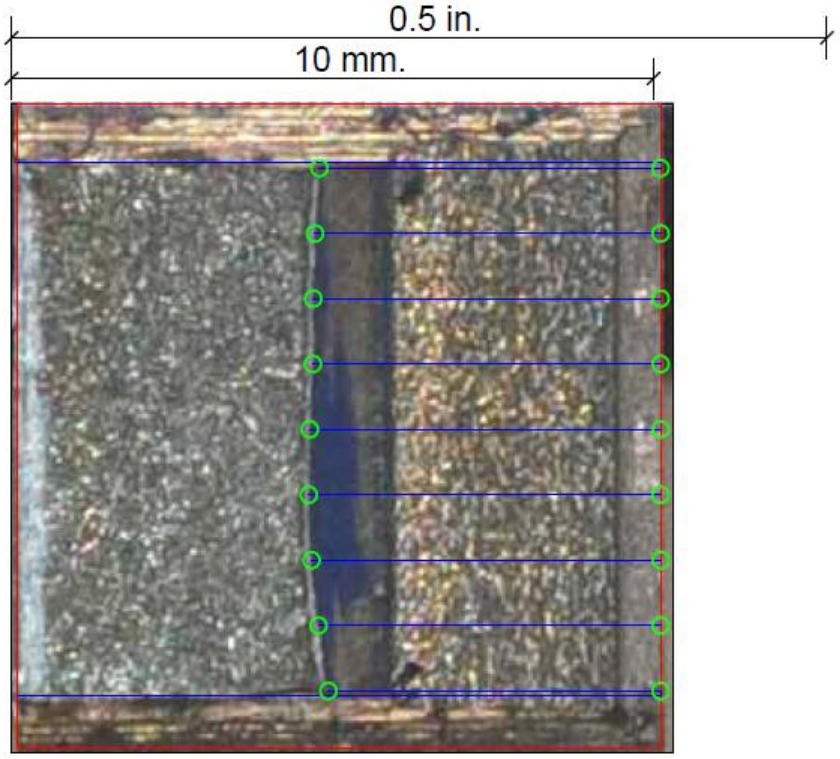

Figure C-46. Specimen D10' Fracture Surface

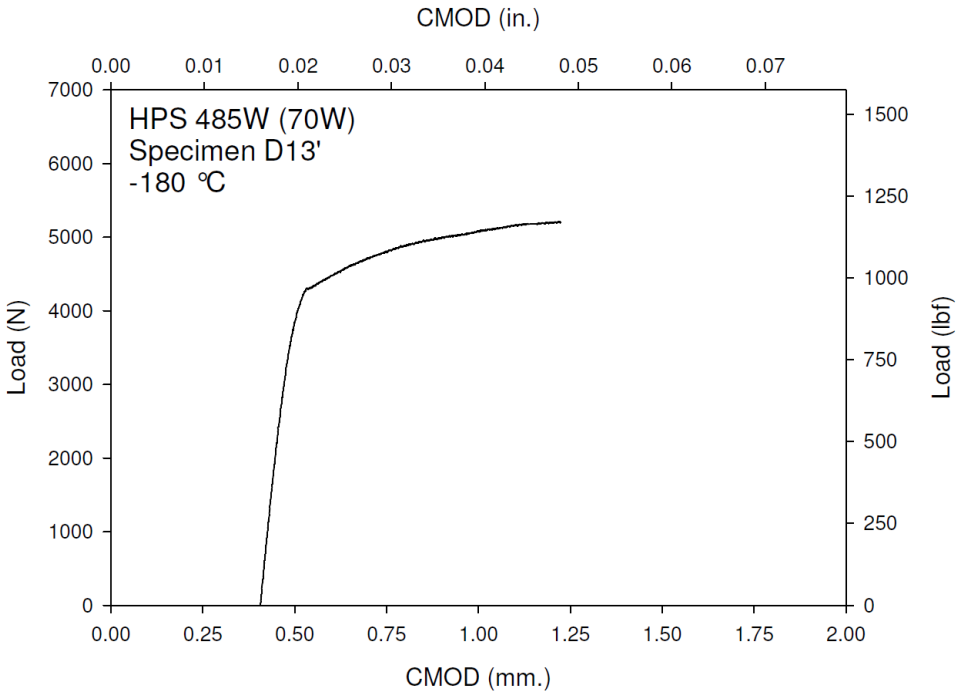

Figure C-47. Specimen D13' Test Record

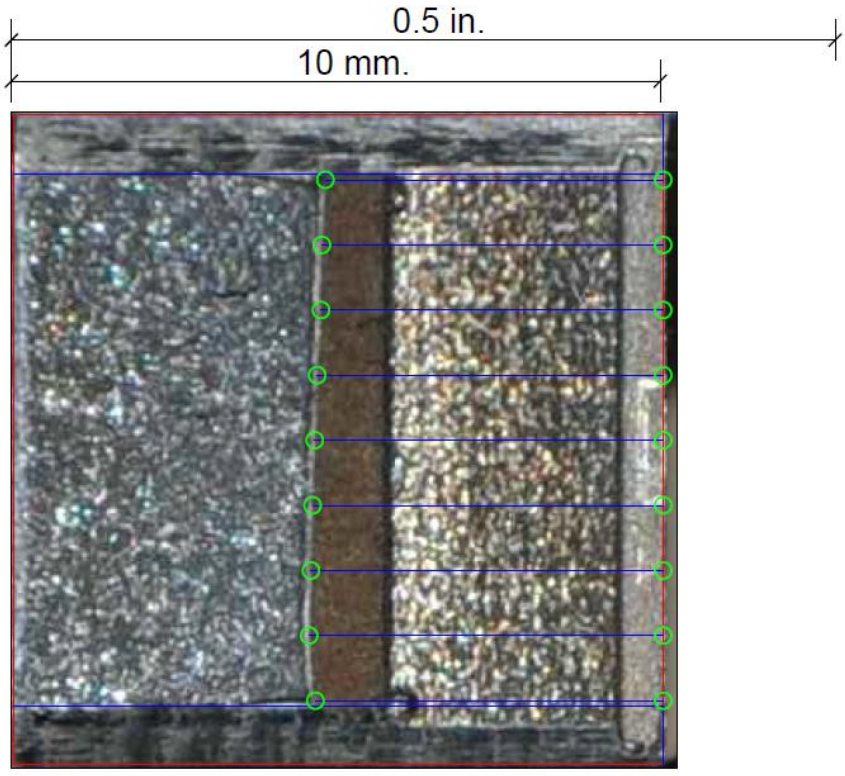

Figure C-48. Specimen D13' Fracture Surface

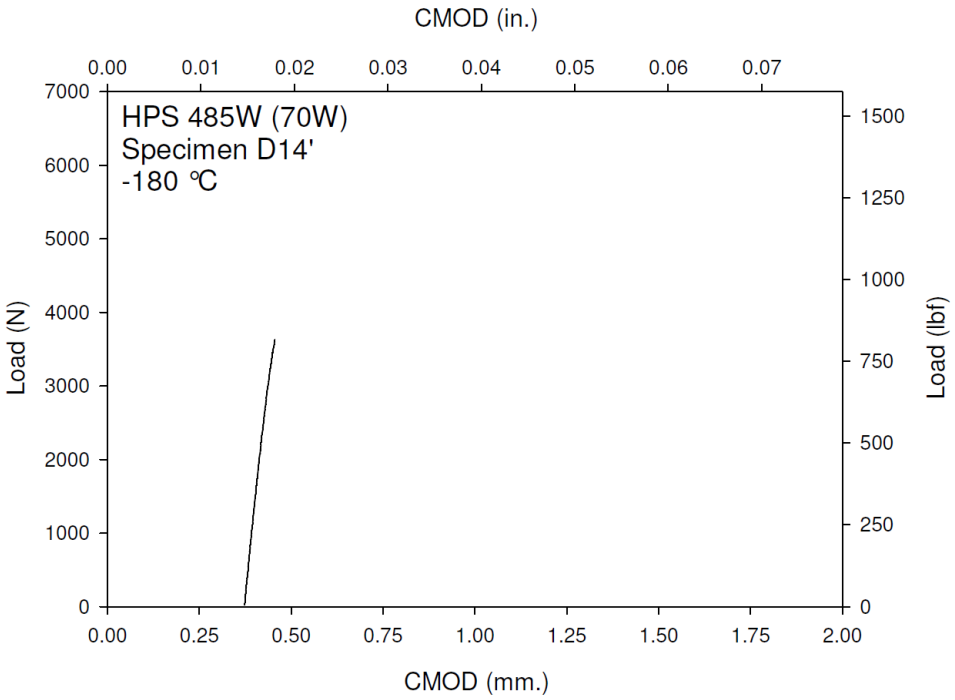

Figure C-49. Specimen D14' Test Record

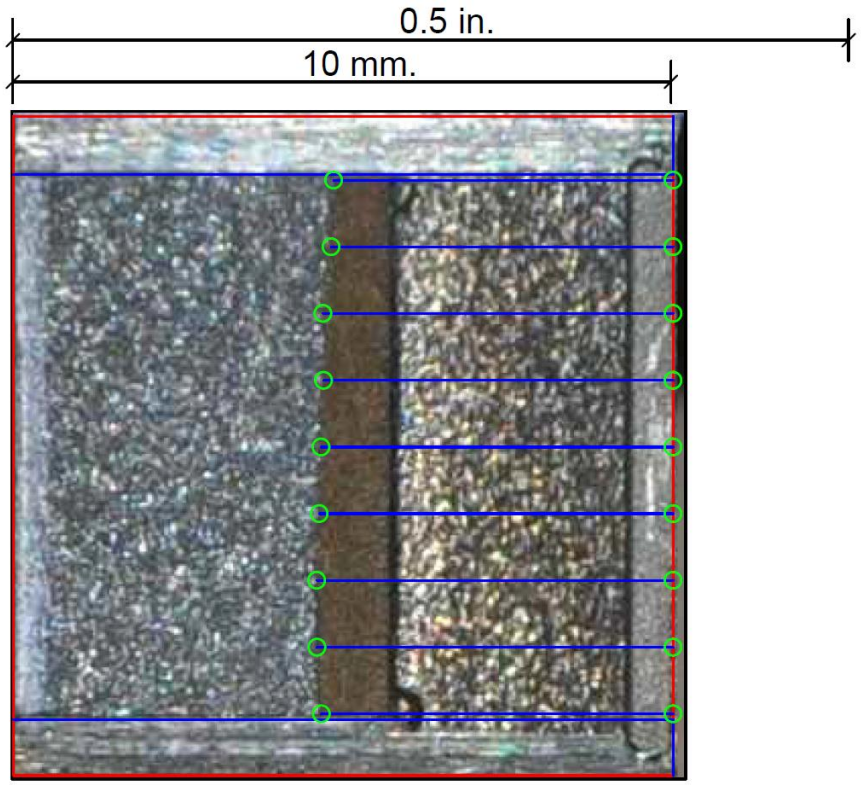

Figure C-50. Specimen D14' Fracture Surface

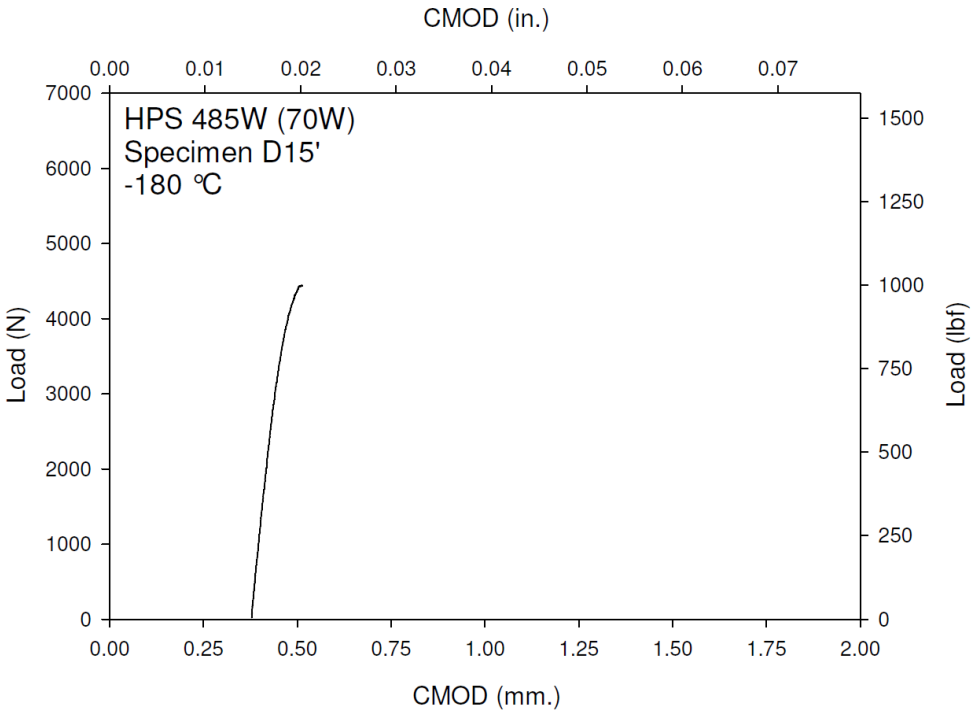

Figure C-51. Specimen D15' Test Record

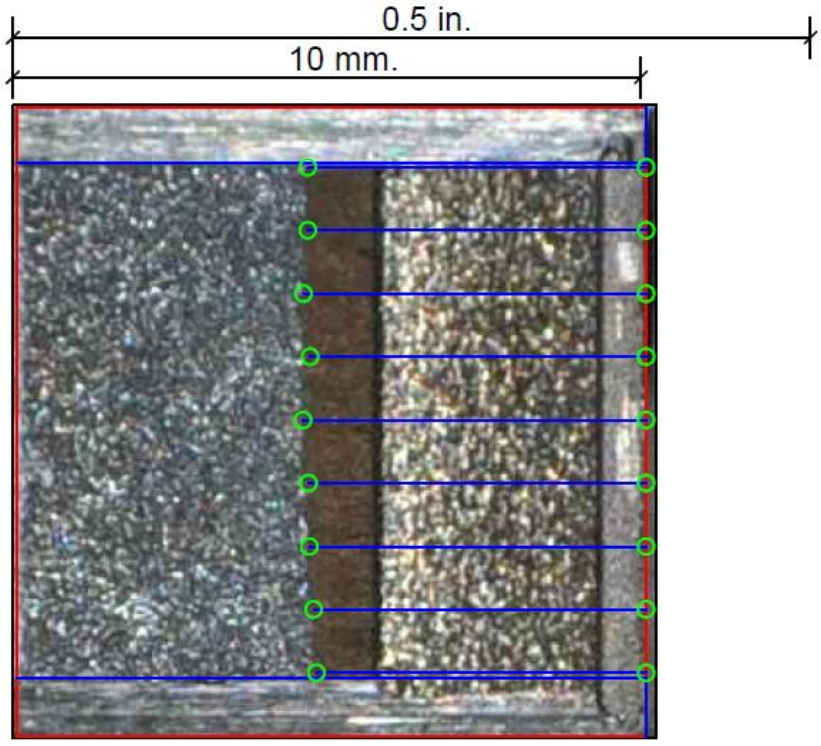

Figure C-52. Specimen D15' Fracture Surface

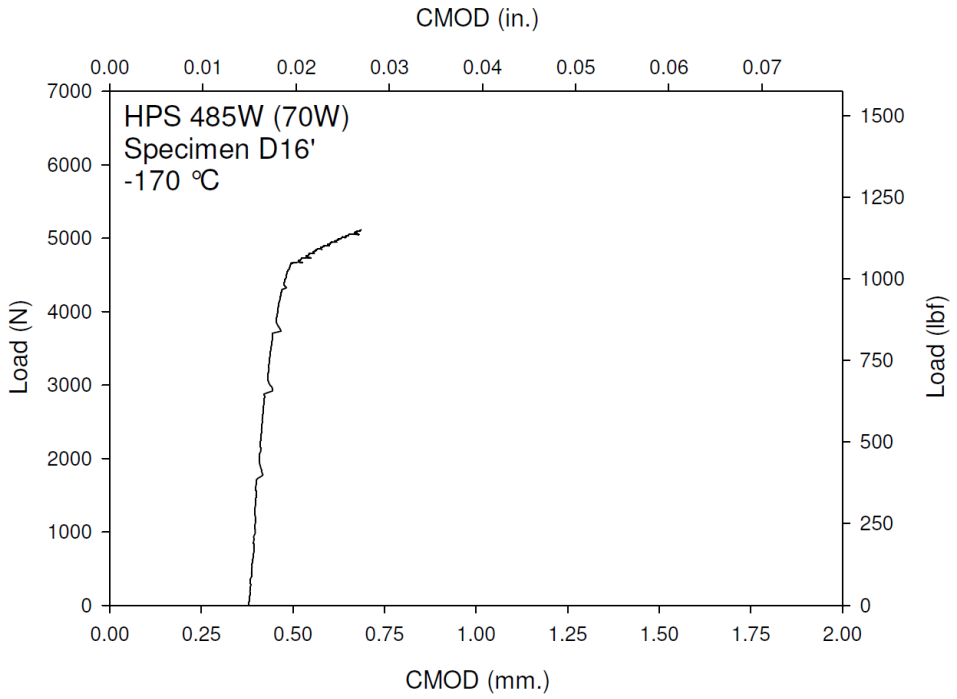

Figure C-53. Specimen D16' Test Record

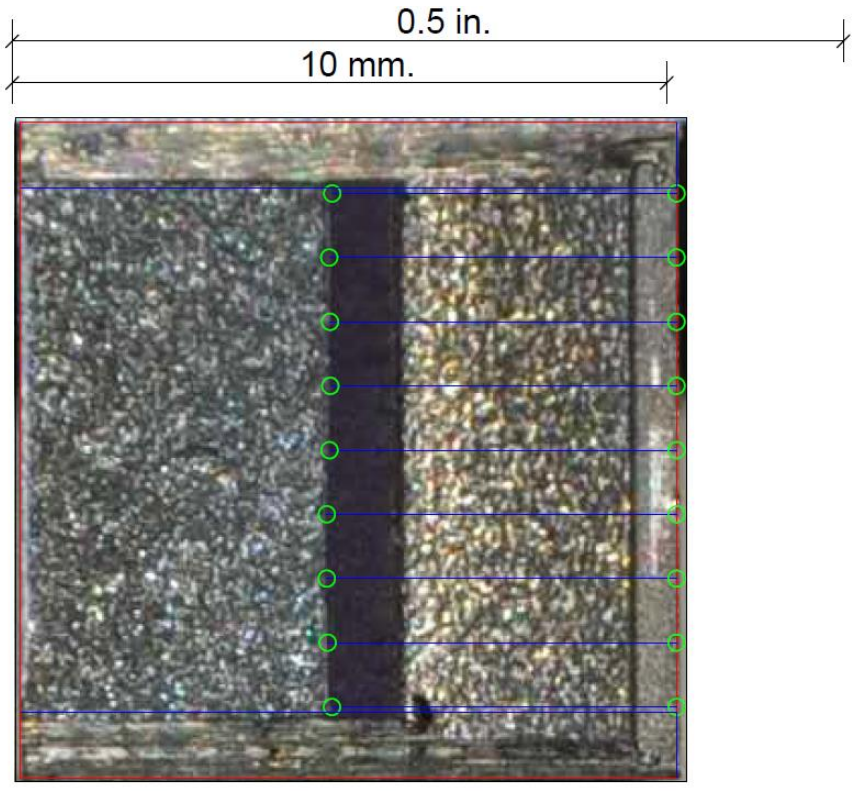

Figure C-54. Specimen D16' Fracture Surface

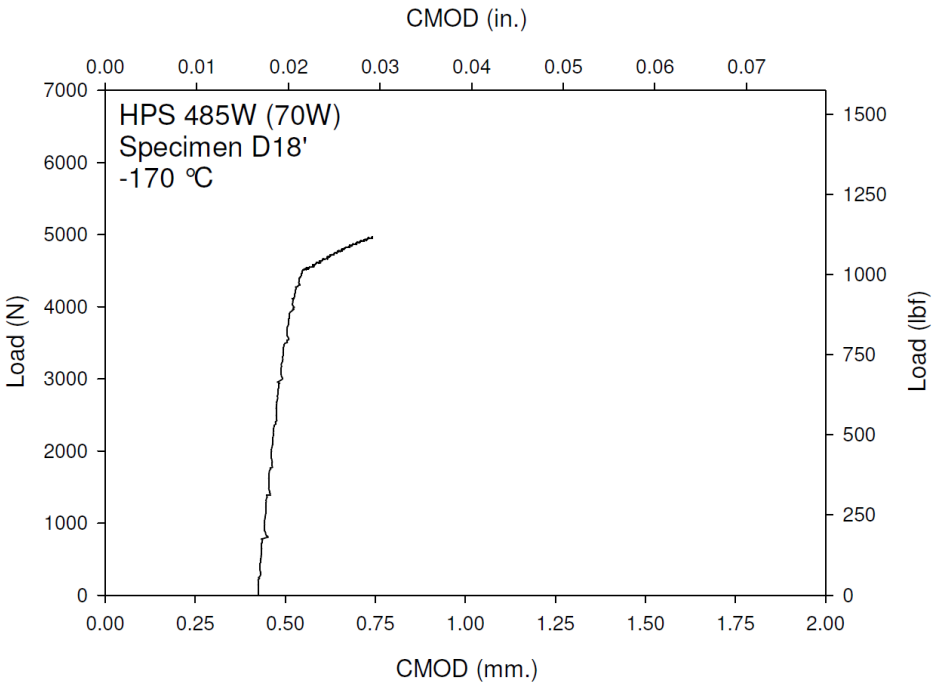

Figure C-55. Specimen D18' Test Record

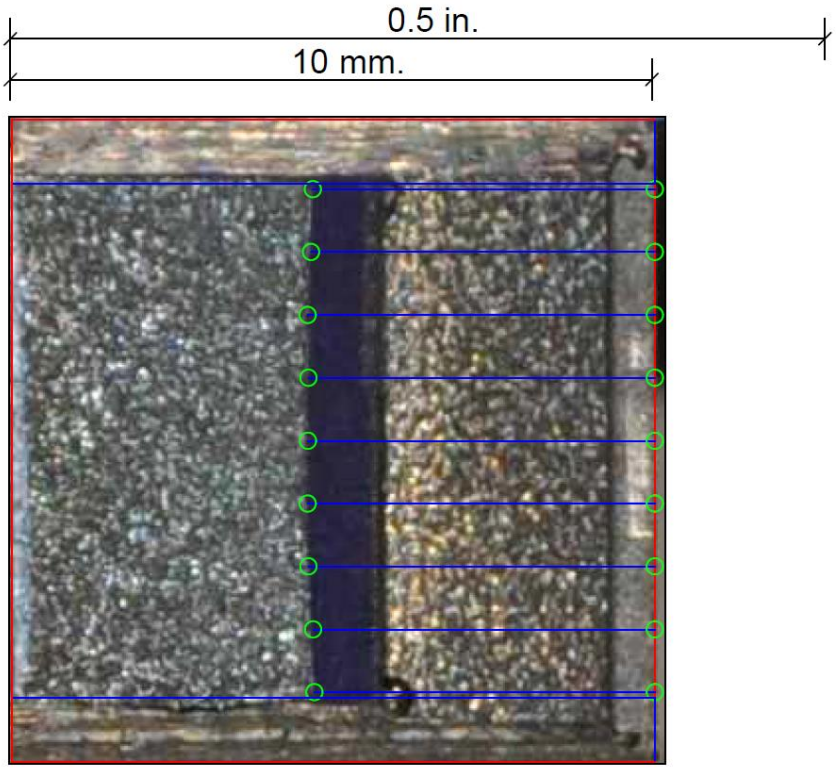

Figure C-56. Specimen D18' Fracture Surface

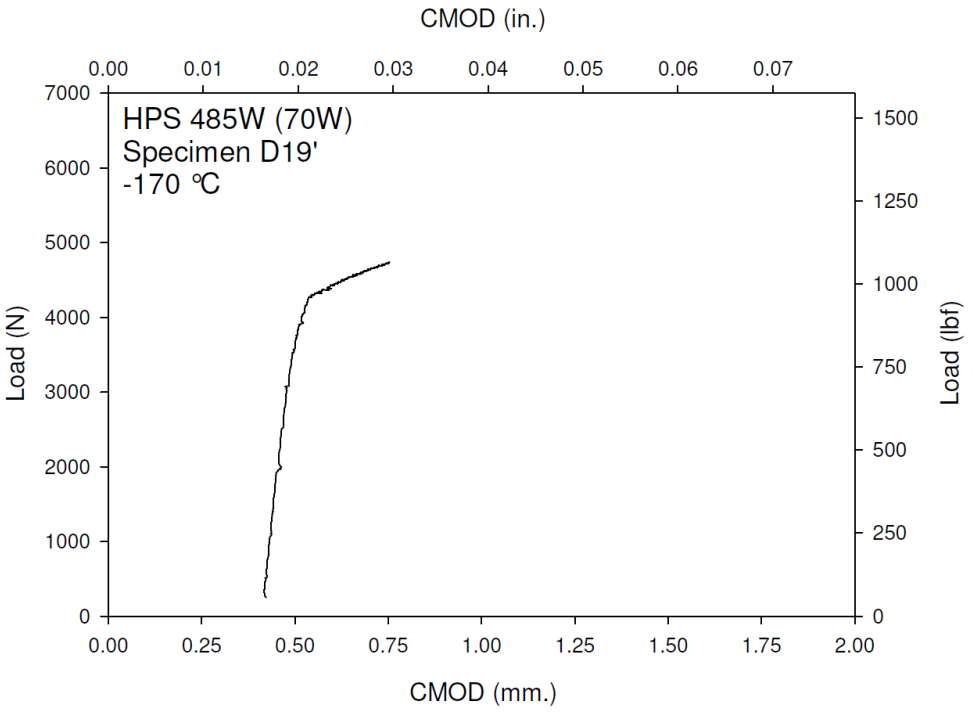

Figure C-57. Specimen D19' Test Record

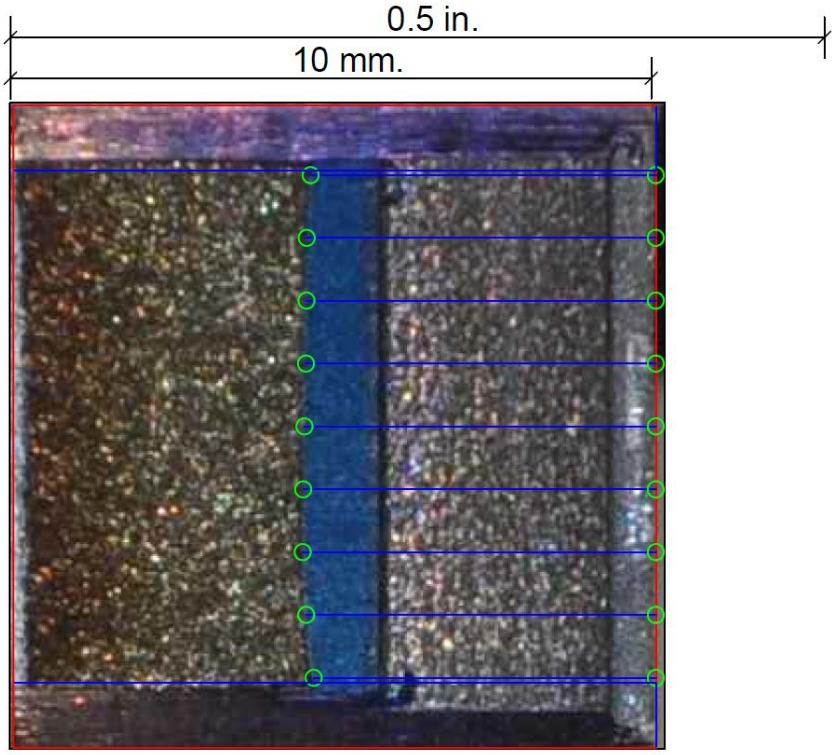

Figure C-58. Specimen D19' Fracture Surface

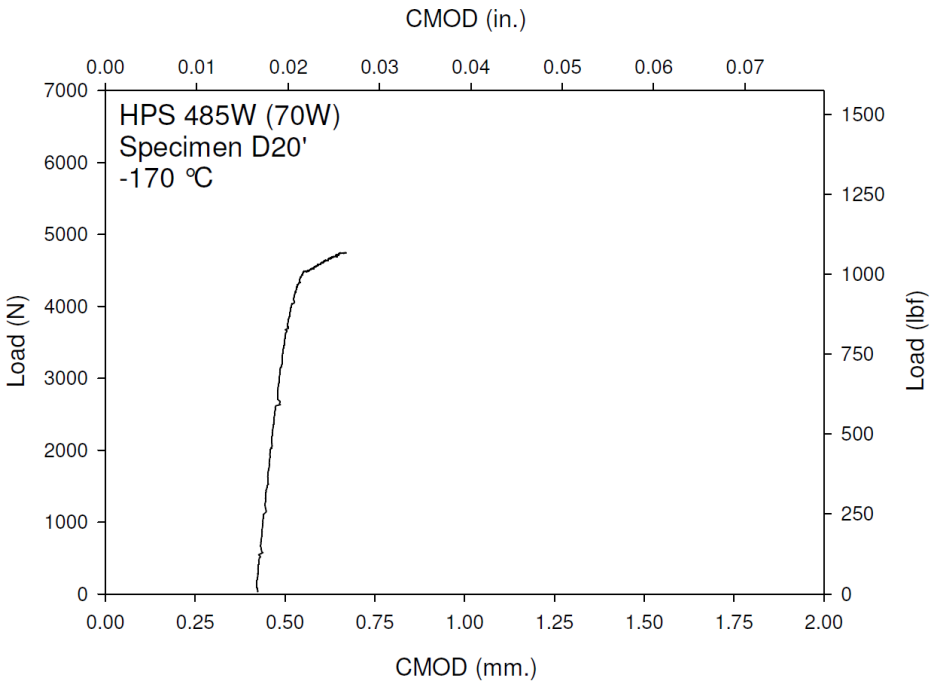

Figure C-59. Specimen D20' Test Record

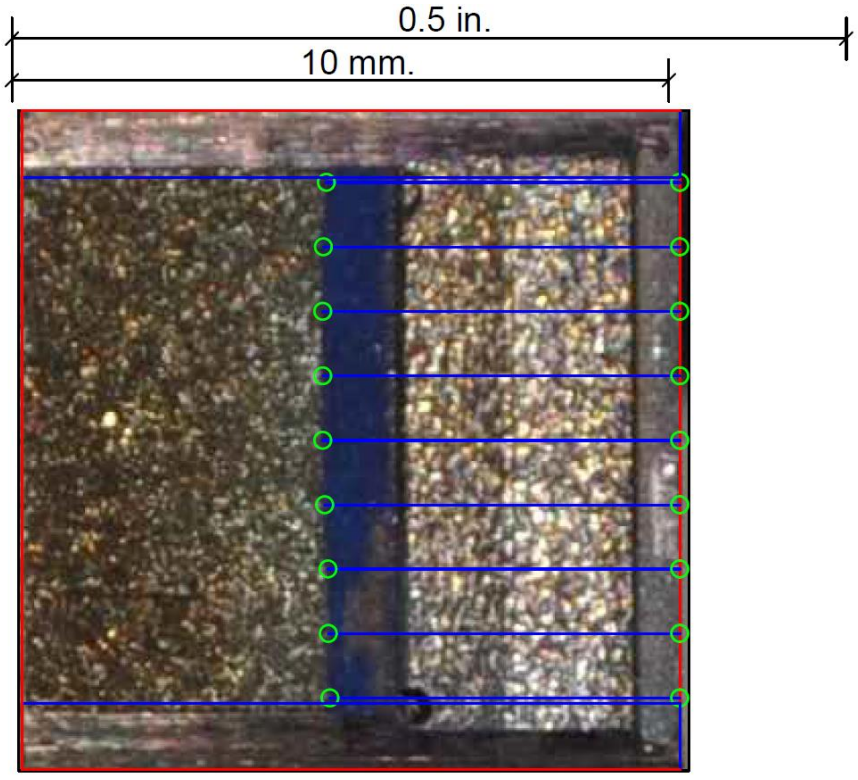

Figure C-60. Specimen D20' Fracture Surface

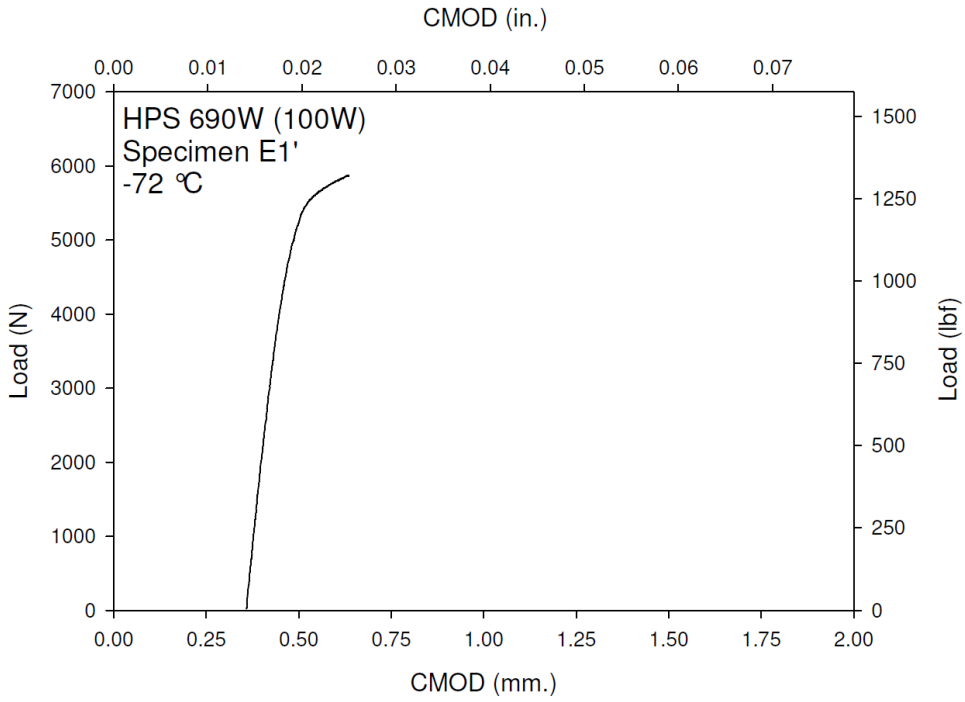

Figure C-61. Specimen E1' Test Record

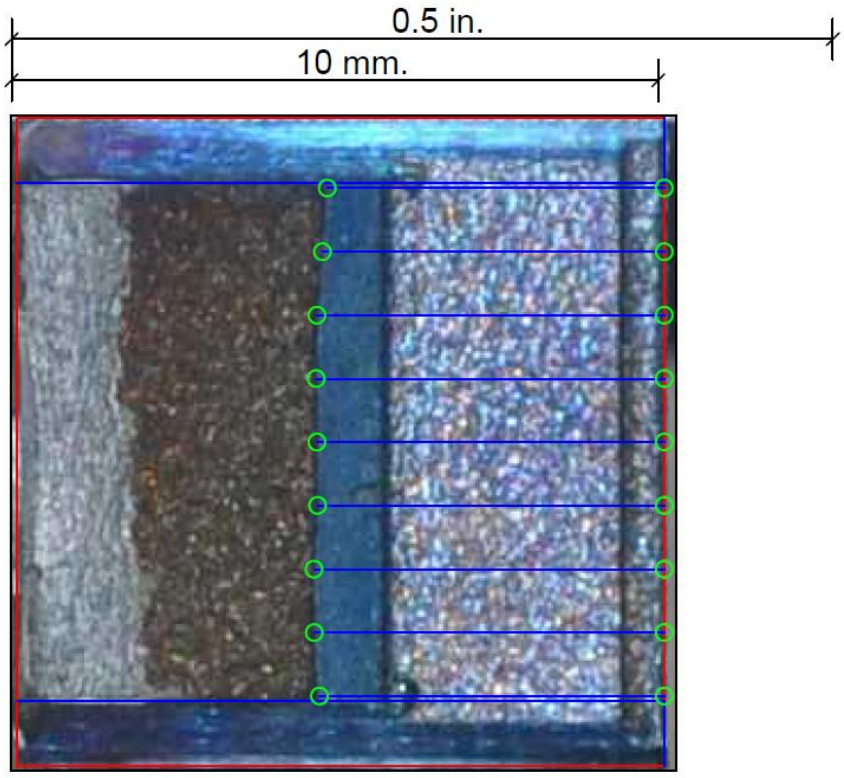

Figure C-62. Specimen E1' Fracture Surface

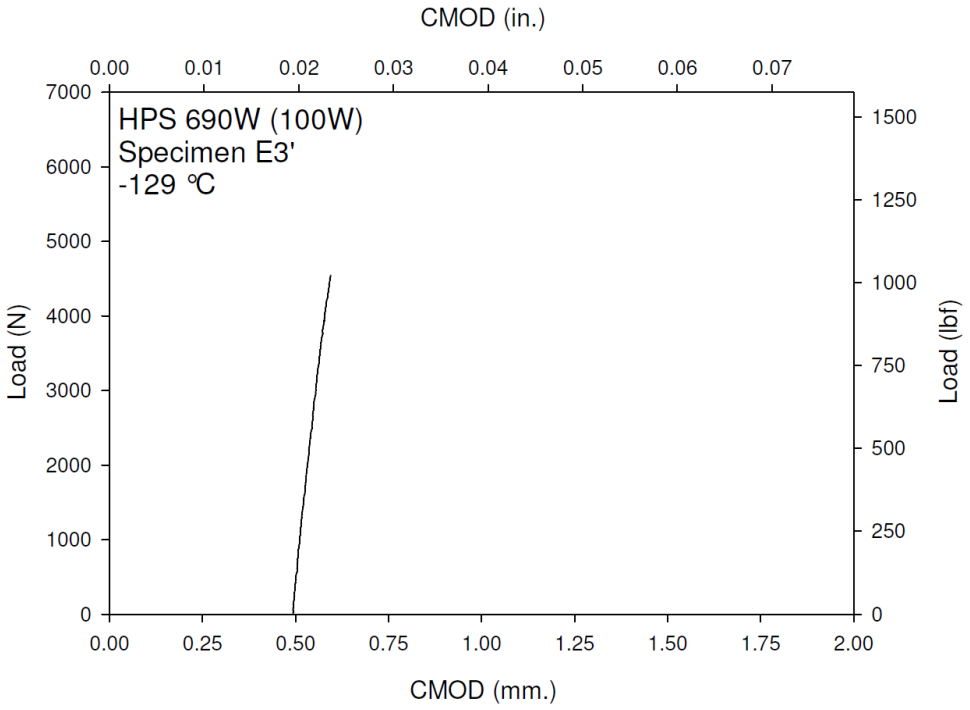

Figure C-63. Specimen E3' Test Record

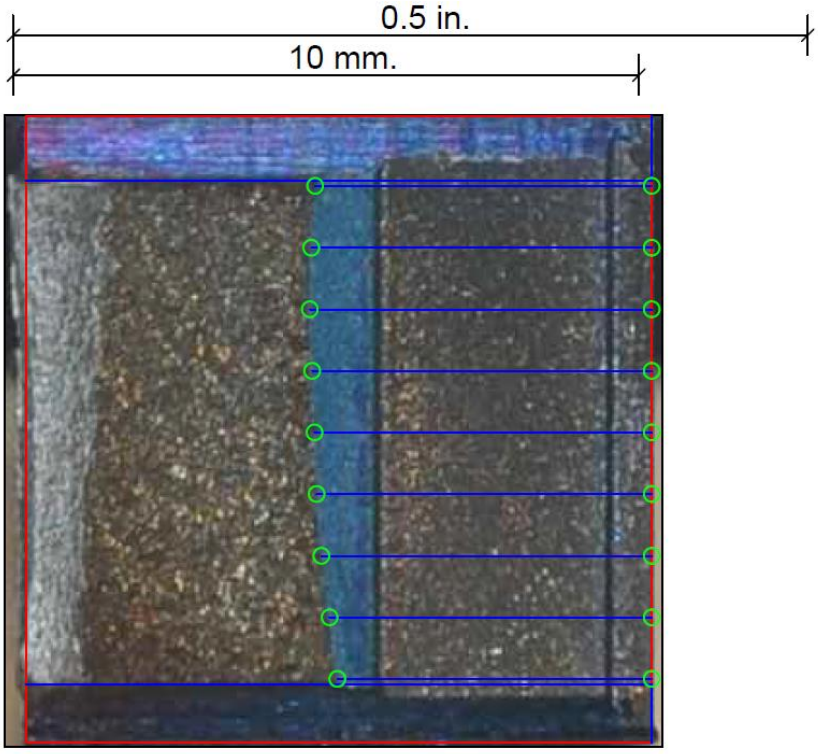

Figure C-64. Specimen E3' Fracture Surface

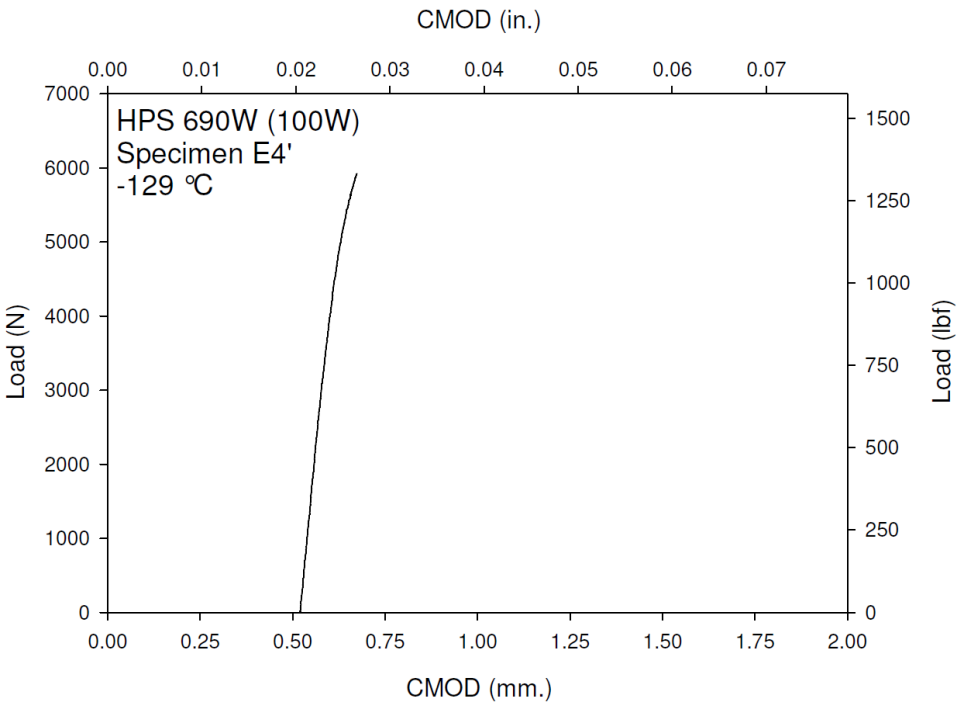

Figure C-65. Specimen E4' Test Record

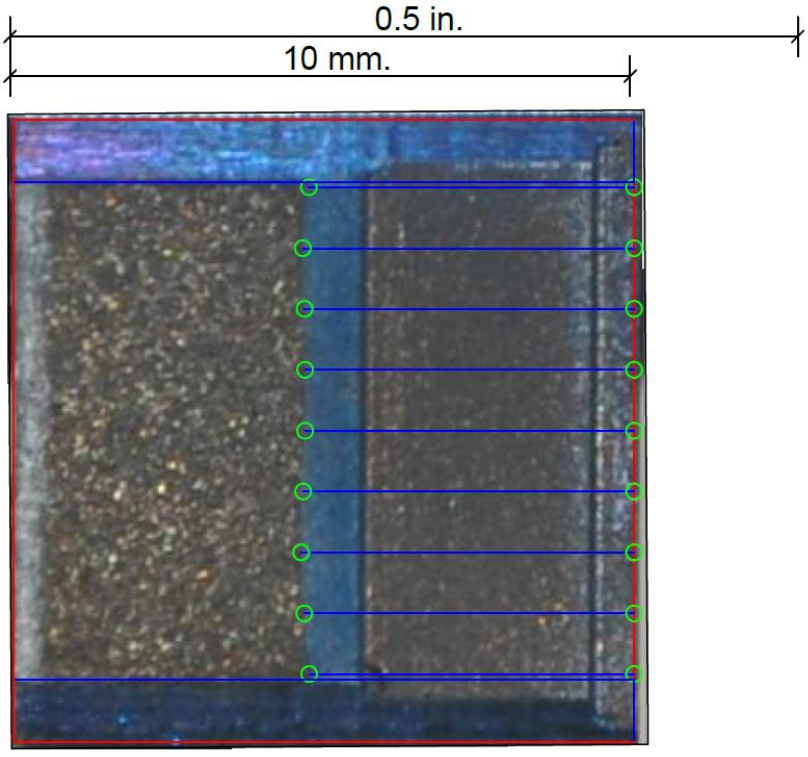

Figure C-66. Specimen E4' Fracture Surface

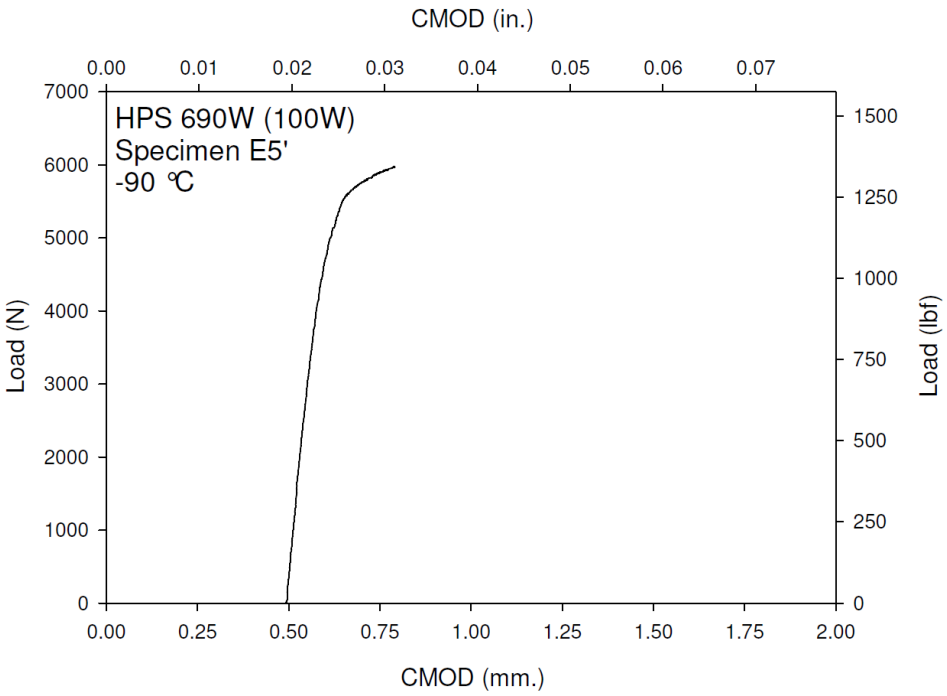

Figure C-67. Specimen E5' Test Record

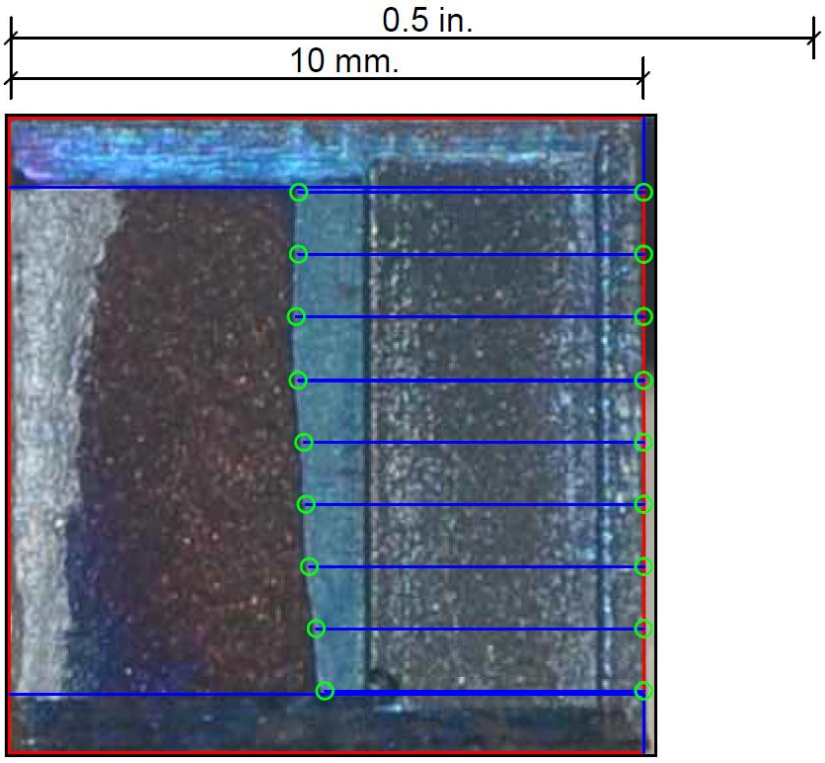

Figure C-68. Specimen E5' Fracture Surface

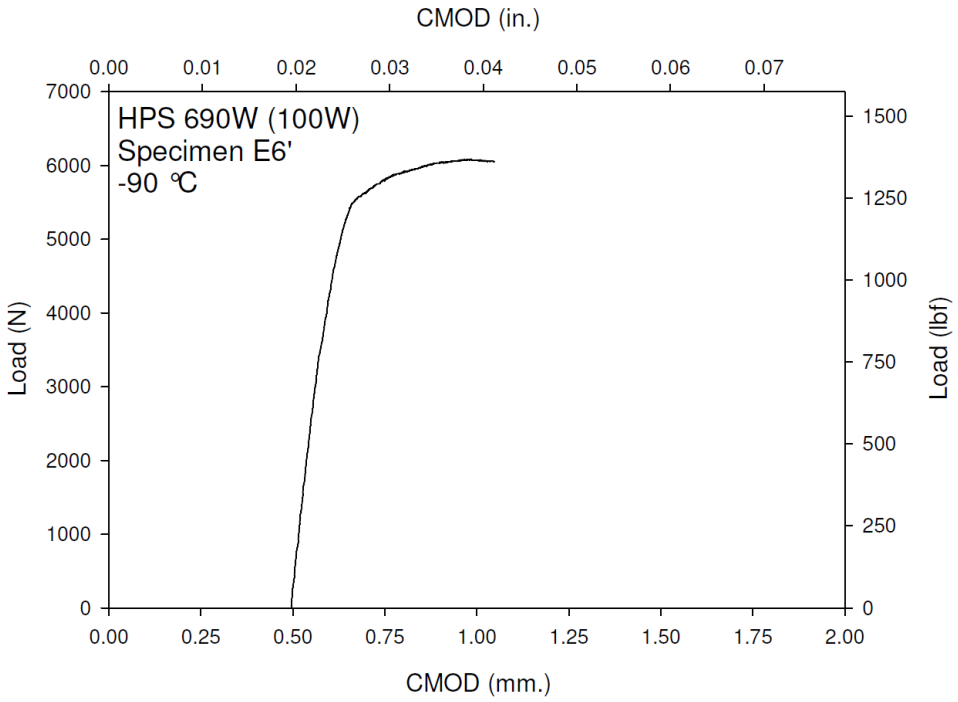

Figure C-69. Specimen E6' Test Record

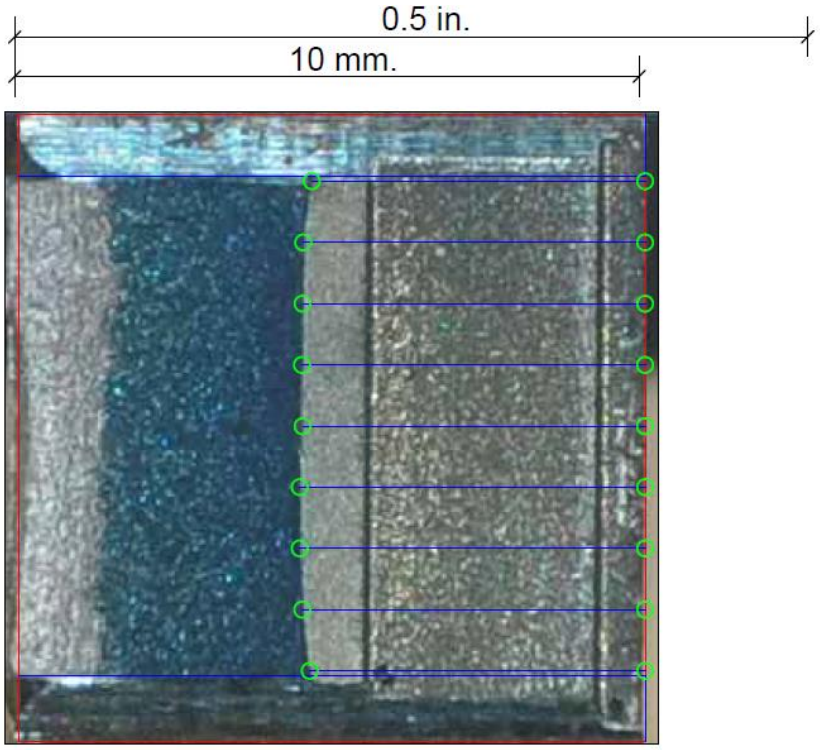

Figure C-70. Specimen E6' Fracture Surface

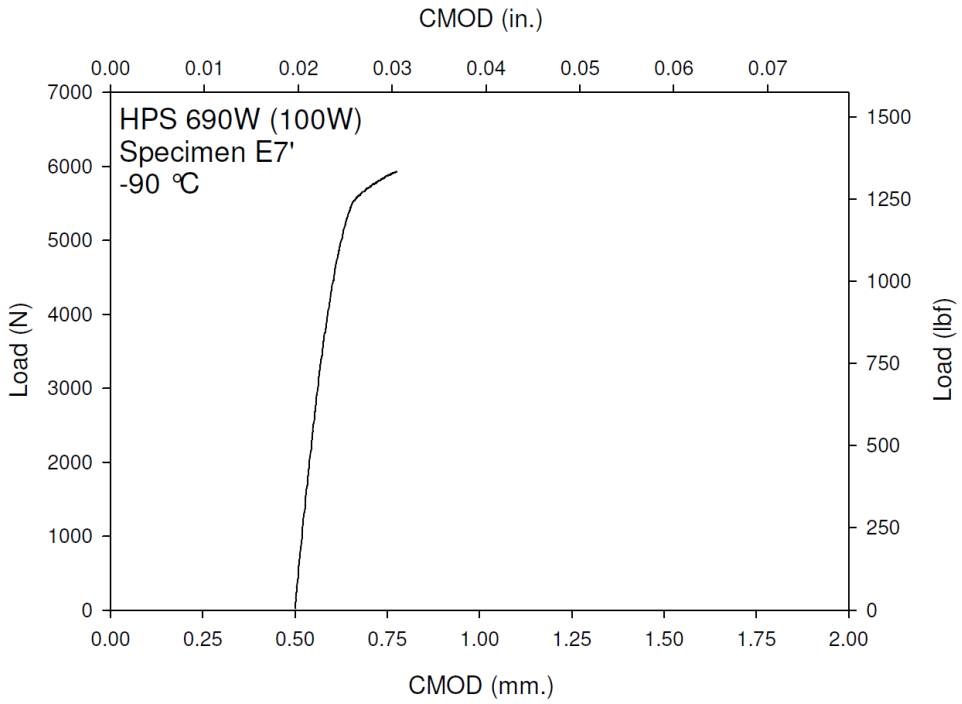

Figure C-71. Specimen E7' Test Record

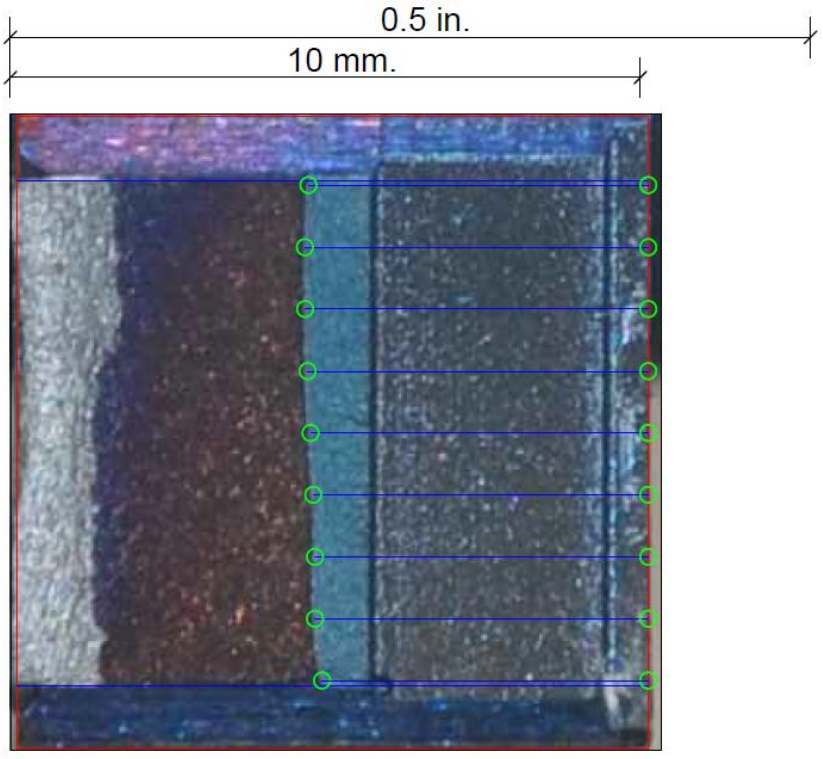

Figure C-72. Specimen E7' Fracture Surface

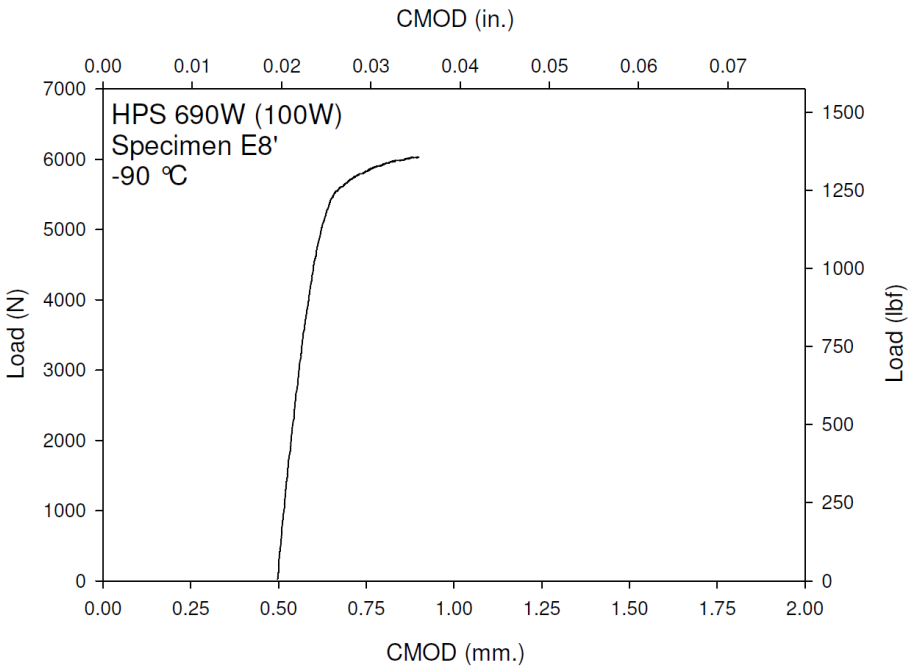

Figure C-73. Specimen E8' Test Record

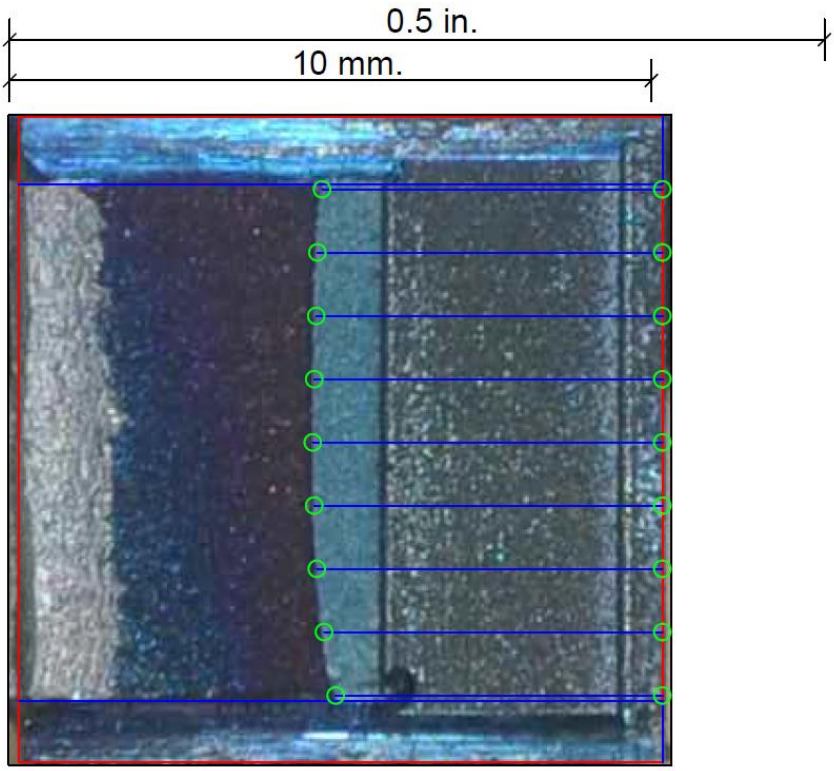

Figure C-74. Specimen E8' Fracture Surface

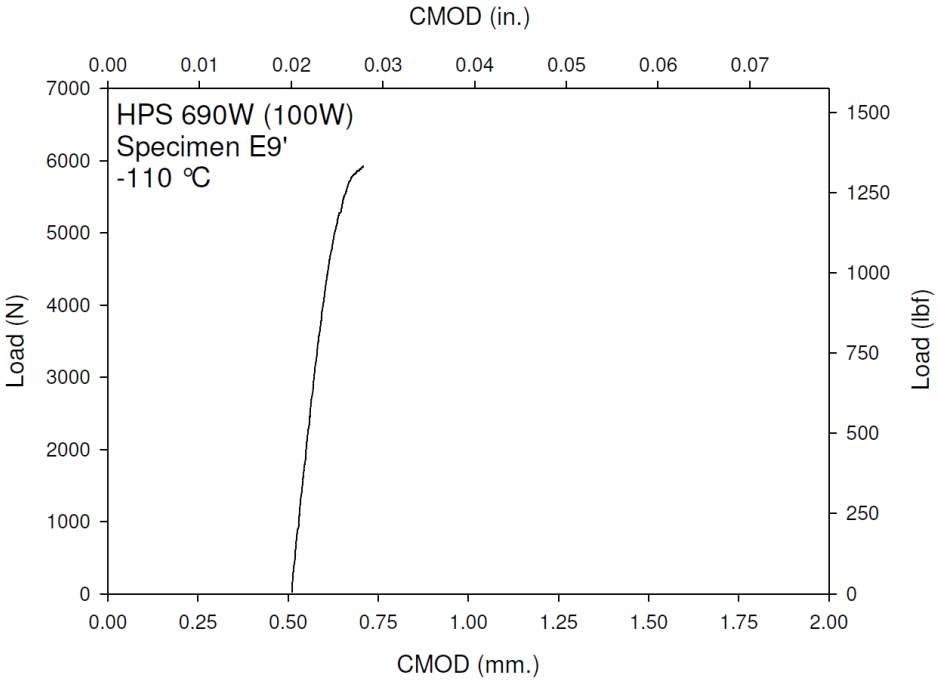

Figure C-75. Specimen E9' Test Record

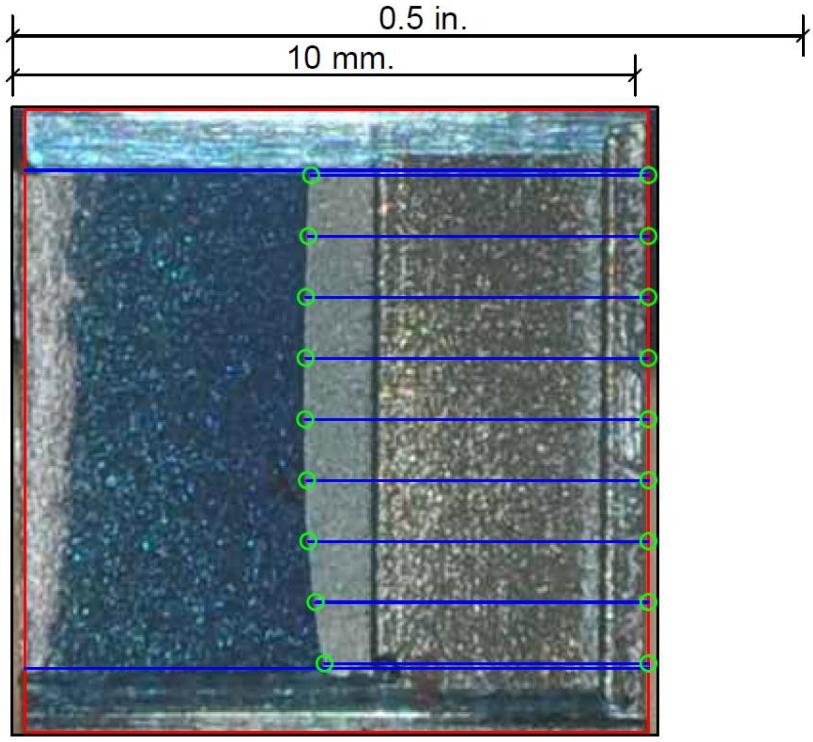

Figure C-76. Specimen E9' Fracture Surface

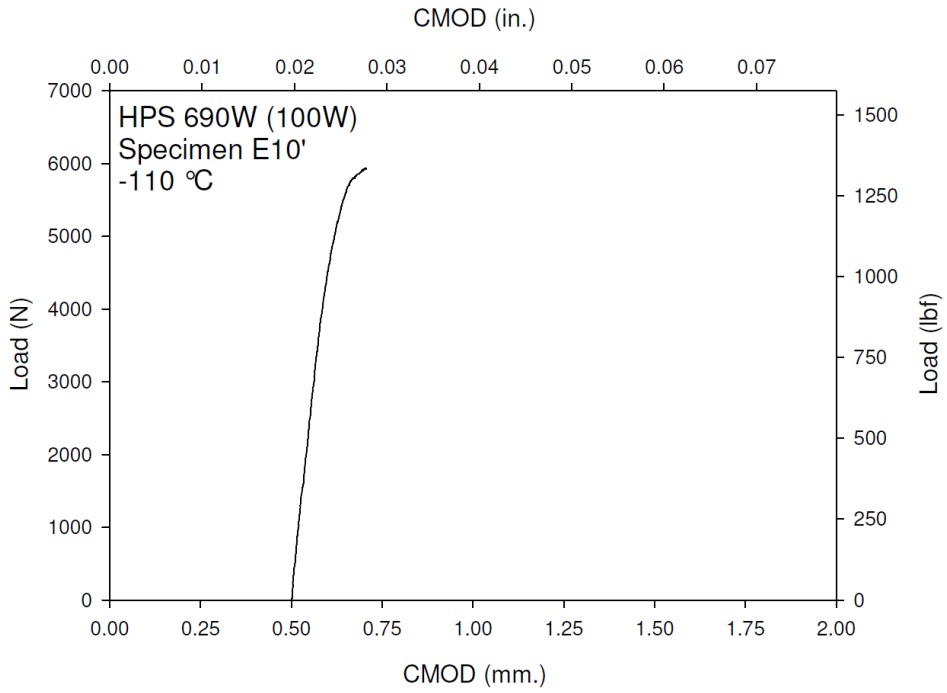

Figure C-77. Specimen E10' Test Record

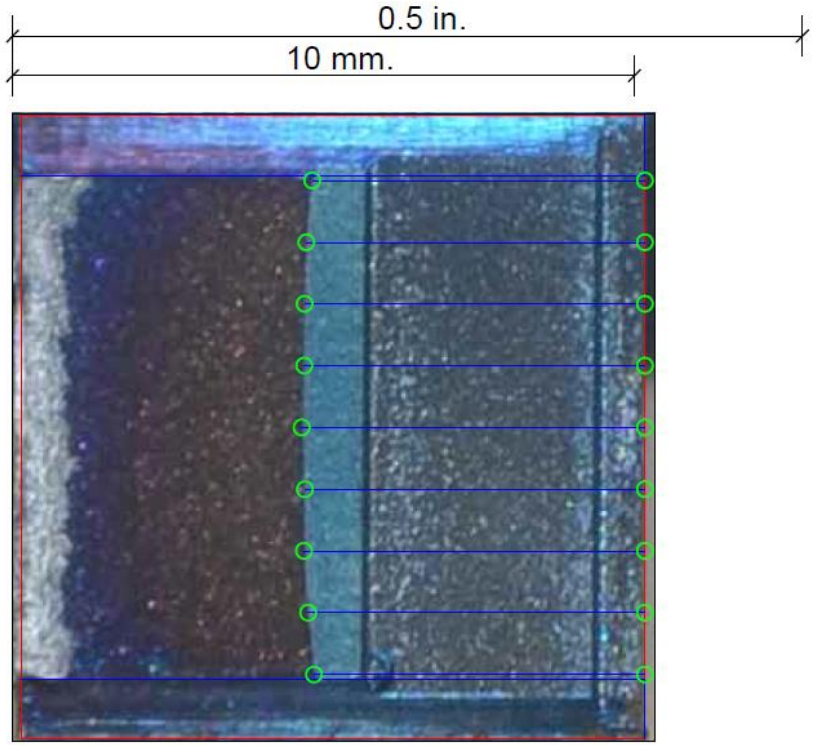

Figure C-78. Specimen E10' Fracture Surface

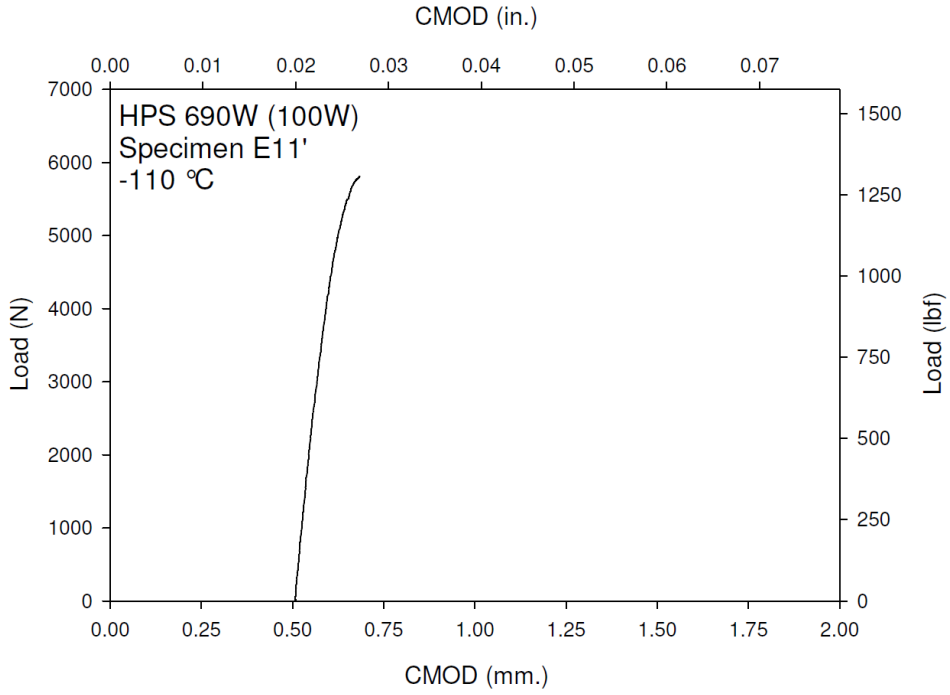

Figure C-79. Specimen E11' Test Record

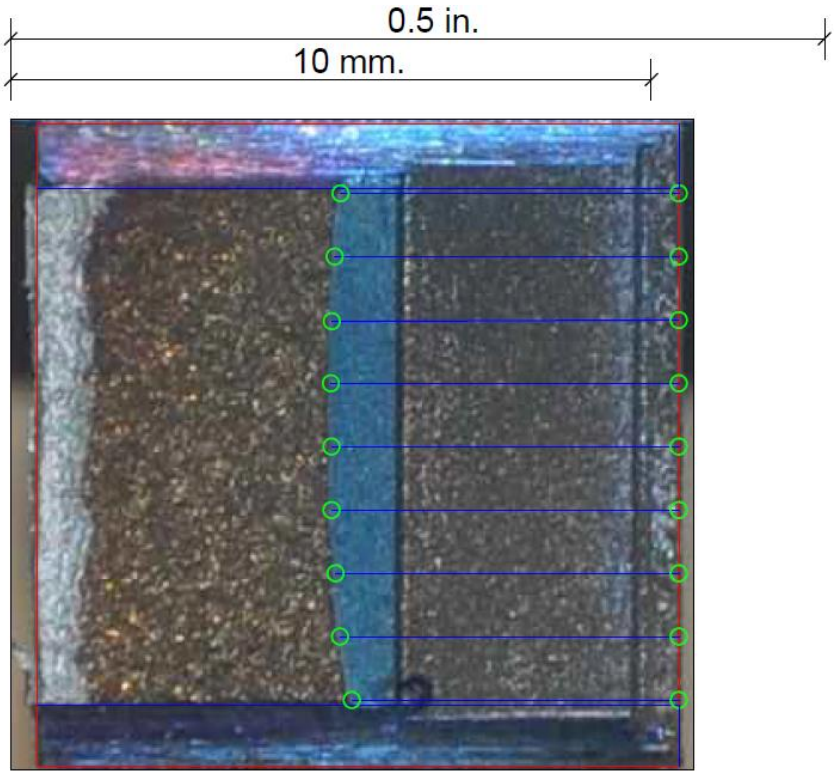

Figure C-80. Specimen E11' Fracture Surface

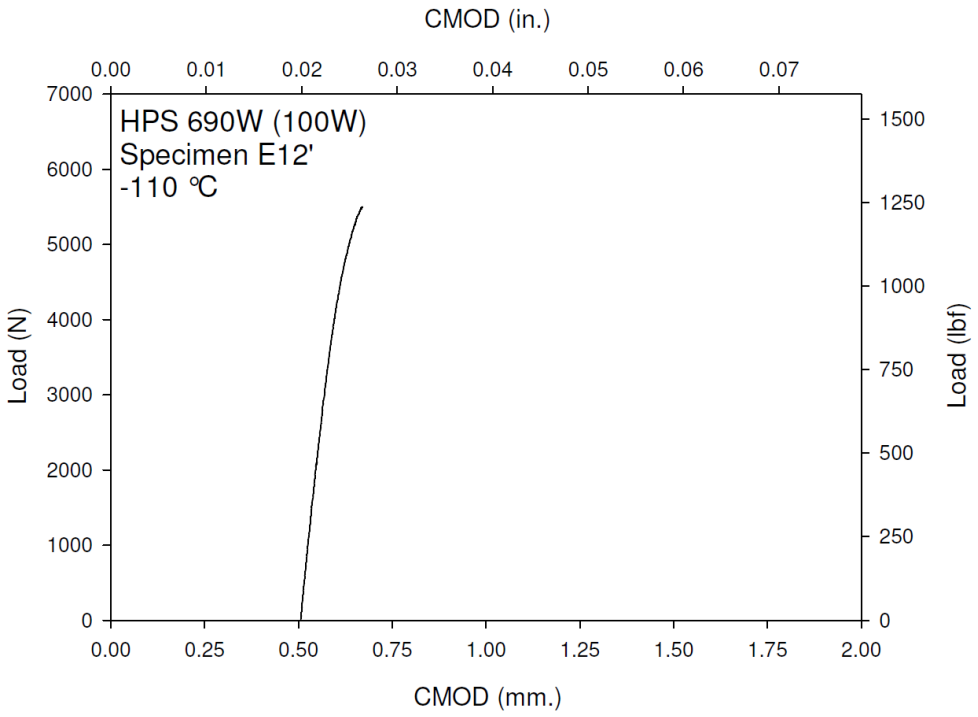

Figure C-81. Specimen E12' Test Record

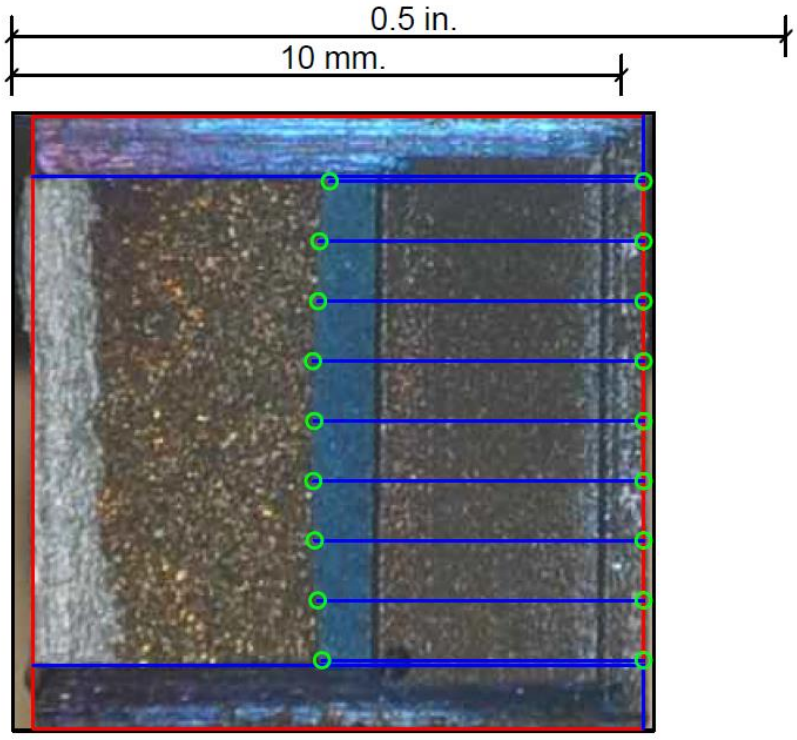

Figure C-82. Specimen E12' Fracture Surface

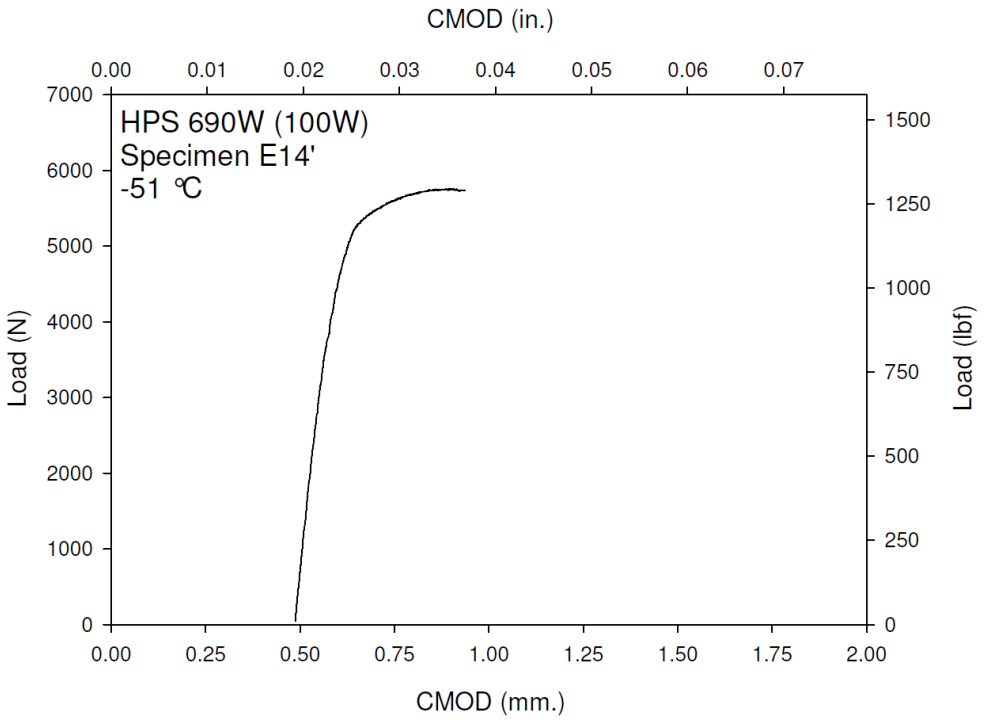

Figure C-83. Specimen E14' Test Record

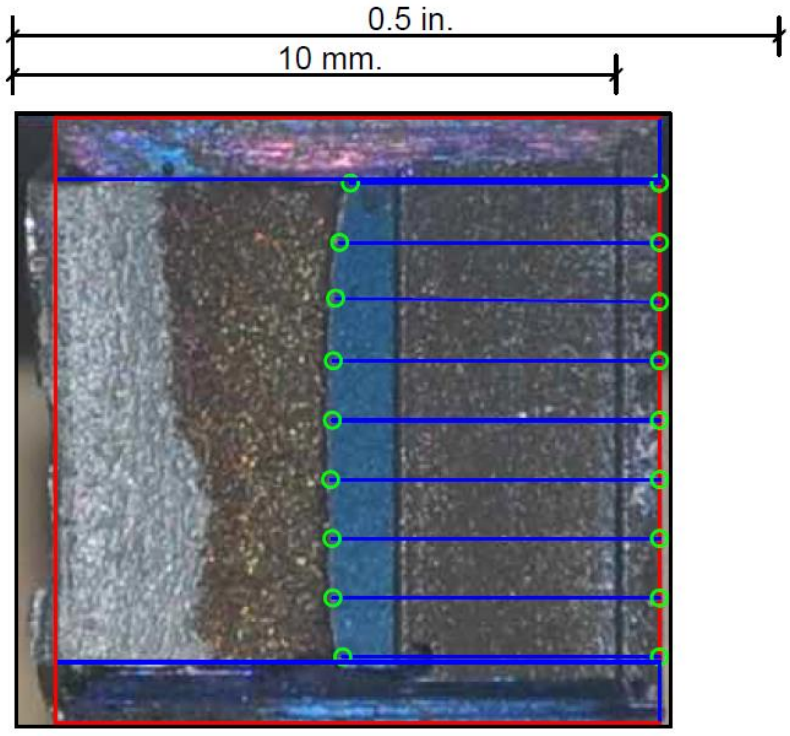

Figure C-84. Specimen E14' Fracture Surface

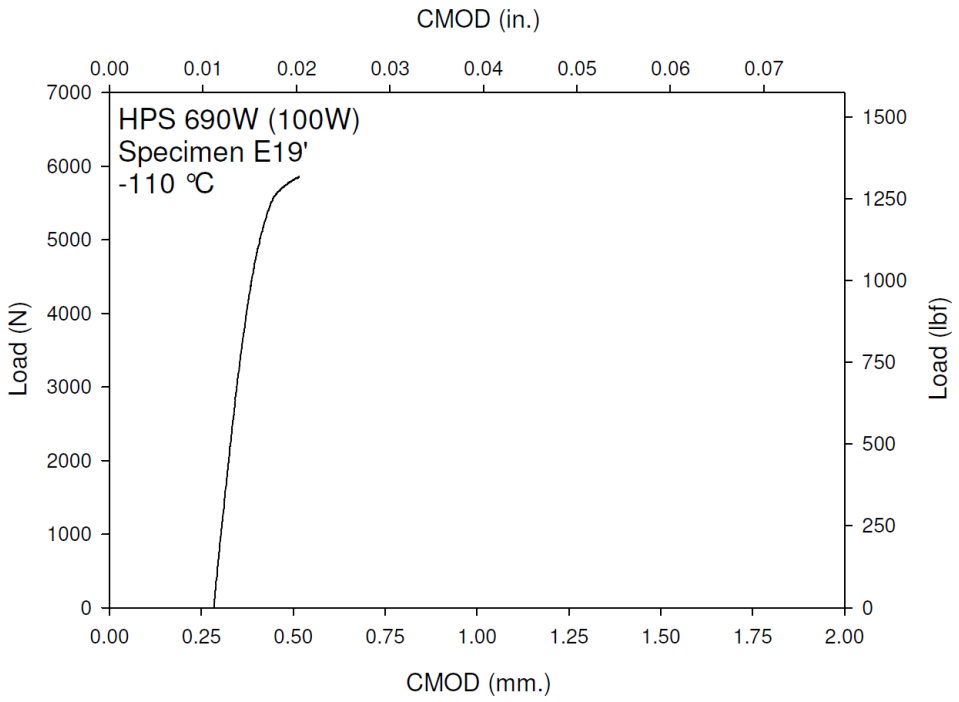

Figure C-85. Specimen E19' Test Record

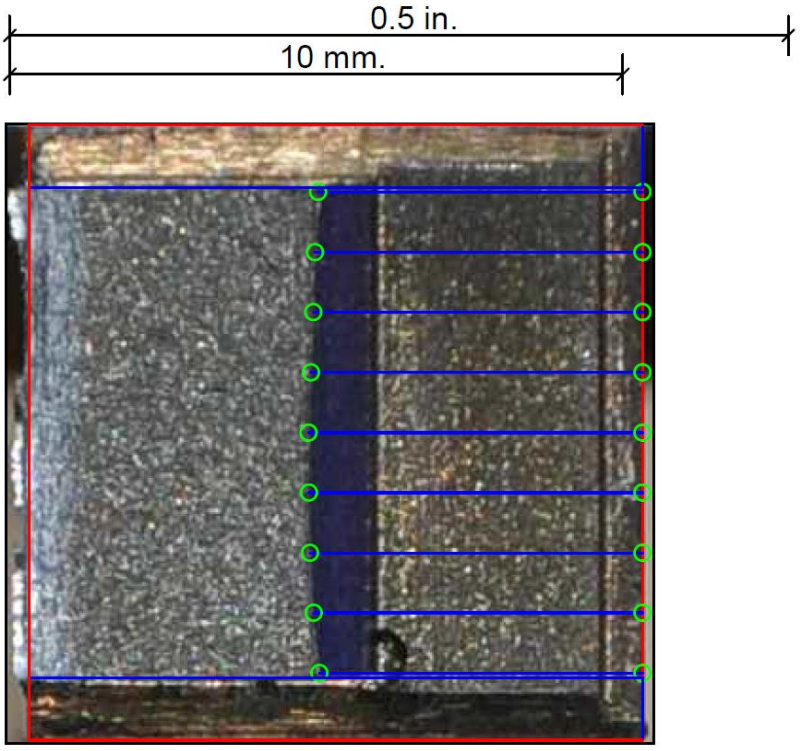

Figure C-86. Specimen E19' Fracture Surface

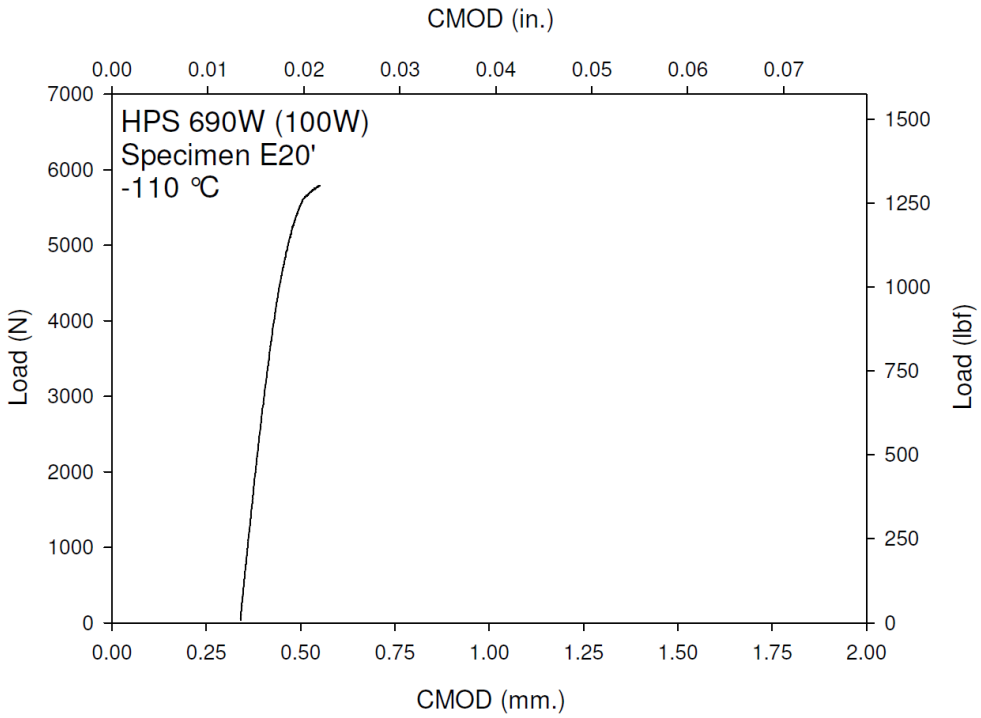

Figure C-87. Specimen E20' Test Record

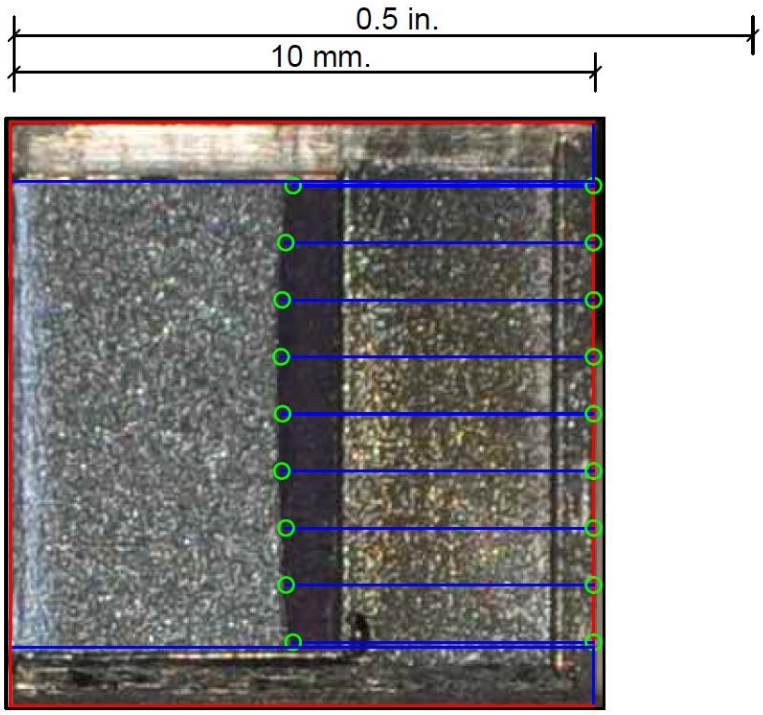

Figure C-88. Specimen E20' Fracture Surface

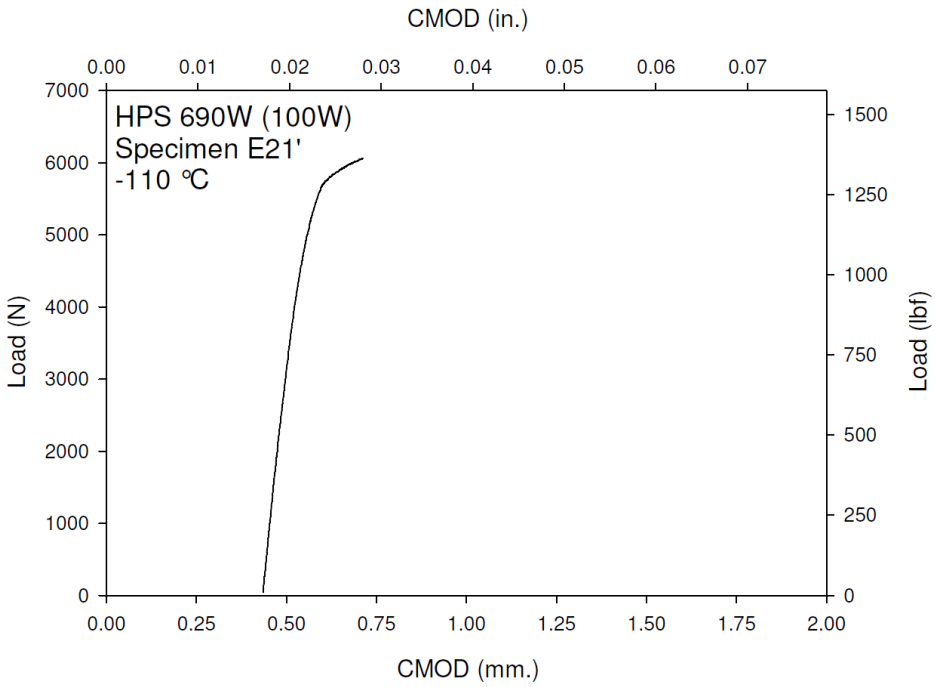

Figure C-89. Specimen E21' Test Record

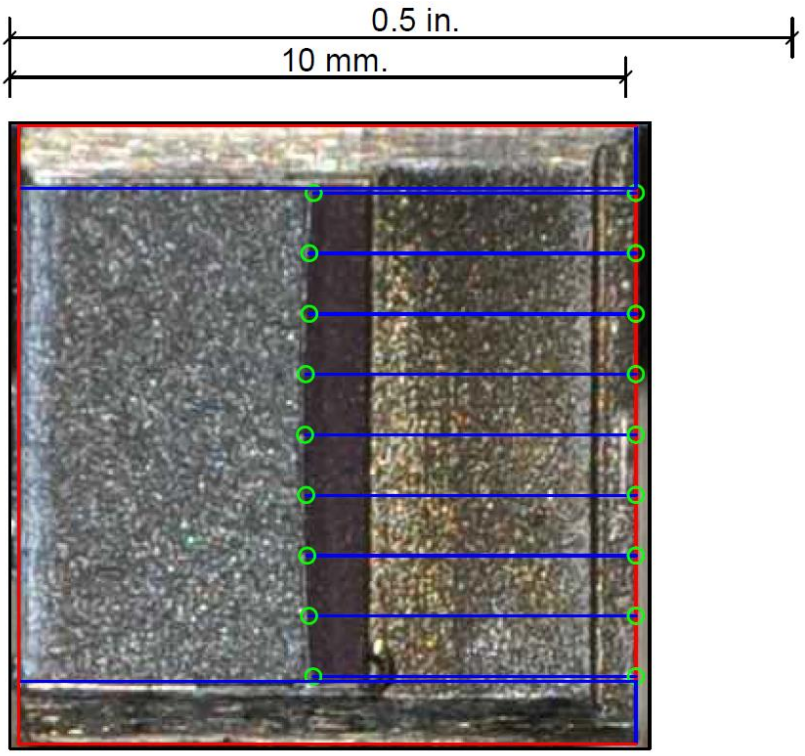

Figure C-90. Specimen E21' Fracture Surface

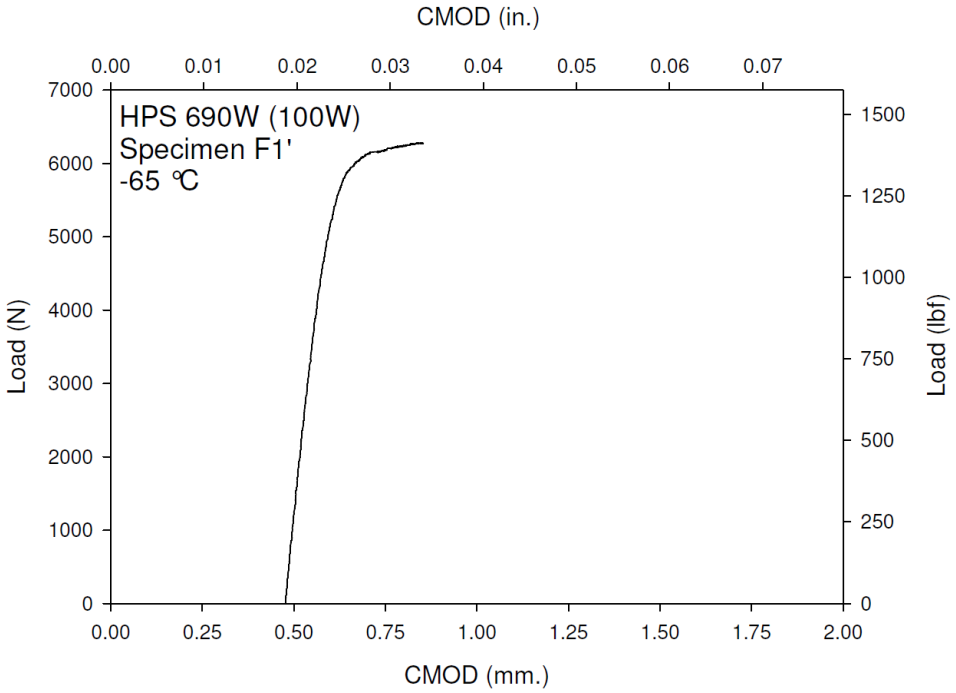

Figure C-91. Specimen F1' Test Record

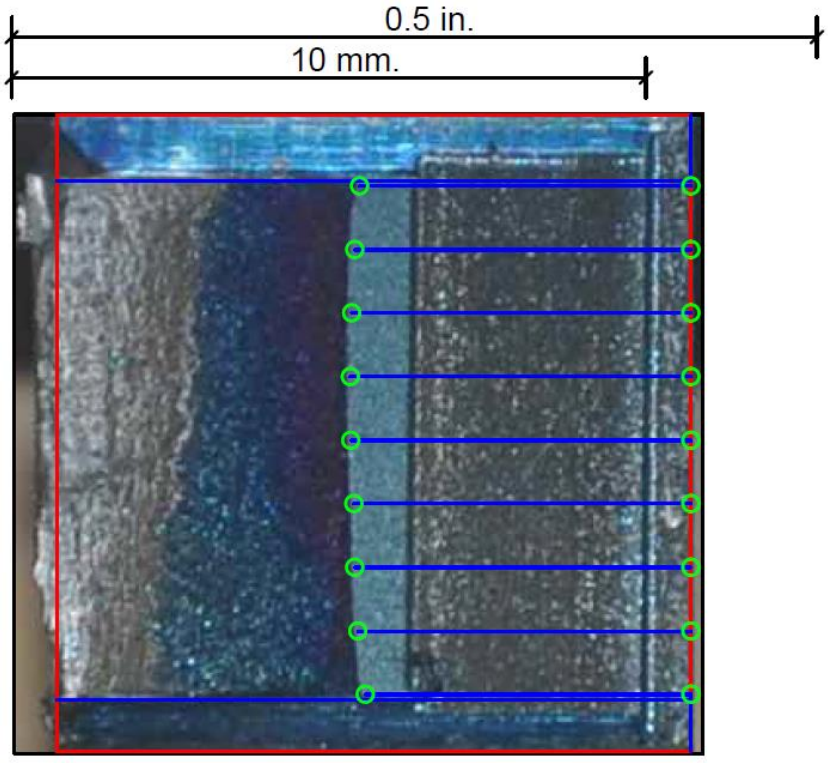

Figure C-92. Specimen F1' Fracture Surface

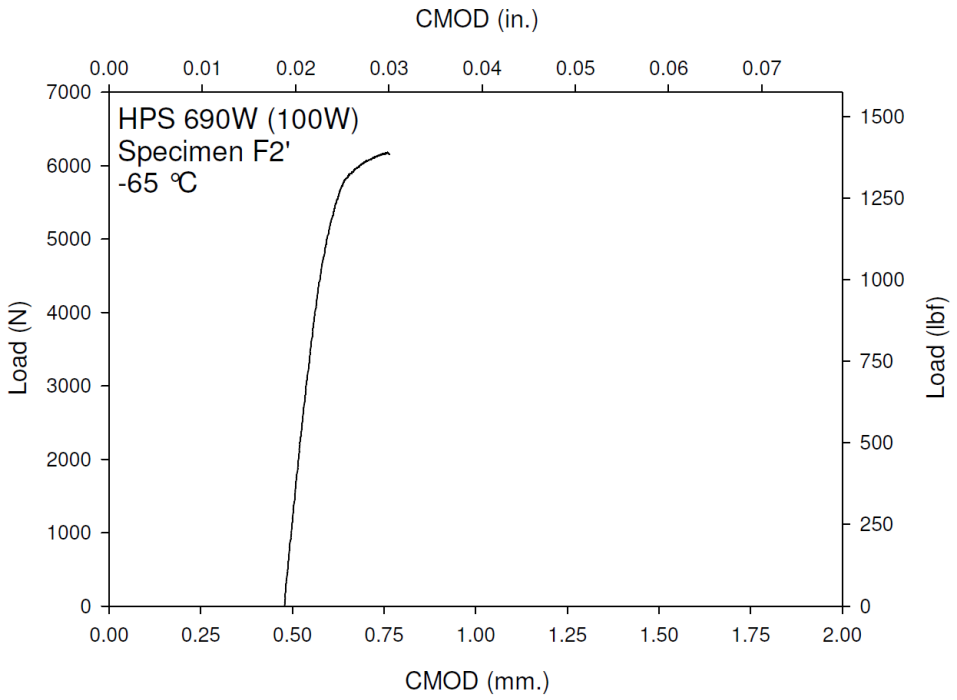

Figure C-93. Specimen F2' Test Record

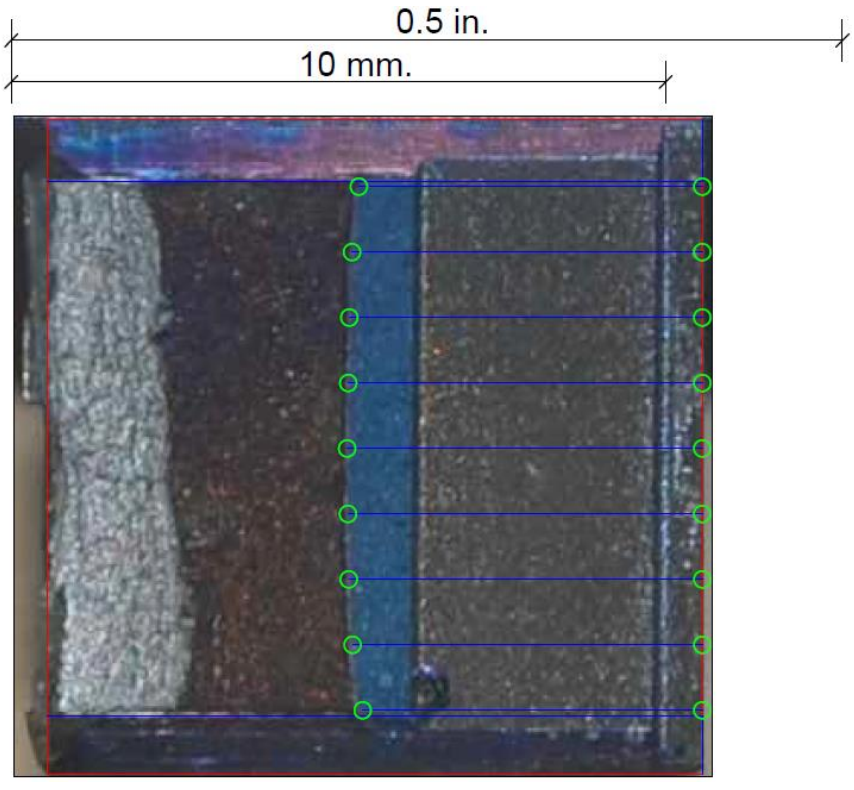

Figure C-94. Specimen F2' Fracture Surface

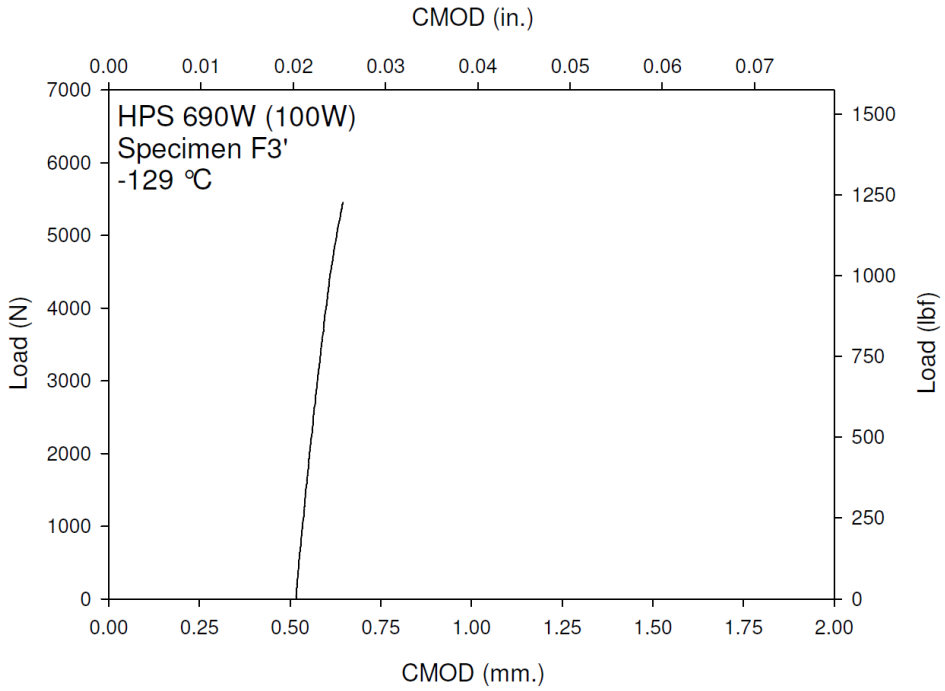

Figure C-95. Specimen F3' Test Record

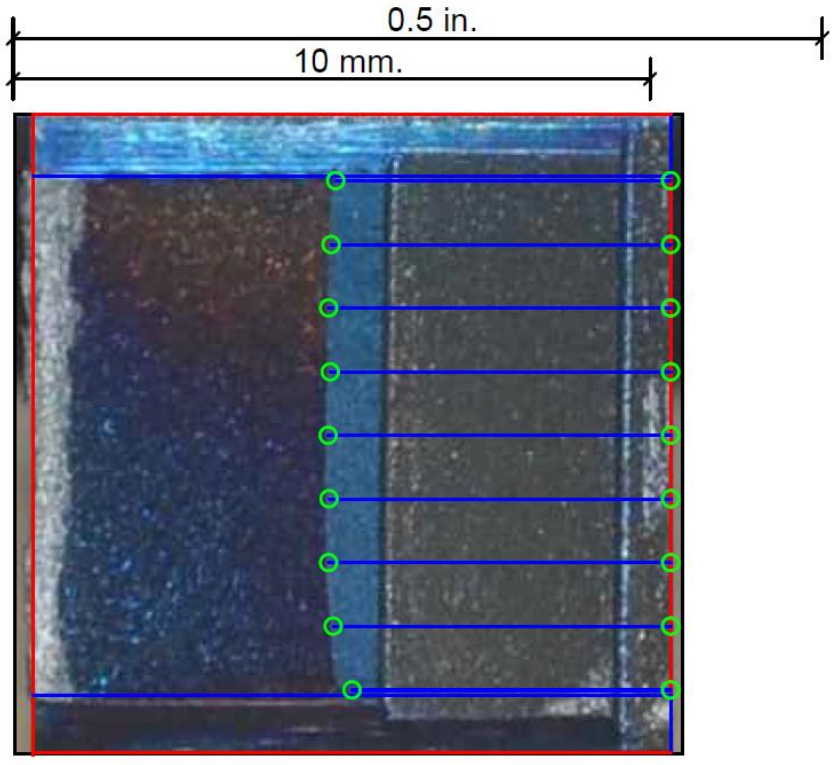

Figure C-96. Specimen F3' Fracture Surface

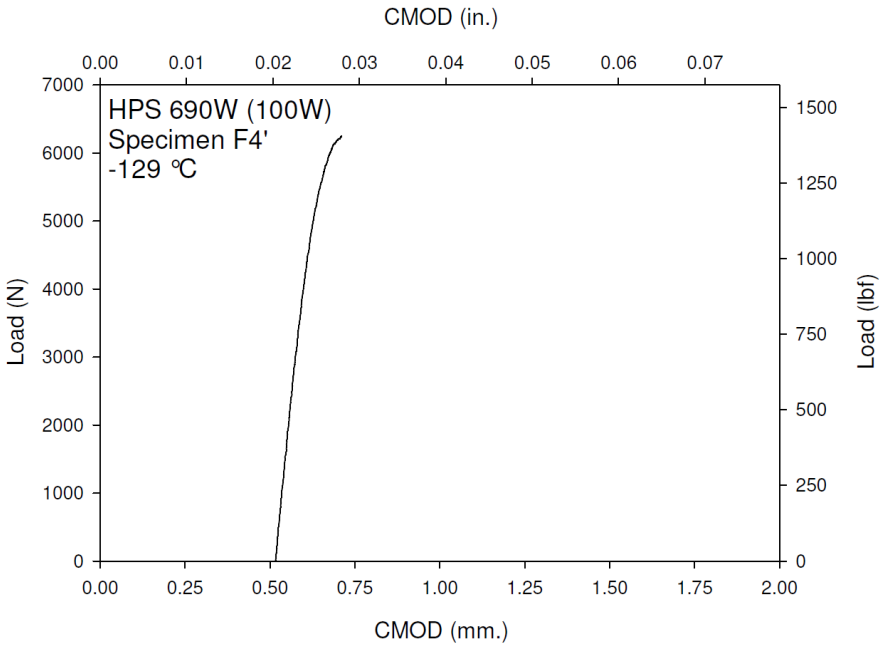

Figure C-97. Specimen F4' Test Record

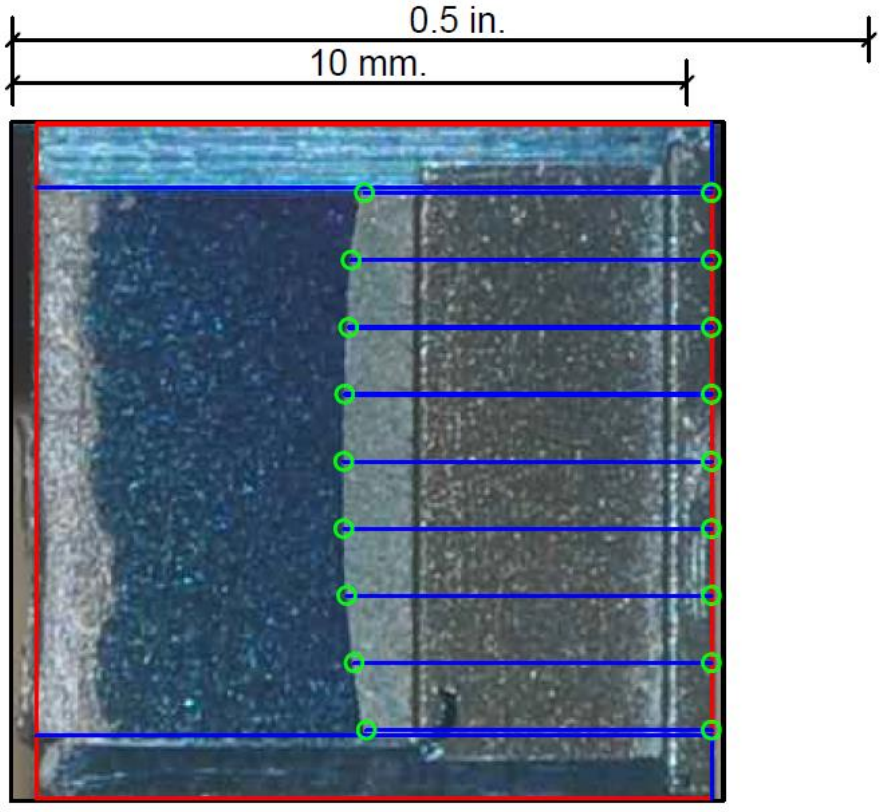

Figure C-98. Specimen F4' Fracture Surface

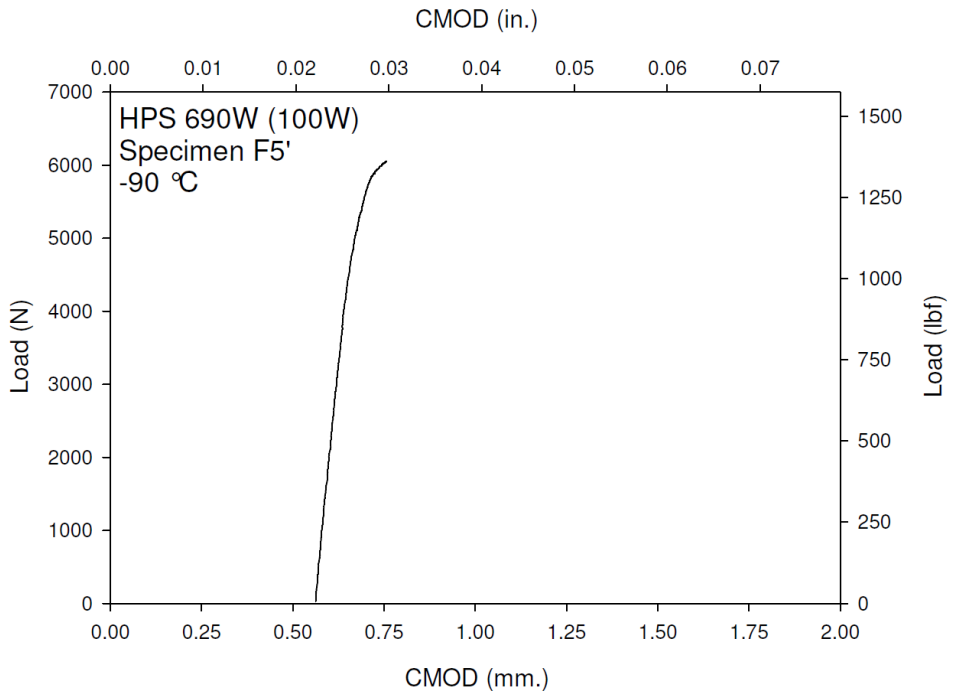

Figure C-99. Specimen F5' Test Record

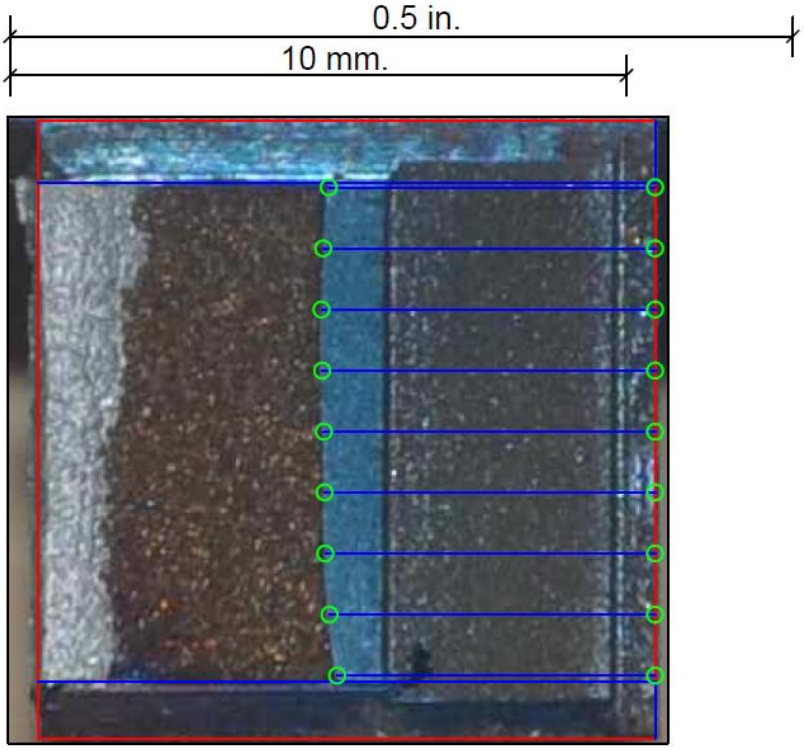

Figure C-100. Specimen F5' Fracture Surface

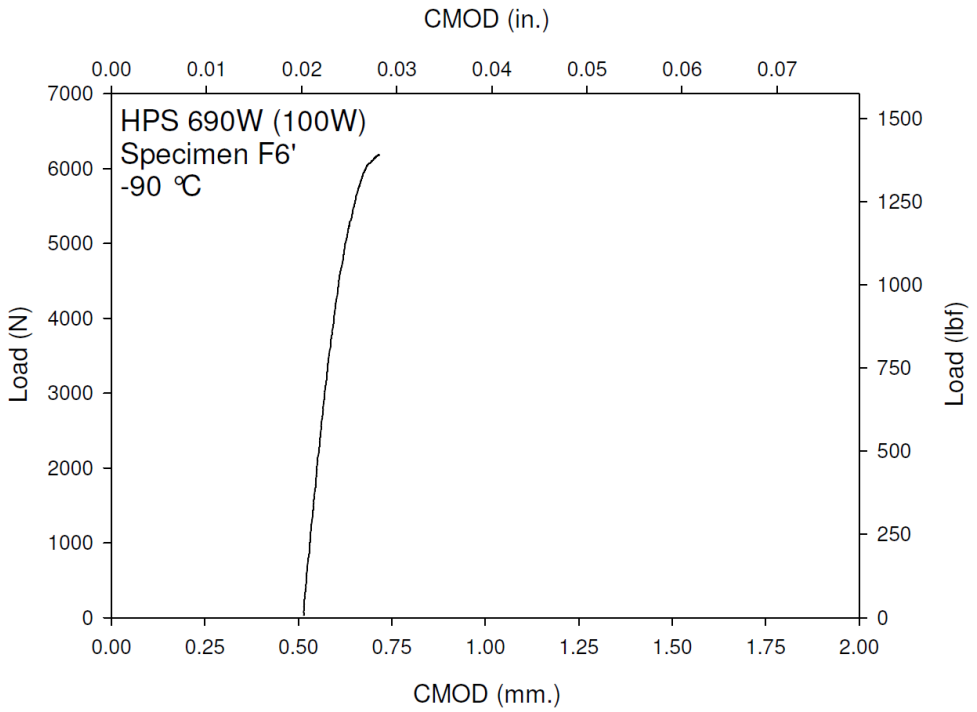

Figure C-101. Specimen F6' Test Record

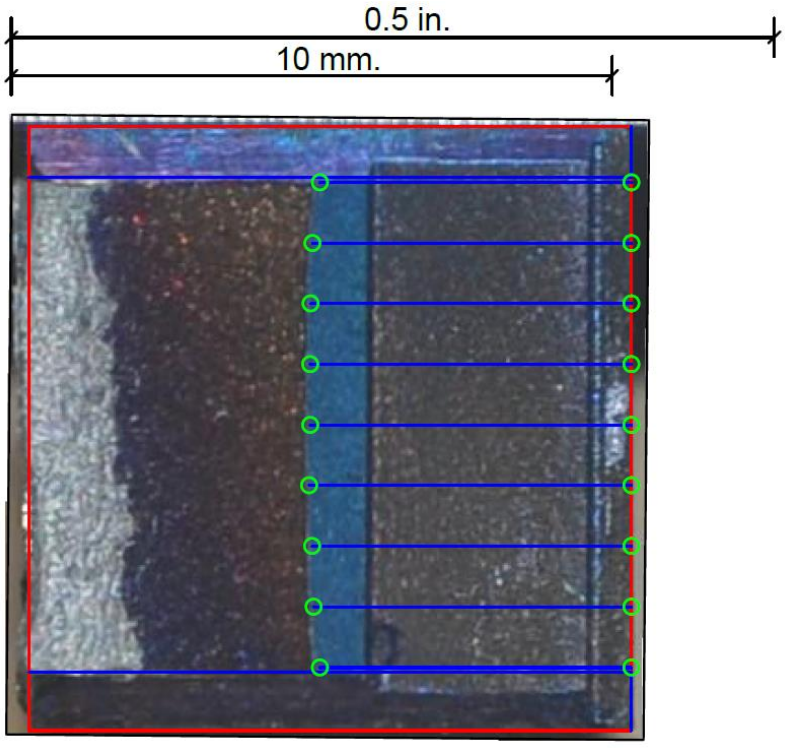

Figure C-102. Specimen F6' Fracture Surface

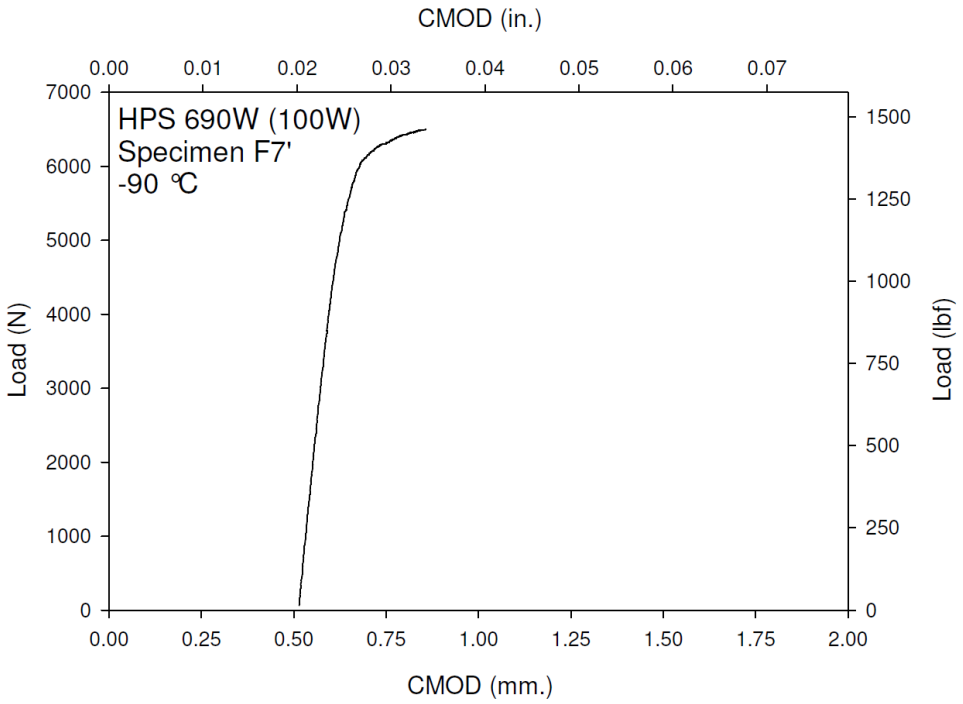

Figure C-103. Specimen F7' Test Record

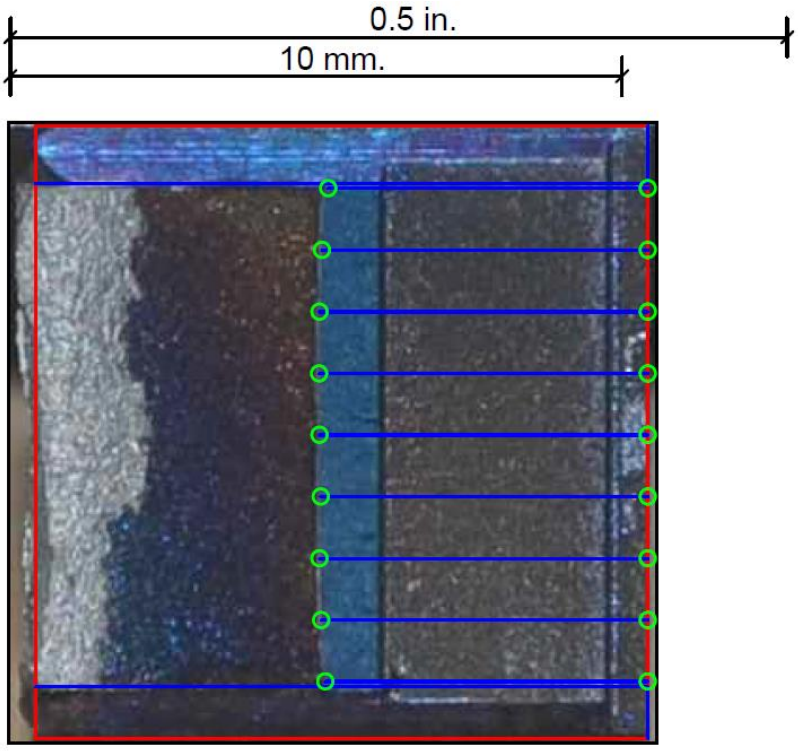

Figure C-104. Specimen F7' Fracture Surface

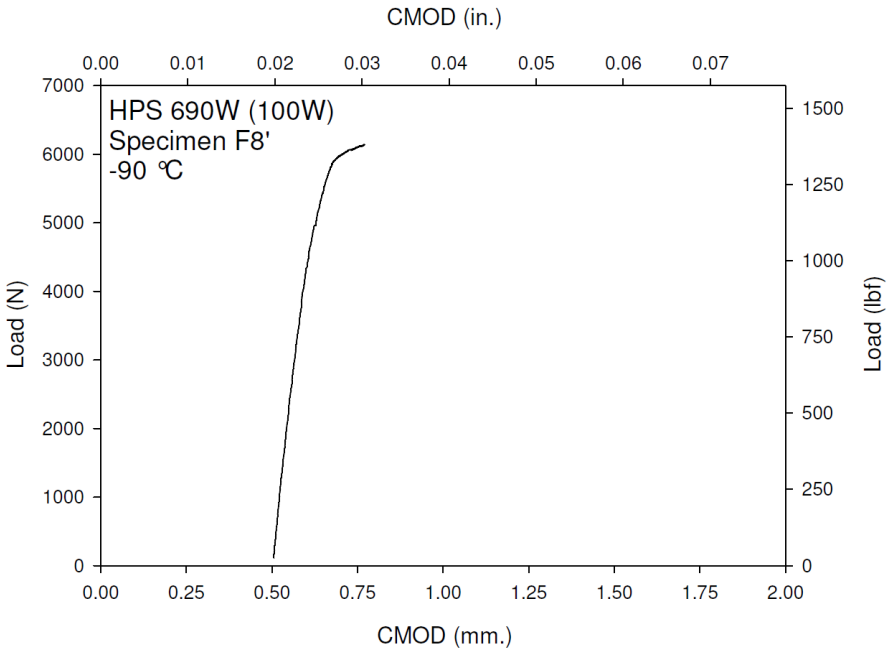

Figure C-105. Specimen F8' Test Record

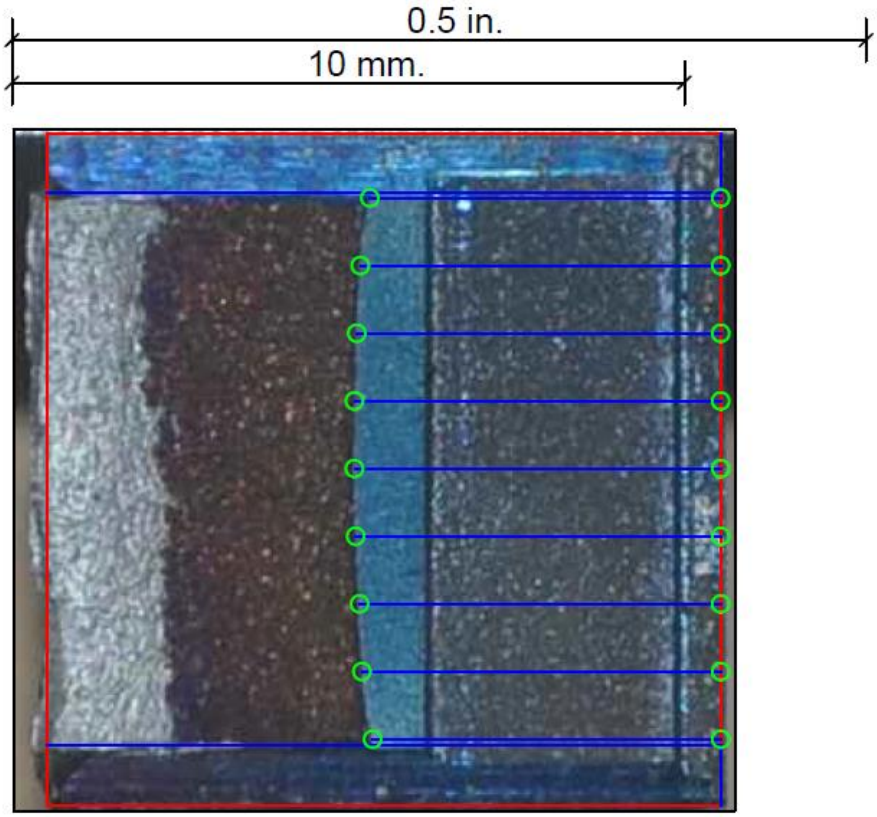

Figure C-106. Specimen F8' Fracture Surface

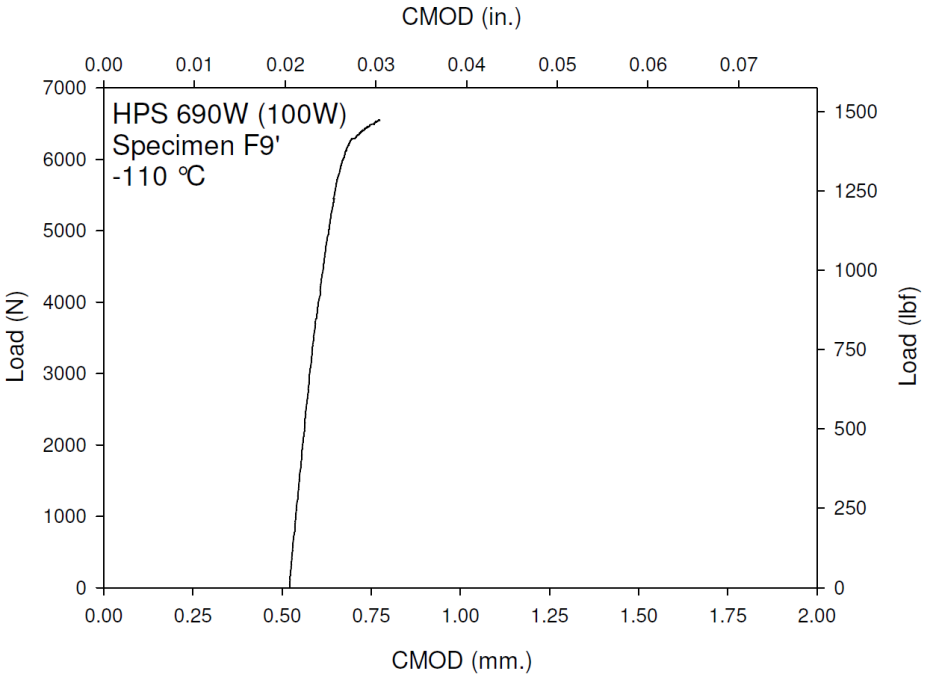

Figure C-107. Specimen F9' Test Record

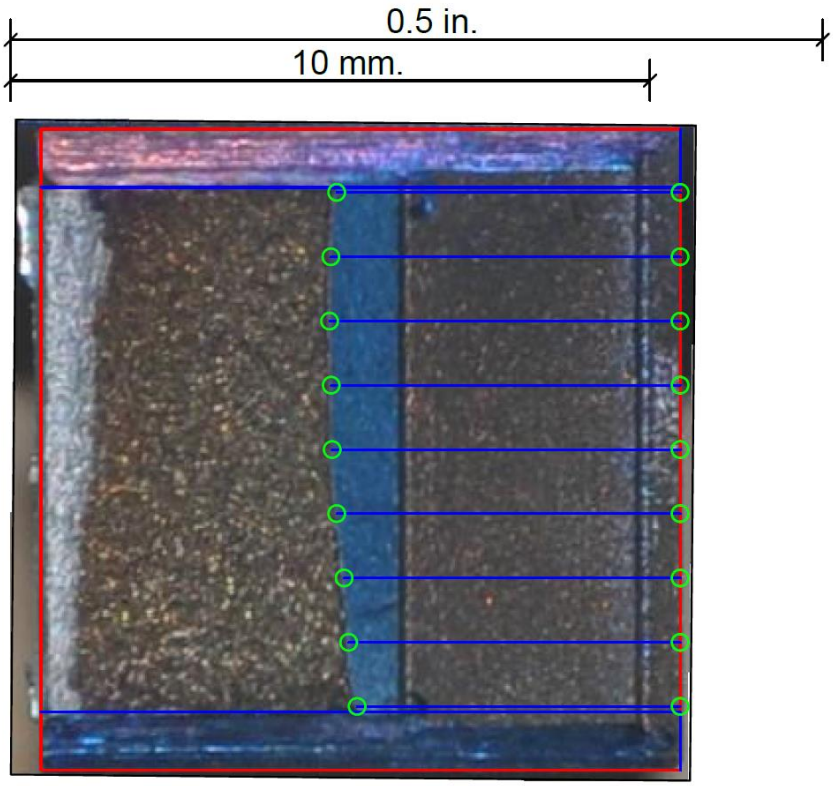

Figure C-108. Specimen F9' Fracture Surface

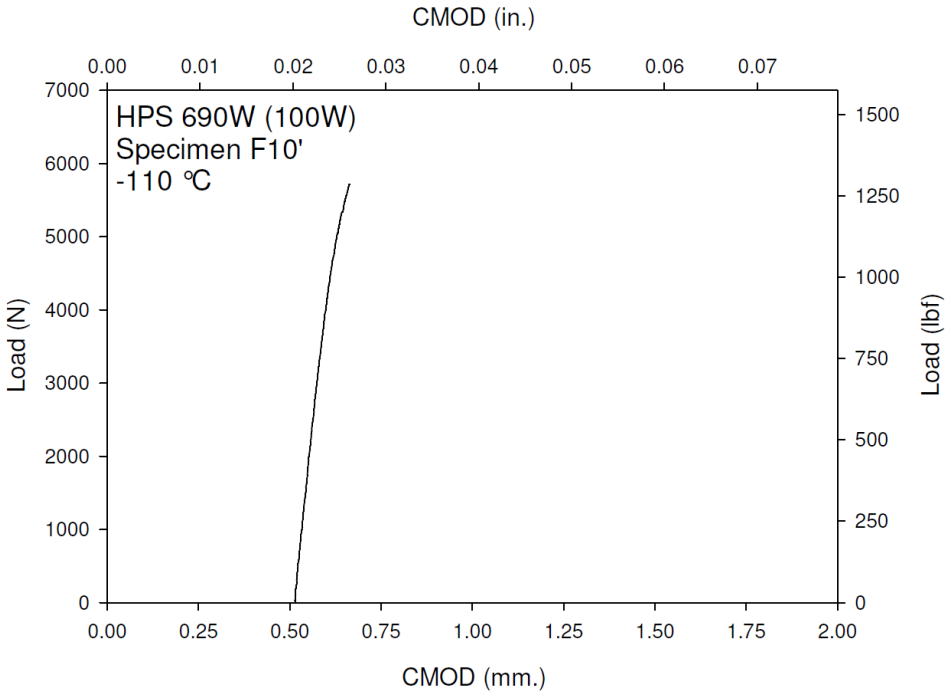

Figure C-109. Specimen F10' Test Record

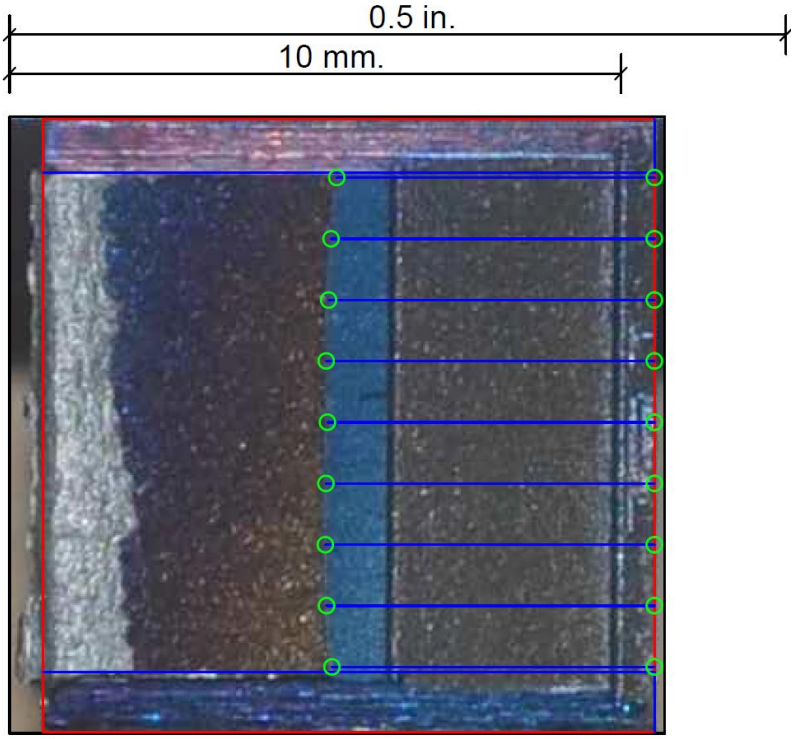

Figure C-110. Specimen F10' Fracture Surface

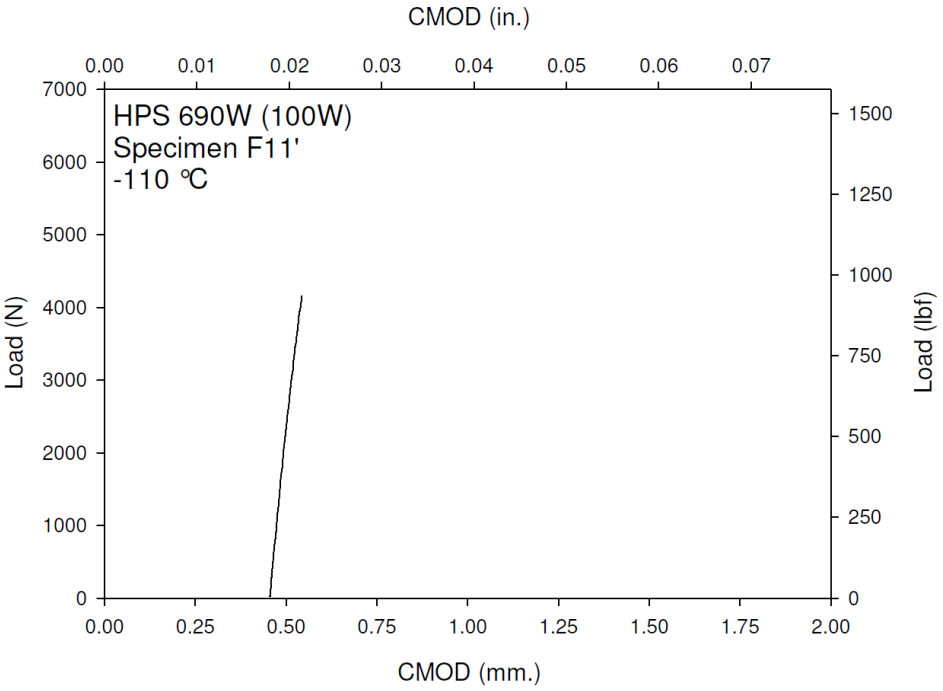

Figure C-111. Specimen F11' Test Record

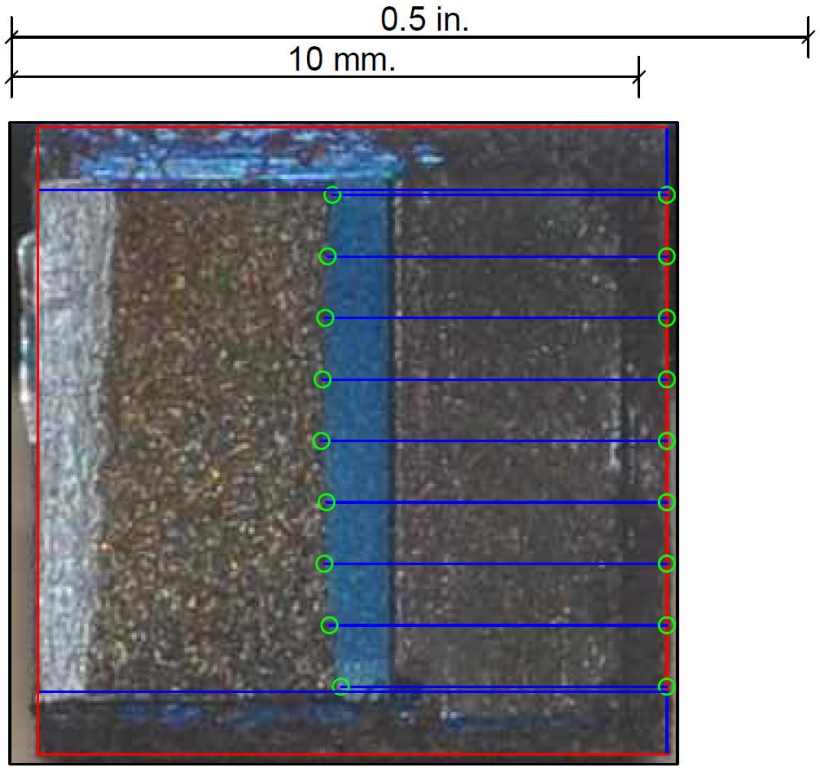

Figure C-112. Specimen F11' Fracture Surface

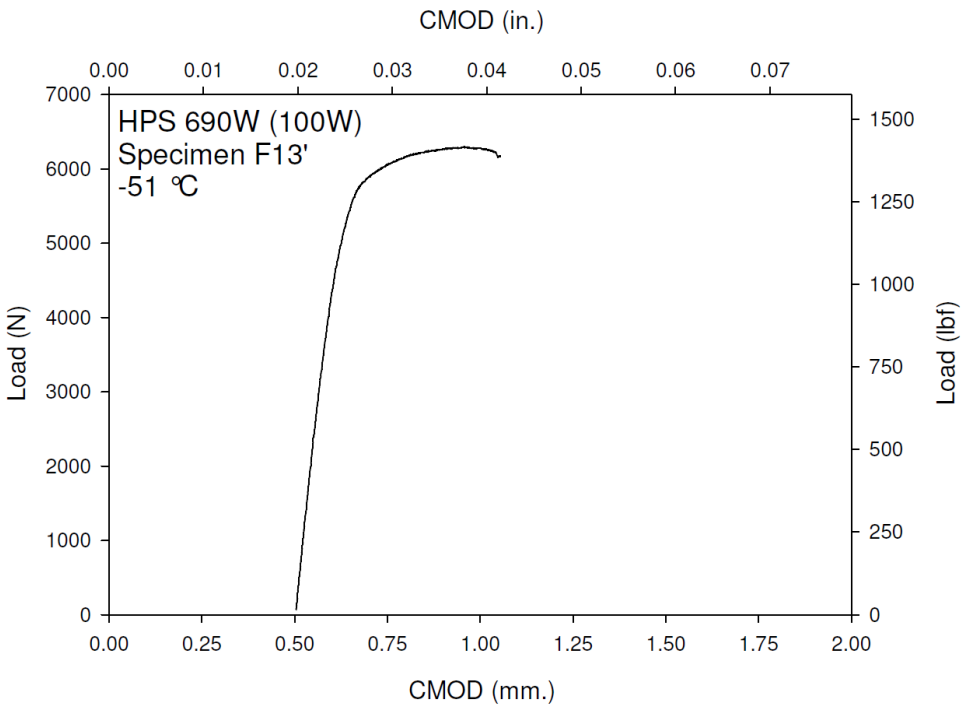

Figure C-113. Specimen F13' Test Record

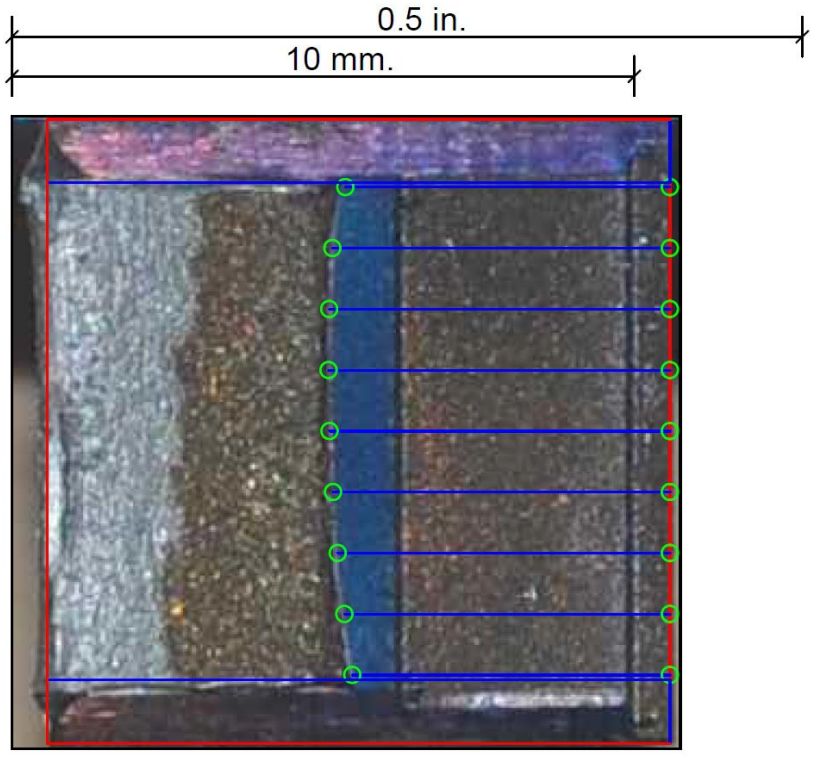

Figure C-114. Specimen F13' Fracture Surface

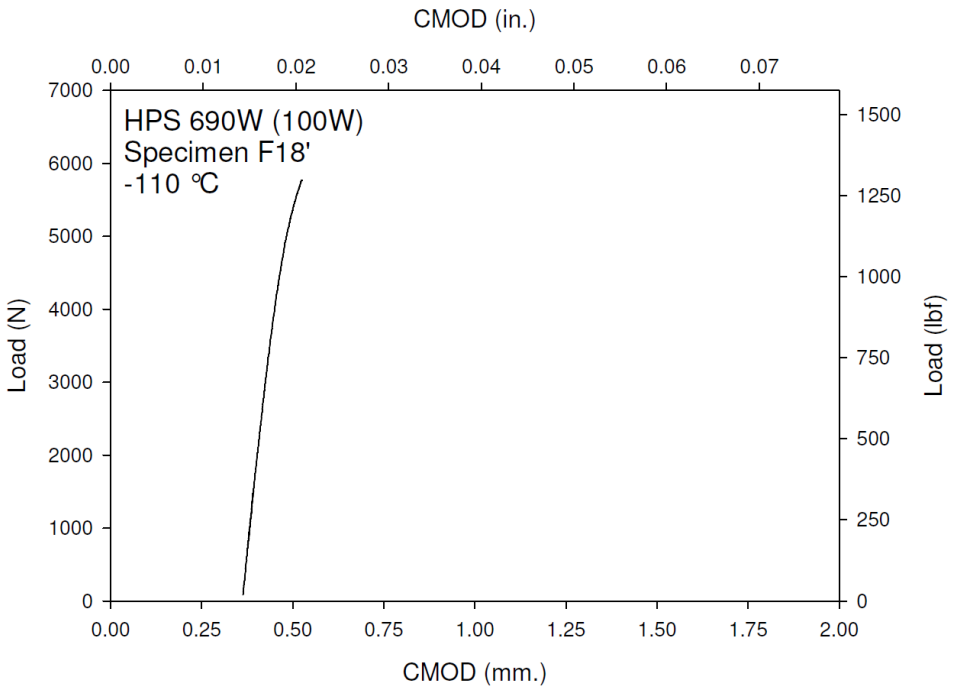

Figure C-115. Specimen F18' Test Record

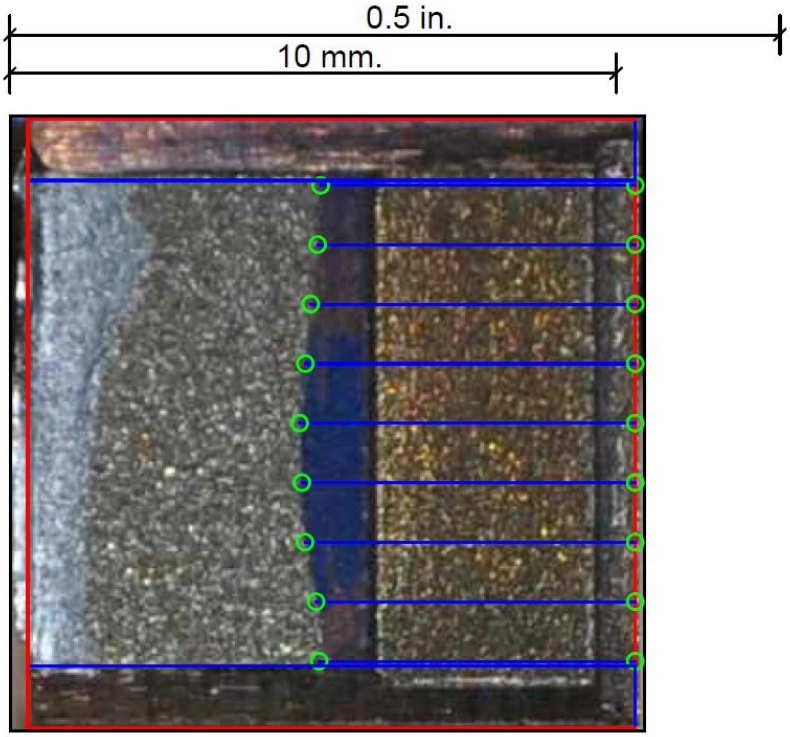

Figure C-116. Specimen F18' Fracture Surface

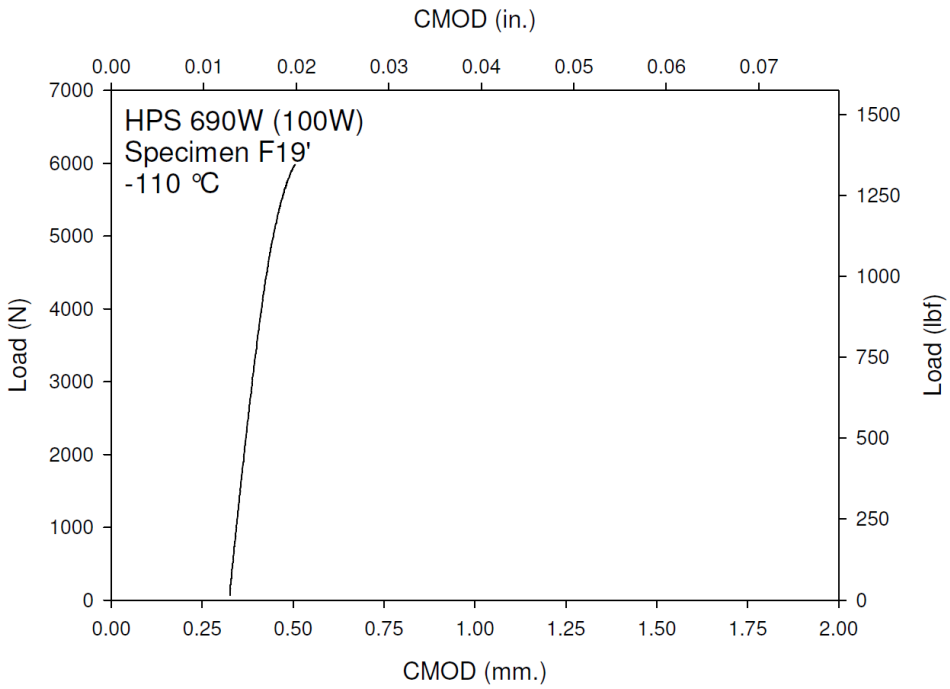

Figure C-117. Specimen F19' Test Record

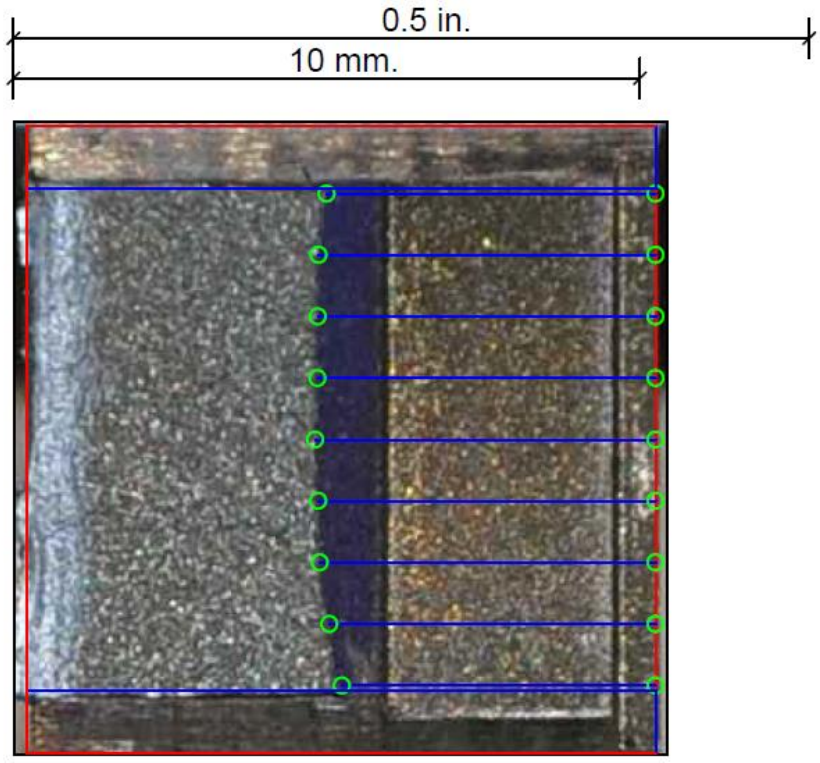

Figure C-118. Specimen F19' Fracture Surface

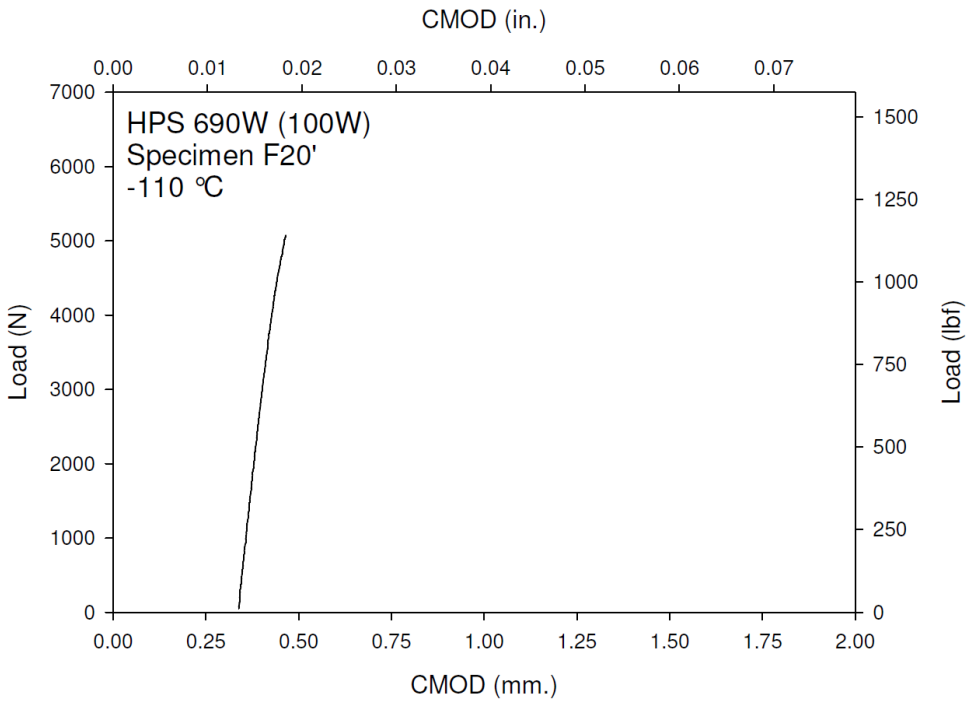

Figure C-119. Specimen F20' Test Record

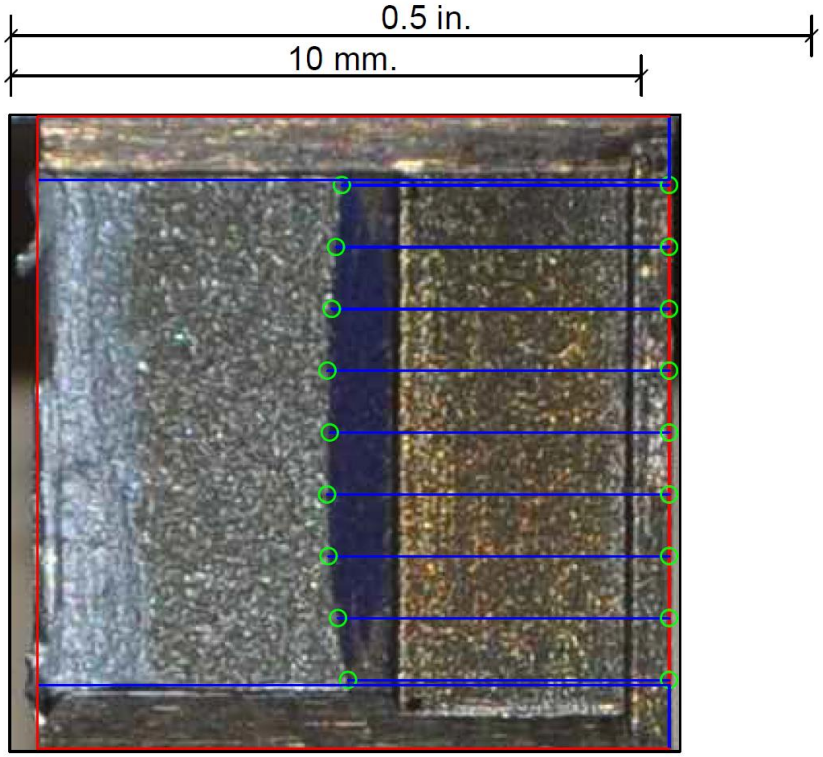

Figure C-120. Specimen F20' Fracture Surface

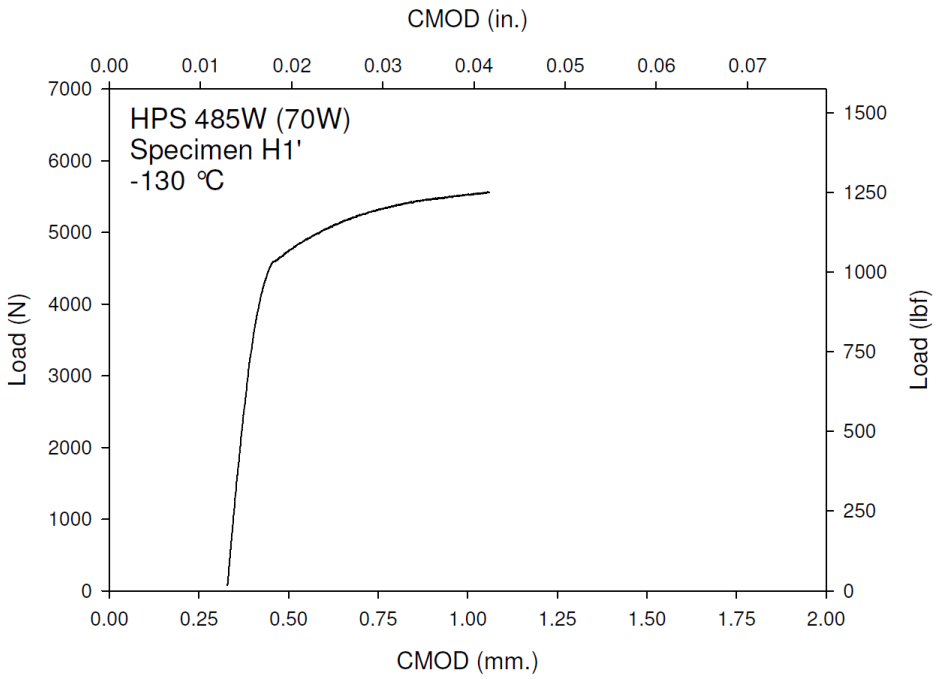

Figure C-121. Specimen H1' Test Record

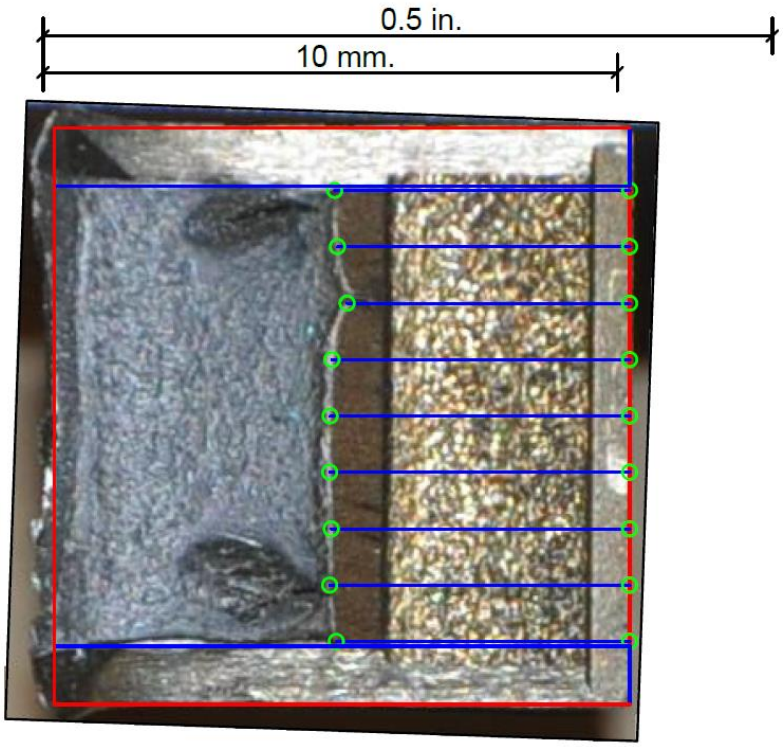

Figure C-122. Specimen H1' Fracture Surface

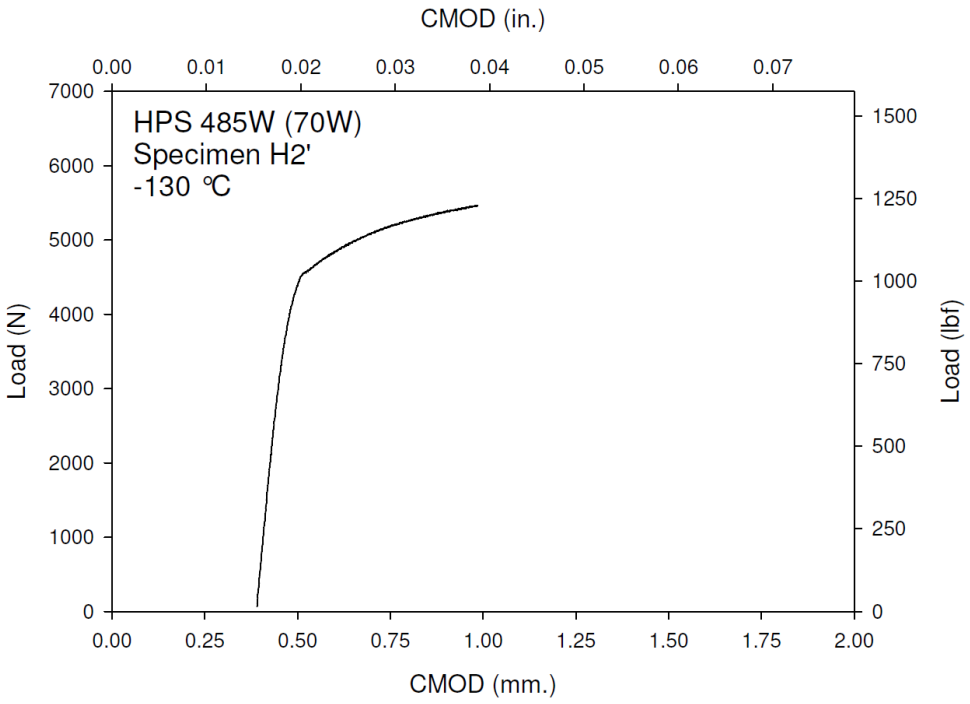

Figure C-123. Specimen H2' Test Record

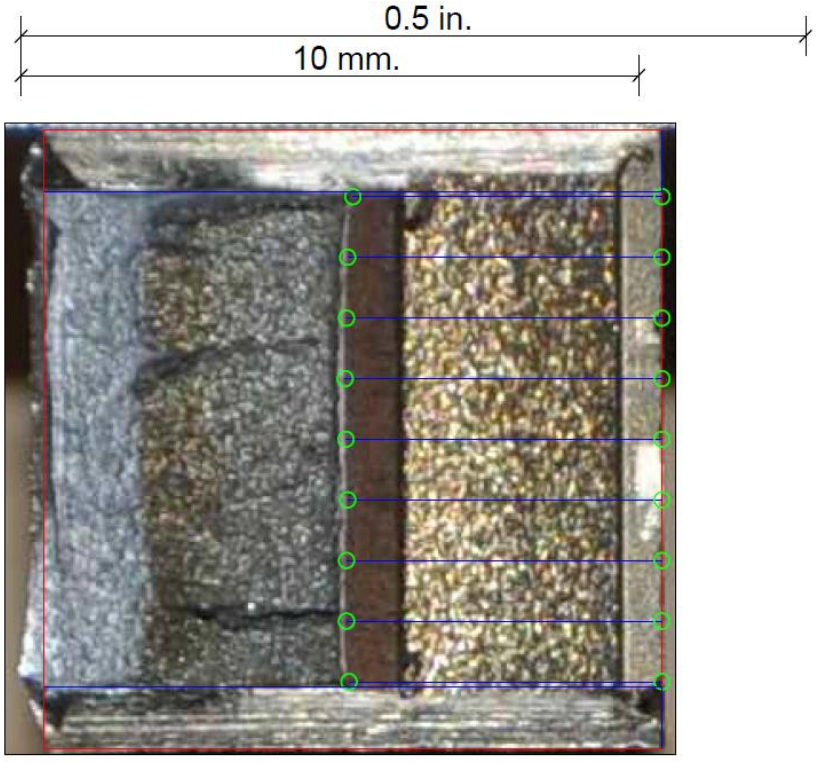

Figure C-124. Specimen H2' Fracture Surface

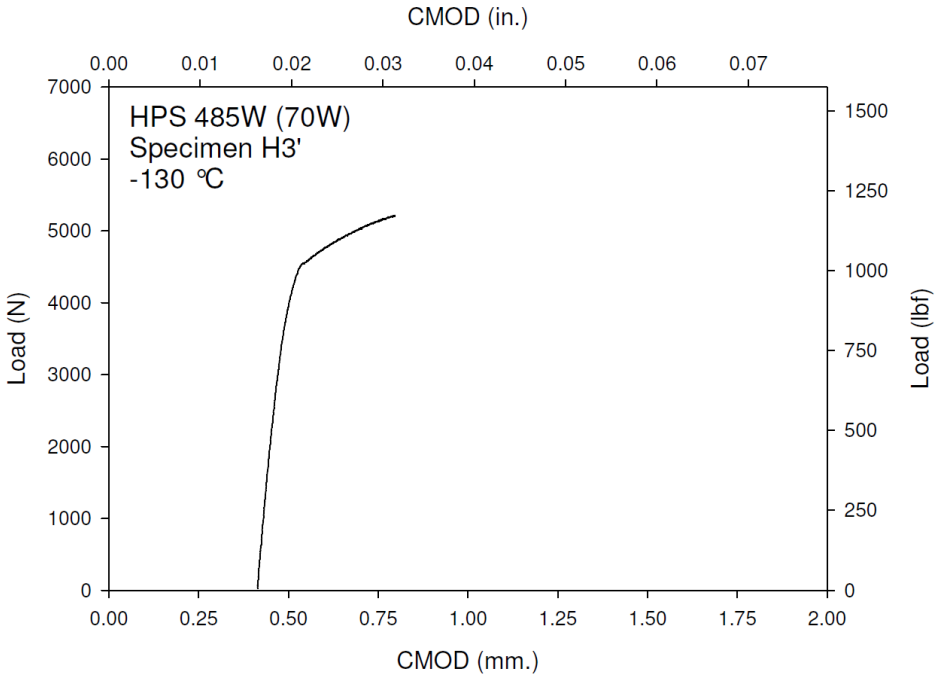

Figure C-125. Specimen H3' Test Record

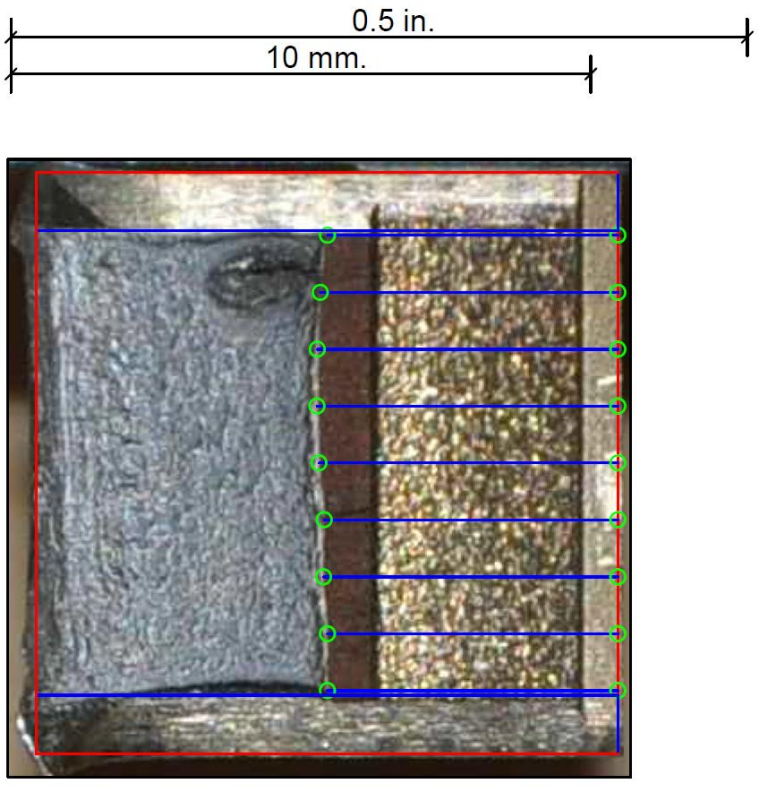

Figure C-126. Specimen H3' Fracture Surface

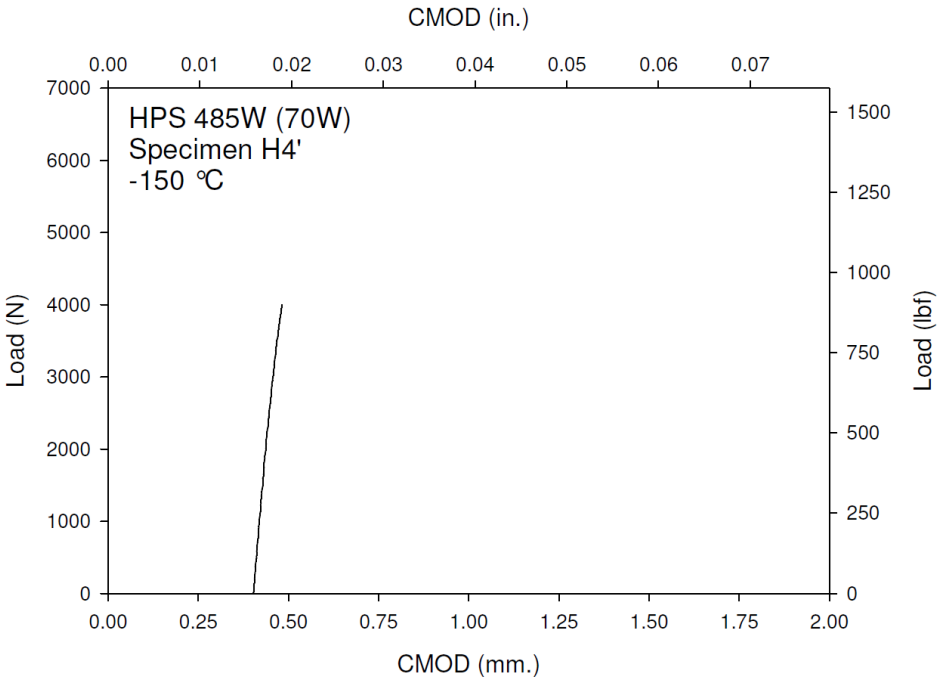

Figure C-127. Specimen H4' Test Record

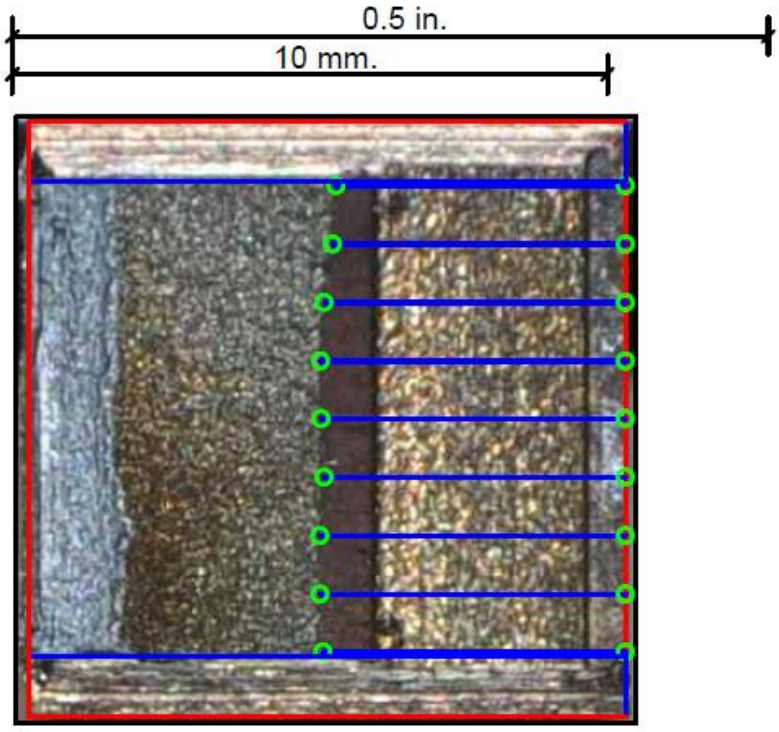

Figure C-128. Specimen H4' Fracture Surface

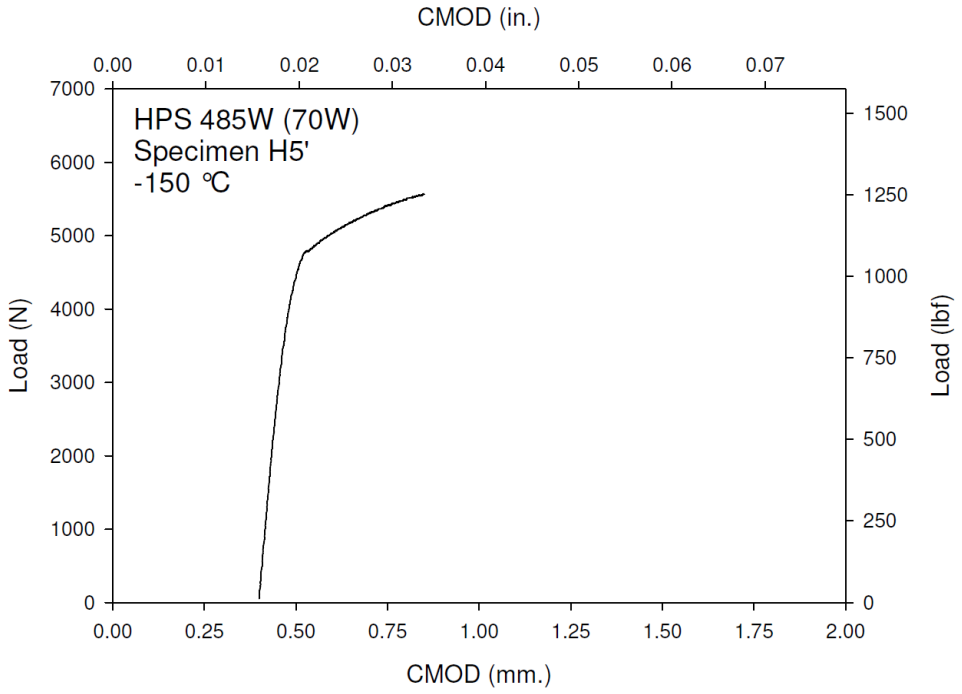

Figure C-129. Specimen H5' Test Record

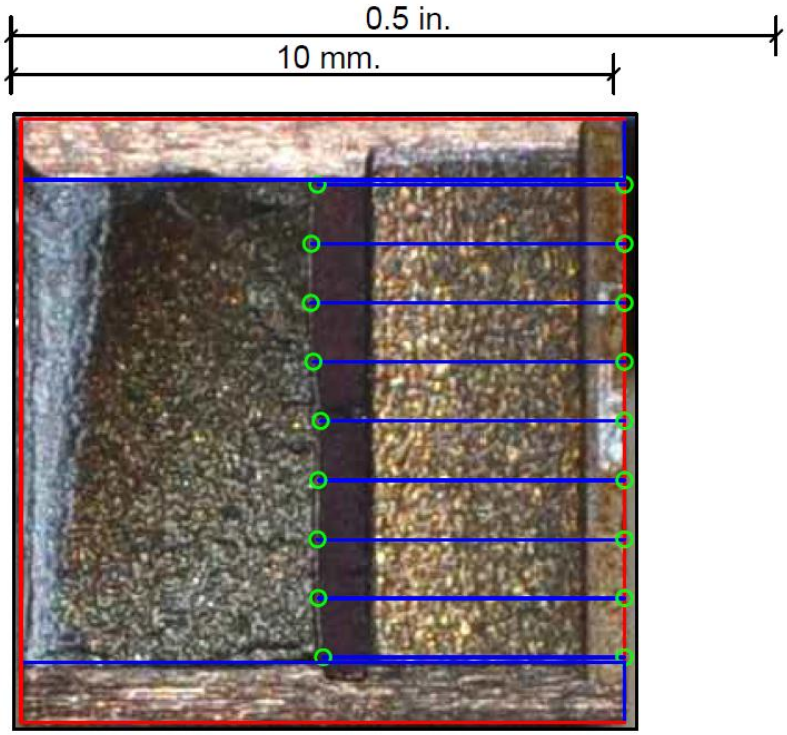

Figure C-130. Specimen H5' Fracture Surface

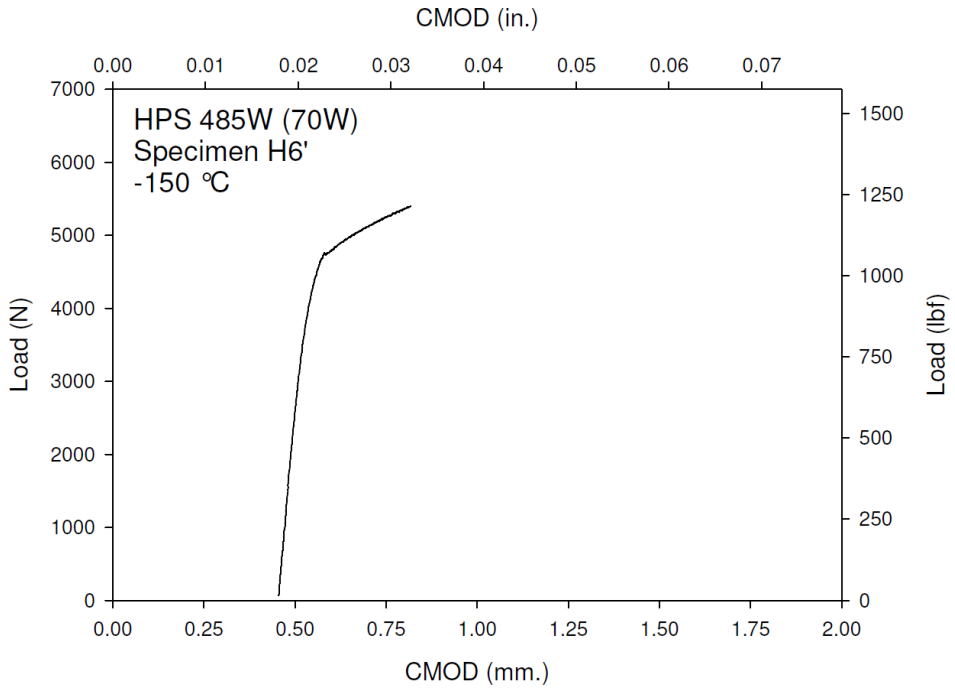

Figure C-131. Specimen H6' Test Record

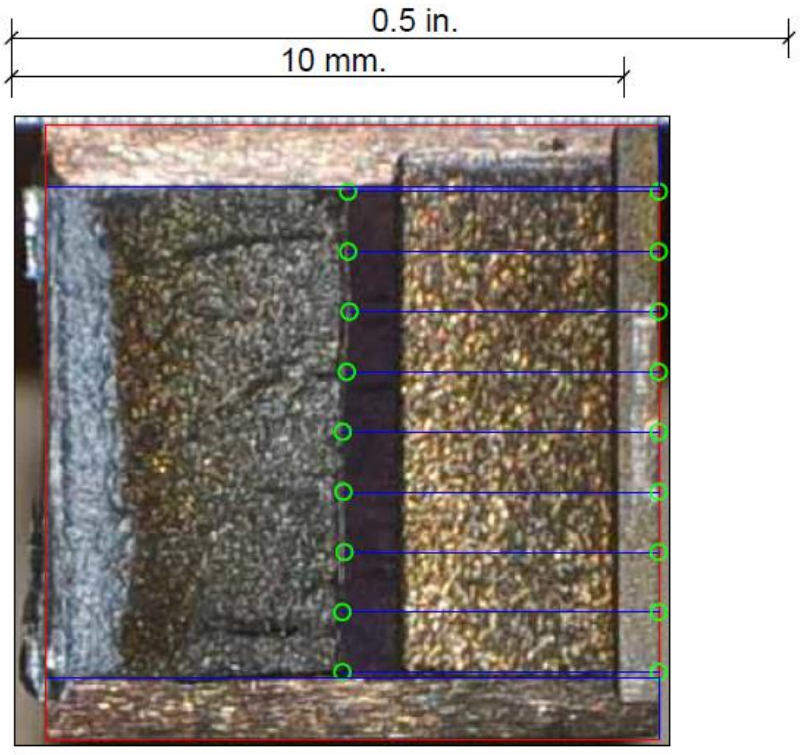

Figure C-132. Specimen H6' Fracture Surface

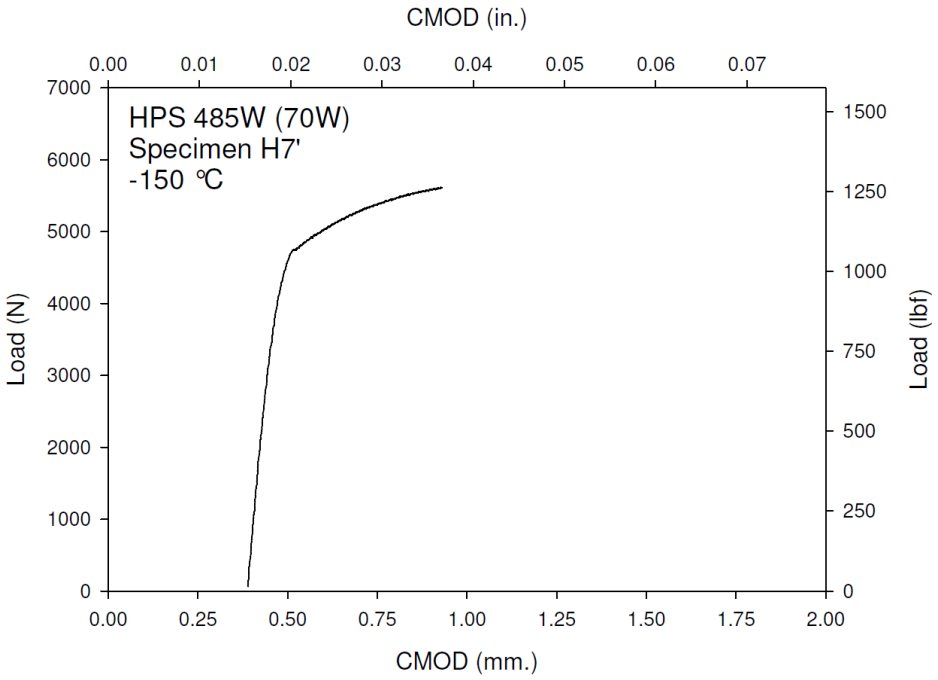

Figure C-133. Specimen H7' Test Record

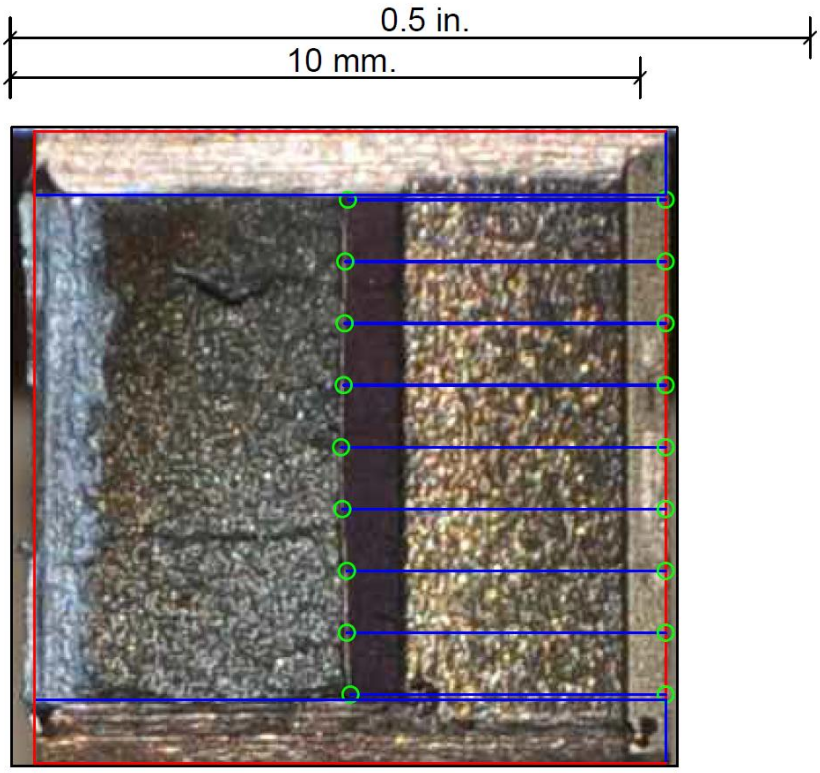

Figure C-134. Specimen H7' Fracture Surface

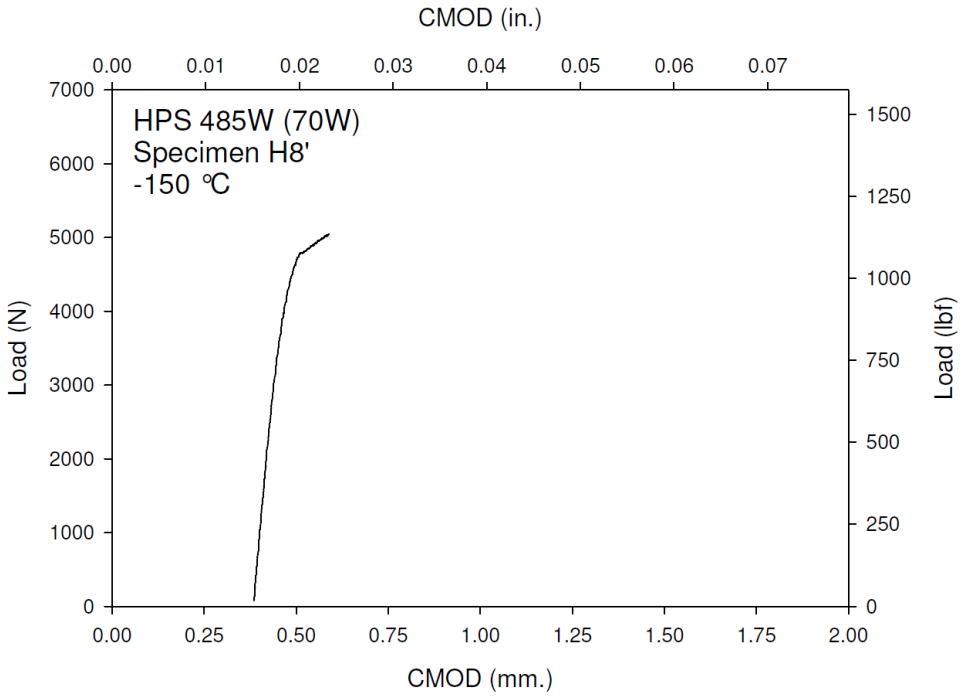

Figure C-135. Specimen H8' Test Record

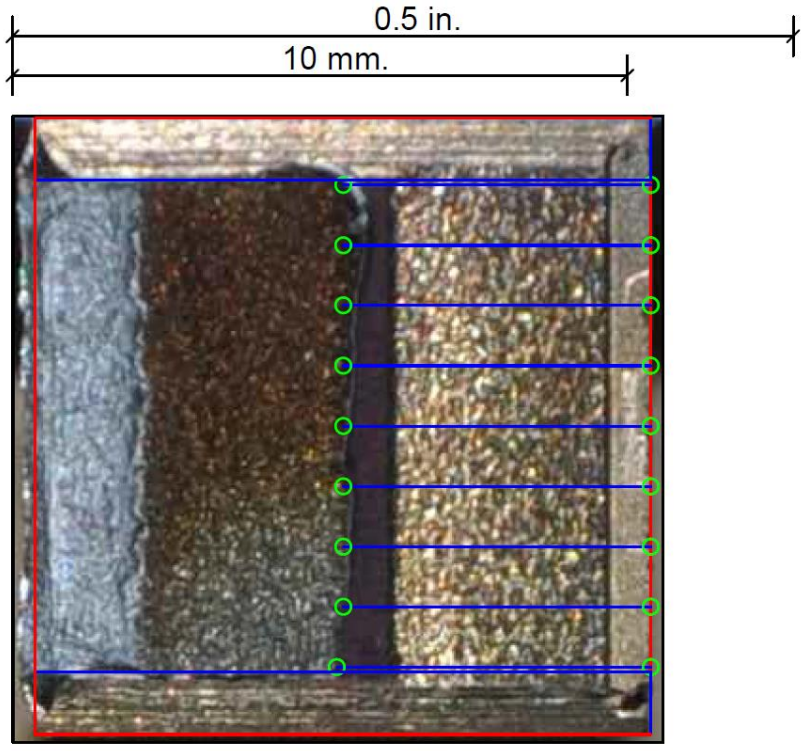

Figure C-136. Specimen H8' Fracture Surface

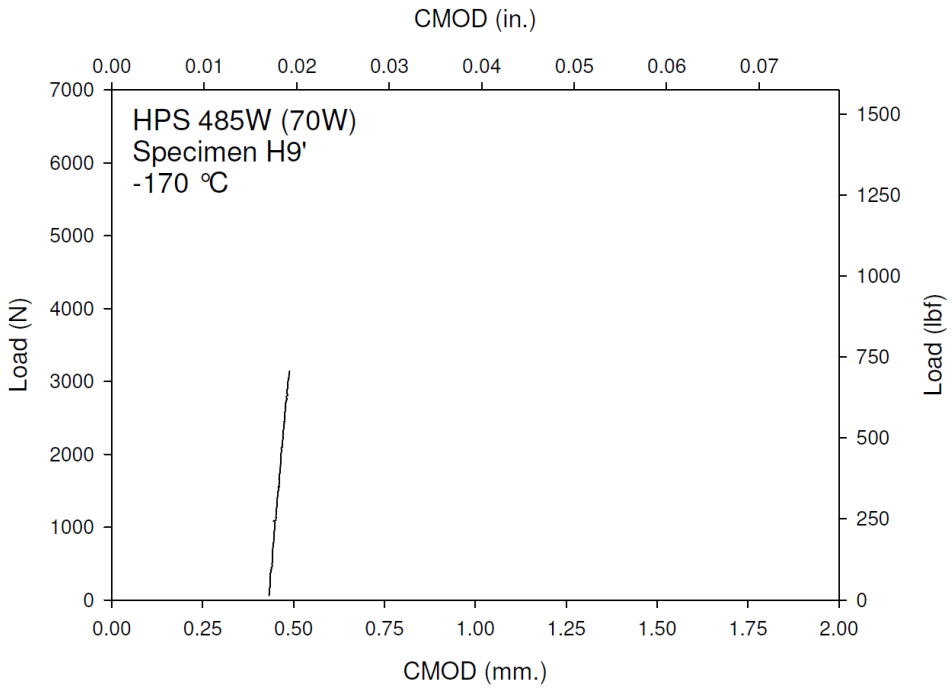

Figure C-137. Specimen H9' Test Record

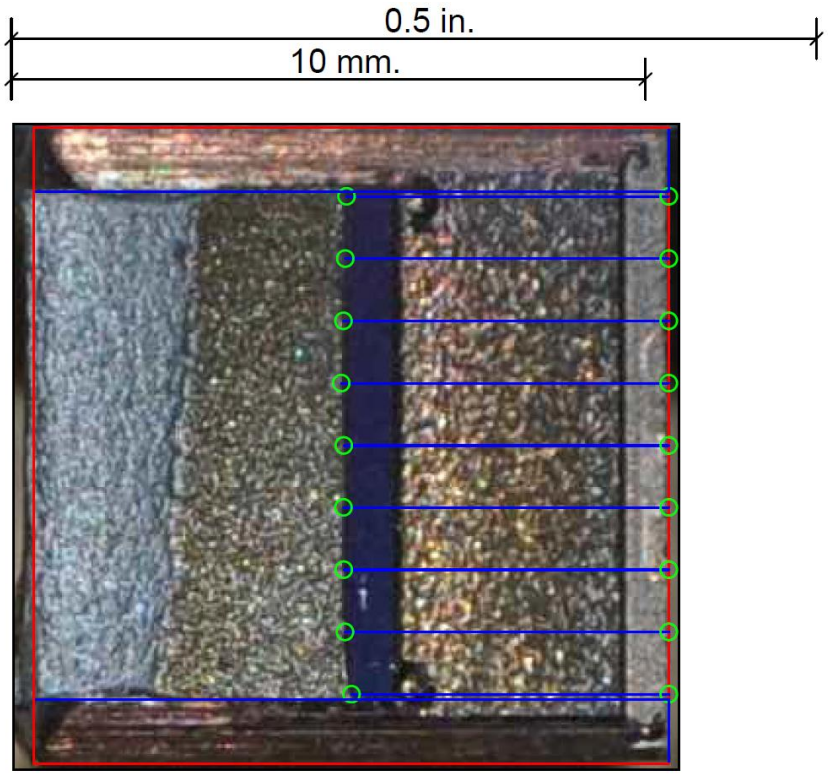

Figure C-138. Specimen H9' Fracture Surface

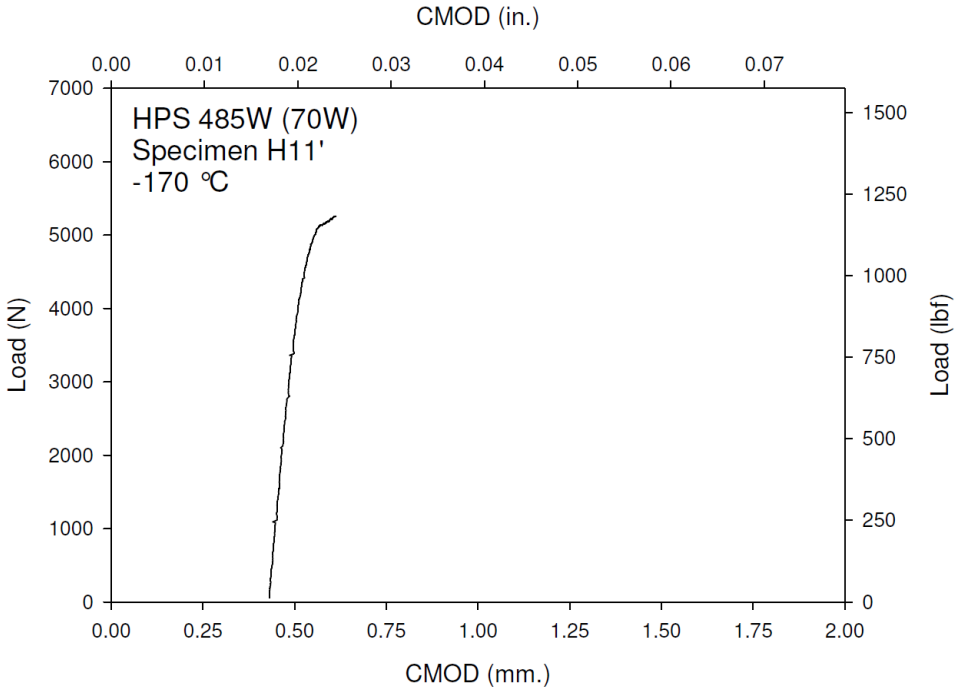

Figure C-139. Specimen H11' Test Record

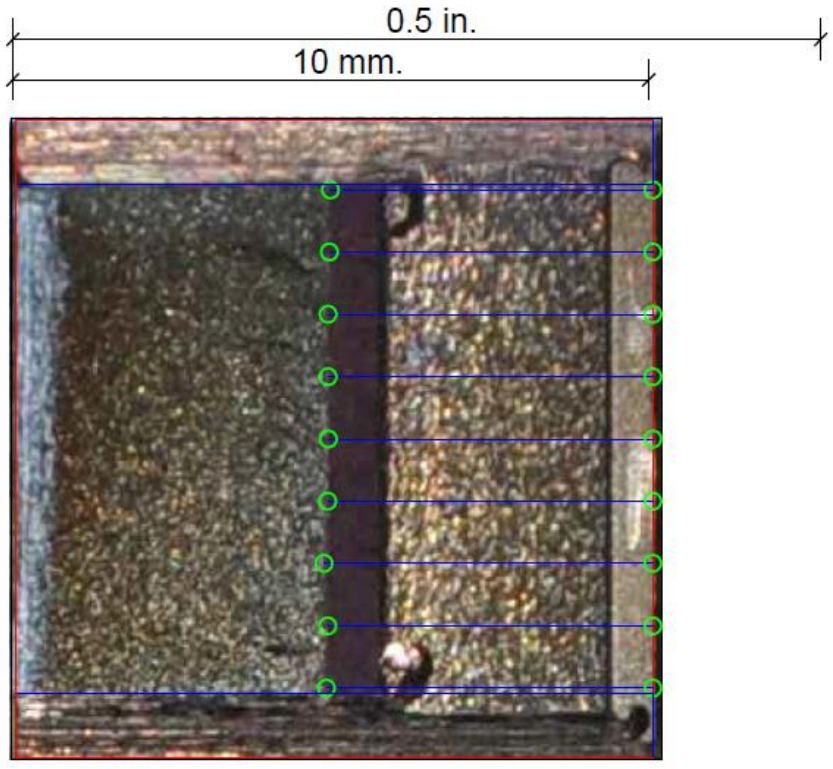

Figure C-140. Specimen H11' Fracture Surface

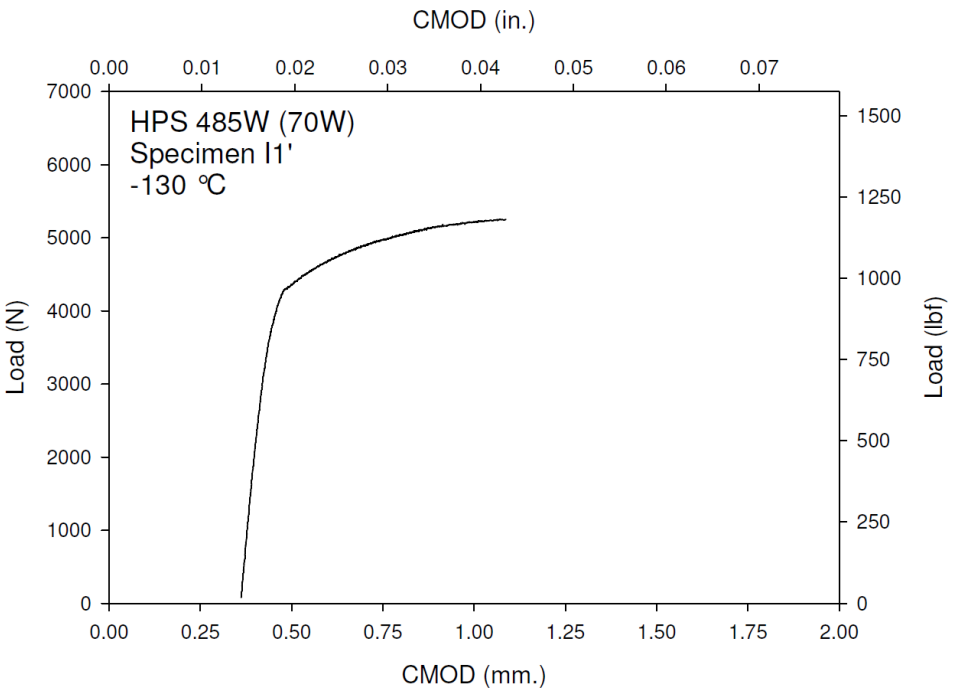

Figure C-141. Specimen I1' Test Record

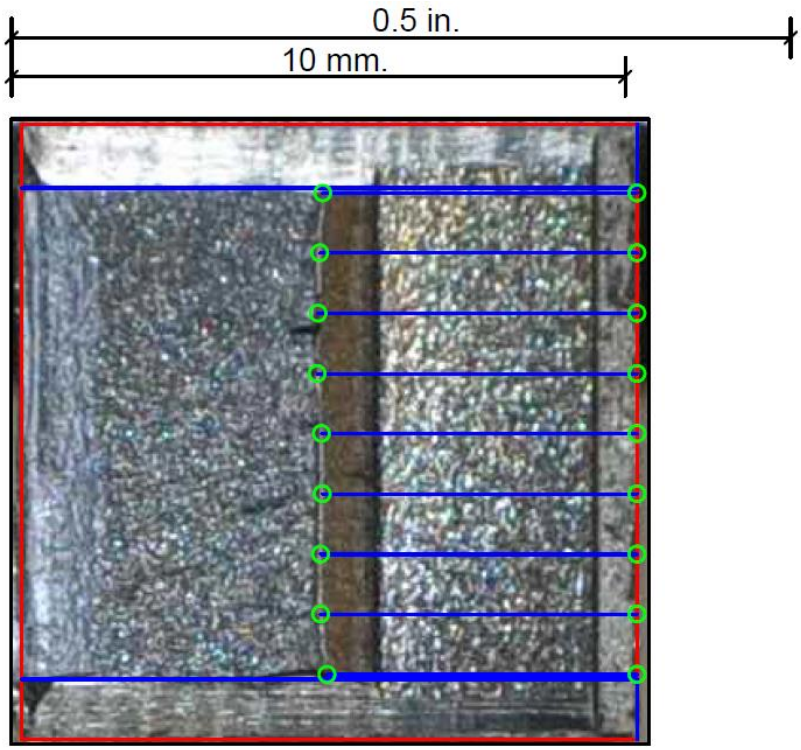

Figure C-142. Specimen I1' Fracture Surface

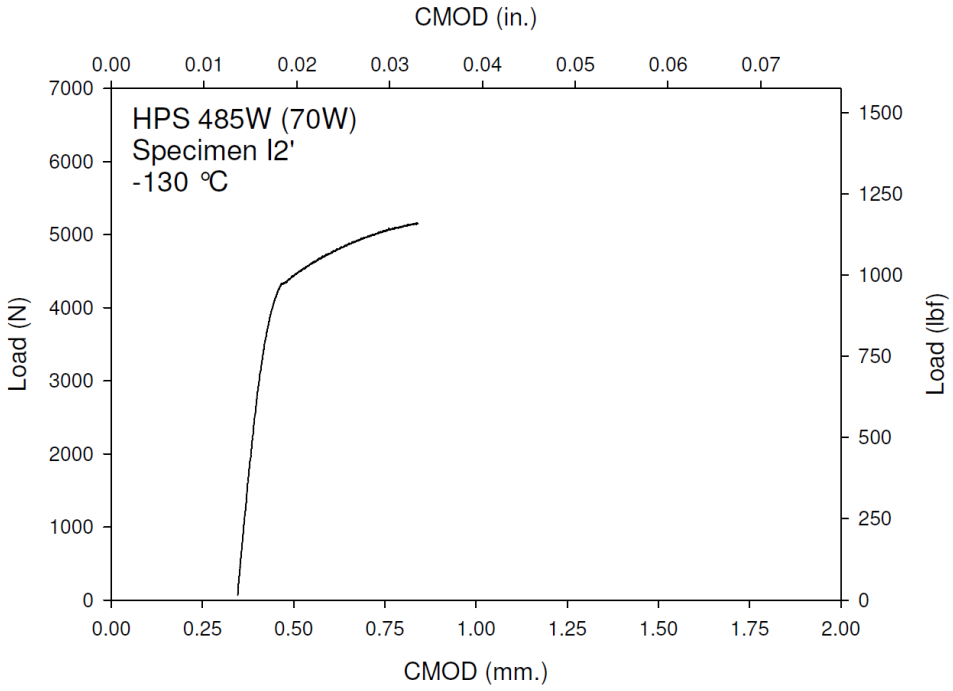

Figure C-143. Specimen I2' Test Record

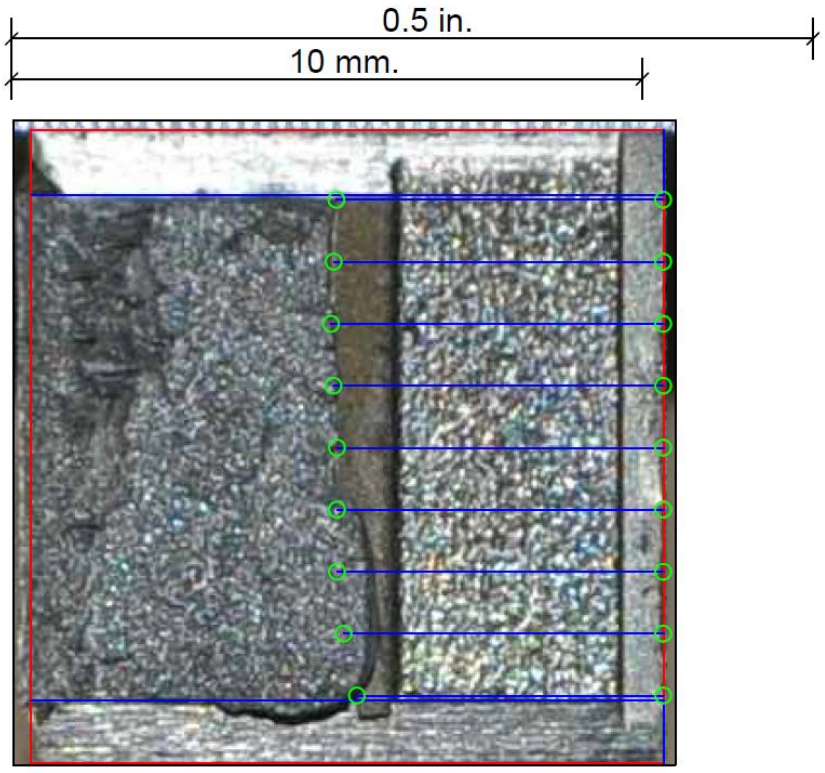

Figure C-144. Specimen I2' Fracture Surface

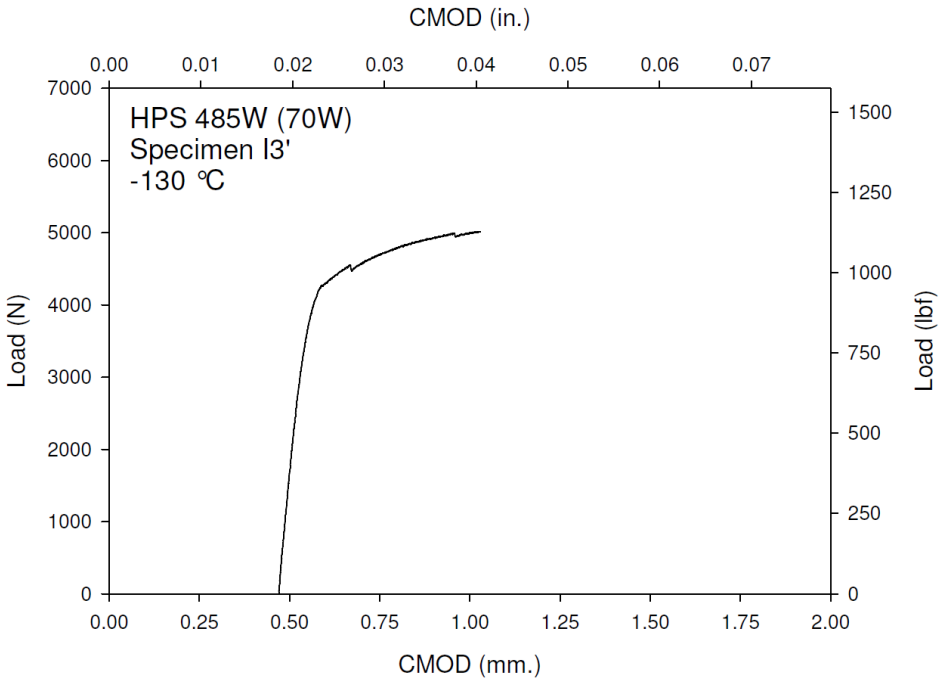

Figure C-145. Specimen I3' Test Record

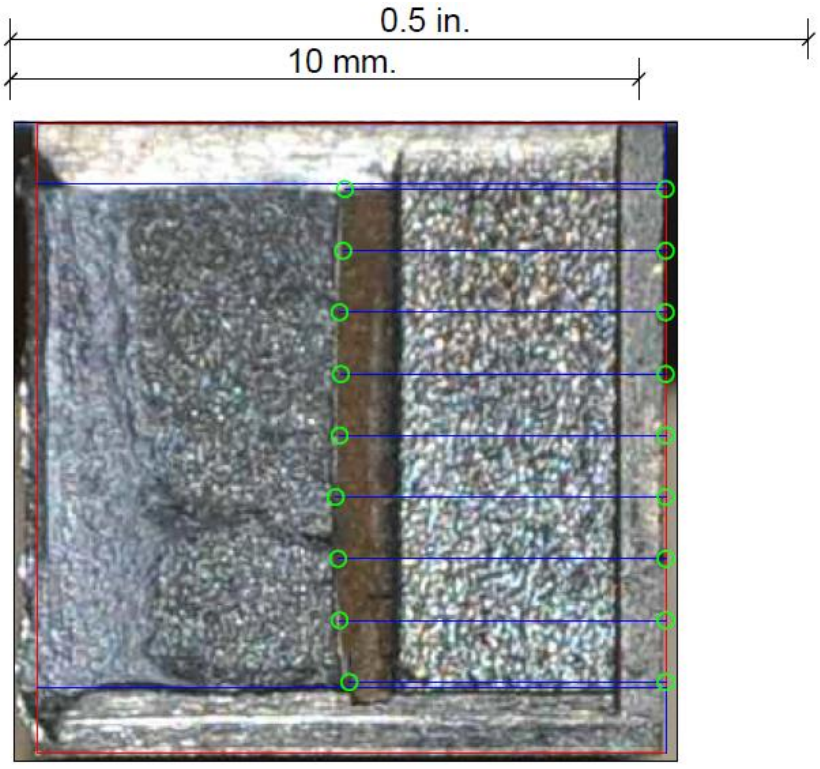

Figure C-146. Specimen I3' Fracture Surface

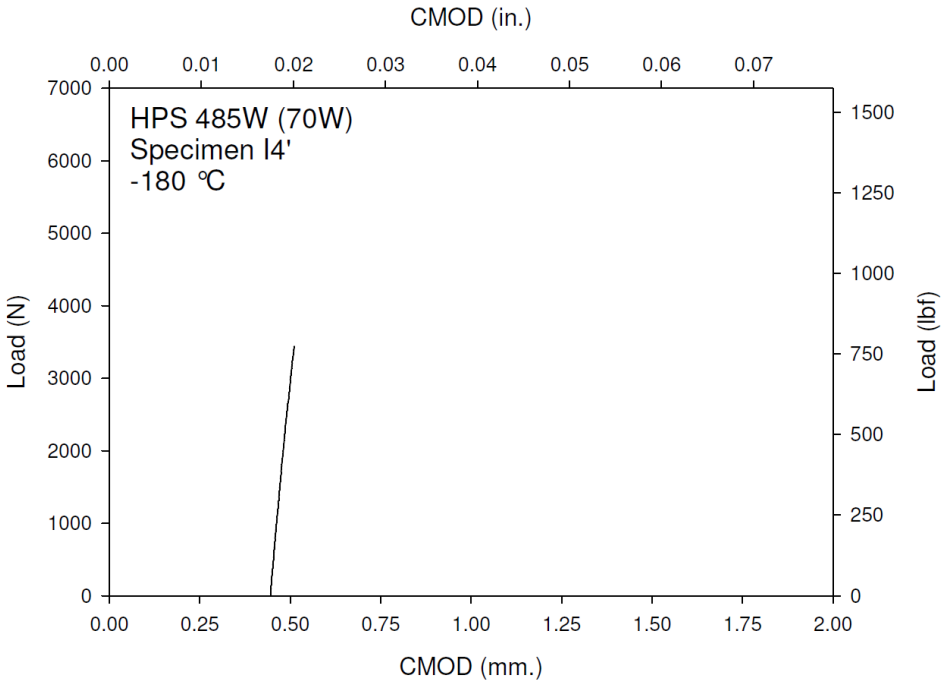

Figure C-147. Specimen I4' Test Record

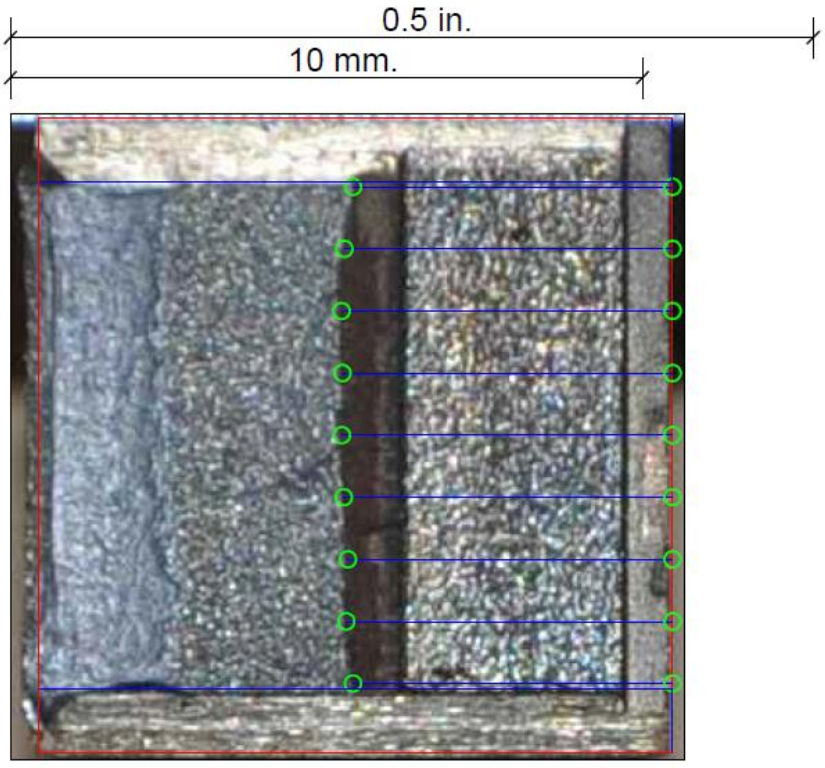

Figure C-148. Specimen I4' Fracture Surface

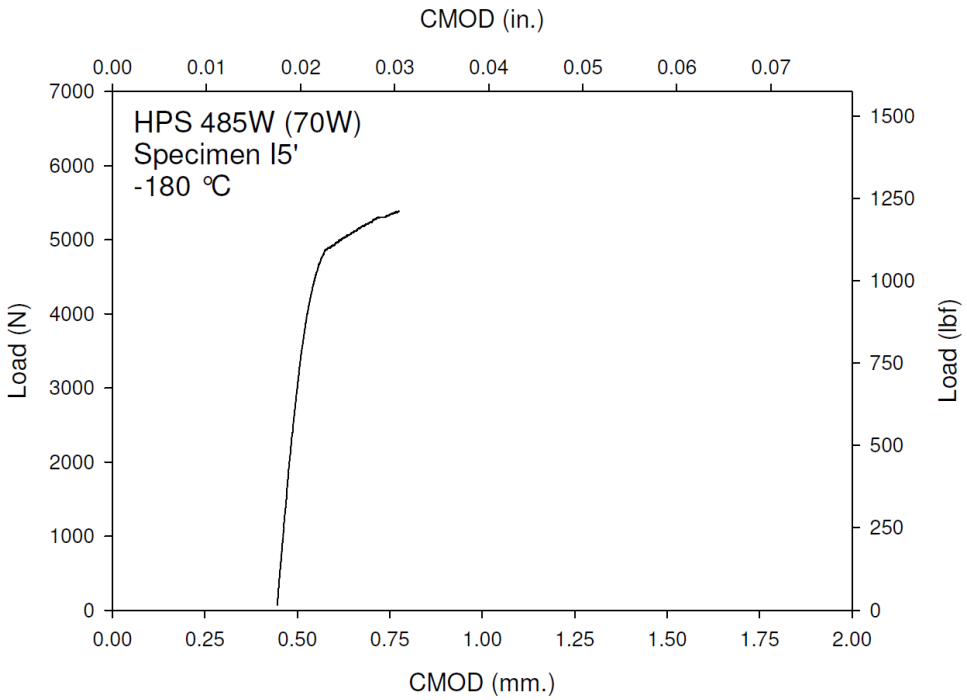

Figure C-149. Specimen I5' Test Record

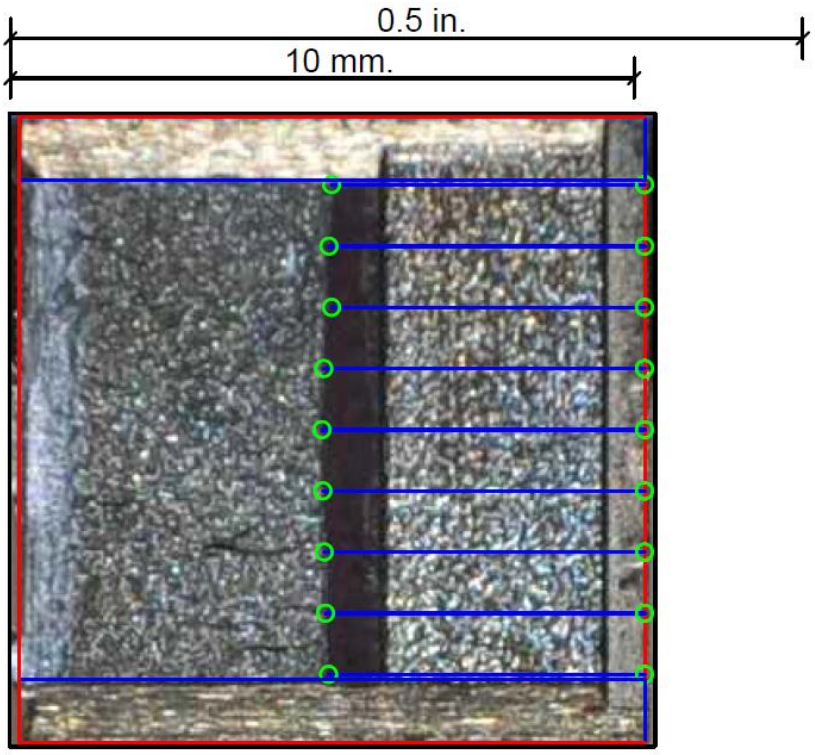

Figure C-150. Specimen I5' Fracture Surface

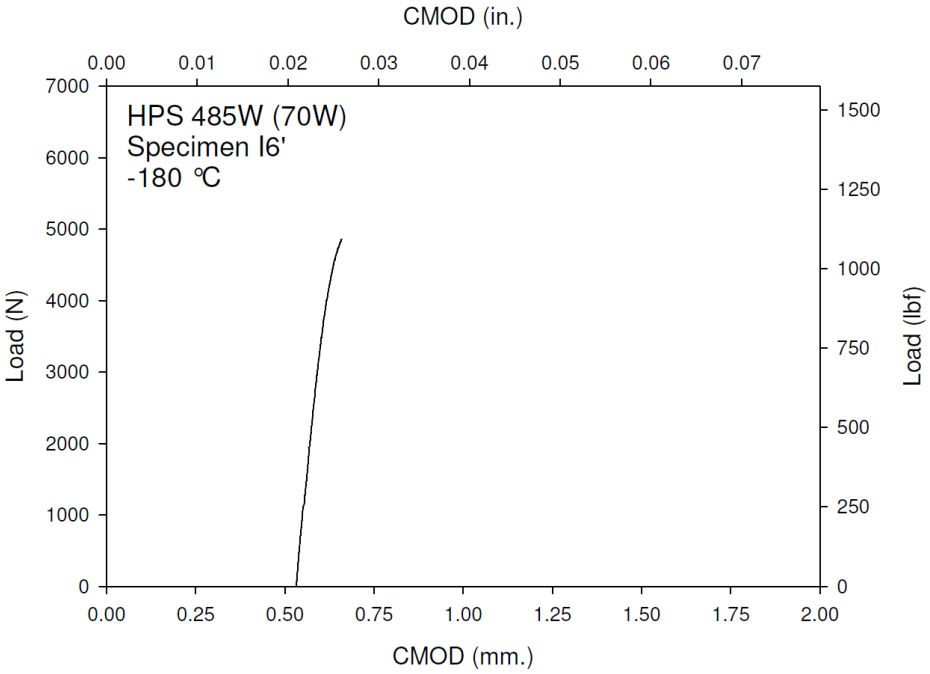

Figure C-151. Specimen I6' Test Record

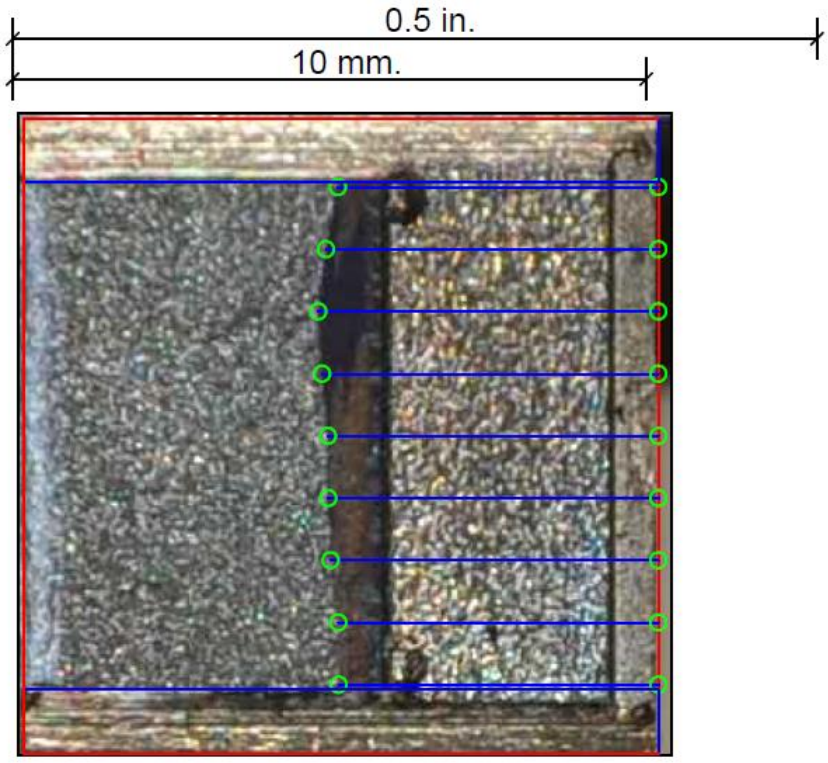

Figure C-152. Specimen I6' Fracture Surface

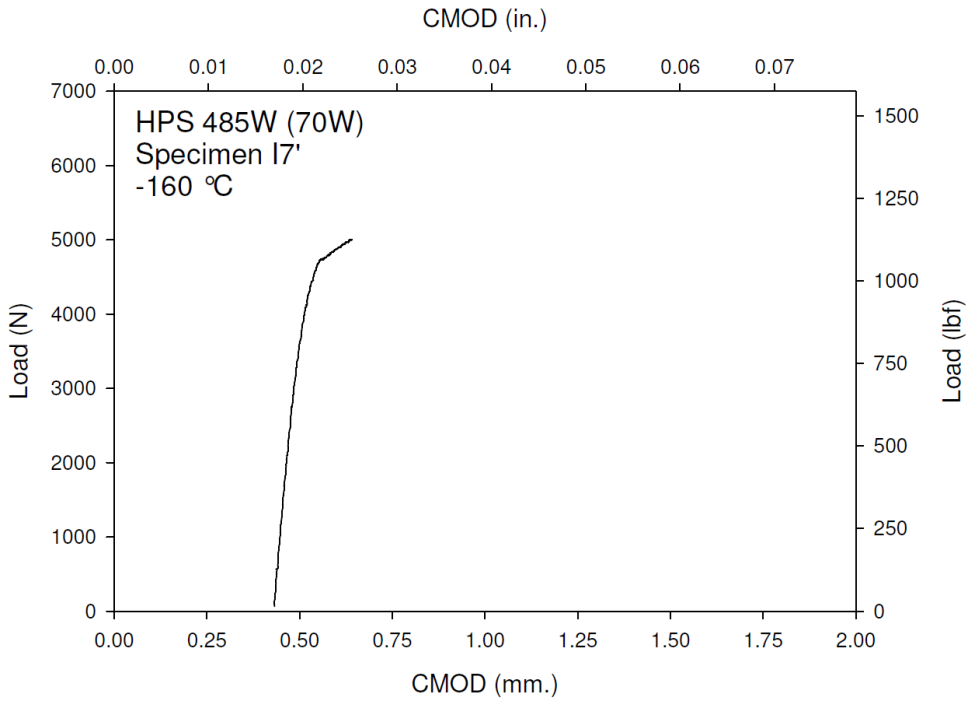

Figure C-153. Specimen I7' Test Record

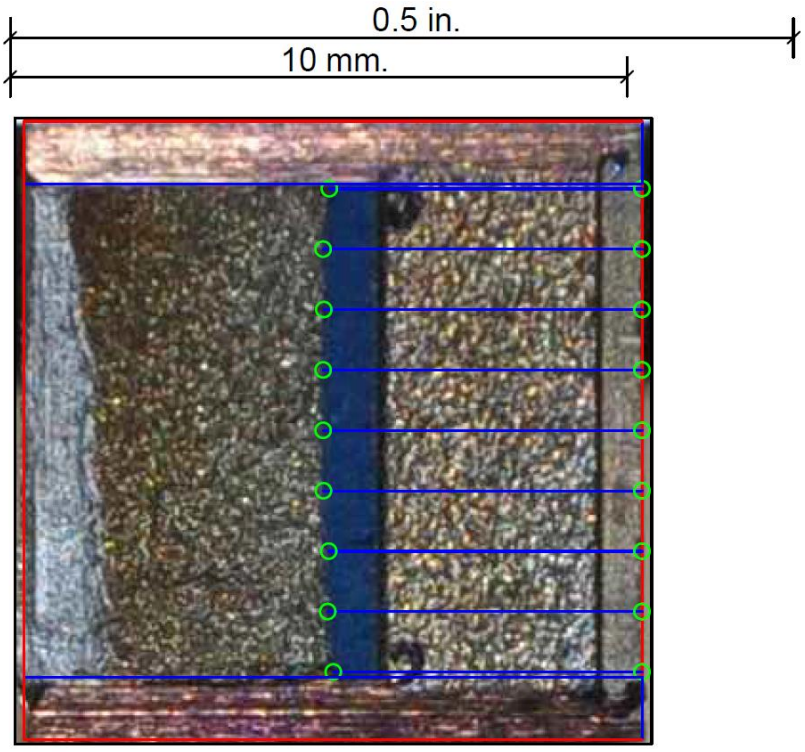

Figure C-154. Specimen I7' Fracture Surface

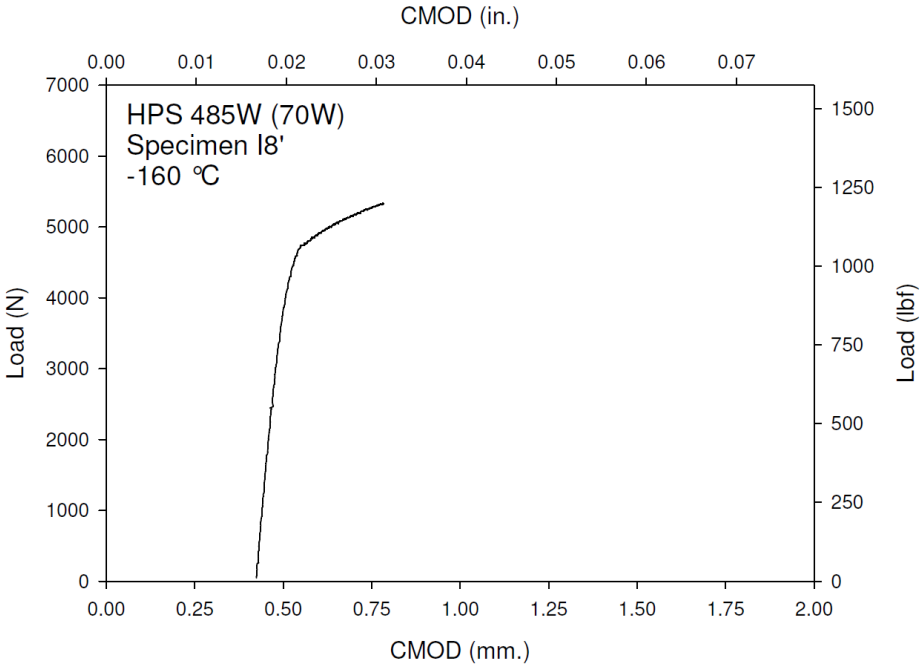

Figure C-155. Specimen I8' Test Record

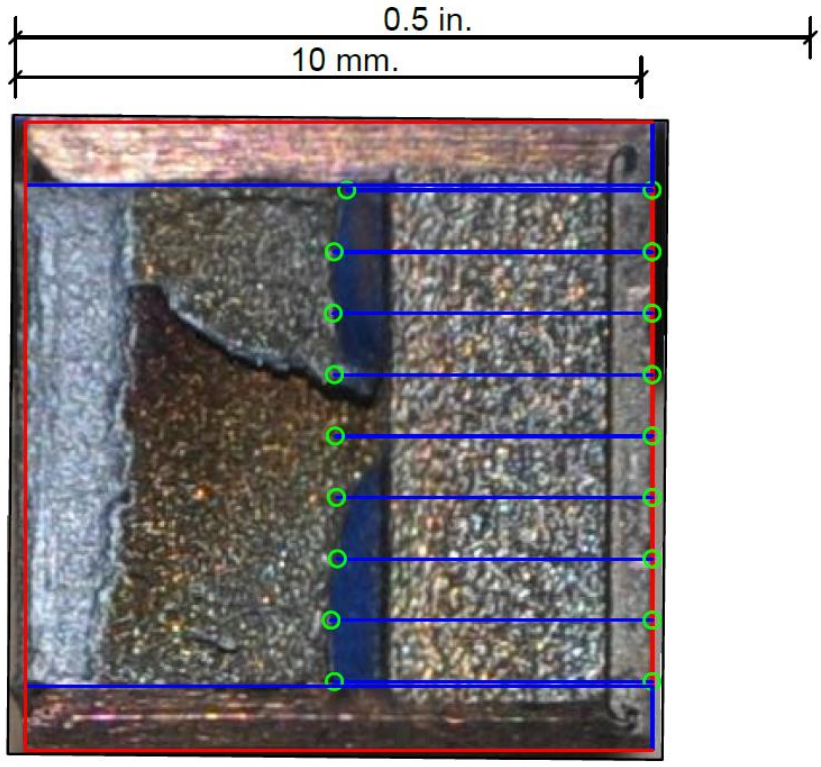

Figure C-156. Specimen I8' Fracture Surface

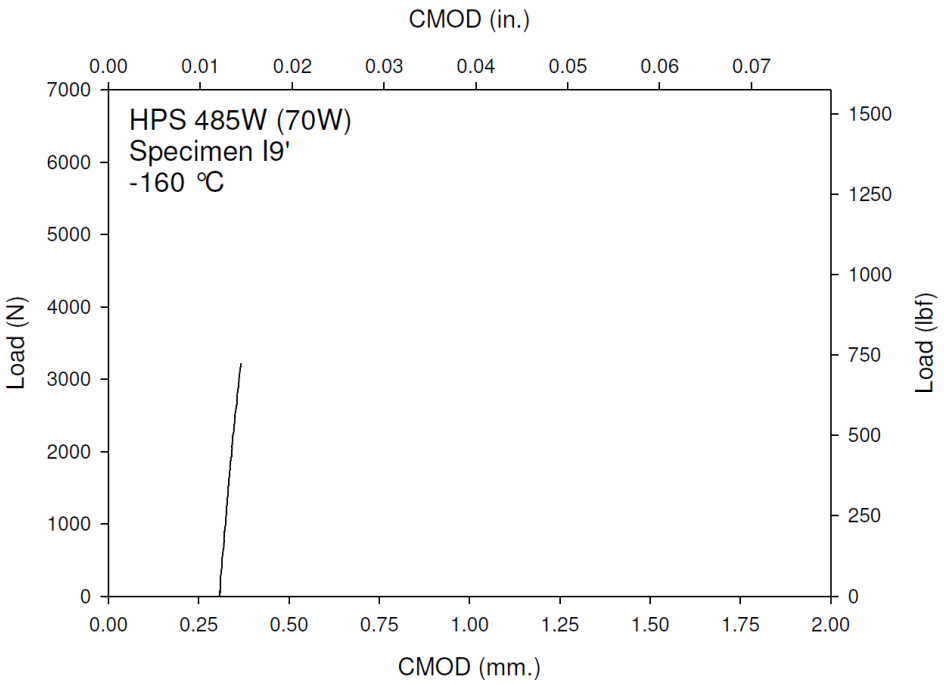

Figure C-157. Specimen I9' Test Record

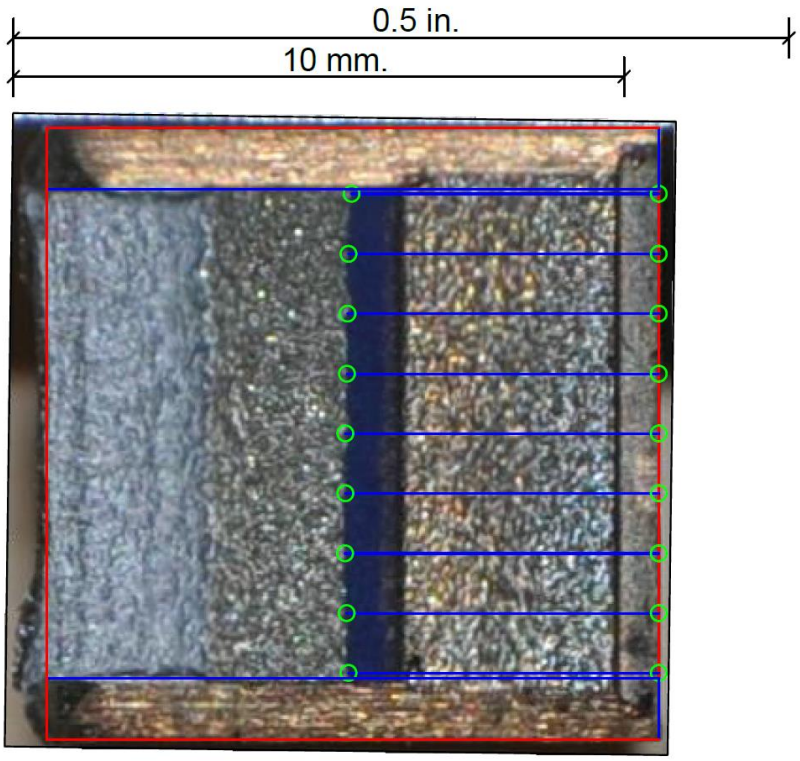

Figure C-158. Specimen I9' Fracture Surface

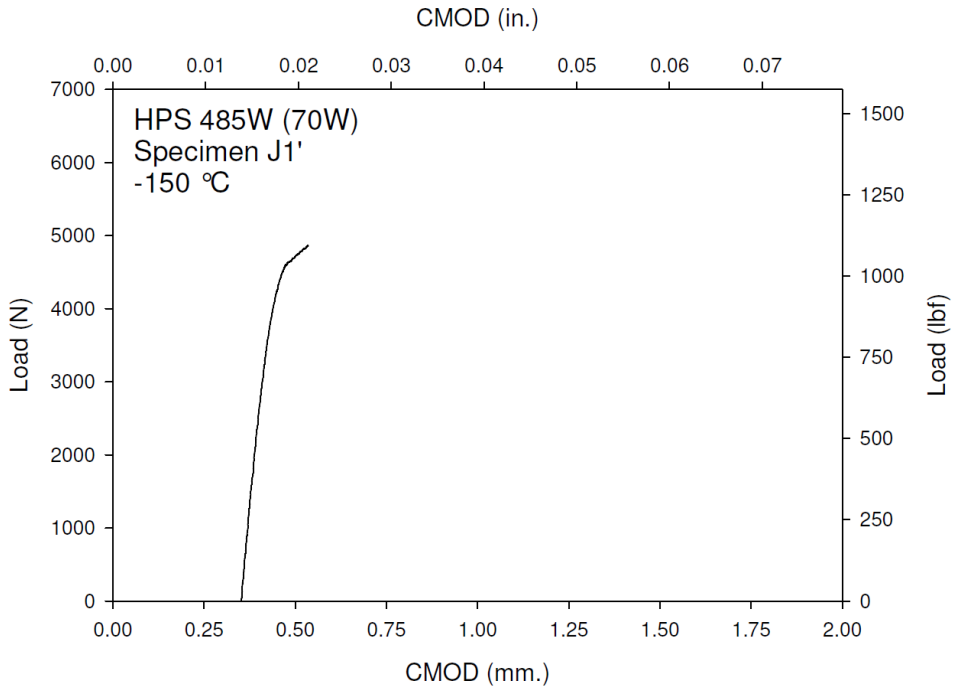

Figure C-159. Specimen J1' Test Record

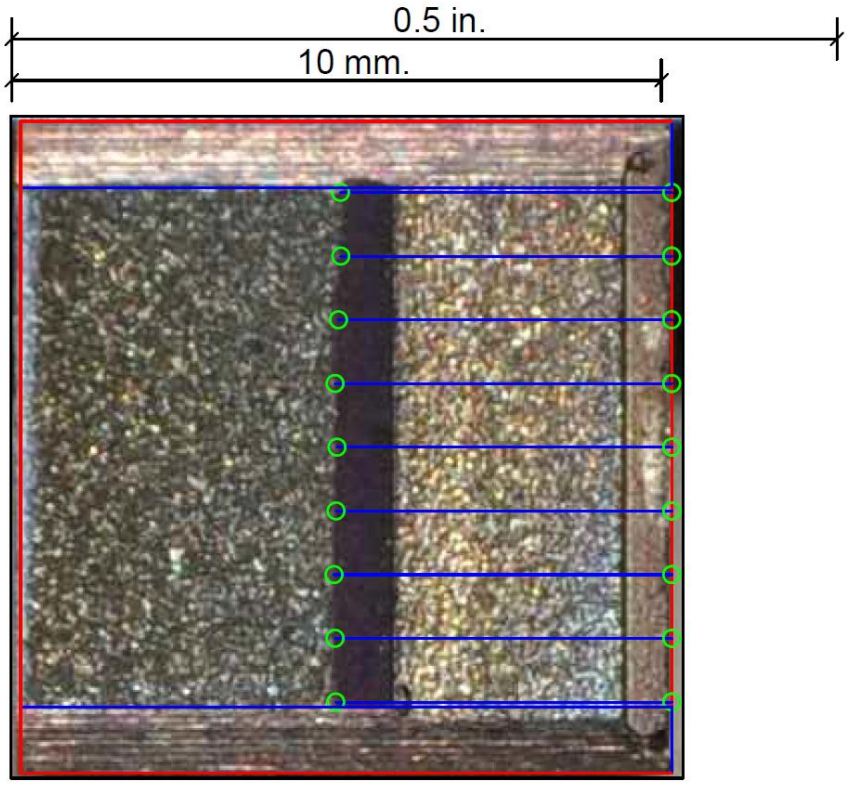

Figure C-160. Specimen J1' Fracture Surface

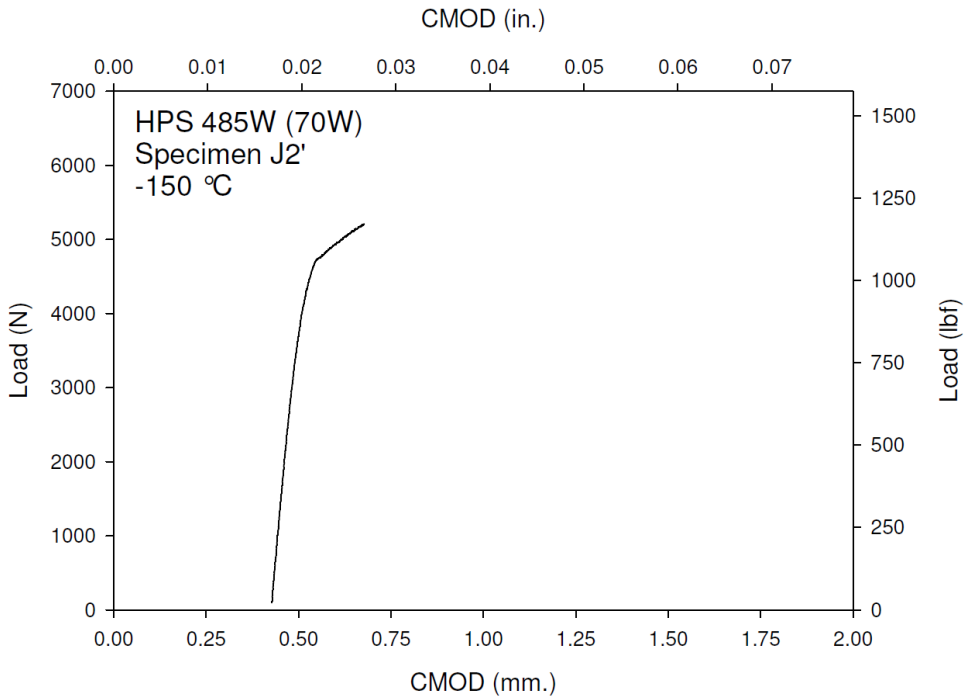

Figure C-161. Specimen J2' Test Record

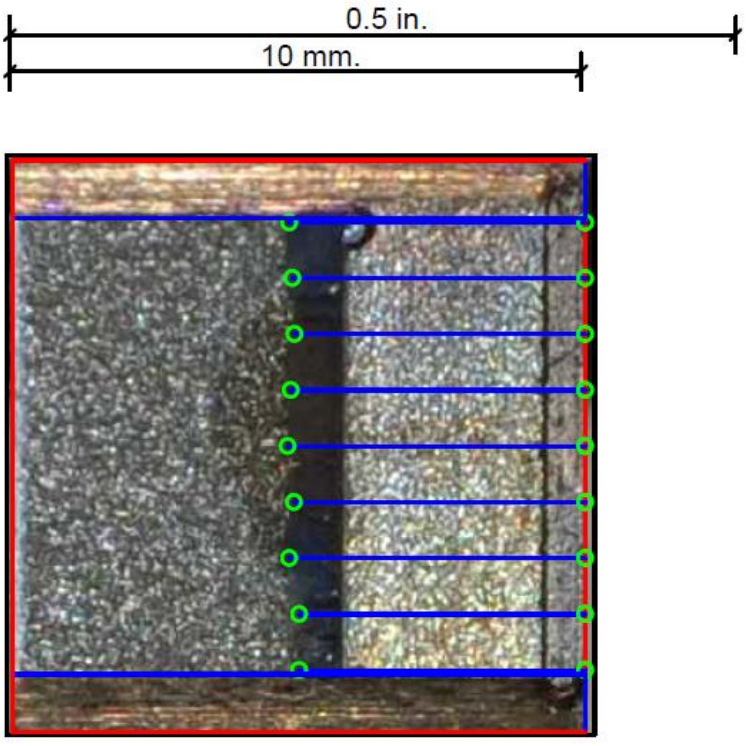

Figure C-162. Specimen J2' Fracture Surface

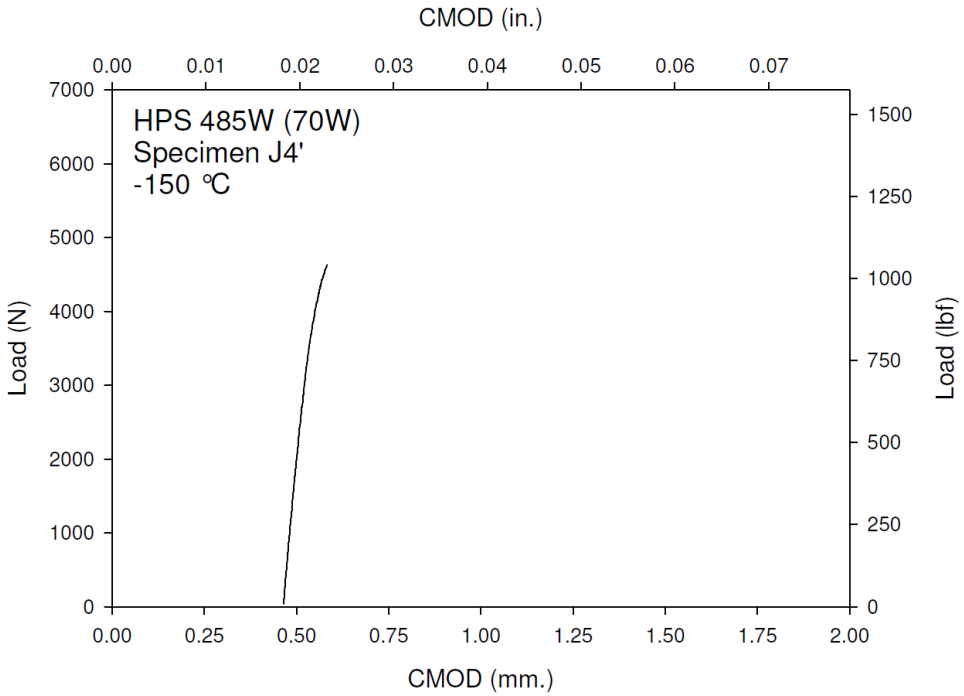

Figure C-163. Specimen J4' Test Record

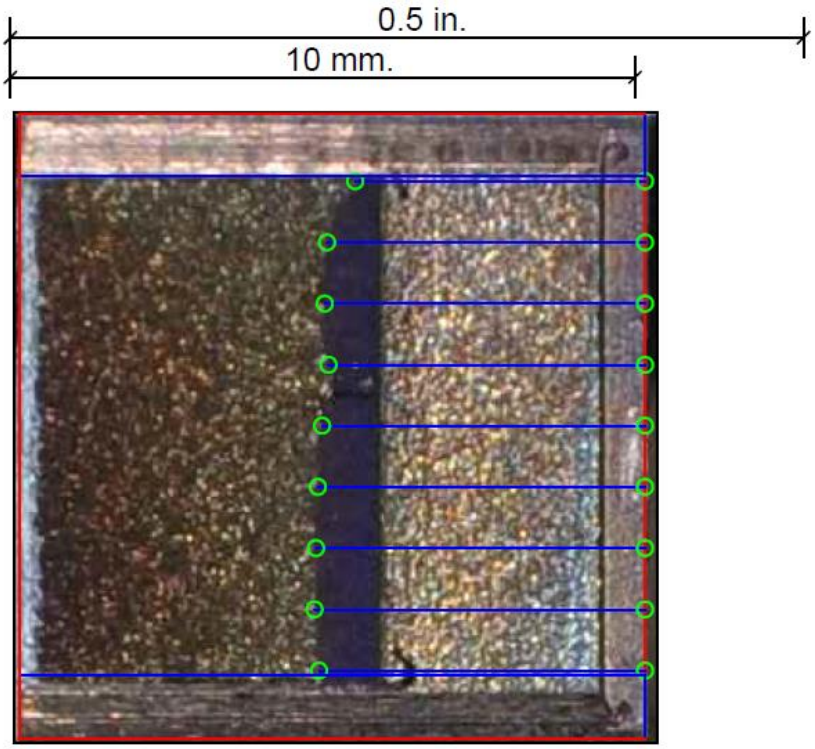

Figure C-164. Specimen J4' Fracture Surface

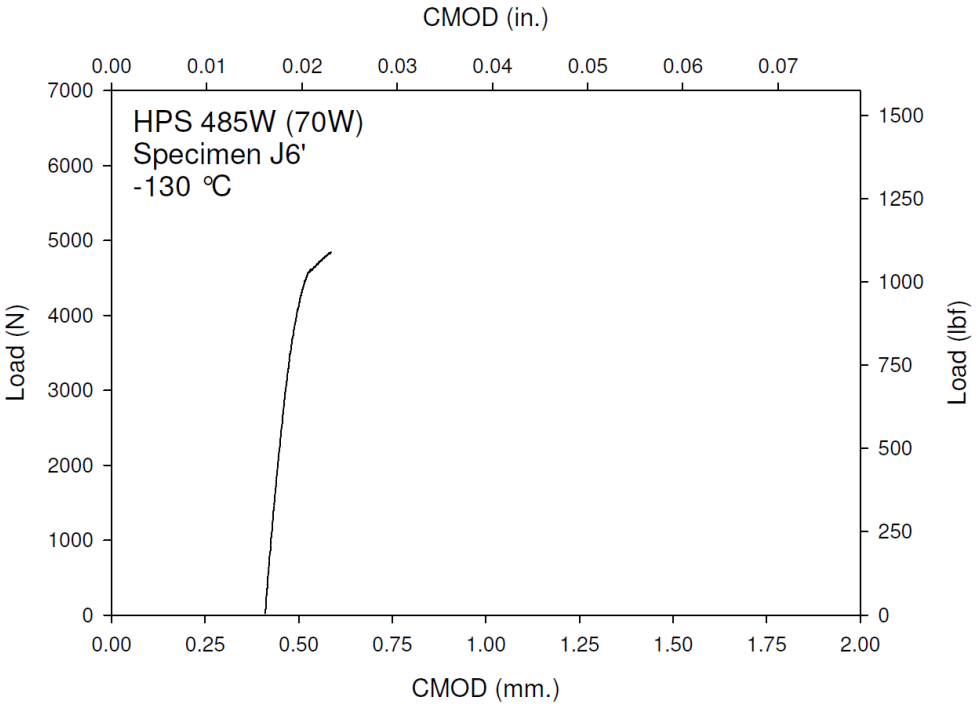

Figure C-165. Specimen J6' Test Record

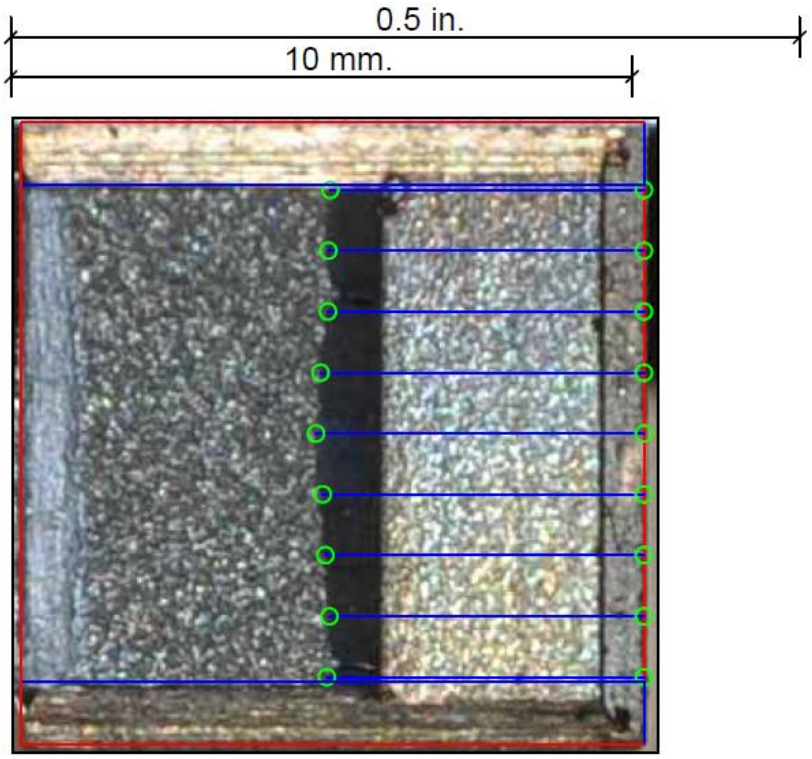

Figure C-166. Specimen J6' Fracture Surface

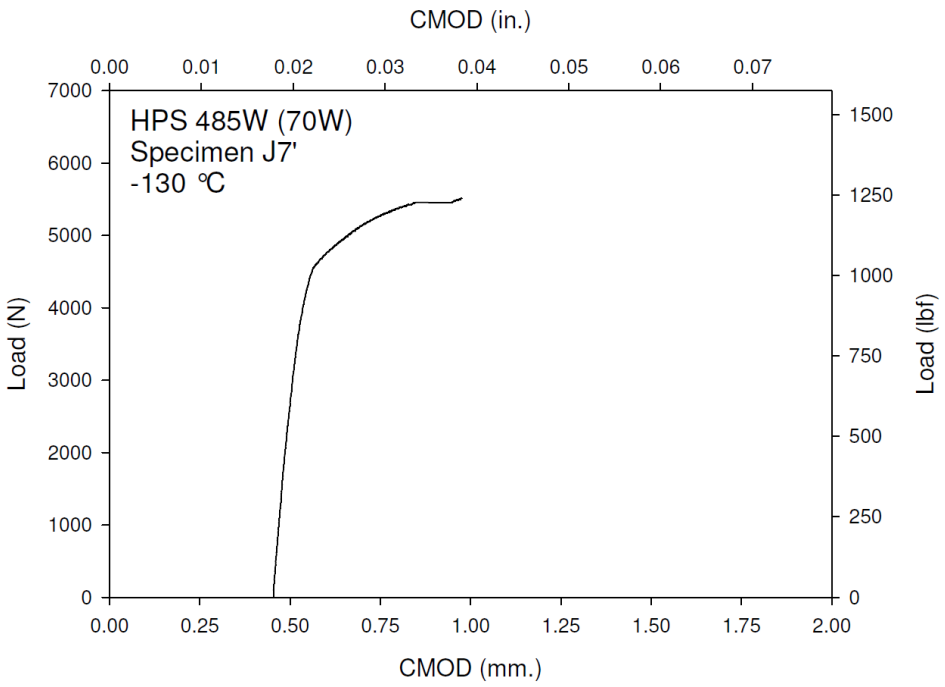

Figure C-167. Specimen J7' Test Record

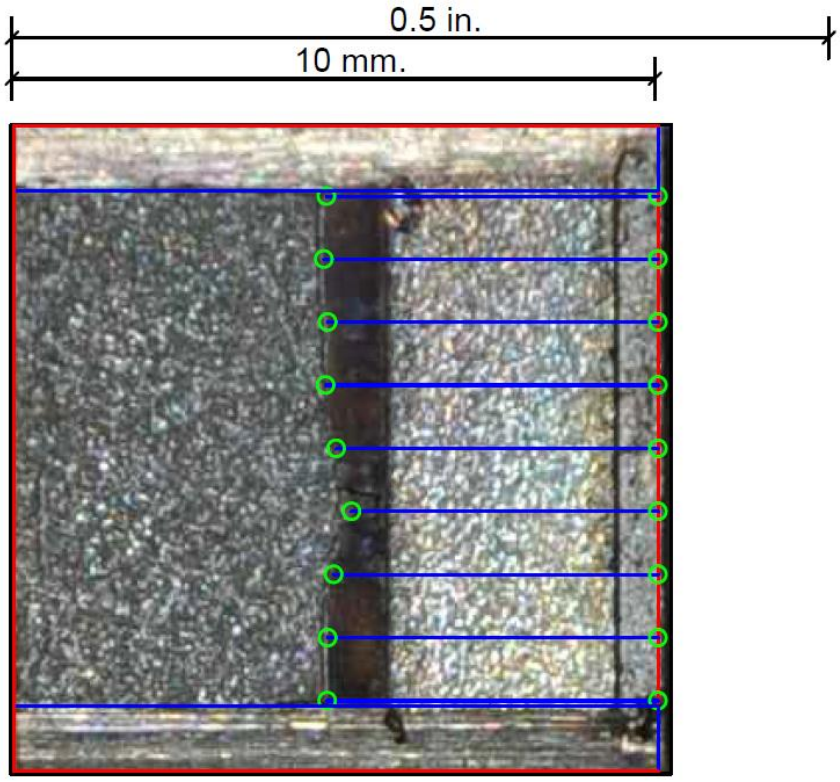

Figure C-168. Specimen J7' Fracture Surface

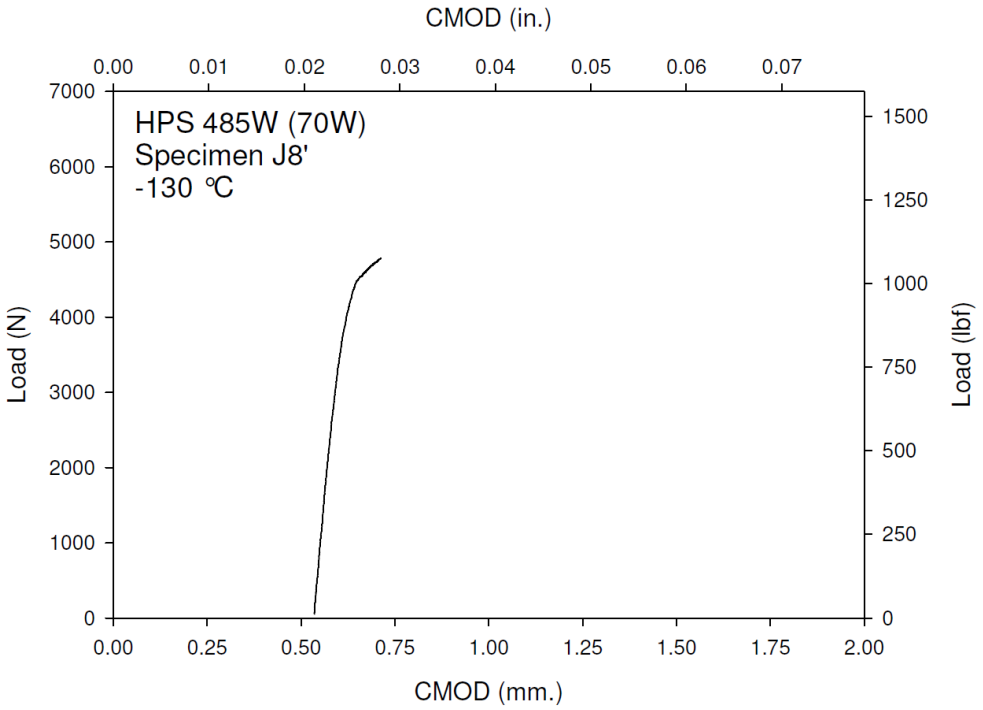

Figure C-169. Specimen J8' Test Record

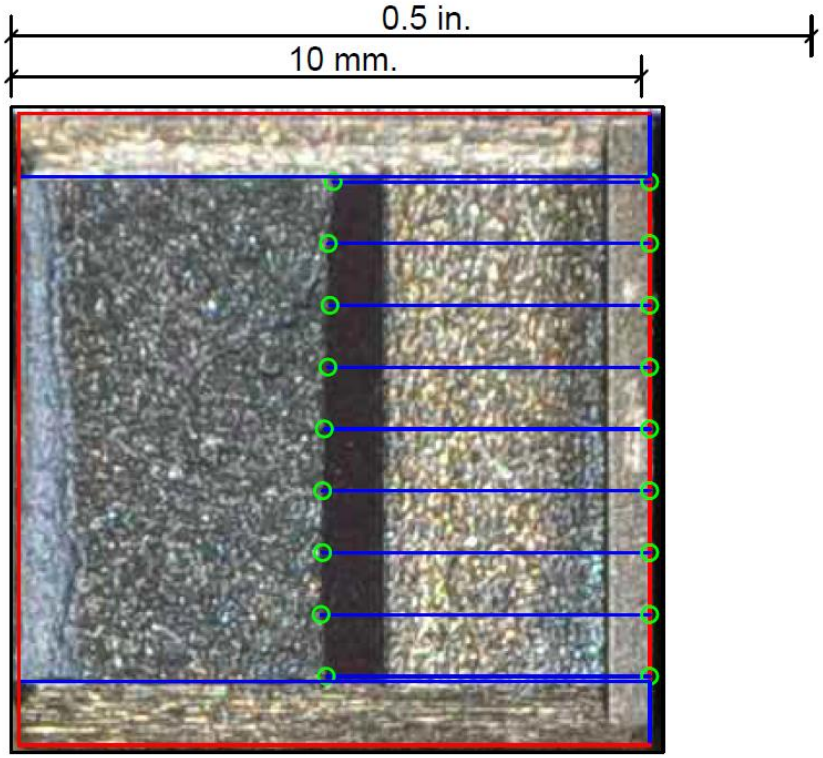

Figure C-170. Specimen J8' Fracture Surface

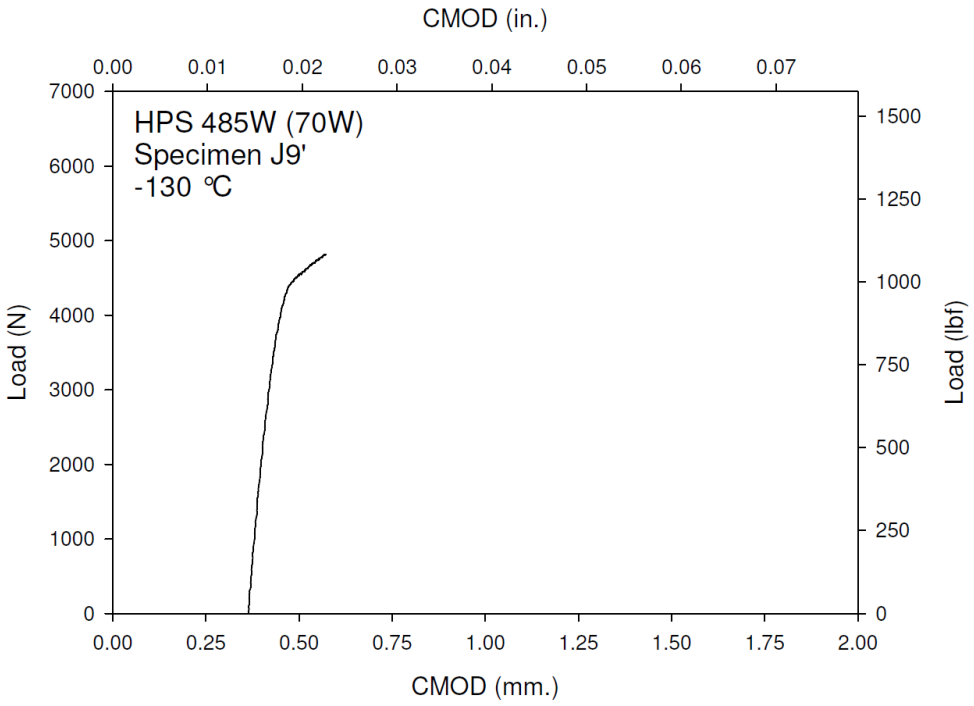

Figure C-171. Specimen J9' Test Record

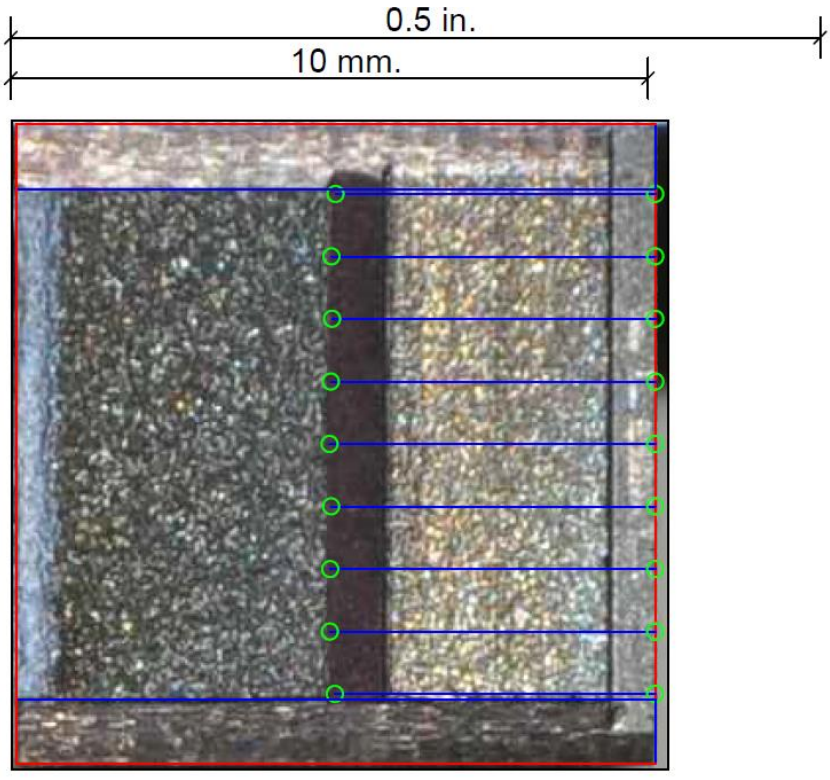

Figure C-172. Specimen J9' Fracture Surface

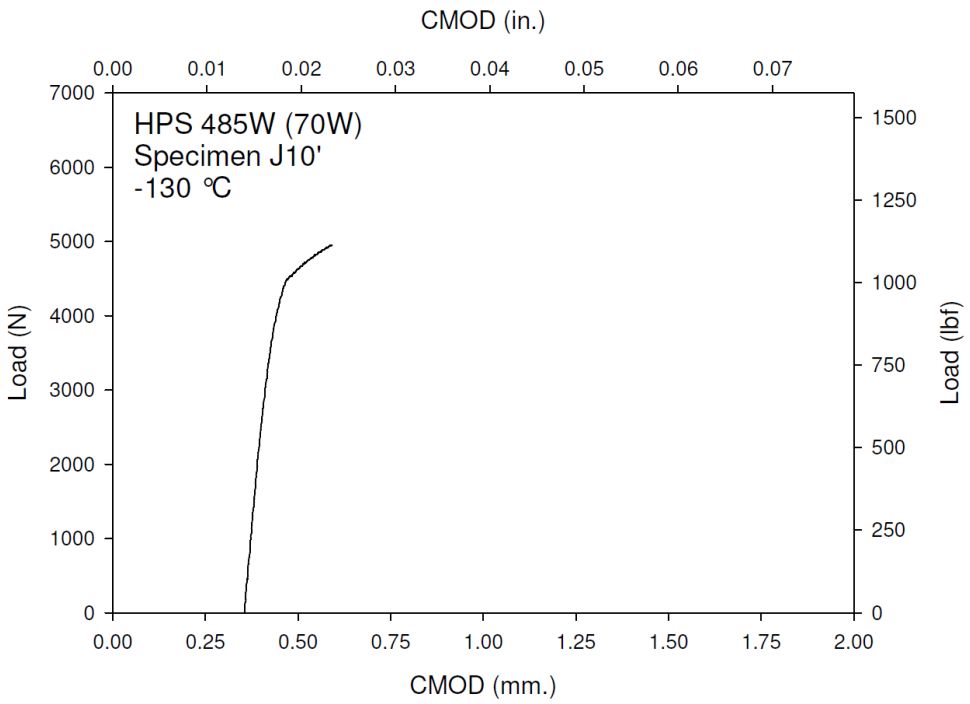

Figure C-173. Specimen J10' Test Record

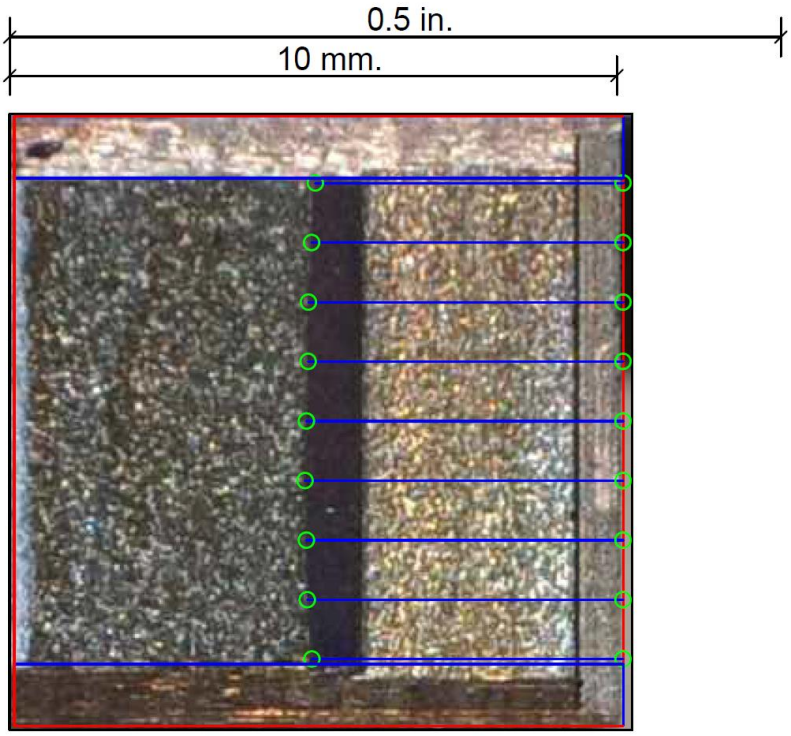

Figure C-174. Specimen J10' Fracture Surface

APPENDIX D: Tabulated HPS Static Fracture Toughness

Table D-1. Static Specimen Information for Plate A, HPS 485W, 25.4 mm.

Specimen ID	W		a_o		B		B_N	
	mm.	in.	mm.	in.	mm.	in.	mm.	in.
A1'	10.02	0.3945	5.16	0.203	10.01	0.3941	8.00	0.315
A2'	10.01	0.3941	5.16	0.203	10.01	0.3941	8.00	0.315
A3'	10.02	0.3945	5.08	0.200	10.01	0.3941	8.00	0.315
A4'	10.01	0.3941	5.10	0.201	10.02	0.3945	8.00	0.315
A5'	10.00	0.3937	5.10	0.201	10.00	0.3937	8.00	0.315
A6'	10.01	0.3941	5.12	0.202	10.02	0.3945	8.00	0.315
A7'	10.01	0.3941	5.18	0.204	10.01	0.3941	8.00	0.315
A8'	10.01	0.3941	5.14	0.202	10.01	0.3941	8.00	0.315
A9'	10.01	0.3941	5.10	0.201	10.01	0.3941	8.00	0.315

Table D-2. Static Test Information for Plate A, HPS 485W, 25.4 mm.

Specimen ID	Test Temperature		Test Result, K_{Jc}		Valid?	Censored?	1T K_{Jc}	
	°C	°F	MPa√m	ksi√in			MPa√m	ksi√in
A1'	-150	-238	150.8	137.2	Yes	No	123.6	112.5
A2'	-150	-238	213.2	194.0	Yes	Yes	141.8	129.1
A3'	-150	-238	193.9	176.4	Yes	Yes	143.1	130.2
A4'	-185	-301	112.0	101.9	Yes	No	92.9	84.6
A5'	-185	-301	71.0	64.6	Yes	No	60.4	55.0
A6'	-185	-301	26.5	24.1	No	No	25.2	22.9
A7'	-170	-274	134.9	122.8	Yes	No	111.0	101.0
A8'	-170	-274	137.4	125.0	Yes	No	113.0	102.8
A9'	-170	-274	130.6	118.8	Yes	No	107.6	97.9

Table D-3. Static Specimen Information for Plate C, HPS 690W, 19 mm.

Specimen ID	W		a_o		B		B_N	
	mm.	in.	mm.	in.	mm.	in.	mm.	in.
C1'	10.02	0.3945	5.12	0.202	10.01	0.3941	8.00	0.3152
C2'	10.01	0.3941	5.14	0.202	10.02	0.3945	8.00	0.3152
C3'	10.03	0.3949	5.15	0.203	10.02	0.3945	8.00	0.3152
C4'	10.03	0.3949	5.15	0.203	10.02	0.3945	8.00	0.3152
C5'	10.02	0.3945	5.15	0.203	10.02	0.3945	8.00	0.3152
C6'	No Results- Data File Corrupted							
C7'	10.02	0.3945	5.09	0.200	10.02	0.3945	8.00	0.3152
C8'	10.03	0.3949	5.12	0.202	10.03	0.3949	8.00	0.3152
C9'	10.02	0.3945	5.16	0.203	10.02	0.3945	8.00	0.3152

Table D-4. Static Test Information for Plate C, HPS 690W, 19 mm.

Specimen ID	Test Temperature		Test Result, K_{Jc}		Valid?	Censored?	1T K_{Jc}	
	°C	°F	MPa√m	ksi√in			MPa√m	ksi√in
C1'	-110	-166	86.0	78.3	Yes	No	72.3	65.8
C2'	-110	-166	82.3	74.9	Yes	No	69.4	63.1
C3'	-110	-166	64.2	58.4	Yes	No	55.0	50.1
C4'	-70	-94	175.1	159.3	Yes	No	142.9	130.1
C5'	-70	-94	170.0	154.7	Yes	No	138.9	126.4
C6'	No Results- Data File Corrupted							
C7'	-90	-130	128.3	116.8	Yes	No	105.8	96.3
C8'	-90	-130	91.5	83.3	Yes	No	76.7	69.8
C9'	-51	-60	155.9	141.9	Yes	No	127.7	116.2

Table D-5. Static Specimen Information for Plate D, HPS 485W, 63.5 mm.

Specimen ID	W		a_o		B		B_N	
	mm.	in.	mm.	in.	mm.	in.	mm.	in.
D3'	10.02	0.394	5.10	0.201	10.00	0.3937	8.00	0.3152
D4'	10.03	0.395	5.33	0.210	10.03	0.3949	8.00	0.3152
D7'	10.02	0.394	5.37	0.211	10.03	0.3949	8.00	0.3152
D8'	10.02	0.394	5.35	0.211	10.03	0.3949	8.00	0.3152
D9'	10.02	0.394	5.31	0.209	10.03	0.3949	8.00	0.3152
D10'	10.02	0.394	5.39	0.212	10.03	0.3949	8.00	0.3152
D13'	10.02	0.394	5.35	0.211	10.03	0.3949	8.00	0.3152
D14'	10.02	0.394	5.33	0.210	10.03	0.3949	8.00	0.3152
D15'	10.02	0.394	5.37	0.211	10.03	0.3949	8.00	0.3152
D16'	10.03	0.395	5.31	0.209	10.02	0.3945	8.00	0.3152
D18'	10.02	0.394	5.38	0.212	10.02	0.3945	8.00	0.3152
D19'	10.03	0.395	5.46	0.215	10.02	0.3945	8.00	0.3152
D20'	10.02	0.394	5.40	0.213	10.02	0.3945	8.00	0.3152

Table D-6. Static Test Information for Plate D, HPS 485W, 63.5 mm.

Specimen ID	Test Temperature		Test Result, K_{Jc}		Valid?	Censored?	1T K_{Jc}	
	°C	°F	MPa√m	ksi√in			MPa√m	ksi√in
D3'	-129	-200	287.6	261.7	Yes	Yes	132.0	120.1
D4'	-129	-200	148.4	135.0	No	No	121.8	110.8
D7'	-150	-238	207.4	188.7	No	Yes	129.9	118.2
D8'	-150	-238	91.3	83.1	Yes	No	76.5	69.6
D9'	-150	-238	200.3	182.3	Yes	Yes	130.7	119.0
D10'	-150	-238	243.3	221.4	Yes	Yes	129.7	118.0
D13'	-180	-292	254.1	231.2	Yes	Yes	143.1	130.2
D14'	-180	-292	52.7	48.0	Yes	No	45.9	41.8
D15'	-180	-292	82.8	75.3	Yes	No	69.8	63.5
D16'	-170	-274	161.3	146.8	No	No	132.0	120.1
D18'	-170	-274	144.6	131.6	Yes	No	118.7	108.1
D19'	-170	-274	147.4	134.1	Yes	No	121.0	110.1
D20'	-170	-274	119.1	108.4	Yes	No	98.5	89.7

Table D-7. Static Specimen Information for Plate E, HPS 690W, 38.1 mm.

Specimen ID	W		a_o		B		B_N	
	mm.	in.	mm.	in.	mm.	in.	mm.	in.
E1'	10.03	0.395	5.37	0.211	10.01	0.3941	8.00	0.3152
E3'	10.01	0.394	5.34	0.210	10.02	0.3945	8.00	0.3152
E4'	10.02	0.394	5.32	0.209	10.01	0.3941	8.00	0.3152
E5'	10.03	0.395	5.35	0.211	10.02	0.3945	8.00	0.3152
E6'	10.03	0.395	5.48	0.216	10.02	0.3945	8.00	0.3152
E7'	10.02	0.394	5.36	0.211	10.01	0.3941	8.00	0.3152
E8'	10.03	0.395	5.37	0.211	10.04	0.3953	8.00	0.3152
E9'	10.02	0.394	5.45	0.215	10.01	0.3941	8.00	0.3152
E10'	10.03	0.395	5.45	0.215	10.01	0.3941	8.00	0.3152
E11'	10.02	0.394	5.36	0.211	10.02	0.3945	8.00	0.3152
E12'	10.02	0.394	5.36	0.211	10.03	0.3949	8.00	0.3152
E14	10.01	0.394	5.37	0.211	10.02	0.3945	8.00	0.3152
E19'	10.01	0.394	5.38	0.212	10.03	0.3949	8.00	0.3152
E20'	10.03	0.395	5.31	0.209	10.02	0.3945	8.00	0.3152
E21'	10.02	0.394	5.32	0.209	10.03	0.3949	8.00	0.3152

Table D-8. Static Test Information for Plate E, HPS 690W, 38.1 mm.

Specimen ID	Test Temperature		Test Result, K_{Jc}		Valid?	Censored?	1T K_{Jc}	
	°C	°F	MPa√m	ksi√in			MPa√m	ksi√in
E1'	-72	-98	133.1	121.1	Yes	No	109.6	99.7
E3'	-129	-200	62.3	56.7	Yes	No	53.5	48.7
E4'	-129	-200	91.5	83.3	No	No	76.7	69.8
E5'	-90	-130	142.5	129.7	No	No	117.1	106.5
E6'	-90	-130	203.3	185.0	Yes	Yes	135.8	123.5
E7'	-90	-130	133.5	121.5	Yes	No	109.9	100.0
E8'	-90	-130	170.3	155.0	Yes	Yes	137.4	125.0
E9'	-110	-166	106.3	96.7	Yes	No	88.4	80.4
E10'	-110	-166	109.4	99.6	Yes	No	90.8	82.7
E11'	-110	-166	99.7	90.7	No	No	83.2	75.7
E12'	-110	-166	91.0	82.8	Yes	No	76.3	69.4
E14	-51	-60	178.1	162.1	Yes	Yes	134.2	122.1
E19'	-110	-166	118.2	107.6	Yes	No	97.8	89.0
E20'	-110	-166	109.7	99.8	Yes	No	91.1	82.9
E21'	-110	-166	135.2	123.0	Yes	No	111.3	101.3

Table D-9. Static Specimen Information for Plate F, HPS 690W, 50.8 mm.

Specimen ID	W		a_o		B		B_N	
	mm.	in.	mm.	in.	mm.	in.	mm.	in.
F1'	10.02	0.394	5.31	0.209	10.00	0.3937	8.00	0.3152
F2'	10.01	0.394	5.37	0.211	10.00	0.3937	8.00	0.3152
F3'	10.02	0.394	5.32	0.209	10.00	0.3937	8.00	0.3152
F4'	10.00	0.394	5.36	0.211	10.01	0.3941	8.00	0.3152
F5'	10.02	0.394	5.34	0.210	10.01	0.3941	8.00	0.3152
F6'	10.02	0.394	5.31	0.209	10.03	0.3949	8.00	0.3152
F7'	10.01	0.394	5.34	0.210	10.00	0.3937	8.00	0.3152
F8'	10.02	0.394	5.37	0.211	10.01	0.3941	8.00	0.3152
F9'	10.00	0.394	5.36	0.211	10.01	0.3941	8.00	0.3152
F10'	10.00	0.394	5.33	0.210	10.03	0.3949	8.00	0.3152
F11'	10.02	0.394	5.42	0.213	10	0.3937	8.00	0.3152
F13'	10.01	0.394	5.37	0.211	10.03	0.3949	8.00	0.3152
F18'	10.02	0.394	5.37	0.211	10.02	0.3945	8.00	0.3152
F19'	10.03	0.395	5.33	0.210	10.01	0.3941	8.00	0.3152
F20'	10.02	0.394	5.33	0.210	10.01	0.3941	8.00	0.3152

Table D-10. Static Test Information for Plate F, HPS 690W, 50.8 mm.

Specimen ID	Test Temperature		Test Result, K_{Jc}		Valid?	Censored?	1T K_{Jc}	
	°C	°F	MPa√m	ksi√in			MPa√m	ksi√in
F1'	-65	-85	180.7	164.4	Yes	Yes	135.1	122.9
F2'	-65	-85	153.2	139.4	Yes	No	125.5	114.2
F3'	-129	-200	84.4	76.8	Yes	No	71.0	64.6
F4'	-129	-200	120.7	109.8	No	No	99.8	90.8
F5'	-90	-130	121.2	110.3	No	No	100.2	91.2
F6'	-90	-130	121.5	110.6	Yes	No	100.5	91.4
F7'	-90	-130	175.7	159.9	Yes	Yes	136.7	124.4
F8'	-90	-130	143.8	130.9	Yes	No	118.1	107.5
F9'	-110	-166	147.6	134.3	No	No	121.1	110.2
F10'	-110	-166	93.5	85.1	Yes	No	78.3	71.2
F11'	-110	-166	61.3	55.8	No	No	52.7	48.0
F13'	-51	-60	228.1	207.6	Yes	Yes	133.3	121.3
F18'	-110	-166	98.8	89.9	Yes	No	82.5	75.0
F19'	-110	-166	105.8	96.3	Yes	No	88.0	80.1
F20'	-110	-166	77.1	70.2	Yes	No	65.2	59.4

Table D-11. Static Specimen Information for Plate H, HPS 485W, 31.8 mm.

Specimen ID	W		a_o		B		B_N	
	mm.	in.	mm.	in.	mm.	in.	mm.	in.
H1'	10.02	0.3945	5.14	0.202	10.02	0.3945	8.00	0.3152
H2'	10.01	0.3941	5.10	0.201	10.02	0.3945	8.00	0.3152
H3'	10.03	0.3949	5.10	0.201	10.01	0.3941	8.00	0.3152
H4'	10.02	0.3945	5.06	0.199	10.01	0.3941	8.00	0.3152
H5'	10.02	0.3945	5.12	0.202	10.01	0.3941	8.00	0.3152
H6'	10.02	0.3945	5.12	0.202	10.03	0.3949	8.00	0.3152
H7'	10.02	0.3945	5.09	0.200	10.01	0.3941	8.00	0.3152
H8'	10.02	0.3945	5.01	0.197	10.02	0.3945	8.00	0.3152
H9'	10.02	0.3945	5.12	0.202	10.02	0.3945	8.00	0.3152
H10'	No Results- Data File Corrupted							
H11'	10.02	0.3945	5.11	0.201	10.03	0.3949	8.00	0.3152

Table D-12. Static Test Information for Plate H, HPS 485W, 31.8 mm.

Specimen ID	Test Temperature		Test Result, K_{Jc}		Valid?	Censored?	1T K_{Jc}	
	°C	°F	MPa√m	ksi√in			MPa√m	ksi√in
H1'	-130	-202	239.8	218.2	Yes	Yes	130.1	118.4
H2'	-130	-202	210.0	191.1	Yes	Yes	130.5	118.7
H3'	-130	-202	162.1	147.5	Yes	No	132.6	120.7
H4'	-150	-238	54.8	49.9	Yes	No	47.6	43.3
H5'	-150	-238	186.6	169.8	Yes	Yes	135.8	123.6
H6'	-150	-238	161.9	147.3	Yes	No	132.5	120.6
H7'	-150	-238	207.6	188.9	Yes	Yes	136.2	124.0
H8'	-150	-238	109.4	99.6	Yes	No	90.9	82.7
H9'	-170	-274	40.2	36.6	Yes	No	36.0	32.8
H10'	No Results- Data File Corrupted							
H11'	-170	-274	105.5	96.0	Yes	No	87.8	79.9

Table D-13. Static Specimen Information for Plate I, HPS 485W, 31.8 mm.

Specimen ID	W		a_o		B		B_N	
	mm.	in.	mm.	in.	mm.	in.	mm.	in.
I1'	10.03	0.3949	5.16	0.203	10.02	0.3945	8.00	0.3152
I2'	10.02	0.3945	5.16	0.203	10.02	0.3945	8.00	0.3152
I3'	10.01	0.3941	5.18	0.204	10.02	0.3945	8.00	0.3152
I4'	10.02	0.3945	5.18	0.204	10.01	0.3941	8.00	0.3152
I5'	10.03	0.3949	5.12	0.202	10.02	0.3945	8.00	0.3152
I6'	10.02	0.3945	5.20	0.205	10.01	0.3941	8.00	0.3152
I7'	10.02	0.3945	5.13	0.202	10.03	0.3949	8.00	0.3152
I8'	10.02	0.3945	5.06	0.199	10.03	0.3949	8.00	0.3152
I9'	10.02	0.3945	5.10	0.201	10.01	0.3941	8.00	0.3152

Table D-14. Static Test Information for Plate I, HPS 485W, 31.8 mm.

Specimen ID	Test Temperature		Test Result, K_{Jc}		Valid?	Censored?	1T K_{Jc}	
	°C	°F	MPa√m	ksi√in			MPa√m	ksi√in
I1'	-130	-202	232.4	211.5	Yes	Yes	127.4	115.9
I2'	-130	-202	185.8	169.1	Yes	Yes	127.3	115.8
I3'	-130	-202	201.8	183.6	Yes	Yes	126.9	115.5
I4'	-180	-292	45.8	41.7	Yes	No	40.4	36.8
I5'	-180	-292	153.9	140.0	Yes	No	126.1	114.8
I6'	-180	-292	76.4	69.5	Yes	No	64.7	58.9
I7'	-160	-256	115.8	105.4	Yes	No	95.9	87.3
I8'	-160	-256	159.7	145.3	Yes	No	130.7	119.0
I9'	-160	-256	42.5	38.7	No	No	37.8	34.4

Table D-15. Static Specimen Information for Plate J, HPS 485W, 38.1 mm.

Specimen ID	W		a_o		B		B_N	
	mm.	in.	mm.	in.	mm.	in.	mm.	in.
J1'	10.02	0.3945	5.15	0.203	10.03	0.3949	8.00	0.3152
J2'	10.03	0.3949	5.12	0.202	10.02	0.3945	8.00	0.3152
J3'	Specimen Damaged in Machining							
J4'	10.03	0.3949	5.15	0.203	10.02	0.3945	8.00	0.3152
J6'	10.03	0.3949	5.14	0.202	10.02	0.3945	8.00	0.3152
J7'	10.02	0.3945	5.08	0.200	10.03	0.3949	8.00	0.3152
J8'	10.02	0.3945	5.14	0.202	10.02	0.3945	8.00	0.3152
J9'	10.03	0.3949	5.08	0.200	10.03	0.3949	8.00	0.3152
J10'	10.03	0.3949	5.18	0.204	10.04	0.3953	8.00	0.3152

Table D-16. Static Test Information for Plate J, HPS 485W, 38.1 mm.

Specimen ID	Test Temperature		Test Result, K_{Jc}		Valid?	Censored?	1T K_{Jc}	
	°C	°F	MPa√m	ksi√in			MPa√m	ksi√in
J1'	-150	-238	102.8	93.5	Yes	No	85.6	77.9
J2'	-150	-238	129.3	117.7	Yes	No	106.6	97.0
J3'	Specimen Damaged in Machining							
J4'	-150	-238	75.0	68.3	Yes	No	63.6	57.9
J6'	-130	-202	102.6	93.4	Yes	No	85.5	77.8
J7'	-130	-202	203.8	185.5	Yes	Yes	131.1	119.3
J8'	-130	-202	101.8	92.6	Yes	No	84.8	77.2
J9'	-130	-202	111.3	101.3	Yes	No	92.4	84.1
J10'	-130	-202	123.4	112.3	Yes	No	102.0	92.8

APPENDIX E: HPS Resistance Curves

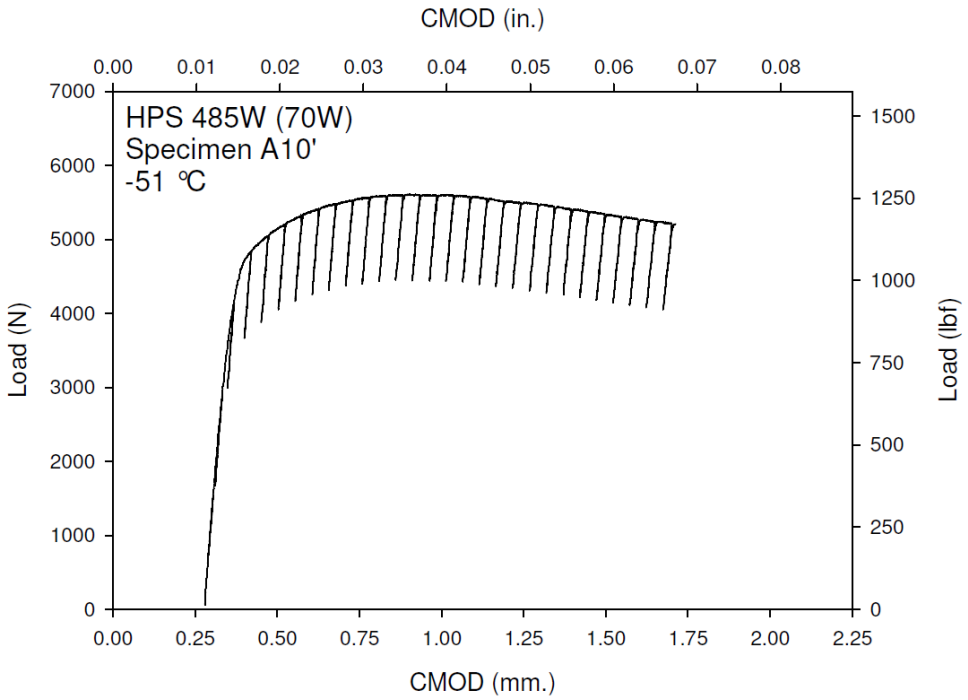

Figure E-1. Specimen A10' Test Record

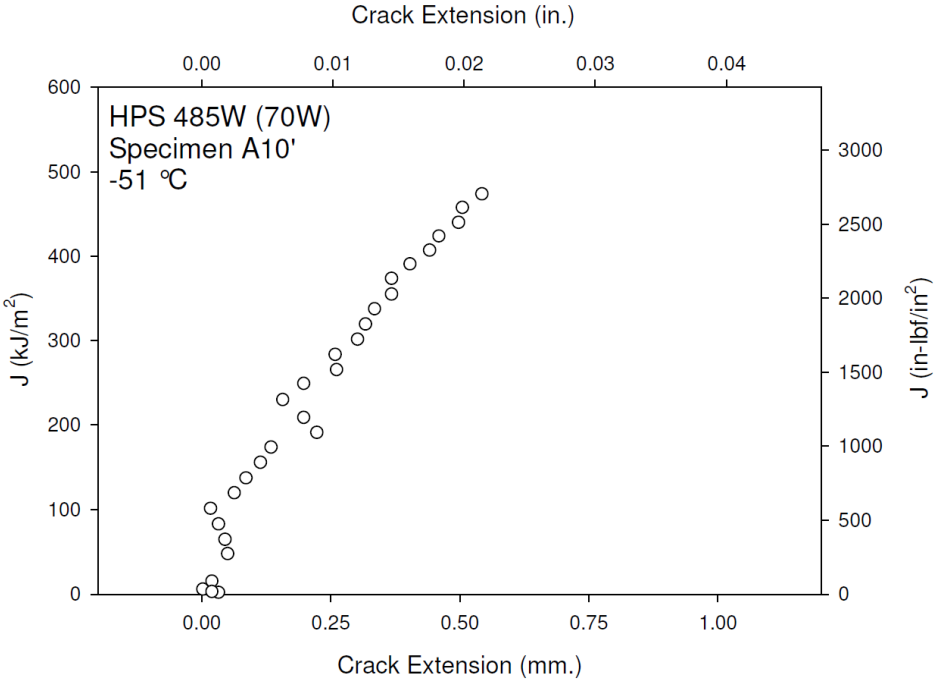

Figure E-2. Specimen A10' Resistance Curve

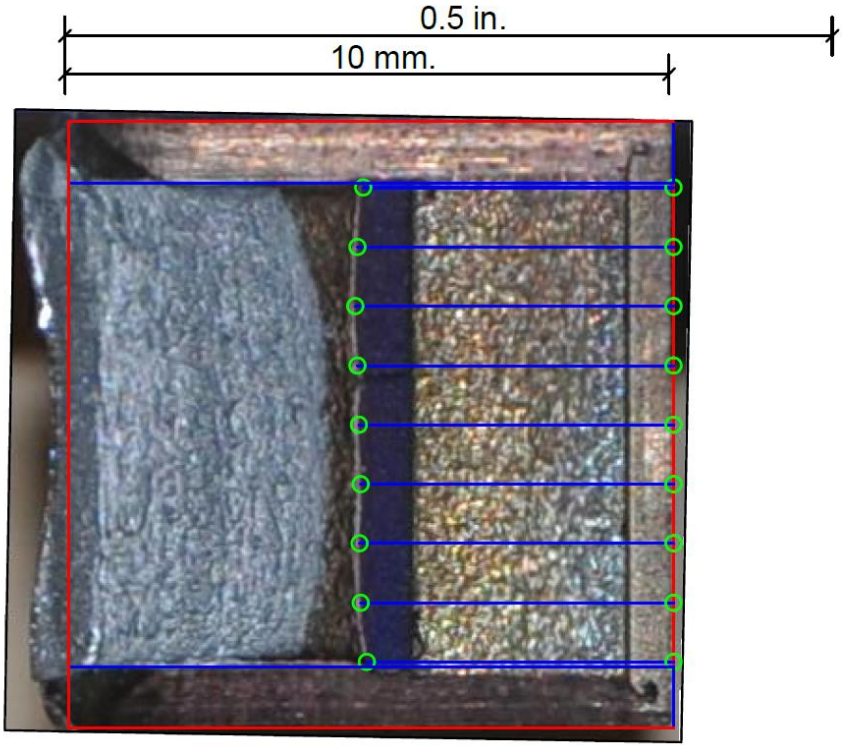

Figure E-3. Specimen A10' Fracture Surface

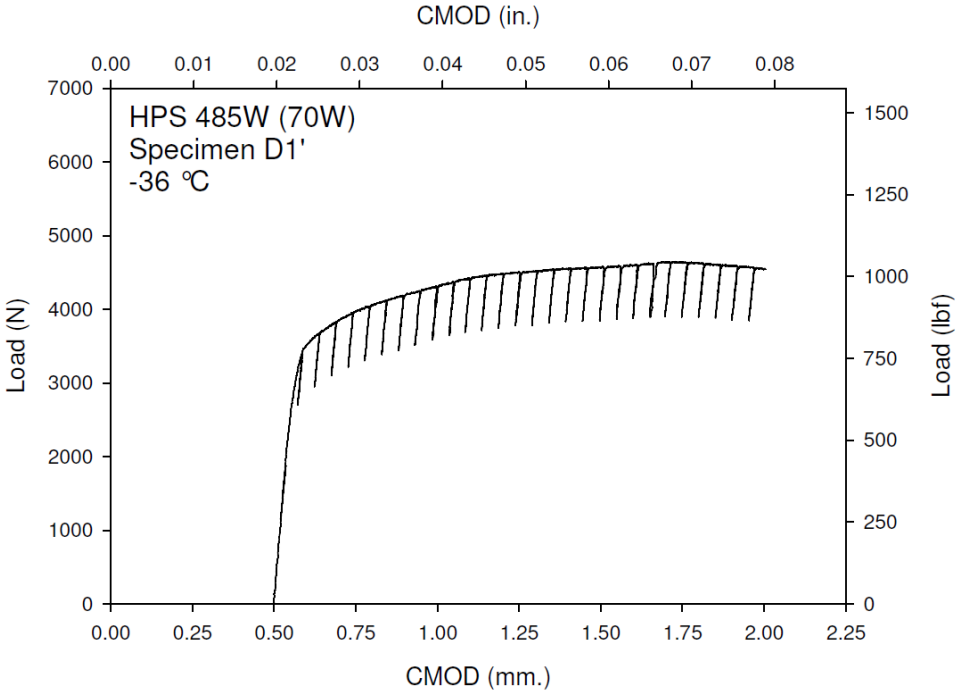

Figure E-4. Specimen D1' Test Record

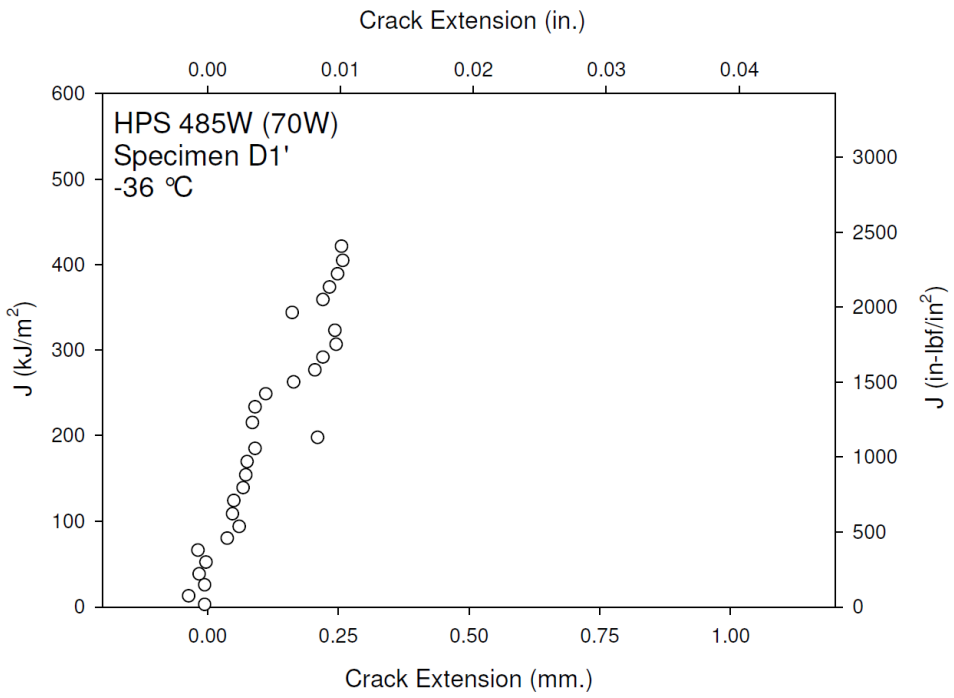

Figure E-5. Specimen D1' Resistance Curve

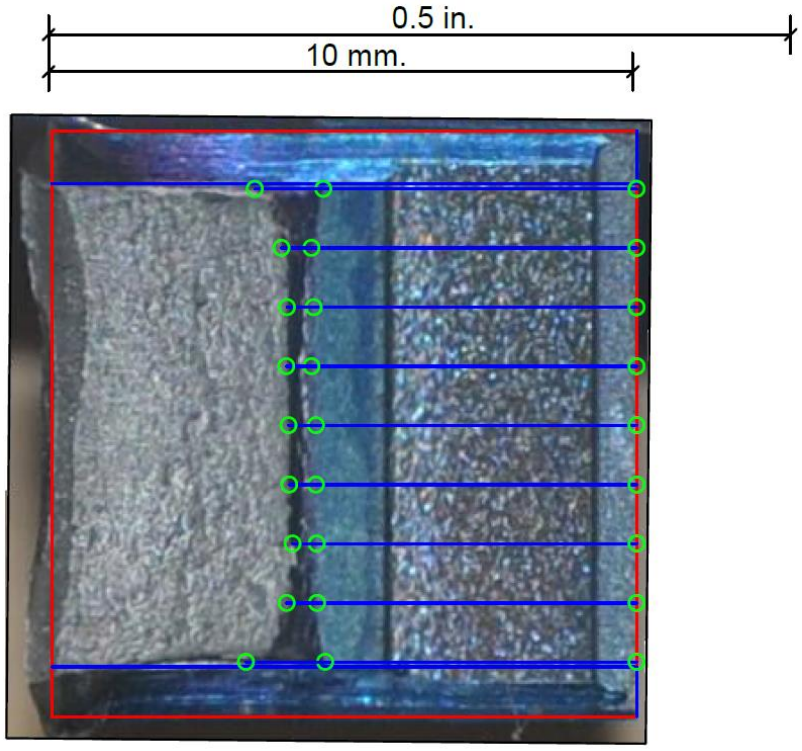

Figure E-6. Specimen D1' Fracture Surface

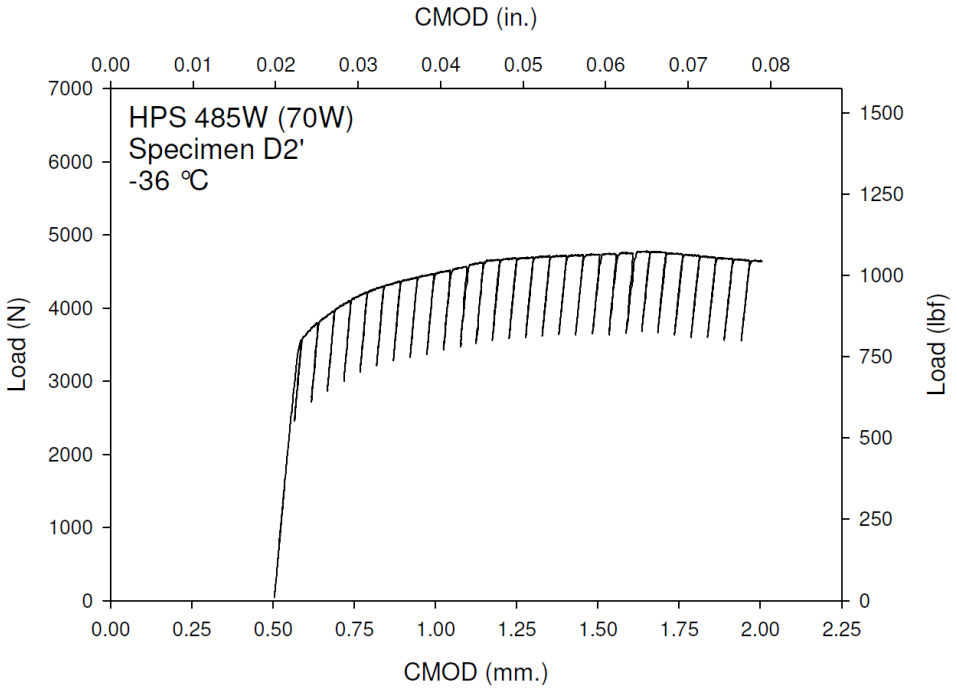

Figure E-7. Specimen D2' Test Record

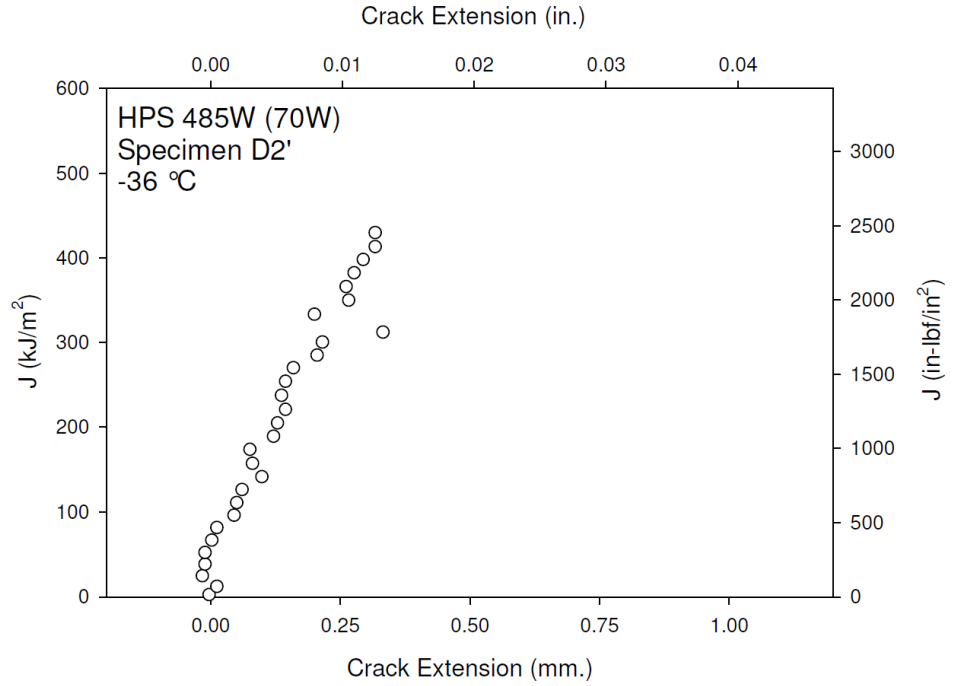

Figure E-8. Specimen D2' Resistance Curve

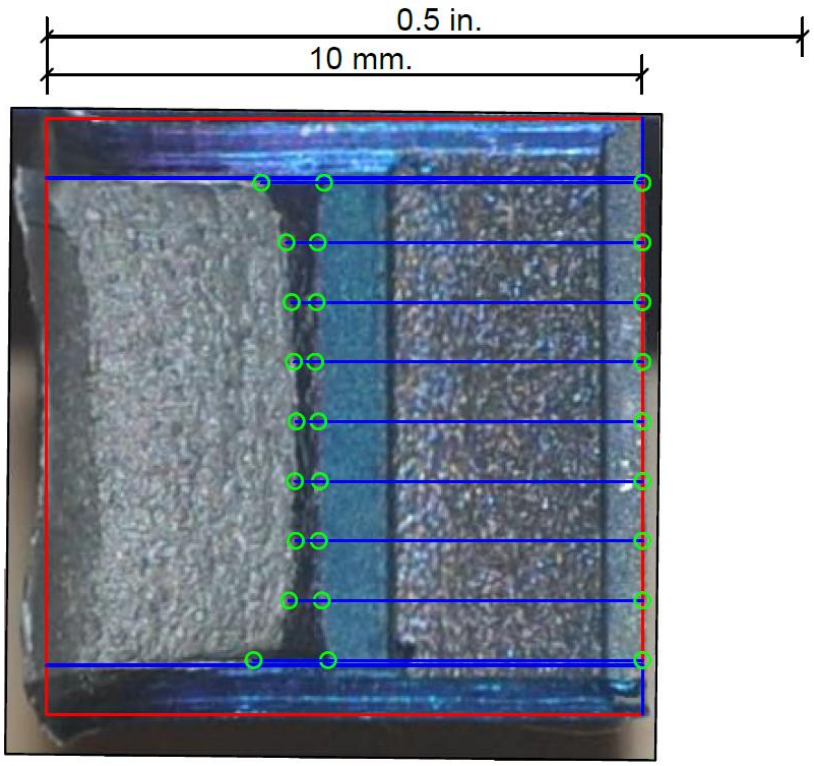

Figure E-9. Specimen D2' Fracture Surface

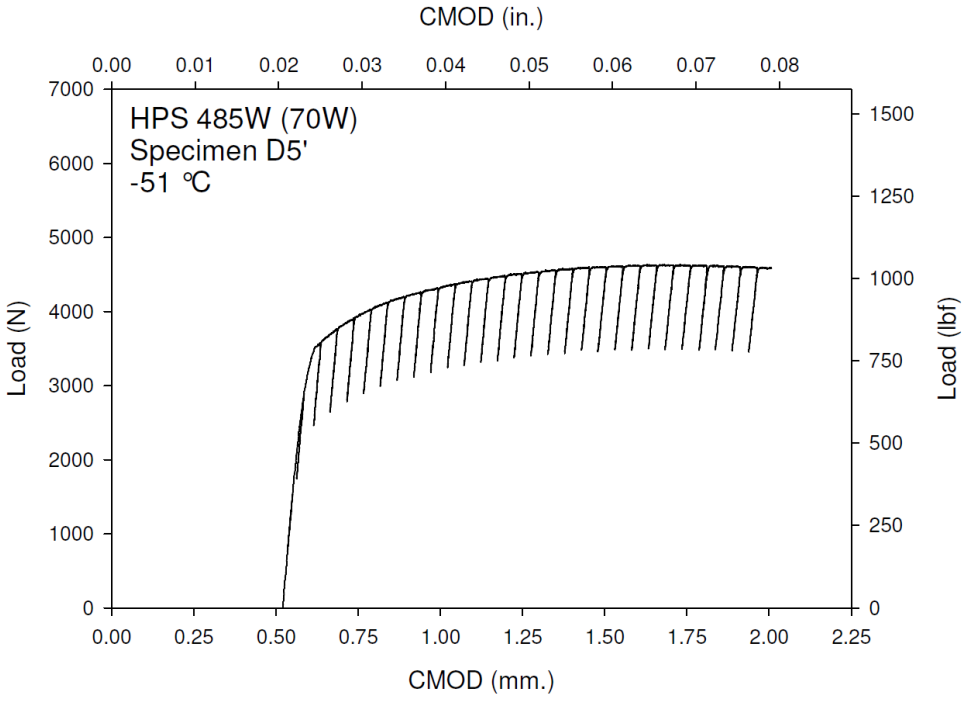

Figure E-10. Specimen D5' Test Record

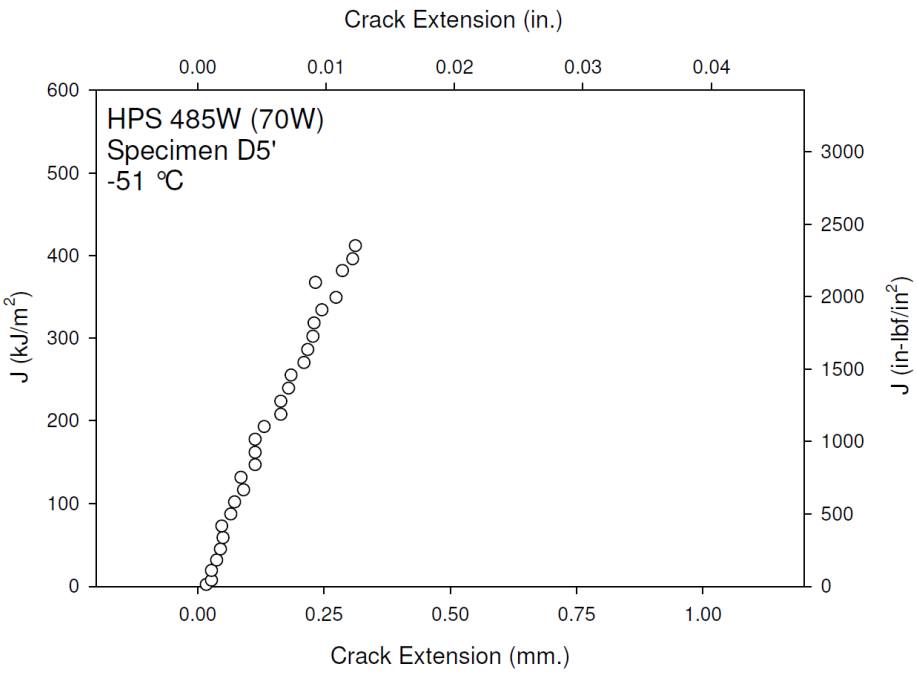

Figure E-11. Specimen D5' Resistance Curve

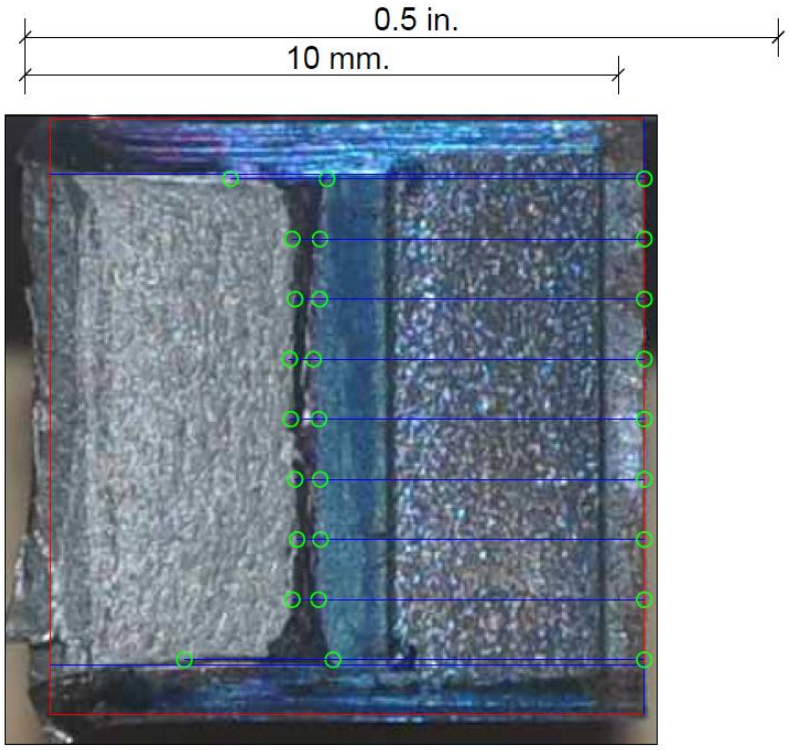

Figure E-12. Specimen D5' Fracture Surface

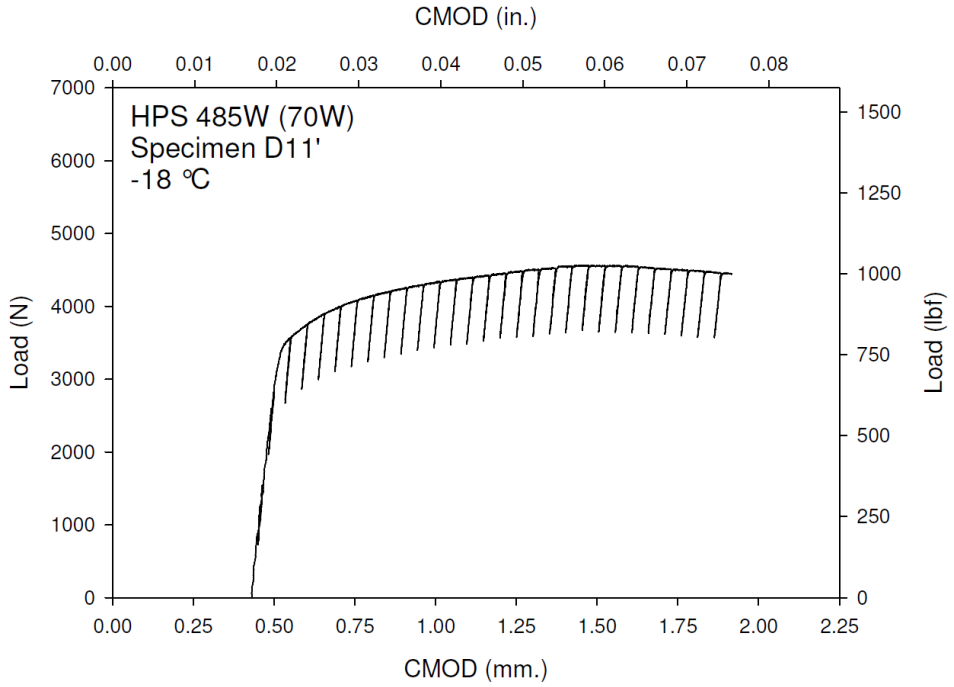

Figure E-13. Specimen D11' Test Record

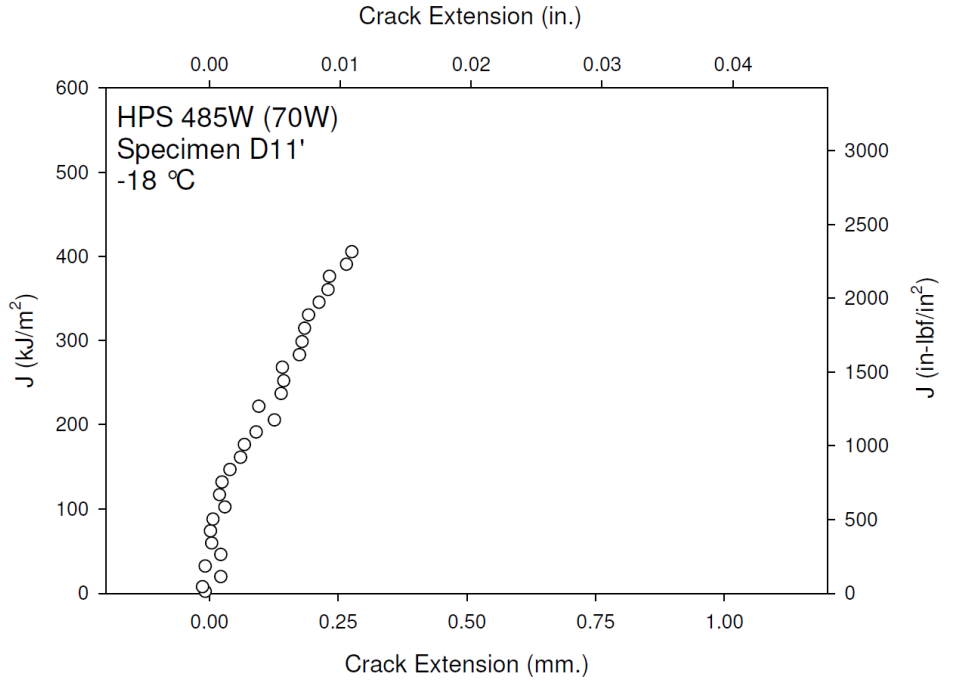

Figure E-14. Specimen D11' Resistance Curve

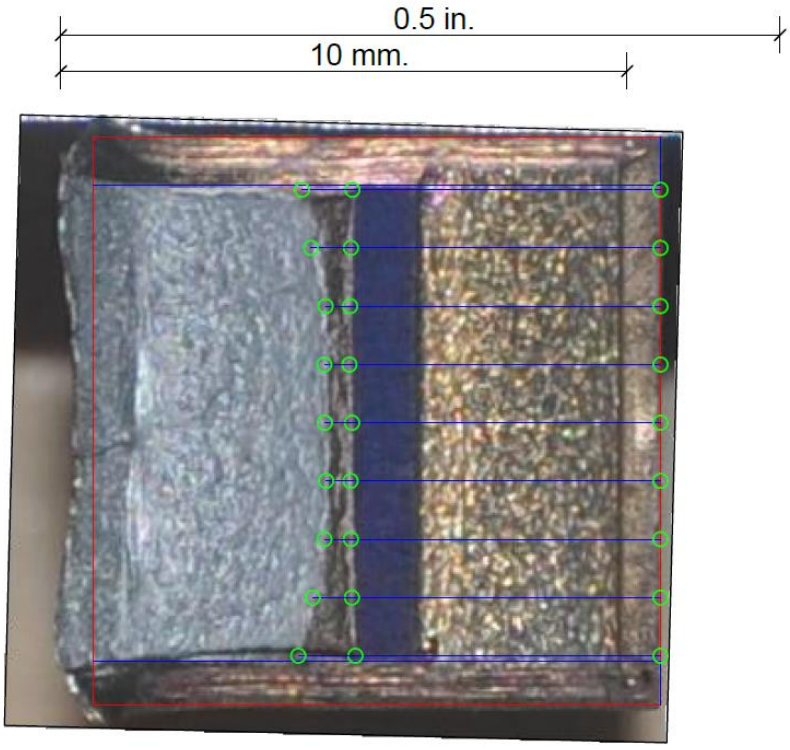

Figure E-15. Specimen D11' Fracture Surface

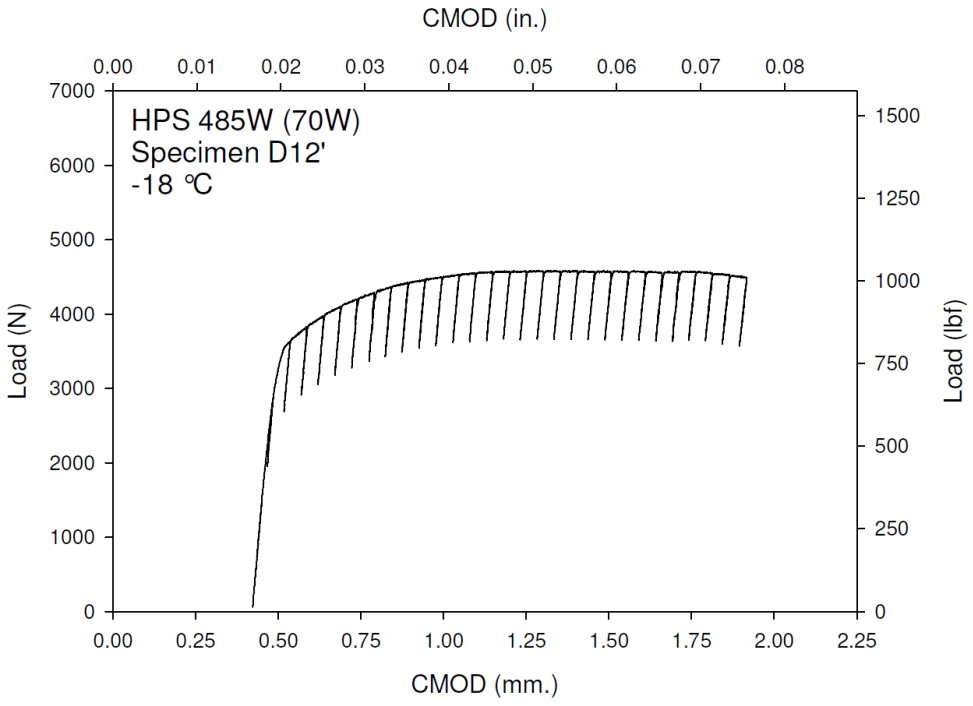

Figure E-16. Specimen D12' Test Record

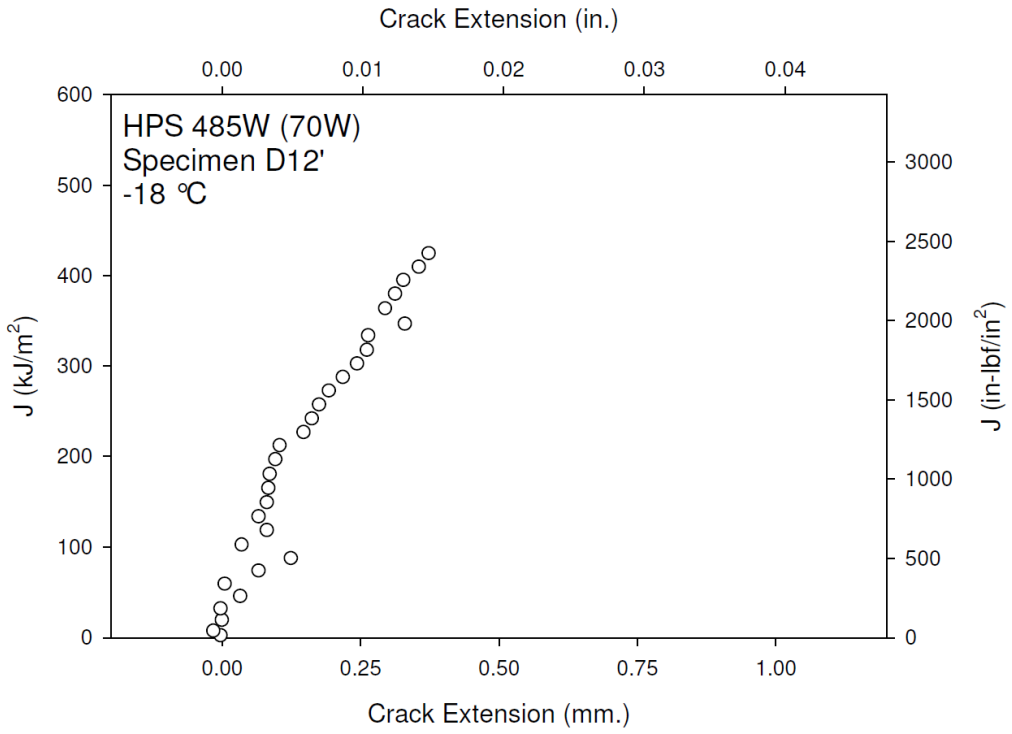

Figure E-17. Specimen D12' Resistance Curve

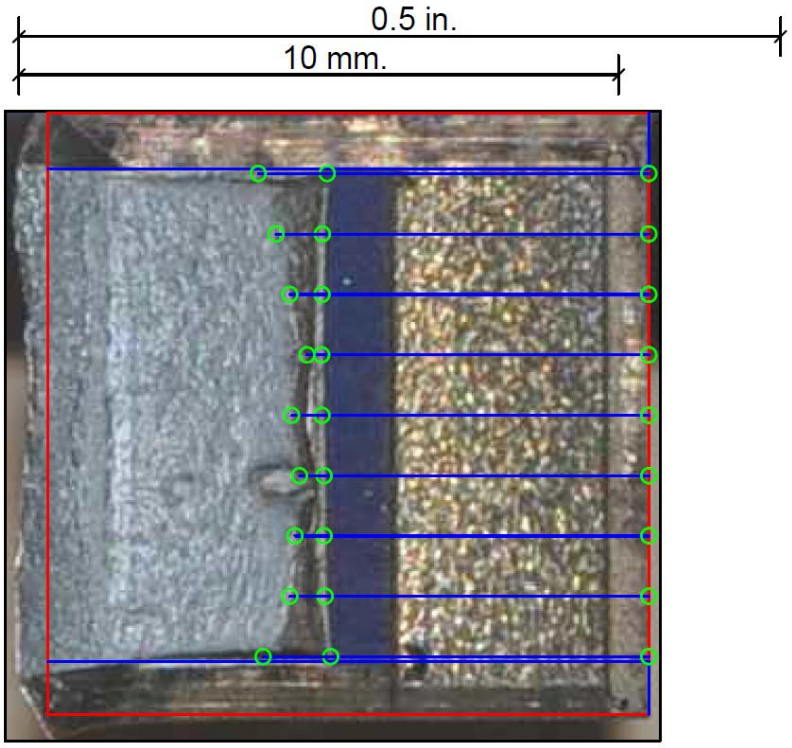

Figure E-18. Specimen D12' Fracture Surface

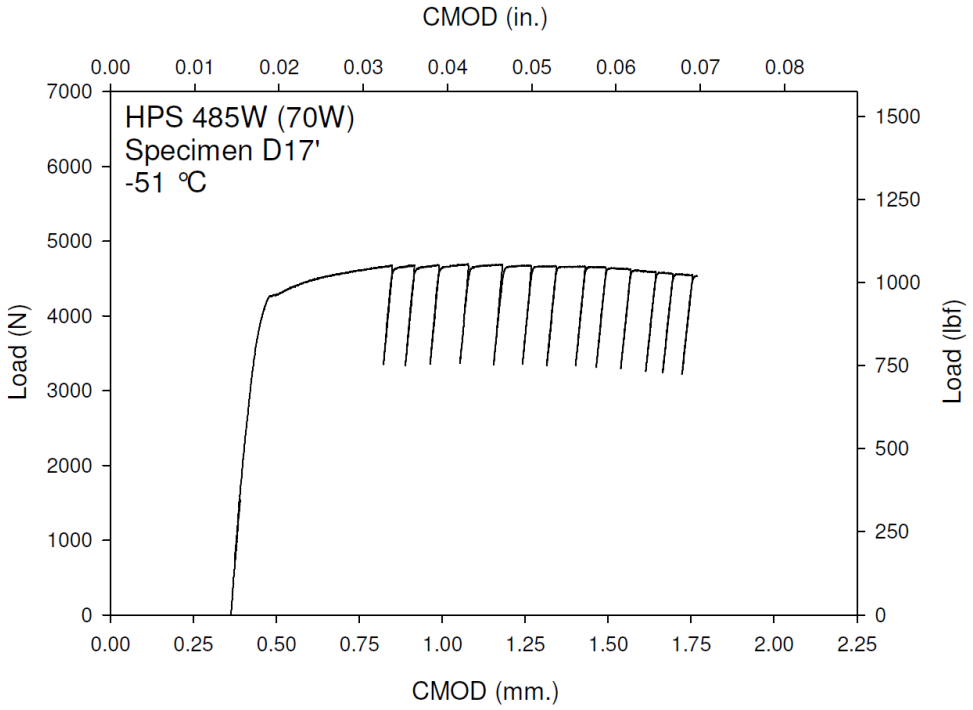

Figure E-19. Specimen D17' Test Record

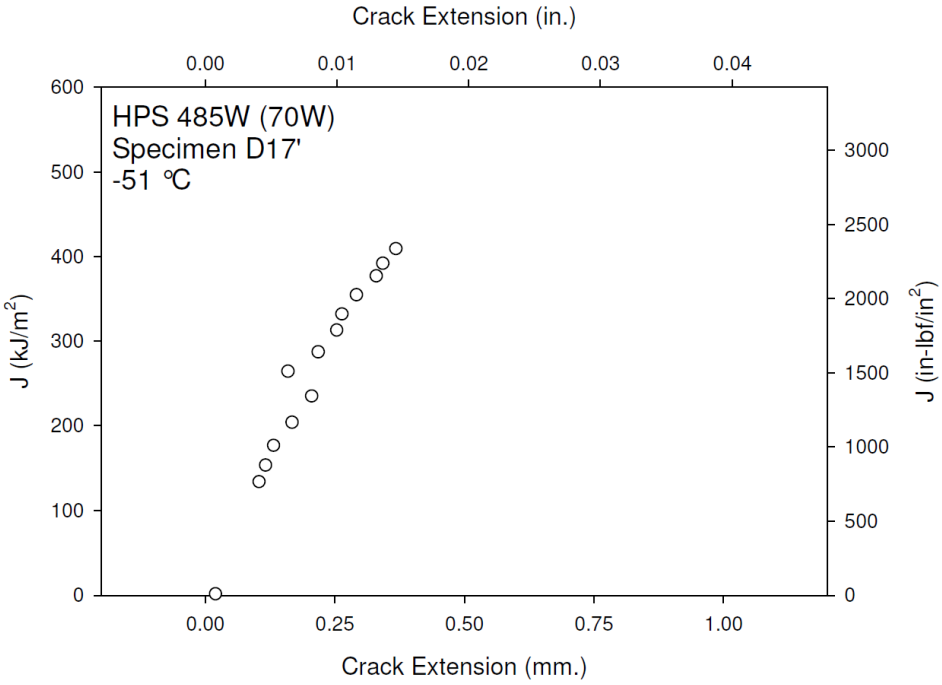

Figure E-20. Specimen D17' Resistance Curve

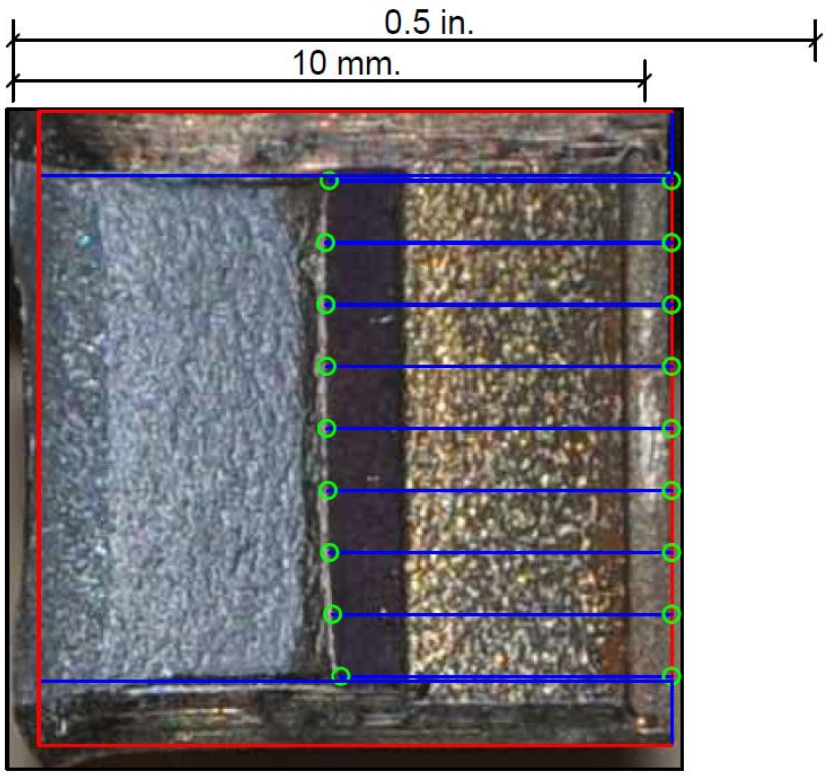

Figure E-21. Specimen D17' Fracture Surface

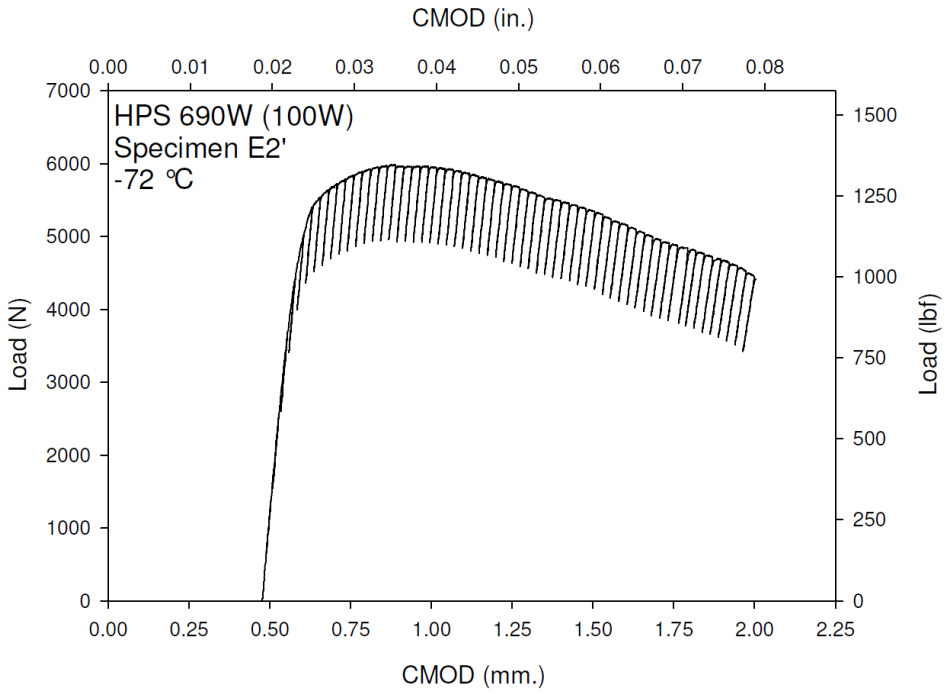

Figure E-22. Specimen E2' Test Record

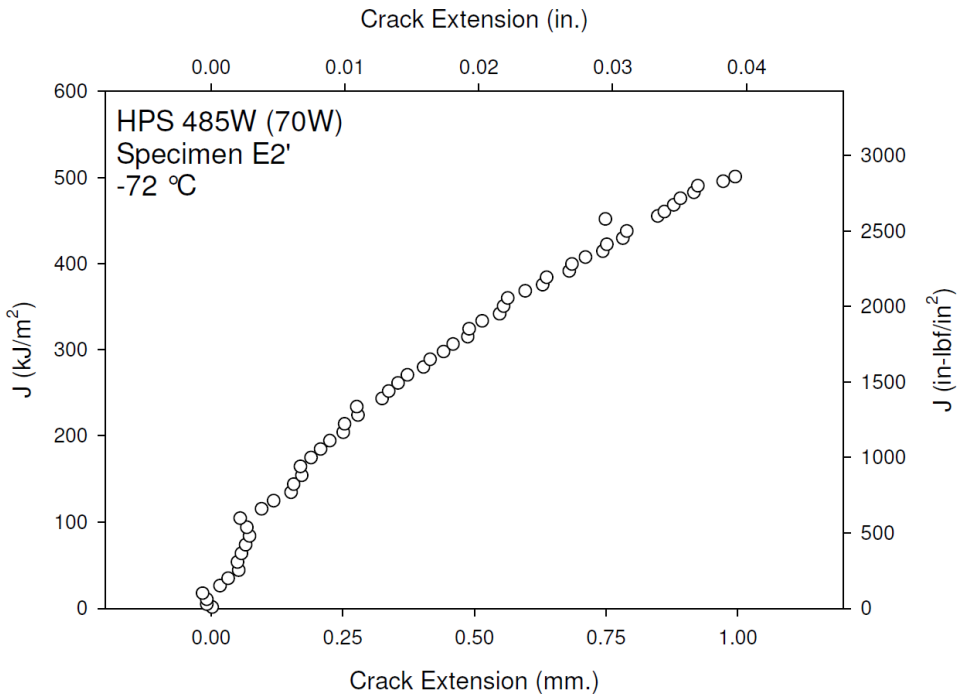

Figure E-23. Specimen E2' Resistance Curve

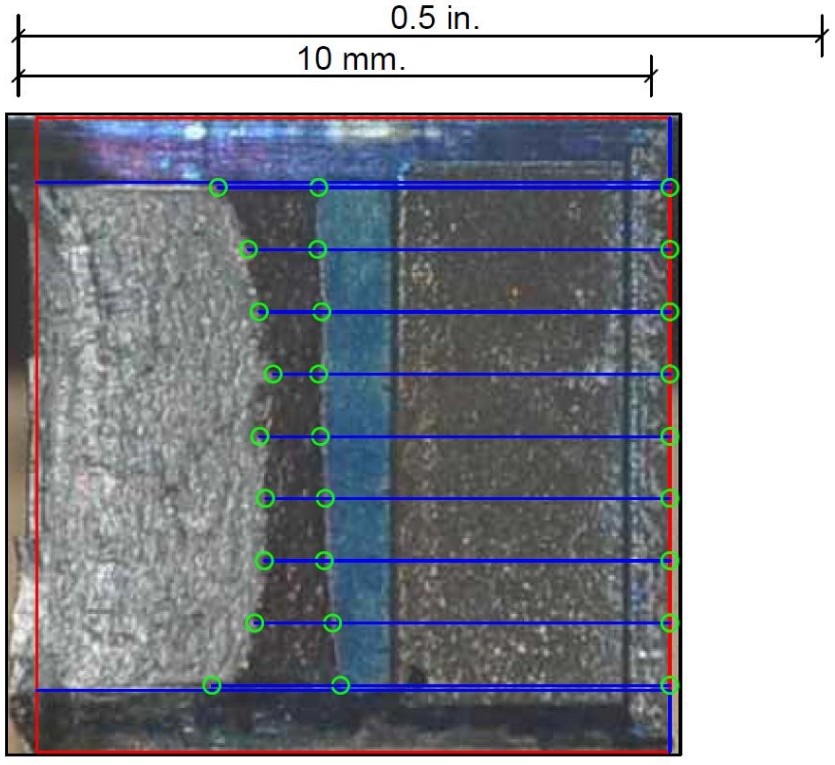

Figure E-24. Specimen E2' Fracture Surface

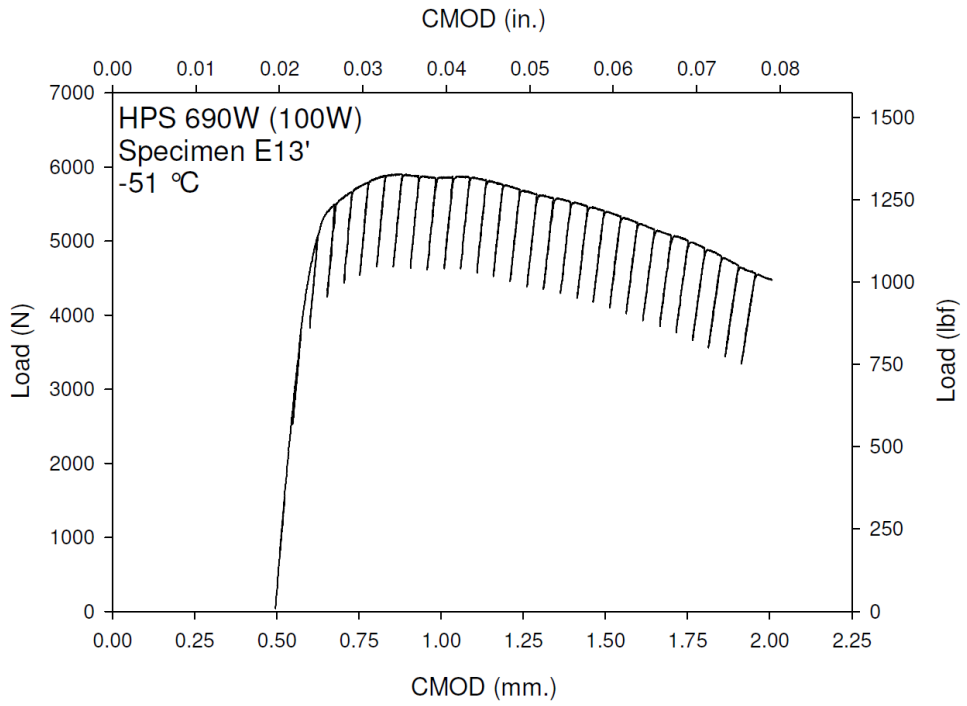

Figure E-25. Specimen E13' Test Record

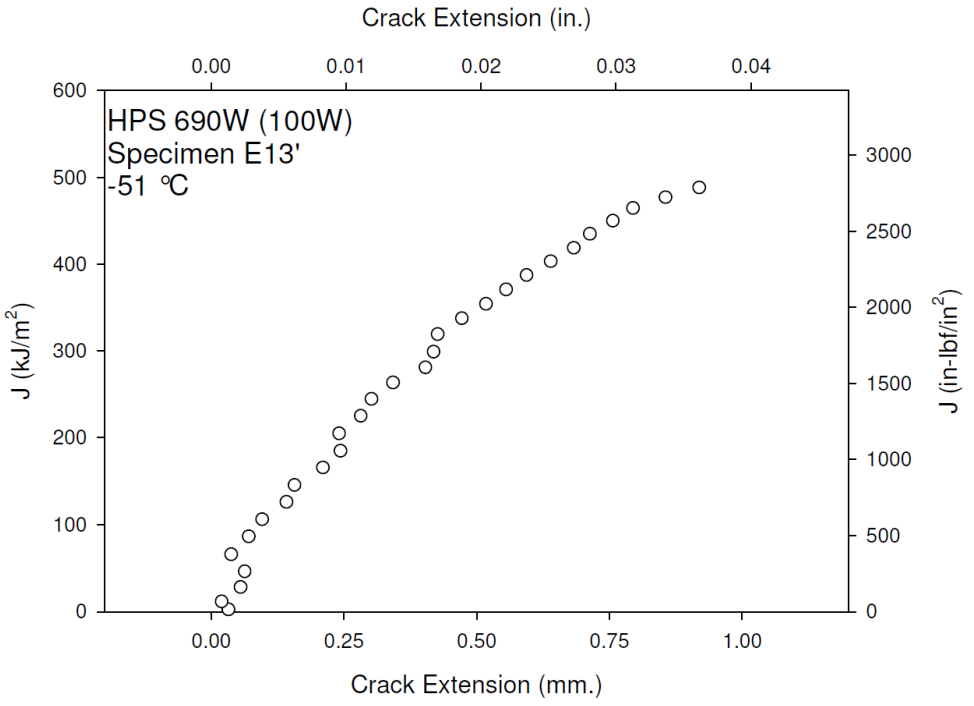

Figure E-26. Specimen E13' Resistance Curve

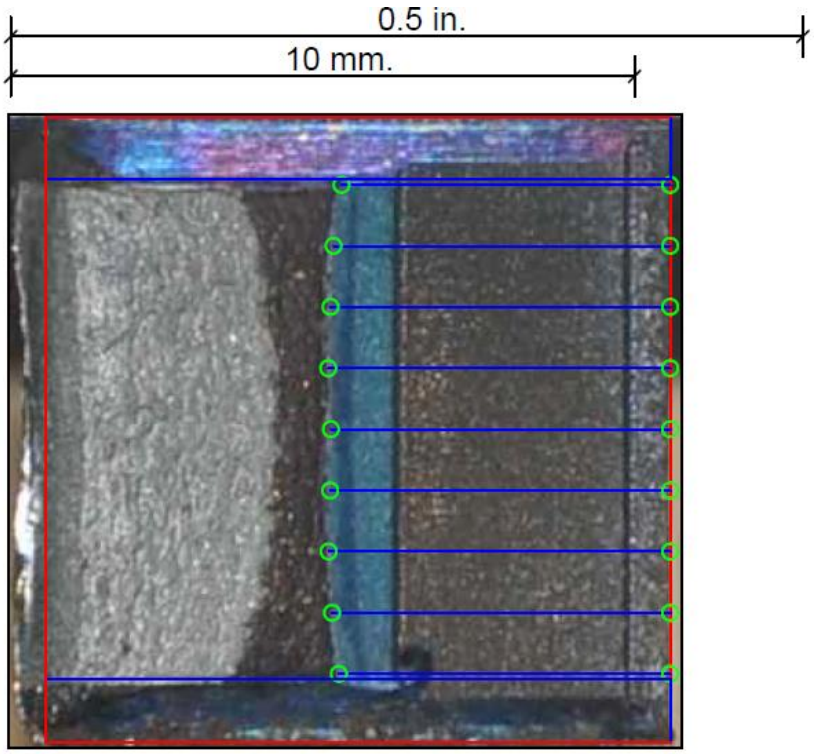

Figure E-27. Specimen E13' Fracture Surface

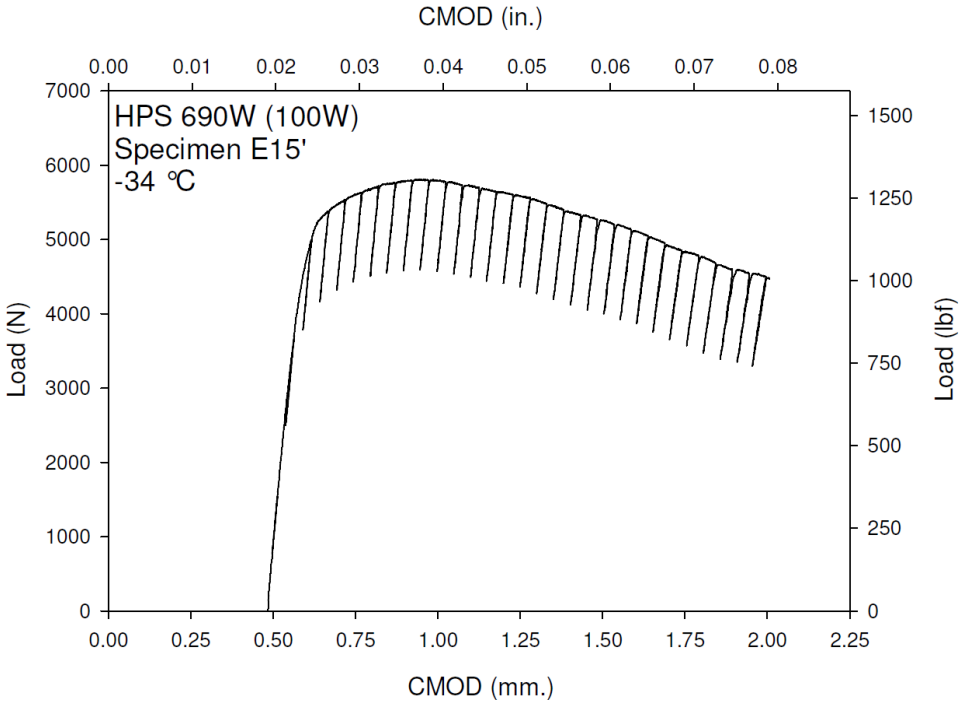

Figure E-28. Specimen E15' Test Record

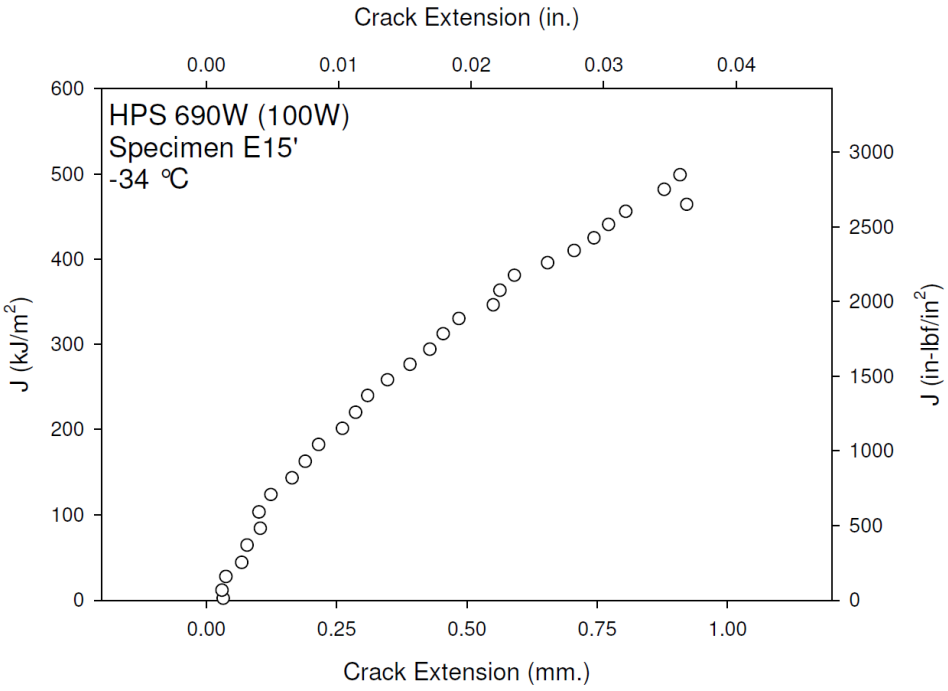

Figure E-29. Specimen E15' Resistance Curve

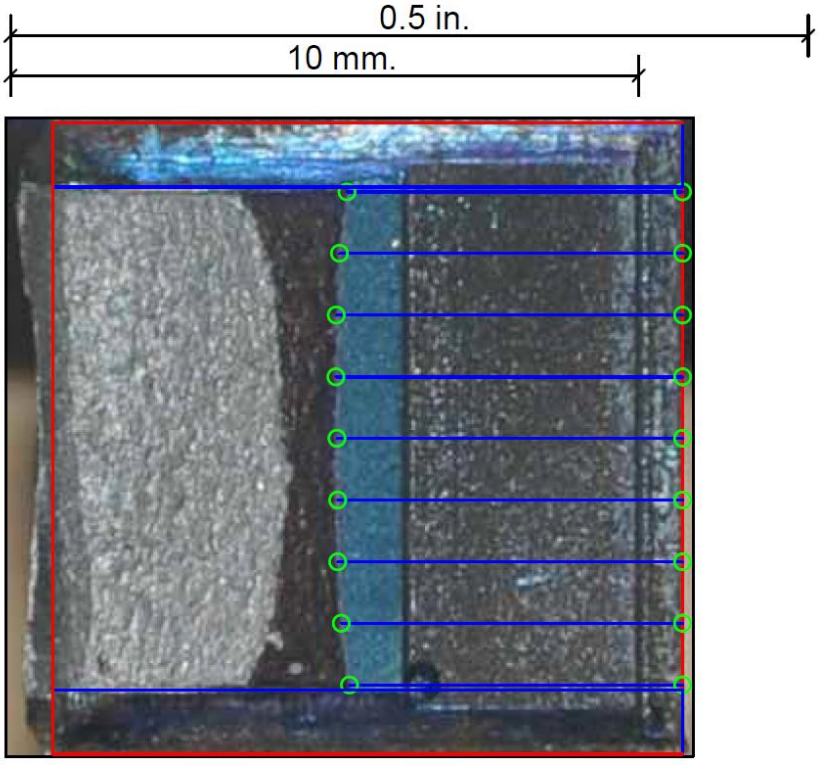

Figure E-30. Specimen E15' Fracture Surface

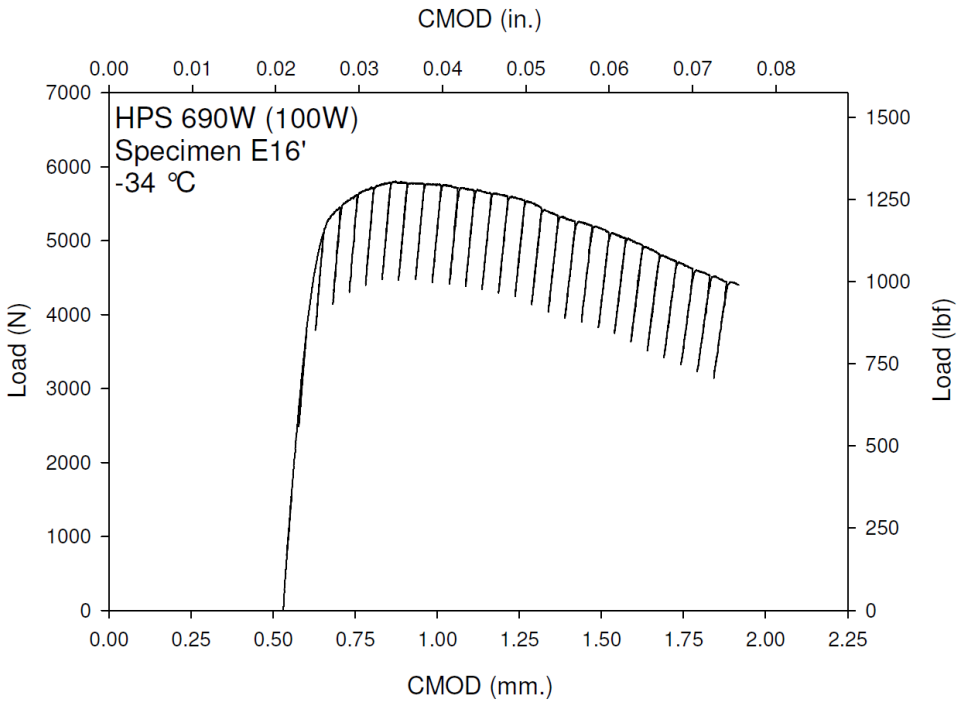

Figure E-31. Specimen E16' Test Record

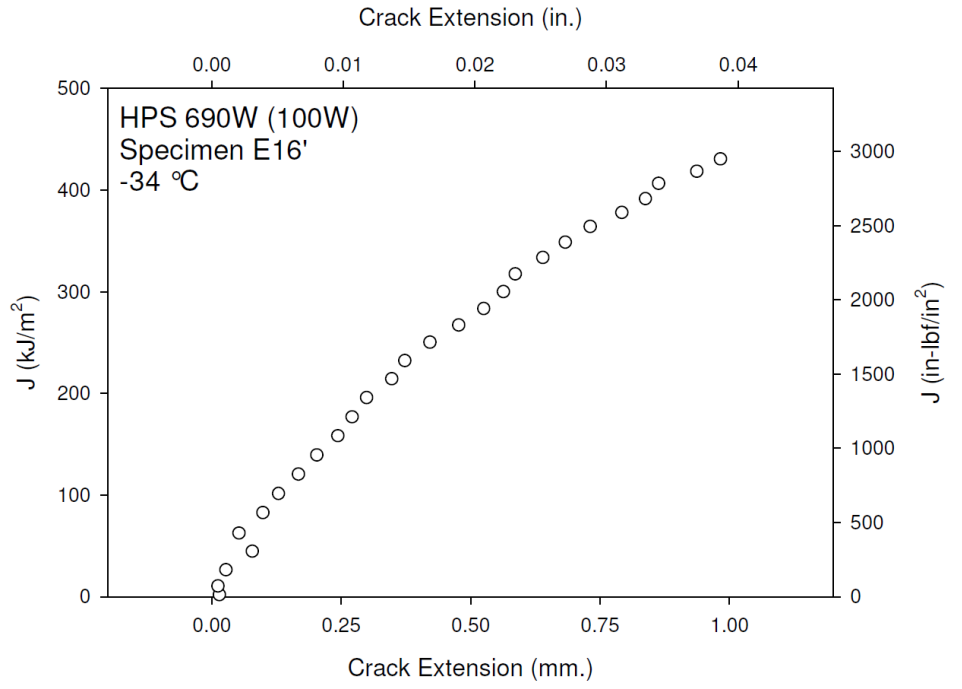

Figure E-32. Specimen E16' Resistance Curve

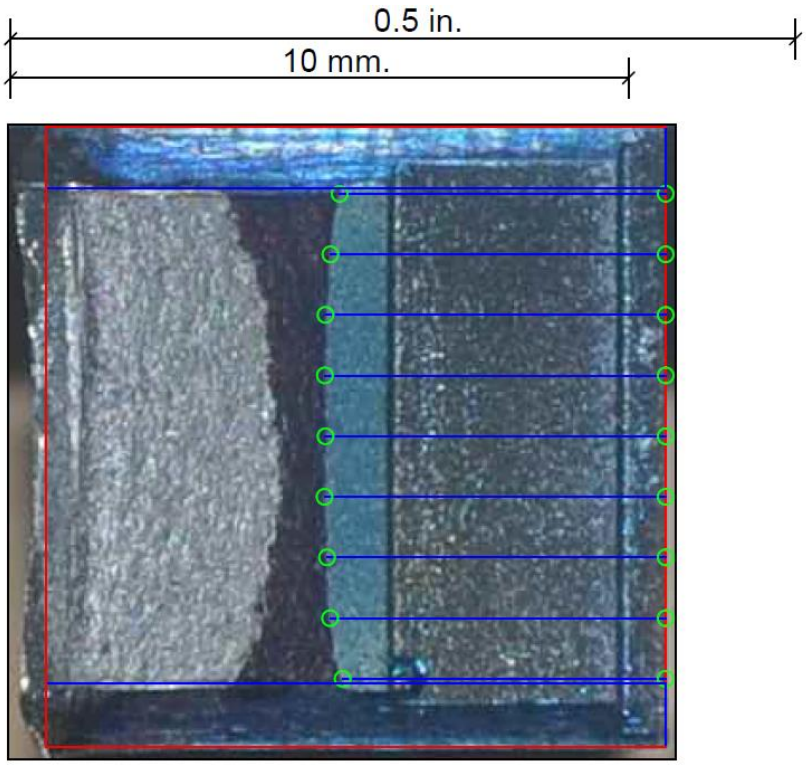

Figure E-33. Specimen E16' Fracture Surface

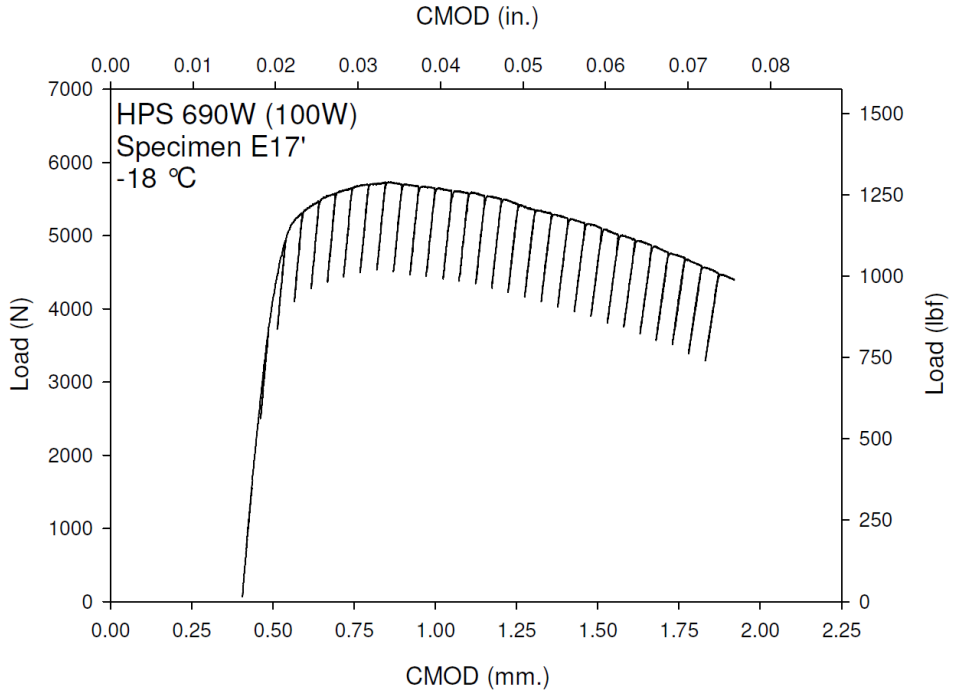

Figure E-34. Specimen E17' Test Record

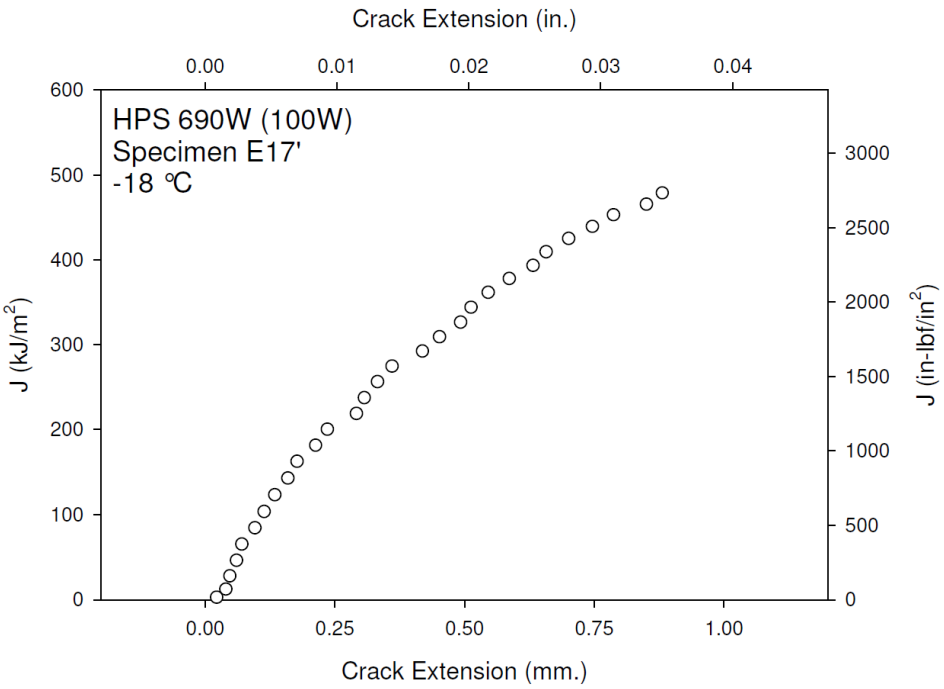

Figure E-35. Specimen E17' Resistance Curve

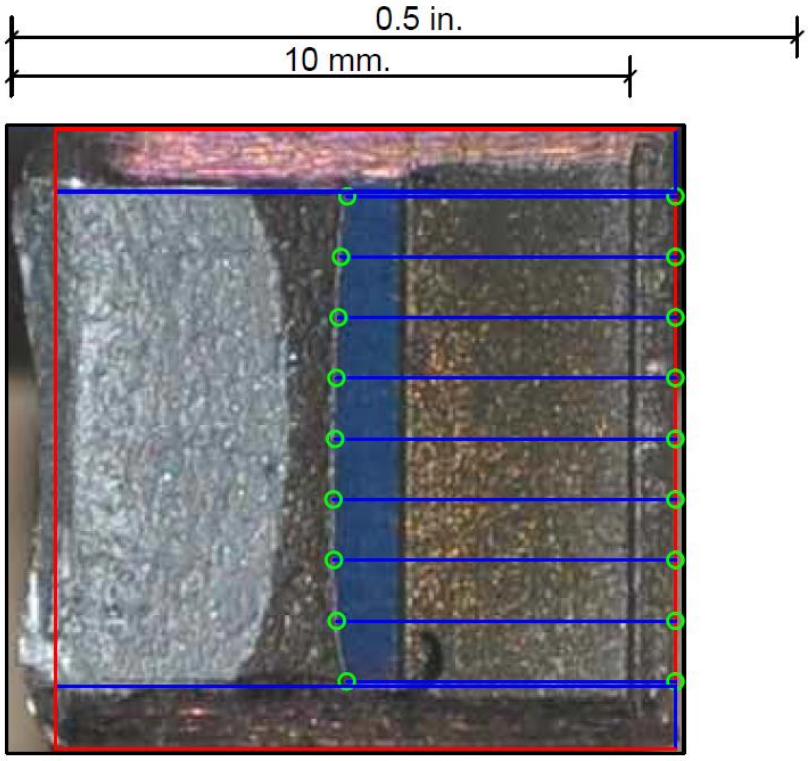

Figure E-36. Specimen E17' Fracture Surface

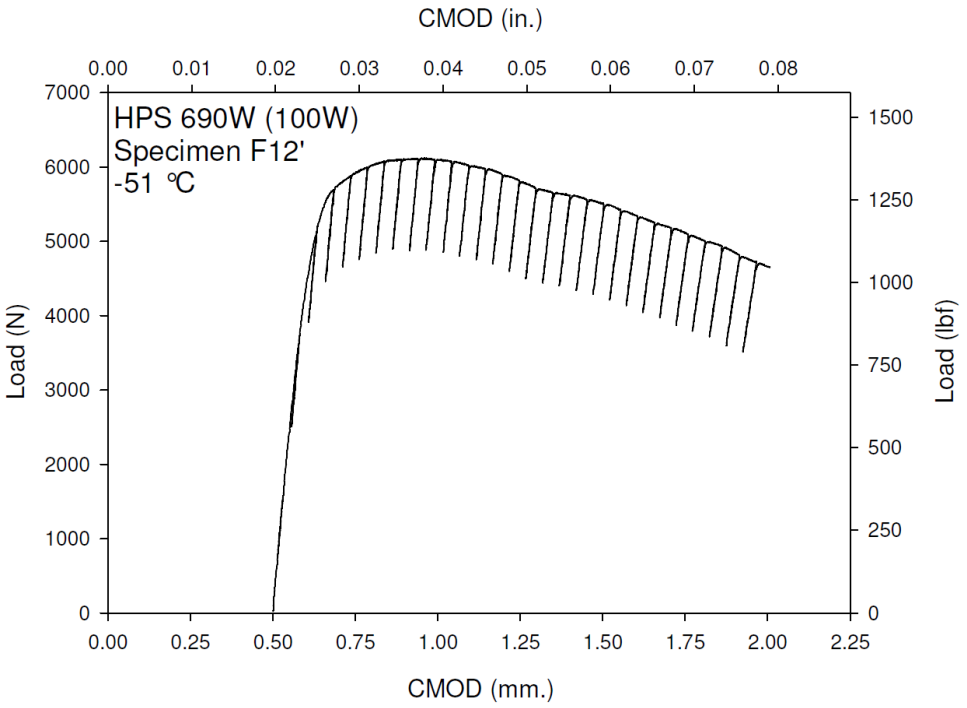

Figure E-37. Specimen F12' Test Record

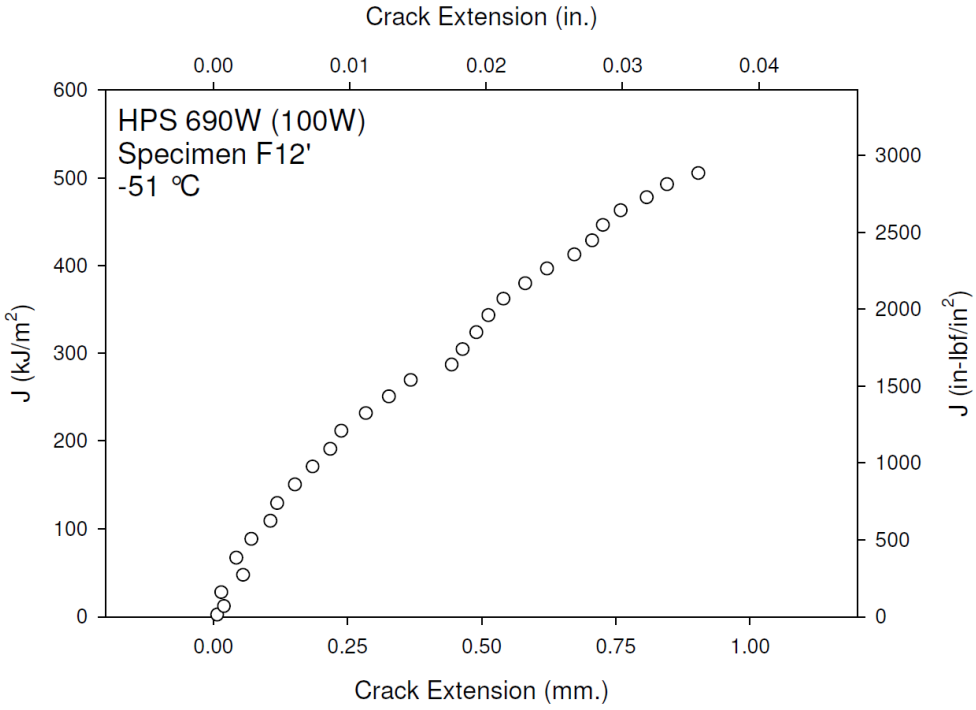

Figure E-38. Specimen F12' Resistance Curve

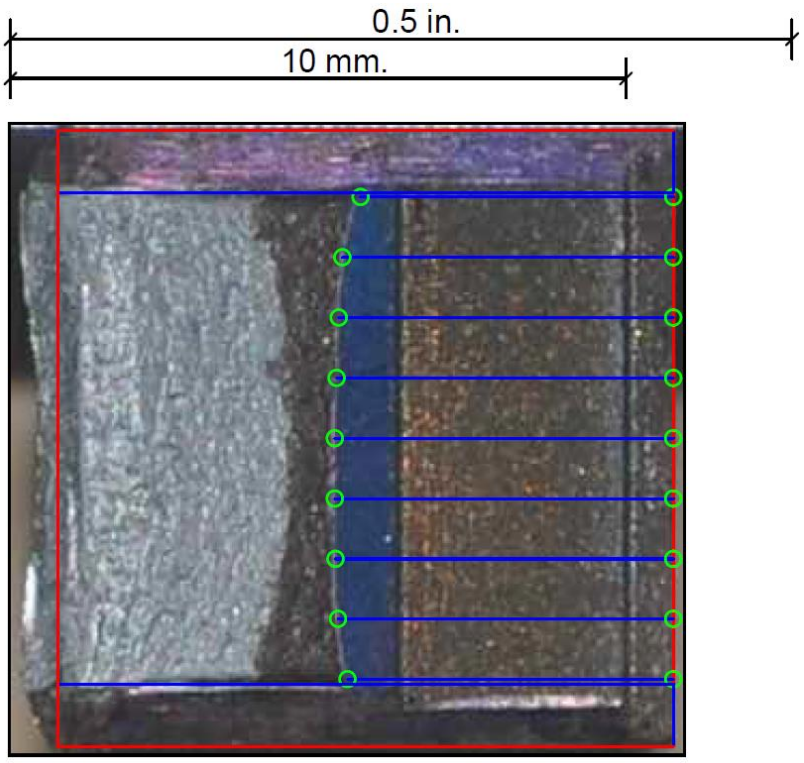

Figure E-39. Specimen F12' Fracture Surface

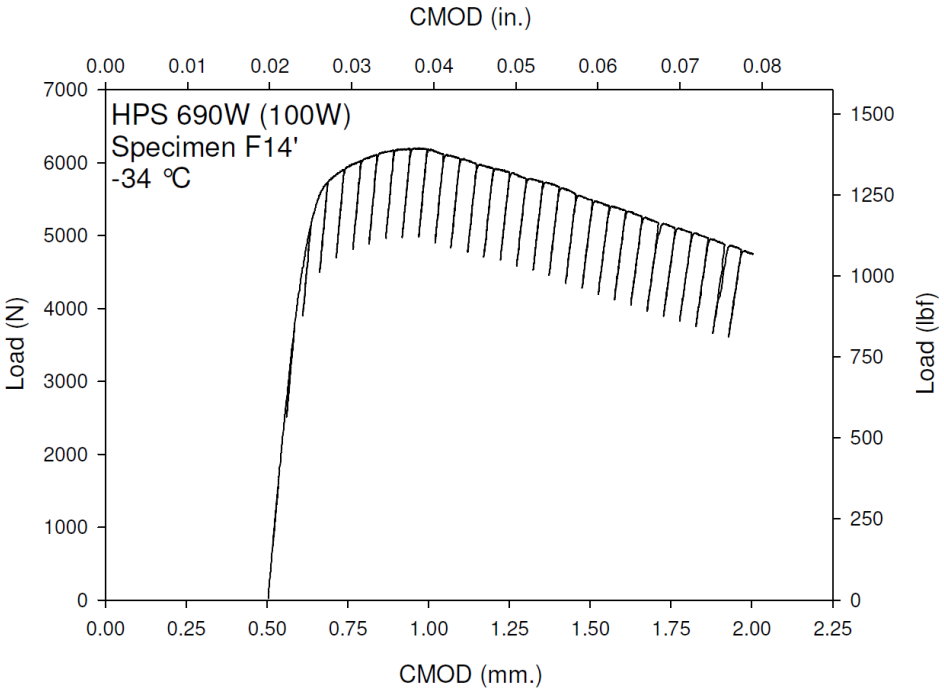

Figure E-40. Specimen F14' Test Record

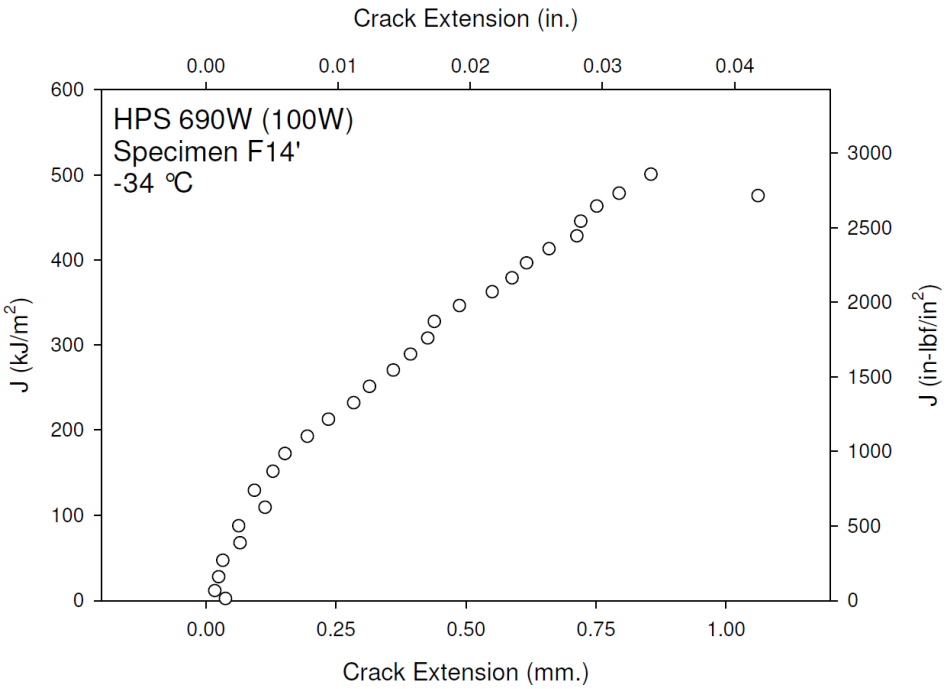

Figure E-41. Specimen F14' Resistance Curve

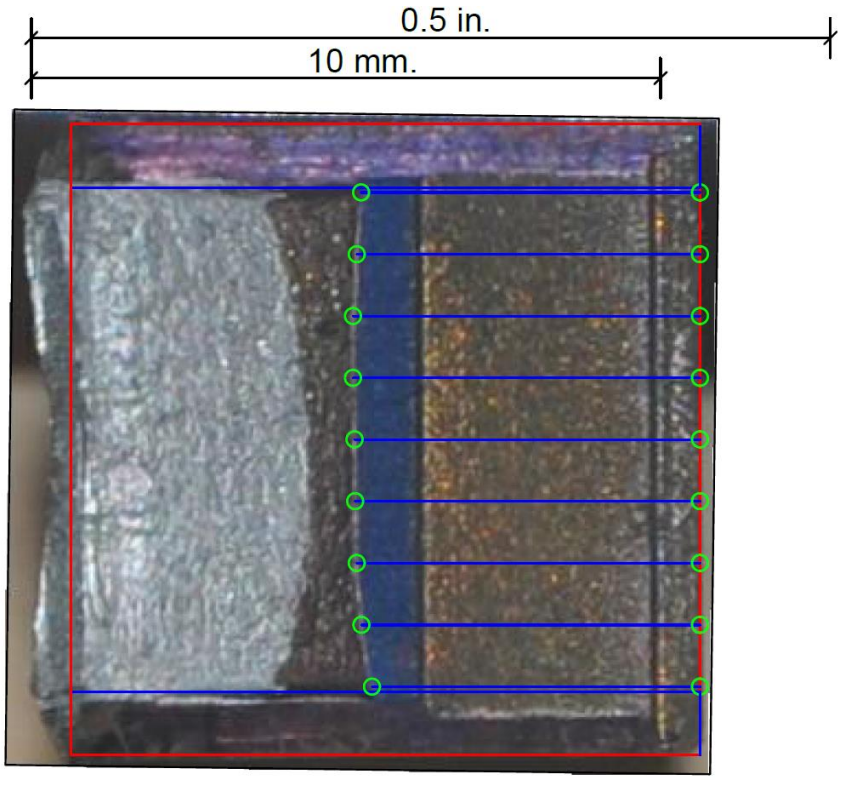

Figure E-42. Specimen F14' Fracture Surface

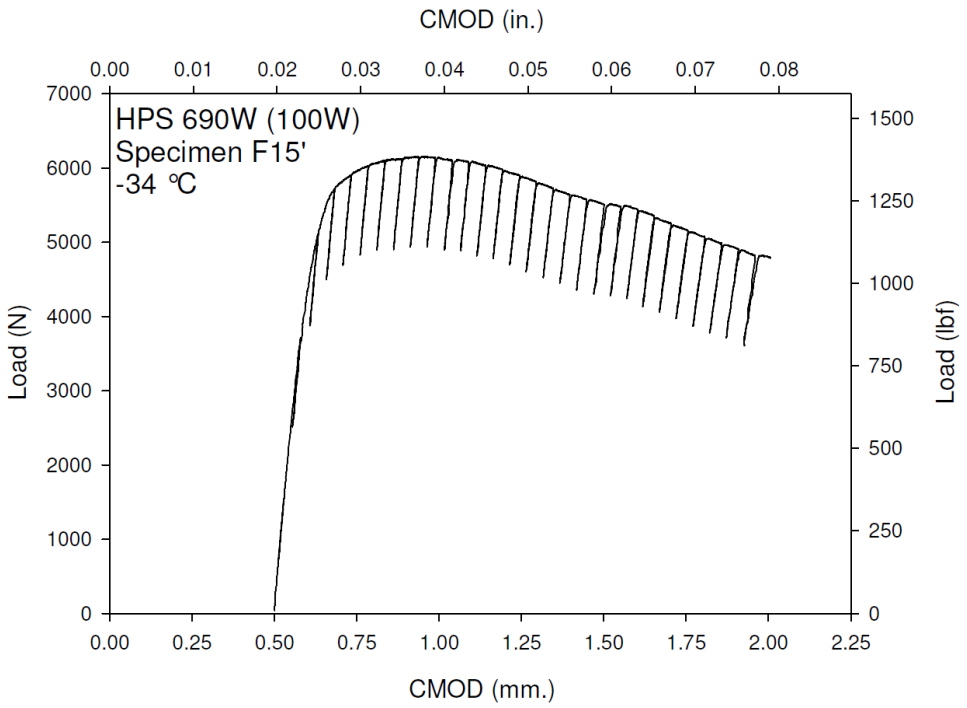

Figure E-43. Specimen F15' Test Record

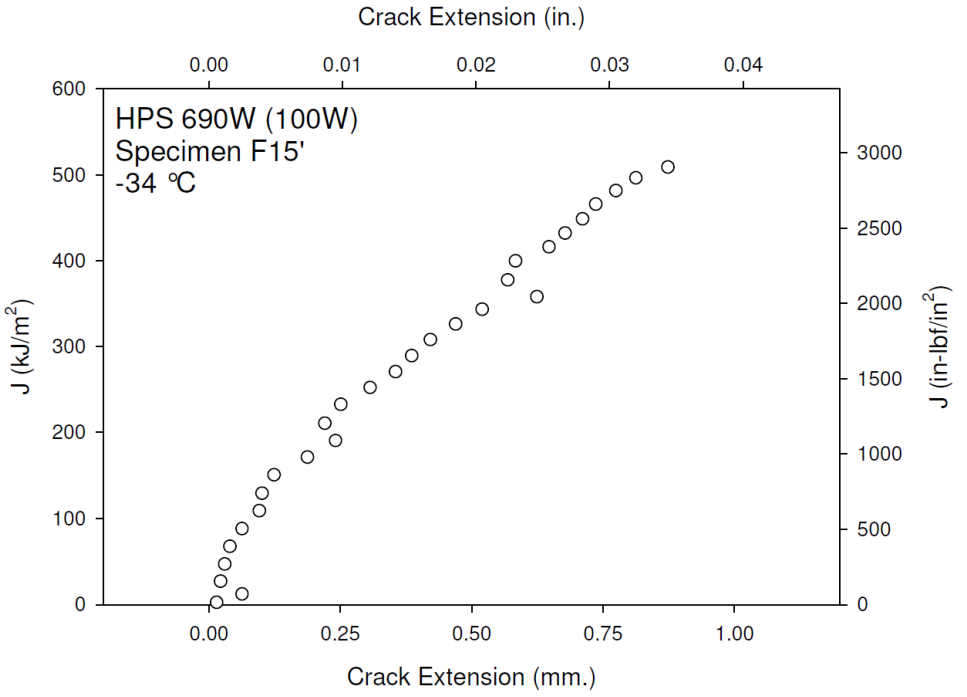

Figure E-44. Specimen F15' Resistance Curve

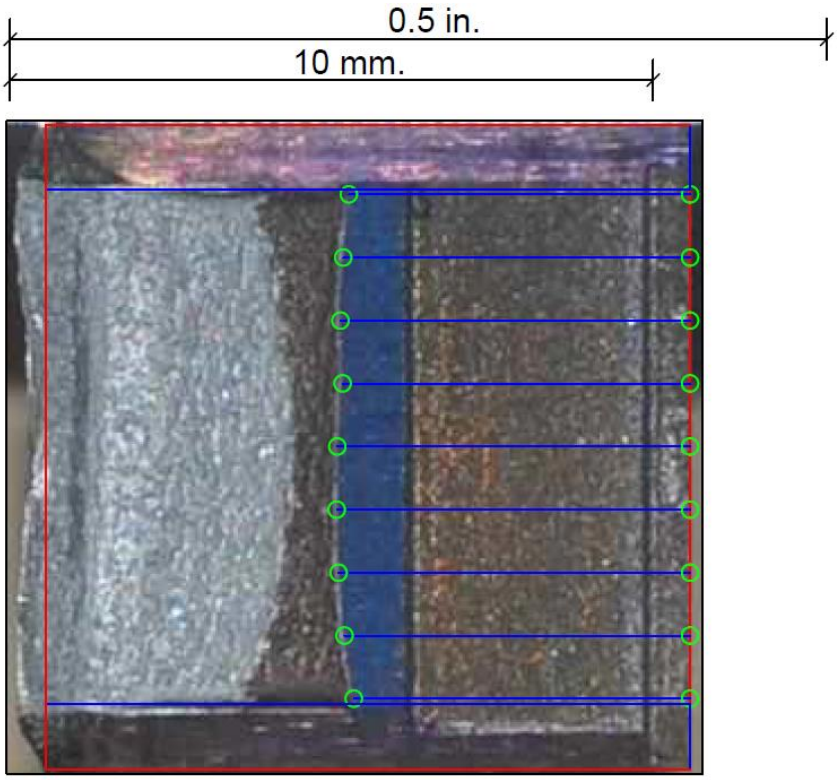

Figure E-45. Specimen F15' Fracture Surface

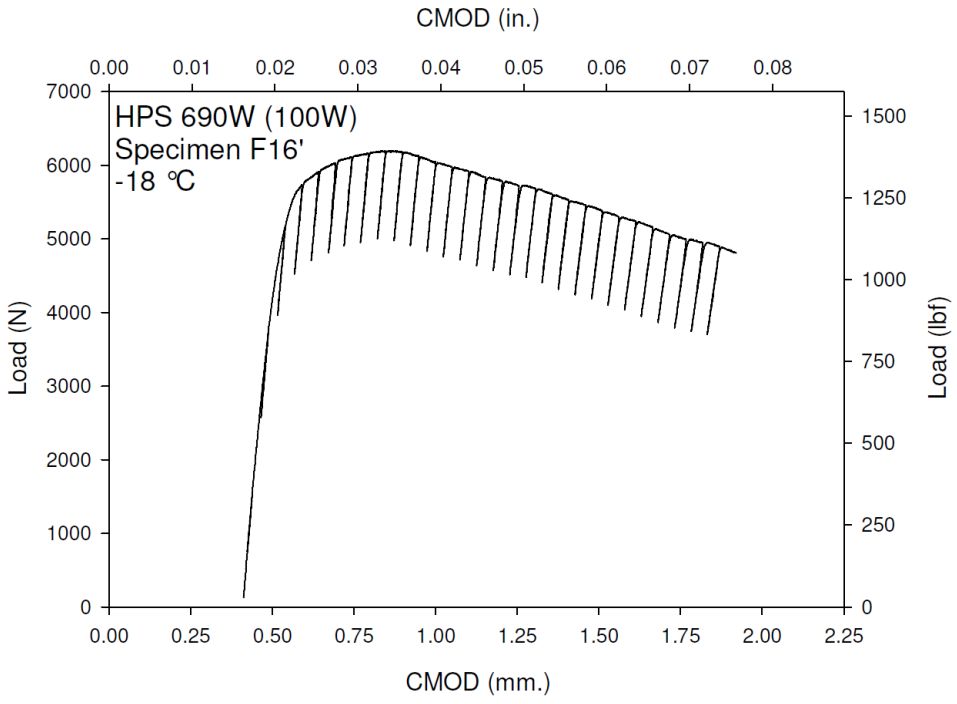

Figure E-46. Specimen F16' Test Record

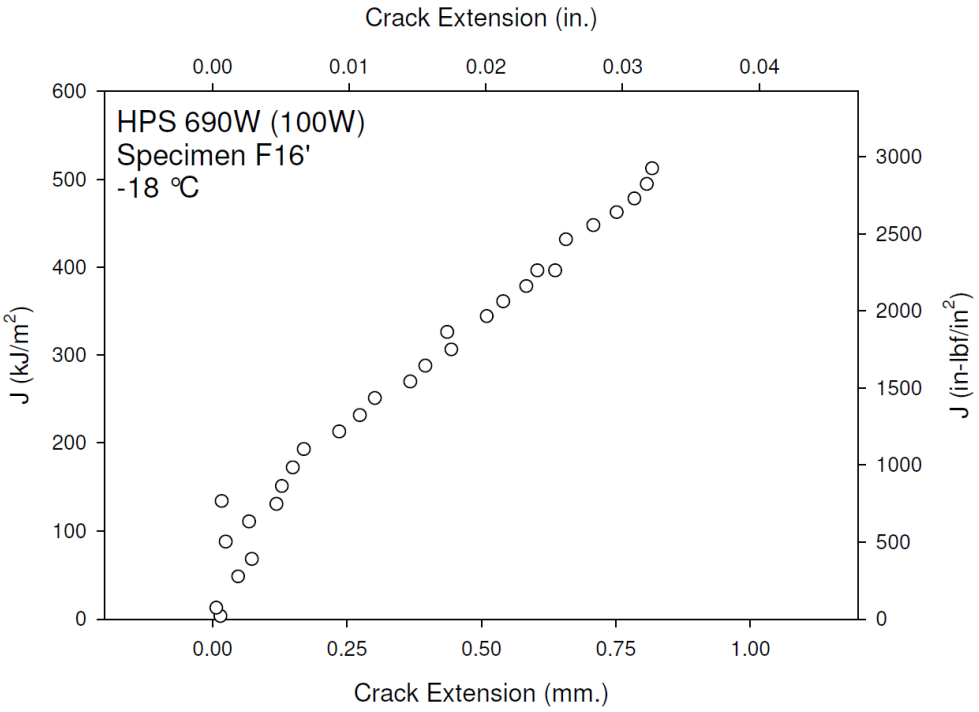

Figure E-47. Specimen F16' Resistance Curve

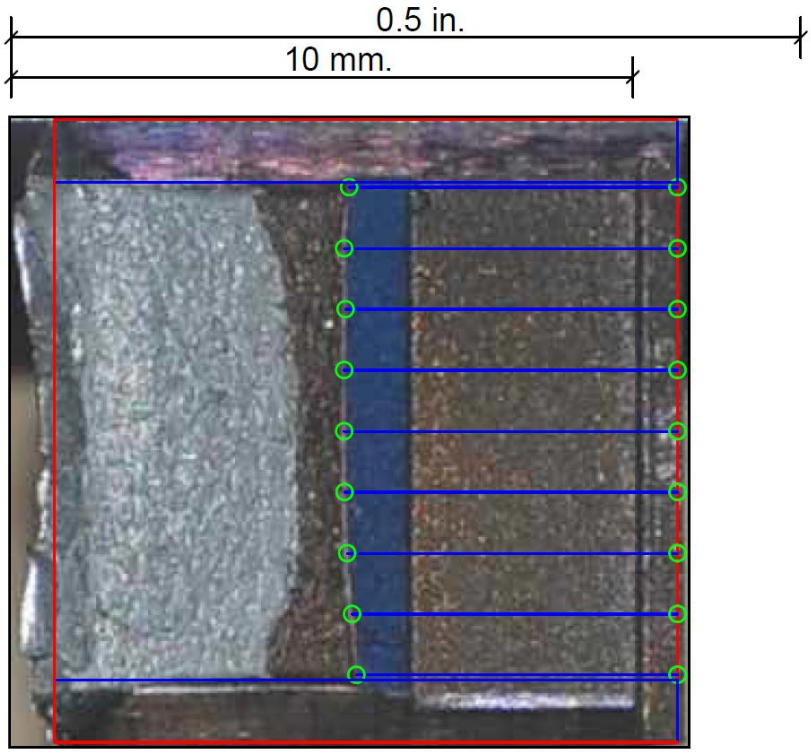

Figure E-48. Specimen F16' Fracture Surface

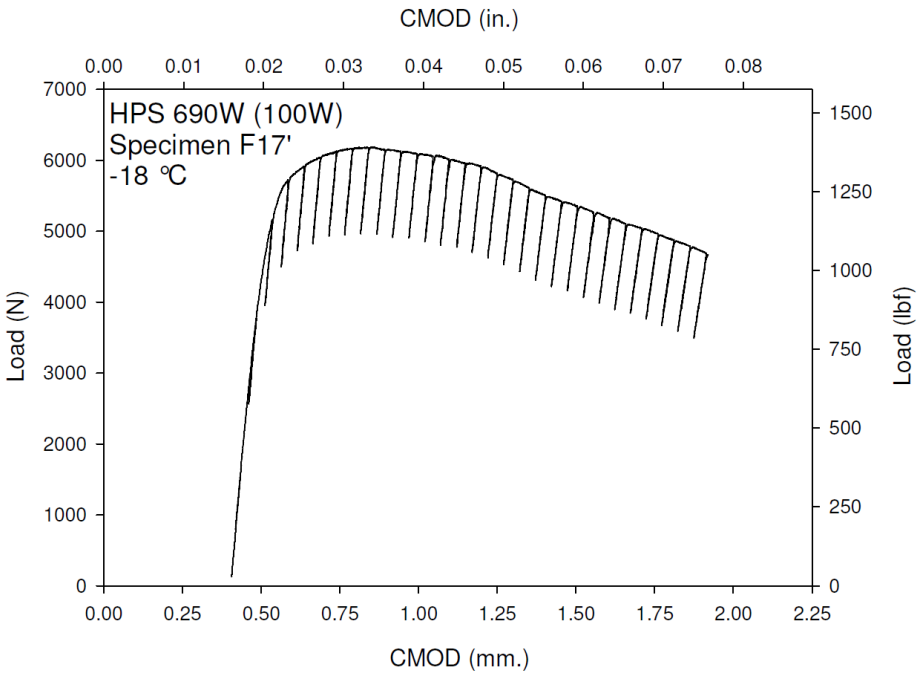

Figure E-49. Specimen F17' Test Record

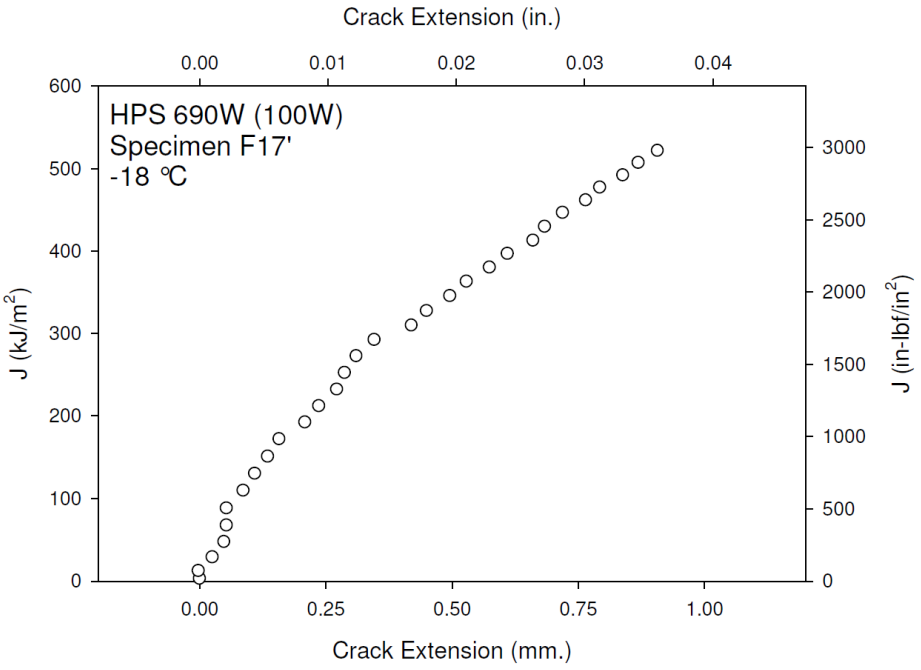

Figure E-50. Specimen F17' Resistance Curve

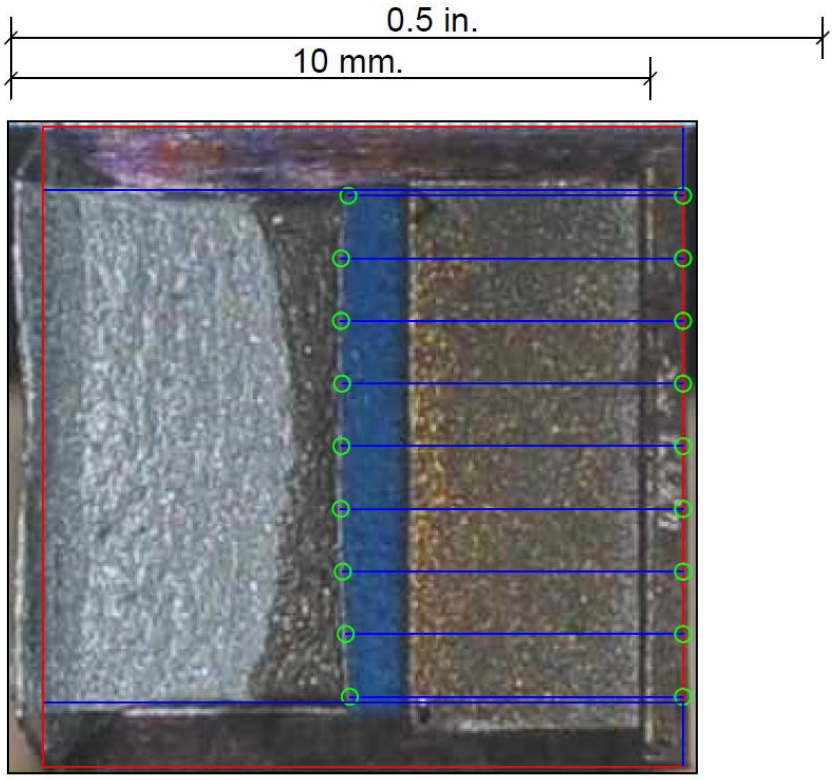

Figure E-51. Specimen F17' Fracture Surface

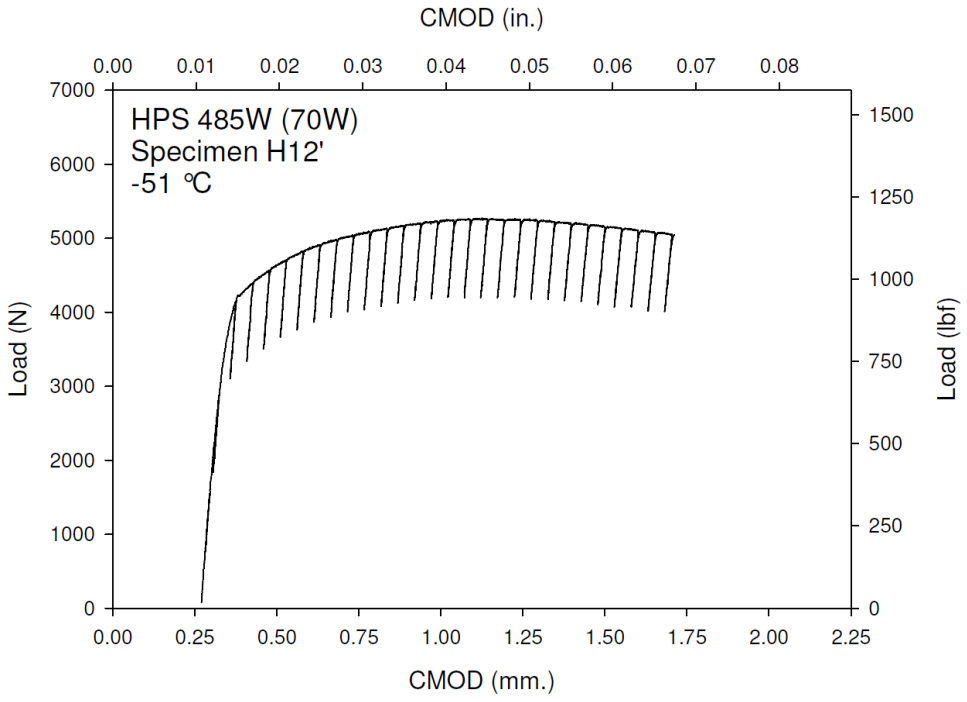

Figure E-52. Specimen H12' Test Record

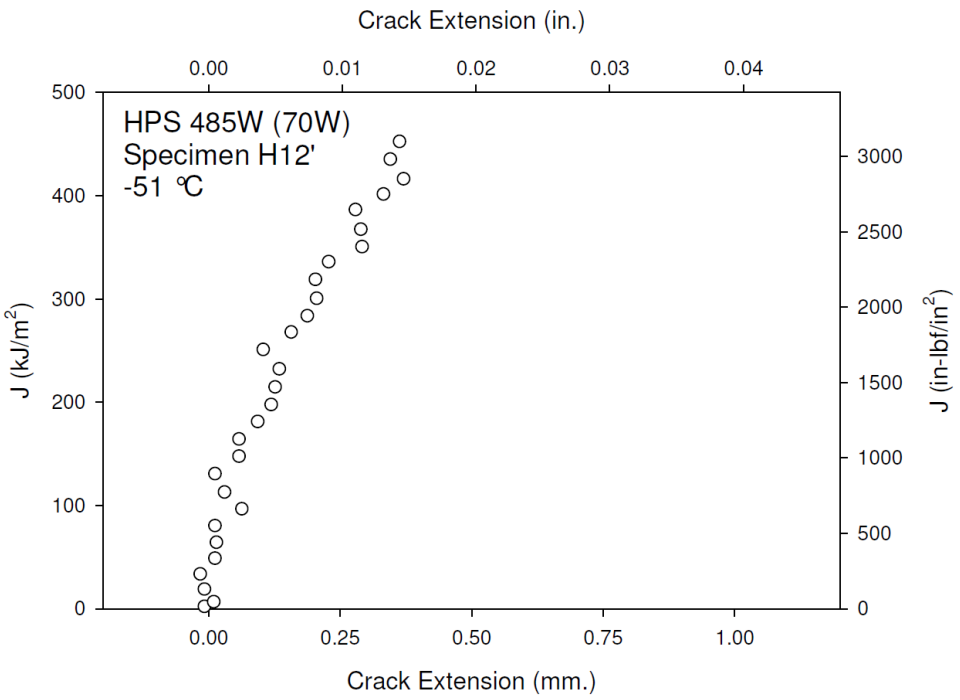

Figure E-53. Specimen H12' Resistance Curve

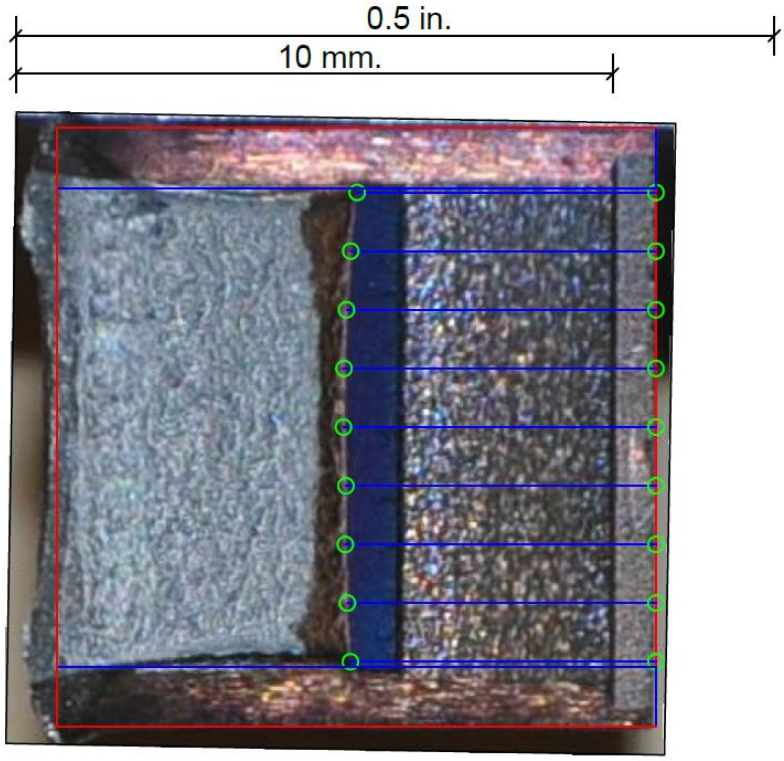

Figure E-54. Specimen H12' Fracture Surface

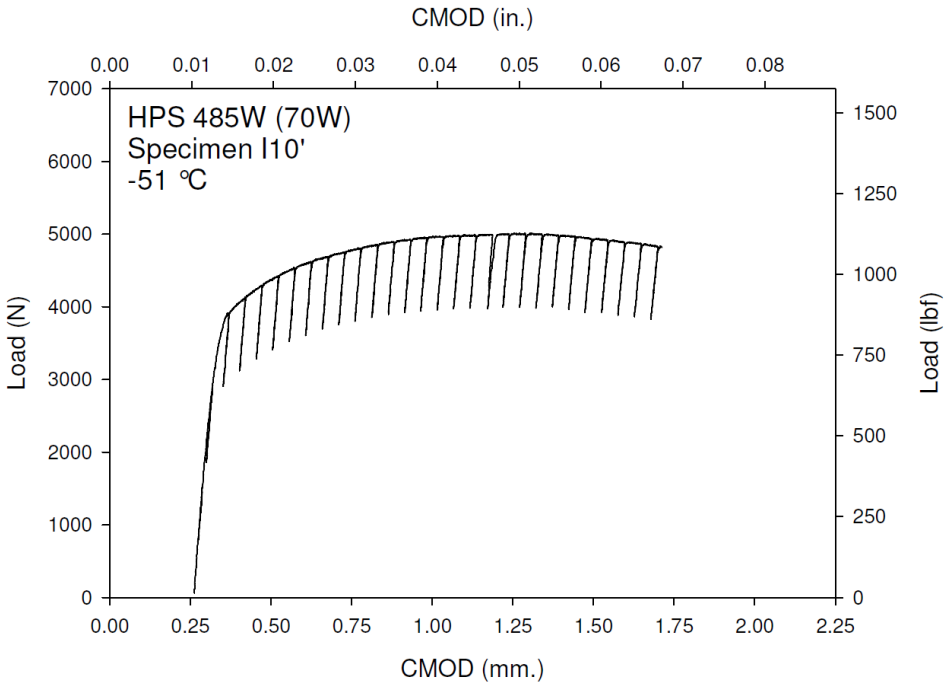

Figure E-55. Specimen I10' Test Record

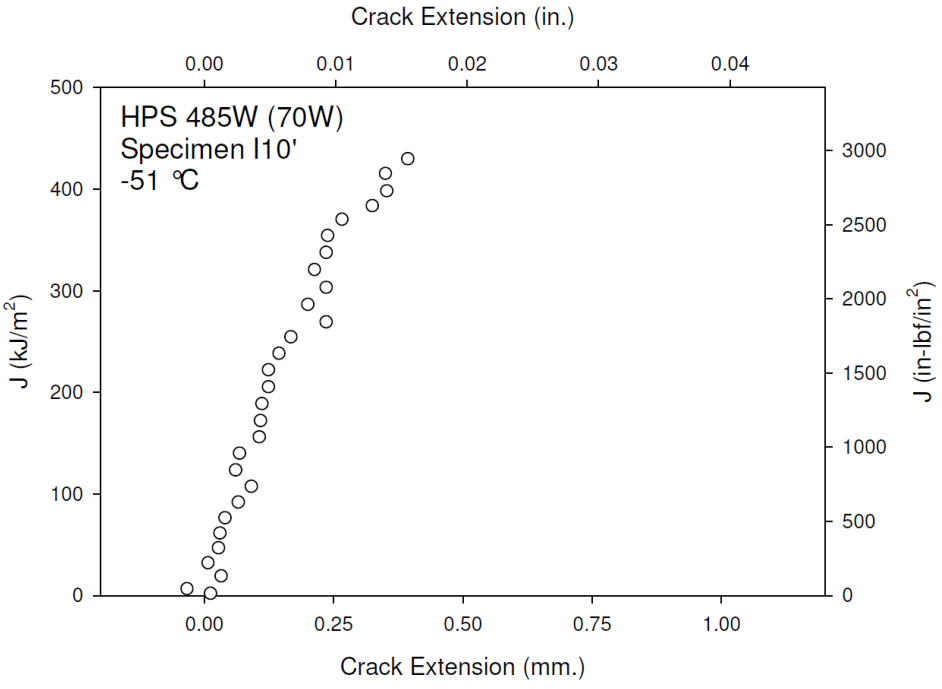

Figure E-56. Specimen I10' Resistance Curve

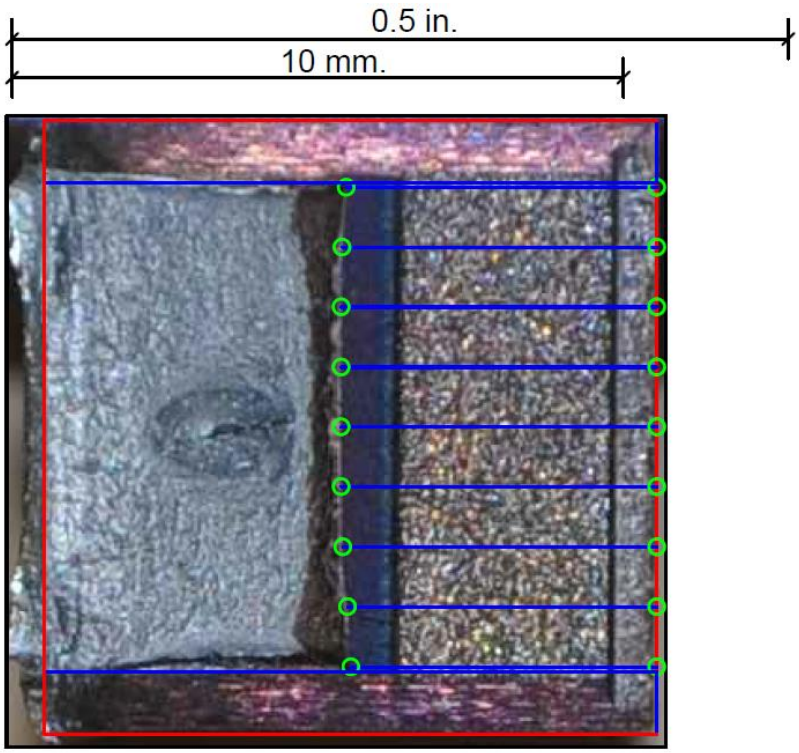

Figure E-57. Specimen I10' Fracture Surface

APPENDIX F: HPS Dynamic Test Records and Fracture Surfaces

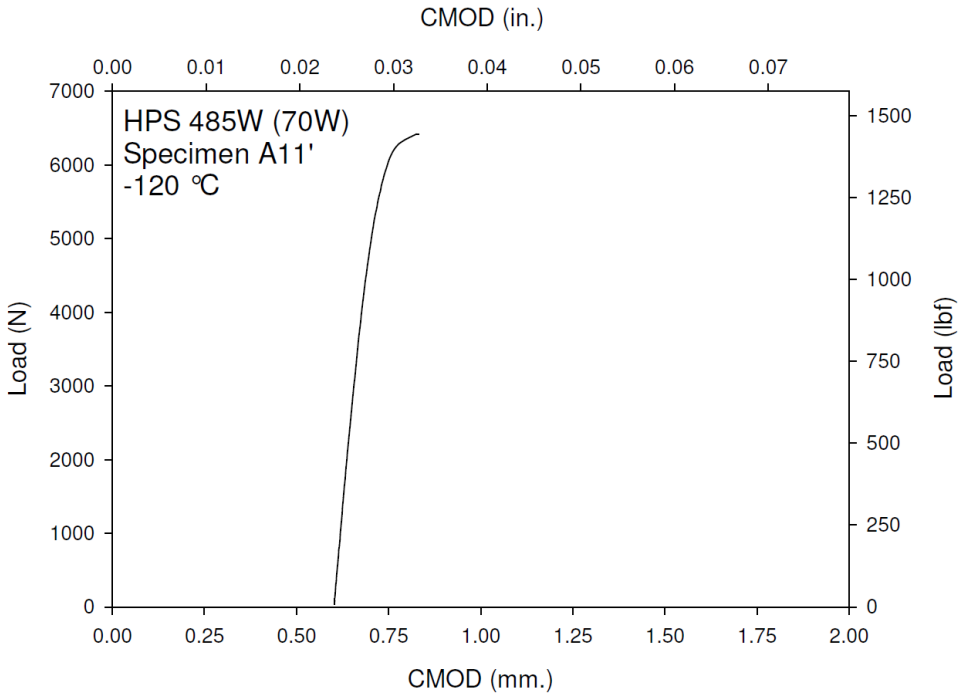

Figure F-1. Specimen A11' Test Record

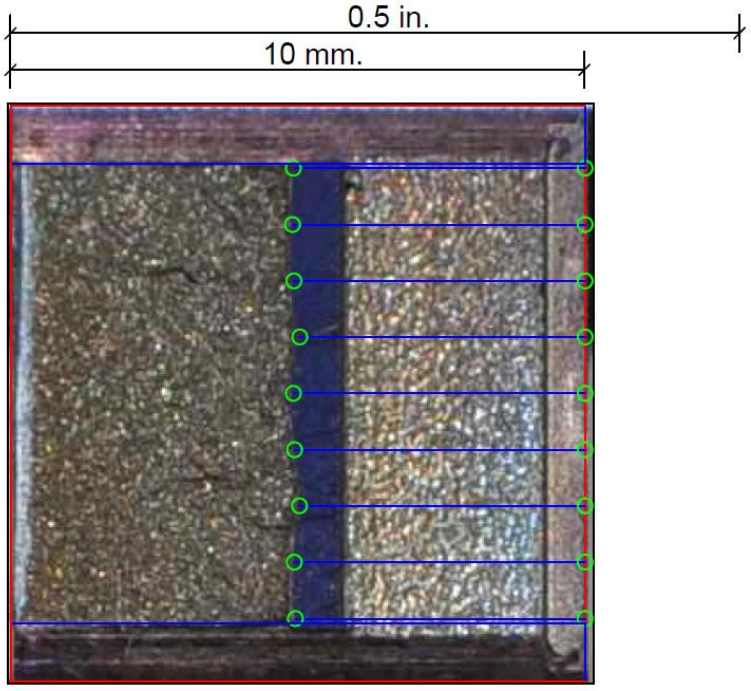

Figure F-2. Specimen A11' Fracture Surface

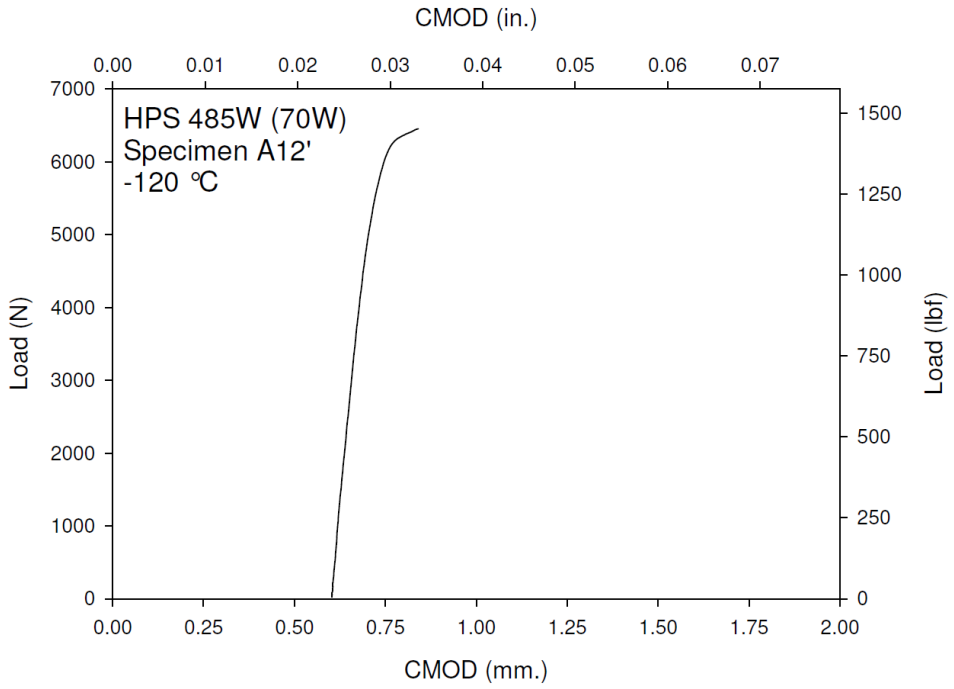

Figure F-3. Specimen A12' Test Record

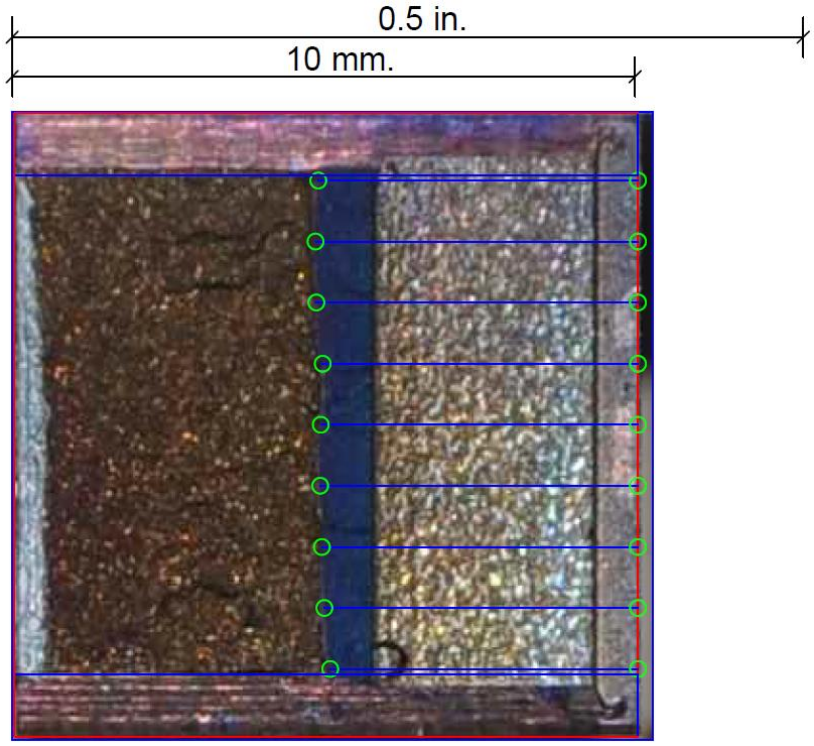

Figure F-4. Specimen A12' Fracture Surface

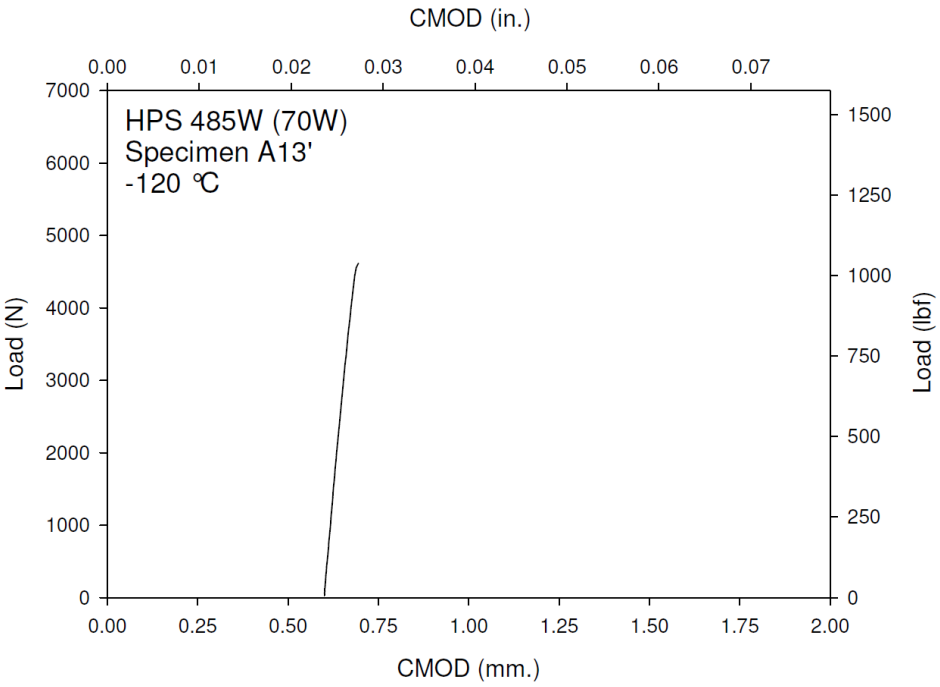

Figure F-5. Specimen A13' Test Record

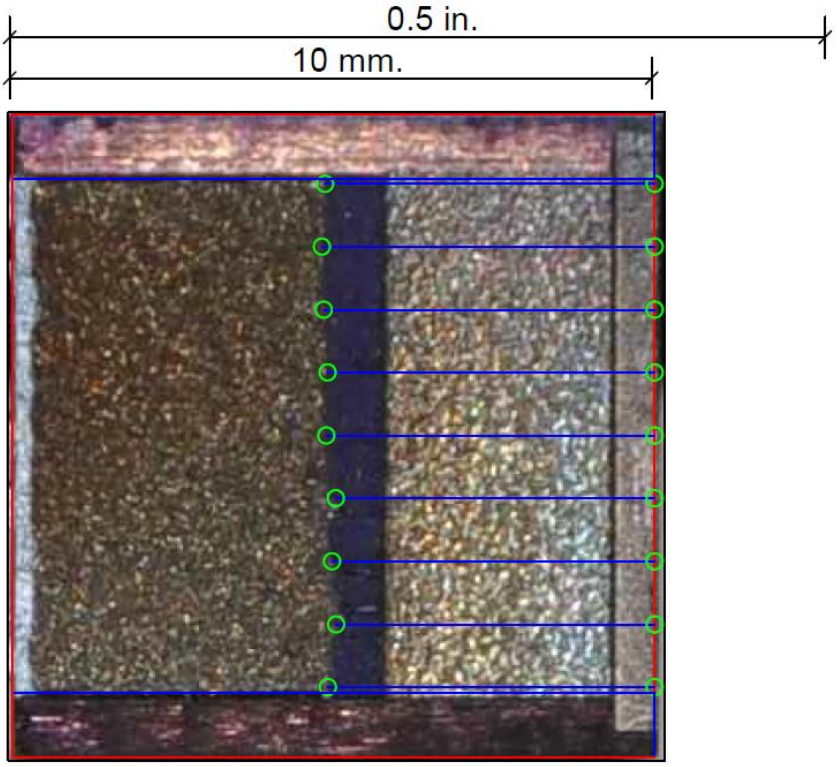

Figure F-6. Specimen A13' Fracture Surface

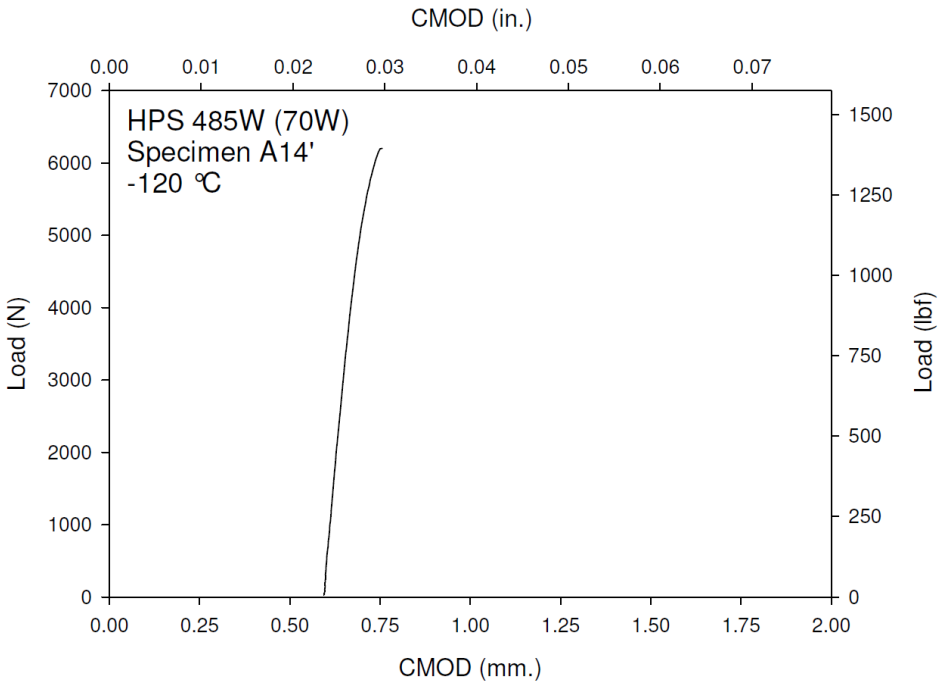

Figure F-7. Specimen A14' Test Record

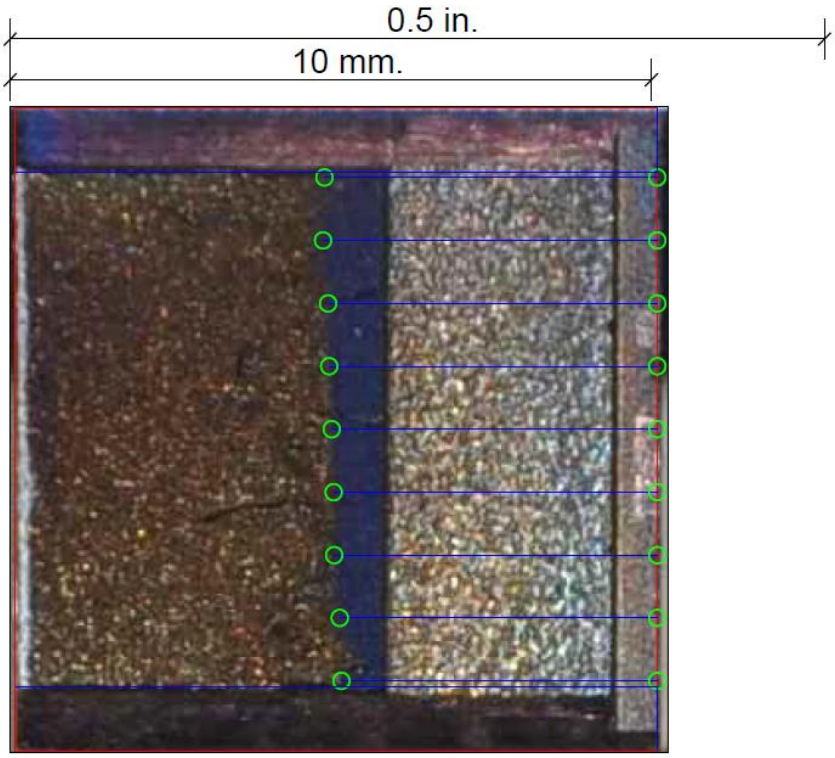

Figure F-8. Specimen A14' Fracture Surface

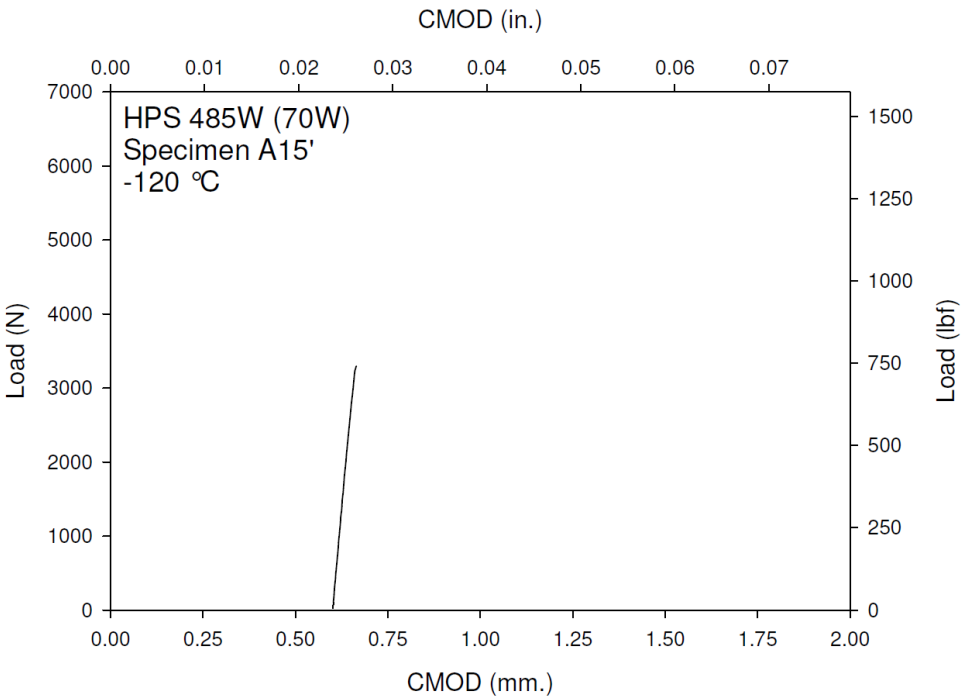

Figure F-9. Specimen A15' Test Record

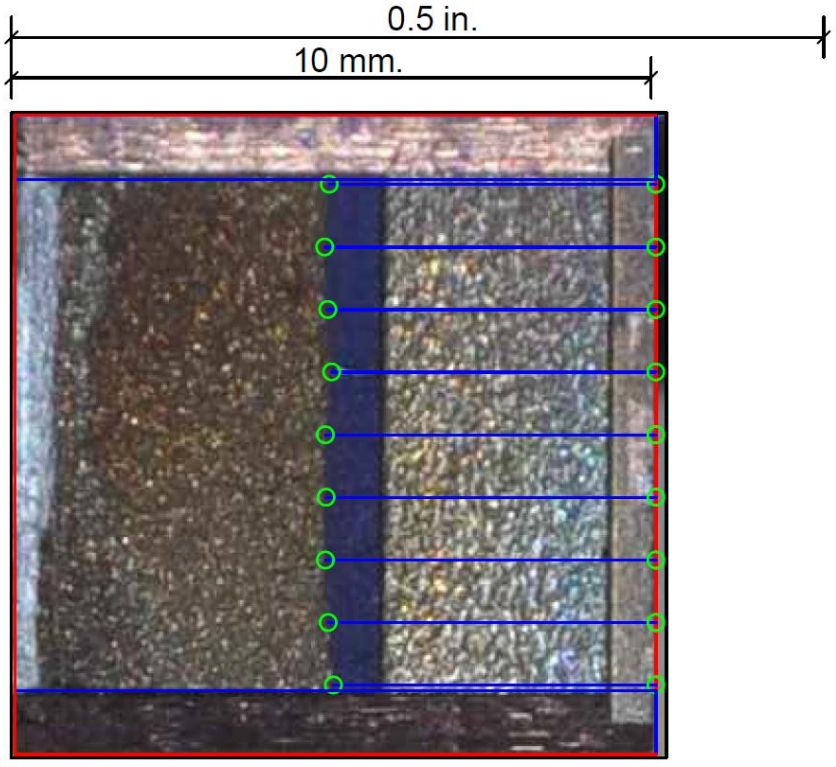

Figure F-10. Specimen A15' Fracture Surface

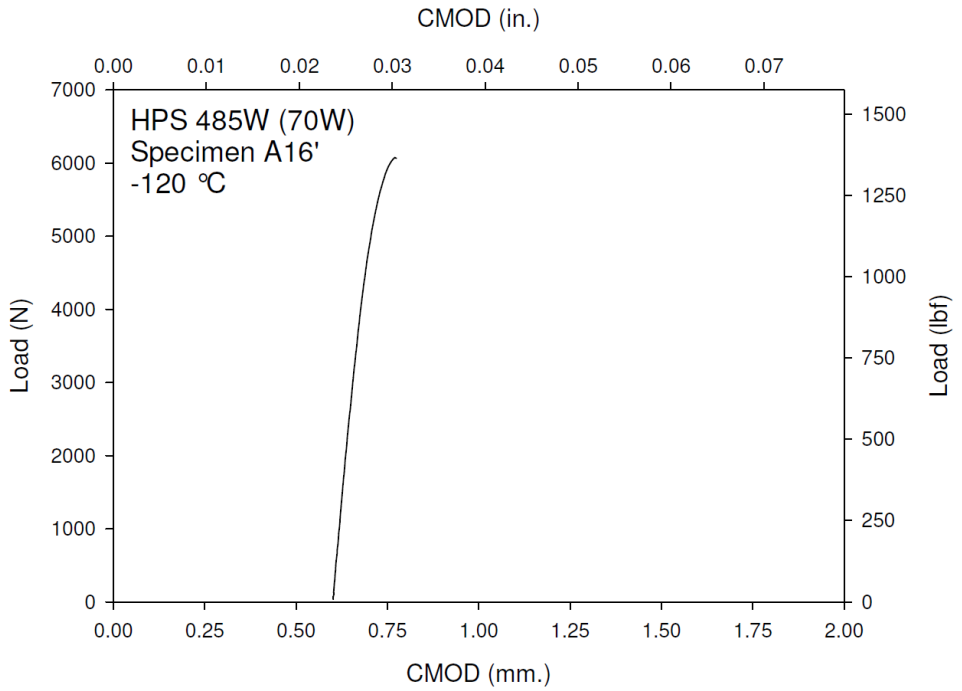

Figure F-11. Specimen A16' Test Record

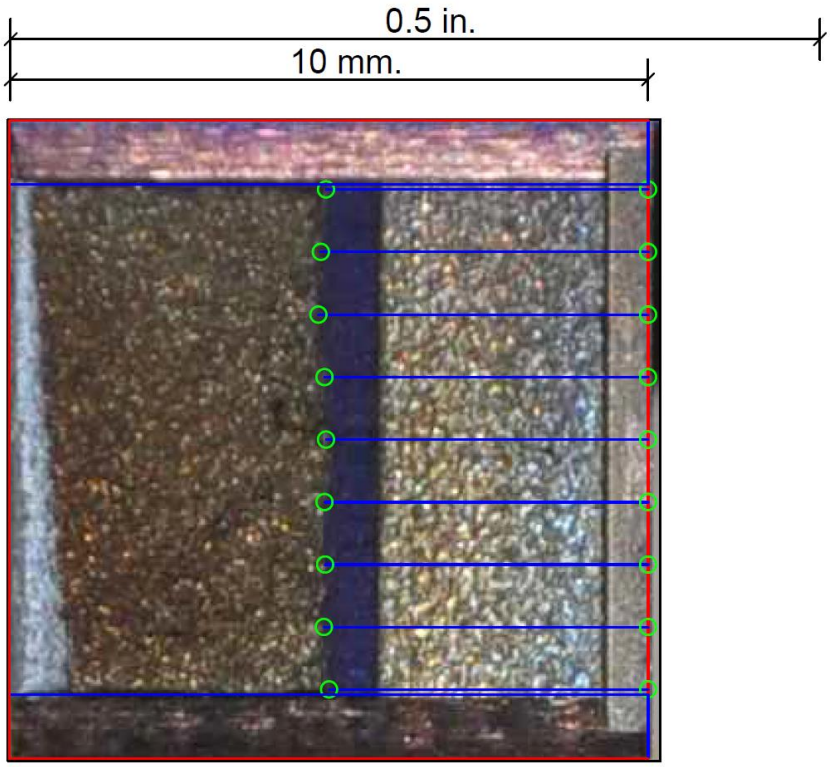

Figure F-12. Specimen A16' Fracture Surface

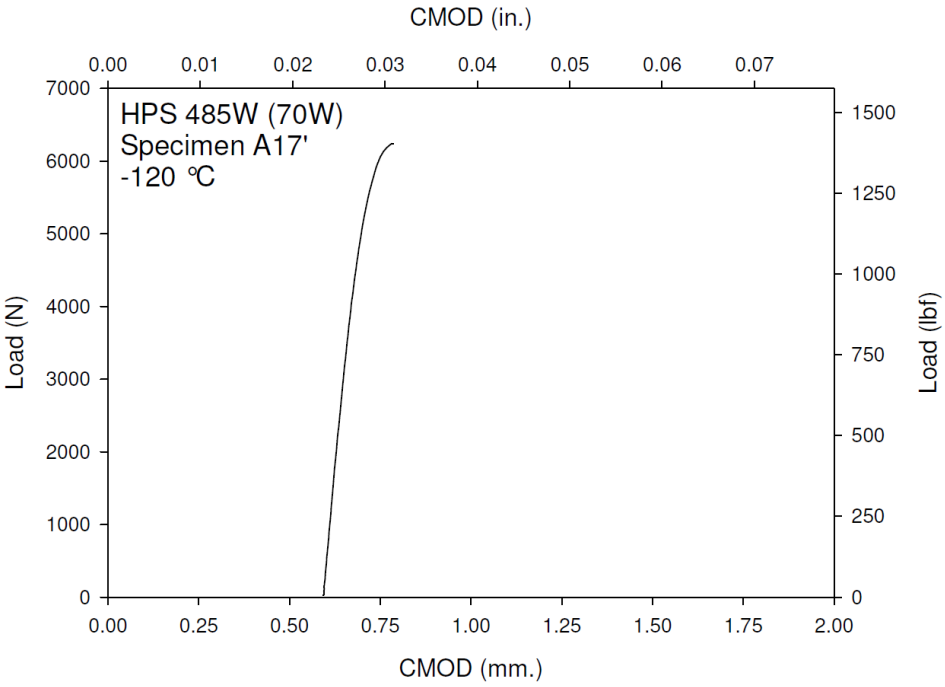

Figure F-13. Specimen A17' Test Record

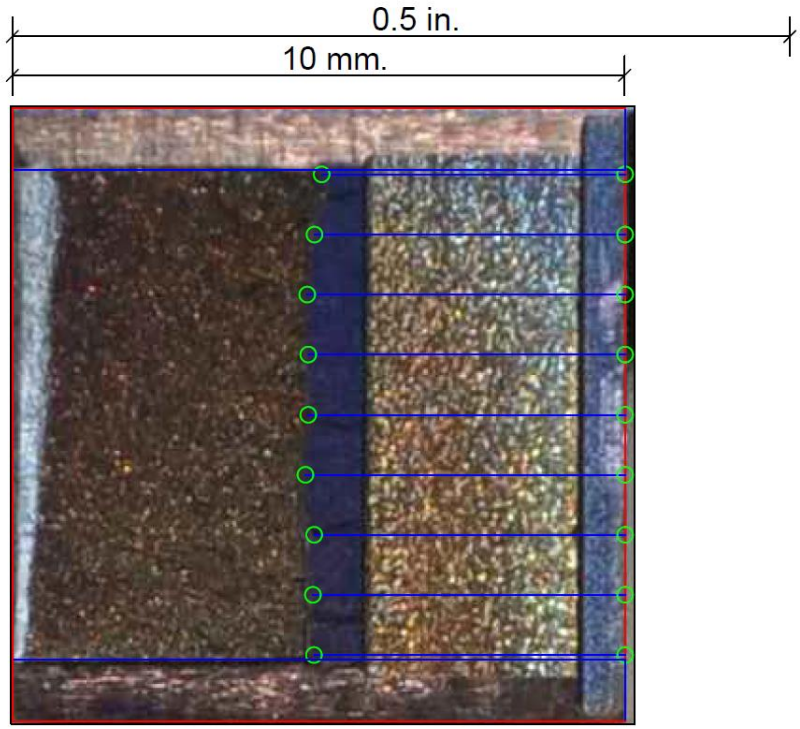

Figure F-14. Specimen A17' Fracture Surface

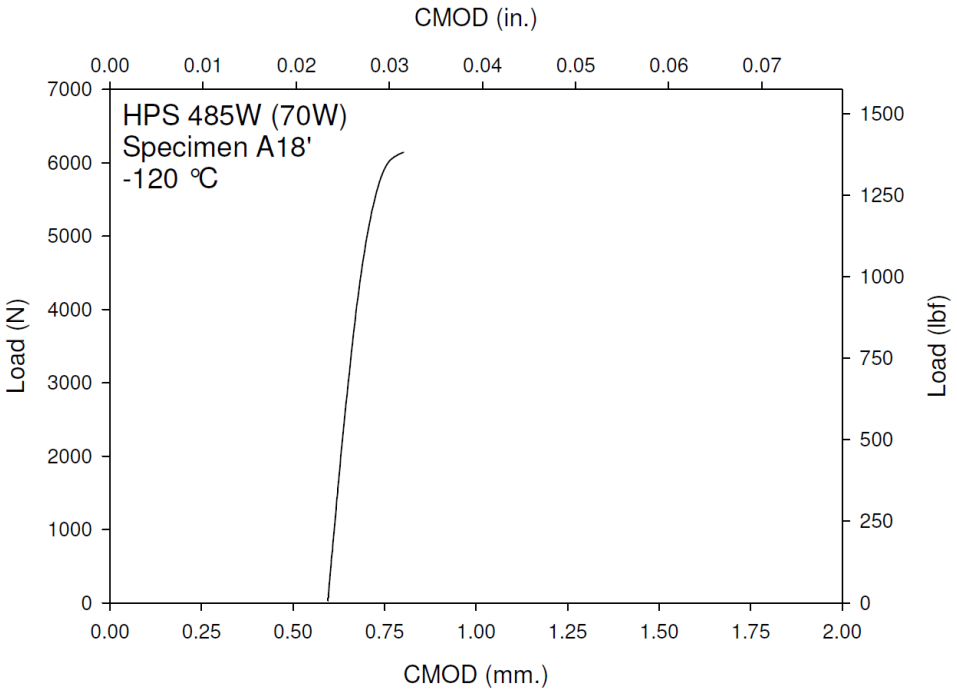

Figure F-15. Specimen A18' Test Record

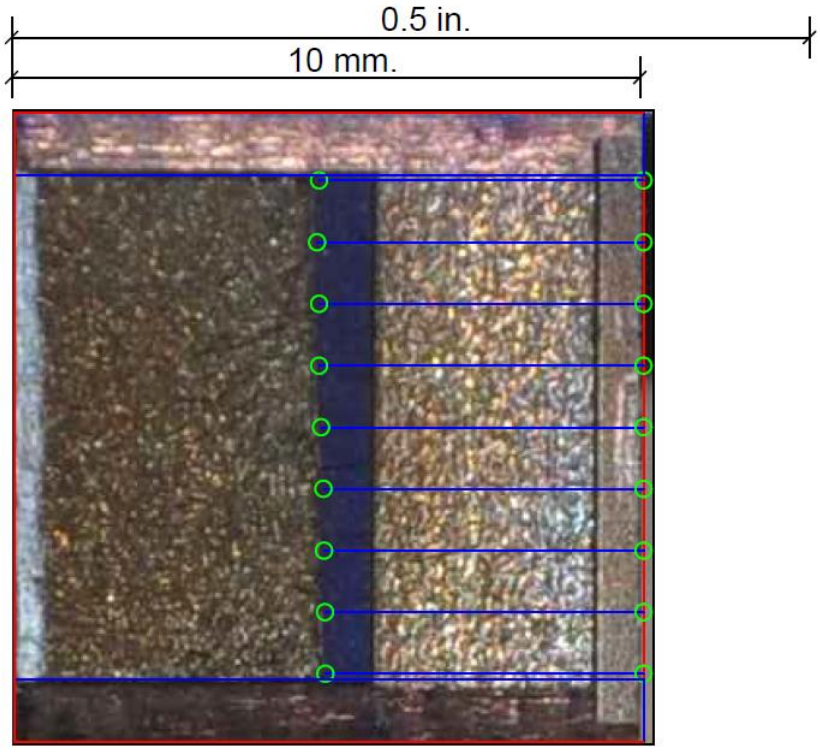

Figure F-16. Specimen A18' Fracture Surface

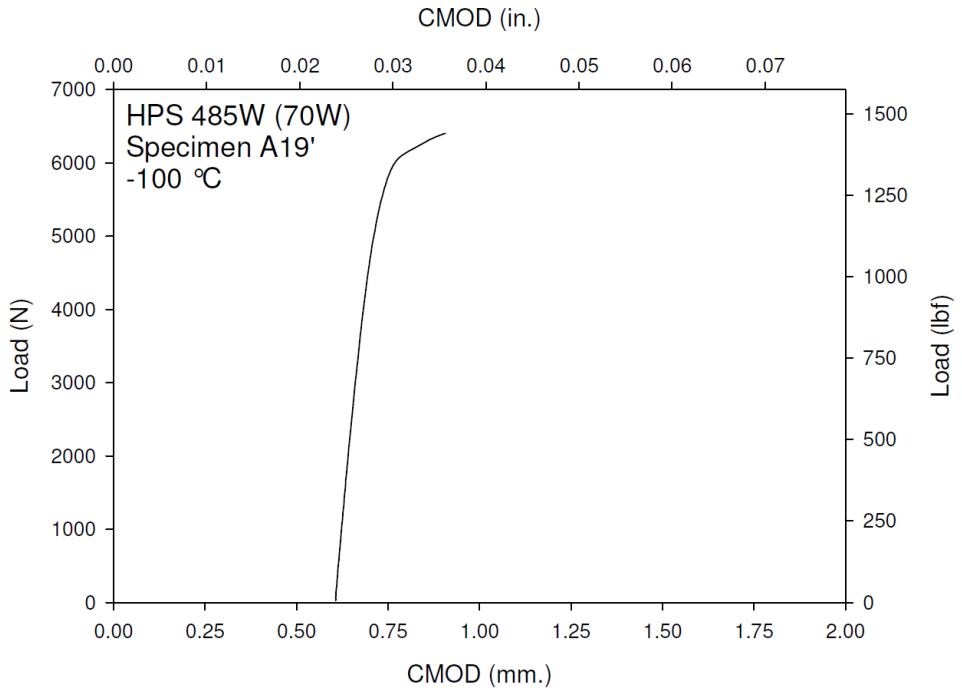

Figure F-17. Specimen A19' Test Record

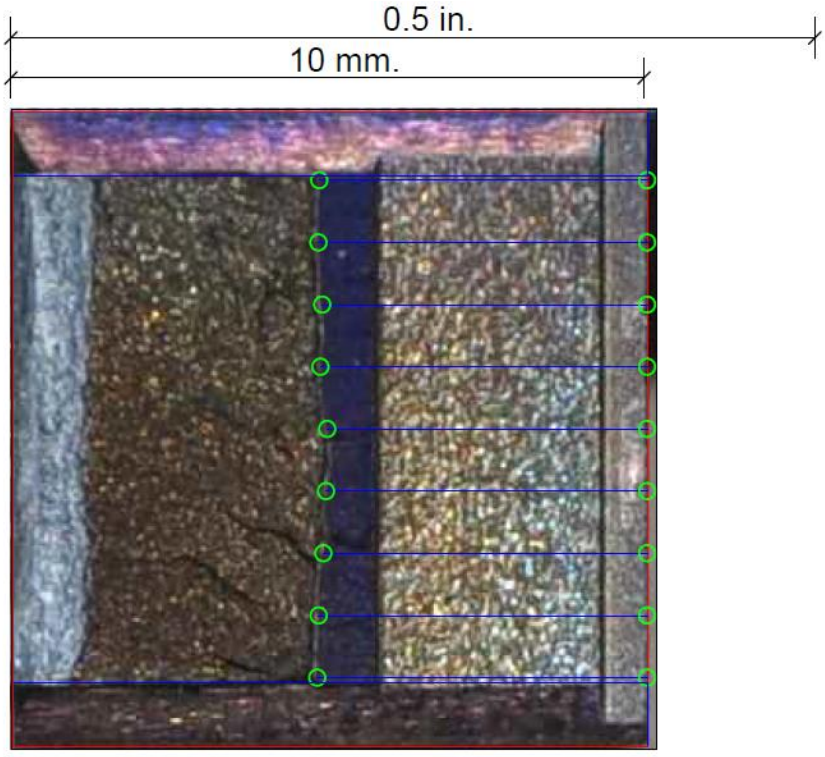

Figure F-18. Specimen A19' Fracture Surface

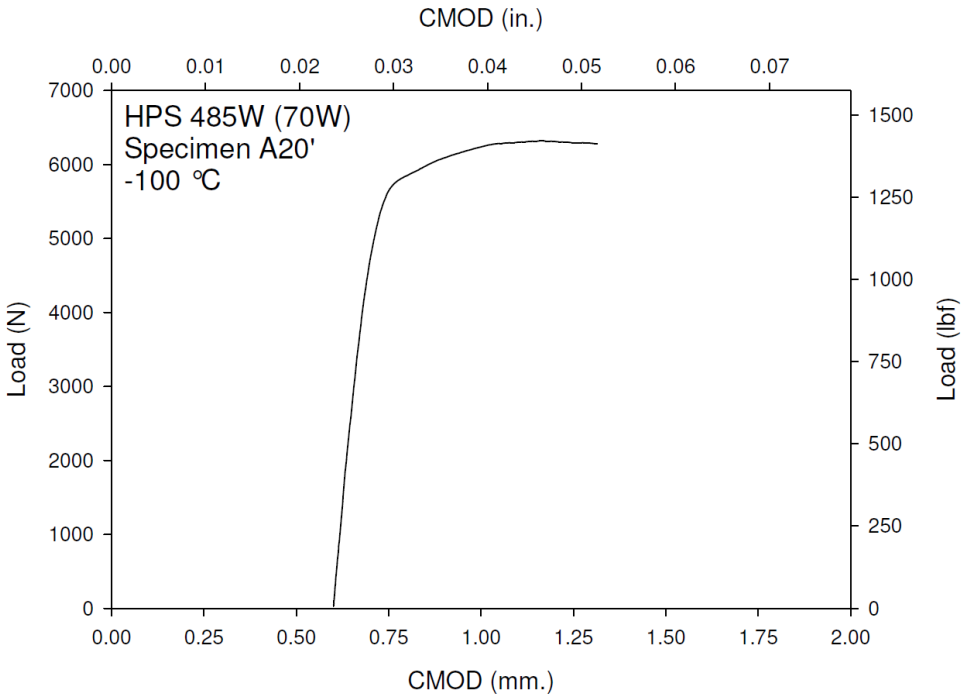

Figure F-19. Specimen A20' Test Record

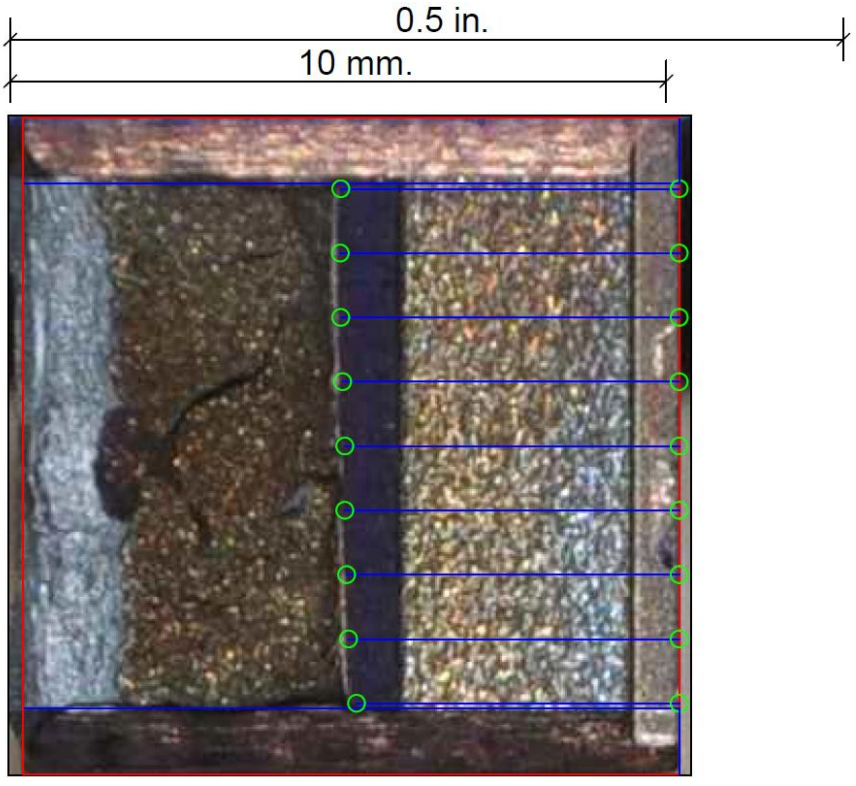

Figure F-20. Specimen A20' Fracture Surface

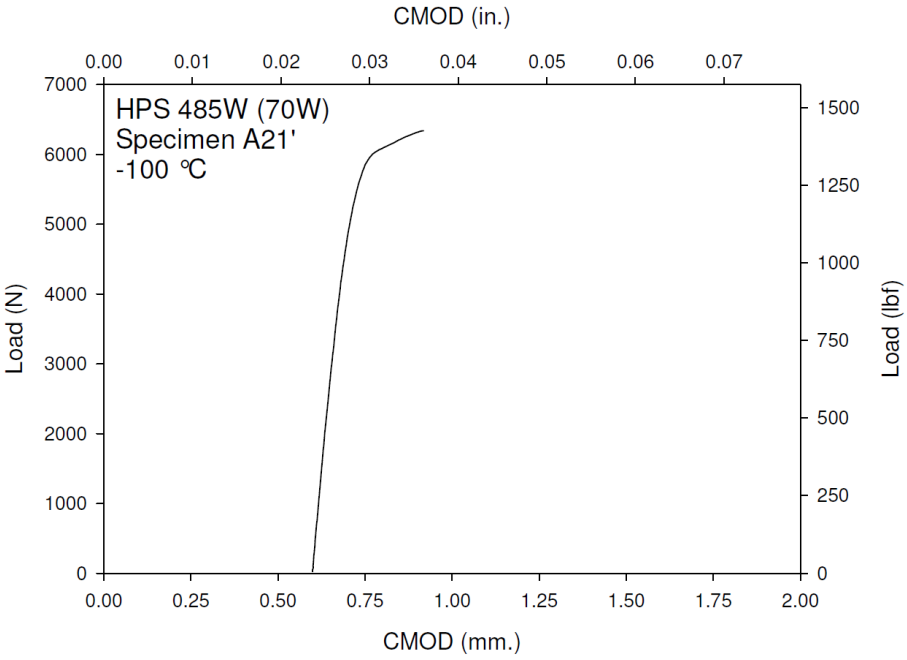

Figure F-21. Specimen A21' Test Record

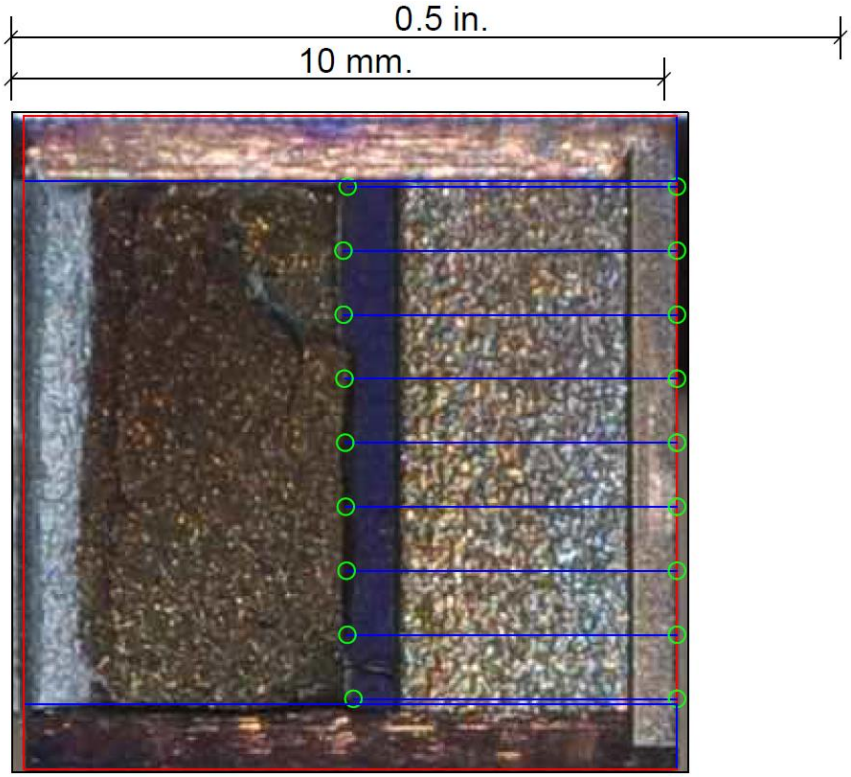

Figure F-22. Specimen A21' Fracture Surface

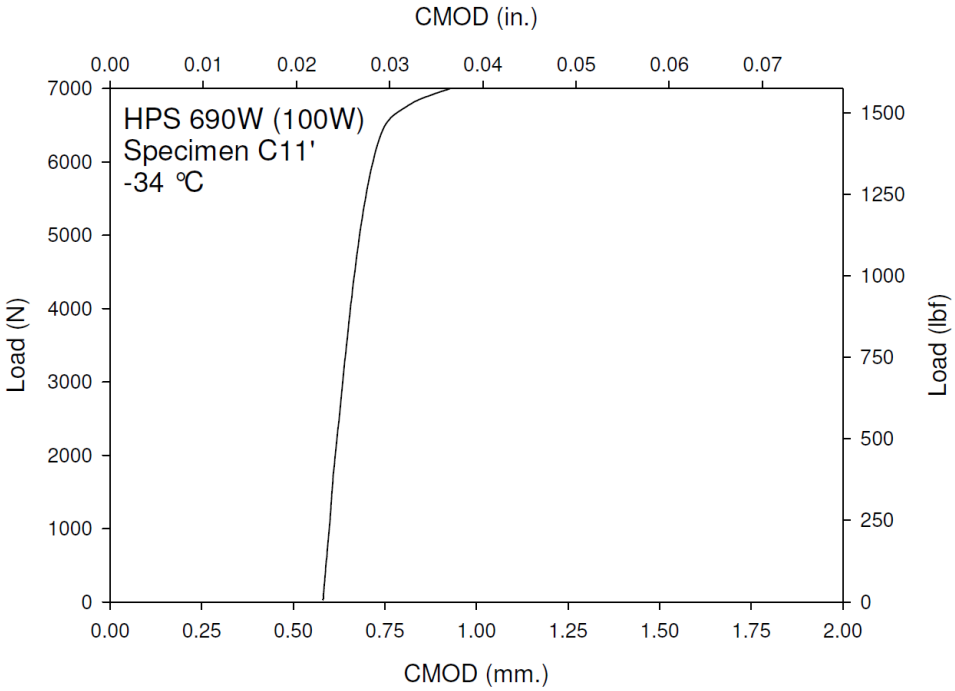

Figure F-23. Specimen C11' Test Record

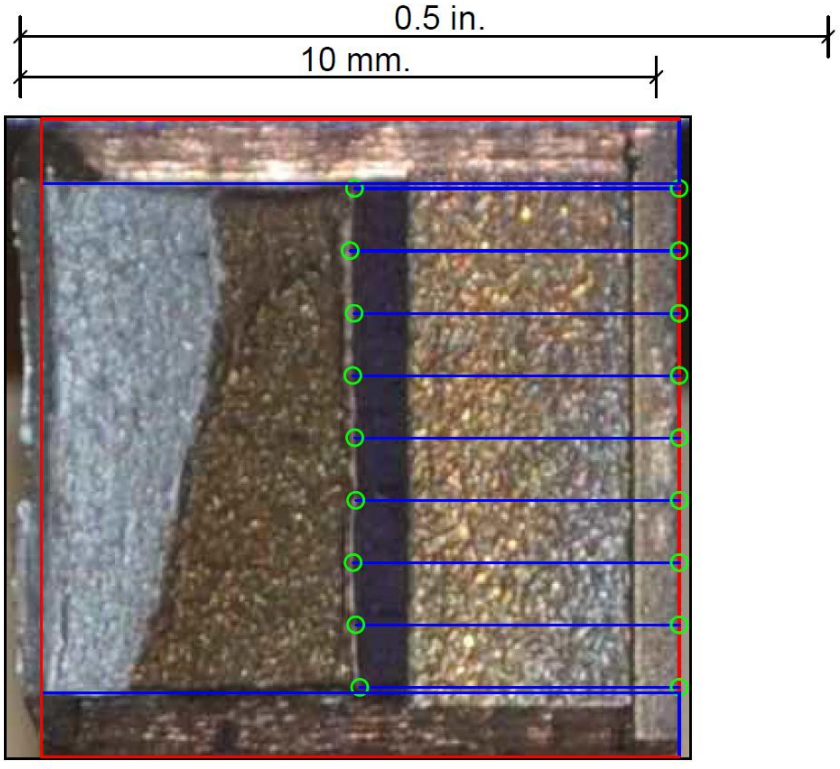

Figure F-24. Specimen C11' Fracture Surface

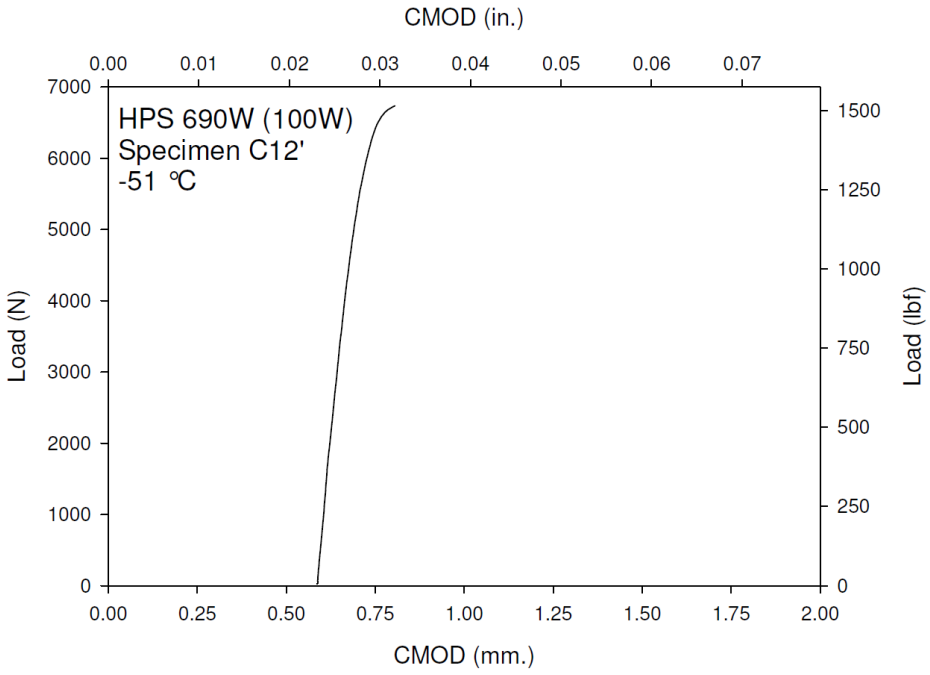

Figure F-25. Specimen C12' Test Record

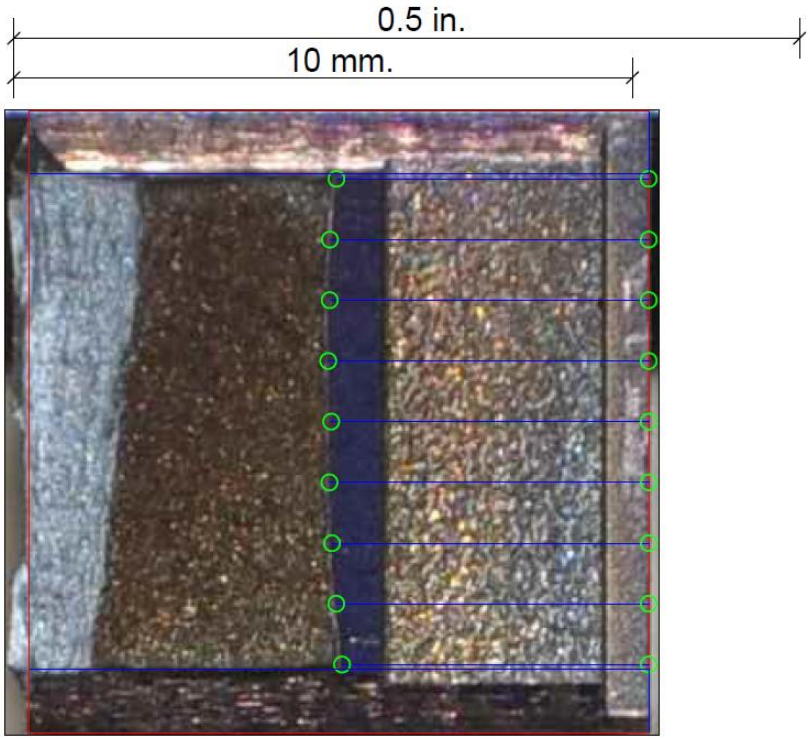

Figure F-26. Specimen C12' Fracture Surface

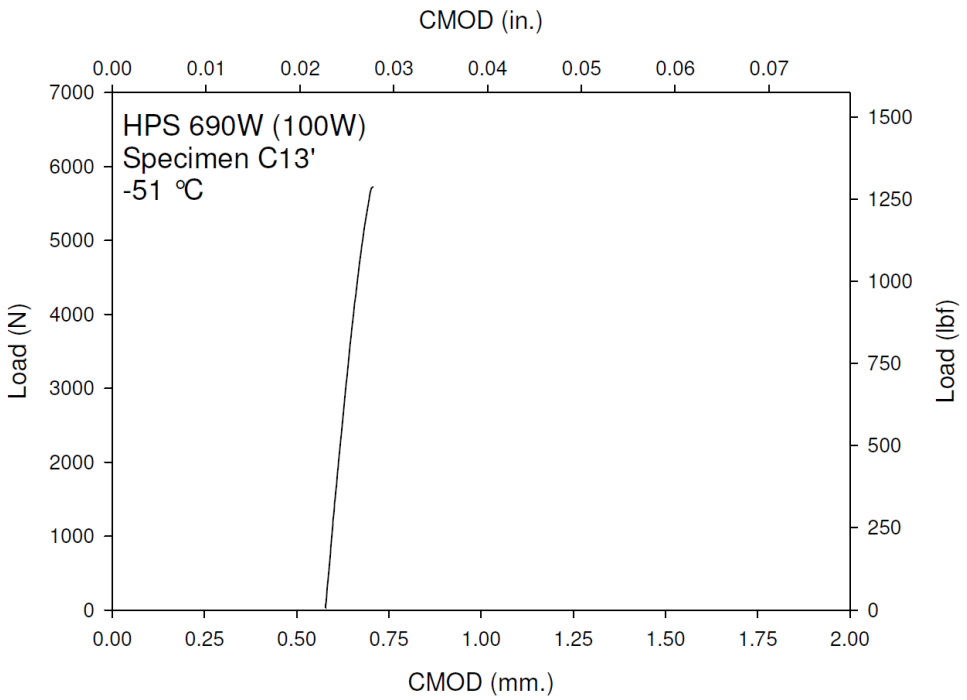

Figure F-27. Specimen C13' Test Record

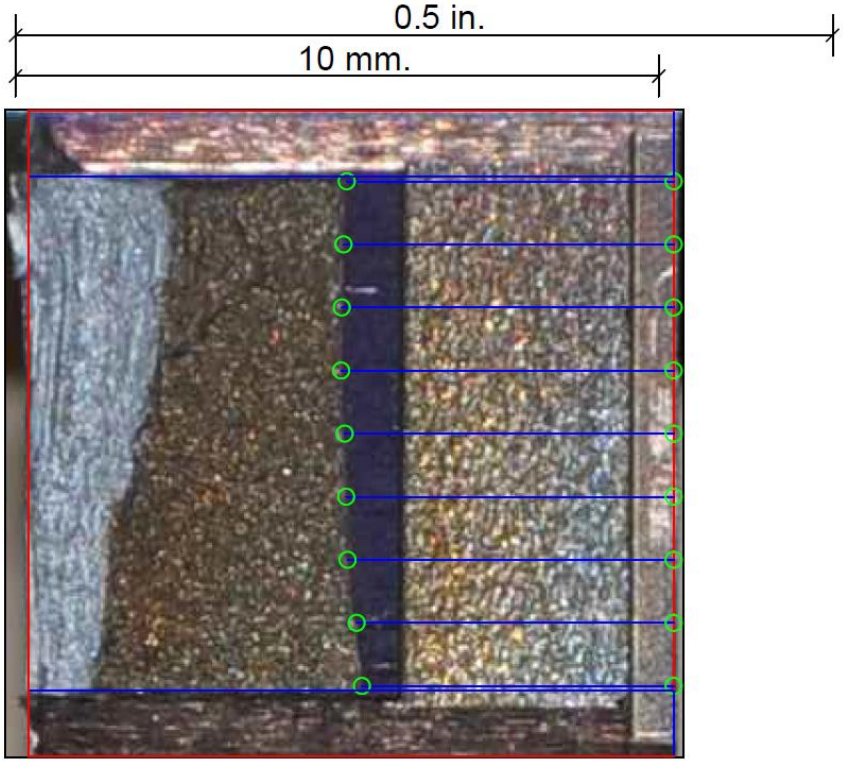

Figure F-28. Specimen C13' Fracture Surface

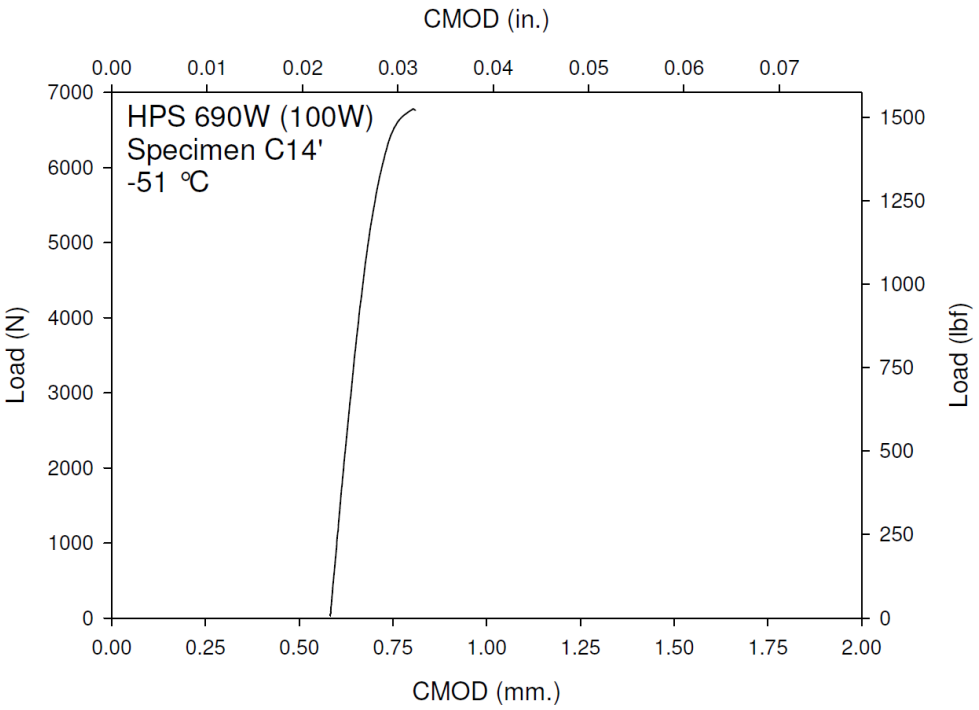

Figure F-29. Specimen C14' Test Record

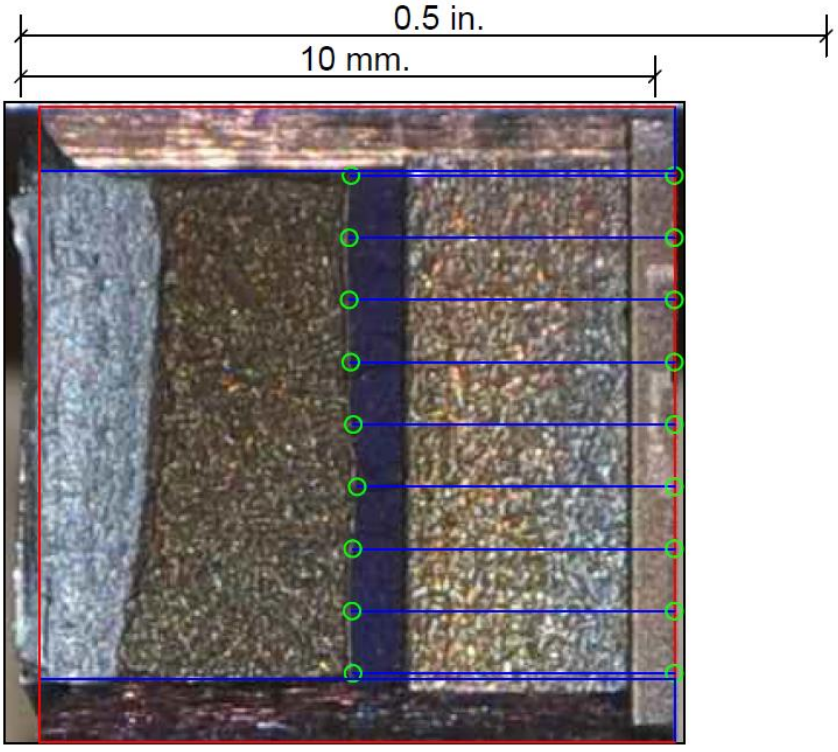

Figure F-30. Specimen C14' Fracture Surface

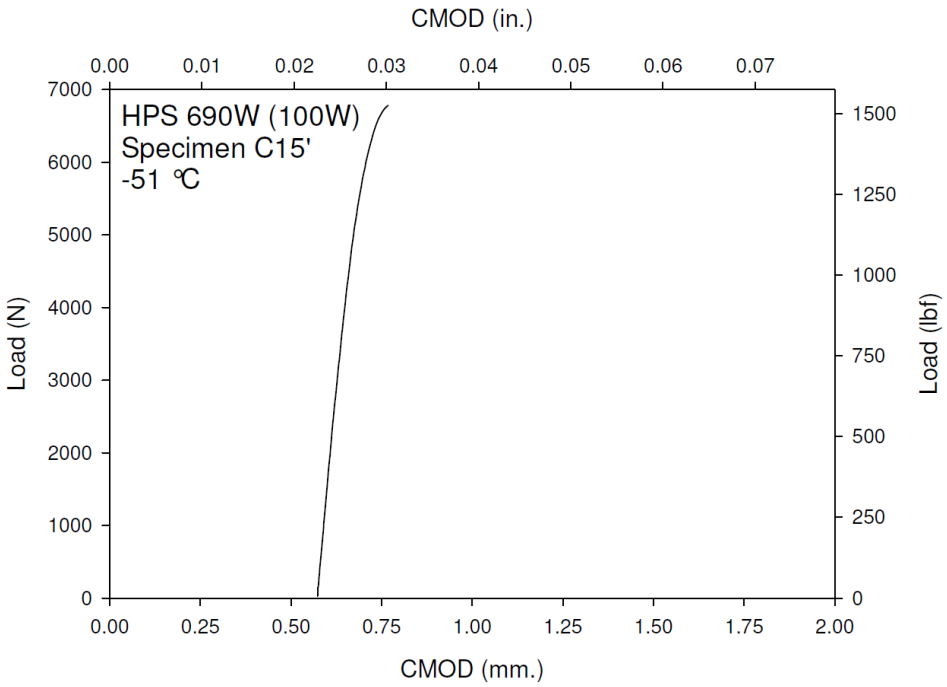

Figure F-31. Specimen C15' Test Record

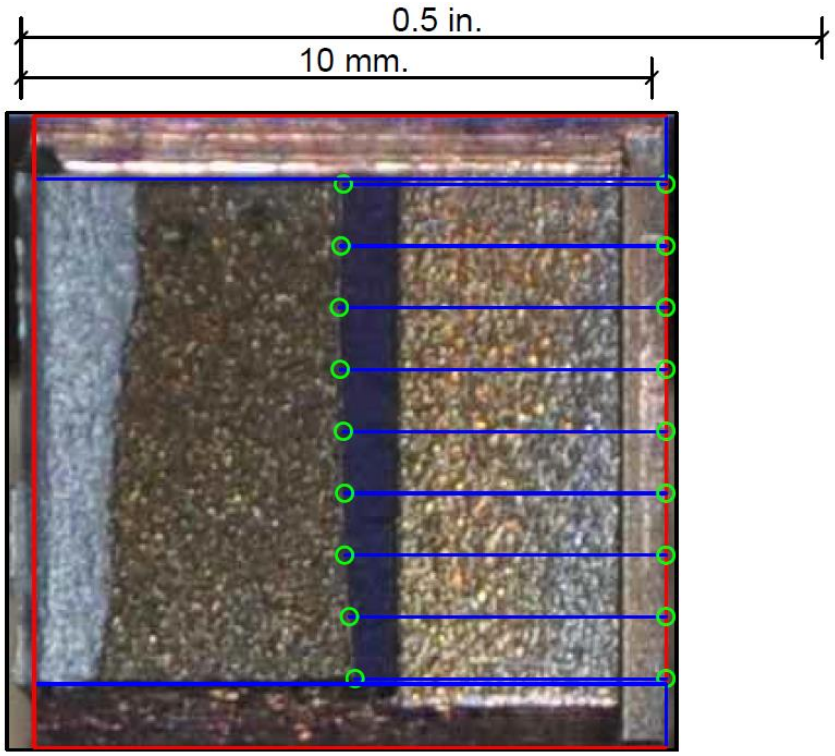

Figure F-32. Specimen C15' Fracture Surface

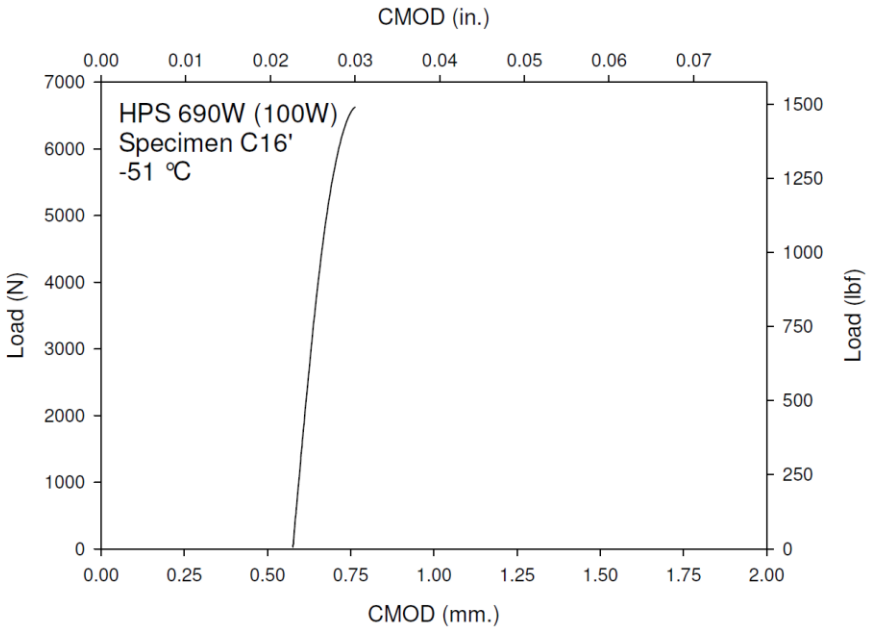

Figure F-33. Specimen C16' Test Record

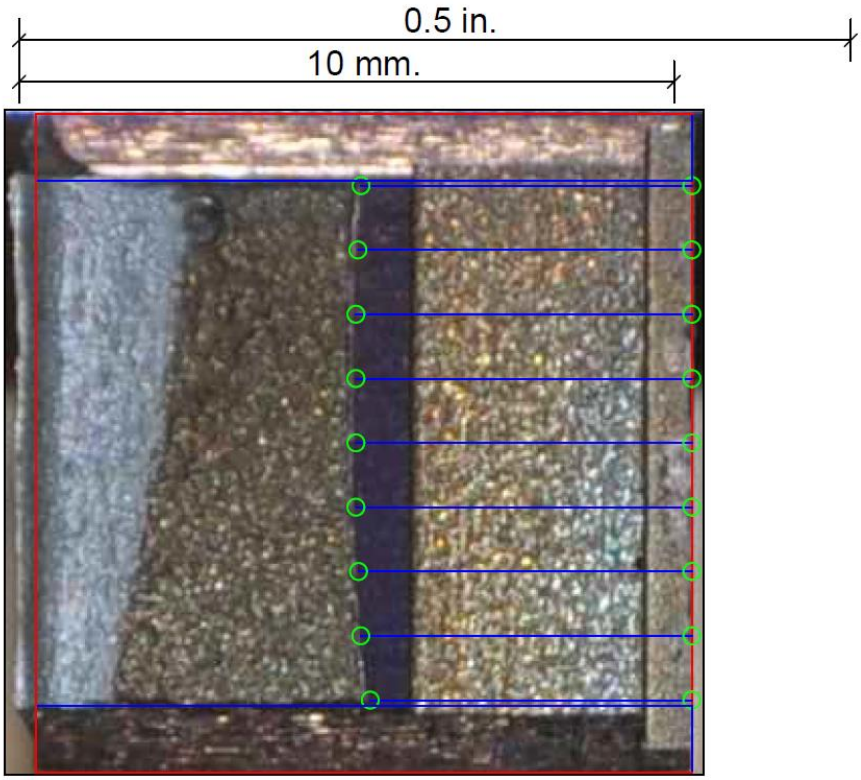

Figure F-34. Specimen C16' Fracture Surface

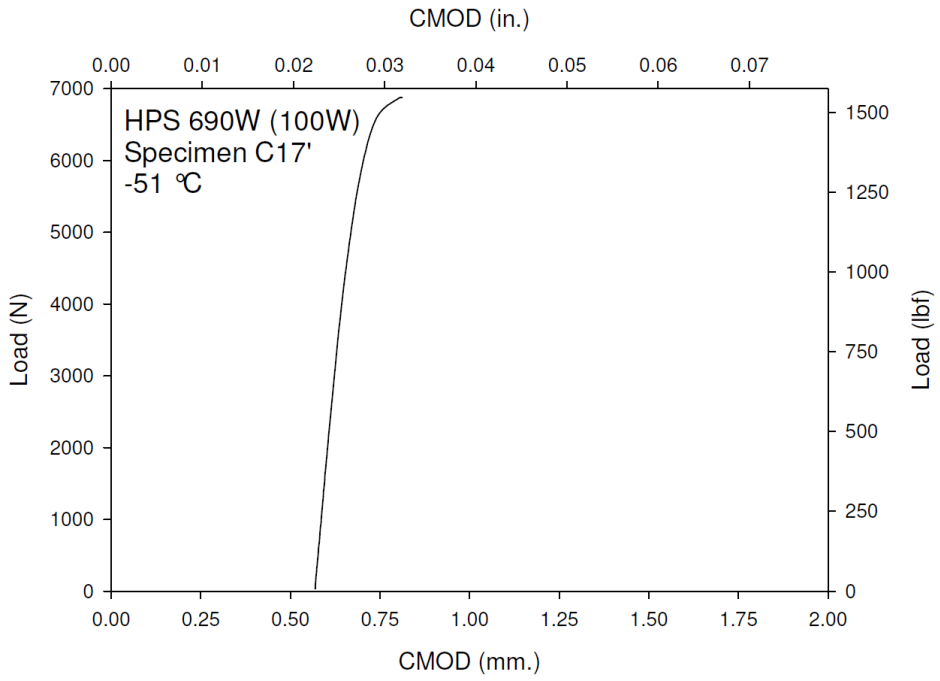

Figure F-35. Specimen C17' Test Record

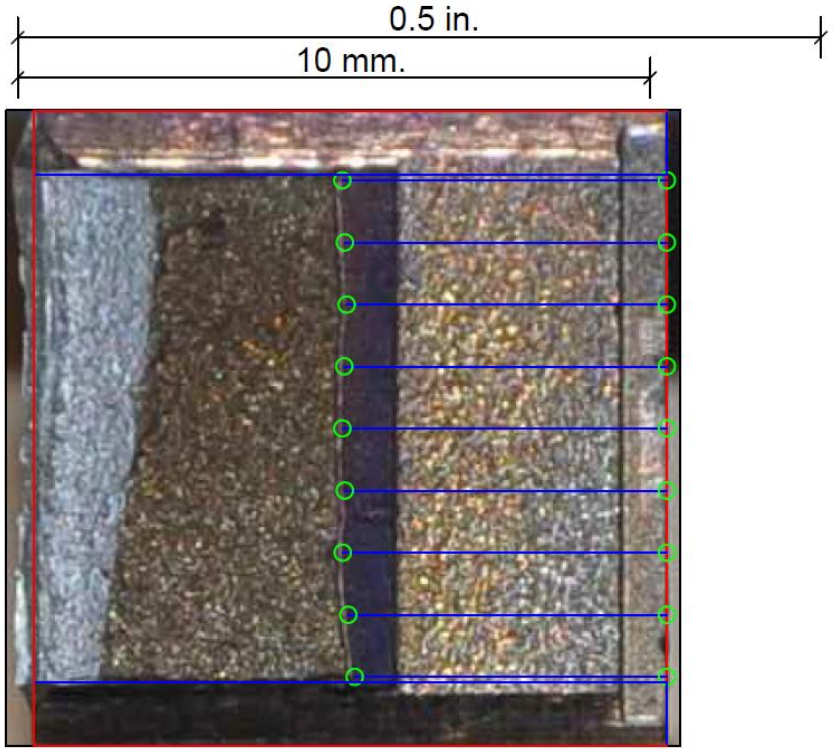

Figure F-36. Specimen C17' Fracture Surface

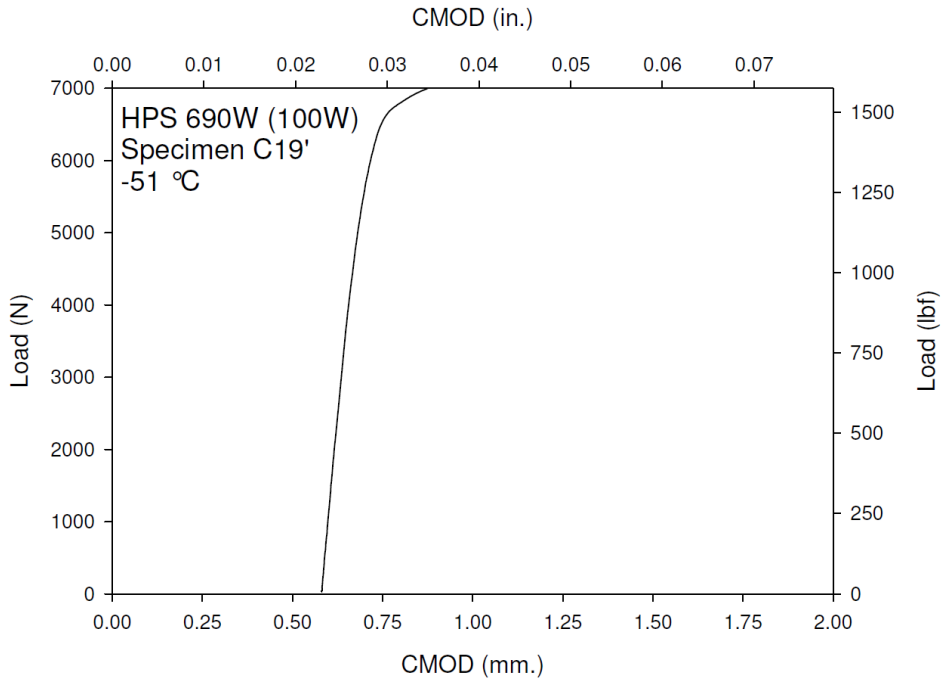

Figure F-37. Specimen C19' Test Record

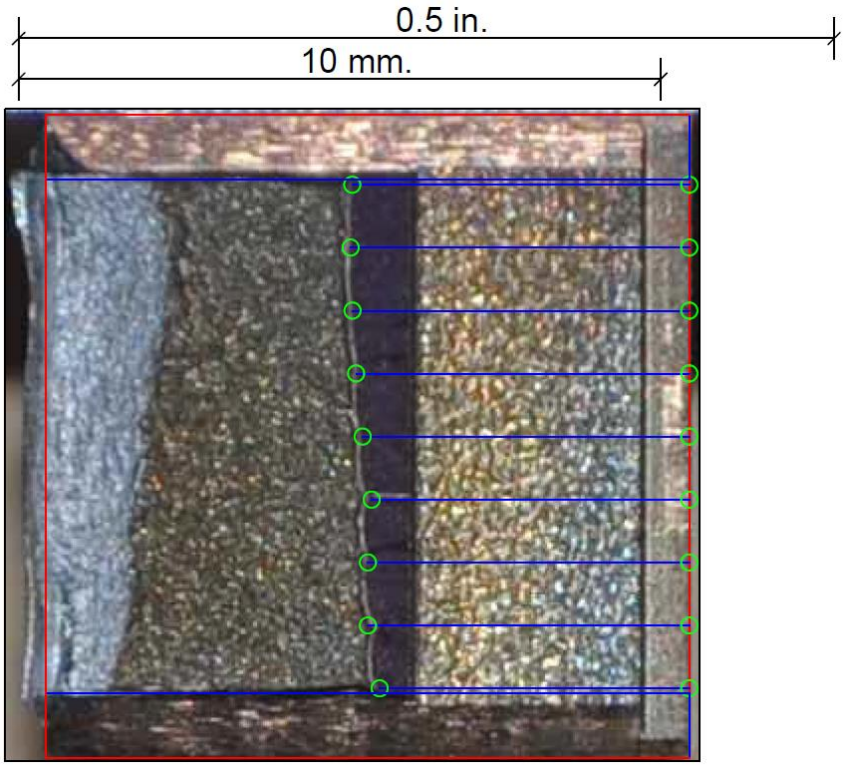

Figure F-38. Specimen C19' Fracture Surface

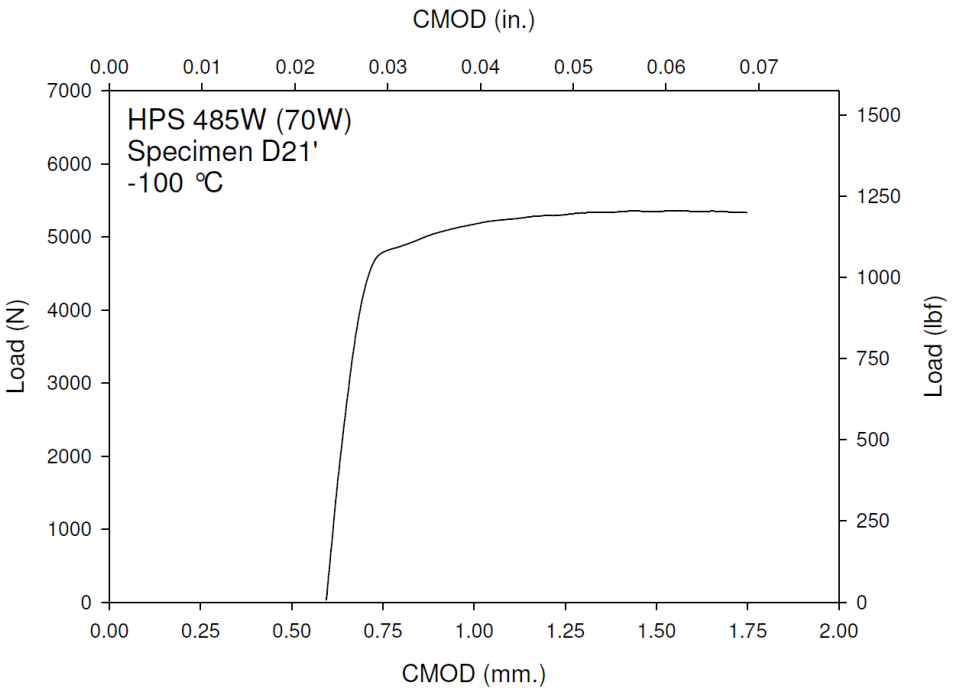

Figure F-39. Specimen D21' Test Record

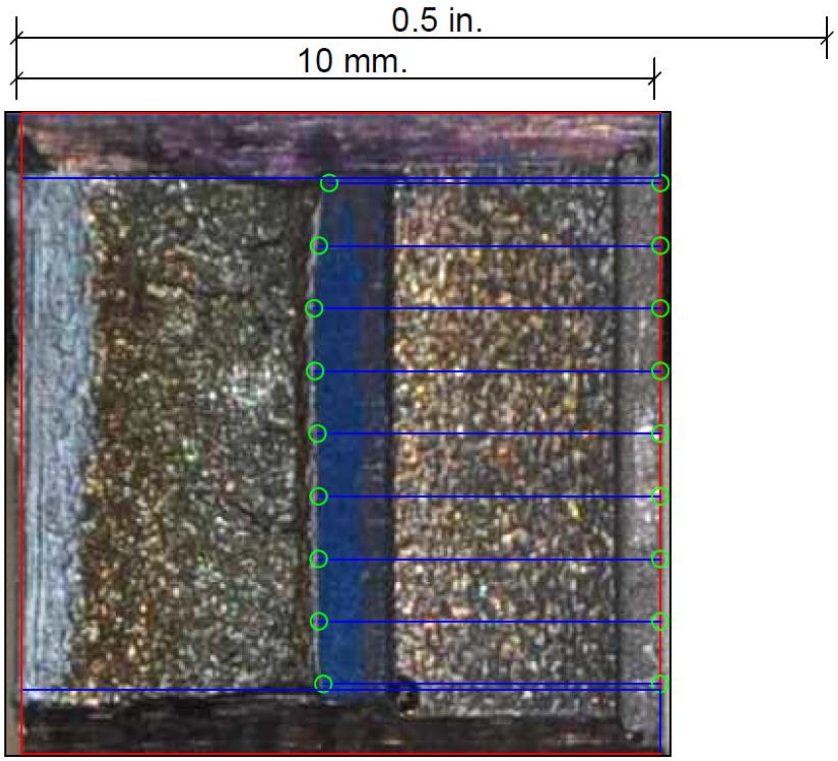

Figure F-40. Specimen D21' Fracture Surface

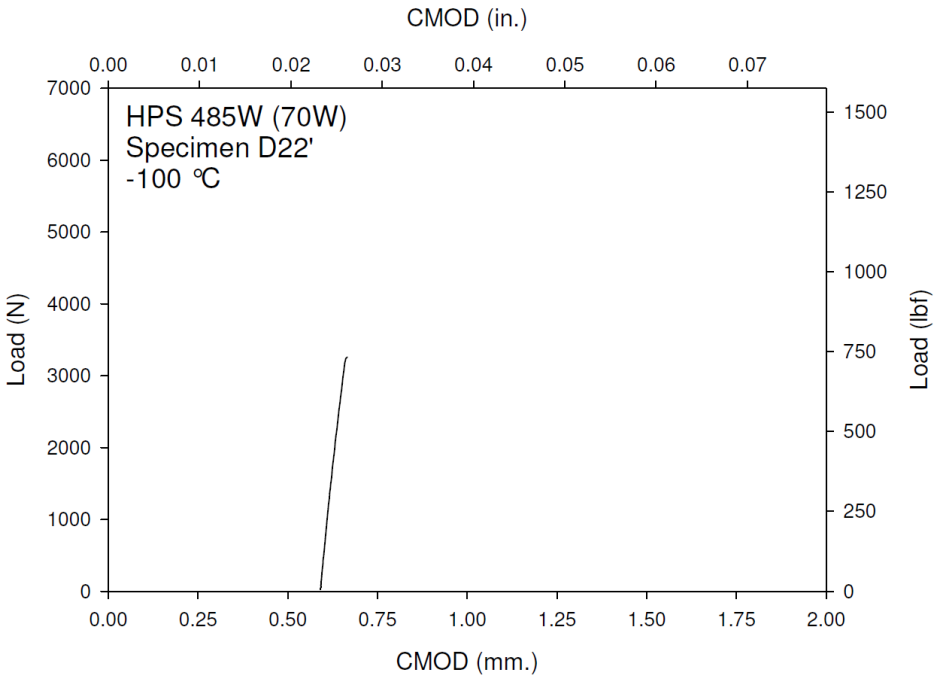

Figure F-41. Specimen D22' Test Record

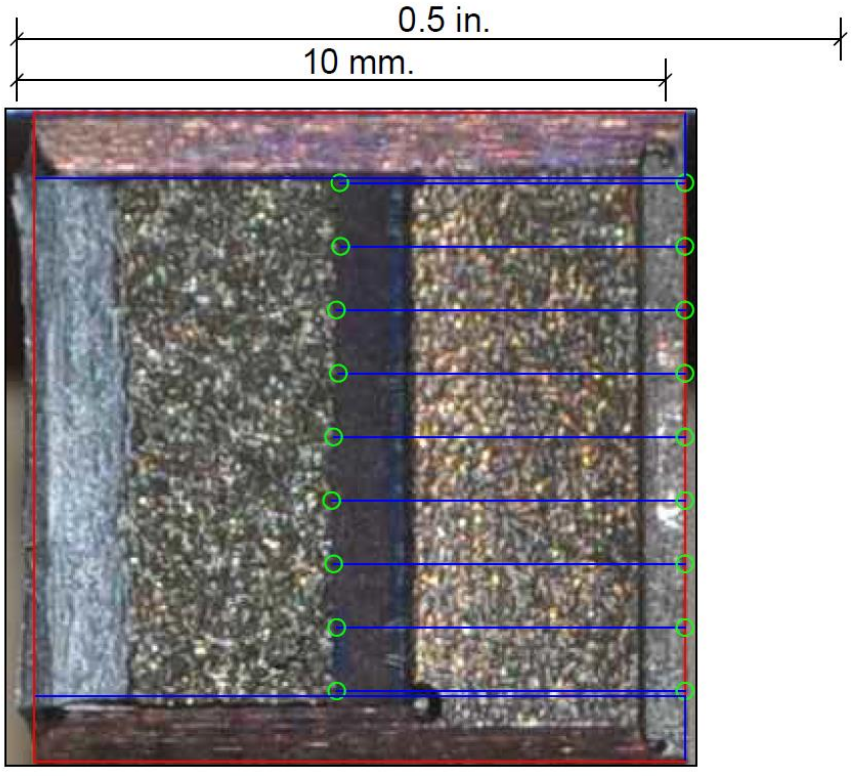

Figure F-42. Specimen D22' Fracture Surface

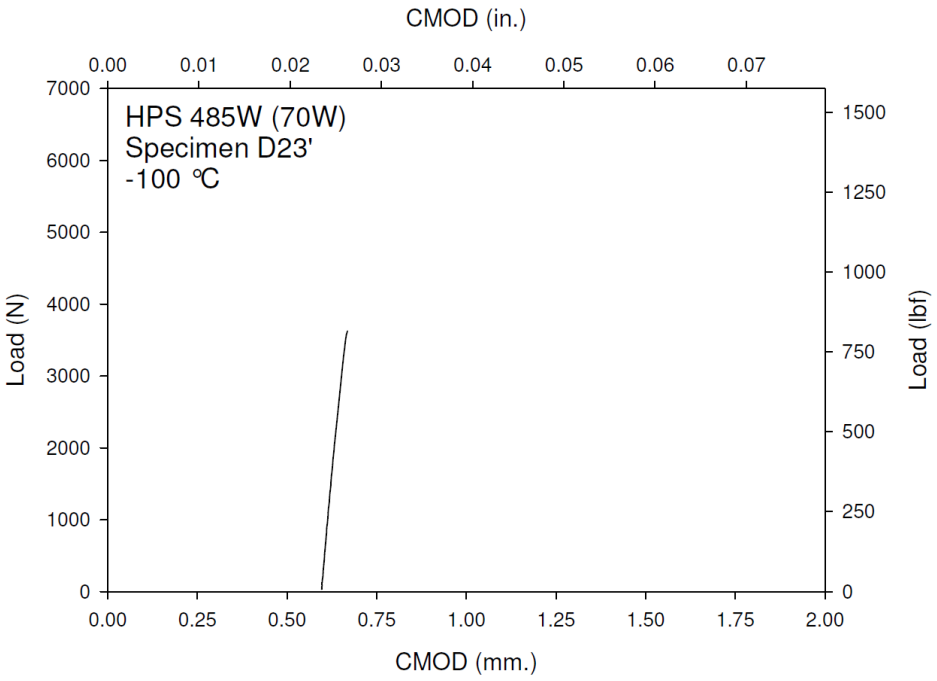

Figure F-43. Specimen D23' Test Record

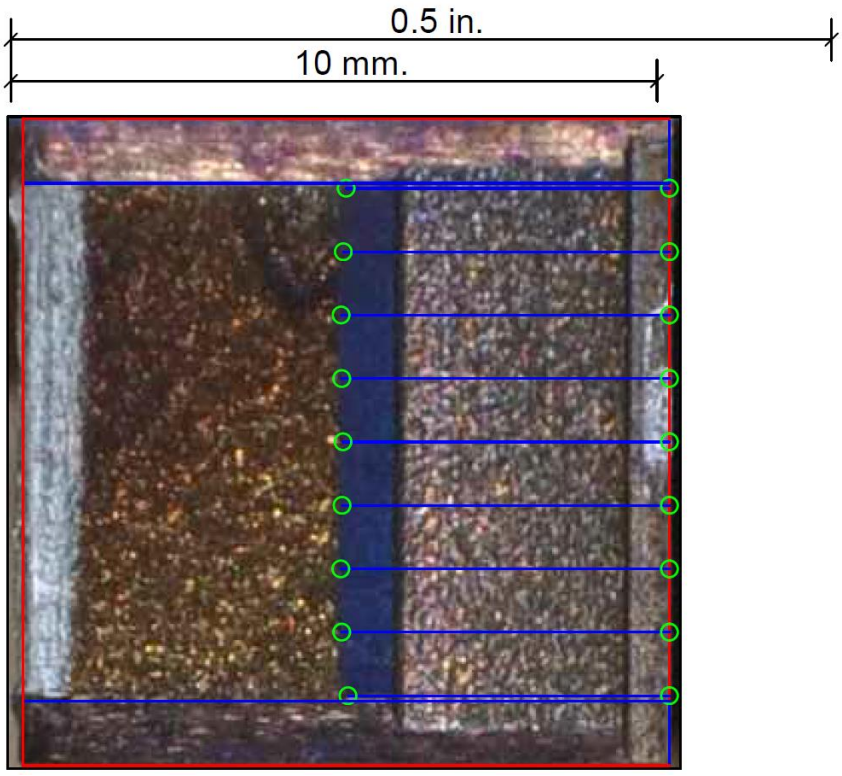

Figure F-44. Specimen D23' Test Record

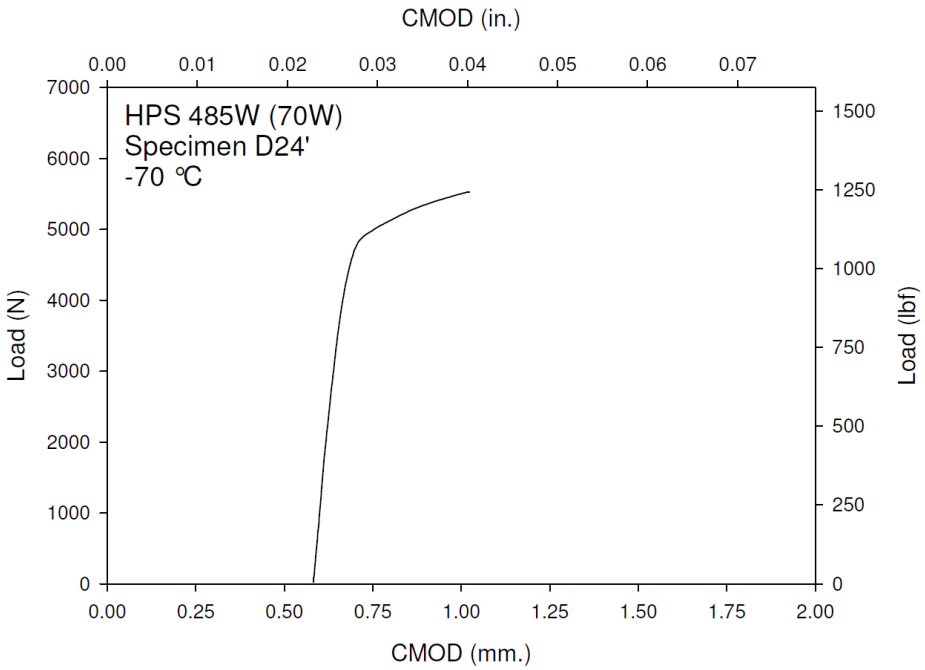

Figure F-45. Specimen D24' Test Record

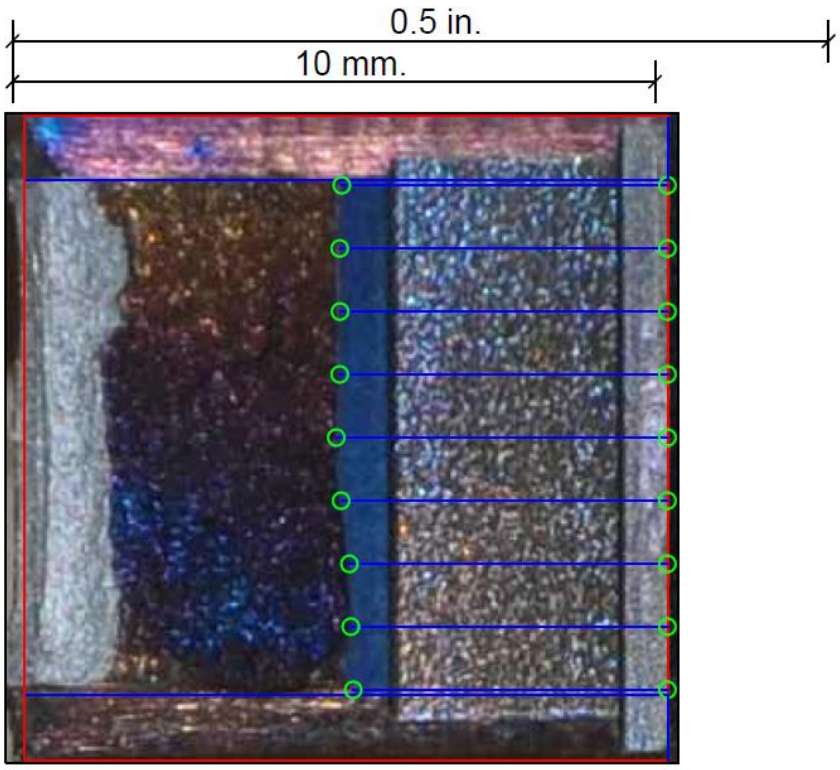

Figure F-46. Specimen D24' Fracture Surface

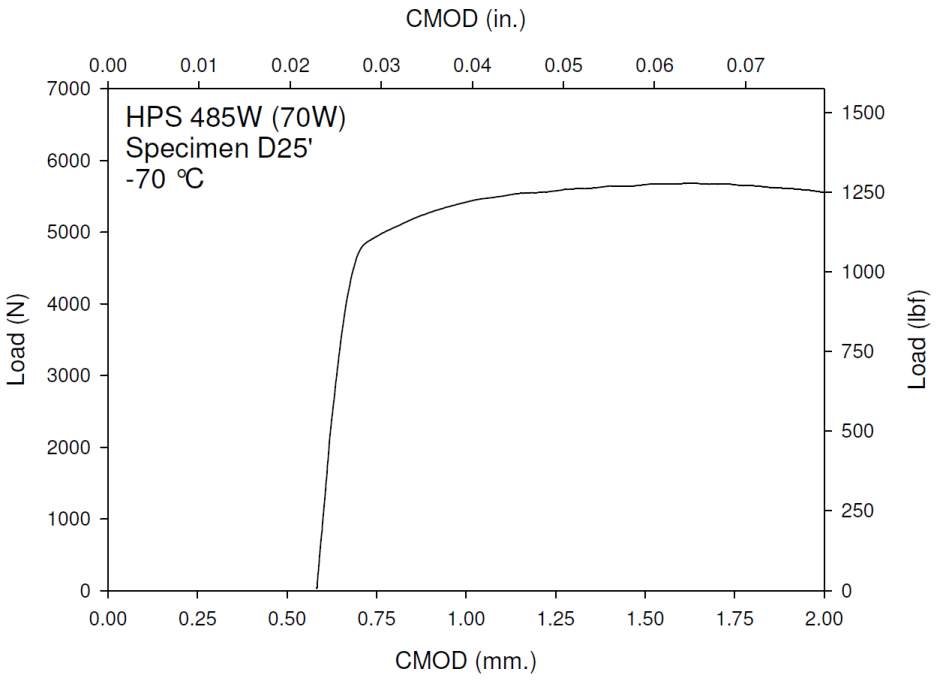

Figure F-47. Specimen D25' Test Record

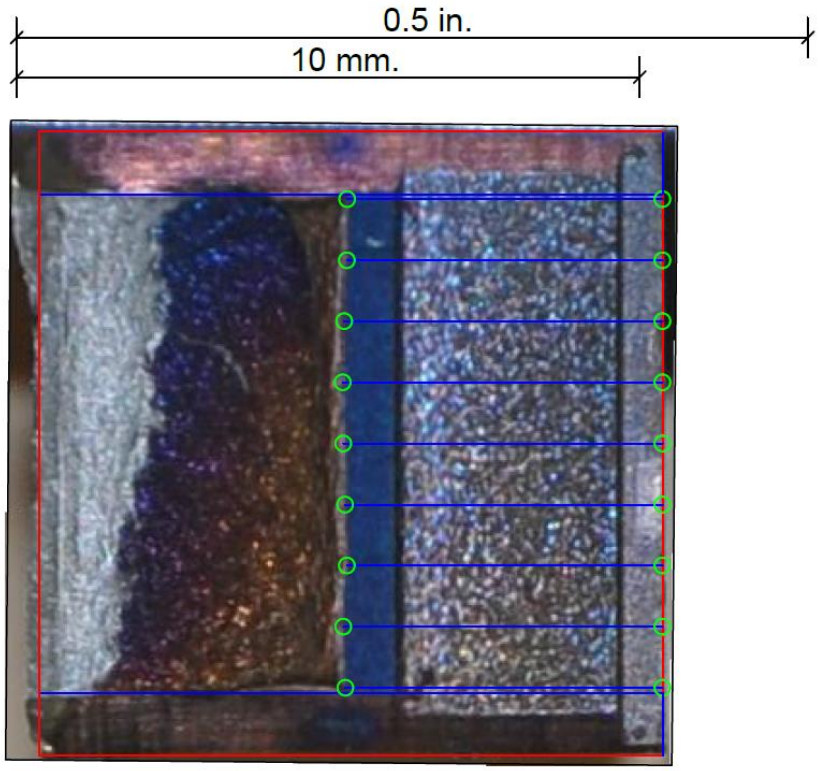

Figure F-48. Specimen D25' Fracture Surface

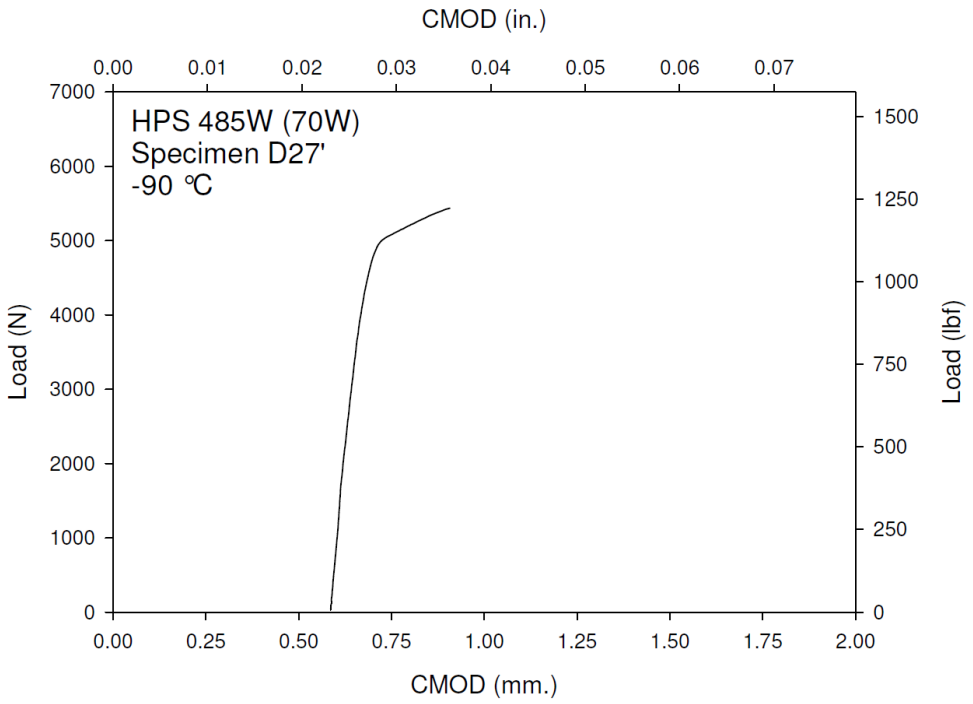

Figure F-49. Specimen D27' Test Record

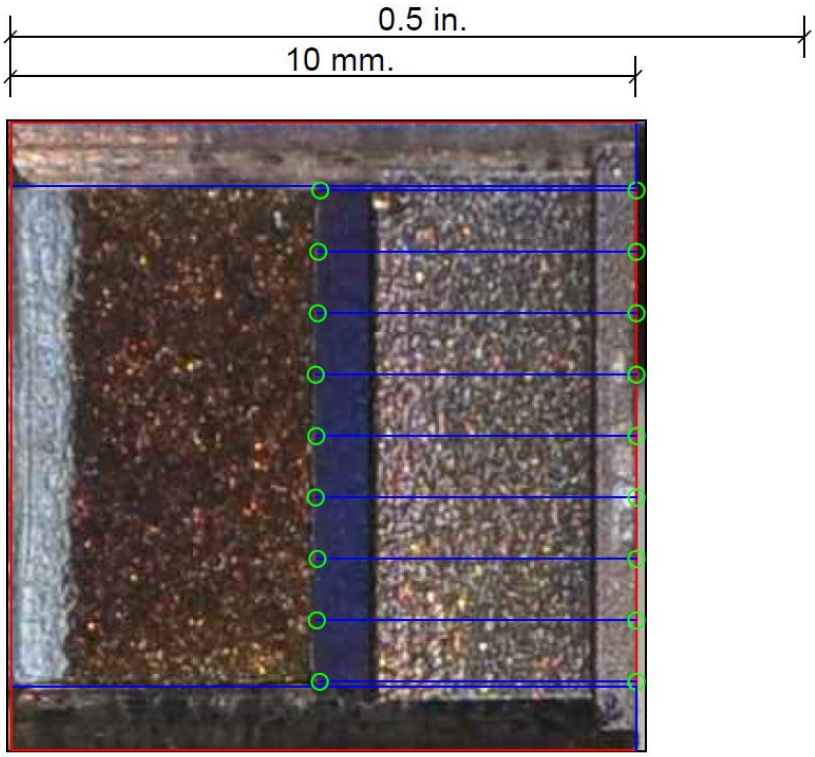

Figure F-50. Specimen D27' Fracture Surface

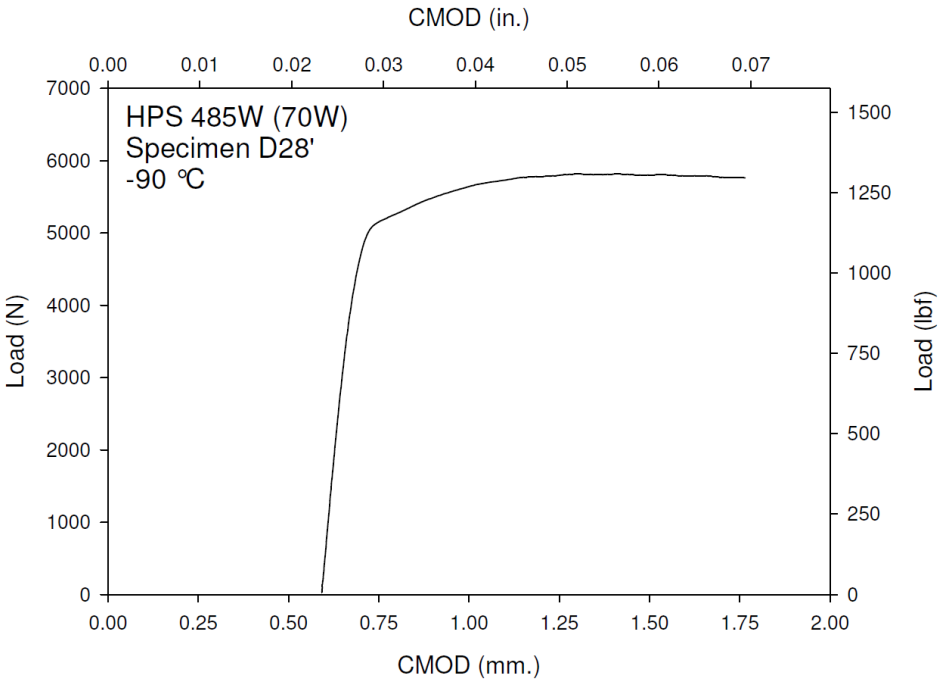

Figure F-51. Specimen D28' Test Record

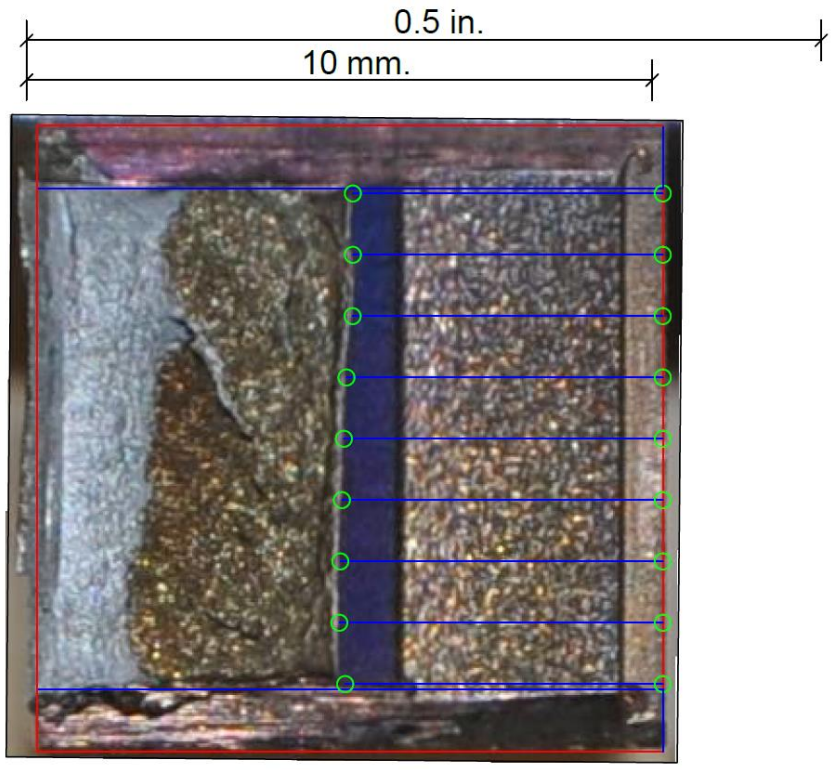

Figure F-52. Specimen D28' Fracture Surface

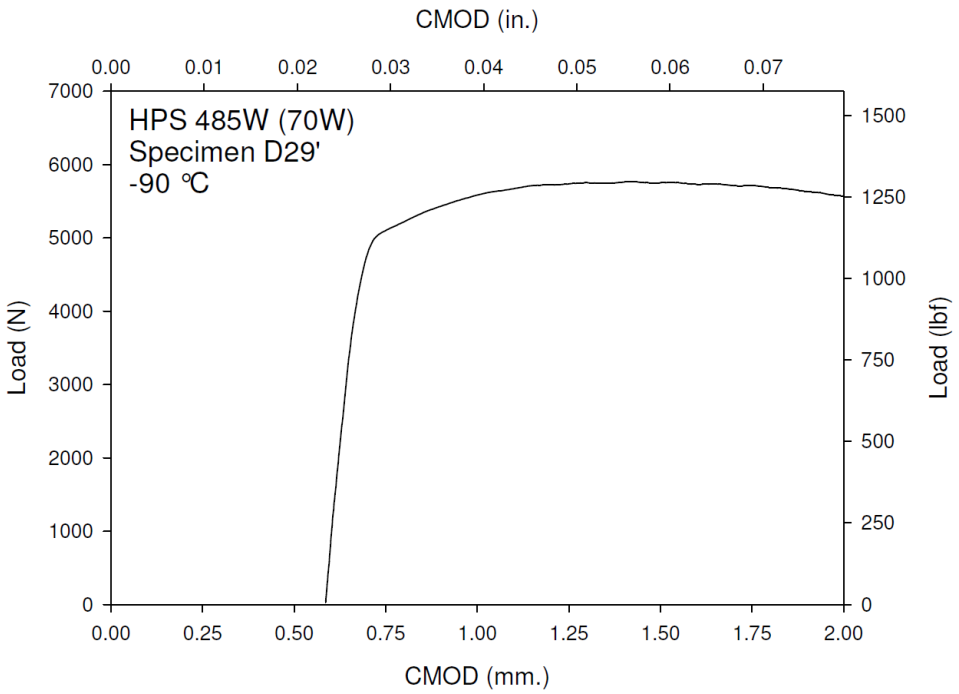

Figure F-53. Specimen D29' Test Record

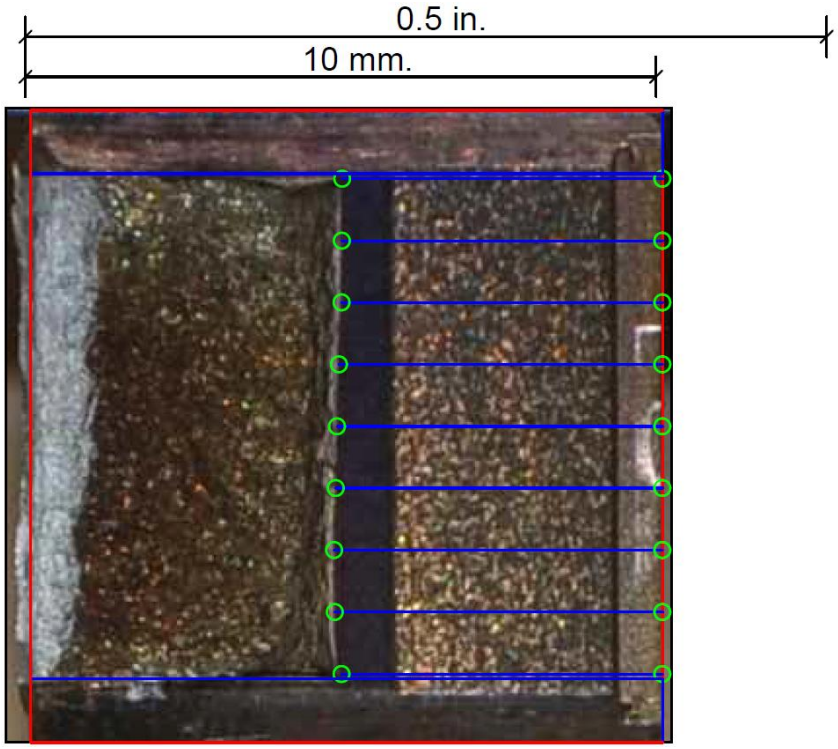

Figure F-54. Specimen D29' Fracture Surface

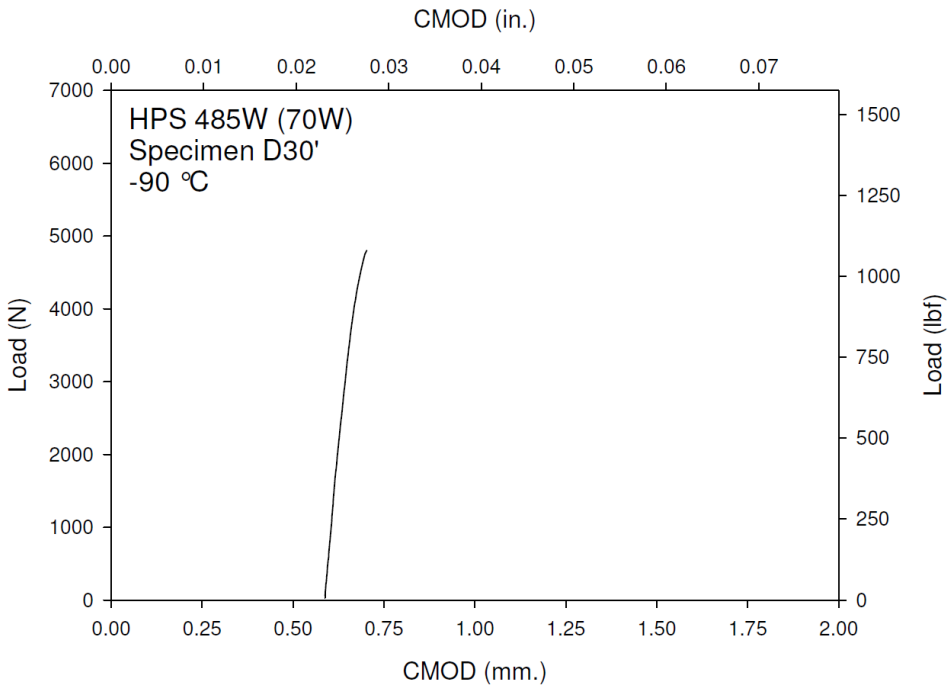

Figure F-55. Specimen D30' Test Record

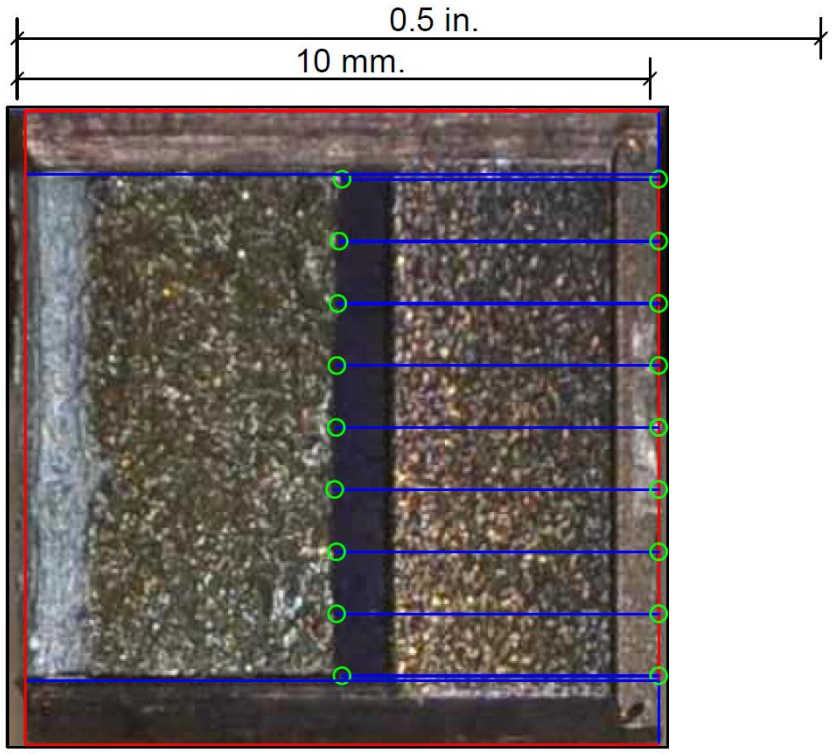

Figure F-56. Specimen D30' Fracture Surface

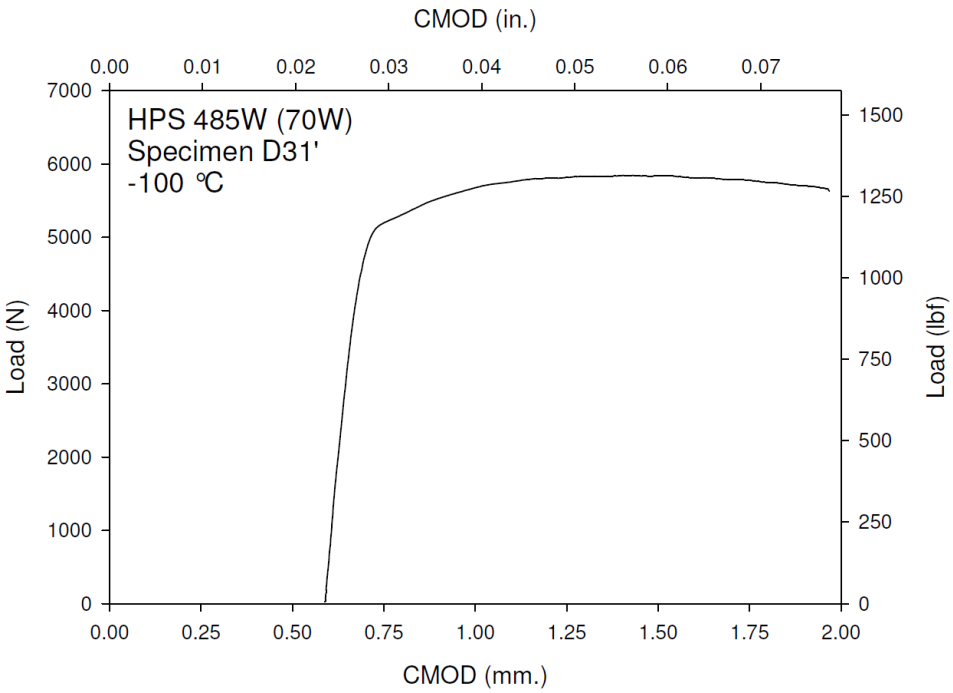

Figure F-57. Specimen D31' Test Record

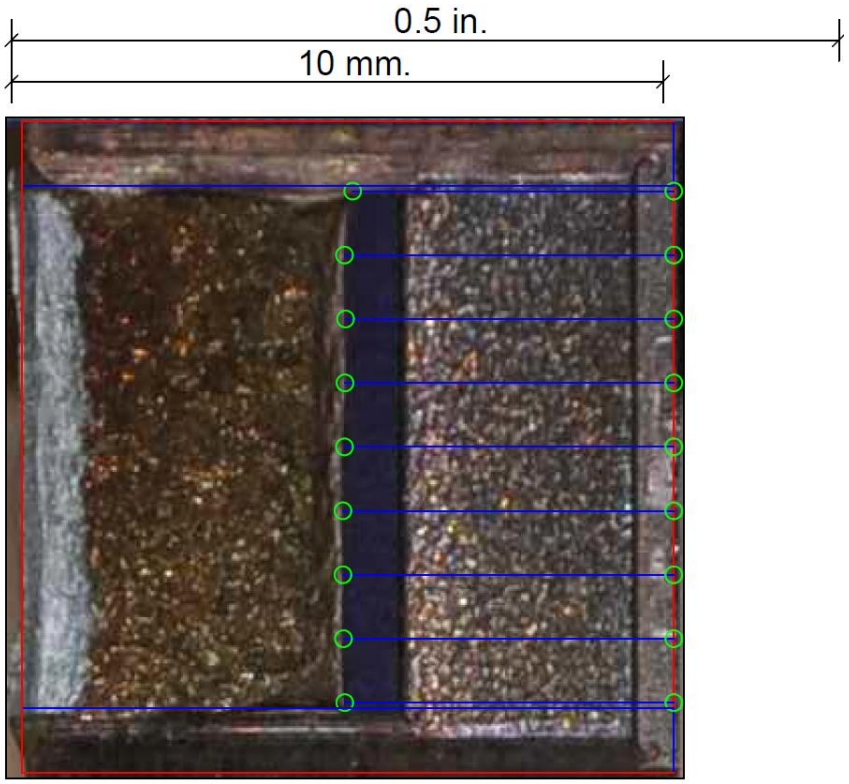

Figure F-58. Specimen D31' Fracture Surface

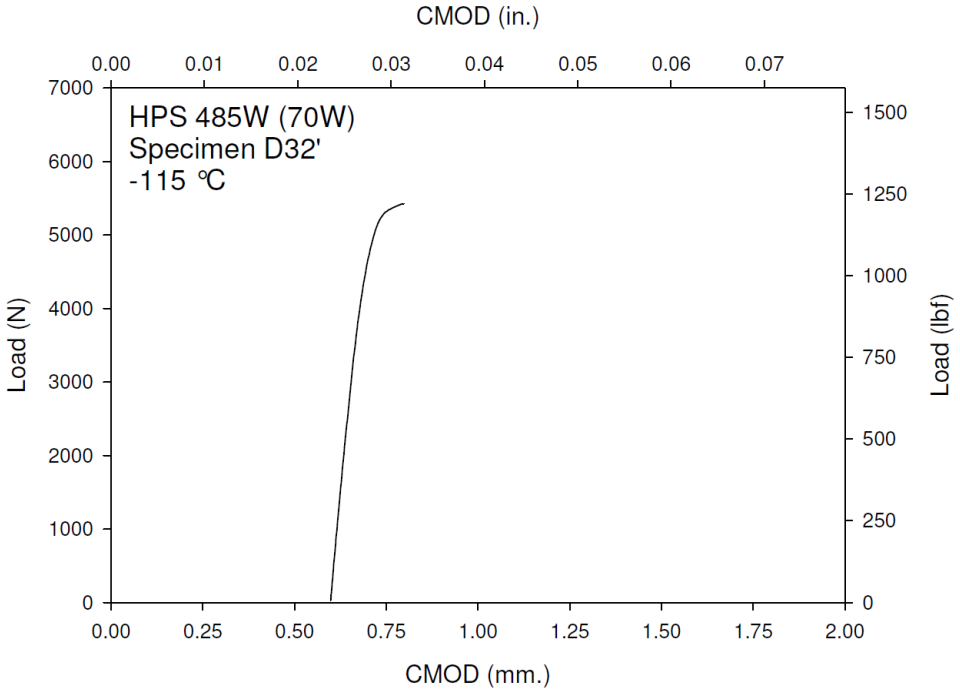

Figure F-59. Specimen D32' Test Record

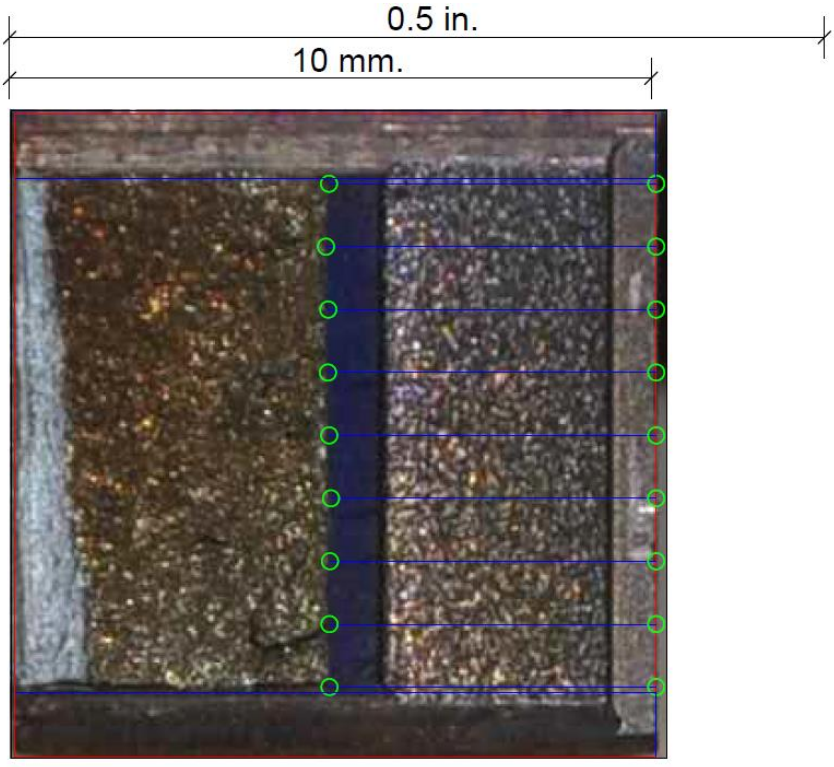

Figure F-60. Specimen D32' Fracture Surface

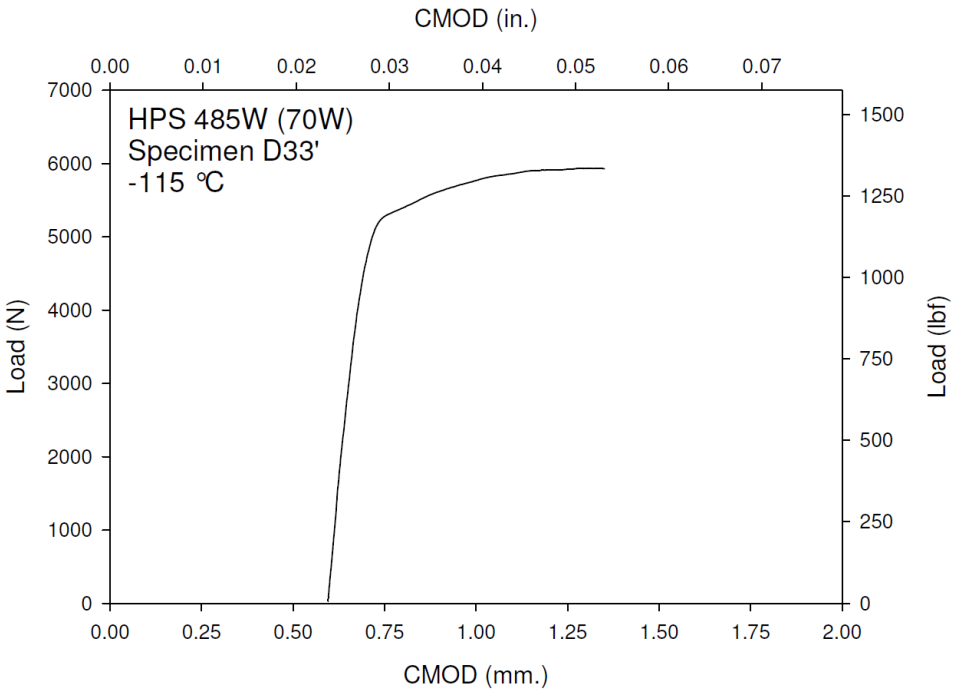

Figure F-61. Specimen D33' Test Record

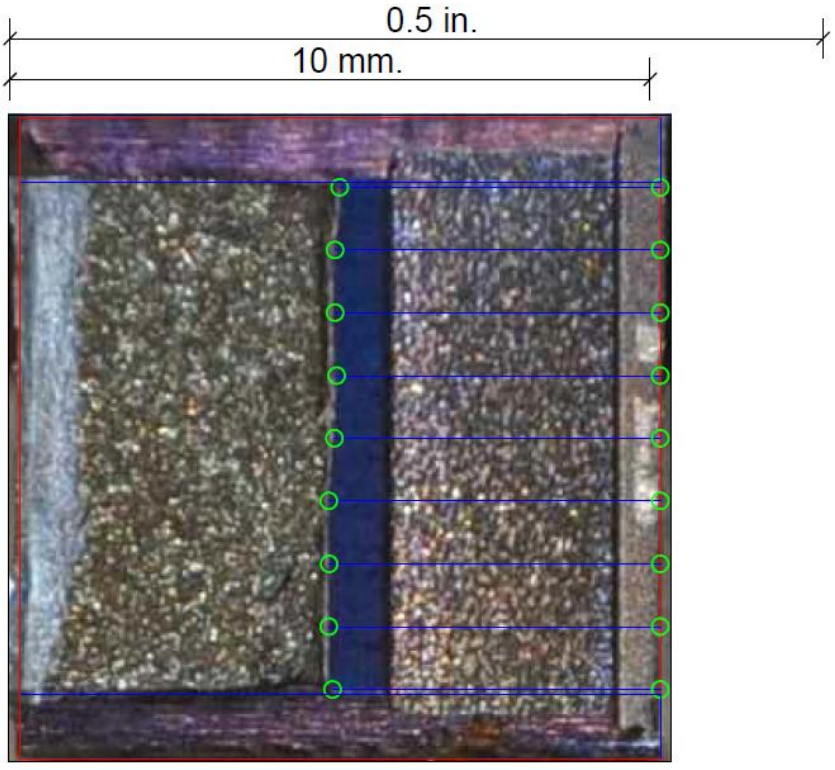

Figure F-62. Specimen D33' Fracture Surface

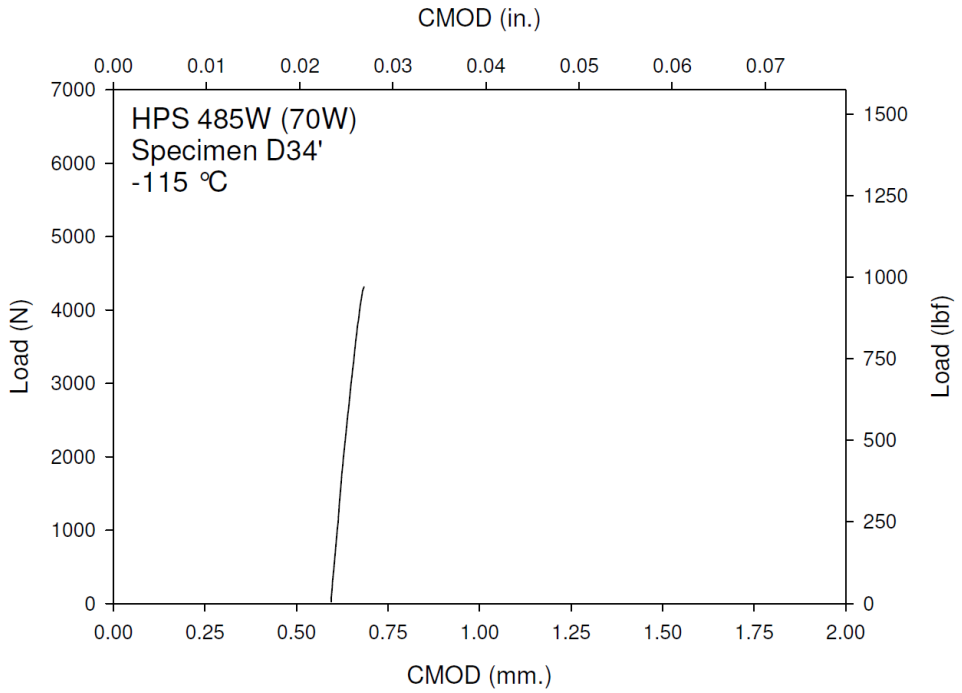

Figure F-63. Specimen D34' Test Record

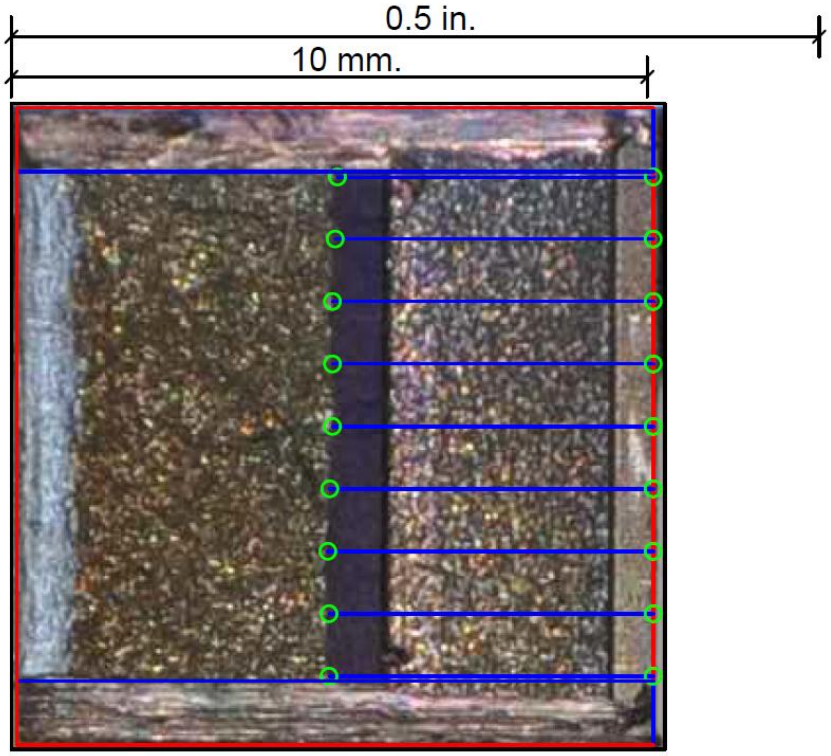

Figure F-64. Specimen D34' Fracture Surface

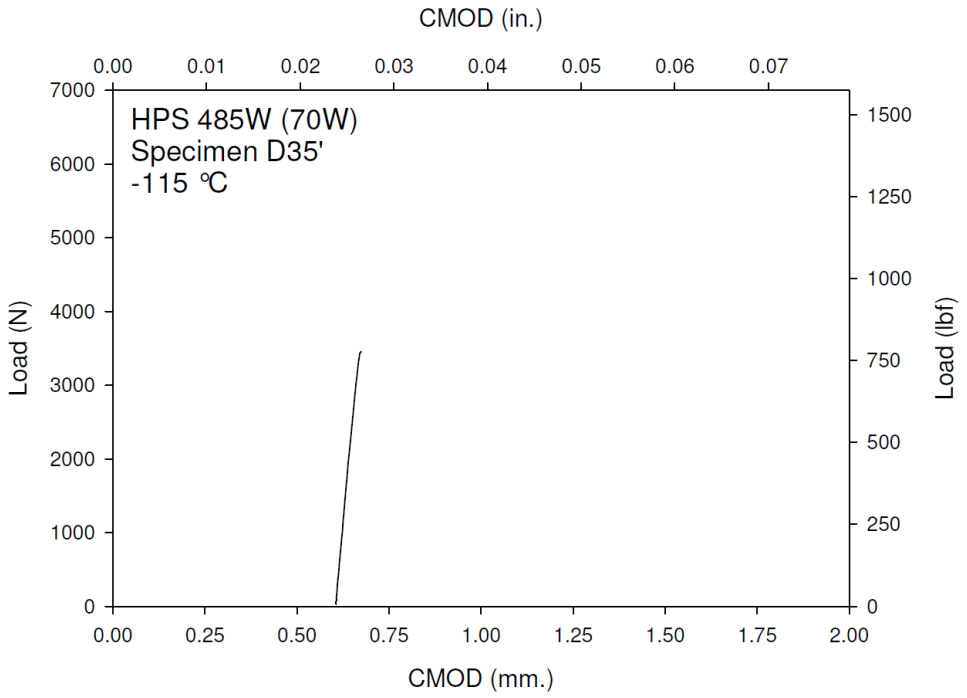

Figure F-65. Specimen D35' Test Record

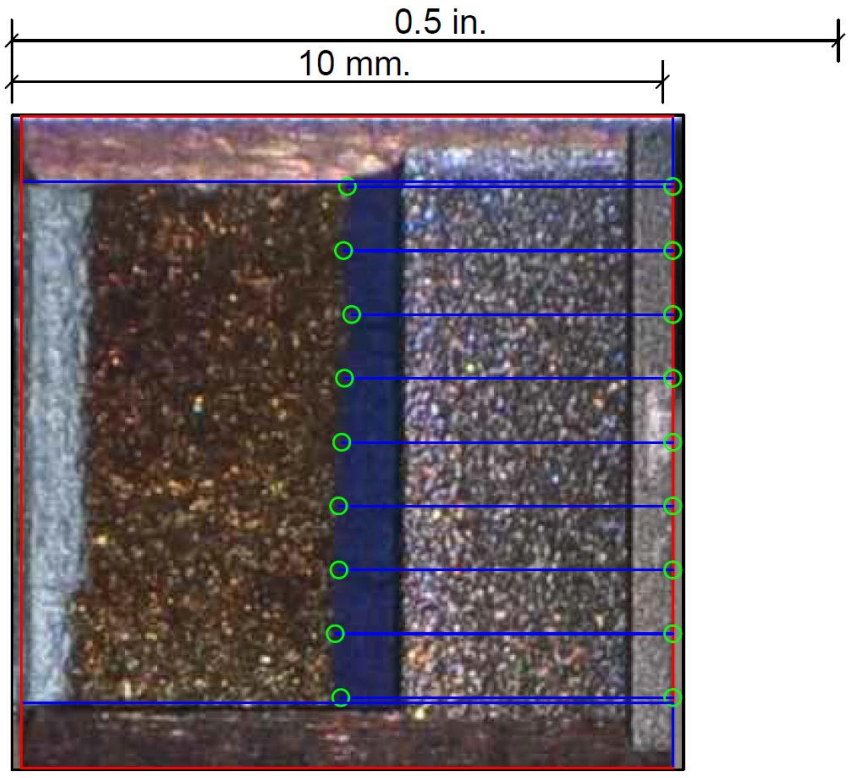

Figure F-66. Specimen D35' Fracture Surface

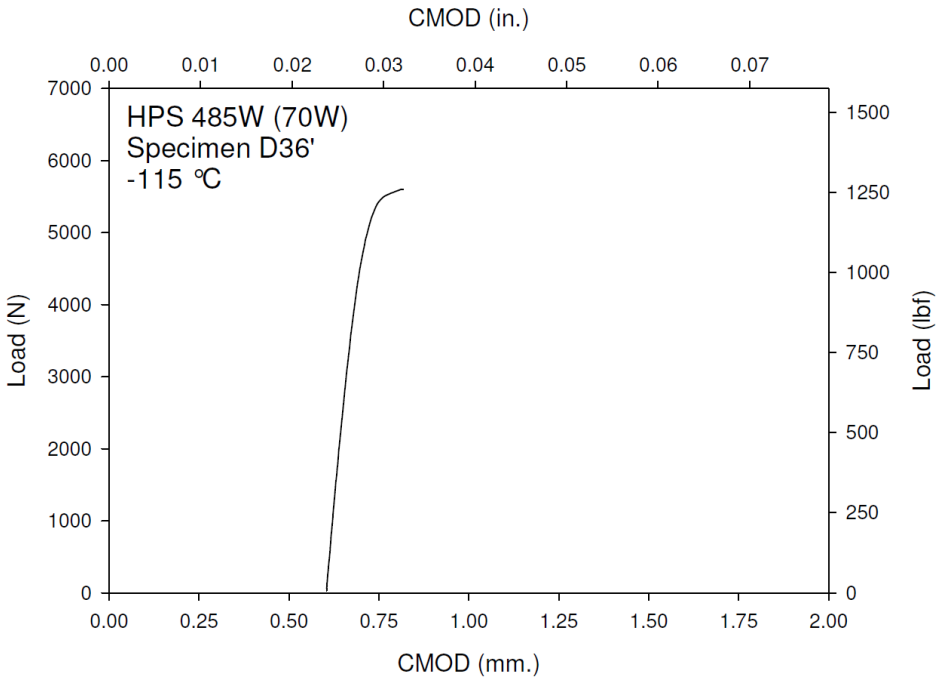

Figure F-67. Specimen D36' Test Record

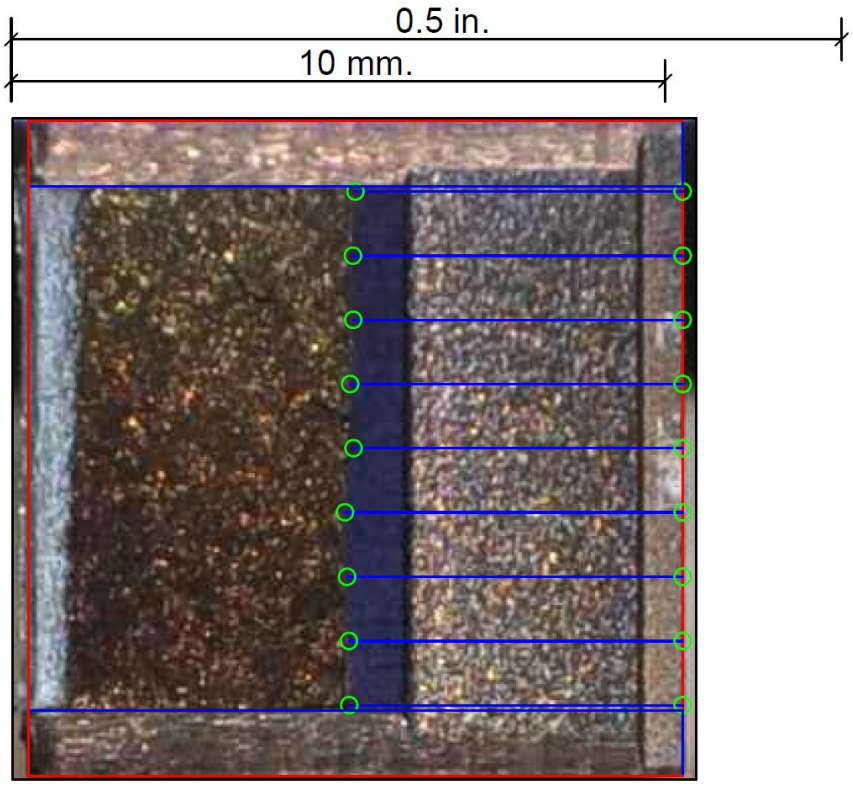

Figure F-68. Specimen D36' Fracture Surface

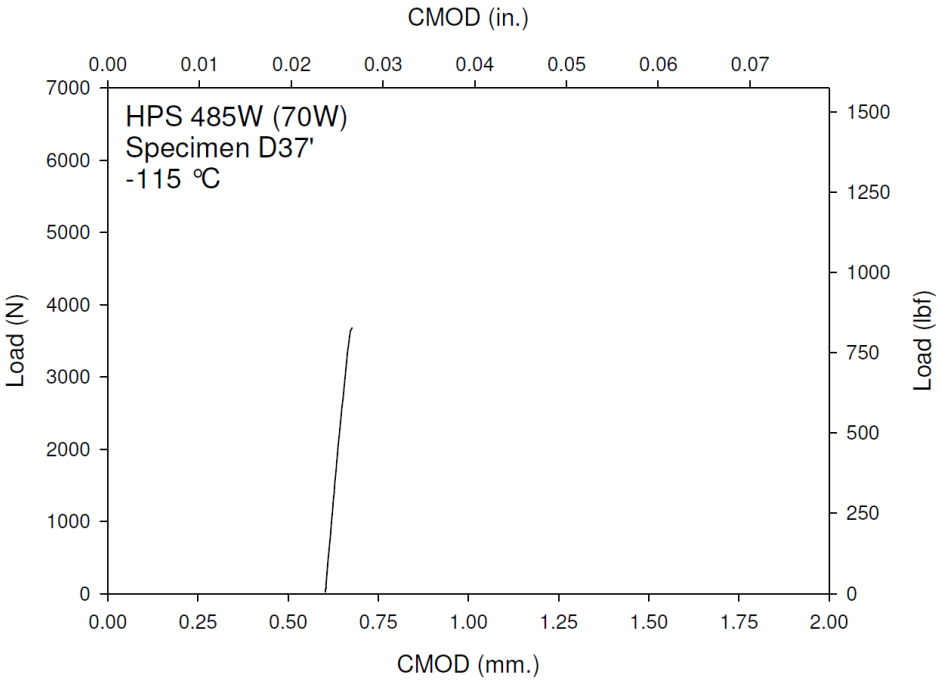

Figure F-69. Specimen D37' Test Record

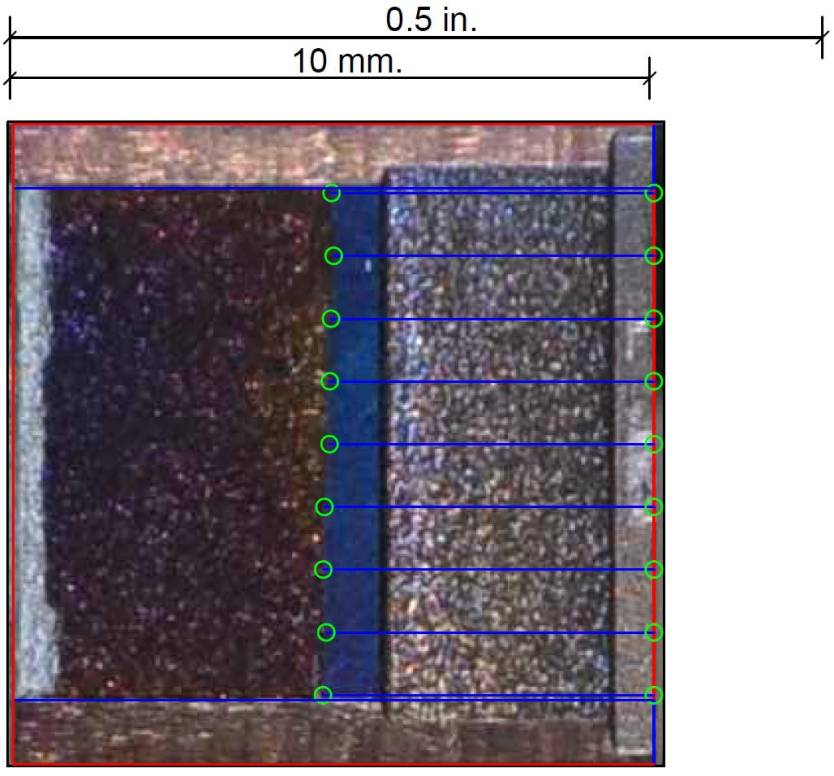

Figure F-70. Specimen D37' Fracture Surface

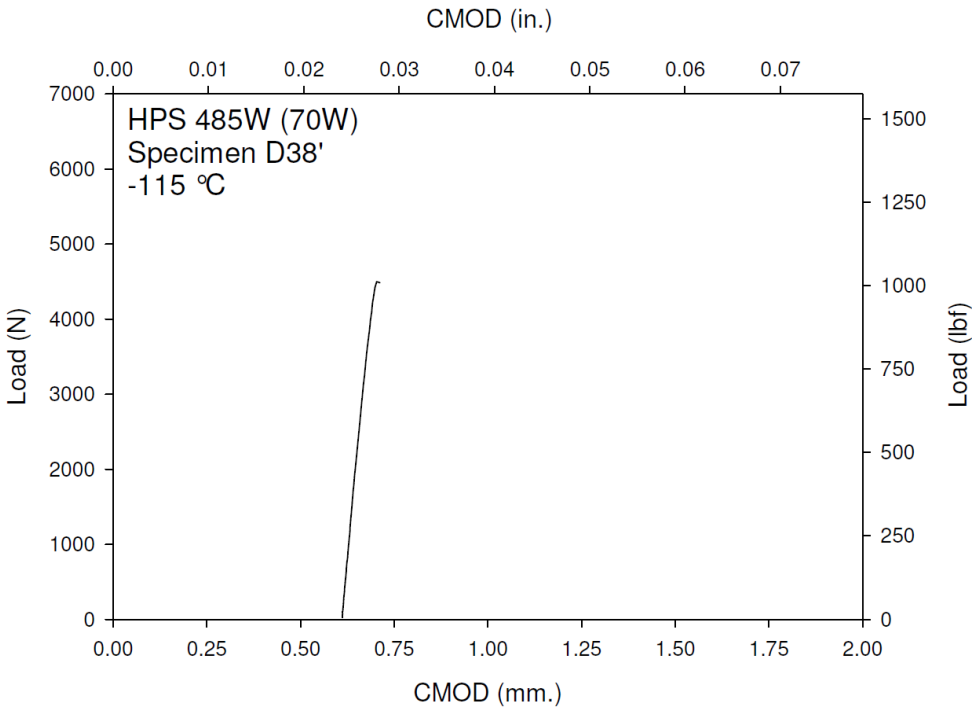

Figure F-71. Specimen D38' Test Record

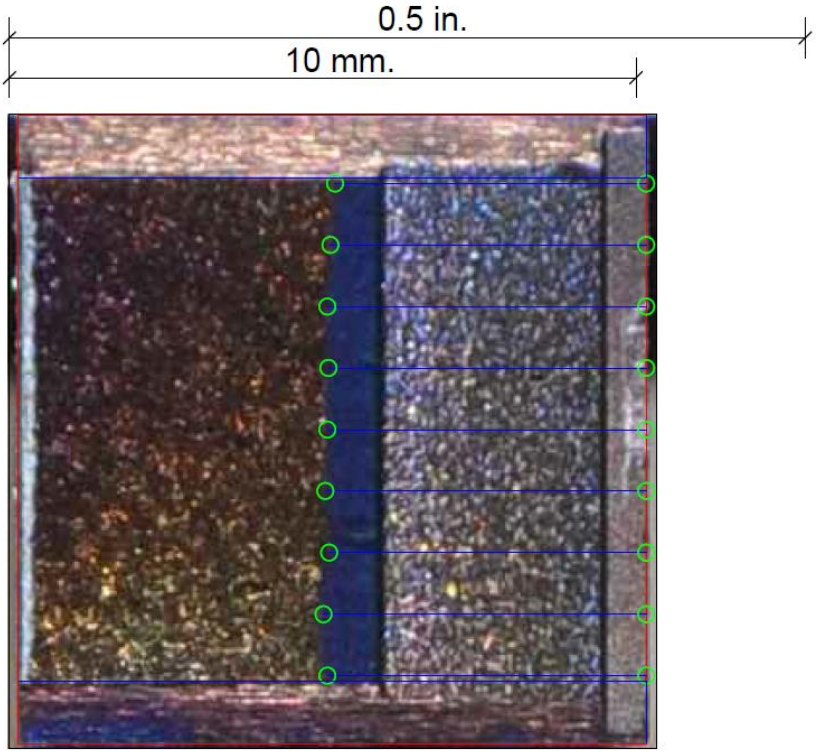

Figure F-72. Specimen D38' Fracture Surface

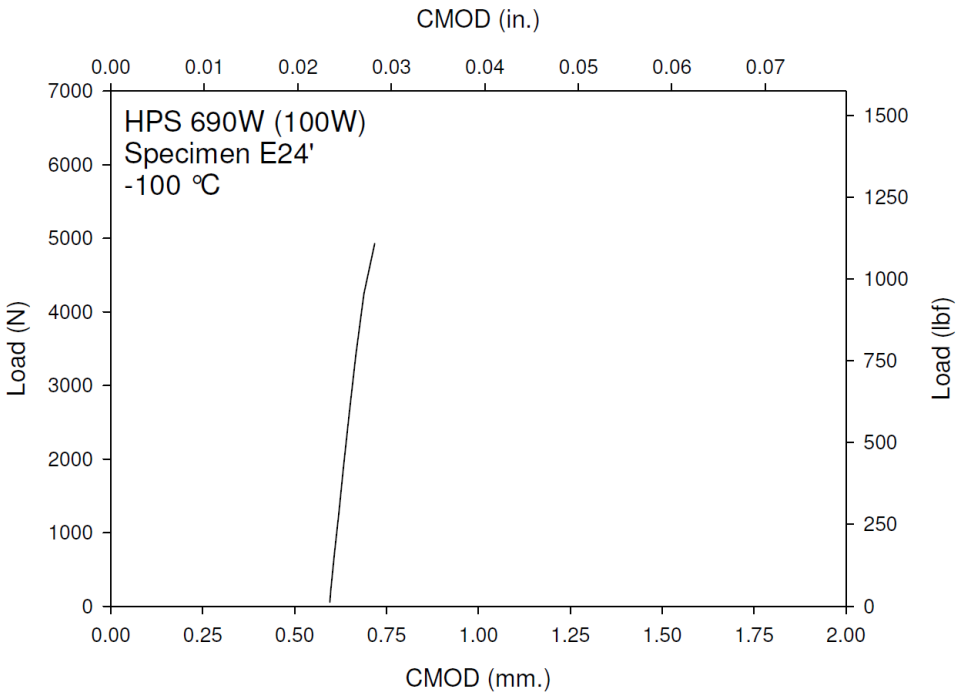

Figure F-73. Specimen E24' Test Record

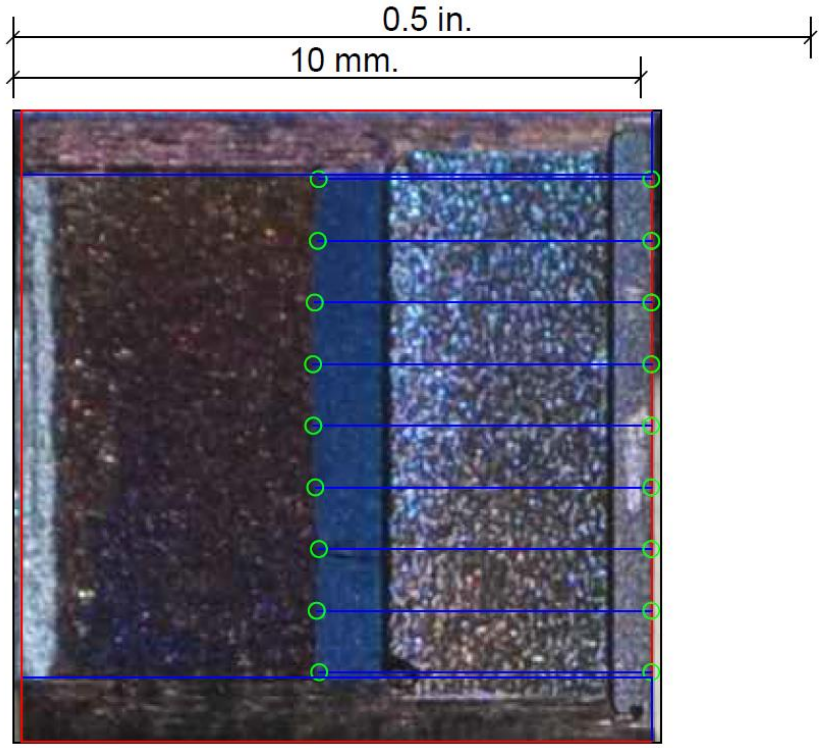

Figure F-74. Specimen E24' Fracture Surface

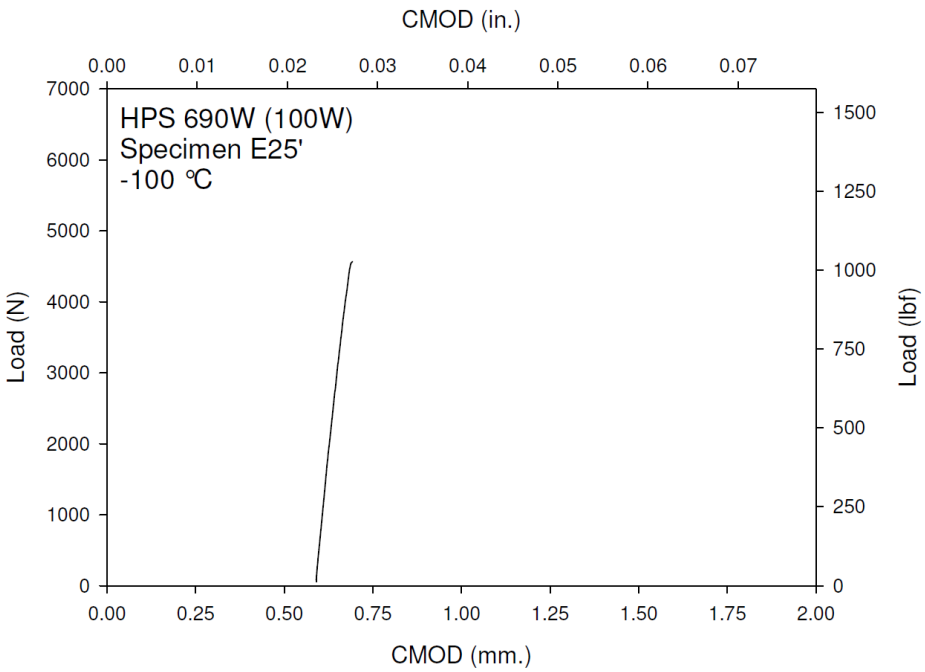

Figure F-75. Specimen E25' Test Record

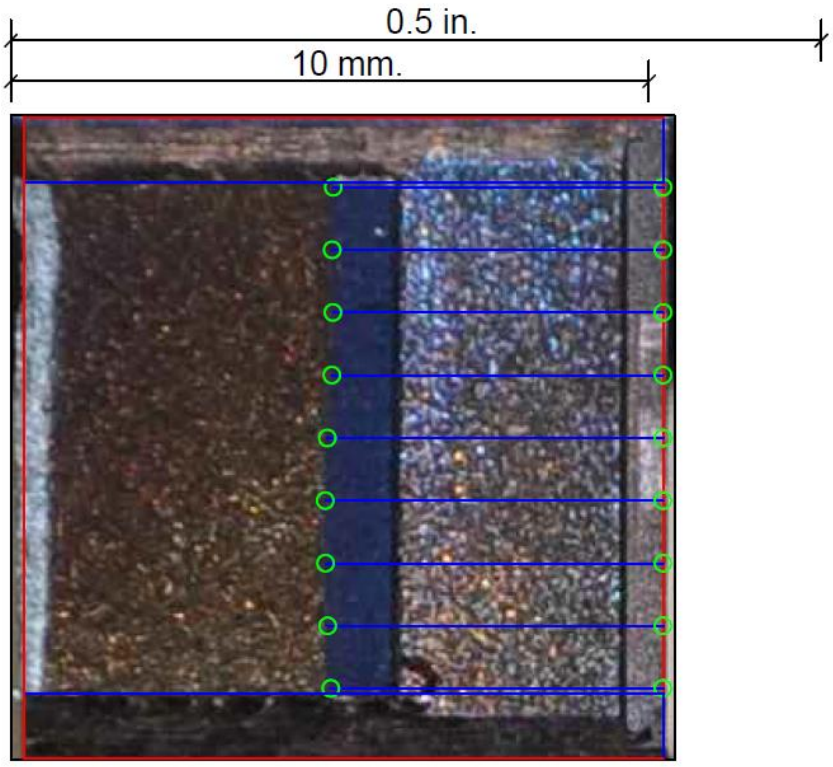

Figure F-76. Specimen E25' Fracture Surface

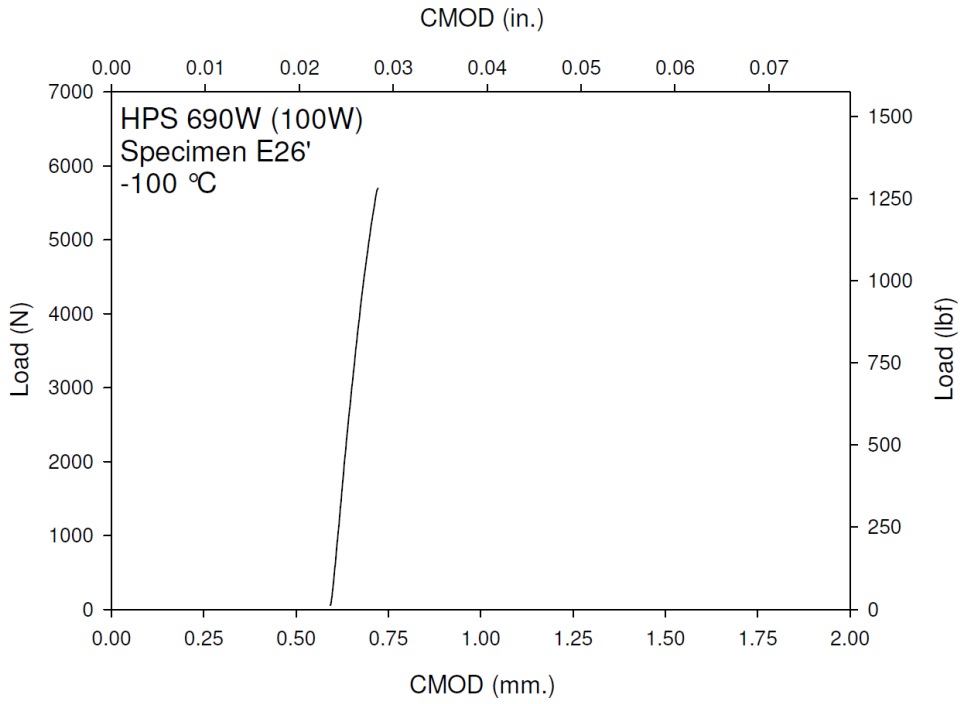

Figure F-77. Specimen E26' Test Record

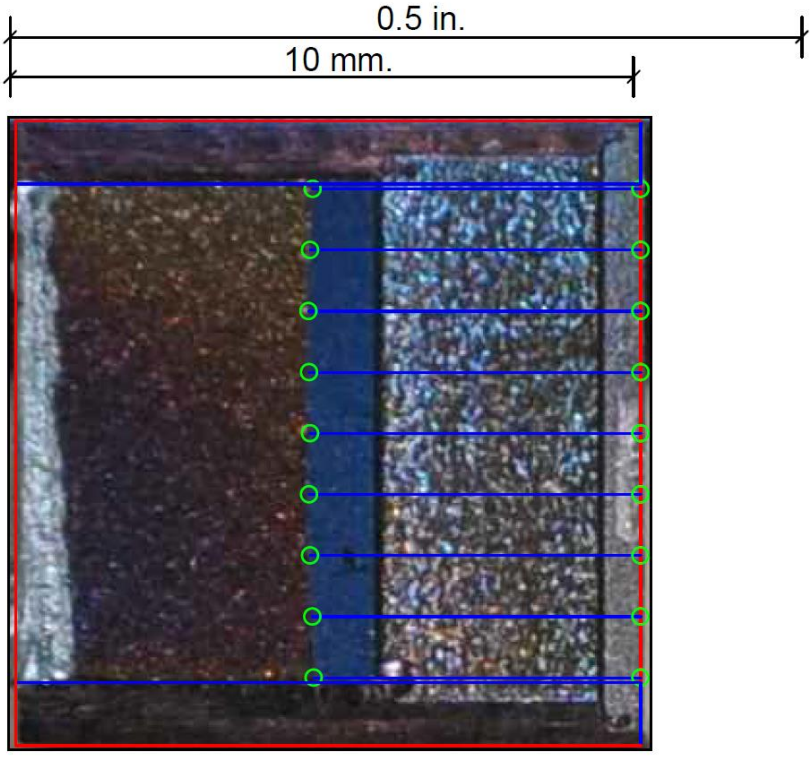

Figure F-78. Specimen E26' Fracture Surface

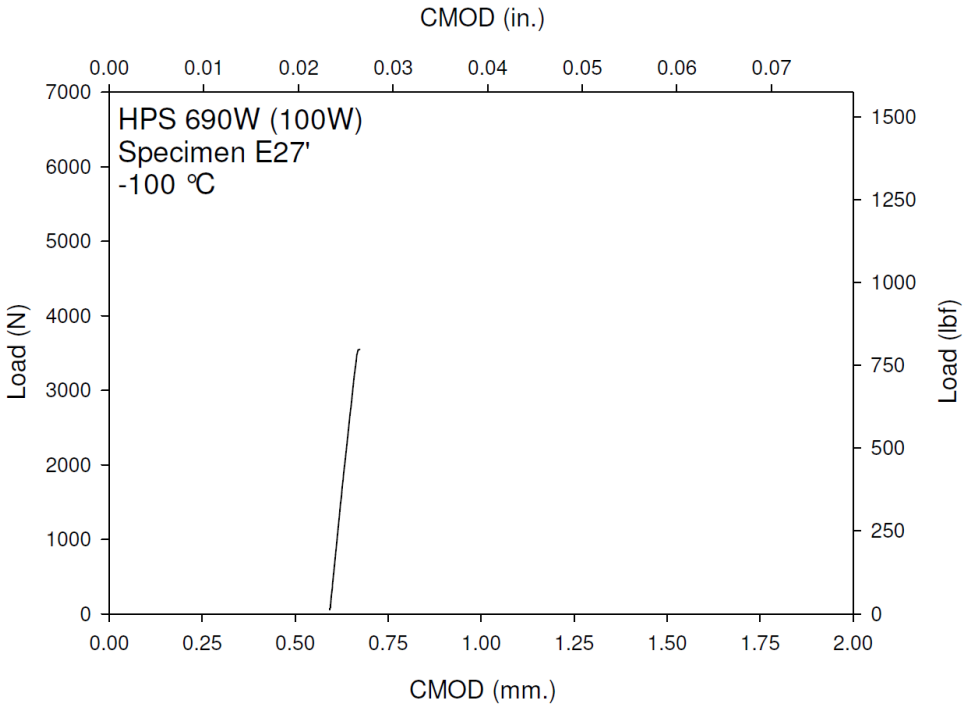

Figure F-79. Specimen E27' Test Record

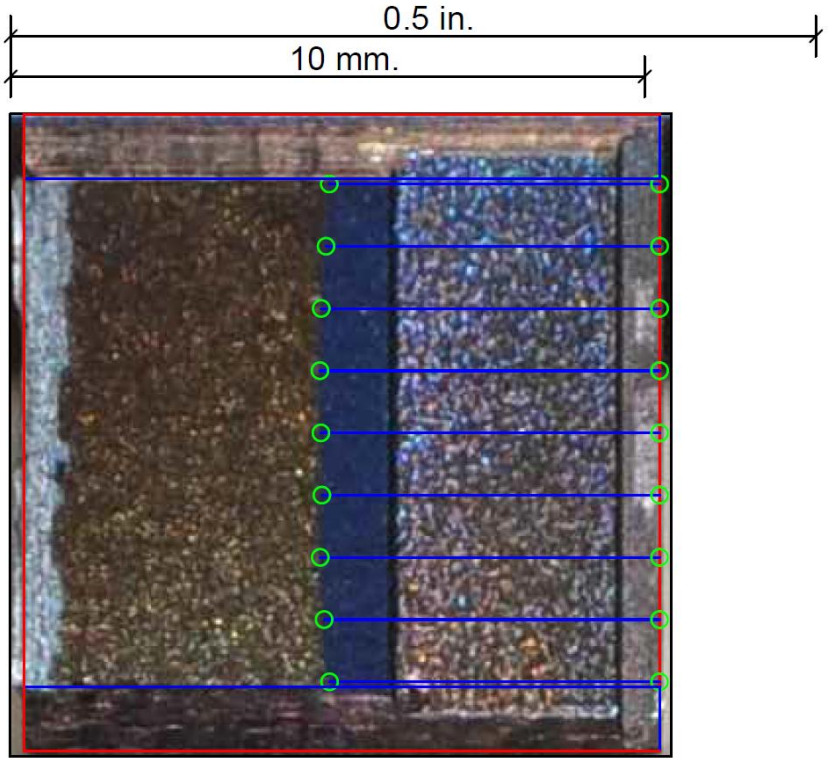

Figure F-80. Specimen E27' Fracture Surface

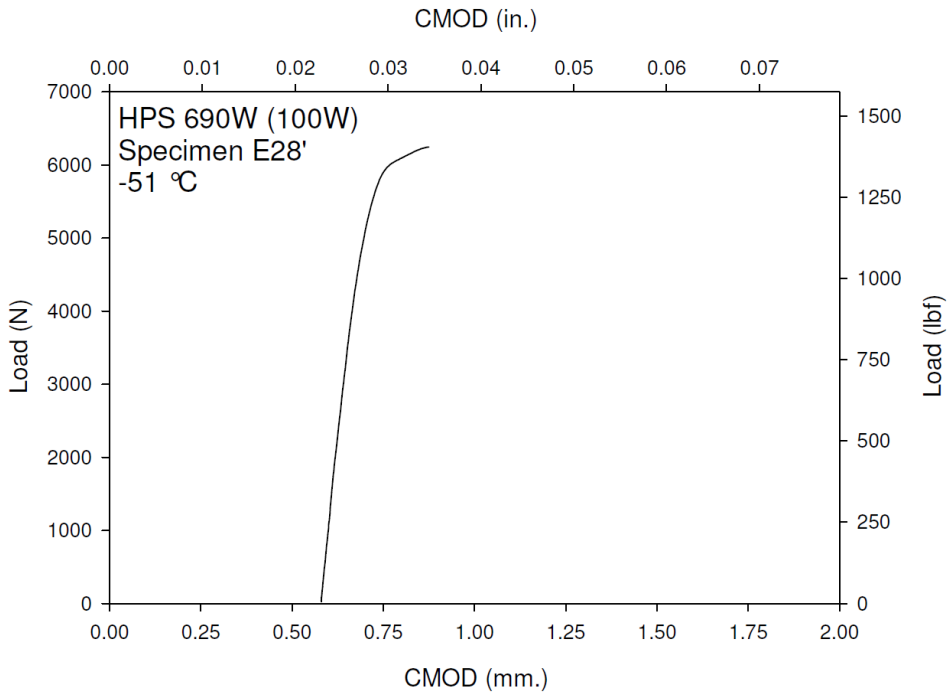

Figure F-81. Specimen E28' Test Record

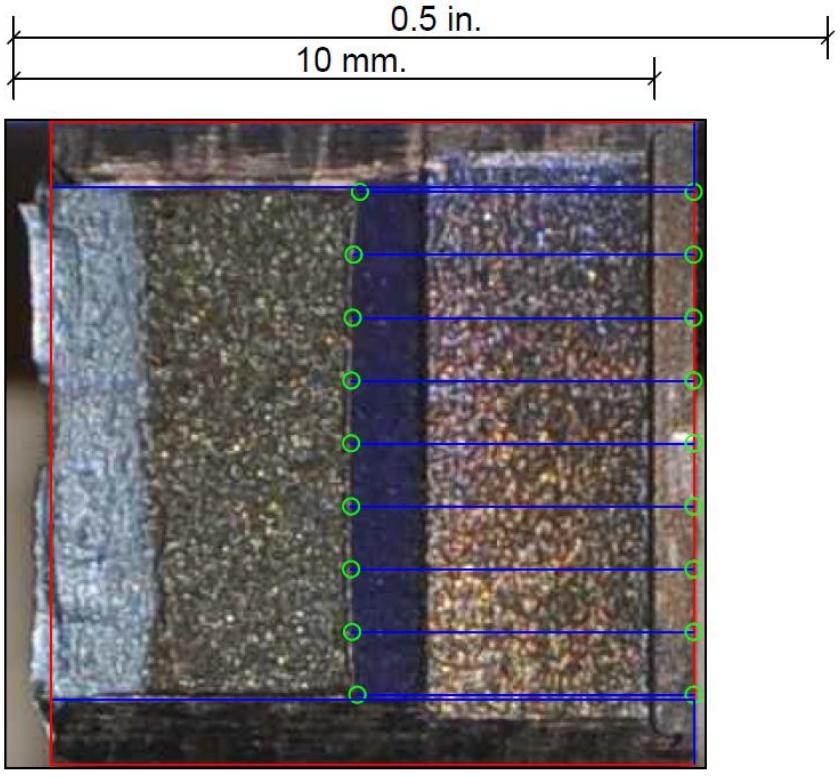

Figure F-82. Specimen E28' Fracture Surface

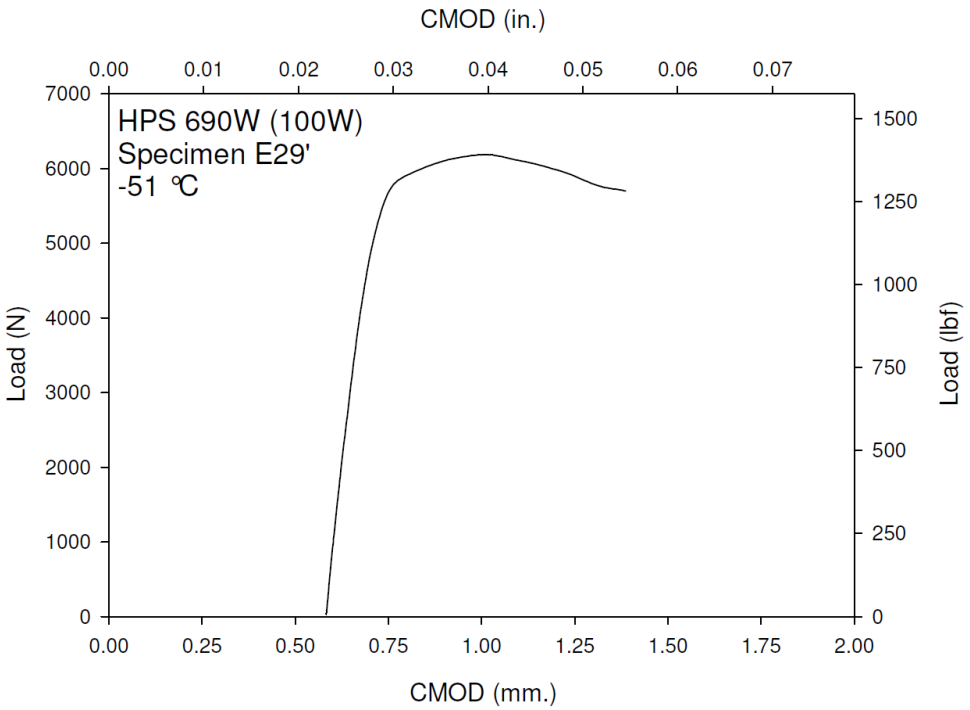

Figure F-83. Specimen E29' Test Record

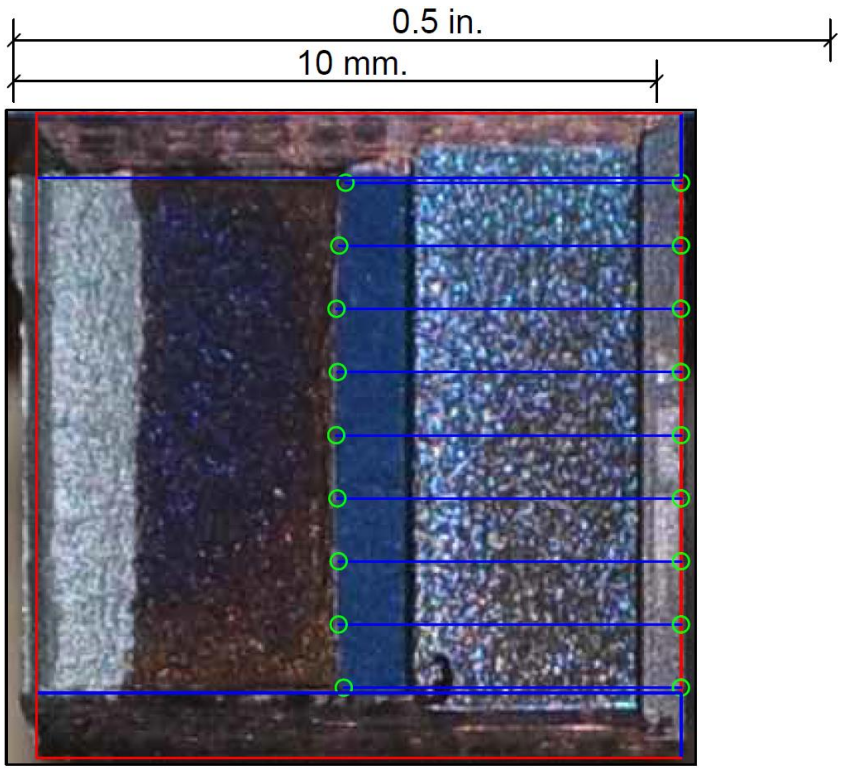

Figure F-84. Specimen E29' Fracture Surface

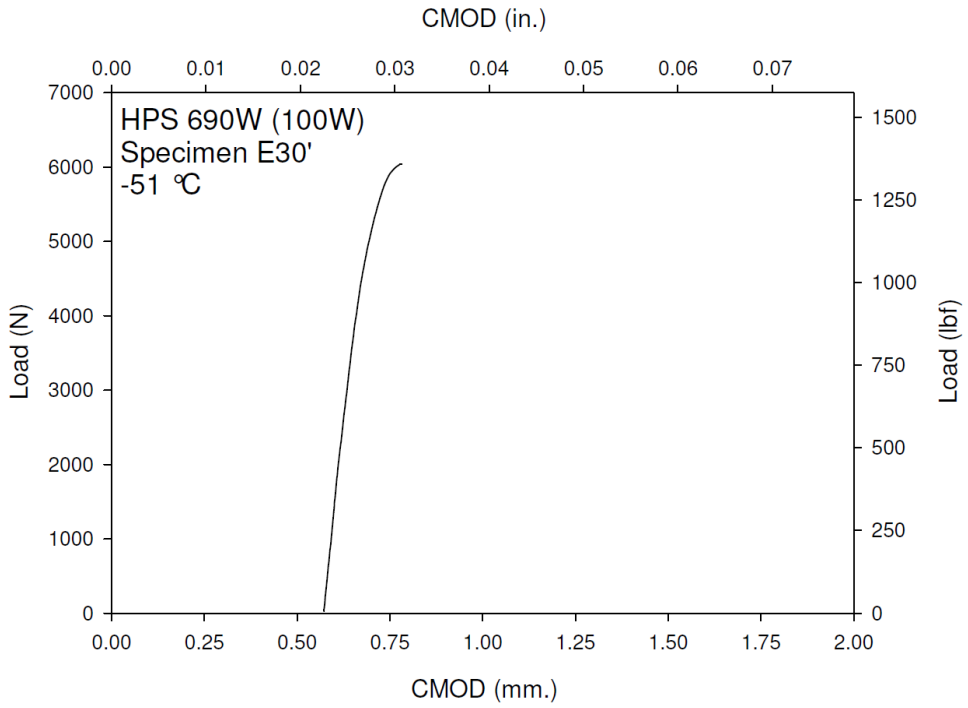

Figure F-85. Specimen E30' Test Record

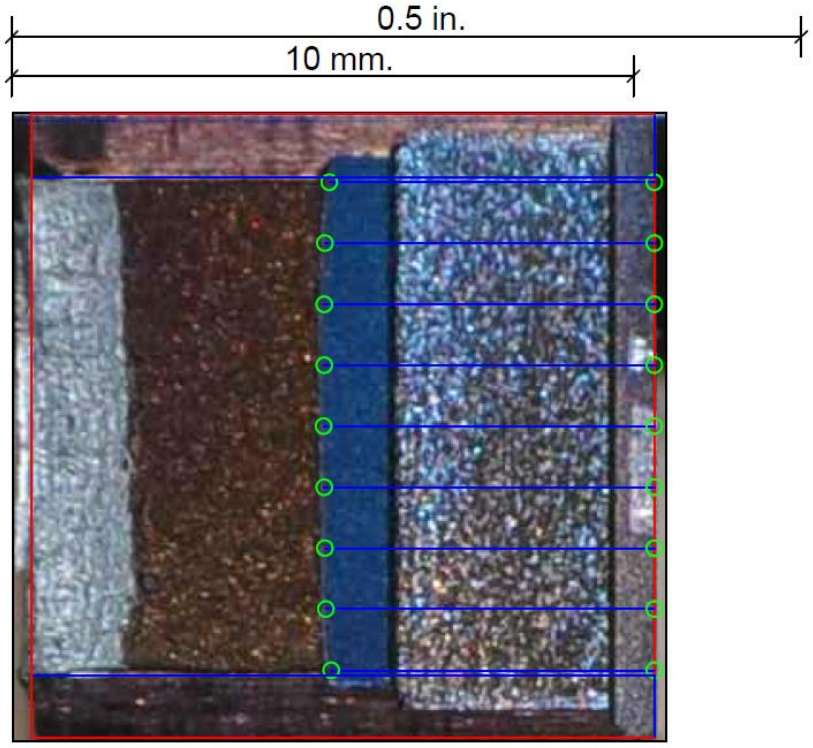

Figure F-86. Specimen E30' Fracture Surface

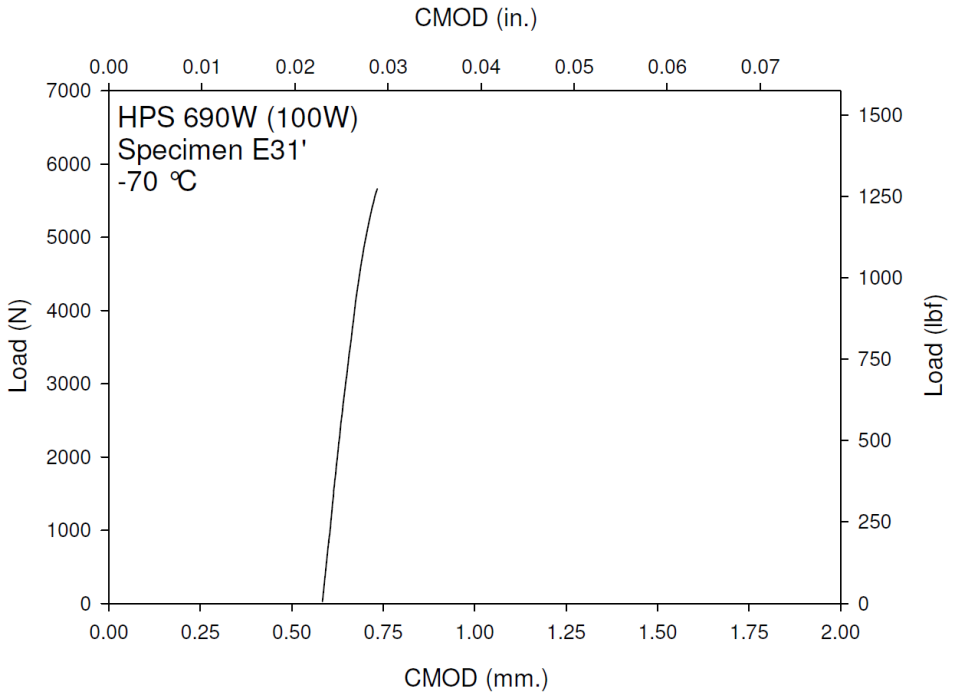

Figure F-87. Specimen E31' Test Record

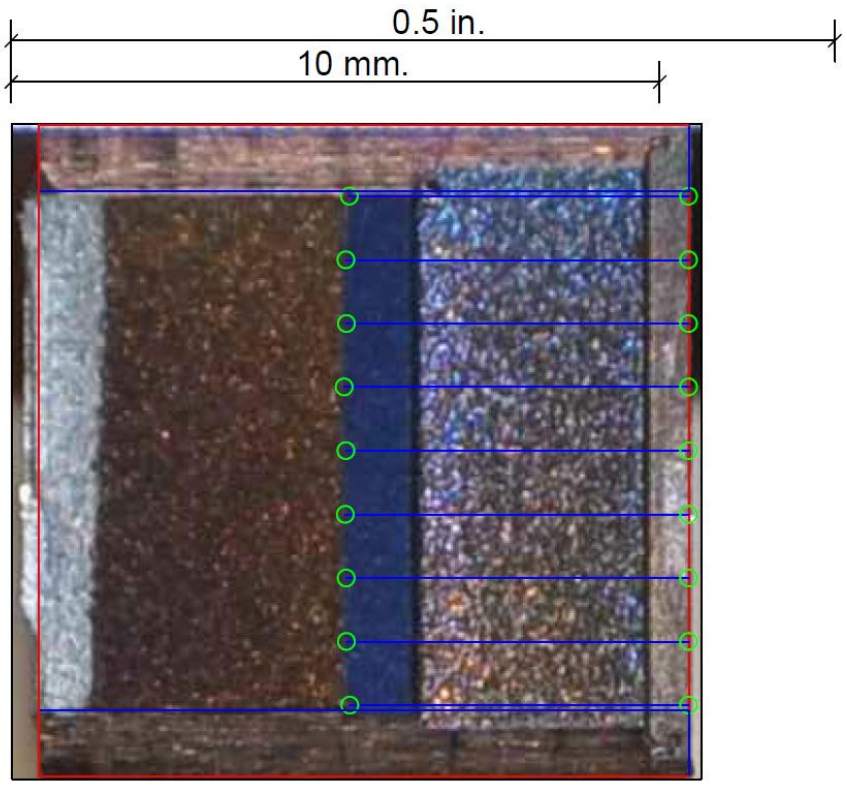

Figure F-88. Specimen E31' Fracture Surface

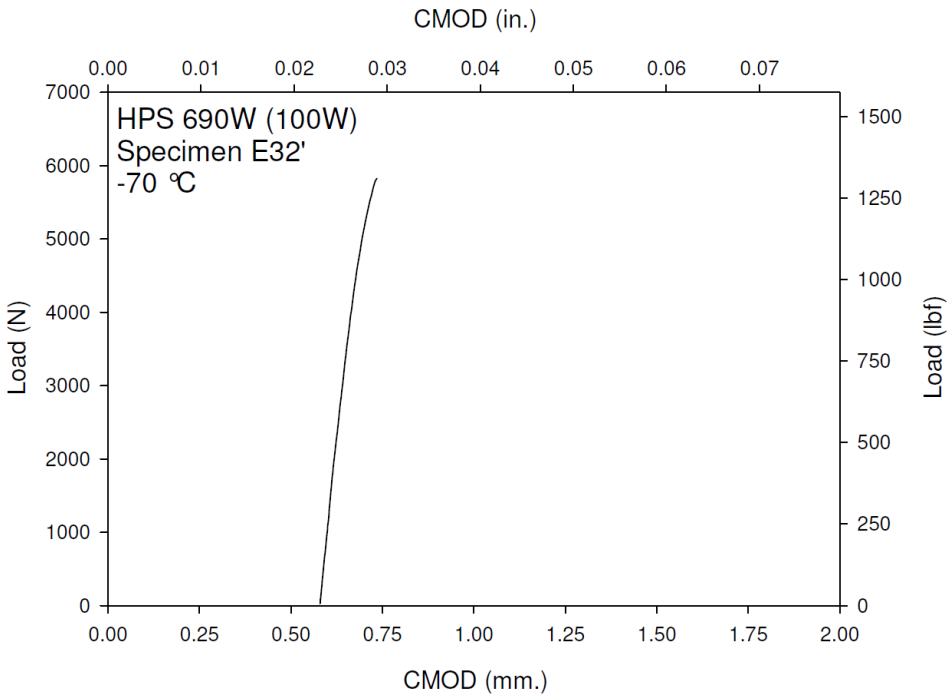

Figure F-89. Specimen E32' Test Record

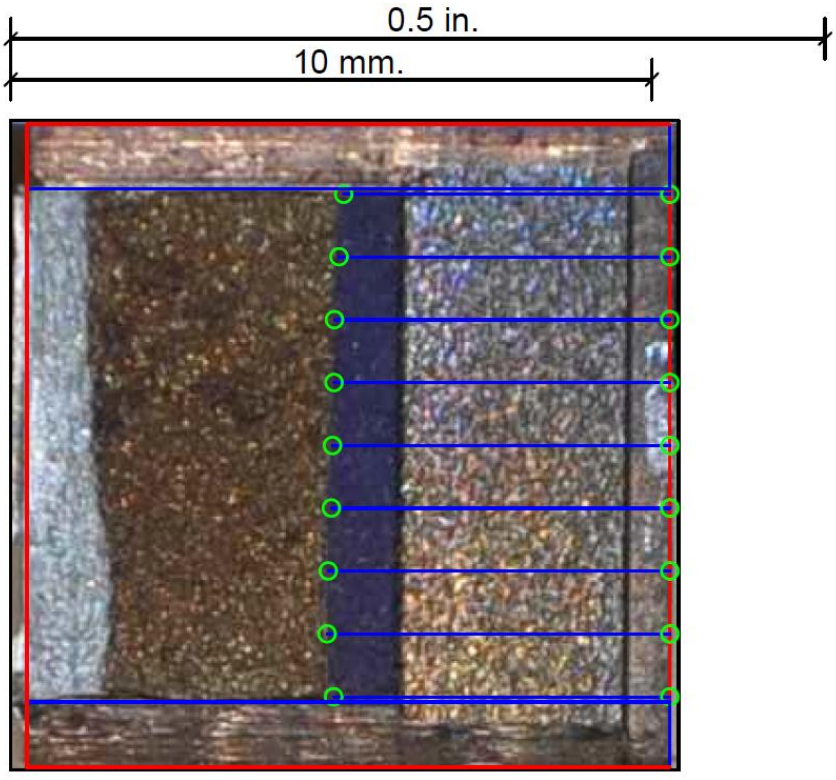

Figure F-90. Specimen E32' Fracture Surface

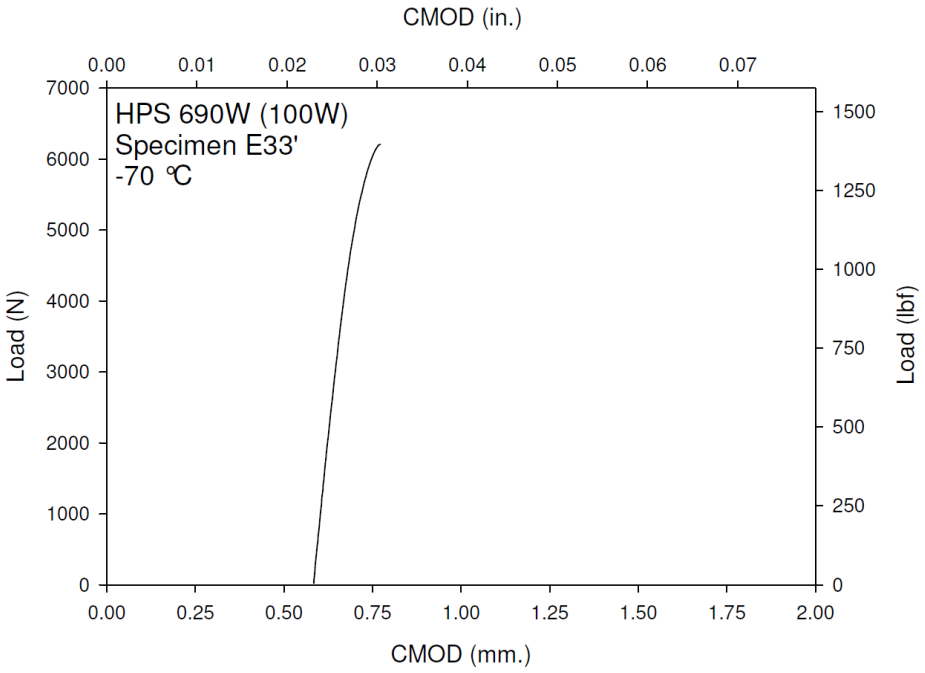

Figure F-91. Specimen E33' Test Record

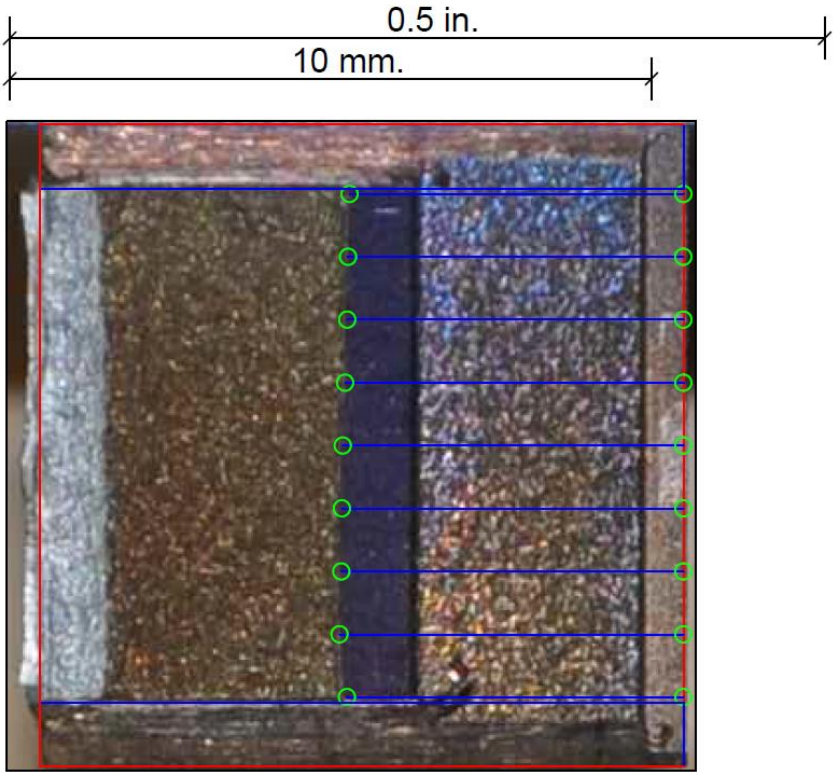

Figure F-92. Specimen E33' Fracture Surface

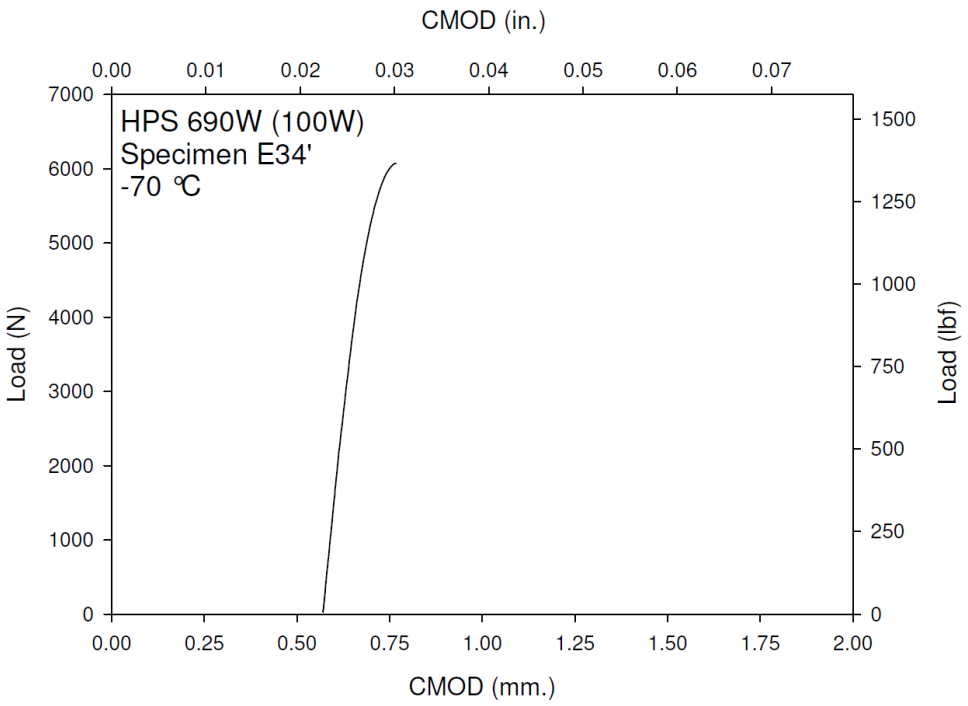

Figure F-93. Specimen E34' Test Record

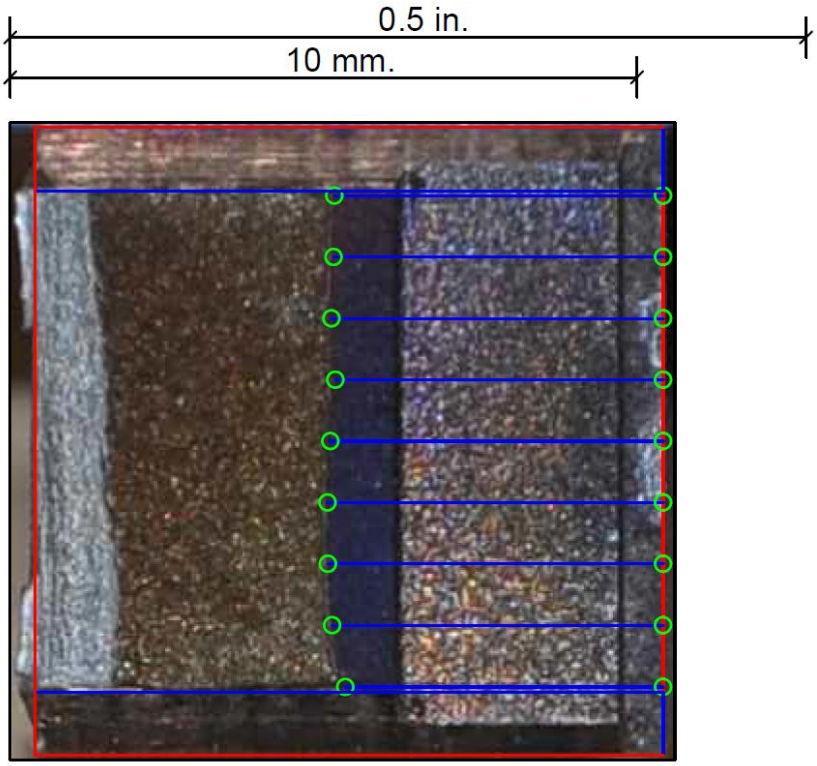

Figure F-94. Specimen E34' Fracture Surface

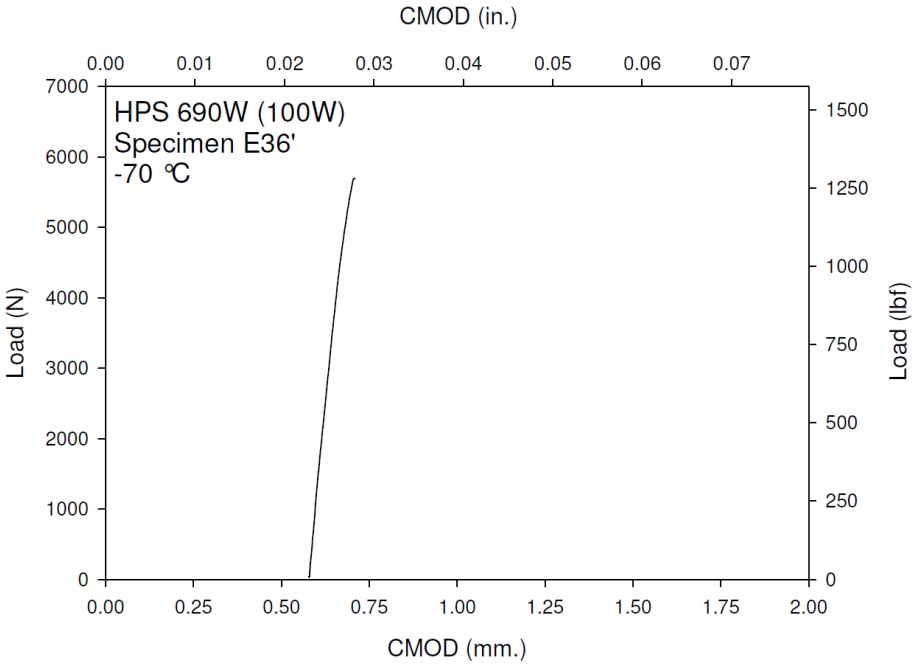

Figure F-95. Specimen E36' Test Record

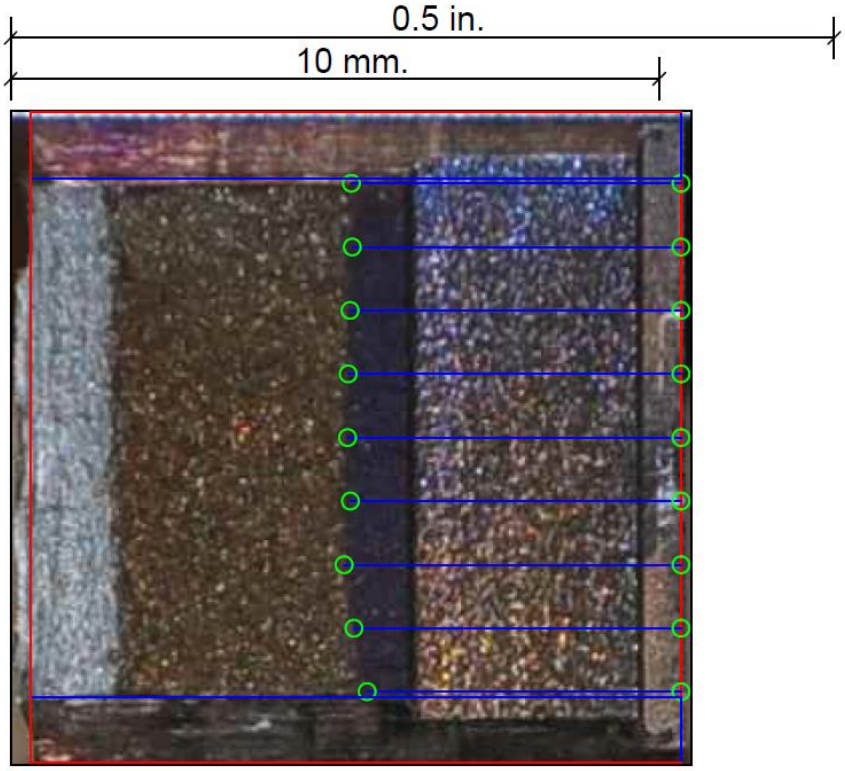

Figure F-96. Specimen E36' Fracture Surface

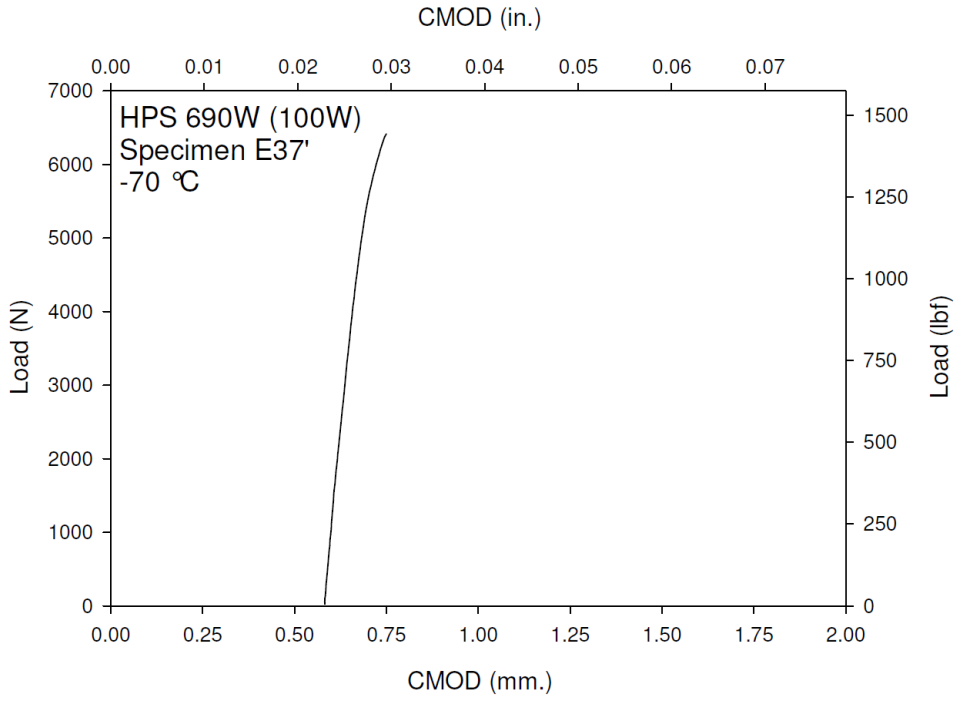

Figure F-97. Specimen E37' Test Record

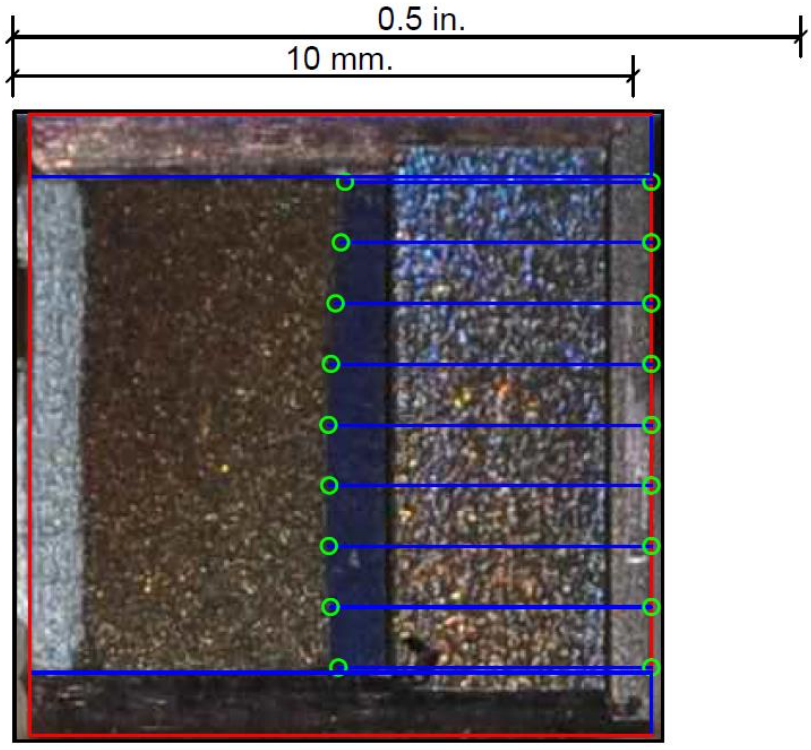

Figure F-98. Specimen E37' Fracture Surface

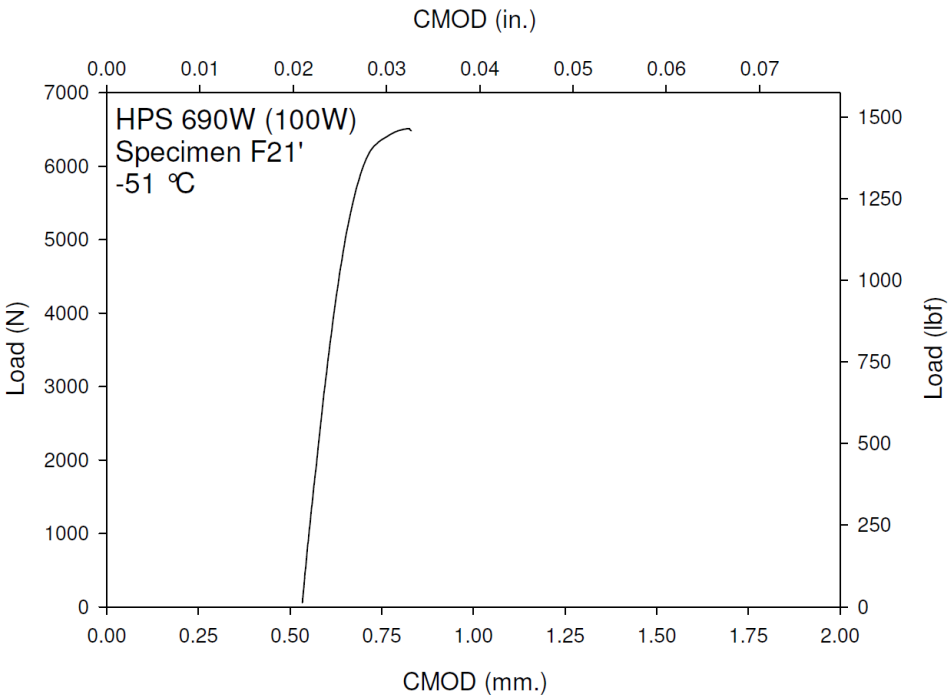

Figure F-99. Specimen F21' Test Record

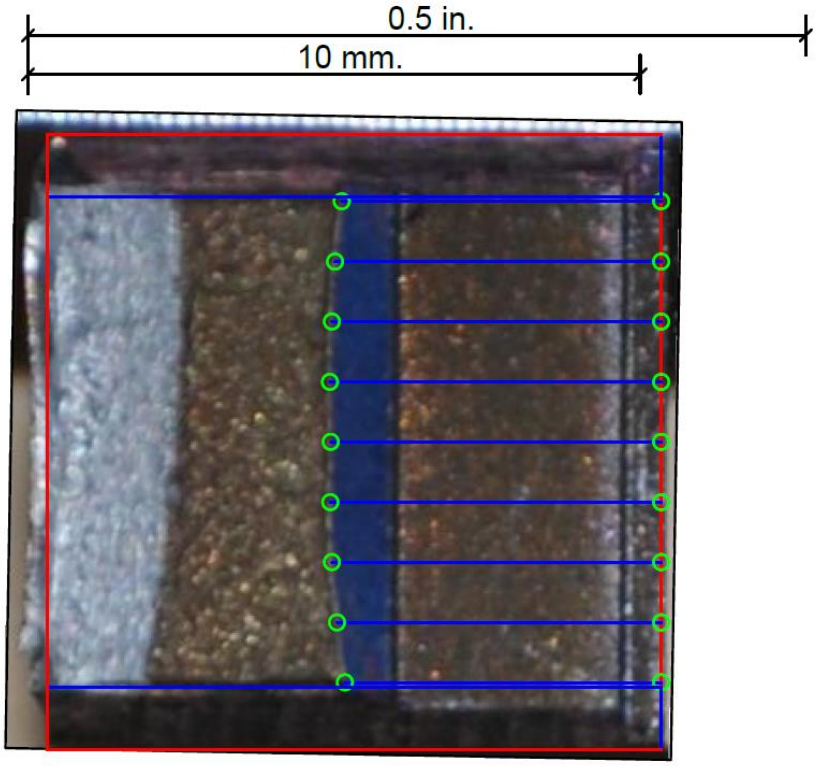

Figure F-100. Specimen F21' Fracture Surface

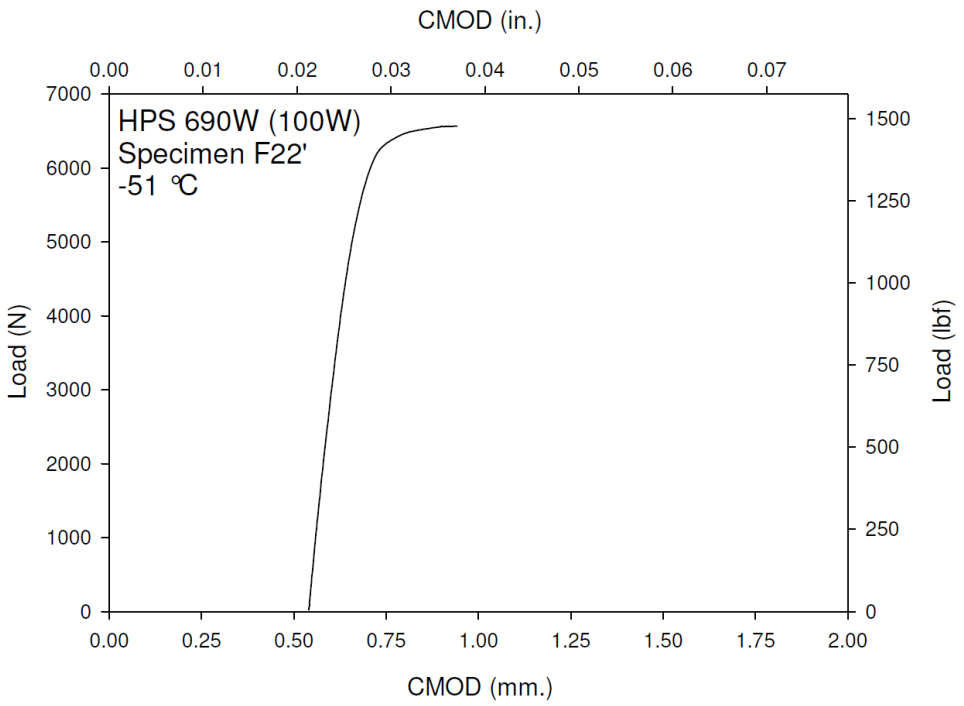

Figure F-101. Specimen F22' Test Record

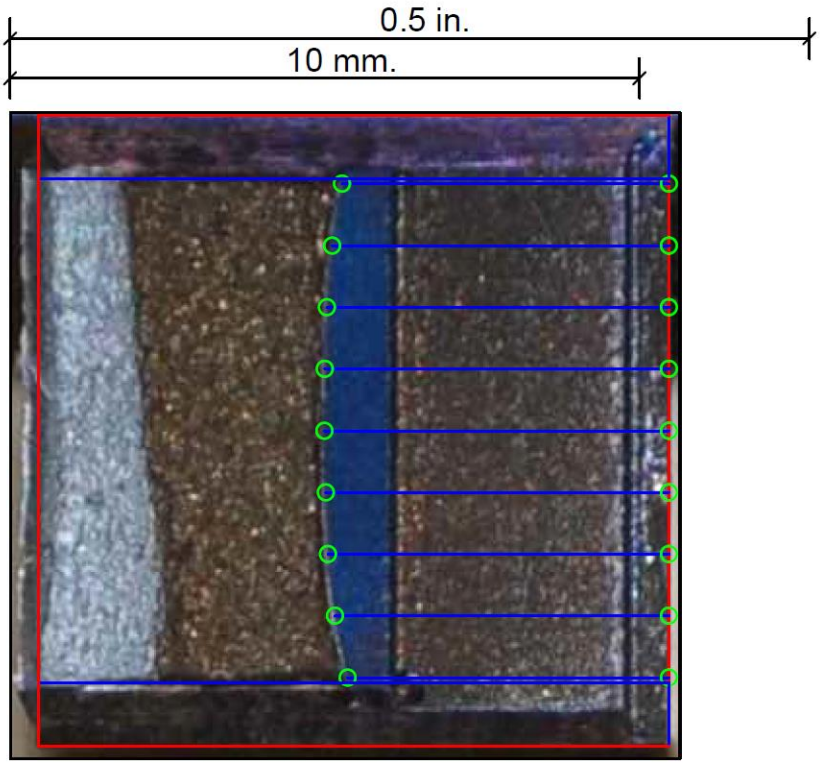

Figure F-102. Specimen F22' Fracture Surface

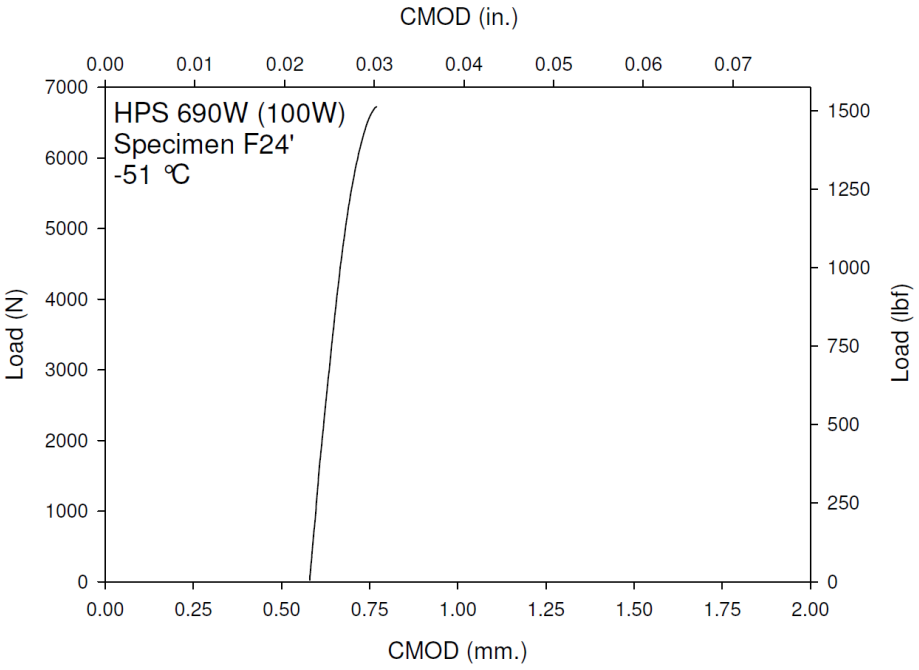

Figure F-103. Specimen F24' Test Record

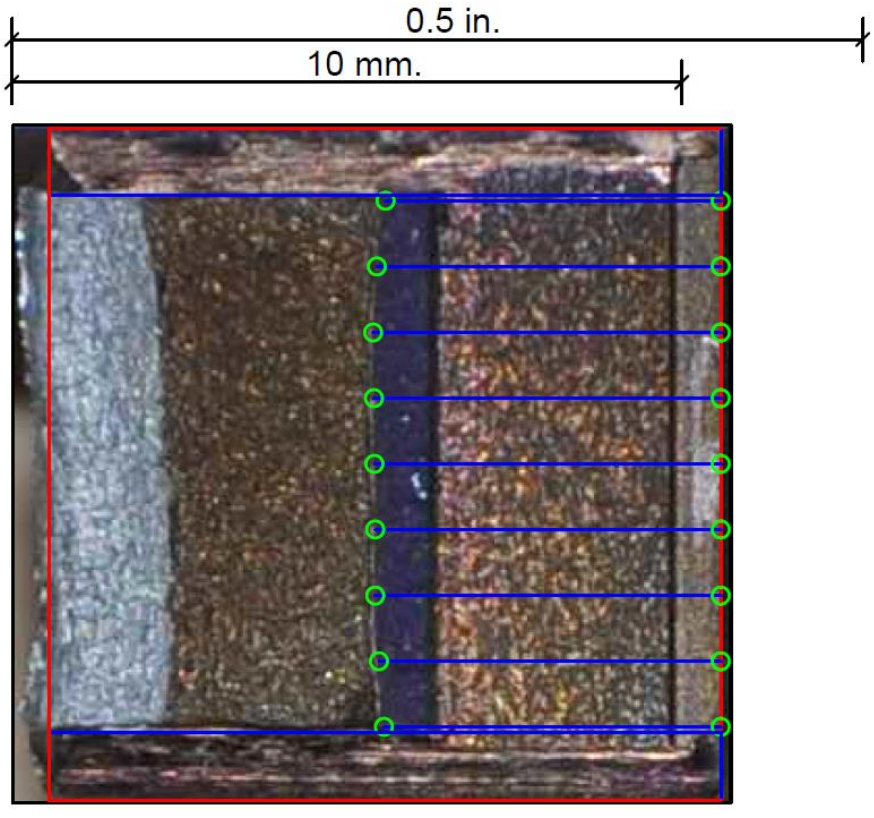

Figure F-104. Specimen F24' Fracture Surface

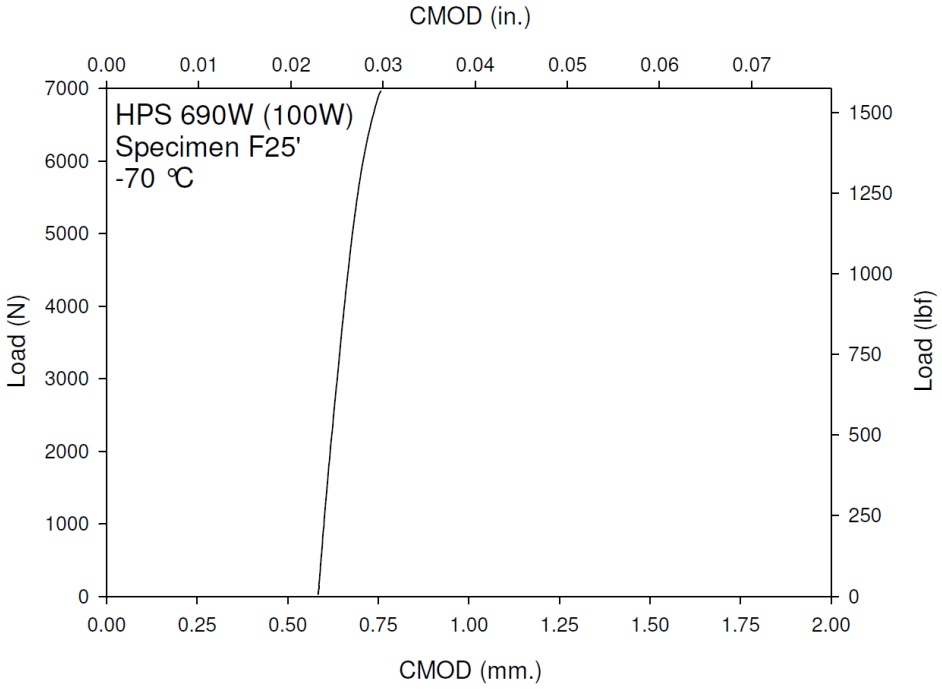

Figure F-105. Specimen F25' Test Record

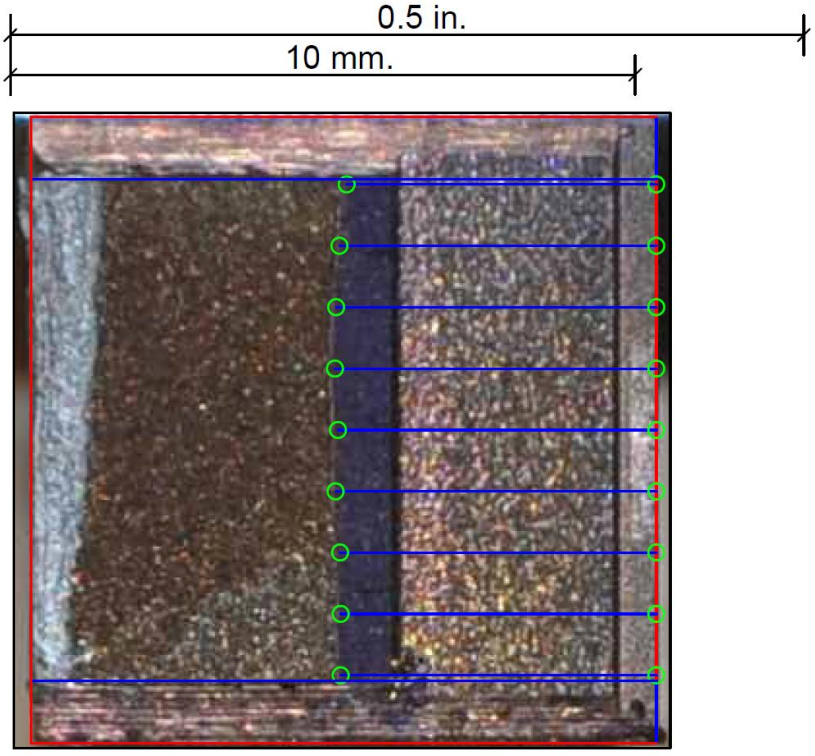

Figure F-106. Specimen F25' Fracture Surface

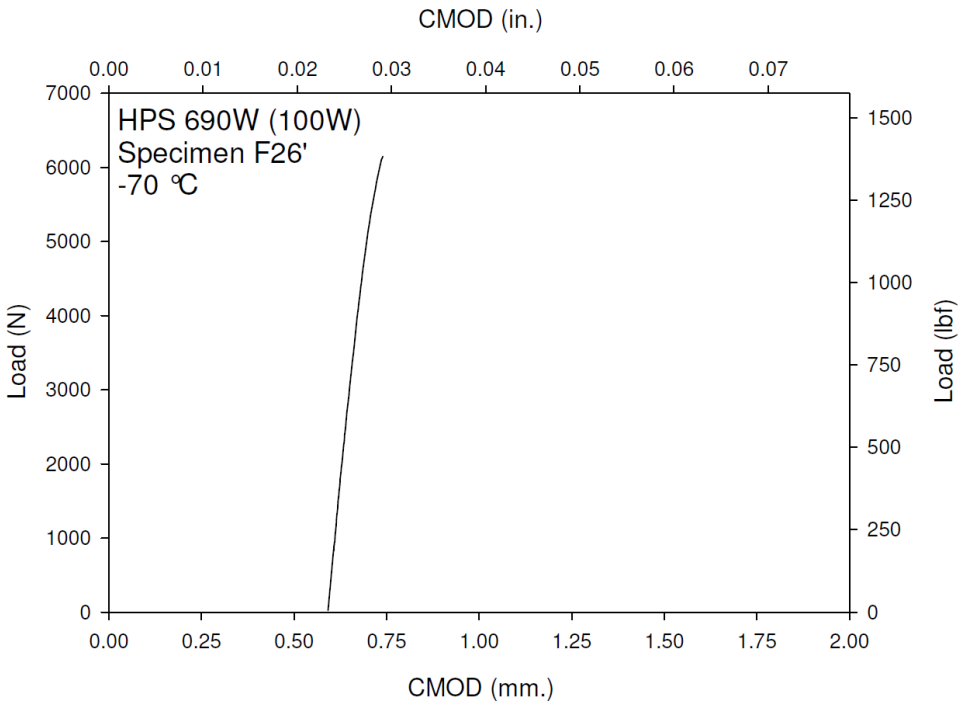

Figure F-107. Specimen F26' Test Record

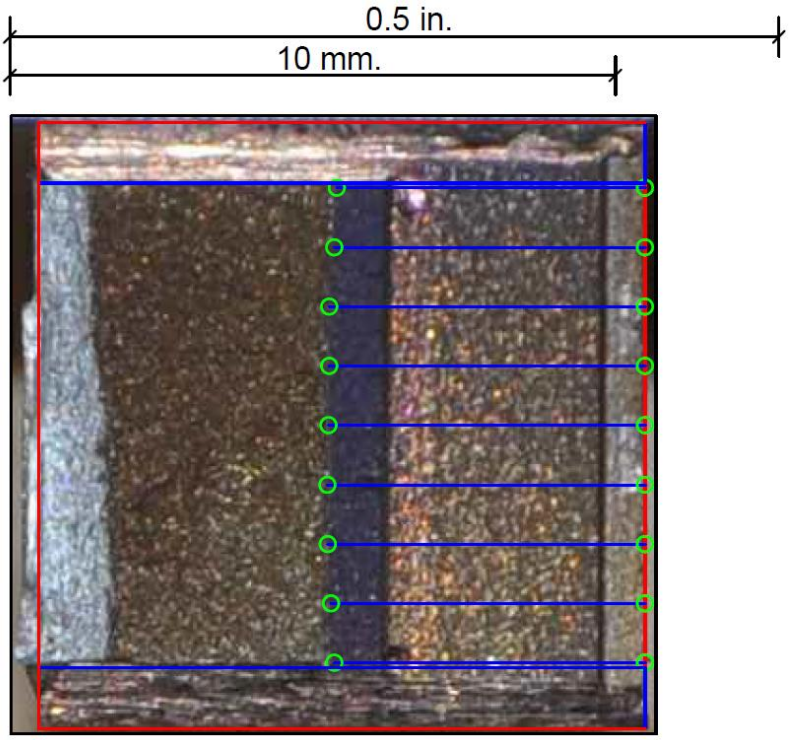

Figure F-108. Specimen F26' Fracture Surface

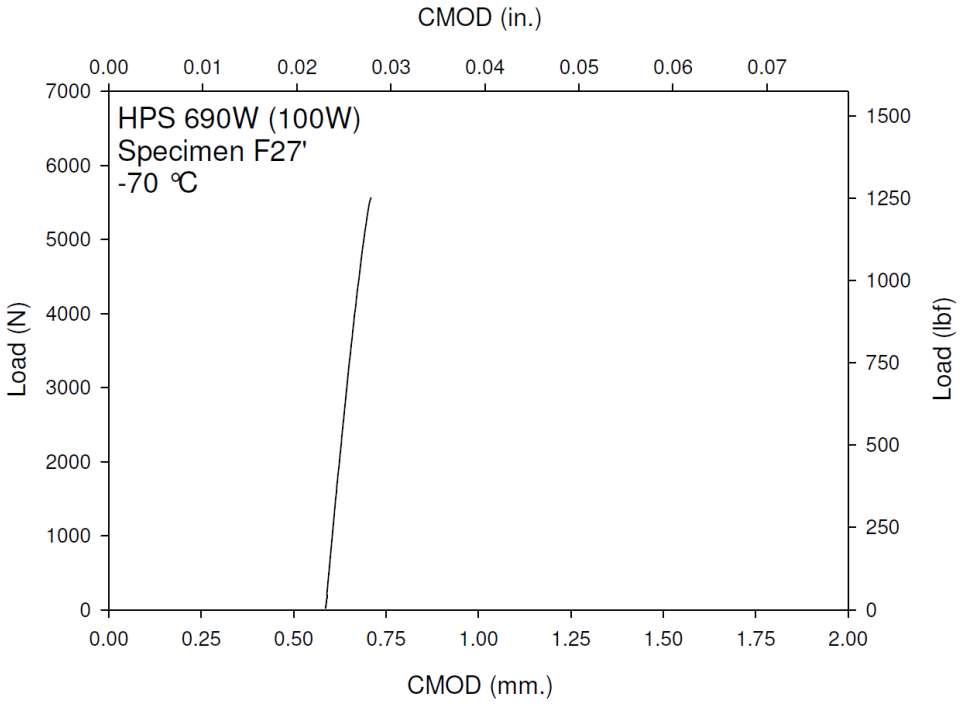

Figure F-109. Specimen F27' Test Record

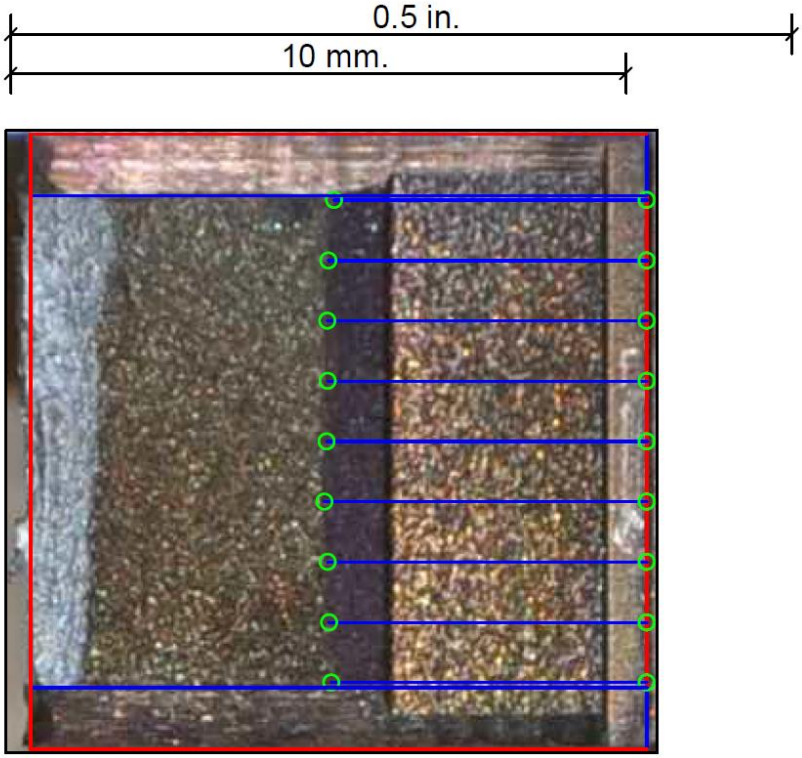

Figure F-110. Specimen F27' Fracture Surface

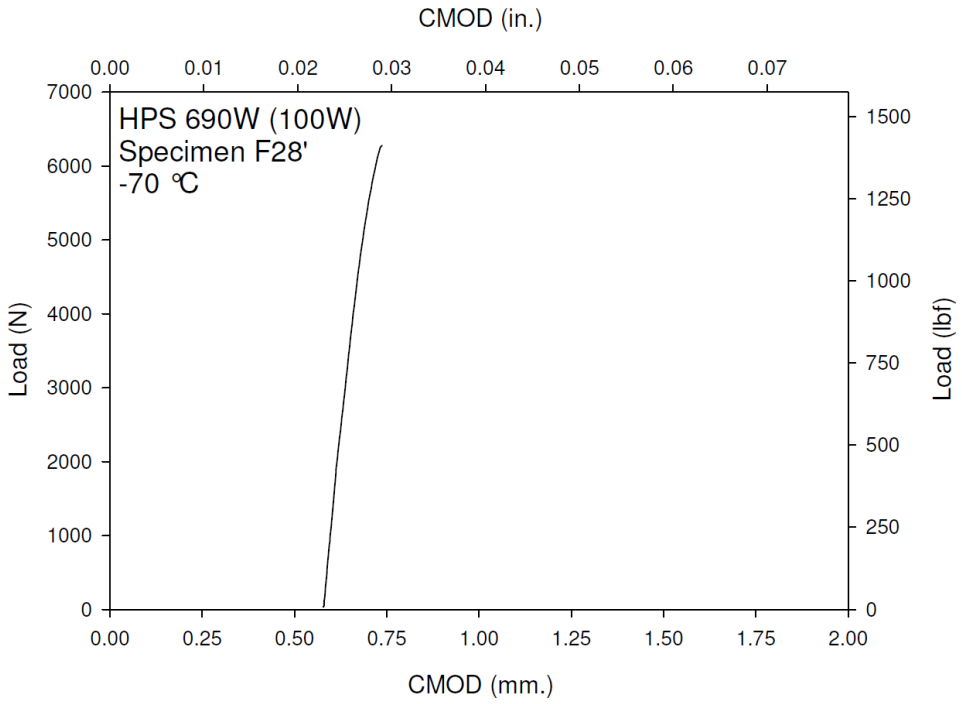

Figure F-111. Specimen F28' Test Record

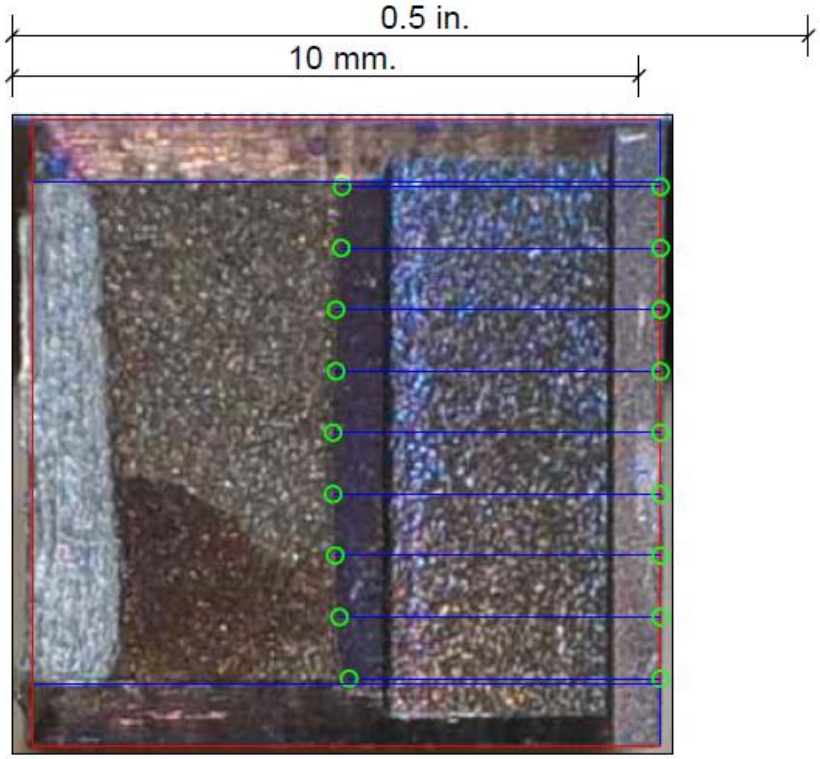

Figure F-112. Specimen F28' Fracture Surface

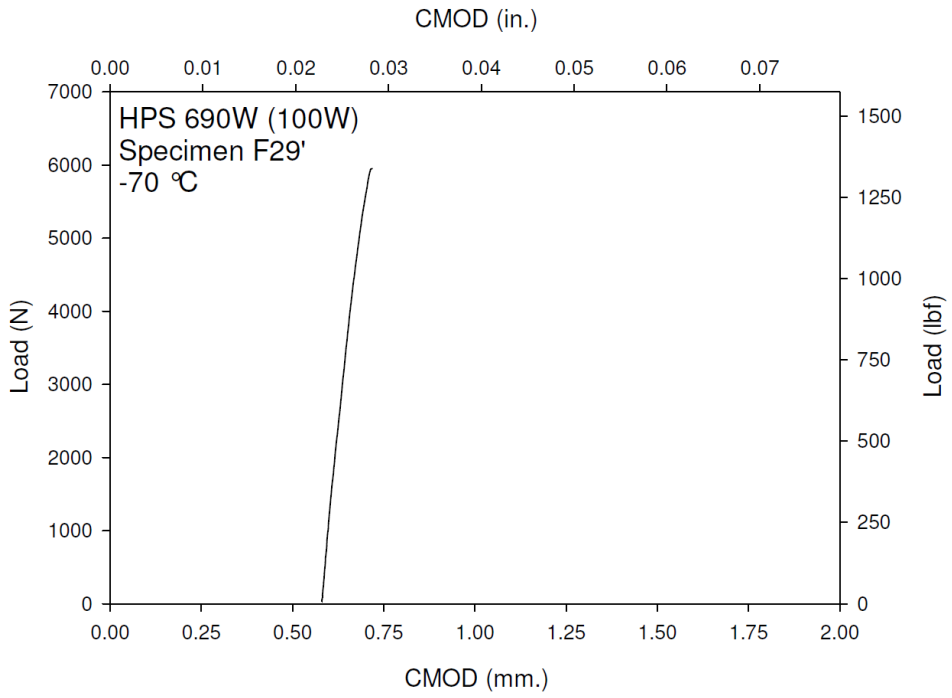

Figure F-113. Specimen F29' Test Record

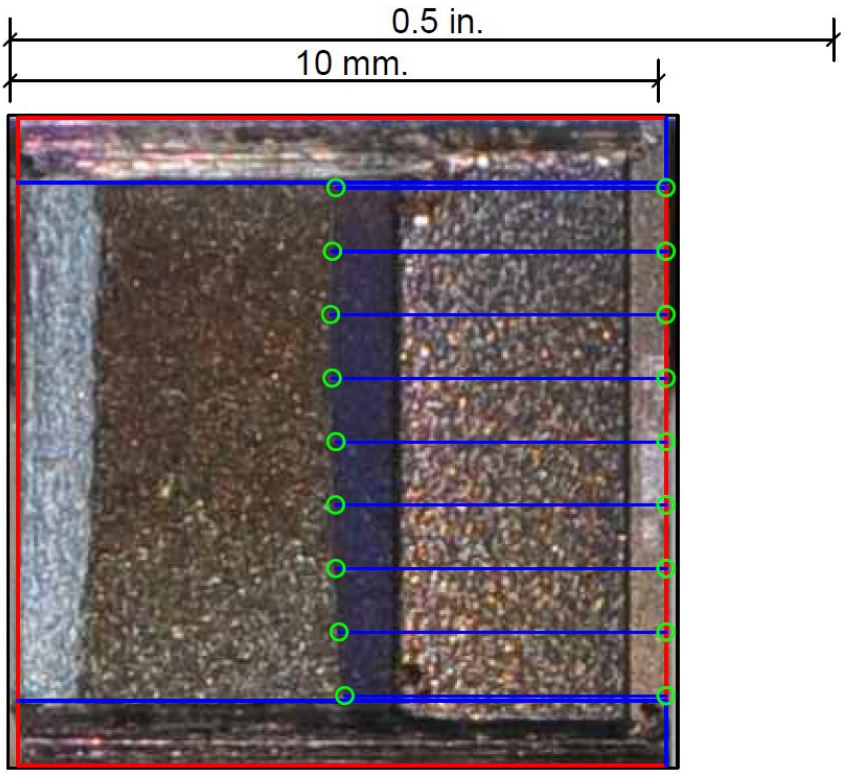

Figure F-114. Specimen F29' Fracture Surface

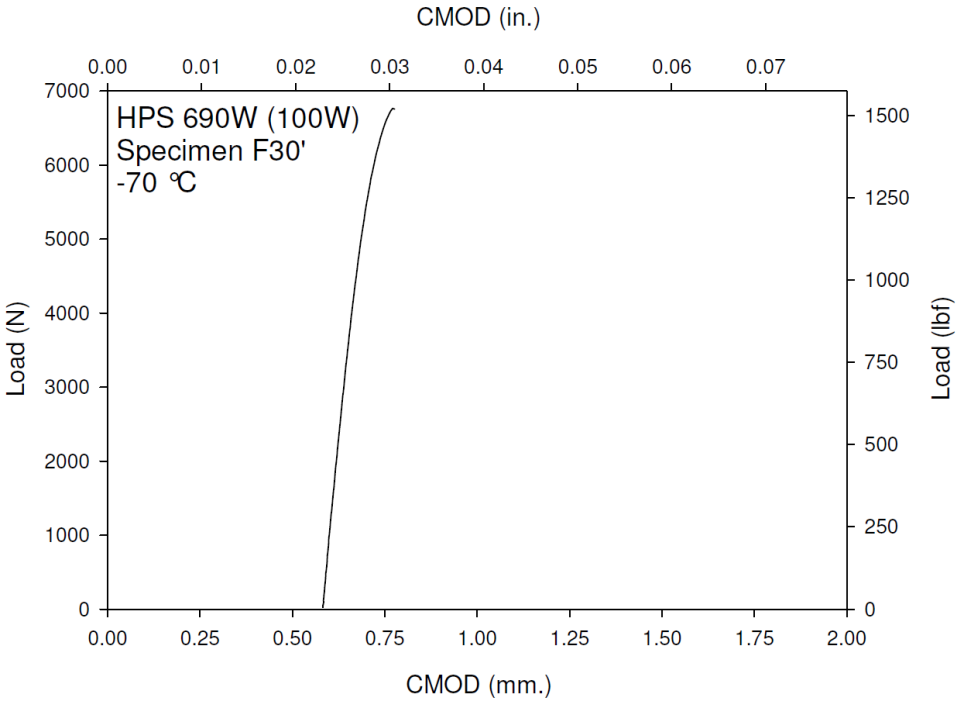

Figure F-115. Specimen F30' Test Record

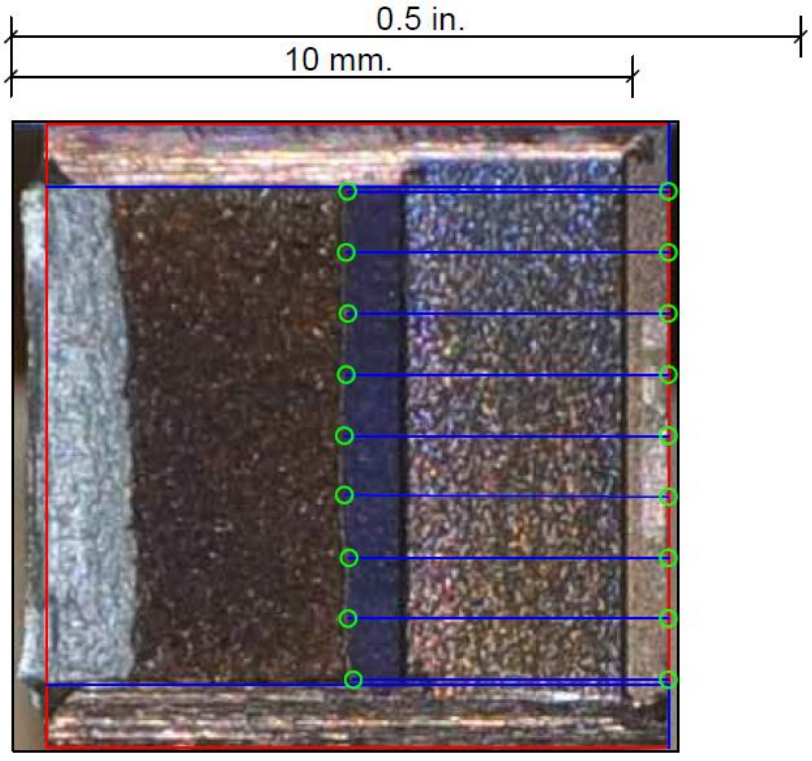

Figure F-116. Specimen F30' Fracture Surface

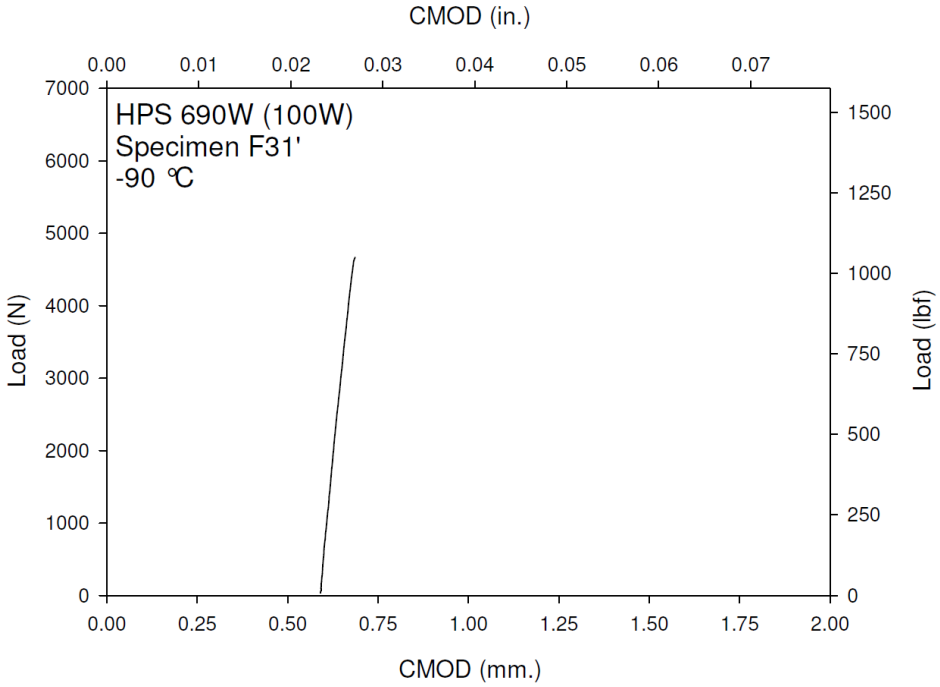

Figure F-117. Specimen F31' Test Record

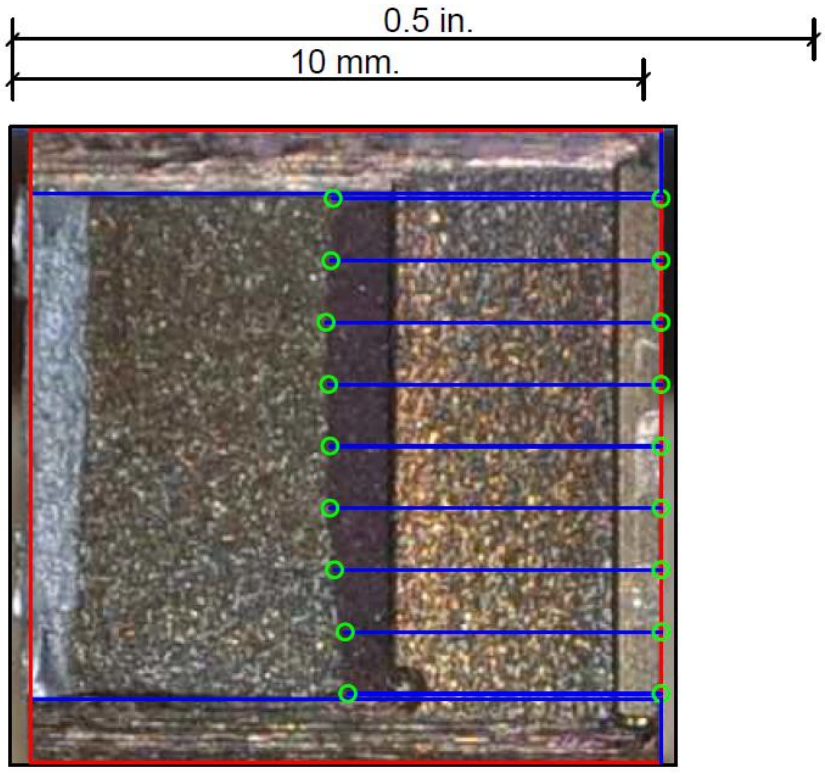

Figure F-118. Specimen F31' Fracture Surface

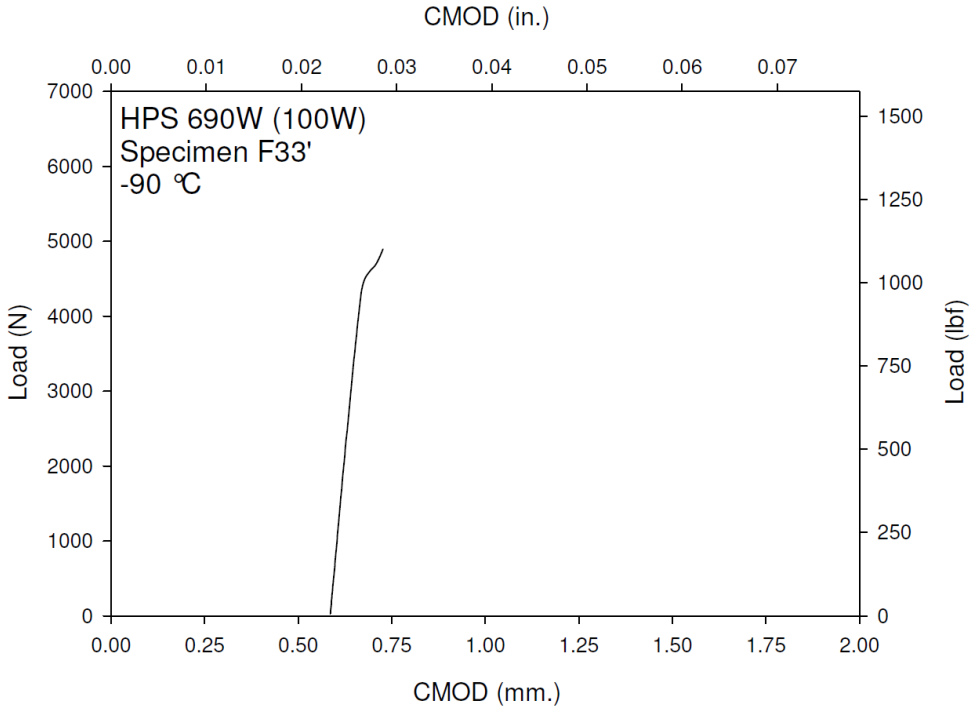

Figure F-119. Specimen F33' Test Record

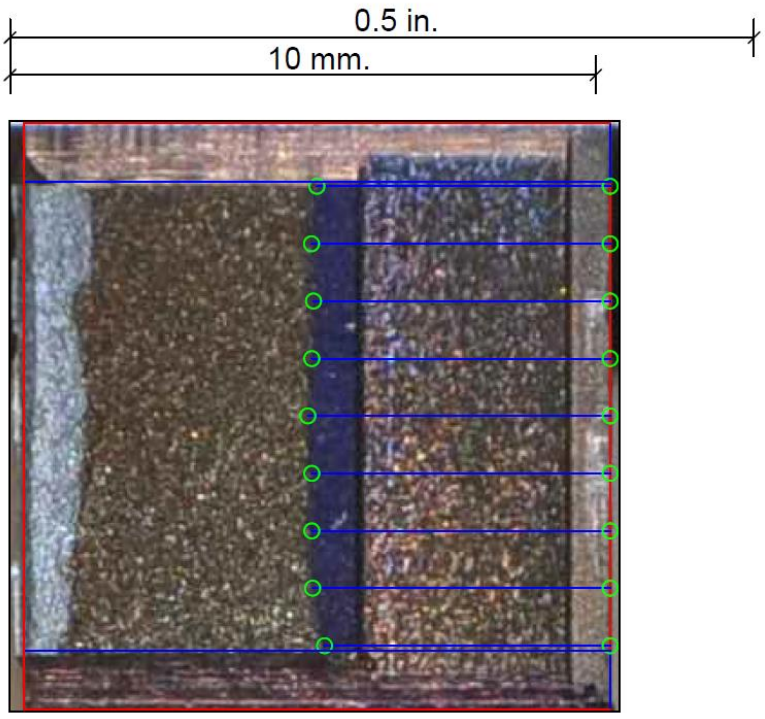

Figure F-120. Specimen F33' Fracture Surface

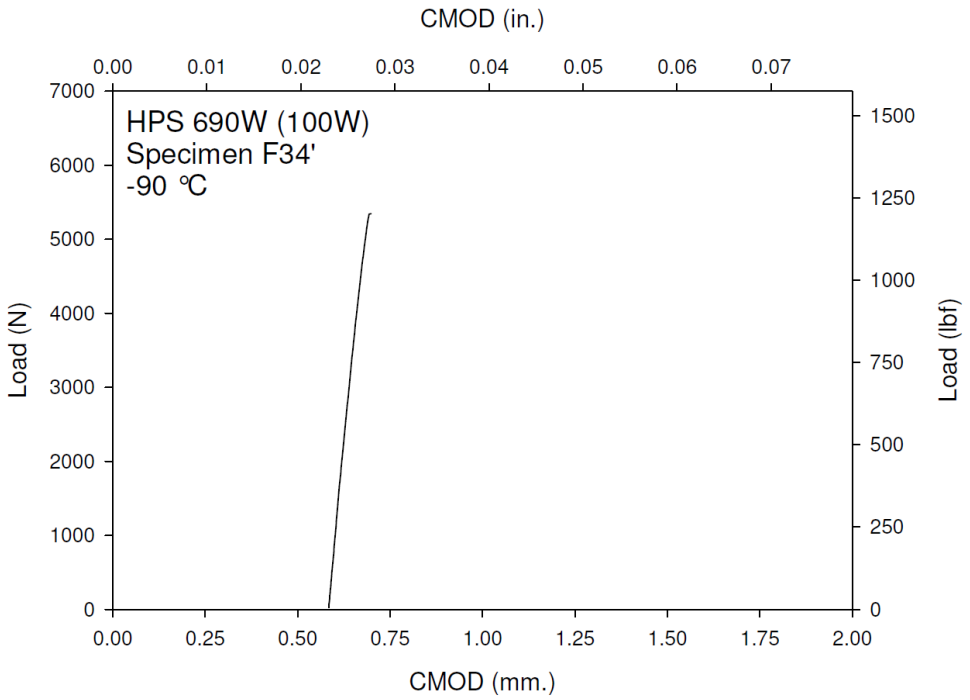

Figure F-121. Specimen F34' Test Record

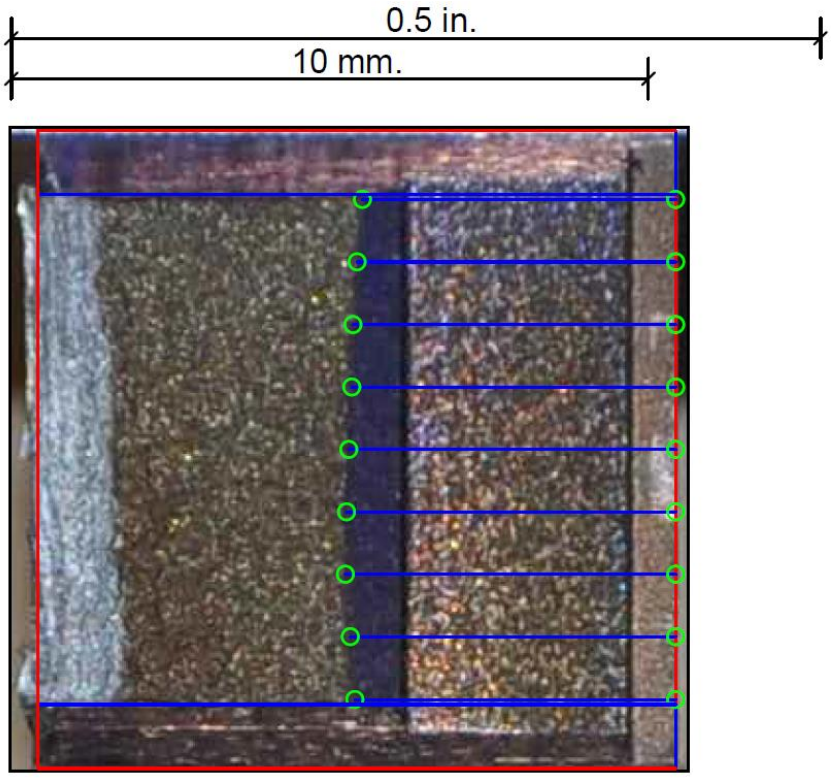

Figure F-122. Specimen F34' Fracture Surface

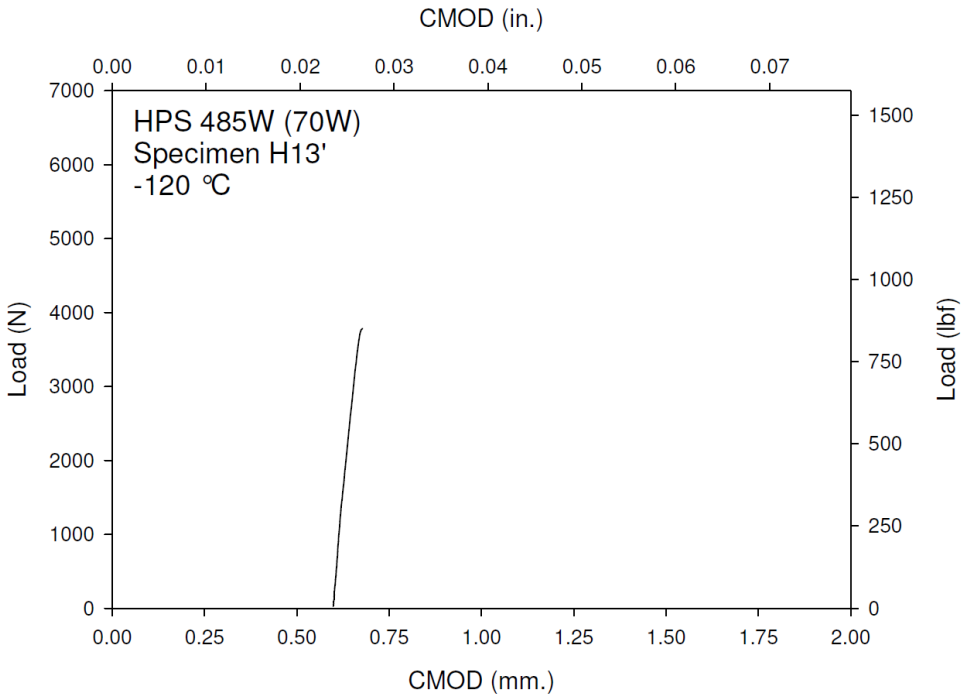

Figure F-123. Specimen H13' Test Record

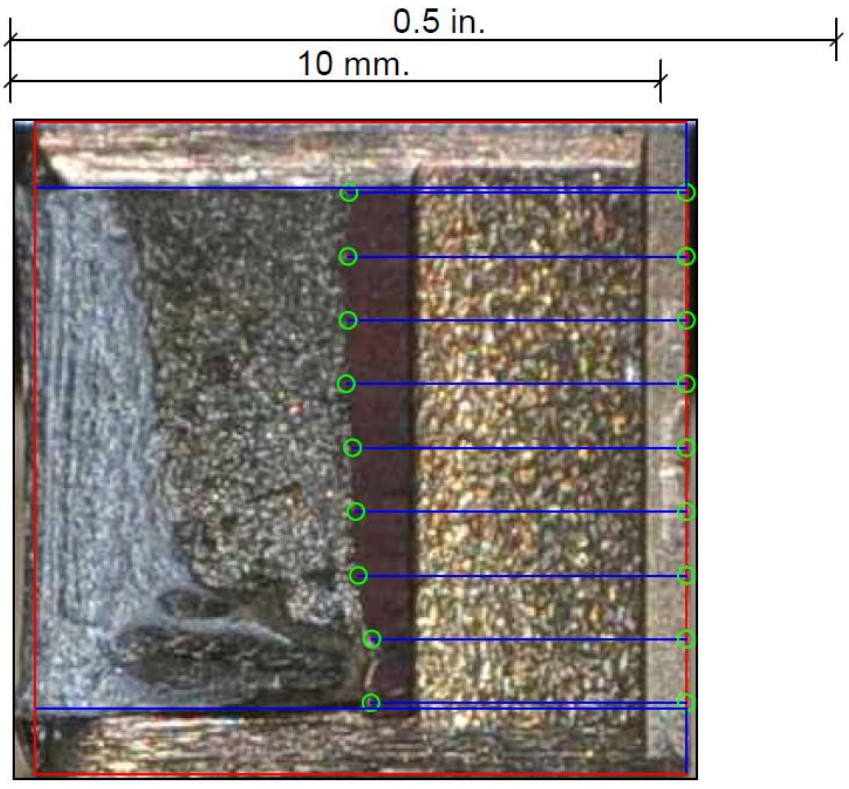

Figure F-124. Specimen H13' Fracture Surface

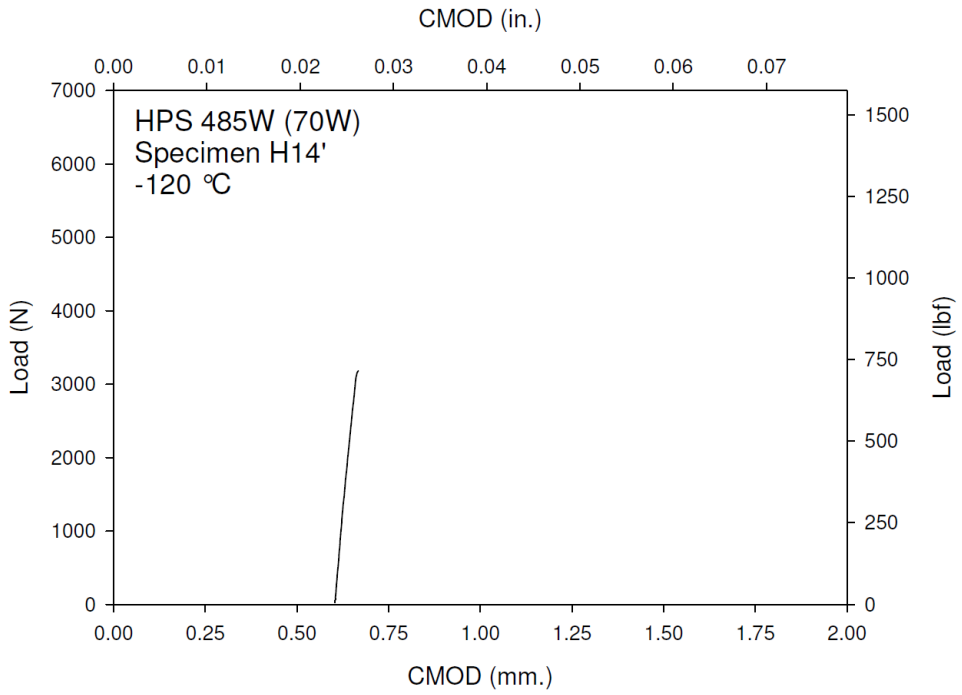

Figure F-125. Specimen H14' Test Record

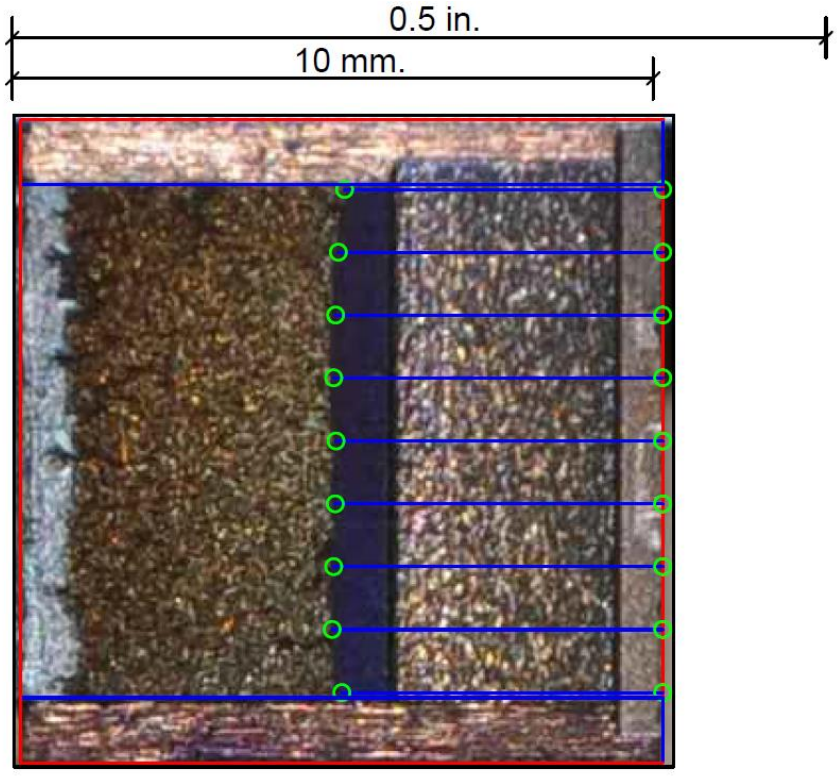

Figure F-126. Specimen H14' Fracture Surface

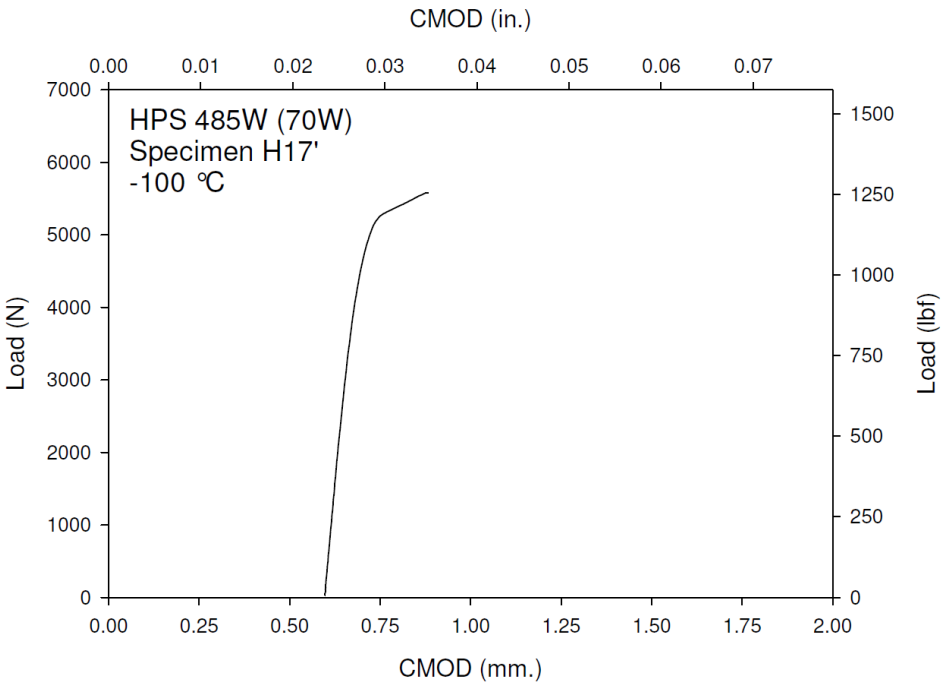

Figure F-127. Specimen H17' Test Record

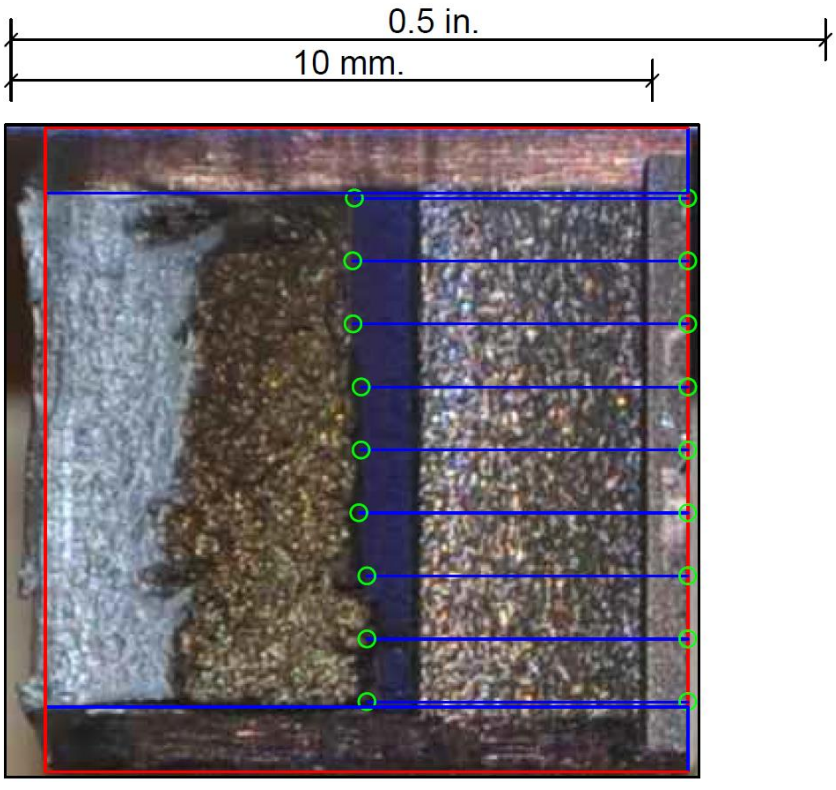

Figure F-128. Specimen H17' Fracture Surface

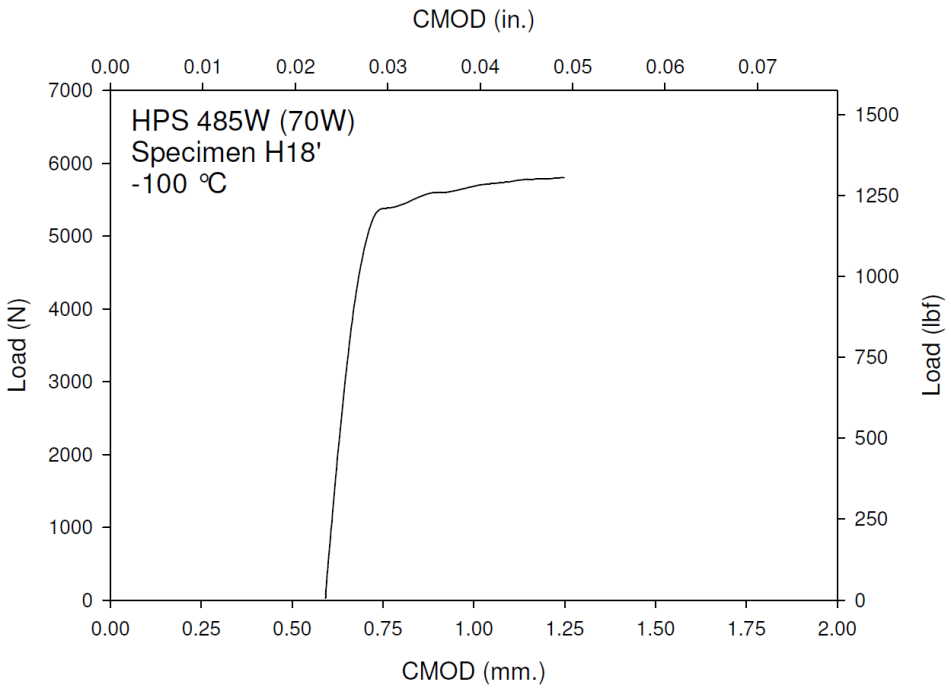

Figure F-129. Specimen H18' Test Record

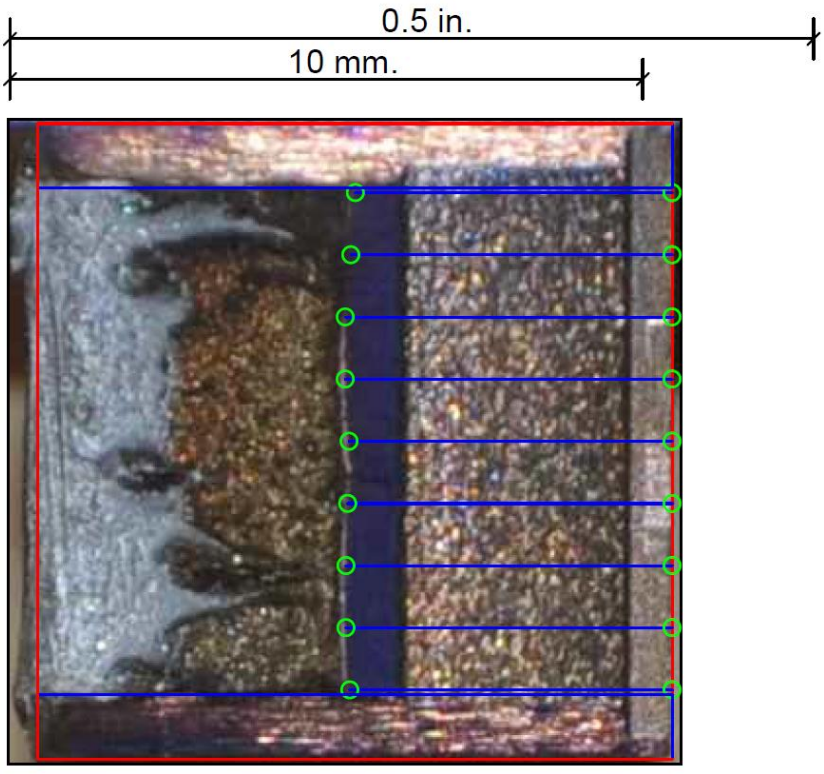

Figure F-130. Specimen H18' Fracture Surface

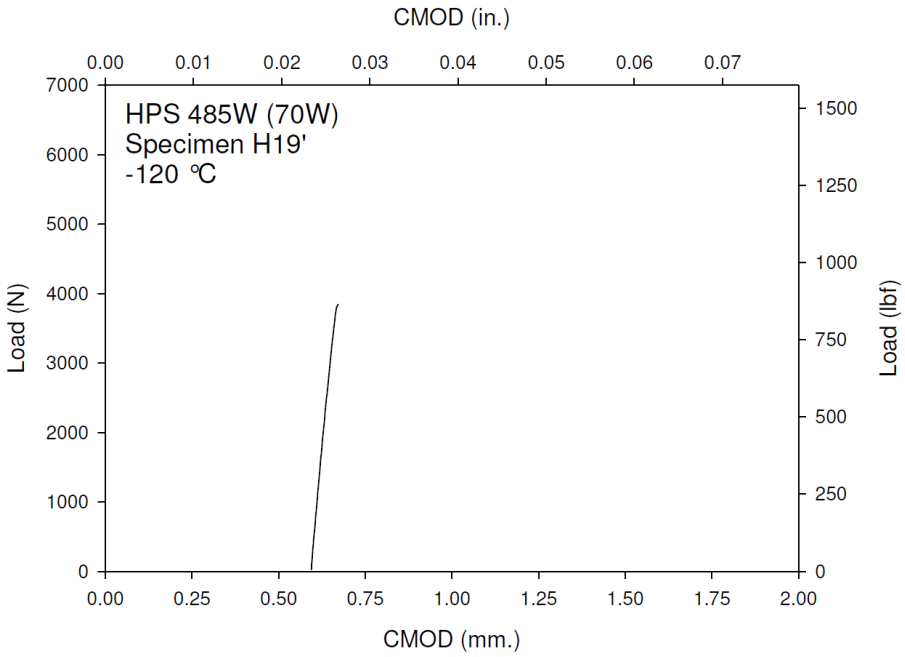

Figure F-131. Specimen H19' Test Record

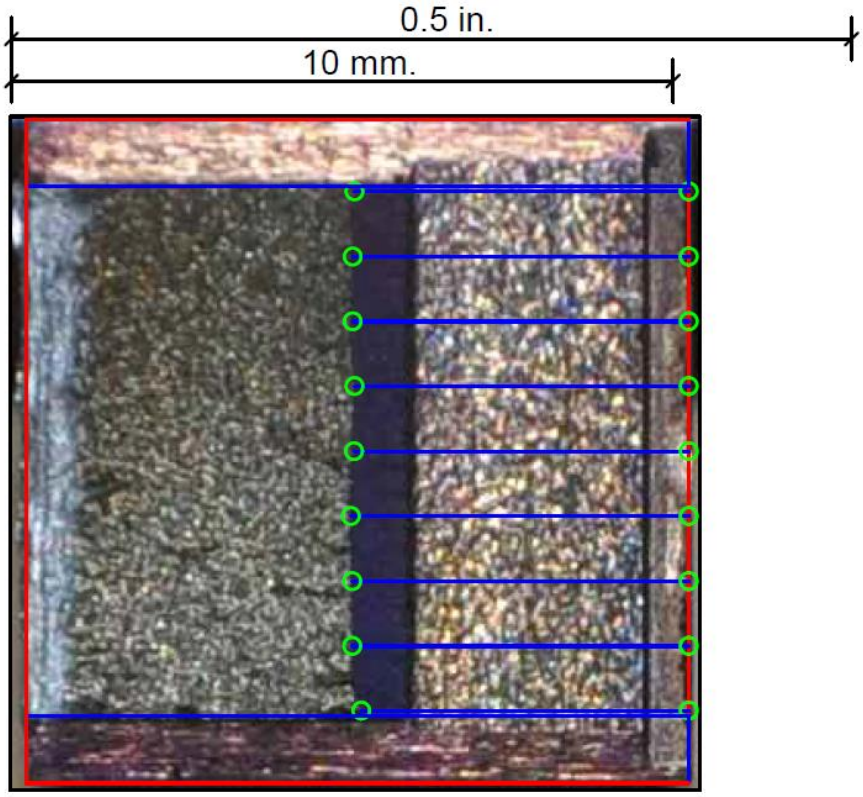

Figure F-132. Specimen H19' Fracture Surface

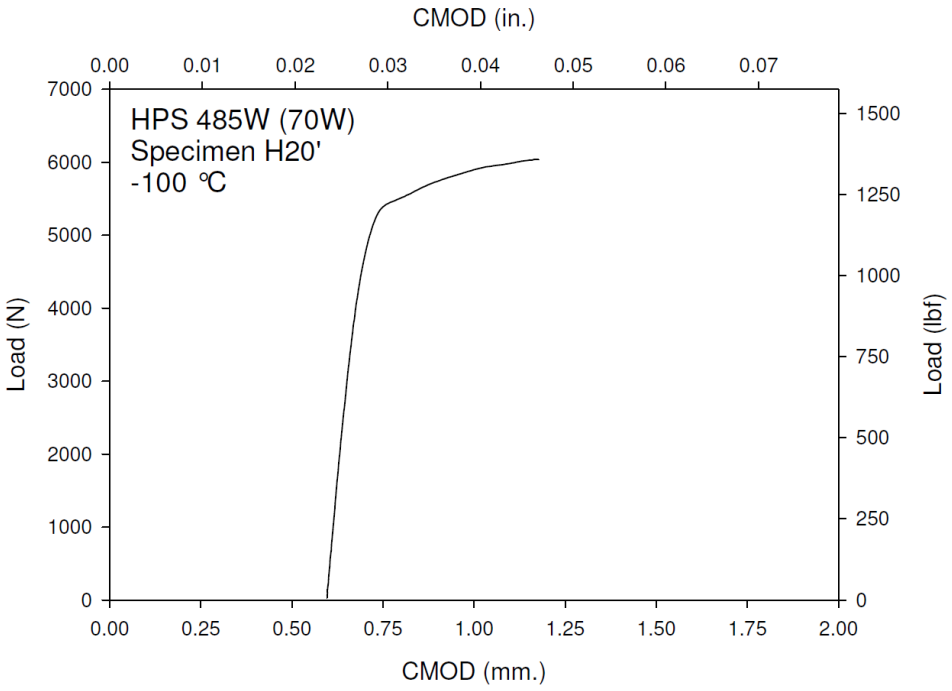

Figure F-133. Specimen H20' Test Record

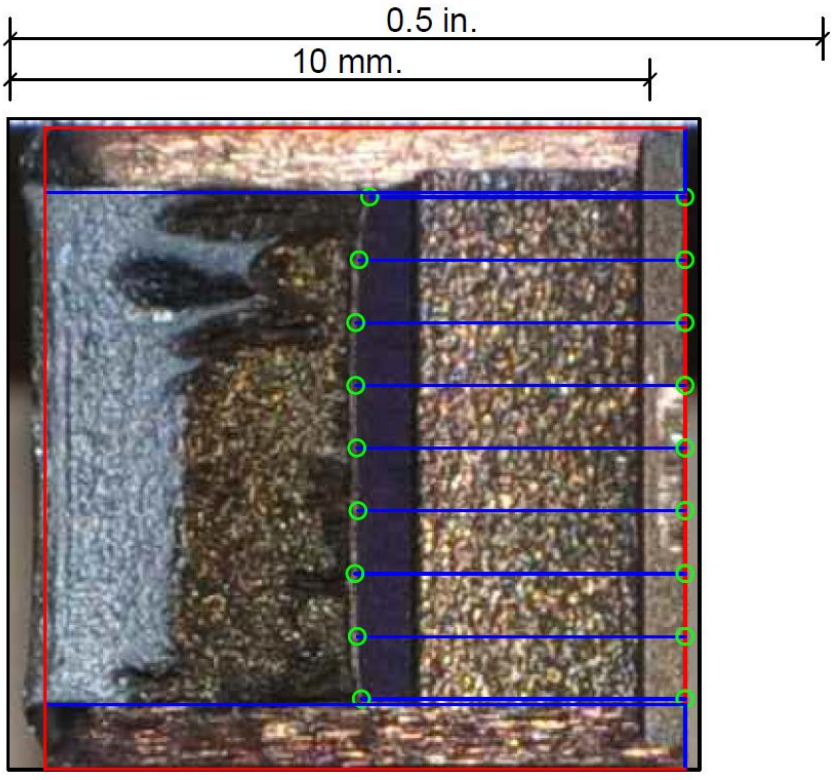

Figure F-134. Specimen H20' Fracture Surface

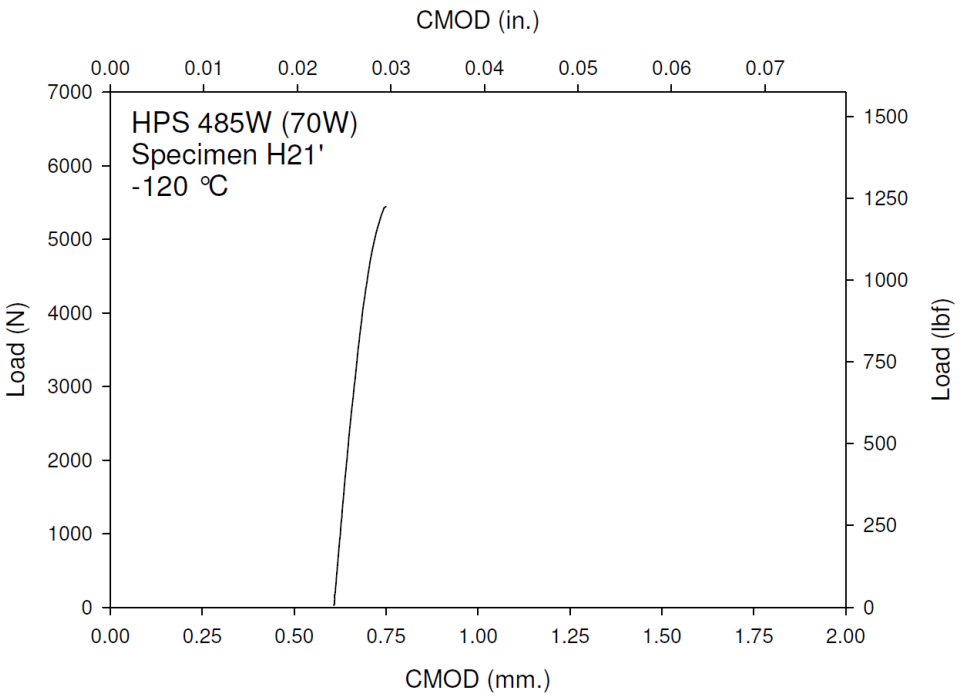

Figure F-135. Specimen H21' Test Record

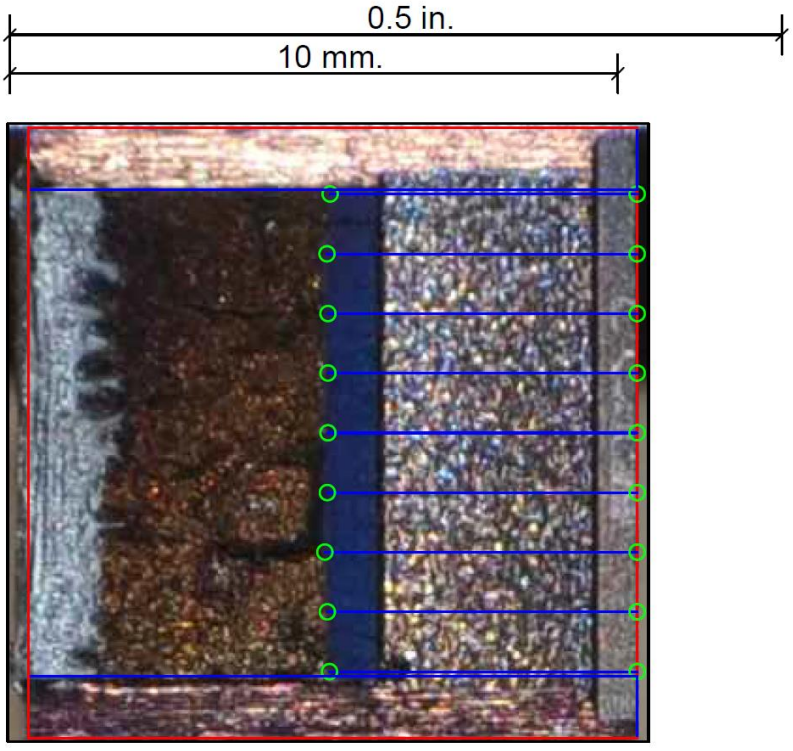

Figure F-136. Specimen H21' Fracture Surface

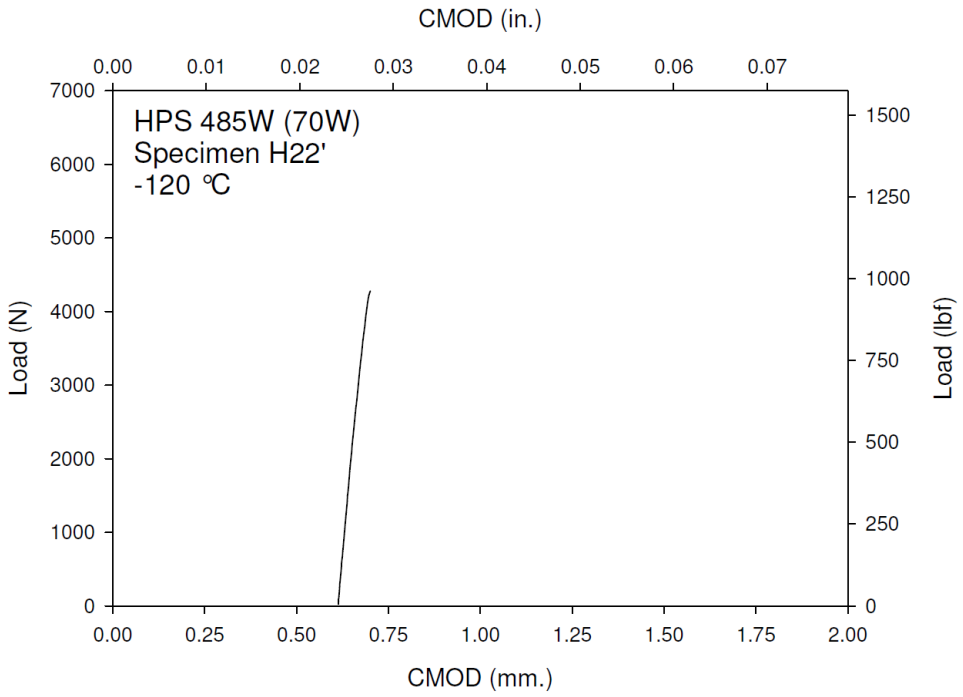

Figure F-137. Specimen H22' Test Record

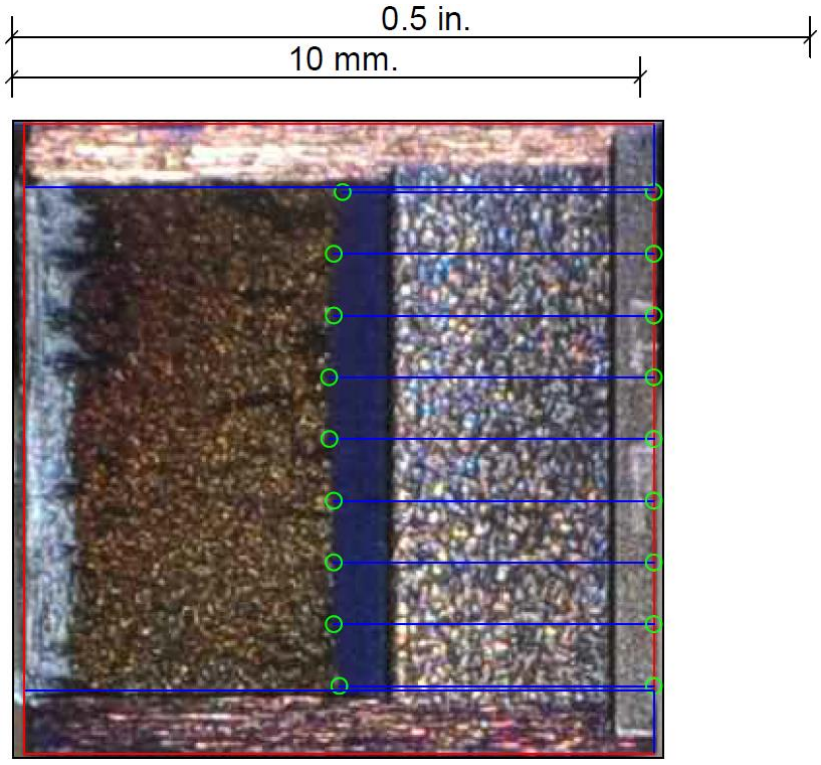

Figure F-138. Specimen H22' Fracture Surface

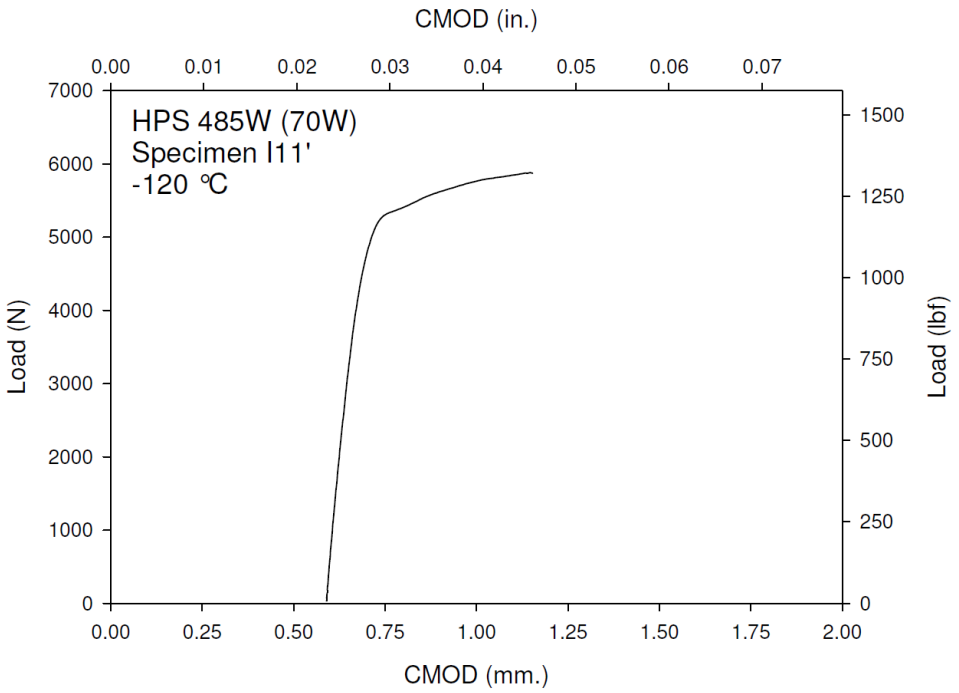

Figure F-139. Specimen I11' Test Record

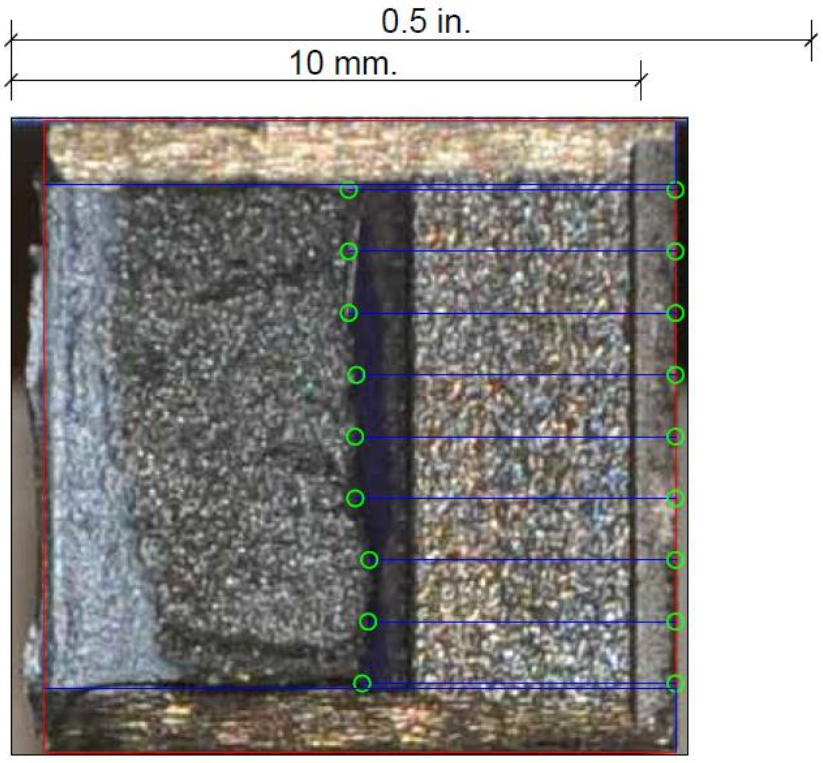

Figure F-140. Specimen I11' Fracture Surface

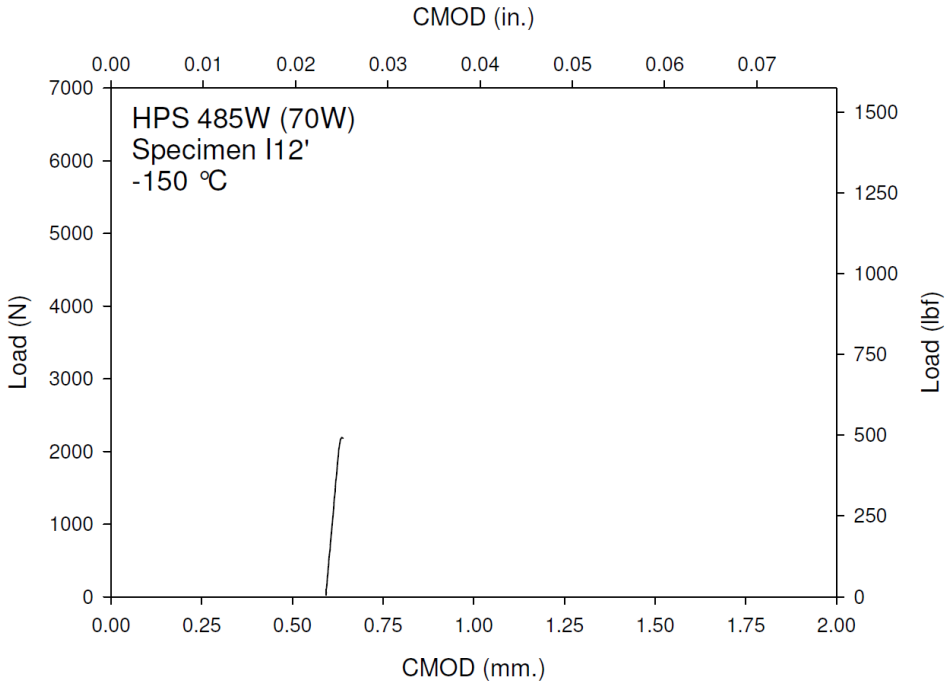

Figure F-141. Specimen I12' Test Record

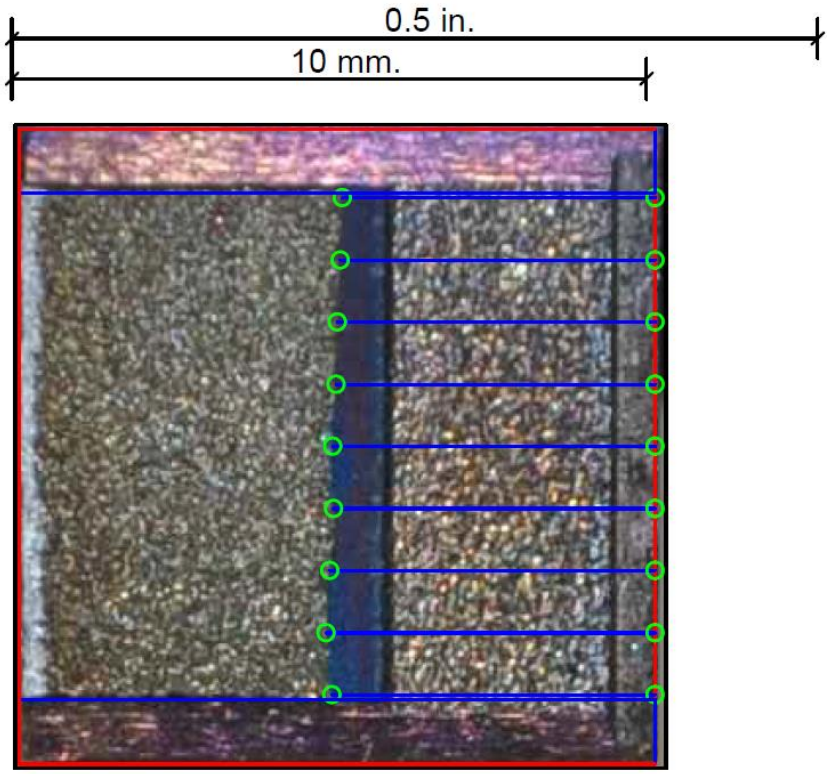

Figure F-142. Specimen I12' Fracture Surface

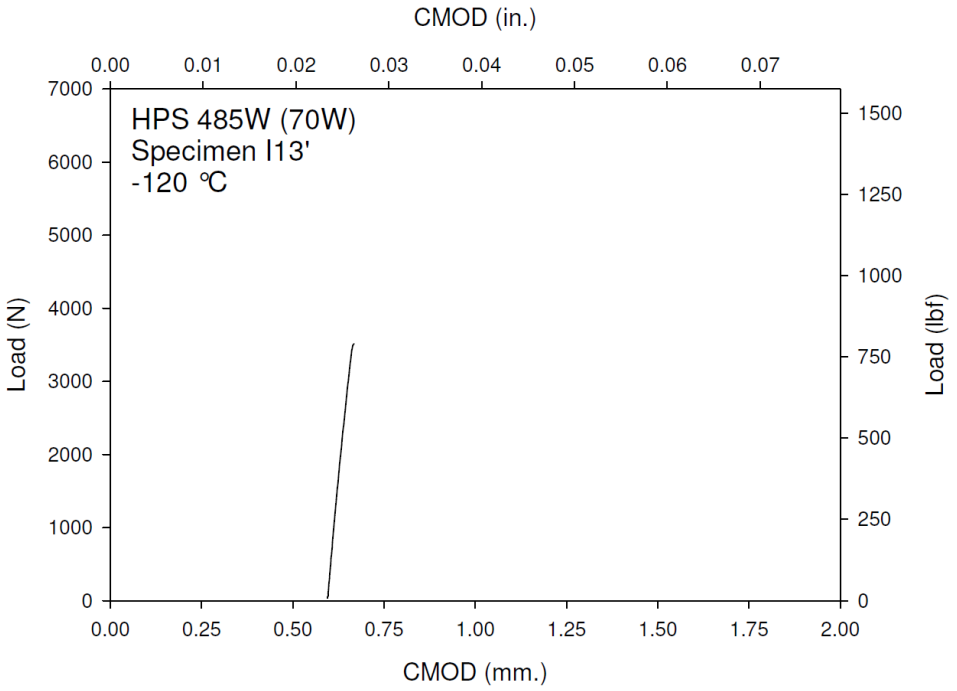

Figure F-143. Specimen I13' Test Record

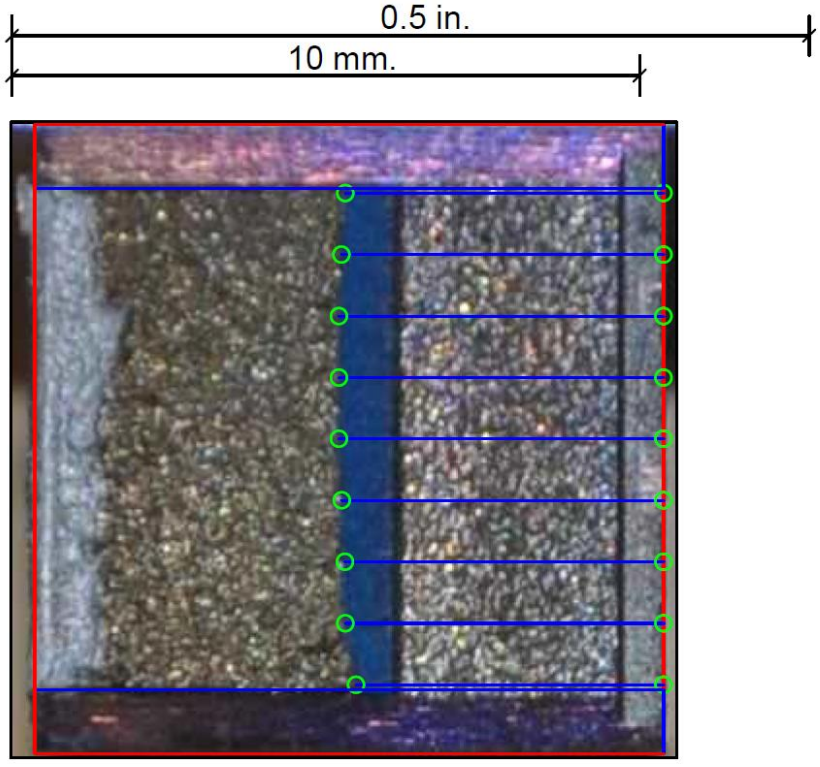

Figure F-144. Specimen I13' Fracture Surface

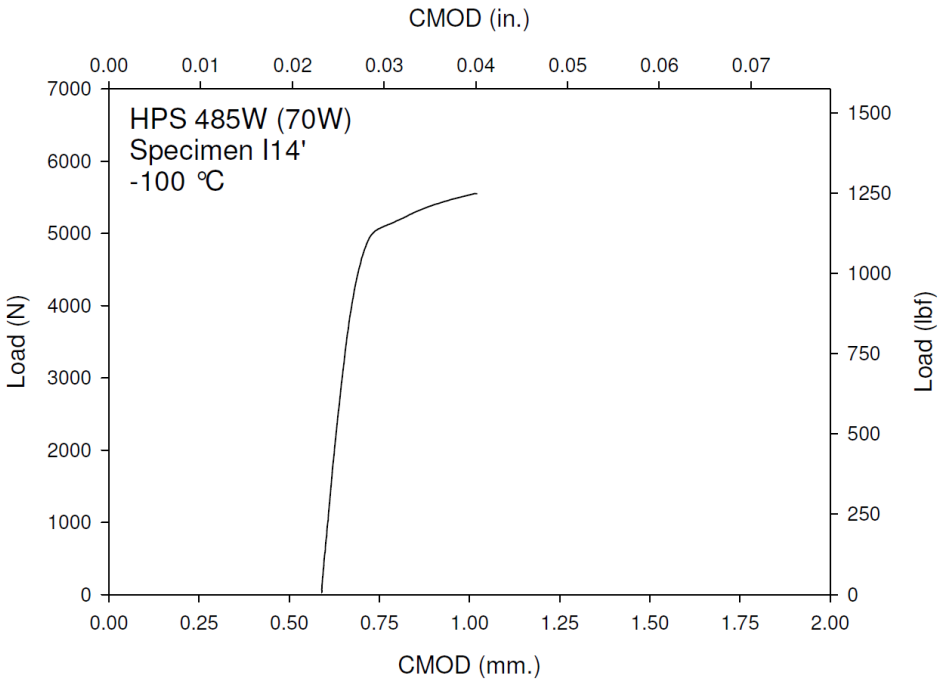

Figure F-145. Specimen I14' Test Record

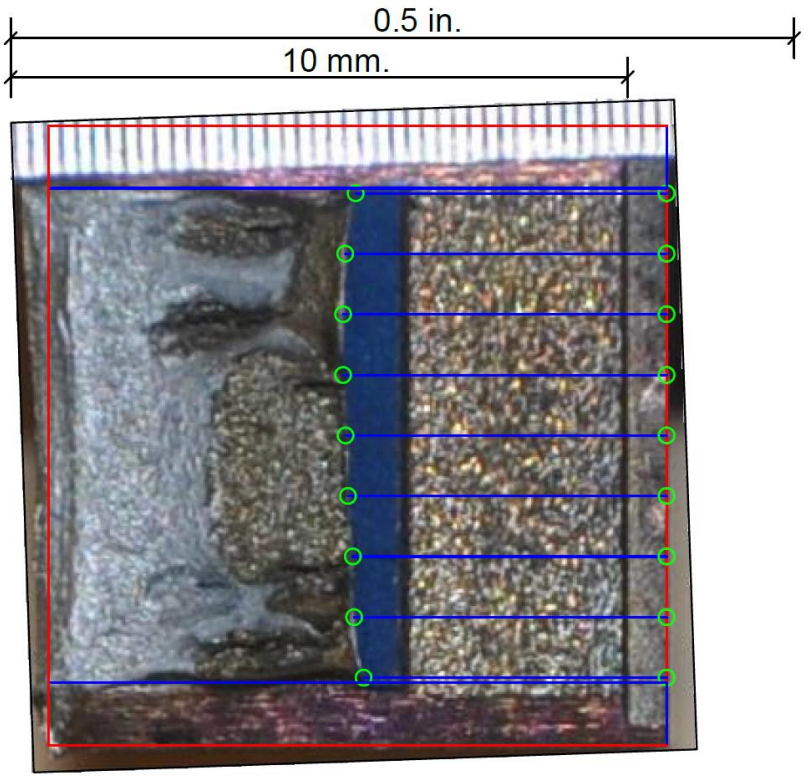

Figure F-146. Specimen I14' Fracture Surface

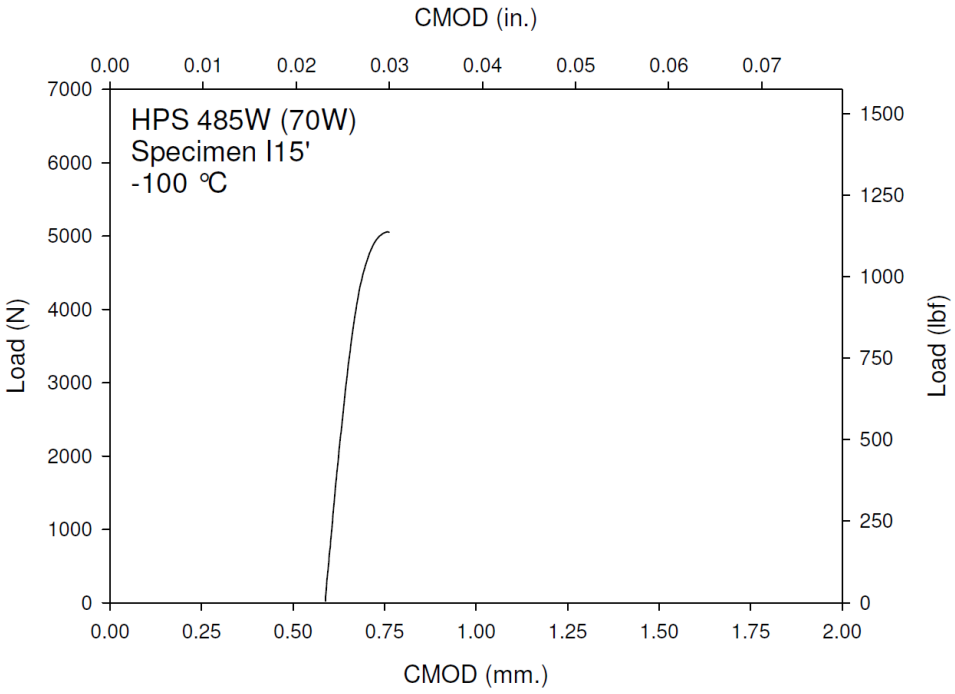

Figure F-147. Specimen I15' Test Record

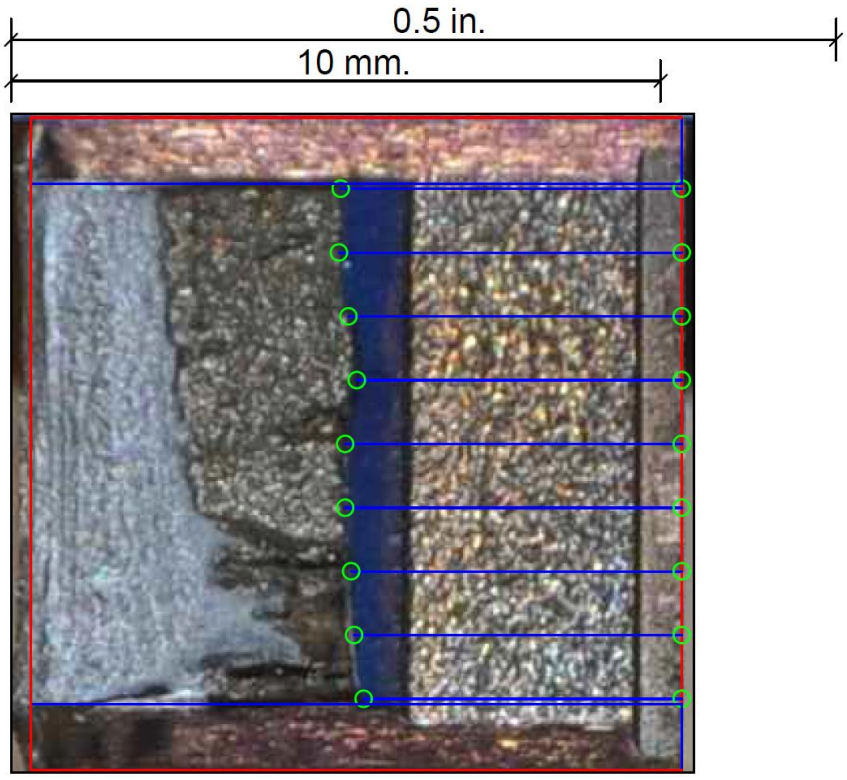

Figure F-148. Specimen I15' Fracture Surface

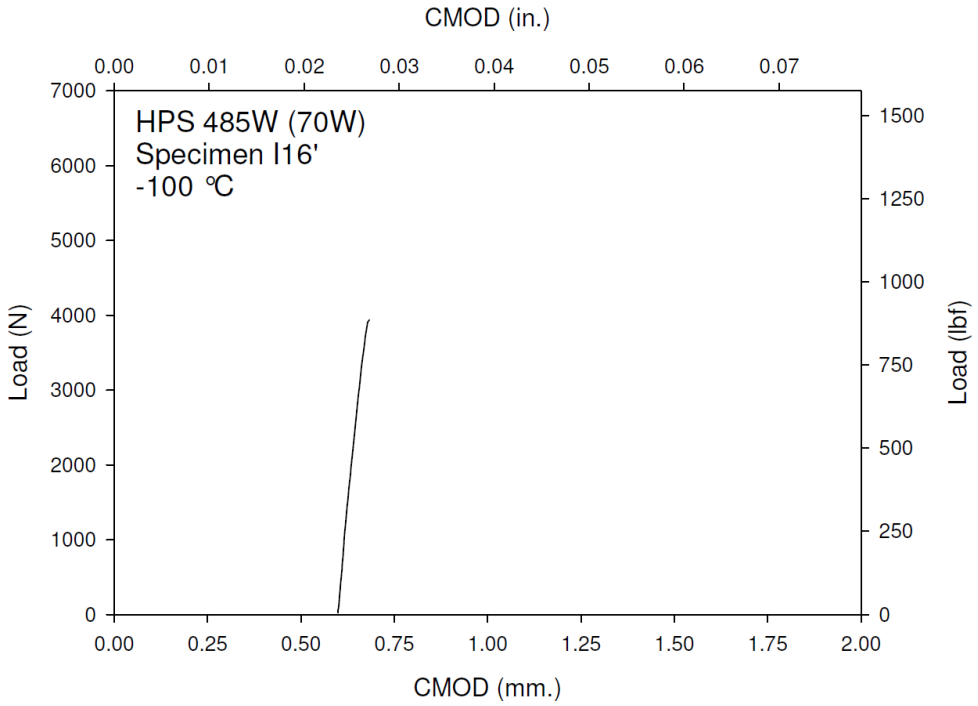

Figure F-149. Specimen I16' Test Record

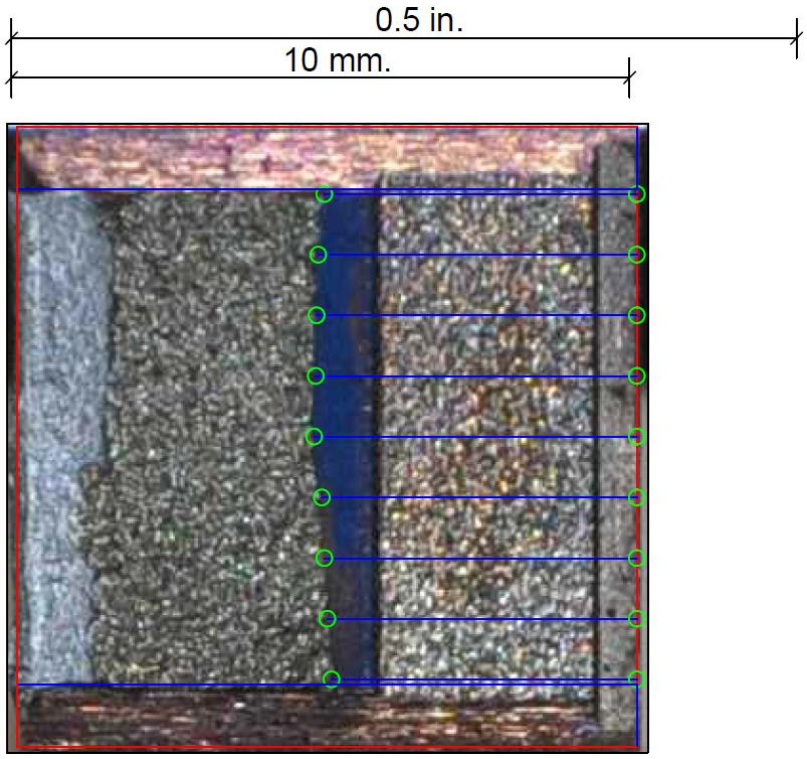

Figure F-150. Specimen I16' Fracture Surface

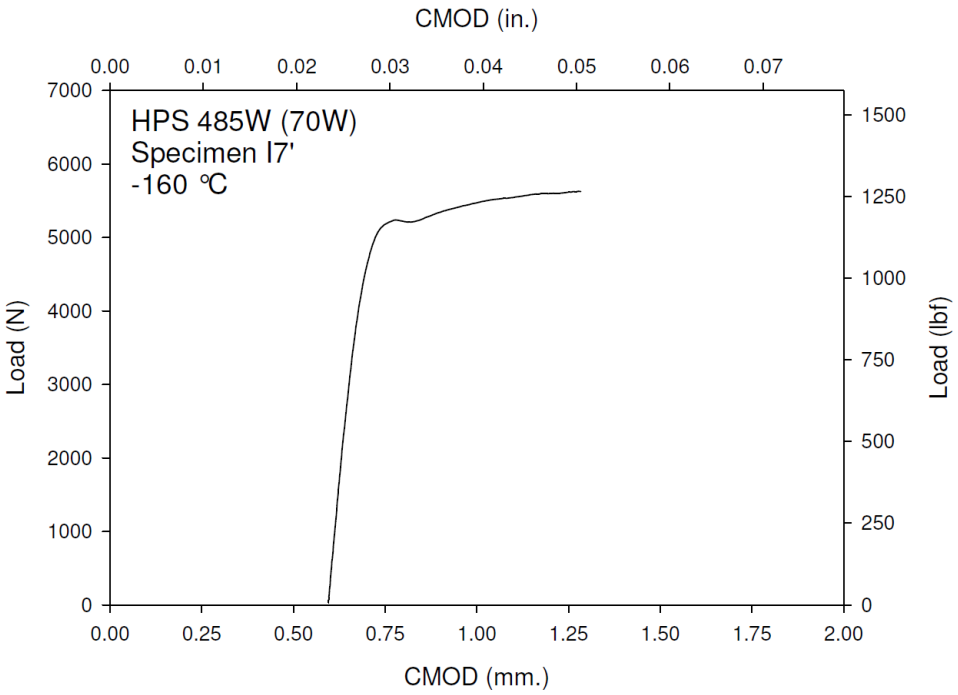

Figure F-151. Specimen I7' Test Record

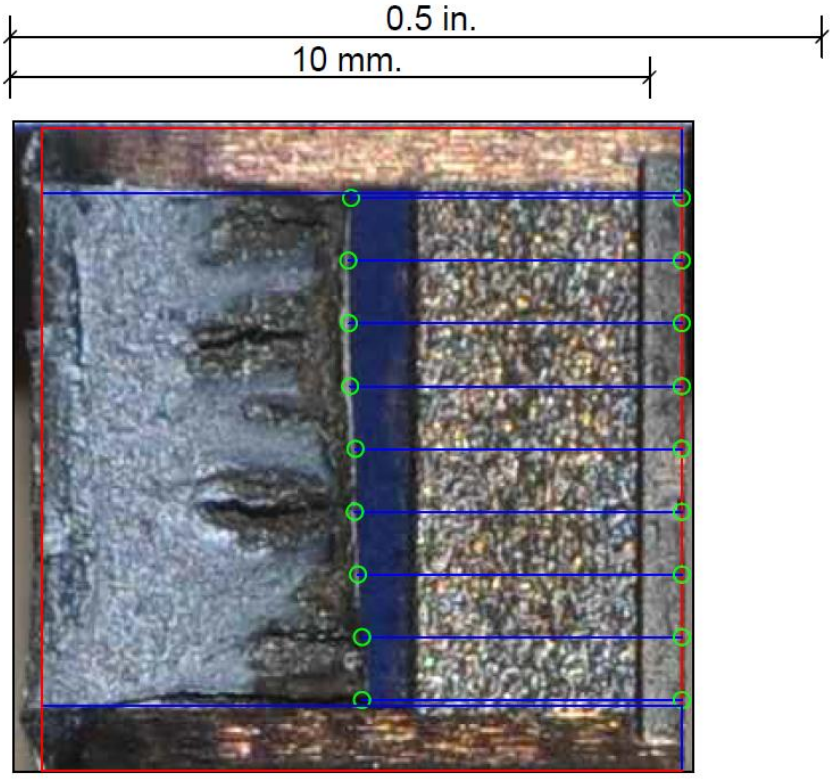

Figure F-152. Specimen I17' Fracture Surface

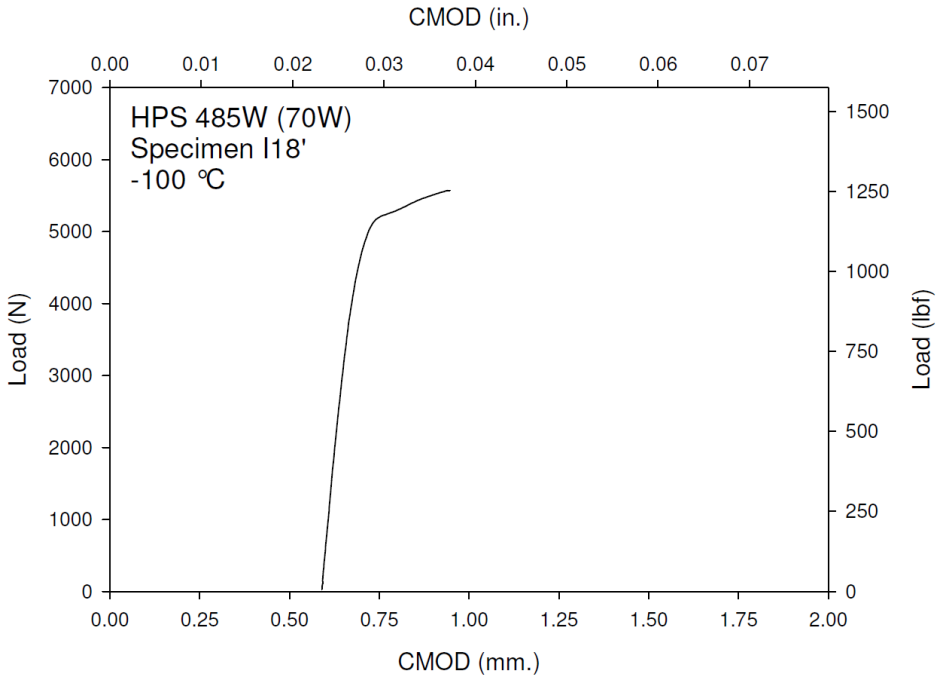

Figure F-153. Specimen I18' Test Record

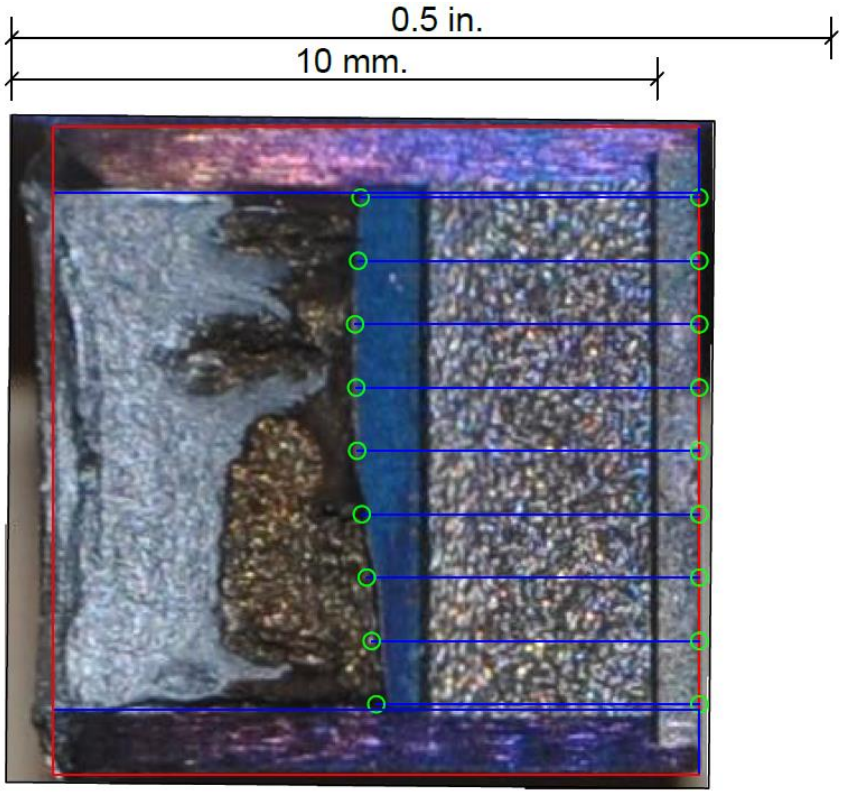

Figure F-154. Specimen I18' Fracture Surface

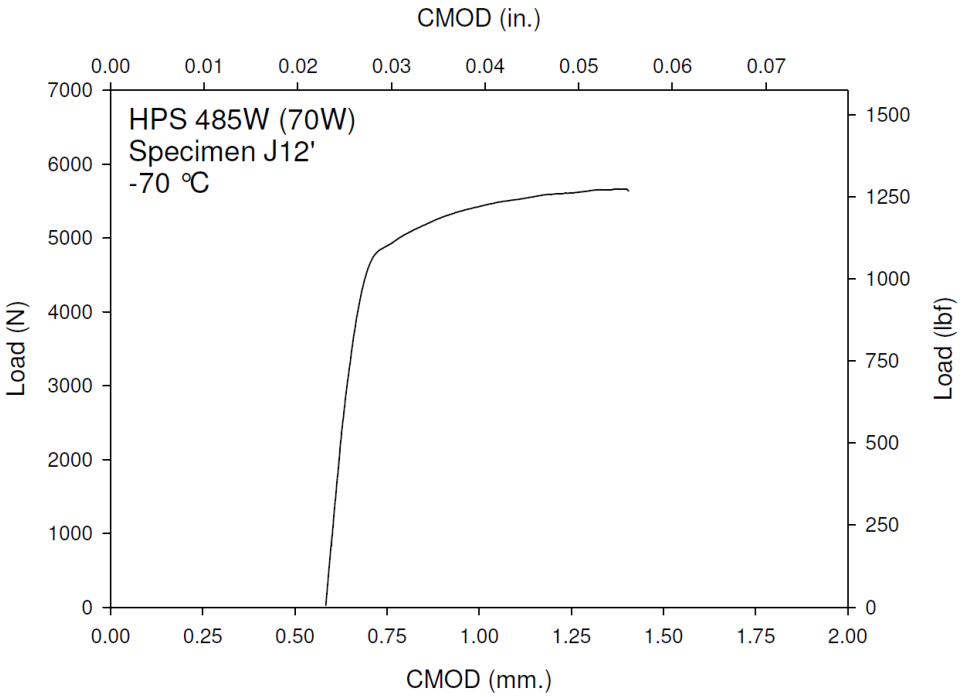

Figure F-155. Specimen J12' Test Record

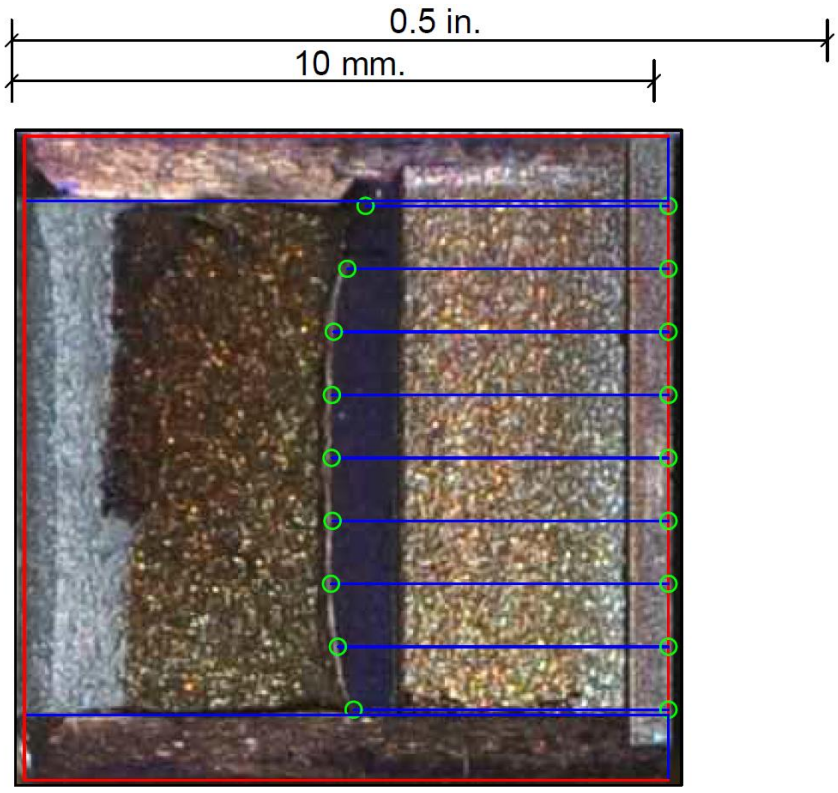

Figure F-156. Specimen J12' Fracture Surface

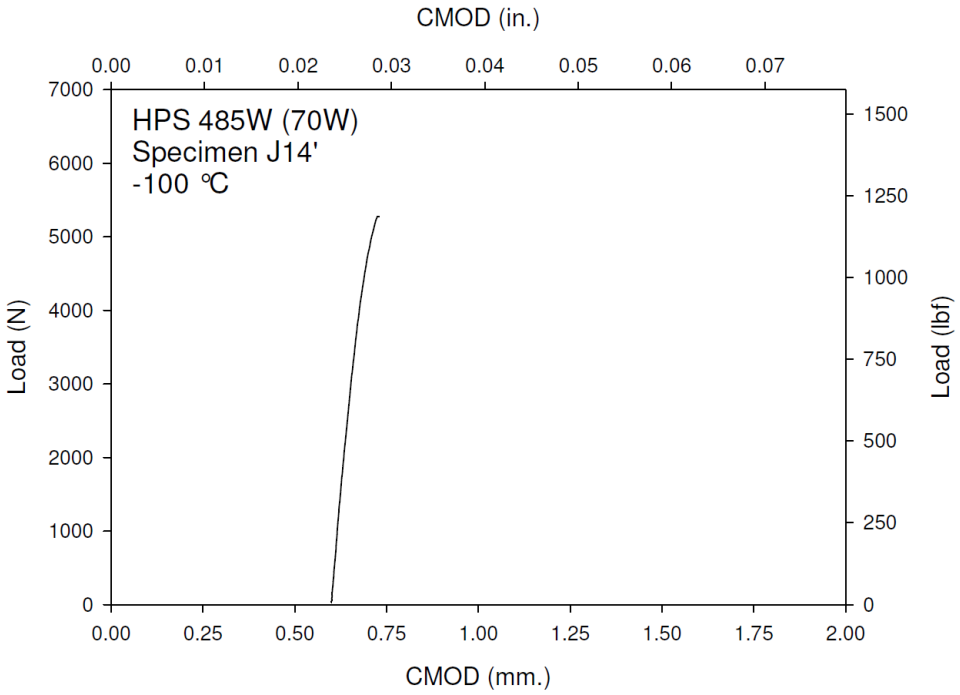

Figure F-157. Specimen J14' Test Record

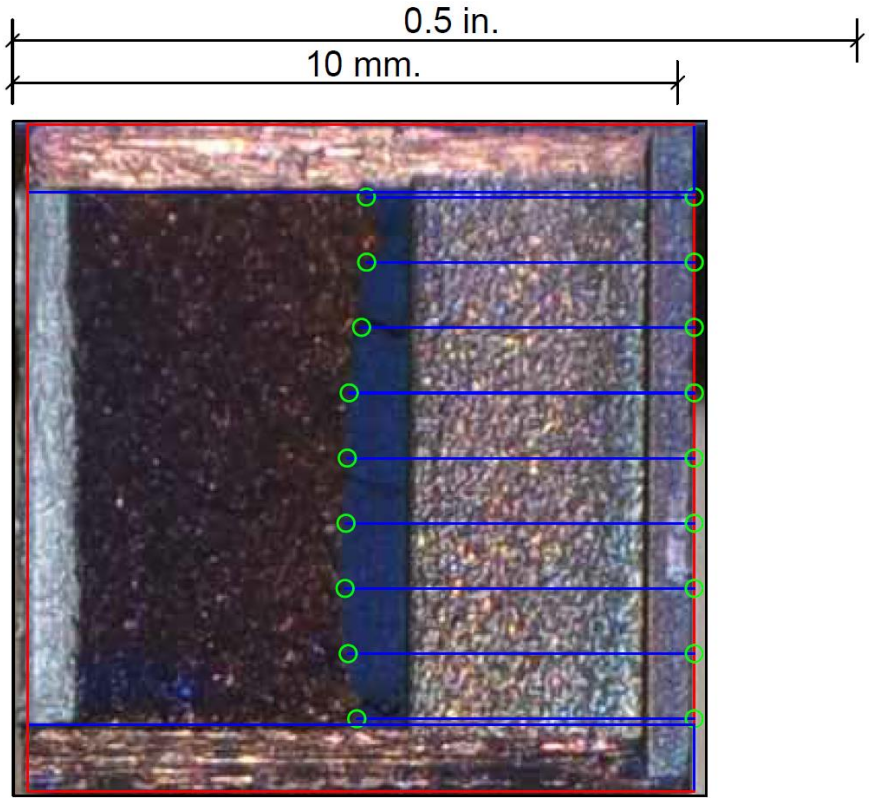

Figure F-158. Specimen J14' Fracture Surface

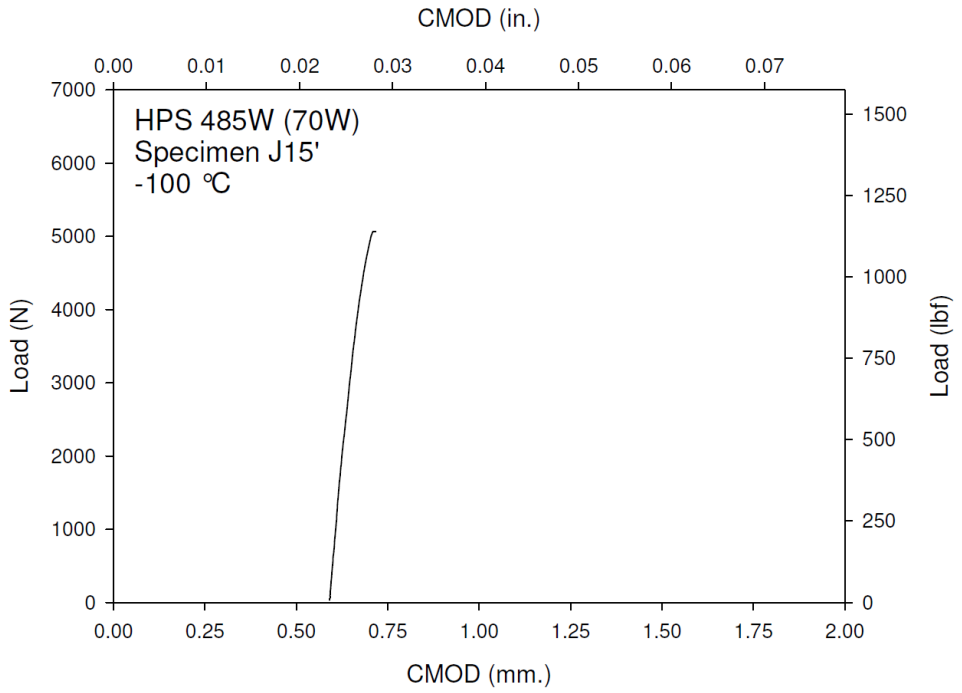

Figure F-159. Specimen J15' Test Record

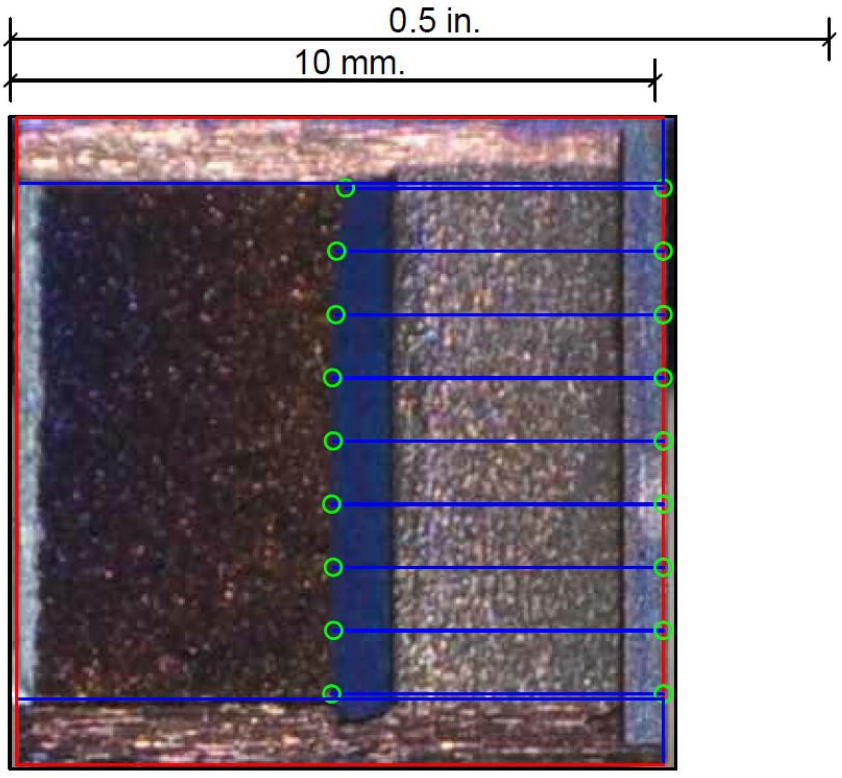

Figure F-160. Specimen J15' Fracture Surface

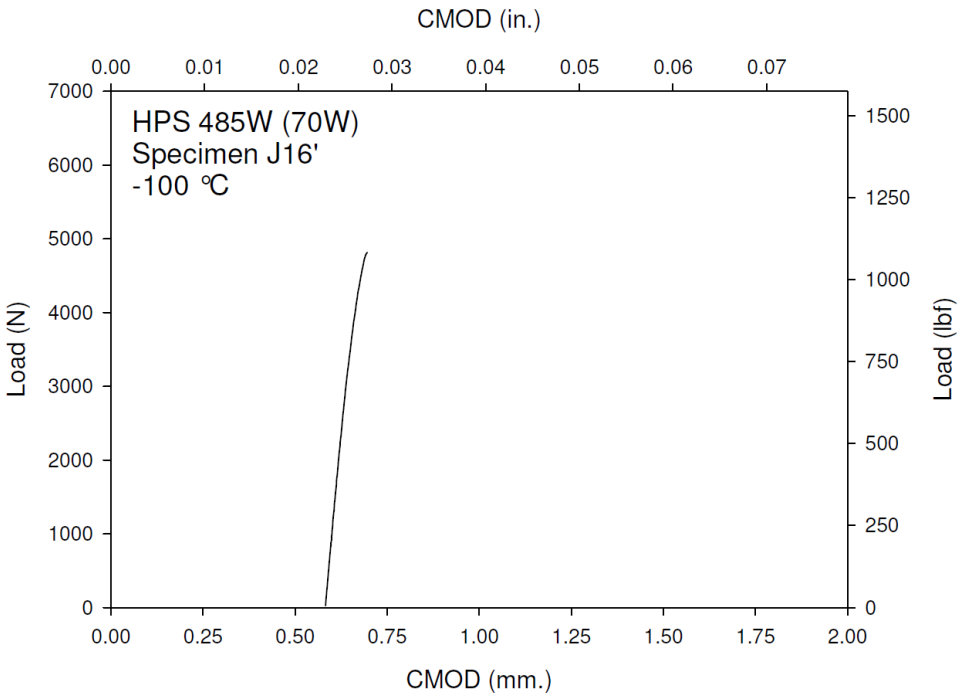

Figure F-161. Specimen J16' Test Record

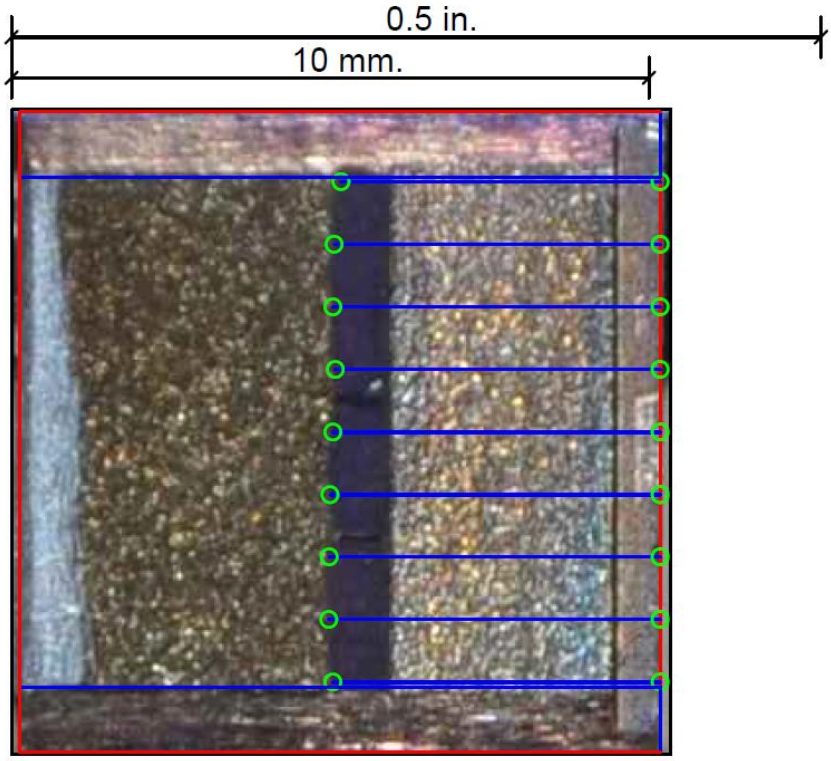

Figure F-162. Specimen J16' Fracture Surface

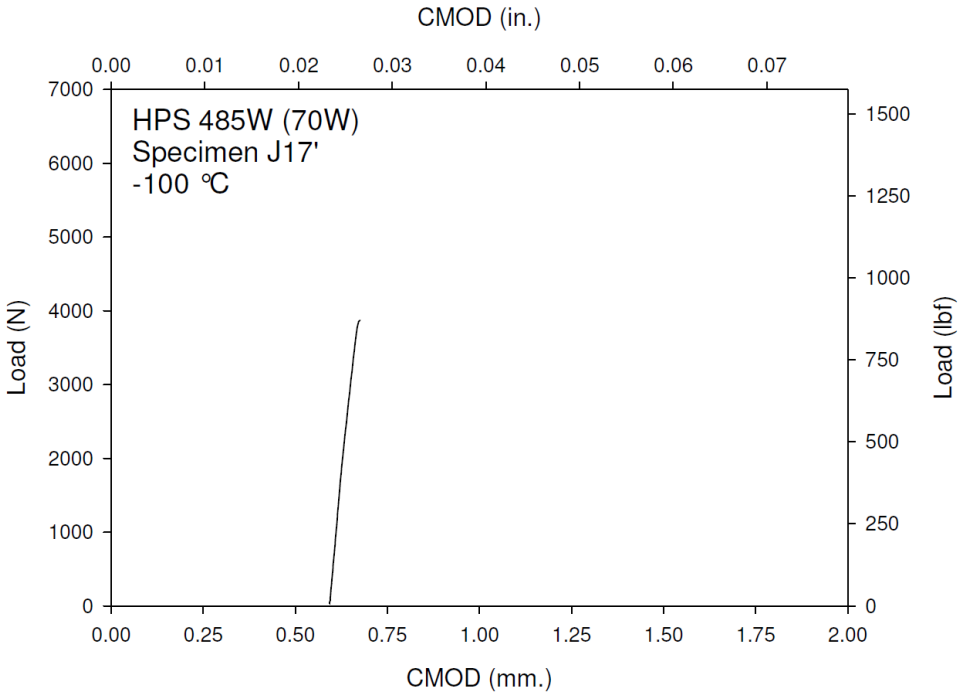

Figure F-163. Specimen J17' Test Record

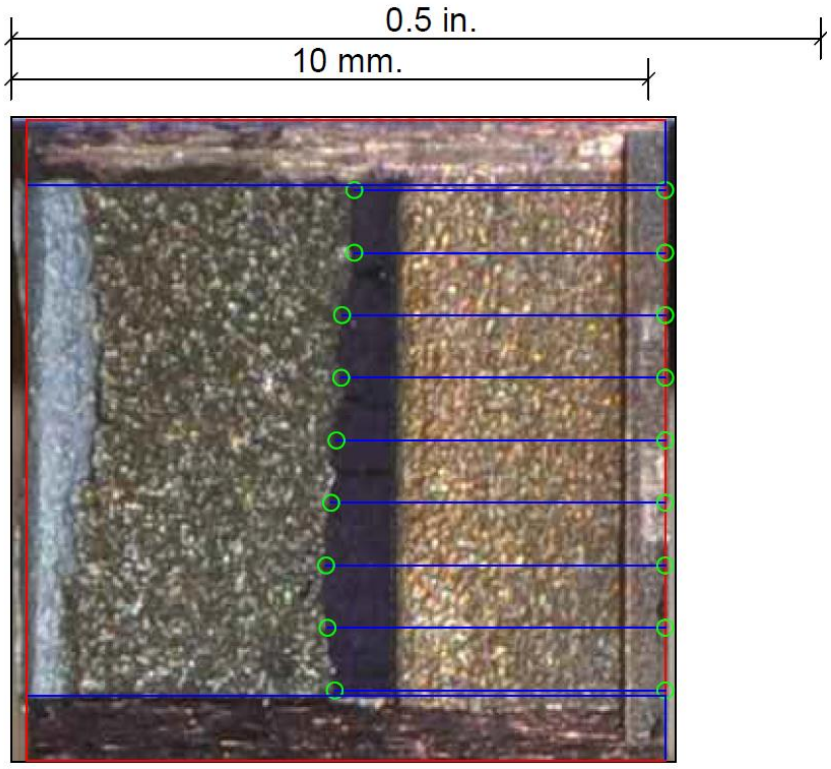

Figure F-164. Specimen J17' Fracture Surface

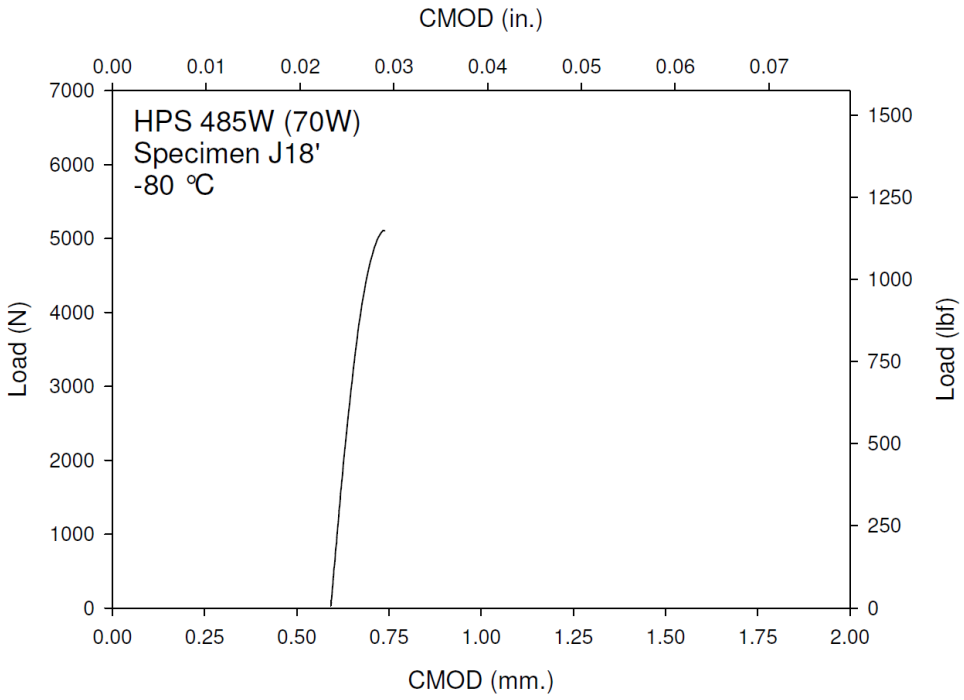

Figure F-165. Specimen J18' Test Record

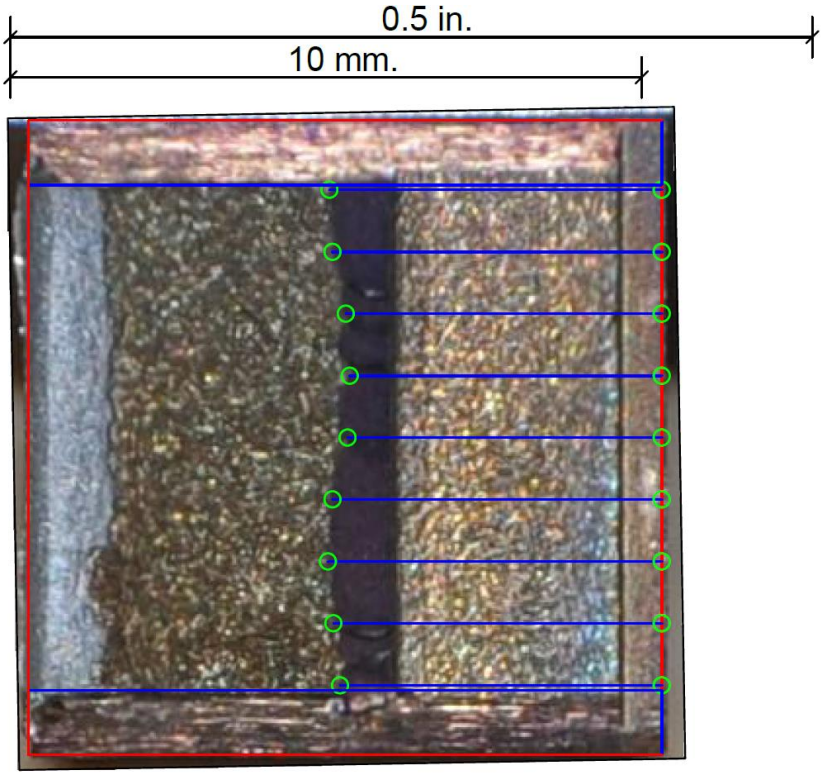

Figure F-166. Specimen J18' Fracture Surface

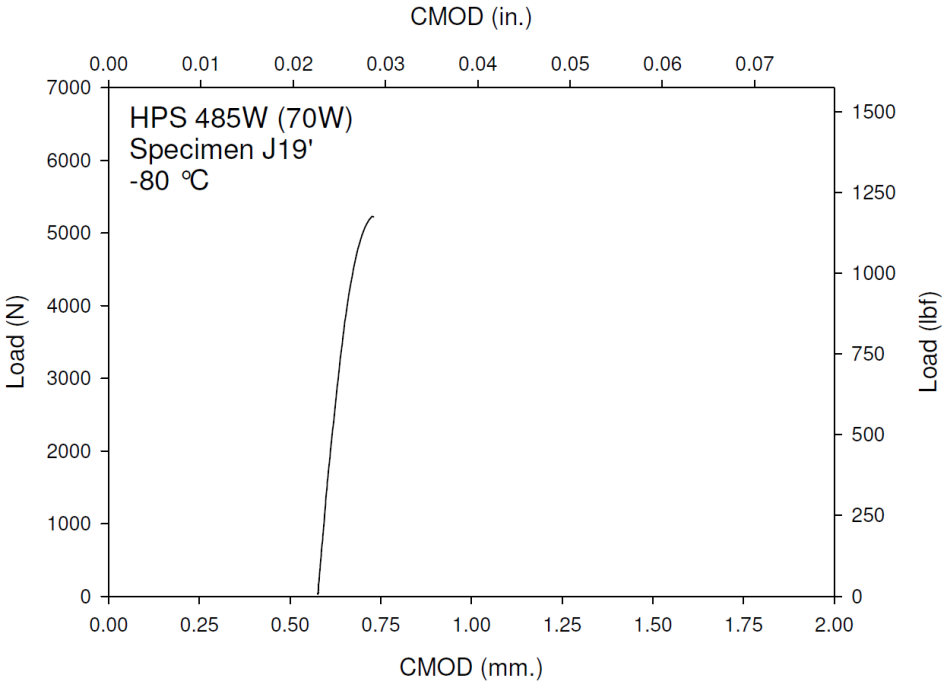

Figure F-167. Specimen J19' Test Record

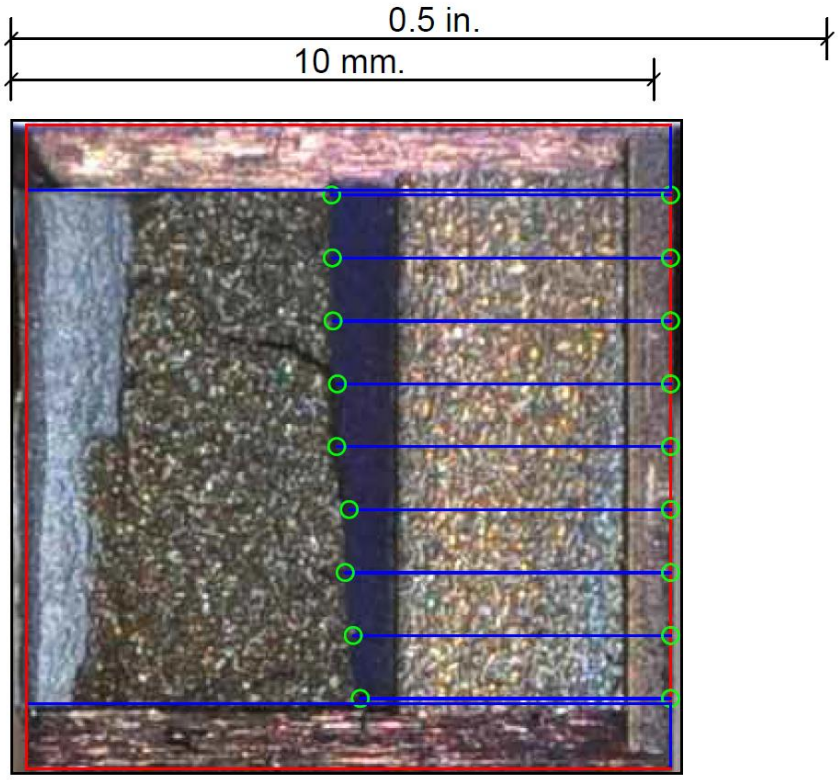

Figure F-168. Specimen J19' Fracture Surface

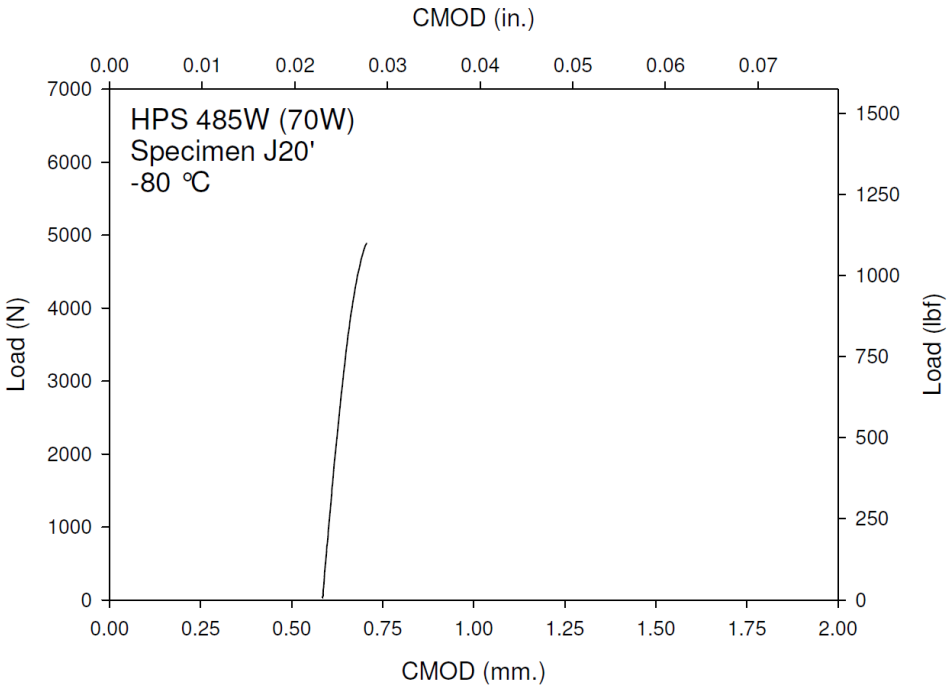

Figure F-169. Specimen J20' Test Record

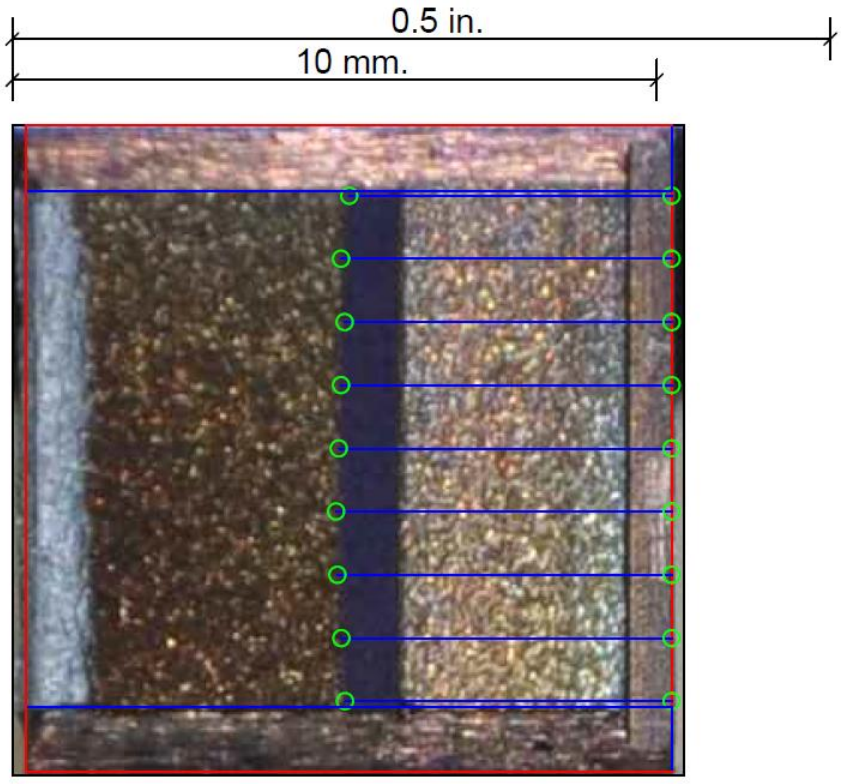

Figure F-170. Specimen J20' Fracture Surface

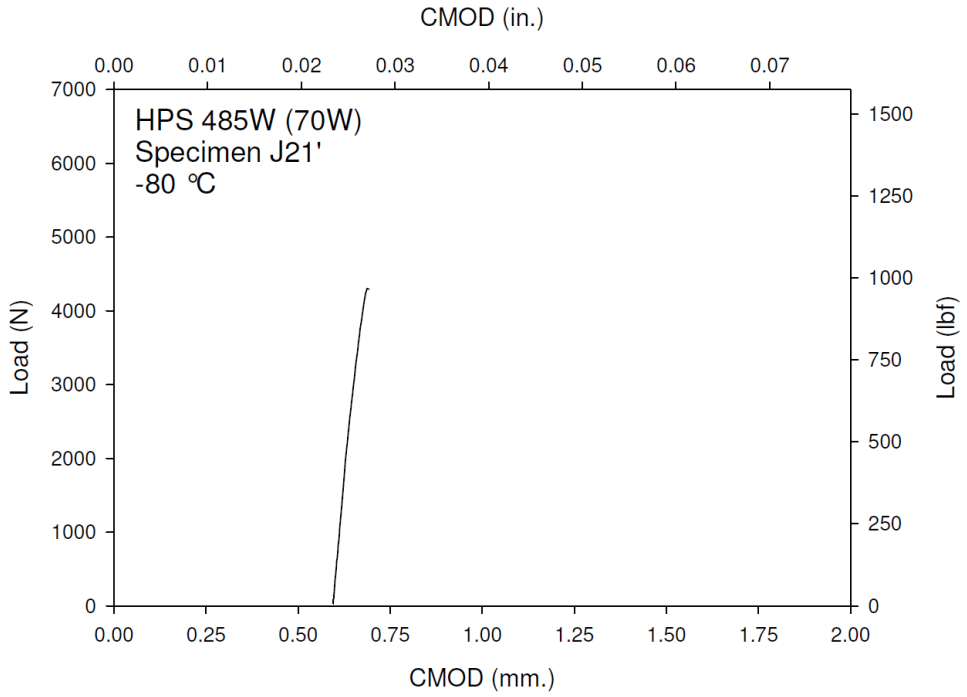

Figure F-171. Specimen J21' Test Record

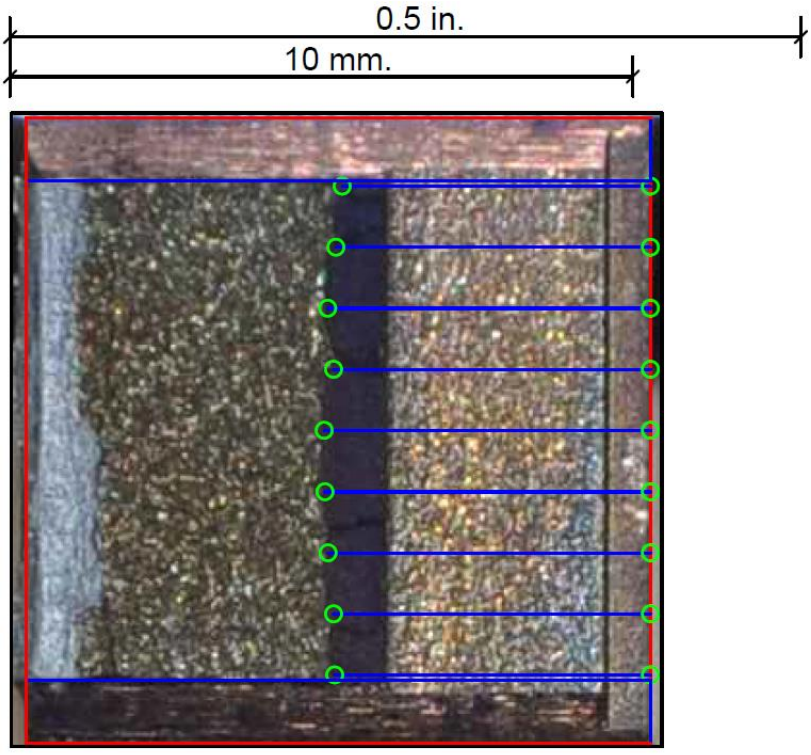

Figure F-172. Specimen J21' Fracture Surface

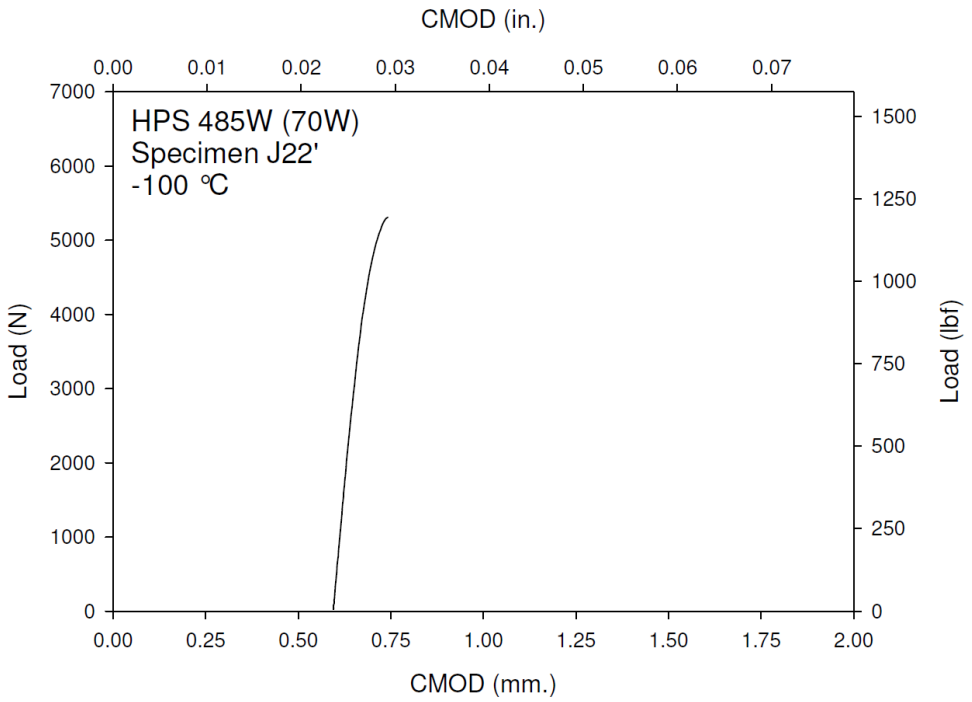

Figure F-173. Specimen J22' Test Record

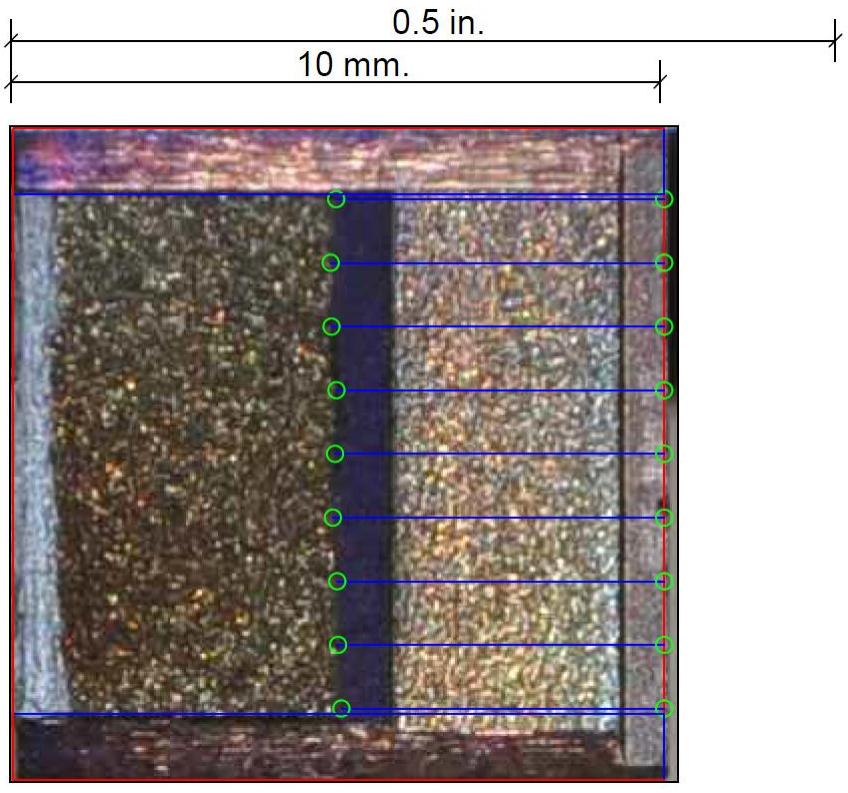

Figure F-174. Specimen J22' Fracture Surface

APPENDIX G: Tabulated HPS Dynamic Fracture Toughness

Table G-1. Dynamic Specimen Information for Plate A, HPS 485W, 25.4 mm.

Specimen ID	W		a_o		B		B_N	
	mm.	in.	mm.	in.	mm.	in.	mm.	in.
A11'	10.01	0.3941	5.05	0.199	10.02	0.3945	8.00	0.3152
A12'	10.01	0.3941	5.09	0.200	10.01	0.3941	8.00	0.3152
A13'	10.01	0.3941	5.07	0.200	10.01	0.3941	8.00	0.3152
A14'	10.01	0.3941	5.08	0.200	10.01	0.3941	8.00	0.3152
A15'	10.02	0.3945	5.13	0.202	10.01	0.3941	8.00	0.3152
A16'	10.02	0.3945	5.09	0.200	10.01	0.3941	8.00	0.3152
A17'	10.01	0.3941	5.13	0.202	10.01	0.3941	8.00	0.3152
A18'	10.01	0.3941	5.12	0.202	10.01	0.3941	8.00	0.3152
A19'	10.01	0.3941	5.14	0.202	10.01	0.3941	8.00	0.3152
A20'	10.00	0.3937	5.10	0.201	10.01	0.3941	8.00	0.3152
A21'	10.01	0.3941	5.07	0.200	10.01	0.3941	8.00	0.3152

Table G-2. Dynamic Test Information for Plate A, HPS 485W, 25.4 mm.

Specimen ID	Test Temperature		Test Result, K_{Jc}		Valid?	Censored?	1T K_{Jc}		Test Rate	
	°C	°F	MPa√m	ksi√in			MPa√m	ksi√in	MPa√m/sec	ksi√in/sec
A11'	-120	-184	131.3	119.5	Yes	No	108.2	98.5	2734	2488
A12'	-120	-184	133.5	121.5	Yes	No	109.9	100.0	2641	2403
A13'	-120	-184	63.5	57.8	Yes	No	54.5	49.6	4326	3937
A14'	-120	-184	101.6	92.5	Yes	No	84.7	77.0	3181	2895
A15'	-120	-184	43.0	39.1	Yes	No	38.2	34.8	5434	4945
A16'	-120	-184	105.1	95.6	Yes	No	87.4	79.6	3177	2891
A17'	-120	-184	116.9	106.4	Yes	No	96.8	88.1	2871	2613
A18'	-120	-184	120.0	109.2	Yes	No	99.2	90.3	2875	2616
A19'	-100	-148	159.0	144.7	No	No	130.1	118.4	2378	2164
A20'	-100	-148	257.5	234.3	Yes	Yes	143.5	130.6	1398	1272
A21'	-100	-148	158.7	144.4	Yes	No	129.9	118.2	2307	2099

Table G-3. Dynamic Specimen Information for Plate C, HPS 690W, 19 mm.

Specimen ID	W		a_o		B		B_N	
	mm.	in.	mm.	in.	mm.	in.	mm.	in.
C11'	10.02	0.3945	5.11	0.201	10.03	0.3949	8.00	0.3152
C12'	10.02	0.3945	5.12	0.202	10.03	0.3949	8.00	0.3152
C13'	10.03	0.3949	5.08	0.200	10.03	0.3949	8.00	0.3152
C14'	10.01	0.3941	5.08	0.200	10.02	0.3945	8.00	0.3152
C15'	10.02	0.3945	5.10	0.201	10.02	0.3945	8.00	0.3152
C16'	10.02	0.3945	5.09	0.200	10.03	0.3949	8.00	0.3152
C17'	10.01	0.3941	5.08	0.200	10.02	0.3945	8.00	0.3152
C19'	10.02	0.3945	5.10	0.201	10.01	0.3941	8.00	0.3152

Table G-4. Dynamic Test Information for Plate C, HPS 690W, 19 mm.

Specimen ID	Test Temperature		Test Result, K_{Jc}		Valid?	Censored?	1T K_{Jc}		Test Rate	
	°C	°F	MPa√m	ksi√in			MPa√m	ksi√in	MPa√m/sec	ksi√in/sec
C11'	-34	-29	200.0	182.0	Yes	Yes	149.3	135.9	1973	1795
C12'	-51	-60	128.1	116.6	Yes	No	105.7	96.2	2724	2479
C13'	-51	-60	84.9	77.3	Yes	No	71.4	65.0	3649	3321
C14'	-51	-60	129.3	117.7	Yes	No	106.6	97.0	2701	2458
C15'	-51	-60	117.4	106.8	Yes	No	97.2	88.4	2913	2651
C16'	-51	-60	110.9	100.9	Yes	No	92.1	83.8	2980	2712
C17'	-51	-60	135.5	123.3	Yes	No	111.5	101.5	2616	2381
C19'	-51	-60	167	152.2	Yes	No	136.7	124.4	2196	1998

Table G-5. Dynamic Specimen Information for Plate D, HPS 485W, 63.5 mm.

Specimen ID	W		a_o		B		B_N	
	mm.	in.	mm.	in.	mm.	in.	mm.	in.
D21'	10.01	0.394	5.36	0.211	10.02	0.3945	8.00	0.3152
D22'	10.03	0.395	5.38	0.212	10.02	0.3945	8.00	0.3152
D23'	10.01	0.394	5.06	0.199	10.00	0.3937	8.00	0.3152
D24'	10.00	0.394	5.05	0.199	10.01	0.3941	8.00	0.3152
D25'	10.00	0.394	5.10	0.201	10.01	0.3941	8.00	0.3152
D26'	Specimen Did Not Fracture- No Test							
D27'	10.00	0.394	5.11	0.201	10.02	0.3945	8.00	0.3152
D28'	10.00	0.394	5.07	0.200	10.01	0.3941	8.00	0.3152
D29'	10.02	0.394	5.14	0.202	10.01	0.3941	8.00	0.3152
D30'	10.01	0.394	5.07	0.200	10.00	0.3937	8.00	0.3152
D31'	10.01	0.394	5.05	0.199	10.00	0.3937	8.00	0.3152
D32'	10.01	0.394	5.10	0.201	10.01	0.3941	8.00	0.3152
D33'	10.01	0.394	5.11	0.201	10.01	0.3941	8.00	0.3152
D34'	10.01	0.394	5.06	0.199	10.00	0.3937	8.00	0.3152
D35'	10.02	0.394	5.08	0.200	10.00	0.3937	8.00	0.3152
D36'	10.01	0.394	5.08	0.200	10.01	0.3941	8.00	0.3152
D37'	10.02	0.394	5.09	0.200	10.00	0.3937	8.00	0.3152
D38'	10.02	0.394	5.07	0.200	10.01	0.3941	8.00	0.3152

Table G-6. Dynamic Test Information for Plate D, HPS 485W, 63.5 mm.

Specimen ID	Test Temperature		Test Result, K_{Jc}		Valid?	Censored?	1T K_{Jc}		Test Rate	
	°C	°F	MPa√m	ksi√in			MPa√m	ksi√in	MPa√m/sec	ksi√in/sec
D21'	-100	-148	308.4	280.6	Yes	Yes	129.8	118.1	941	856
D22'	-100	-148	48.5	44.1	Yes	No	42.6	38.8	5100	4641
D23'	-100	-148	47.6	43.3	Yes	No	41.9	38.1	5034	4581
D24'	-70	-94	178.0	162.0	Yes	Yes	128.4	116.8	1893	1723
D25'	-70	-94	370.4	337.1	Yes	Yes	127.7	116.2	318	289
D26'	Specimen Did Not Fracture- No Test									
D27'	-90	-130	151.5	137.9	Yes	No	124.2	113.0	2294	2088
D28'	-90	-130	318.1	289.5	Yes	Yes	131.6	119.7	940	855
D29'	-90	-130	358.5	326.2	Yes	Yes	130.9	119.1	722	657
D30'	-90	-130	74.0	67.3	Yes	No	62.8	57.1	3984	3625
D31'	-100	-148	343.0	312.1	Yes	Yes	133.9	121.8	766	697
D32'	-115	-175	110.9	100.9	Yes	No	92.0	83.7	2950	2685
D33'	-115	-175	251.3	228.7	Yes	Yes	136.3	124.0	1348	1227
D34'	-115	-175	59.3	54.0	Yes	No	51.1	46.5	4495	4090
D35'	-115	-175	46.9	42.7	Yes	No	41.3	37.6	5231	4760
D36'	-115	-175	117.6	107.0	Yes	No	97.3	88.6	2824	2570
D37'	-130	-202	49.5	45.0	Yes	No	43.4	39.5	4918	4475
D38'	-130	-202	65.9	60.0	Yes	No	56.4	51.3	4260	3877

Table G-7. Dynamic Specimen Information for Plate E, HPS 690W, 38.1 mm.

Specimen ID	W		a_o		B		B_N	
	mm.	in.	mm.	in.	mm.	in.	mm.	in.
E22'	Specimen Reserved							
E23'	Specimen Used to Check Dynamic Test Method							
E24'	10.03	0.395	5.34	0.210	10.03	0.3949	8.00	0.3152
E25'	10.02	0.394	5.23	0.206	10.03	0.3949	8.00	0.3152
E26'	10.02	0.394	5.30	0.209	10.03	0.3949	8.00	0.3152
E27'	10.03	0.395	5.31	0.209	10.03	0.3949	8.00	0.3152
E28'	10.03	0.395	5.32	0.209	10.02	0.3945	8.00	0.3152
E29'	10.02	0.394	5.32	0.209	10.01	0.3941	8.00	0.3152
E30'	10.02	0.394	5.29	0.208	10.02	0.3945	8.00	0.3152
E31'	10.03	0.395	5.28	0.208	10.02	0.3945	8.00	0.3152
E32'	10.03	0.395	5.25	0.207	10.03	0.3949	8.00	0.3152
E33'	10.03	0.395	5.28	0.208	10.01	0.3941	8.00	0.3152
E34'	10.03	0.395	5.28	0.208	10.03	0.3949	8.00	0.3152
E35'	Specimen Used to Check Pre-Crack Procedure							
E36'	10.03	0.395	5.09	0.200	10.03	0.3949	8.00	0.3152
E37'	10.03	0.395	5.12	0.202	10.02	0.3945	8.00	0.3152

Table G-8. Dynamic Test Information for Plate E, HPS 690W, 38.1 mm.

Specimen ID	Test Temperature		Test Result, K_{Jc}		Valid?	Censored?	1T K_{Jc}		Test Rate	
	°C	°F	MPa√m	ksi√in			MPa√m	ksi√in	MPa√m/sec	ksi√in/sec
E22'	Specimen Reserved									
E23'	Specimen Used to Check Dynamic Test Method									
E24'	-100	-148	71.8	65.3	Yes	No	61.1	55.6	3838	3493
E25'	-100	-148	67.7	61.6	Yes	No	57.8	52.6	3998	3638
E26'	-100	-148	82.9	75.4	Yes	No	69.9	63.6	3790	3449
E27'	-100	-148	51.4	46.8	Yes	No	44.9	40.9	4737	4311
E28'	-51	-60	154.4	140.5	Yes	No	126.5	115.1	2345	2134
E29'	-51	-60	277.4	252.4	Yes	Yes	140.1	127.5	1241	1129
E30'	-51	-60	116.9	106.4	Yes	No	96.8	88.1	2806	2553
E31'	-70	-94	90.7	82.5	Yes	No	76.0	69.2	3742	3405
E32'	-70	-94	94.3	85.8	Yes	No	78.9	71.8	3302	3005
E33'	-70	-94	111.9	101.8	Yes	No	92.8	84.5	2939	2674
E34'	-70	-94	113.7	103.5	Yes	No	94.3	85.8	2976	2708
E35'	Specimen Used to Check Pre-Crack Procedure									
E36'	-70	-94	78.6	71.5	Yes	No	66.5	60.5	3642	3314
E37'	-70	-94	104.2	94.8	Yes	No	86.7	78.9	3210	2921

Table G-9. Dynamic Specimen Information for Plate F, HPS 690W, 50.8 mm.

Specimen ID	W		a_o		B		B_N	
	mm.	in.	mm.	in.	mm.	in.	mm.	in.
F21'	10.03	0.395	5.35	0.211	10.03	0.3949	8.00	0.3152
F22'	10.03	0.395	5.38	0.212	10.03	0.3949	8.00	0.3152
F23'	Specimen Used to Check Pre-Crack Procedure							
F24'	10.03	0.395	5.14	0.202	10.03	0.3949	8.00	0.3152
F25'	10.01	0.394	5.08	0.200	10.00	0.3937	8.00	0.3152
F26'	10.01	0.394	5.20	0.205	10.01	0.3941	8.00	0.3152
F27'	10.02	0.394	5.18	0.204	10.00	0.3937	8.00	0.3152
F28'	10.02	0.394	5.15	0.203	10.00	0.3937	8.00	0.3152
F29'	10.00	0.394	5.10	0.201	10.00	0.3937	8.00	0.3152
F30'	10.00	0.394	5.16	0.203	10.00	0.3937	8.00	0.3152
F31'	10.00	0.394	5.19	0.204	10.02	0.3945	8.00	0.3152
F32'	Specimen Damaged in Machining							
F33'	10.00	0.394	5.07	0.200	10.02	0.3945	8.00	0.3152
F34'	10.00	0.394	5.09	0.200	10.02	0.3945	8.00	0.3152

Table G-10. Dynamic Test Information for Plate F, HPS 690W, 50.8 mm.

Specimen ID	Test Temperature		Test Result, K_{Jc}		Valid?	Censored?	1T K_{Jc}		Test Rate	
	°C	°F	MPa√m	ksi√in			MPa√m	ksi√in	MPa√m/sec	ksi√in/sec
F21'	-51	-60	154.5	140.6	Yes	No	126.6	115.2	2294	2088
F22'	-51	-60	192.9	175.5	Yes	Yes	143.0	130.1	1942	1767
F23'	Specimen Used to Check Pre-Crack Procedure									
F24'	-51	-60	116.0	105.6	Yes	No	96.1	87.5	2875	2616
F25'	-70	-94	112.3	102.2	Yes	No	93.1	84.7	2986	2717
F26'	-70	-94	95.2	86.6	Yes	No	79.6	72.4	3599	3275
F27'	-70	-94	79.0	71.9	Yes	No	66.7	60.7	3558	3238
F28'	-70	-94	96.6	87.9	Yes	No	80.7	73.4	3245	2953
F29'	-70	-94	90.4	82.3	Yes	No	75.8	68.9	3474	3161
F30'	-70	-94	109.6	99.7	Yes	No	91.0	82.8	2929	2665
F31'	-90	-130	64.1	58.3	Yes	No	55.0	50.0	4353	3961
F32'	Specimen Damaged in Machining									
F33'	-90	-130	85.1	77.4	Yes	No	71.6	65.1	3640	3312
F34'	-90	-130	73.9	67.2	Yes	No	62.7	57.1	3857	3510

Table G-11. Dynamic Specimen Information for Plate H, HPS 485W, 31.8 mm.

Specimen ID	W		a_o		B		B_N	
	mm.	in.	mm.	in.	mm.	in.	mm.	in.
H13'	10.02	0.3945	5.09	0.200	10.02	0.3945	8.00	0.3152
H14'	10.02	0.3945	5.10	0.201	10.03	0.3949	8.00	0.3152
H15'	Specimen Did Not Fracture- No Test							
H16'	Specimen Damaged in Machining							
H17'	10.02	0.3945	5.11	0.201	10.02	0.3945	8.00	0.3152
H18'	10.02	0.3945	5.12	0.202	10.02	0.3945	8.00	0.3152
H19'	10.02	0.3945	5.07	0.200	10.02	0.3945	8.00	0.3152
H20'	10.01	0.3941	5.12	0.202	10.02	0.3945	8.00	0.3152
H21'	10.02	0.3945	5.10	0.201	10.02	0.3945	8.00	0.3152
H22'	10.02	0.3945	5.10	0.201	10.01	0.3941	8.00	0.3152

Table G-12. Dynamic Test Information for Plate H, HPS 485W, 31.8 mm.

Specimen ID	Test Temperature		Test Result, K_{Jc}		Valid?	Censored?	1T K_{Jc}		Test Rate	
	°C	°F	MPa√m	ksi√in			MPa√m	ksi√in	MPa√m/sec	ksi√in/sec
H13'	-120	-184	49.9	45.4	Yes	No	43.7	39.8	4647	4229
H14'	-120	-184	41.4	37.7	Yes	No	37.0	33.6	5334	4854
H15'	Specimen Did Not Fracture- No Test									
H16'	Specimen Damaged in Machining									
H17'	-100	-148	141.6	128.9	Yes	No	116.4	105.9	2480	2257
H18'	-100	-148	237.5	216.1	Yes	Yes	137.1	124.7	1463	1331
H19'	-120	-184	52.4	47.7	Yes	No	45.7	41.6	4742	4315
H20'	-100	-148	224.3	204.1	Yes	Yes	136.9	124.6	1603	1459
H21'	-120	-184	89.2	81.2	Yes	No	74.8	68.1	3483	3170
H22'	-120	-184	58.7	53.4	Yes	No	50.7	46.1	4559	4149

Table G-13. Dynamic Specimen Information for Plate I, HPS 485W, 31.8 mm.

Specimen ID	W		a_o		B		B_N	
	mm.	in.	mm.	in.	mm.	in.	mm.	in.
I11'	10.03	0.3949	5.05	0.199	10.02	0.3945	8.00	0.3152
I12'	10.02	0.3945	5.06	0.199	10.02	0.3945	8.00	0.3152
I13'	10.02	0.3945	5.11	0.201	10.04	0.3953	8.00	0.3152
I14'	10.02	0.3945	5.15	0.203	10.03	0.3949	8.00	0.3152
I15'	10.01	0.3941	5.12	0.202	10.03	0.3949	8.00	0.3152
I16'	10.02	0.3945	5.10	0.201	10.03	0.3949	8.00	0.3152
I17'	10.02	0.3945	5.12	0.202	10.03	0.3949	8.00	0.3152
I18'	10.01	0.3941	5.23	0.206	10.03	0.3949	8.00	0.3152

Table G-14. Dynamic Test Information for Plate I, HPS 485W, 31.8 mm.

Specimen ID	Test Temperature		Test Result, K_{Jc}		Valid?	Censored?	1T K_{Jc}		Test Rate	
	°C	°F	MPa√m	ksi√in			MPa√m	ksi√in	MPa√m/sec	ksi√in/sec
I11'	-120	-184	212.4	193.3	Yes	Yes	140.7	128.0	1637	1490
I12'	-150	-238	31.5	28.7	Yes	No	29.1	26.5	6625	6029
I13'	-120	-184	48.2	43.9	Yes	No	42.4	38.5	5223	4753
I14'	-100	-148	179.1	163.0	Yes	Yes	134.1	122.0	1922	1749
I15'	-100	-148	99.8	90.8	Yes	No	83.3	75.8	3167	2882
I16'	-100	-148	55.2	50.2	Yes	No	47.9	43.6	4642	4224
I17'	-100	-148	237.8	216.4	Yes	Yes	134.5	122.4	1446	1316
I18'	-100	-148	164.1	149.3	Yes	Yes	132.9	120.9	2135	1943

Table G-15. Dynamic Specimen Information for Plate J, HPS 485W, 38.1 mm.

Specimen ID	W		a_o		B		B_N	
	mm.	in.	mm.	in.	mm.	in.	mm.	in.
J12'	10.03	0.3949	5.14	0.202	10.02	0.3945	8.00	0.3152
J13'	Specimen Damaged in Machining							
J14'	10.03	0.3949	5.13	0.202	10.03	0.3949	8.00	0.3152
J15'	10.03	0.3949	5.10	0.201	10.03	0.3949	8.00	0.3152
J16'	10.04	0.3953	5.14	0.202	10.03	0.3949	8.00	0.3152
J17'	10.03	0.3949	5.14	0.202	10.03	0.3949	8.00	0.3152
J18'	10.03	0.3949	5.13	0.202	10.04	0.3953	8.00	0.3152
J19'	10.03	0.3949	5.12	0.202	10.02	0.3945	8.00	0.3152
J20'	10.03	0.3949	5.13	0.202	10.03	0.3949	8.00	0.3152
J21'	10.03	0.3949	5.13	0.202	10.03	0.3949	8.00	0.3152
J22'	10.03	0.3949	5.07	0.200	10.02	0.3945	8.00	0.3152

Table G-16. Dynamic Test Information for Plate J, HPS 485W, 38.1 mm.

Specimen ID	Test Temperature		Test Result, K_{Jc}		Valid?	Censored?	1T K_{Jc}		Test Rate	
	°C	°F	MPa√m	ksi√in			MPa√m	ksi√in	MPa√m/sec	ksi√in/sec
J12'	-70	-94	263.6	239.9	Yes	Yes	131.0	119.2	1285	1169
J13'	Specimen Damaged in Machining									
J14'	-100	-148	84.5	76.9	Yes	No	71.1	64.7	3681	3350
J15'	-100	-148	80.1	72.9	Yes	No	67.6	61.6	3859	3512
J16'	-100	-148	72.8	66.2	Yes	No	61.9	56.3	4470	4068
J17'	-100	-148	55.0	50.1	Yes	No	47.7	43.4	4632	4215
J18'	-80	-112	89.9	81.8	Yes	No	75.4	68.6	3526	3209
J19'	-80	-112	93.5	85.1	Yes	No	78.3	71.2	3384	3079
J20'	-80	-112	77.0	70.1	Yes	No	65.2	59.3	3849	3503
J21'	-80	-112	64.2	58.4	Yes	No	55.0	50.1	4389	3994
J22'	-100	-148	88.7	80.7	Yes	No	74.4	67.7	3452	3141

APPENDIX H: HPS Crack Arrest Test Records and Fracture Surfaces

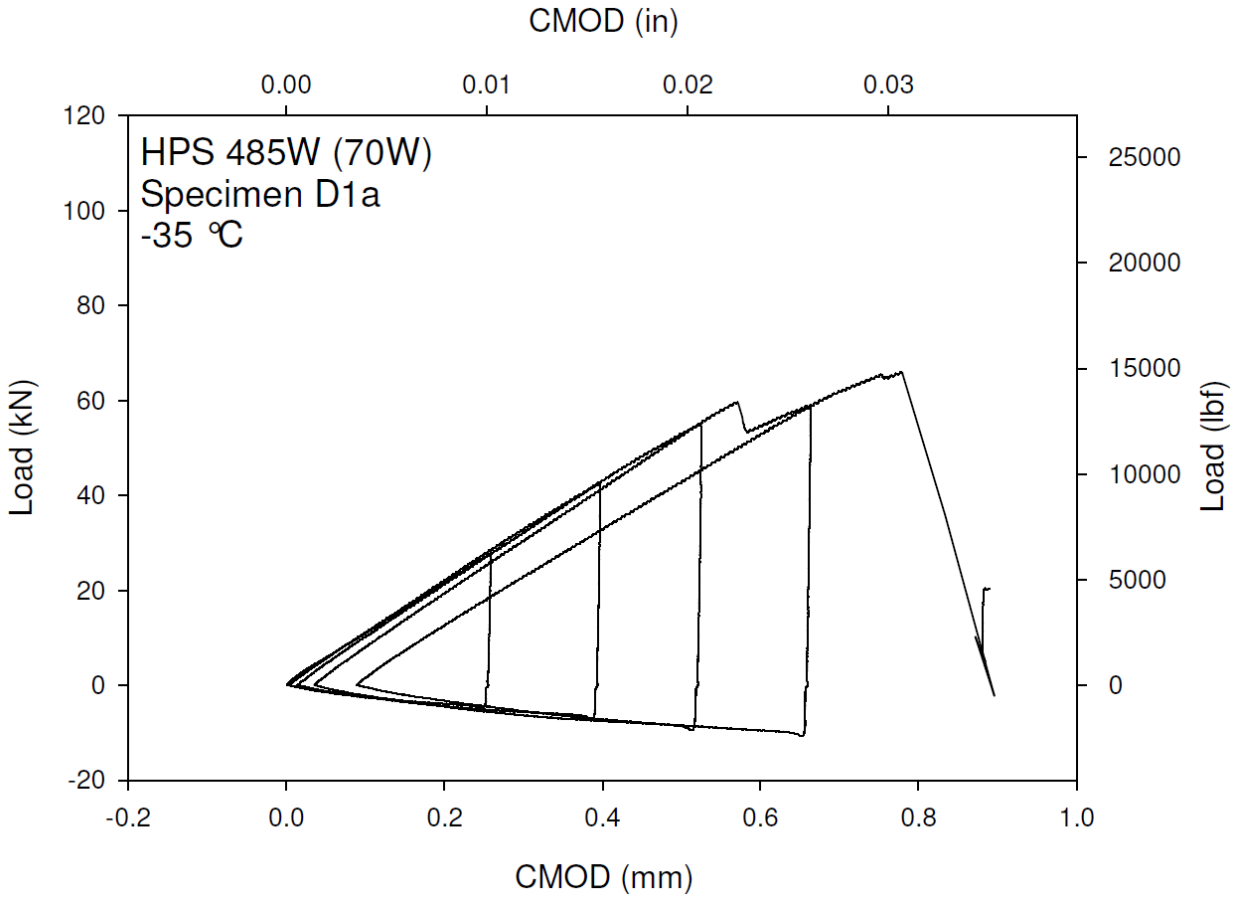

Figure H-1. Specimen D1a Test Record

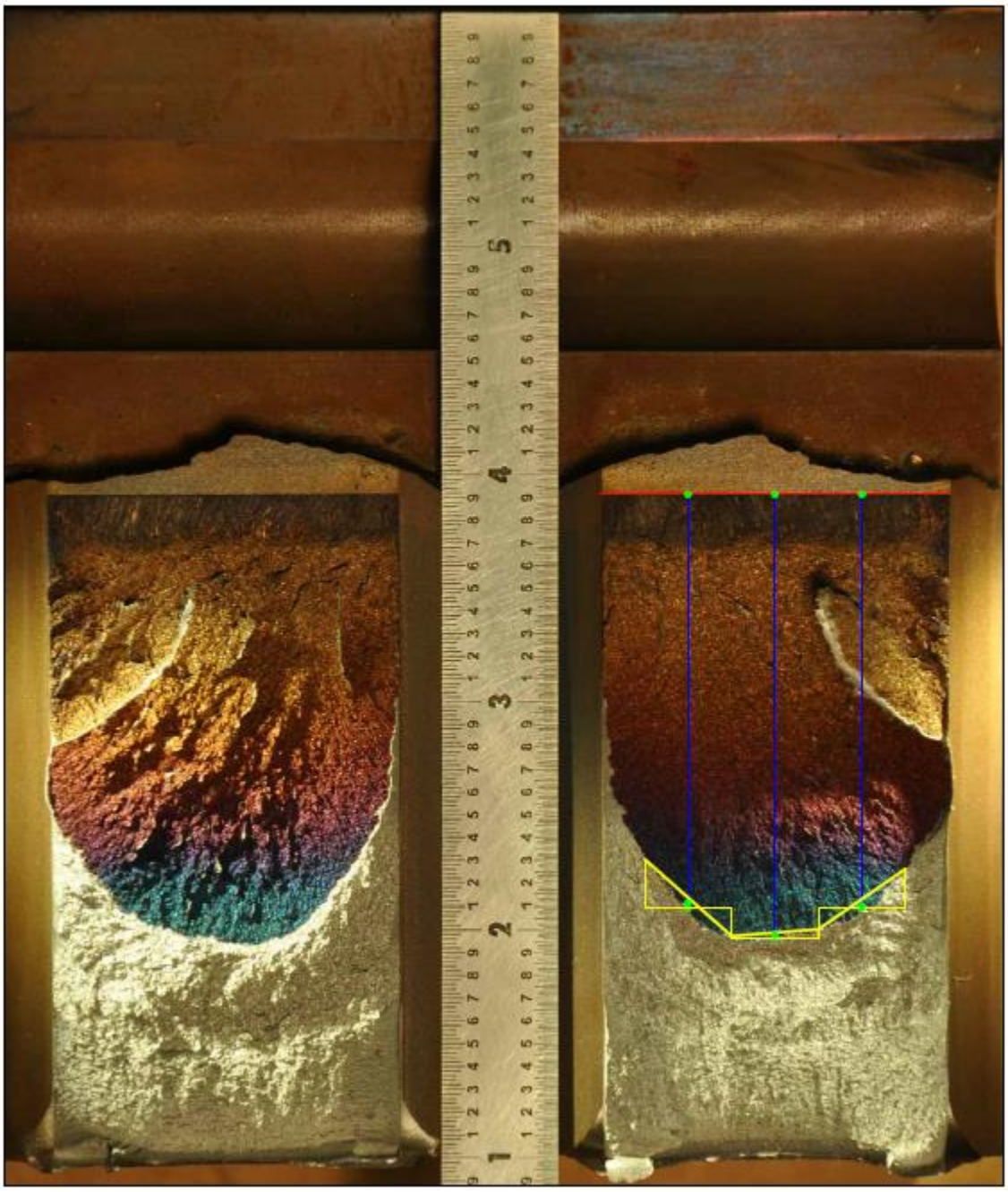

Figure H-2. Specimen D1a Fracture Surface

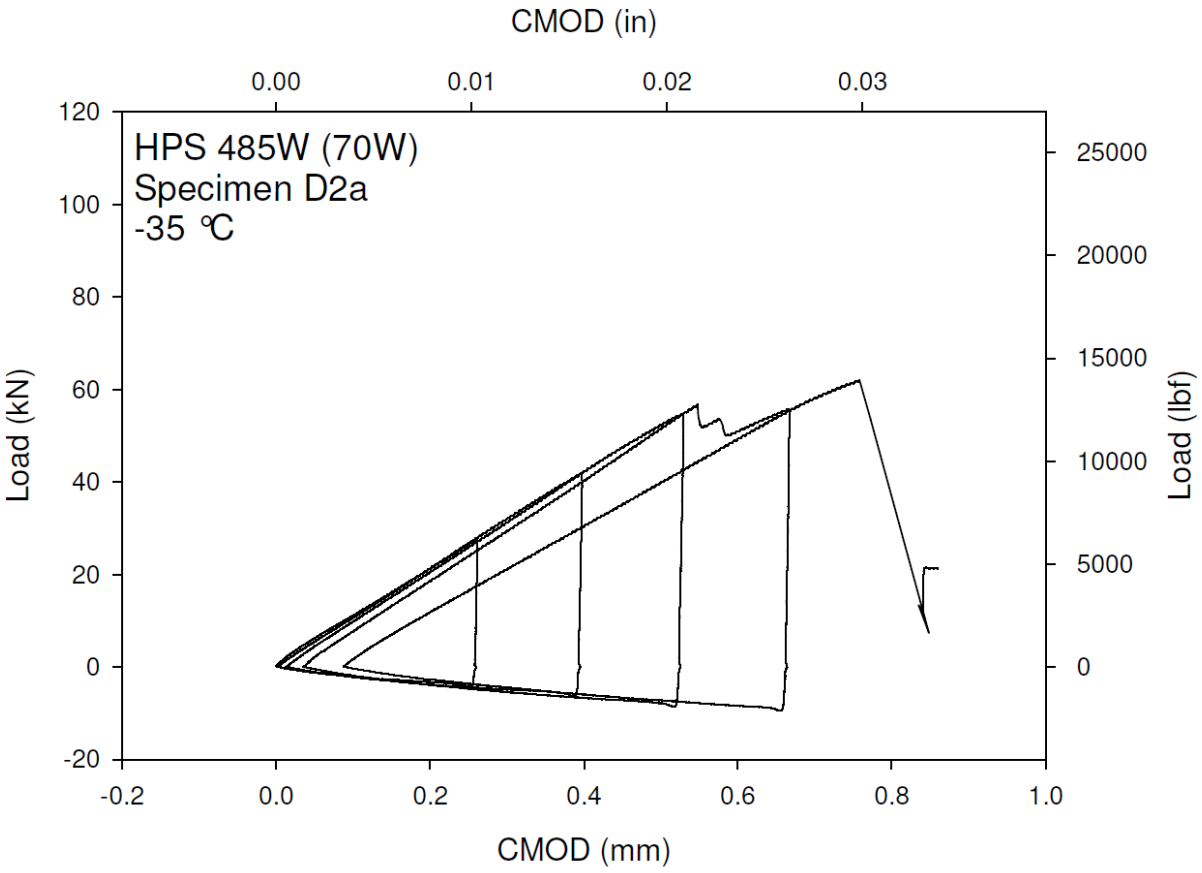

Figure H-3. Specimen D2a Test Record

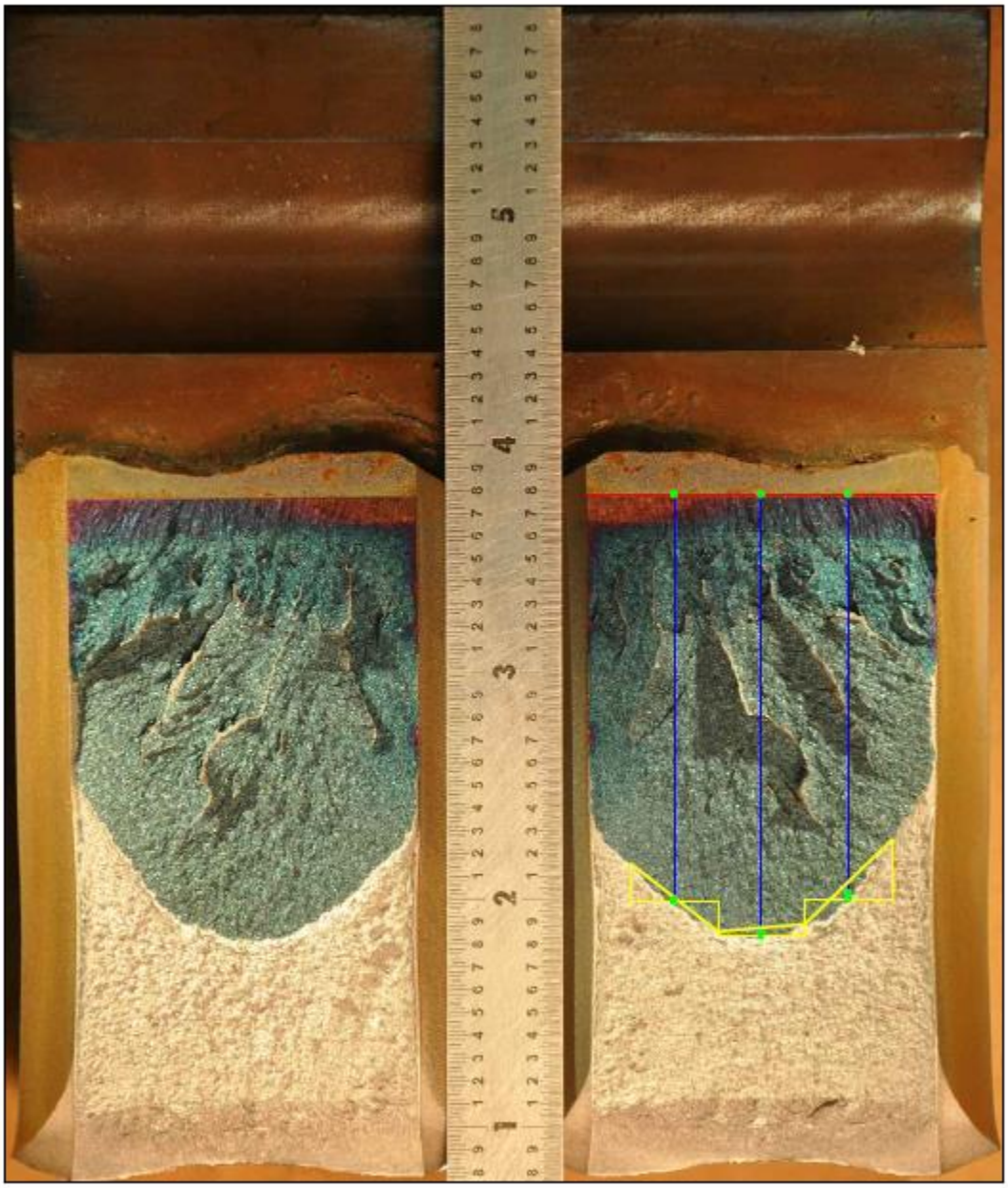

Figure H-4. Specimen D2a Fracture Surface

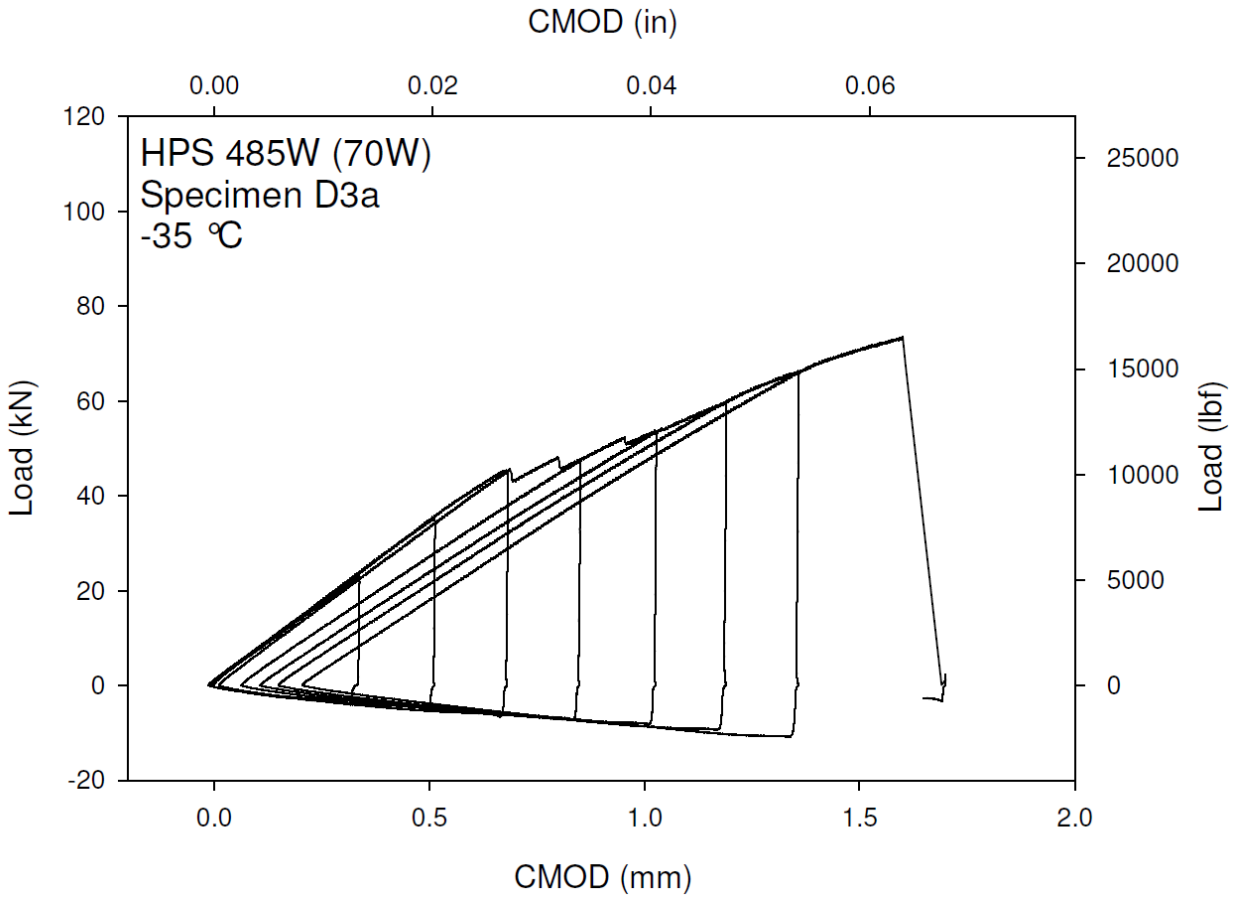

Figure H-5. Specimen D3a Test Record

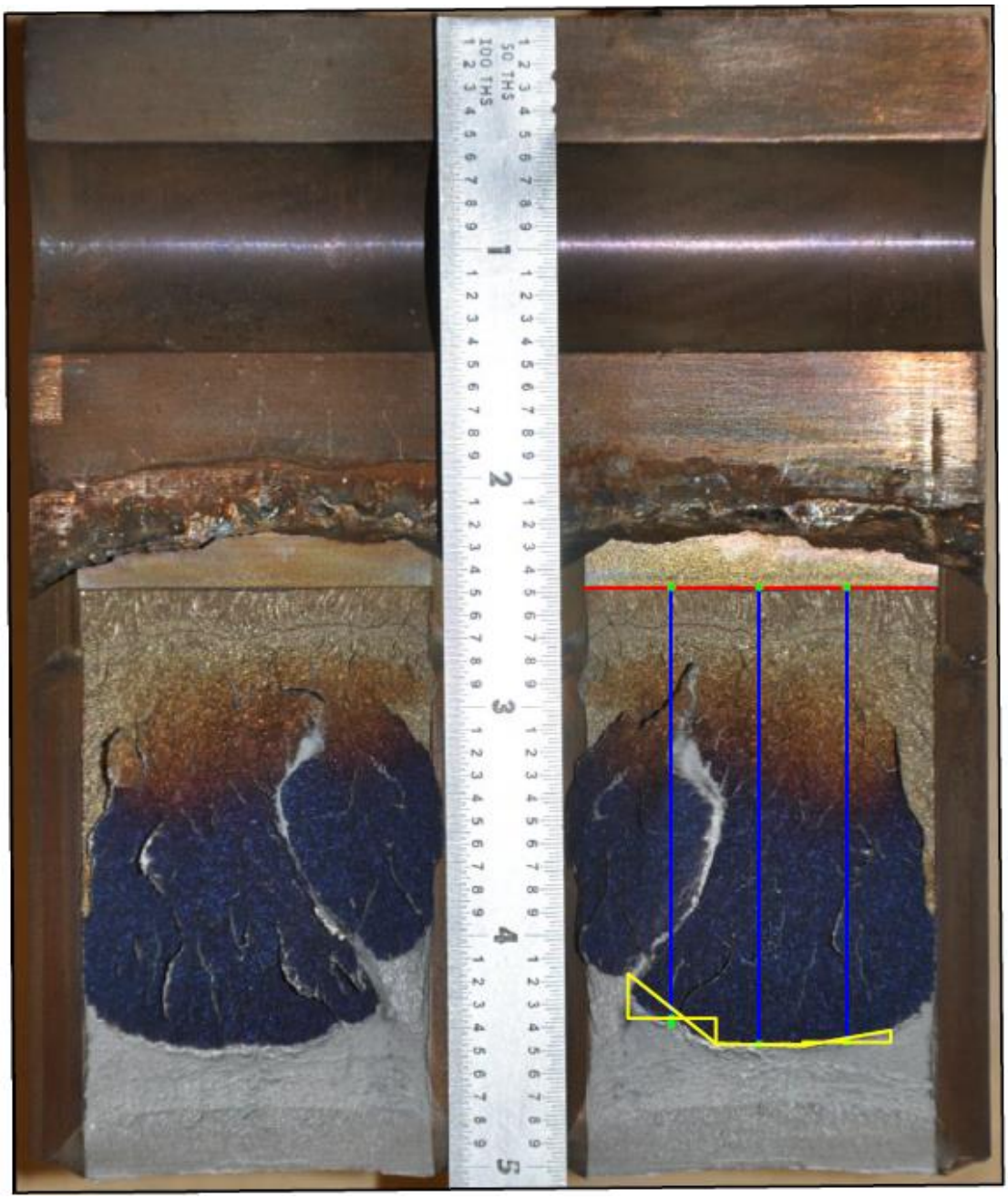

Figure H-6. Specimen D3a Fracture Surface

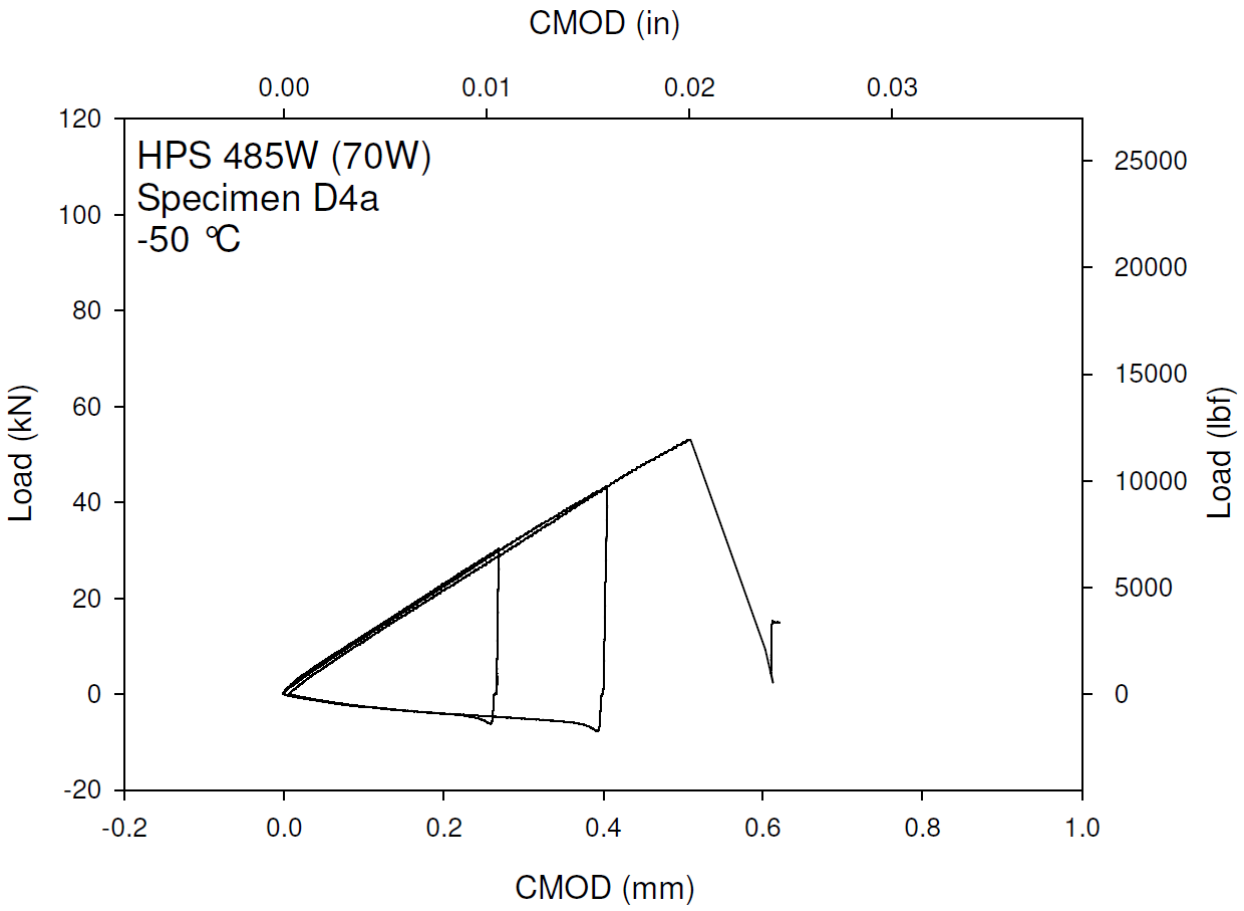

Figure H-7. Specimen D4a Test Record

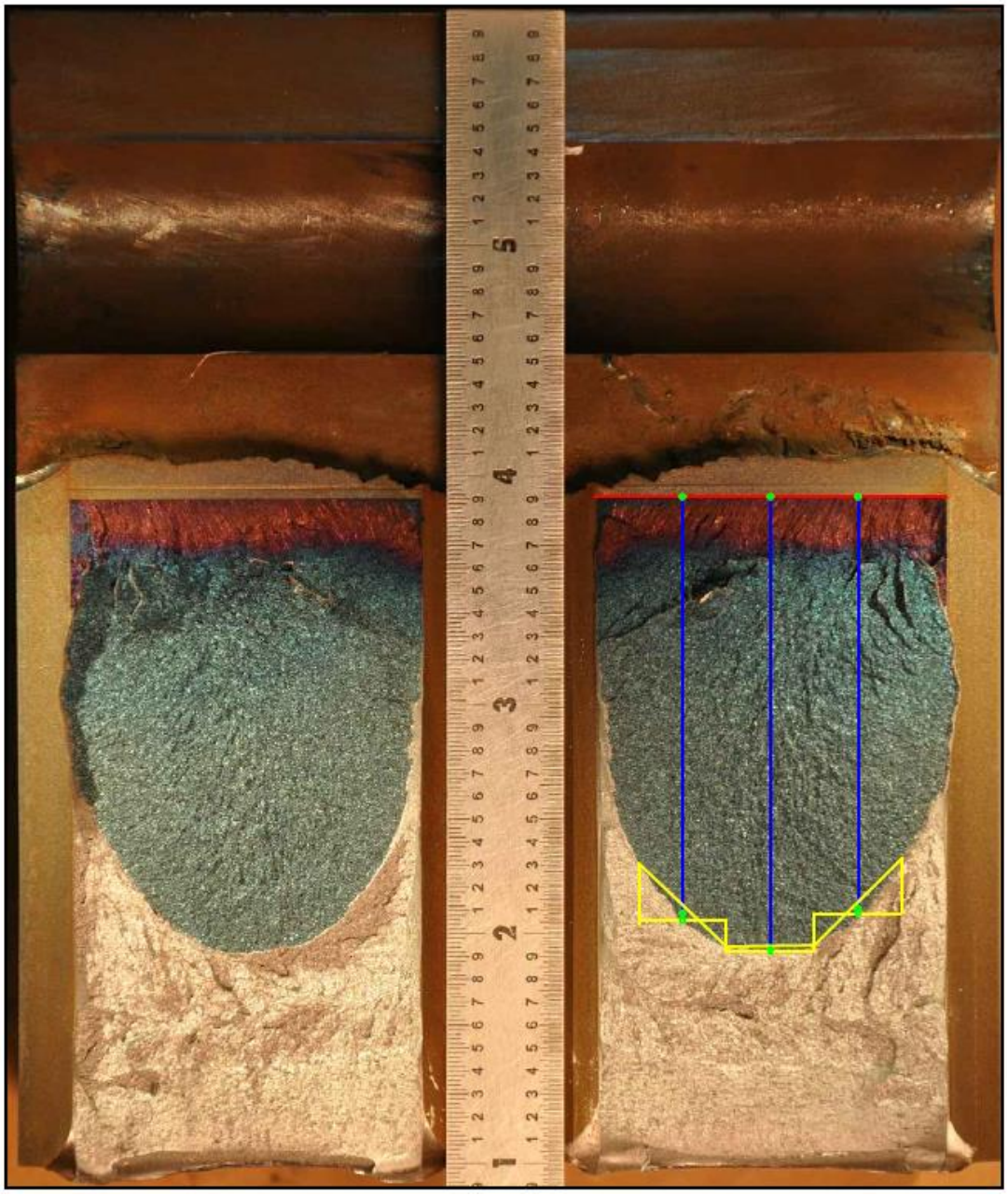

Figure H-8. Specimen D4a Fracture Surface

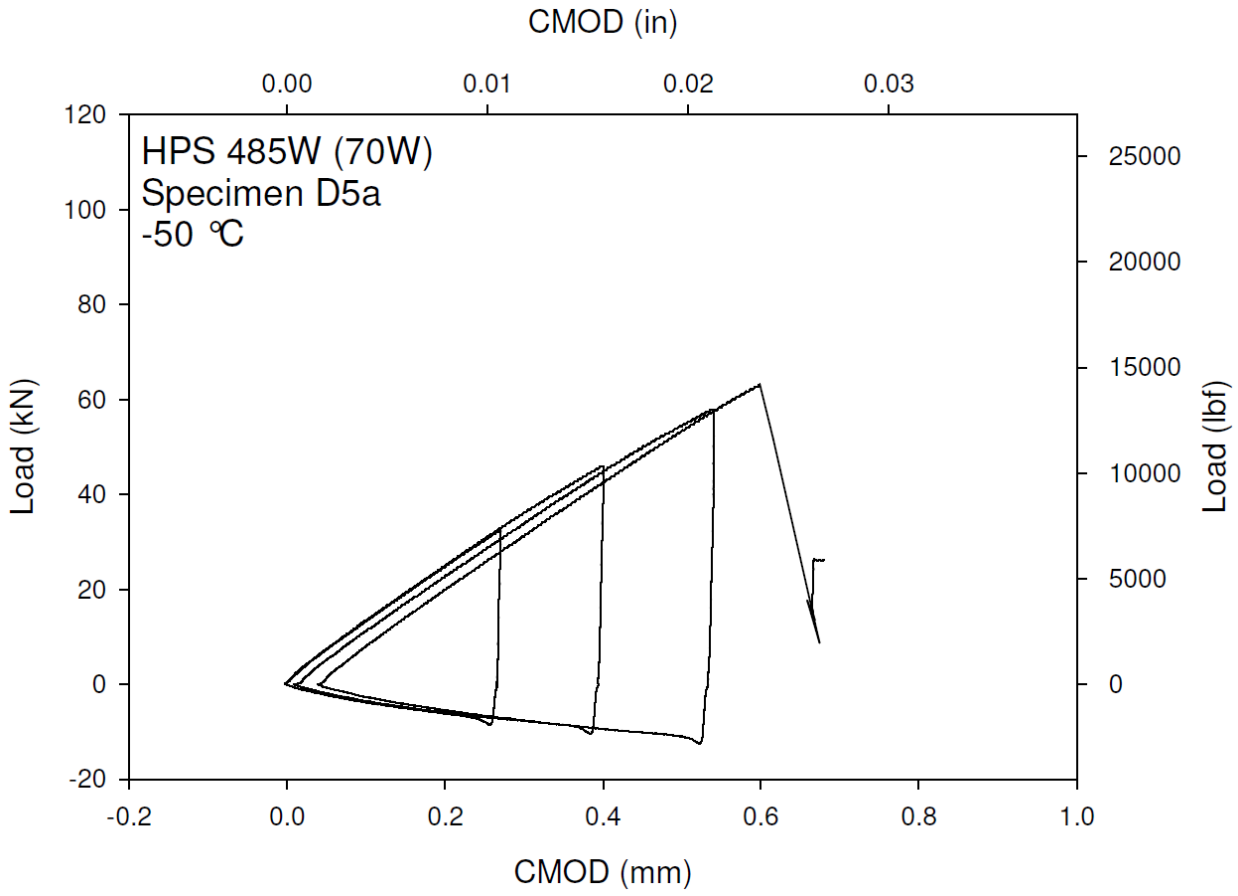

Figure H-9. Specimen D5a Test Record

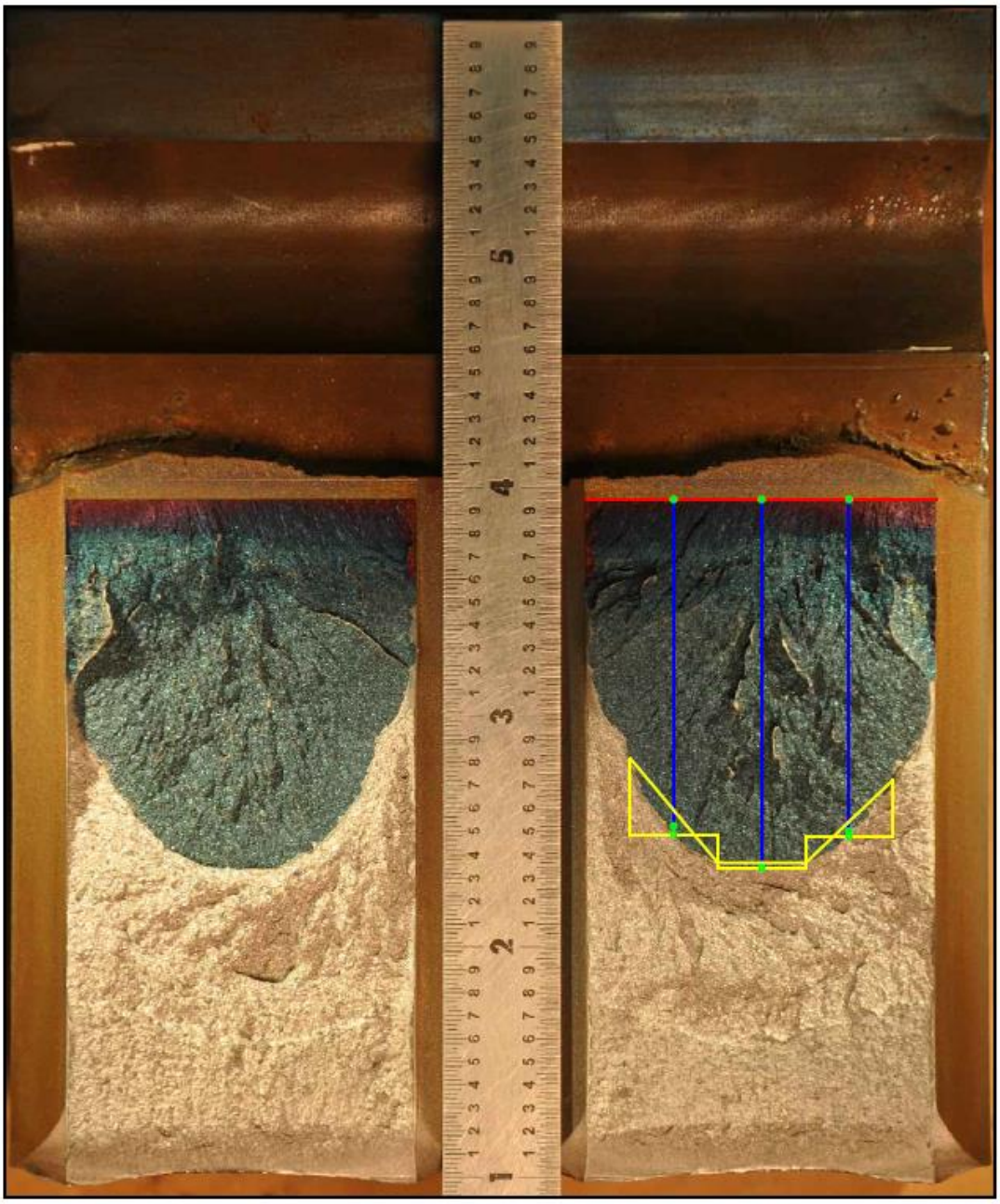

Figure H-10. Specimen D5a Fracture Surface

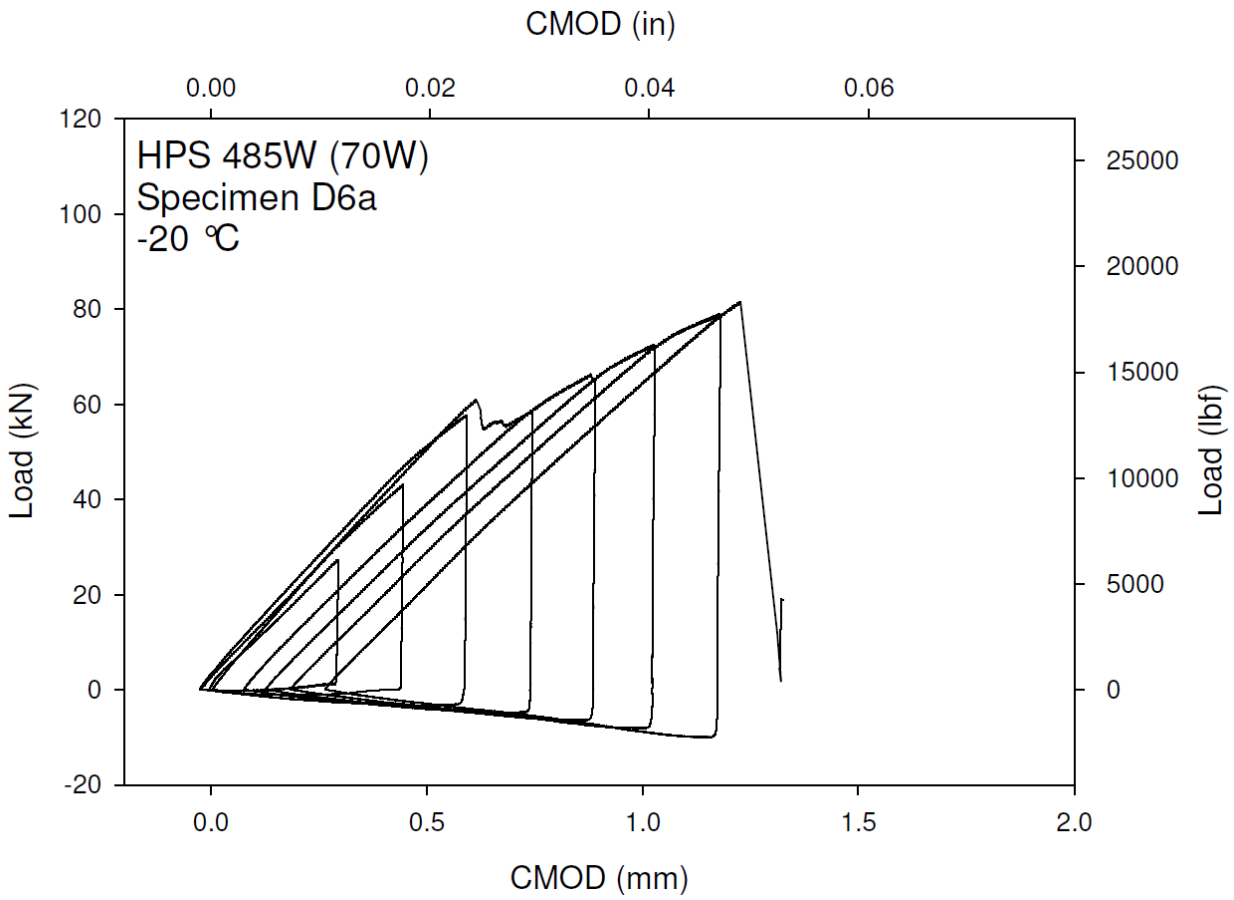

Figure H-11. Specimen D6a Test Record

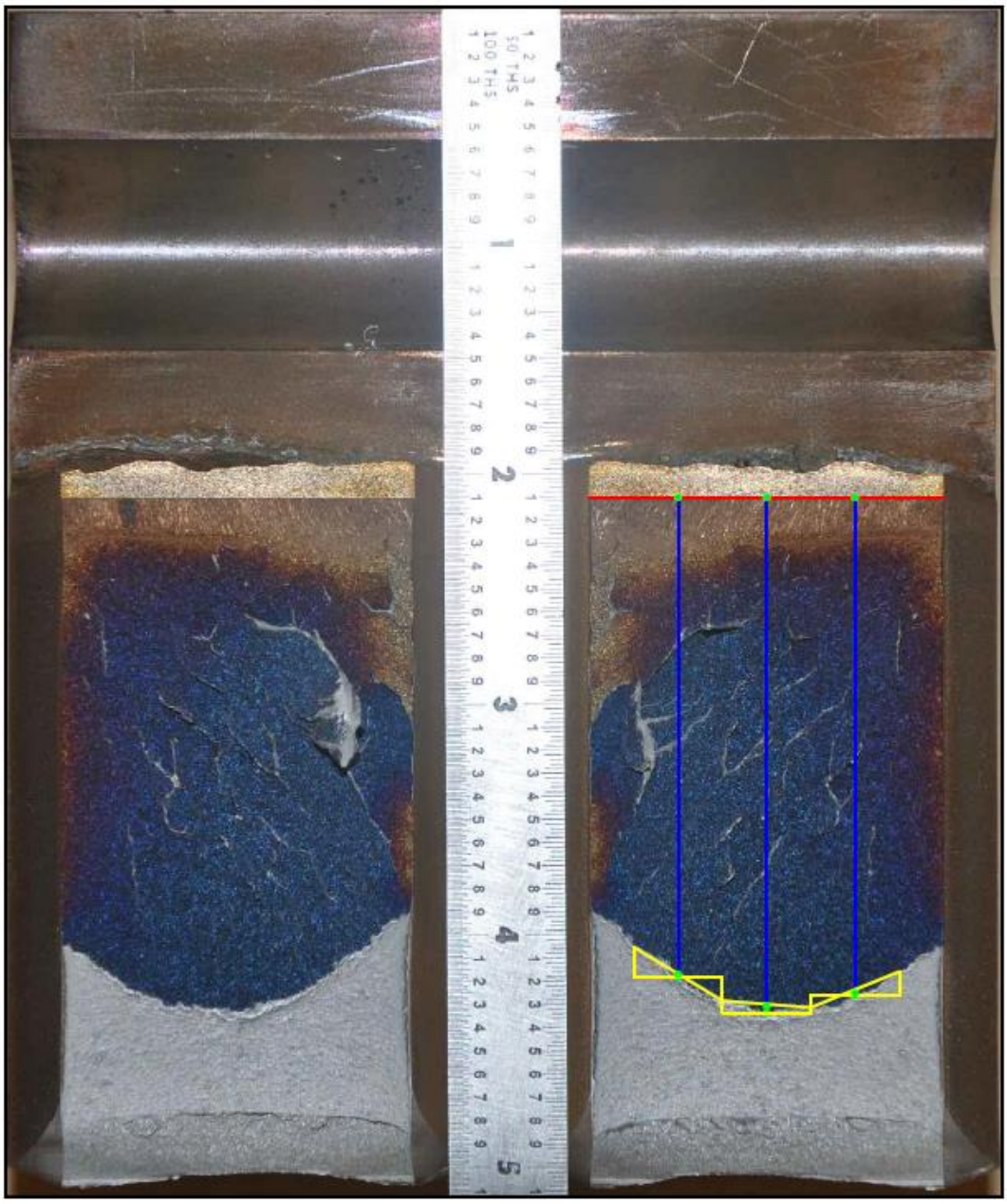

Figure H-12. Specimen D6a Fracture Surface

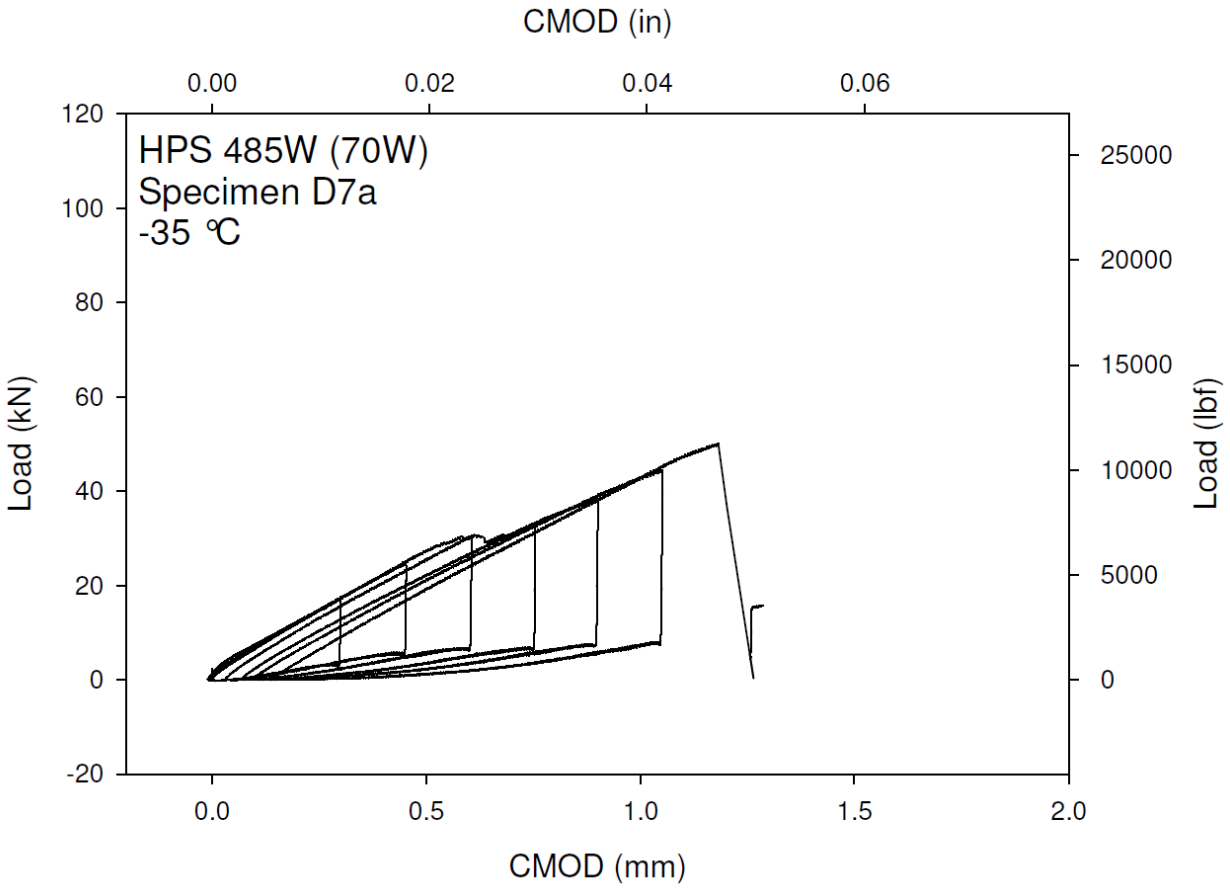

Figure H-13. Specimen D7a Test Record

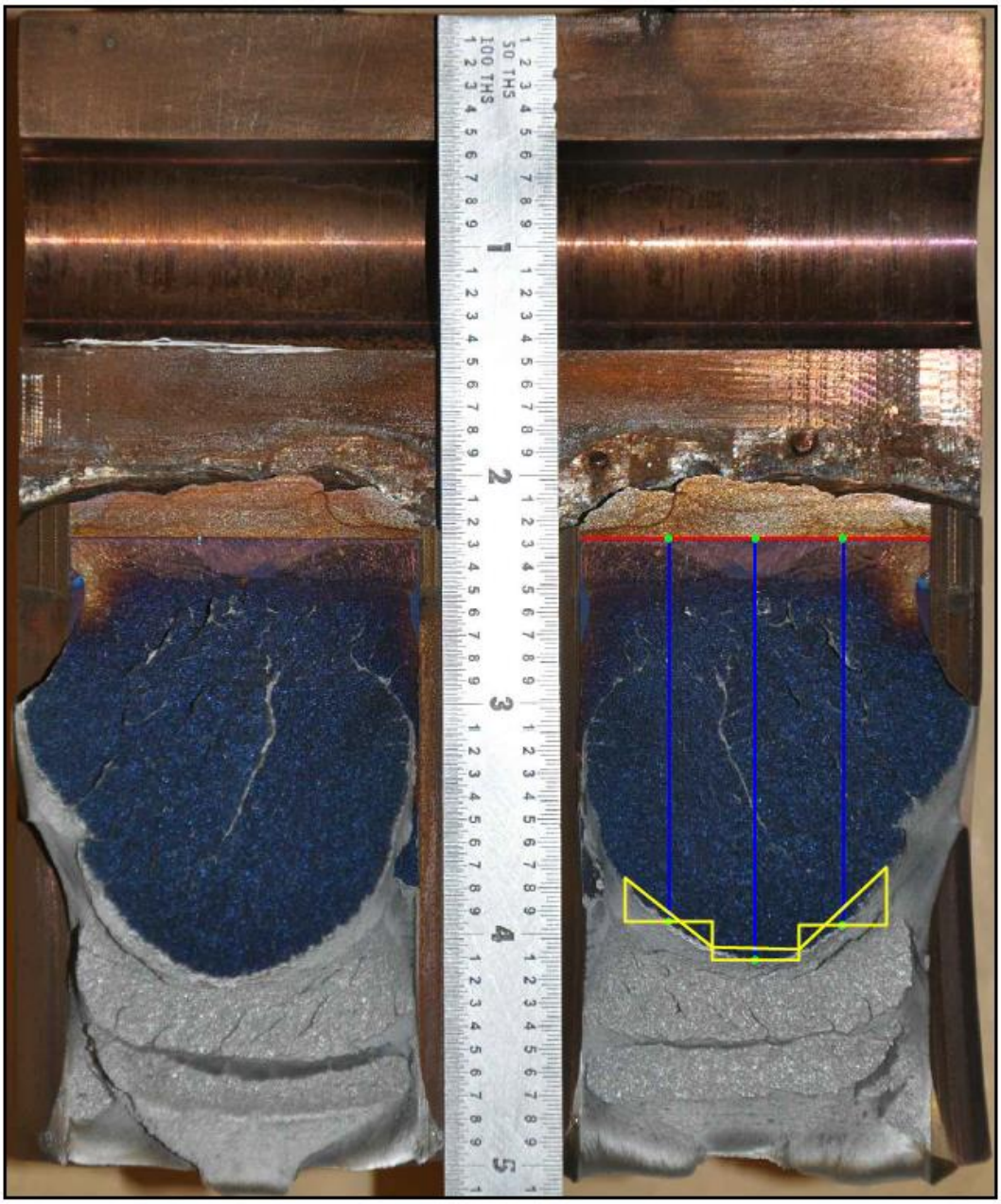

Figure H-14. Specimen D7a Fracture Surface

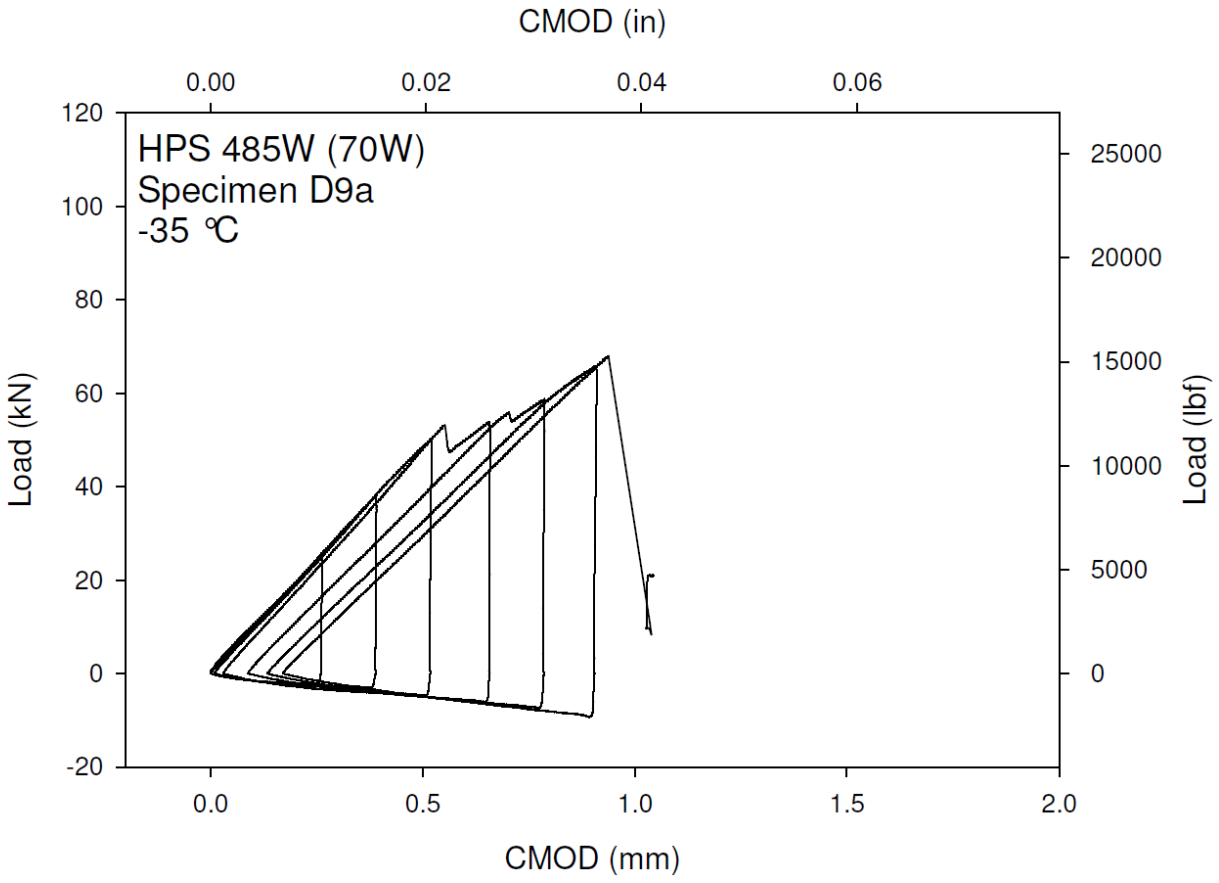

Figure H-15. Specimen D9a Test Record

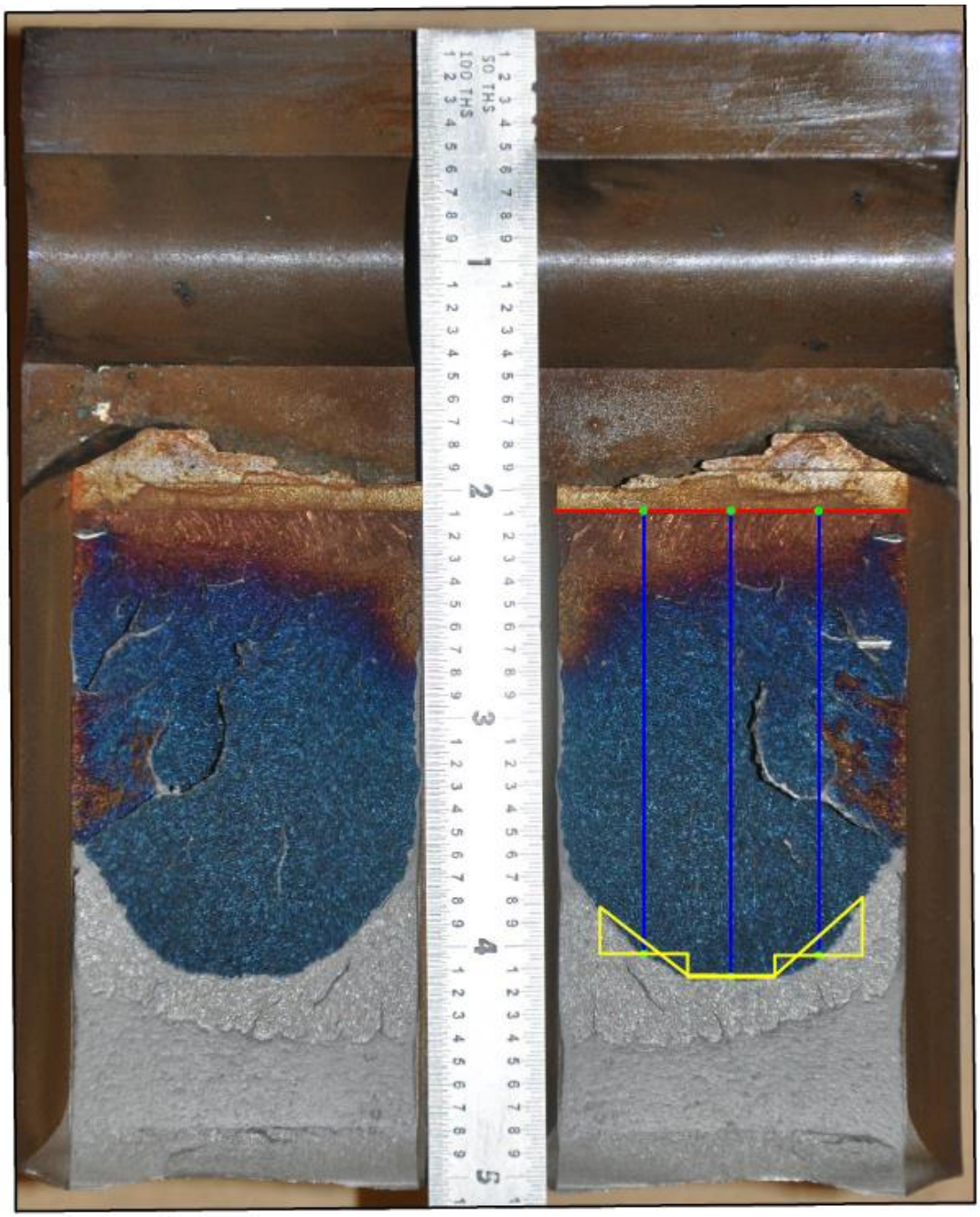

Figure H-16. Specimen D9a Fracture Surface

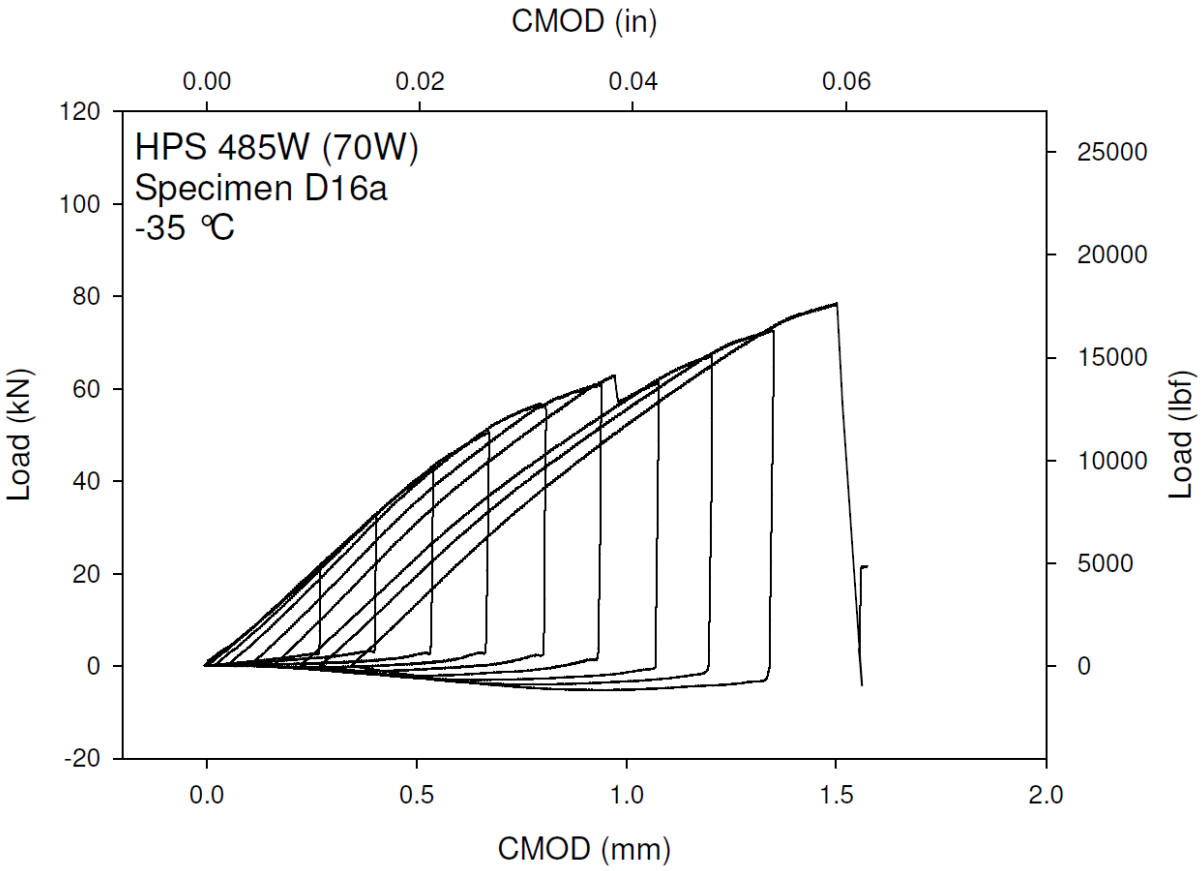

Figure H-17. Specimen D16a Test Record

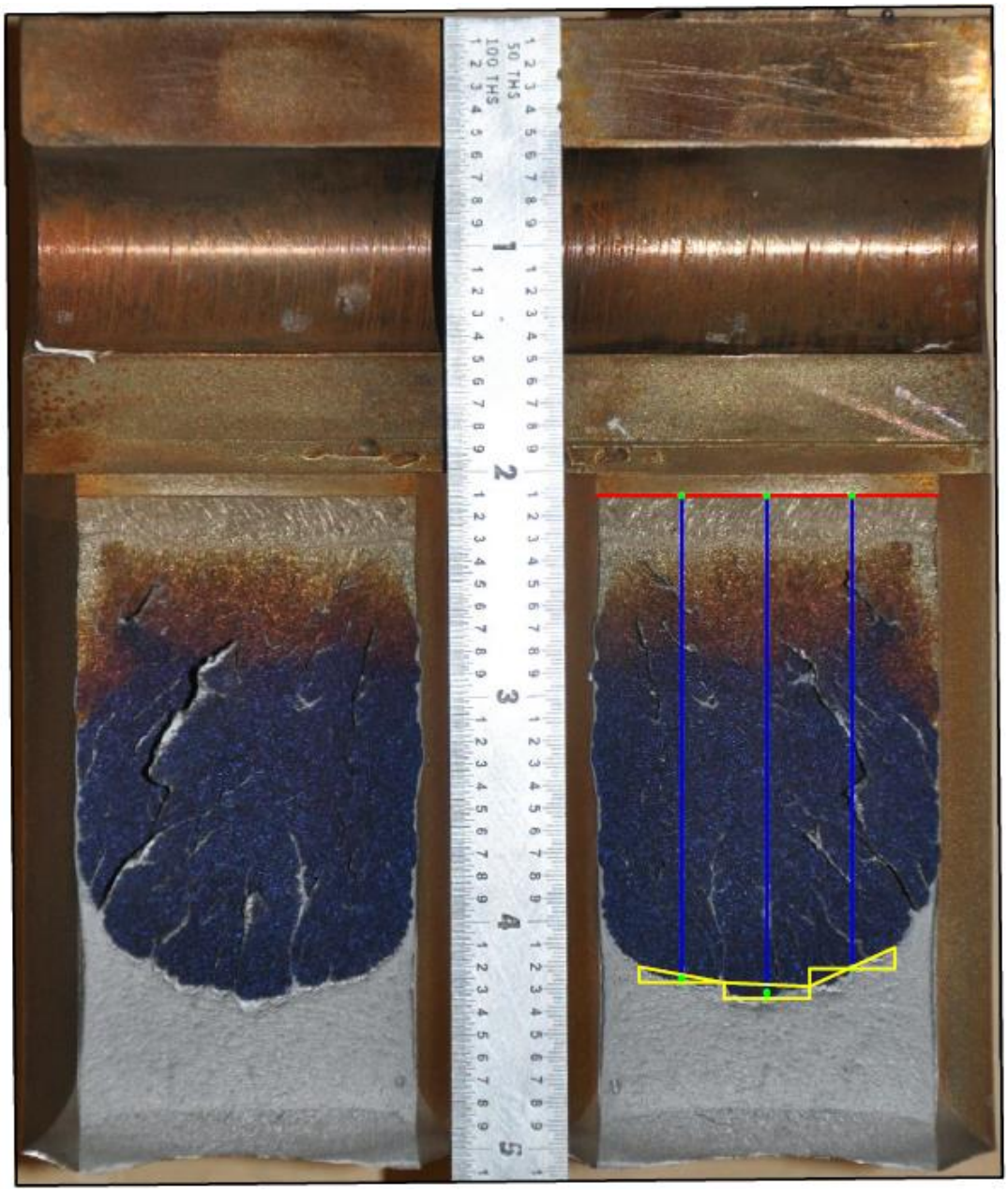

Figure H-18. Specimen D16a Fracture Surface

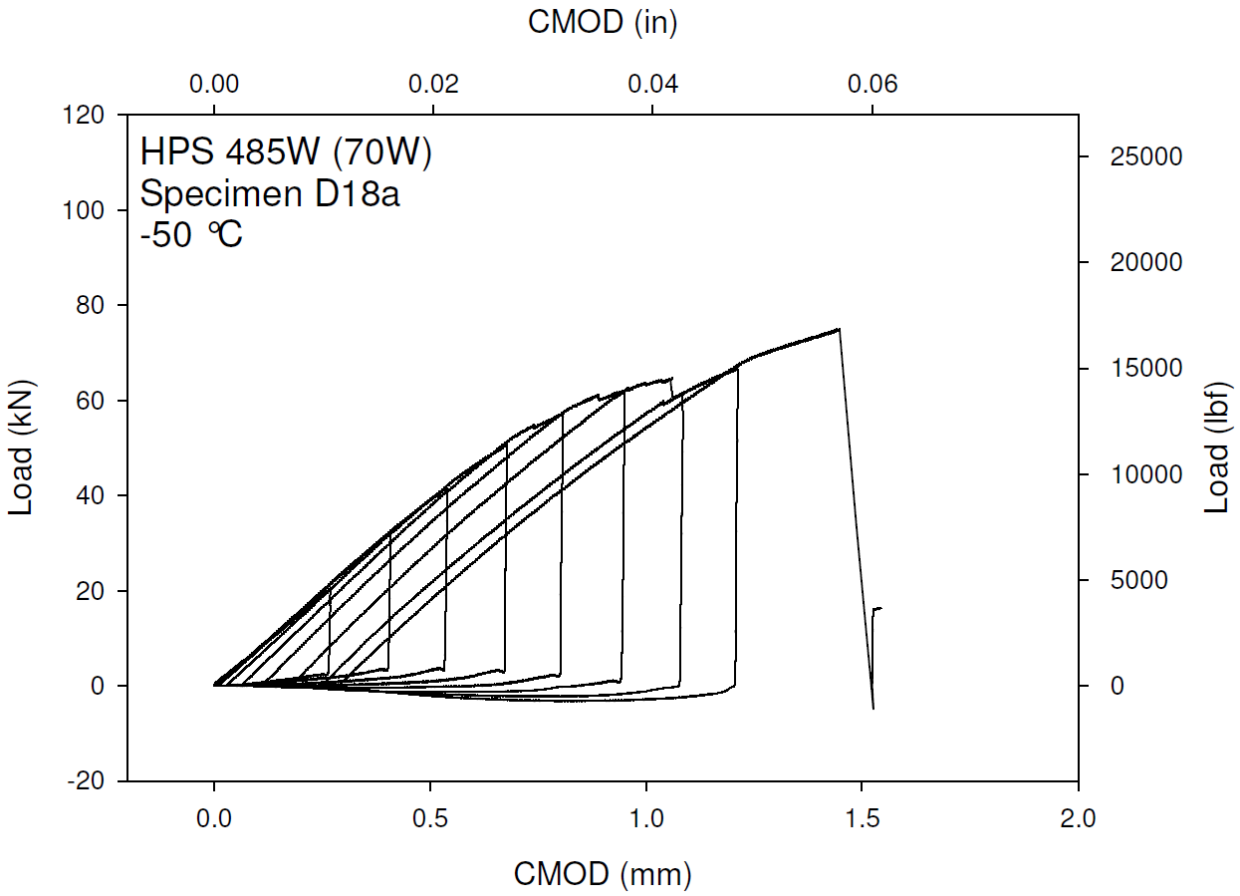

Figure H-19. Specimen D18a Test Record

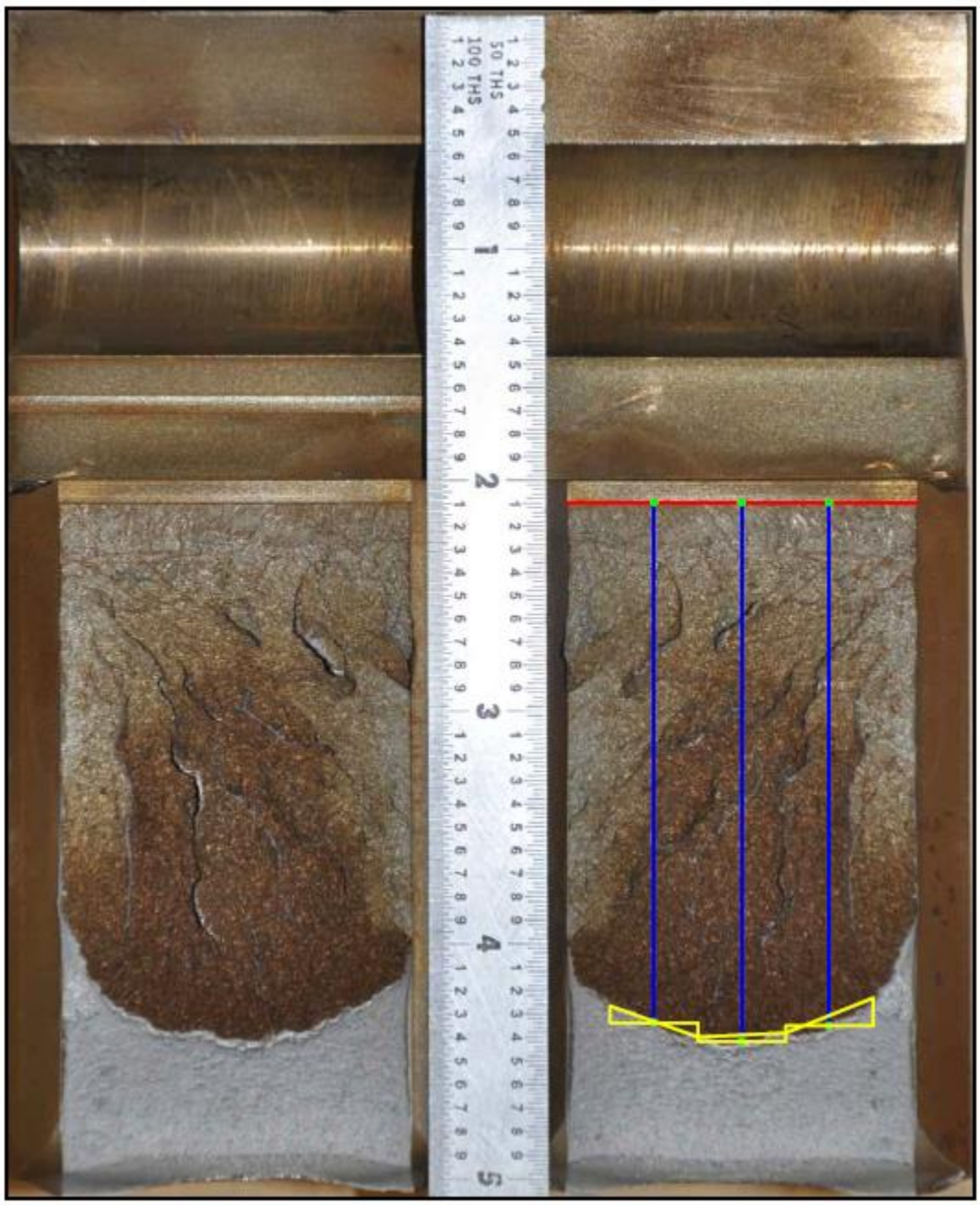

Figure H-20. Specimen D18a Fracture Surface

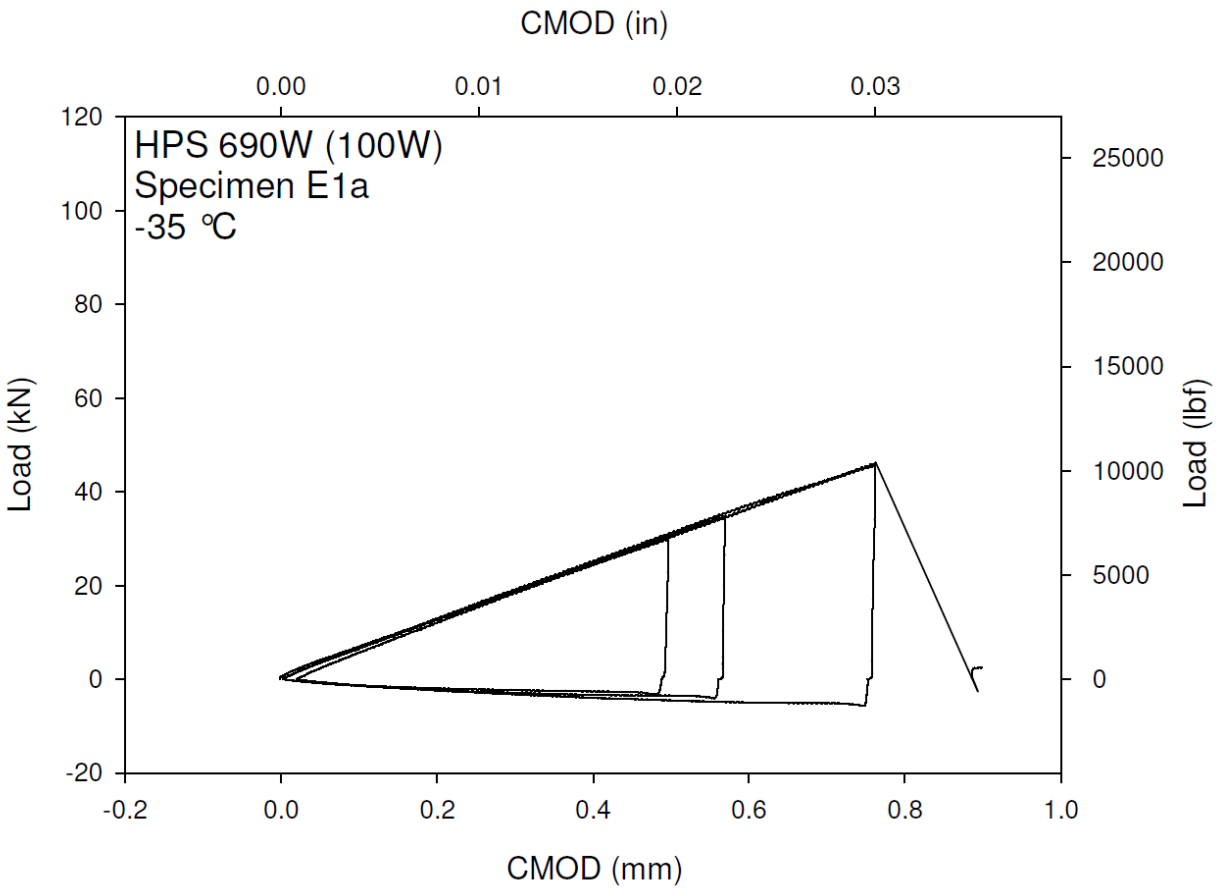

Figure H-21. Specimen E1a Test Record

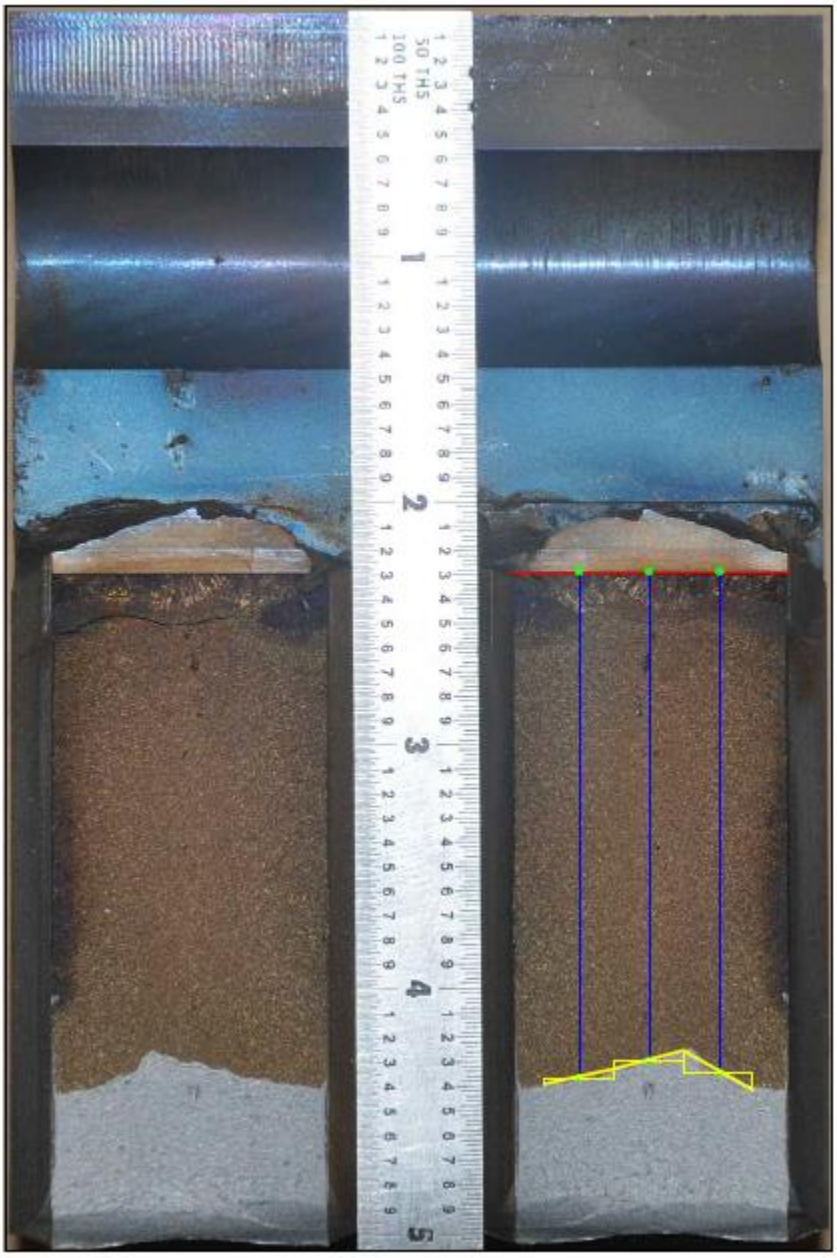

Figure H-22. Specimen E1a Fracture Surface

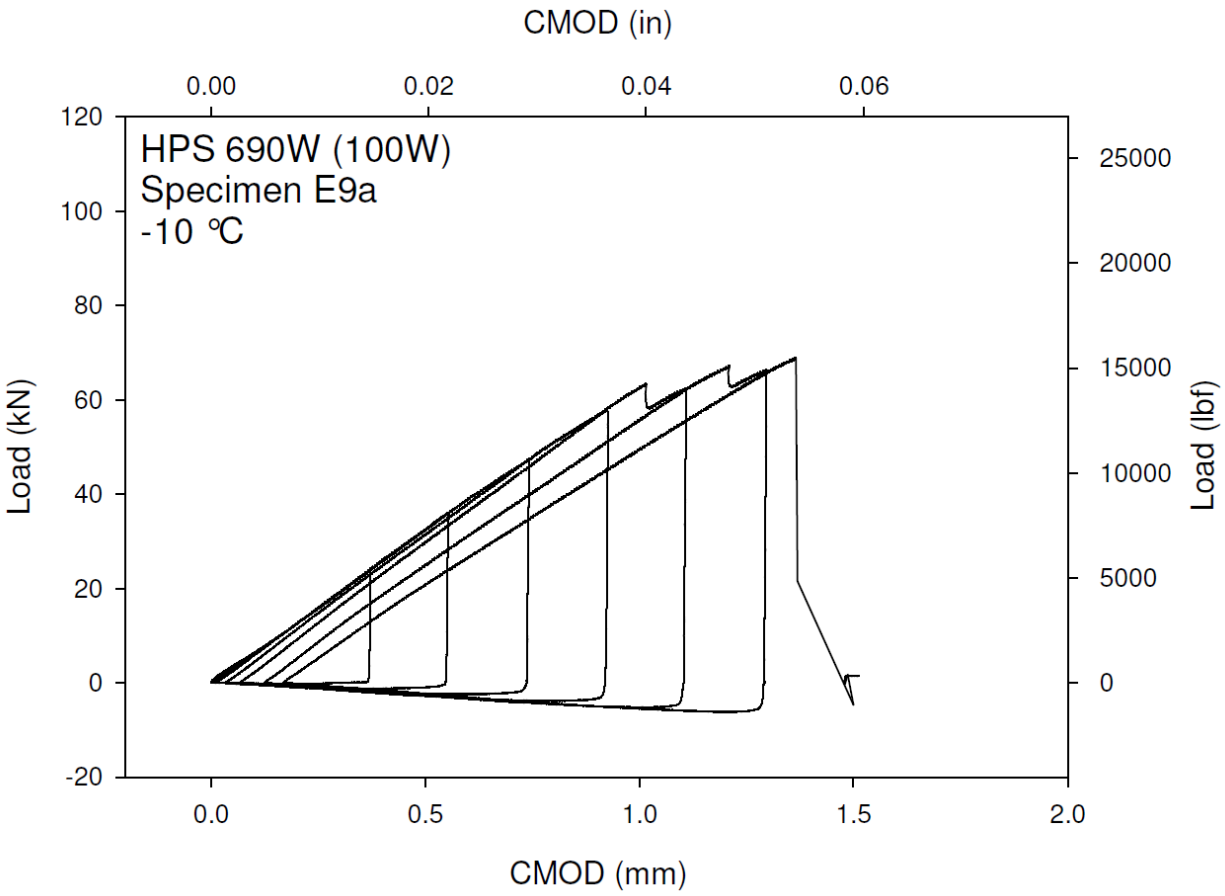

Figure H-23. Specimen E9a Test Record

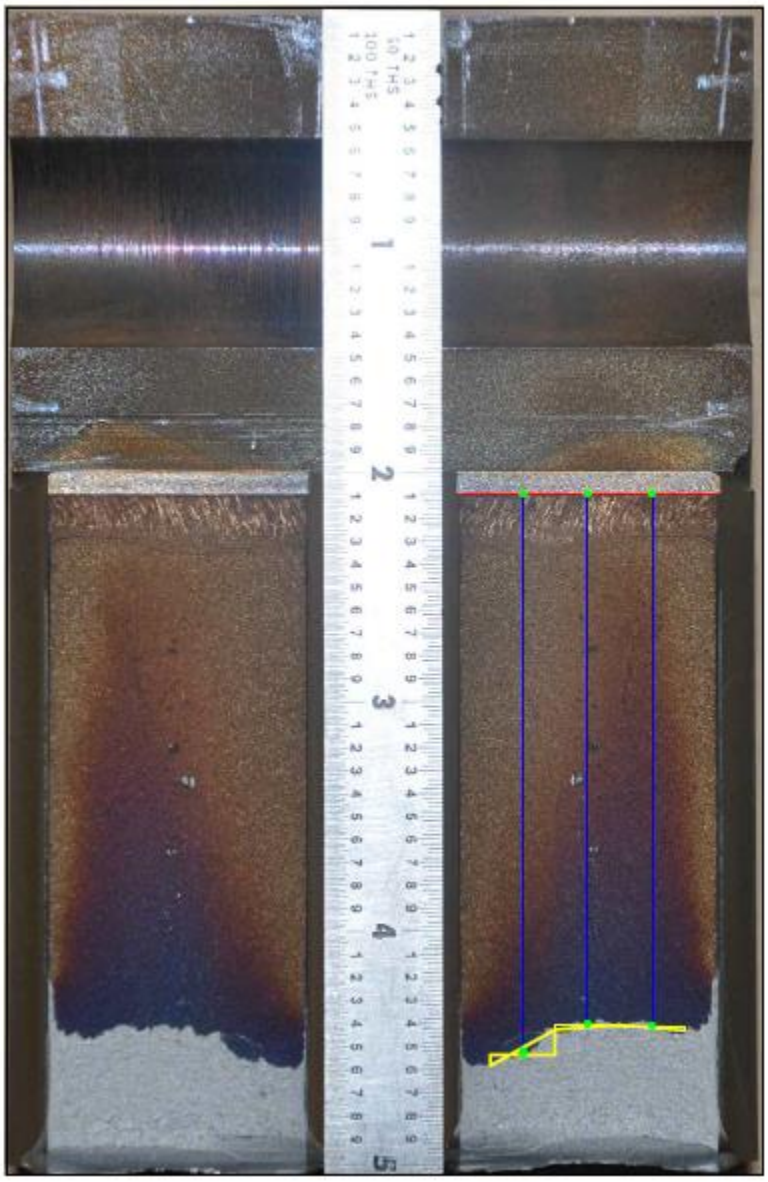

Figure H-24. Specimen E9a Fracture Surface

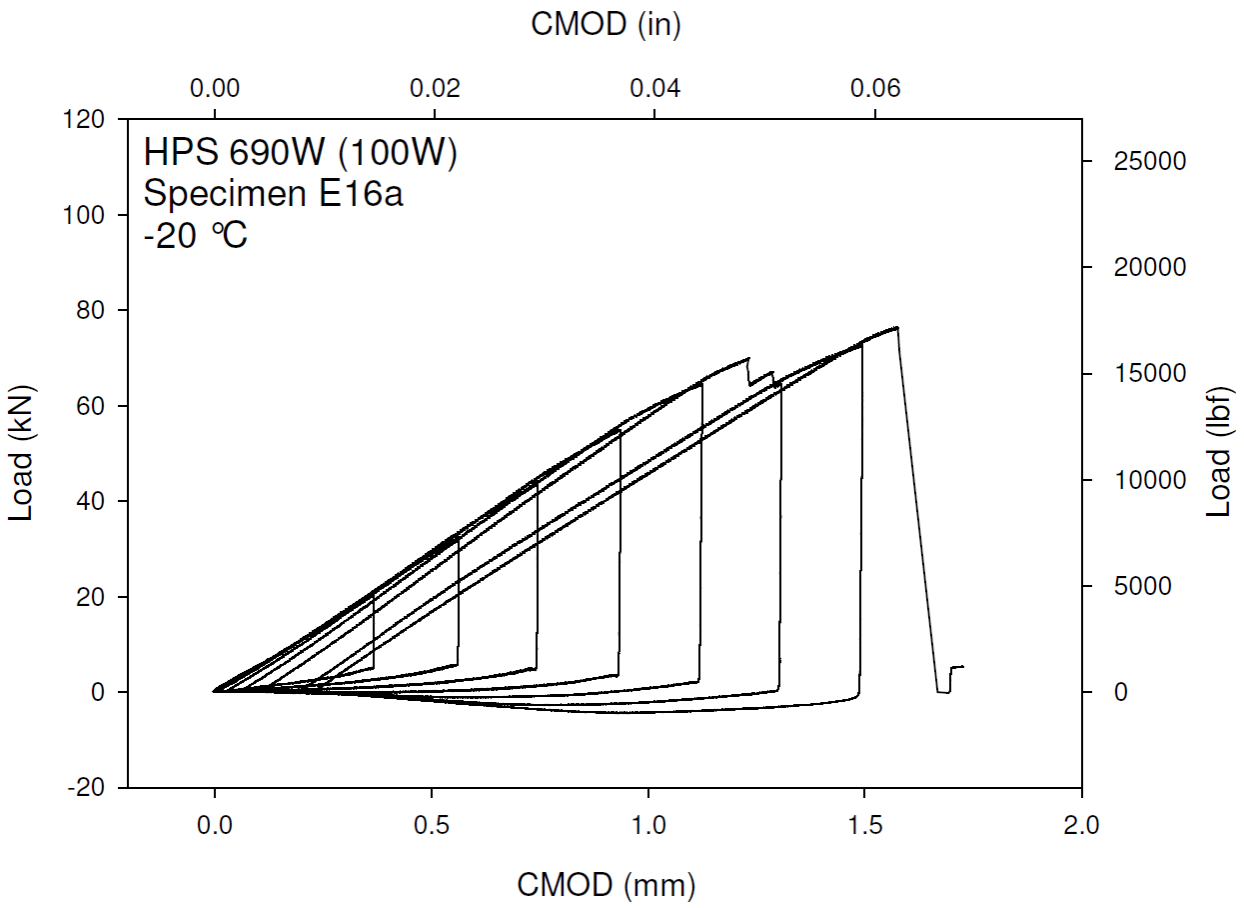

Figure H-25. Specimen E16a Test Record

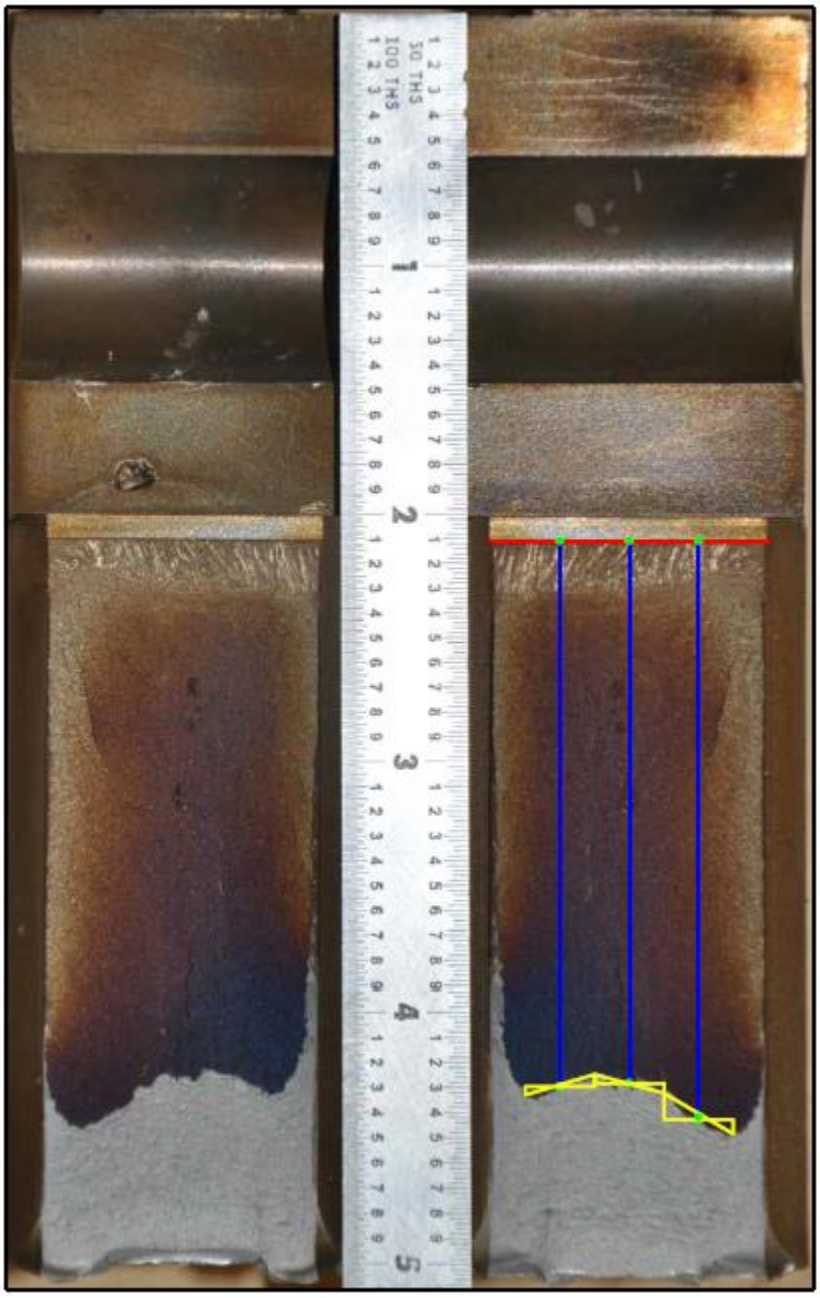

Figure H-26. Specimen E16a Fracture Surface

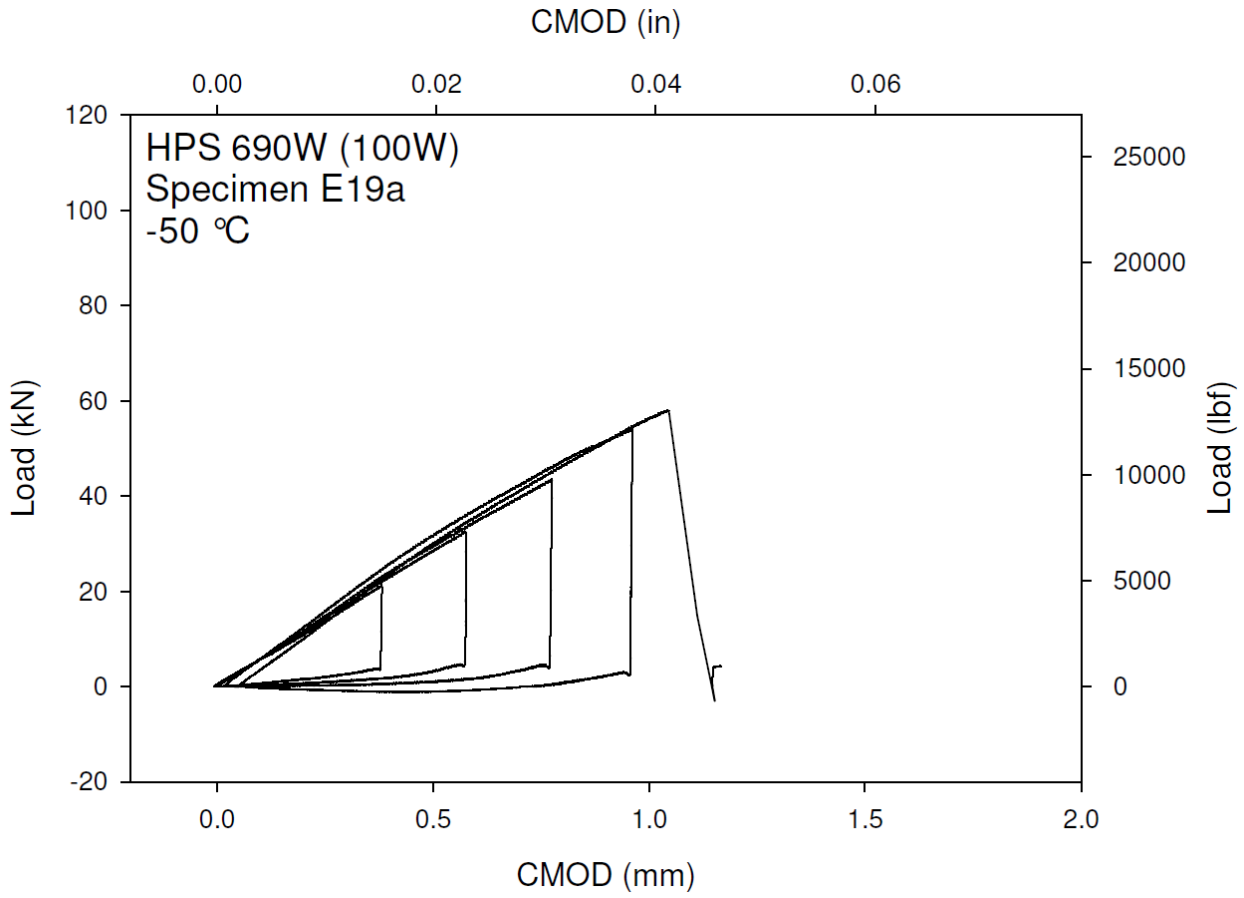

Figure H-27. Specimen E19a Test Record

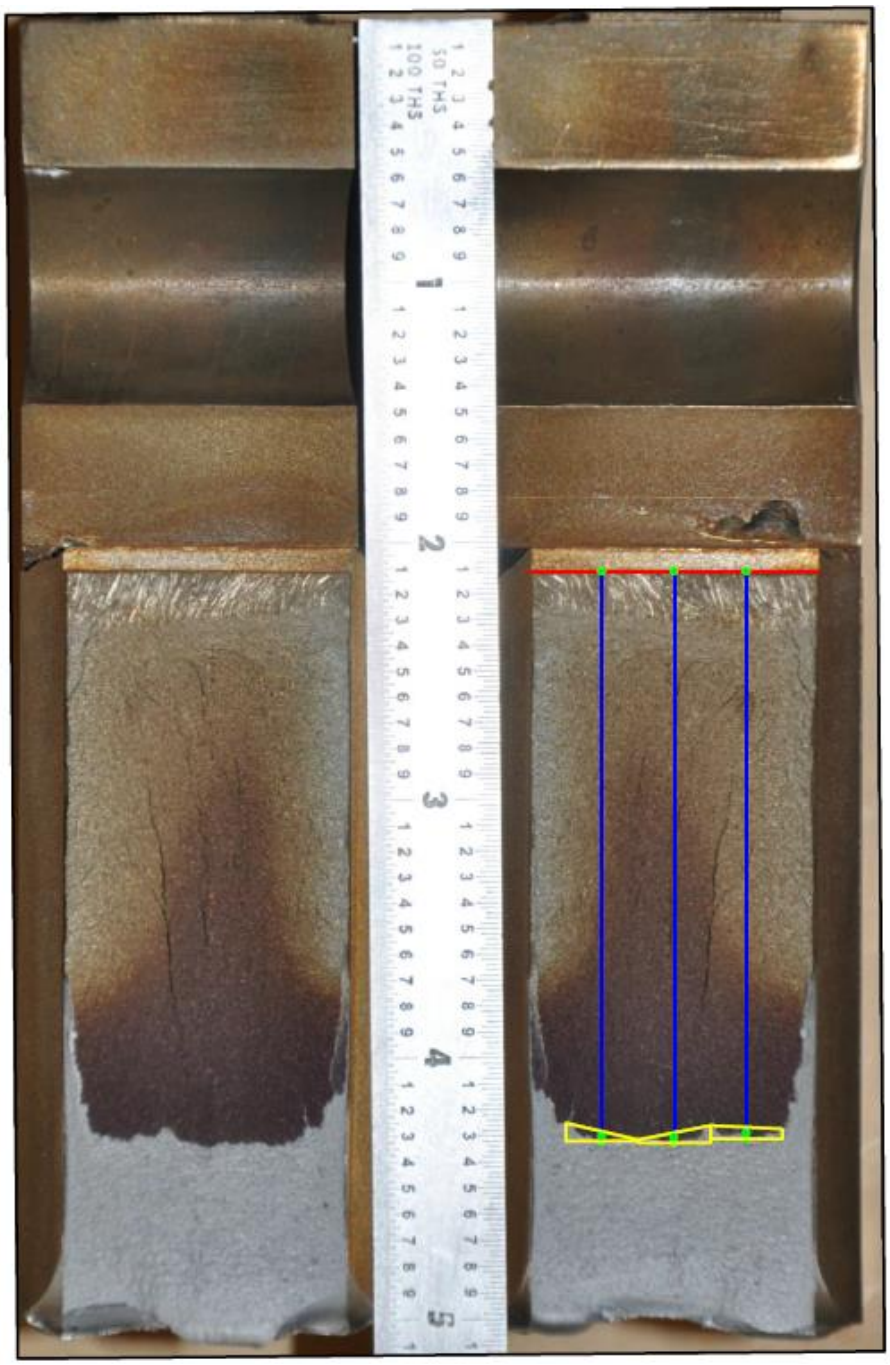

Figure H-28. Specimen E19a Fracture Surface

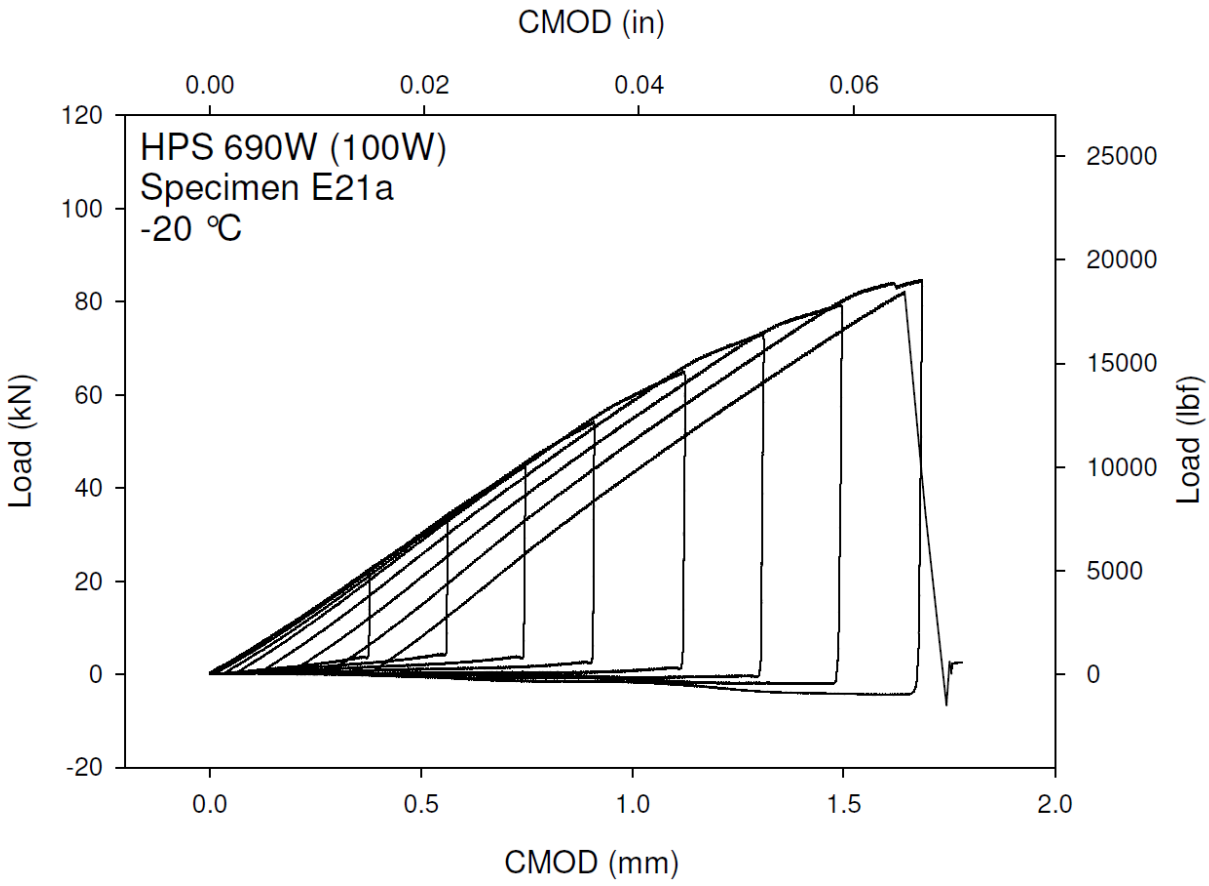

Figure H-29. Specimen E21a Test Record

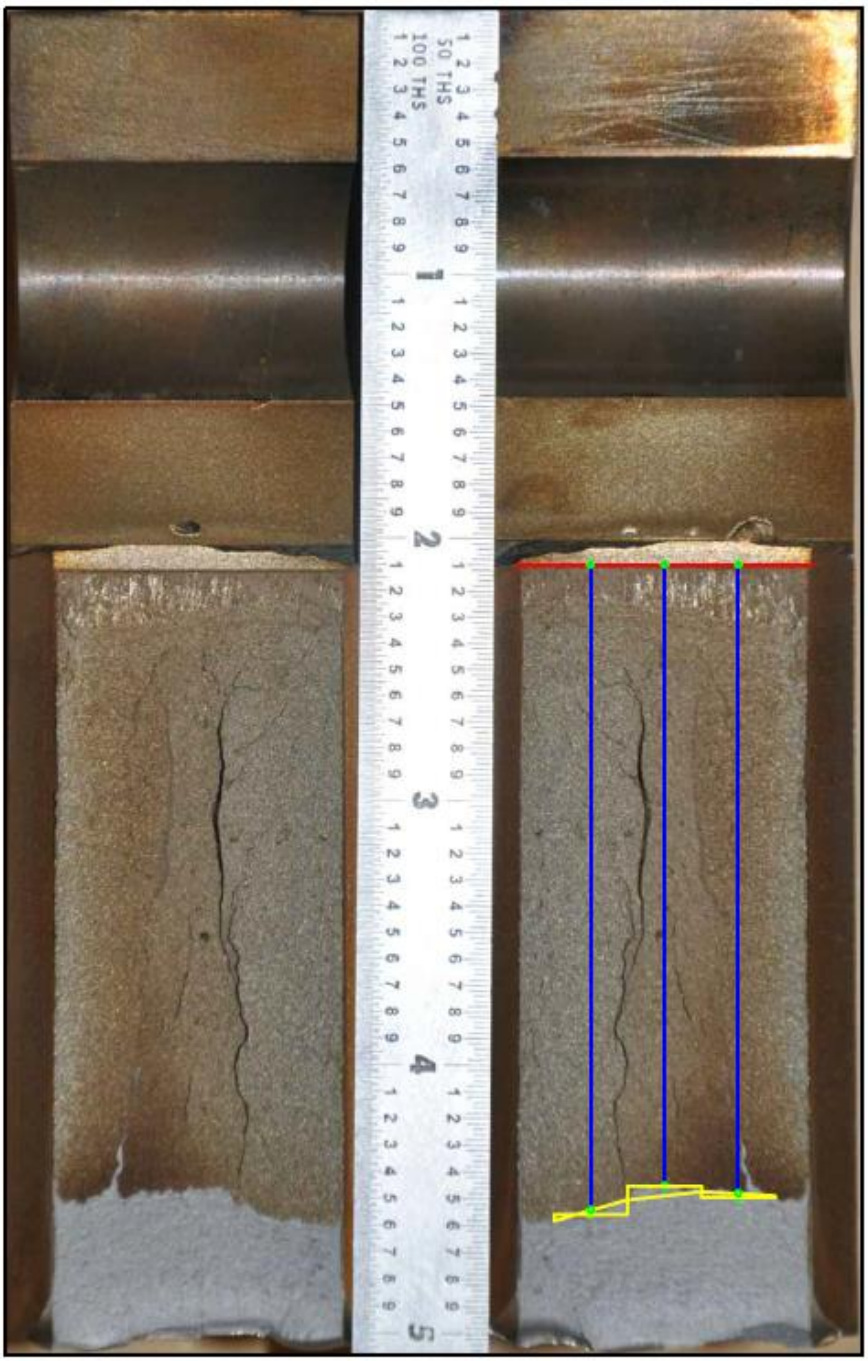

Figure H-30. Specimen E21a Fracture Surface

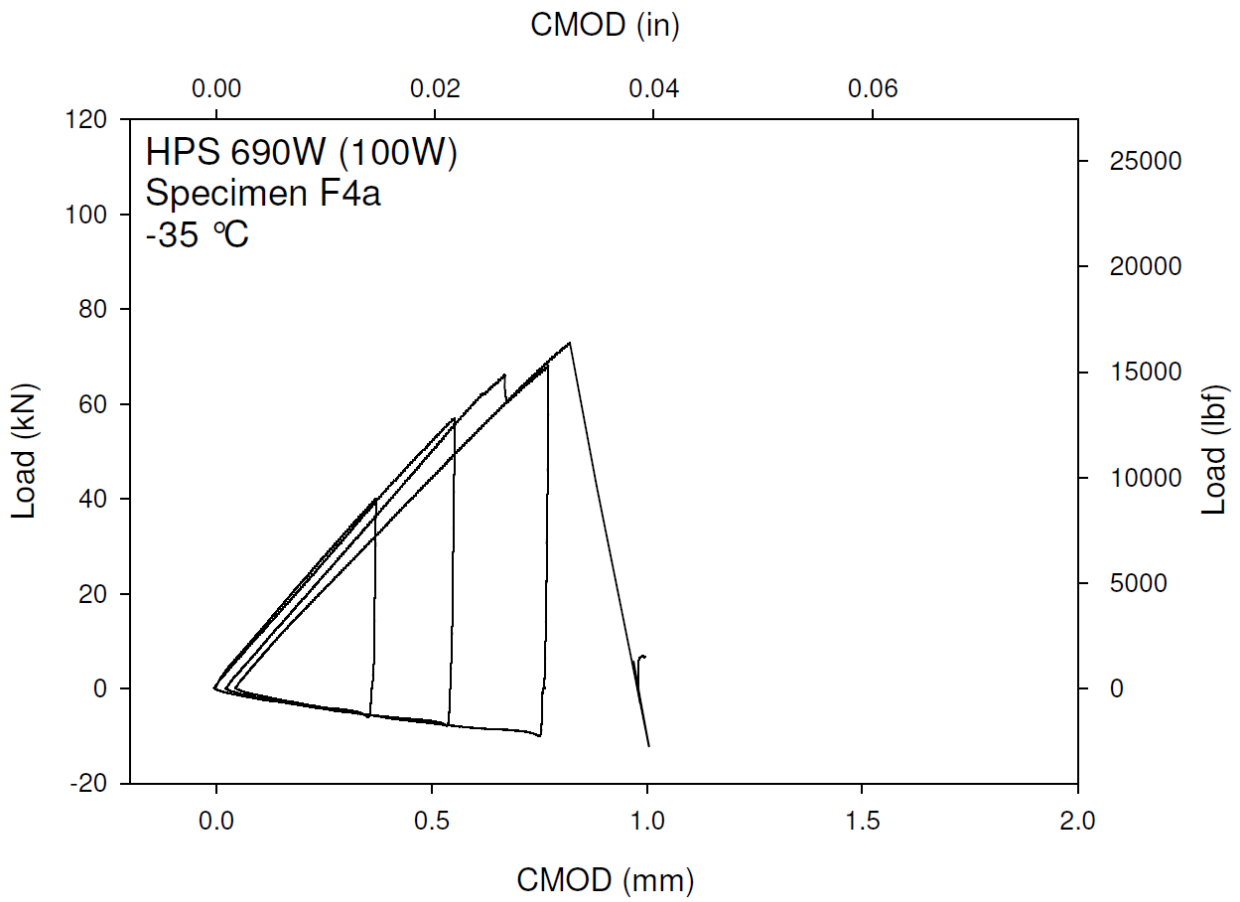

Figure H-31. Specimen F4a Test Record

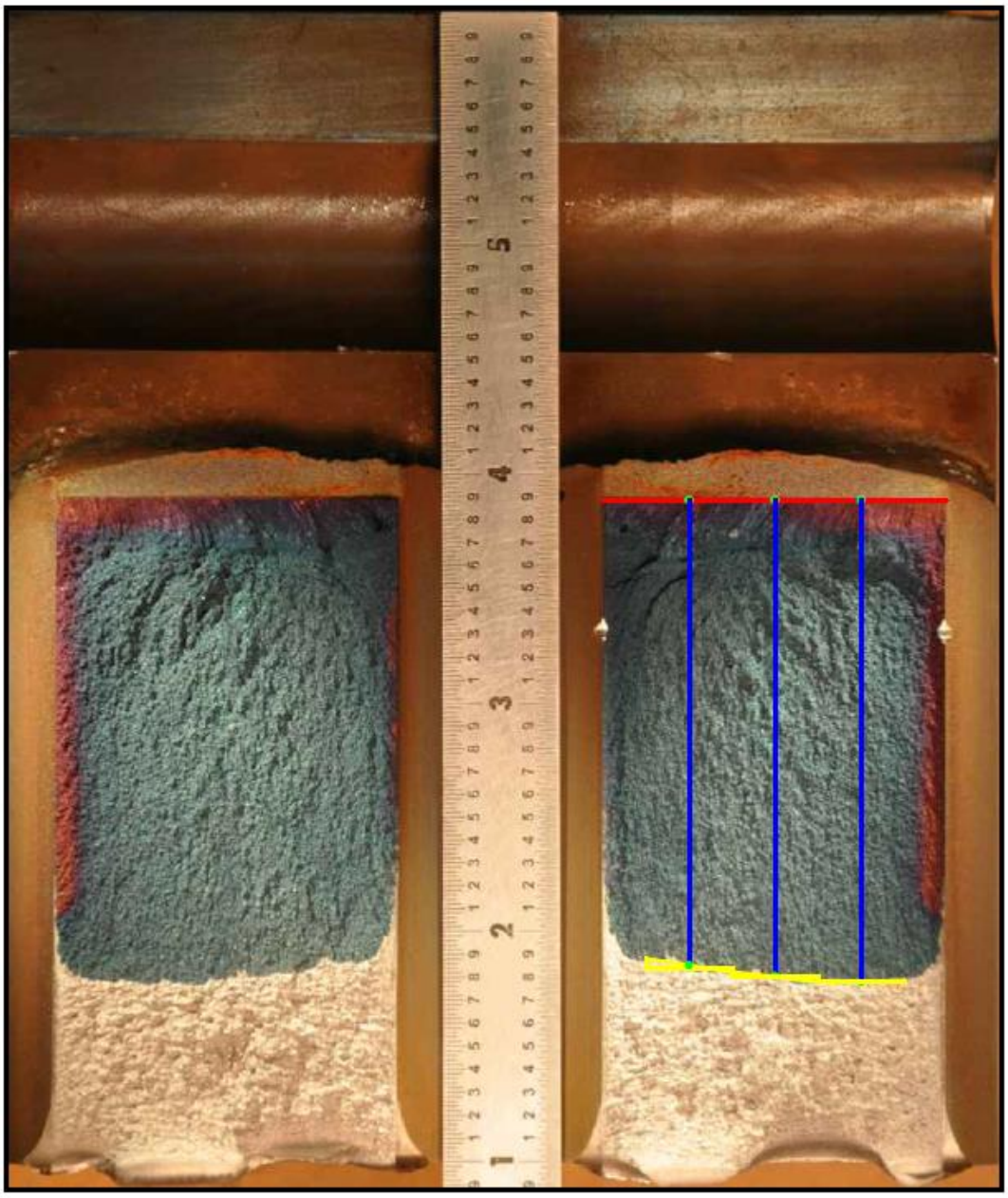

Figure H-32. Specimen F4a Fracture Surface

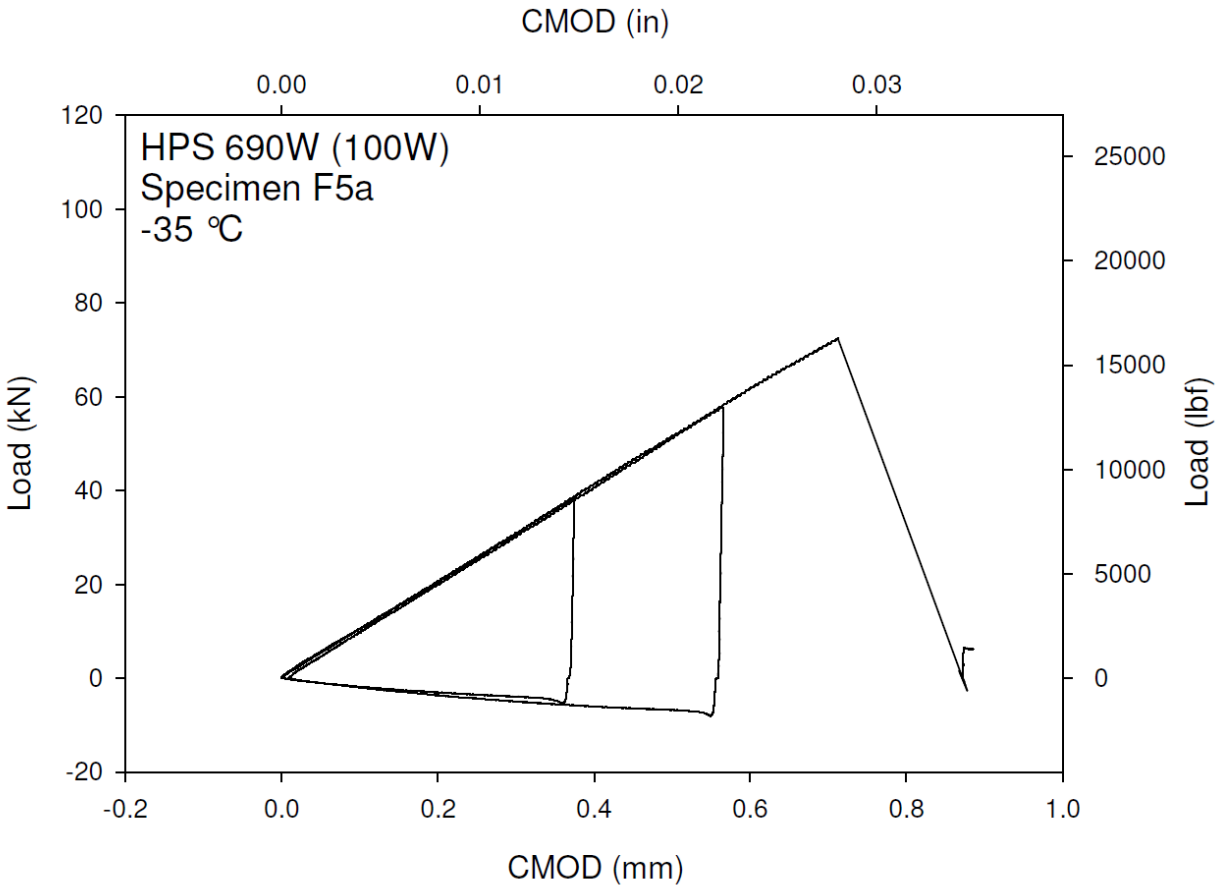

Figure H-33. Specimen F5a Test Record

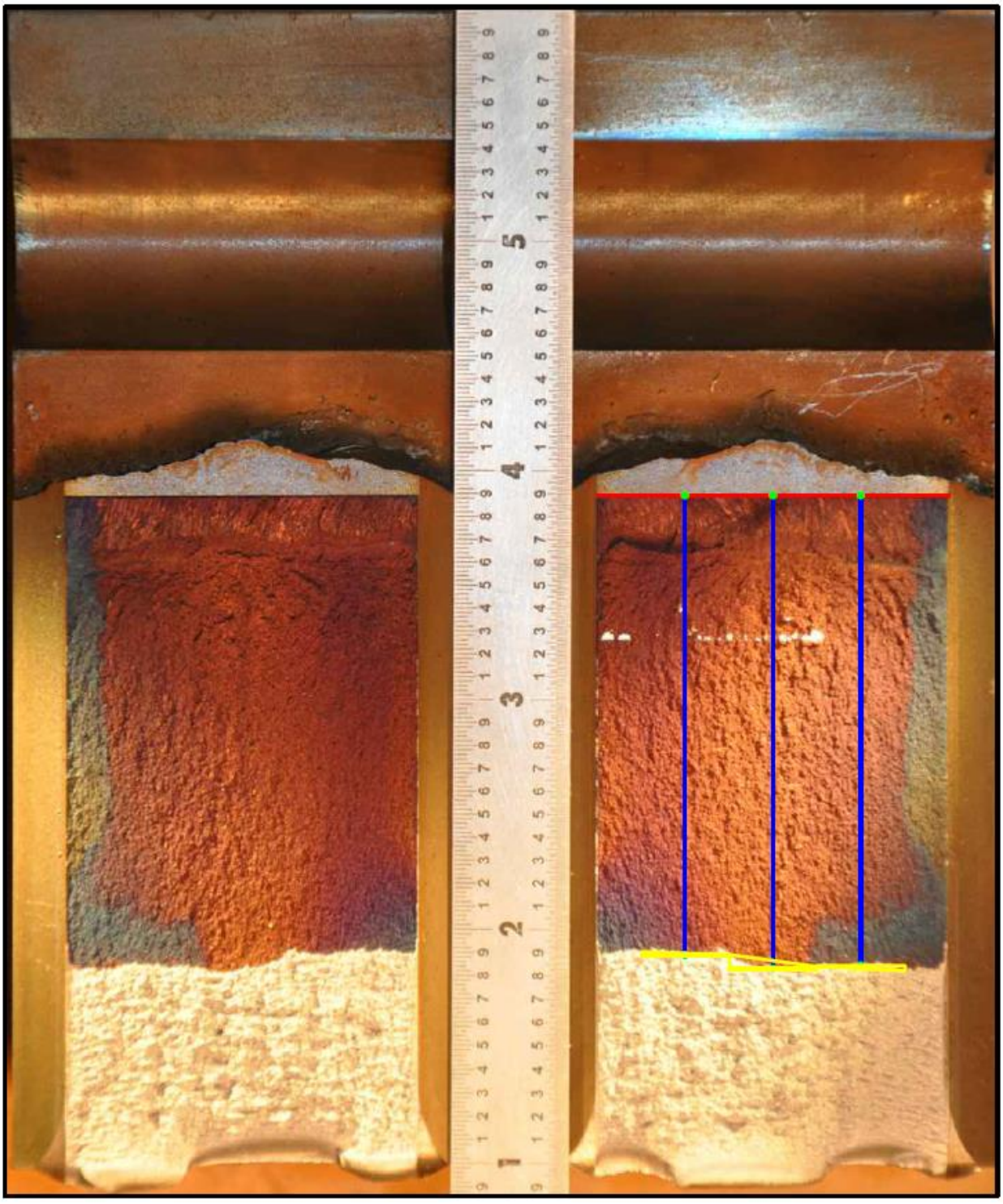

Figure H-34. Specimen F5a Fracture Surface

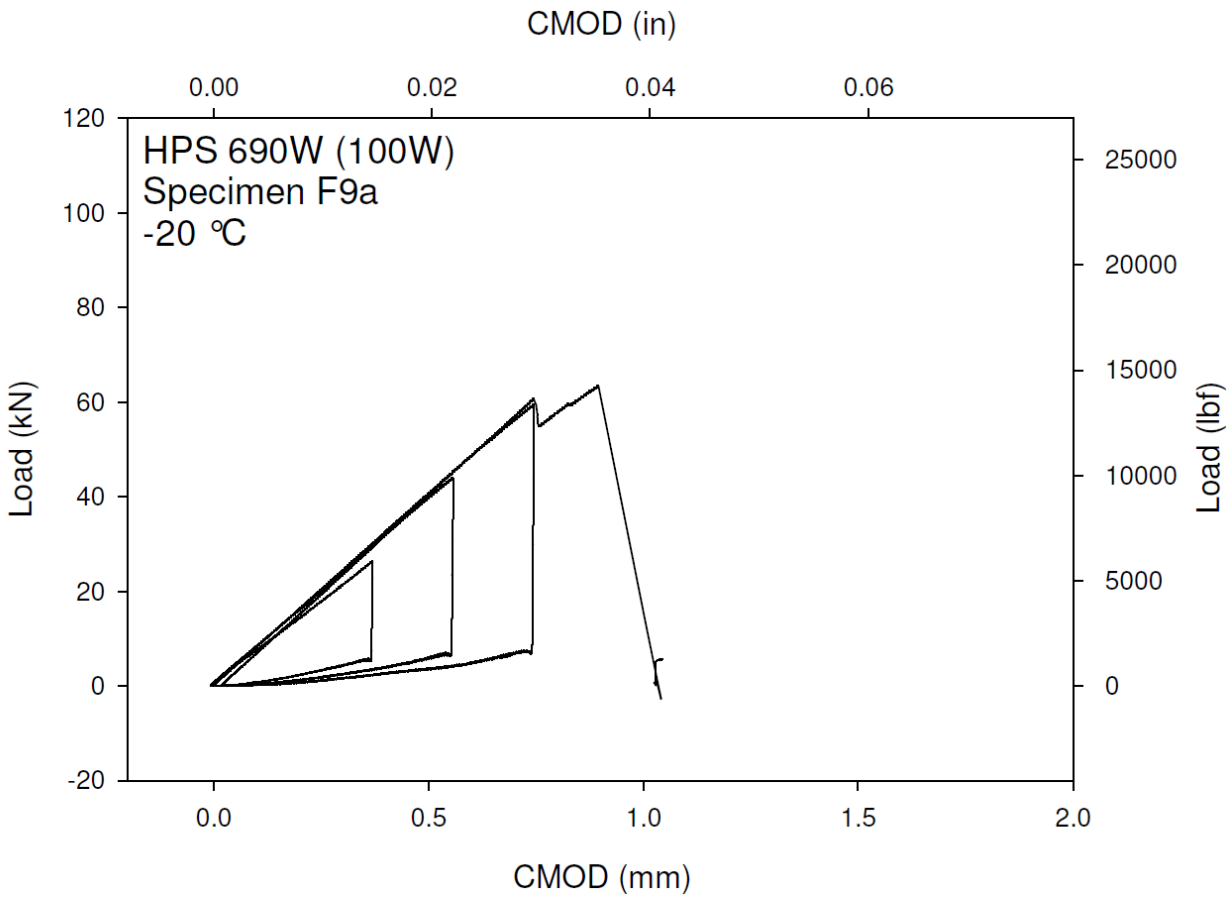

Figure H-35. Specimen F9a Test Record

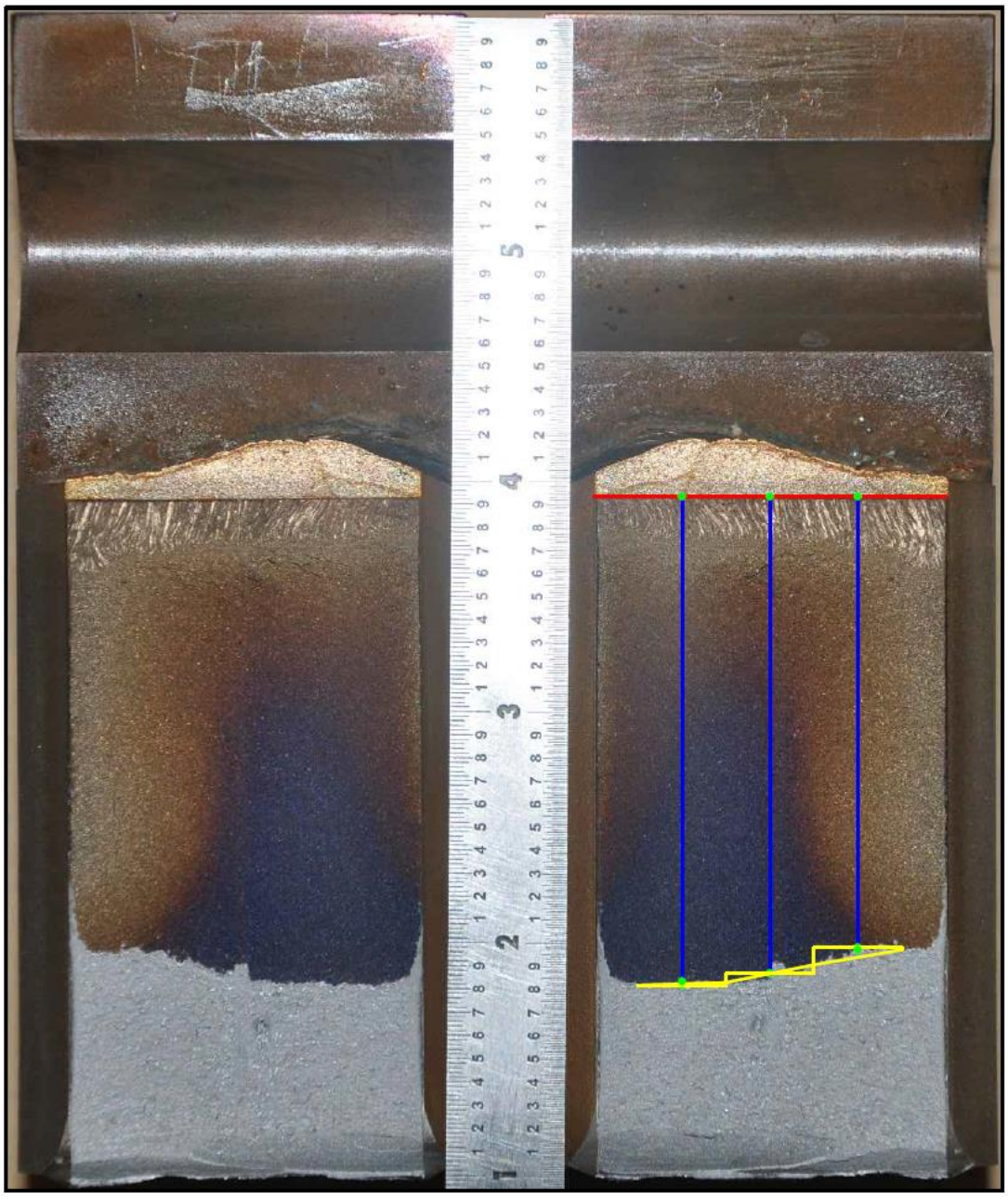

Figure H-36. Specimen F9a Fracture Surface

APPENDIX I: Tabulated HPS Crack Arrest Toughness

Table I-1. Valid Arrest Specimen Information

Specimen ID	Test Temperature		W		a_o		B		B_N		a_a		N	
	°C	°F	mm.	in.	mm.	in.	mm.	in.	mm.	in.	mm.	in.	mm.	in.
D1a	-35	-31	101.63	4.001	27.84	1.0961	50.90	2.004	39.00	1.535	74.88	2.9481	9.86	0.388
D2a	-35	-31	101.60	4.000	28.07	1.1053	50.83	2.001	38.90	1.532	74.35	2.9273	10.03	0.395
D4a	-50	-58	101.79	4.007	27.97	1.1010	50.88	2.003	39.03	1.537	75.44	2.9700	10.01	0.394
D5a	-50	-58	101.63	4.001	28.06	1.1049	50.90	2.004	38.88	1.531	65.97	2.5972	10.11	0.398
D9a	-35	-31	101.62	4.001	27.76	1.0928	50.95	2.006	38.99	1.535	77.96	3.0694	10.01	0.394
E1a	-35	-31	101.13	3.982	32.64	1.2849	37.47	1.475	29.05	1.144	84.72	3.3354	10.85	0.427
E19a	-50	-58	102.06	4.018	27.94	1.1001	36.98	1.456	28.45	1.120	83.52	3.2880	10.11	0.398
F4a	-35	-31	102.40	4.032	28.44	1.1195	50.14	1.974	38.33	1.509	80.89	3.1847	9.88	0.389
F5a	-35	-31	101.93	4.013	27.76	1.0930	50.32	1.981	38.89	1.531	79.38	3.1251	10.08	0.397
F9a	-20	-4	101.32	3.989	27.72	1.0913	49.99	1.968	38.77	1.527	79.75	3.1396	10.08	0.397

Table I-2. Valid Arrest Test Record Information

Specimen ID	δ_o		δ_a		δ_{R1}		$\delta_{R\text{-}last}$		K_o		K_{Ia}	
	mm.	in.	mm.	in.	mm.	in.	mm.	in.	MPa√m	ksi√in	MPa√m	ksi√in
D1a	0.7795	0.03069	0.8806	0.03467	0.0025	0.0001	0.0892	0.0035	155.9	141.9	69.1	62.9
D2a	0.7584	0.02986	0.8402	0.03308	0.0033	0.0001	0.0881	0.0035	150.7	137.1	67.4	61.3
D4a	0.5093	0.02005	0.6101	0.02402	-0.0010	0.0000	0.0069	0.0003	113.1	102.9	48.6	44.2
D5a	0.5987	0.02357	0.6650	0.02618	-0.0025	-0.0001	0.0411	0.0016	125.4	114.1	64.6	58.8
D9a	0.9378	0.03692	1.0282	0.04048	0.0005	0.0000	0.1709	0.0067	173.8	158.2	73.6	67.0
E1a	0.7625	0.03002	0.8865	0.03490	0.0015	0.0001	0.0198	0.0008	147.3	134.0	53.7	48.9
E19a	1.046	0.04118	1.1466	0.04514	-0.0061	-0.0002	0.0503	0.0020	224.2	204.0	75.7	68.9
F4a	0.8207	0.03231	0.9784	0.03852	-0.0046	-0.0002	0.0452	0.0018	173.1	157.5	67.7	61.6
F5a	0.7125	0.02805	0.8717	0.03432	0.0000	0.00000	0.0094	0.00037	158.7	144.4	62.3	56.7
F9a	0.8954	0.03525	1.0284	0.04049	-0.0069	-0.00027	0.0175	0.00069	197.7	179.9	74.1	67.4

Table I-3. Invalid Arrest Specimen Information

Specimen ID	Test Temperature		W		a_o		B		B_N		a_a		N	
	°C	°F	mm.	in.	mm.	in.	mm.	in.	mm.	in.	mm.	in.	mm.	in.
D3a	-35	-31	101.17	3.983	37.84	1.4898	50.90	2.004	39.01	1.536	87.90	3.4605	10.03	0.395
D6a	-20	-4	101.51	3.996	27.92	1.0990	50.93	2.005	38.96	1.534	82.21	3.2365	10.16	0.400
D7a	-35	-31	101.60	4.000	32.80	1.2913	50.93	2.005	38.71	1.524	76.93	3.0287	9.96	0.392
D16a	-35	-31	101.65	4.002	27.77	1.0935	50.83	2.001	38.48	1.515	82.39	3.2438	10.03	0.395
D18a	-50	-58	101.71	4.005	27.81	1.0950	50.42	1.985	38.51	1.516	85.72	3.3749	10.08	0.397
E9a	-10	14	101.49	3.996	27.71	1.0910	37.36	1.471	28.66	1.128	87.47	3.4436	10.52	0.414
E16a	-20	-4	102.20	4.024	27.80	1.0943	37.19	1.464	28.45	1.120	84.69	3.3344	10.21	0.402
E21a	-20	-4	102.05	4.018	27.59	1.0864	37.01	1.457	28.50	1.122	88.74	3.4936	10.21	0.402

Table I-4. Invalid Arrest Test Record Information

Specimen ID	δ_o		δ_a		δ_{R1}		$\delta_{R\text{-}last}$		K_o		K_{Ia}	
	mm.	in.	mm.	in.	mm.	in.	mm.	in.	MPa√m	ksi√in	MPa√m	ksi√in
D3a	1.6002	0.06300	1.6990	0.06689	-0.0127	-0.0005	0.2047	0.0081	246.5	224.3	91.1	82.9
D6a	1.2271	0.04831	1.3185	0.05191	-0.0185	-0.0007	0.3759	0.0148	192.1	174.8	79.7	72.5
D7a	1.1816	0.04652	1.2581	0.04953	-0.0094	-0.0004	0.1417	0.0056	207.8	189.1	97.5	88.7
D16a	1.5019	0.05913	1.5565	0.06128	-0.0056	-0.0002	0.3470	0.0137	263.1	239.4	99.2	90.3
D18a	1.4475	0.05699	1.5235	0.05998	0.0010	0.0000	0.2911	0.0115	262.0	238.4	87.3	79.4
E9a	1.3658	0.05377	1.4803	0.05828	0.0020	0.0001	0.1689	0.0067	271.2	246.8	80.8	73.5
E16a	1.5761	0.06205	1.6970	0.06681	-0.0023	-0.0001	0.2283	0.0090	305.6	278.1	104.1	94.7
E21a	1.6436	0.06471	1.7556	0.06912	0.0018	0.0001	0.3790	0.0149	287.3	261.4	87.7	79.8

APPENDIX J: Legacy Data CVN Plots

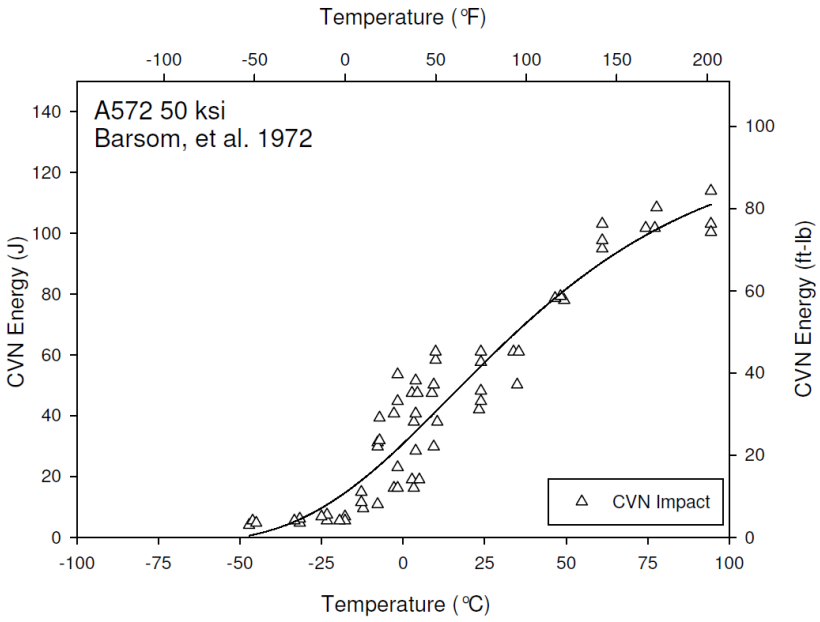

Figure J-1. CVN Data for A572 50, Barsom, et al. 1972

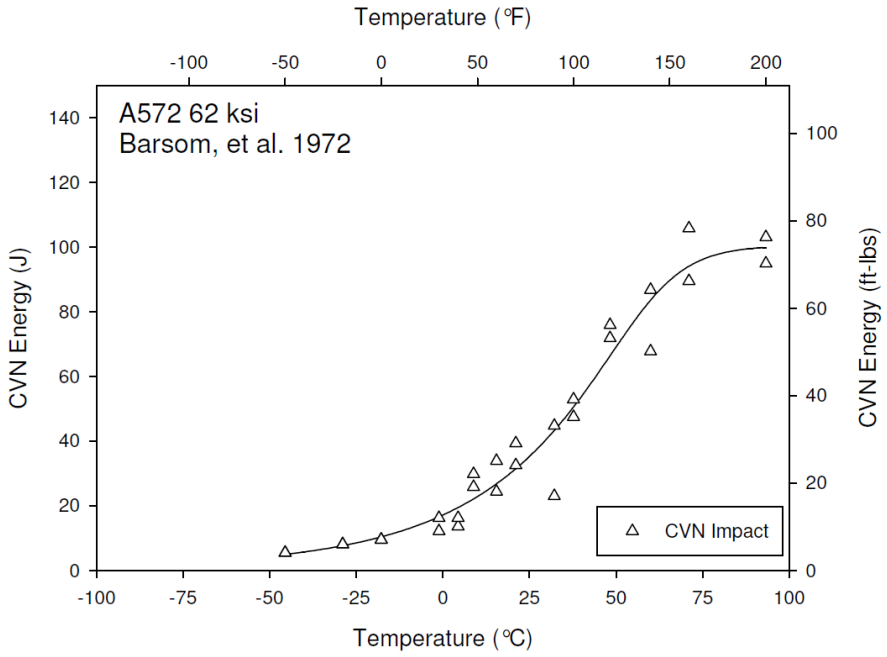

Figure J-2. CVN Data for A572 60, Barsom, et al. 1972

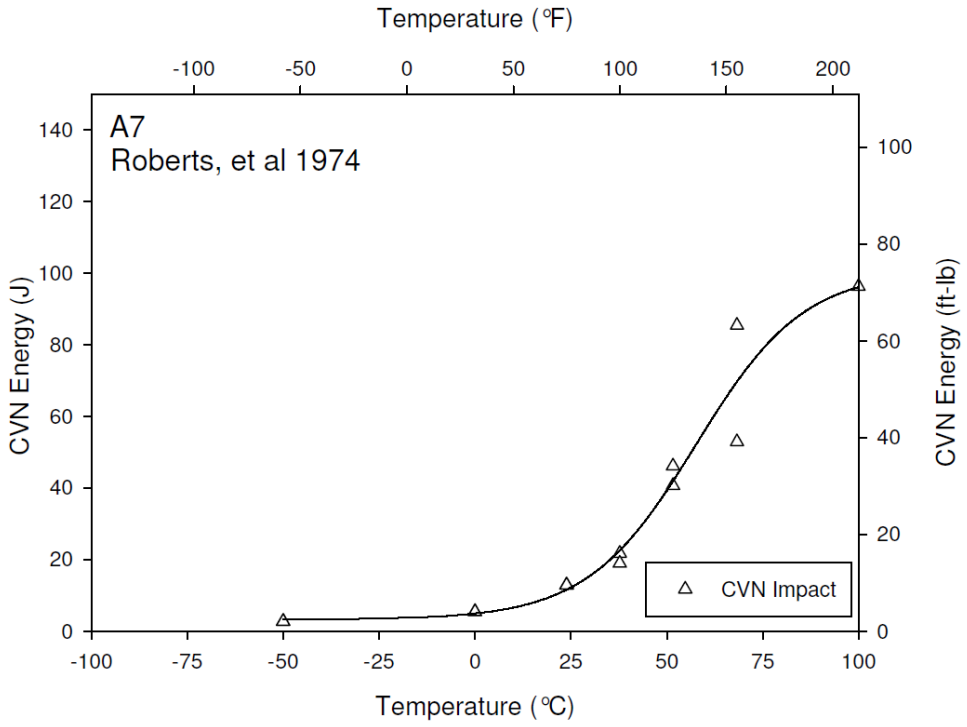

Figure J-3. CVN Data for A7, Roberts, at al. 1974

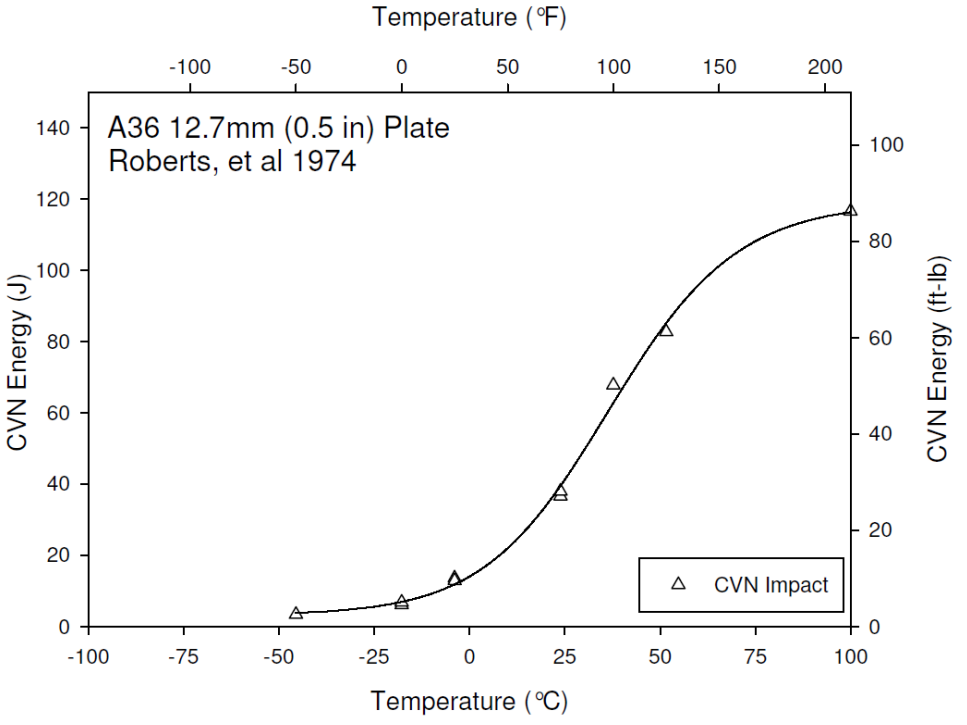

Figure J-4. CVN Data for A36 0.5", Roberts, et al. 1974

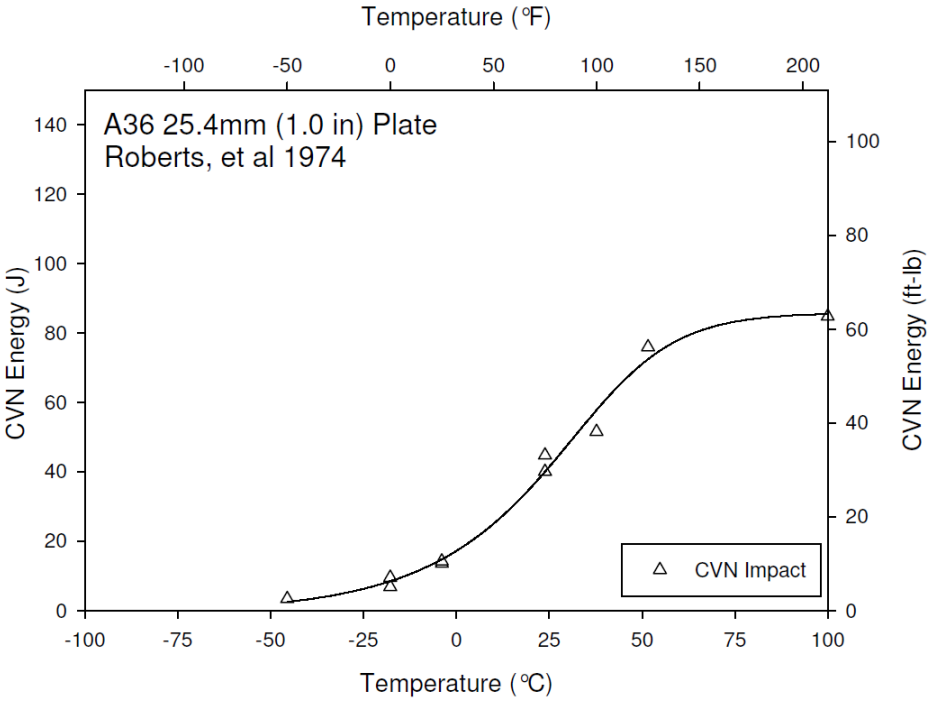

Figure J-5. CVN Data for A36 1.0", Roberts, et al. 1974

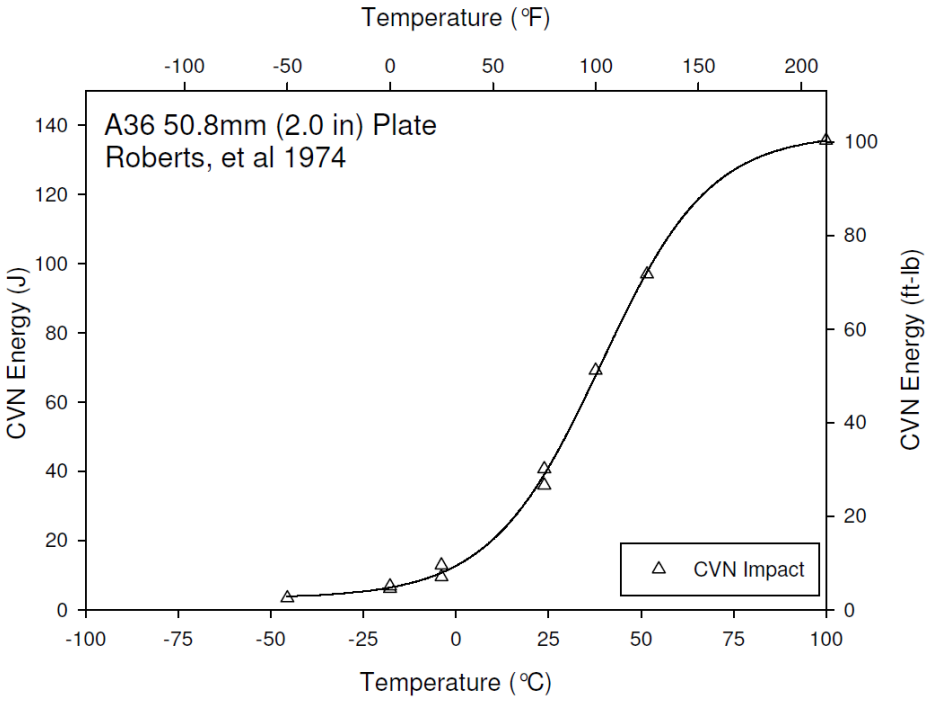

Figure J-6. CVN Data for A36 2.0", Roberts, et al. 1974

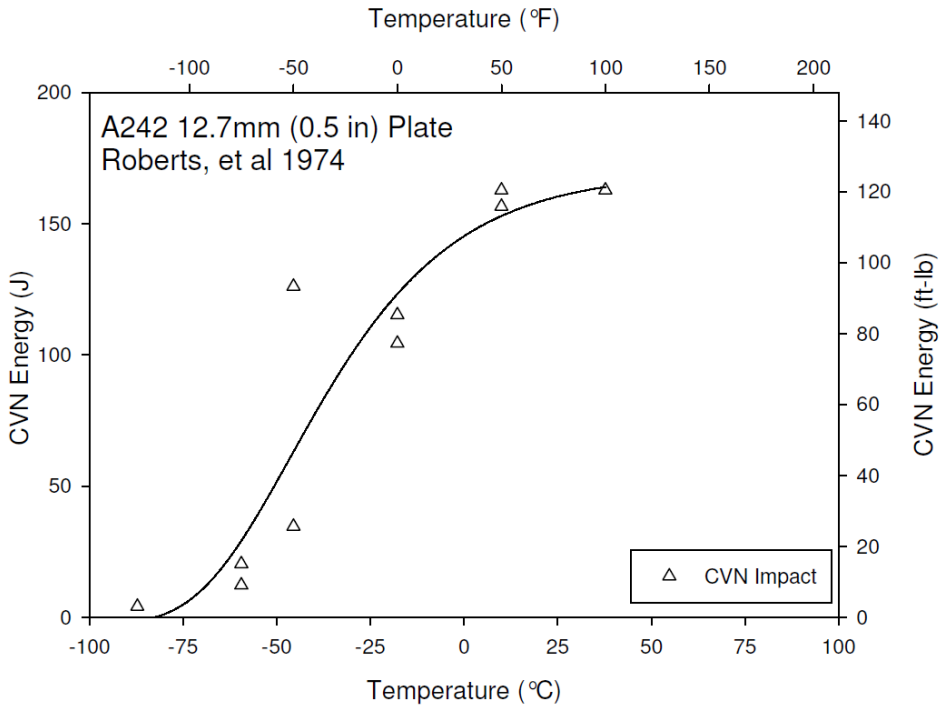

Figure J-7. CVN Data for A242 0.5", Roberts, et al. 1974

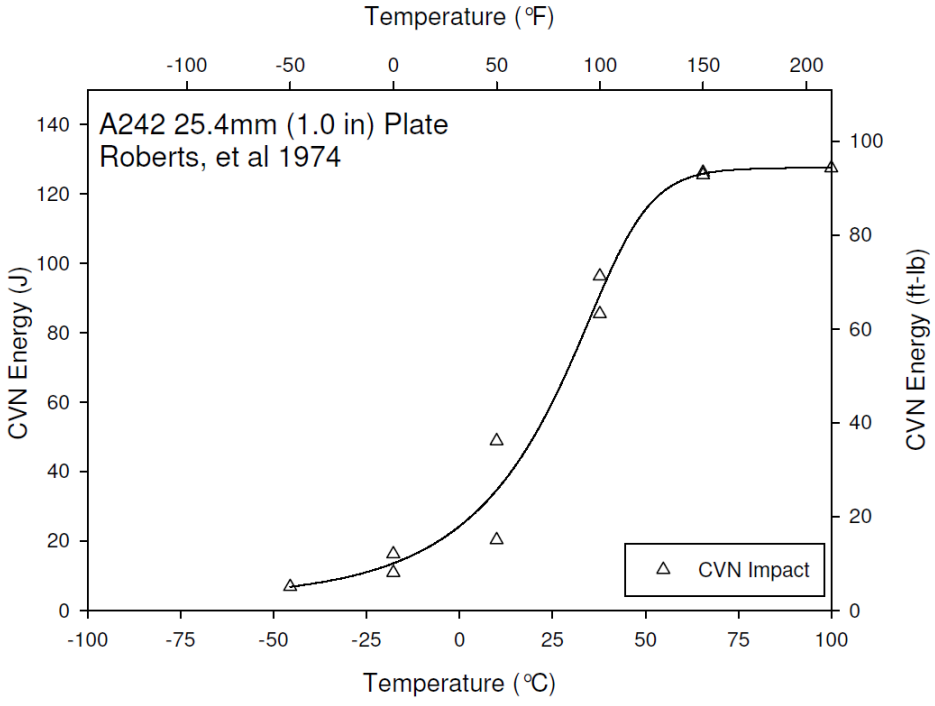

Figure J-8. CVN Data for A242 1.0", Roberts, et al. 1974

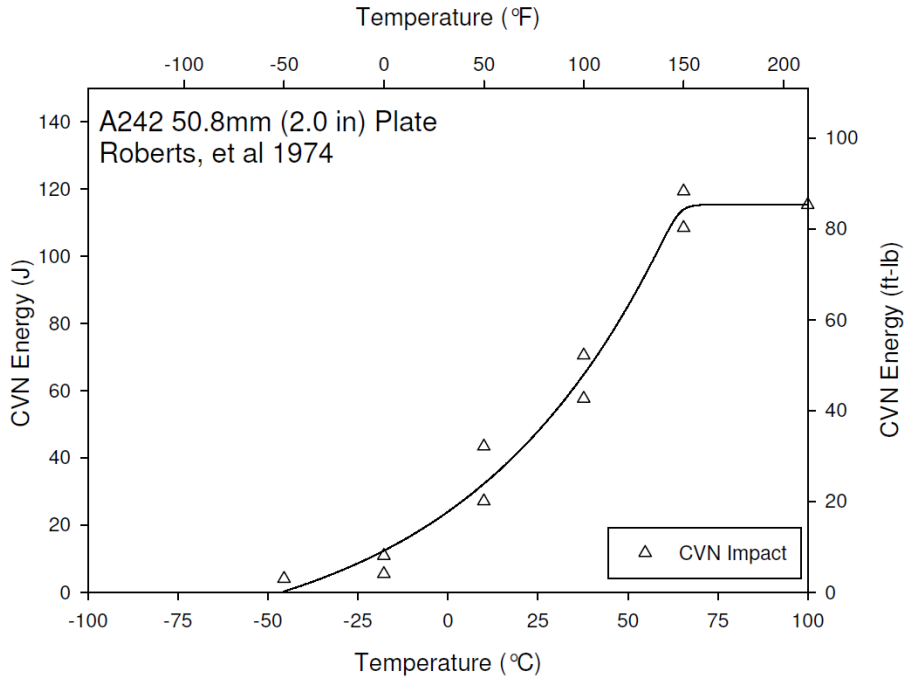

Figure J-9. CVN Data for A242 2.0", Roberts, et al. 1974

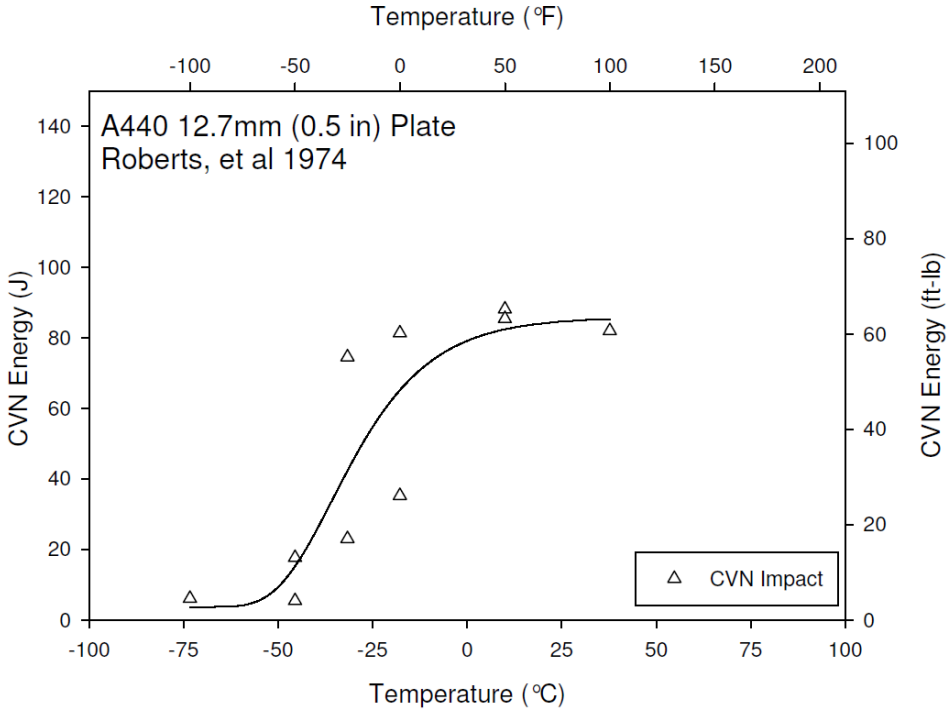

Figure J-10. CVN Data for A440 0.5", Roberts, et al. 1974

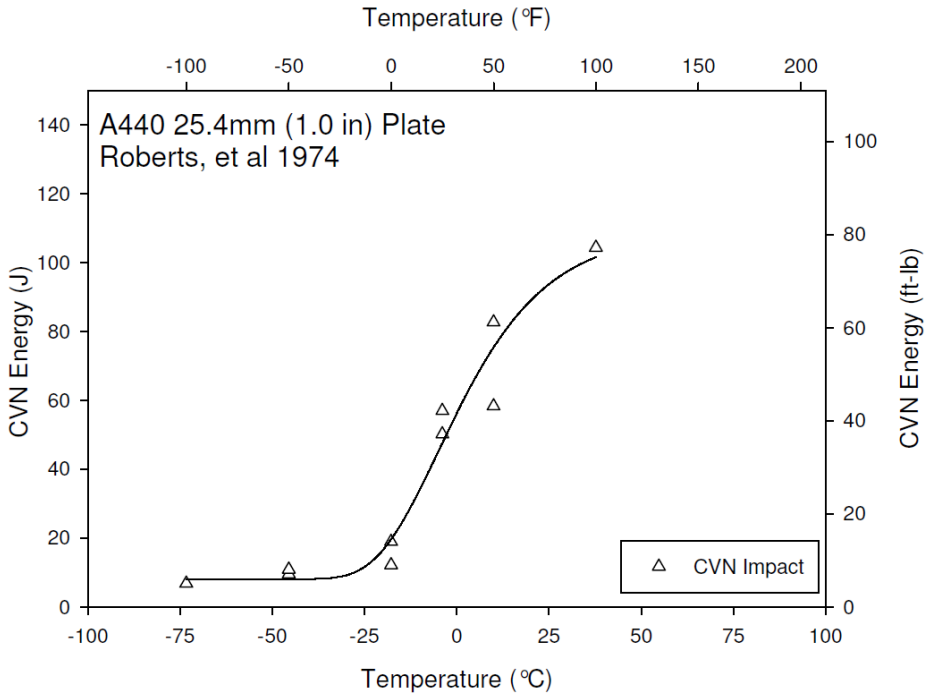

Figure J-11. CVN Data for A440 1.0", Roberts, et al. 1974

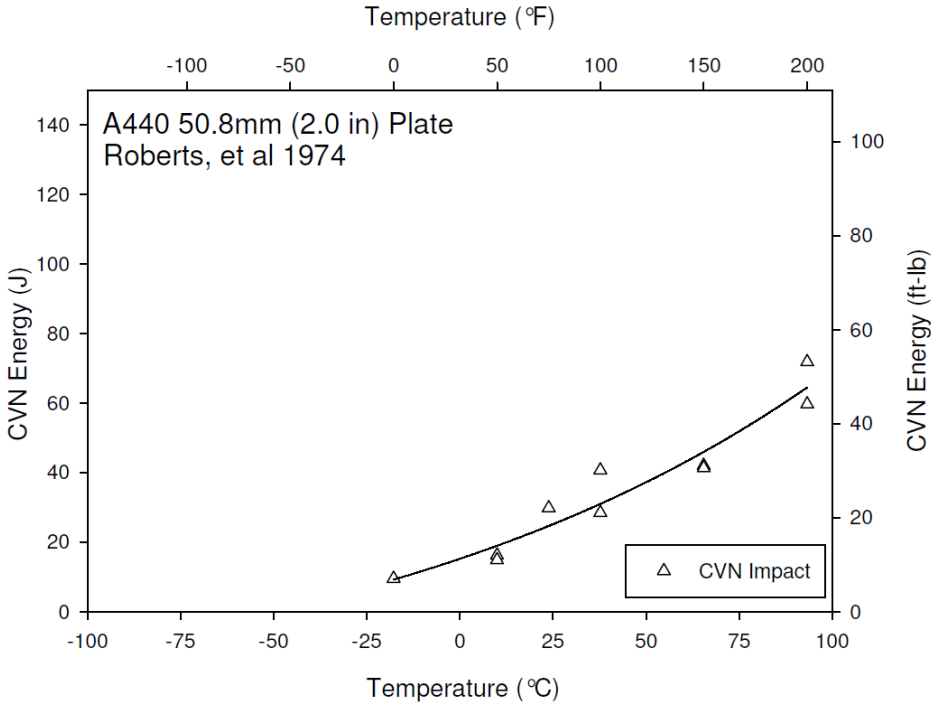

Figure J-12. CVN Data for A440 2.0", Roberts, et al. 1974

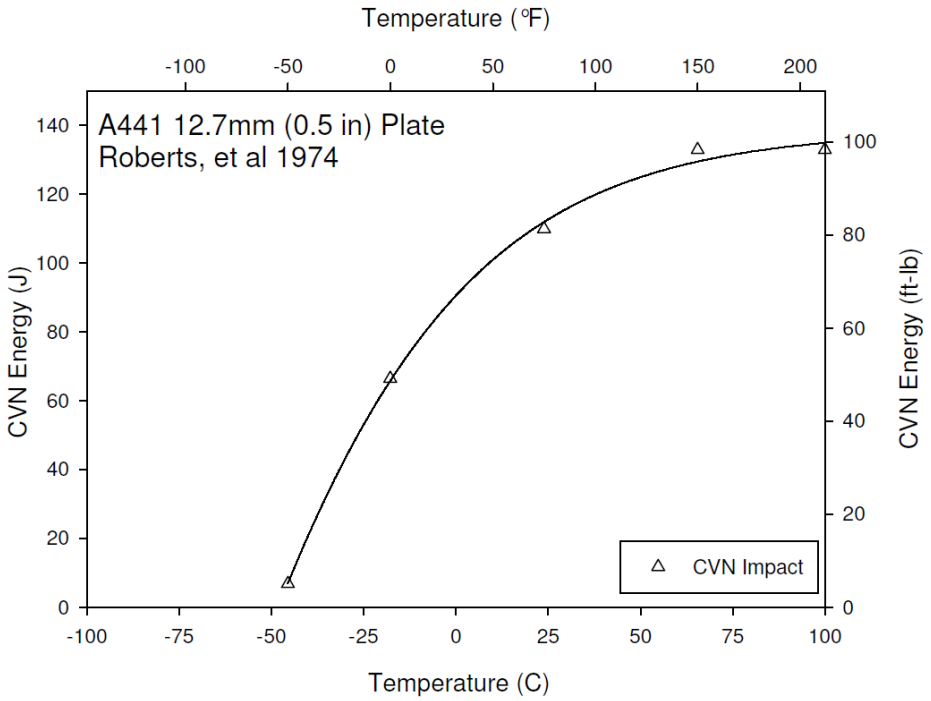

Figure J-13. CVN Data for A441 0.5", Roberts, et al. 1974

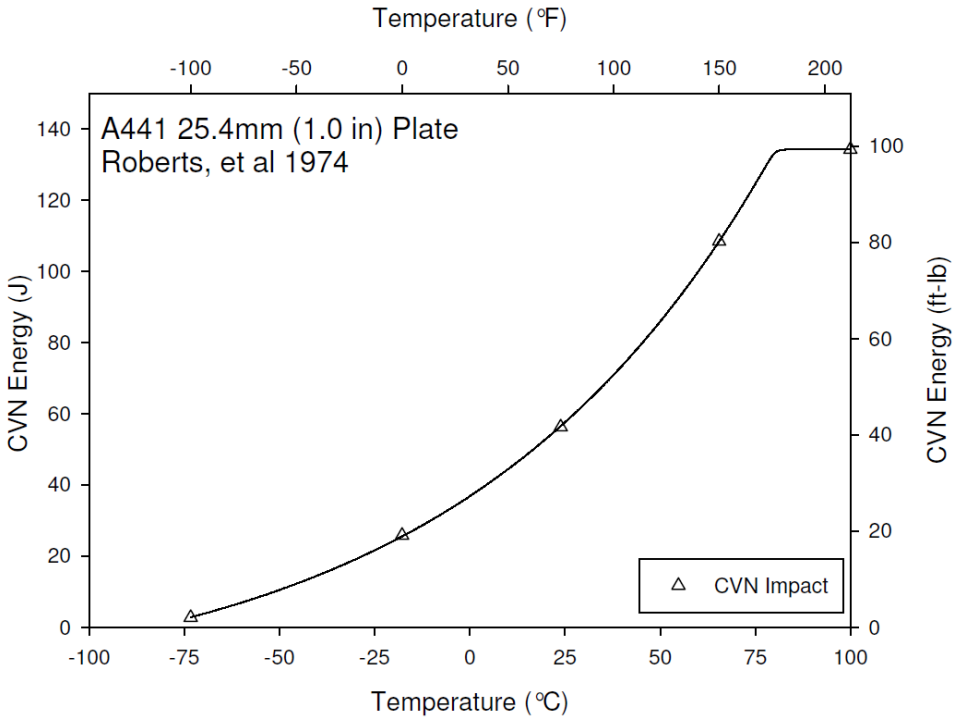

Figure J-14. CVN Data for A441 1.0", Roberts, et al. 1974

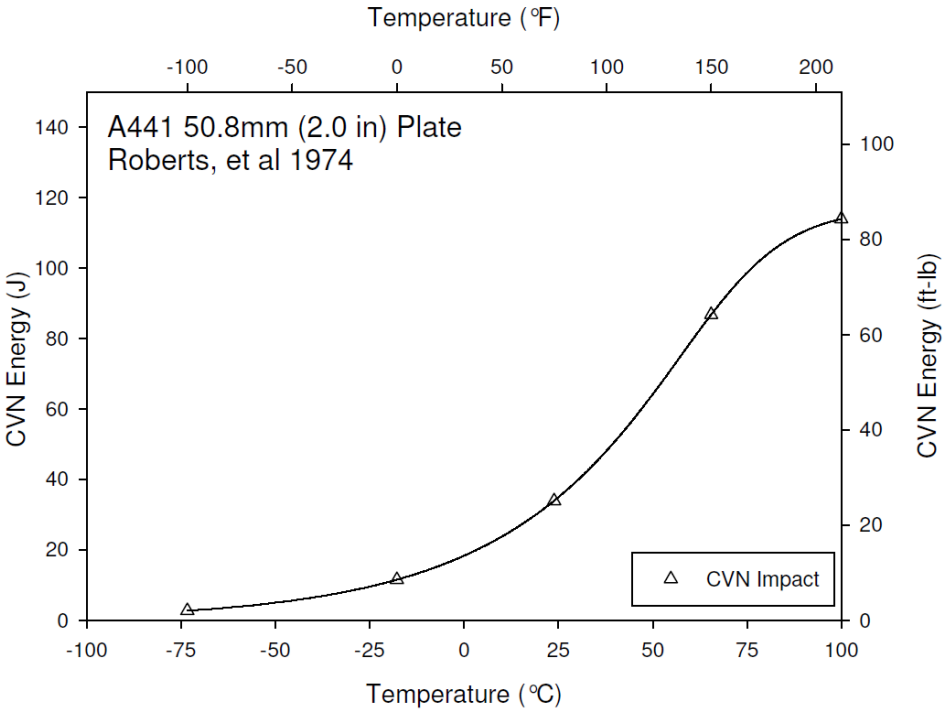

Figure J-15. CVN Data for A441 2.0", Roberts, et al. 1974

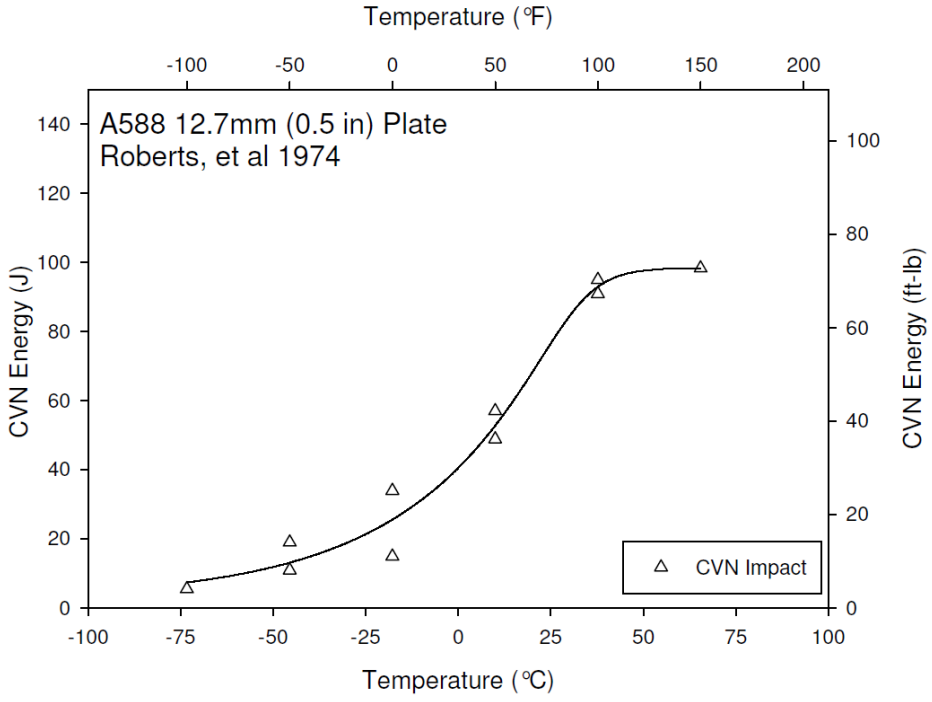

Figure J-16. CVN Data for A588 0.5", Roberts, et al. 1974

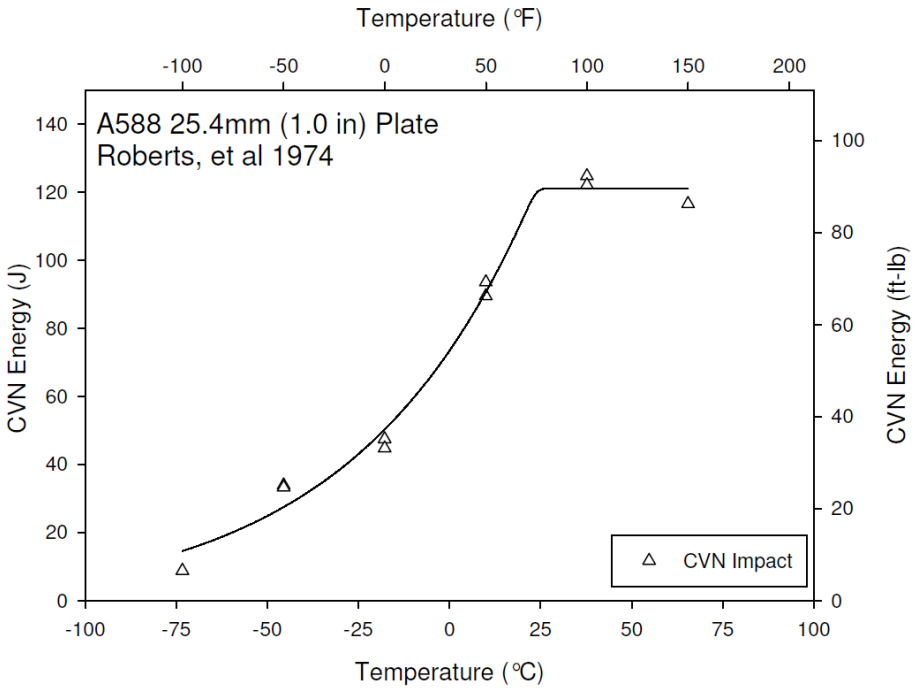

Figure J-17. CVN Data for A588 1.0", Roberts, et al. 1974

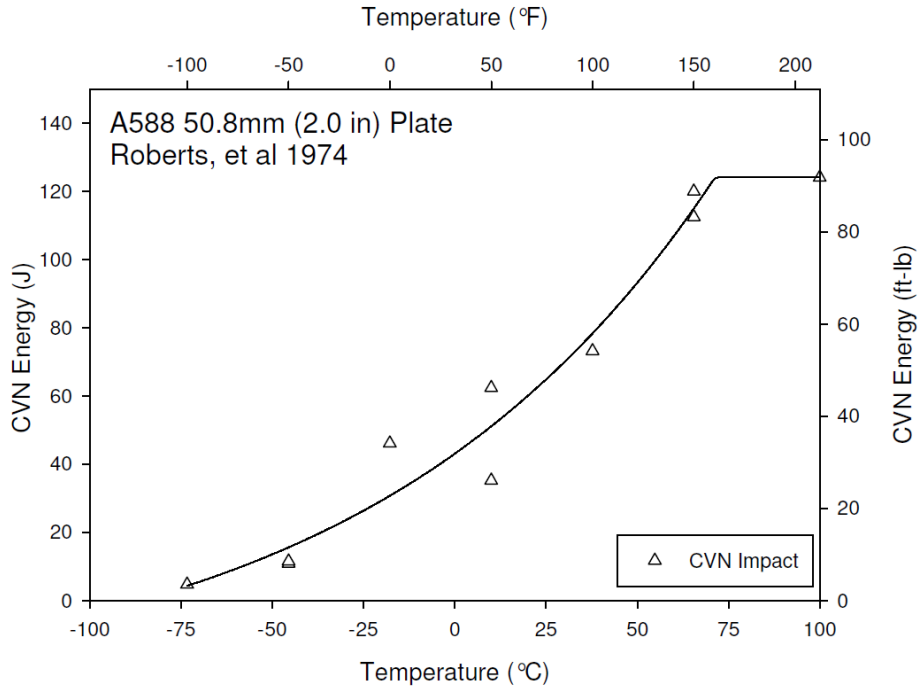

Figure J-18. CVN Data for A588 2.0", Roberts, et al. 1974

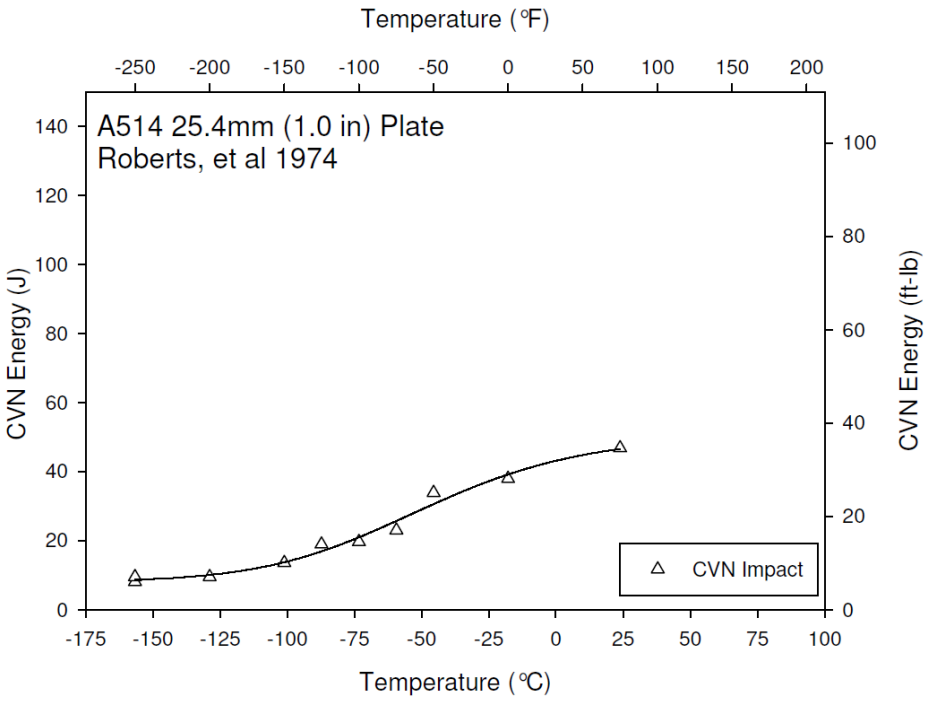

Figure J-19. CVN Data for A514 1.0", Roberts, et al. 1974

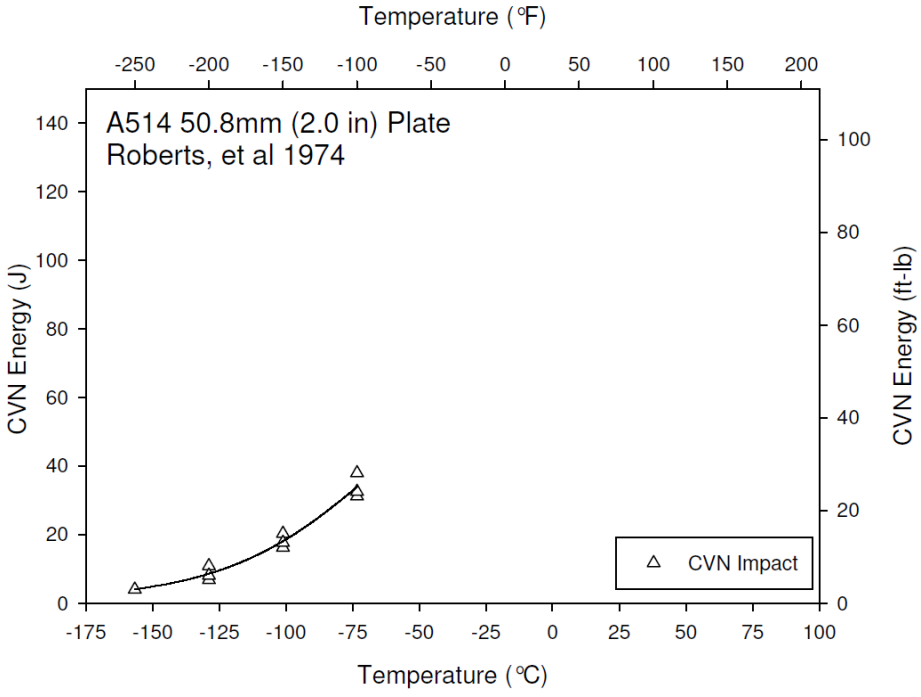

Figure J-20. CVN Data for A514 2.0", Roberts, et al. 1974

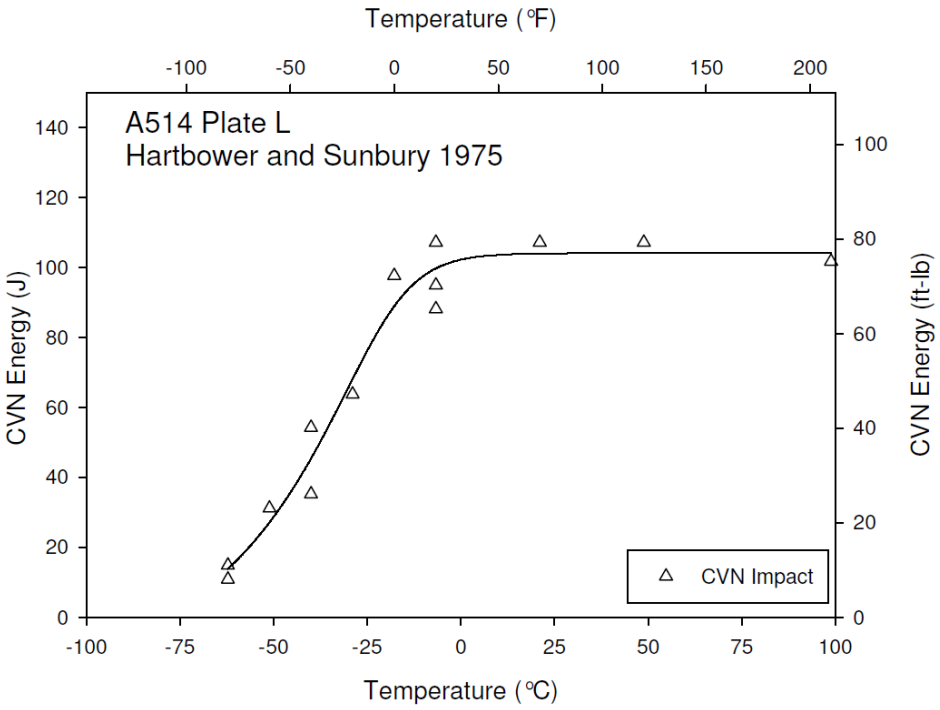

Figure J-21. CVN Data for A514 Plate L, Hartbower and Sunbury 1975

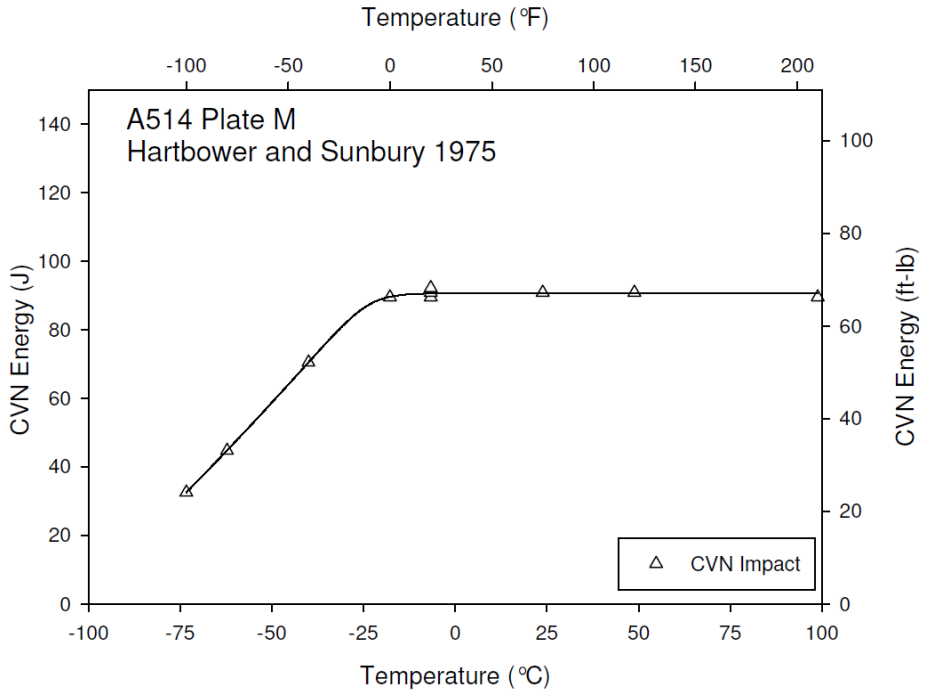

Figure J-22. CVN Data for A514 Plate M, Hartbower and Sunbury 1975

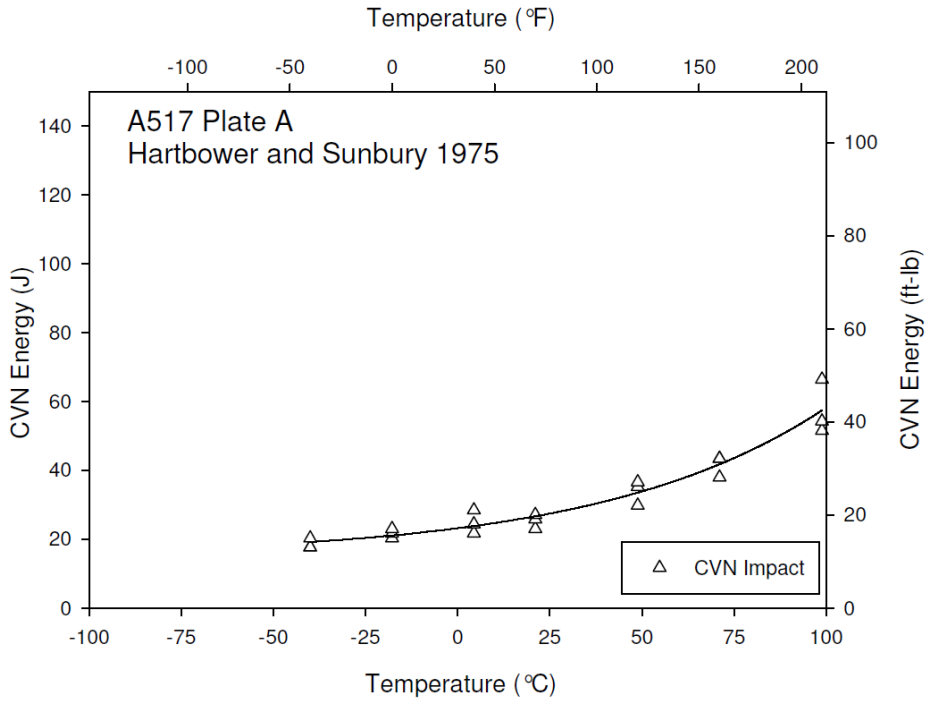

Figure J-23. CVN Data for A517 Plate A, Hartbower and Sunbury 1975

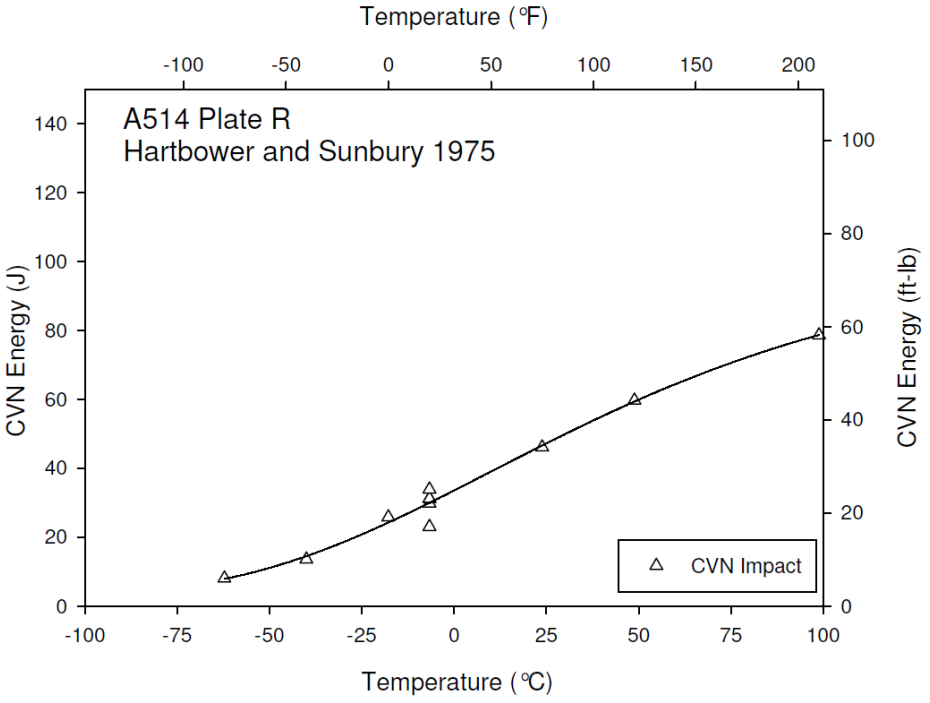

Figure J-24. CVN Data for A514 Plate R, Hartbower and Sunbury 1975

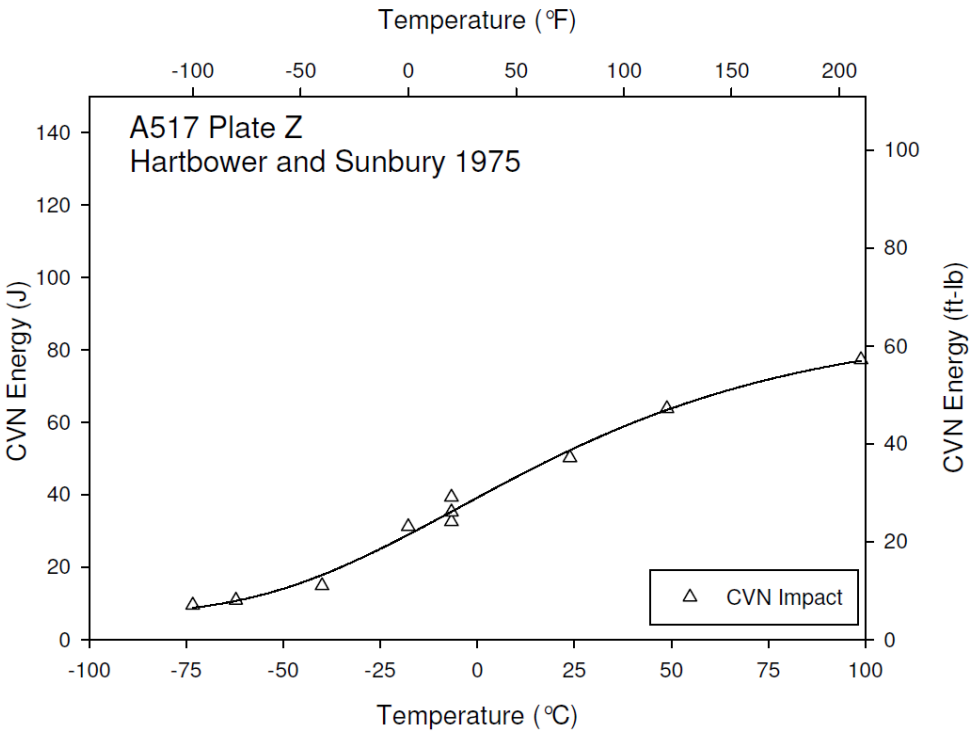

Figure J-25. CVN Data for A517 Plate Z, Hartbower and Sunbury 1975

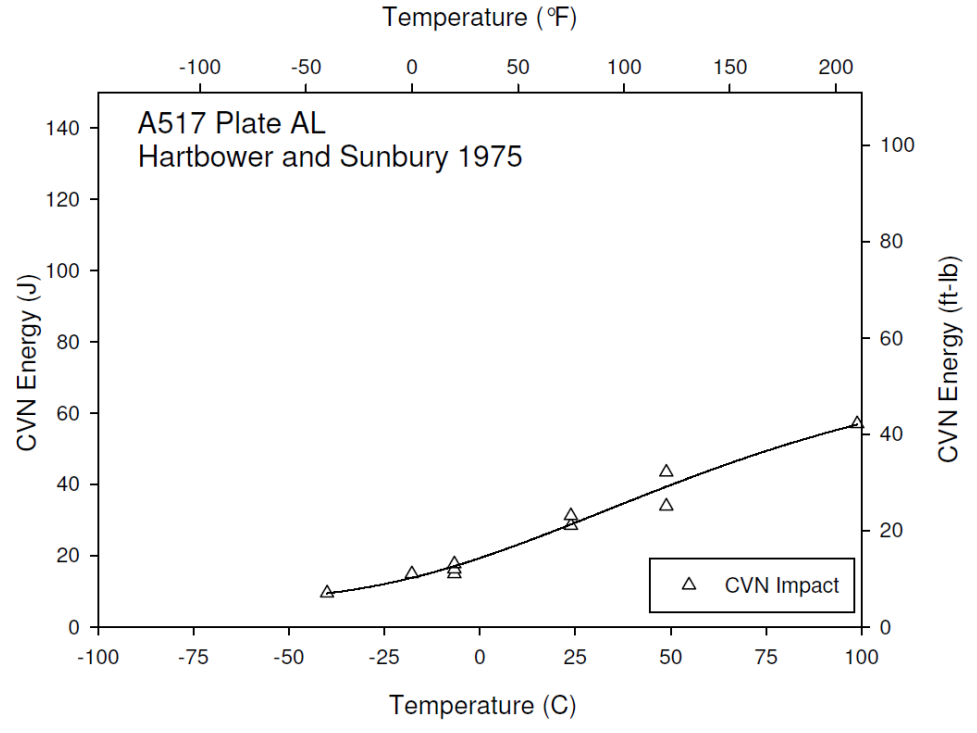

Figure J-26. CVN Data for A517 Plate AL, Hartbower and Sunbury 1975

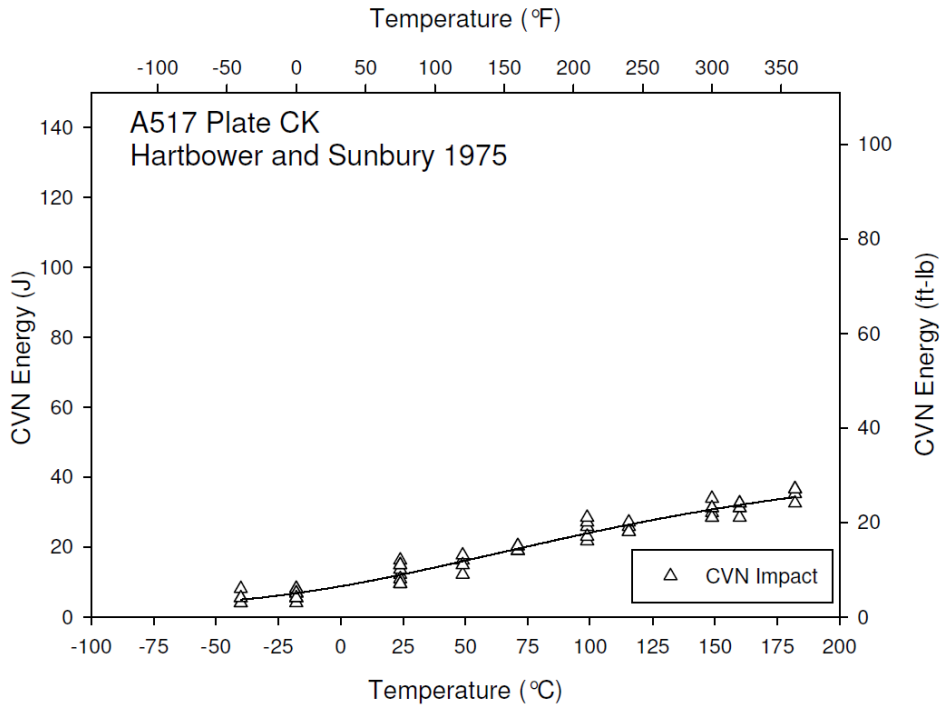

Figure J-27. CVN Data for A517 Plate CK, Hartbower and Sunbury

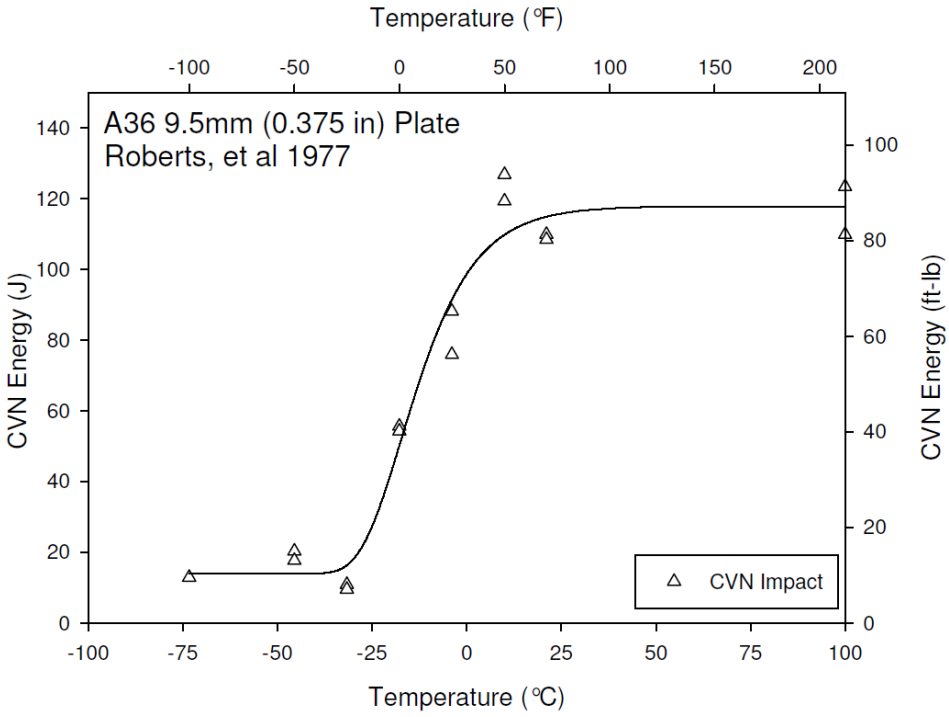

Figure J-28. CVN Data for A36 0.375", Roberts, et al. 1977

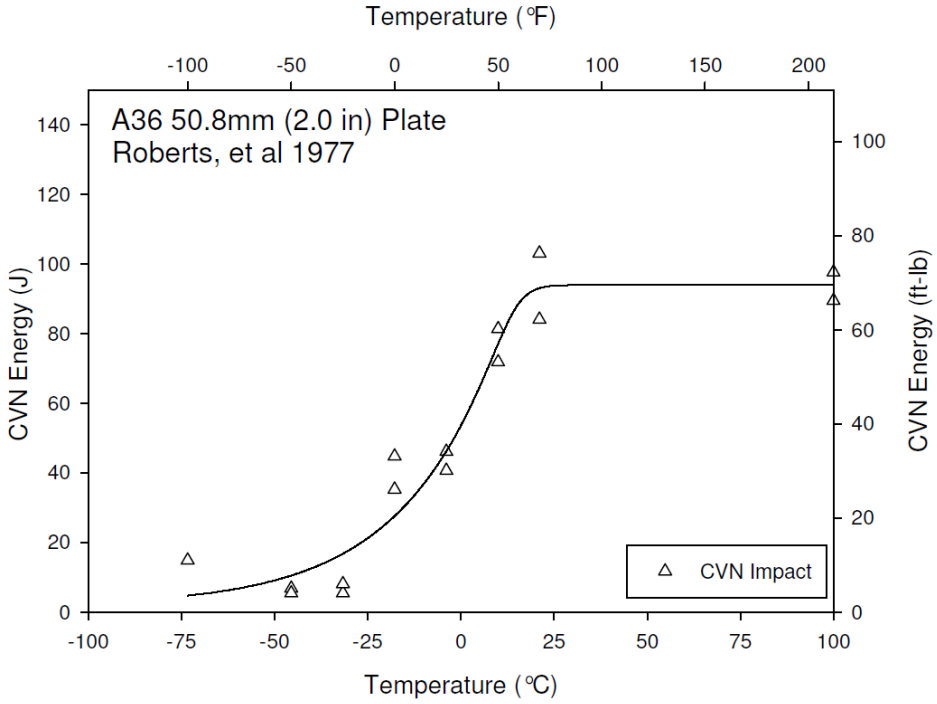

Figure J-29. CVN Data for A36 2.0", Roberts, et al. 1977

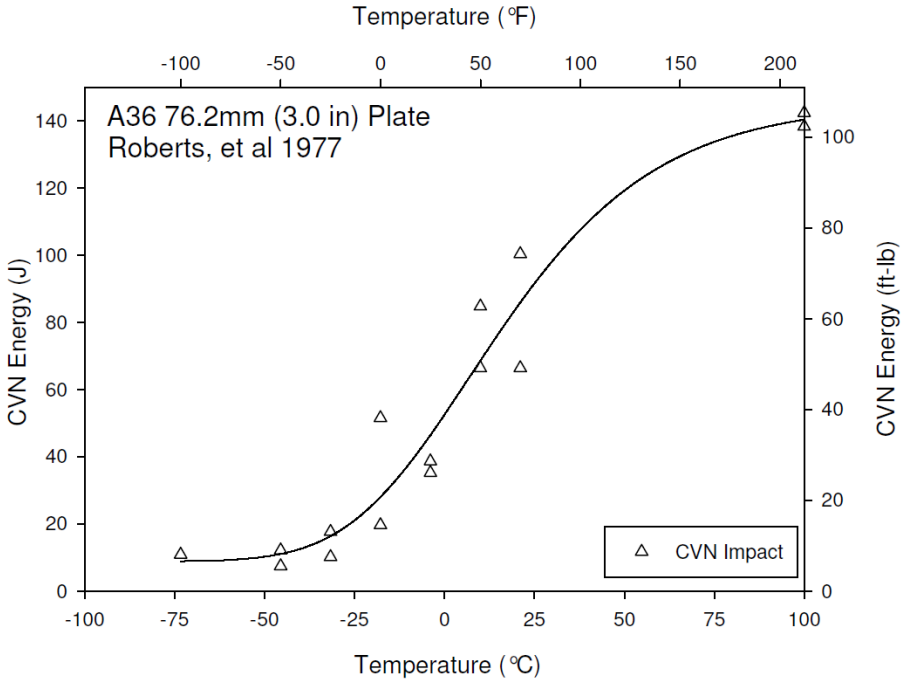

Figure J-30. CVN Data for A36 3.0", Roberts, et al. 1977

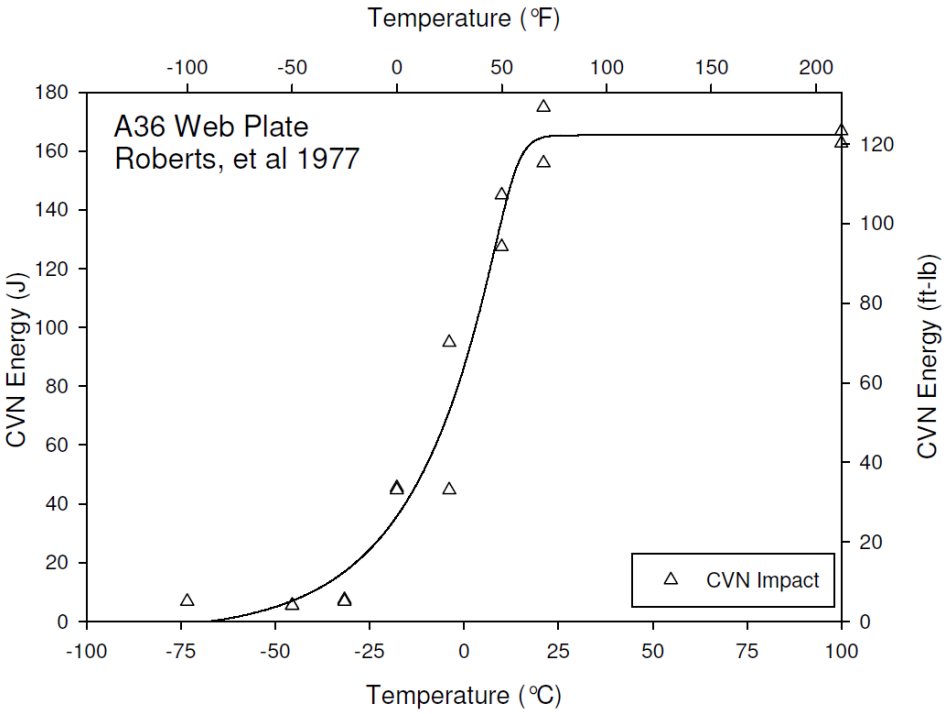

Figure J-31. CVN Data for A36 Web, Roberts, et al. 1977

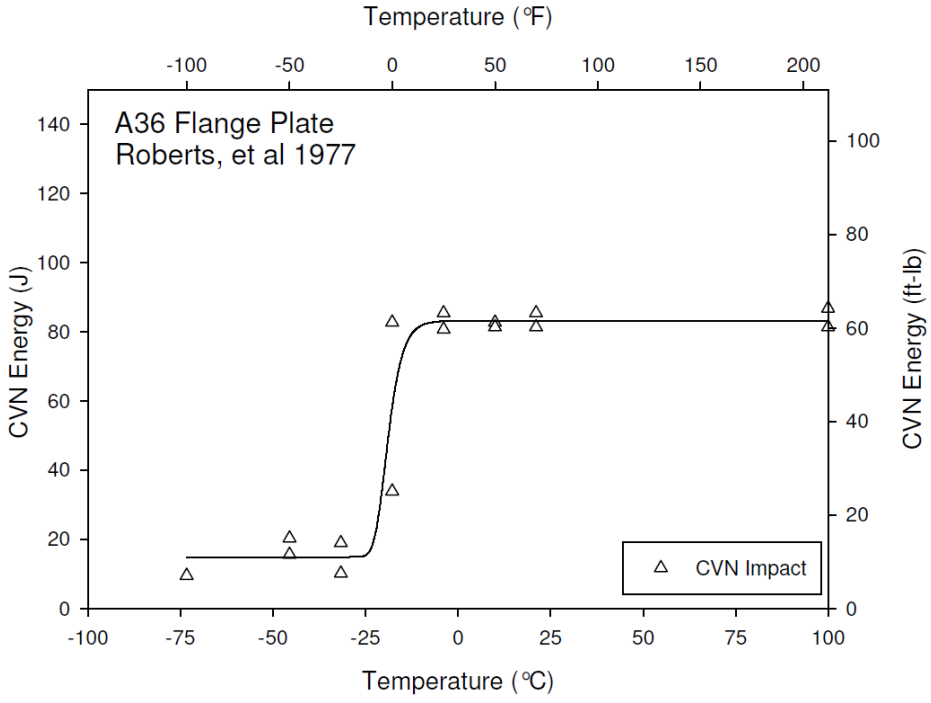

Figure J-32. CVN Data for A36 Flange, Roberts, et al. 1977

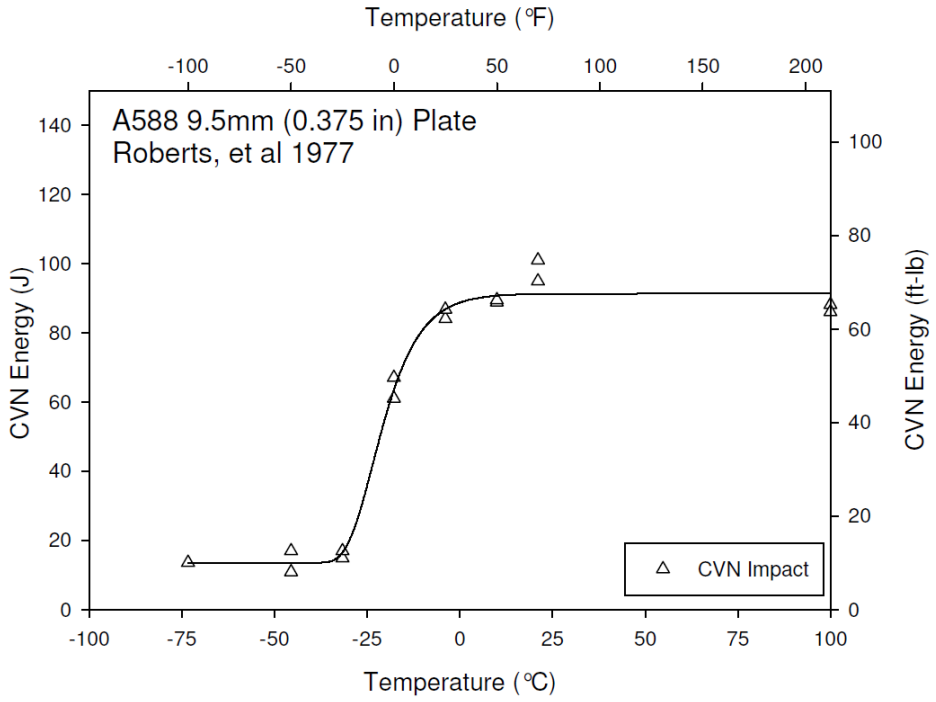

Figure J-33. CVN Data for A588 0.375", Roberts, et al. 1977

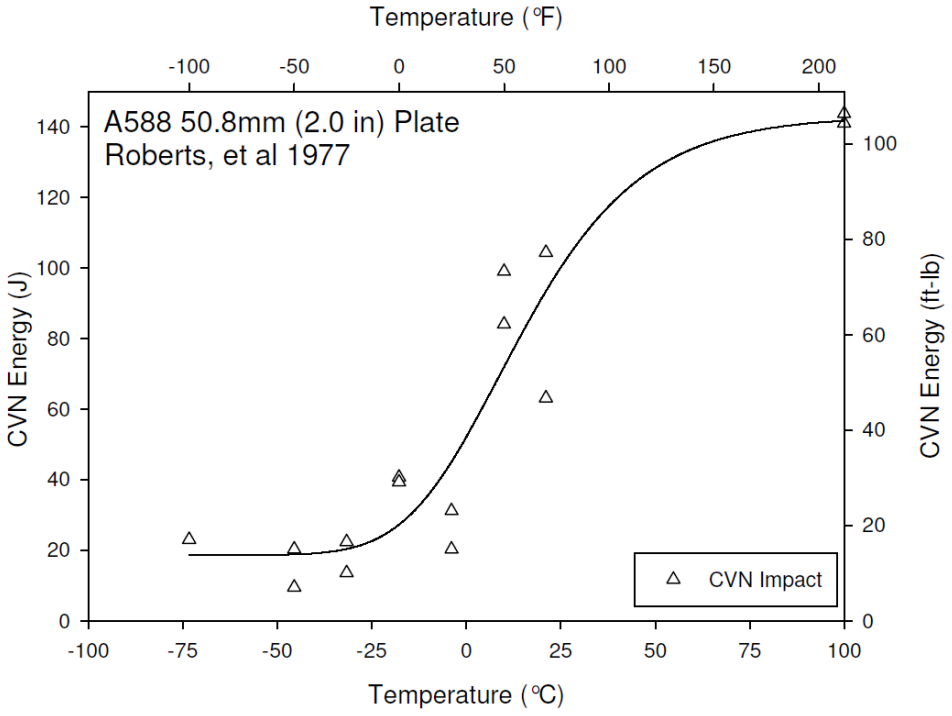

Figure J-34. CVN Data for A588 2.0", Roberts, et al. 1977

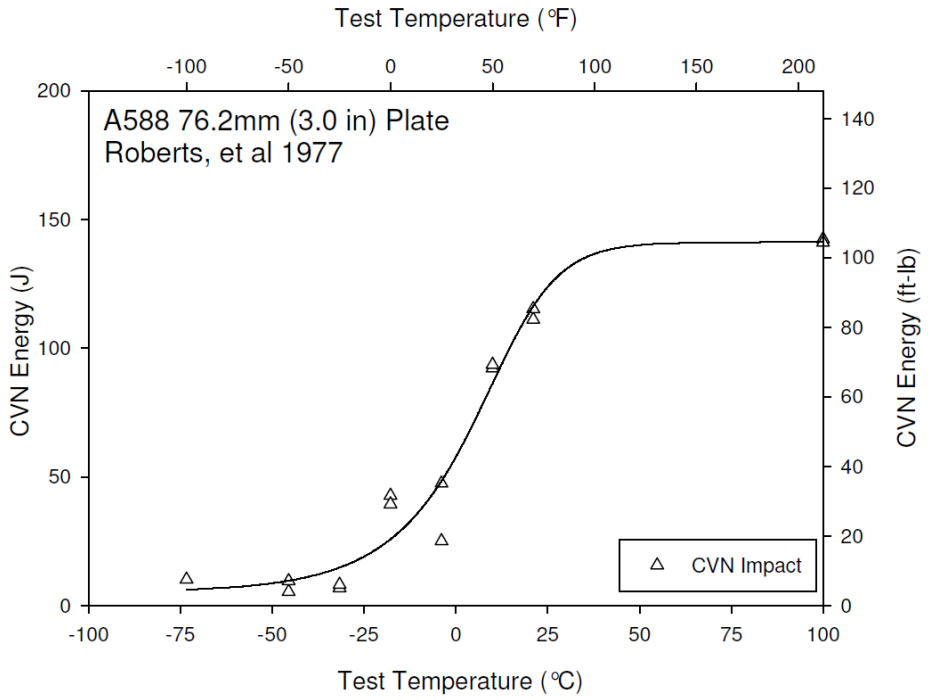

Figure J-35. CVN Data for A588 3.0", Roberts, et al. 1977

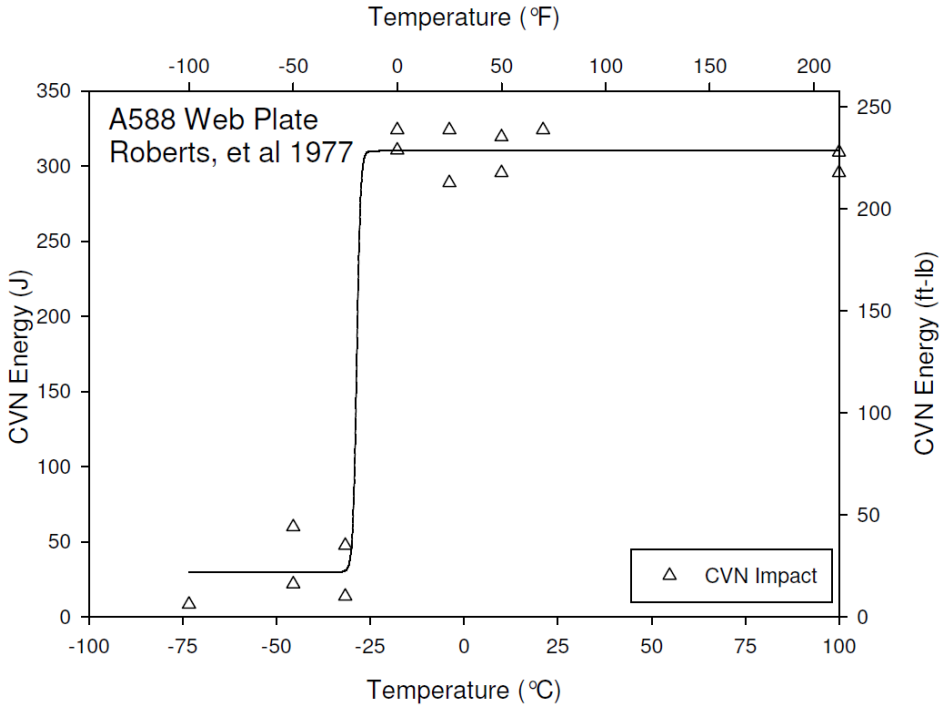

Figure J-36. CVN Data for A588 Web, Roberts, et al. 1977

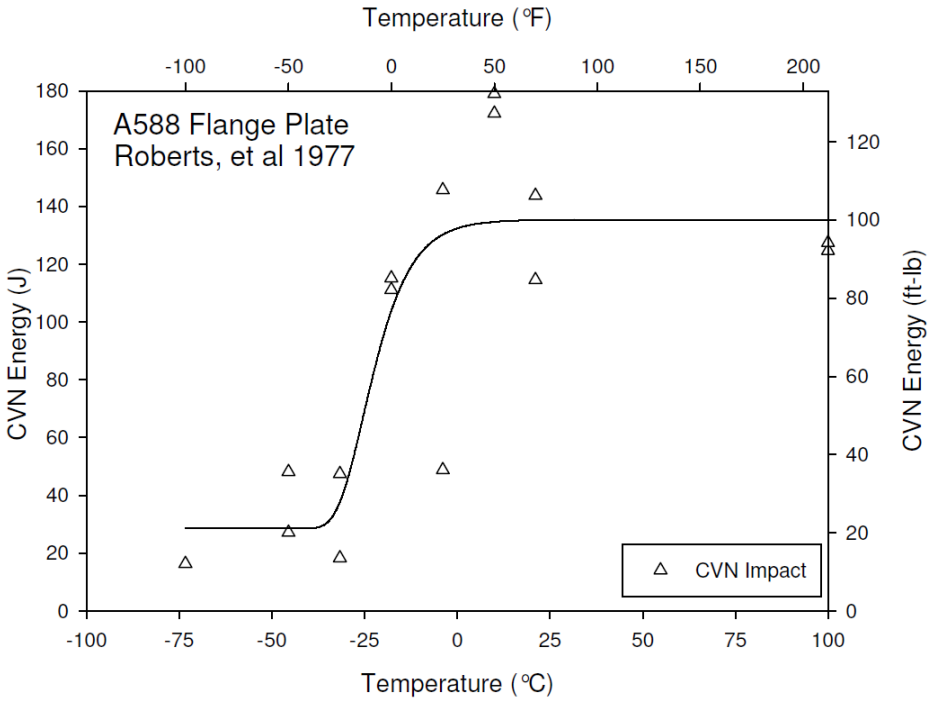

Figure J-37. CVN Data for A588 Flange, Roberts, et al. 1977

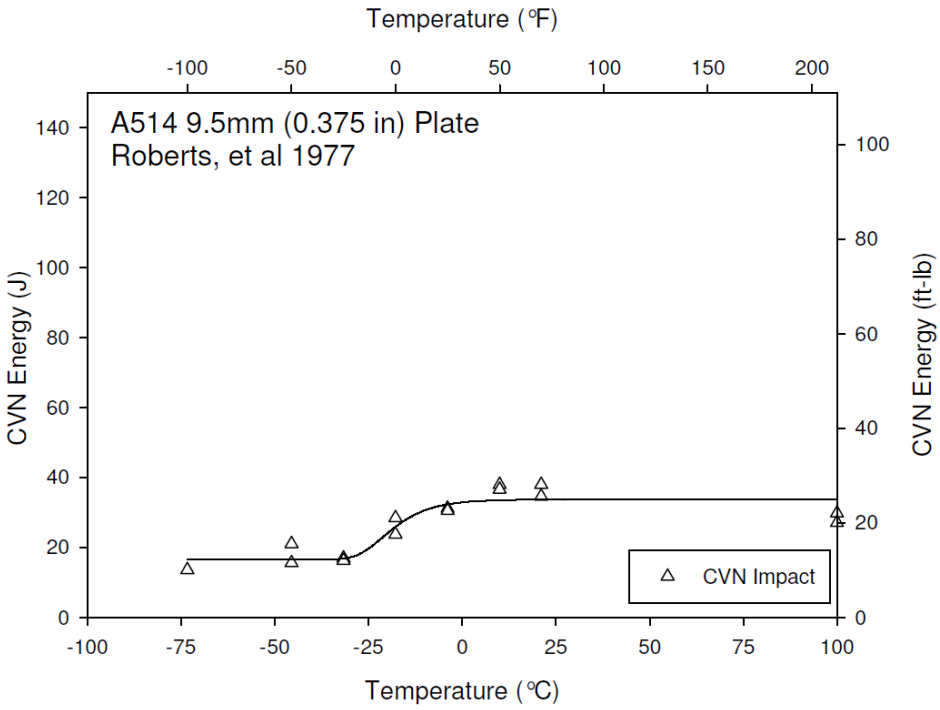

Figure J-38. CVN Data for A514 0.375", Roberts, et al. 1977

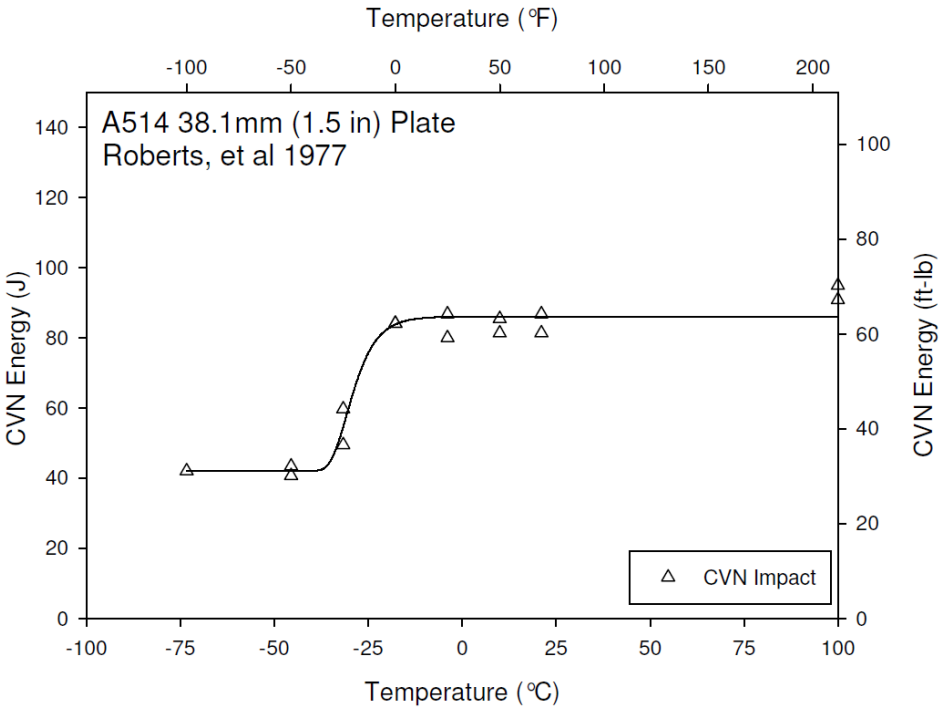

Figure J-39. CVN Data for A514 1.5", Roberts, et al. 1977

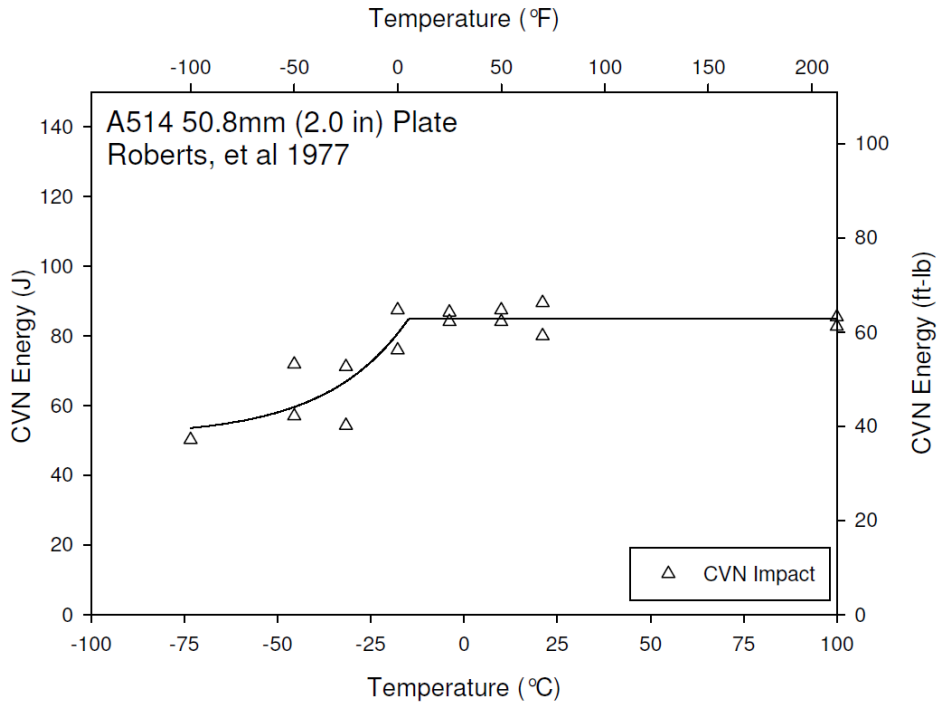

Figure J-40. CVN Data for A514 2.0", Roberts, et al. 1977

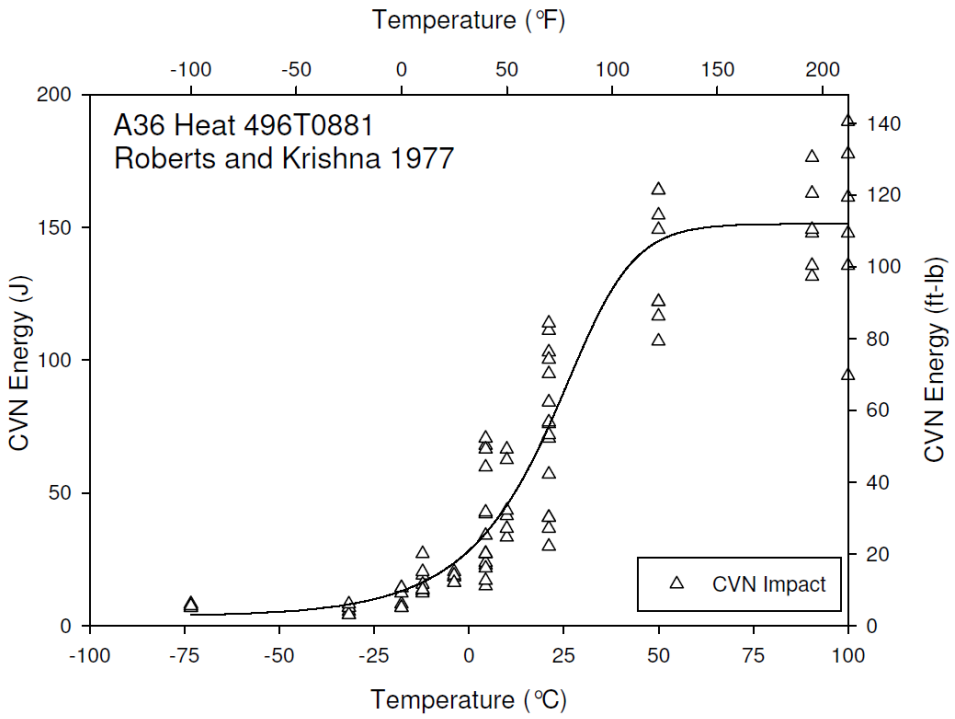

Figure J-41. CVN Data for A36 496T0881, Roberts and Krishna 1977

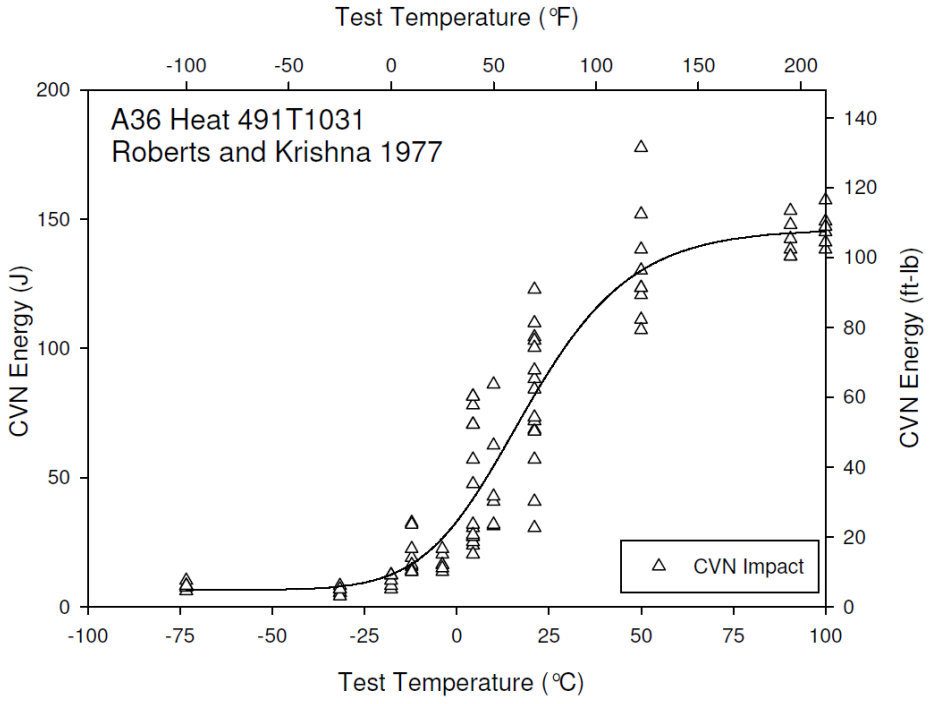

Figure J-42. CVN Data for A36 49T1031, Roberts and Krishna 1977

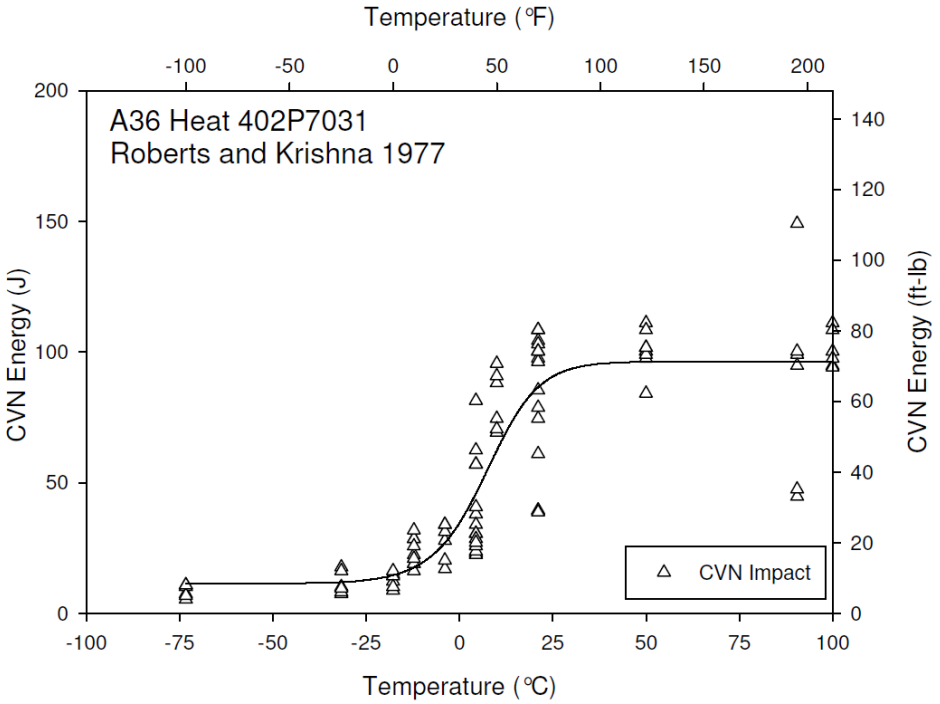

Figure J-43. CVN Data for A36 402P7031, Roberts and Krishna 1977

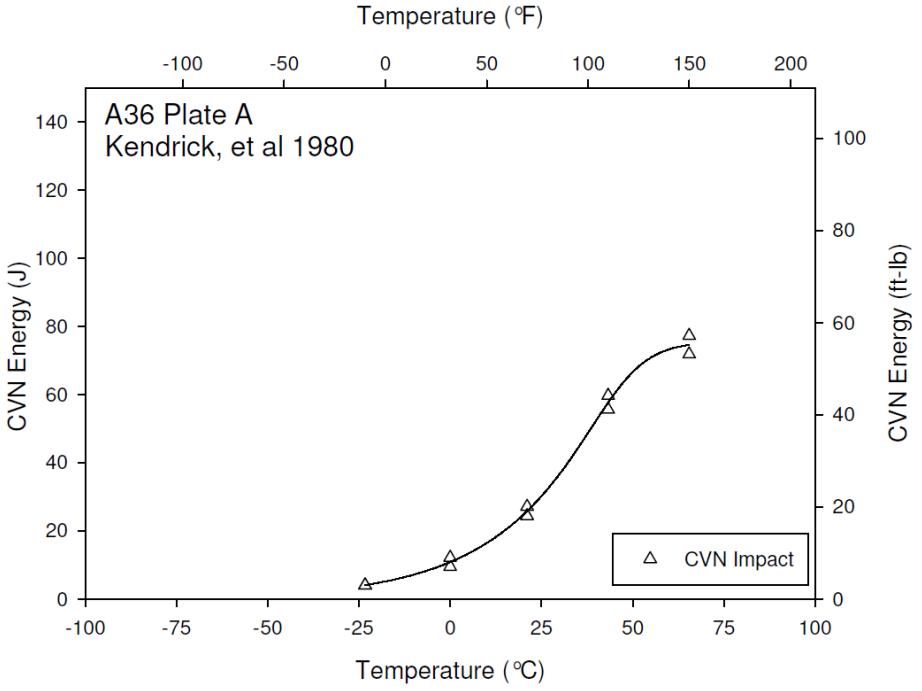

Figure J-44. CVN Data for A36 Plate A, Kendrick, et al. 1980

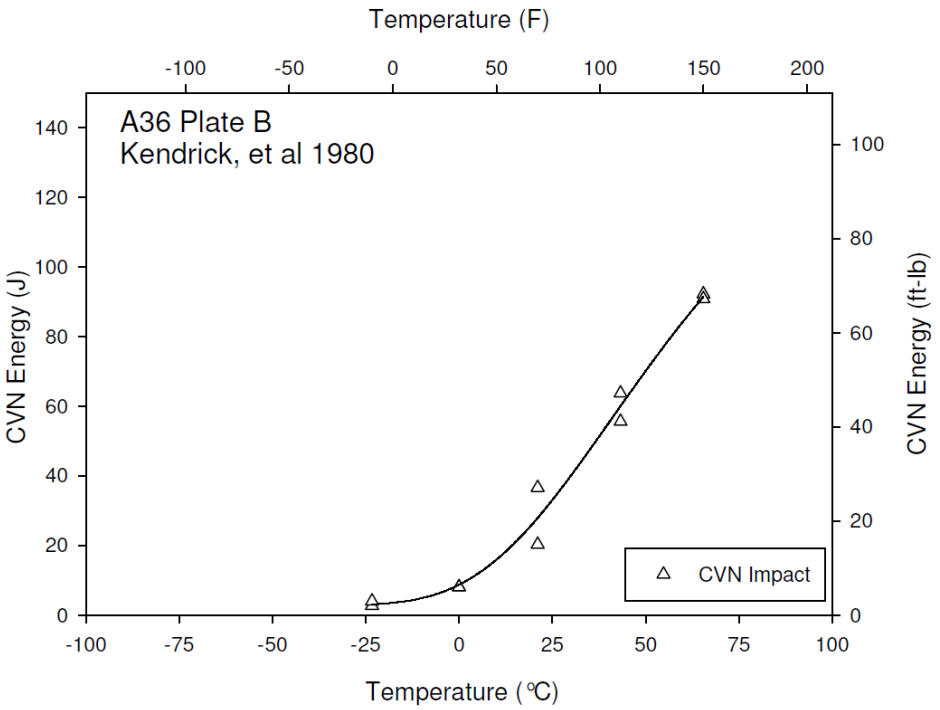

Figure J-45. CVN Data for A36 Plate B, Kendrick, et al. 1980

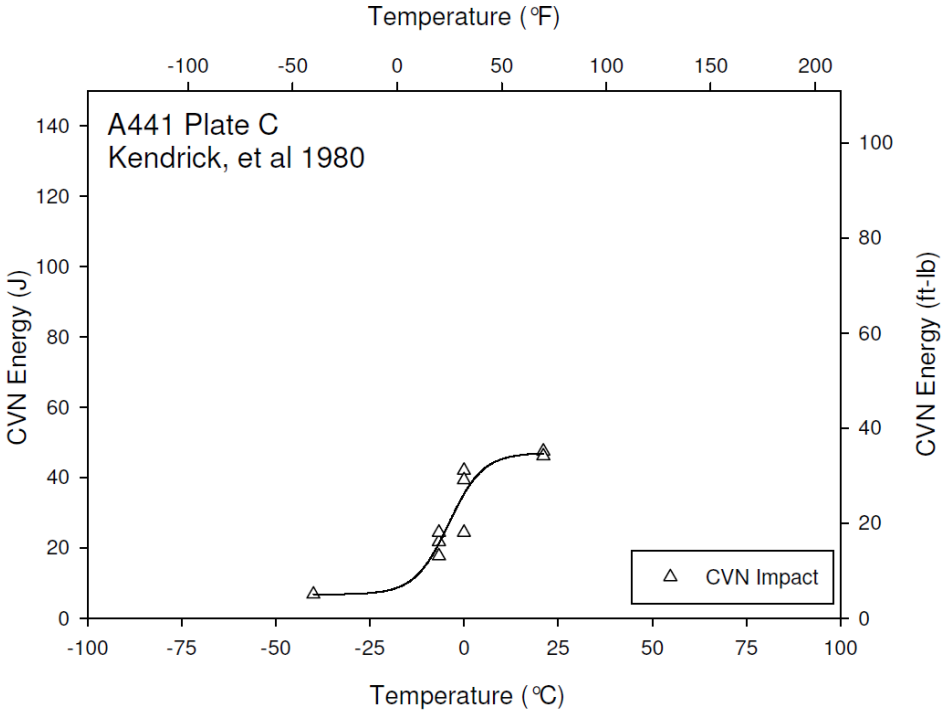

Figure J-46. CVN Data A441 Plate C, Kendrick, et al. 1980

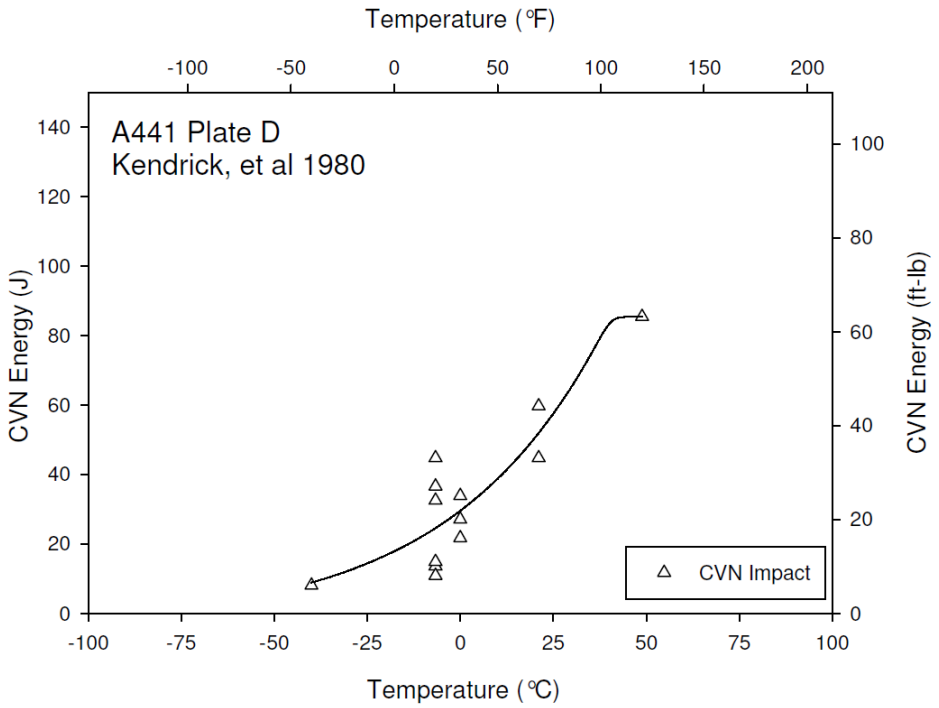

Figure J-47. CVN Data for A441 Plate D, Kendrick, et al. 1980

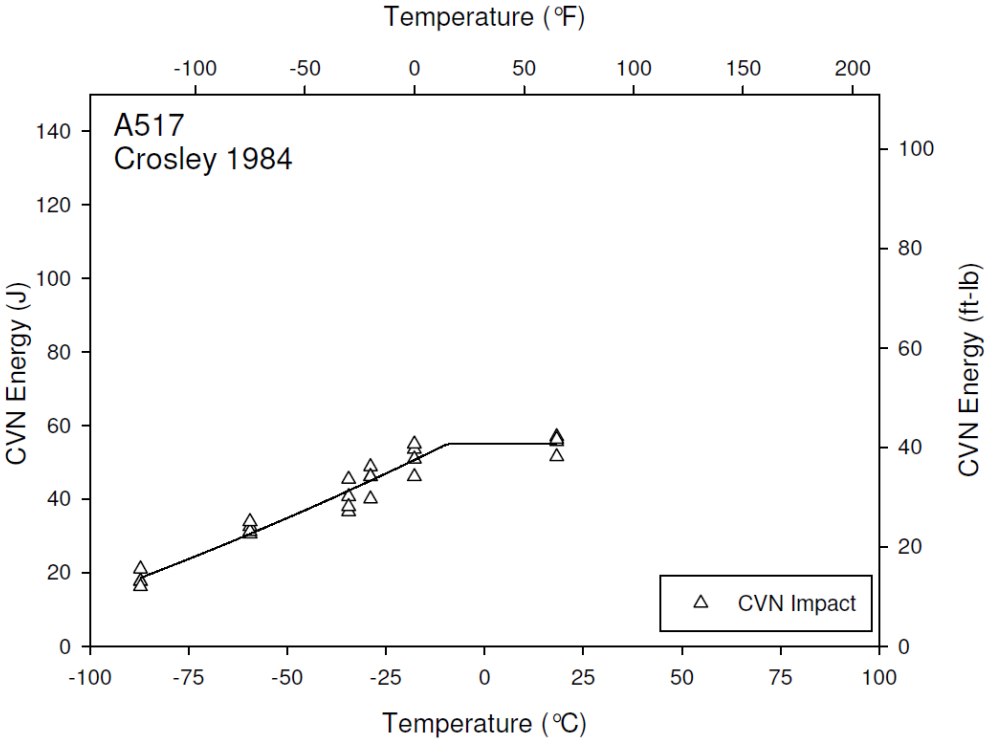

Figure J-48. CVN Data for A517, Crosley 1984

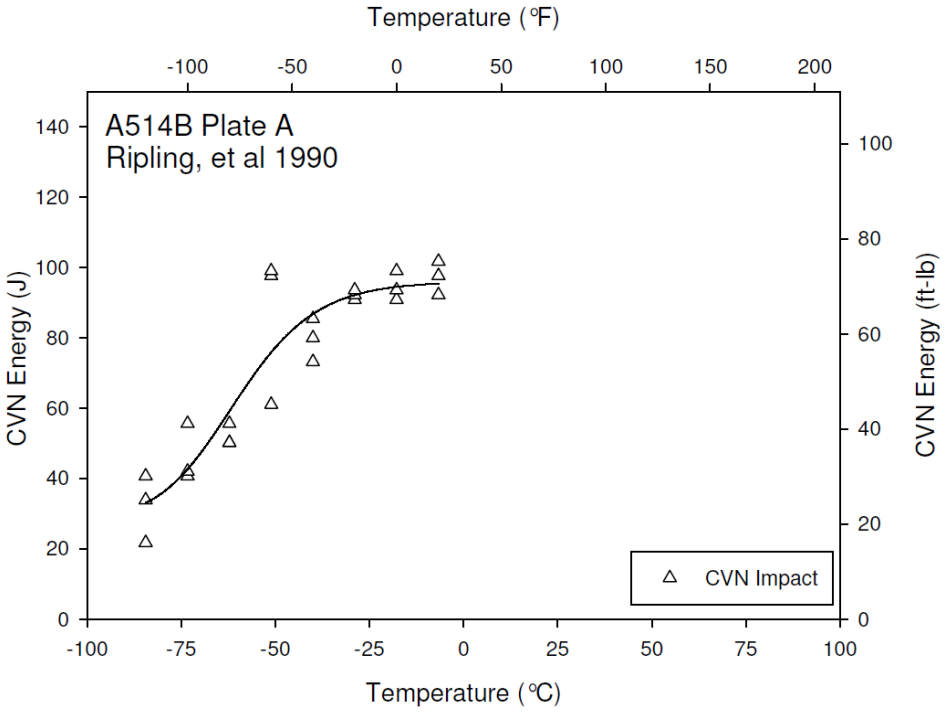

Figure J-49. CVN Data for A514B Plate A, Ripling, et al. 1990

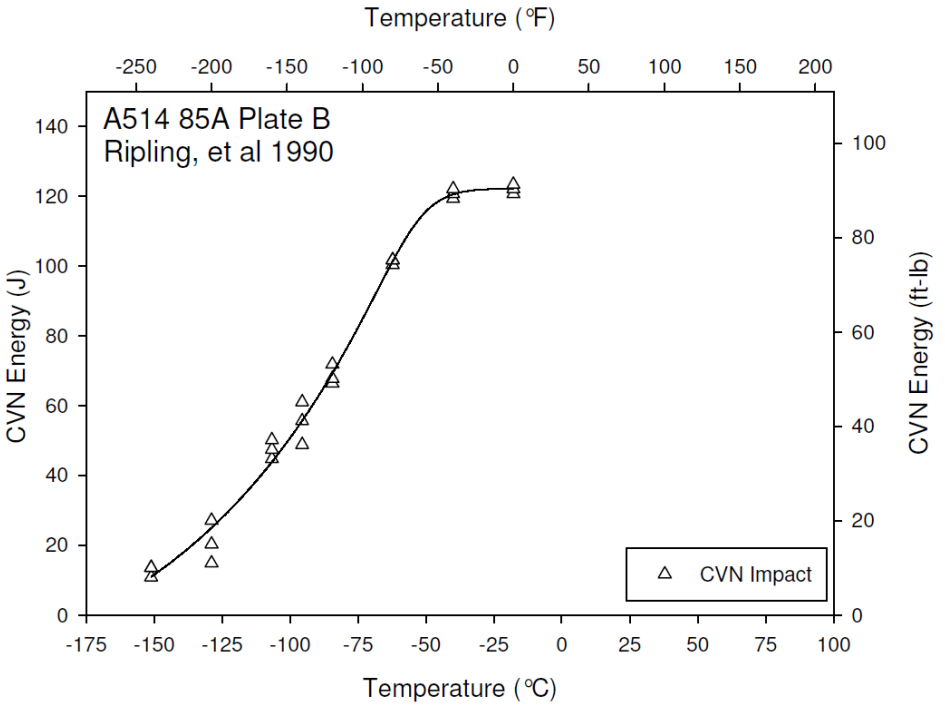

Figure J-50. CVN Data for A514-85A Plate B, Ripling, et al. 1990

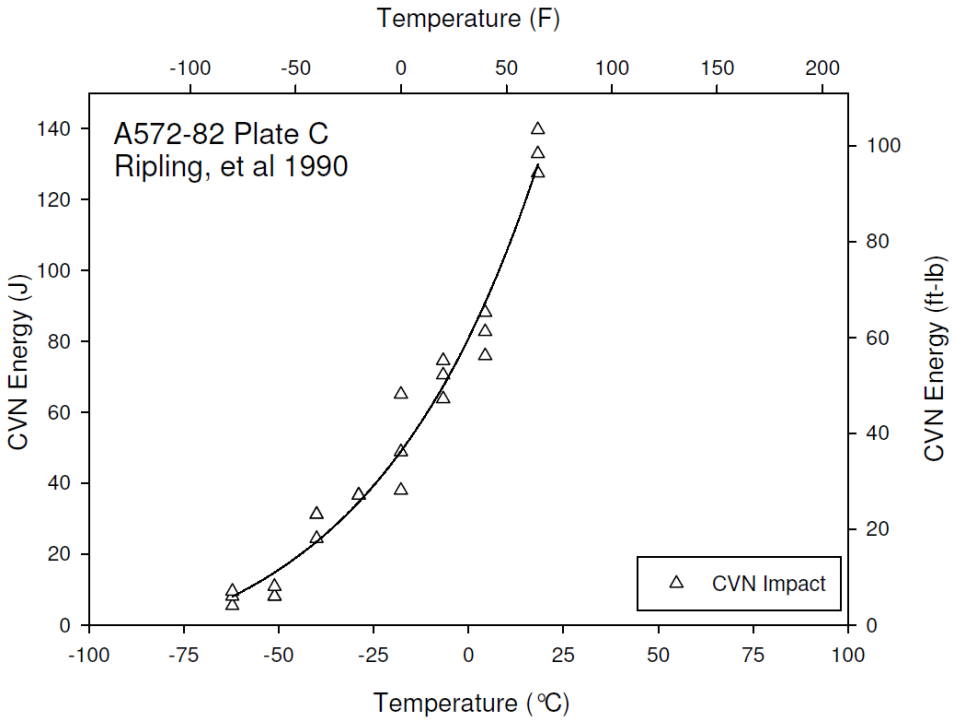

Figure J-51. CVN Data for A572-82 Plate C, Ripling, et al. 1990

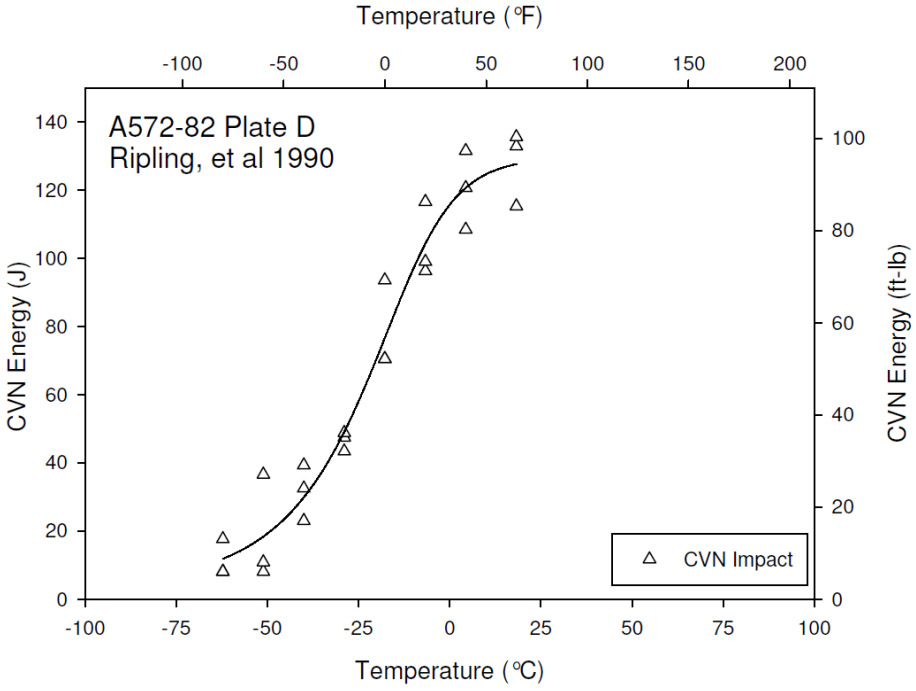

Figure J-52. CVN Data for A572-82 Plate D, Ripling, et al. 1990

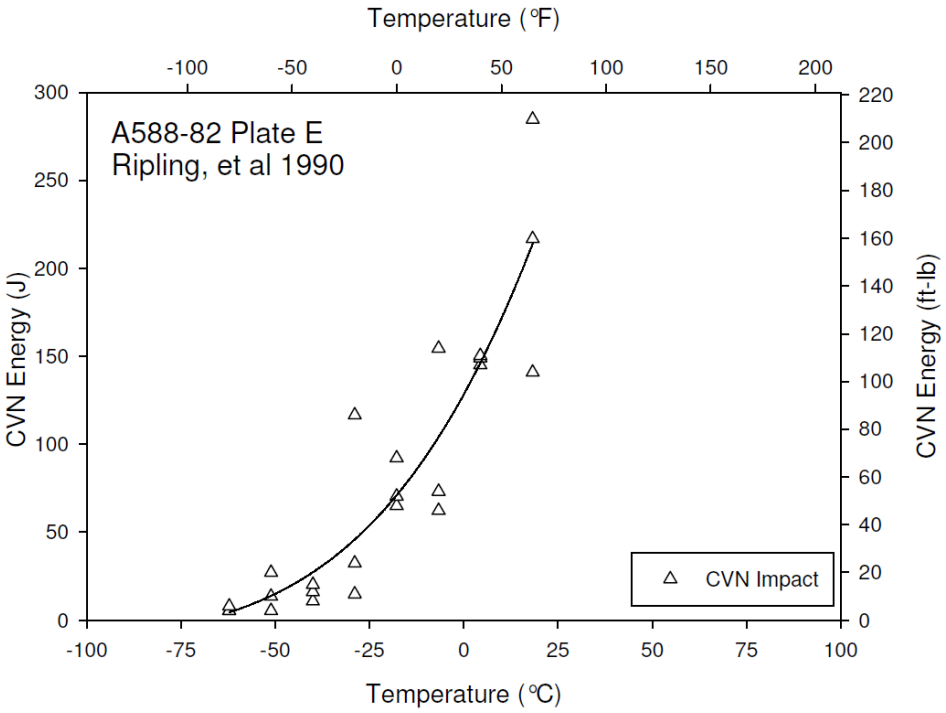

Figure J-53. CVN Data for A588-82 Plate E, Ripling, et al. 1990

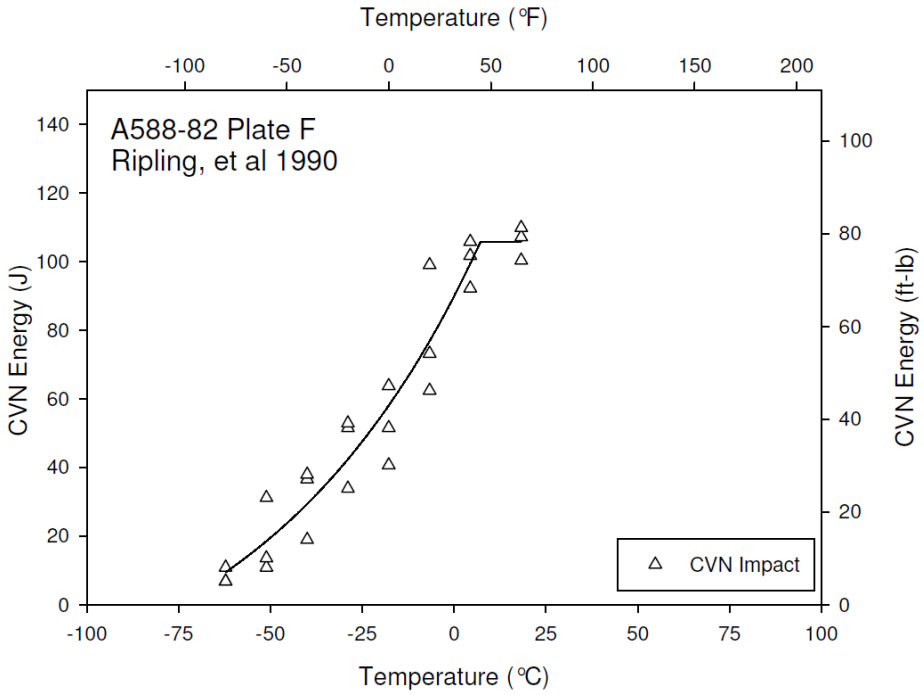

Figure J-54. CVN Data for A588-82 Plate F, Ripling, et al. 1990

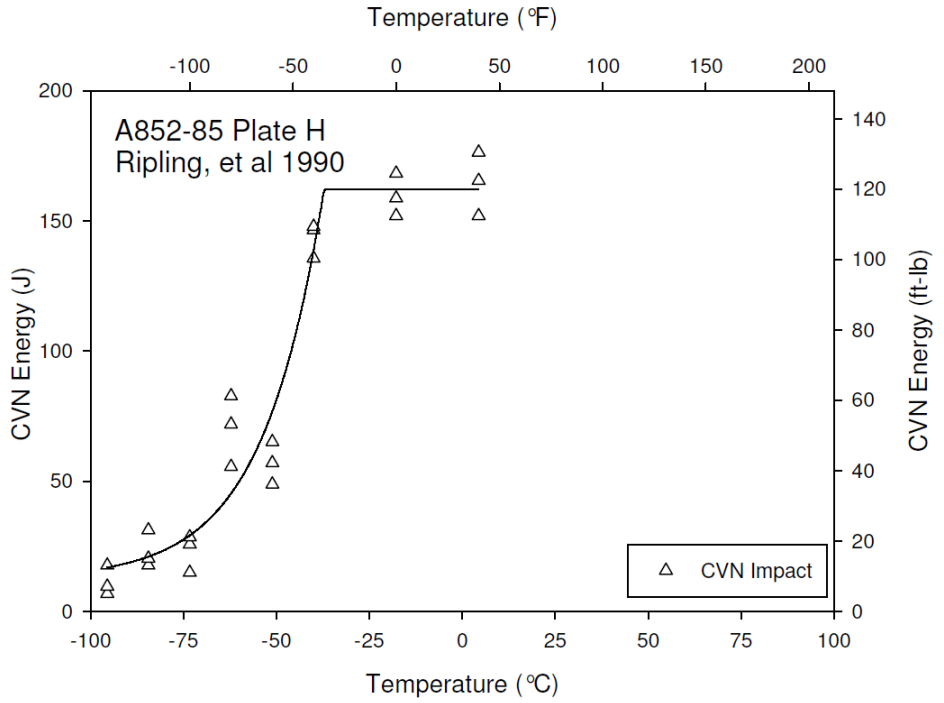

Figure J-55. CVN Data for A852-85 Plate H, Ripling, et al. 1990

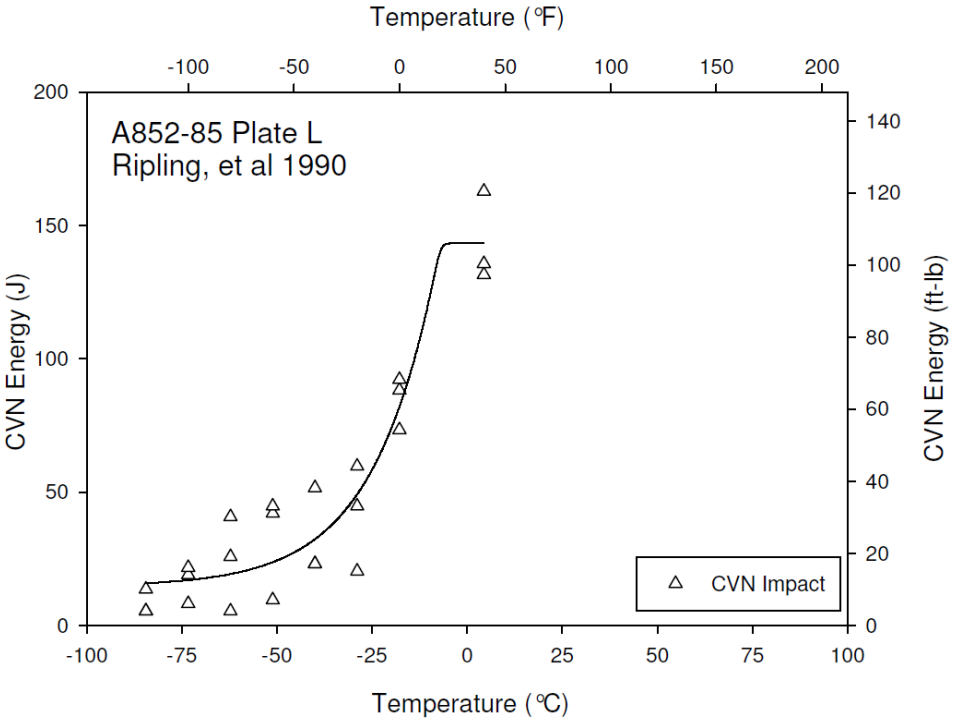

Figure J-56. CVN Data for A852-85 Plate L, Ripling, et al. 1990

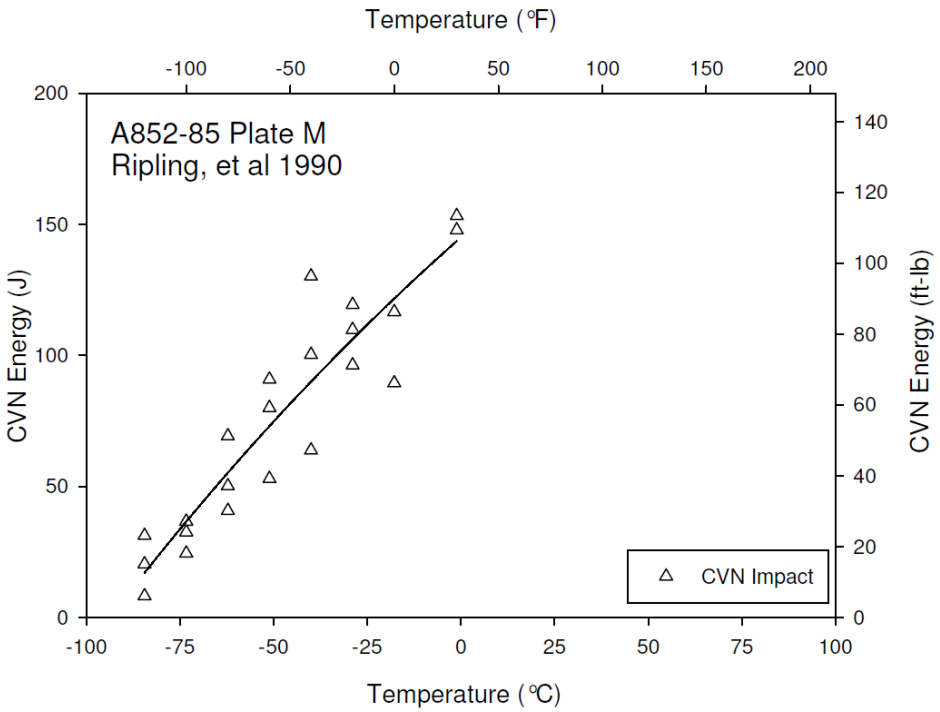

Figure J-57. CVN Data for A852-85 Plate M, Ripling, et al. 1990

APPENDIX K: Legacy Data Master Curve Plots

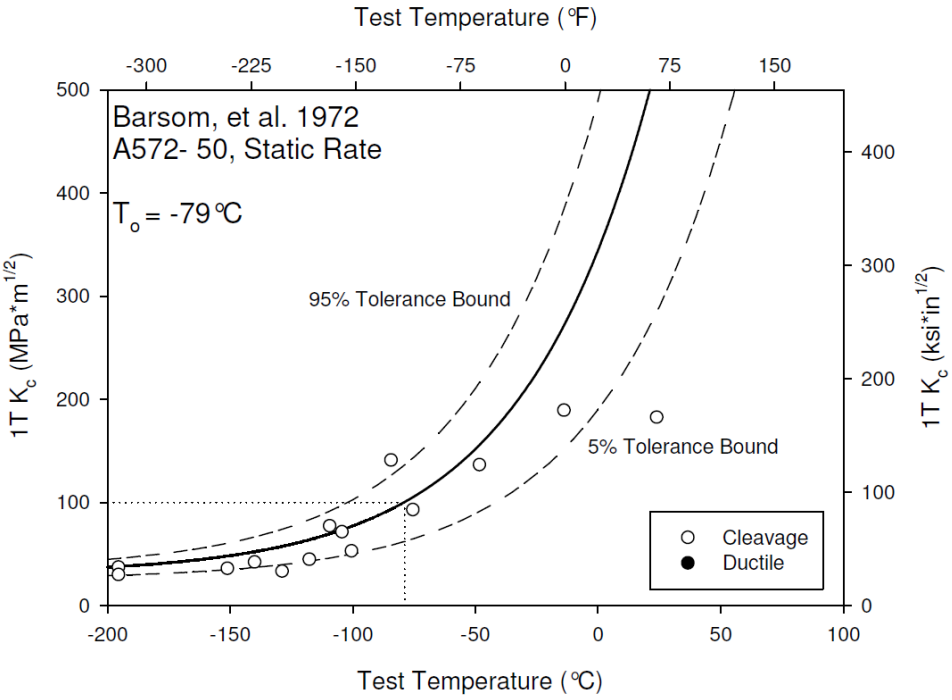

Figure K-1. Master Curve for A572 50 Static, Barsom, et al. 1972

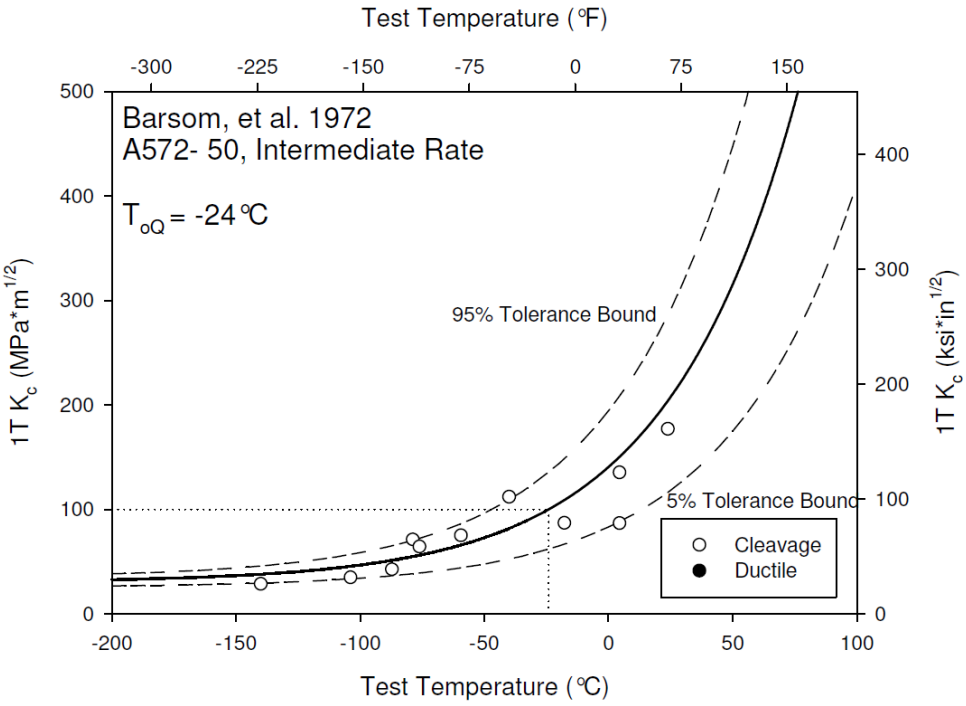

Figure K-2. Master Curve for A572 50 Intermediate, Barsom, et al. 1972

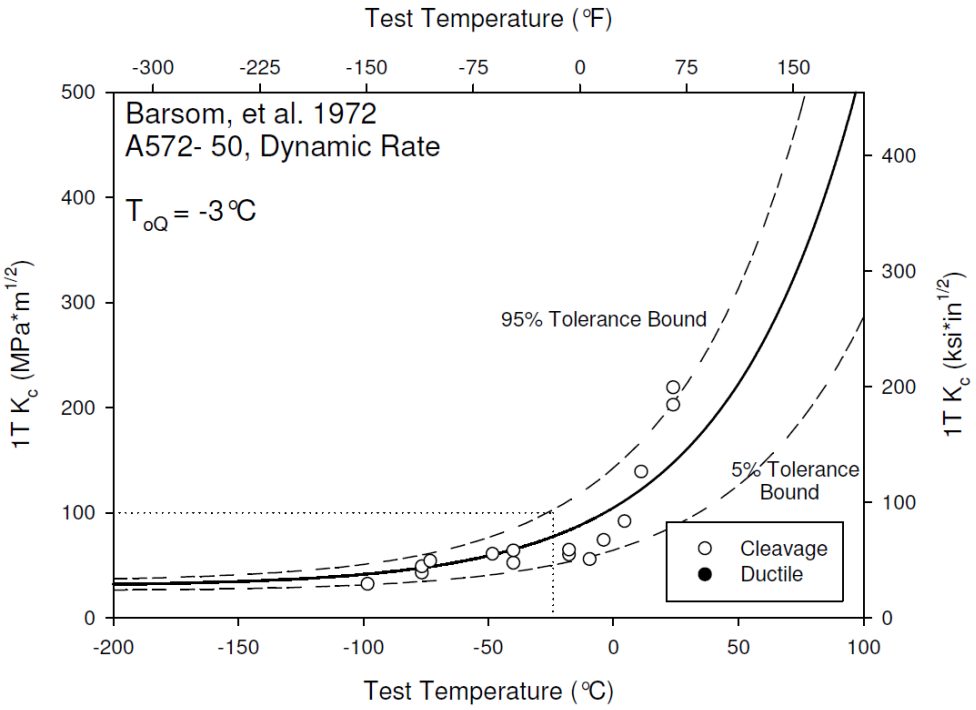

Figure K-3. Master Curve for A572 50 Dynamic, Barsom, et al. 1972

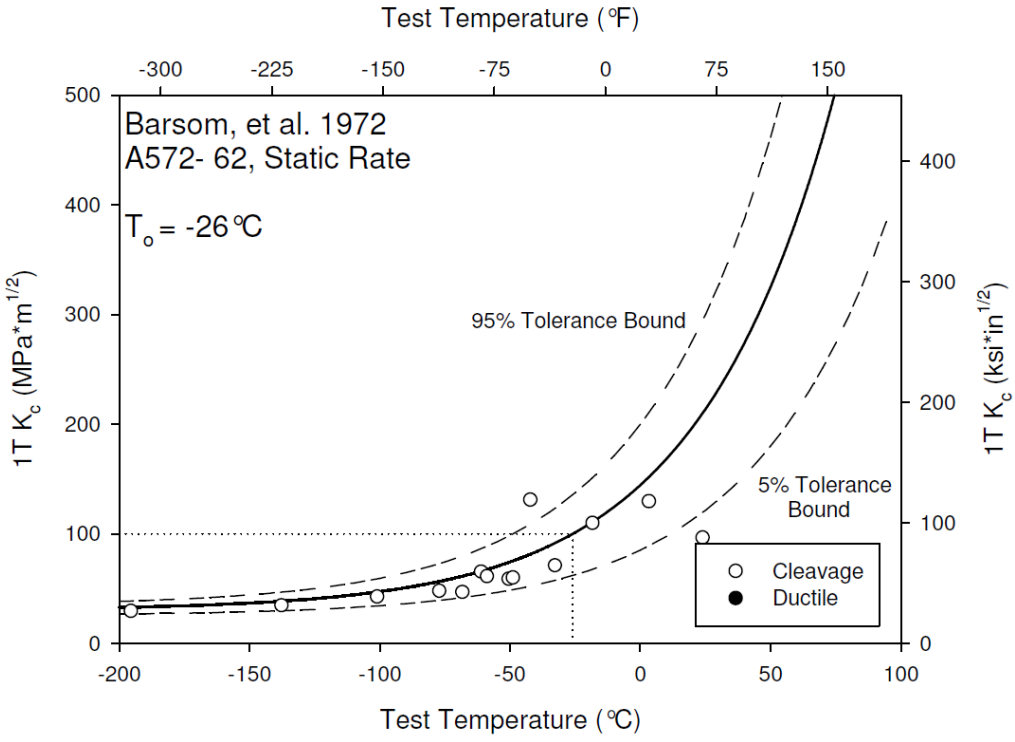

Figure K-4. Master Curve for A572 62 Static, Barsom, et al. 1972

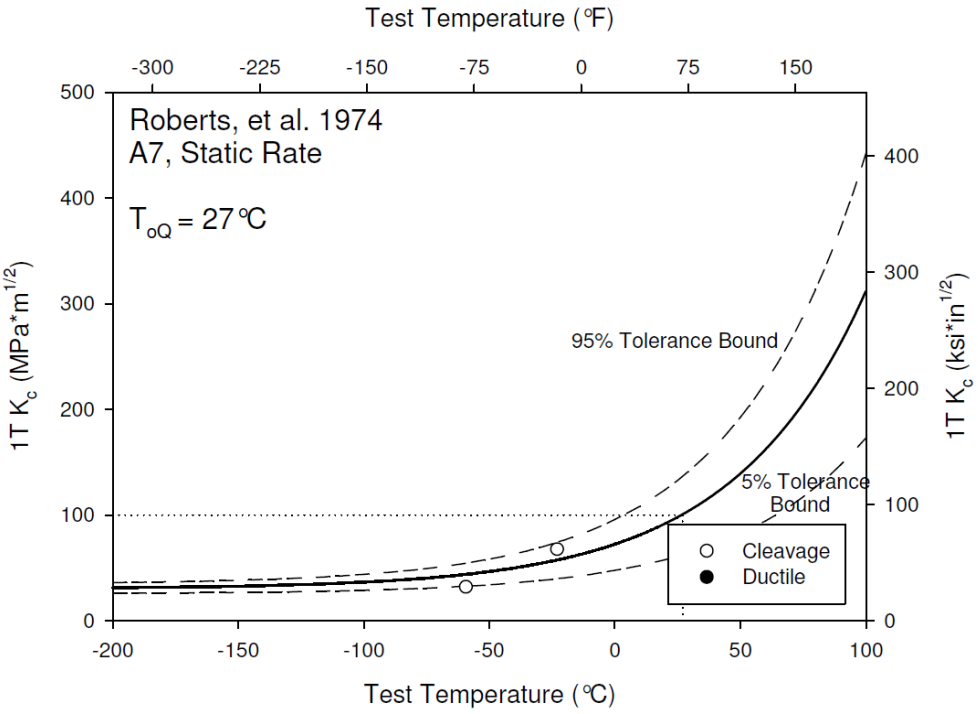

Figure K-5. Master Curve for A7 Static, Roberts, et al. 1974

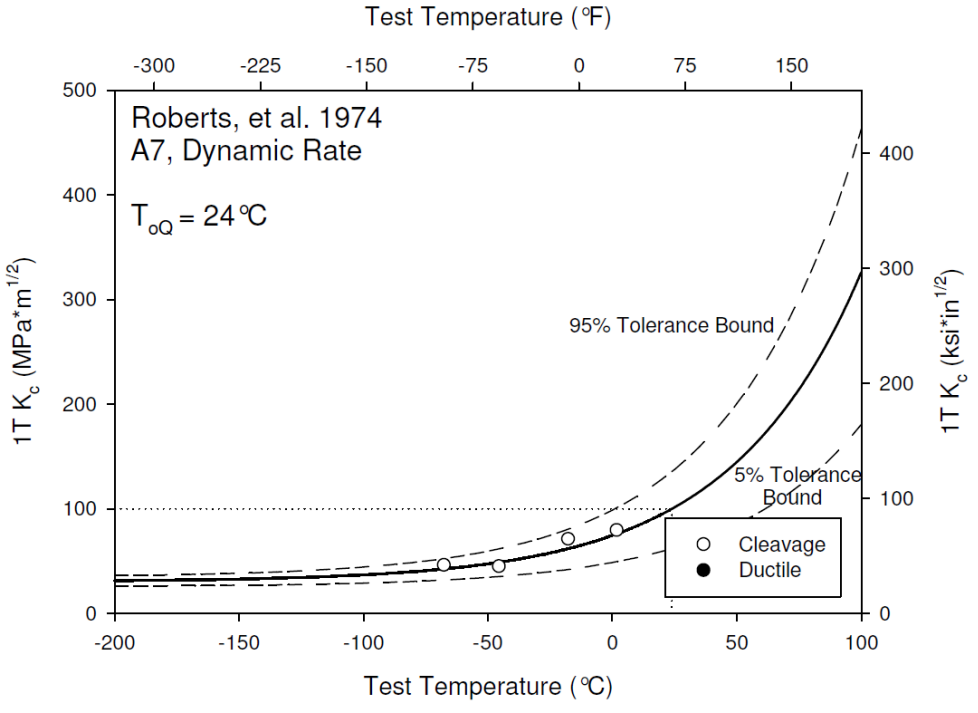

Figure K-6. Master Curve for A7 Dynamic, Roberts, et al. 1974

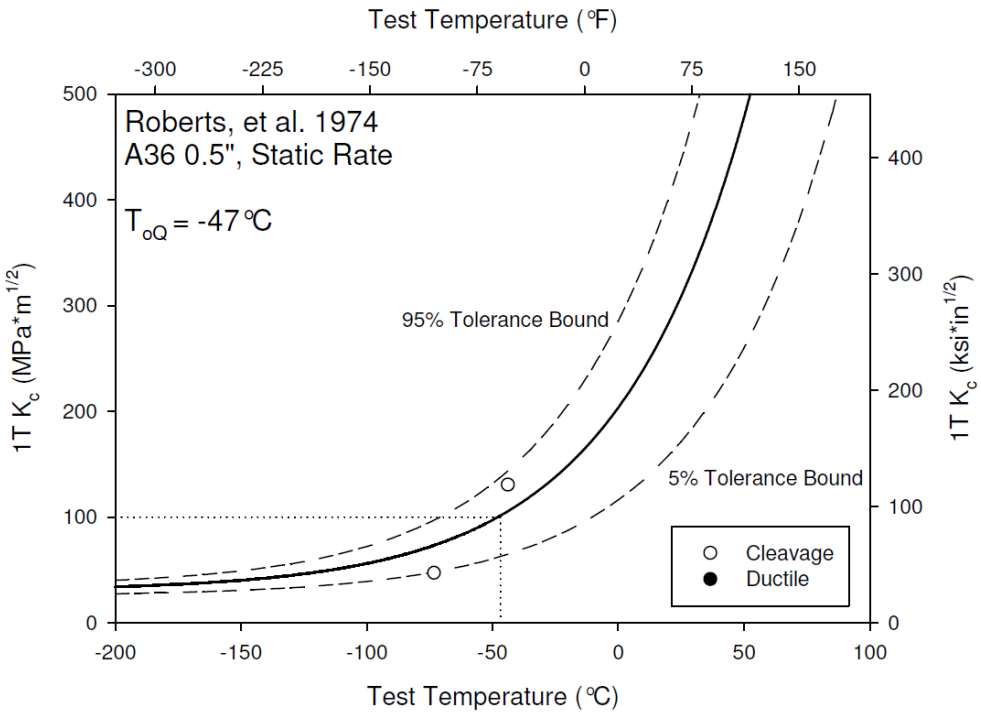

Figure K-7. Master Curve for A36 0.5" Static, Roberts, et al. 1974

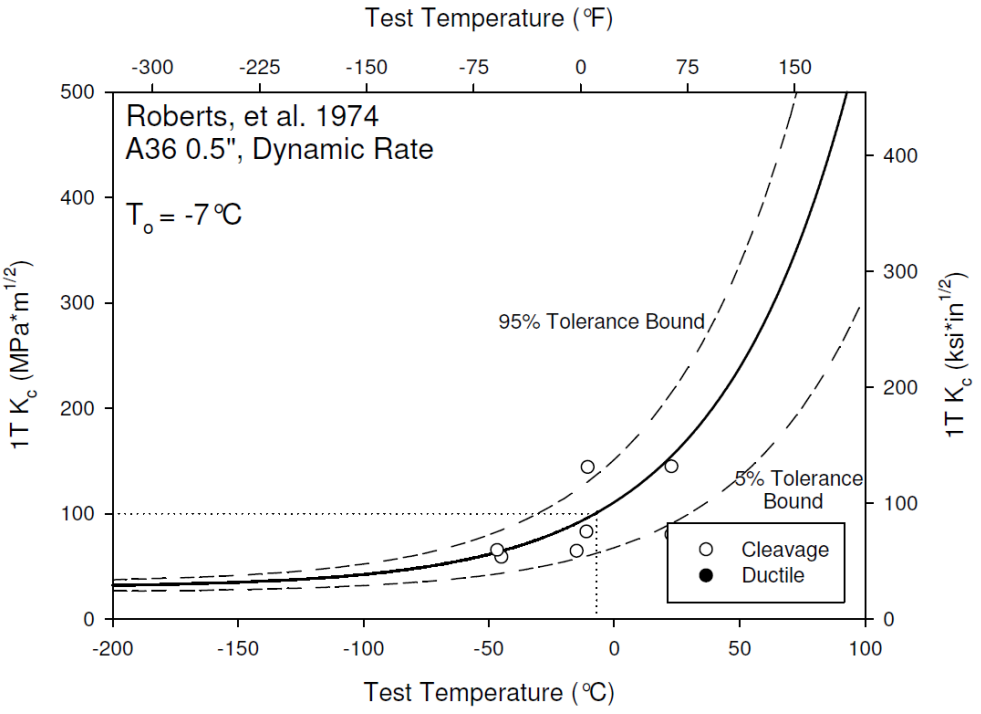

Figure K-8. Master Curve for A36 0.5" Dynamic, Roberts, et al. 1974

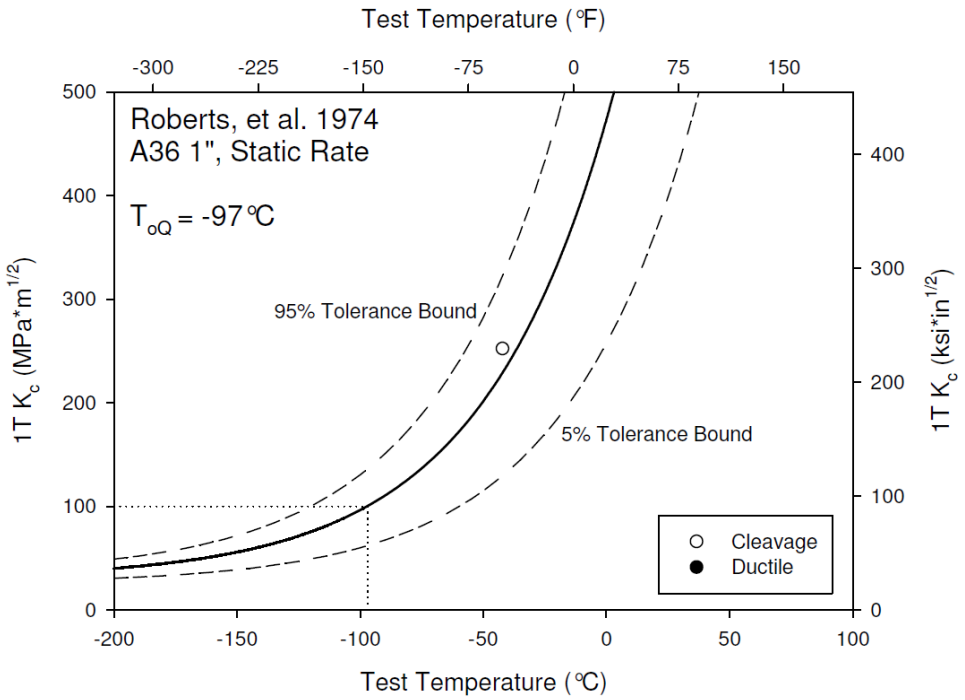

Figure K-9. Master Curve for A36 1.0" Static, Roberts, et al. 1974

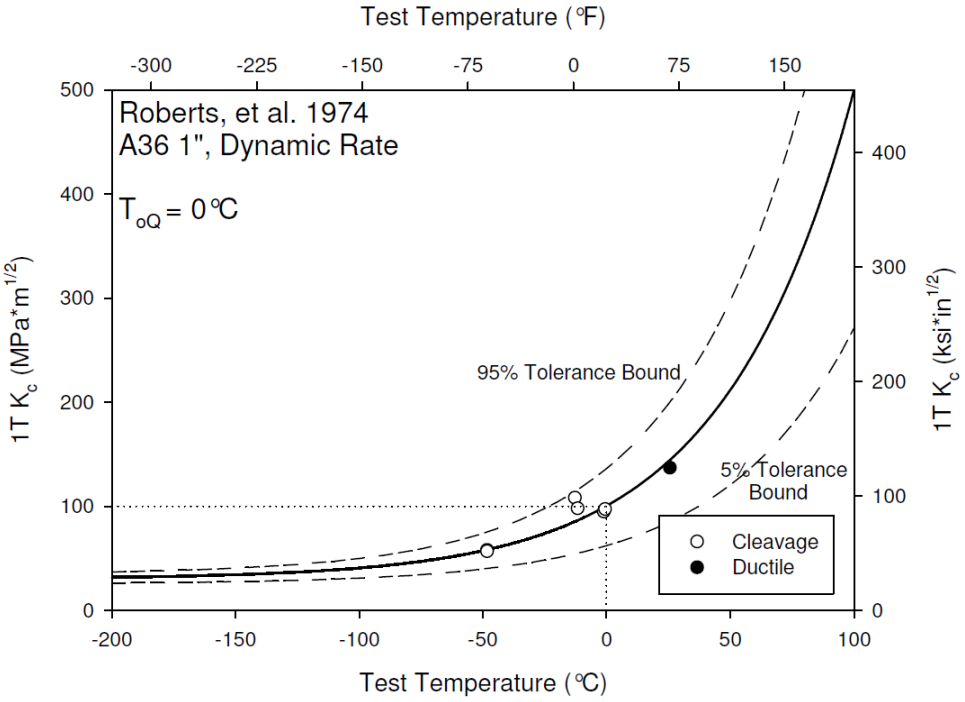

Figure K-10. Master Curve for A36 1.0" Dynamic, Roberts, et al. 1974

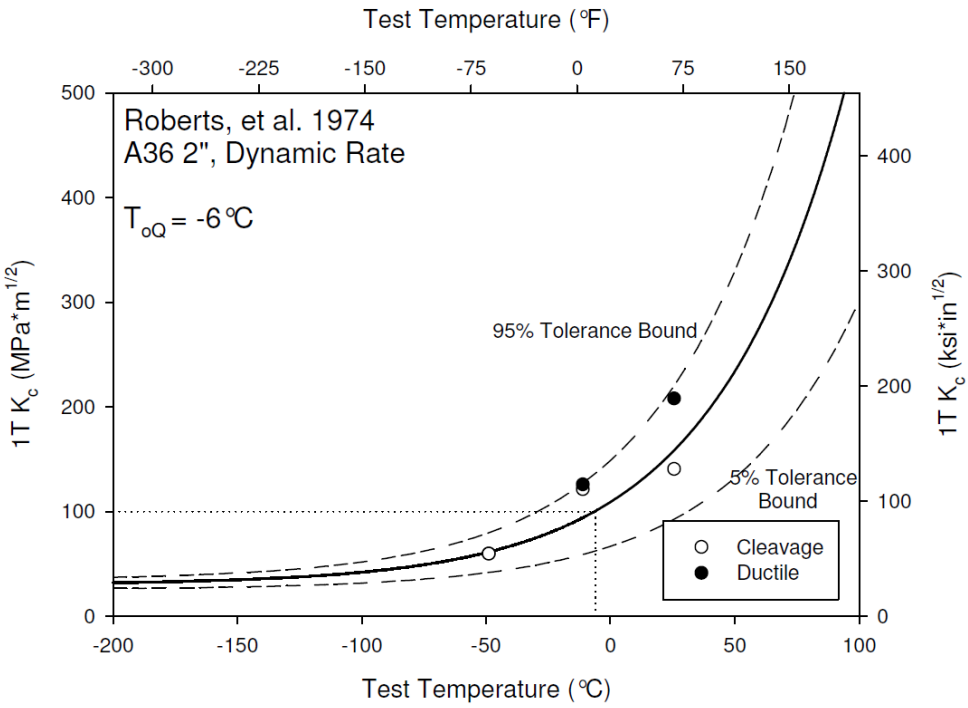

Figure K-11. Master Curve for A36 2" Dynamic, Roberts, et al. 1974

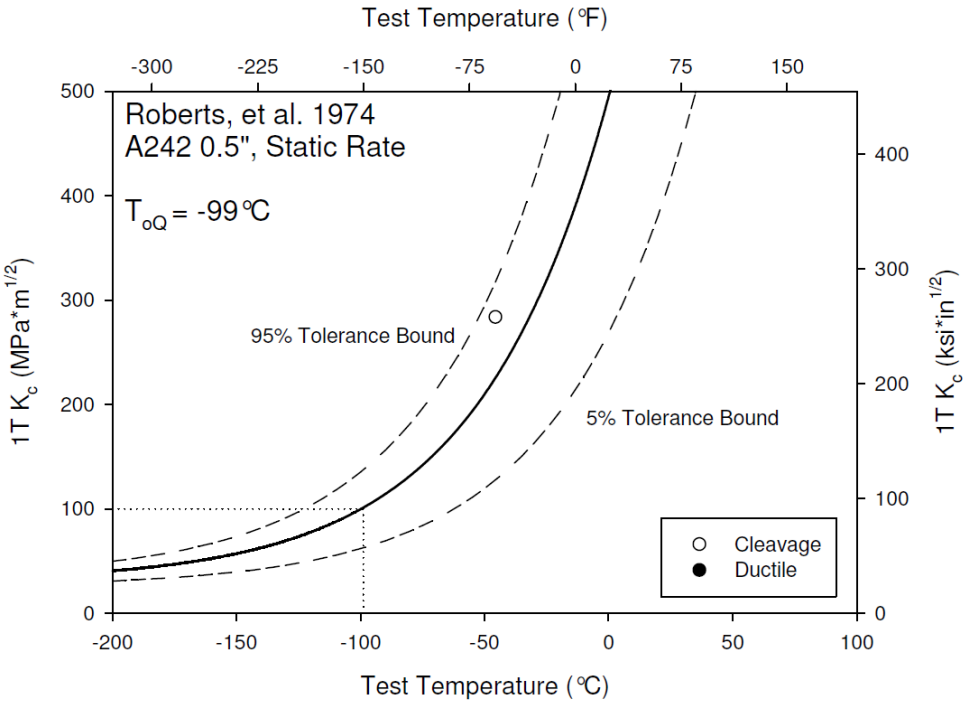

Figure K-12. Master Curve for A242 0.5" Static, Roberts, et al. 1974

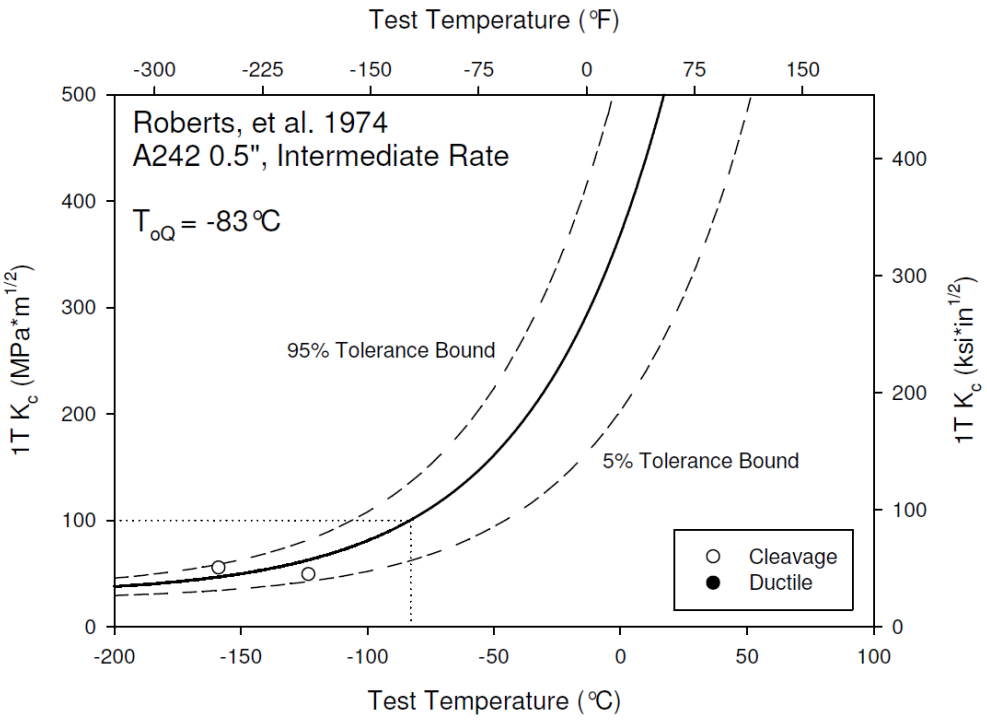

Figure K-13. Master Curve for A242 0.5" Intermediate, Roberts, et al. 1974

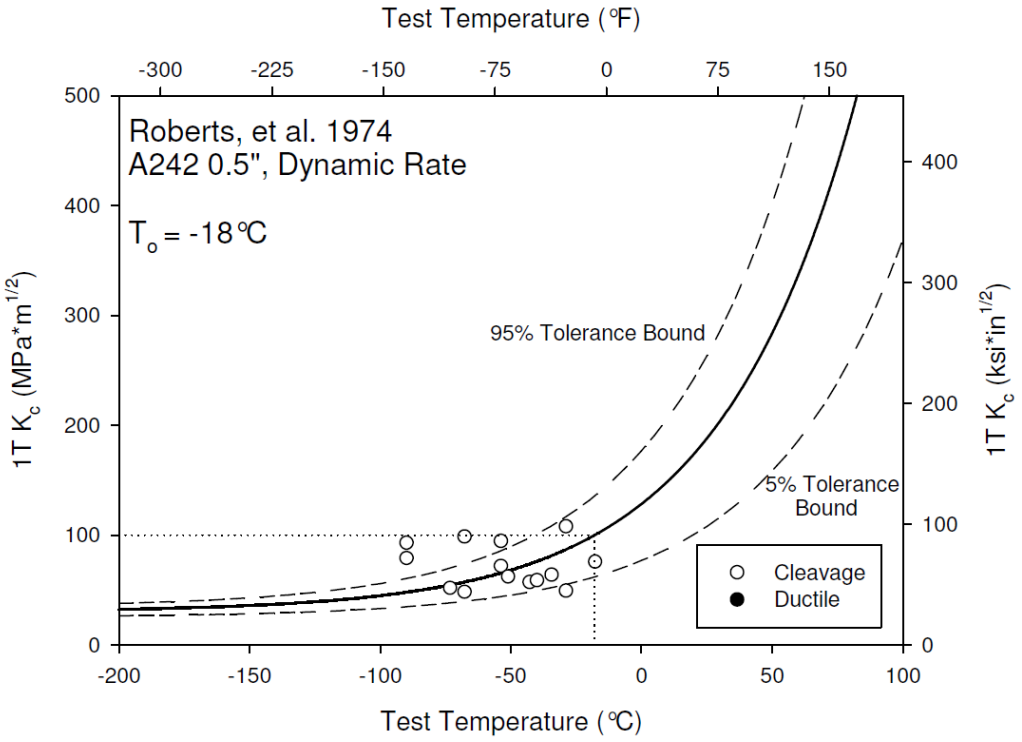

Figure K-14. Master Curve for A242 0.5" Dynamic, Roberts, et al. 1974

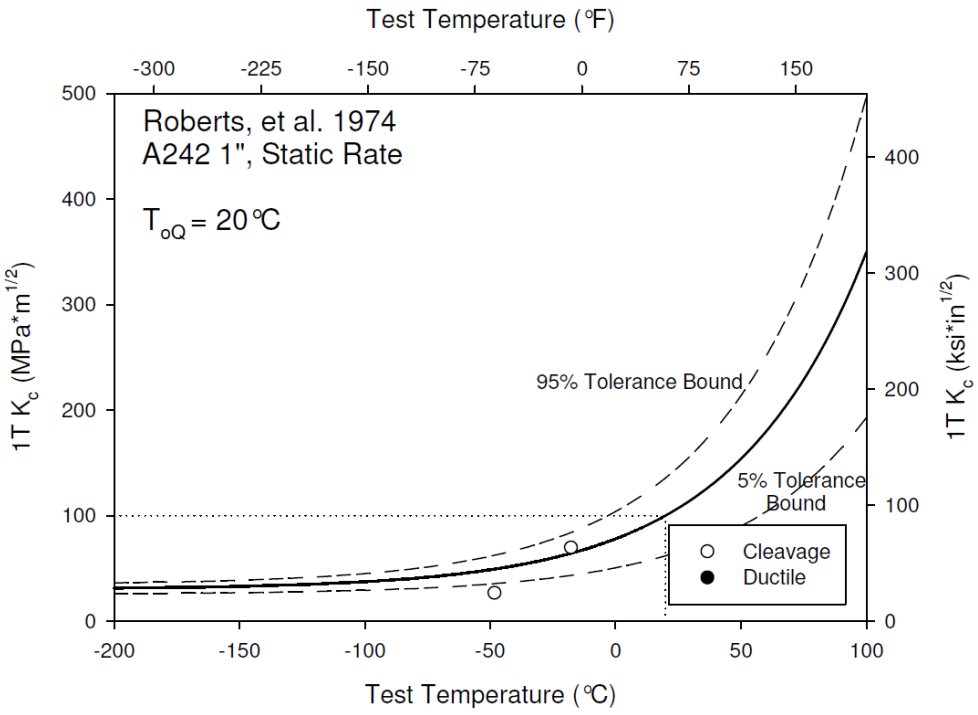

Figure K-15. Master Curve for A242 1.0" Static, Roberts, et al. 1974

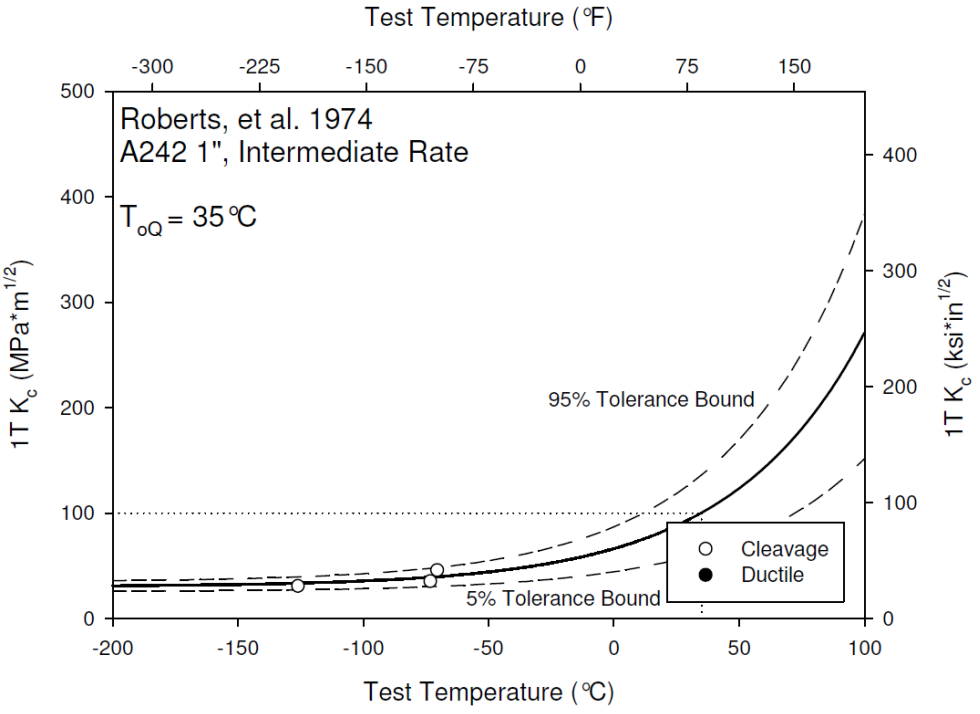

Figure K-16. Master Curve for A242 1.0" Intermediate, Roberts, et al. 1974

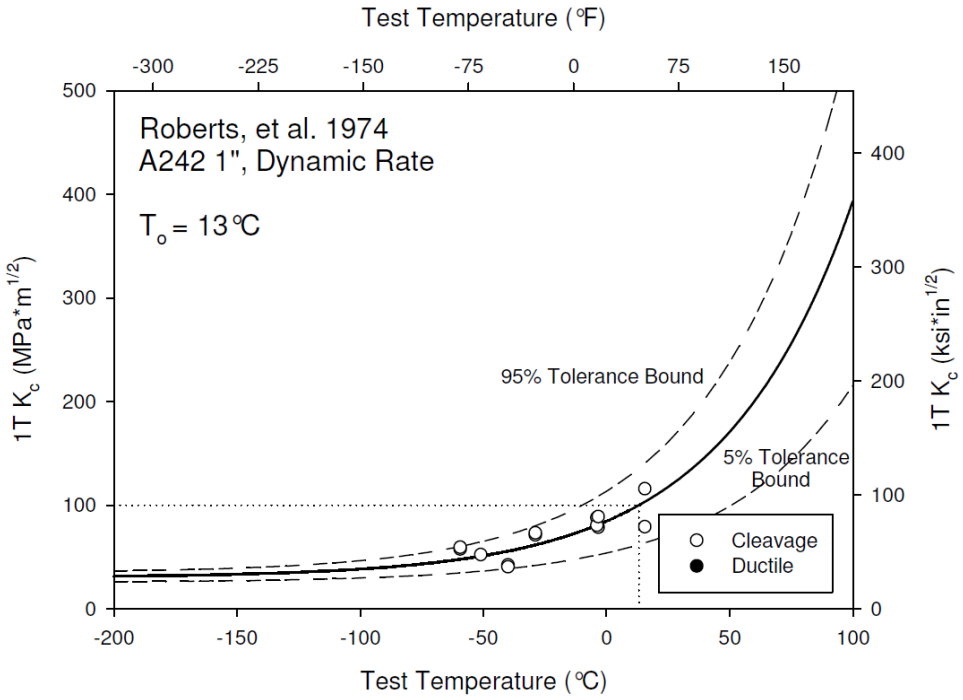

Figure K-17. Master Curve for A242 1.0" Dynamic, Roberts, et al. 1974

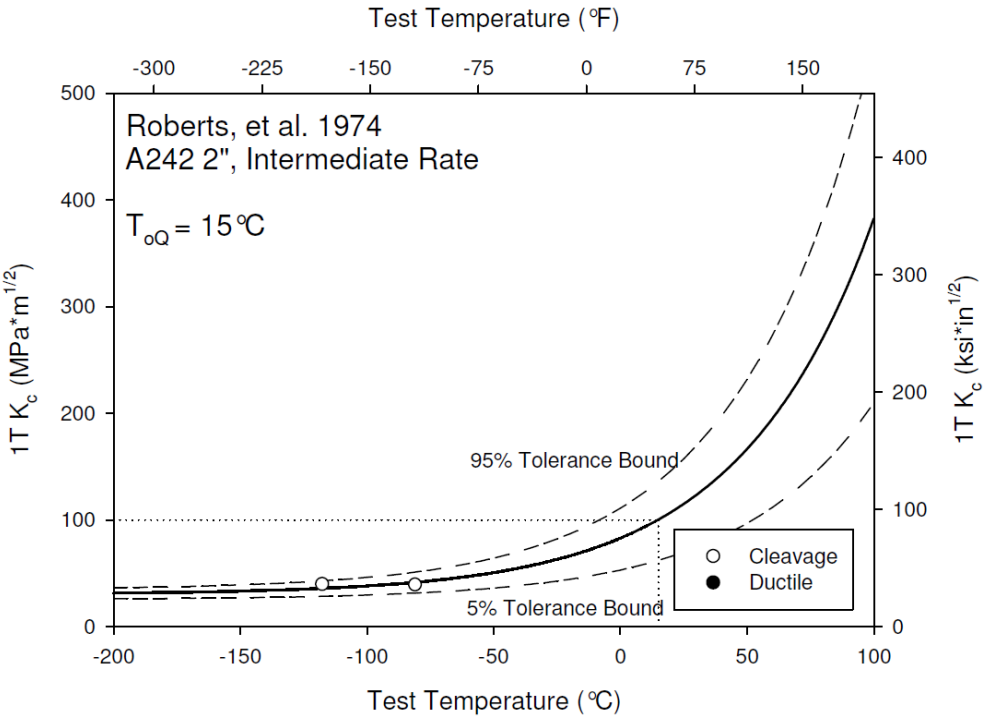

Figure K-18. Master Curve for A242 2.0" Intermediate, Roberts, et al. 1974

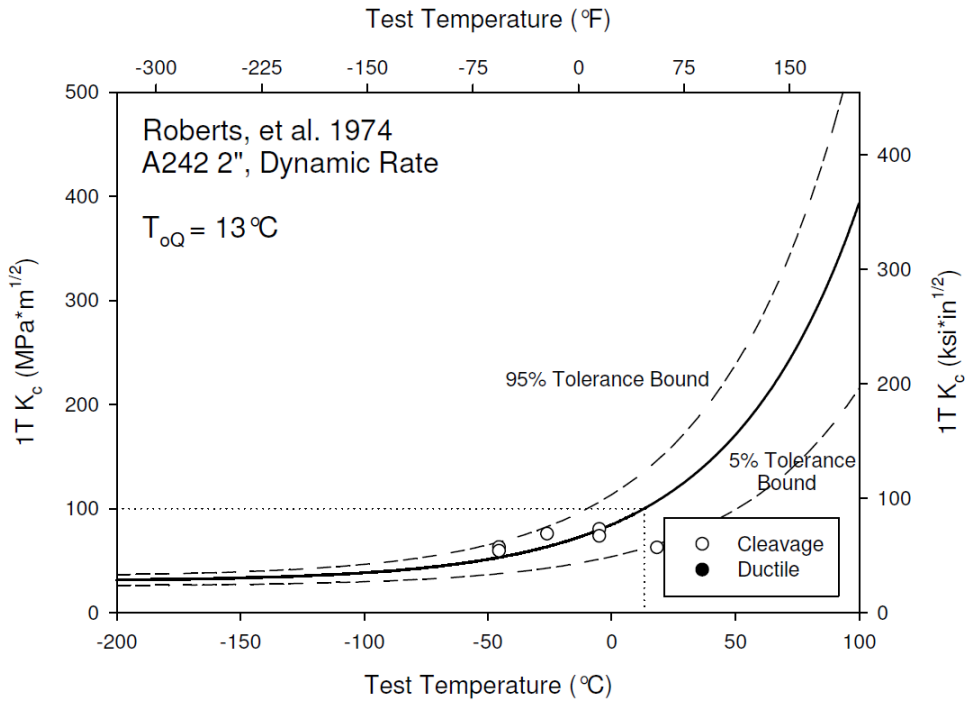

Figure K-19. Master Curve for A242 2.0" Dynamic, Roberts, et al. 1974

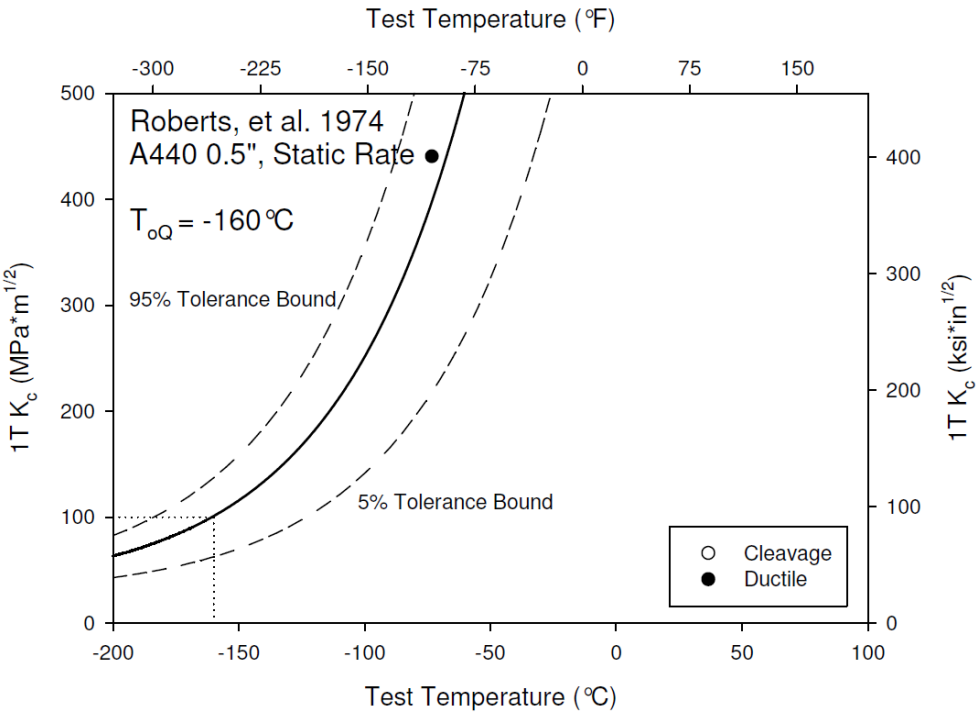

Figure K-20. Master Curve for A440 0.5" Static, Roberts, et al. 1974

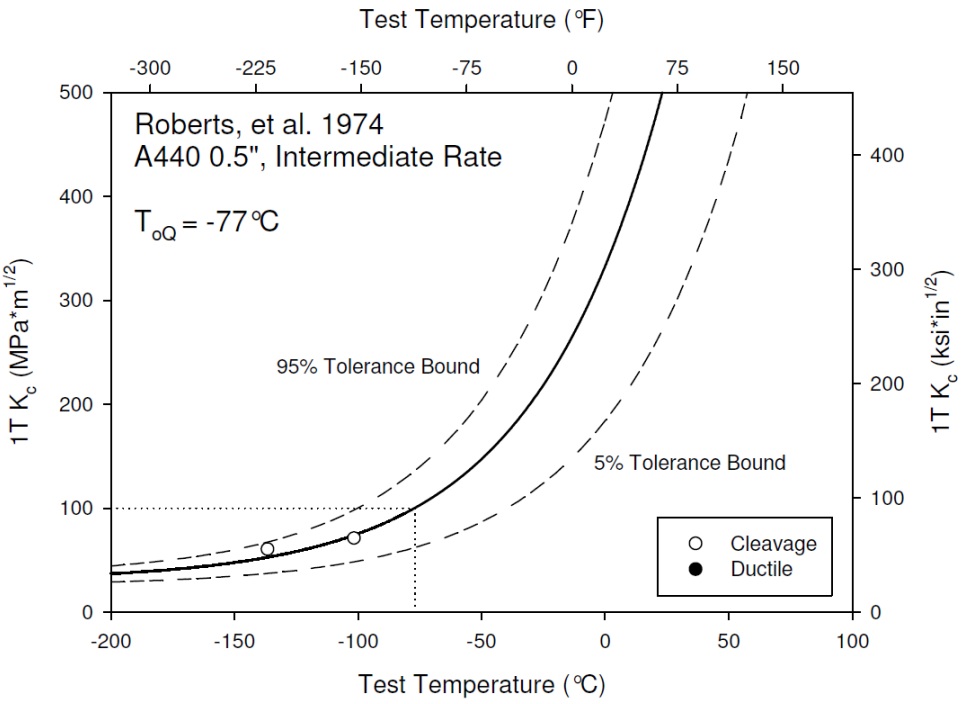

Figure K-21. Master Curve for A440 0.5" Intermediate, Roberts, et al. 1974

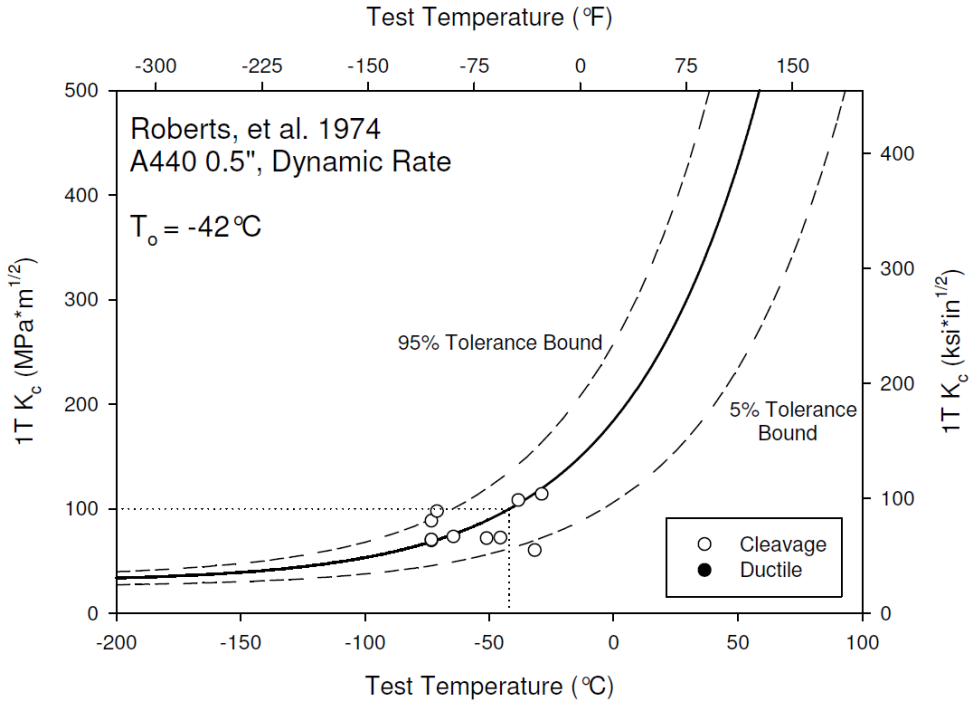

Figure K-22. Master Curve for A440 0.5" Dynamic, Roberts, et al. 1974

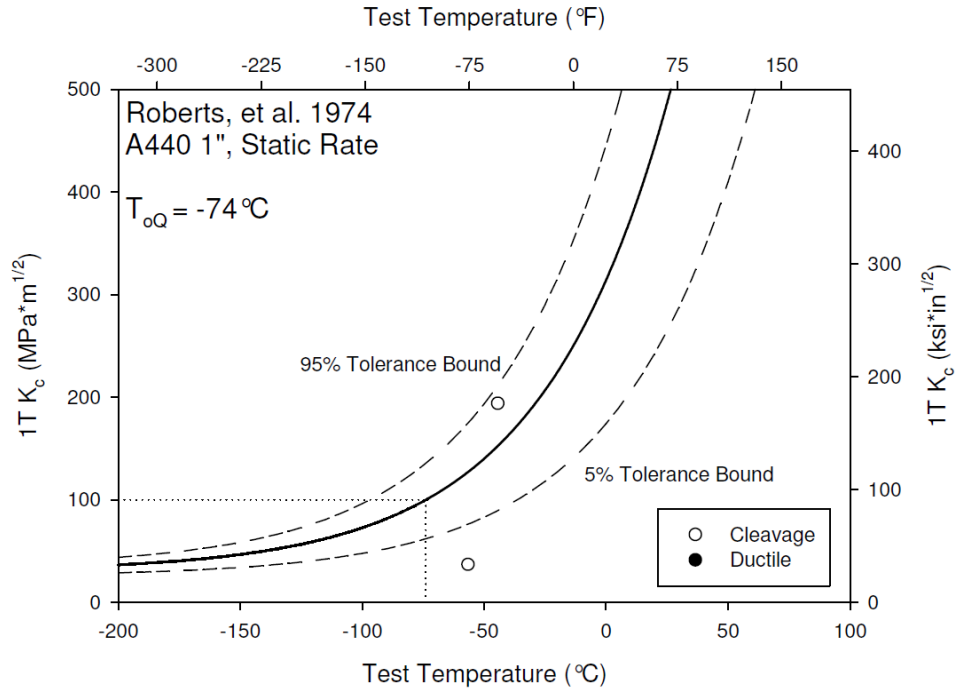

Figure K-23. Master Curve for A440 1.0" Static, Roberts, et al. 1974

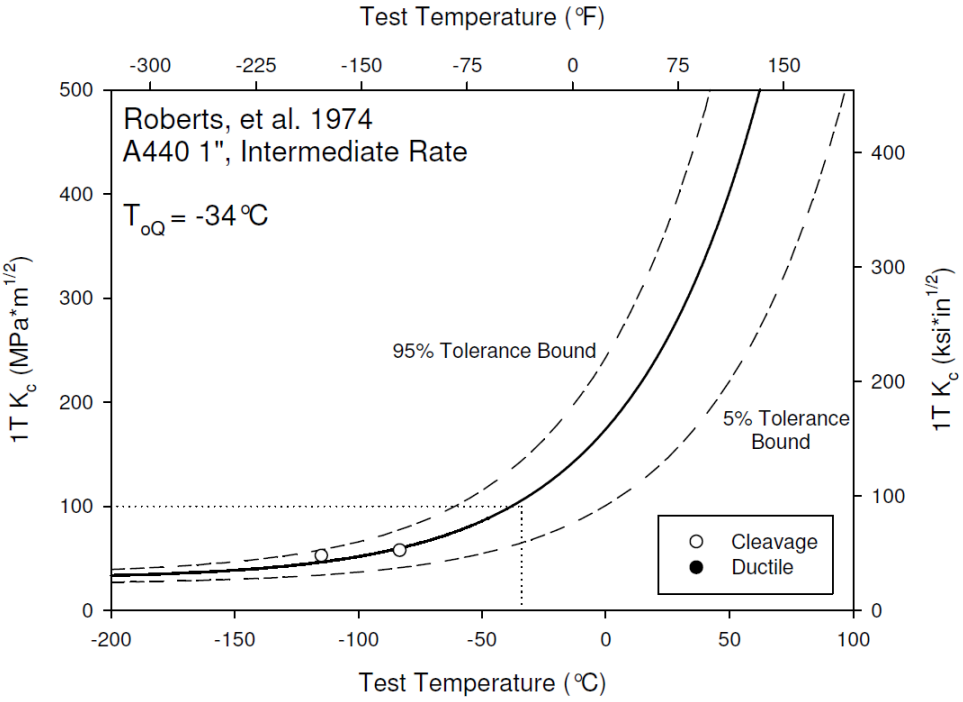

Figure K-24. Master Curve for A440 1.0" Intermediate, Roberts, et al. 1974

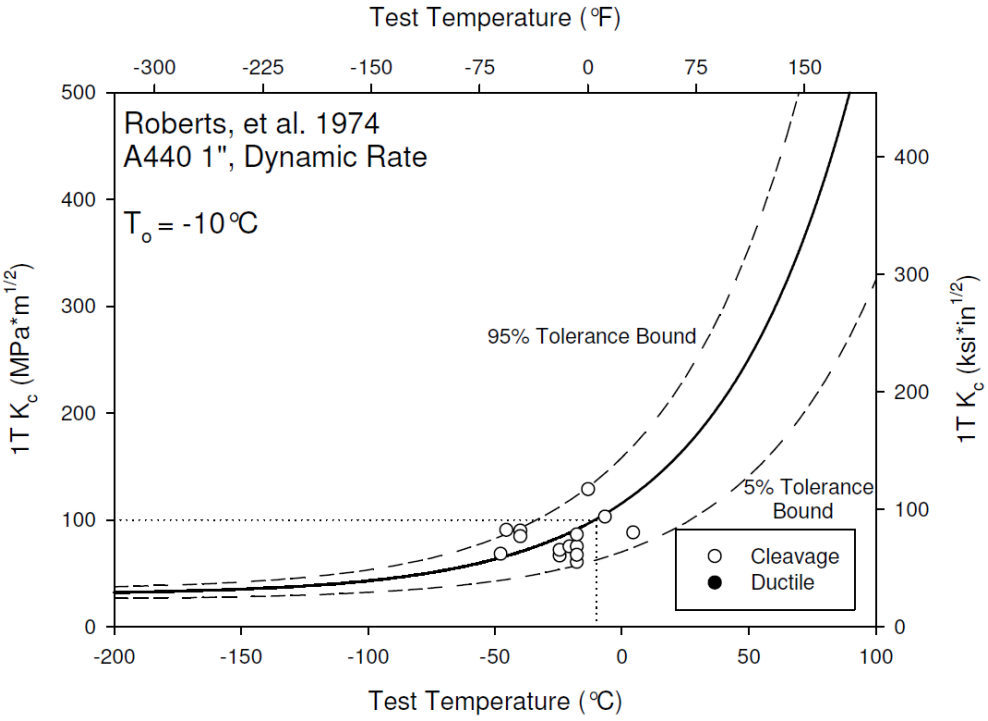

Figure K-25. Master Curve for A440 1.0" Dynamic, Roberts, et al. 1974

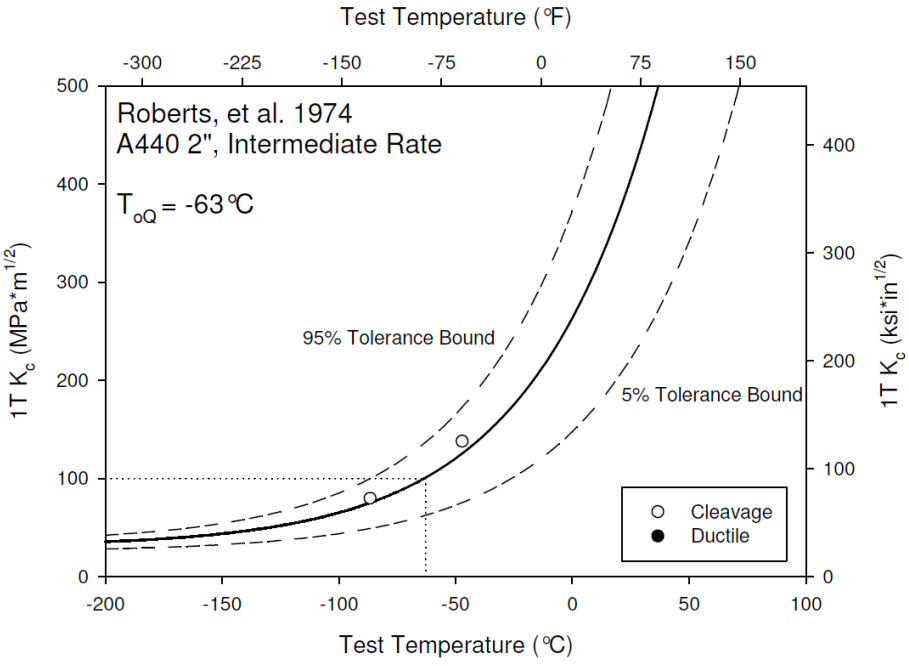

Figure K-26. Master Curve for A440 2.0" Intermediate, Roberts, et al. 1974

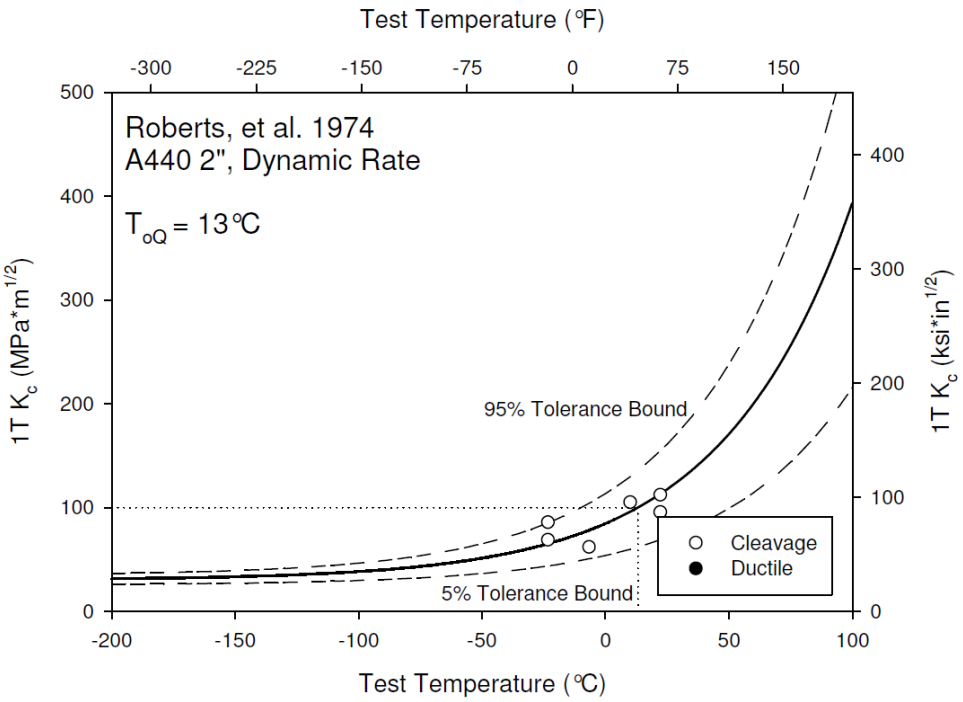

Figure K-27. Master Curve for A440 2.0" Dynamic, Roberts, et al. 1974

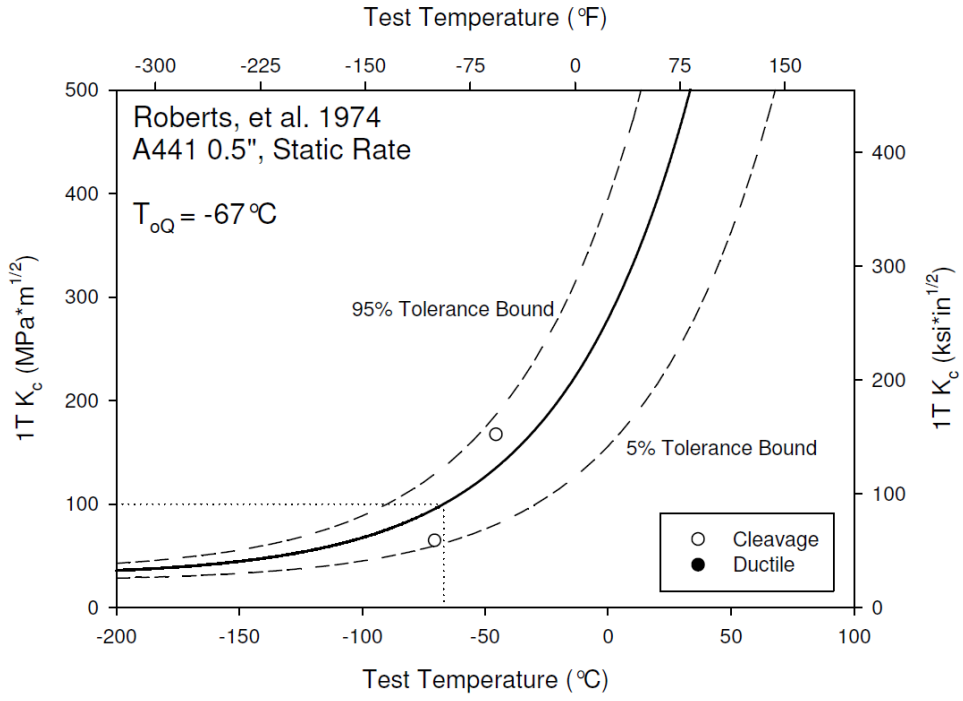

Figure K-28. Master Curve for A441 0.5" Static, Roberts, et al. 1974

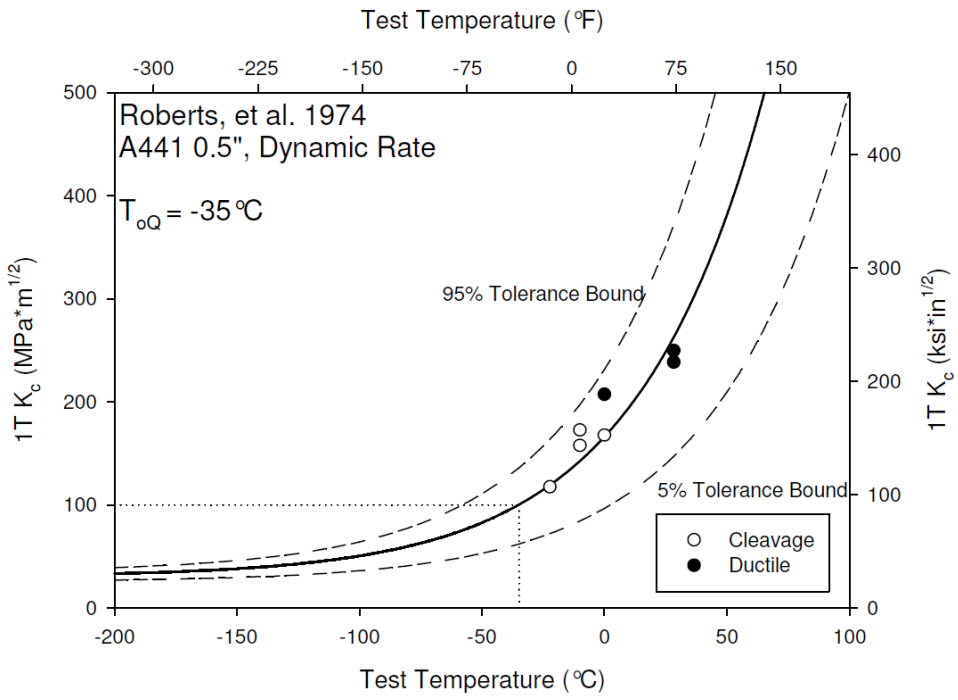

Figure K-29. Master Curve for A441 0.5" Dynamic, Roberts, et al. 1974

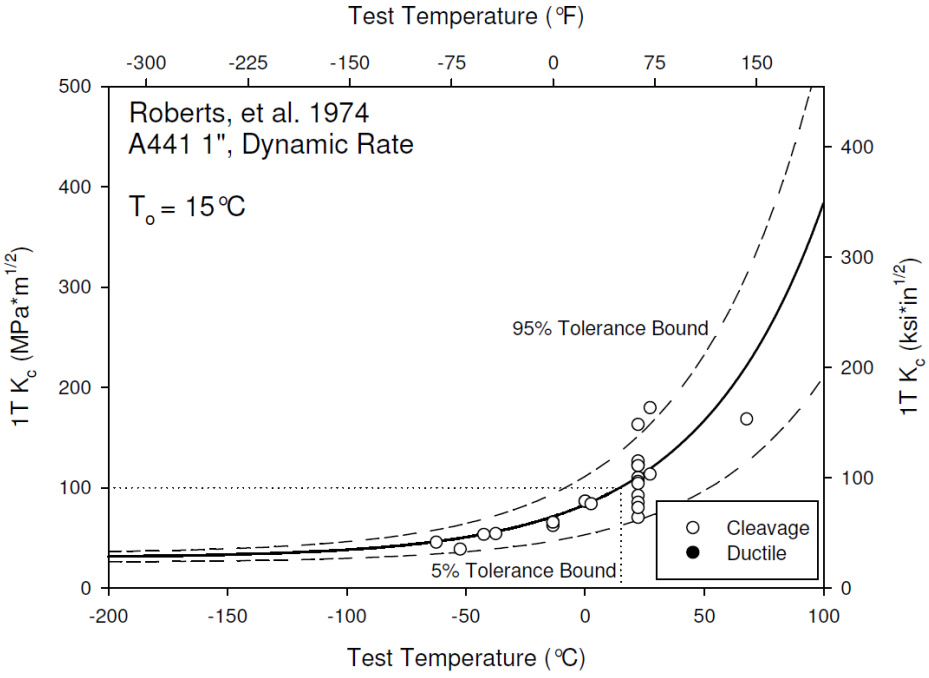

Figure K-30. Master Curve for A441 1.0" Dynamic, Roberts, et al. 1974

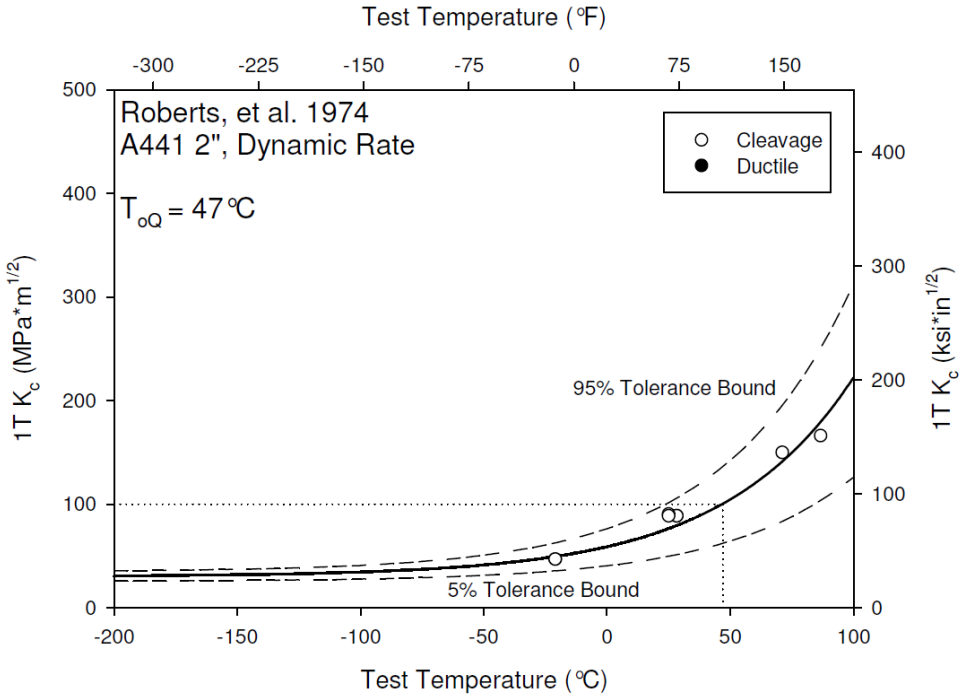

Figure K-31. Master Curve for A441 2.0" Dynamic, Roberts, et al. 1974

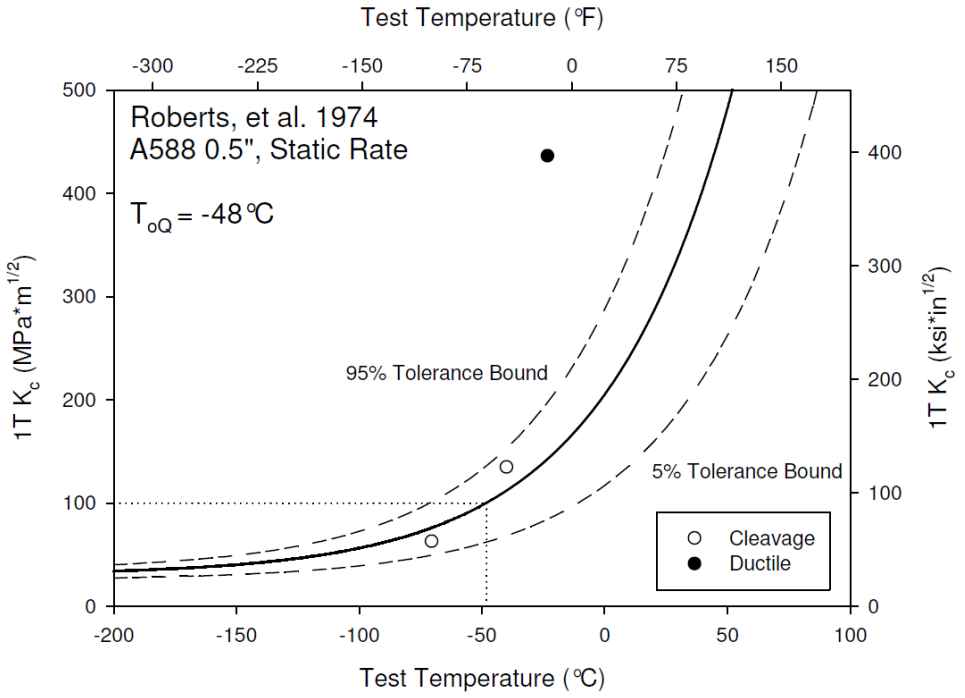

Figure K-32. Master Curve for A588 0.5" Static, Roberts, et al. 1974

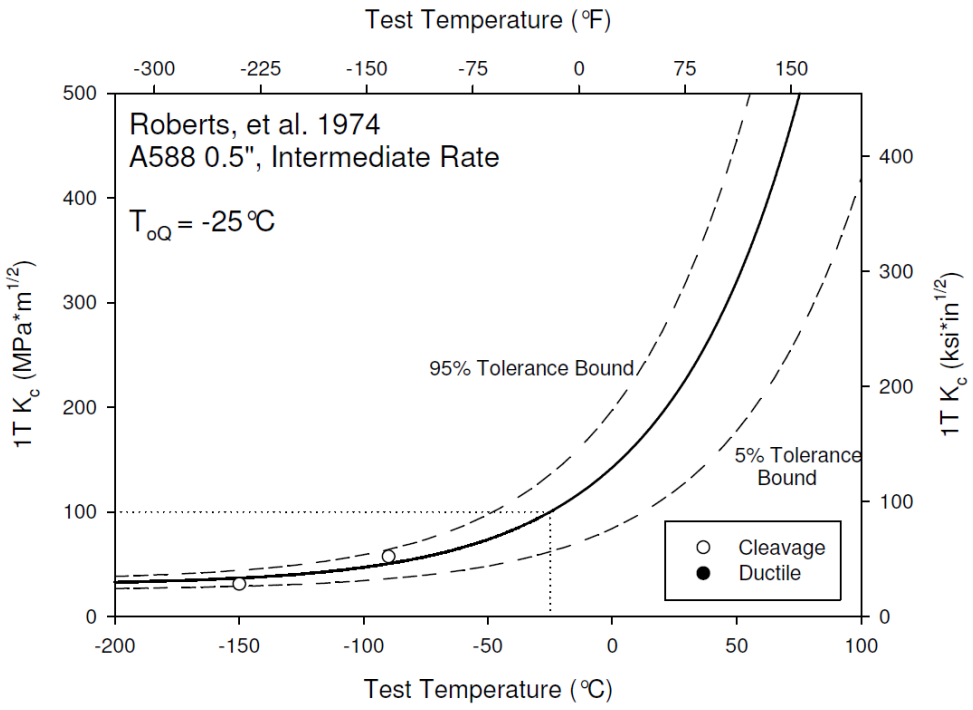

Figure K-33. Master Curve for A588 0.5" Intermediate, Roberts, et al. 1974

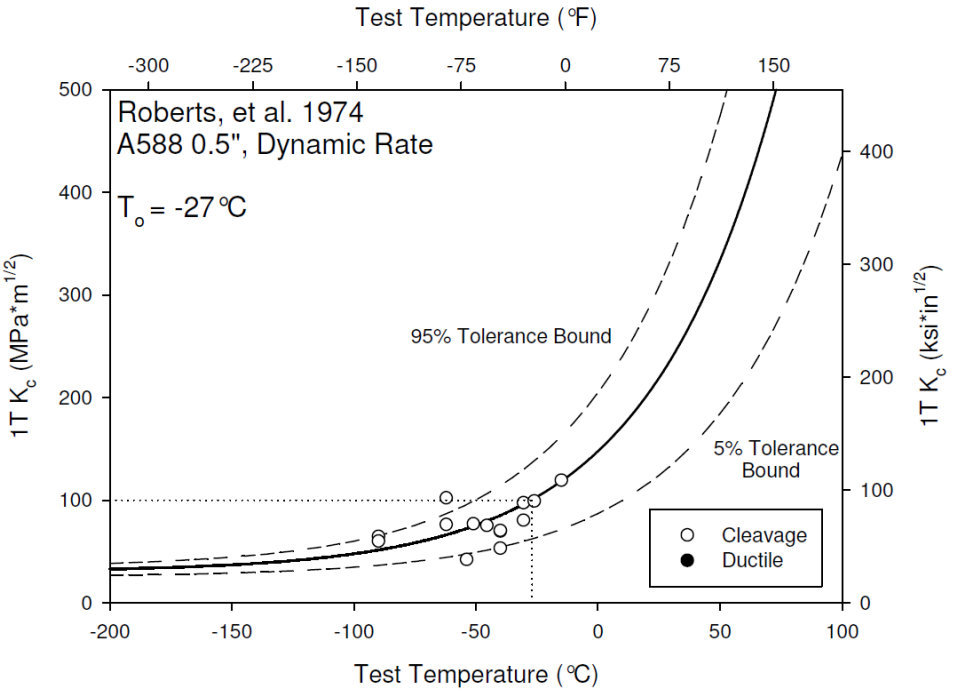

Figure K-34. Master Curve for A588 0.5" Dynamic, Roberts, et al. 1974

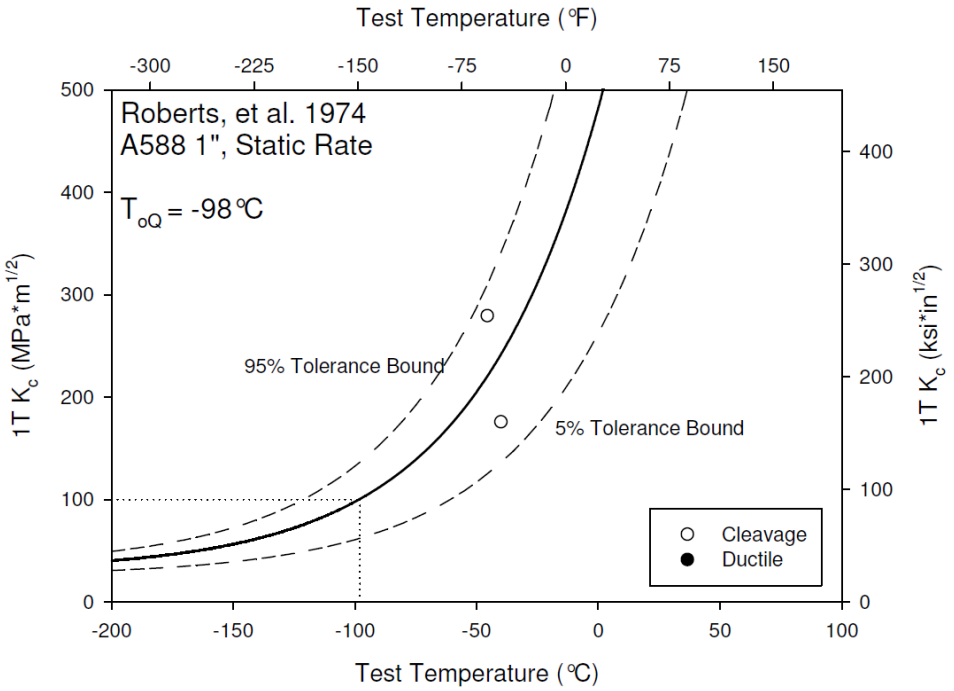

Figure K-35. Master Curve for A588 1.0" Static, Roberts, et al. 1974

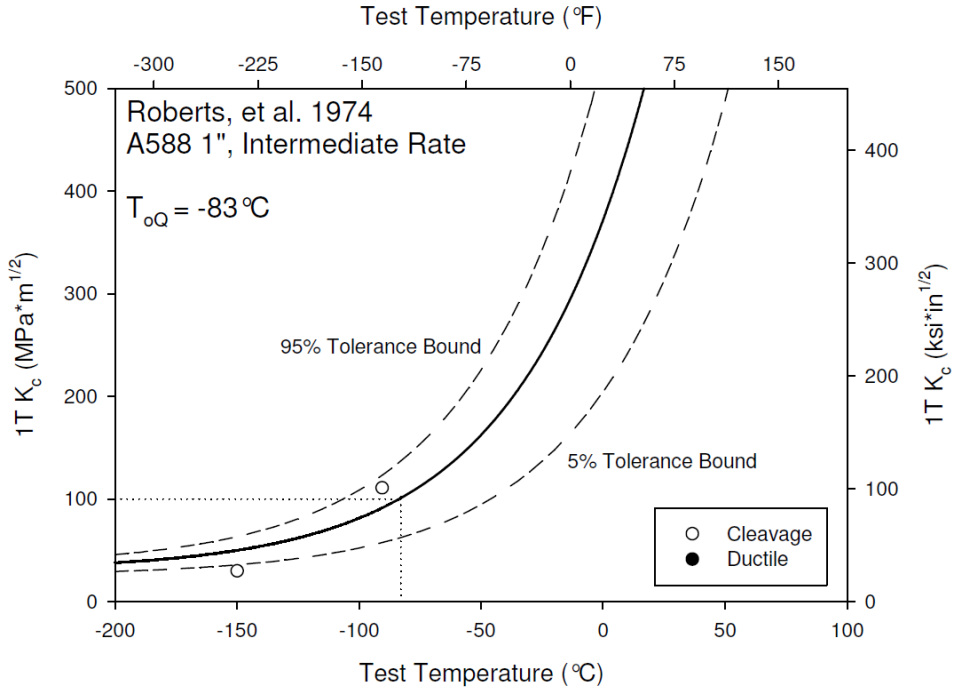

Figure K-36. Master Curve for A588 1.0" Intermediate, Roberts, et al. 1974

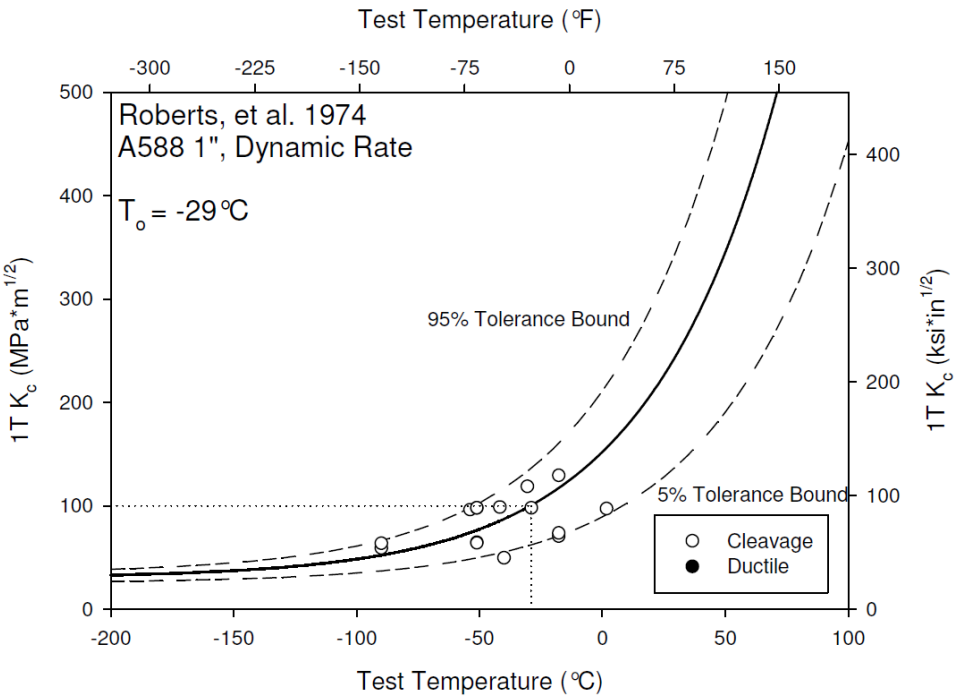

Figure K-37. Master Curve for A588 1.0" Dynamic, Roberts, et al. 1974

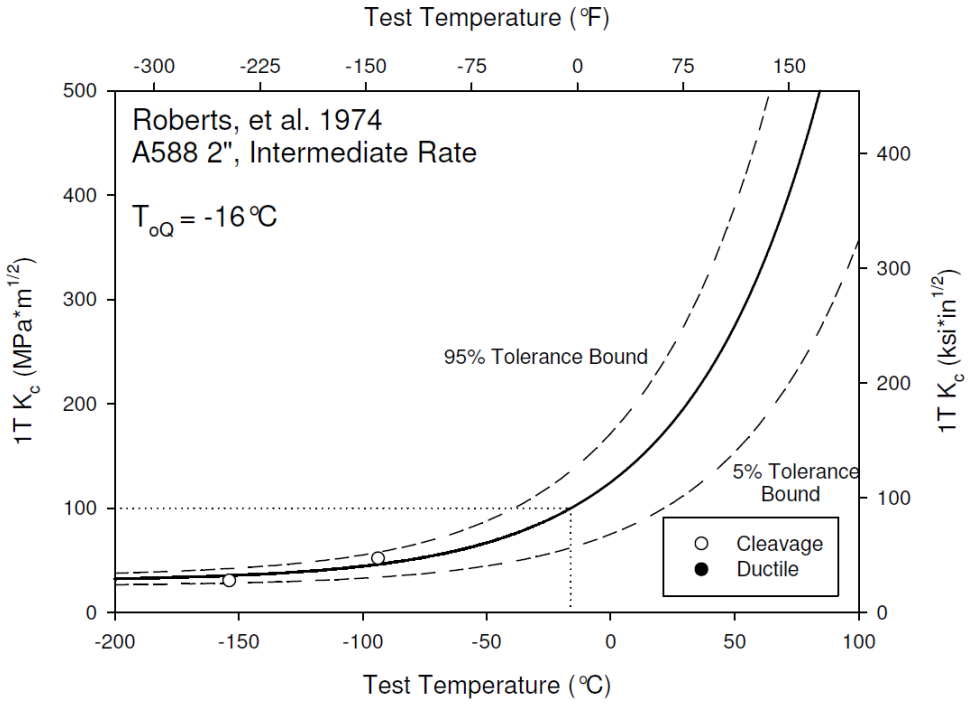

Figure K-38. Master Curve for A588 2.0" Intermediate, Roberts, et al. 1974

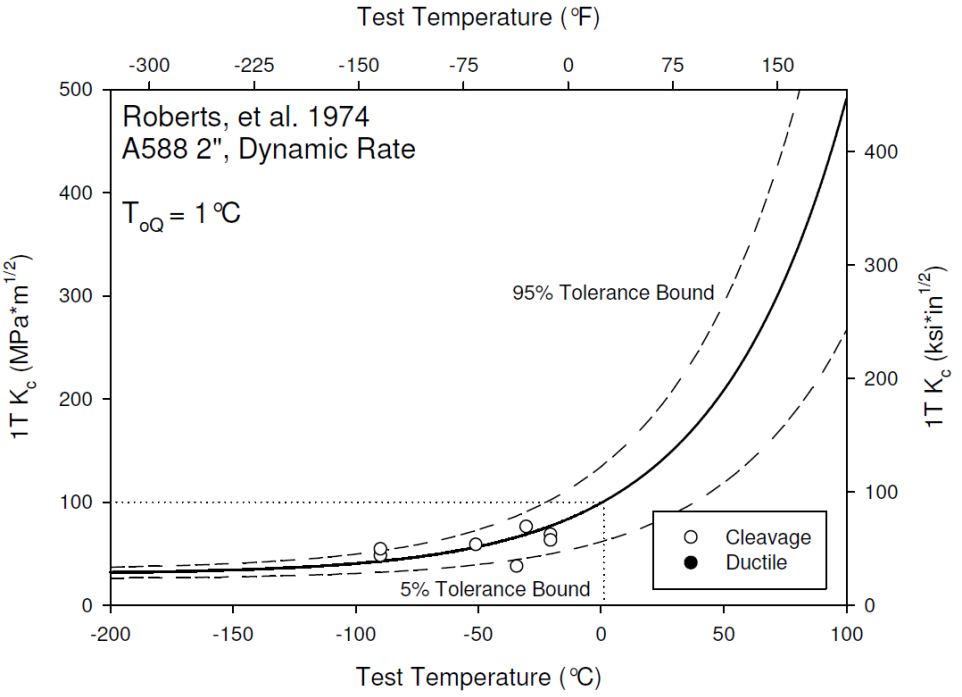

Figure K-39. Master Curve for A588 2.0" Dynamic, Roberts, et al. 1974

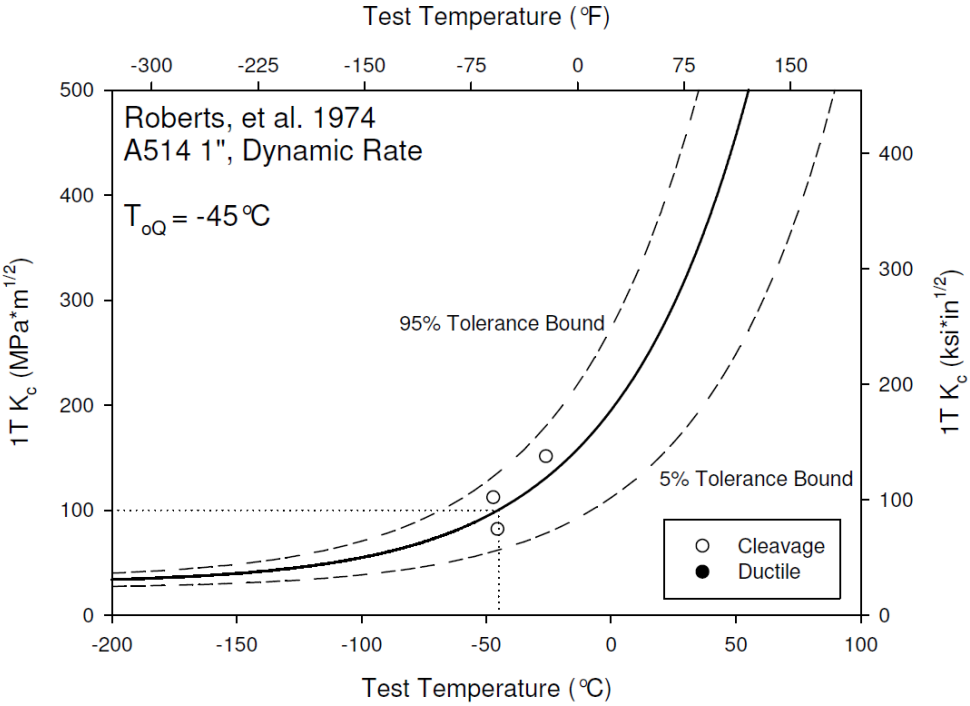

Figure K-40. Master Curve for A514 1.0" Dynamic, Roberts, et al. 1974

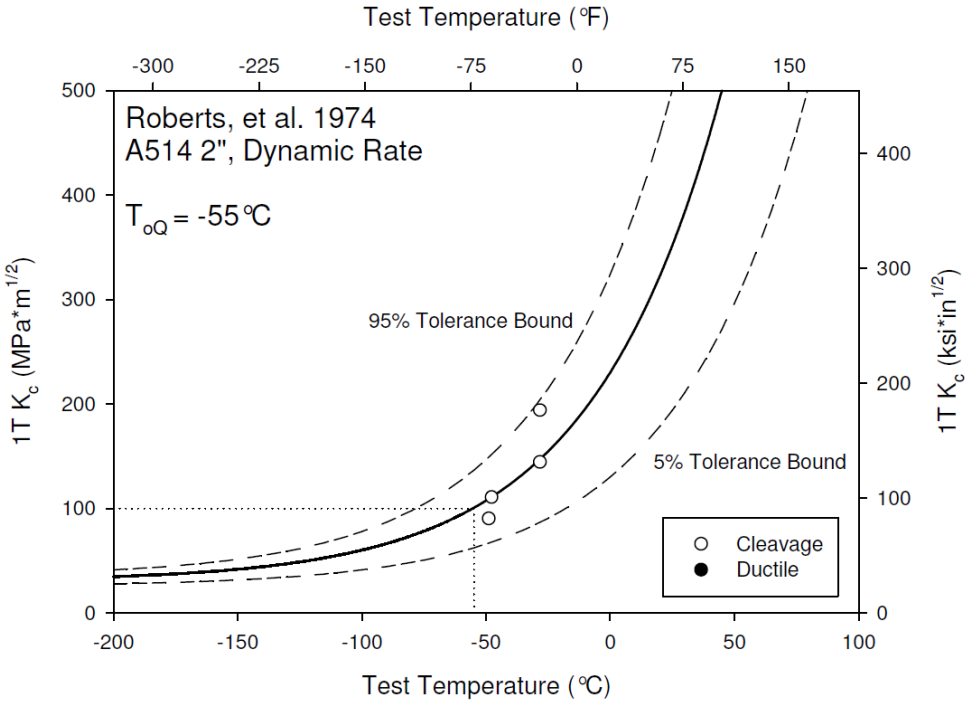

Figure K-41. Master Curve for A514 2.0" Dynamic, Roberts, et al. 1974

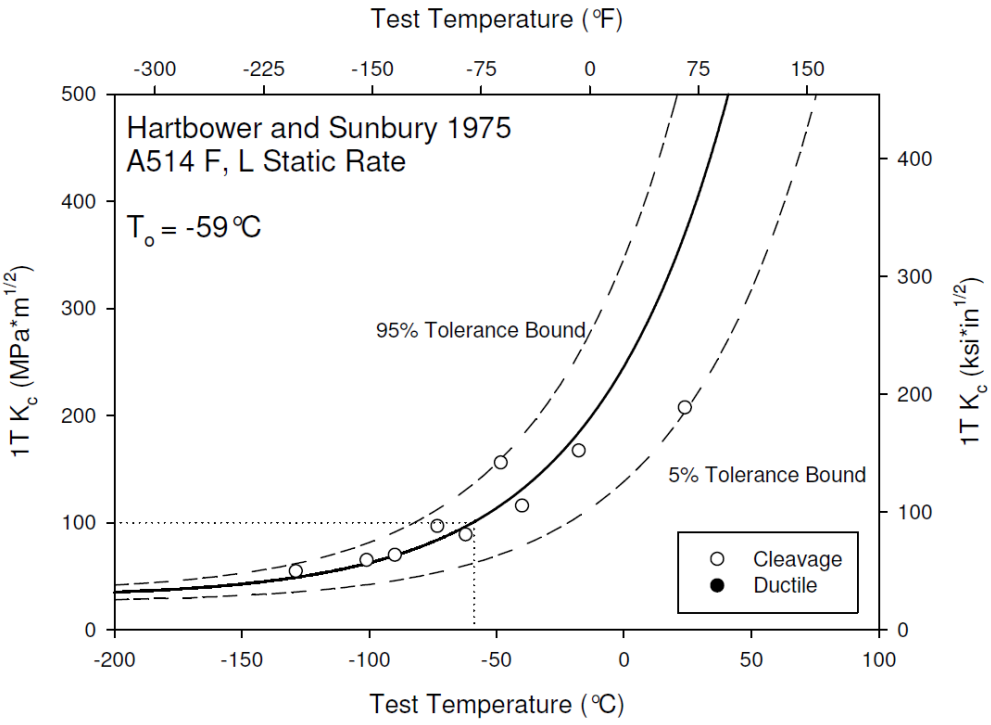

Figure K-42. Master Curve for A514 Plate L Static, Hartbower and Sunbury 1975

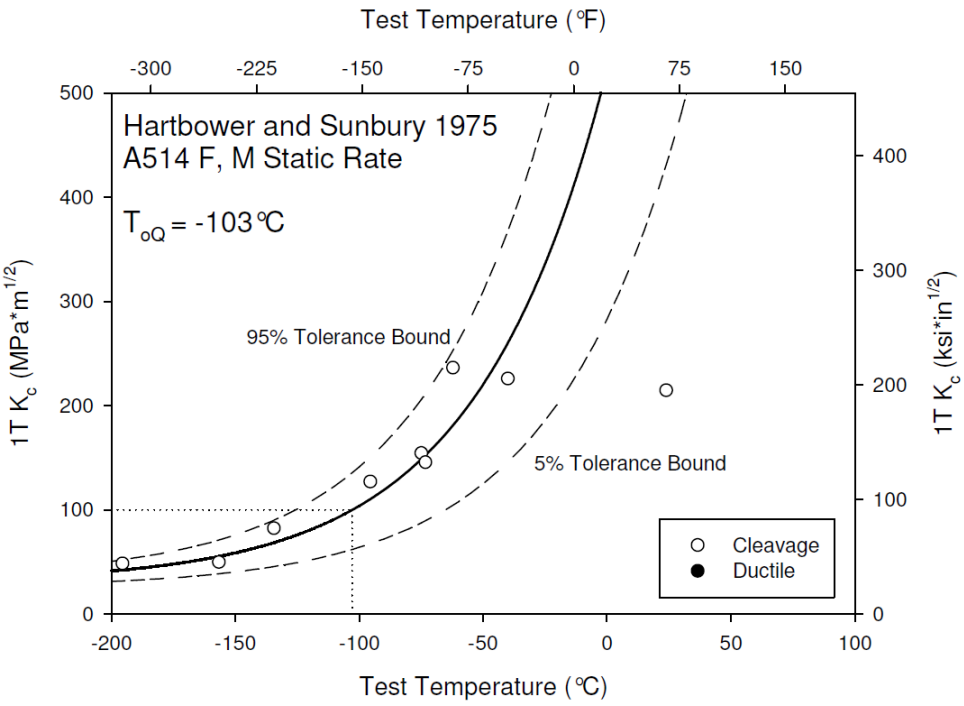

Figure K-43. Master Curve for A514 Plate M Static, Hartbower and Sunbury 1975

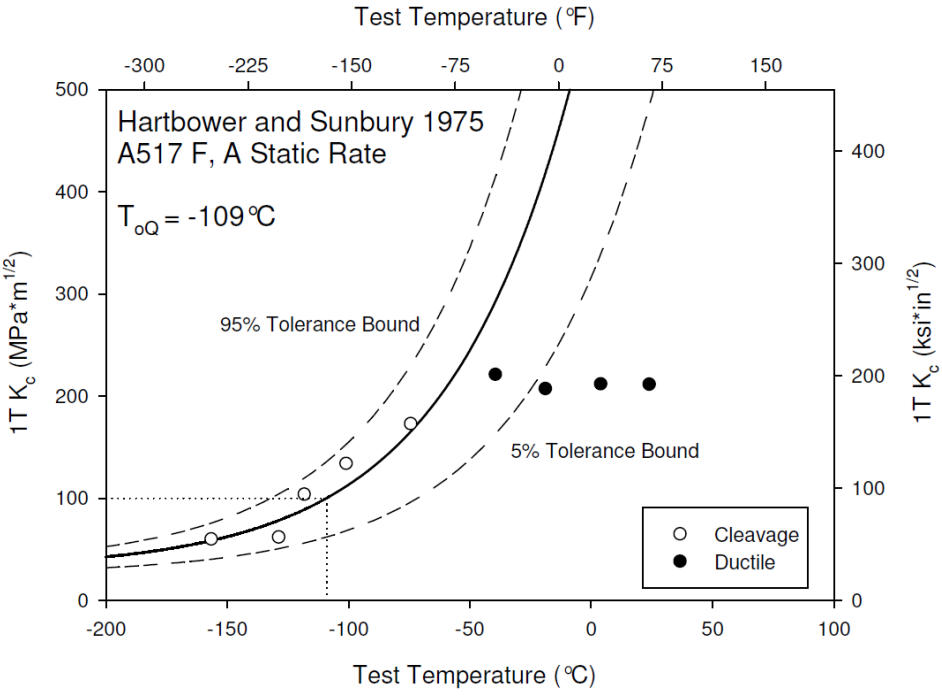

Figure K-44. Master Curve for A517 Plate A Static, Hartbower and Sunbury 1975

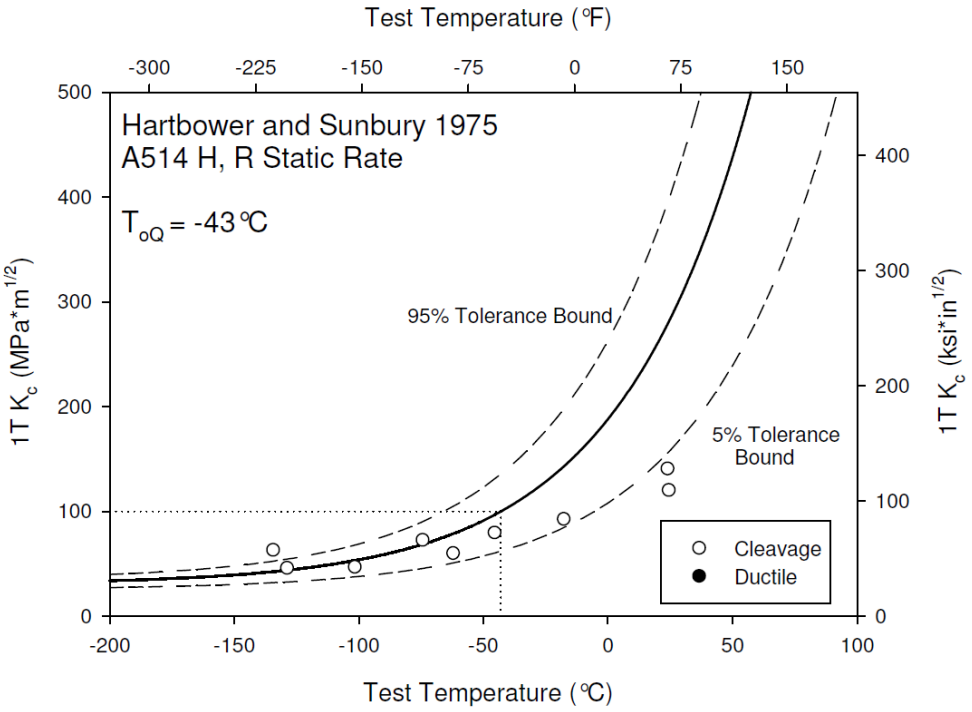

Figure K-45. Master Curve for A514 Plate R Static, Hartbower and Sunbury 1975

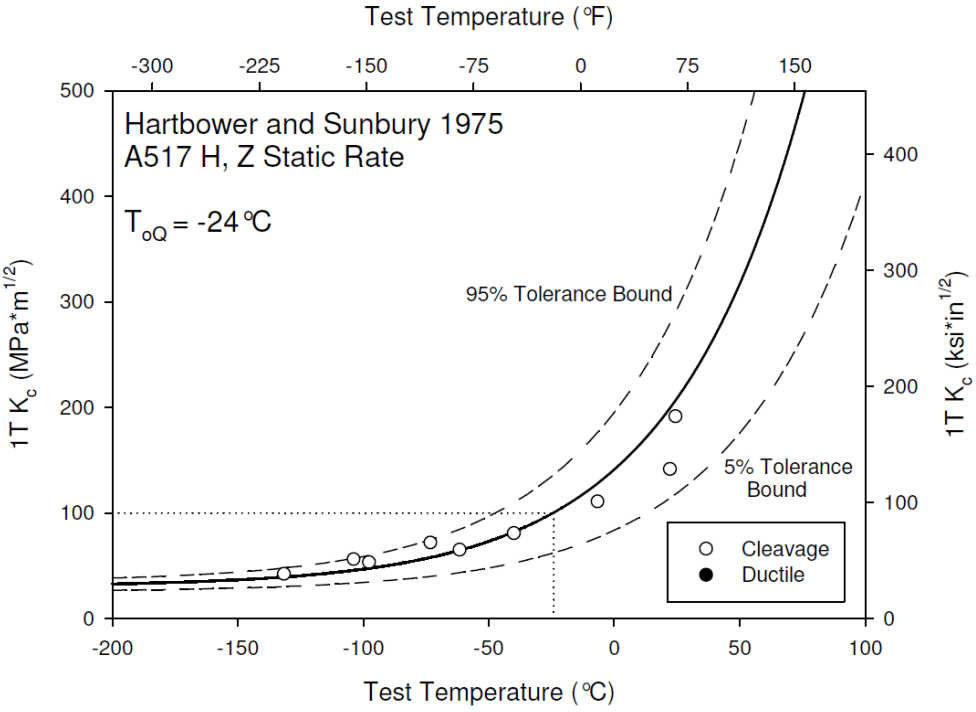

Figure K-46. Master Curve for A517 Plate Z Static, Hartbower and Sunbury 1975

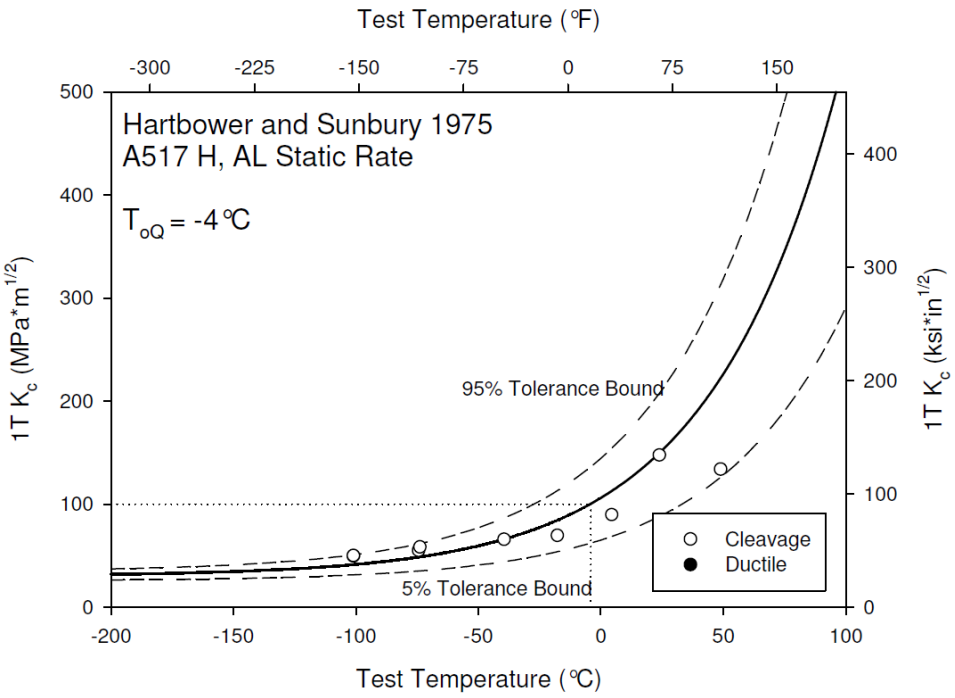

Figure K-47. Master Curve for A517 Plate AL Static, Hartbower and Sunbury 1975

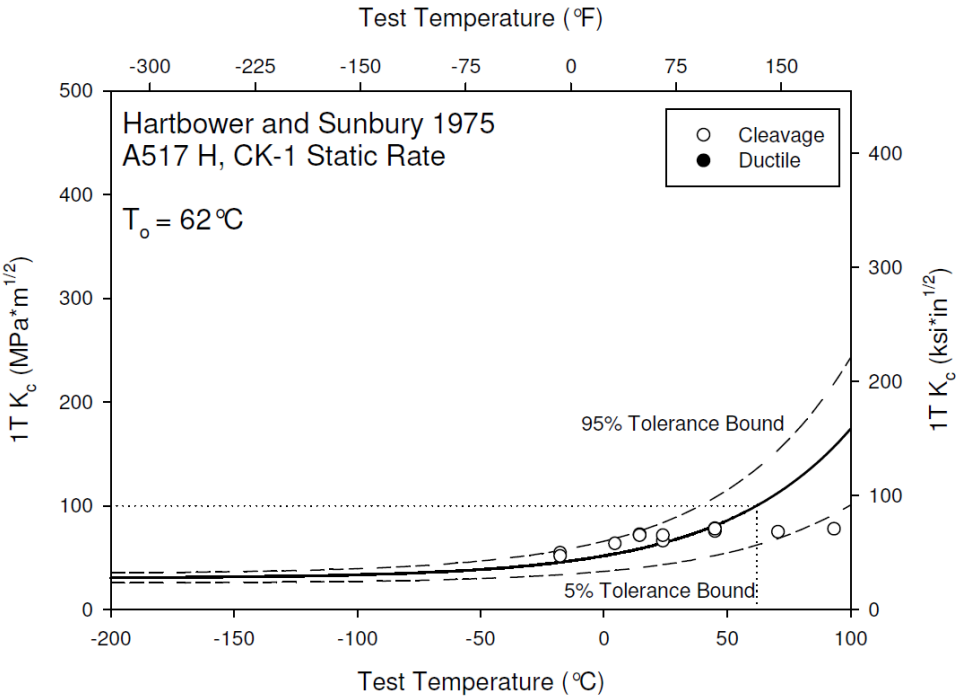

Figure K-48. Master Curve for A517 Plate CK-1 Static, Hartbower and Sunbury 1975

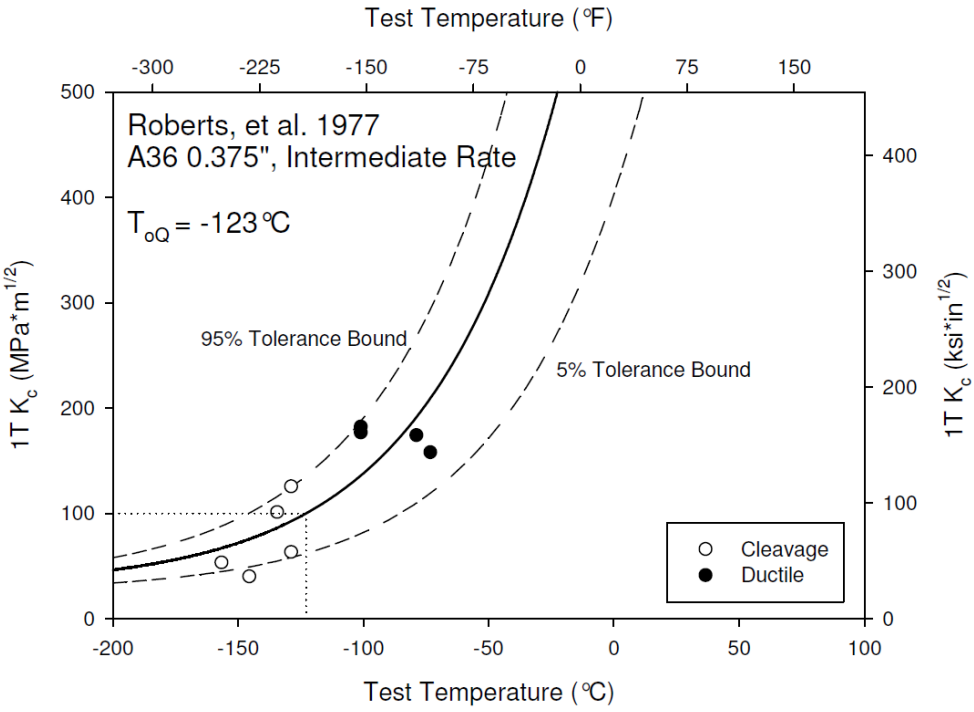

Figure K-49. Master Curve for A36 0.375" Intermediate, Roberts, et al. 1977

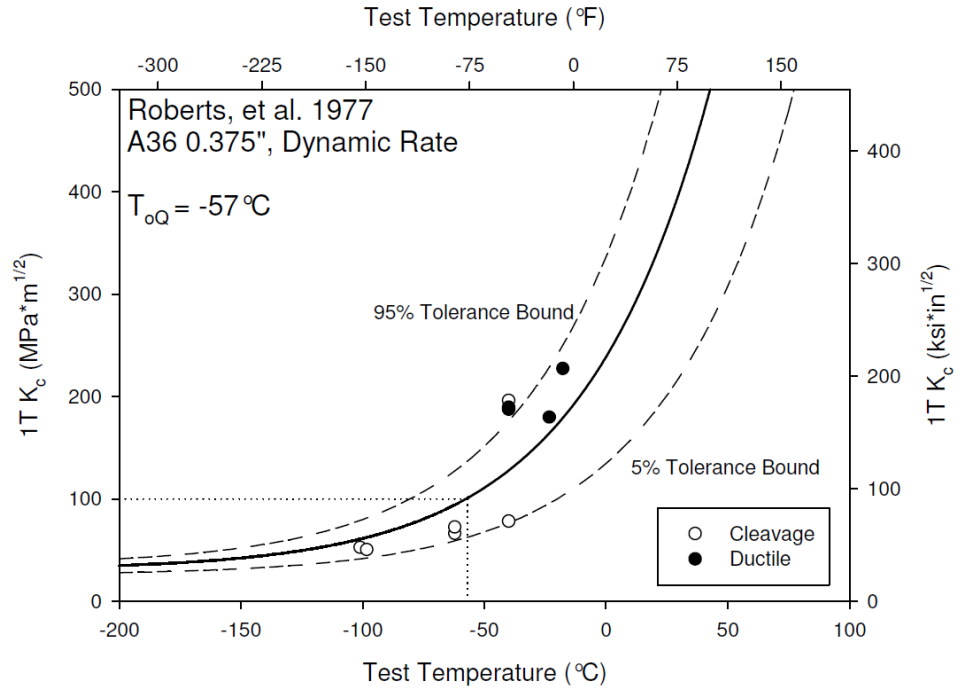

Figure K-50. Master Curve for A36 0.375" Dynamic, Roberts, et al. 1977

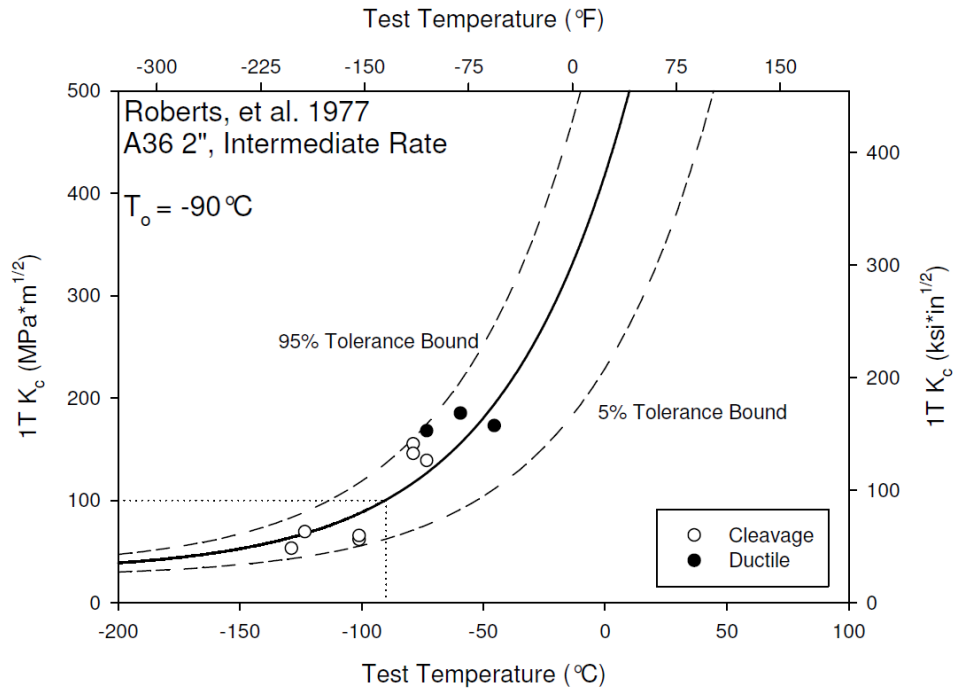

Figure K-51. Master Curve for A36 2.0" Intermediate, Roberts, et al. 1977

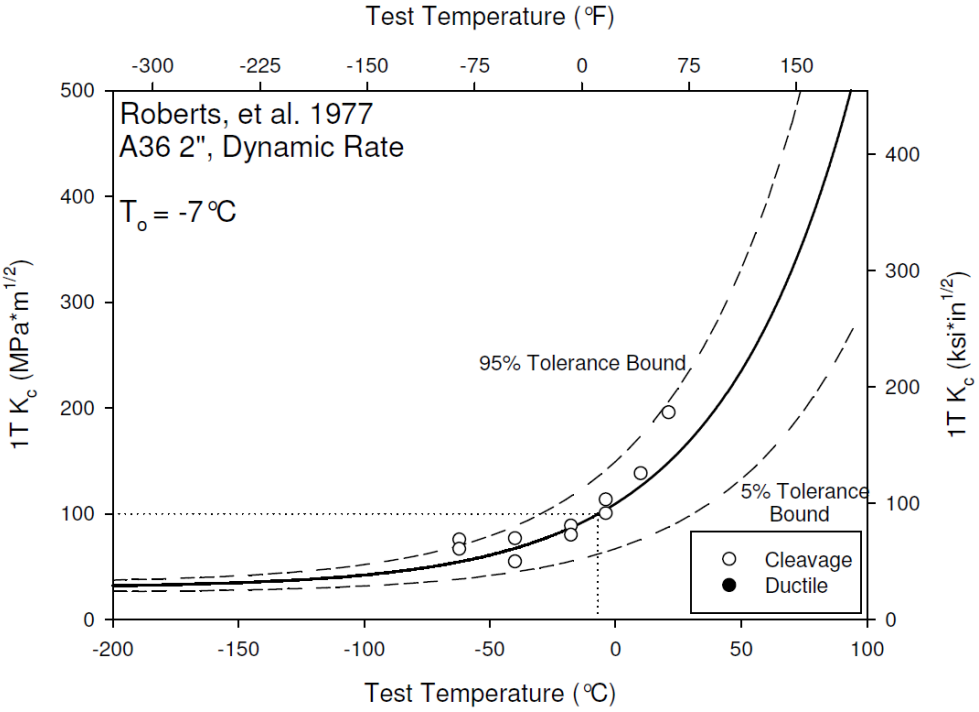

Figure K-52. Master Curve for A36 2.0" Dynamic, Roberts, et al. 1977

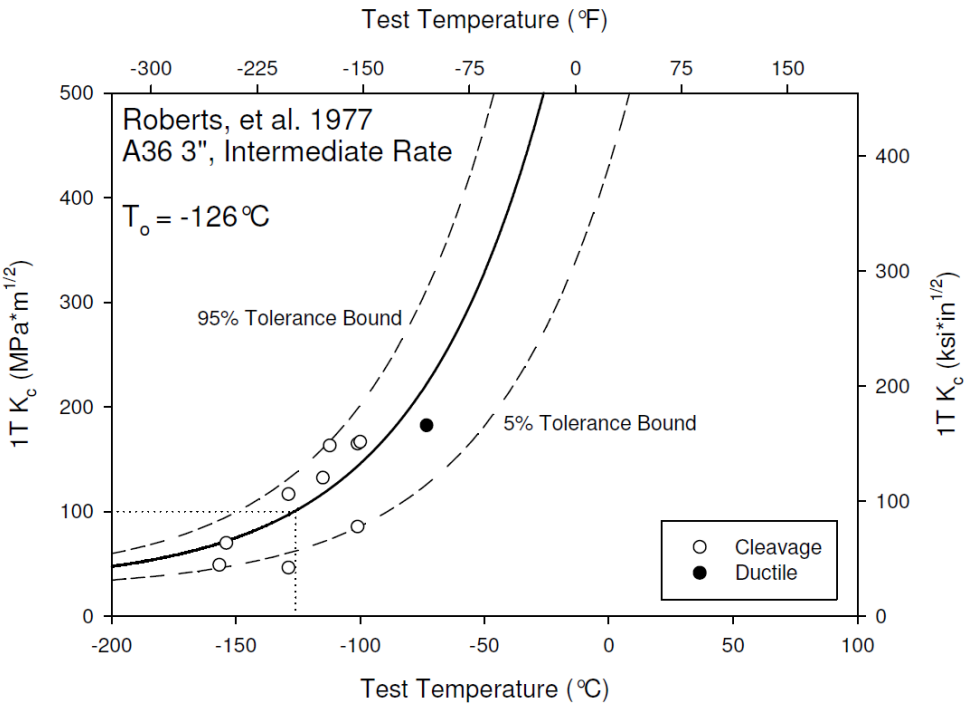

Figure K-53. Master Curve for A36 3.0" Intermediate, Roberts, et al. 1977

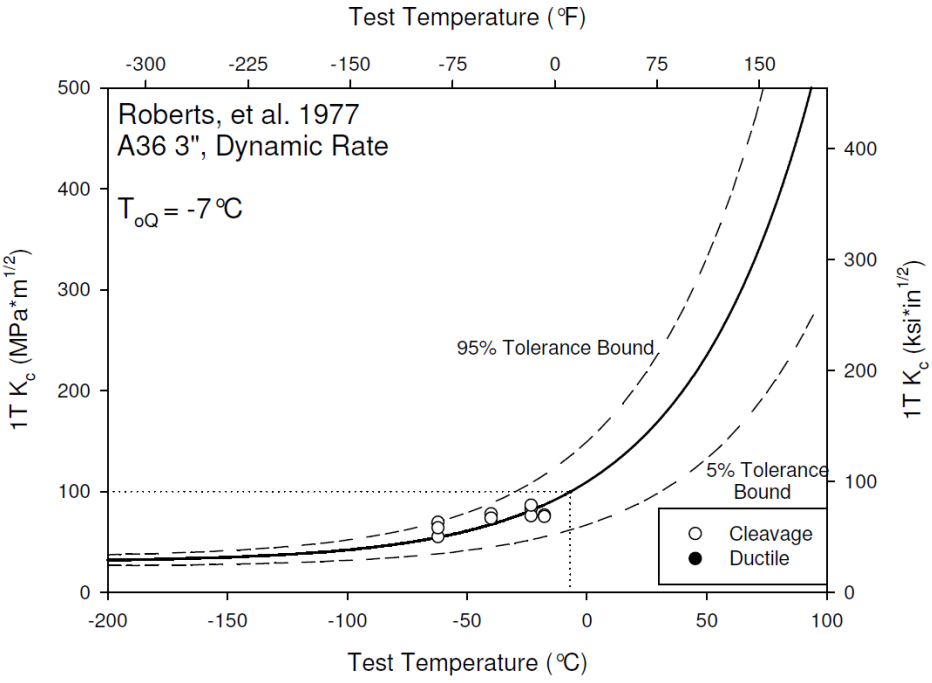

Figure K-54. Master Curve for A36 3.0" Dynamic, Roberts, et al. 1977

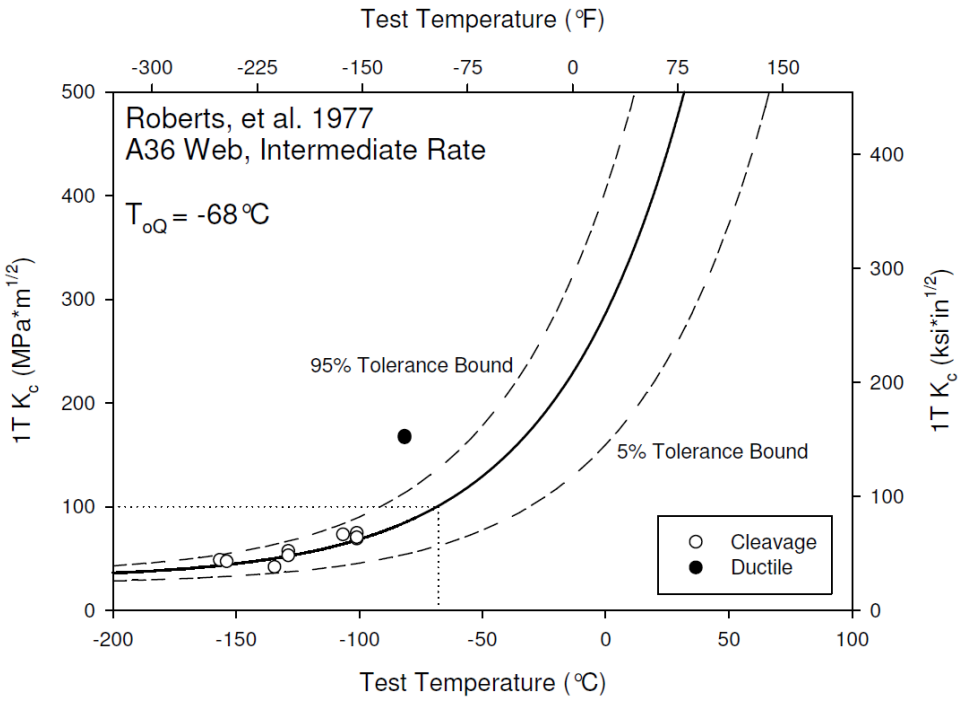

Figure K-55. Master Curve for A36 Web Intermediate, Roberts, et al. 1977

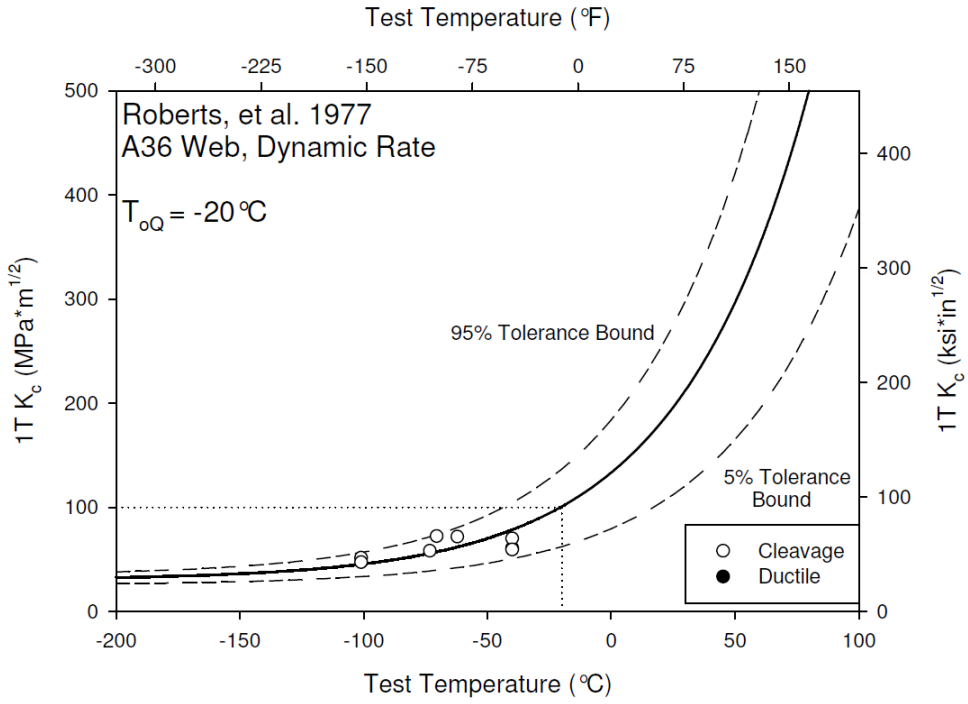

Figure K-56. Master Curve for A36 Web Dynamic, Roberts, et al. 1977

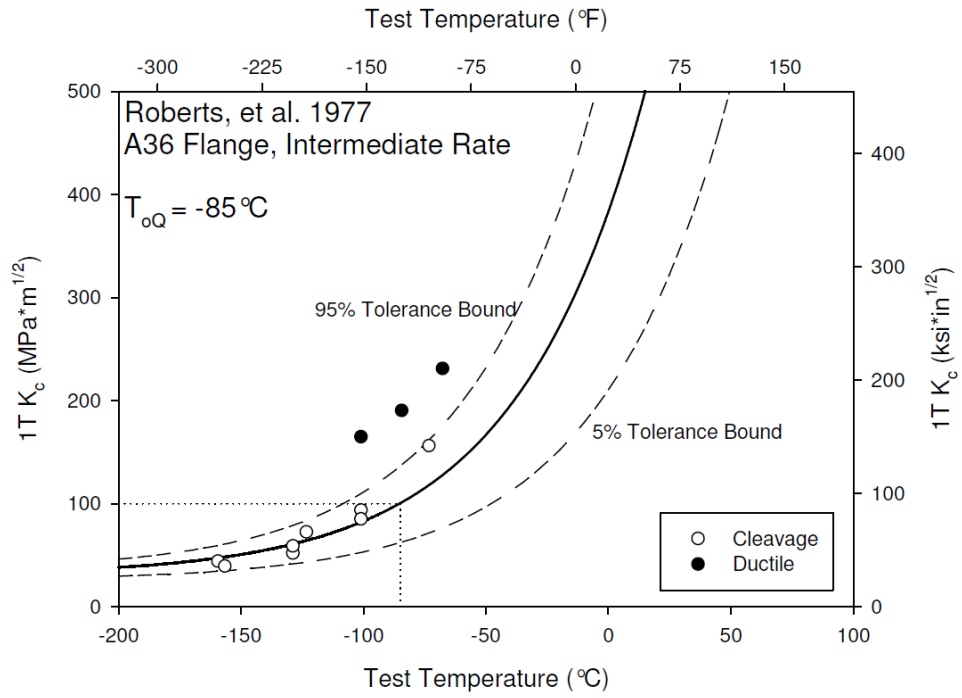

Figure K-57. Master Curve for A36 Flange Intermediate, Roberts, et al. 1977

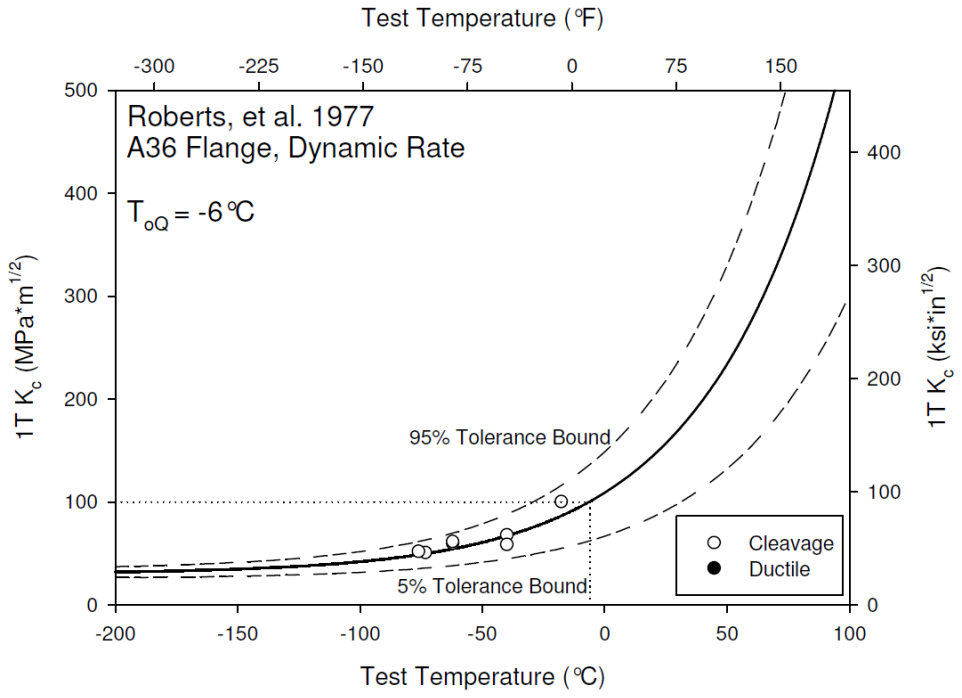

Figure K-58. Master Curve for A36 Flange Dynamic, Roberts, et al. 1977

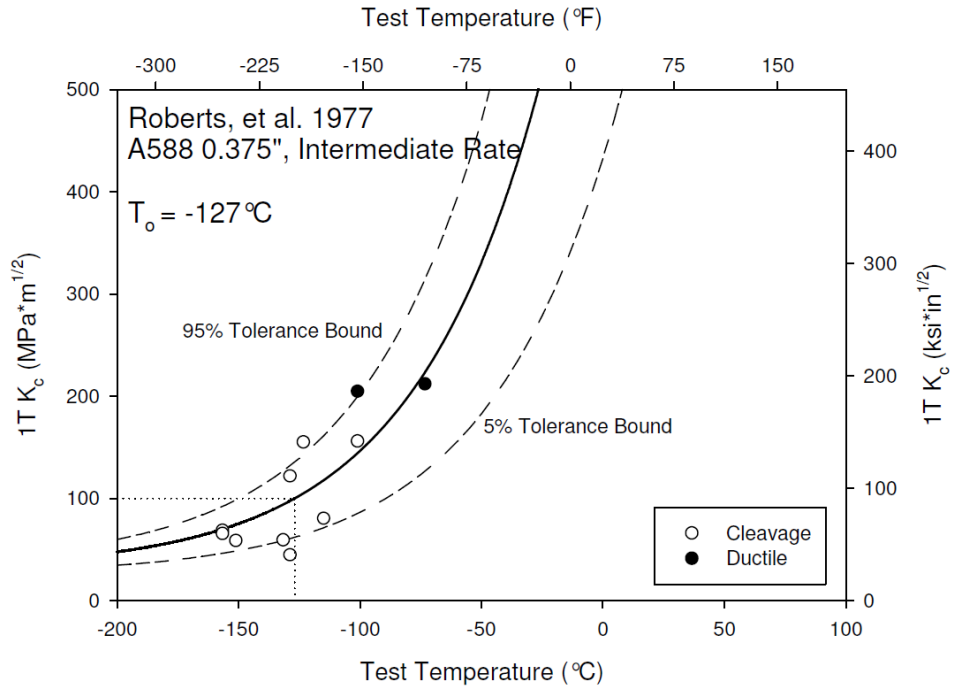

Figure K-59. Master Curve for A588 0.375" Intermediate, Roberts, et al. 1977

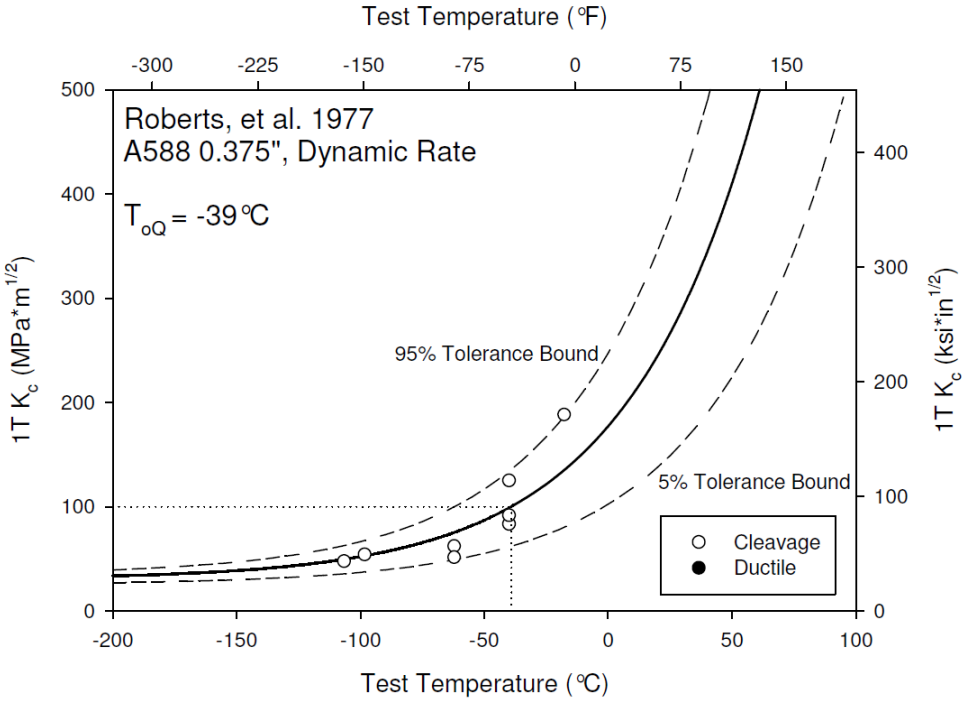

Figure K-60. Master Curve for A588 0.375" Dynamic, Roberts, et al. 1977

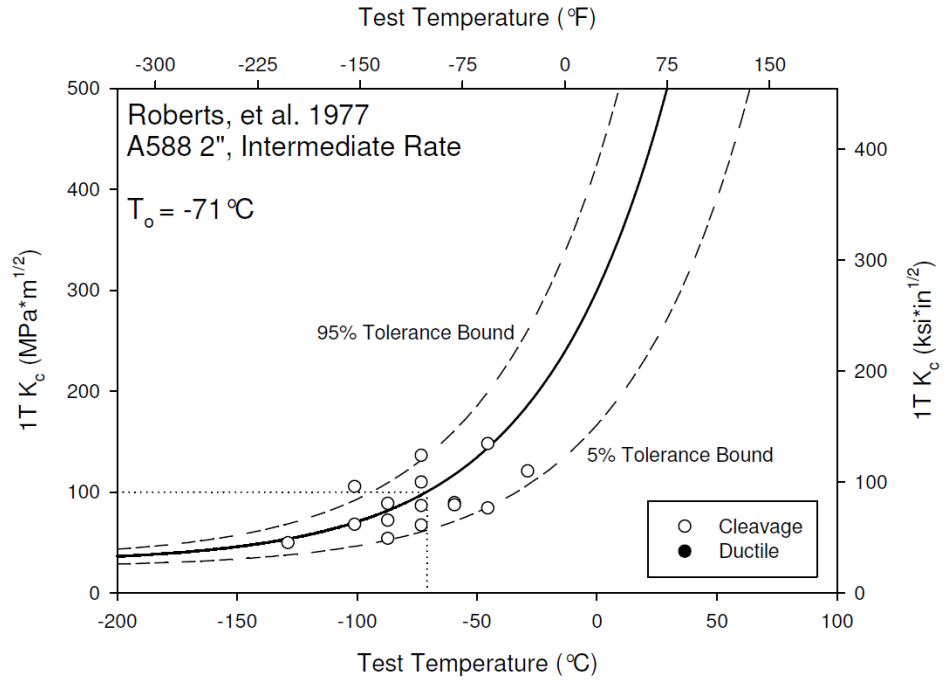

Figure K-61. Master Curve for A588 2.0" Intermediate, Roberts, et al. 1977

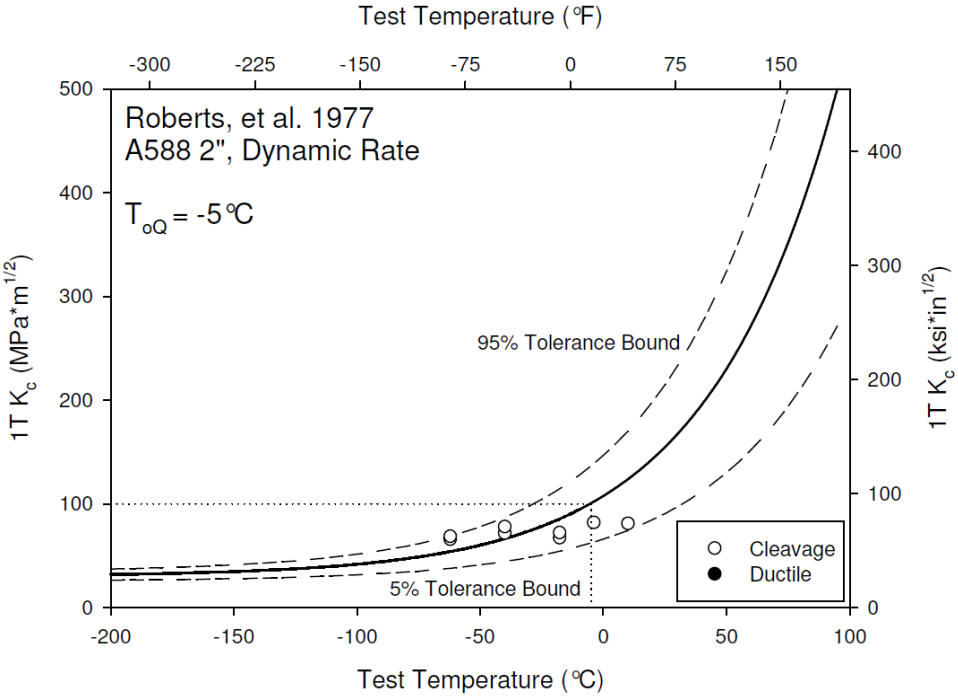

Figure K-62. Master Curve for A588 2.0" Dynamic, Roberts, et al. 1977

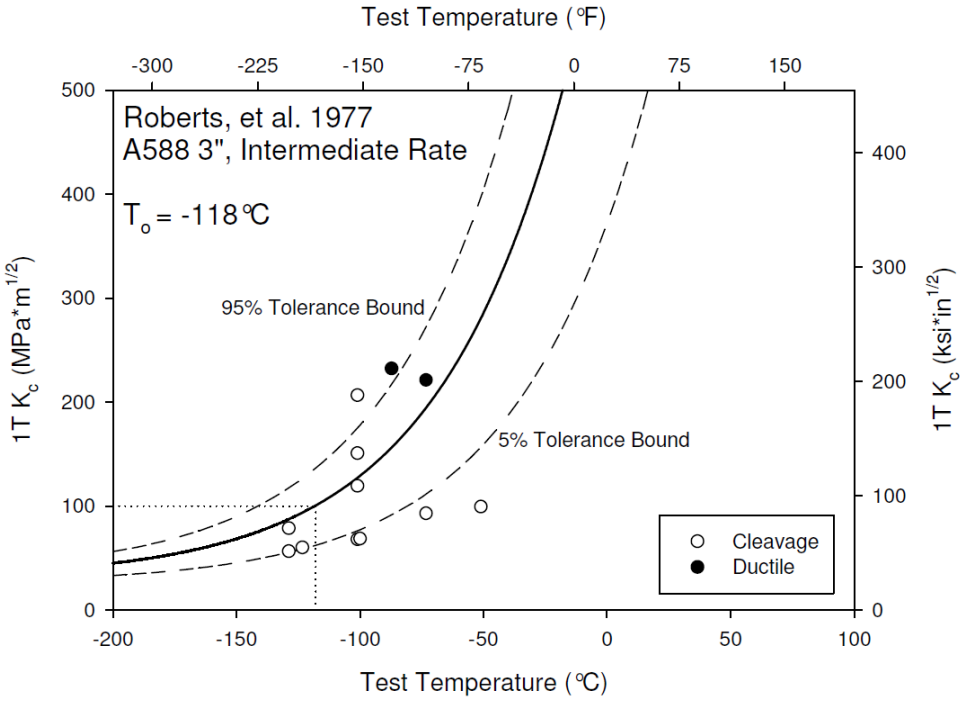

Figure K-63. Master Curve for A588 3.0" Intermediate, Roberts, et al. 1977

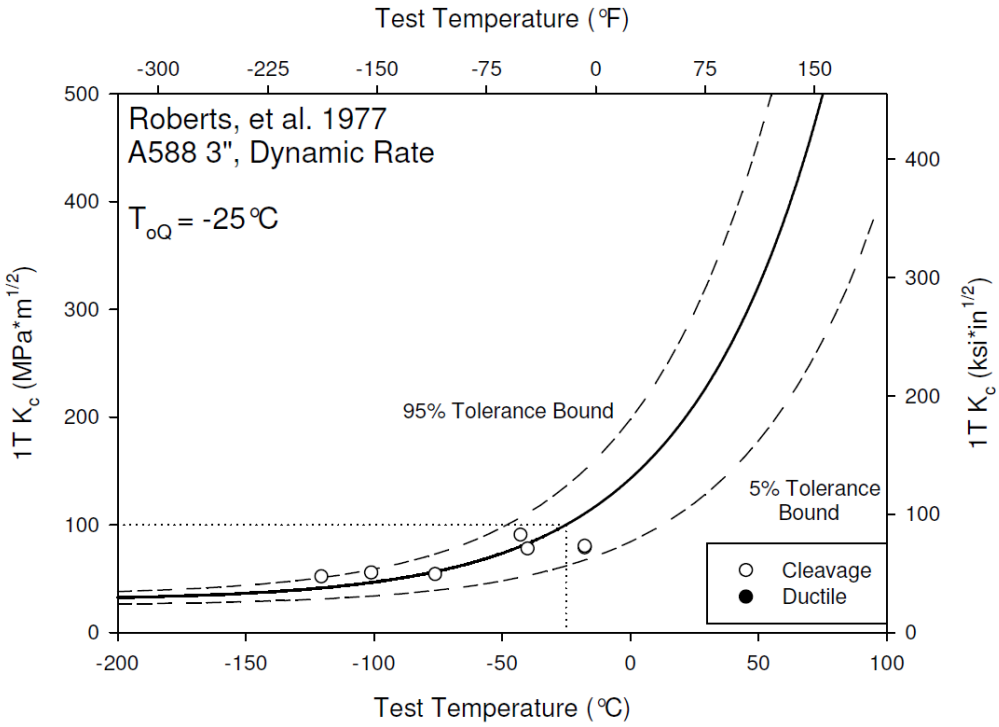

Figure K-64. Master Curve for A588 3.0" Dynamic, Roberts, et al. 1977

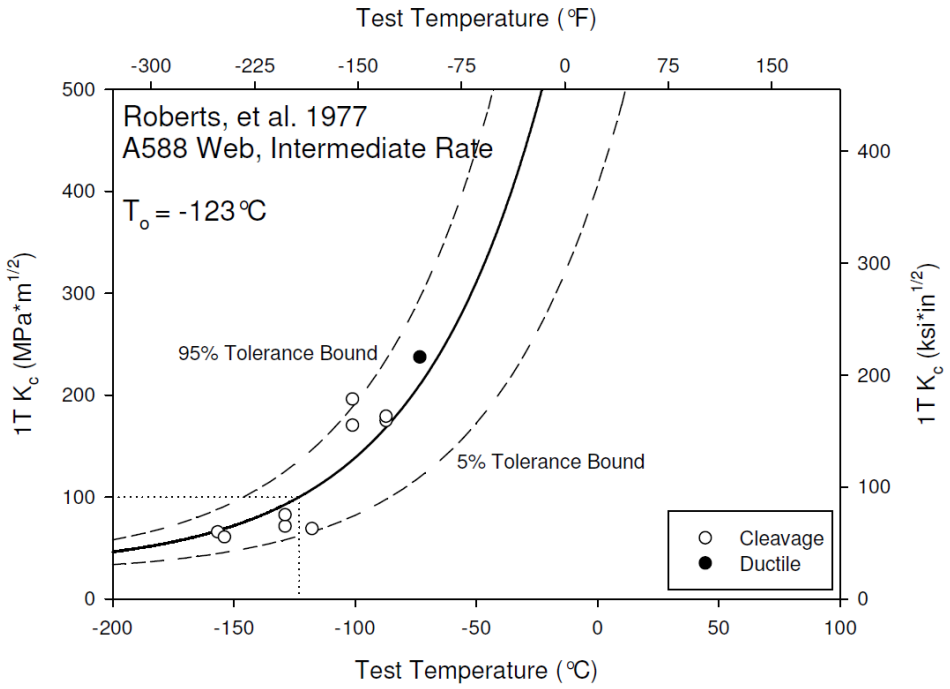

Figure K-65. Master Curve for A588 Web Intermediate, Roberts, et al. 1977

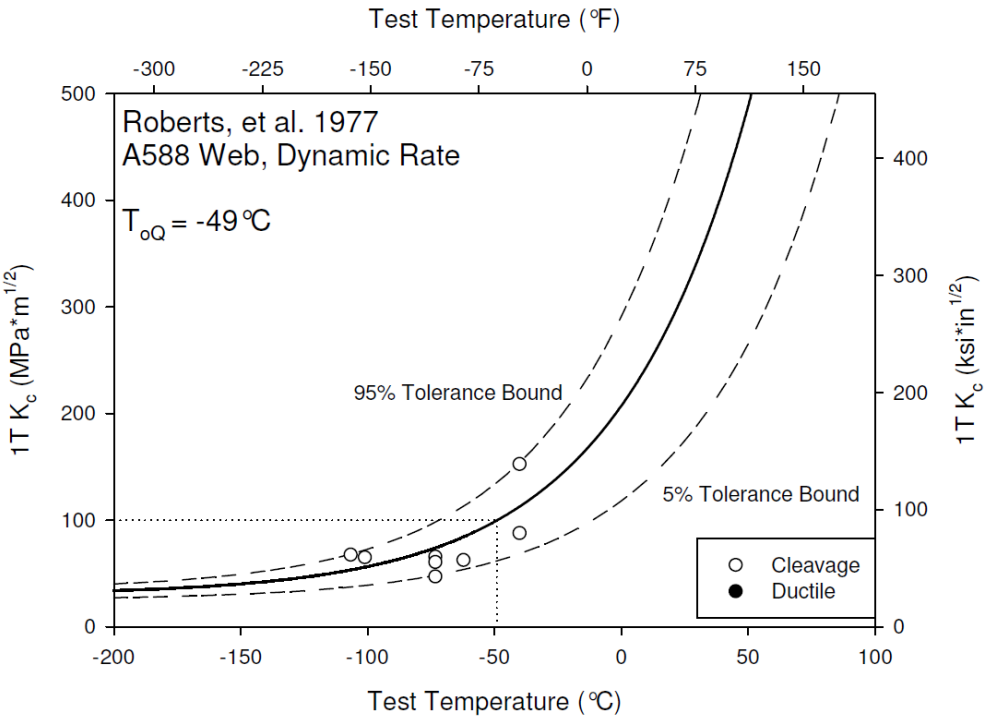

Figure K-66. Master Curve for A588 Web Dynamic, Roberts, et al. 1977

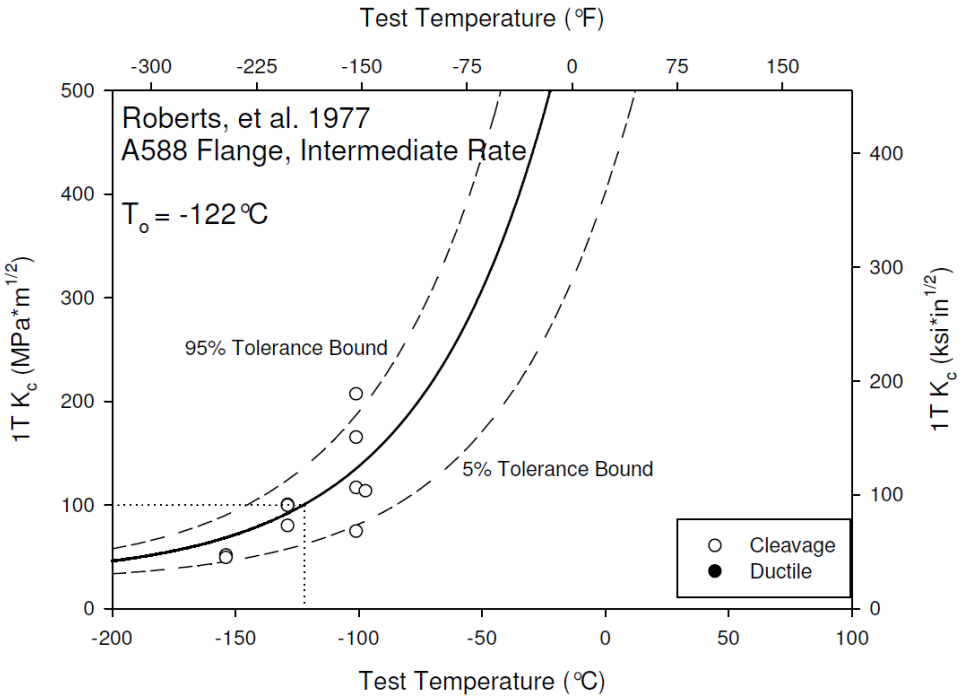

Figure K-67. Master Curve for A588 Flange Intermediate, Roberts, et al. 1977

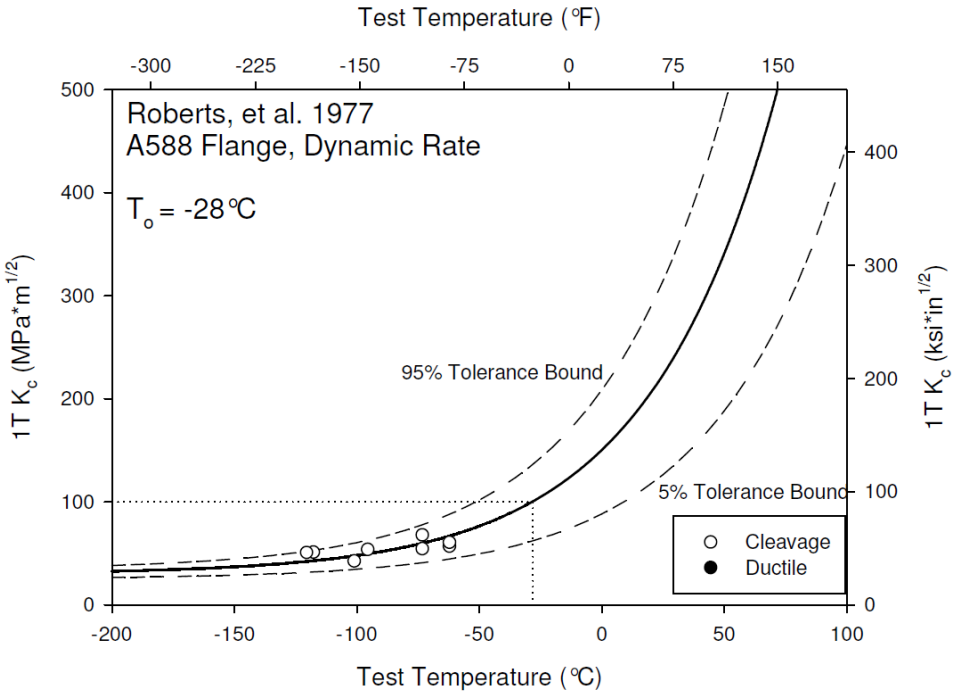

Figure K-68. Master Curve for A588 Flange Dynamic, Roberts, et al. 1977

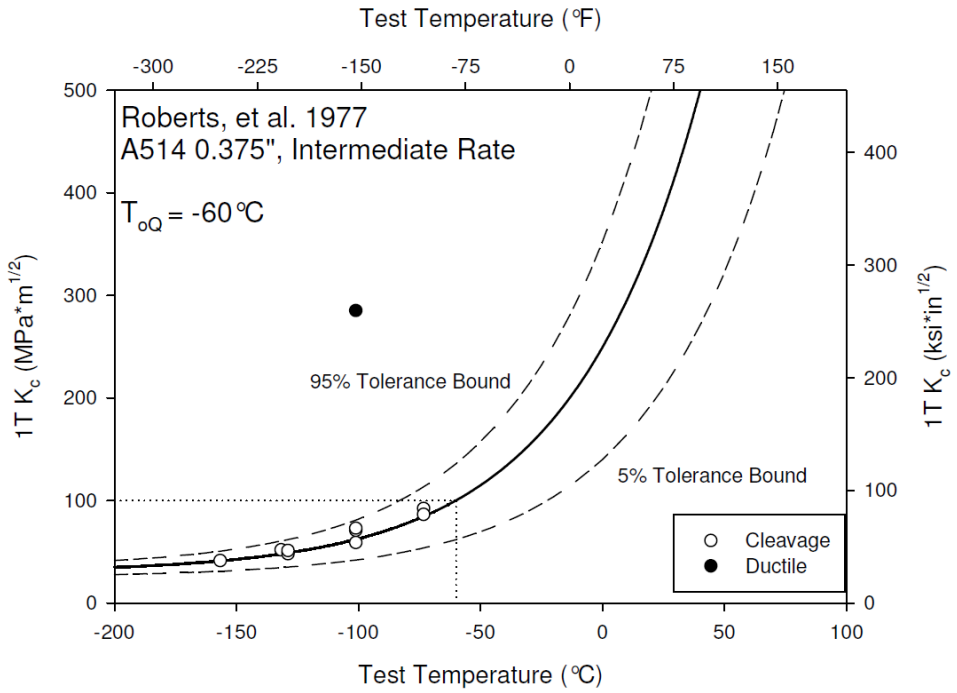

Figure K-69. Master Curve for A514 0.375" Intermediate, Roberts, et al. 1977

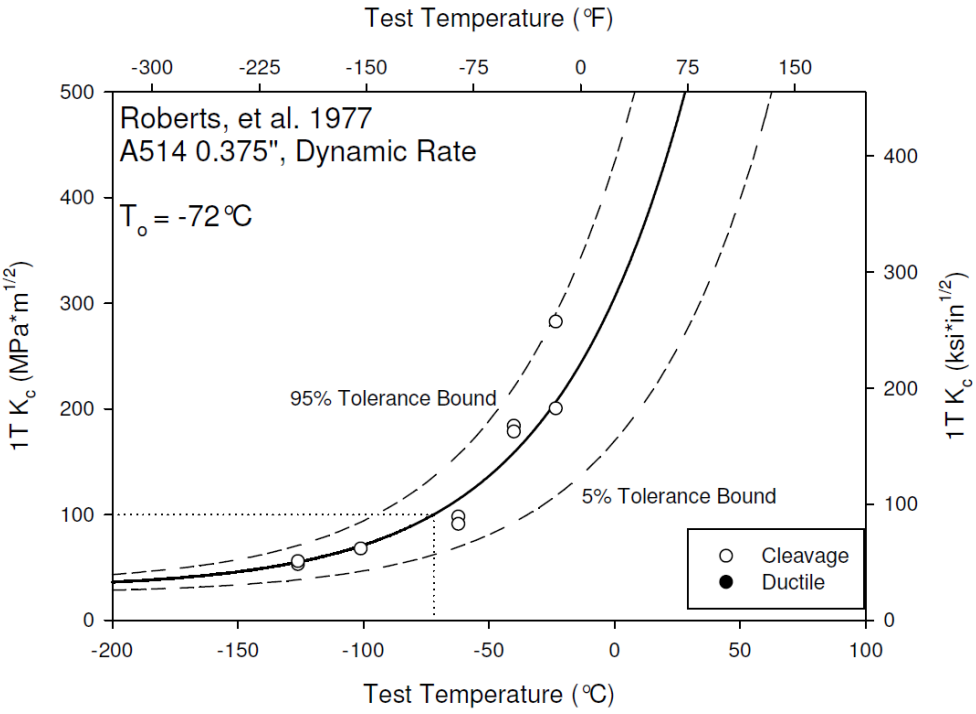

Figure K-70. Master Curve for A514 0.375" Dynamic, Roberts, et al. 1977

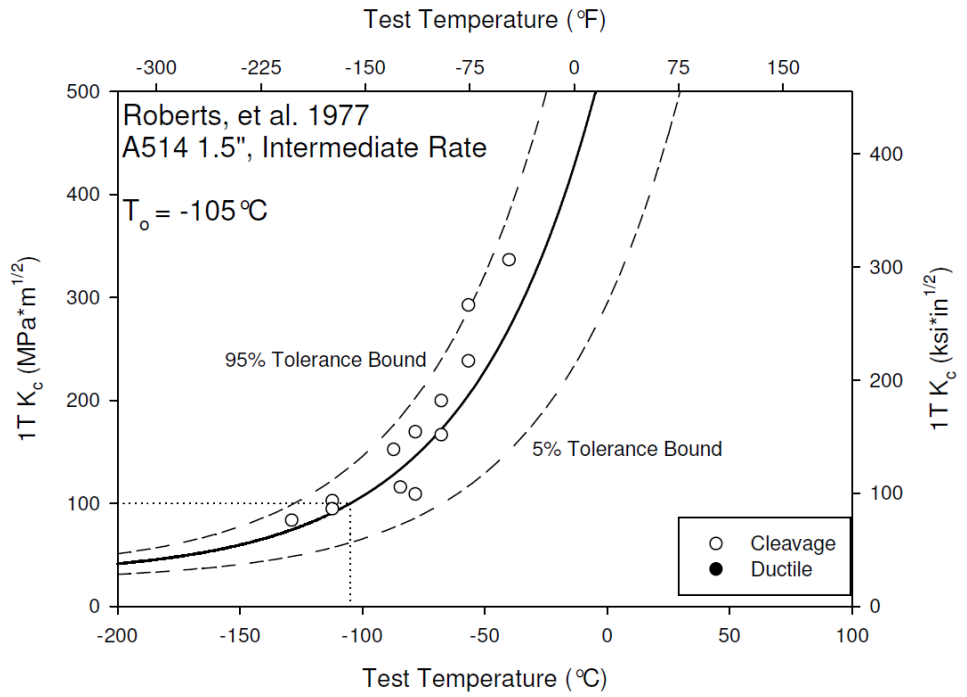

Figure K-71. Master Curve for A514 1.5" Intermediate, Roberts, et al. 1977

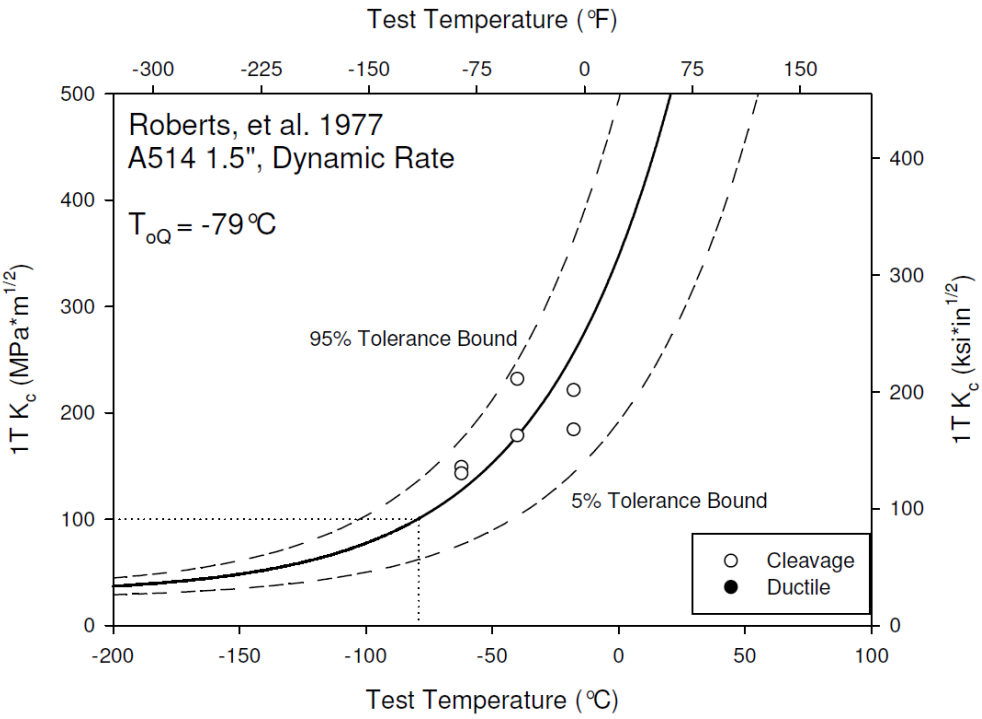

Figure K-72. Master Curve for A514 1.5" Dynamic, Roberts, et al. 1977

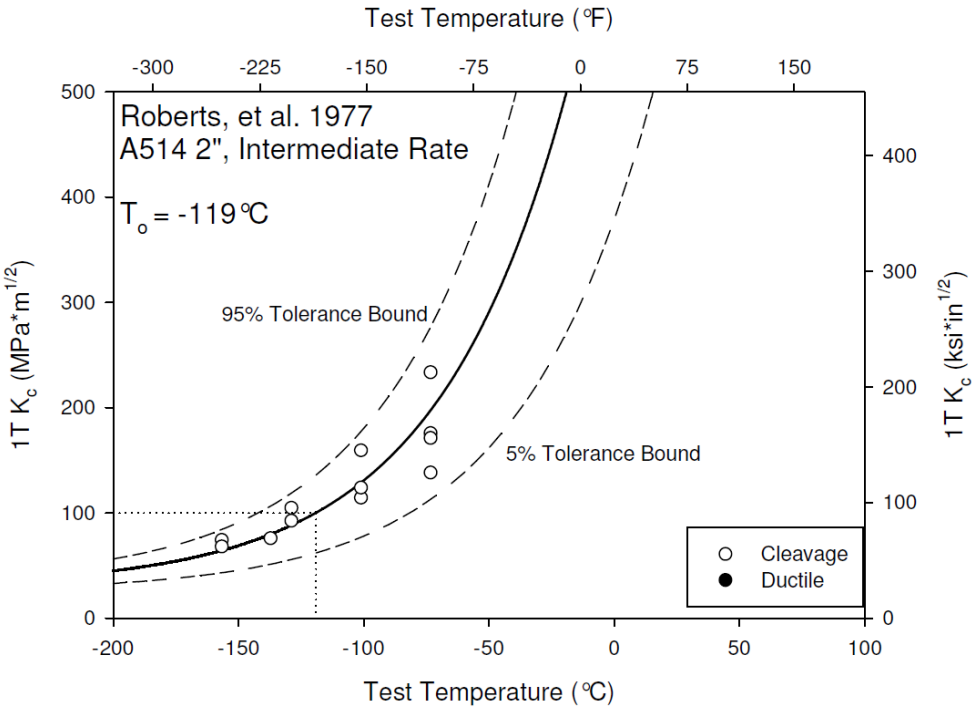

Figure K-73. Master Curve for A514 2.0" Intermediate, Roberts, et al. 1977

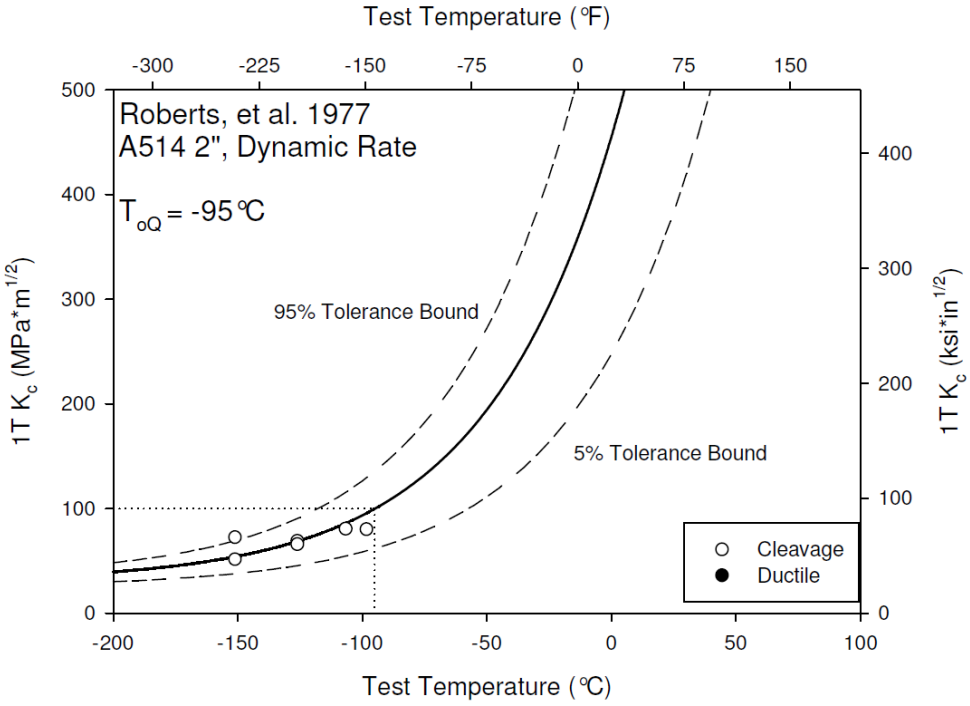

Figure K-74. Master Curve for A514 2.0" Dynamic, Roberts, et al. 1977

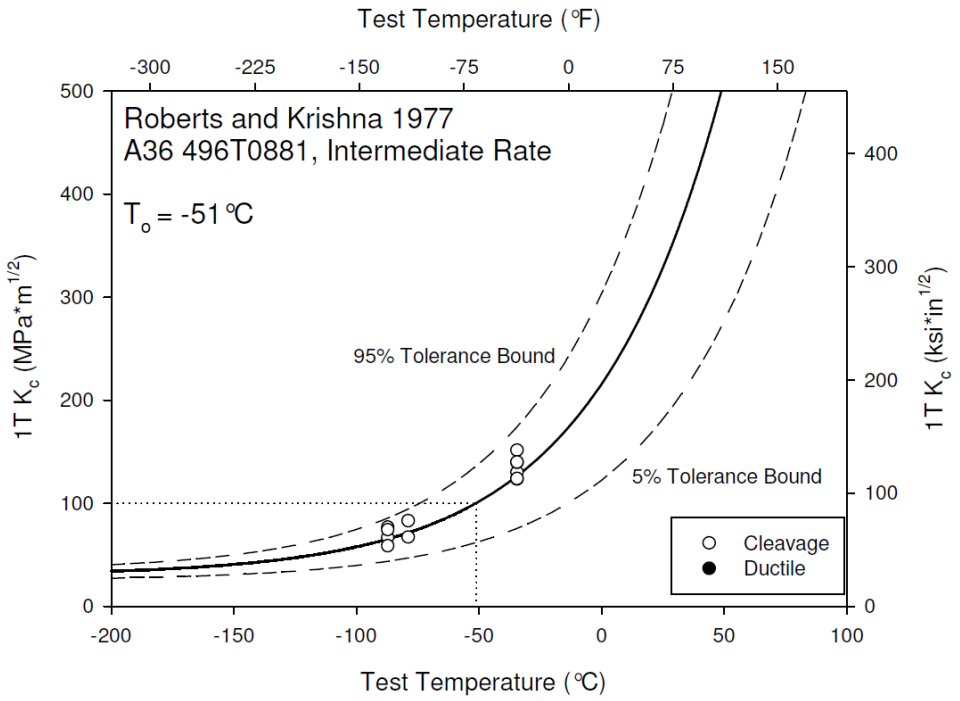

Figure K-75. Master Curve for A36 496T0881 Intermediate, Roberts and Krishna 1977

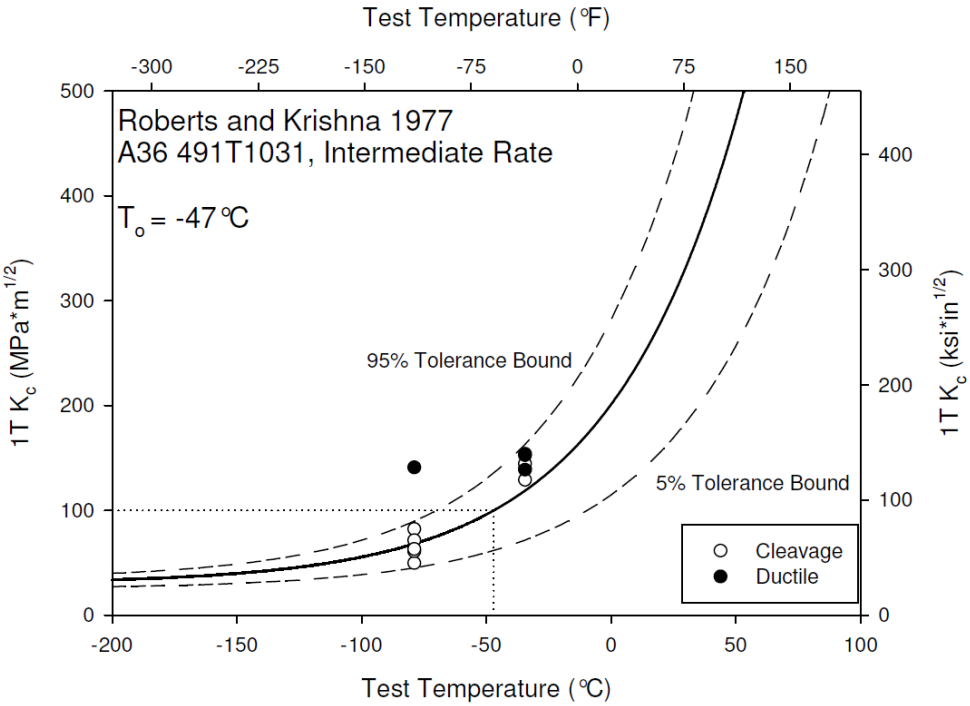

Figure K-76. Master Curve for A36 491T1031 Intermediate, Roberts and Krishna 1977

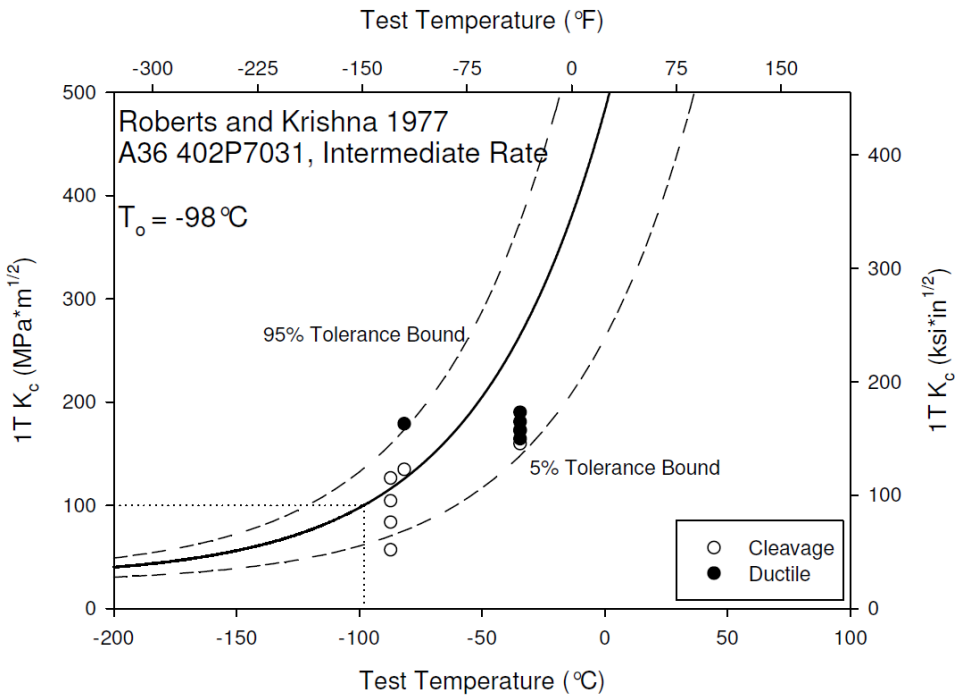

Figure K-77. Master Curve for A36 402P7031 Intermediate, Roberts and Krishna 1977

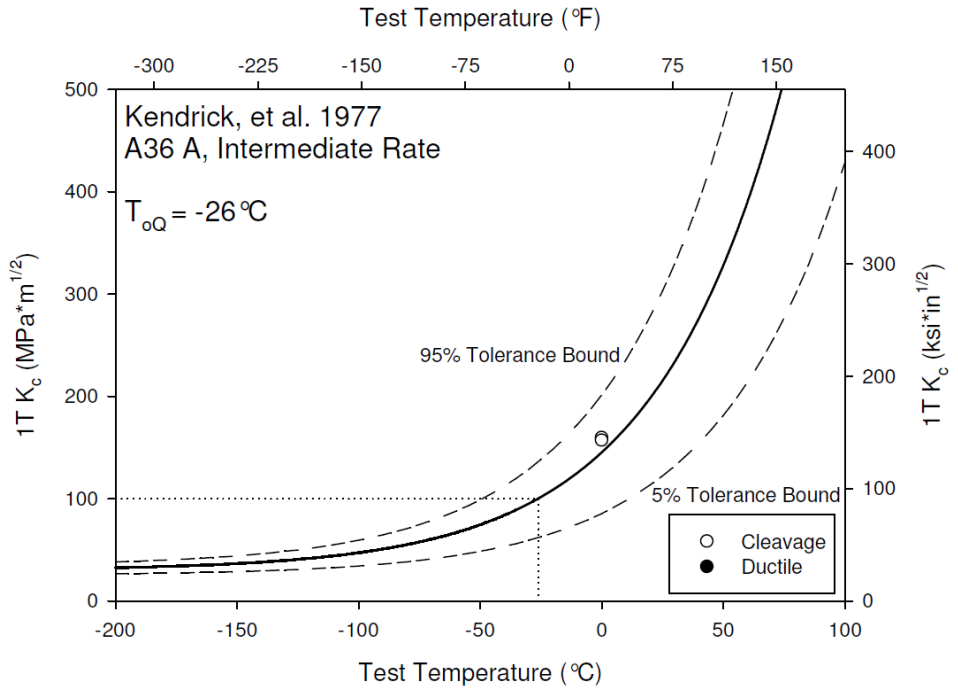

Figure K-78. Master Curve for A36 Plate A Intermediate, Kendrick, et al. 1977

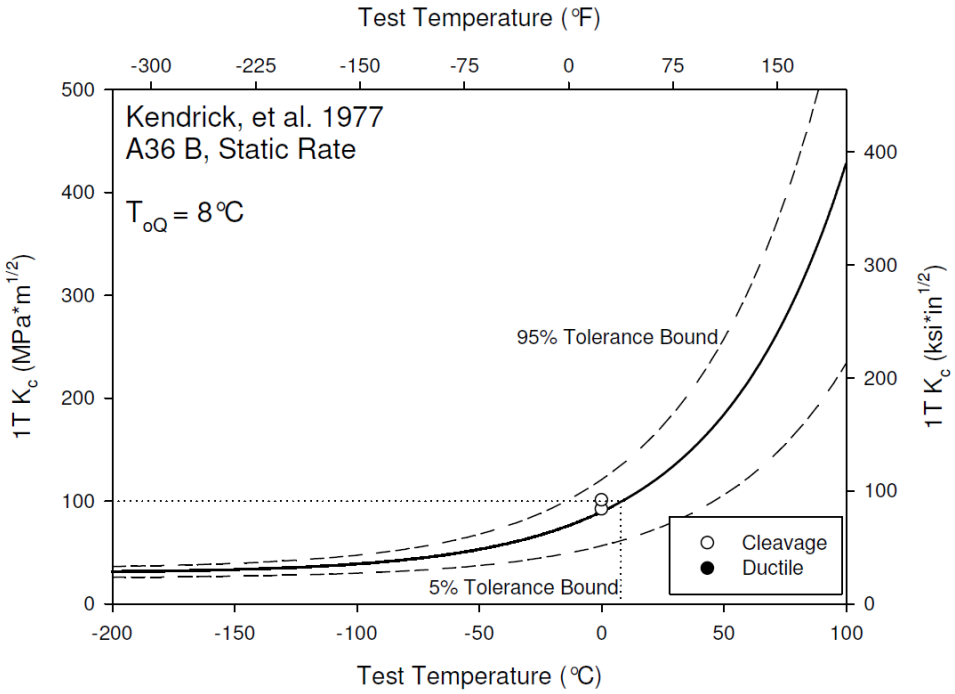

Figure K-79. Master Curve for A36 Plate B Static, Kendrick, et al. 1977

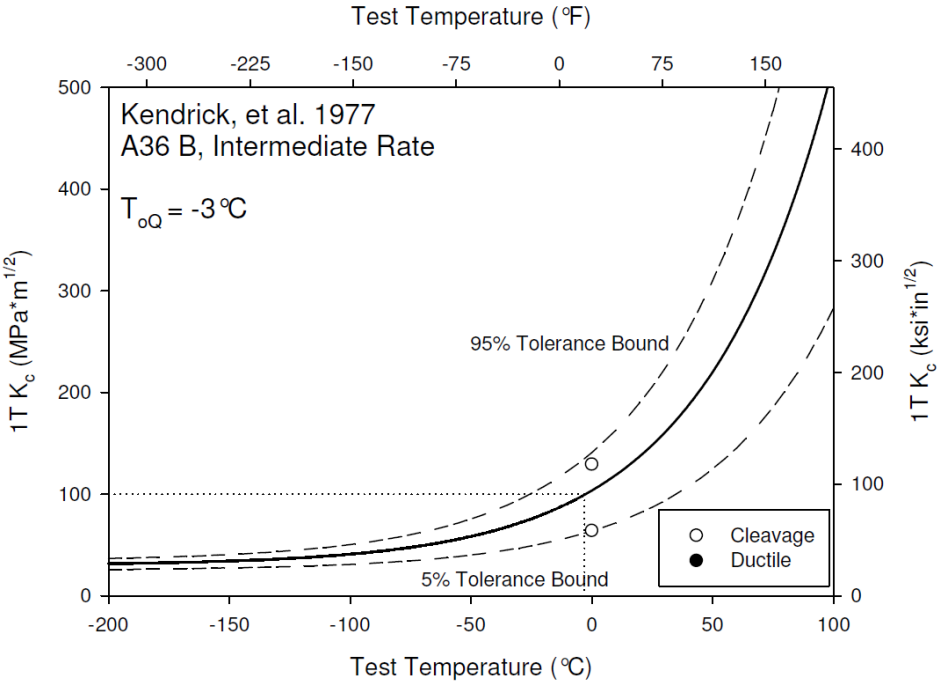

Figure K-80. Master Curve for A36 Plate B Intermediate, Kendrick, et al. 1977

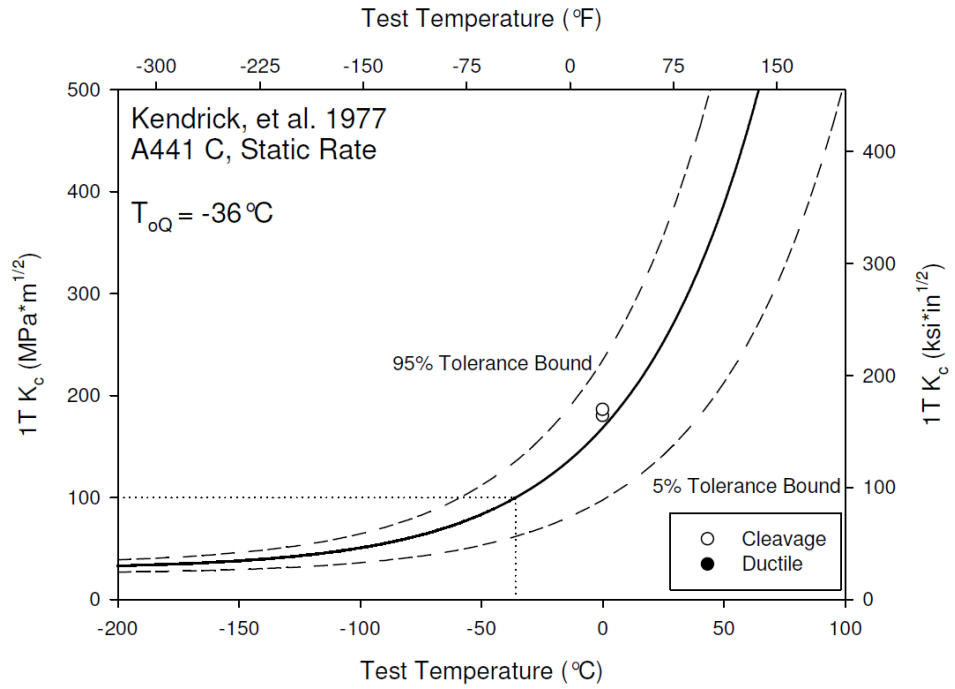

Figure K-81. Master Curve for A441 Plate C Static, Kendrick, et al. 1977

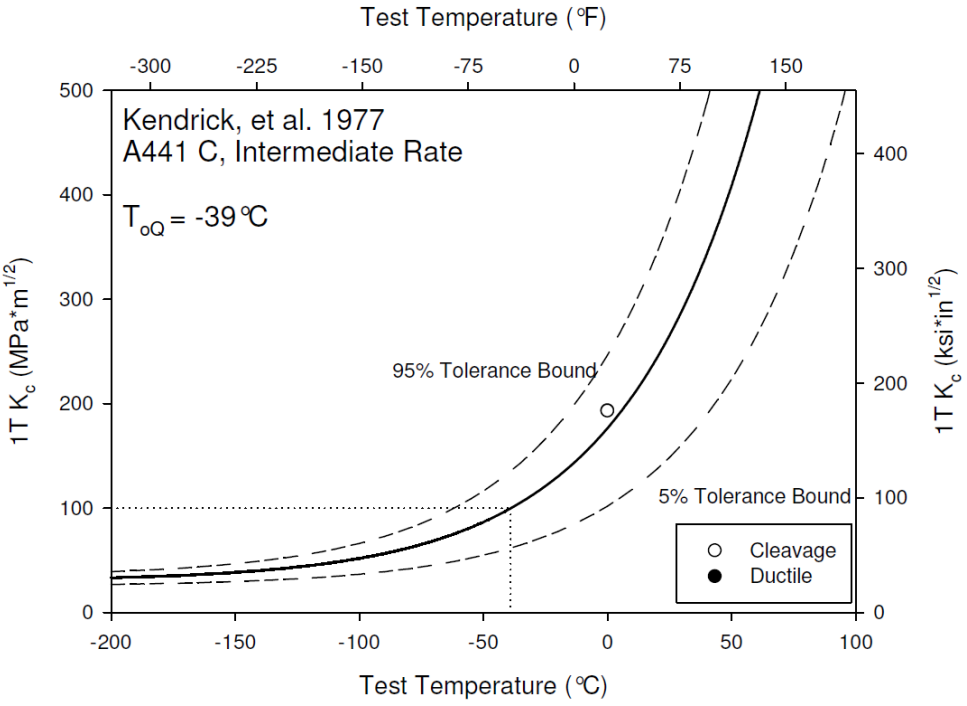

Figure K-82. Master Curve for A441 Plate C Intermediate, Kendrick, et al. 1977

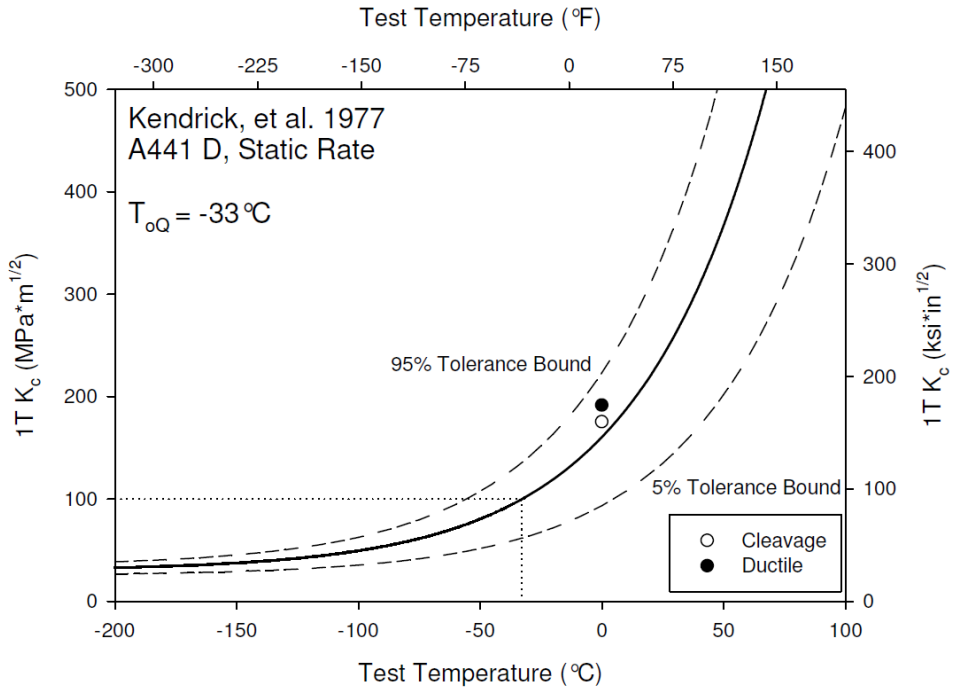

Figure K-83. Master Curve for A441 Plate D Static, Kendrick, et al. 1977

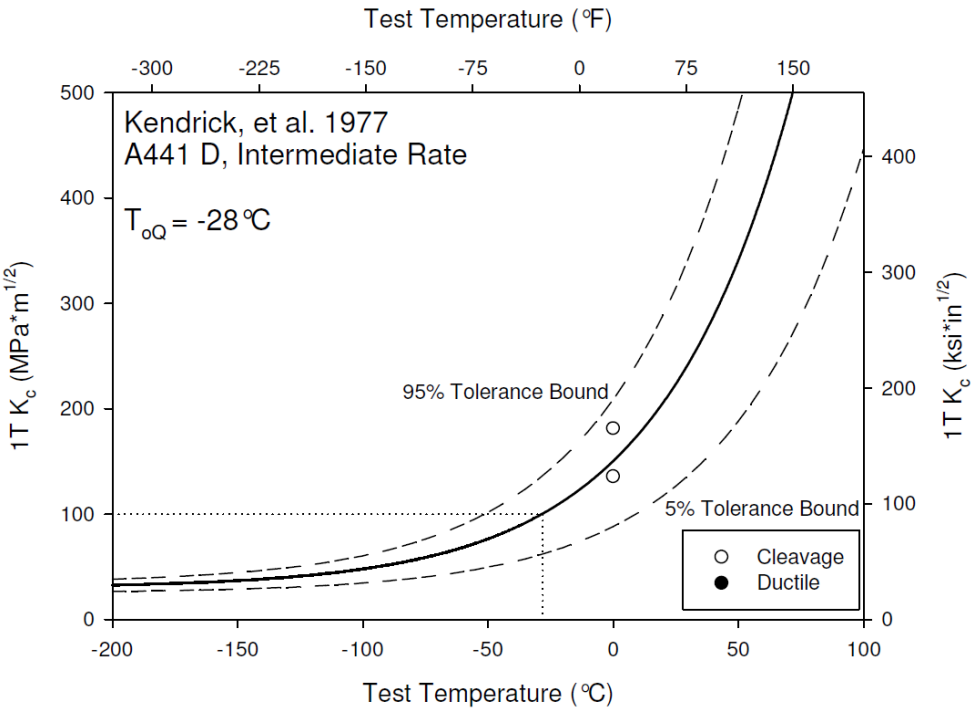

Figure K-84. Master Curve for A441 Plate D Intermediate, Kendrick, et al. 1977

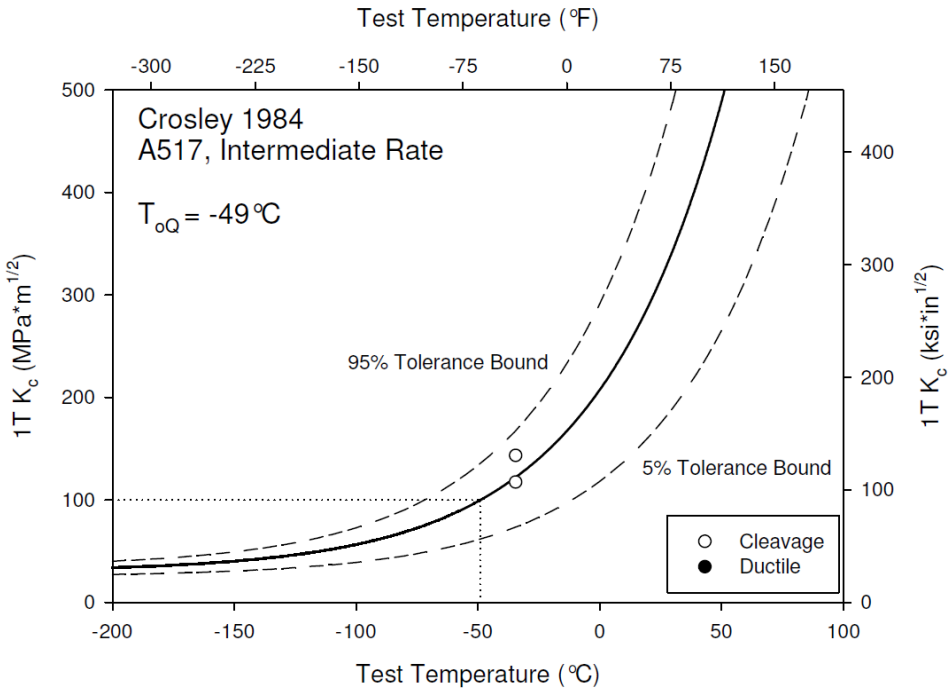

Figure K-85. Master Curve for A517 Intermediate, Crosley 1984

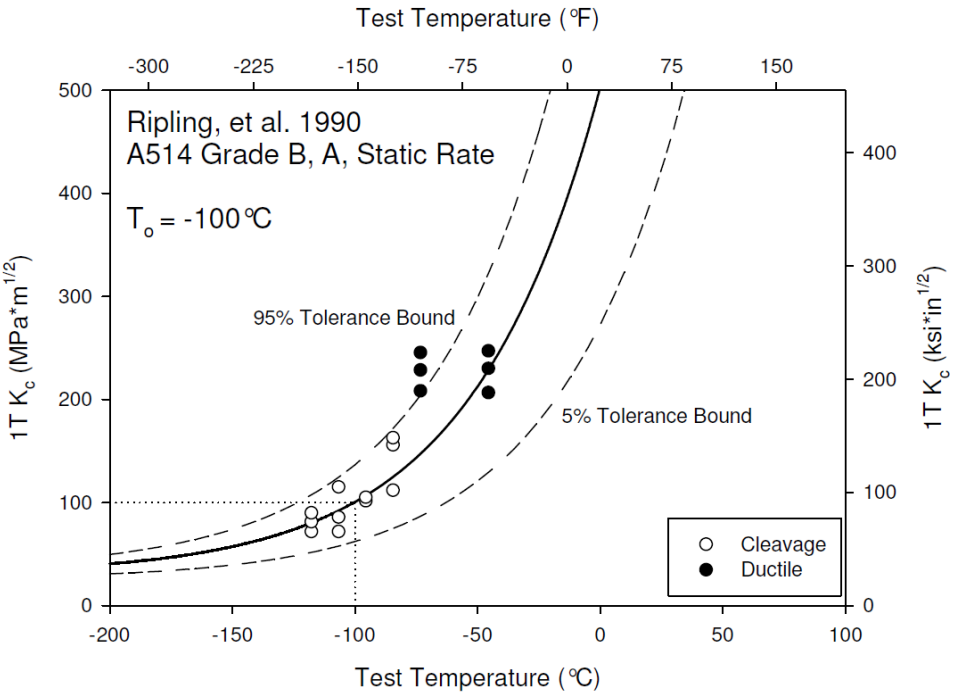

Figure K-86. Master Curve for A514B Plate A, Ripling, et al. 1990

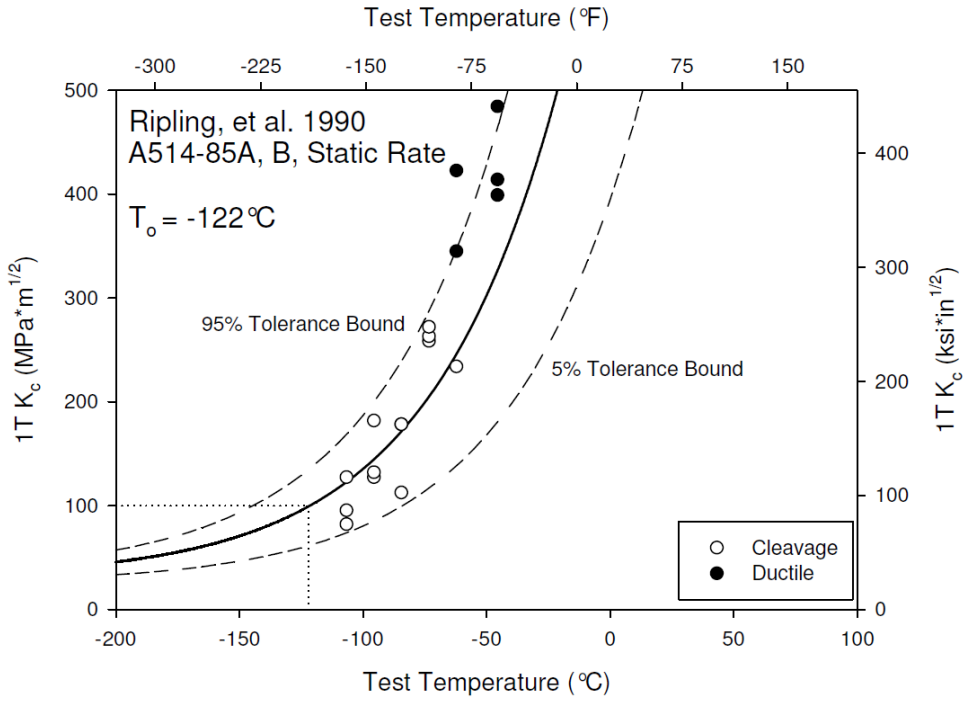

Figure K-87. Master Curve for A514-85A Plate B Static, Ripling, et al. 1990

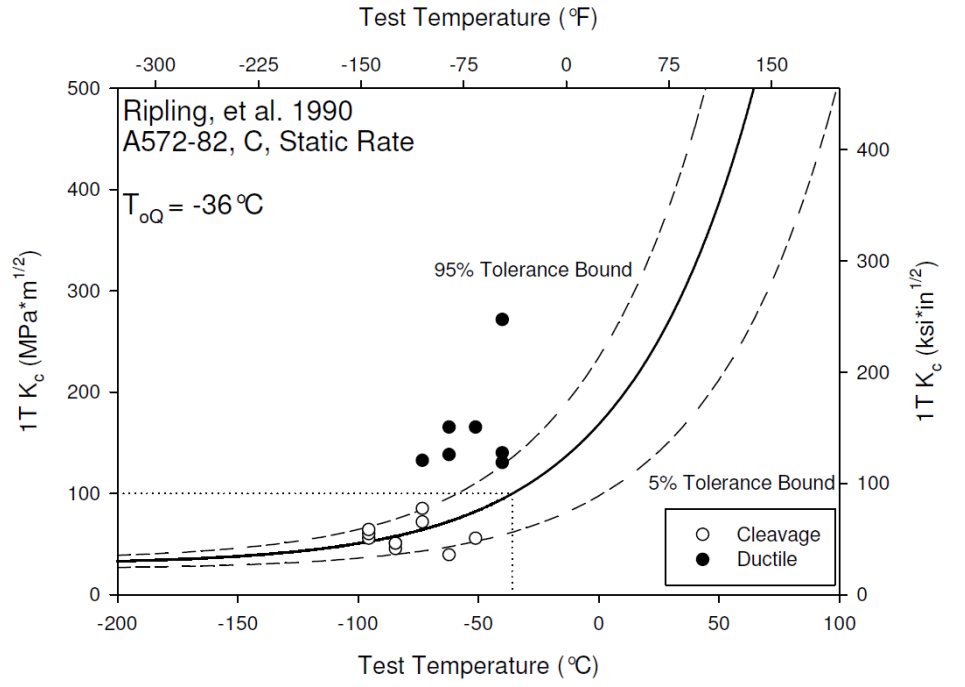

Figure K-88. Master Curve for A572-82 Plate C Static, Ripling, et al. 1990

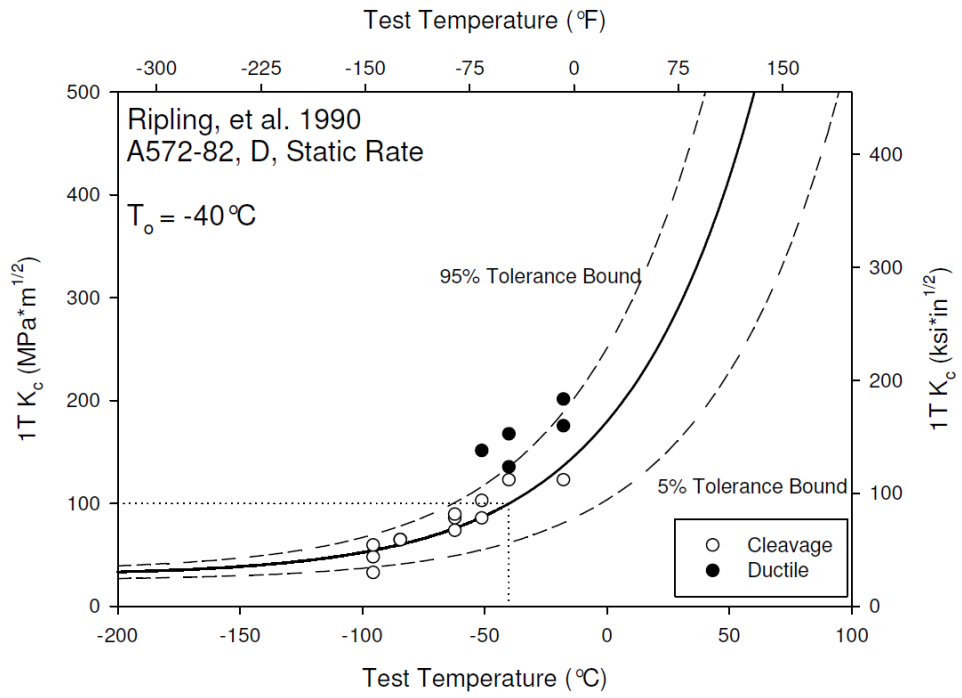

Figure K-89. Master Curve for A572-82 Plate D Static, Ripling, et al. 1990

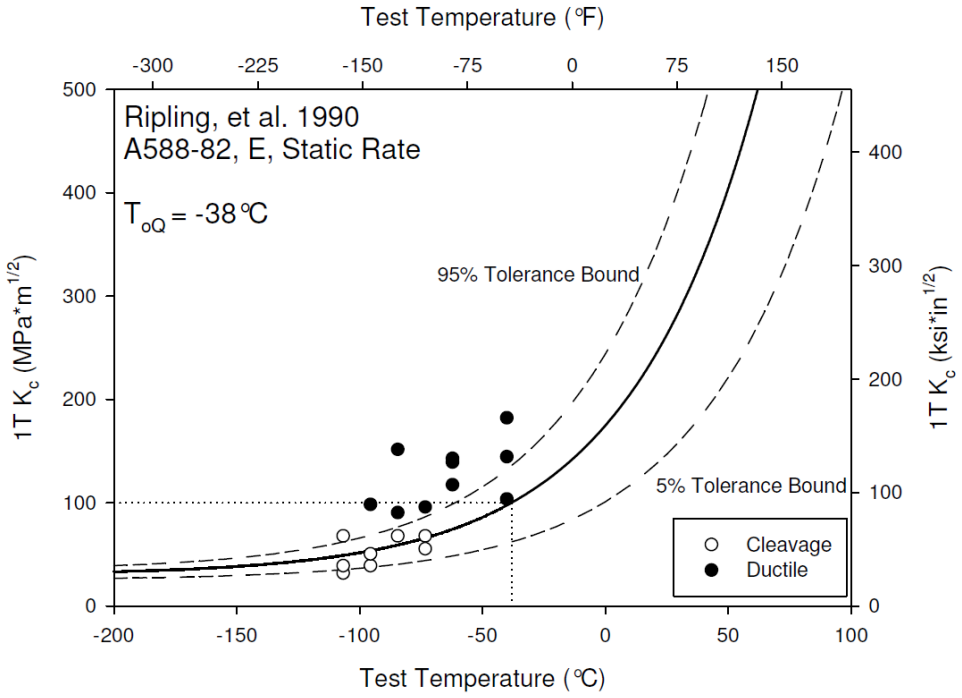

Figure K-90. Master Curve for A588-82 Plate E Static, Ripling, et al. 1990

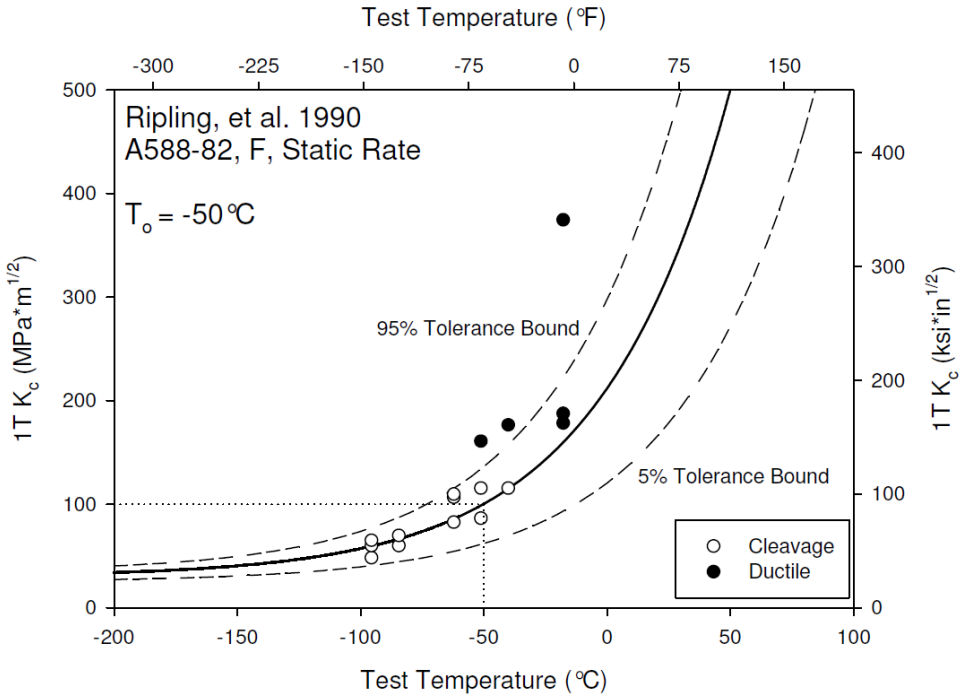

Figure K-91. Master Curve for A588-82 Plate F Static, Ripling, et al. 1990

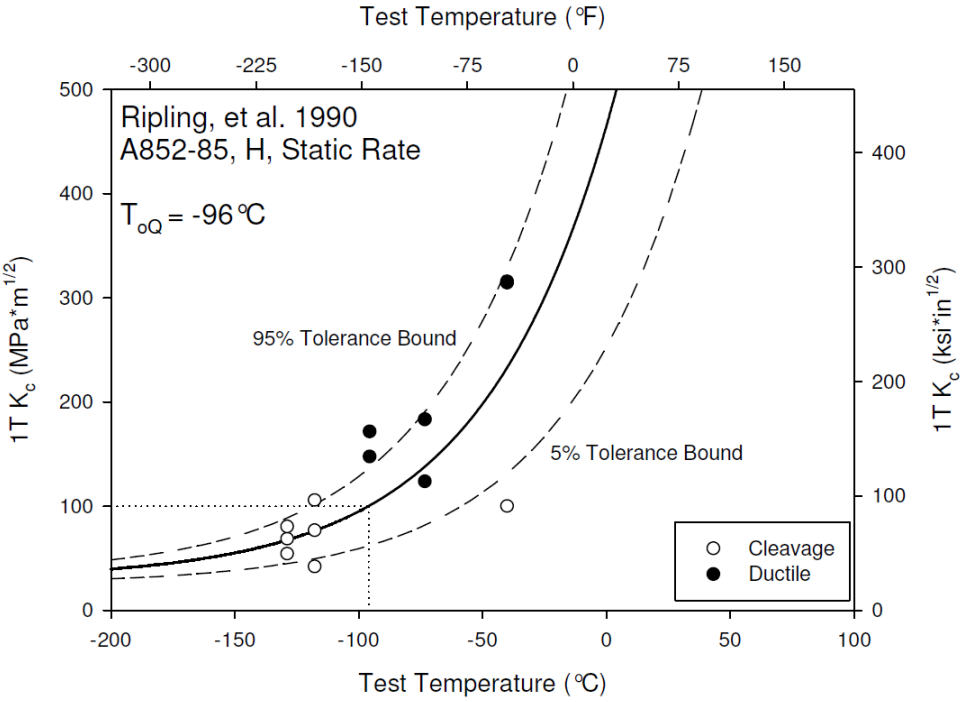

Figure K-92. Master Curve for A852-85 Plate H Static, Ripling, et al. 1990

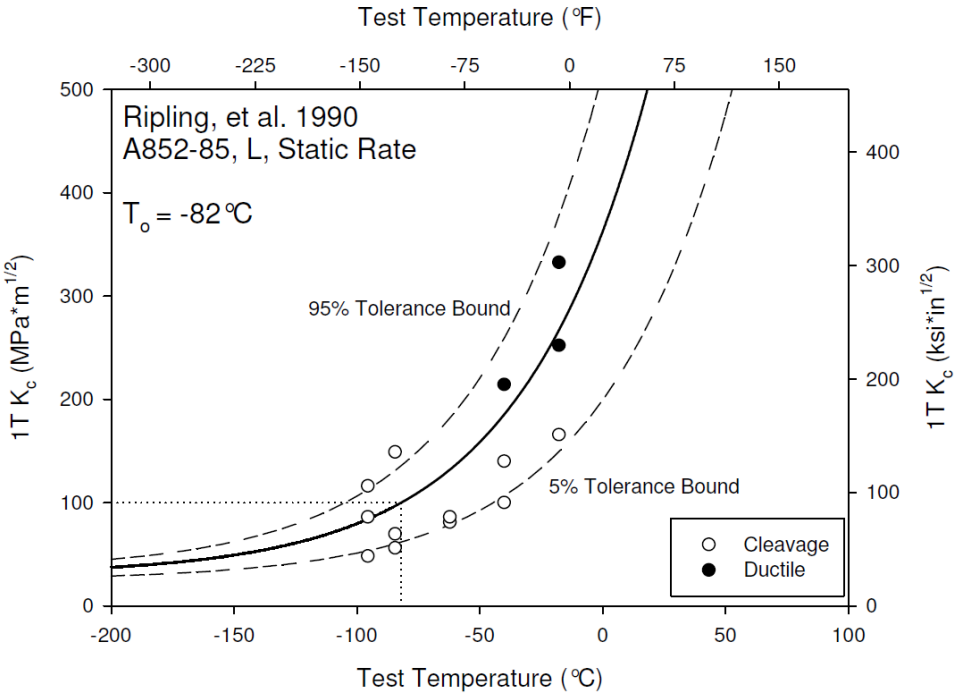

Figure K-93. Master Curve for A852-85 Plate L Static, Ripling, et al. 1990

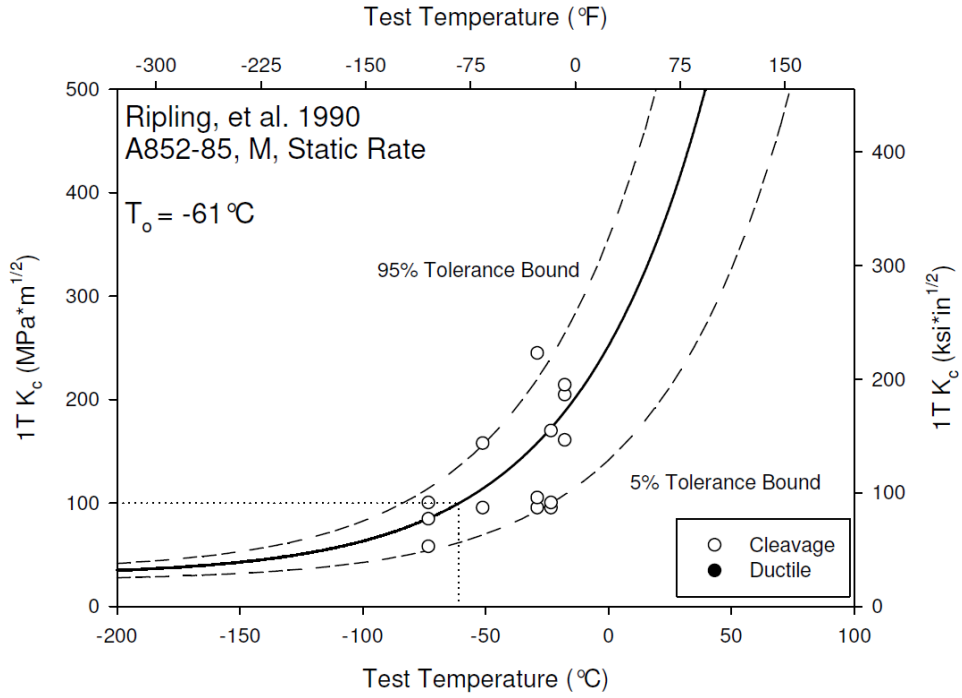

Figure K-94. Master Curve for A852-85 Plate M Static, Ripling, et al. 1990

APPENDIX L: Legacy Data Correlation Plots

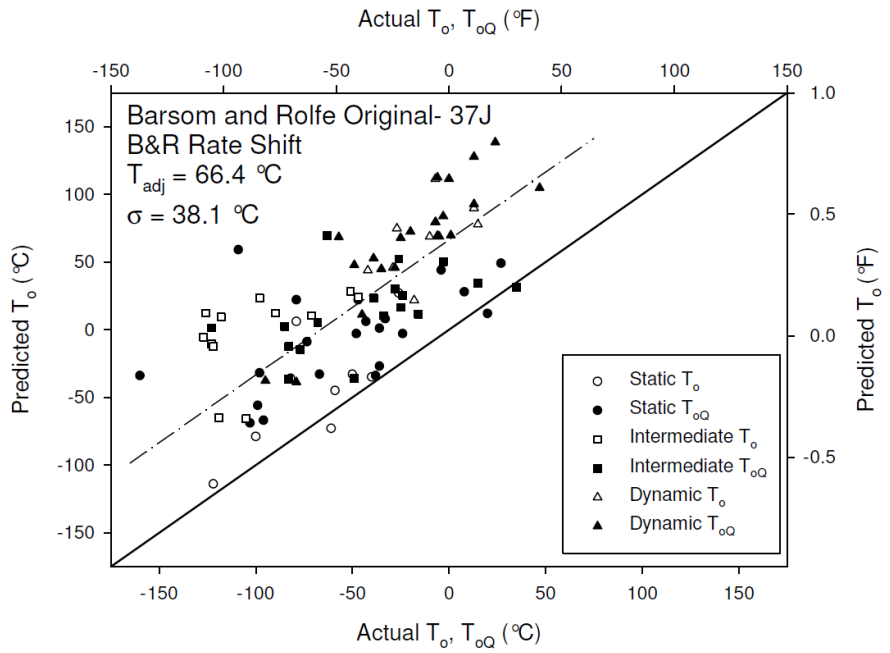

Figure L-1. Barsom and Rolfe Original Evaluated at 37J with B&R Shift

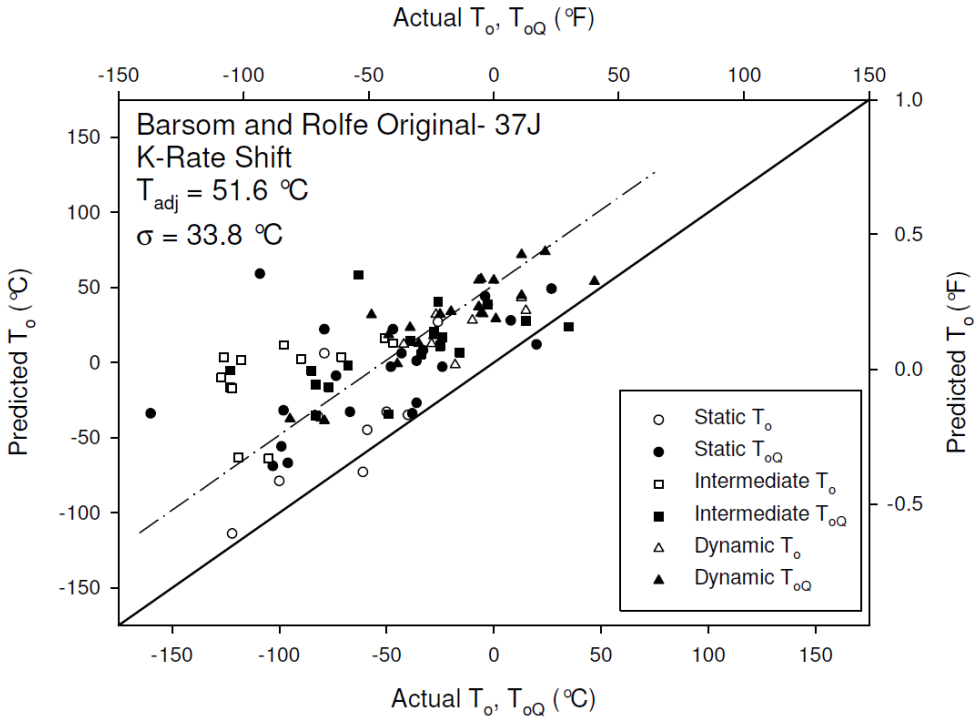

Figure L-2. Barsom and Rolfe Original Evaluated at 37J with K-Rate Shift

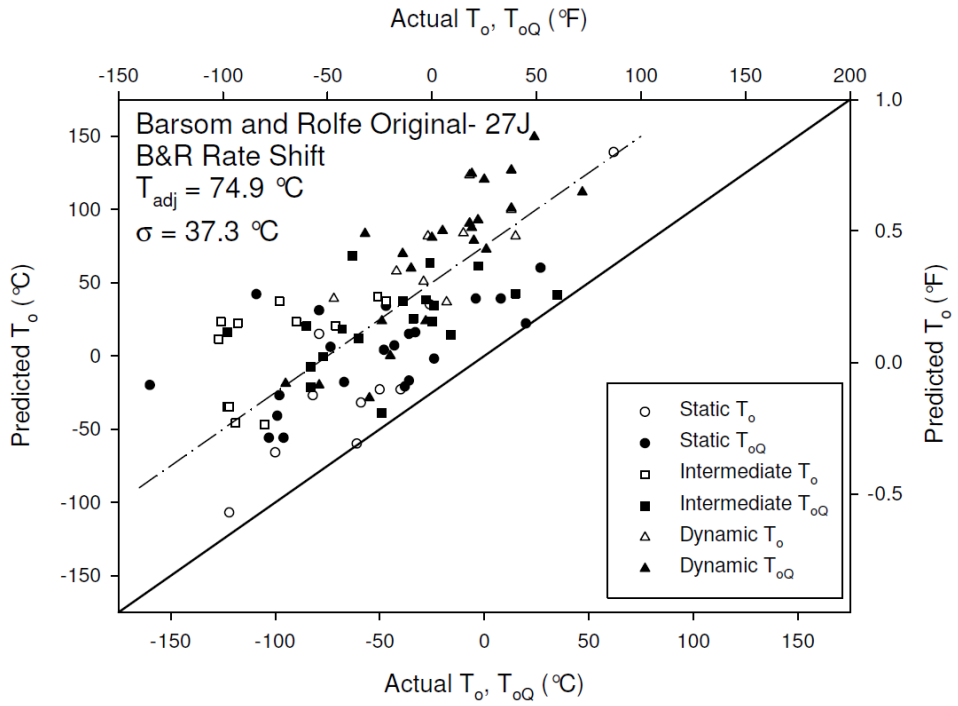

Figure L-3. Barsom and Rolfe Original Evaluated at 27J with B&R Shift

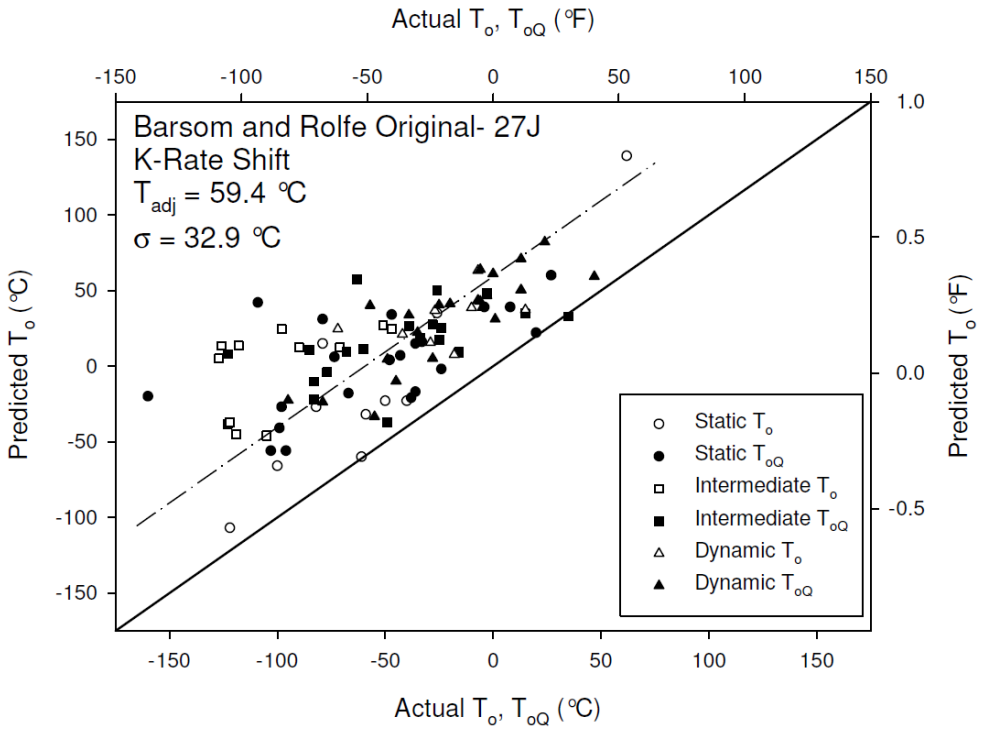

Figure L-4. Barsom and Rolfe Original Evaluated at 27J with K-Rate Shift

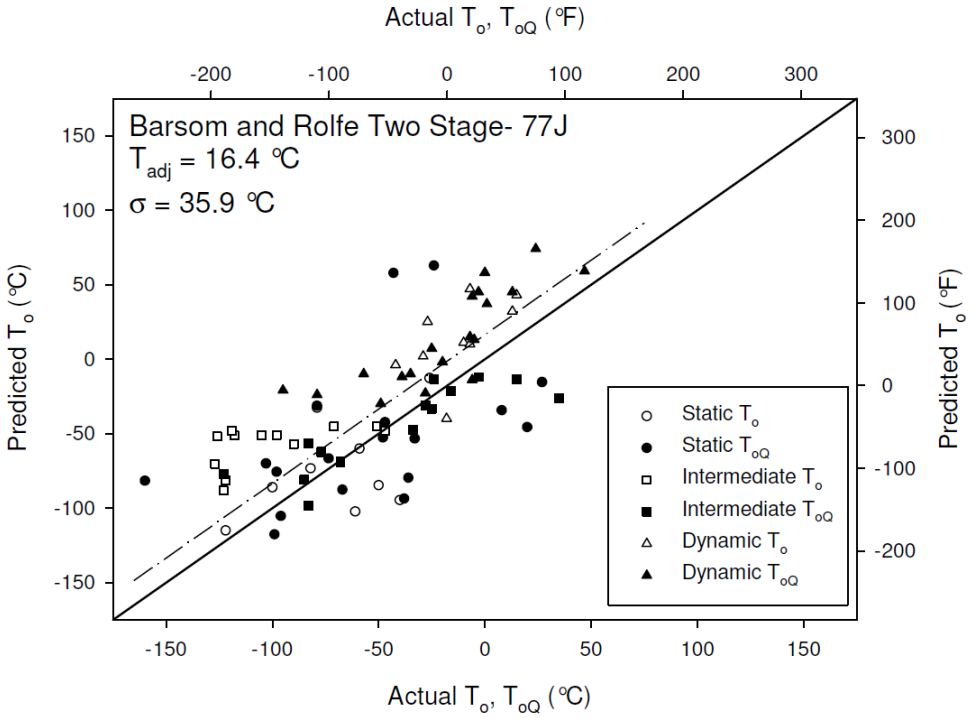

Figure L-5. Barsom and Rolfe Two Stage Evaluated at 77J

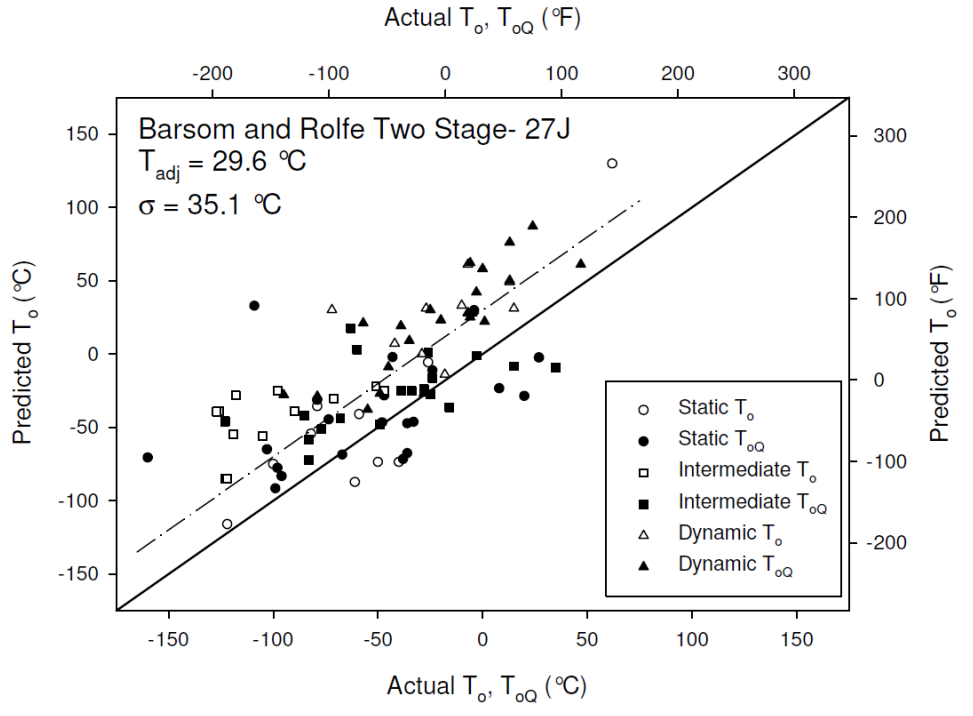

Figure L-6. Barsom and Rolfe Two Stage Evaluated at 27J

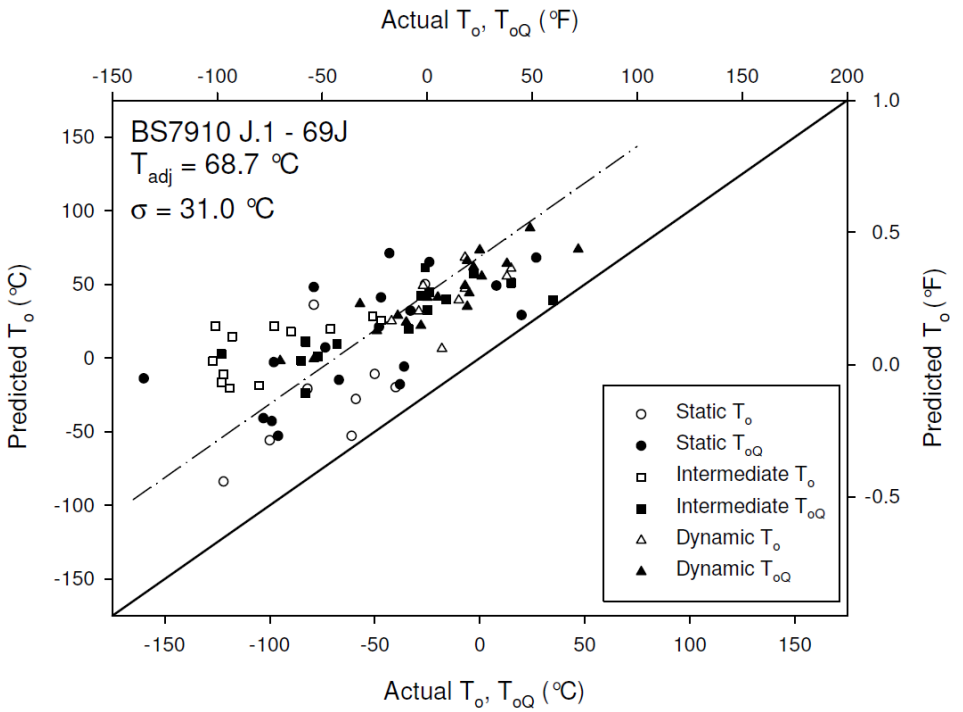

Figure L-7. BS 7910 J.1

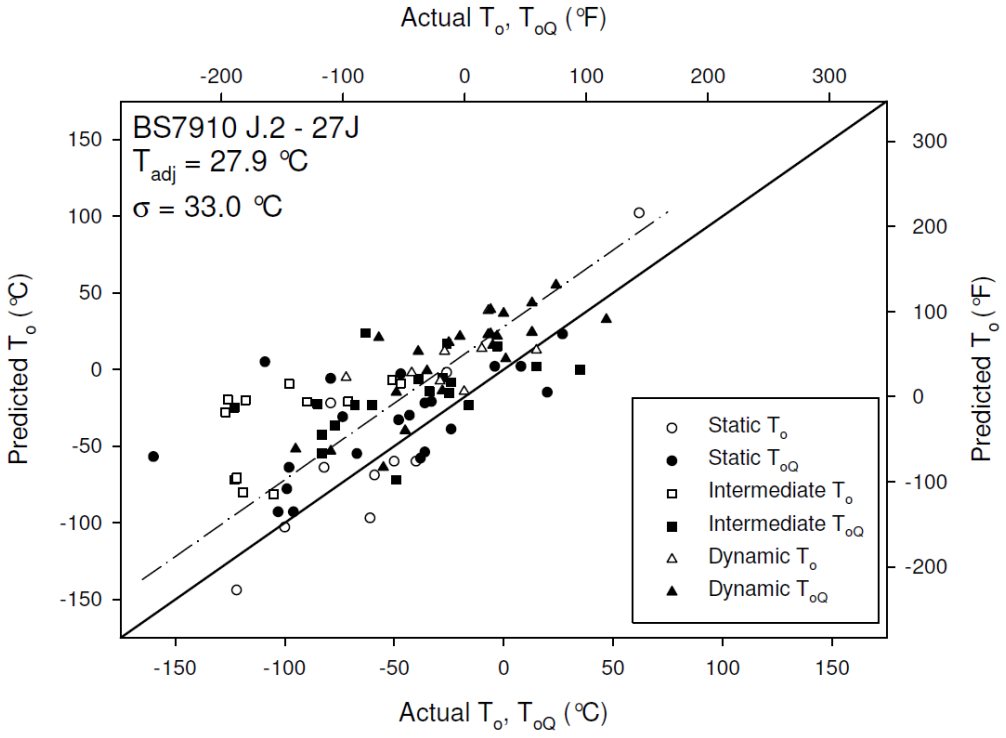

Figure L-8. BS 7910 J.2

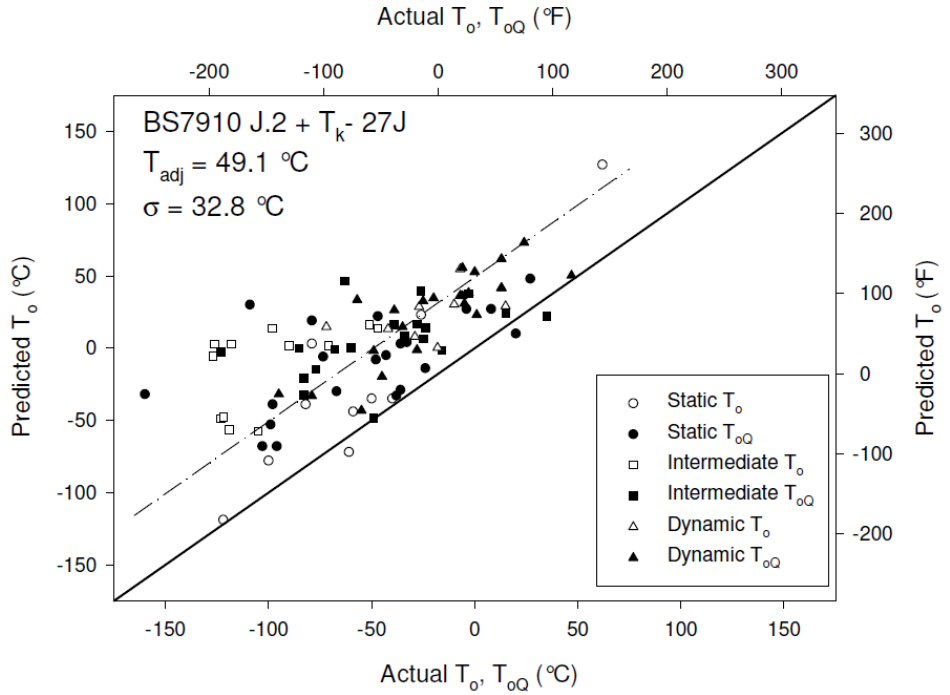

Figure L-9. BS 7910 J.2 +T_k

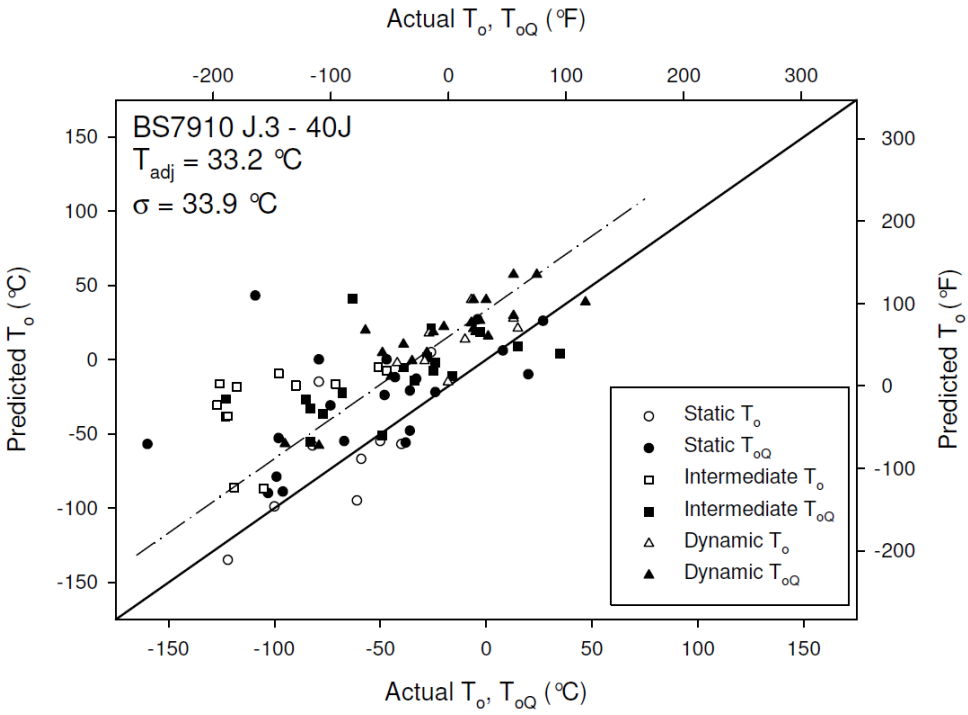

Figure L-10. BS 7910 J.3

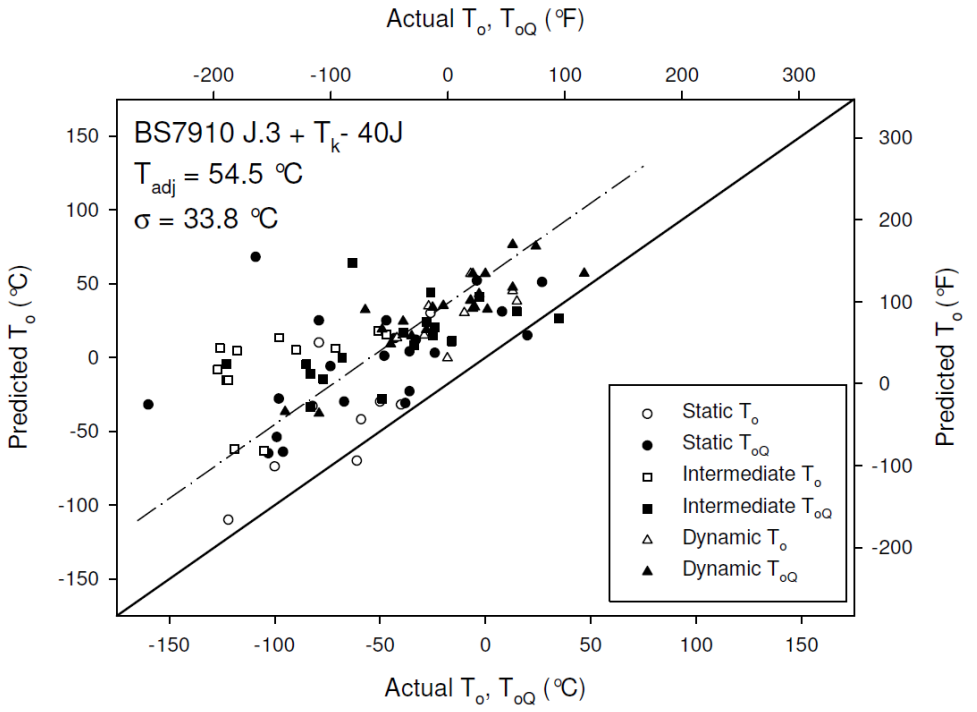

Figure L-11. BS 7910 J.3 + T_k

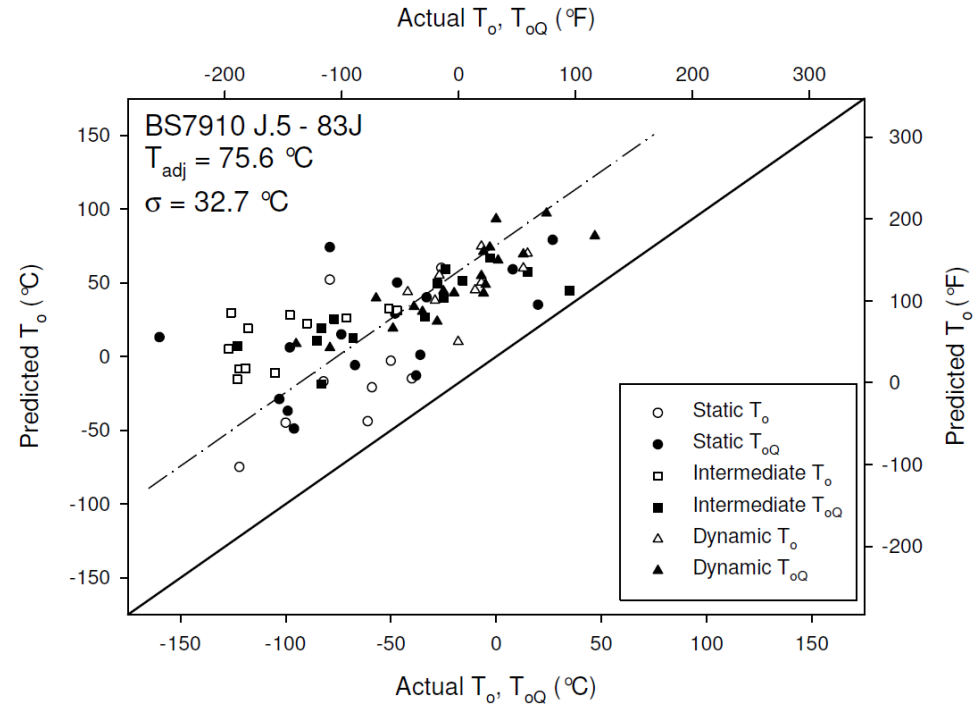

Figure L-12. BS 7910 J.5

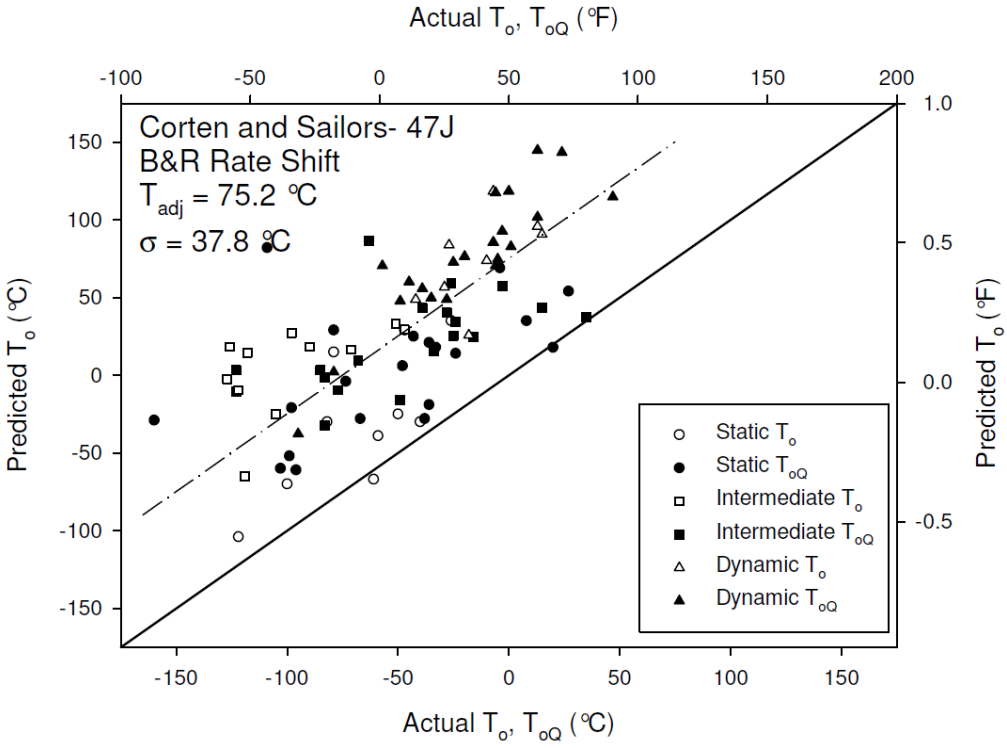

Figure L-13. Corten and Sailors Evaluated at 47J with B&R Shift

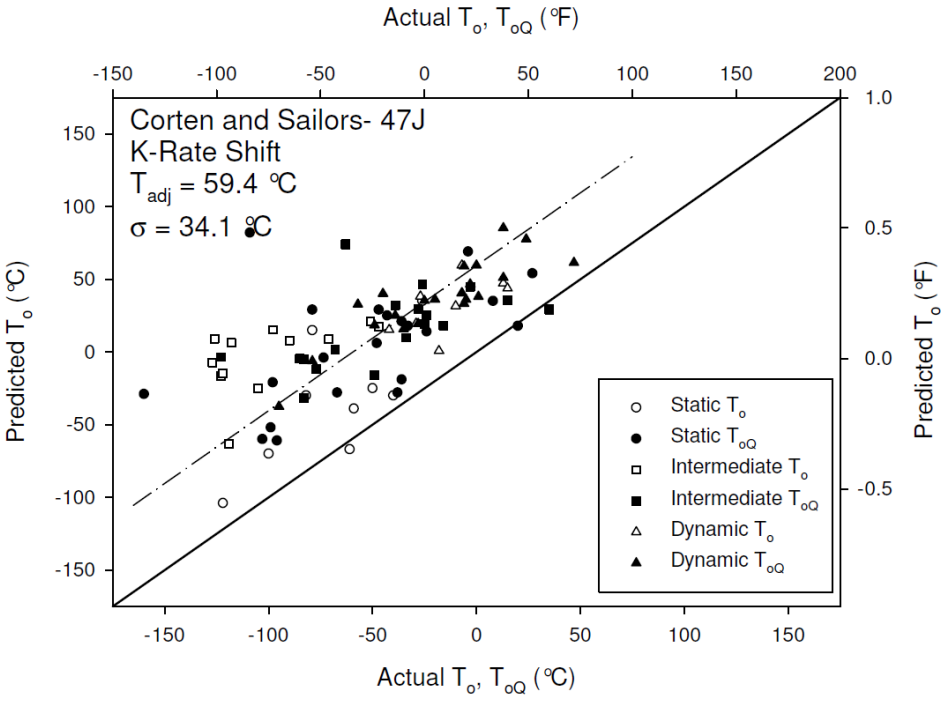

Figure L-14. Corten and Sailors Evaluated at 47J with K-Rate Shift

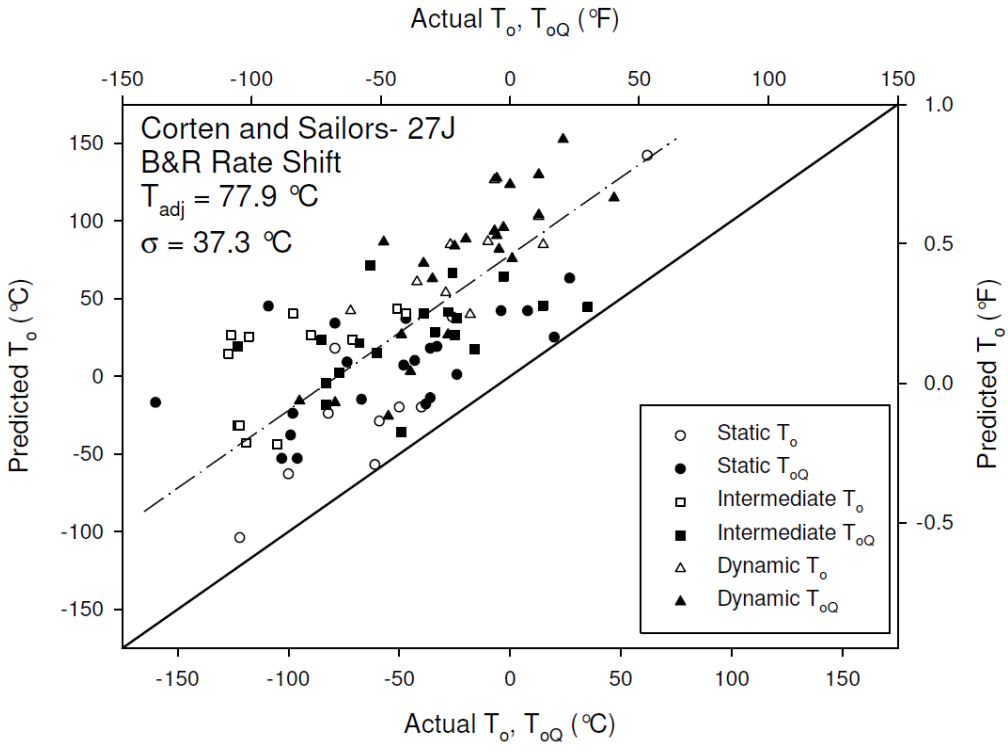

Figure L-15. Corten and Sailors Evaluated at 27J with B&R Shift

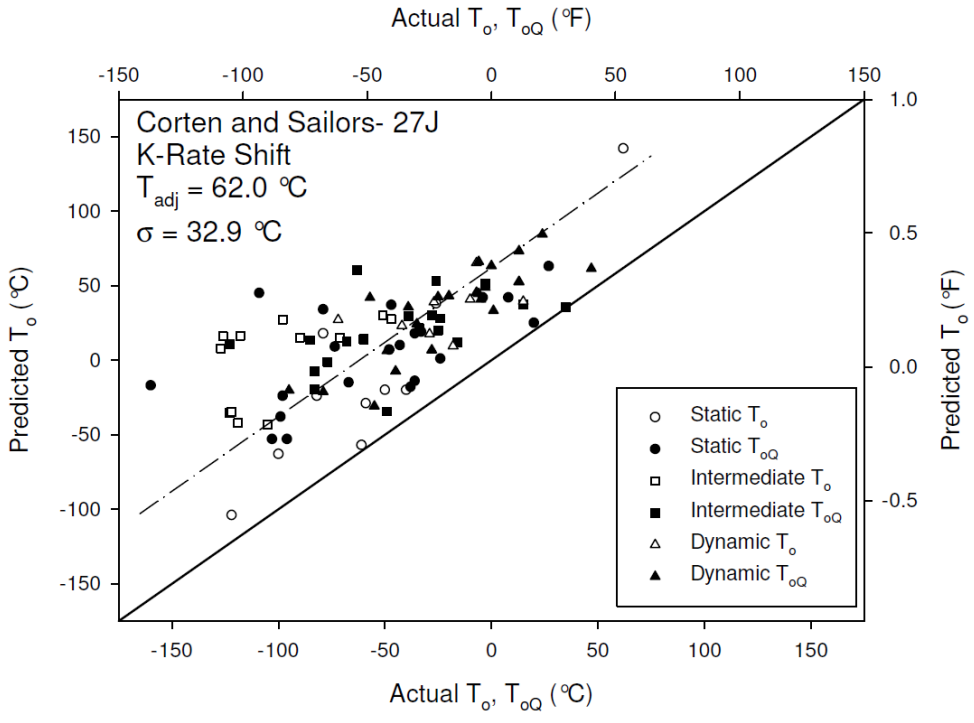

Figure L-16. Corten and Sailors Evaluated at 27J with K-Rate Shift

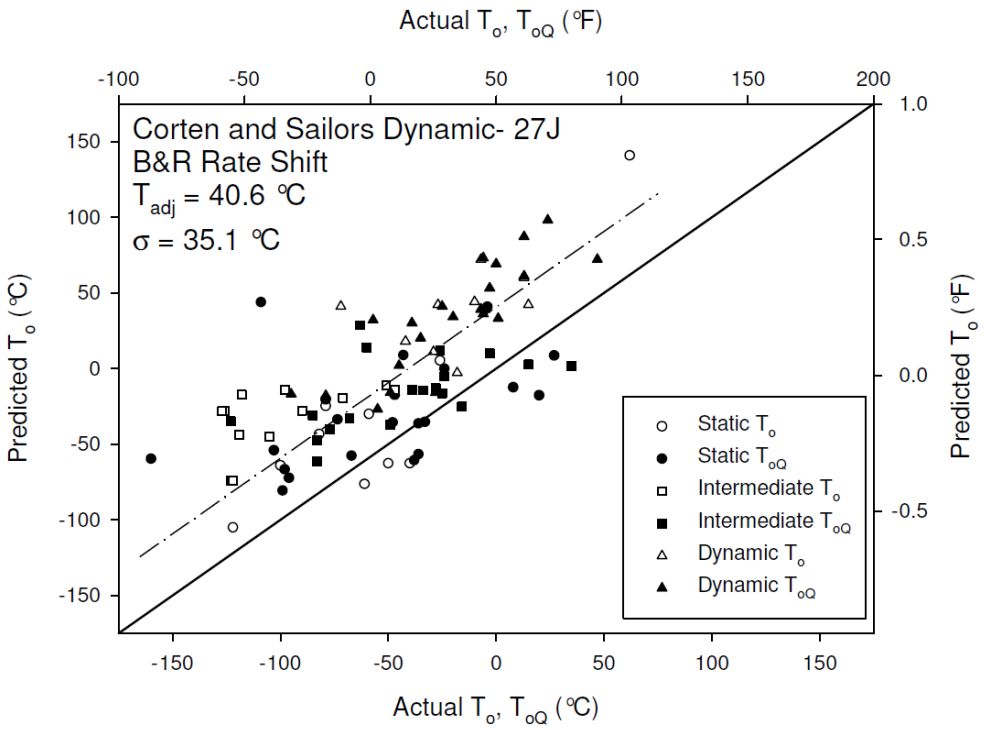

Figure L-17. Corten and Sailors Dynamic with B&R Shift

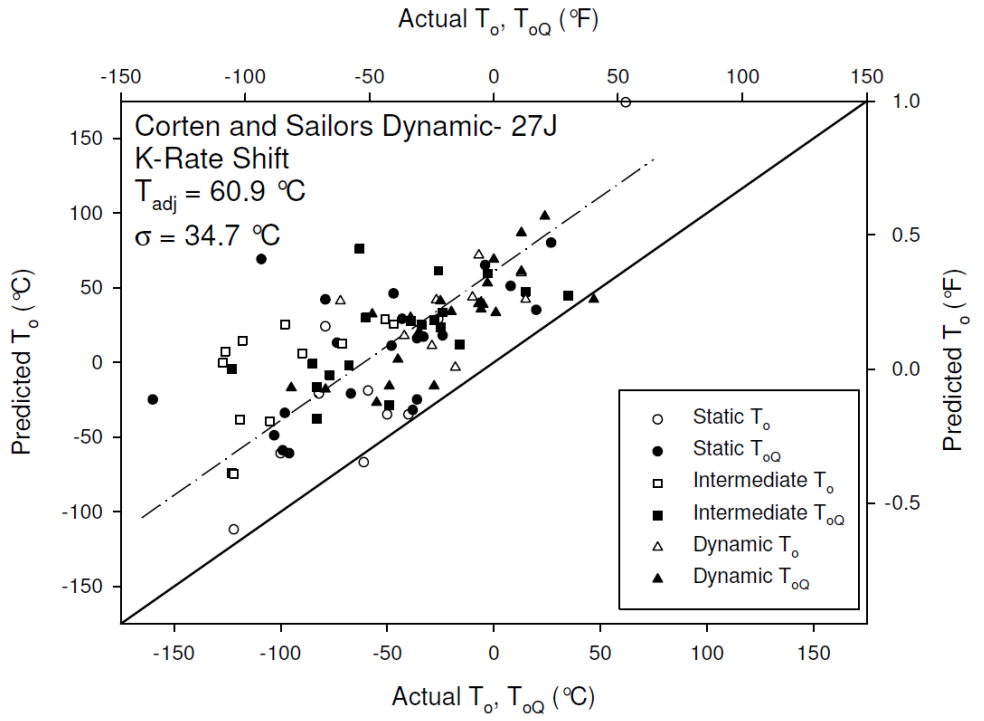

Figure L-18. Corten and Sailors Dynamic with K-Rate Shift

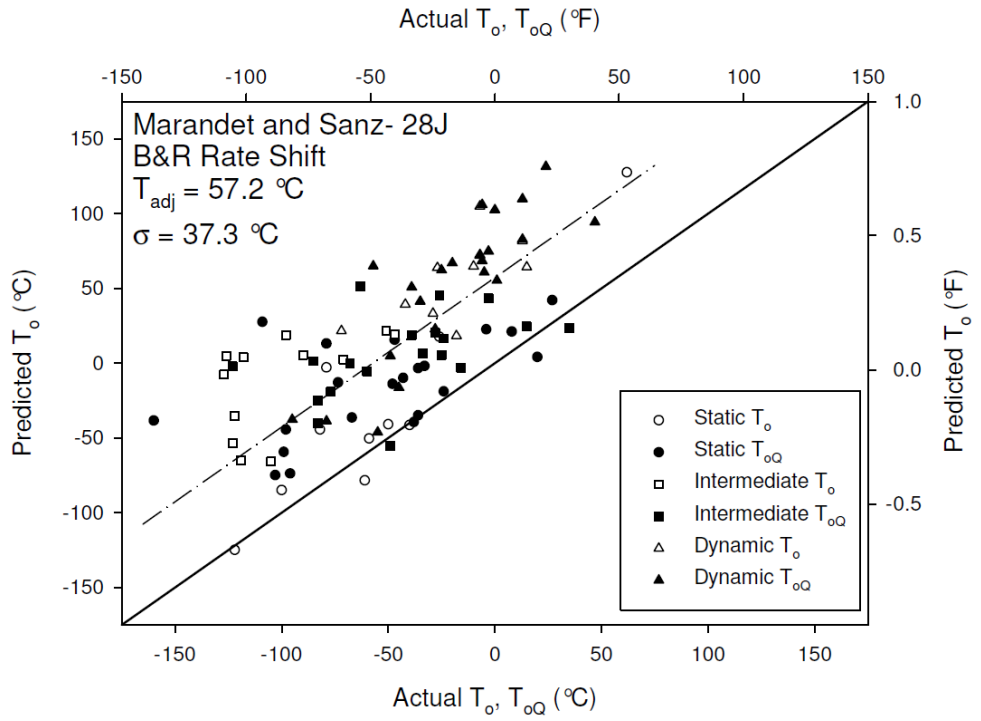

Figure L-19. Marandet and Sanz with B&R Shift

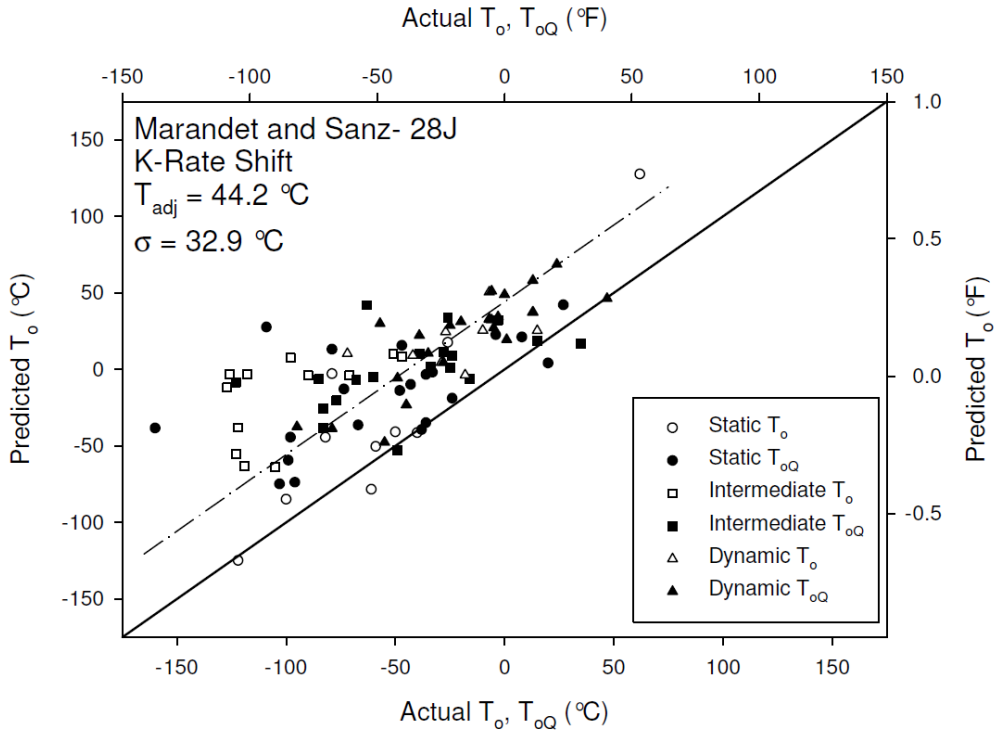

Figure L-20. Marandet and Sanz with K-Rate Shift

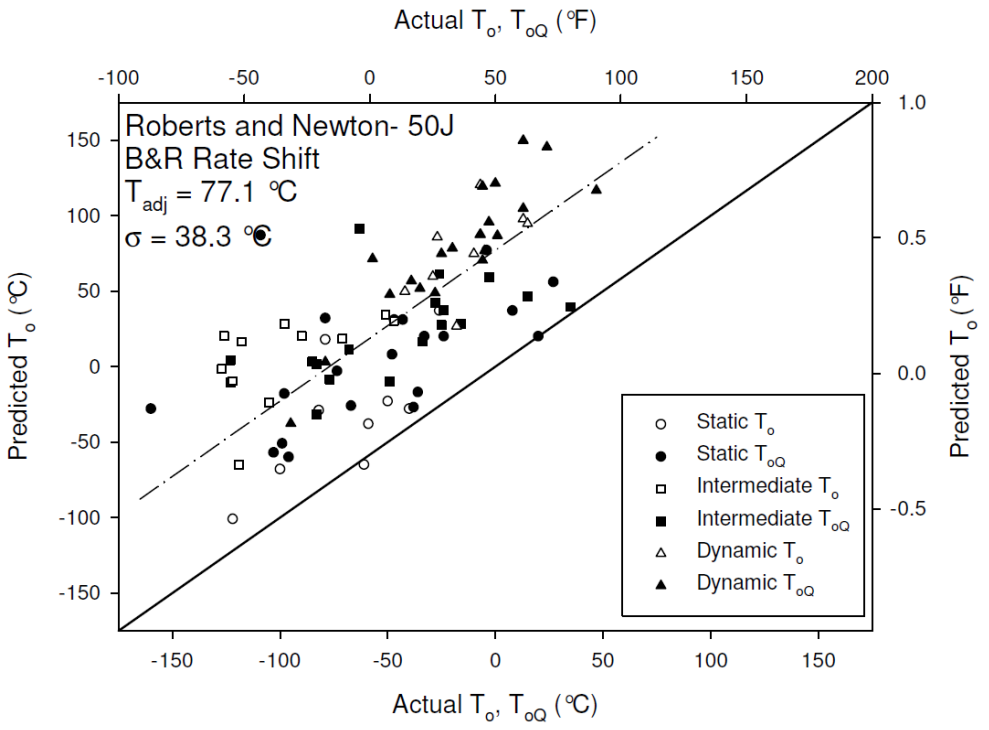

Figure L-21. Roberts and Newton Evaluated at 50J with B&R Shift

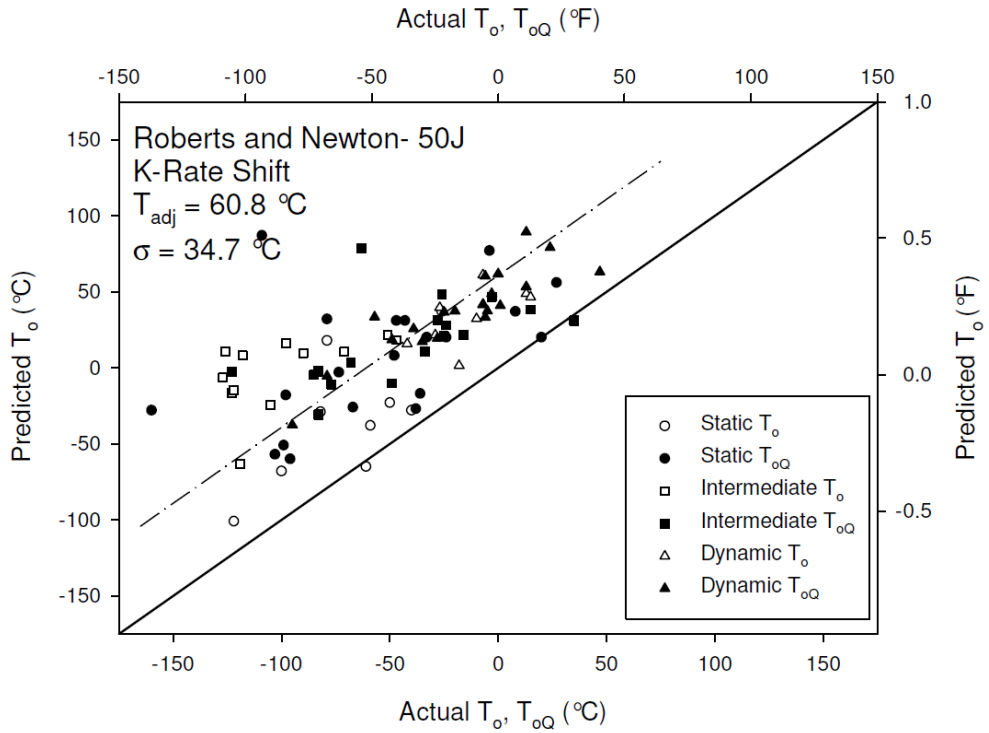

Figure L-22. Roberts and Newton Evaluated at 50J with K-Rate Shift

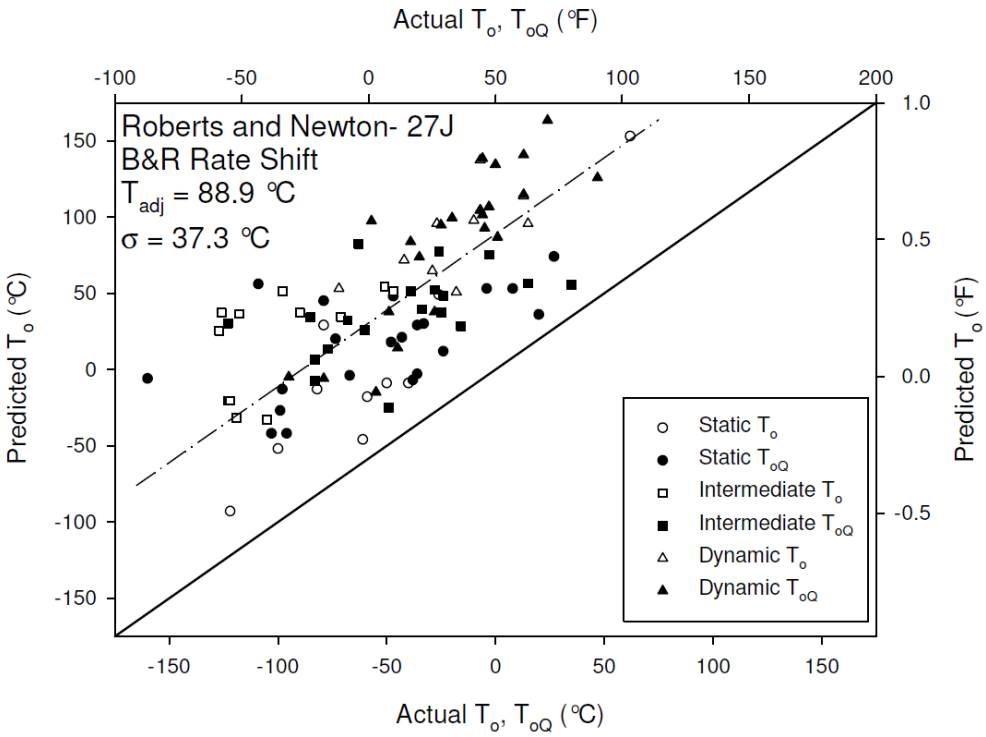

Figure L-23. Roberts and Newton Evaluated at 27J with B&R Shift

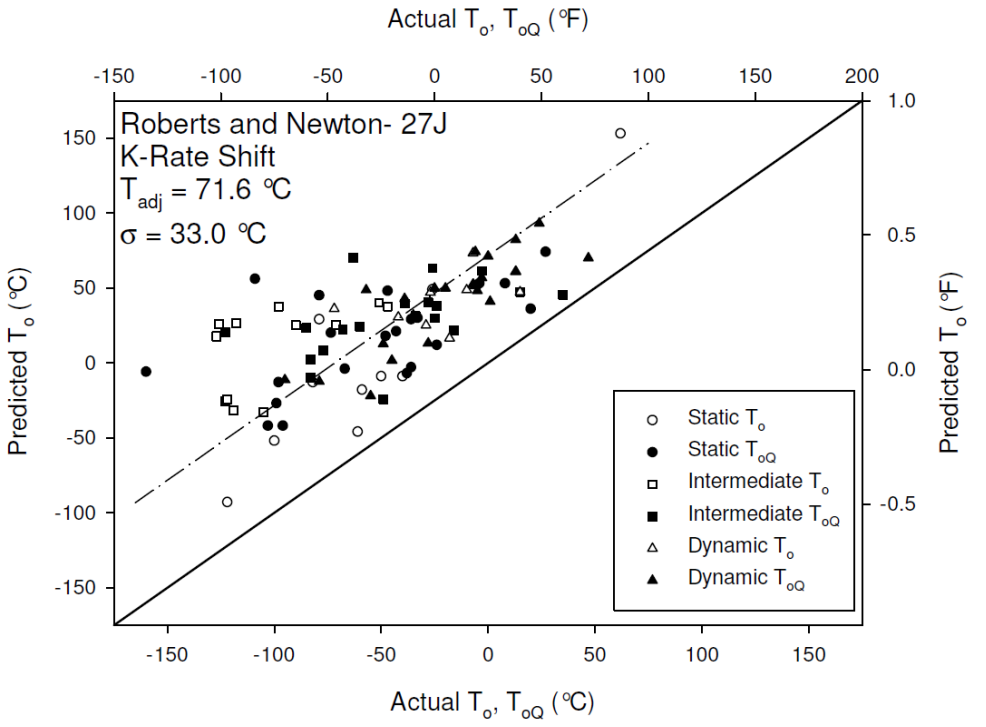

Figure L-24. Roberts and Newton Evaluated at 27J with K-Rate Shift

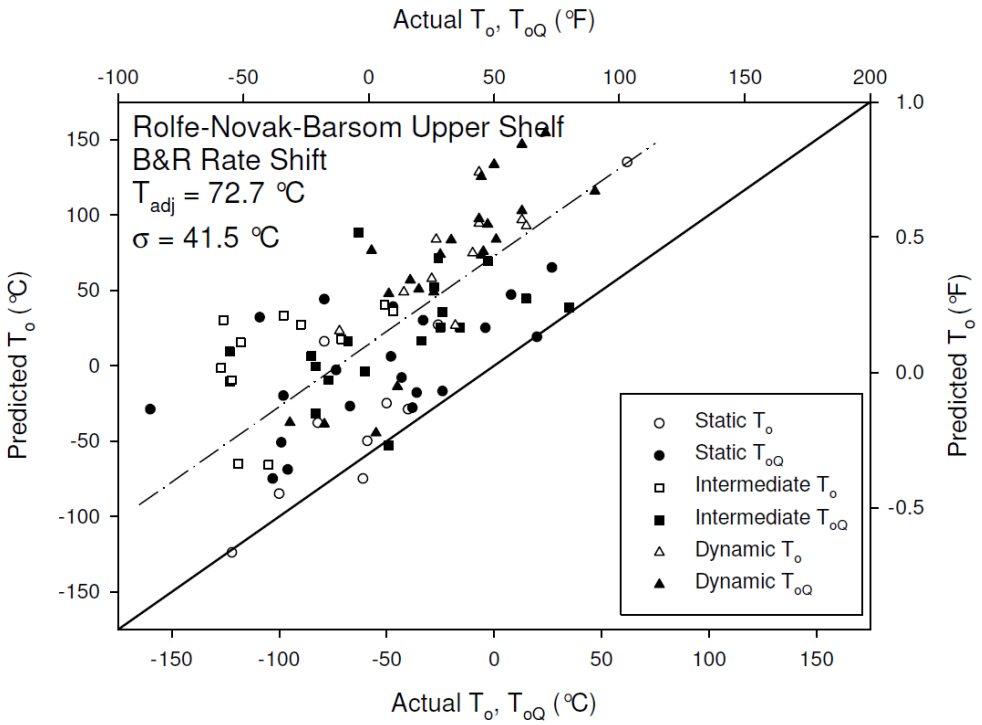

Figure L-25. RNB Upper Shelf with B&R Shift

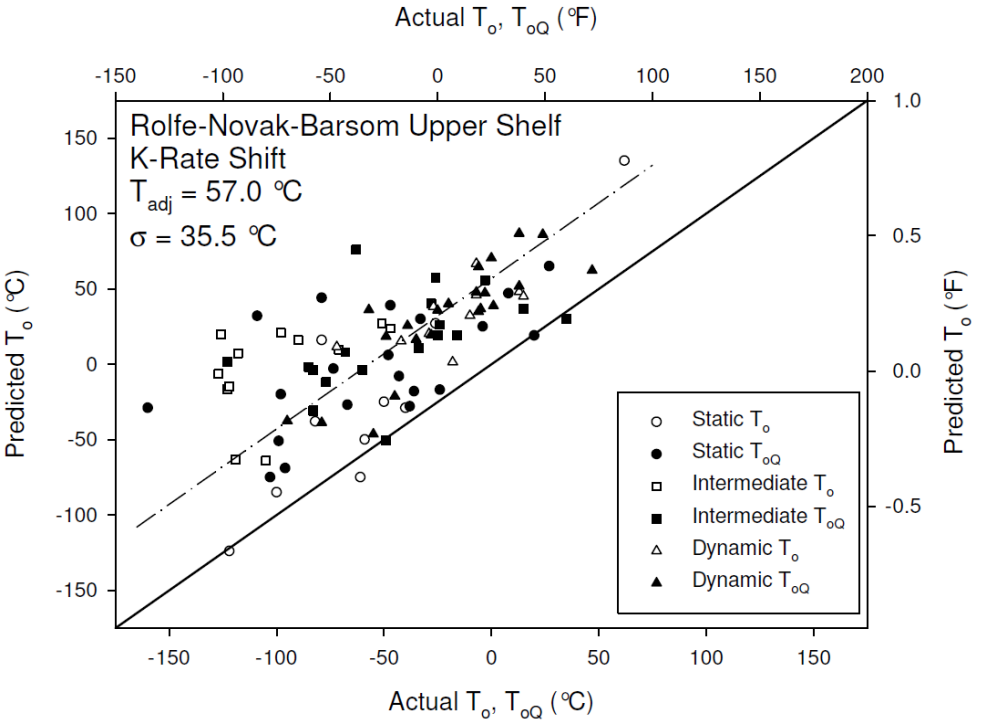

Figure L-26. RNB Upper Shelf with K-Rate Shift

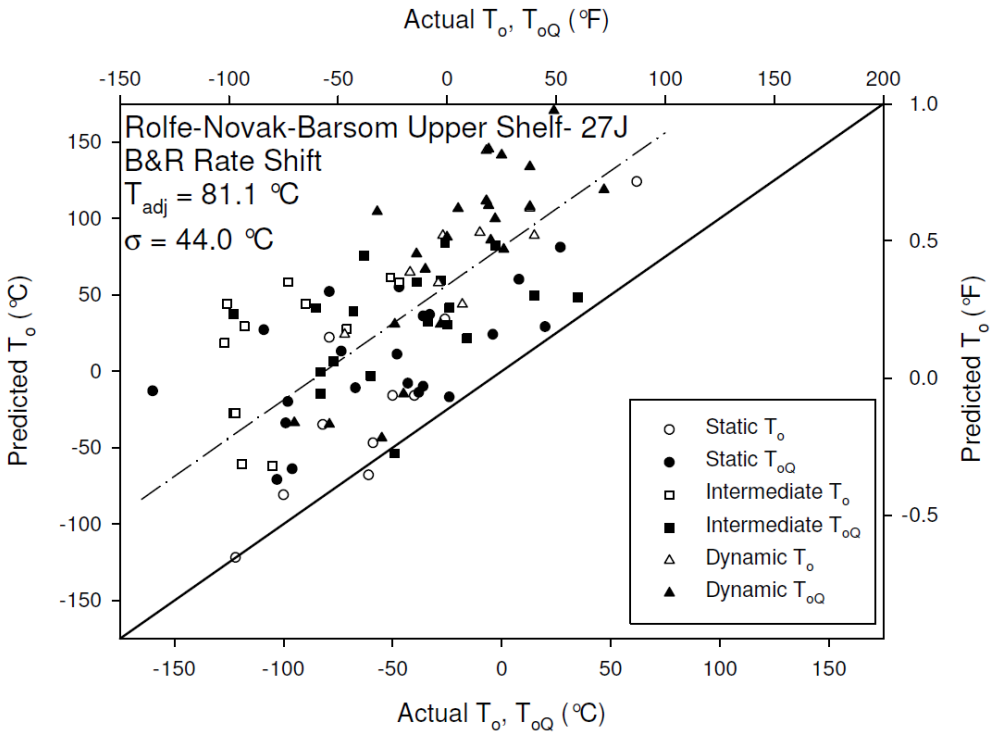

Figure L-27. RNB Upper Shelf Evaluated at 27J with B&R Shift

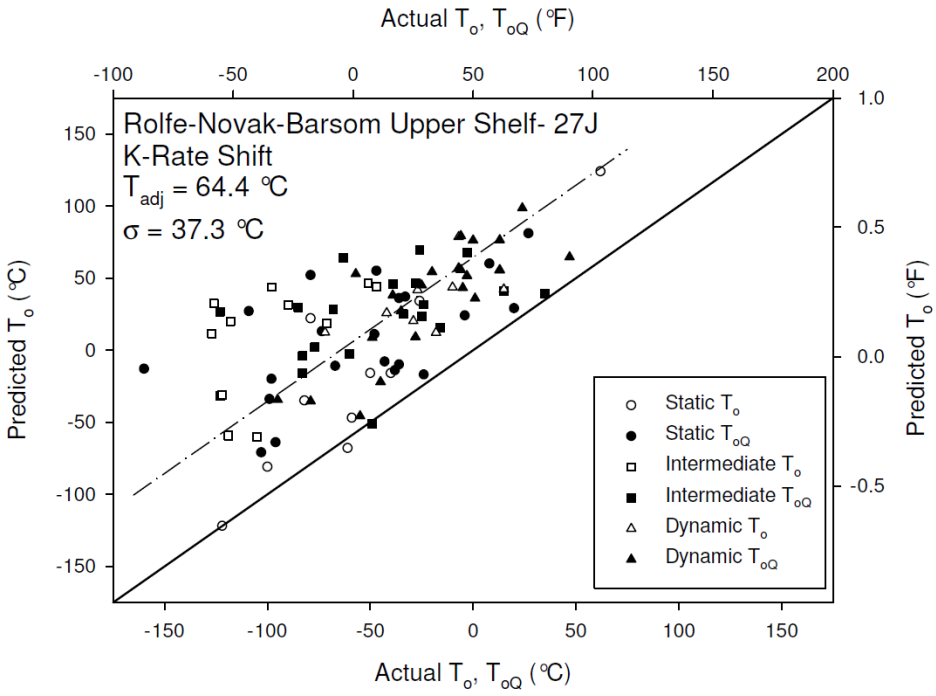

Figure L-28. RNB Upper Shelf Evaluated at 27J with K-Rate Shift

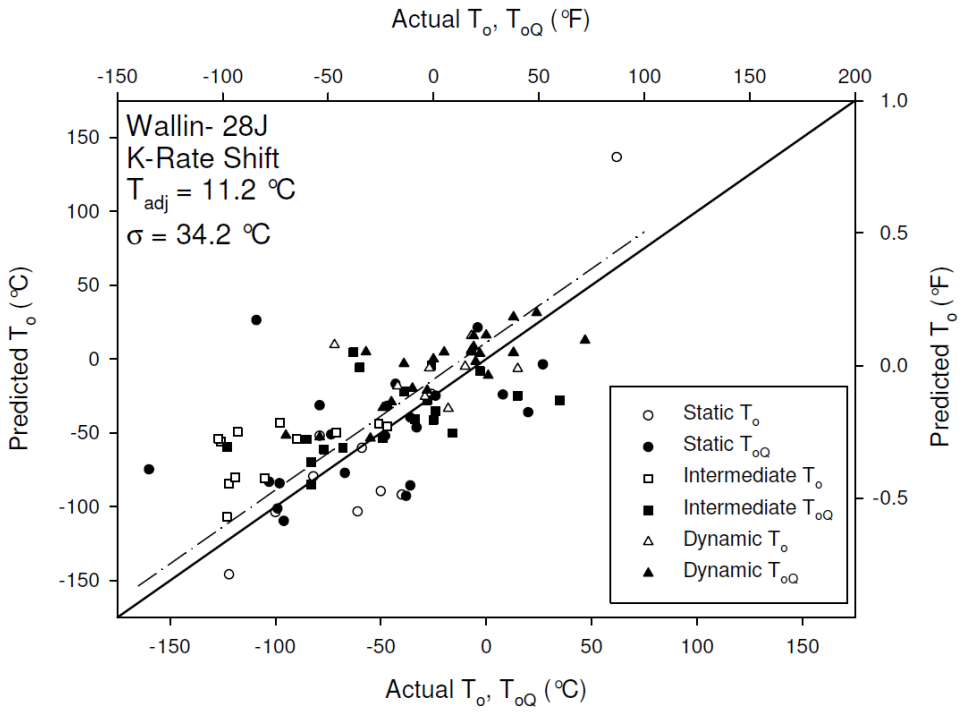

Figure L-29. Wallin with K-Rate Shift

APPENDIX M: Conventional Steel Test Records and Fracture Surfaces

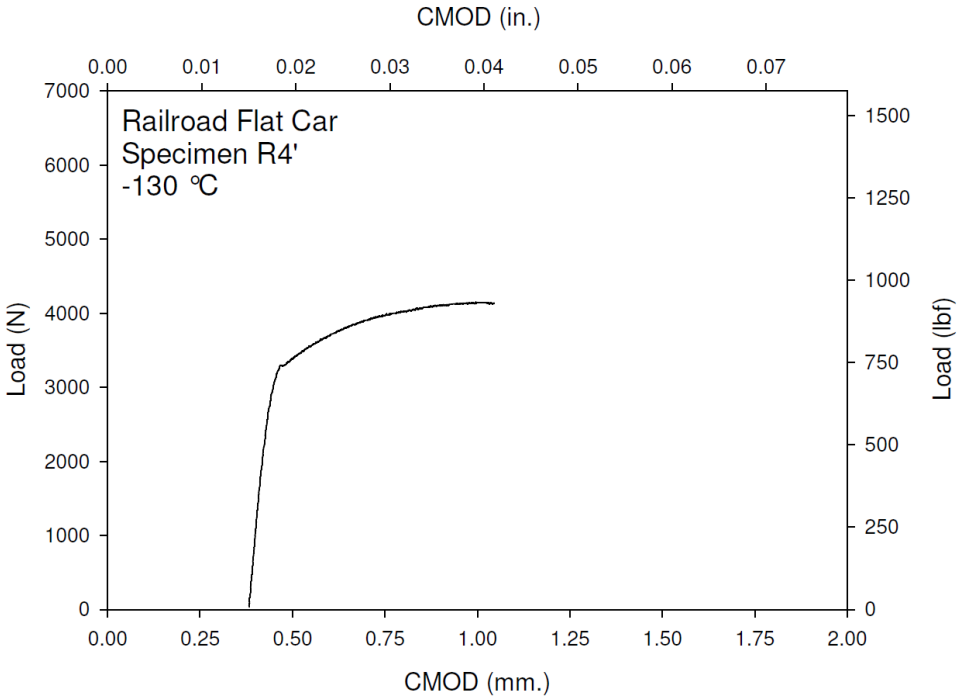

Figure M-1. Specimen R4' Test Record

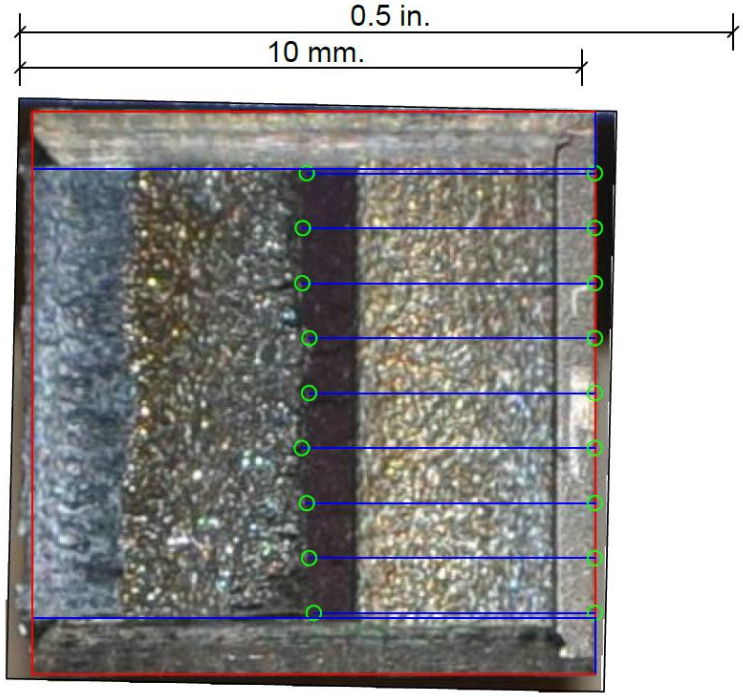

Figure M-2. Specimen R4' Fracture Surface

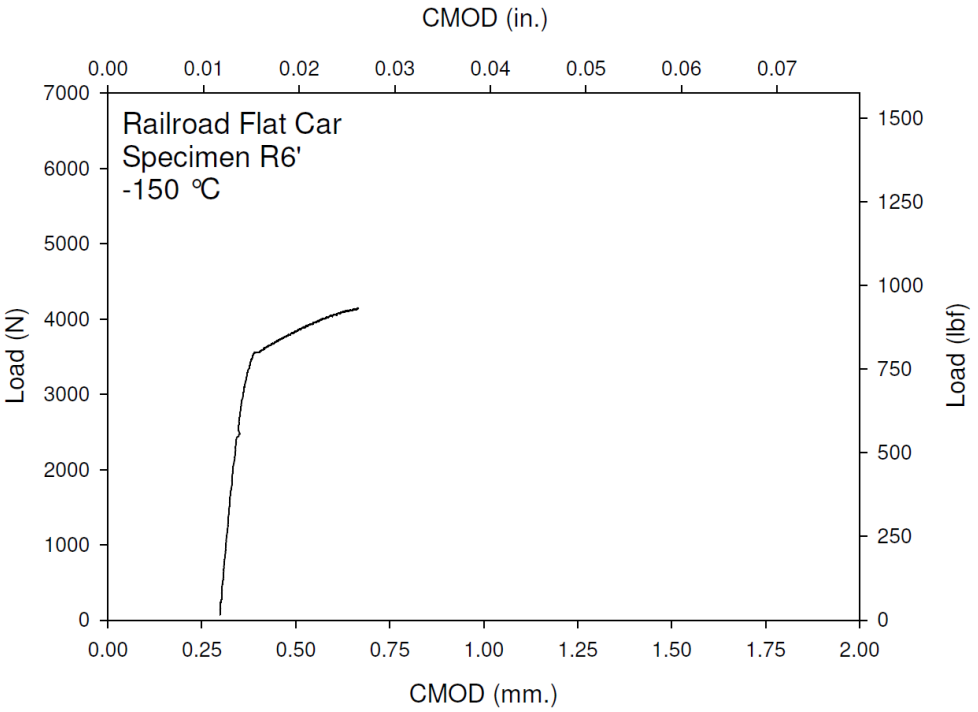

Figure M-3. Specimen R6' Test Record

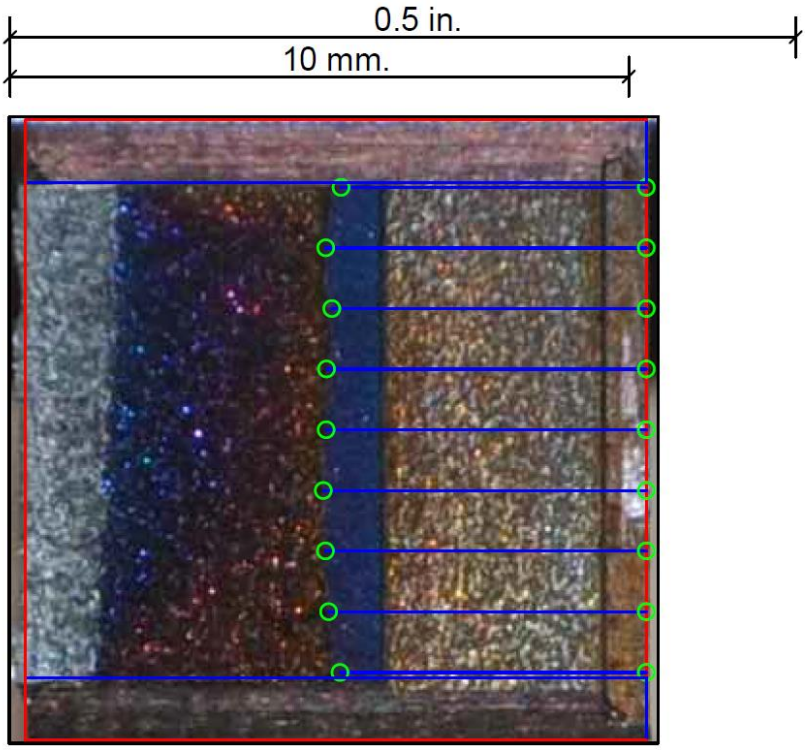

Figure M-4. Specimen R6' Fracture Surface

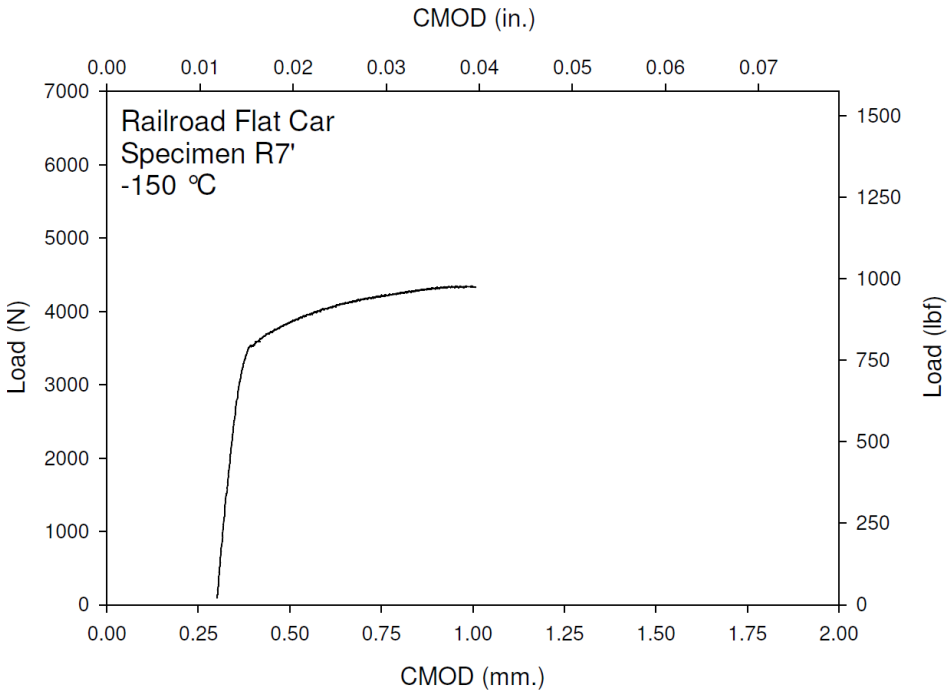

Figure M-5. Specimen R7' Test Record

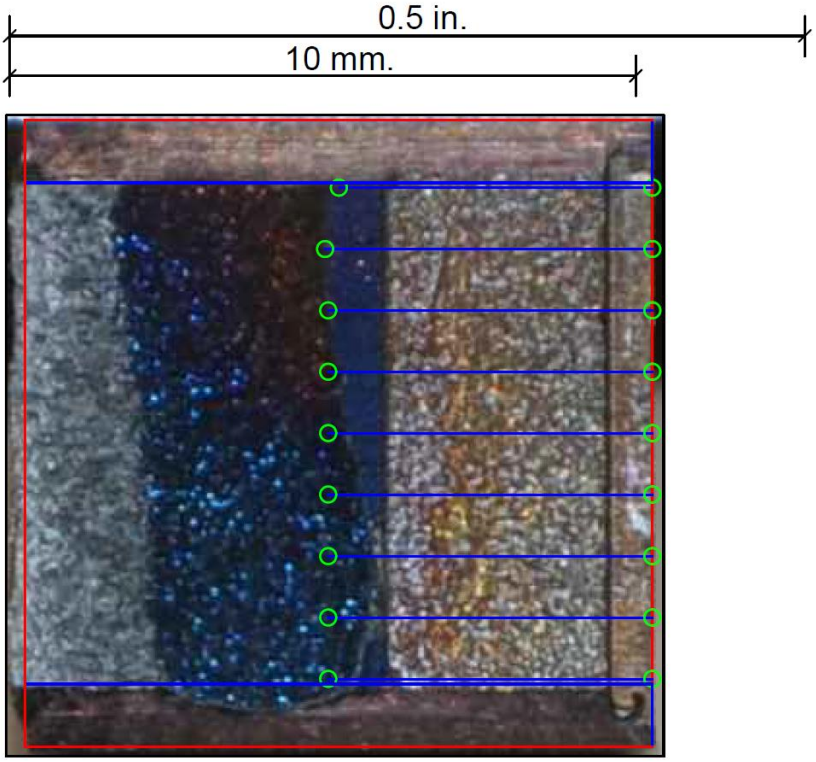

Figure M-6. Specimen R7' Fracture Surface

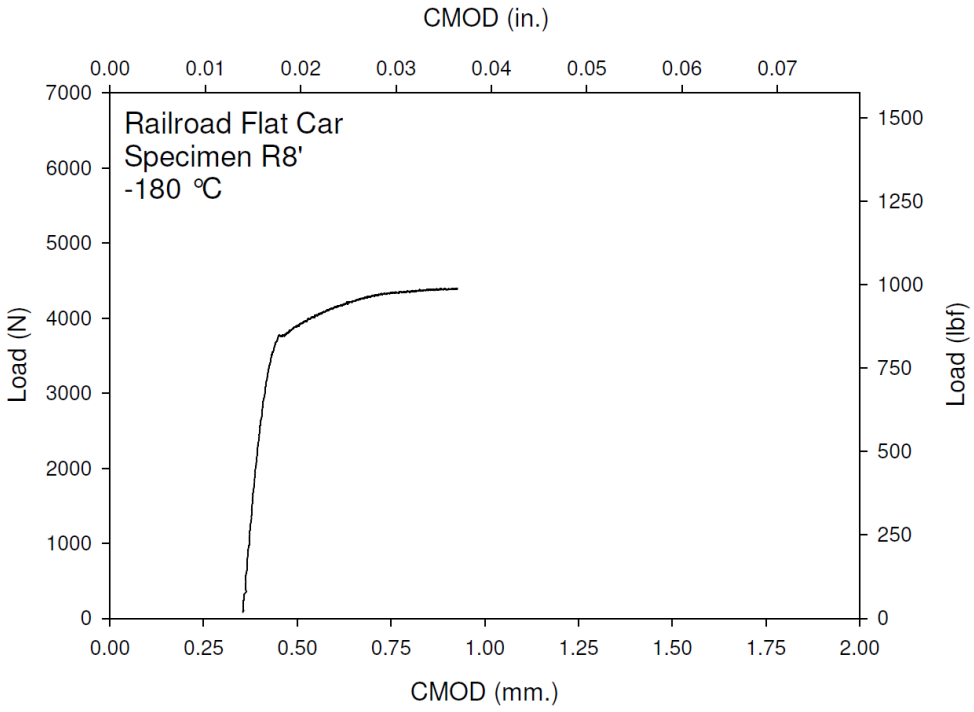

Figure M-7. Specimen R8' Test Record

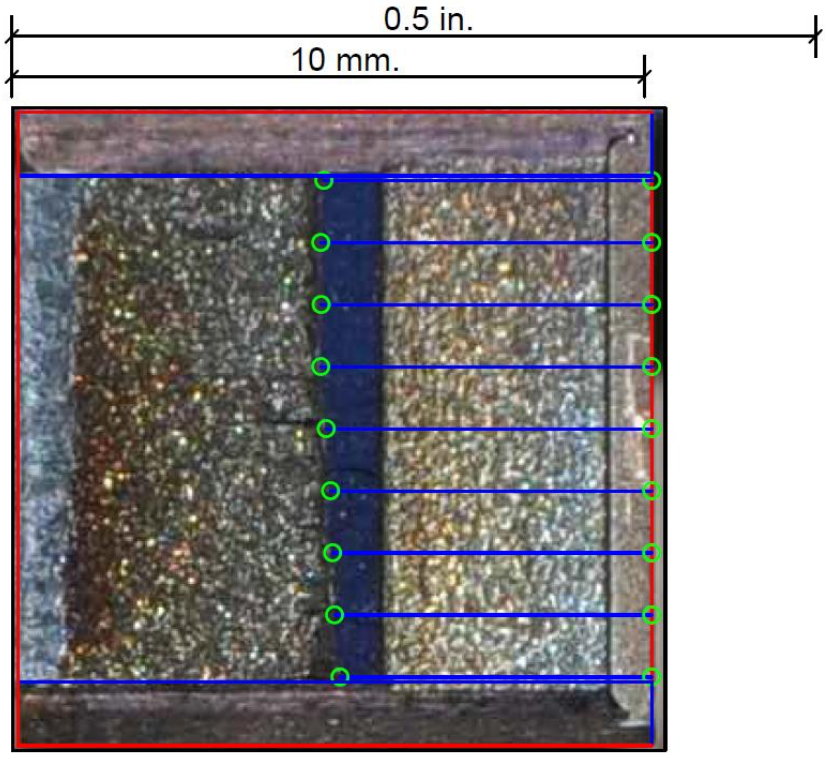

Figure M-8. Specimen R8' Fracture Surface

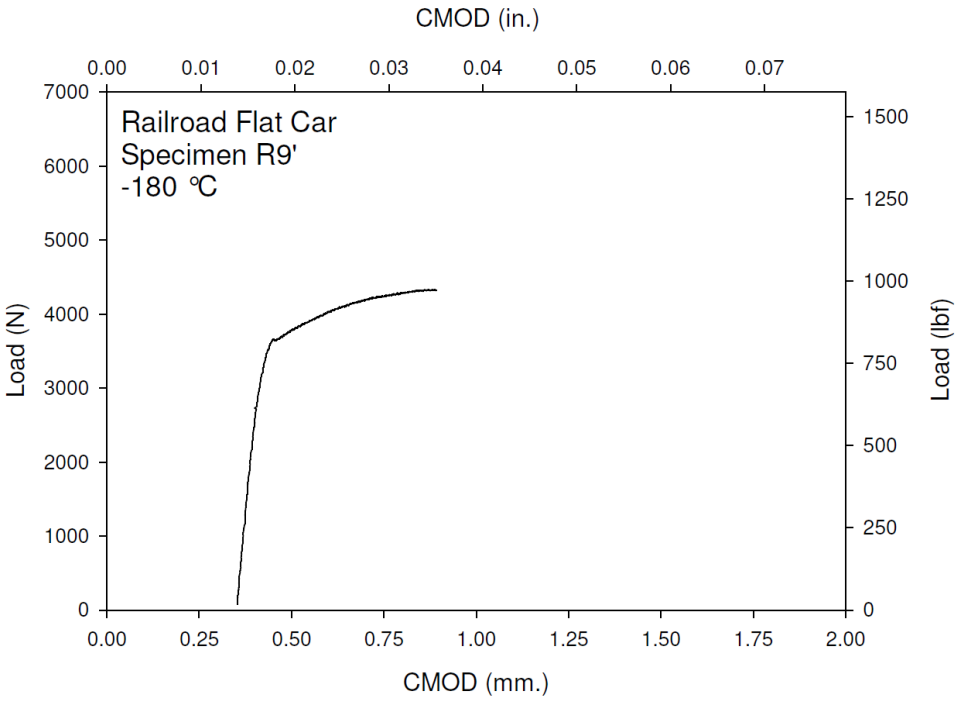

Figure M-9. Specimen R9' Test Record

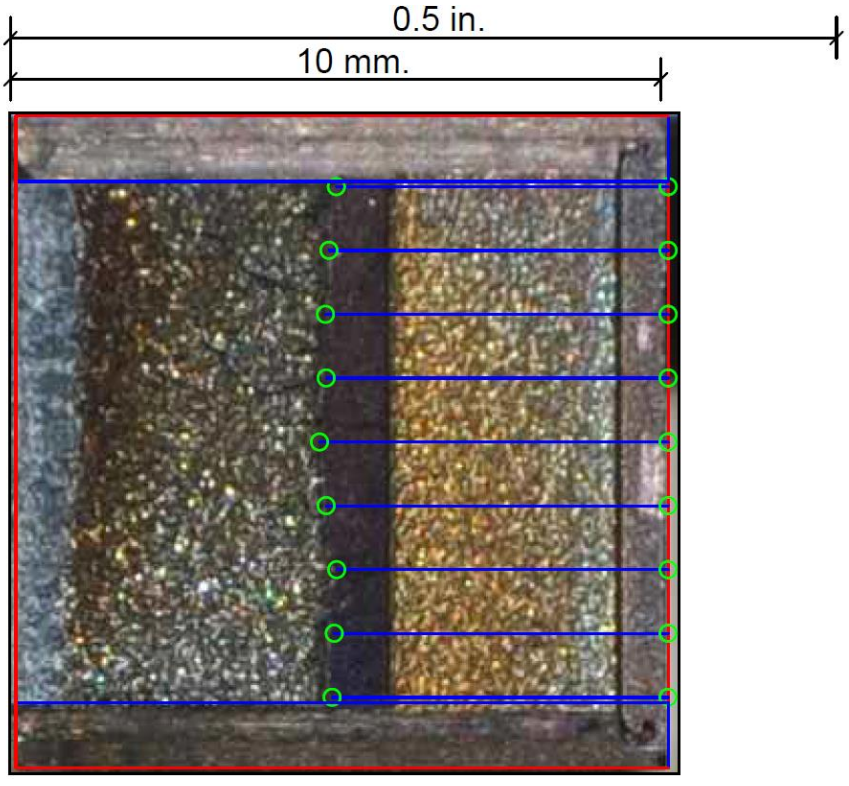

Figure M-10. Specimen R9' Fracture Surface

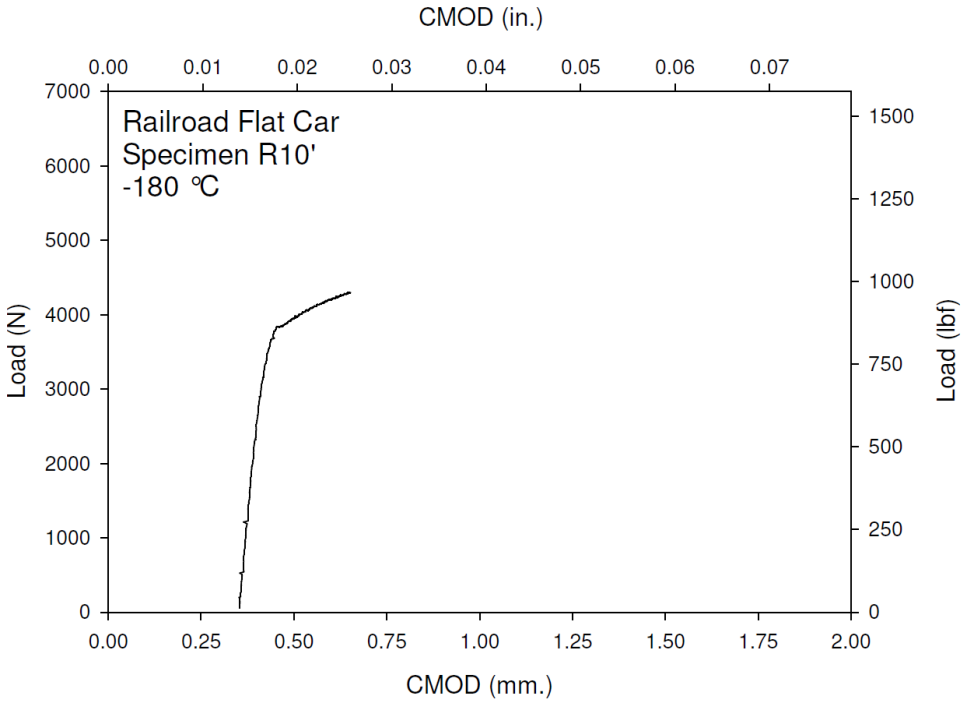

Figure M-11. Specimen R10' Test Record

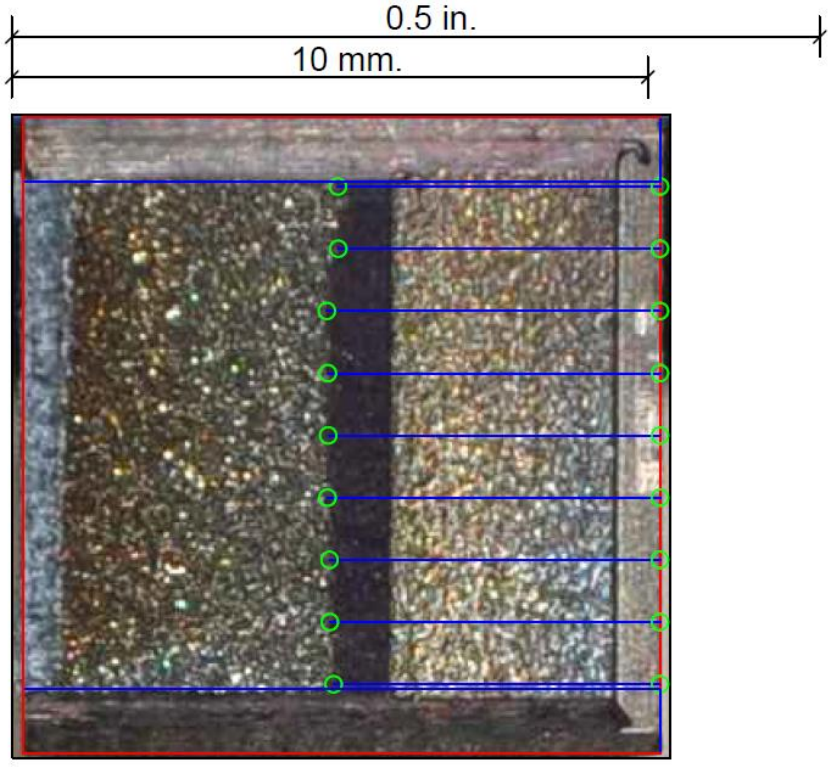

Figure M-12. Specimen R10' Fracture Surface

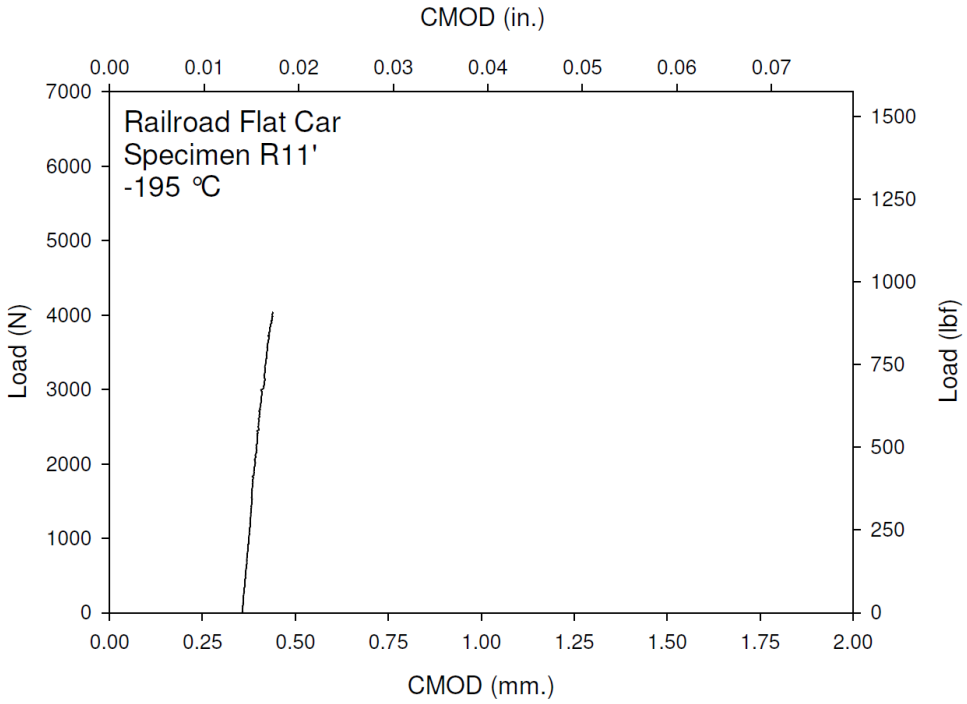

Figure M-13. Specimen R11' Test Record

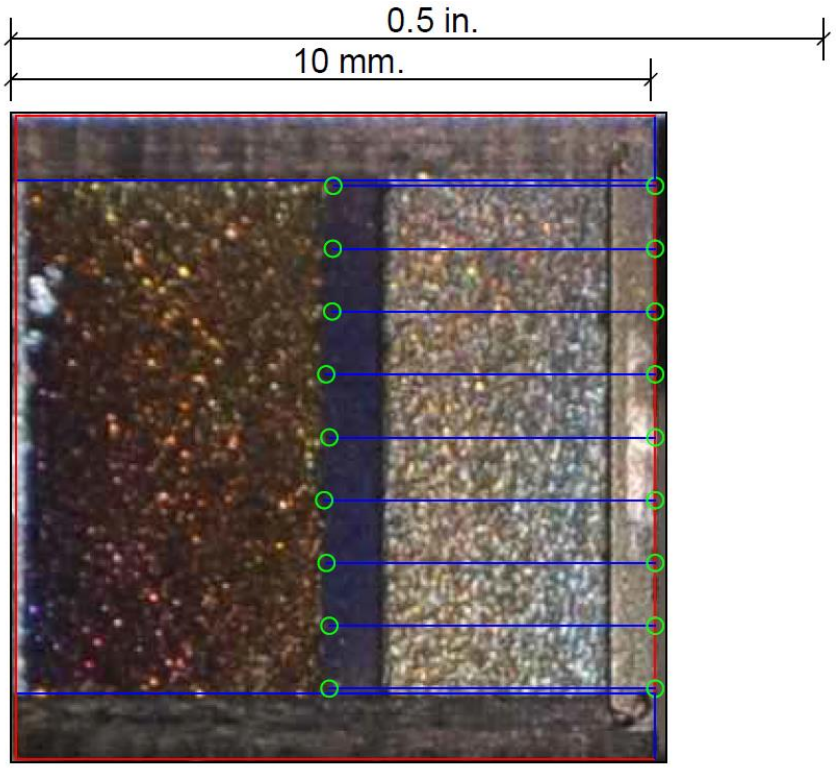

Figure M-14. Specimen R11' Fracture Surface

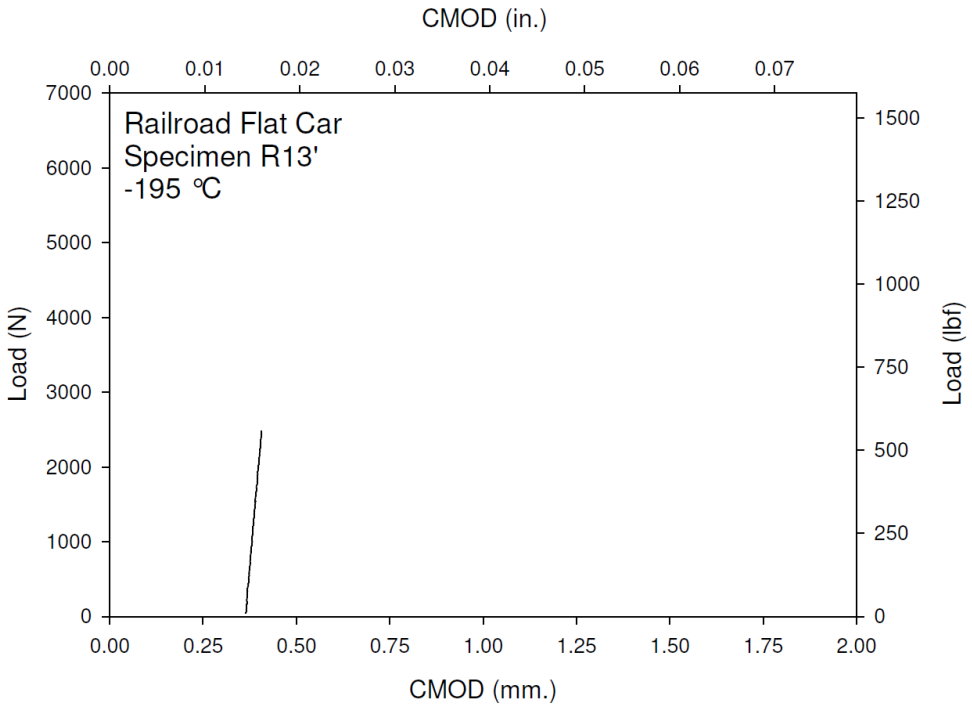

Figure M-15. Specimen R13' Test Record

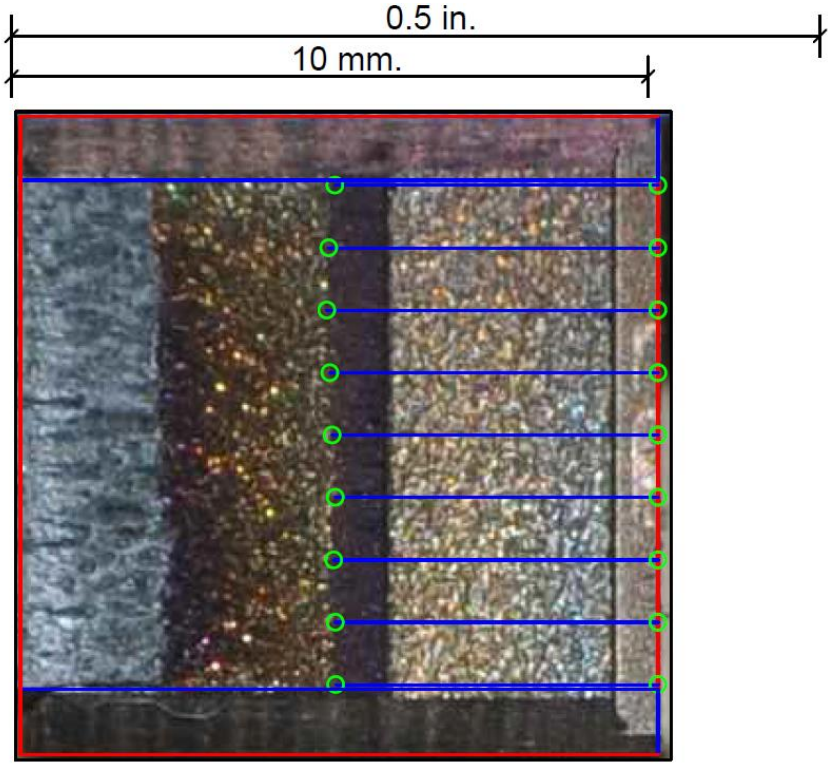

Figure M-16. Specimen R13' Fracture Surface

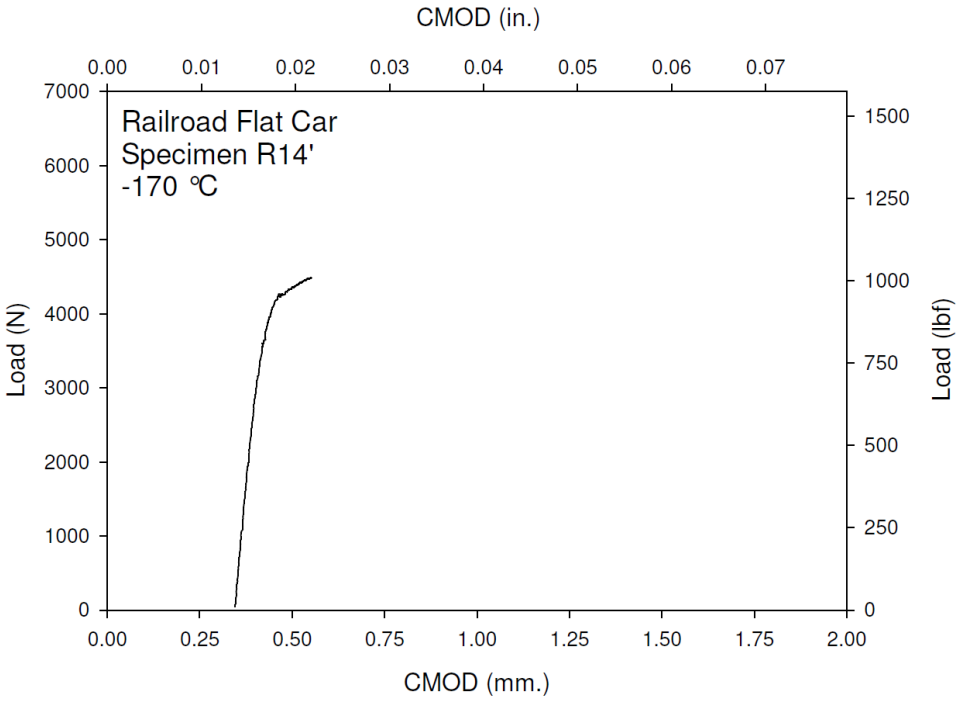

Figure M-17. Specimen R14' Test Record

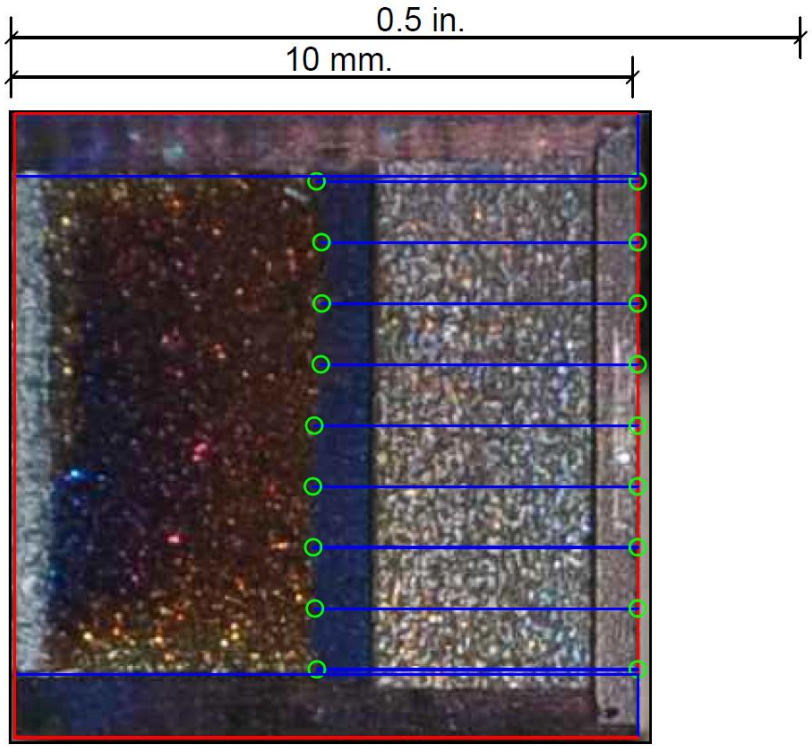

Figure M-18. Specimen R14' Fracture Surface

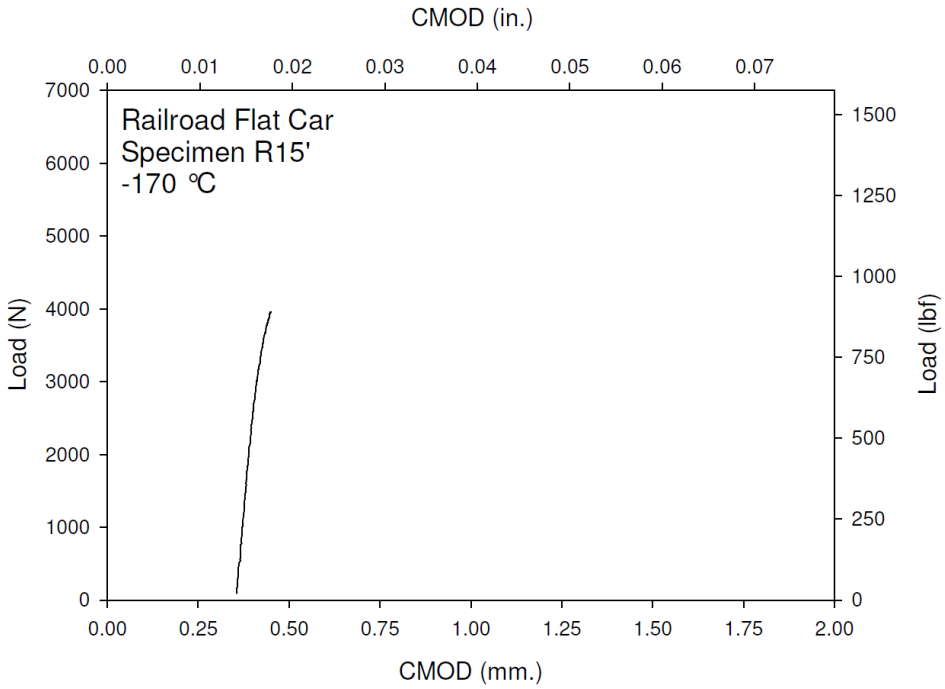

Figure M-19. Specimen R15' Test Record

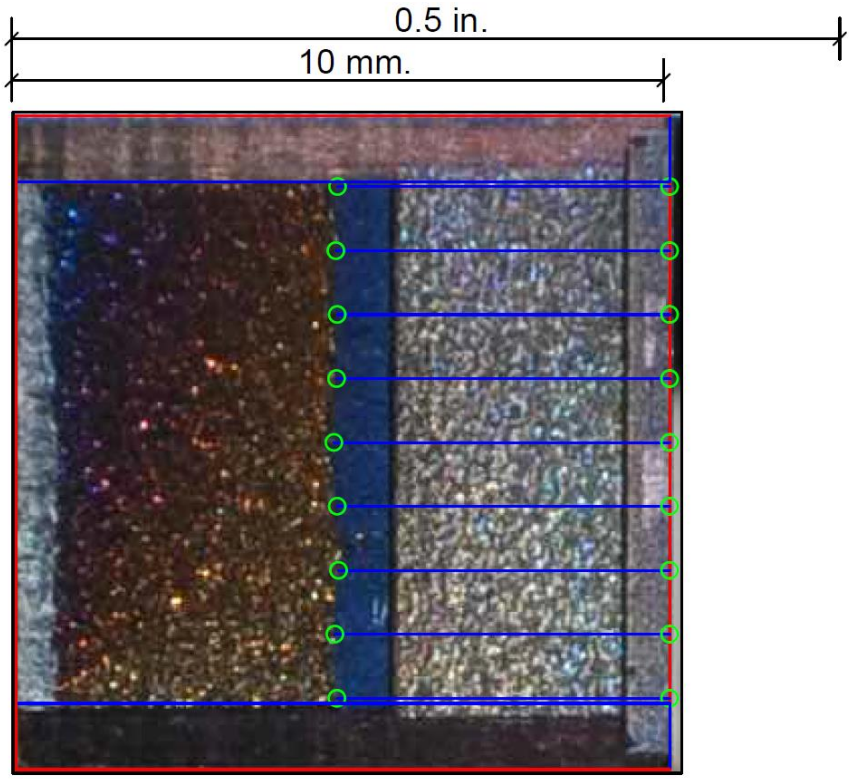

Figure M-20. Specimen R15' Fracture Surface

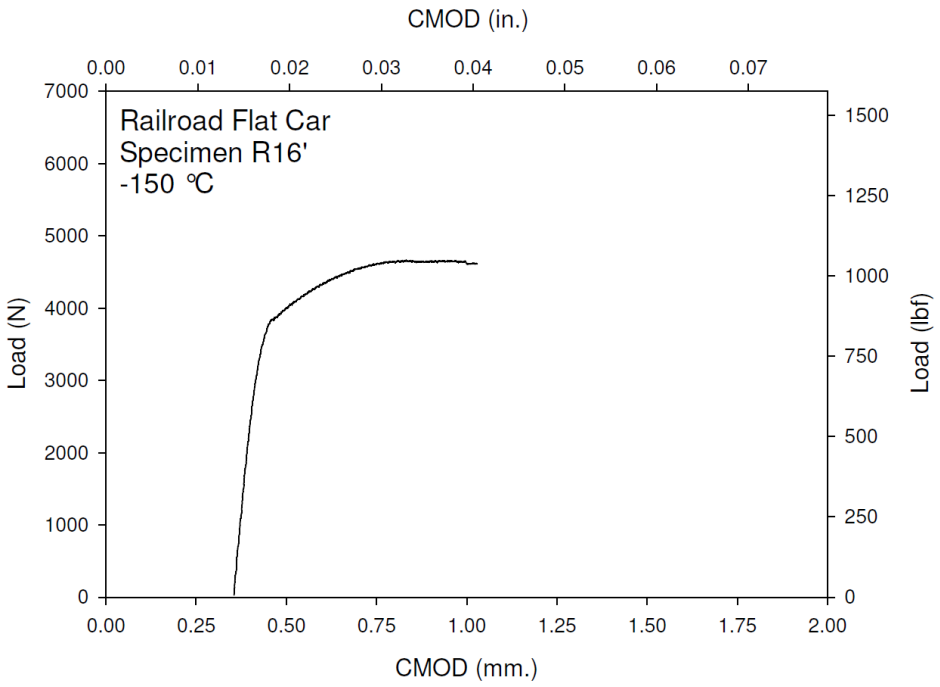

Figure M-21. Specimen R16' Test Record

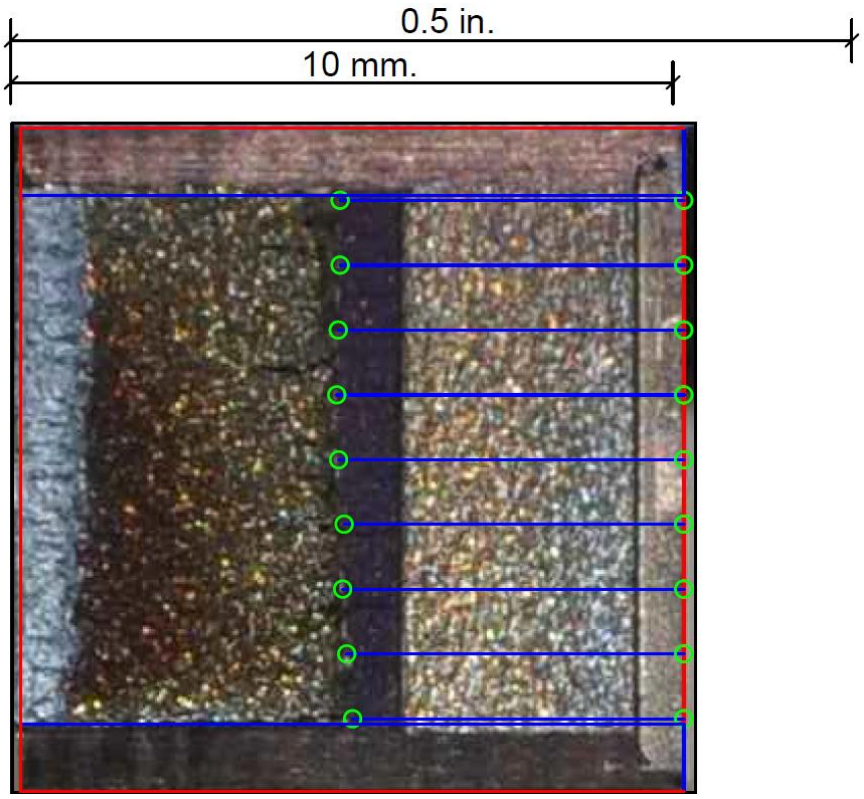

Figure M-22. Specimen R16' Fracture Surface

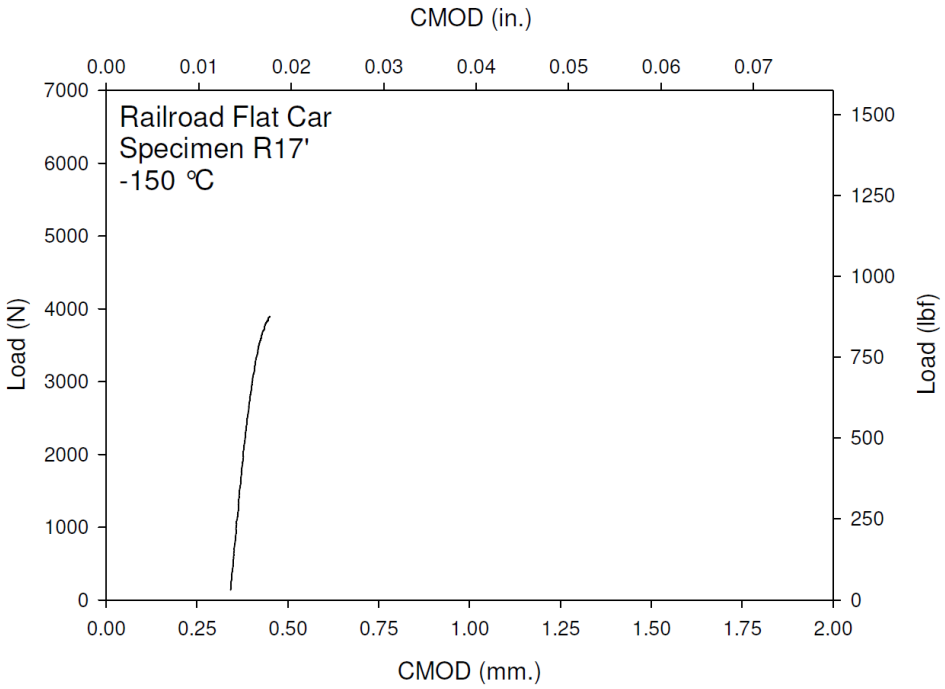

Figure M-23. Specimen R17' Test Record

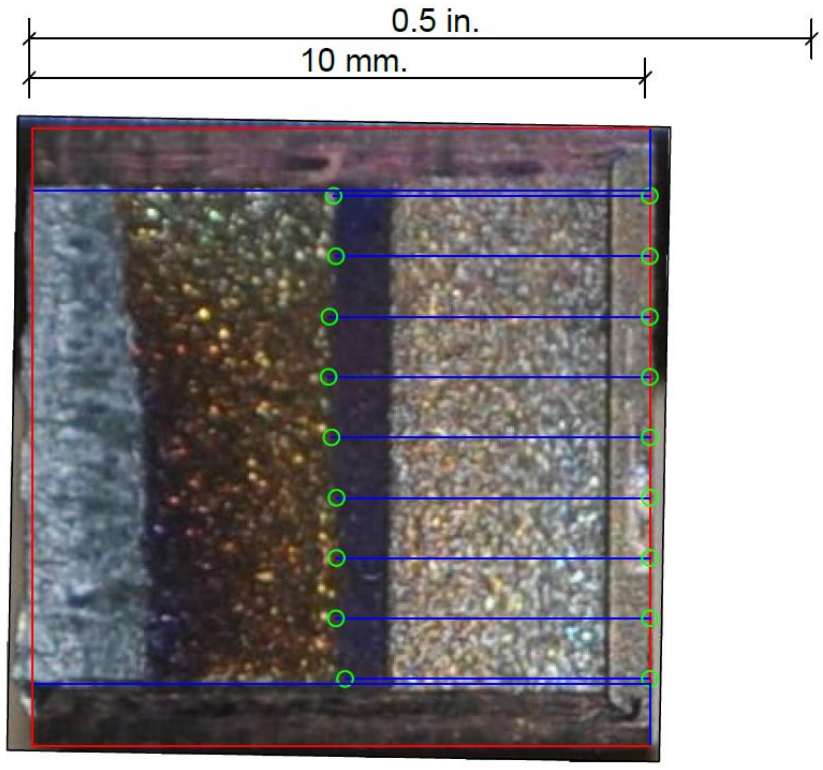

Figure M-24. Specimen R17' Fracture Surface

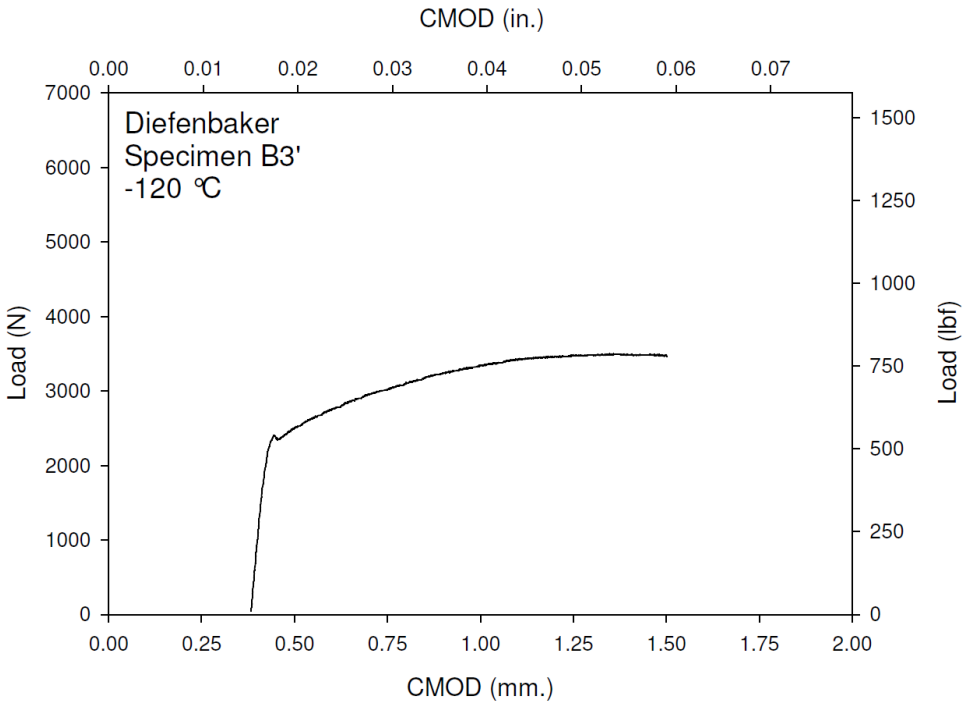

Figure M-25. Specimen B3' Test Record

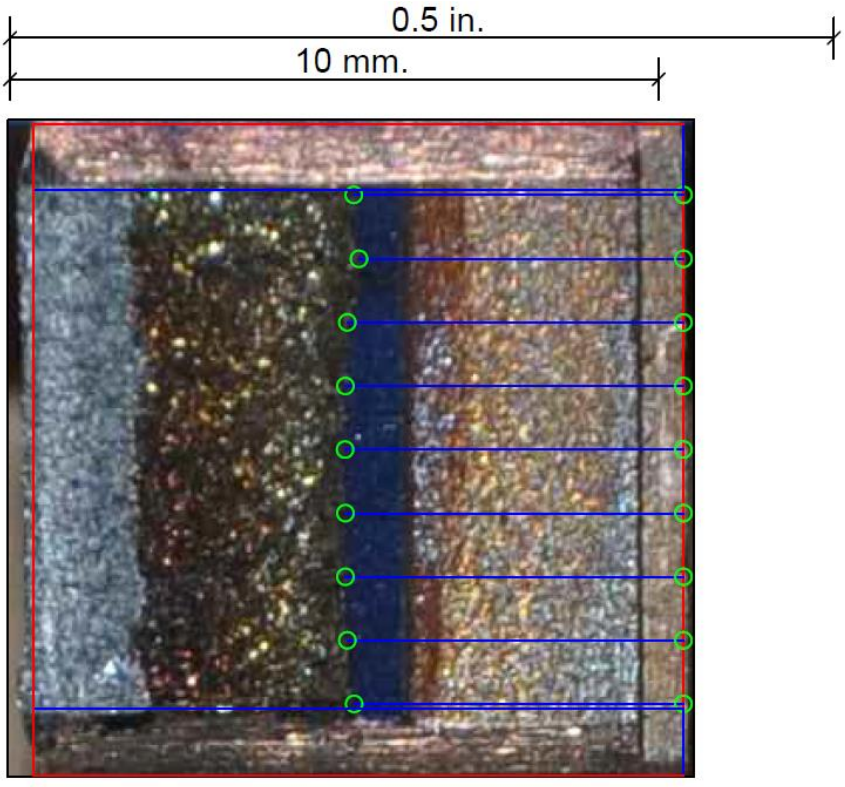

Figure M-26. Specimen B3' Fracture Surface

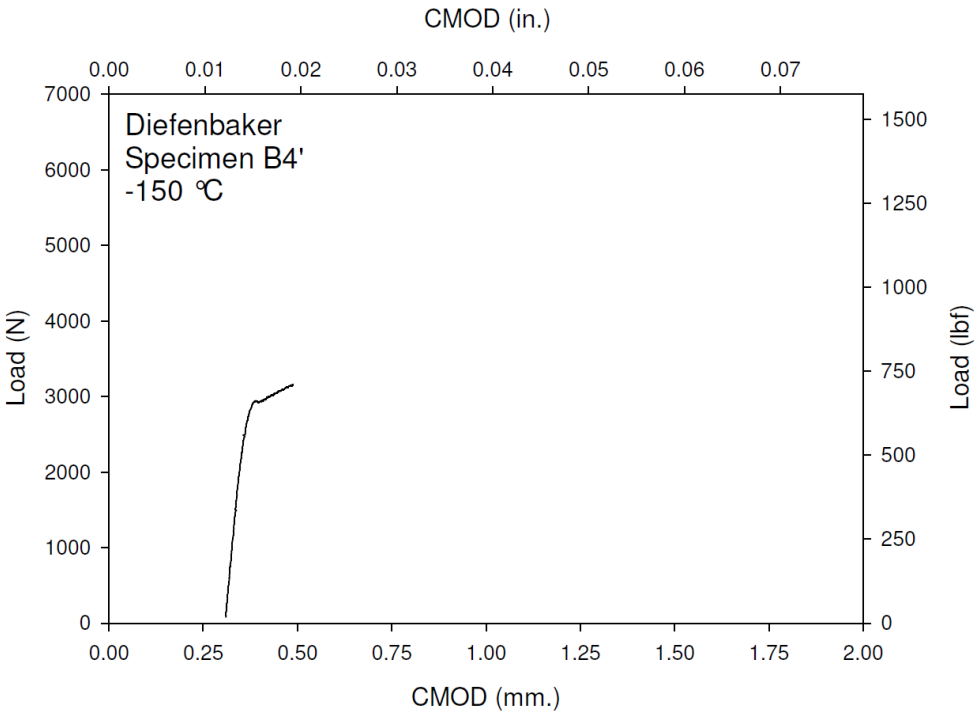

Figure M-27. Specimen B4' Test Record

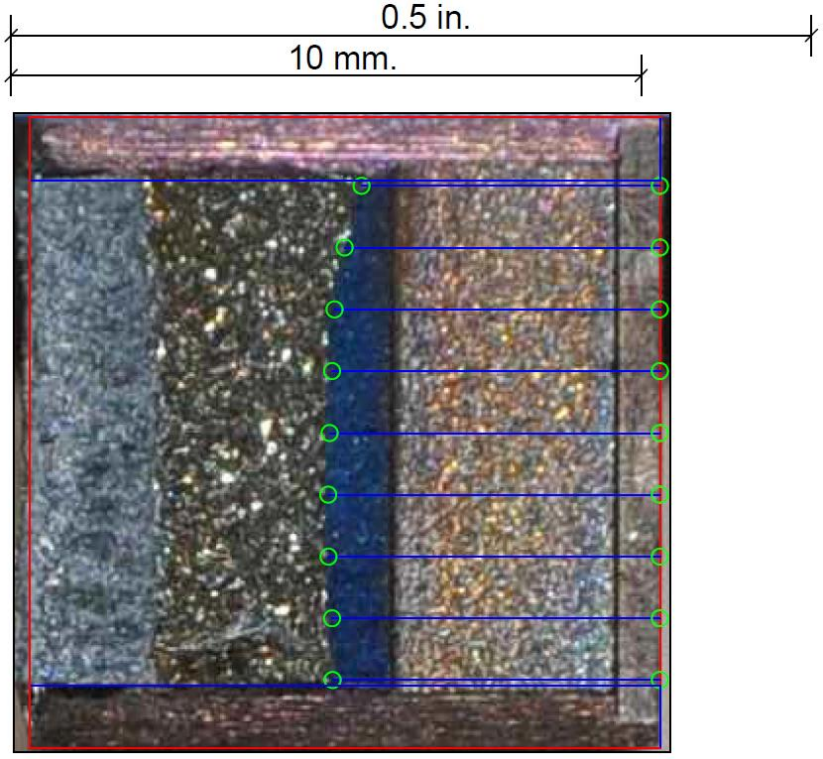

Figure M-28. Specimen B4' Fracture Surface

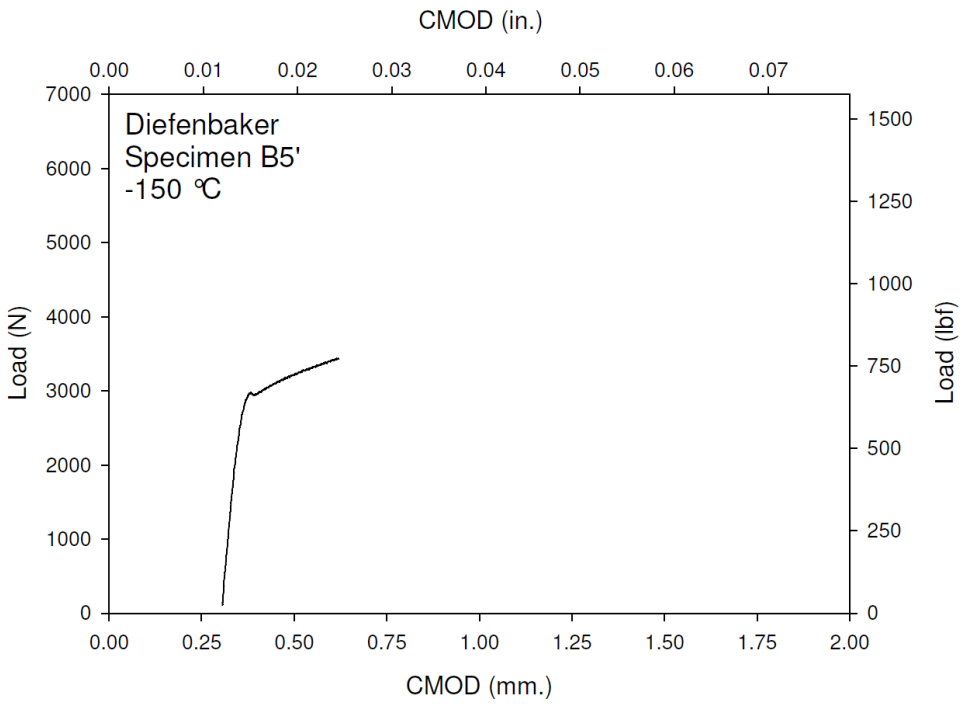

Figure M-29. Specimen B5' Test Record

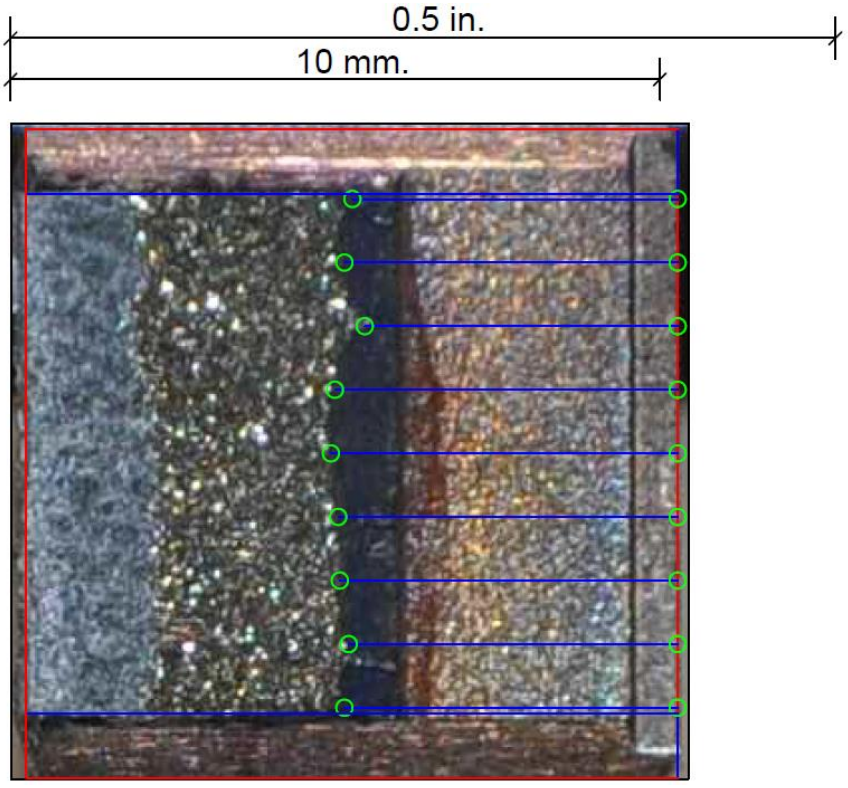

Figure M-30. Specimen B5' Fracture Surface

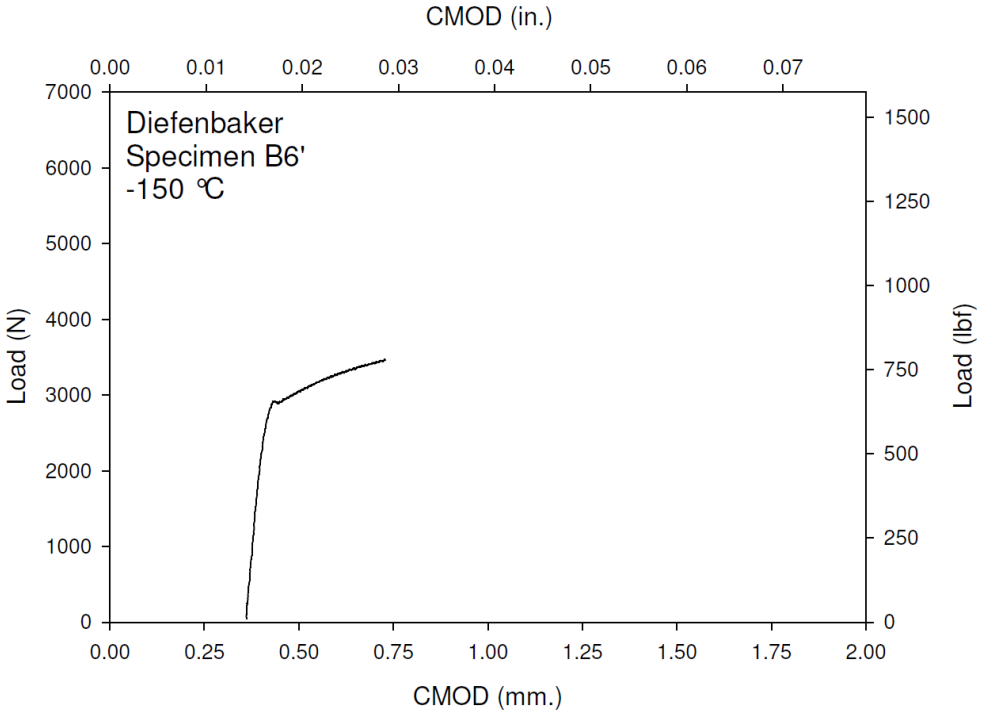

Figure M-31. Specimen B6' Test Record

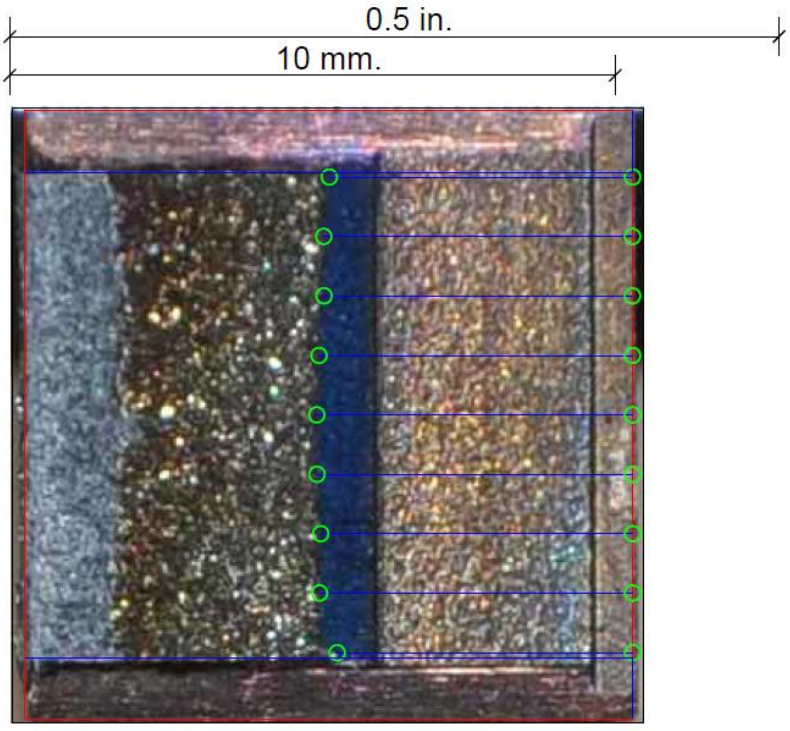

Figure M-32. Specimen B6' Fracture Surface

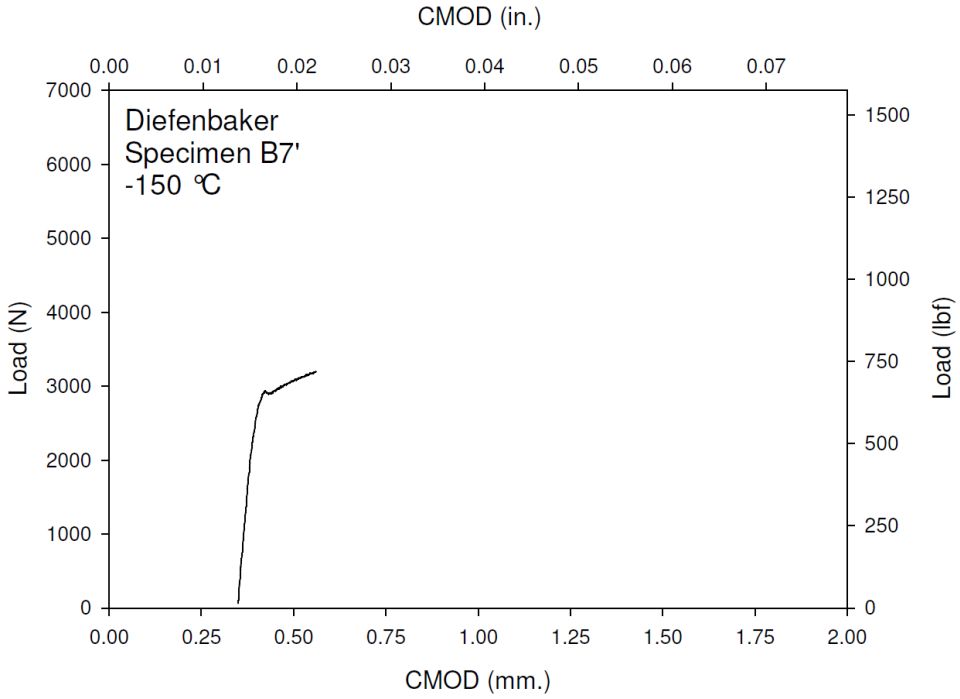

Figure M-33. Specimen B7' Test Record

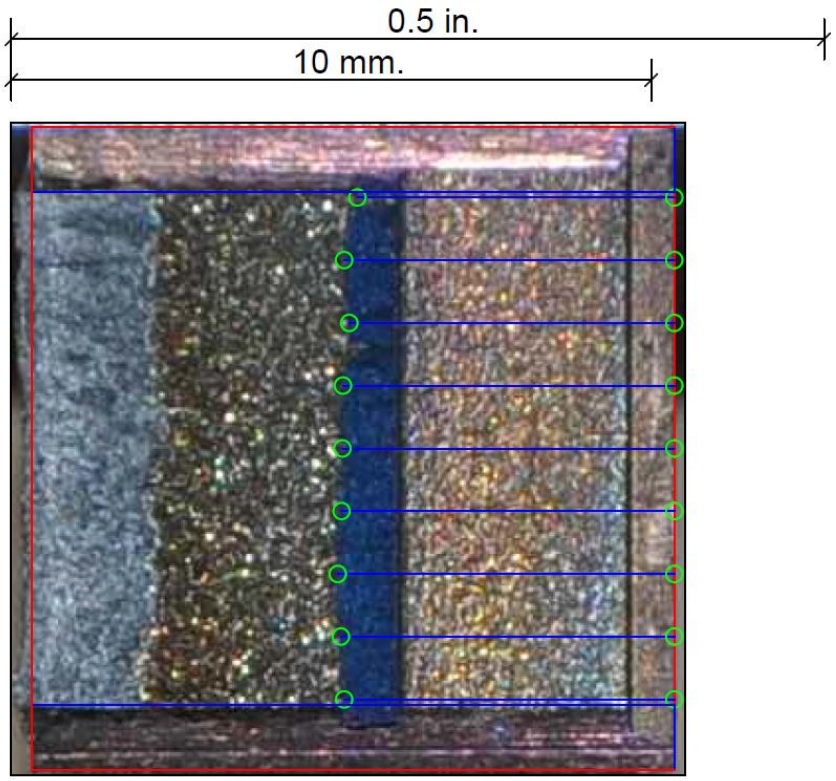

Figure M-34. Specimen B7' Fracture Surface

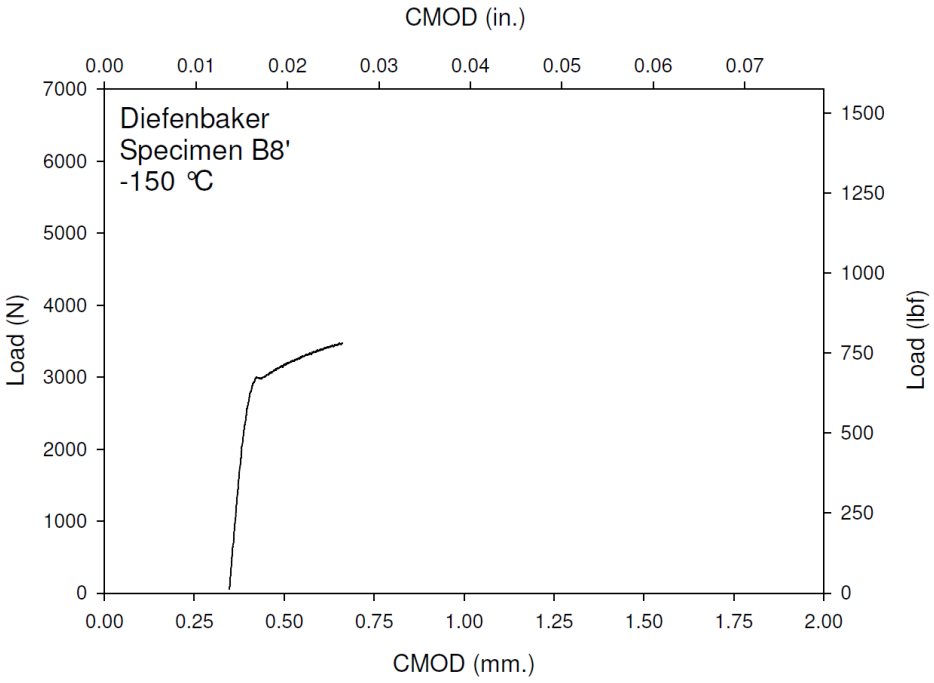

Figure M-35. Specimen B8' Test Record

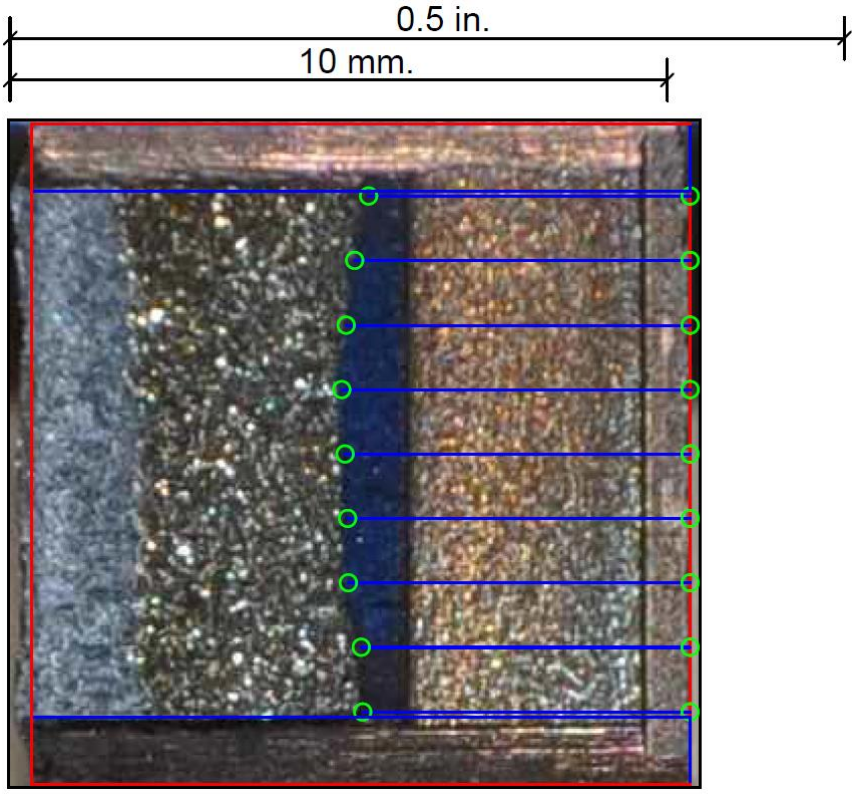

Figure M-36. Specimen B8' Fracture Surface

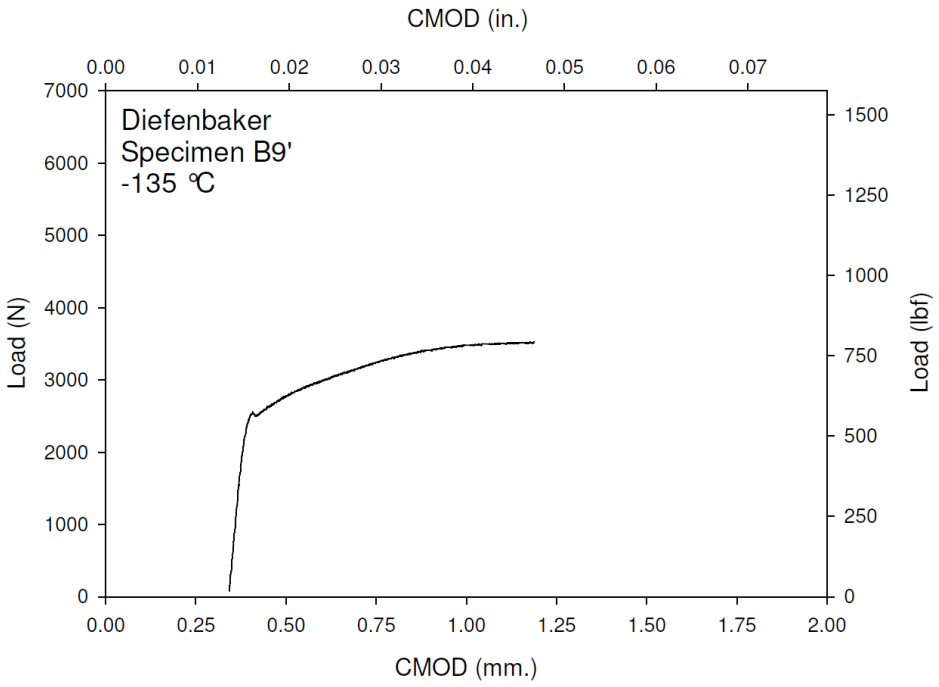

Figure M-37. Specimen B9' Test Record

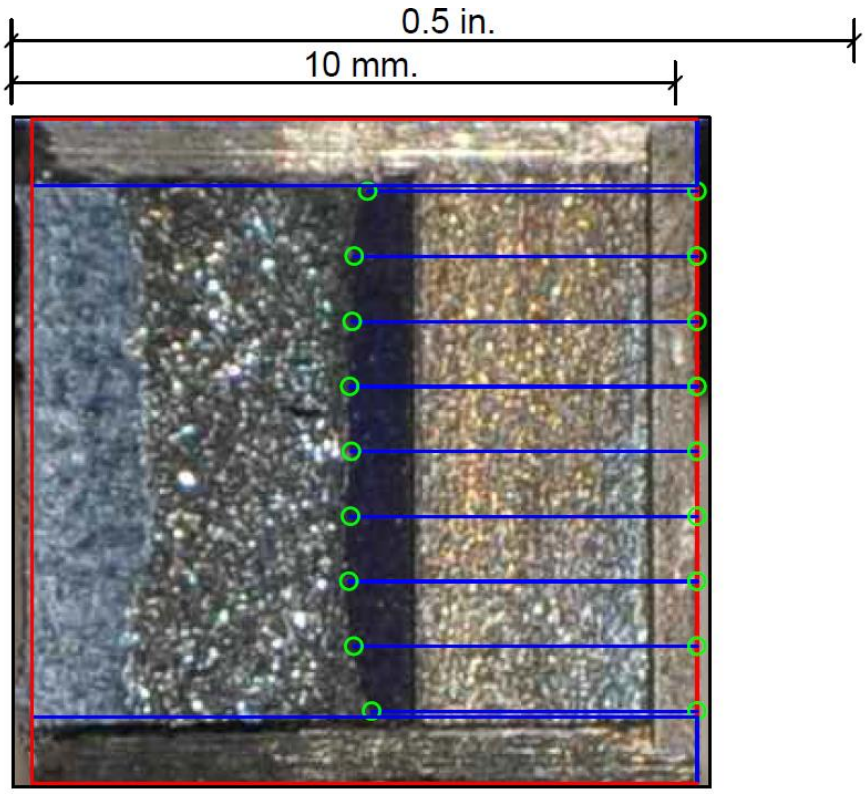

Figure M-38. Specimen B9' Fracture Surface

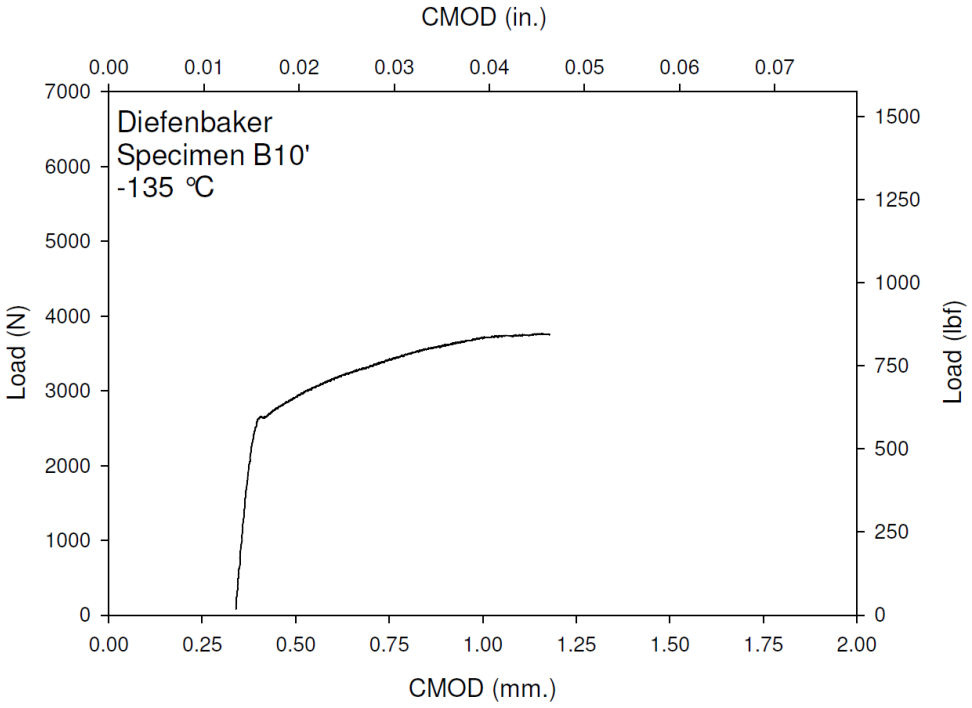

Figure M-39. Specimen B10' Test Record

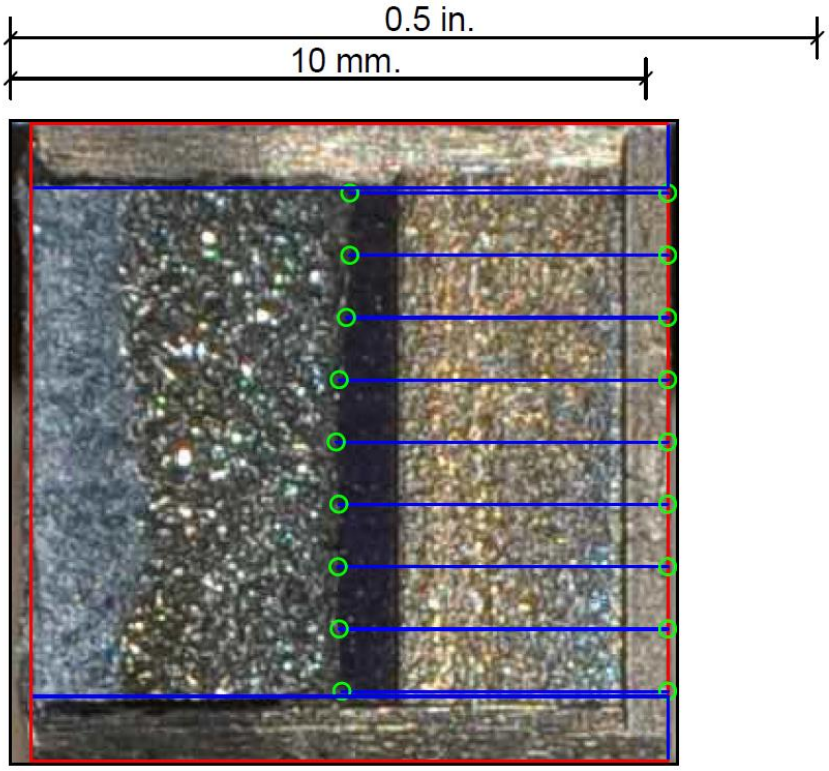

Figure M-40. Specimen B10' Fracture Surface

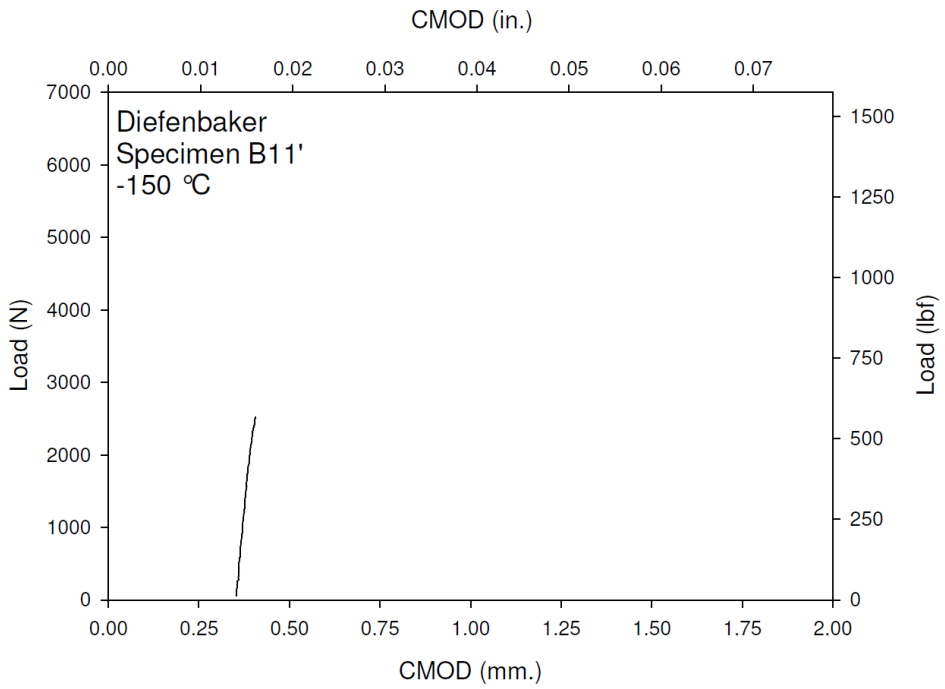

Figure M-41. Specimen B11' Test Record

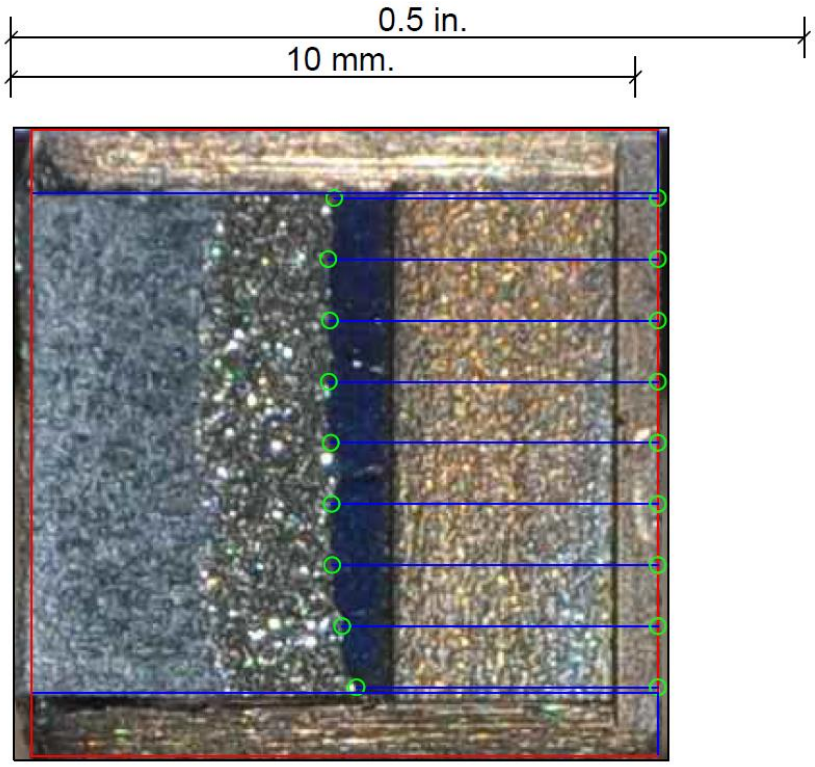

Figure M-42. Specimen B11' Fracture Surface

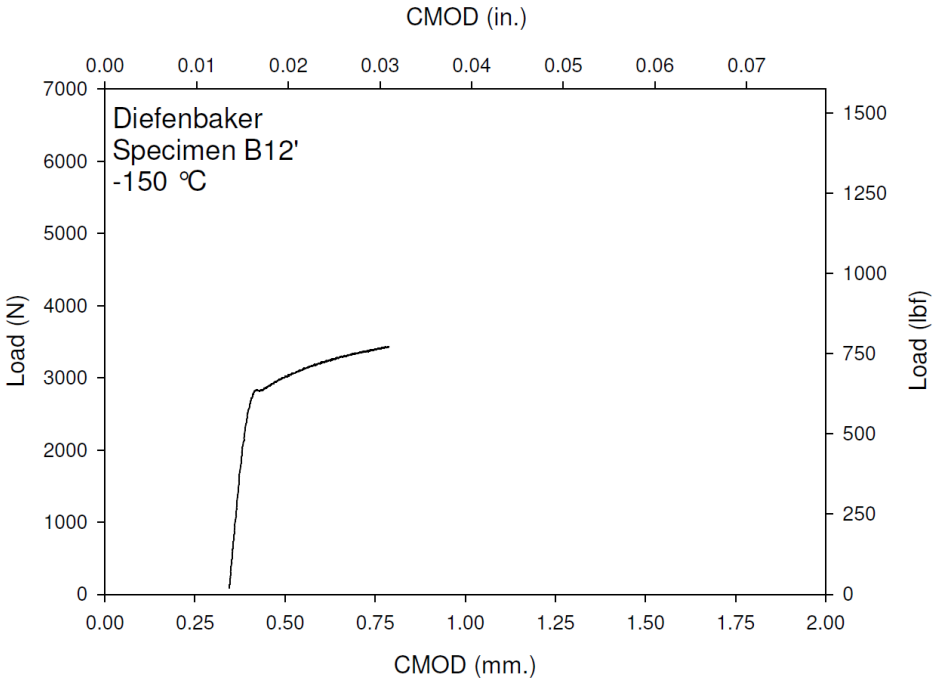

Figure M-43. Specimen B12' Test Record

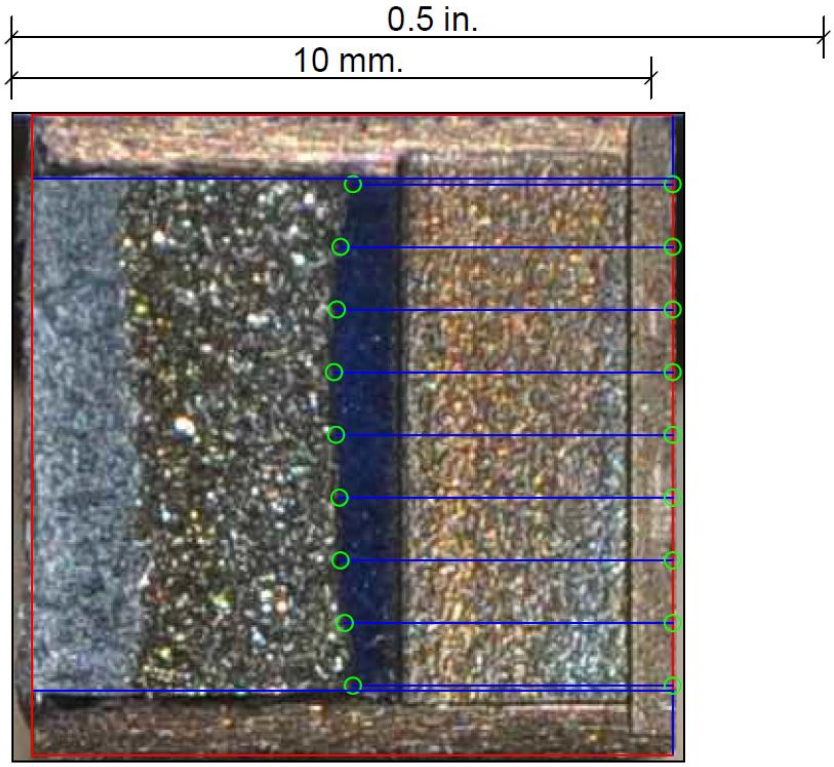

Figure M-44. Specimen B12' Fracture Surface

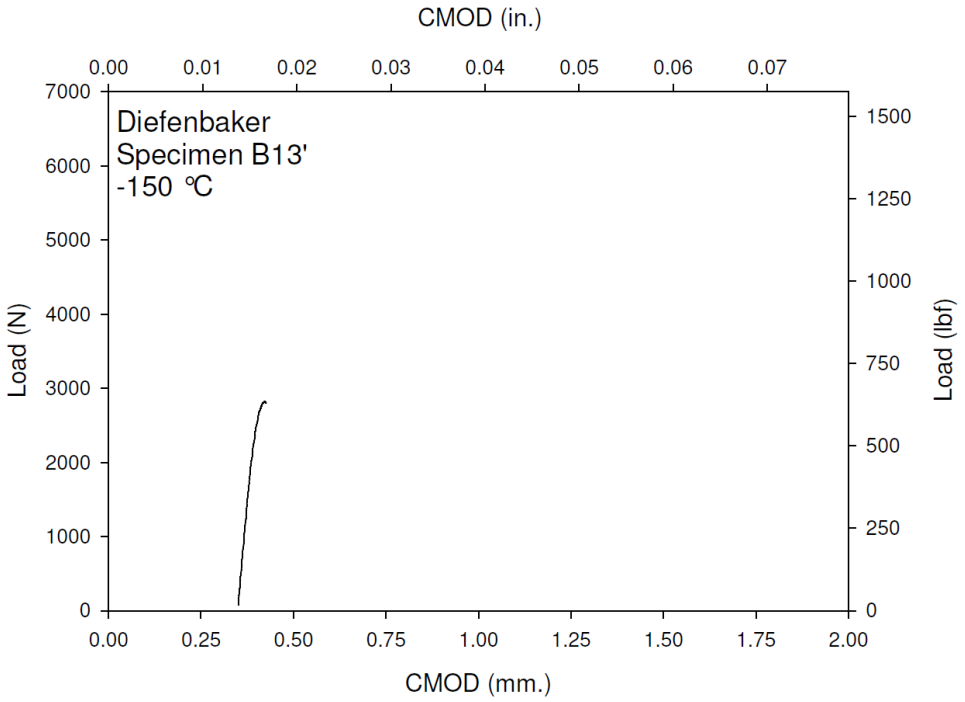

Figure M-45. Specimen B13' Test Record

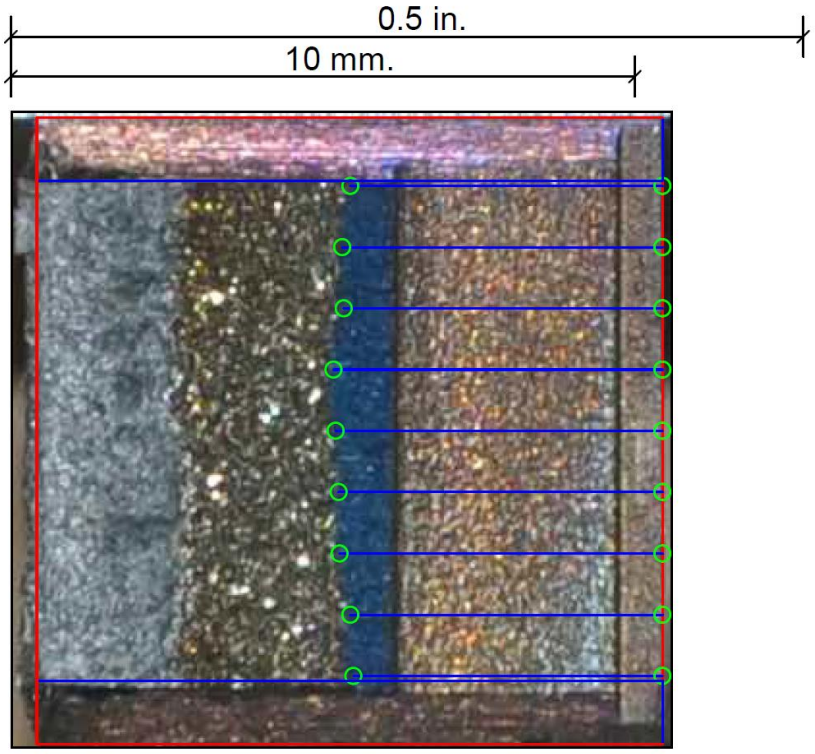

Figure M-46. Specimen B13' Fracture Surface

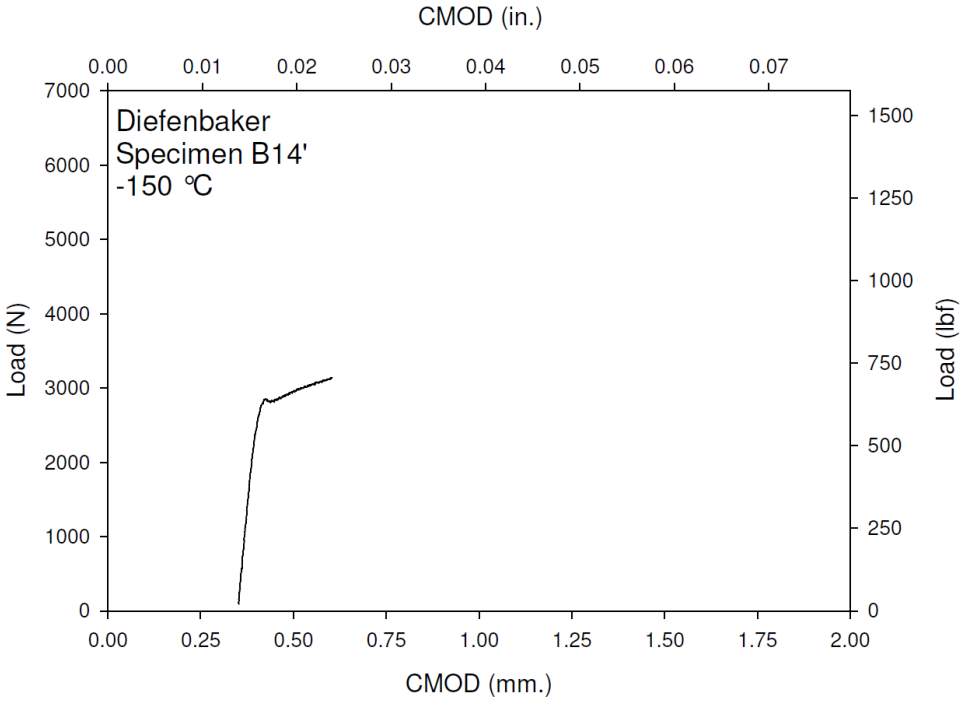

Figure M-47. Specimen B14' Test Record

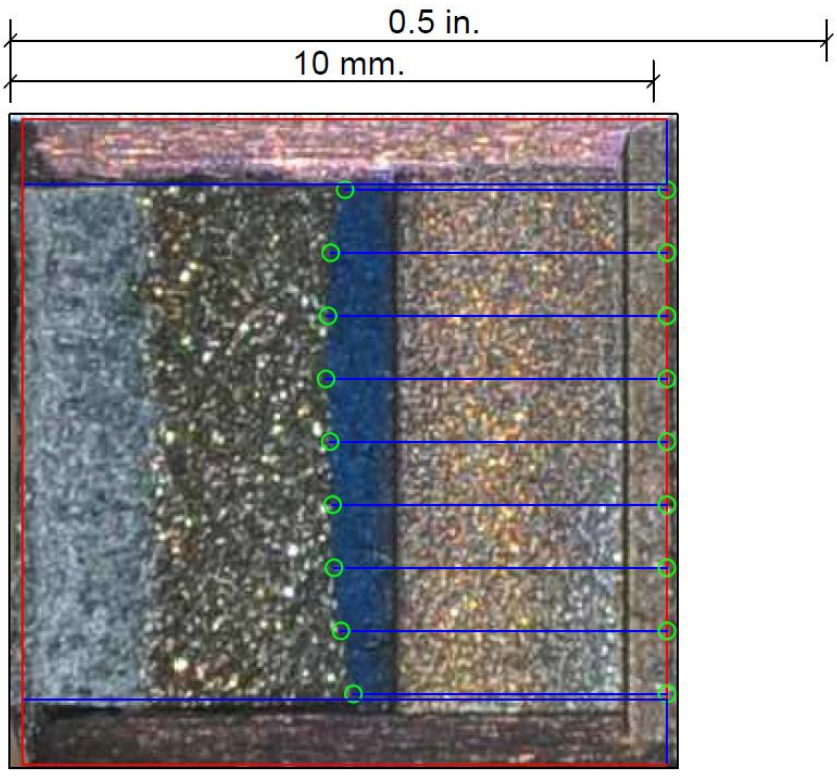

Figure M-48. Specimen B14' Fracture Surface

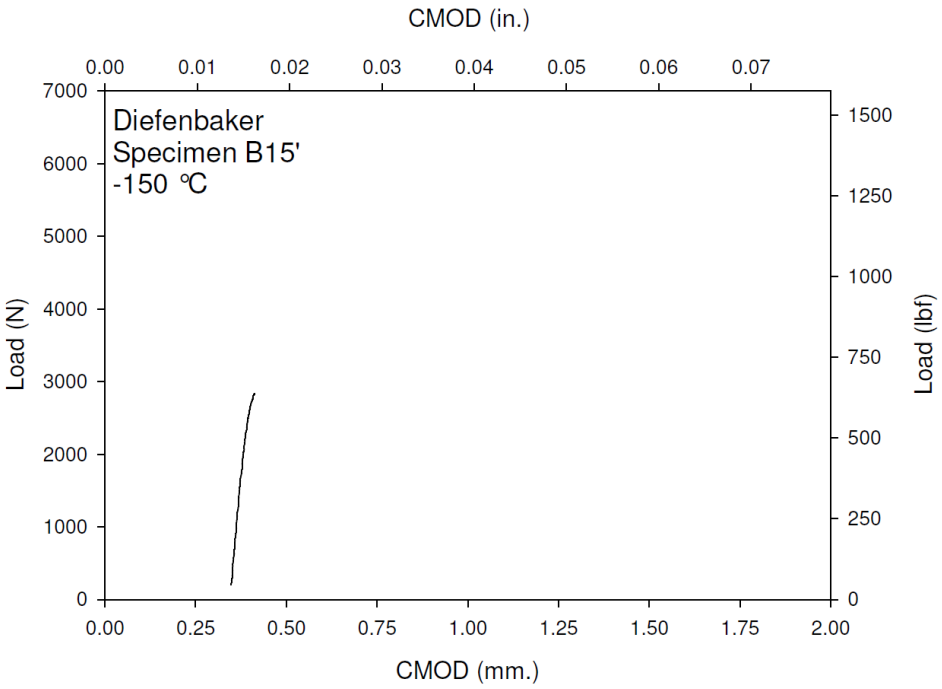

Figure M-49. Specimen B15' Test Record

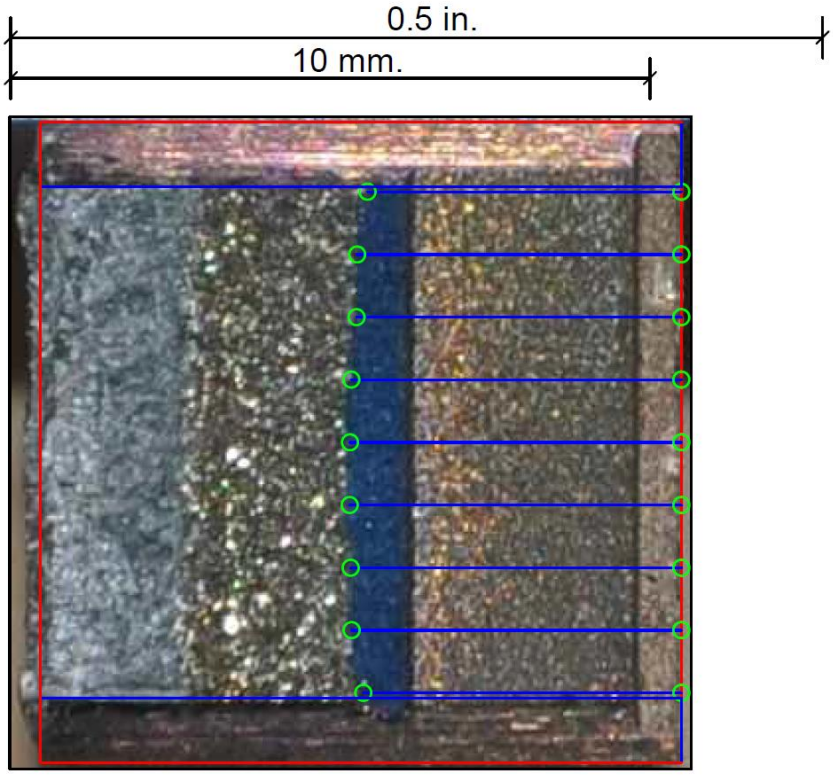

Figure M-50. Specimen B15' Fracture Surface

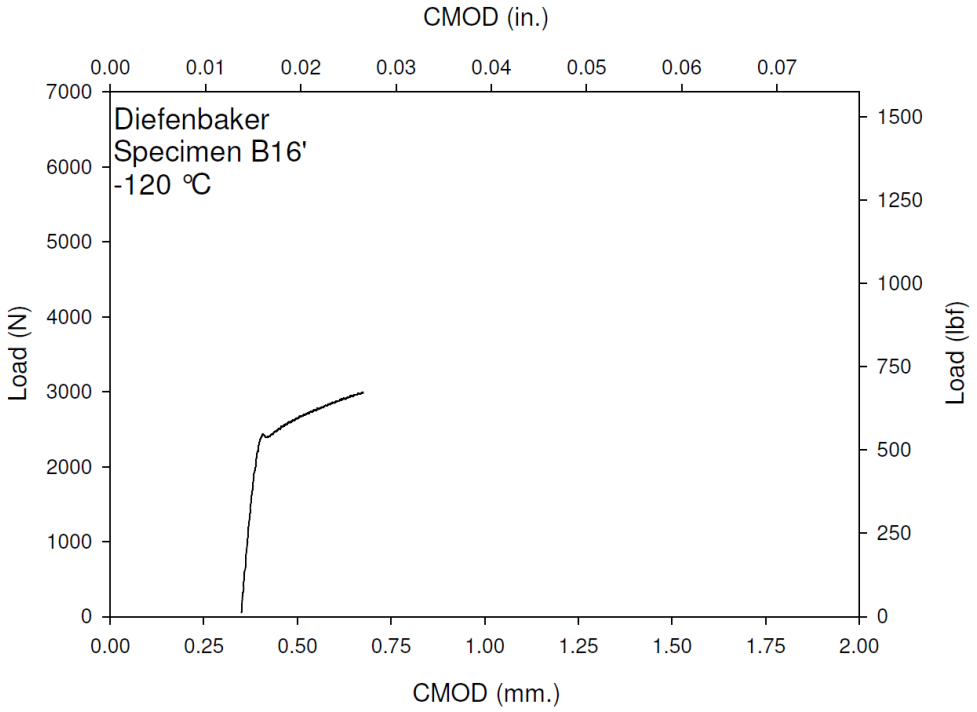

Figure M-51. Specimen B16' Test Record

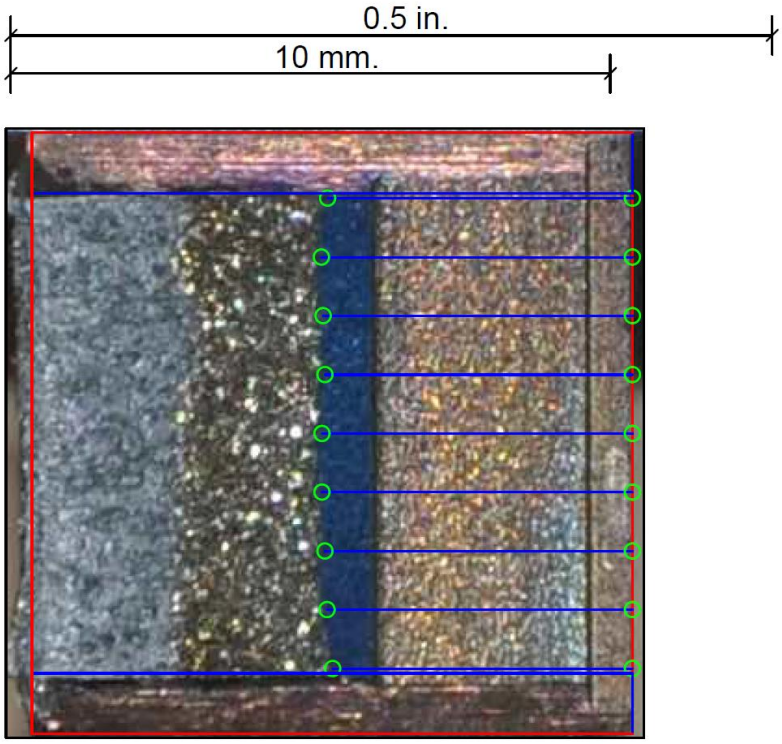

Figure M-52. Specimen B16' Fracture Surface

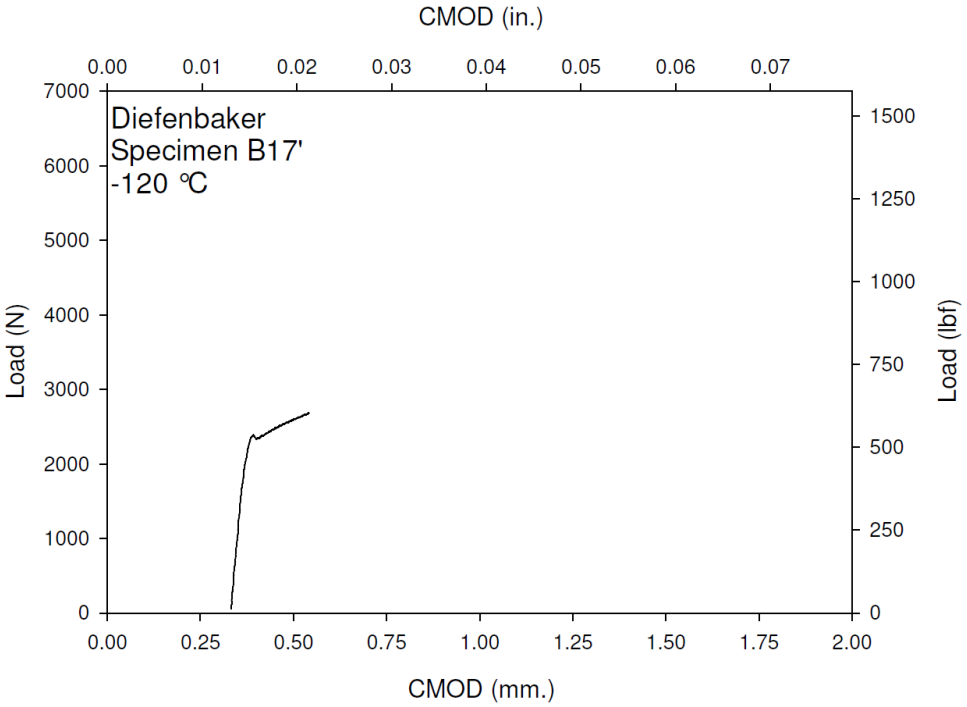

Figure M-53. Specimen B17' Test Record

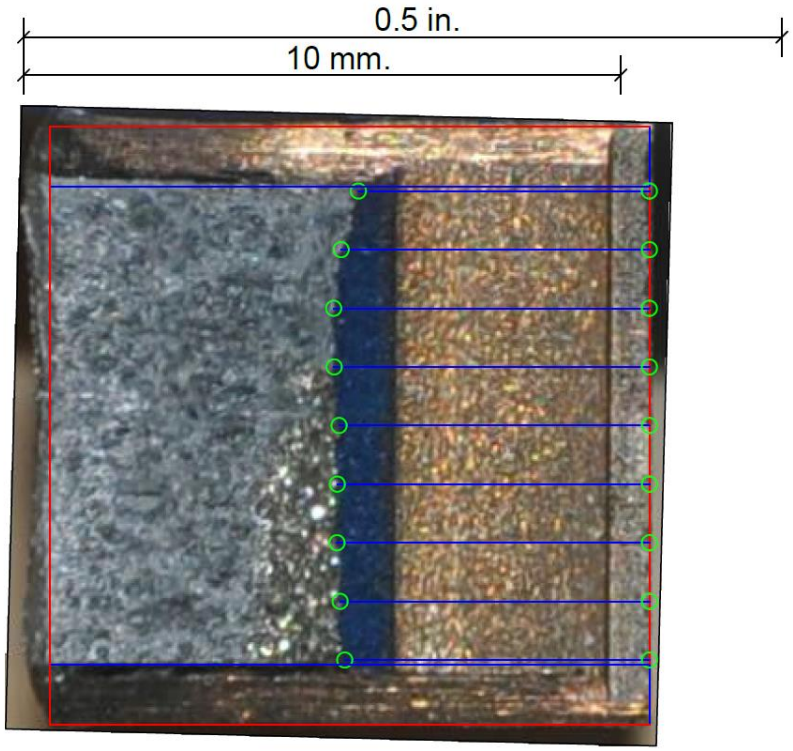

Figure M-54. Specimen B17' Fracture Surface

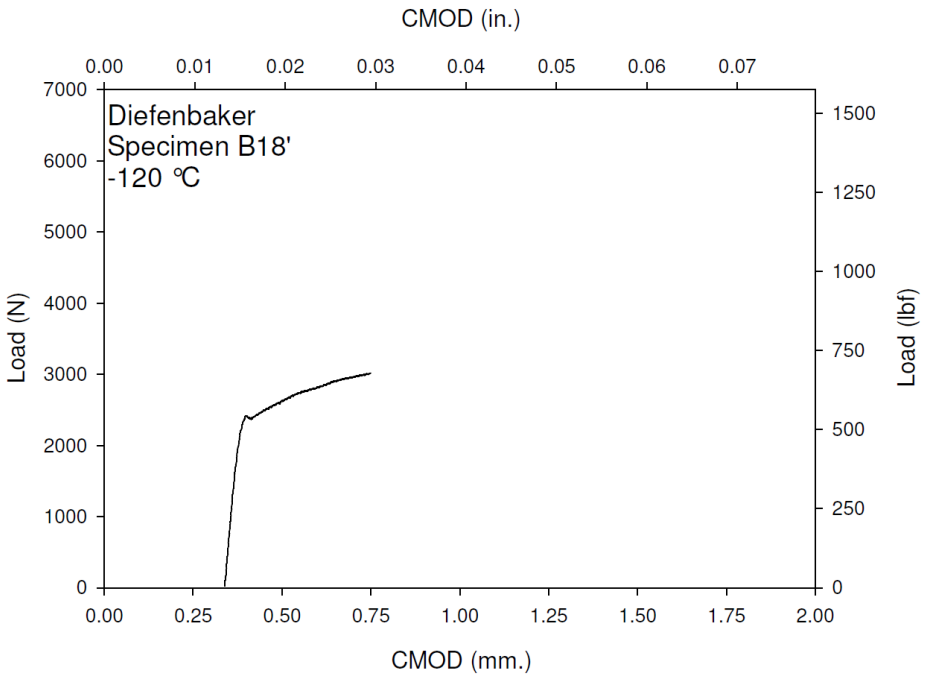

Figure M-55. Specimen B18' Test Record

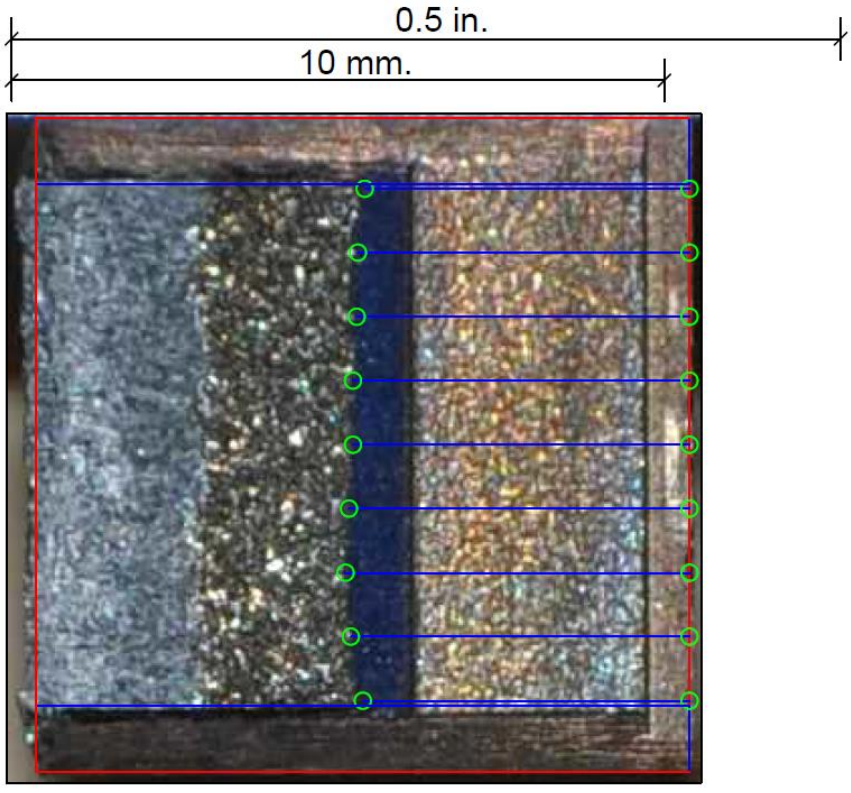

Figure M-56. Specimen B18' Fracture Surface

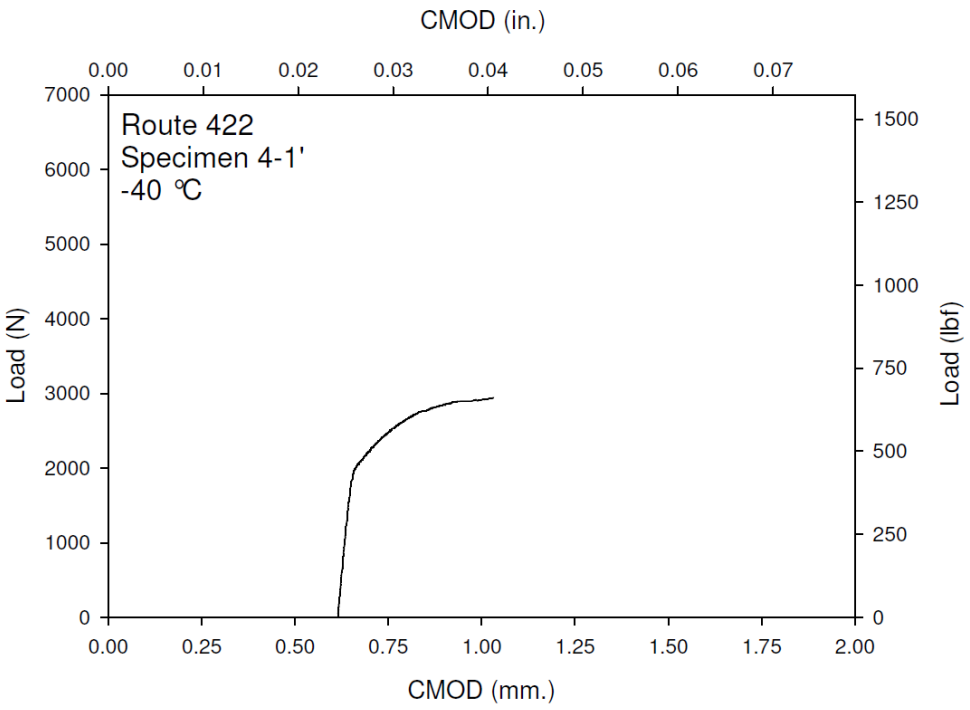

Figure M-57. Specimen 4-1' Test Record

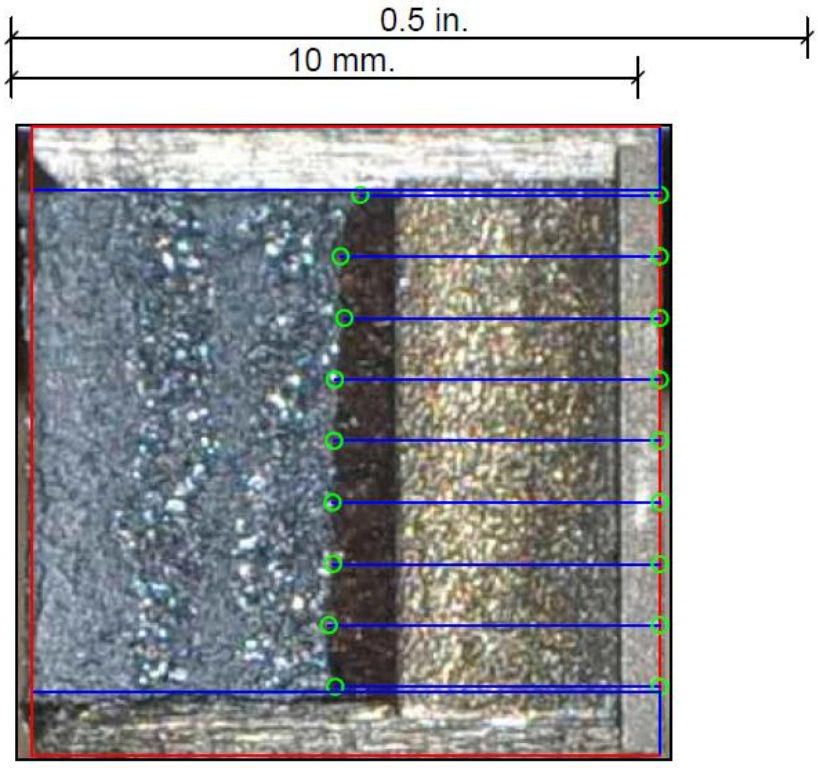

Figure M-58. Specimen 4-1' Fracture Surface

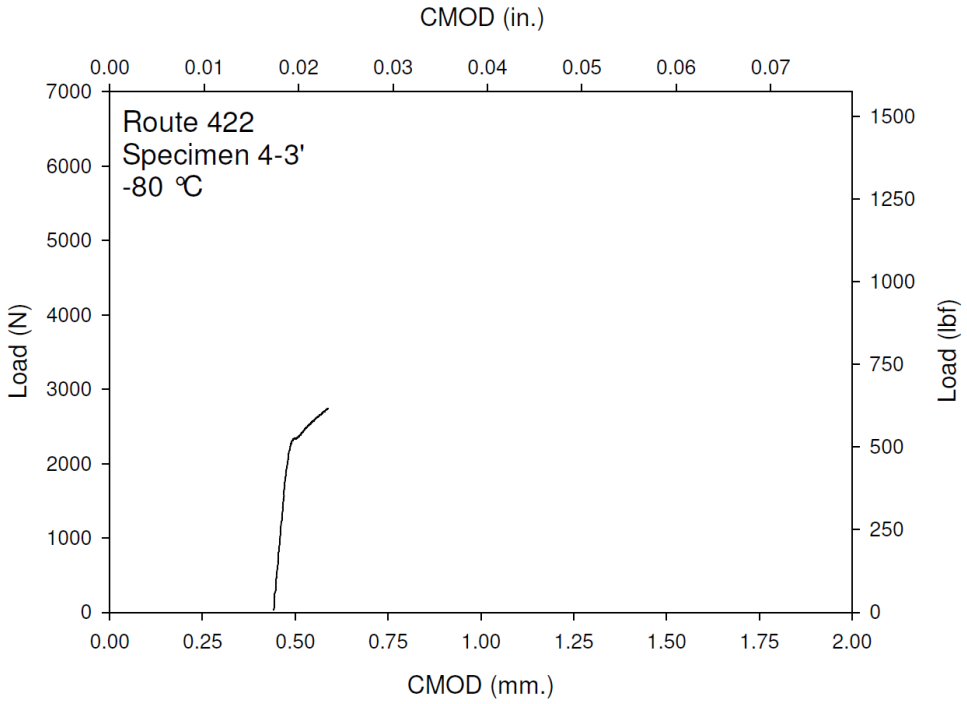

Figure M-59. Specimen 4-3' Test Record

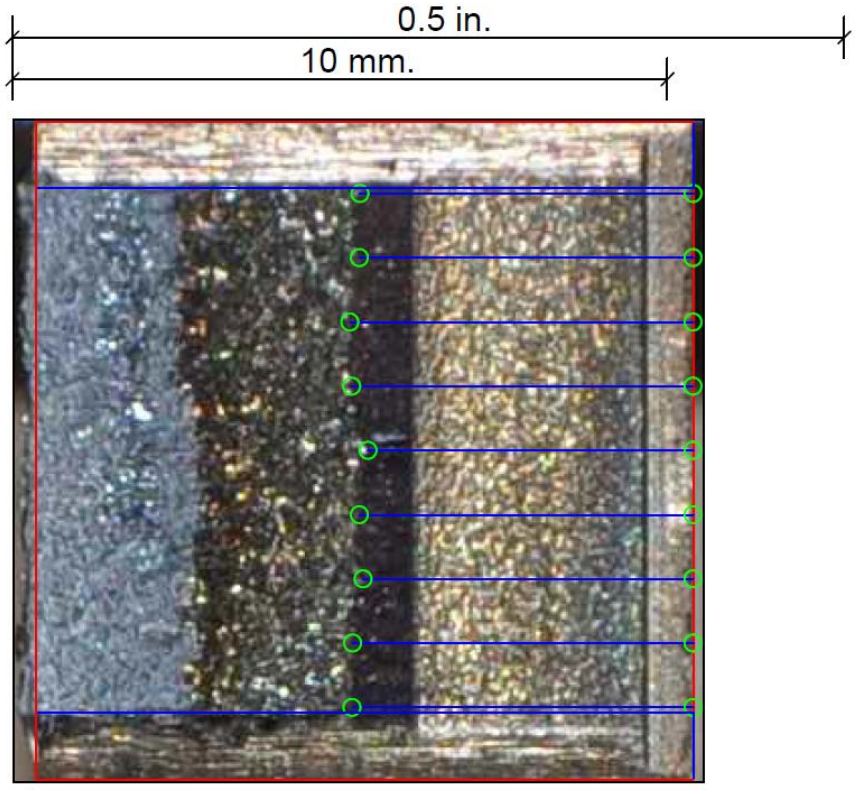

Figure M-60. Specimen 4-3' Fracture Surface

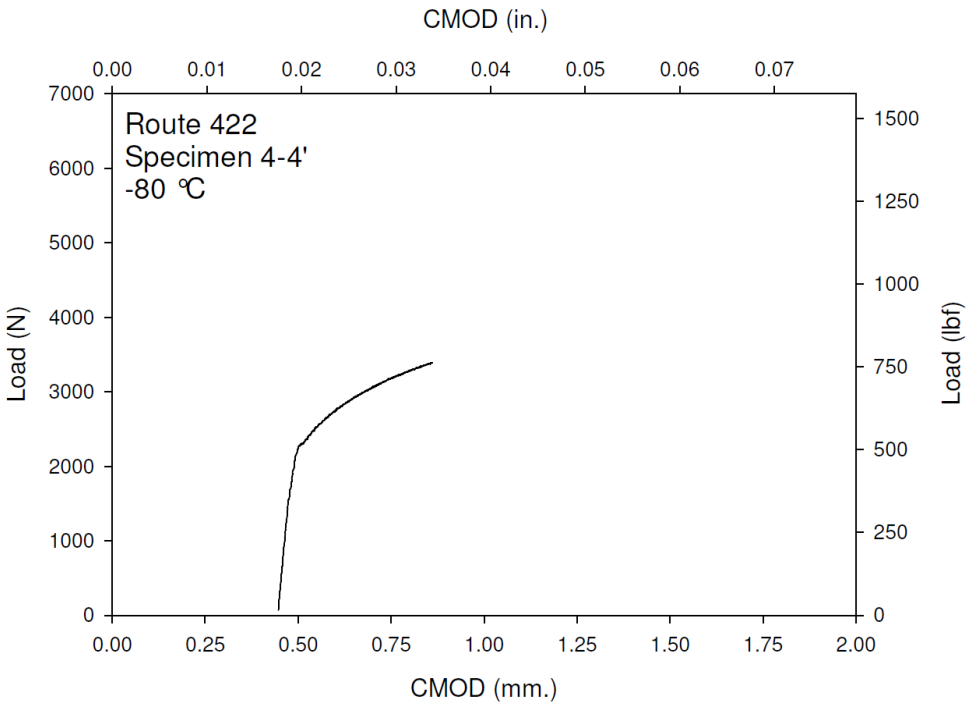

Figure M-61. Specimen 4-4' Test Record

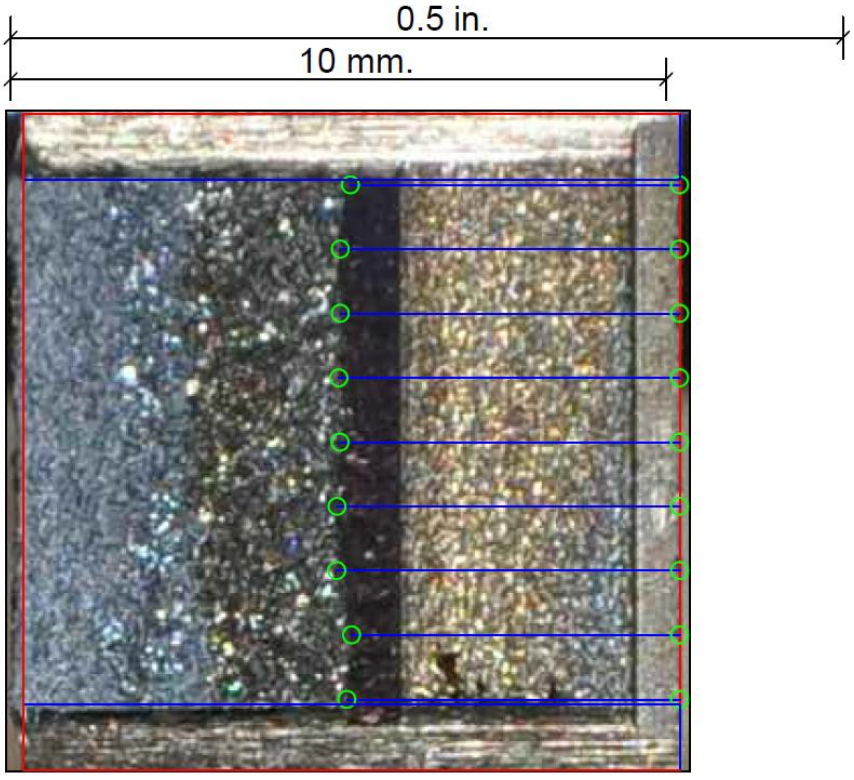

Figure M-62. Specimen 4-4' Fracture Surface

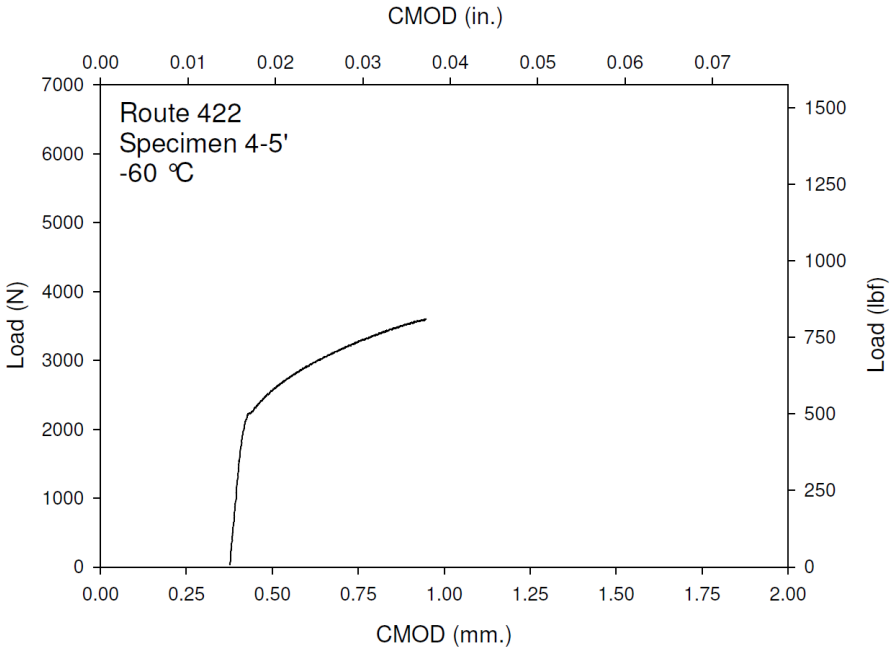

Figure M-63. Specimen 4-5' Test Record

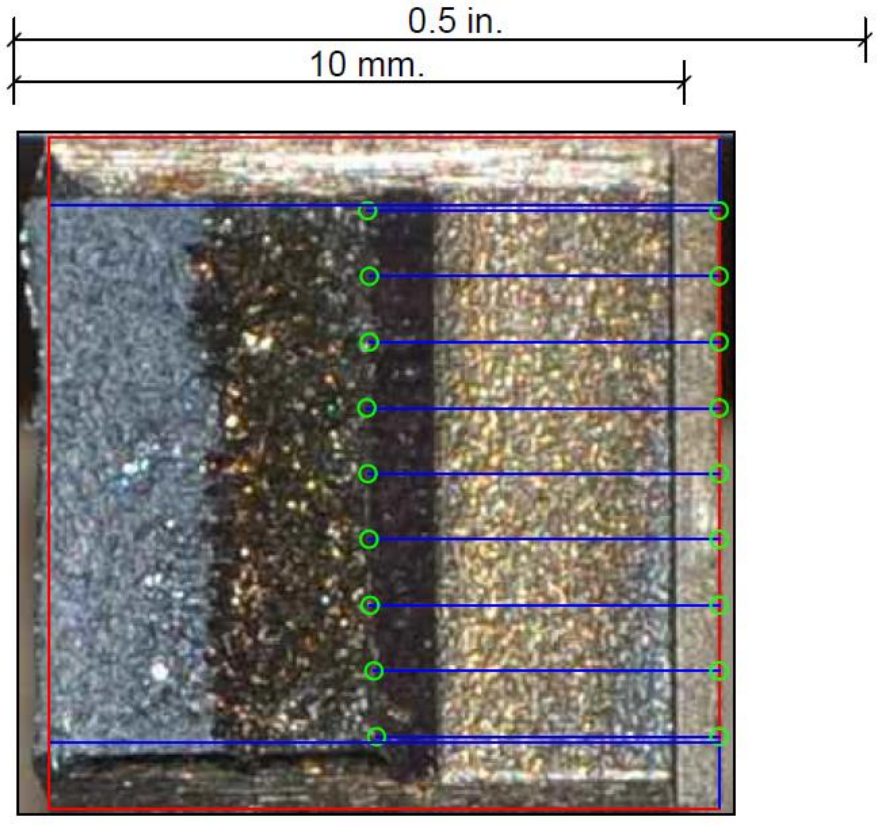

Figure M-64. Specimen 4-5' Fracture Surface

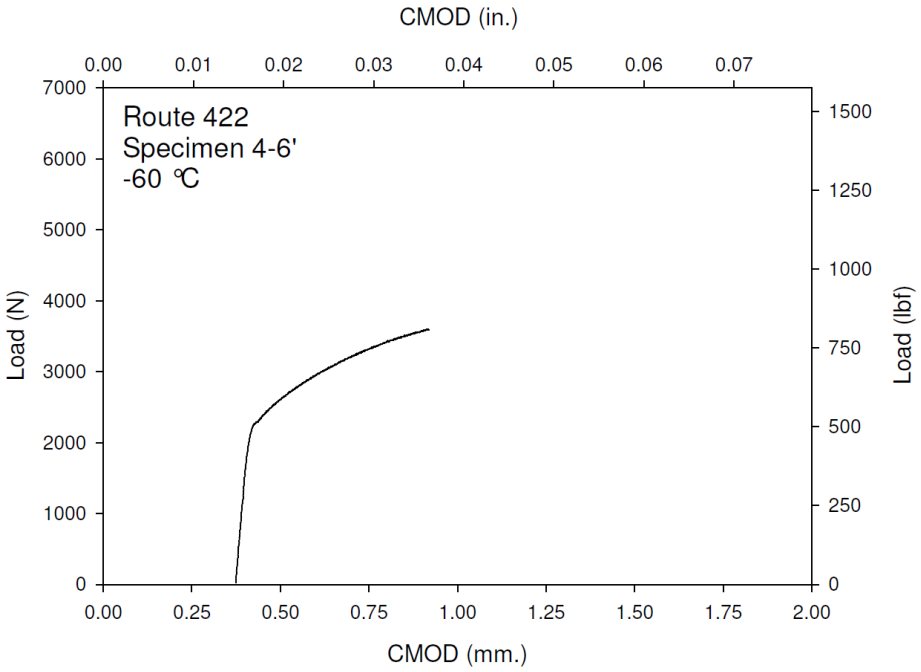

Figure M-65. Specimen 4-6' Test Record

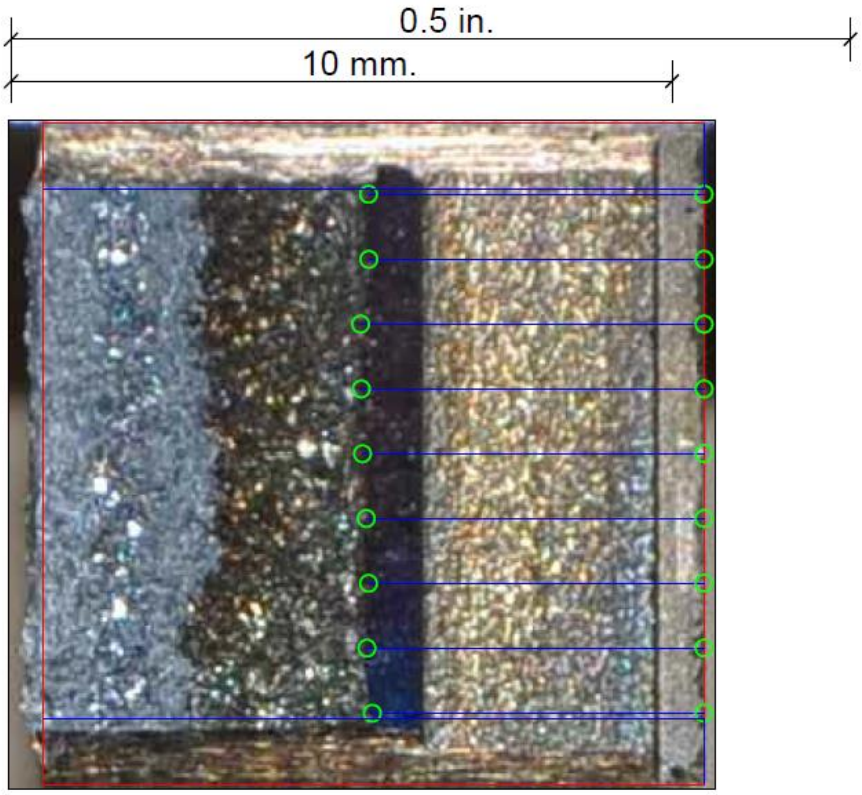

Figure M-66. Specimen 4-6' Fracture Surface

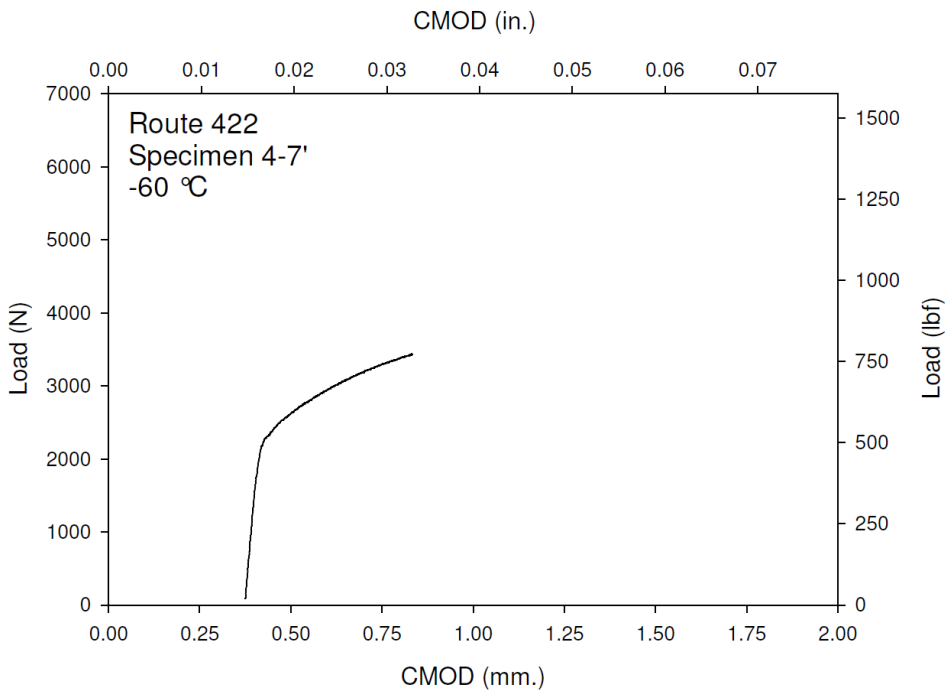

Figure M-67. Specimen 4-7' Test Record

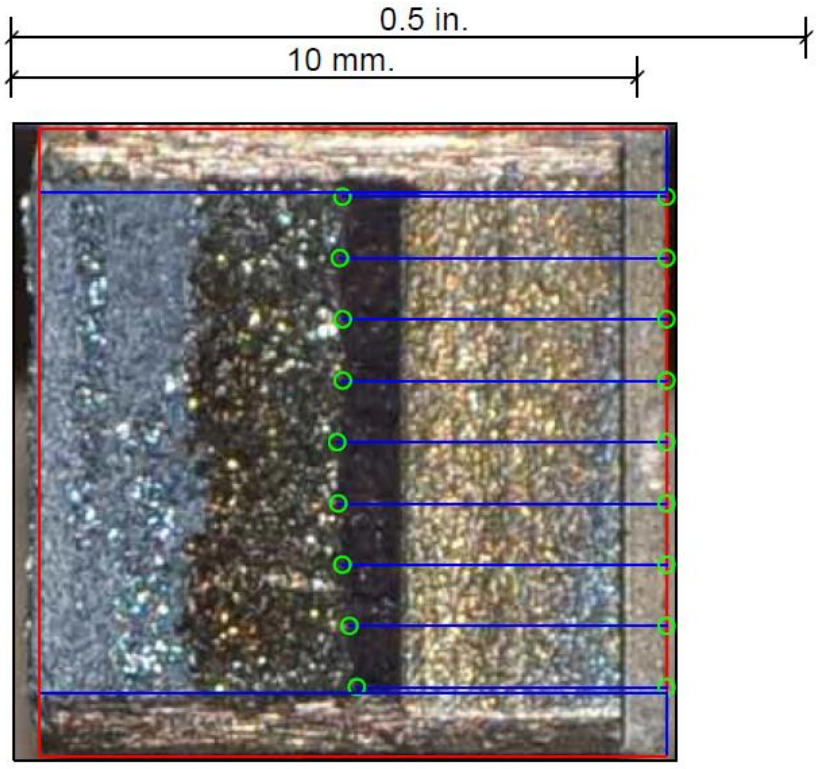

Figure M-68. Specimen 4-7' Fracture Surface

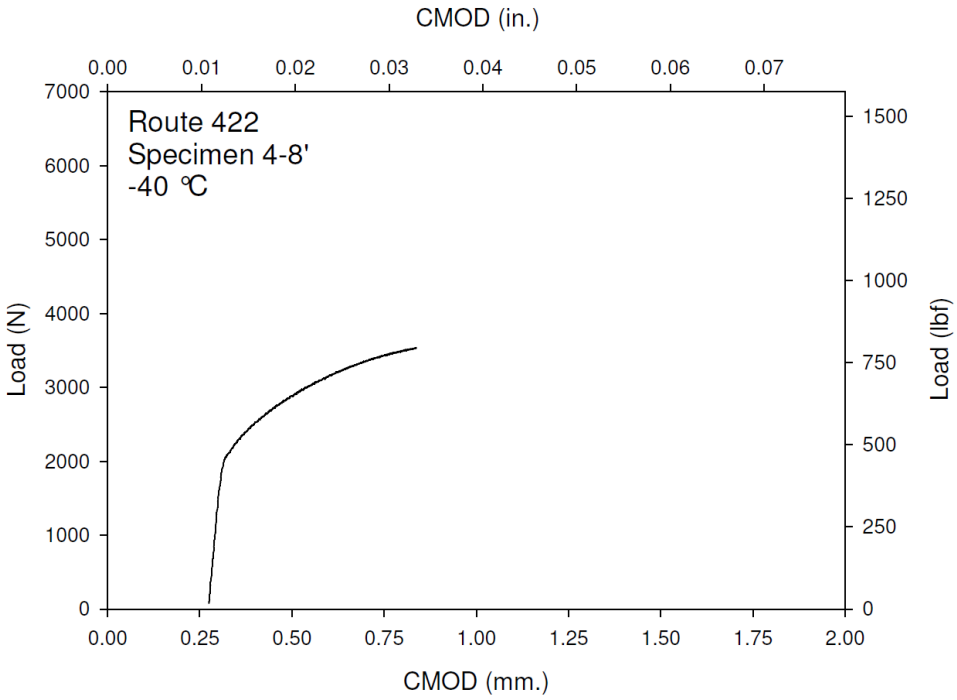

Figure M-69. Specimen 4-8' Test Record

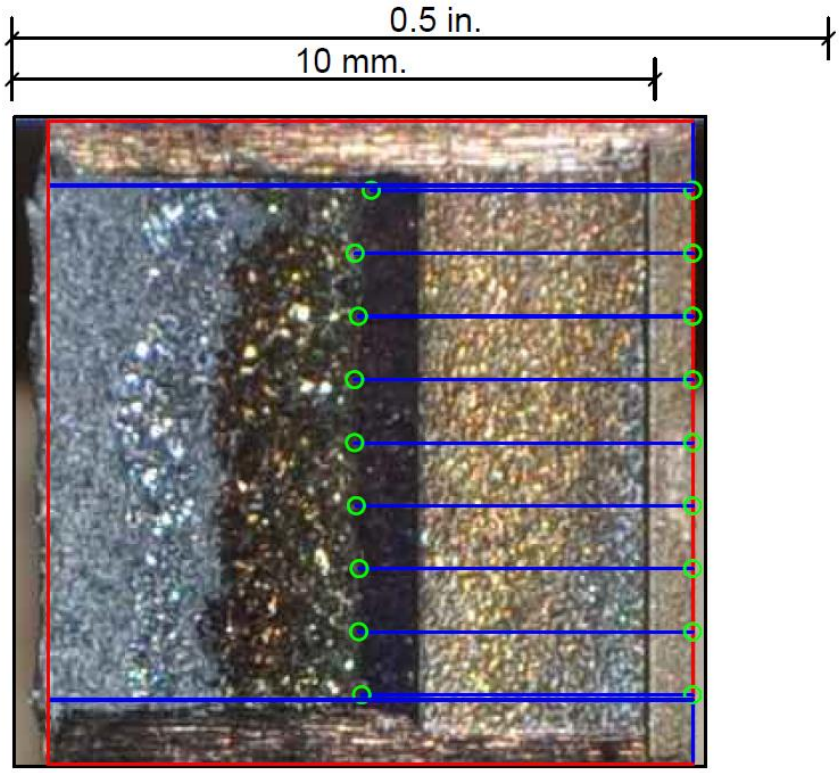

Figure M-70. Specimen 4-8' Fracture Surface

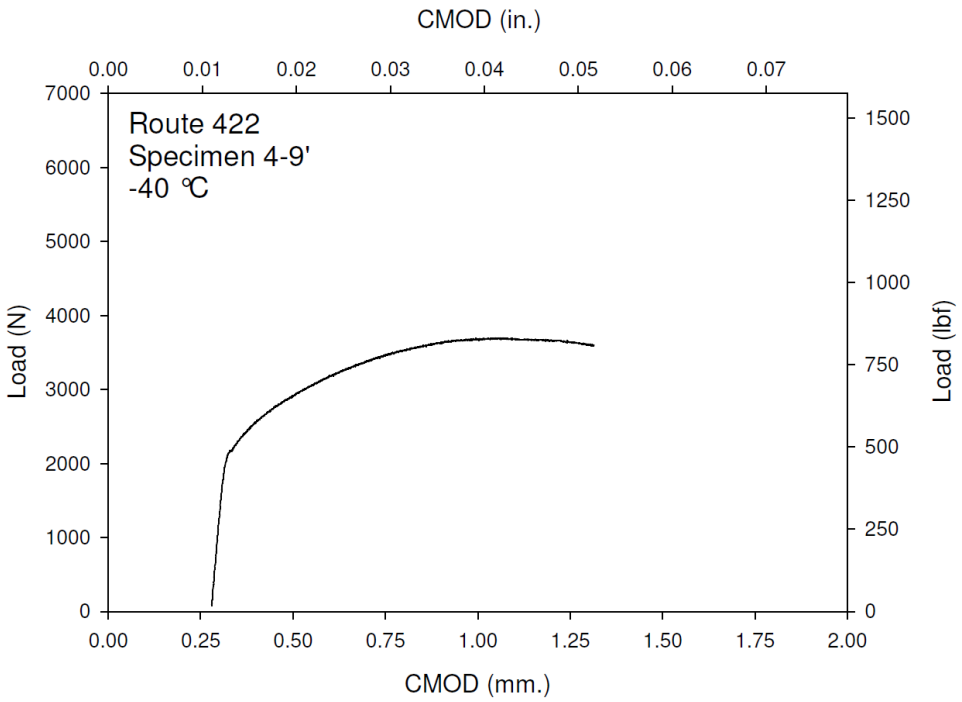

Figure M-71. Specimen 4-9' Test Record

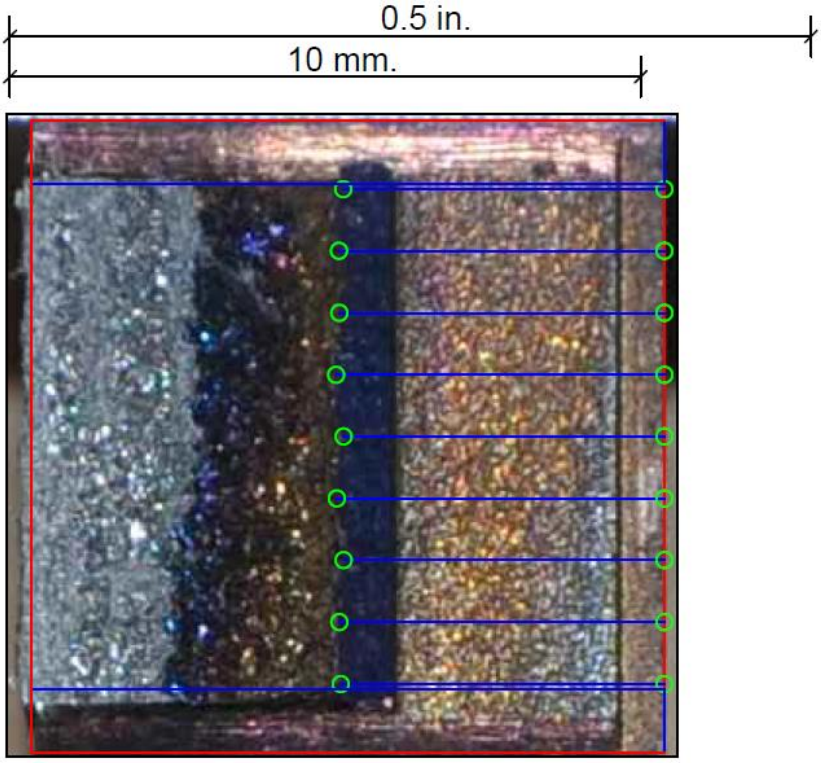

Figure M-72. Specimen 4-9' Fracture Surface

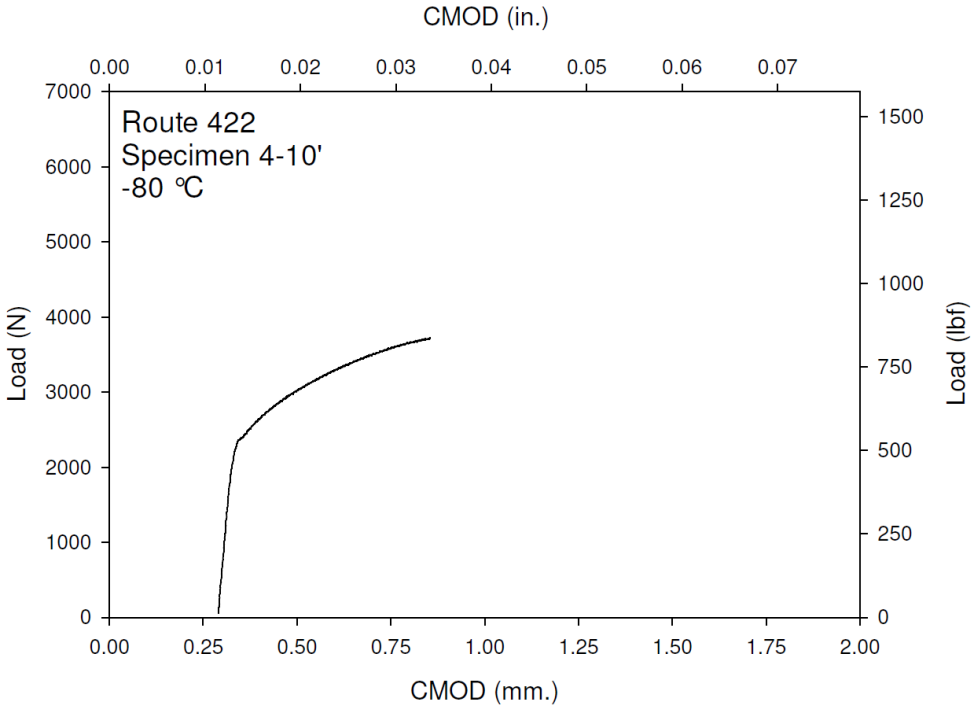

Figure M-73. Specimen 4-10' Test Record

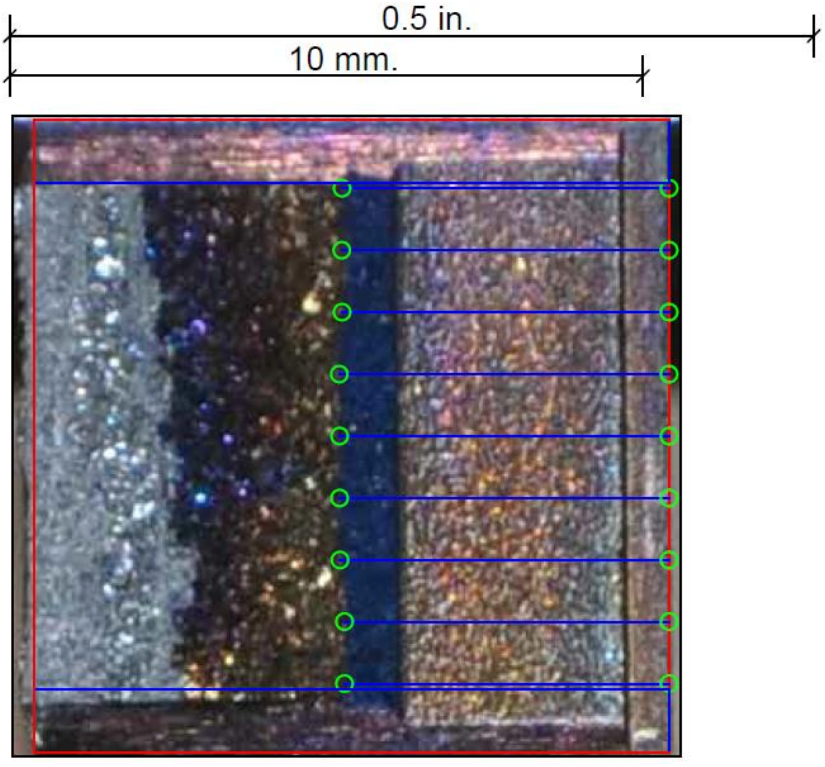

Figure M-74. Specimen 4-10' Fracture Surface

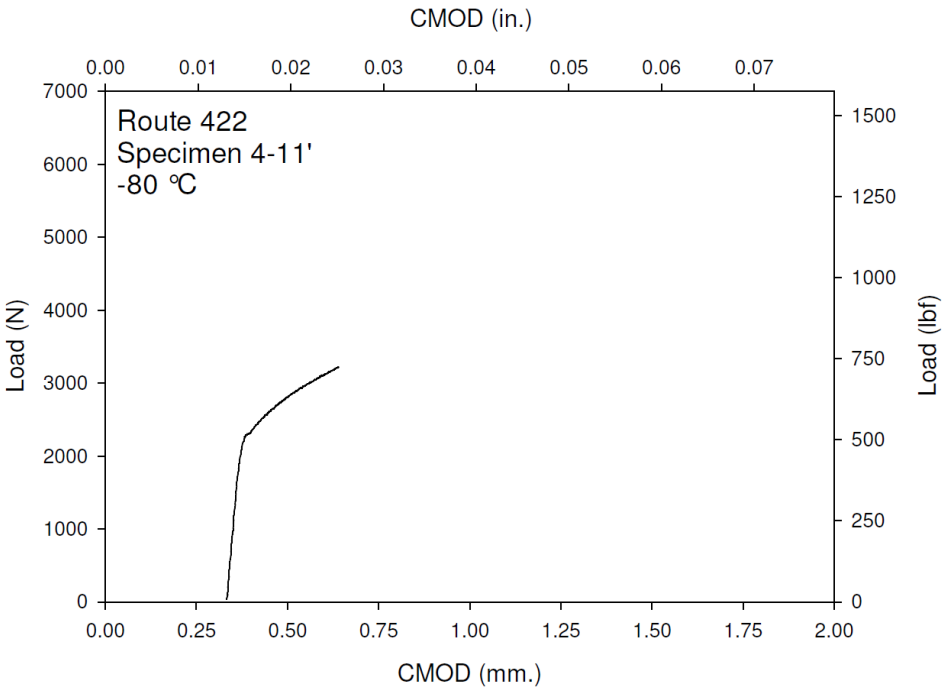

Figure M-75. Specimen 4-11' Test Record

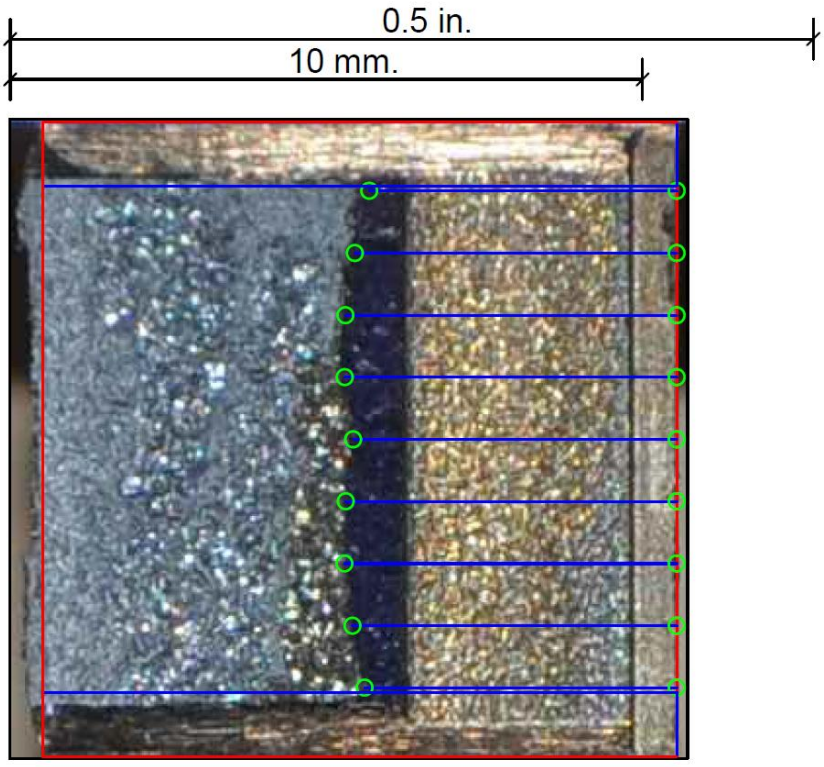

Figure M-76. Specimen 4-11' Fracture Surface

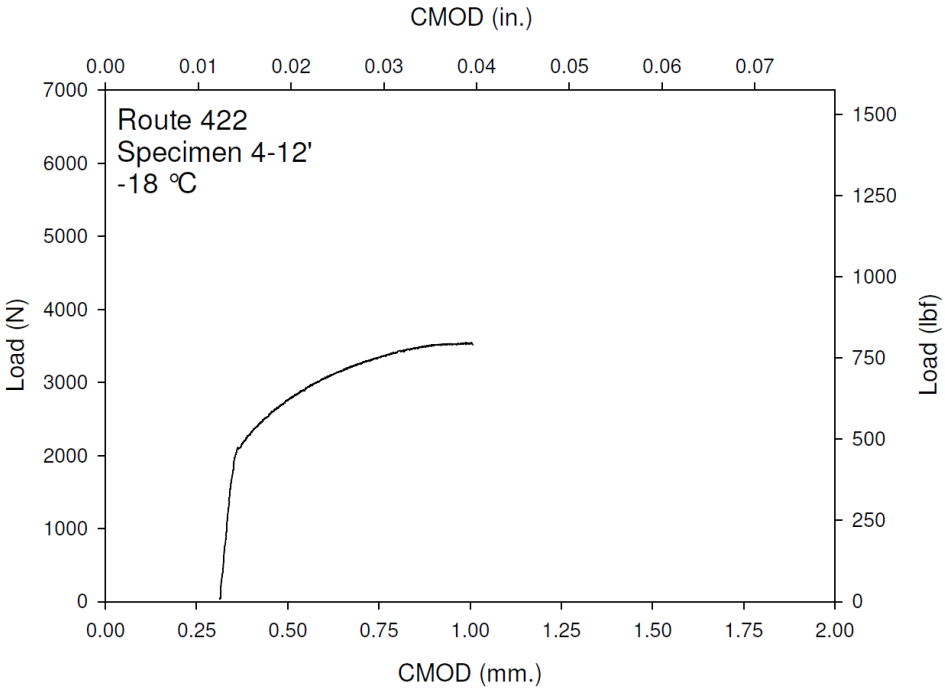

Figure M-77. Specimen 4-12' Test Record

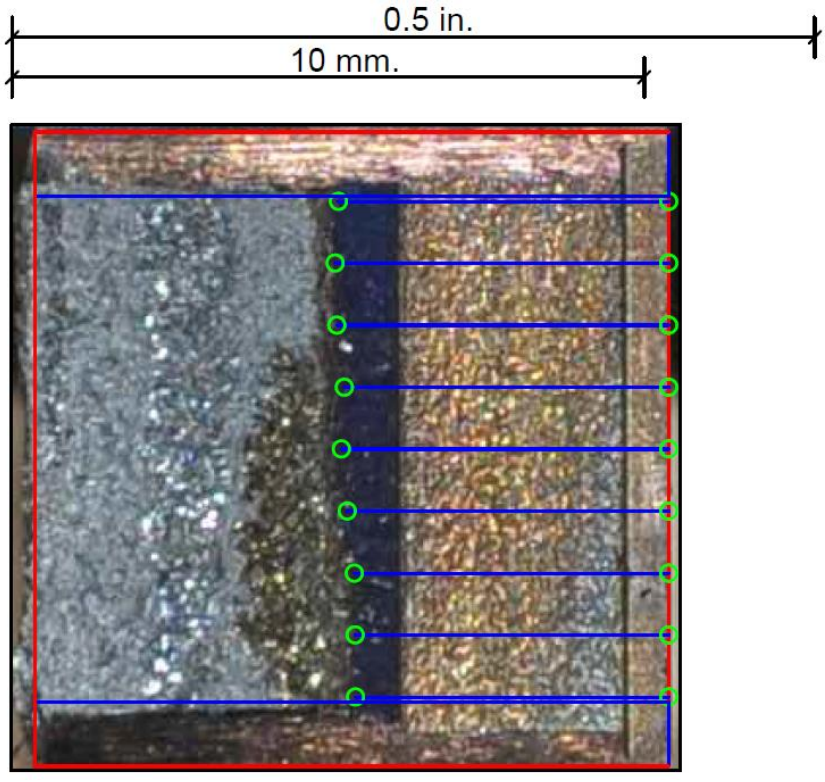

Figure M-78. Specimen 4-12' Fracture Surface

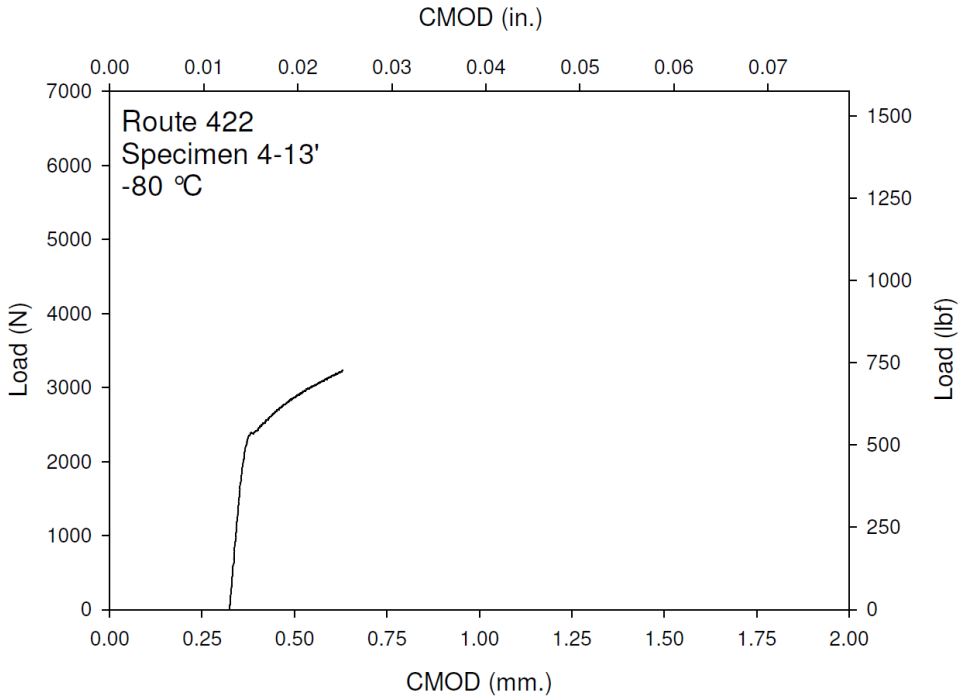

Figure M-79. Specimen 4-13' Test Record

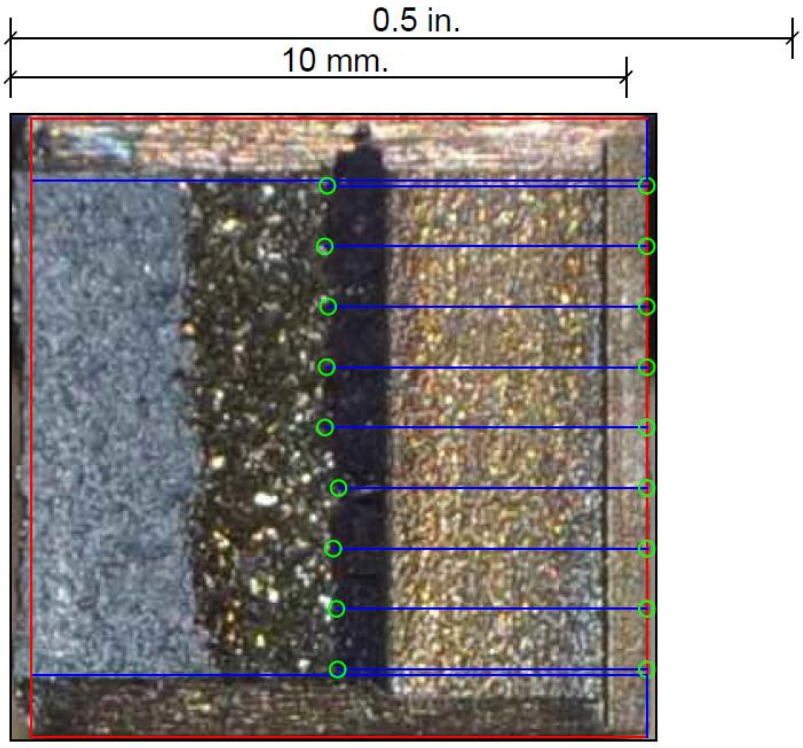

Figure M-80. Specimen 4-13' Fracture Surface

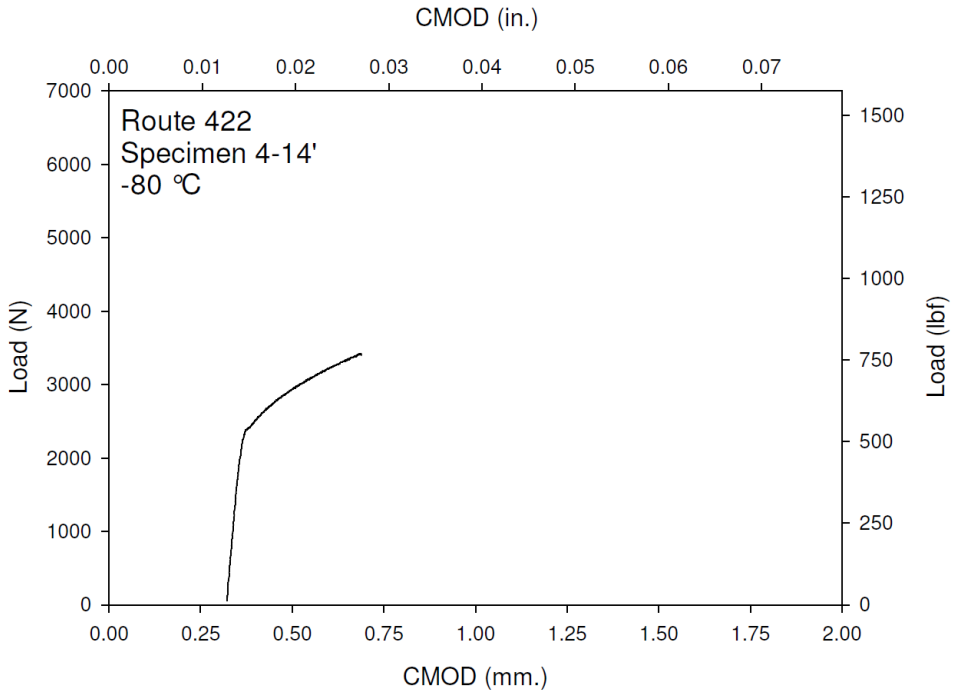

Figure M-81. Specimen 4-14' Test Record

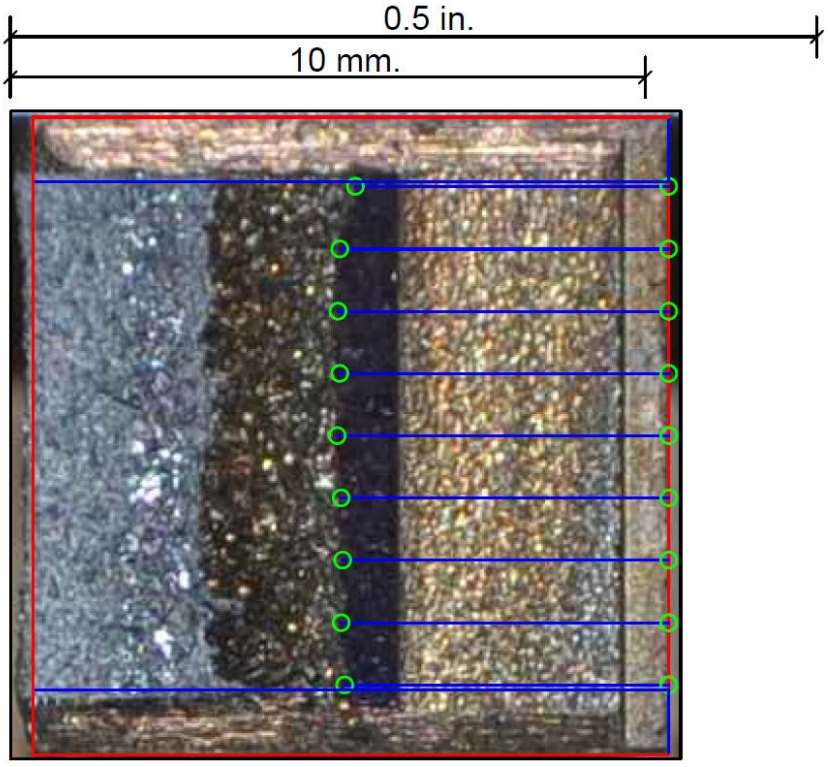

Figure M-82. Specimen 4-14' Fracture Surface

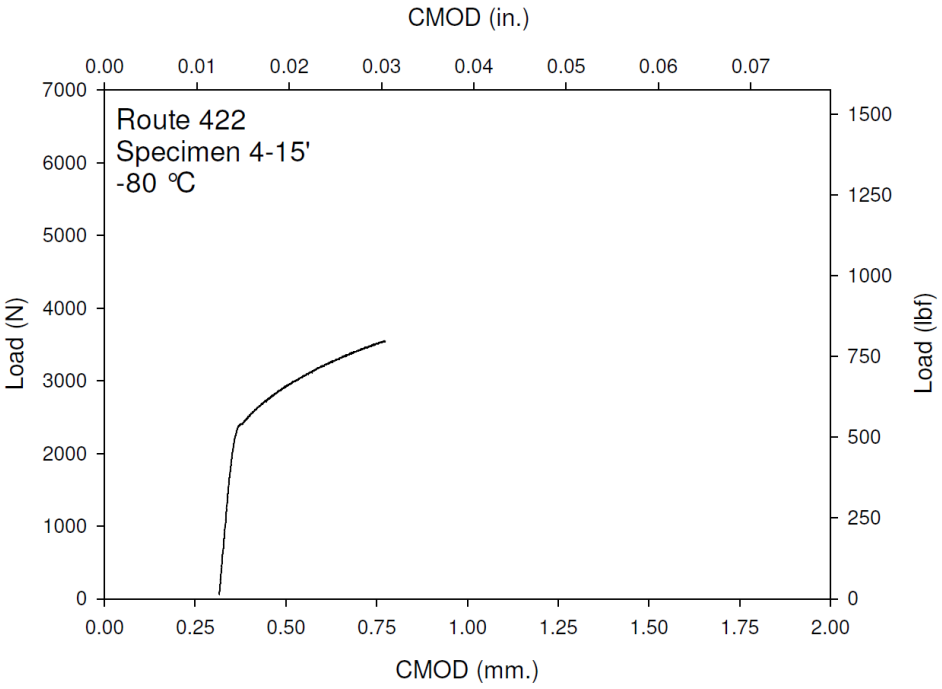

Figure M-83. Specimen 4-15' Test Record

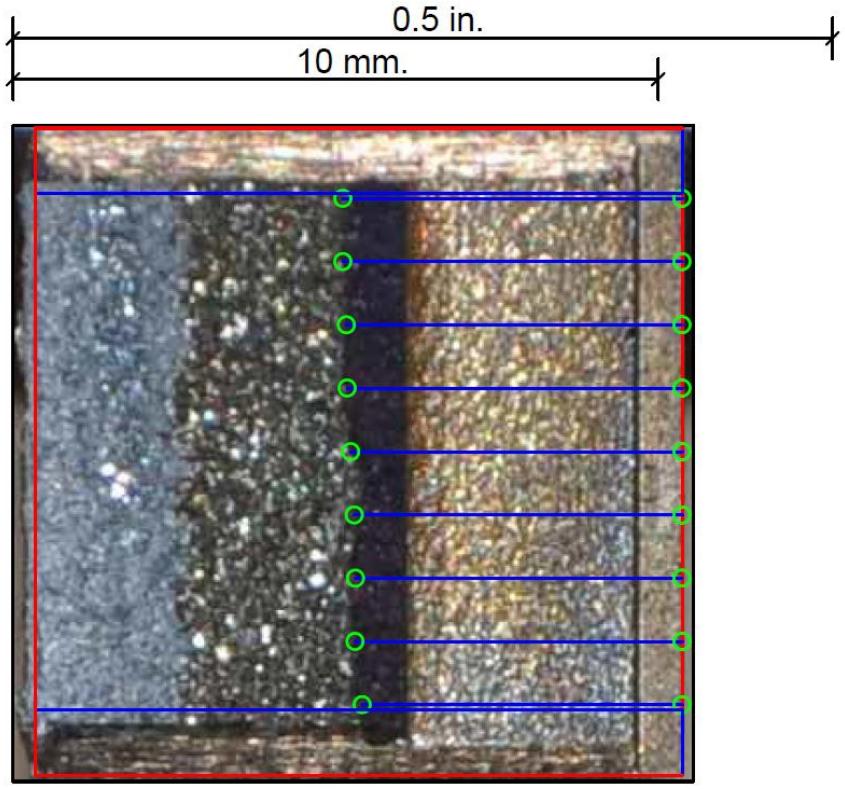

Figure M-84. Specimen 4-15' Fracture Surface

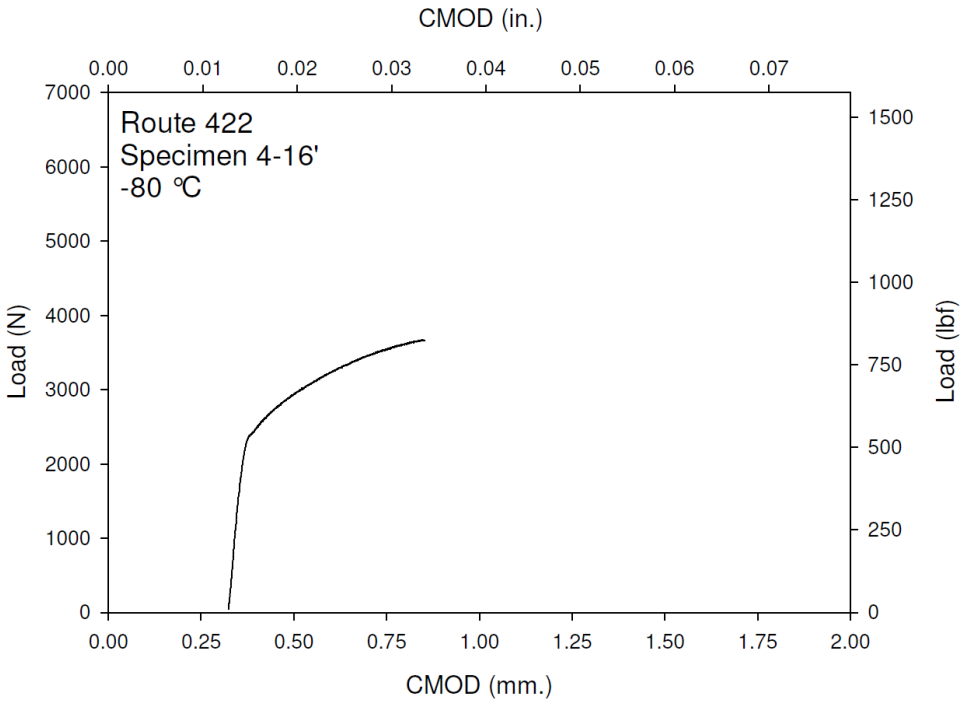

Figure M-85. Specimen 4-16' Test Record

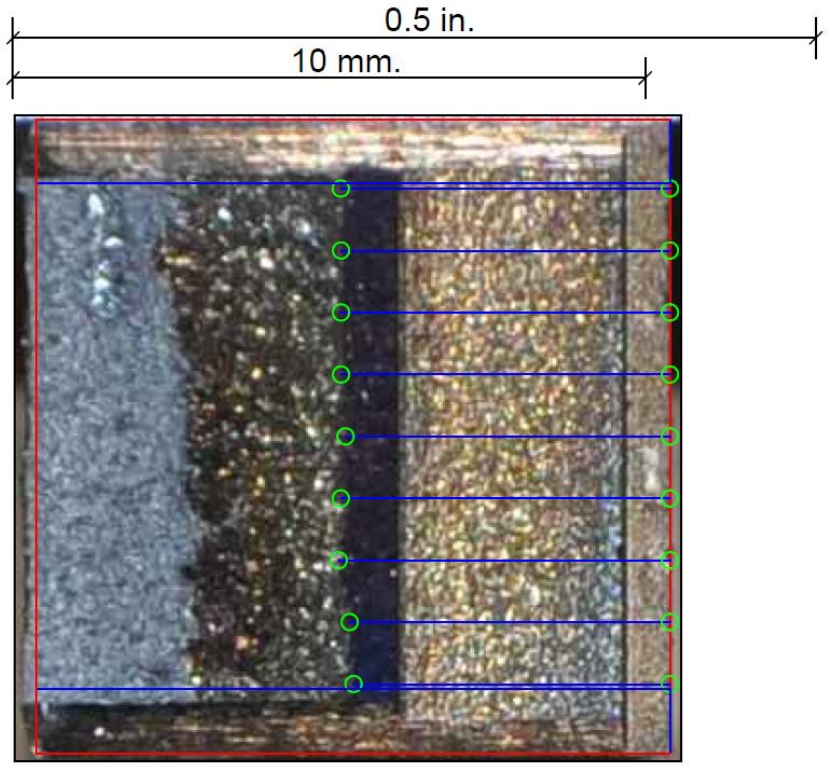

Figure M-86. Specimen 4-16' Fracture Surface

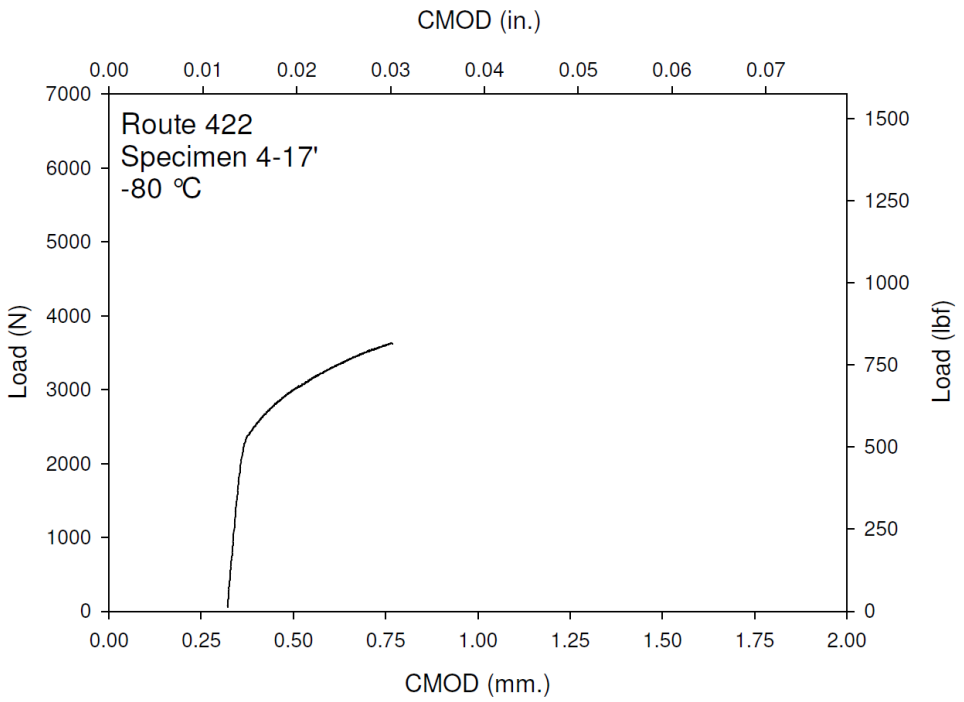

Figure M-87. Specimen 4-17' Test Record

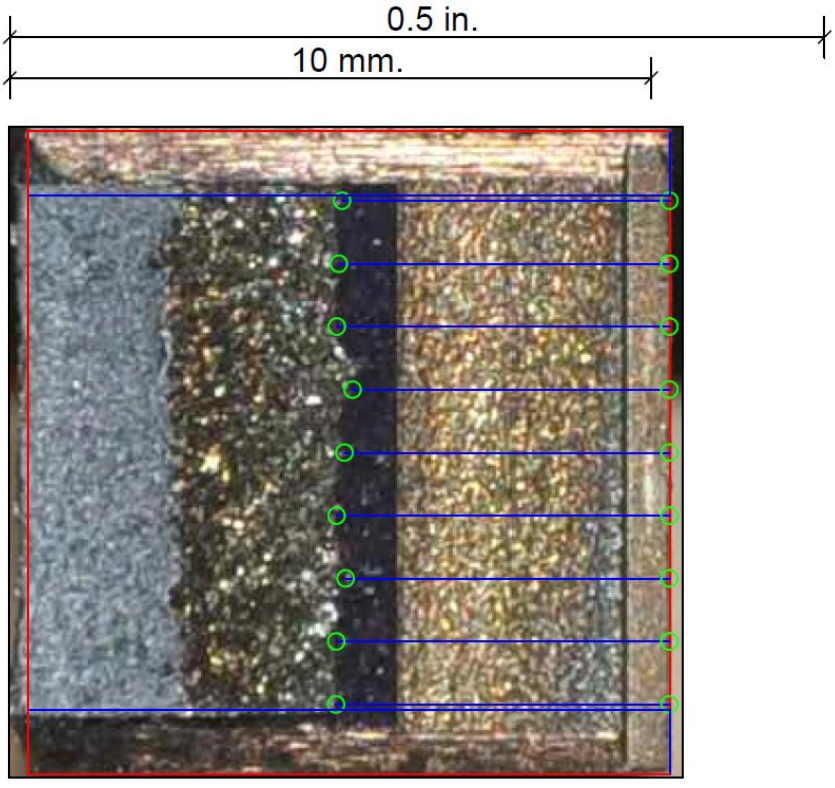

Figure M-88. Specimen 4-17' Fracture Surface

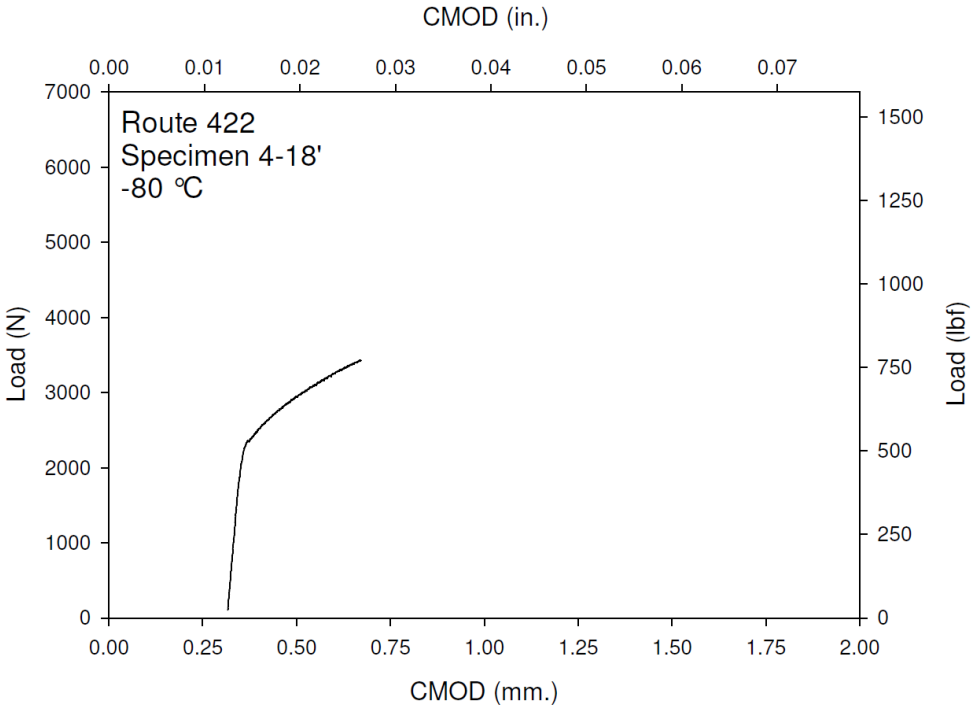

Figure M-89. Specimen 4-18' Test Record

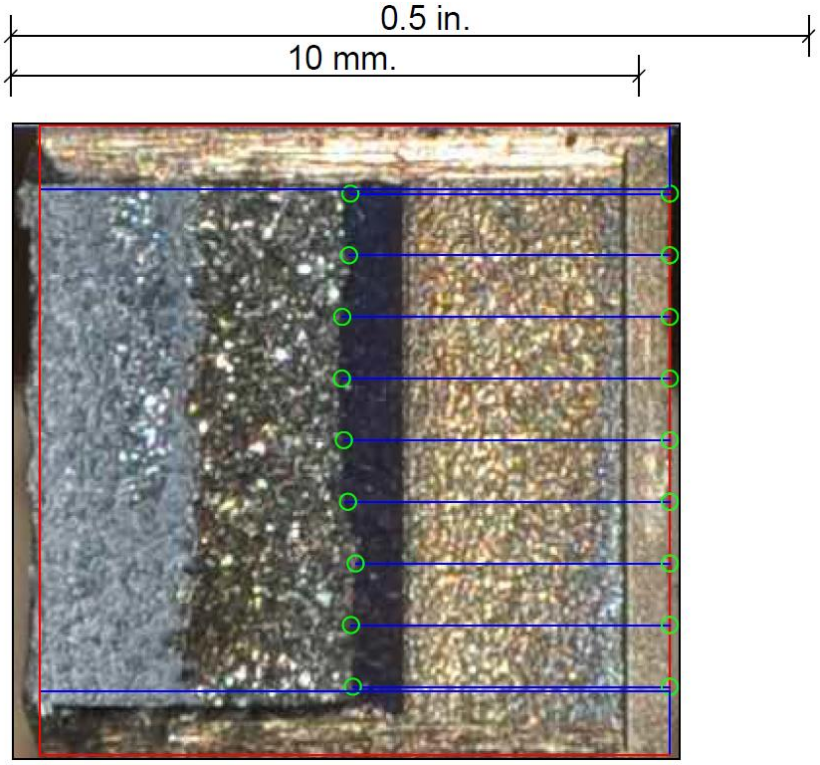

Figure M-90. Specimen 4-18' Fracture Surface

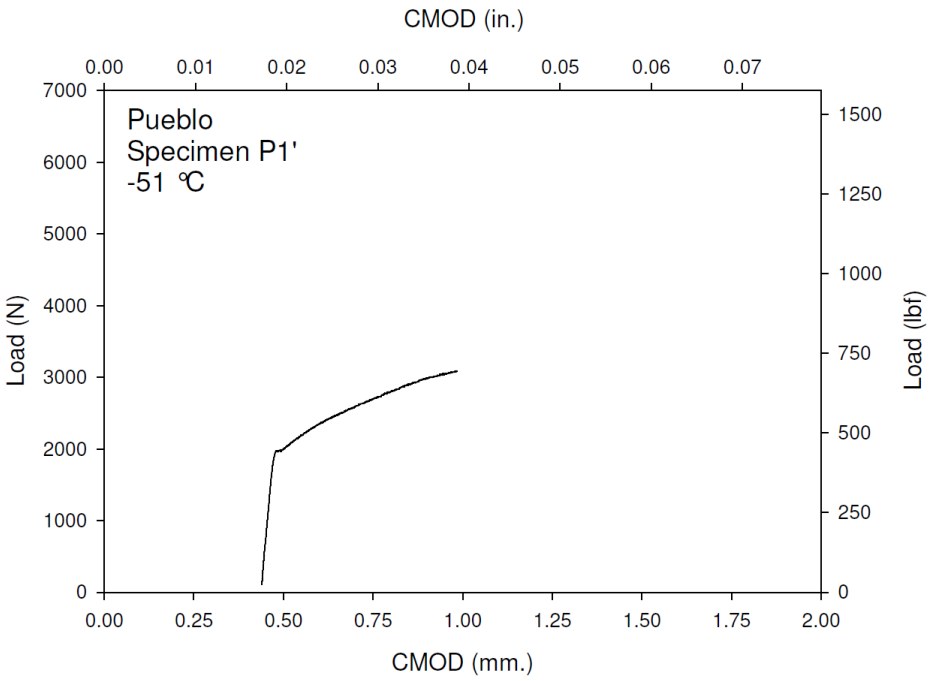

Figure M-91. Specimen P1' Test Record

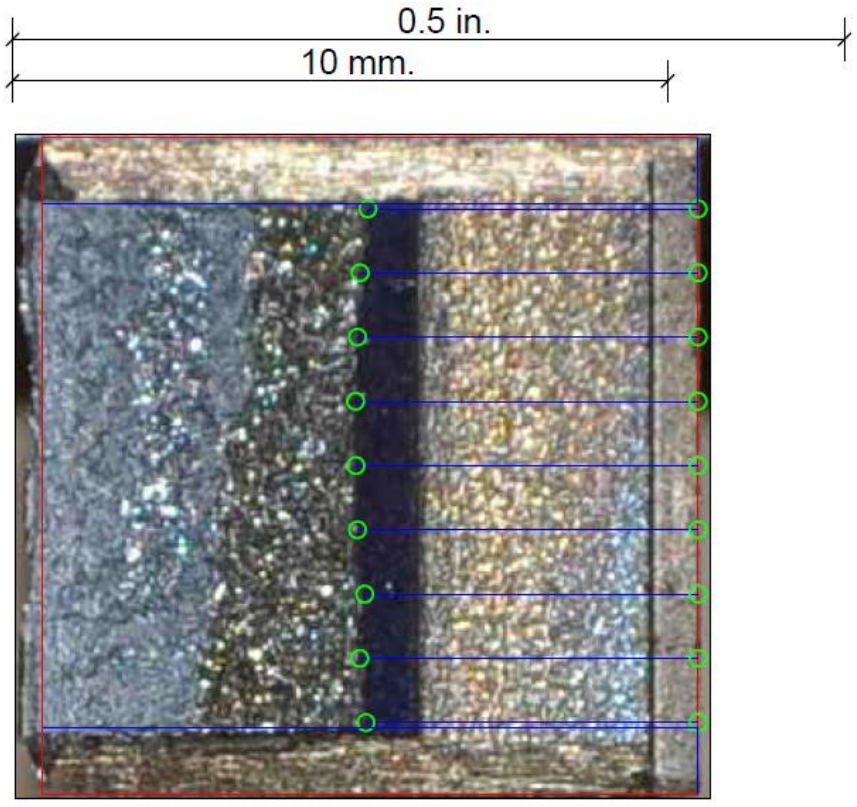

Figure M-92. Specimen P1' Fracture Surface

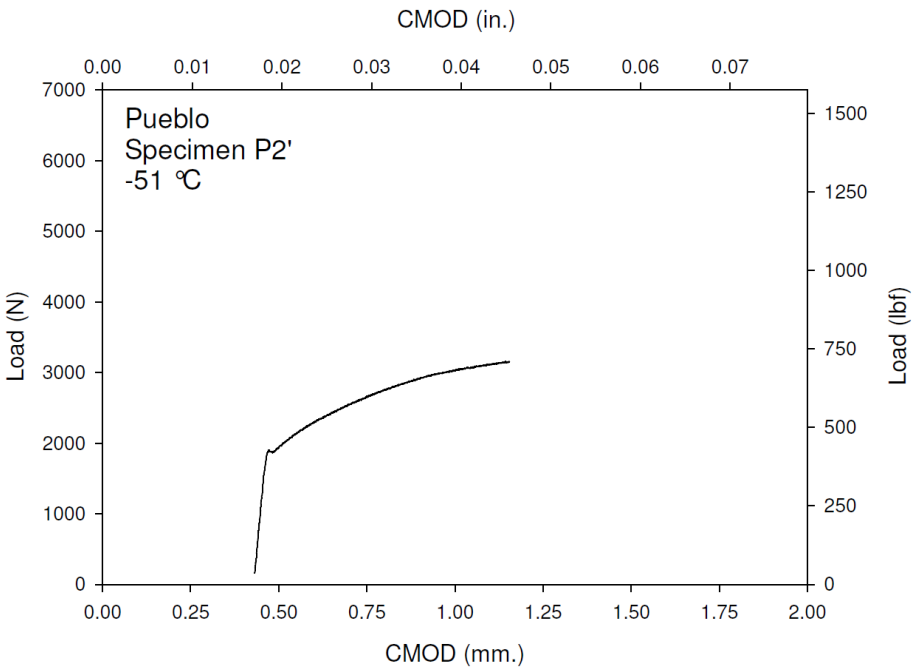

Figure M-93. Specimen P2' Test Record

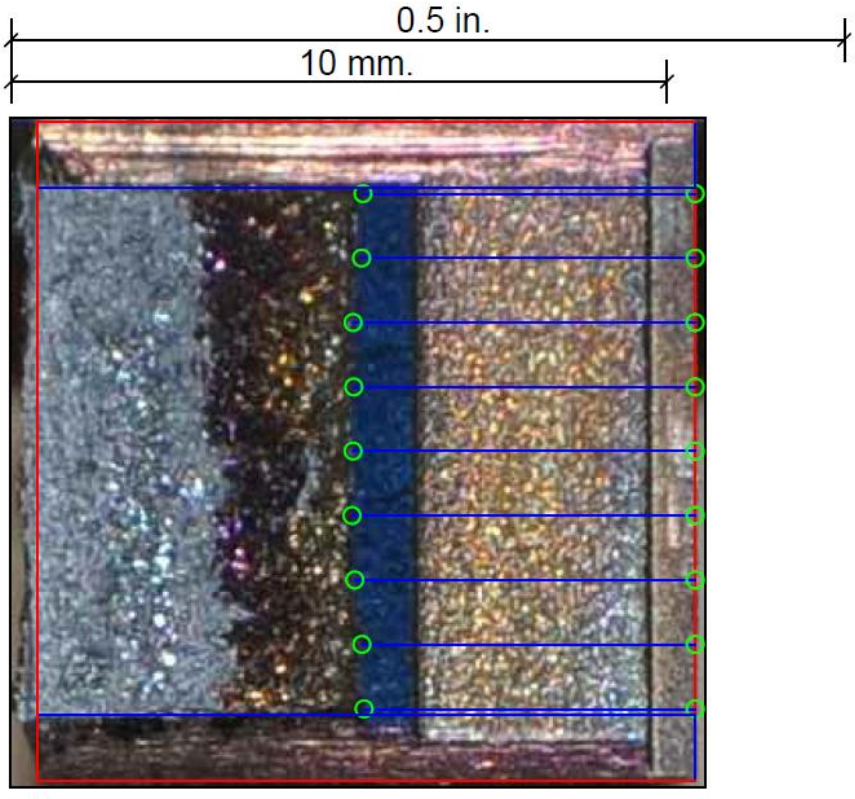

Figure M-94. Specimen P2' Fracture Surface

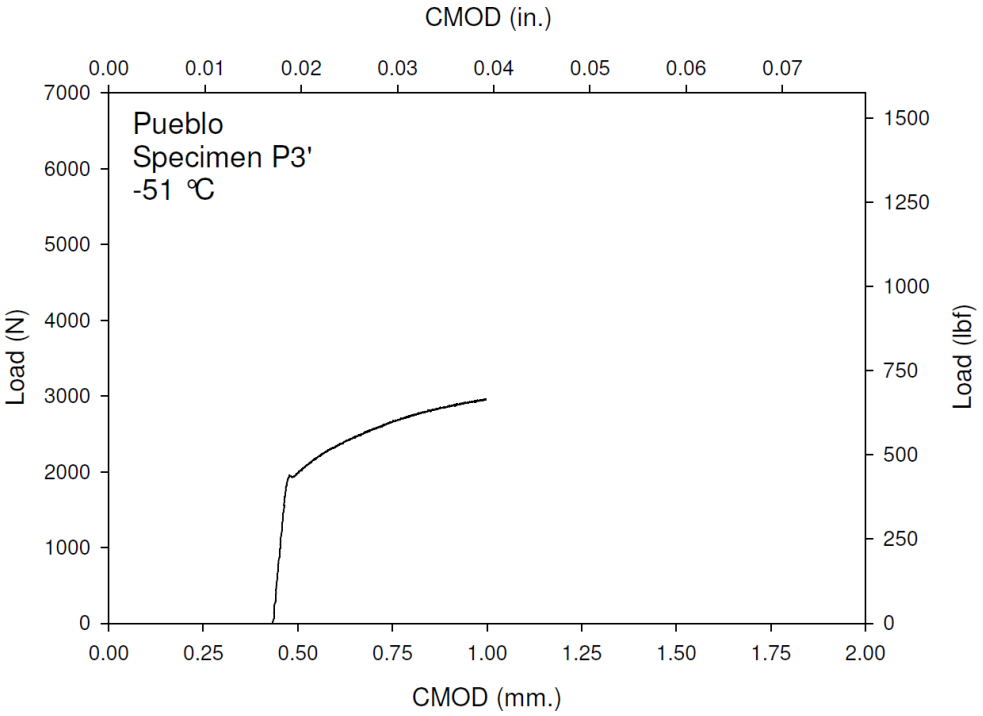

Figure M-95. Specimen P3' Test Record

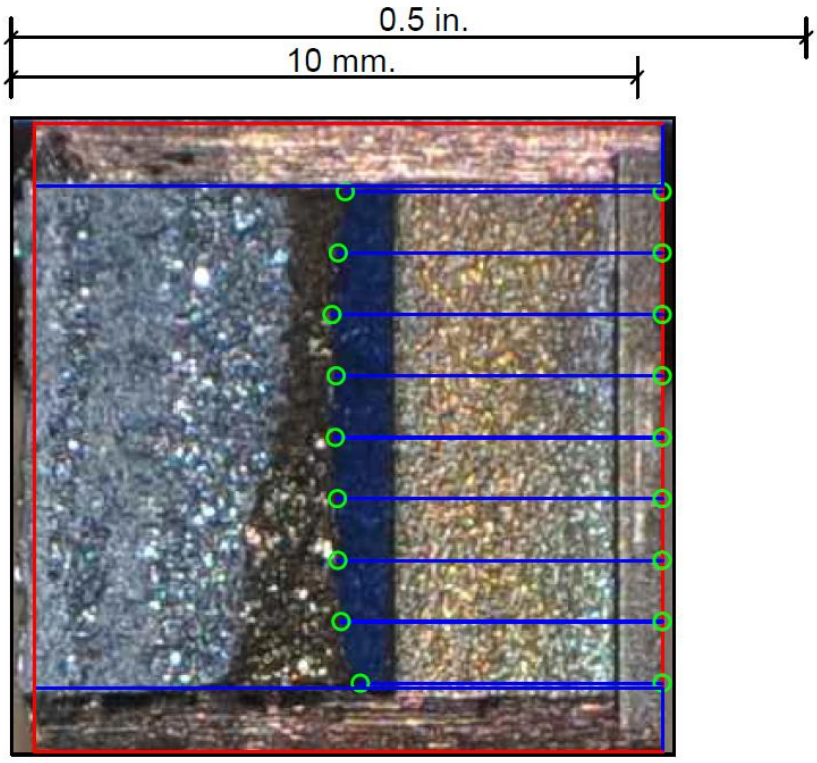

Figure M-96. Specimen P3' Fracture Surface

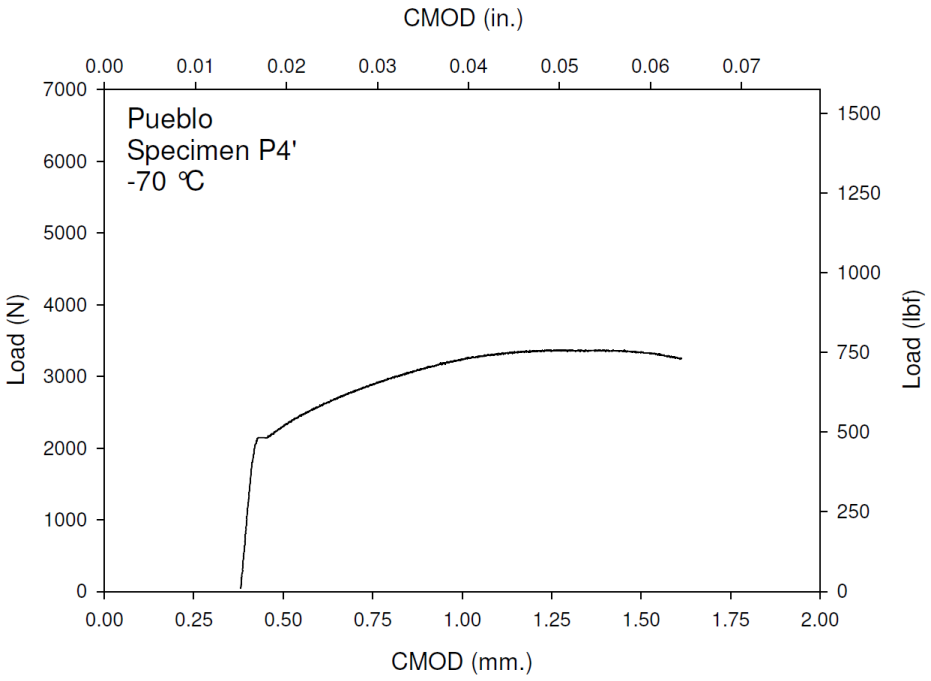

Figure M-97. Specimen P4' Test Record

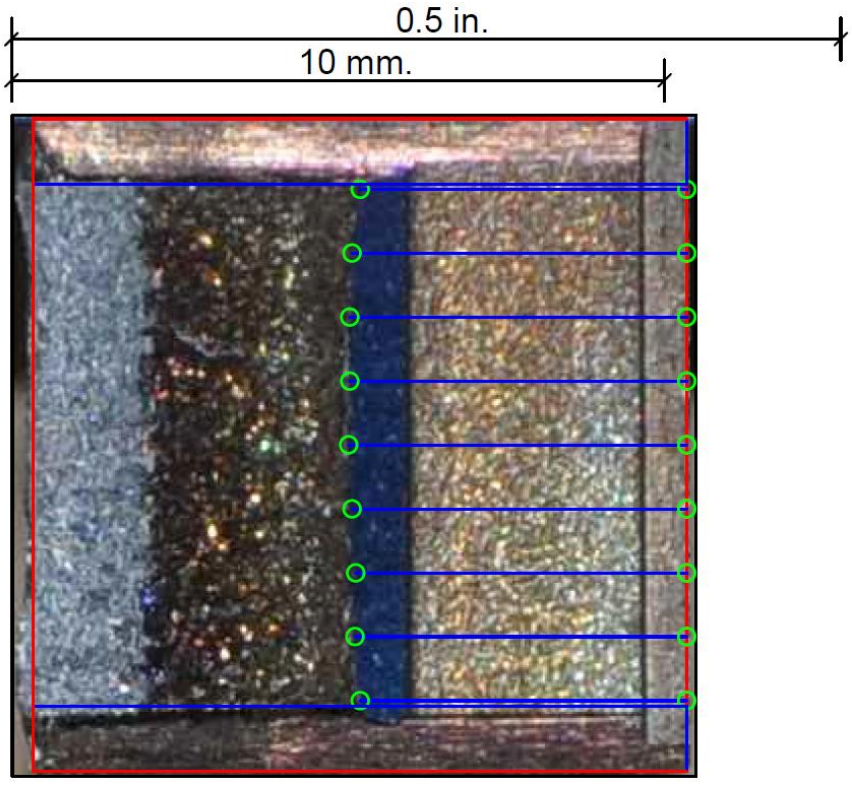

Figure M-98. Specimen P4' Fracture Surface

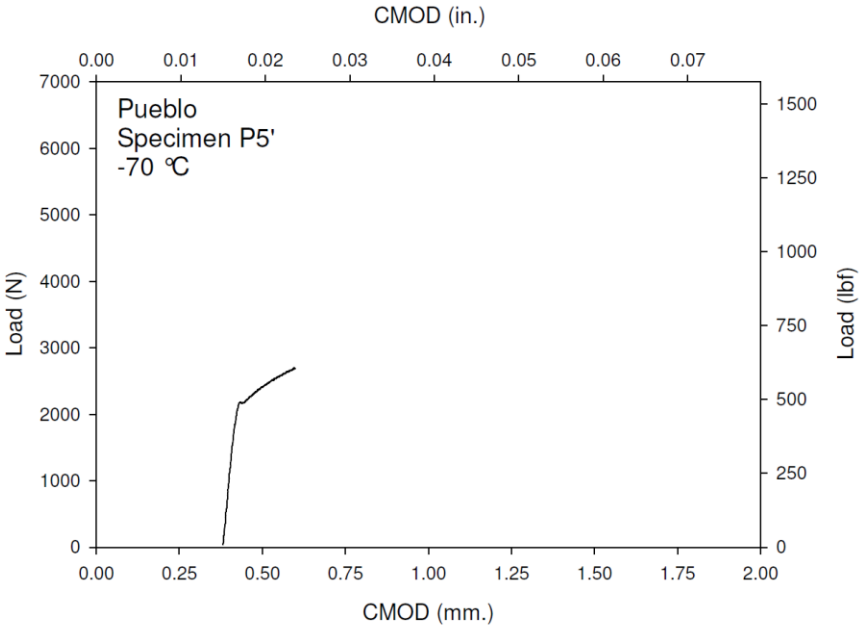

Figure M-99. Specimen P5' Test Record

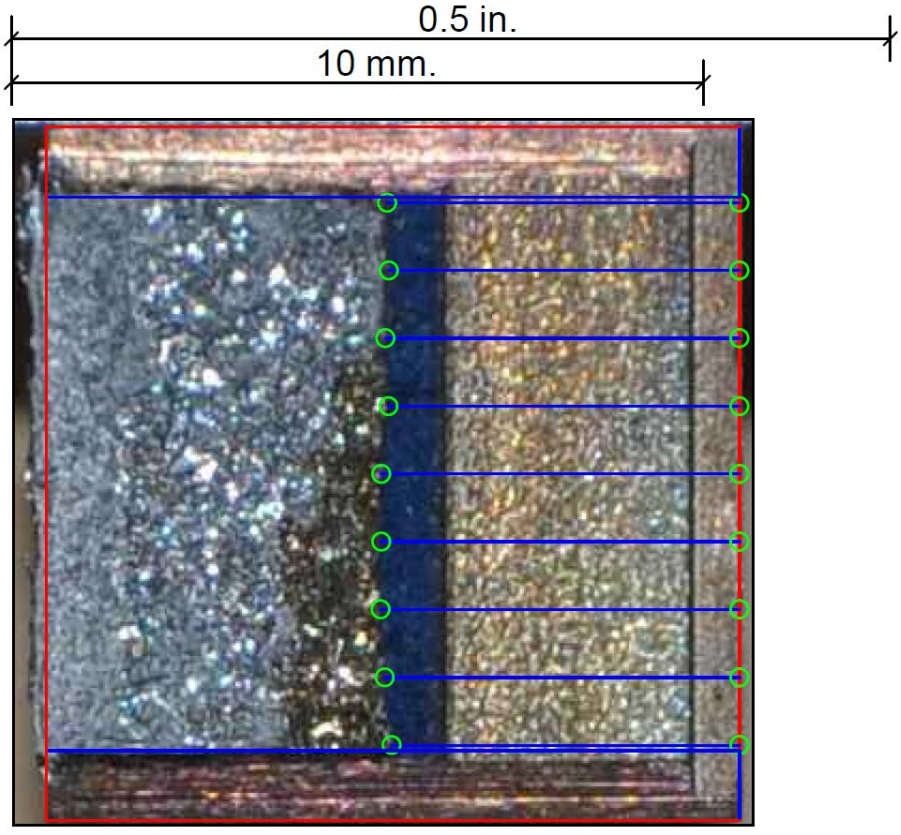

Figure M-100. Specimen P5' Fracture Surface

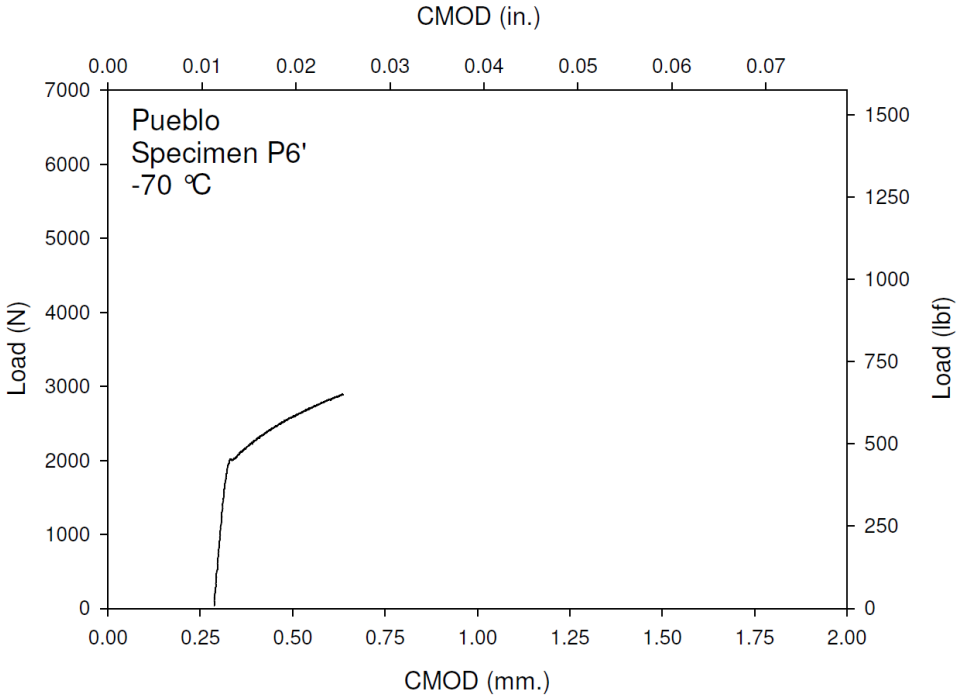

Figure M-101. Specimen P6' Test Record

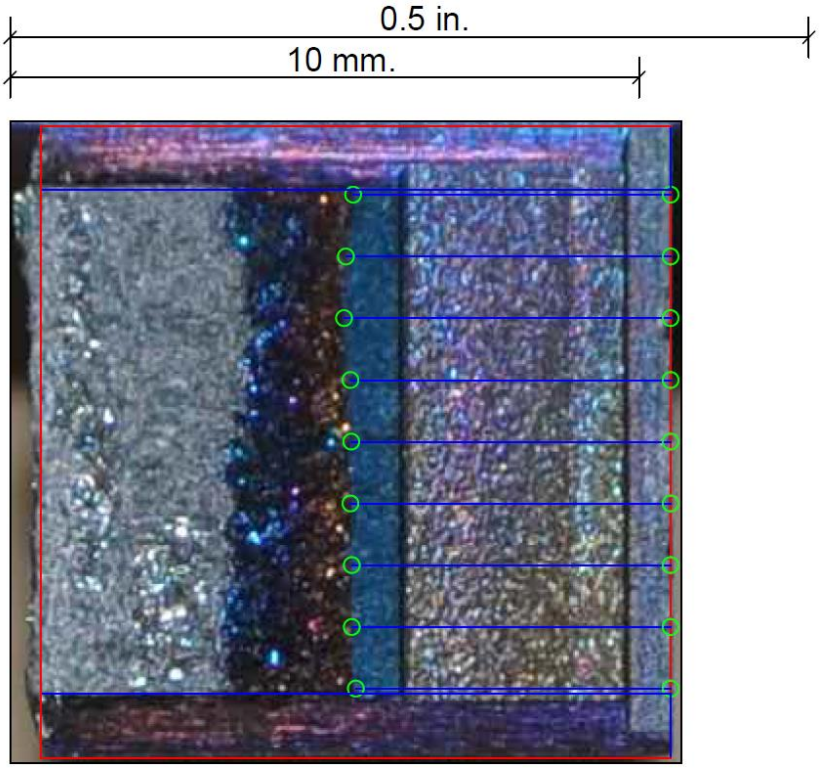

Figure M-102. Specimen P6' Fracture Surface

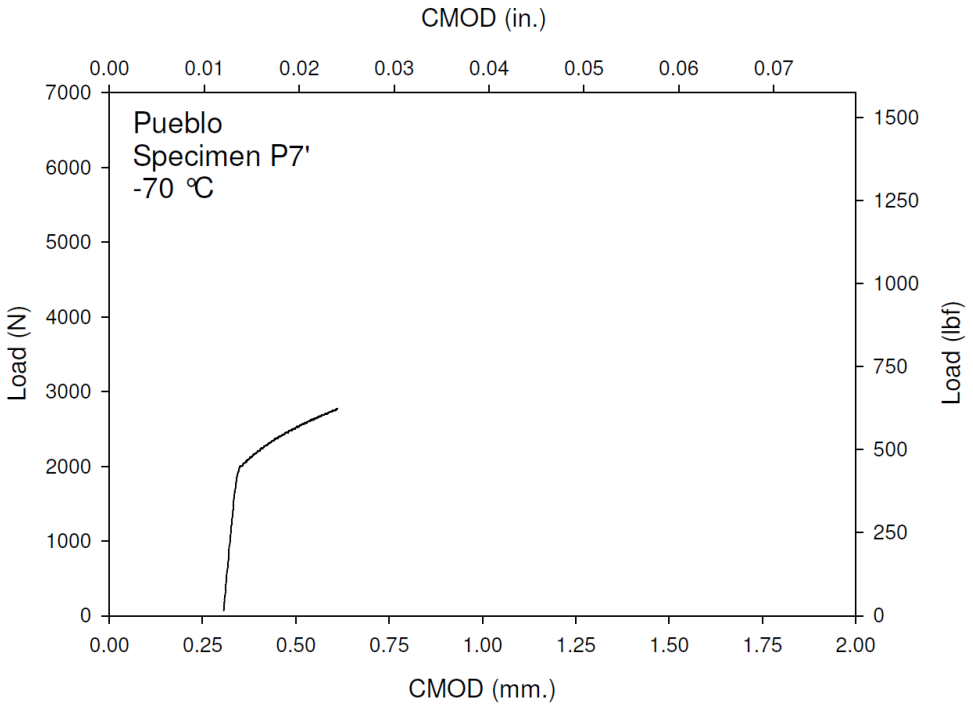

Figure M-103. Specimen P7' Test Record

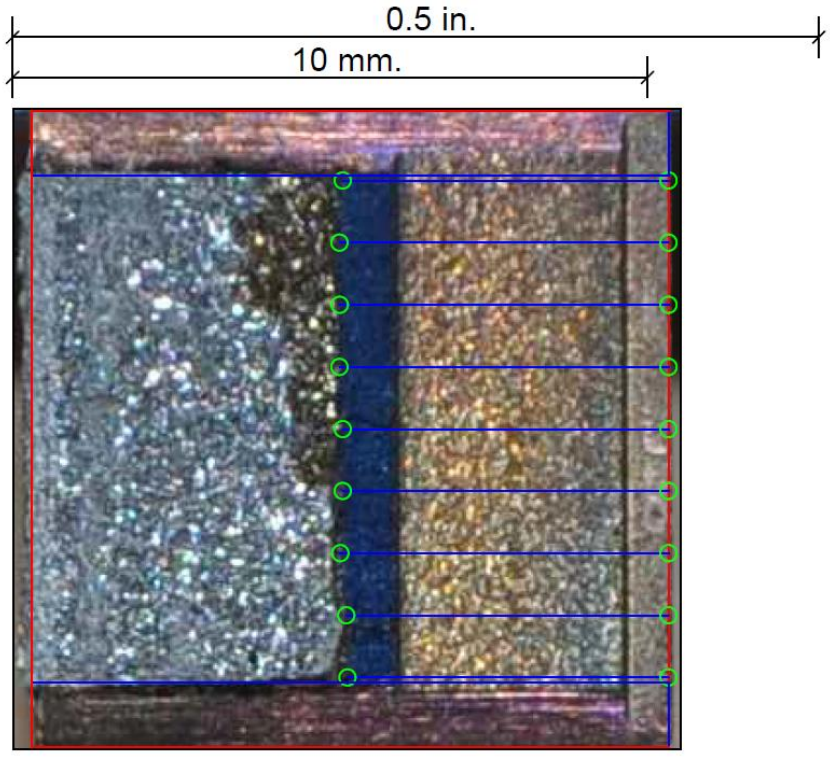

Figure M-104. Specimen P7' Fracture Surface

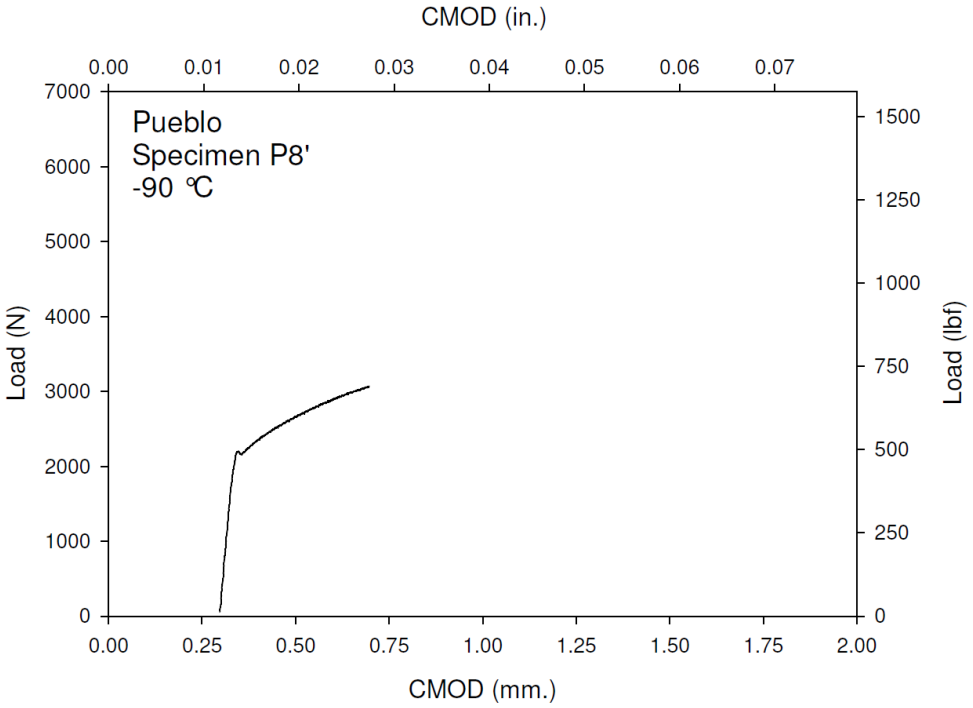

Figure M-105. Specimen P8' Test Record

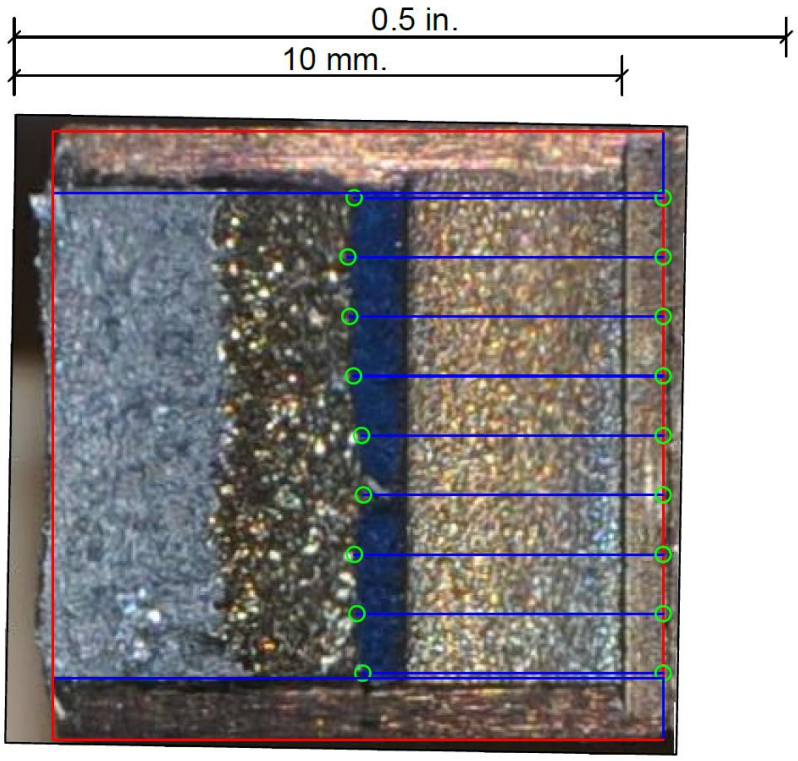

Figure M-106. Specimen P8' Fracture Surface

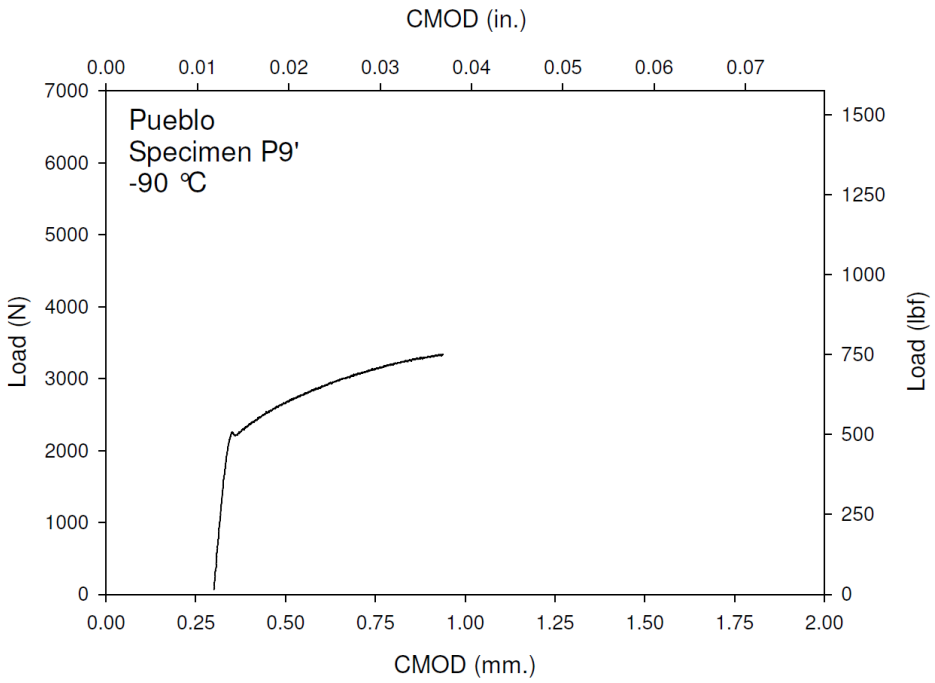

Figure M-107. Specimen P9' Test Record

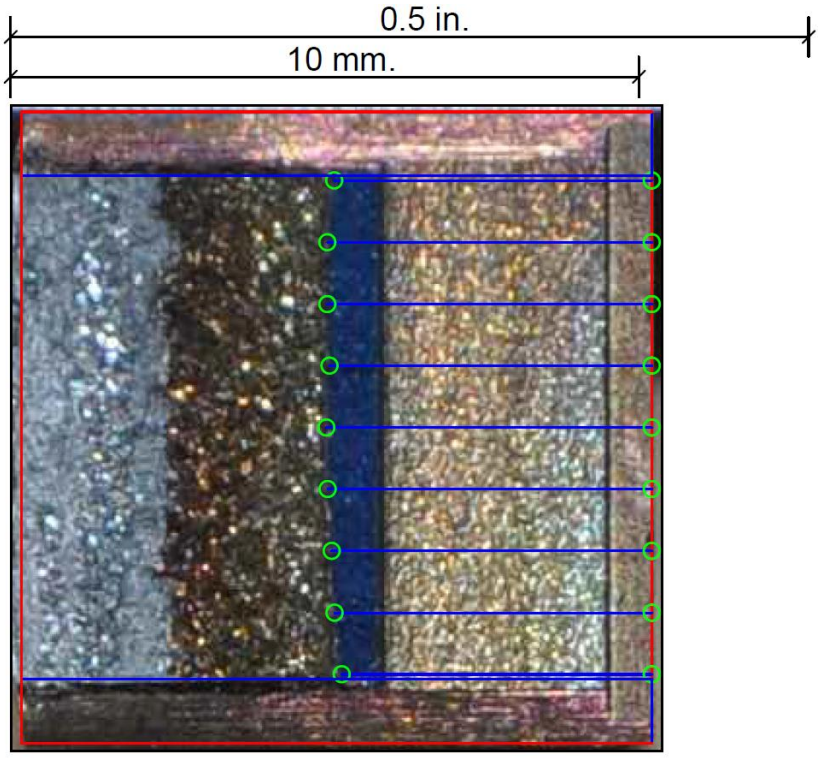

Figure M-108. Specimen P9' Fracture Surface

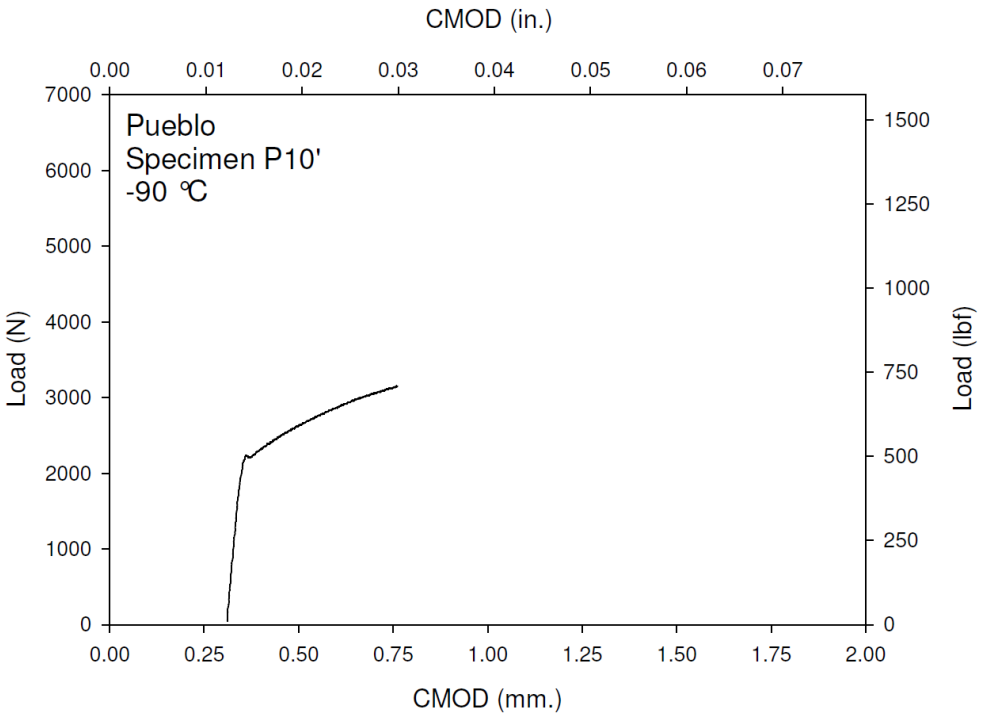

Figure M-109. Specimen P10' Test Record

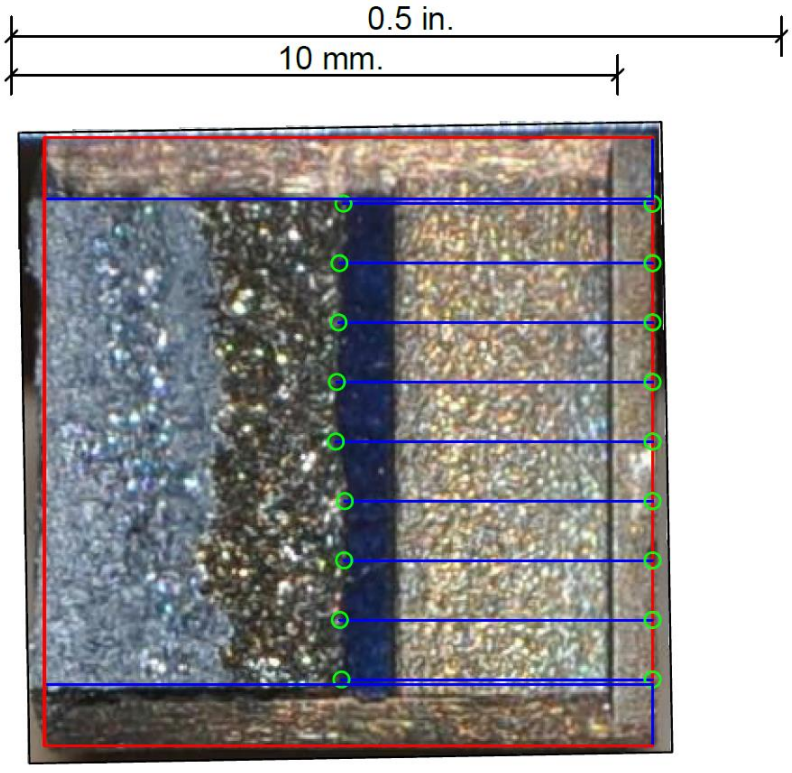

Figure M-110. Specimen P10' Fracture Surface

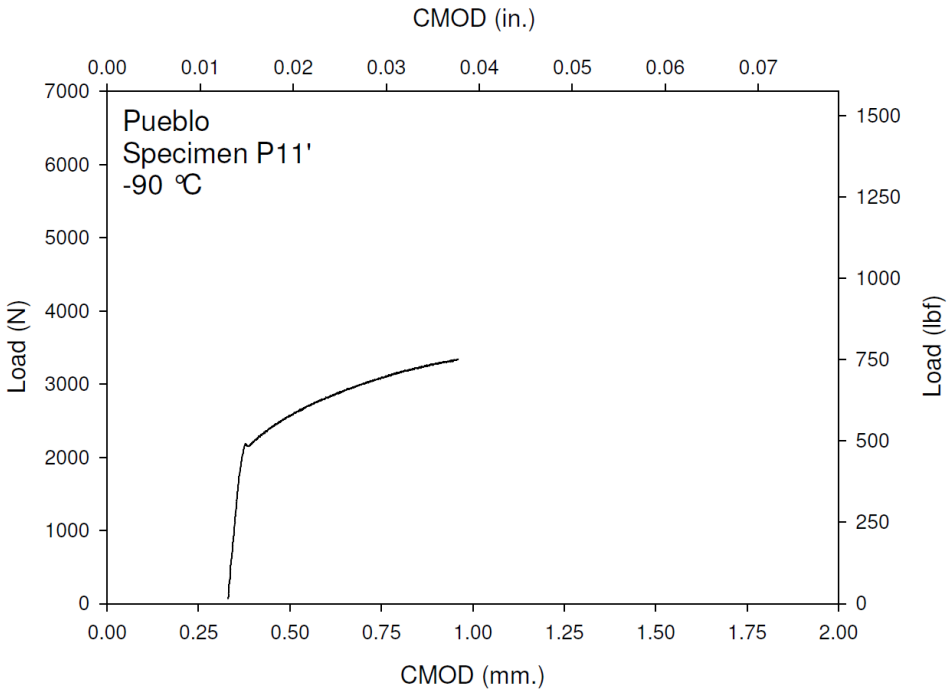

Figure M-111. Specimen P11' Test Record

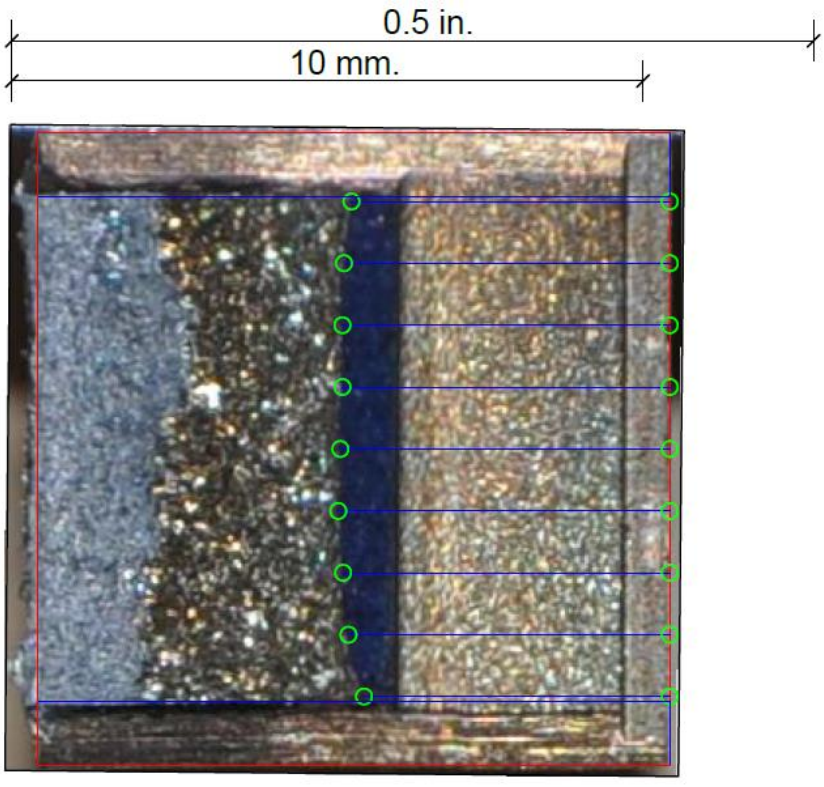

Figure M-112. Specimen P11' Fracture Surface

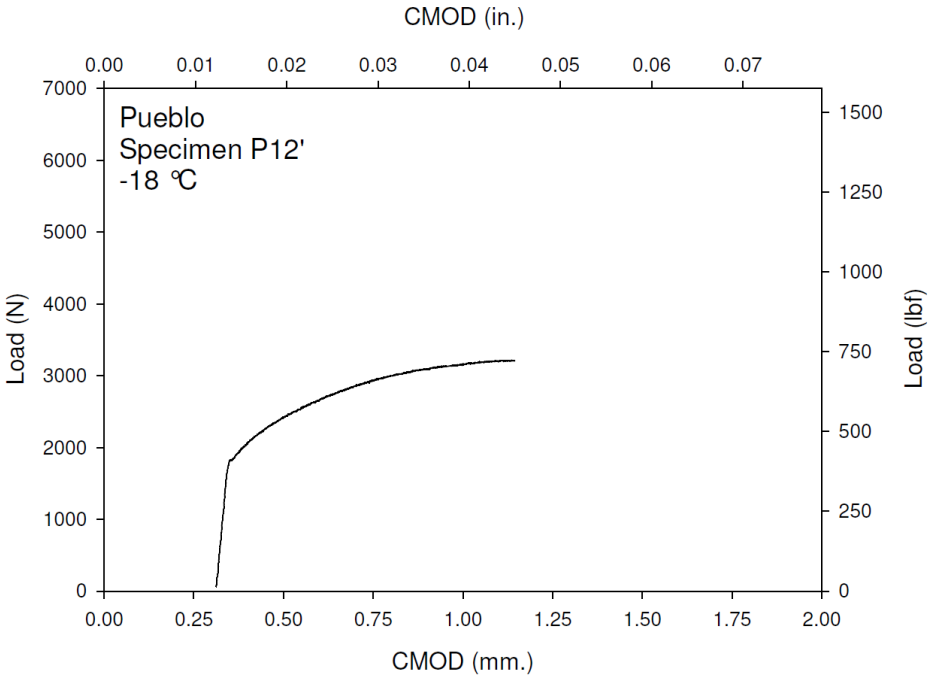

Figure M-113. Specimen P12' Test Record

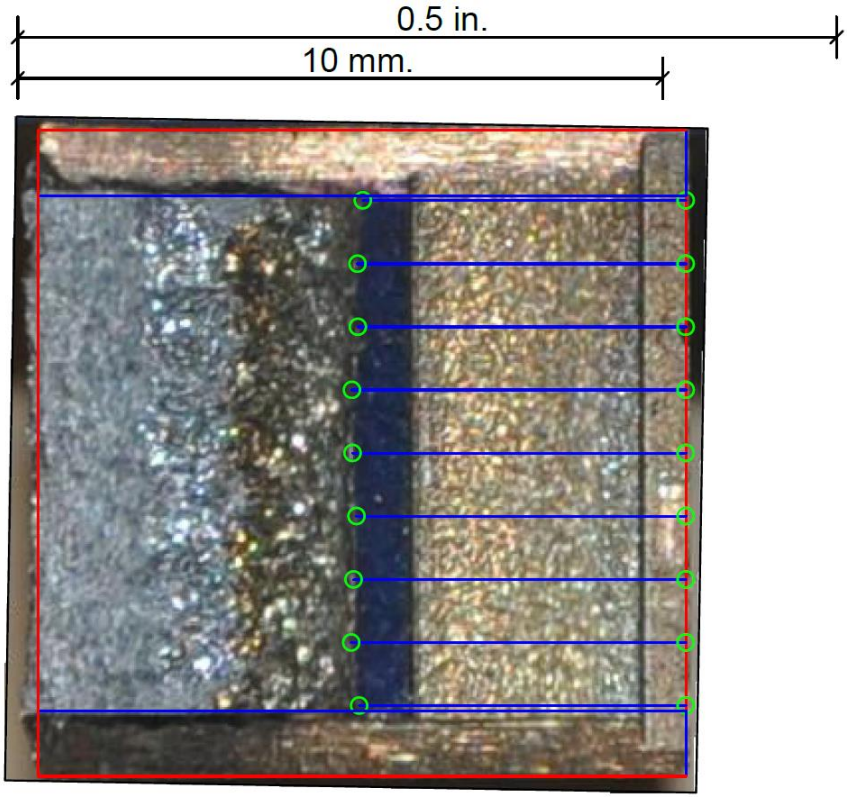

Figure M-114. Specimen P12' Fracture Surface

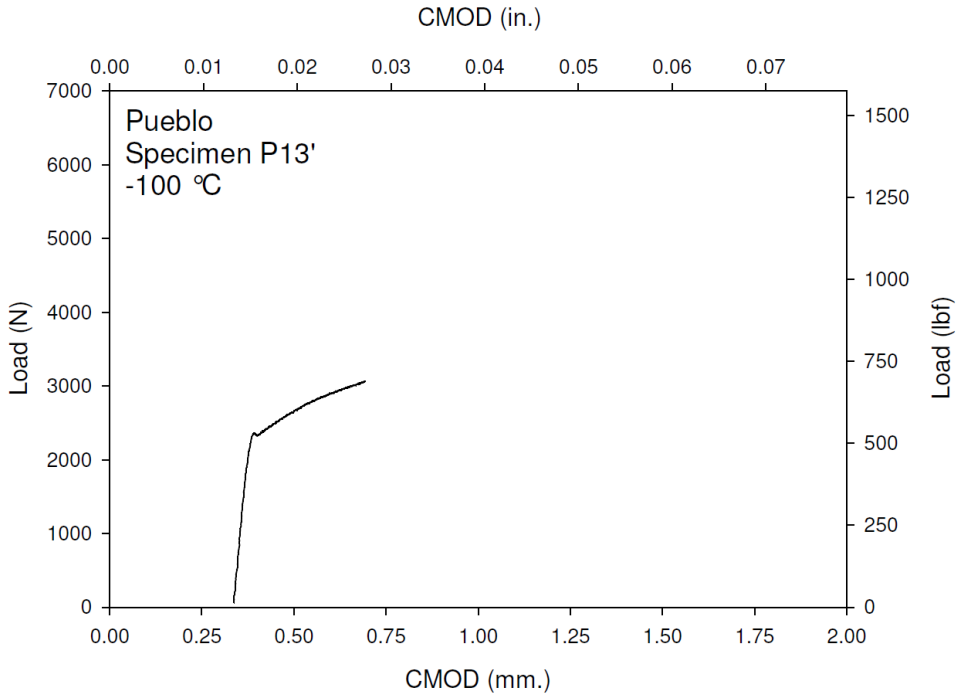

Figure M-115. Specimen P13' Test Record

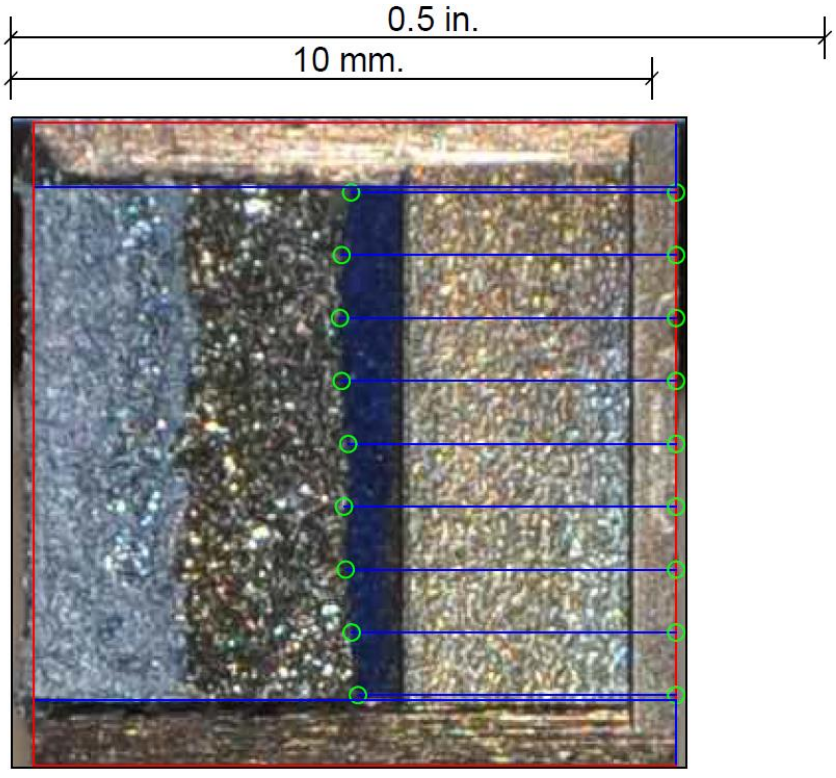

Figure M-116. Specimen P13' Fracture Surface

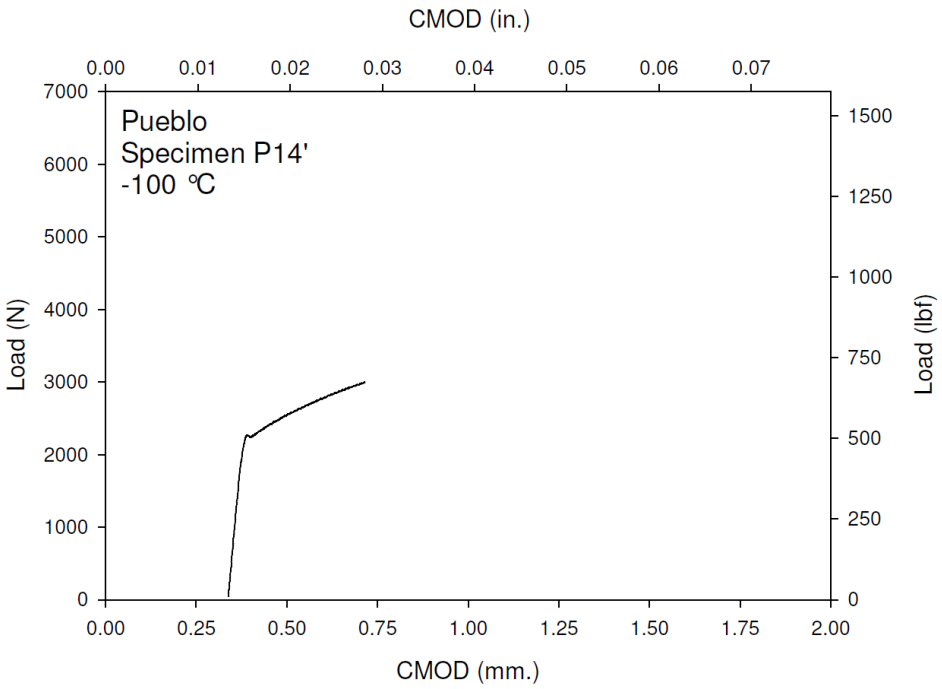

Figure M-117. Specimen P14' Test Record

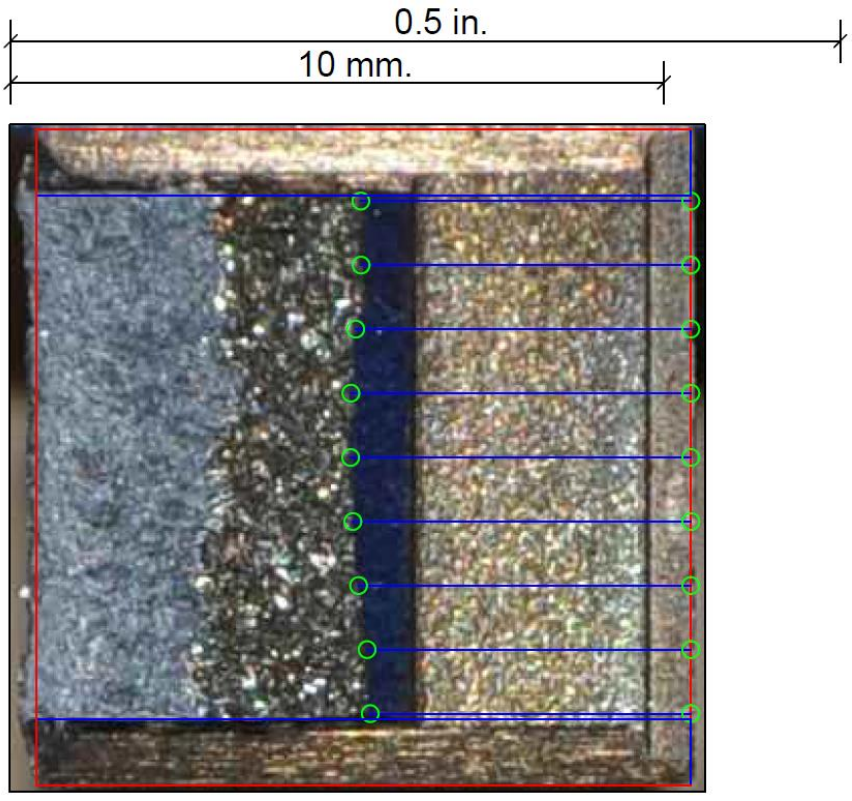

Figure M-118. Specimen P14' Fracture Surface

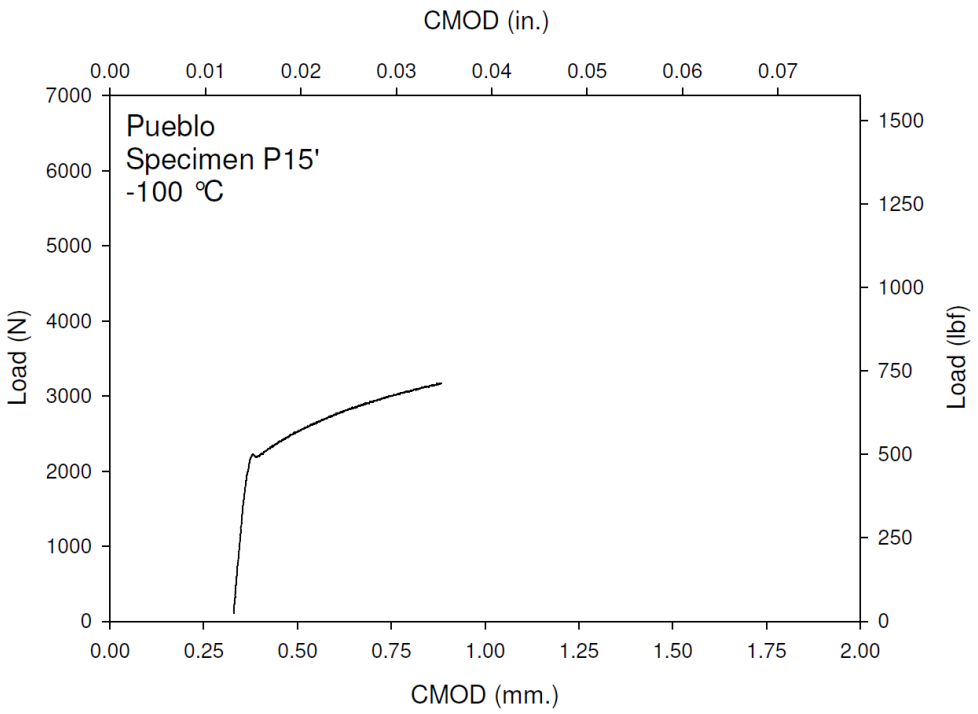

Figure M-119. Specimen P15' Test Record

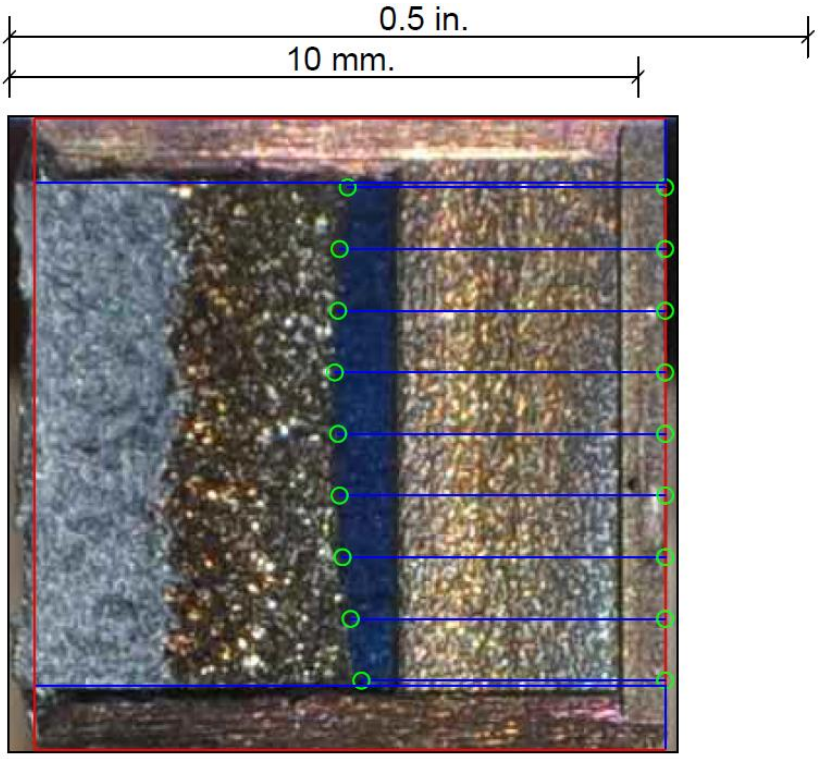

Figure M-120. Specimen P15' Fracture Surface

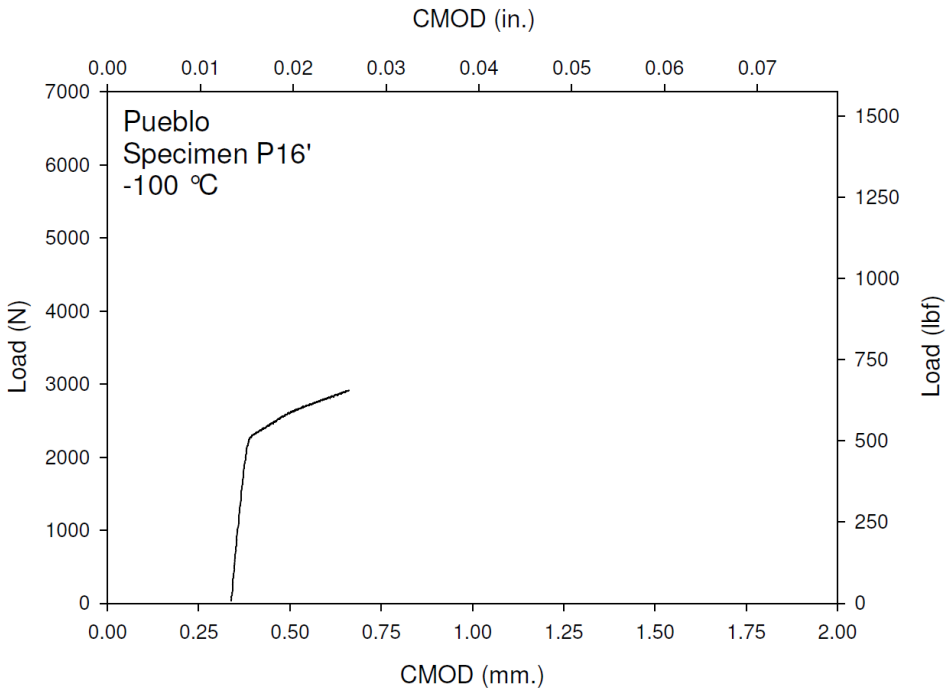

Figure M-121. Specimen P16' Test Record

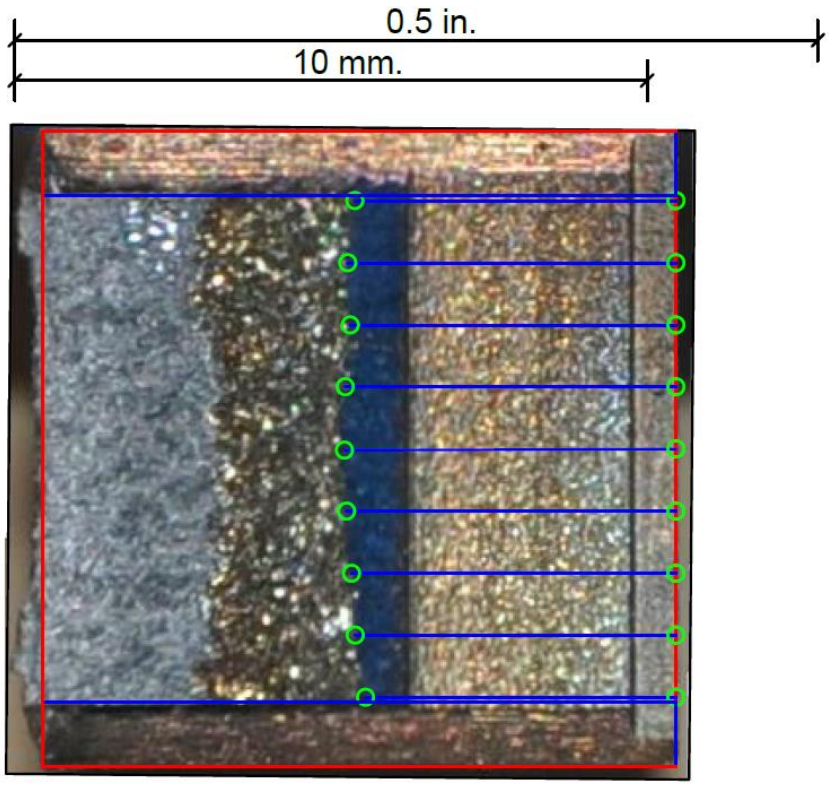

Figure M-122. Specimen P16' Fracture Surface

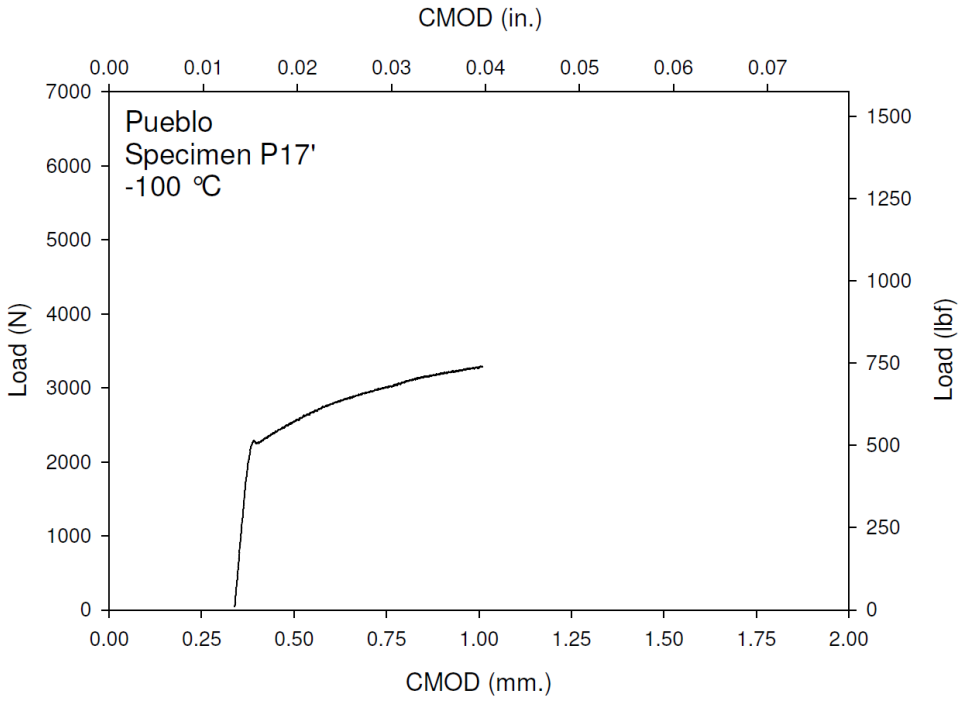

Figure M-123. Specimen P17' Test Record

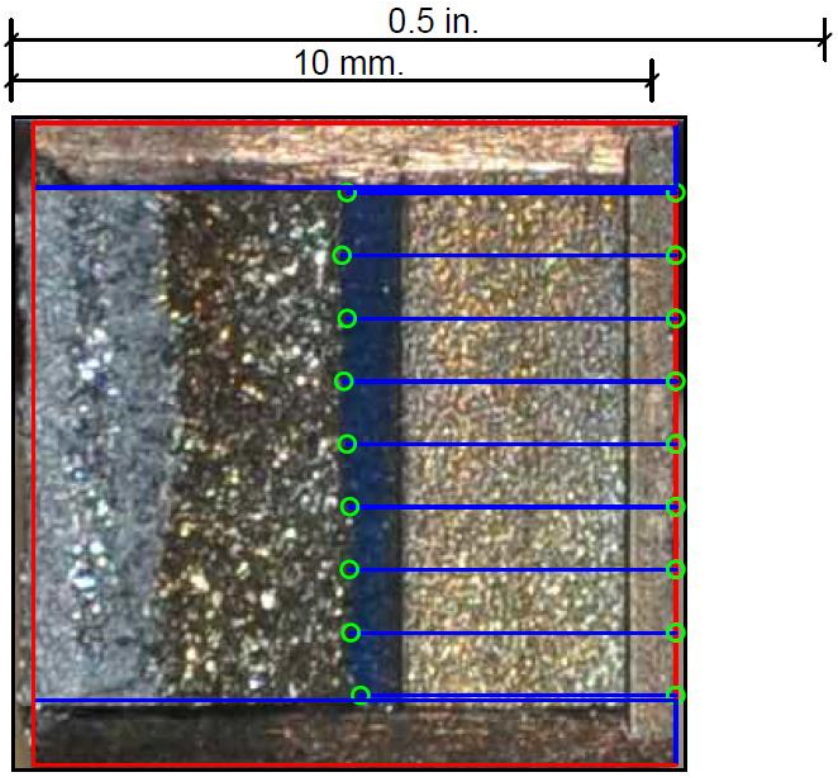

Figure M-124. Specimen P17' Fracture Surface

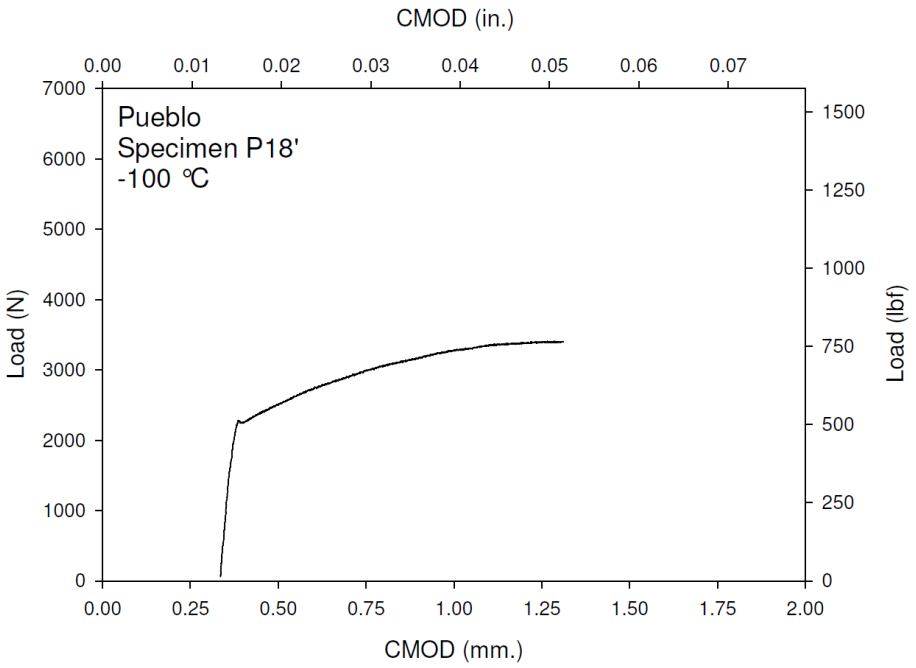

Figure M-125. Specimen P18' Test Record

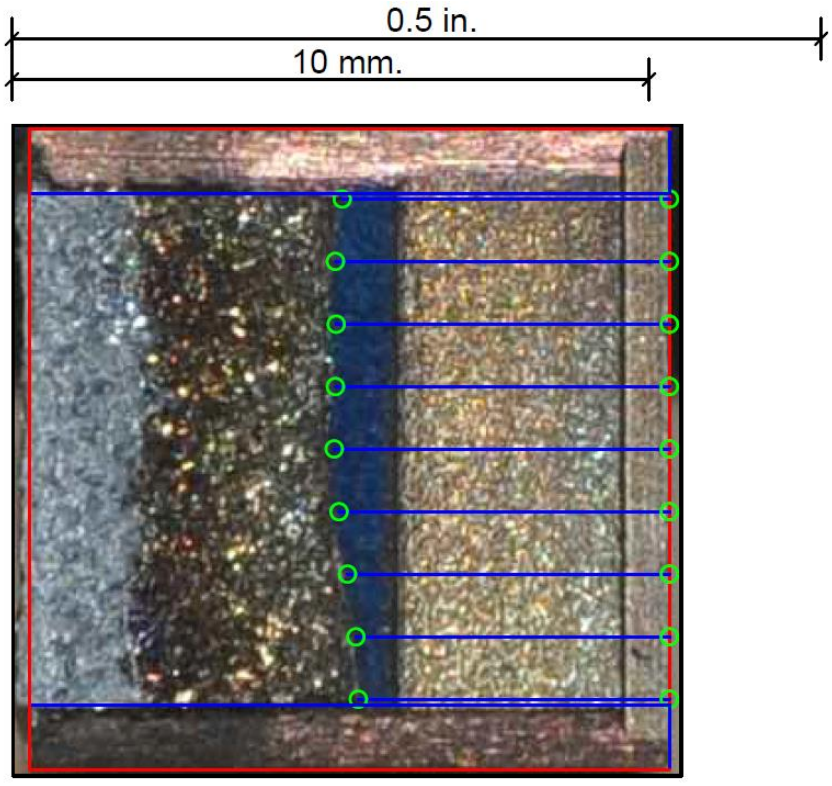

Figure M-126. Specimen P18' Fracture Surface

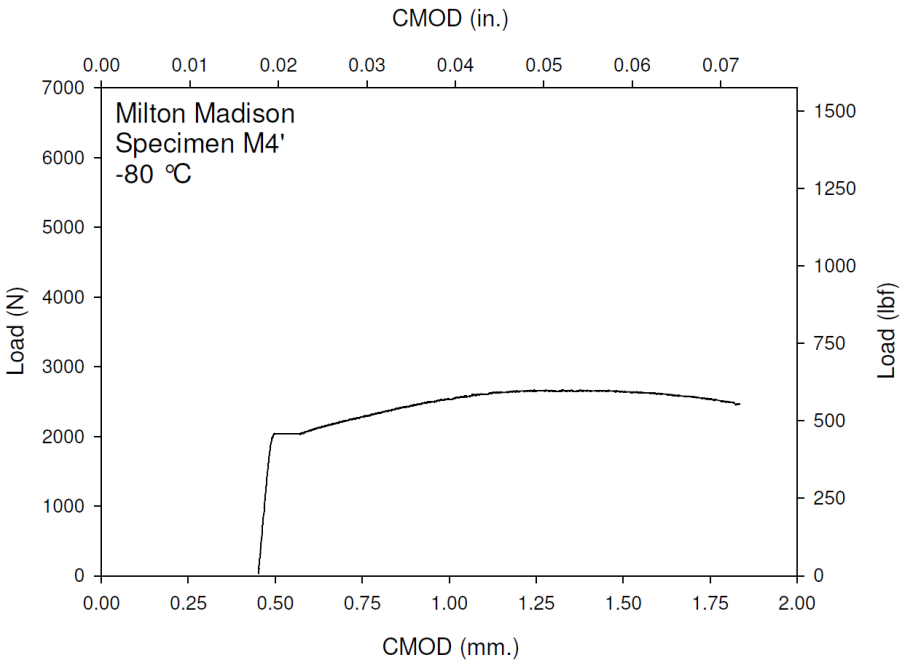

Figure M-127. Specimen M4' Test Record

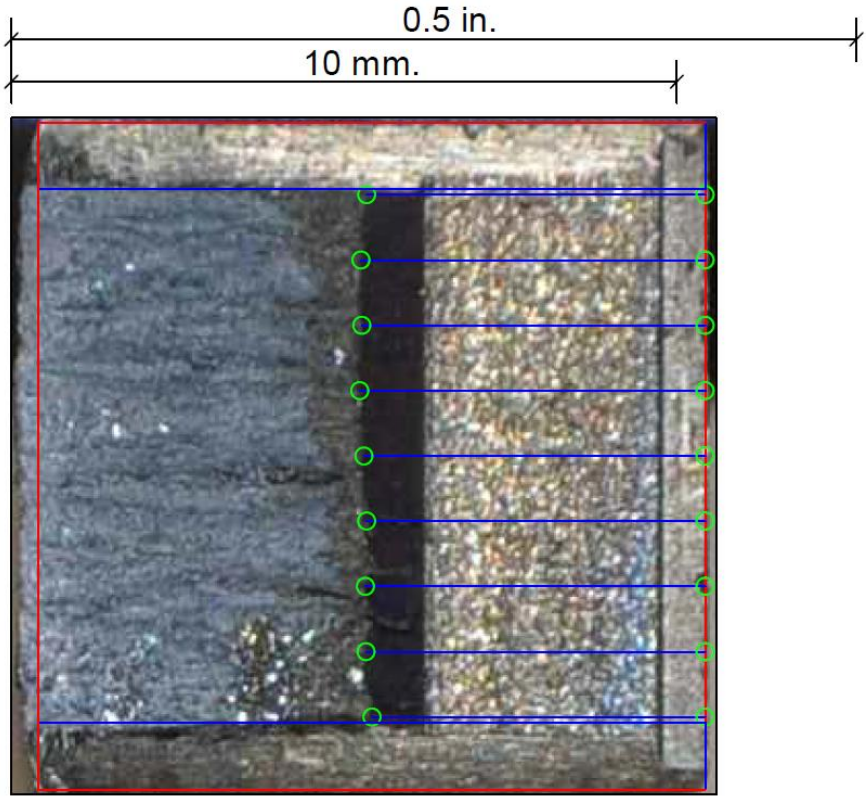

Figure M-128. Specimen M4' Fracture Surface

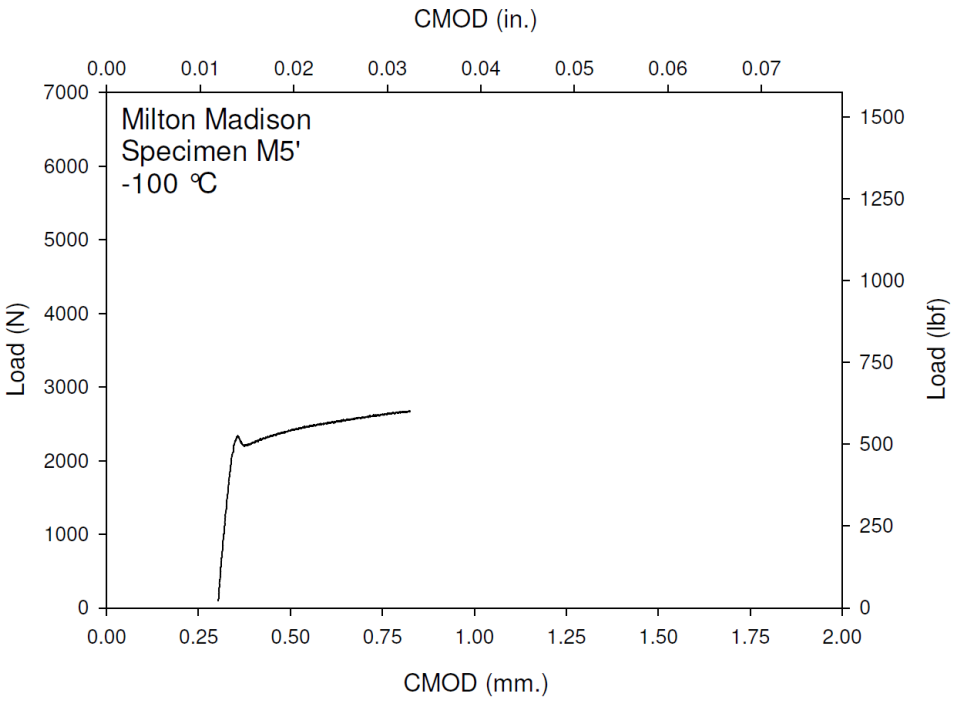

Figure M-129. Specimen M5' Test Record

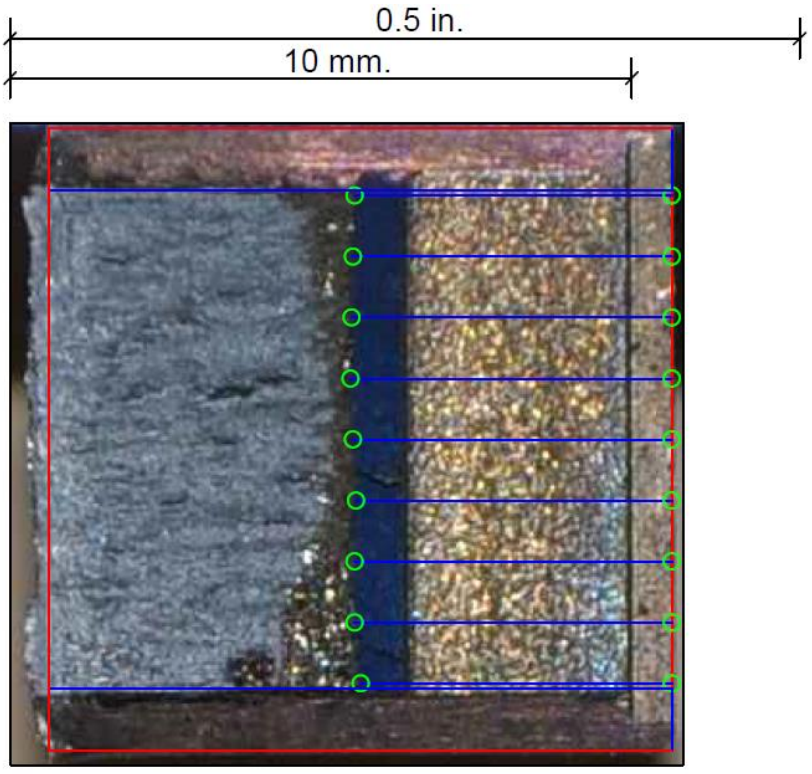

Figure M-130. Specimen M5' Fracture Surface

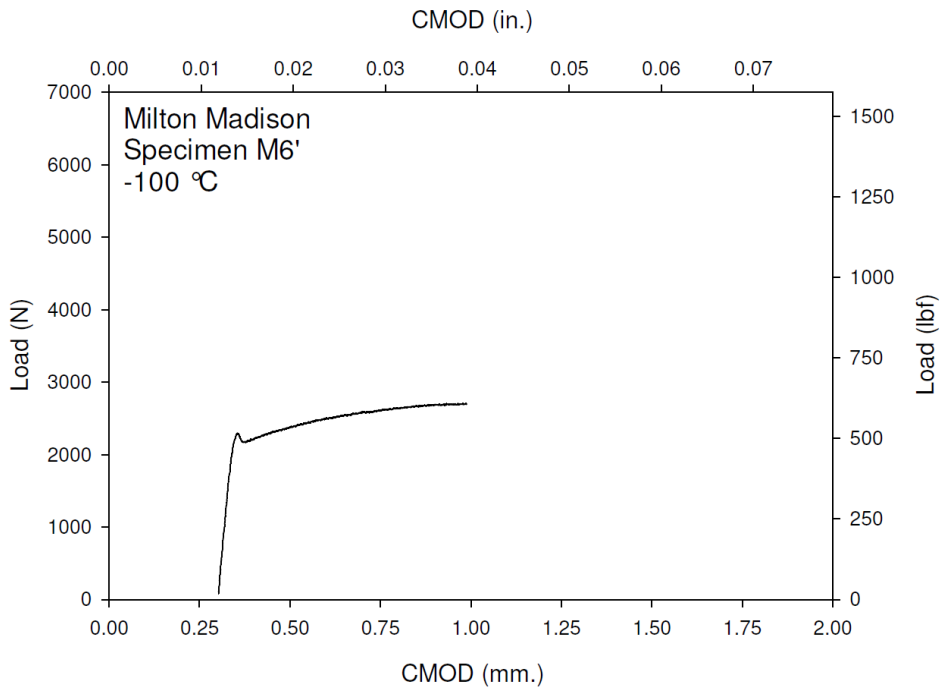

Figure M-131. Specimen M6' Test Record

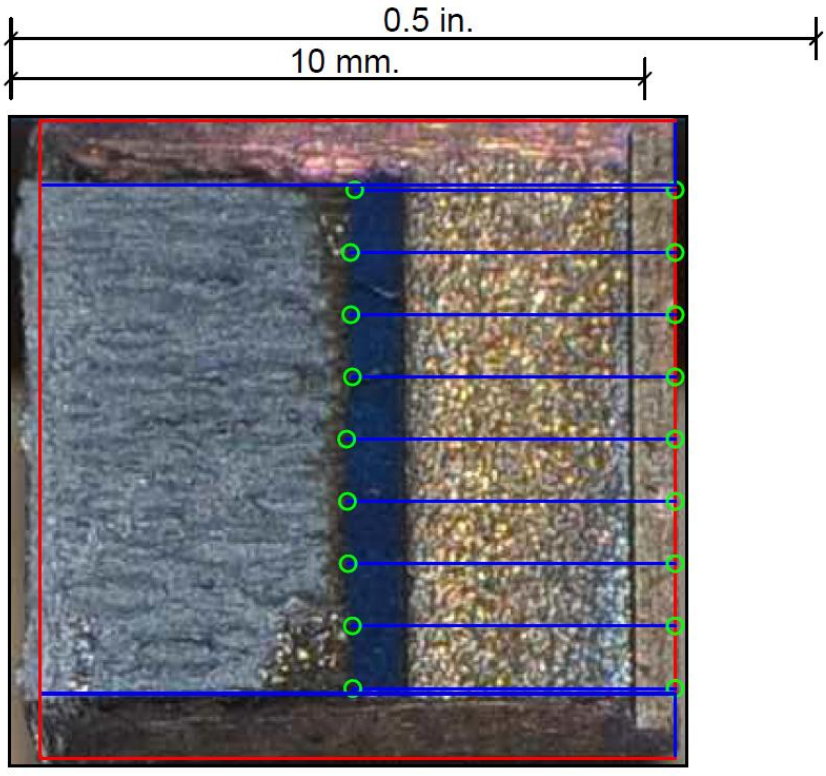

Figure M-132. Specimen M6' Fracture Surface

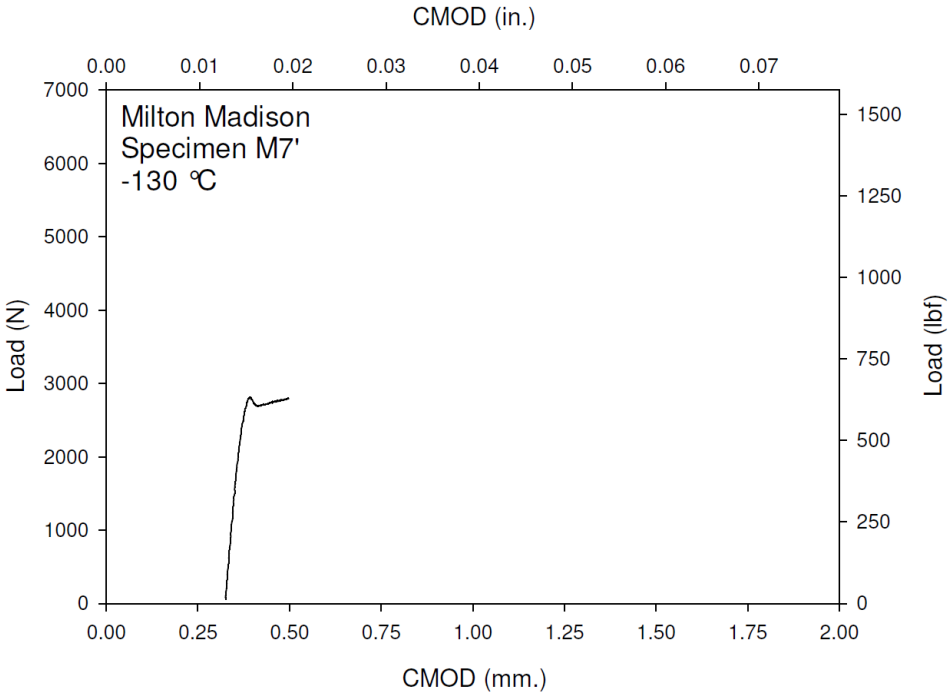

Figure M-133. Specimen M7' Test Record

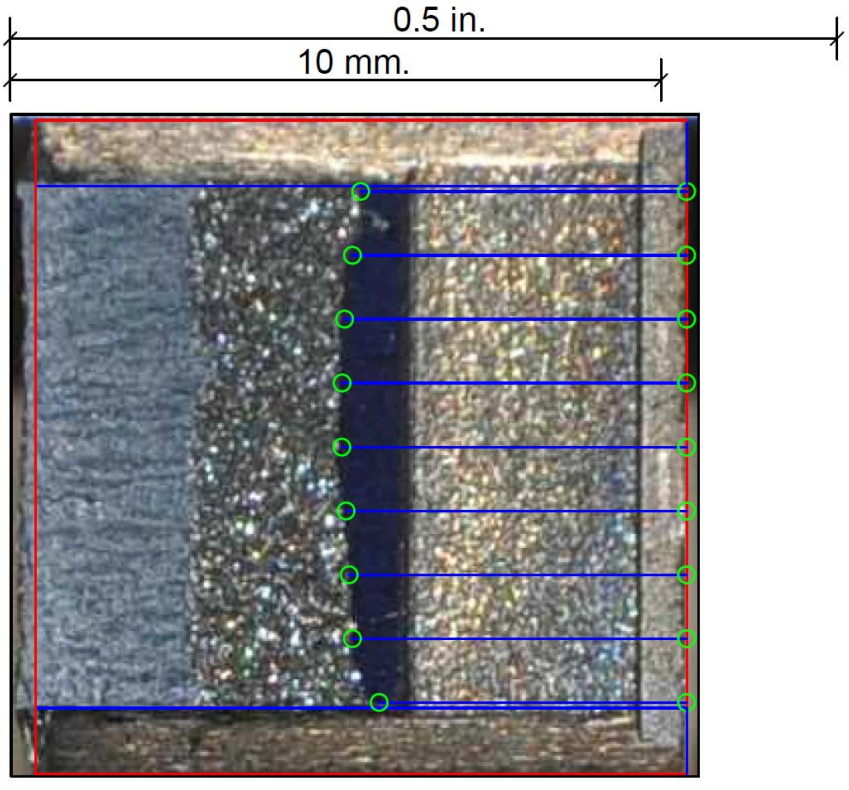

Figure M-134. Specimen M7' Fracture Surface

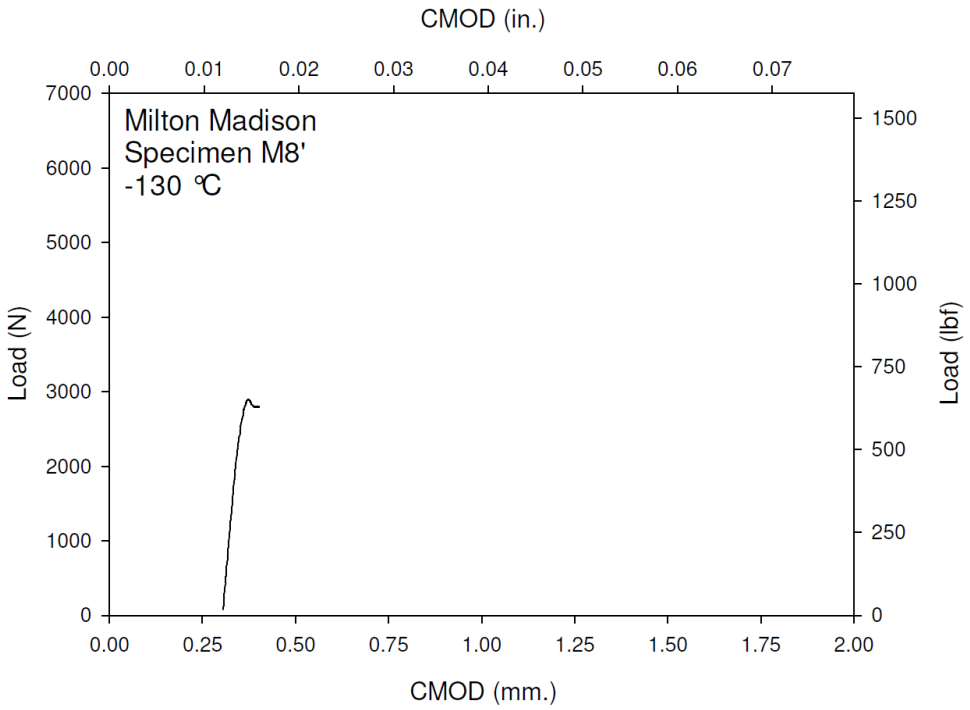

Figure M-135. Specimen M8' Test Record

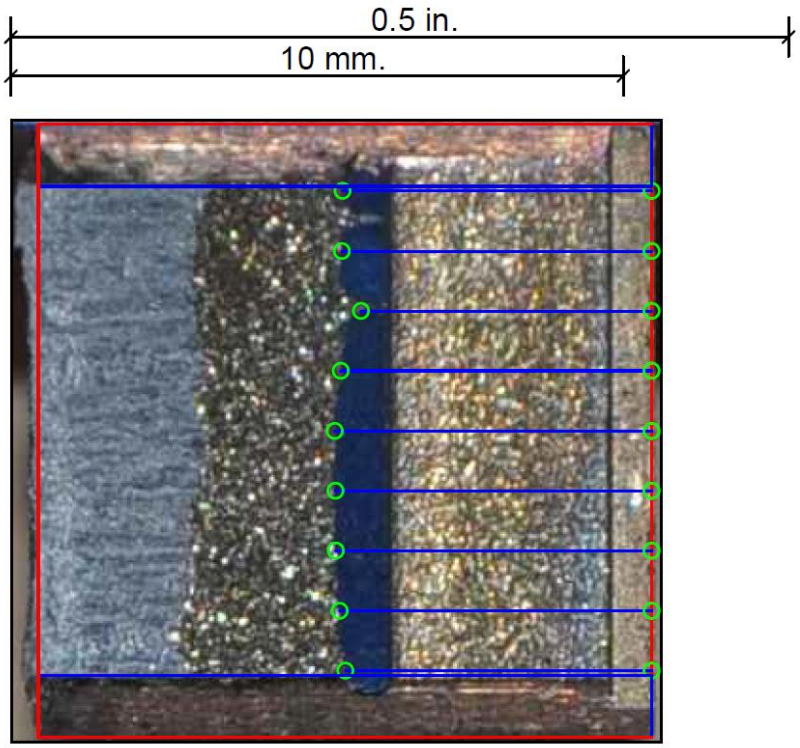

Figure M-136. Specimen M8' Fracture Surface

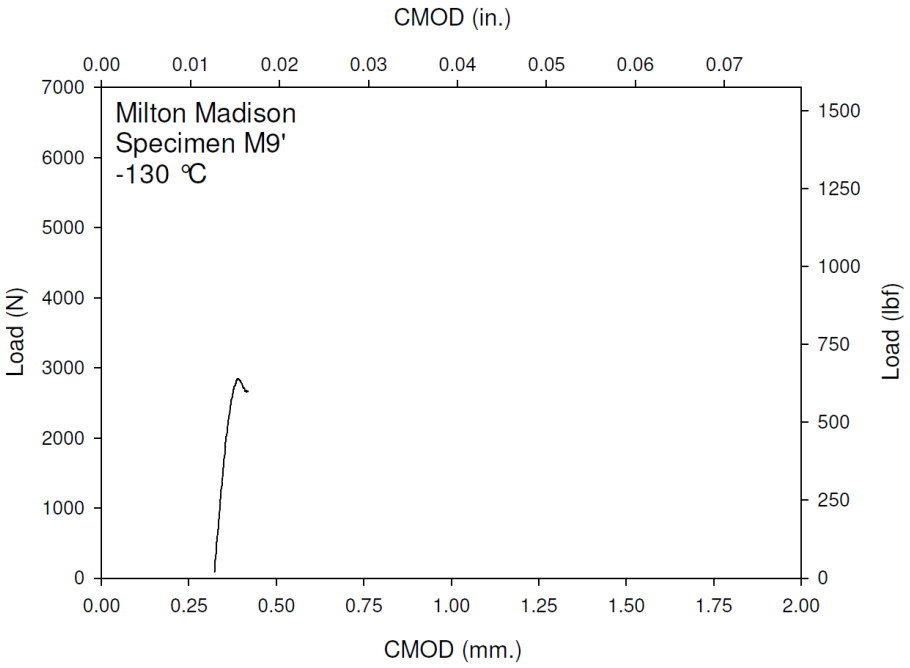

Figure M-137. Specimen M9' Test Record

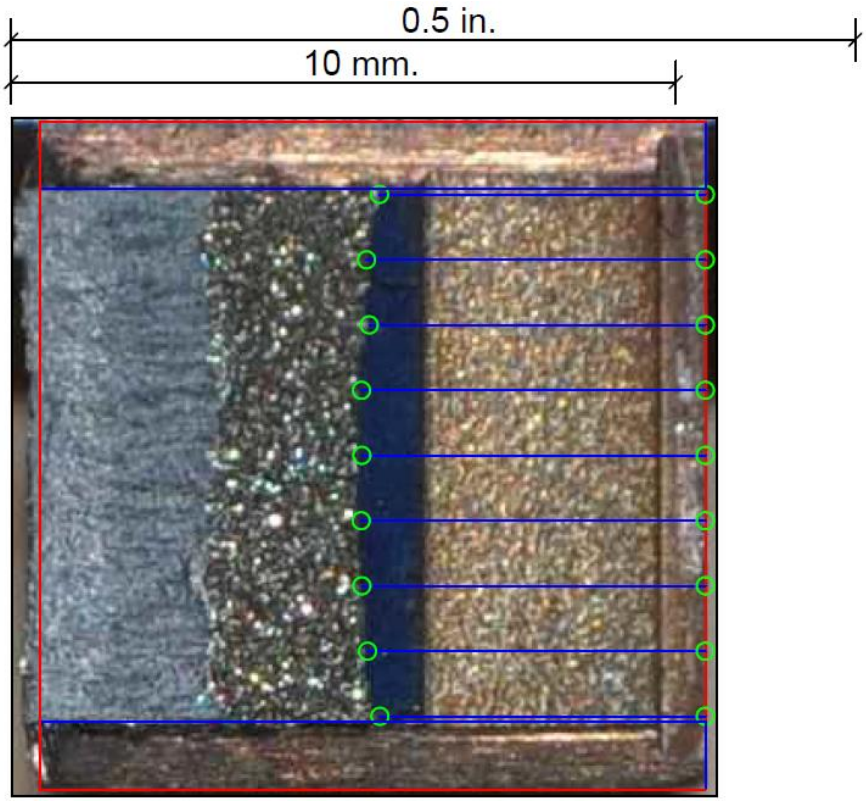

Figure M-138. Specimen M9' Fracture Surface

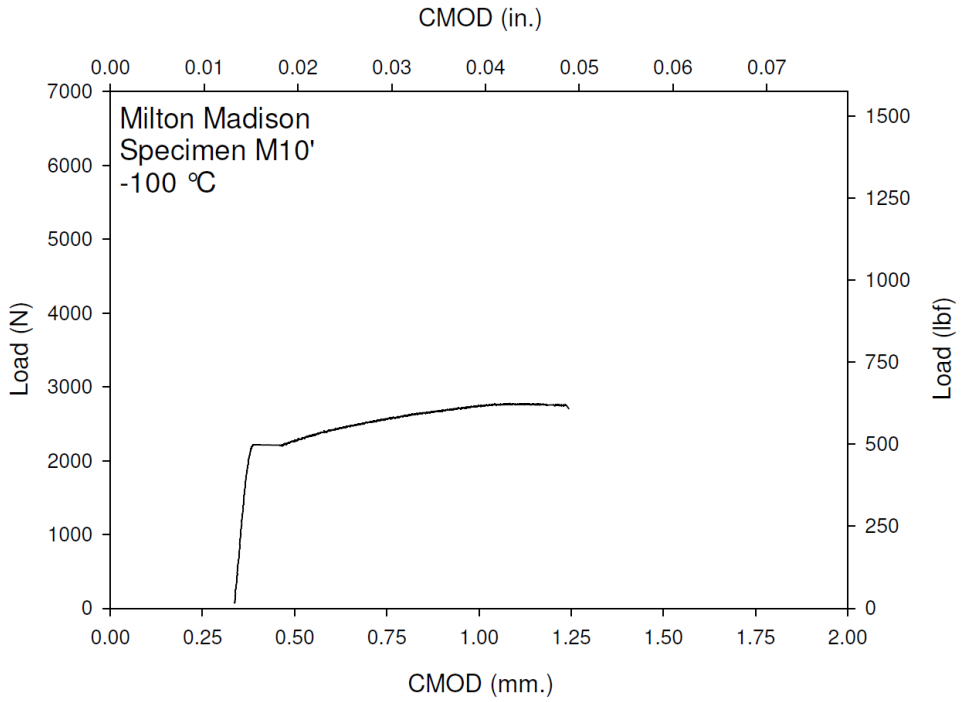

Figure M-139. Specimen M10' Test Record

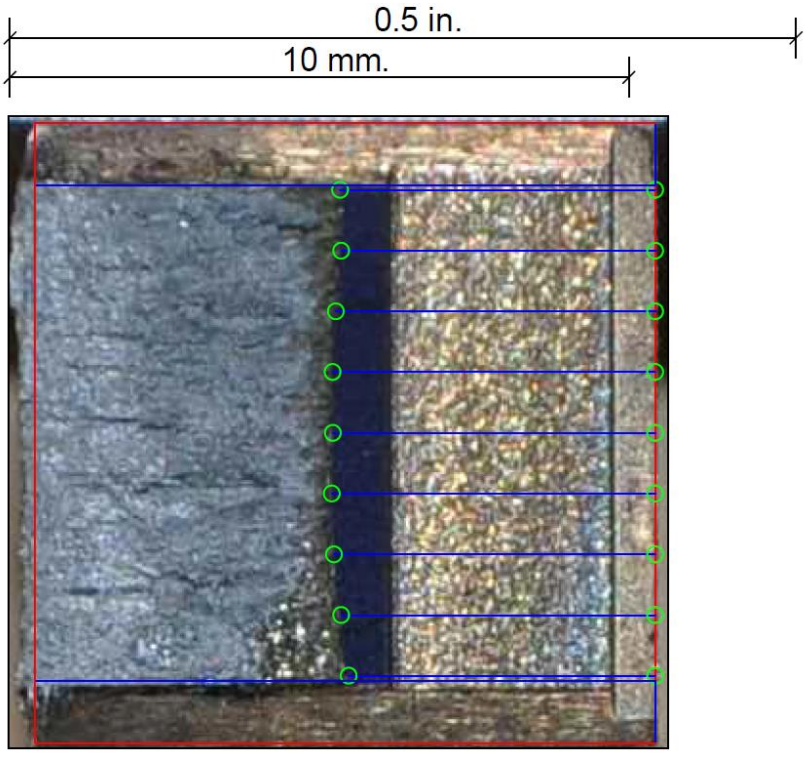

Figure M-140. Specimen M10' Fracture Surface

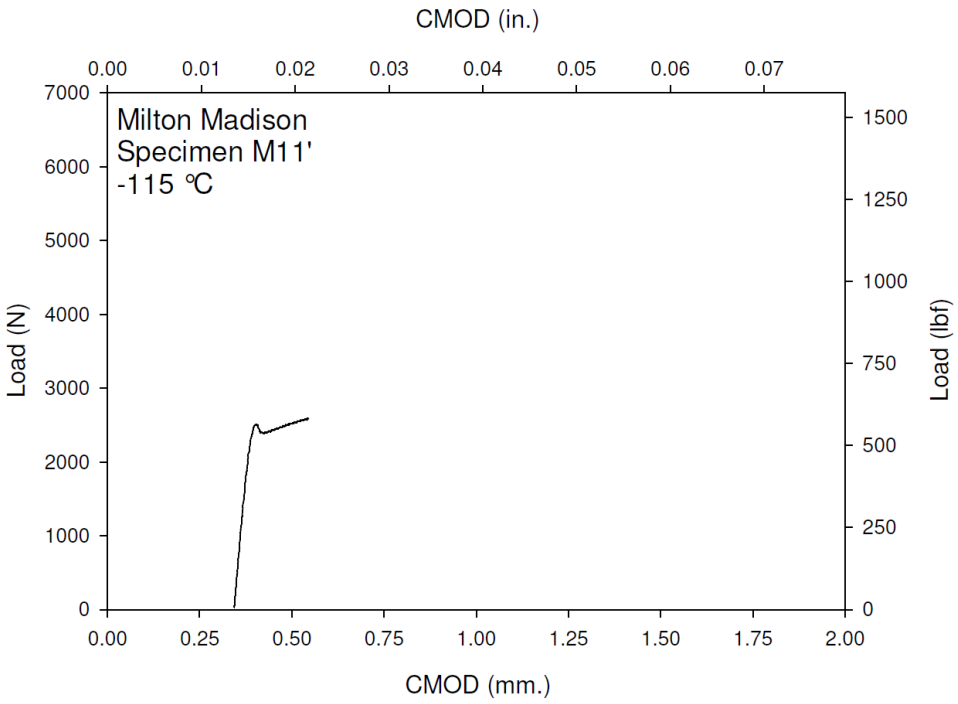

Figure M-141. Specimen M11' Test Record

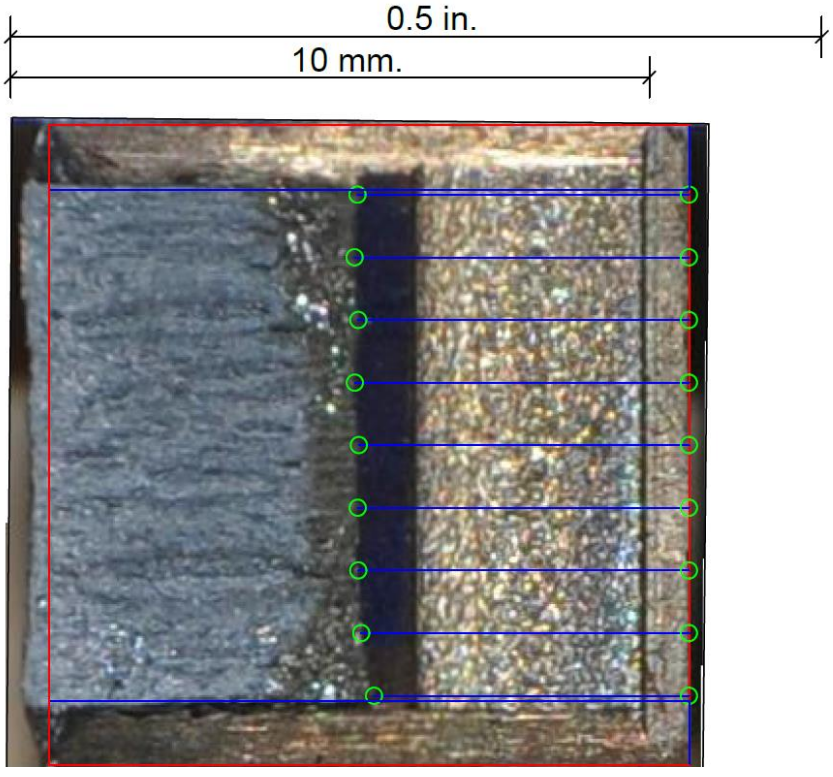

Figure M-142. Specimen M11' Fracture Surface

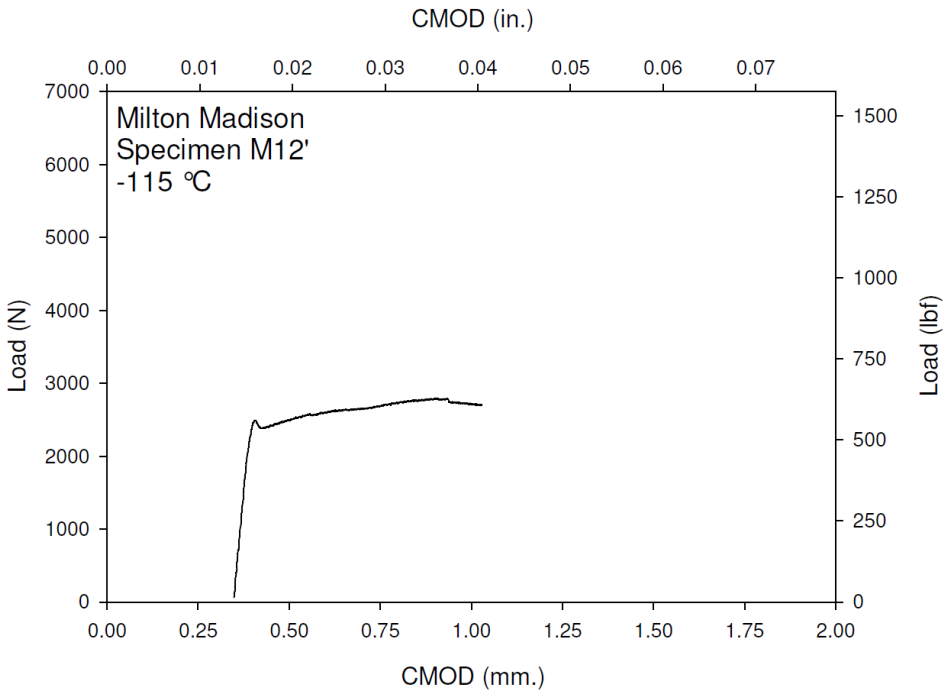

Figure M-143. Specimen M12' Test Record

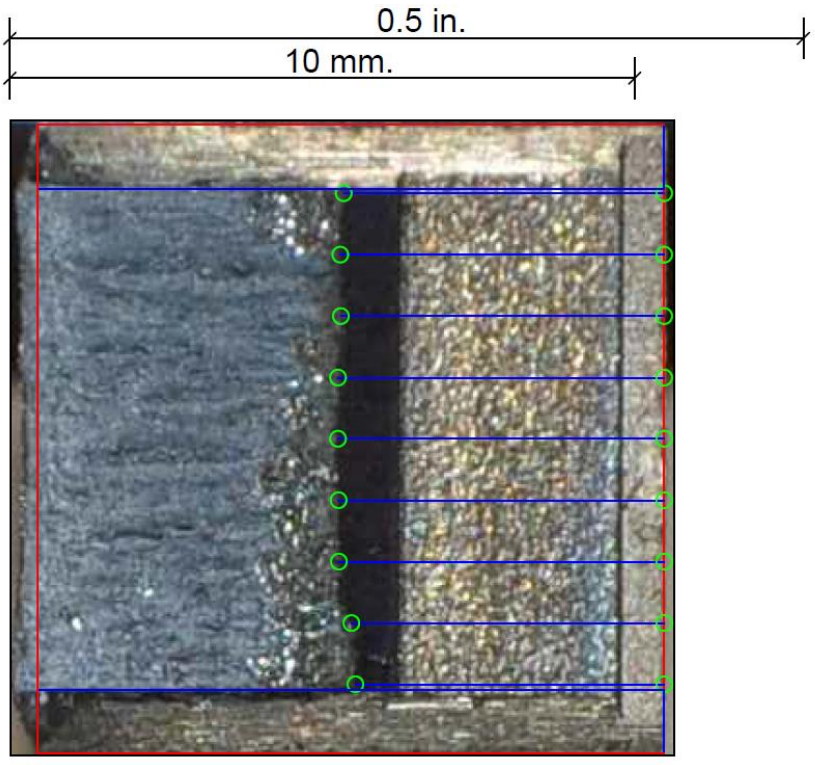

Figure M-144. Specimen M12' Fracture Surface

APPENDIX N: Tabulated Conventional Steel Fracture Toughness

Table N-1. Specimen Information for Plate R

Specimen ID	W		a_o		B		B_N	
	mm.	in.	mm.	in.	mm.	in.	mm.	in.
R1'	Specimen Used to Check Pre-Crack Procedure							
R4'	10.02	0.394	5.14	0.202	10.02	0.3945	8.00	0.3152
R5'	Specimen Damaged in Machining							
R6'	10.03	0.395	5.13	0.202	10.03	0.3949	8.00	0.3152
R7'	10.02	0.394	5.17	0.204	10.01	0.3941	8.00	0.3152
R8'	10.02	0.394	5.13	0.202	10.01	0.3941	8.00	0.3152
R9'	10.03	0.395	5.21	0.205	10.01	0.3941	8.00	0.3152
R10'	10.02	0.394	5.18	0.204	10.02	0.3945	8.00	0.3152
R11'	10.00	0.394	5.10	0.201	10.02	0.3945	8.00	0.3152
R13'	10.02	0.394	5.12	0.202	10.02	0.3945	8.00	0.3152
R14'	10.03	0.395	5.16	0.203	10.02	0.3945	8.00	0.3152
R15'	10.03	0.395	5.11	0.201	10.03	0.3949	8.00	0.3152
R16'	10.02	0.394	5.17	0.204	10.02	0.3945	8.00	0.3152
R17'	10.02	0.394	5.12	0.202	10.03	0.3949	8.00	0.3152

Table N-2. Test Information for Plate R

Specimen ID	Test Temperature		Test Result, K_{Jc}		Valid?	Censored?	1T K_{Jc}	
	°C	°F	MPa√m	ksi√in			MPa√m	ksi√in
R1'	Specimen Used to Check Pre-Crack Procedure							
R4'	-130	-202	202.2	184.0	Yes	Yes	112.8	102.6
R5'	Specimen Damaged in Machining							
R6'	-150	-238	145.2	132.1	Yes	No	119.2	108.5
R7'	-150	-238	206.2	187.6	Yes	Yes	118.7	108.1
R8'	-180	-292	195.0	177.5	Yes	Yes	132.6	120.7
R9'	-180	-292	186.1	169.4	Yes	Yes	131.7	119.9
R10'	-180	-292	131.4	119.6	Yes	No	108.3	98.5
R11'	-195	-319	56.0	51.0	Yes	No	48.5	44.2
R13'	-195	-319	30.6	27.8	Yes	No	28.4	25.8
R14'	-170	-274	108.0	98.3	Yes	No	89.7	81.7
R15'	-170	-274	62.5	56.9	Yes	No	53.7	48.9
R16'	-150	-238	214.1	194.8	Yes	Yes	118.8	108.1
R17'	-150	-238	65.4	59.5	Yes	No	56.0	51.0

Table N-3. Specimen Information for Plate B

Specimen ID	W		a_o		B		B_N	
	mm.	in.	mm.	in.	mm.	in.	mm.	in.
B3'	10.03	0.3949	5.16	0.203	10.03	0.3949	8.00	0.3152
B4'	10.01	0.3941	5.16	0.203	10.01	0.3941	8.00	0.3152
B5'	10.03	0.3949	5.14	0.202	10.00	0.3937	8.00	0.3152
B6'	10.00	0.3937	5.13	0.202	10.03	0.3949	8.00	0.3152
B7'	10.04	0.3953	5.16	0.203	10.04	0.3953	8.00	0.3152
B8'	10.03	0.3949	5.16	0.203	10.04	0.3953	8.00	0.3152
B9'	10.02	0.3945	5.17	0.204	10.01	0.3941	8.00	0.3152
B10'	10.03	0.3949	5.13	0.202	10.02	0.3945	8.00	0.3152
B11'	10.03	0.3949	5.19	0.204	10.03	0.3949	8.00	0.3152
B12'	10.03	0.3949	5.19	0.204	10.00	0.3937	8.00	0.3152
B13'	10.03	0.3949	5.14	0.202	10.02	0.3945	8.00	0.3152
B14'	10.03	0.3949	5.18	0.204	10.04	0.3953	8.00	0.3152
B15'	10.02	0.3945	5.12	0.202	10.02	0.3945	8.00	0.3152
B16'	10.02	0.3945	5.14	0.202	10.03	0.3949	8.00	0.3152
B17'	10.04	0.3953	5.19	0.204	10.00	0.3937	8.00	0.3152
B18'	10.02	0.3945	5.14	0.202	10.00	0.3937	8.00	0.3152

Table N-4. Test Information for Plate B

Specimen ID	Test Temperature		Test Result, K_{Jc}		Valid?	Censored?	1T K_{Jc}	
	°C	°F	MPa√m	ksi√in			MPa√m	ksi√in
B3'	-120	-184	236.2	214.9	Yes	Yes	104.8	95.4
B4'	-150	-238	86.4	78.6	Yes	No	72.6	66.1
B5'	-150	-238	123.8	112.7	Yes	No	102.2	93.0
B6'	-150	-238	133.4	121.4	Yes	No	109.9	100.0
B7'	-150	-238	99.3	90.4	No	No	82.9	75.4
B8'	-150	-238	125.3	114.0	Yes	No	103.5	94.2
B9'	-135	-211	207.0	188.4	Yes	Yes	108.9	99.1
B10'	-135	-211	210.3	191.4	Yes	Yes	109.4	99.6
B11'	-150	-238	35.5	32.3	Yes	No	32.3	29.4
B12'	-150	-238	147.2	134.0	Yes	Yes	113.8	103.6
B13'	-150	-238	48.9	44.5	Yes	No	42.9	39.0
B14'	-150	-238	105.3	95.8	Yes	No	87.6	79.7
B15'	-150	-238	44.4	40.4	Yes	No	39.3	35.8
B16'	-120	-184	117.0	106.5	Yes	No	96.9	88.2
B17'	-120	-184	88.0	80.1	Yes	No	73.9	67.2
B18'	-120	-184	133	120.8	Yes	Yes	104.9	95.4

Table N-5. Specimen Information for Plate 4

Specimen ID	W		a_o		B		B_N	
	mm.	in.	mm.	in.	mm.	in.	mm.	in.
4-1'	10.02	0.3945	5.15	0.203	10.02	0.3945	8.00	0.3152
4-2'	No Test- Clip Gage Malfunction							
4-3'	10.03	0.3949	5.12	0.202	10.03	0.3949	8.00	0.3152
4-4'	10.02	0.3945	5.16	0.203	10.01	0.3941	8.00	0.3152
4-5'	10.01	0.3941	5.21	0.205	10.00	0.3937	8.00	0.3152
4-6'	10.01	0.3941	5.12	0.202	10.02	0.3945	8.00	0.3152
4-7'	10.02	0.3945	5.17	0.204	10.03	0.3949	8.00	0.3152
4-8'	10.03	0.3949	5.21	0.205	10.00	0.3937	8.00	0.3152
4-9'	10.03	0.3949	5.14	0.202	10.04	0.3953	8.00	0.3152
4-10'	10.04	0.3953	5.18	0.204	10.01	0.3941	8.00	0.3152
4-11'	10.03	0.3949	5.15	0.203	10.01	0.3941	8.00	0.3152
4-12'	10.03	0.3949	5.12	0.202	10.03	0.3949	8.00	0.3152
4-13'	10.00	0.3937	5.13	0.202	10.02	0.3945	8.00	0.3152
4-14'	10.02	0.3945	5.16	0.203	10.03	0.3949	8.00	0.3152
4-15'	10.02	0.3945	5.14	0.202	10.02	0.3945	8.00	0.3152
4-16'	10.03	0.3949	5.17	0.204	10.02	0.3945	8.00	0.3152
4-17'	10.01	0.3941	5.12	0.202	10.03	0.3949	8.00	0.3152
4-18'	10.02	0.3945	5.13	0.202	10.02	0.3945	8.00	0.3152

Table N-6. Test Information for Plate 4

Specimen ID	Test Temperature		Test Result, K_{Jc}		Valid?	Censored?	1T K_{Jc}	
	°C	°F	MPa√m	ksi√in			MPa√m	ksi√in
4-1'	-40	-40	125.5	114.2	Yes	Yes	84.9	77.2
4-2'	No Test- Clip Gage Malfunction							
4-3'	-80	-112	71.1	64.7	Yes	No	60.5	55.1
4-4'	-80	-112	131.6	119.8	Yes	Yes	91.3	83.1
4-5'	-60	-76	166.5	151.5	Yes	Yes	87.3	79.4
4-6'	-60	-76	163.4	148.7	Yes	Yes	88.1	80.2
4-7'	-60	-76	147.0	133.8	Yes	Yes	87.8	79.9
4-8'	-40	-40	165.6	150.7	Yes	Yes	84.4	76.8
4-9'	-40	-40	236.6	215.3	Yes	Yes	85.1	77.4
4-10'	-80	-112	171.4	156.0	Yes	Yes	91.3	83.1
4-11'	-80	-112	115.5	105.1	Yes	Yes	91.5	83.3
4-12'	-18	0	174.8	159.1	Yes	Yes	82.3	74.9
4-13'	-80	-112	166.0	151.1	Yes	Yes	91.4	83.2
4-14'	-80	-112	131.7	119.8	Yes	Yes	91.4	83.1
4-15'	-80	-112	149.1	135.7	Yes	Yes	91.5	83.3
4-16'	-80	-112	163.5	148.8	Yes	Yes	91.3	83.1
4-17'	-80	-112	148.3	135.0	Yes	Yes	91.6	83.4
4-18'	-80	-112	129.6	117.9	No	Yes	91.6	83.4

Table N-7. Specimen Information for Plate P

Specimen ID	W		a_o		B		B_N	
	mm.	in.	mm.	in.	mm.	in.	mm.	in.
P1'	10.02	0.394	5.17	0.204	10.02	0.3945	8.00	0.3152
P2'	10.03	0.395	5.16	0.203	10.04	0.3953	8.00	0.3152
P3'	10.02	0.394	5.16	0.203	10.03	0.3949	8.00	0.3152
P4'	10.01	0.394	5.12	0.202	10.01	0.3941	8.00	0.3152
P5'	10.02	0.394	5.12	0.202	10.03	0.3949	8.00	0.3152
P6'	10.02	0.394	5.10	0.201	10.03	0.3949	8.00	0.3152
P7'	10.03	0.395	5.14	0.202	10.04	0.3953	8.00	0.3152
P8'	10.04	0.395	5.06	0.199	10.02	0.3945	8.00	0.3152
P9'	10.03	0.395	5.12	0.202	10.03	0.3949	8.00	0.3152
P10'	10.03	0.395	5.15	0.203	10.04	0.3945	8.00	0.3152
P11'	10.02	0.394	5.15	0.203	10.04	0.3953	8.00	0.3152
P12'	10.03	0.395	5.12	0.202	10.02	0.3945	8.00	0.3152
P13'	10.03	0.395	5.15	0.203	10.02	0.3945	8.00	0.3152
P14'	10.02	0.394	5.10	0.201	10.02	0.3945	8.00	0.3152
P15'	10.03	0.395	5.14	0.202	10.03	0.3949	8.00	0.3152
P16'	10.03	0.395	5.15	0.203	10.02	0.3945	8.00	0.3152
P17'	10.03	0.395	5.11	0.201	10.02	0.3945	8.00	0.3152
P18'	10.03	0.395	5.16	0.203	10.02	0.3945	8.00	0.3152

Table N-8. Test Information for Plate P

Specimen ID	Test Temperature		Test Result, K_{Jc}		Valid?	Censored?	1T K_{Jc}	
	°C	°F	MPa√m	ksi√in			MPa√m	ksi√in
P1'	-51	-60	150.2	136.7	Yes	Yes	78.8	71.7
P2'	-51	-60	168.7	153.5	Yes	Yes	78.9	71.8
P3'	-51	-60	149.1	135.7	Yes	Yes	78.8	71.7
P4'	-70	-94	246.2	224.0	Yes	Yes	82.5	75.0
P5'	-70	-94	85.2	77.5	Yes	No	71.7	65.2
P6'	-70	-94	113.8	103.6	Yes	Yes	82.7	75.3
P7'	-70	-94	102.8	93.5	Yes	Yes	82.5	75.1
P8'	-90	-130	125.1	113.8	Yes	Yes	87.4	79.5
P9'	-90	-130	167.2	152.2	Yes	Yes	86.8	79.0
P10'	-90	-130	139.0	126.5	Yes	Yes	86.6	78.8
P11'	-90	-130	167.6	152.5	Yes	Yes	86.5	78.7
P12'	-18	0	185.8	169.1	Yes	Yes	74.2	67.5
P13'	-100	-148	121.4	110.5	Yes	Yes	88.9	80.9
P14'	-100	-148	120.8	109.9	Yes	Yes	89.3	81.2
P15'	-100	-148	153.0	139.2	Yes	Yes	89.0	81.0
P16'	-100	-148	109.5	99.6	Yes	Yes	88.9	80.9
P17'	-100	-148	173.9	158.2	Yes	Yes	89.3	81.2
P18'	-100	-148	216.5	197.0	Yes	Yes	88.8	80.8

Table N-9. Specimen Information for Plate M

Specimen ID	W		a_o		B		B_N	
	mm.	in.	mm.	in.	mm.	in.	mm.	in.
M1'	No Test- Specimen Did Not Fracture							
M2'	No Test- Clip Gage Malfunction							
M4'	10.02	0.394	5.12	0.202	10.02	0.3945	8.00	0.3152
M5'	10.02	0.394	5.12	0.202	10.01	0.3941	8.00	0.3152
M6'	10.02	0.394	5.12	0.202	10.03	0.3949	8.00	0.3152
M7'	10.00	0.394	5.17	0.204	10.03	0.3949	8.00	0.3152
M8'	10.02	0.394	5.06	0.199	10.02	0.3945	8.00	0.3152
M9'	10.02	0.394	5.10	0.201	10.03	0.3949	8.00	0.3152
M10'	10.02	0.394	5.14	0.202	10.01	0.3941	8.00	0.3152
M11'	10.02	0.394	5.17	0.204	10.01	0.3941	8.00	0.3152
M12'	10.03	0.395	5.16	0.203	10.03	0.3949	8.00	0.3152

Table N-10. Test Information for Plate M

Specimen ID	Test Temperature		Test Result, K_{Jc}		Valid?	Censored?	1T K_{Jc}	
	°C	°F	MPa√m	ksi√in			MPa√m	ksi√in
M1'	No Test- Specimen Did Not Fracture							
M2'	No Test- Clip Gage Malfunction							
M4'	-80	-112	230.7	209.9	Yes	Yes	96.4	87.7
M5'	-100	-148	141.8	129.0	Yes	Yes	100.3	91.3
M6'	-100	-148	163.0	148.3	Yes	Yes	100.4	91.3
M7'	-130	-202	85.2	77.5	No	No	71.7	65.2
M8'	-130	-202	58.2	53.0	Yes	No	50.3	45.7
M9'	-130	-202	57.7	52.5	Yes	No	49.9	45.4
M10'	-100	-148	192.0	174.7	Yes	Yes	100.1	91.1
M11'	-115	-175	87.0	79.2	Yes	No	73.1	66.5
M12'	-115	-175	167.4	152.3	Yes	Yes	103.6	94.2

APPENDIX O: Conventional Steel Resistance Curves

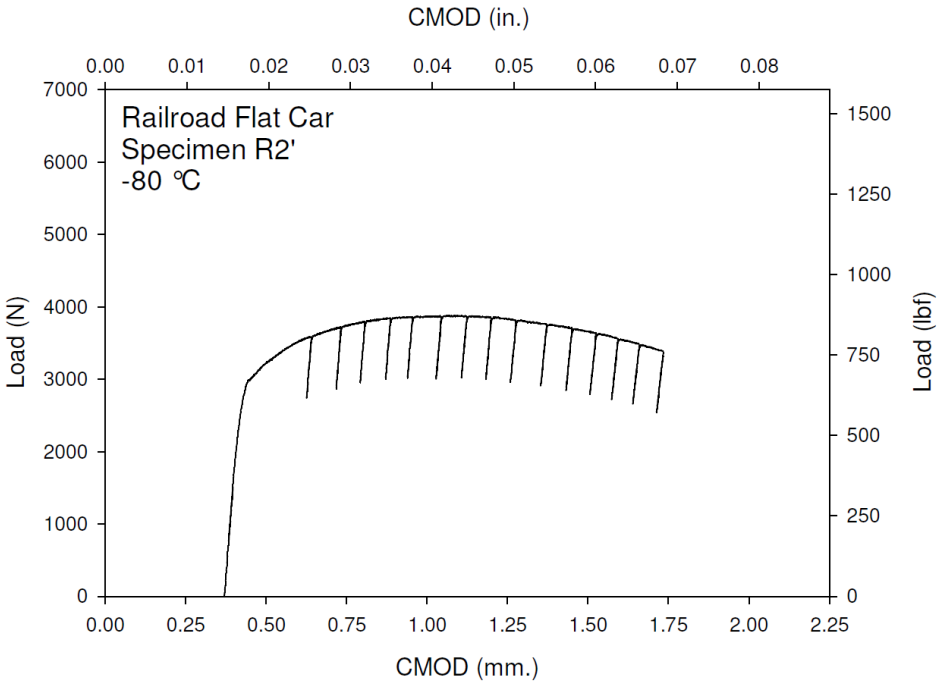

Figure O-1. Specimen R2' Test Record

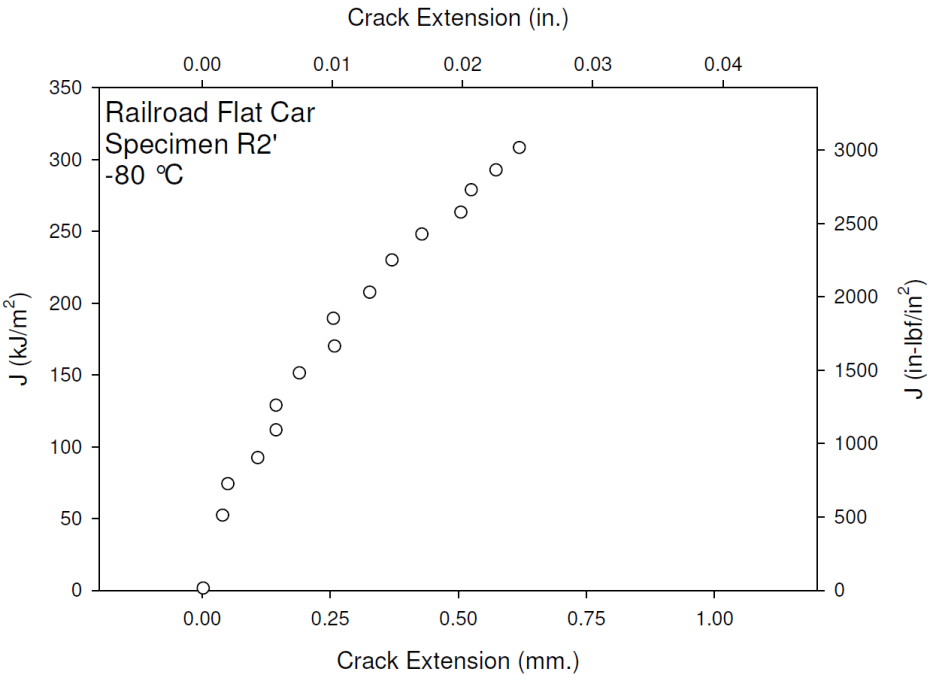

Figure O-2. Specimen R2' Resistance Curve

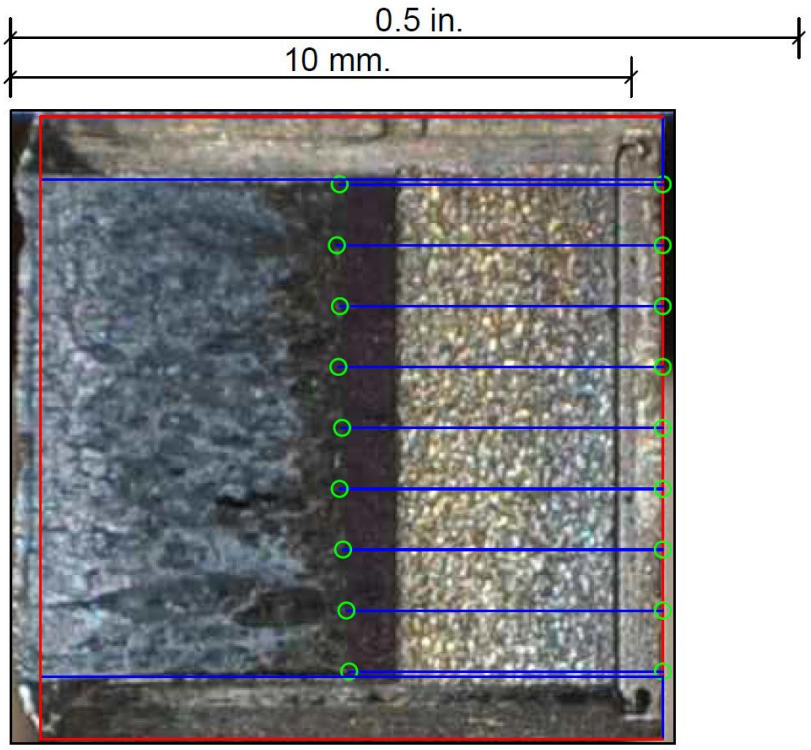

Figure O-3. Specimen R2' Fracture Surface

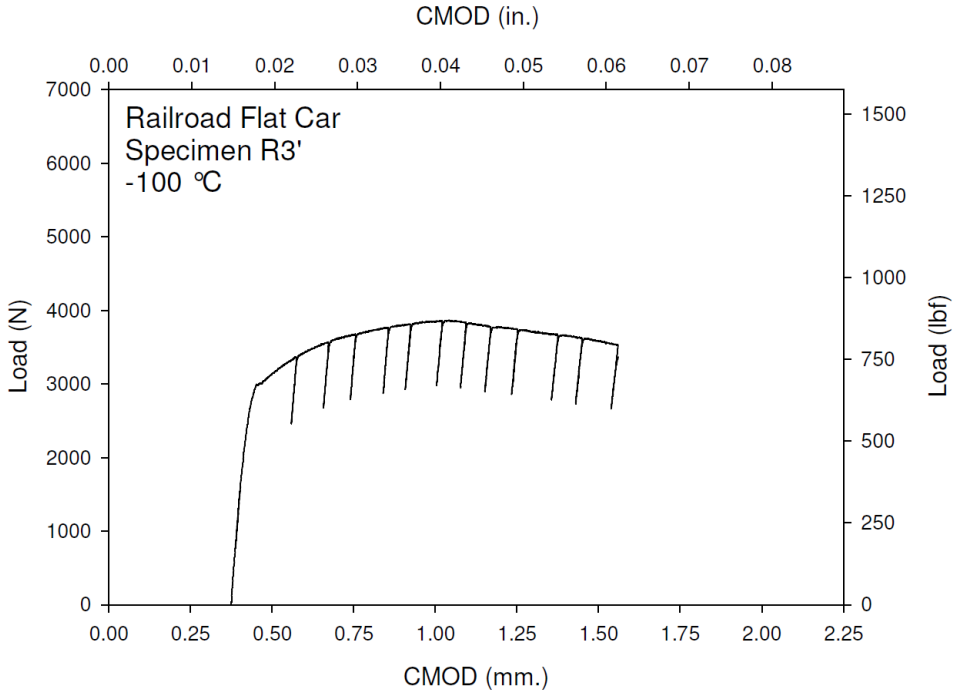

Figure O-4. Specimen R3' Test Record

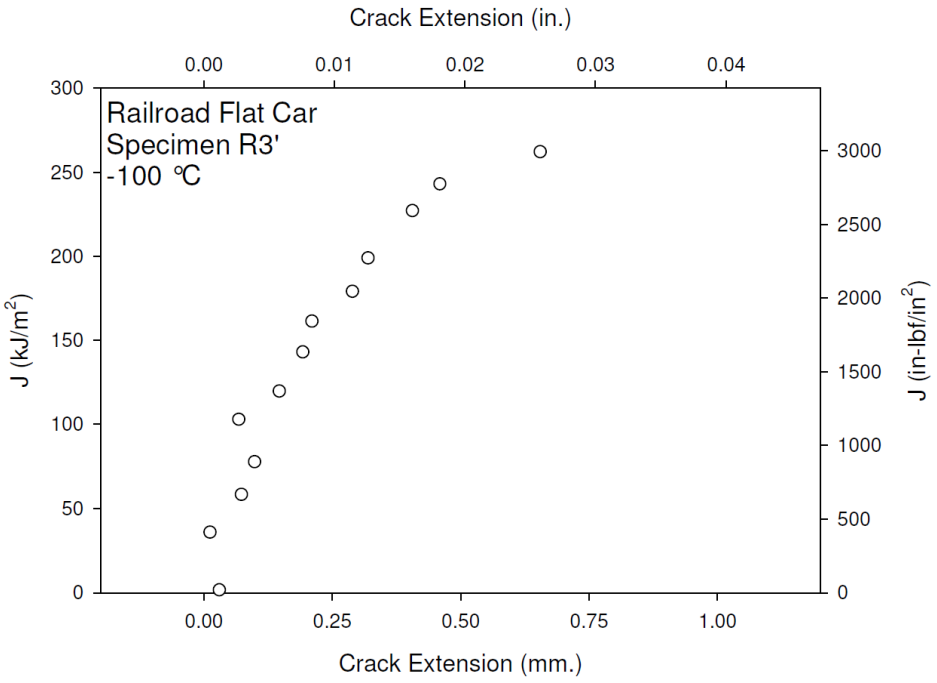

Figure O-5. Specimen R3' Resistance Curve

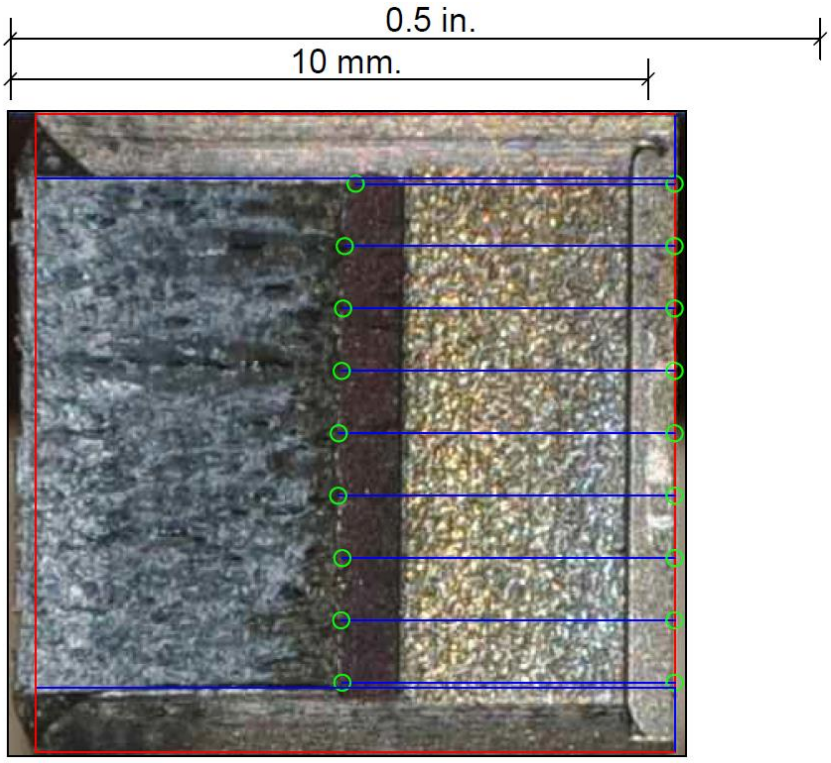

Figure O-6. Specimen R3' Fracture Surface

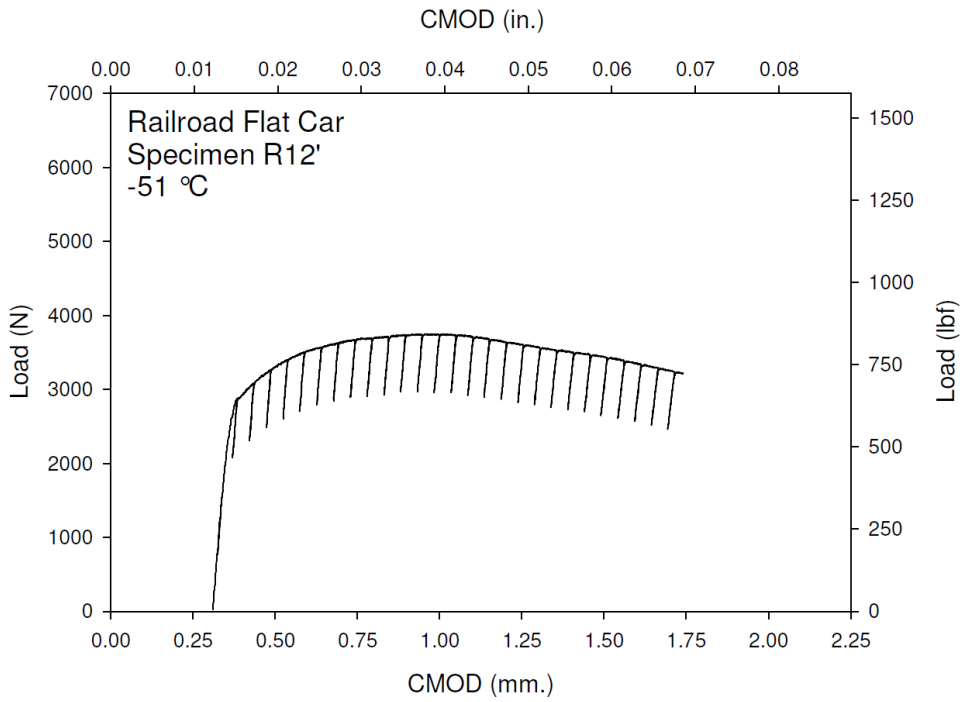

Figure O-7. Specimen R12' Test Record

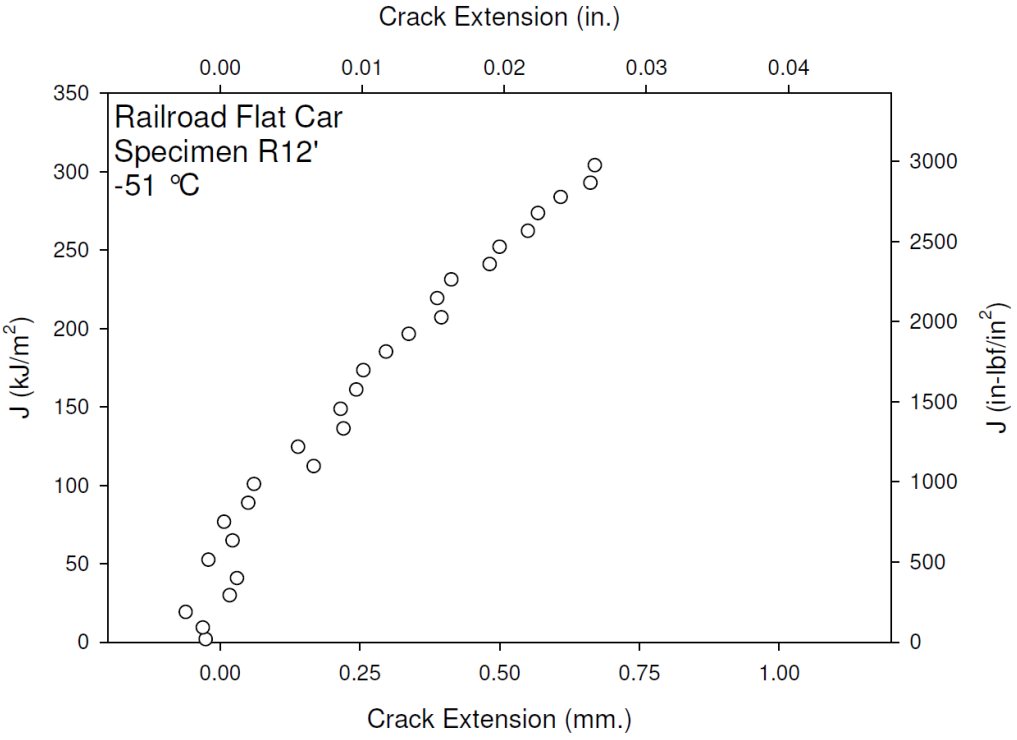

Figure O-8. Specimen R12' Resistance Curve

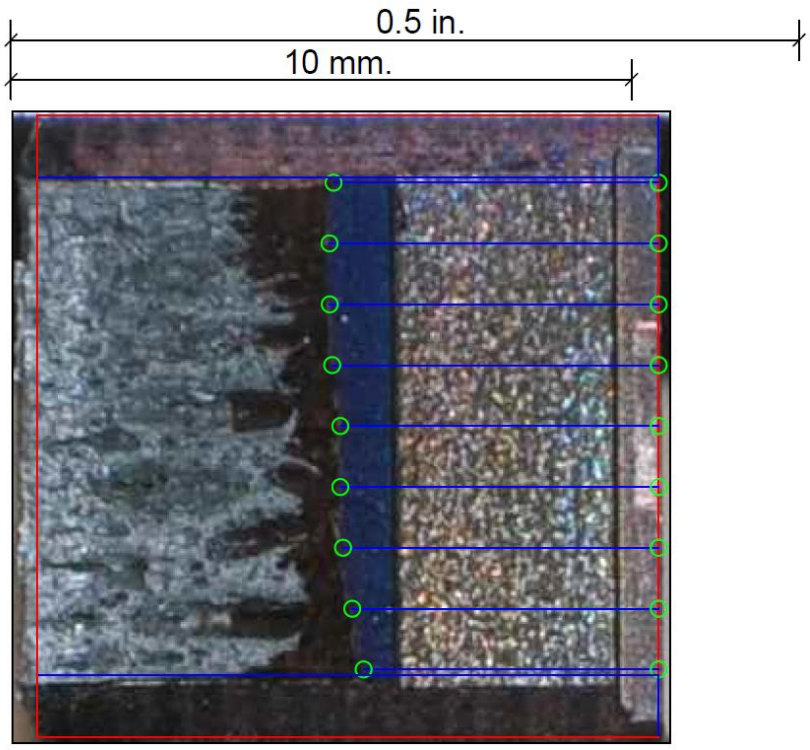

Figure O-9. Specimen R12' Fracture Surface

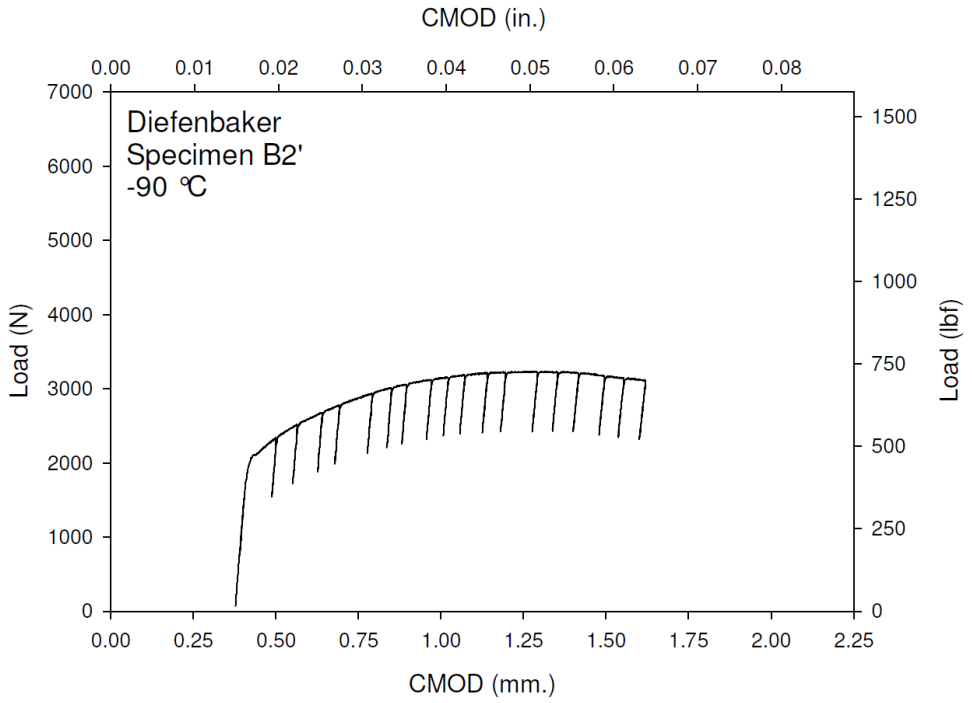

Figure O-10. Specimen B2' Test Record

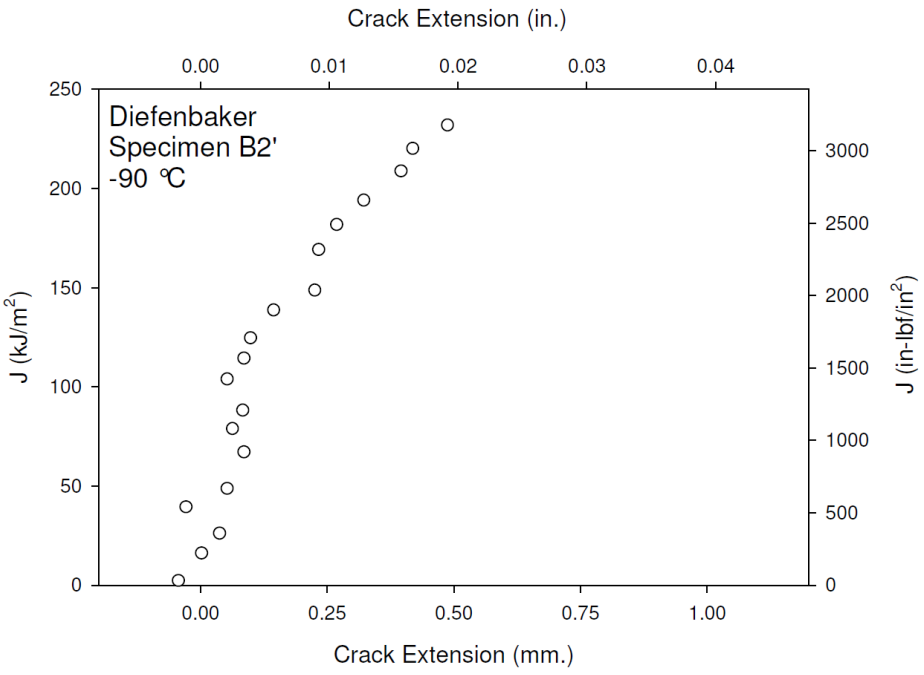

Figure O-11. Specimen B2' Resistance Curve

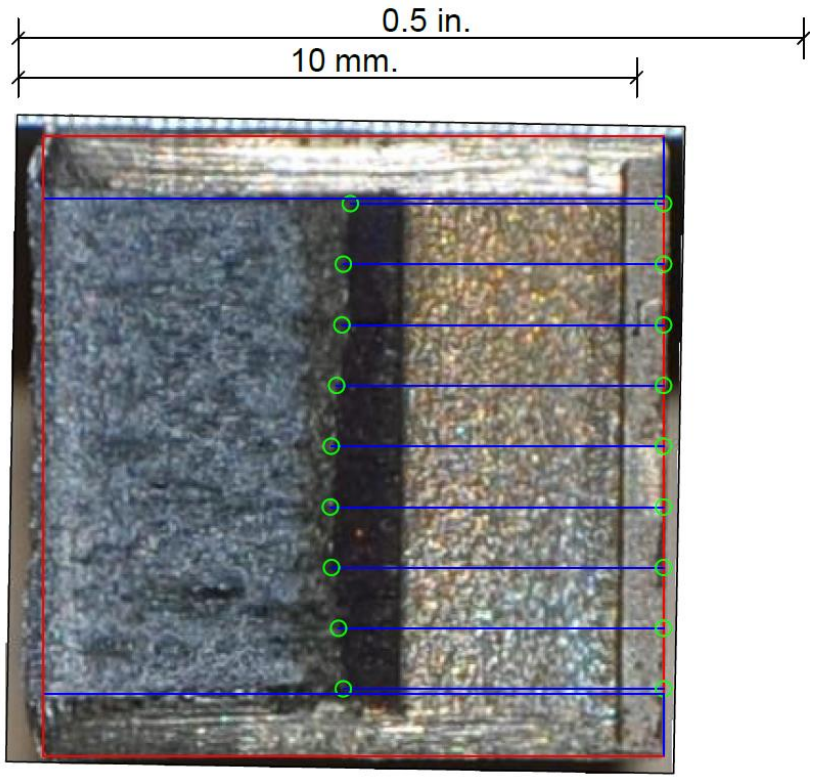

Figure O-12. Specimen B2' Fracture Surface

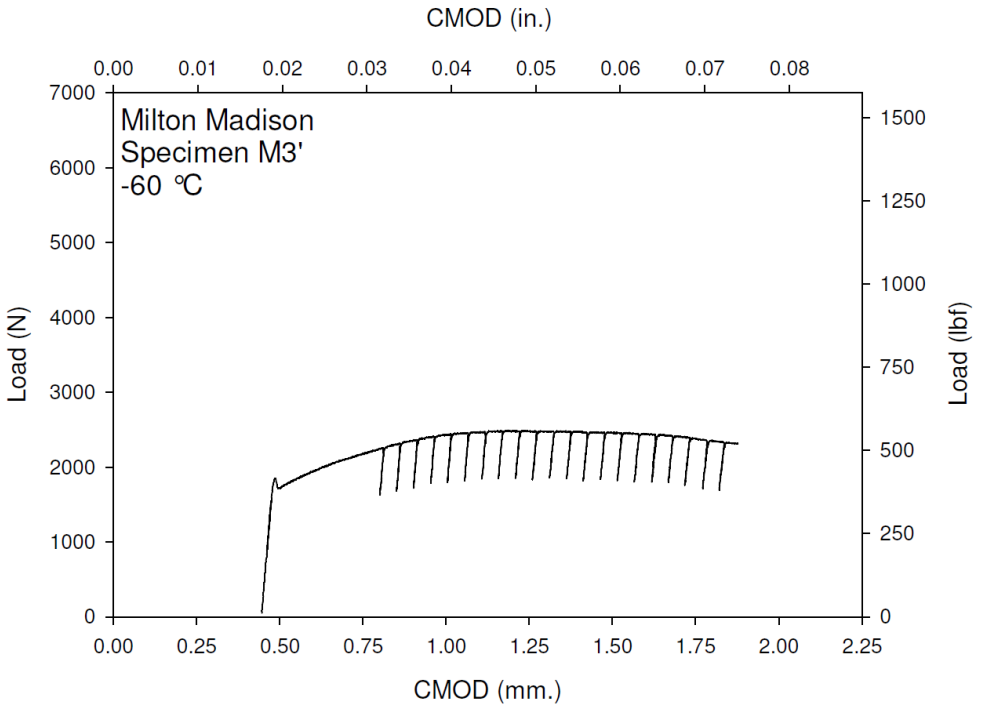

Figure O-13. Specimen M3' Test Record

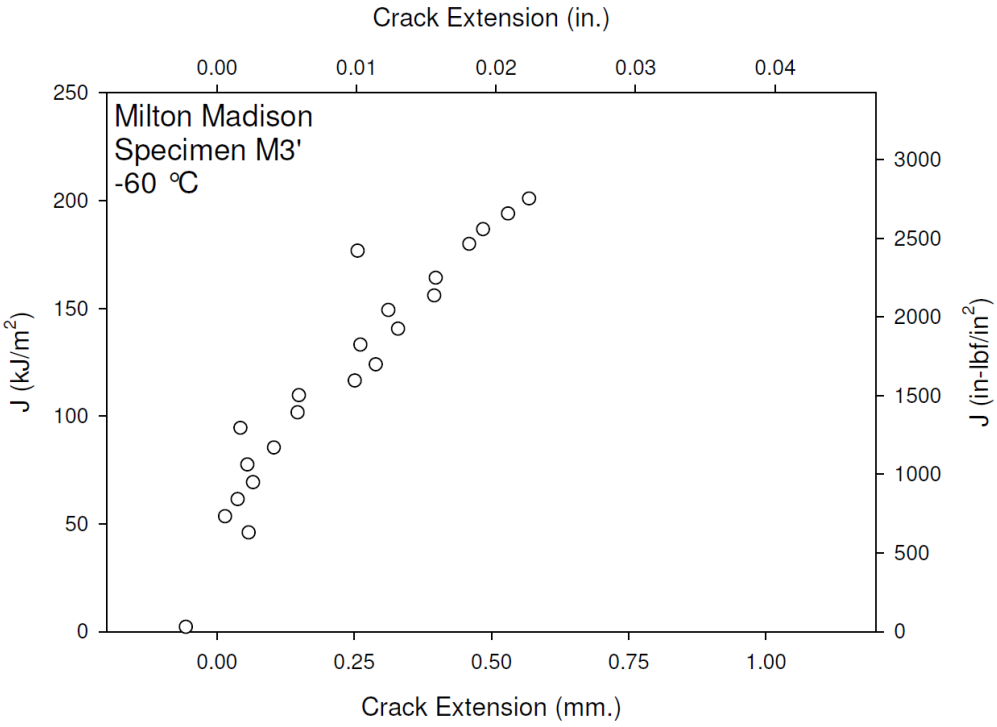

Figure O-14. Specimen M3' Resistance Curve

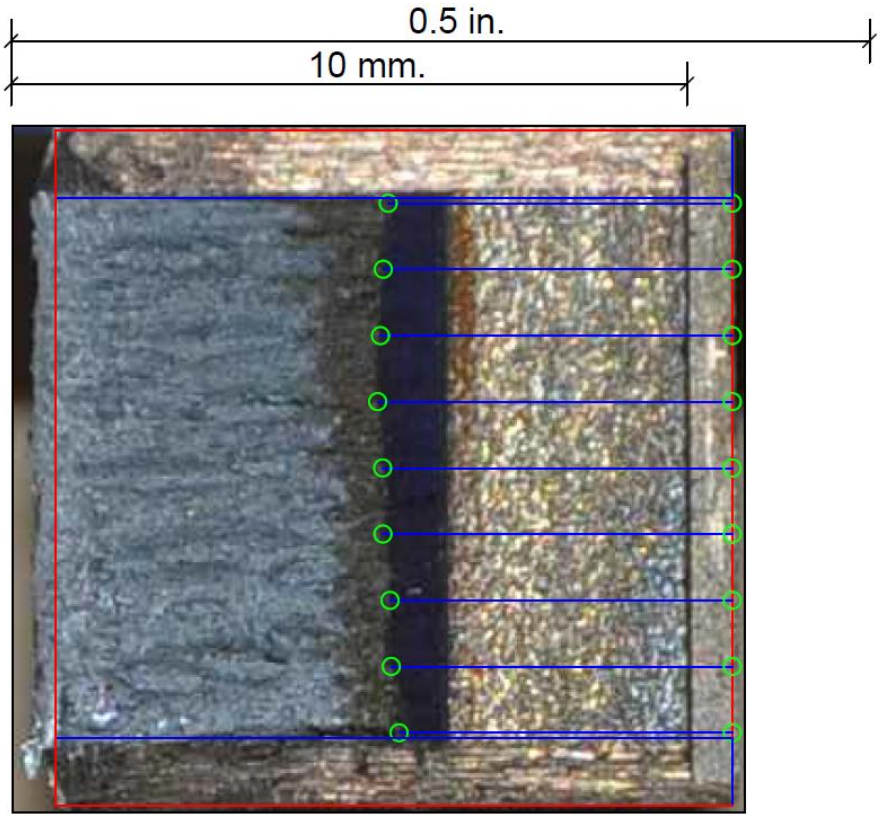

Figure O-15. Specimen M3' Fracture Surface